MODELING FOR PREDICTION OF RADIATION-INDUCED TOXICITY TO IMPROVE THERAPEUTIC RATIO IN THE MODERN RADIATION THERAPY ERA

EDITED BY: Ester Orlandi, Tiziana Rancati, Giuseppe Sanguineti, Claudio Fiorino and Riccardo Valdagni

PUBLISHED IN: Frontiers in Oncology

frontiers Research Topics

ISSN 1664-8714
ISBN 978-2-88971-088-1
DOI 10.3389/978-2-88971-088-1

About Frontiers

Frontiers is more than just an open-access publisher of scholarly articles: it is a pioneering approach to the world of academia, radically improving the way scholarly research is managed. The grand vision of Frontiers is a world where all people have an equal opportunity to seek, share and generate knowledge. Frontiers provides immediate and permanent online open access to all its publications, but this alone is not enough to realize our grand goals.

Frontiers Journal Series

The Frontiers Journal Series is a multi-tier and interdisciplinary set of open-access, online journals, promising a paradigm shift from the current review, selection and dissemination processes in academic publishing. All Frontiers journals are driven by researchers for researchers; therefore, they constitute a service to the scholarly community. At the same time, the Frontiers Journal Series operates on a revolutionary invention, the tiered publishing system, initially addressing specific communities of scholars, and gradually climbing up to broader public understanding, thus serving the interests of the lay society, too.

Dedication to Quality

Each Frontiers article is a landmark of the highest quality, thanks to genuinely collaborative interactions between authors and review editors, who include some of the world's best academicians. Research must be certified by peers before entering a stream of knowledge that may eventually reach the public - and shape society; therefore, Frontiers only applies the most rigorous and unbiased reviews.
Frontiers revolutionizes research publishing by freely delivering the most outstanding research, evaluated with no bias from both the academic and social point of view. By applying the most advanced information technologies, Frontiers is catapulting scholarly publishing into a new generation.

What are Frontiers Research Topics?

Frontiers Research Topics are very popular trademarks of the Frontiers Journals Series: they are collections of at least ten articles, all centered on a particular subject. With their unique mix of varied contributions from Original Research to Review Articles, Frontiers Research Topics unify the most influential researchers, the latest key findings and historical advances in a hot research area! Find out more on how to host your own Frontiers Research Topic or contribute to one as an author by contacting the Frontiers Editorial Office: frontiersin.org/about/contact

MODELING FOR PREDICTION OF RADIATION-INDUCED TOXICITY TO IMPROVE THERAPEUTIC RATIO IN THE MODERN RADIATION THERAPY ERA

Topic Editors:
Ester Orlandi, Istituto Nazionale dei Tumori (IRCCS), Italy
Tiziana Rancati, Istituto Nazionale dei Tumori (IRCCS), Italy
Giuseppe Sanguineti, Regina Elena National Cancer Institute (IRCCS), Italy
Claudio Fiorino, San Raffaele Hospital (IRCCS), Italy
Riccardo Valdagni, University of Milan, Italy

Citation: Orlandi, E., Rancati, T., Sanguineti, G., Fiorino, C., Valdagni, R., eds. (2021). Modeling for Prediction of Radiation-Induced Toxicity to Improve Therapeutic Ratio in the Modern Radiation Therapy Era. Lausanne: Frontiers Media SA. doi: 10.3389/978-2-88971-088-1

Table of Contents

frontiers in Oncology

EDITORIAL
published: 26 May 2021
doi: 10.3389/fonc.2021.690649

Editorial: Modeling for Prediction of Radiation-Induced Toxicity to Improve Therapeutic Ratio in the Modern Radiation Therapy Era

Tiziana Rancati[1]*, *Claudio Fiorino*[2], *Giuseppe Sanguineti*[3], *Riccardo Valdagni*[1,4,5] *and Ester Orlandi*[6]

[1] Prostate Cancer Program, Fondazione IRCCS Istituto Nazionale dei Tumori, Milan, Italy, [2] Unit of Medical Physics, San Raffaele Hospital, Milan, Italy, [3] Unit of Radiation Oncology, Regina Elena National Cancer Institute (IRCCS), Rome, Italy, [4] Department of Oncology and Hemato-Oncology, Università degli Studi di Milano, Milan, Italy, [5] Unit of Radiation Oncology 1, Fondazione IRCCS Istituto Nazionale dei Tumori, Milan, Italy, [6] Radiation Oncology Clinical Department, National Center for Oncological Hadrontherapy (CNAO), Pavia, Italy

Keywords: radiotherapy, toxicity, modeling, normal tissue complication probability, dose-response

Editorial on the Research Topic

Modeling for Prediction of Radiation-Induced Toxicity to Improve Therapeutic Ratio in the Modern Radiation Therapy Era

OPEN ACCESS

Edited and reviewed by:
Ira Ida Skvortsova, Innsbruck Medical University, Austria

***Correspondence:**
Tiziana Rancati
Tiziana.rancati@istitutotumori.mi.it

Specialty section:
This article was submitted to Radiation Oncology, a section of the journal Frontiers in Oncology

Received: *03 April 2021*
Accepted: *10 May 2021*
Published: *26 May 2021*

Citation:
Rancati T, Fiorino C, Sanguineti G, Valdagni R and Orlandi E (2021) Editorial: Modeling for Prediction of Radiation-Induced Toxicity to Improve Therapeutic Ratio in the Modern Radiation Therapy Era. Front. Oncol. 11:690649. doi: 10.3389/fonc.2021.690649

INTRODUCTION

Radiation therapy (RT) represents a mainstay of treatment for many cancer types, either as a single modality or within a multidisciplinary approach, including surgery and systemic therapy. From a general perspective, when planning a curative radiotherapy course, its potential benefits should be weighed against the risk of acute and late tissue/organ damage. In other words, the main goal of radiotherapy is to improve the clinical outcome by increasing the therapeutic ratio, i.e., the ratio between tumor control probability (TCP) and normal tissue complication probability (NTCP). Although modern radiotherapy techniques, such as Intensity Modulated RT (IMRT), often coupled with advanced in-room imaging (Image Guided RT, IGRT), Stereotactic Body RT (SBRT), particle RT, including proton ion and carbon ion RT, allow a better sparing of normal tissues due to their improved conformity and precision, radiation-induced toxicity is still a matter of concern. Indeed, dose tolerance of many healthy tissues, called organs at risk, is a little less than or equal to the dose needed to eradicate cancers.

It is acknowledged that the risk of some induced side effects during and after the course of curative radiotherapy may be related to radiation doses delivered to multiple organs at risk rather than to the dose received by a specific organ. Additionally, various patient-related factors, including comorbidities and genetic, genomic and biological/microenvironment features, may act as modifiers of the dose-response curve. Thus, predicting toxicity by analyzing the relationship among all determinants of radiation response of healthy tissues could improve the therapeutic ratio and the management of side effects.

The QUANTEC (Quantitative Analyses of Normal Tissue Effects in the Clinic) collaboration (1) presented a synthesis of data and models available in 2010. It derived recommendations based on what we knew at that moment. The document gave clear and exhaustive recommendations in the (few)

situations where consistent results were available. In the case of controversial results or still more of a lack of reliable information, the document critically discussed the controversial points, often suggesting urgent lines of research and giving clear warnings around the uncertainty of the proposed recommendations.

During the "post-QUANTEC" years, the field's progress has been relevant, confirming its vitality, with many research groups continuously contributing with ideas and new data. Besides, new challenges entered into the arena, substantially modifying the traditional aspects dealing with clinical dose-volume effects studies (2).

Among them, probably the most important is the shift from NTCP dose-based modelling to the broader field of more "comprehensive" predictive models. In the hypothetical case that two patients receive exactly the "same dose distribution", the risk of toxicity is always modulated by the single individual profile.

The fact that "dose is not enough" was clear from the early days of radiobiology. It is receiving constantly growing attention in the current "omics" era (3): the availability of individual information characterizing the patients and potentially influencing their reaction to radiation is more and more essential, especially in the era of image-guided IMRT in which organs are efficiently spared in most patients.

This implies the need to have access to data including individually assessed clinical, biological and genetic information and to face the issue of modeling the response of normal tissue to radiation in a more and more "phenomenological" approach (4), requiring robust methods for the selection of the most predictive variables (both dosimetric and non-dosimetric) and the adoption of advanced data mining/machine learning methods to manage large databases, including a large number of patients and lots of variables.

Treatment planning optimization is driven by the knowledge, often not exhaustive, of quantitative dose-volume effect relationships. NTCP models are also increasingly used in protocols of model-based selection of patients for proton therapy (5–7), impacting both the single patient treatment and National Health Systems (efficiency and costs). Therefore, every progress in this field has a vast and rapid impact on how patients are treated everywhere. This is an active field of research and practice, involving many radiation oncologists, medical physicists, biologists, and data scientists in a multiprofessional scenario.

TOPICS COVERED IN THIS RESEARCH TOPIC

This Research Topic includes Original Research Papers, Reviews, Mini Reviews and Perspective and Opinion articles focusing on:

- The state-of-the-art of modeling approaches and their contribution towards personalized cancer treatment;
- The improvements of knowledge on dose-volume relationships for different organs;
- The integration of clinical/genetic/genomic/biological/microenvironment/imaging features in prediction models;
- Pre-clinical research on radiation induced damage to normal tissues using animal models;
- Voxel-based approaches to analysis of radiation induced toxicity.

PAPERS INCLUDED IN THIS RESEARCH TOPIC

This Research Topic includes 30 original articles, 2 review, 1 mini-review and 1 perspective article.

The papers are from 160 authors and 18 countries on four continents. In particular, there are 19 works involving several centers and countries from one continent (10 from Europe, 6 from Asia, 2 from United States, and 1 from Australia) 9 international papers including countries both from Europe and other continents, and 6 papers from Italian centers. Authors' affiliations are equally distributed among academies and hospitals. These summary statistics mirror the broad interest in modeling radiation-induced toxicity, the highly multidisciplinary background of people involved in the field, and the vital relationship between academic and clinical research teams.

Four pre-clinical studies are presented: McKelvey et al. consider the interaction between immunotherapy and radiotherapy, Wang et al. studied the mitigation of side-effects by removing senescent cells, Li et al. present results in mice on aerosolized thyroid hormone in preventing lung fibrosis, and Zuppone et al. propose a review of pre-clinical research on bladder toxicity

Four manuscript focus on general/methodological issues: Barry et al. evaluate the propagation of uncertainties in biologically driven treatment planning systems, Thor et al. reinforce the value of registering study analysis plans and proposes some guidelines, Isaksoon et al. review machine learning methods applied to modeling of radiotherapy outcomes, while Desideri et al. propose a mini-review on available models including radiomics features in models.

Most papers (26/34) report original research on modeling toxicity outcomes in clinical cohorts. Cancer sites include brain tumors, head-and-neck and thoracic diseases (mainly breast cancer, lung and esophageal cancers), prostate cancer. Twenty-one out 26 papers focus on photon external beam radiotherapy. At the same time, one considers proton-therapy (Palma et al.), one carbon ions (Dale et al.), one brachytherapy (Panettieri et al.) and one radioligand therapy (Belli et al.). A last work considers modeling secondary malignancy in the frame of comparison of photons and protons radiotherapy (Konig et al.). This uneven distribution is associated with a more mature experience in toxicity modeling after external beam RT; simultaneously, it highlights recent interest from the environment of more modern therapies.

Thirteen out of 26 papers consider more established modeling methods, including clinical and dosimetric risk factors (Jasper et al.; Zhao et al.; Lee et al.; Dupic et al.; Scoccianti et al.; Palma et al.; Panettieri et al.; Bresolin et al.; Onjukka et al.; Dale et al.;

Belli et al.; Rattay et al.; Meng et al.). Some papers consider the inclusion of radiomics (Avanzo et al.; Du et al.), genetic information (Palumbo et al.; Massi et al.) and patient-specific biomarkers (Luo et al.; von Reibnitz et al.; Dulong et al.).

Evaluation of models including advanced dosimetric features beyond the dose-volume-histograms is presented in two papers: Heemsbergen et al. considering rectum dose maps and Marcello et al. conducting three-dimensional voxel-based analysis.

Interestingly four papers consider external validation of previously published models and or clinical/dosimetric/genetic features (Shi et al.; Panettieri et al.; Massi et al.; Rattay et al.), investigating when models can be generalized to populations other than the ones used for their training, how well this works and which cautious should be considered.

Two papers put the use of models in the perspective of modern radiotherapy: Bijman et al. consider automated radiotherapy planning to explore at the single-patient level the trade-off between tumor coverage and predicted toxicity; Lafond et al. investigate the feasibility and the added value of planning which considers specific organ sub-regions while preserving the dose to the target for prostate radiotherapy.

CONCLUSIONS

The QUANTEC papers were published as a special issue of the Red Journal in March 2010 and became hugely successful with copies of QUANTEC dose constraints tables hanging in most dose-planning office spaces and hundreds to a thousand citations each of the published papers. However, as we passed the tenth anniversary of QUANTEC, there is a need for a renewed coordinated effort to take the use of mathematical bioeffect models for decision support and treatment plan comparison in radiation oncology to the next level for a range of reasons, including: (i) understanding that patient related risk factors may substantially impact organ tolerance, (ii) documented problems with external validation of dose-response models, (iii) more complicated associations of dose distribution to toxicity than a single dose-volume metric in a well-defined tissue structure, (iv) normal tissue effect models are being proposed for comparing competing high-cost treatment options (e.g. hadrons *vs.* photons).

The 34 papers published in this Research Topic constitute a vital contribution to the field. New interesting results are included, new topics and challenges are approached. The Research Topic witnesses the broad involvement of multidisciplinary teams towards a better understanding of the complex relationships between dose and biological response of healthy tissues, with the final aim of reaching improved optimization and personalization of radiotherapy treatments.

AUTHOR CONTRIBUTIONS

All authors listed have made a substantial, direct and intellectual contribution to the work, and approved it for publication.

REFERENCES

1. Bentzen SM, Constine LS, Deasy JO, Eisbruch A, Jackson A, Marks LB, et al. Quantitative Analyses of Normal Tissue Effects in the Clinic (QUANTEC): An Introduction to the Scientific Issues. *Int J Radiat Oncol Biol Phys* (2010) 76(3 Suppl):S3–9. doi: 10.1016/j.ijrobp.2009.09.040
2. Rancati T, Fiorino C. *Modelling Radiotherapy Side Effects: Practical Applications for Planning Optimization*. Boca Raton, FL: CRC press, Taylor and Francis group (2019). Available at: https://www.crcpress.com/Modelling-Radiotherapy-Side-Effects-Practical-Applications-for-Planning/Rancati-Fiorino/p/book/9781138198098.
3. Bentzen SM. Preventing or Reducing Late Side Effects of Radiation Therapy: Rraqdiobiology Meets Molecular Pathology. *Nat Rev Cancer* (2006) 6:702–13. doi: 10.1038/nrc1950
4. van der Schaaf A, Langendijk JA, Fiorino C, Rancati T. Embracing Phenomenological Approaches to Normal Tissue Complication Probability Modeling: A Question of Method. *Int J Radiat Oncol Biol Phys* (2015) 91 (3):468–71. doi: 10.1016/j.ijrobp.2014.10.017
5. Chaikh A, Calugaru V, Bondiau PY, Thariat J, Balosso J. Impact of the NTCP Modeling on Medical Decision to Select Eligible Patient for Proton Therapy: The Usefulness of EUD as an Indicator to Rank Modern Photon vs Proton Treatment Plans. *Int J Radiat Biol* (2018) 94(9):789–97. doi: 10.1080/09553002.2018.1486516
6. Hansen CR, Friborg J, Jensen K, Samsøe E, Johnsen L, Zukauskaite R, et al. NTCP Model Validation Method for DAHANCA Patient Selection of Protons Versus Photons in Head and Neck Cancer Radiotherapy. *Acta Oncol* (2019) 58 (10):1410–5. doi: 10.1080/0284186X.2019.1654129
7. Tambas M, Steenbakkers RJHM, van der Laan HP, Wolters AM, Kierkels RGJ, Scandurra D, et al. First Experience With Model-Based Selection of Head and Neck Cancer Patients for Proton Therapy. *Radiother Oncol* (2020) 151:206–13. doi: 10.1016/j.radonc.2020.07.056

Conflict of Interest: The authors declare that the research was conducted in the absence of any commercial or financial relationships that could be construed as a potential conflict of interest.

frontiers in Oncology

ORIGINAL RESEARCH
published: 01 October 2019
doi: 10.3389/fonc.2019.00991

Evaluation of the Hippocampal Normal Tissue Complication Model in a Prospective Cohort of Low Grade Glioma Patients—An Analysis Within the EORTC 22033 Clinical Trial

Jaap Jaspers[1], Alejandra Mèndez Romero[1], Mischa S. Hoogeman[1], Martin van den Bent[2], Ruud G. J. Wiggenraad[3], Martin J. B. Taphoorn[4], Danielle B. P. Eekers[5], Frank J. Lagerwaard[6], Anna Maria Lucas Calduch[7], Brigitta G. Baumert[8†] and Martin Klein[9†]*

[1] Department of Radiation Oncology, Erasmus Medical Center Cancer Institute, Rotterdam, Netherlands, [2] Department of Neurology, Erasmus Medical Center, Rotterdam, Netherlands, [3] Department of Radiation Oncology, Haaglanden Medical Center, Leidschendam, Netherlands, [4] Department of Neurology, Haaglanden Medical Center, The Hague, Netherlands, [5] Department of Radiotherapy, School for Oncology and Developmental Biology, Maastricht University, Maastricht, Netherlands, [6] Department of Radiation Oncology, Medical Center, VU University Amsterdam, Amsterdam, Netherlands, [7] Department of Radiation Oncology, Catalan Institute of Oncology, Barcelona, Spain, [8] Department of Radiation Oncology, University Hospital Bonn, Bonn, Germany, [9] Department of Medical Psychology, University Medical Center Amsterdam, Amsterdam, Netherlands

OPEN ACCESS

Edited by:
Tiziana Rancati, National Tumor Institute, Italy

Reviewed by:
Vivek Verma, Allegheny General Hospital, United States
Wenyin Shi, Thomas Jefferson University, United States

***Correspondence:**
Jaap Jaspers
j.jaspers@erasmusmc.nl

† These authors have contributed equally to this work

Specialty section:
This article was submitted to Radiation Oncology, a section of the journal Frontiers in Oncology

Received: *20 June 2019*
Accepted: *16 September 2019*
Published: *01 October 2019*

Citation:
Jaspers J, Mèndez Romero A, Hoogeman MS, van den Bent M, Wiggenraad RGJ, Taphoorn MJB, Eekers DBP, Lagerwaard FJ, Lucas Calduch AM, Baumert BG and Klein M (2019) Evaluation of the Hippocampal Normal Tissue Complication Model in a Prospective Cohort of Low Grade Glioma Patients—An Analysis Within the EORTC 22033 Clinical Trial. Front. Oncol. 9:991. doi: 10.3389/fonc.2019.00991

Purpose: To evaluate the performance of the hippocampal normal tissue complication model that relates dose to the bilateral hippocampus to memory impairment at 18 months post-treatment in a population of low-grade glioma (LGG) patients.

Methods: LGG patients treated within the radiotherapy-only arm of the EORTC 22033-26033 trial were analyzed. Hippocampal dose parameters were calculated from the original radiotherapy plans. Difference in Rey Verbal Auditory Learning test delayed recall (AVLT-DR) performance pre-and 18 (±4) months post-treatment was compared to reference data from the Maastricht Aging study. The NTCP model published by Gondi et al. was applied to the dosimetric data and model predictions were compared to actual neurocognitive outcome.

Results: A total of 29 patients met inclusion criteria. Mean dose in EQD2 Gy to the bilateral hippocampus was 39.8 Gy (95% CI 34.3–44.4 Gy), the median dose to 40% of the bilateral hippocampus was 47.2 EQD2 Gy. The model predicted a risk of memory impairment exceeding 99% in 22 patients. However, only seven patients were found to have a significant decline in AVLT-dr score.

Conclusions: In this dataset of only LGG patients treated with radiotherapy the hippocampus NTCP model did not perform as expected to predict cognitive decline based on dose to 40% of the bilateral hippocampus. Caution should be taken when extrapolating this model outside of the range of dose-volume parameters in which it was developed.

Keywords: NTCP (normal tissue complication probability) model, low grade glioma (LGG), model verification and validation, neurocognition, memory, late effect of cancer treatment, radiotherapy—adverse effects

INTRODUCTION

Low grade glioma (LGG) are a group of relatively slow growing primary brain neoplasms, mainly occurring in those between 30 and 50 years of age (1, 2). Modern treatment for LGG patients comprises surgery followed by radiotherapy and adjuvant chemotherapy (3). Overall survival was recently reported to be 13.3 years (4), but can vary with molecular subtype.

With many LGG patients living for many years or even decades after treatment, the late adverse effects of treatment on quality of life and neurocognitive functioning are of increasing importance. Although both the tumor itself, as well as the use of anticonvulsant therapy, have a deleterious effect on neurocognitive function (5, 6), radiotherapy (RT) in particular has been associated with a negative impact on neurocognitive function. This late effect of radiotherapy was found in several series with a longer follow-up (7, 8), however, it was not found in several studies that limited observation to the first 5 years (9–12).

A dose response relationship with decreasing neurocognitive performance (specifically memory) has been attributed to the hippocampal area (13). A NTCP model for memory impairment was proposed by Gondi et al. (14). In this study, 18 patients undergoing fractionated stereotactic radiotherapy for benign and low-grade tumors (9 vestibular schwannomas, 2 pituitary adenomas, 3 meningiomas, and 4 low grade gliomas) completed a comprehensive baseline neurocognitive assessment and a repeat assessment at 18 months. A control group of 6 non-irradiated subjects was tested as well, allowing for the use of Z scores for performance change. Dose in excess of 7.3 EQD2 Gy to 40% of bilateral hippocampus were found to be significantly correlated to a decrease in Wechsler Memory Scale III–Word Lists delayed recall score, a test that measures verbal memory performance.

Although this model is routinely used in the clinic, its performance has not yet been quantified in the setting of partial brain irradiation in a population of LGG patients. We analyzed data from a recently completed and published randomized phase III trial, where LGG patients in the control arm were treated exclusively with focal radiotherapy up to 50.4 Gy (15) and compared the predicted risk of neuropsychological impairment with the actual outcome.

MATERIALS AND METHODS

Patient Population

Data was acquired within the EORTC 22033-26033 (NCT00182819) trial, which is a prospective, randomized, open-label, phase 3 Intergroup study (European Organisation for Research and Treatment of Cancer [EORTC] Radiotherapy and Brain Tumor Groups, National Cancer Institute of Canada [NCIC] Clinical Trials Group, Trans Tasman Radiation Oncology Group [TROG], Medical Research Council [MRC] Clinical Trials Unit). The study was approved by the institutional review boards and ethics committees of all participating centers. All patients provided written informed consent at the time of registration (15).

In the aforementioned trial, patients of 18 years of age or older with histologically confirmed and centrally reviewed low-grade (WHO 2) glioma (diffuse astrocytoma, oligoastrocytoma and oligodendroglioma, WHO classification 2006) with at least one high-risk feature (age >40 years, progressive disease, tumor size >5 cm, tumor crossing midline, any focal neurological deficit) were randomly assigned to treatment with either radiotherapy (28 × 1.8 Gy) or temozolomide chemotherapy. Between September 2005 and March 2010 477 patients were randomized. The study design, treatment details and the results of the primary analysis have been described elsewhere (15). A total of 103 patients from preselected medical centers also underwent a detailed neurocognitive examination consisting of the Rey Auditory Verbal Learning test (AVLT), Concept Shifting test, Categoric Word Fluency test, and the Digit-Symbol Substitution test. Neurocognitive tests were conducted at randomization and then every 6 months until to tumor progression or death.

The analysis presented herein contains patients with retrievable radiotherapy planning data and neuropsychological testing at both baseline and 18 (±4 months). The neurocognitive analysis for the entire patient population of EORTC 22033-26033 is reported elsewhere (16). The present study was conducted according to the principles of the Declaration of Helsinki (59th WMA General Assembly, Seoul, October 2008) and in accordance with the local medical research regulations. The study protocol has been presented to the local Medical Ethics Committee (MEC-2017-321). No ethical approval was deemed necessary and the requirement for additional informed consent was waived.

Neuropsychological Assessments

One of the tests in the neuropsychological assessment is the AVLT, which calls for various aspects of learning and recall. The delayed recall condition (AVLT-dr) requires patients to memorize a list of 15 words for five consecutive tests, and to recall these 15 words after 20 min. The maximal score is 15 out of 15. This test is conceptually identical to the delayed recall condition in the Wechsler Memory Scale 3—word lists used by Gondi et al. as the primary outcome measure.

In contrast to the original paper by Gondi et al., EORTC22033-26033 does not include a control group of healthy volunteers. Normal data for AVLT-dr, with test-retest changes, has been published by the Maastricht Aging Study group (17). This study tested healthy volunteers using several neuropsychological tests at 2.5 year intervals and gives parameters for a regression-based change analysis of test-retest performance. The following relationship between age and change in AVLT-dr retest score was found.

$$E = 1.025 - 0.035 * (age - 62.5) \quad (1)$$

Where E is the expected change between test and retest-score. This can be converted to a Z score using the standardized residual (which was found to be 2.362 in this test condition).

$$Z = \frac{O - E}{2.362} \quad (2)$$

Where O is the observed retest score, and E is the predicted retest score. As reported in the paper by Gondi et al., a neurocognitive

event was defined as a reduction in AVLT-dr score at 18 months corresponding to a Z score lower than −1.5.

Radiotherapy Treatment

Patients were treated with photon radiotherapy using 3D conformal radiotherapy (3DCT), fractionated stereotactic radiotherapy (FSRT) or intensity modulated radiotherapy (IMRT) techniques depending on the availability at the institution. Gross tumor volume (GTV) was defined by the region of high signal intensity on T2 weighted MRI of FLAIR sequences, or, in case of prior surgery, the resection cavity and the residual tumor. Clinical target volume (CTV) margin was 10–15 mm. Planning target volume (PTV) margin was 7 mm for all patients. As required per protocol the contralateral hemisphere was spared, but no specific attempt at sparing one or both hippocampi was made.

Delineation and DVH Analysis

A rigid registration was applied between the planning CT and MRI using MIMSoftware (Cleveland, OH, USA). Hippocampus delineation followed the instructions of the publicly available atlas from RTOG0933 (18). In case no registration was possible, delineation was performed on CT using anatomical landmarks visible on MRI. Dose volume histograms (DVH) and subsequent DVH parameters were generated for left and right hippocampus individually and for composite bilateral hippocampi. As presented in the paper by Gondi et al., we assumed an α/β value of 2 to convert physical dose to biologically equivalent dose in 2 Gy fractions (EQD2 Gy). The Dx% of bilateral hippocampus was defined as the dose in EQD2 Gy received by x % of bilateral hippocampal volume.

Statistical Approach

Descriptive statistics were generated for age, tumor laterality, tumor lobe, anti-epileptic drug treatment (AED), education, CTV volume, and hippocampal dosimetry (**Table 1**). The model used by Gondi et al. is based on the Lyman model (19). Their formulation was presented as follows:

$$P_{NTCP} = \frac{1}{\sqrt{2\pi}} \int_{-\infty}^{t} e^{\frac{-u^2}{2}} du \tag{3}$$

Where t is a function of TD_{50}, the dose to 40% of hippocampus at which the probability of neurocognitive decline is 50%, and m, is a slope parameter (see below).

$$t = \frac{D - TD_{50}}{m\ TD_{50}} \tag{4}$$

In the paper published by Gondi et al., the obtained values of TD_{50} and m were 14.88 and 0.54, respectively. We applied this model to generate predicted NTCP values for the dose distributions in our study population. Cases were grouped in three bins of equal size, according to ascending NTCP. In order to compute the observed risk the incidence of a neuropsychological event in each bin is computed. The predicted NTCP was plotted against observed NTCP in a calibration plot. Next, a linear regression was performed. The regression coefficients can be used to calibrate the model to the dataset, the constant can be used as offset parameter and the slope indicates over- or underestimation of the observed risk.

In order to quantify model performance, the Brier score (*BS*) was calculated for the original formulation of the model. *BS* is a measure of the accuracy of a prediction with a binary outcome:

$$BS = \frac{1}{n} \sum_{a=1}^{n} (f_a - o_a)^2 \tag{5}$$

Where n is the number of observations, f_a is the probability that was forecast, and o_a is the outcome (1 if the event occurs and 0 if it does not occur). A low Brier score is indicative of good model performance, it reflects a strong correlation between forecast and outcome.

TABLE 1 | Patient characteristics.

Age (years)	**43.0**	**(95% CI 27.8–69.4)**	
Sex	Male	18	62.1%
	Female	11	37.9%
Handedness	Right	24	82.8%
	Left	5	17.2%
Years of education	13.8	(95% CI 12.0–14.4)	
Hemisphere	Right	10	34.5%
	Left	16	55.2%
	Both	3	10.3%
Lobe	Frontal	10	34.5%
	Temporal	6	20.7%
	Parietal	2	6.9%
	Multifocal	10	34.5%
	Other	1	3.4%
CTV volume (cc)	337	(95% CI 278–403)	
Number of AEDs	0	3	10.3%
	1	2	6.9%
	2	24	82.8%
Epilepsy	No seizures	9	31.0%
	Generalized tonic-clonic seizures	4	13.8%
	Partial seizures	12	41.4%
	Other	4	13.8%
Technique	3DCT	23	79.3%
	IMRT	3	10.3%
	FSRT	3	10.3%
Resection status	Biopsy	15	51.7%
	Partial removal	12	41.4%
	Total removal	2	6.9%
IDH mutation	Present	27	98.1%
	Absent	1	3.4%
	Undetermined	1	3.4%
1p/19q codeletion	Present	10	34.4%
	Absent	14	48.3%
	Undetermined	5	17.2%

For age, CTV volume, and years of education the mean is reported along with the 95% confidence interval.

Other Predictive Parameters

In addition to evaluating the performance of the NTCP model, we investigated if CTV volume, laterality, age, handedness, and WHO performance score were associated with cognitive deterioration. To this end, using Spearman's correlation coefficient, a correlation matrix was made to identify if bilateral and contralateral hippocampal DVH parameters correlated with cognitive deterioration.

Power Considerations

In the paper by Gondi et al., a lower rate of neurocognitive impairment was found in the group of patients with a low dose to bilateral hippocampi, defined as dose to 40% of bilateral hippocampus volume in EQD2 Gy (D40%BH) ≤7.3 Gy (11.1 vs. 66.7%). In order to detect this difference in our group with 80% power and 2-sided significance level $\alpha = 0.05$, using a Fischer exact test, and assuming the low-dose and the high-dose group are equally sized, 15 patients are required per group. The power calculation was done in SAS software version 14.1, all other statistics were done in IBM SPSS Version 24 except for the Brier score, which was calculated in MATLAB v2017a.

RESULTS

Patient Data

Of 477 patients within EORTC 22033-26033, 103 patients underwent full neurocognitive testing. Of these, 54 patients were treated with radiotherapy-only. Of these, 33 patients had a complete neurocognitive assessment at baseline and at a median follow up of 18.5 months (95% CI 17.3–18.9). Complete original dosimetry data was available for 31 patients. Two patients were excluded due to clinically progressive disease at time of neurocognitive outcome assessment (**Figure 1**).

Data of 29 patients from 1 Spanish and 4 Dutch institutes is summarized in **Table 1**. Median age of patients at randomization was 43 years (95% CI 39–47). Only three patients did not require anti-epileptic medication. Sixteen tumors were left sided, 10 right sided, and three were bilateral. Final resection status was biopsy only in 15 patients, gross total resection in two patients, and partial resection in twelve patients. An IDH mutation was present in 27 patients, absent in one patient and undetermined in one patient. An 1p/19q codeletion was present in 10 patients, absent in 14 patients, and undetermined in five patients. Twenty-eight patients were treated to a dose of 50.4 Gy in 28 fractions, one patient was treated to a dose of 54 Gy in 30 fractions. Twenty-five patients were treated with 3DCT, three with IMRT and two with fractionated stereotactic radiotherapy. Mean CTV volume was 340 cc (95% CI 276–403). Mean dose in EQD2 Gy to bilateral hippocampi was 31.4 Gy (95% CI 27.2–35.6). The mean D40%BH was 40.9 Gy (95% CI 35.8–46.0), and the median D40%BH was 47.2 Gy. Only one patient had a D40%BH lower than 7.3 Gy. Mean dose in EQD2 Gy to contralateral hippocampus was 21.6 Gy (95% CI 16.7–26.9). Overall, there was no significant difference between pre- and post-radiotherapy AVLT-dr score (95% CI 1.09–2.16; **Figure 2**). A cognitive event was scored in seven patients (24.1%). At the time of analysis, the median time to progression in 14 patients was 2.9 years (95% CI 2.2–3.6). Fifteen patients were free of progressive disease after a median follow-up duration of 3.3 years. We compared the subgroup of patients with available data ($n = 31$) with the rest of the study population ($n = 446$). The groups were comparable with respect to tumor laterality, tumor lobe, performance status, progression free survival, and presence of an 1p/19q codeletion. However, the number of IDH wildtype tumors was significantly lower in the study population (3.2 vs. 14%, $p = 0.025$, see **Supplementary Data**).

Model Performance

We were unable to compare the incidence of cognitive events between the high and low dose group as described in the paper by Gondi et al. (D40%BH < 7.3 Gy) as there was only one case in the low dose group. However, there was no difference in the incidence of a cognitive event between the group that received a D40%BH above vs. below the median (47.2 Gy) in this study (14 vs. 25%, $p = 0.68$). NTCP values are presented in **Table 2** with dosimetry and neurocognitive results. A calibration plot is presented in **Figure 3**. Linear regression showed a constant of 0.03 ($p = 0.60$) and a slope of 0.24 ($p < 0.01$) at an r^2 of 0.346. The Brier score of the model was 0.63.

Dosimetric Parameters

A heat map of the correlation matrix is presented in **Figure 4**. Increasing age ($p = 0.04$) and tumor localization in the left hemisphere ($p = 0.01$) were related to poorer neurocognitive outcome at 18 (±4) months. None of the bilateral hippocampal dose volume parameters (D10%, D20%, D30% up to D90%, D95% and mean dose) did exhibit a significant correlation with outcome.

DISCUSSION

To the best of our knowledge, this is the first attempt to quantify the performance of the hippocampal NTCP model within a group of only LGG patients treated with partial brain irradiation. This model was used in RTOG 0933—hippocampal sparing whole brain radiotherapy vs. standard whole brain therapy in brain metastases and in the recently presented phase III trial exploring WBRT plus memantine, with or without hippocampal avoidance (NRG-CC001) (18, 20). Brain metastases are almost never observed in the hippocampus, and selective avoidance of this region is not likely to result in a higher risk of intracranial recurrence (21). This is less clear in LGG where tumor cells are known to be present within the entire brain (22). Moreover, subventricular zone involvement has been shown to be a biomarker for poor prognosis (23), making the hippocampus a potential treatment target.

In the calibration procedure, the positive slope in the linear regression indicates an overestimation of NTCP values by the model in this dataset. The high Brier score indicates poor model performance. In comparing the two study groups, the incidence of a neurocognitive event is similar (29.2 vs. 24.1% in this study) but the range of hippocampal dose is quite different. The median D40%BH in the paper by Gondi et al. was 7.3 Gy, at above which a NTCP of 66.7% was observed. By contrast, the median D40%BH in this paper is 47.2 Gy and all but one of the patients

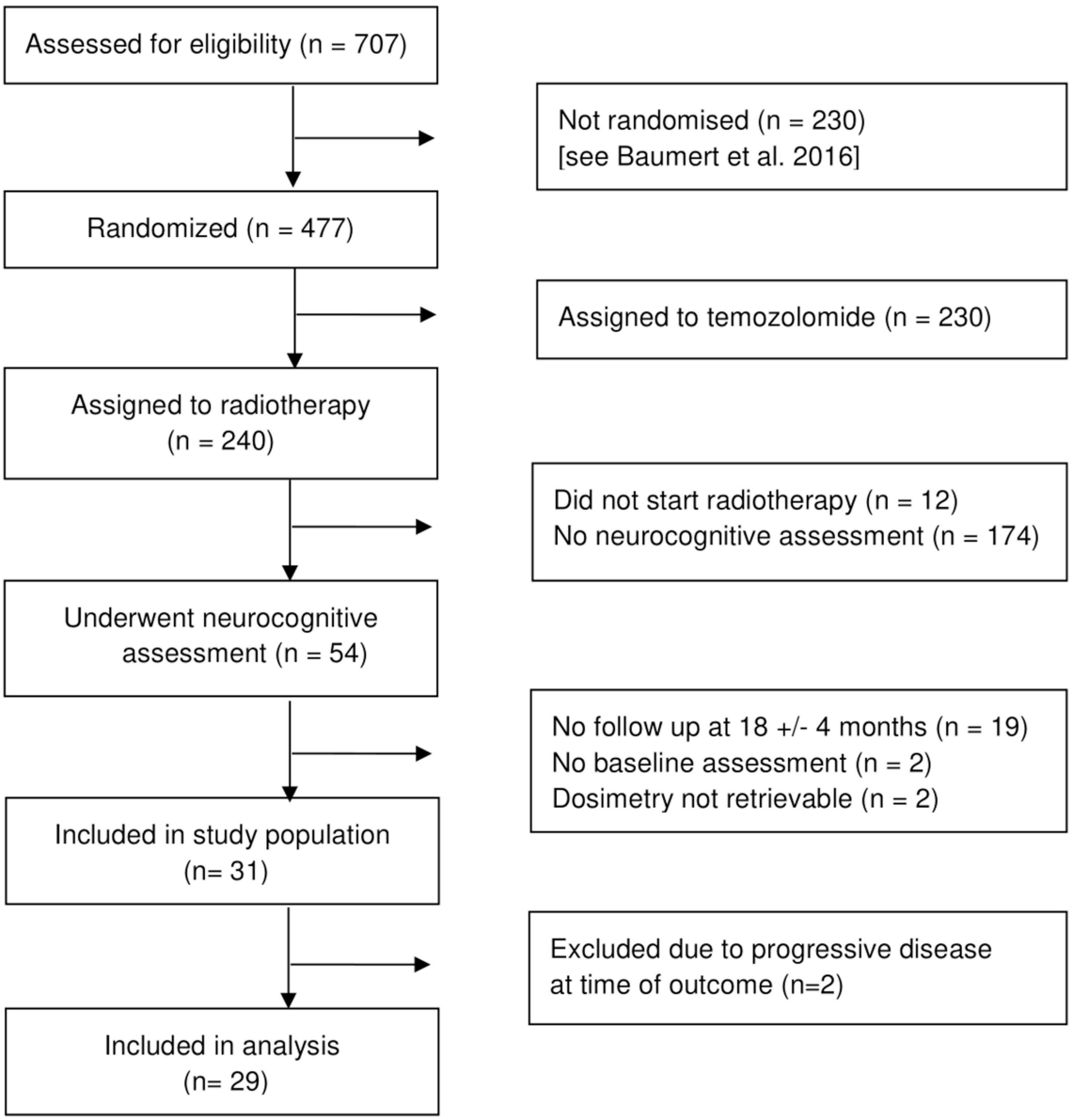

FIGURE 1 | Inclusion of patients.

in the present study received a D40%BH in excess of 7.3 Gy. In comparing the two groups, there are substantial differences in the delivery technique and target volume. In the paper by Gondi et al., most patients were treated without a CTV expansion and with limited PTV margins (2 mm) using highly conformal dose distributions. In the present study, patients were treated with a CTV margin of 10–15 mm and a larger PTV (7 mm) resulting in substantially larger target volumes, and the delivery technique was mainly 3DCRT. It is likely that this resulted in higher doses to bilateral hippocampus in this study, to a degree that almost none of the patients were in the low dose group. As such, we were unable to compare the incidence of neurocognitive impairment between the high dose and the low dose group. However, the hippocampal doses in this study group are probably a good representation of the hippocampal dose range found in LGG patients undergoing radiotherapy. Therefore, this study should not be read as a formal disapproval of the hippocampal NTCP model, but rather as a caution toward extrapolating a NTCP model beyond the dose range in which it was developed. A similar issue was encountered by Moiseenko in comparing NTCP models for radiation toxicity to the visual apparatus (24). Since no significant correlation between dosimetric parameters and outcome was observed, we were unable to generate an alternative model from this dataset.

The choice of endpoint, neurocognitive failure at 18 months after radiotherapy, is debatable in LGG patients. Trials that found

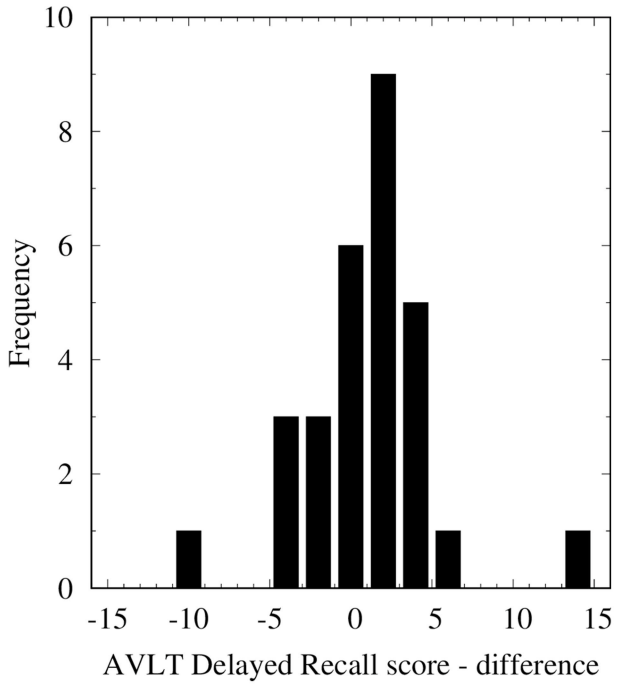

FIGURE 2 | Histogram of differences in AVLT-dr score per patient (baseline minus follow-up). Overall, there was no significant difference between pre- and post-radiotherapy AVLT-dr score.

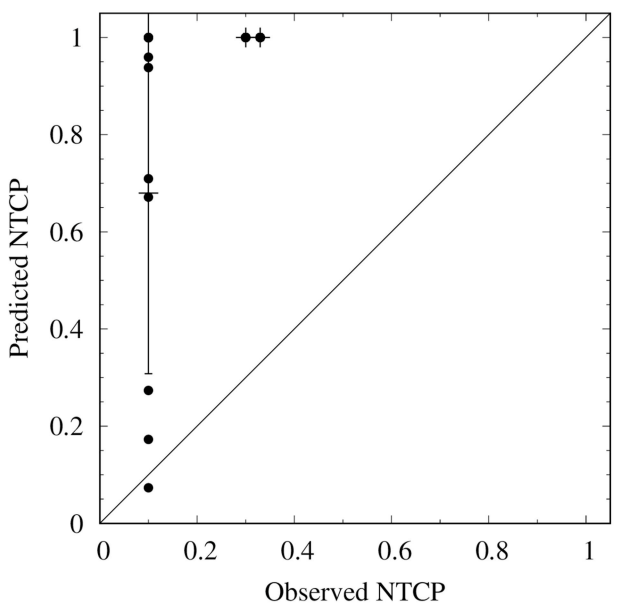

FIGURE 3 | Calibration plot of the original model in this dataset. The predicted NTCP is calculated using the NTCP model. The observed NTCP is calculated by sorting the cases in three bins of ascending risk (horizontal axis), and computing the incidence of a neuropsychological event in each bin (vertical axis). The intercept line represents agreement between predicted and observed NTCP. Error bars are 95% confidence intervals.

TABLE 2 | Dosimetric parameters, expected values derived from the NTCP model, and cognitive event (see text for definition).

Age	Dose to 40% of bilateral hippocampus (EQD2 Gy)	Predicted NTCP (NTCP model)	Cognitive event
48.7	3.21	0.07	No
48.0	7.30	0.17	No
36.3	10.04	0.27	No
69.4	18.45	0.67	Yes
49.2	19.31	0.71	No
45.5	27.24	0.94	No
42.3	28.89	0.96	No
40.3	40.62	>0.99	No
32.9	44.30	>0.99	No
50.8	45.51	>0.99	No
37.1	46.27	>0.99	Yes
35.6	46.52	>0.99	No
40.6	46.79	>0.99	No
41.6	47.08	>0.99	No
50.1	47.18	>0.99	Yes
34.7	47.31	>0.99	No
48.5	47.42	>0.99	No
60.2	47.50	>0.99	Yes
35.9	47.61	>0.99	No
36.3	47.87	>0.99	No
42.5	47.91	>0.99	No
29.5	47.91	>0.99	No
35.2	48.00	>0.99	No
66.5	48.13	>0.99	No
44.3	48.20	>0.99	Yes
34.0	48.43	>0.99	No
50.6	48.73	>0.99	Yes
32.0	48.95	>0.99	No
27.8	50.74	>0.99	No

a significant effect of radiotherapy on neurocognitive function typically only did so after a follow-up >5 years (7, 8), whereas several trials with a shorter follow-up found no significant, or only transient, deleterious effects (9–12, 25). This begs the question whether neurocognitive impairment at 18 months is indeed indicative of a persistent neurocognitive deficit.

Although preclinical and radiological (26, 27) data demonstrated appreciable changes within the hippocampus after radiotherapy, a relationship between cognitive performance and a D40% as low as 7.3 EQD2 Gy was not found in the current study but also not in other studies. In the setting of prophylactic WBRT in small cell lung cancer and partial brain irradiation for glioblastoma multiforme, Ma et al. (28) demonstrated D50% of 22.1 Gy to be associated with a 20% risk of a significant decline in Hopkins Verbal Learning Test (HVLT)—delayed recall score. Peiffer et al. (29) identified the volume of bilateral hippocampi receiving 60 Gy as a possible predictor for cognitive decline. The analysis by

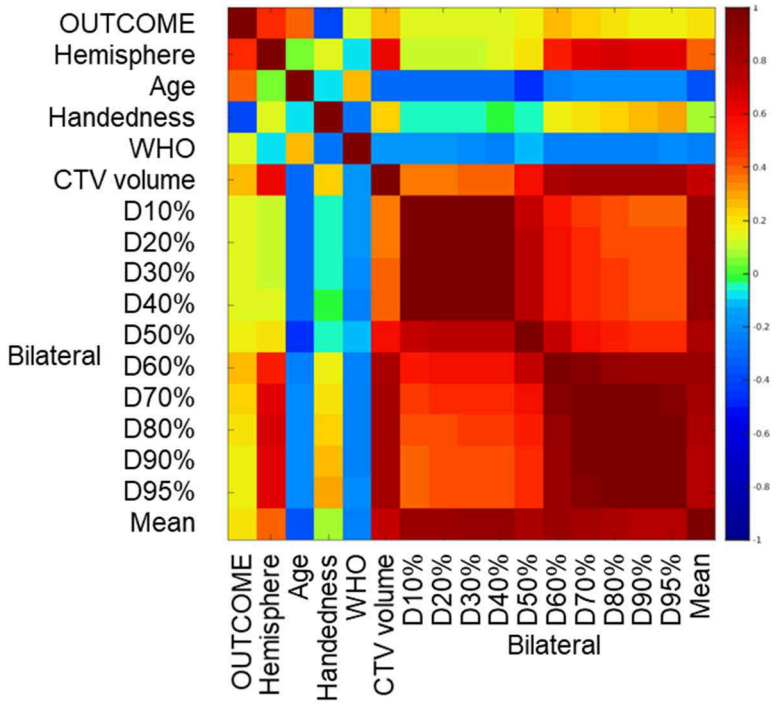

FIGURE 4 | Correlation matrix of clinical and dosimetric parameters. Outcome: neurocognitive event, binary (for definition, see "Methods"), WHO, World Health Organization Performance score; D10%, 20%, etc., dose absorbed by 10, 20%, etc. of bilateral hippocampus volume. Color: Spearman correlation coefficient. There are significant correlations between age and outcome, laterality and outcome, and between individual dosimetric parameters.

Okoukoni et al. (30) established a correlation between post-treatment HVLT score (no baseline measurement was done) and even higher doses to the bilateral hippocampi. Here, hippocampal V55 Gy of 0, 25, and 50% were associated with post-radiation impairment rates of 14.9, 45.9, and 80.6%, respectively.

In this study, we used prospectively acquired baseline and follow up data from the recently completed EORTC22033-26033 trial, ensuring a homogenous patient group with good adherence to protocol. The subset of patients included in this analysis is a relatively small proportion of the radiotherapy-only group (15%). The main reason for this is that neurocognitive testing was not mandatory, and a number of centers did no neurocognitive testing. However, we found no significant differences in clinical variables (save for presence of IDH mutation) and time to progressive disease between our subset of and rest of the study population. In comparing our neurocognitive event-definition to the one used in the paper by Gondi et al., we did not utilize a control group but published test-retest data from the Maastricht Aging study. This data is derived from a study group that is older (49–56 years), than the average patient in our study (43 years), and the test-retest interval is twice as long (3 years).

In this dataset of only LGG patients, the NTCP model did not perform as expected in predicting cognitive decline based on dose to bilateral hippocampus. Clearly, the understanding of the relationship between dose to subsites in the CNS and neurocognitive functioning is still limited, and there exists a paucity of prospective neuropsychological and dosimetric parameters with an adequate duration of follow-up.

DATA AVAILABILITY STATEMENT

The datasets generated for this study are available on request to the corresponding author.

ETHICS STATEMENT

This study was carried out in accordance with the Dutch Medical Research (Human Subjects) Act (WMO). The protocol was approved by the Medical Research Ethics Committee Erasmus MC. All subjects gave written informed consent in accordance with the Declaration of Helsinki.

AUTHOR CONTRIBUTIONS

The study was conceptualized and the manuscript was written by JJ and AM. The statistical analysis was done by JJ and MH. MB, MT, and MK helped interpreting the data. JJ, RW, DE, FL, and AL were involved in data collection. All authors critically reviewed the manuscript and commented on the final version. The final authorship position is shared between BB and MK.

ACKNOWLEDGMENTS

We acknowledge Jacobus van Wingerden and Wilco Schillemans for their work on data recovery from the initially non-DICOM compatible HELAX treatment planning system. We also acknowledge Thierry Gorlia for his work transferring the clinical data from the EORTC headquarters office and comparisons with the full dataset, and Roger Stupp for his contributions that improved the quality of the manuscript.

SUPPLEMENTARY MATERIAL

The Supplementary Material for this article can be found online at: https://www.frontiersin.org/articles/10.3389/fonc.2019.00991/full#supplementary-material

REFERENCES

1. Forst DA, Nahed BV, Loeffler JS, Batchelor TT. Low-grade gliomas. *Oncologist*. (2014) 19:403–13. doi: 10.1634/theoncologist.2013-0345
2. Louis DN, Perry A, Reifenberger G, von Deimling A, Figarella-Branger D, Cavenee WK, et al. The 2016 World Health Organization classification of tumors of the central nervous system: a summary. *Acta Neuropathol.* (2016) 131:803–20. doi: 10.1007/s00401-016-1545-1
3. Shaw EG, Wang M, Coons SW, Brachman DG, Buckner JC, Stelzer KJ, et al. Randomized trial of radiation therapy plus procarbazine, lomustine, and vincristine chemotherapy for supratentorial adult low-grade glioma: initial results of RTOG 9802. *J Clin Oncol.* (2012) 30:3065–70. doi: 10.1200/JCO.2011.35.8598
4. Buckner JC, Shaw EG, Pugh SL, Chakravarti A, Gilbert MR, Barger GR, et al. Radiation plus procarbazine, CCNU, and vincristine in low-grade glioma. *N Engl J Med*. (2016) 374:1344–55. doi: 10.1056/NEJMoa1500925
5. Taphoorn MJ. Neurocognitive sequelae in the treatment of low-grade gliomas. *Semin Oncol*. (2003) 30(Suppl. 19):45–8. doi: 10.1053/j.seminoncol.2003.11.023
6. McAleer MF, Brown PD. Neurocognitive function following therapy for low-grade gliomas. *Semin Radiat Oncol*. (2015) 25:210–8. doi: 10.1016/j.semradonc.2015.02.005
7. Surma-aho O, Niemela M, Vilkki J, Kouri M, Brander A, Salonen O, et al. Adverse long-term effects of brain radiotherapy in adult low-grade glioma patients. *Neurology*. (2001) 56:1285–90. doi: 10.1212/WNL.56.10.1285
8. Douw L, Klein M, Fagel SS, van den Heuvel J, Taphoorn MJ, Aaronson NK, et al. Cognitive and radiological effects of radiotherapy in patients with low-grade glioma: long-term follow-up. *Lancet Neurol.* (2009) 8:810–8. doi: 10.1016/S1474-4422(09)70204-2
9. Taphoorn MJ, Schiphorst AK, Snoek FJ, Lindeboom J, Wolbers JG, Karim AB, et al. Cognitive functions and quality of life in patients with low-grade gliomas: the impact of radiotherapy. *Ann Neurol.* (1994) 36:48–54. doi: 10.1002/ana.410360111
10. Vigliani MC, Sichez N, Poisson M, Delattre JY. A prospective study of cognitive functions following conventional radiotherapy for supratentorial gliomas in young adults: 4-year results. *Int J Radiat Oncol Biol Phys*. (1996) 35:527–33. doi: 10.1016/S0360-3016(96)80015-0
11. Laack NN, Brown PD, Ivnik RJ, Furth AF, Ballman KV, Hammack JE, et al. Cognitive function after radiotherapy for supratentorial low-grade glioma: a North Central Cancer Treatment Group prospective study. *Int J Radiat Oncol Biol Phys*. (2005) 63:1175–83. doi: 10.1016/j.ijrobp.2005.04.016
12. Buglione M, Pedretti S, Gipponi S, Todeschini A, Pegurri L, Costa L, et al. Radiotherapy in low-grade glioma adult patients: a retrospective survival and neurocognitive toxicity analysis. *Radiol Med*. (2014) 119:432–9. doi: 10.1007/s11547-013-0347-y
13. Tome WA, Gokhan S, Gulinello ME, Brodin NP, Heard J, Mehler MF, et al. Hippocampal-dependent neurocognitive impairment following cranial irradiation observed in pre-clinical models: current knowledge and possible future directions. *Br J Radiol*. (2016) 89:20150762. doi: 10.1259/bjr.20150762
14. Gondi V, Hermann BP, Mehta MP, Tome WA. Hippocampal dosimetry predicts neurocognitive function impairment after fractionated stereotactic radiotherapy for benign or low-grade adult brain tumors. *Int J Radiat Oncol Biol Phys*. (2012) 83:e487–93. doi: 10.1016/j.ijrobp.2011.10.021
15. Baumert BG, Hegi ME, van den Bent MJ, von Deimling A, Gorlia T, Hoang-Xuan K, et al. Temozolomide chemotherapy versus radiotherapy in high-risk low-grade glioma (EORTC 22033-26033): a randomised, open-label, phase 3 intergroup study. *Lancet Oncol*. (2016) 17:1521–32. doi: 10.1016/S1470-2045(16)30313-8
16. Klein M, Drijver J, van den Bent MJ, Hoang-Xuan K, Taphoorn MJB, Reijneveld JC, et al. Memory functioning in low-grade glioma patients treated with either radiotherapy (RTx) or temozolomide (TMZ) chemotherapy. A correlative analysis of the European Organization for Research and Treatment (EORTC) study 22033-26033. *Neuro Oncol*. (2018) 19(Suppl. 6):vi139. doi: 10.1093/neuonc/nox168.568
17. Van der Elst W, Van Boxtel MP, Van Breukelen GJ, Jolles J. Detecting the significance of changes in performance on the Stroop Color-Word Test, Rey's Verbal Learning Test, and the Letter Digit Substitution Test: the regression-based change approach. *J Int Neuropsychol Soc*. (2008) 14:71–80. doi: 10.1017/S1355617708080028
18. Gondi V, Pugh SL, Tome WA, Caine C, Corn B, Kanner A, et al. Preservation of memory with conformal avoidance of the hippocampal neural stem-cell compartment during whole-brain radiotherapy for brain metastases (RTOG 0933): a phase II multi-institutional trial. *J Clin Oncol*. (2014) 32:3810–6. doi: 10.1200/JCO.2014.57.2909
19. Lyman JT. Complication probability as assessed from dose-volume histograms. *Radiat Res.* (1985) 104(Suppl. 8):S13–19. doi: 10.2307/3583506
20. Gondi V, Deshmukh S, Brown PD, Wefel JS, Tome WA, Bruner DW, et al. Preservation of neurocognitive function (NCF) with conformal avoidance of the hippocampus during whole-brain radiotherapy (HA-WBRT) for brain metastases: preliminary results of phase III trial NRG oncology CC001. *Int J Radiat Oncol Biol Phys*. (2018) 102:1607. doi: 10.1016/j.ijrobp.2018.08.056
21. Han YM, Cai G, Chai WM, Xu C, Cao L, Ou D, et al. Radiological distribution of brain metastases and its implication for the hippocampus avoidance in whole brain radiotherapy approach. *Br J Radiol*. (2017) 90:20170099. doi: 10.1259/bjr.20170099
22. Sahm F, Capper D, Jeibmann A, Habel A, Paulus W, Troost D, et al. Addressing diffuse glioma as a systemic brain disease with single-cell analysis. *Arch Neurol*. (2012) 69:523–6. doi: 10.1001/archneurol.2011.2910
23. Liu S, Wang Y, Fan X, Ma J, Ma W, Wang R, et al. Anatomical involvement of the subventricular zone predicts poor survival outcome in low-grade astrocytomas. *PLoS ONE*. (2016) 11:e0154539. doi: 10.1371/journal.pone.0154539
24. Moiseenko V, Song WY, Mell LK, Bhandare N. A comparison of dose-response characteristics of four NTCP models using outcomes of radiation-induced optic neuropathy and retinopathy. *Radiat Oncol*. (2011) 6:61. doi: 10.1186/1748-717X-6-61
25. Klein M, Heimans JJ, Aaronson NK, van der Ploeg HM, Grit J, Muller M, et al. Effect of radiotherapy and other treatment-related factors on mid-term to long-term cognitive sequelae in low-grade gliomas: a comparative study. *Lancet.* (2002) 360:1361–8. doi: 10.1016/S0140-6736(02)11398-5
26. Farjam R, Pramanik P, Aryal MP, Srinivasan A, Chapman CH, Tsien CI, et al. A radiation-induced hippocampal vascular injury surrogate marker predicts late neurocognitive dysfunction. *Int J Radiat Oncol Biol Phys*. (2015) 93:908–15. doi: 10.1016/j.ijrobp.2015.08.014
27. Seibert TM, Karunamuni R, Bartsch H, Kaifi S, Krishnan AP, Dalia Y, et al. Radiation dose–dependent hippocampal atrophy detected with longitudinal volumetric magnetic resonance imaging. *Int J Radiat Oncol Biol Phys*. (2017) 97:263–9. doi: 10.1016/j.ijrobp.2016.10.035

28. Ma TM, Grimm J, McIntyre R, Anderson-Keightly H, Kleinberg LR, Hales RK, et al. A prospective evaluation of hippocampal radiation dose volume effects and memory deficits following cranial irradiation. *Radiother Oncol.* (2017) 125:234–40. doi: 10.1016/j.radonc.2017.09.035
29. Peiffer AM, Leyrer CM, Greene-Schloesser DM, Shing E, Kearns WT, Hinson WH, et al. Neuroanatomical target theory as a predictive model for radiation-induced cognitive decline. *Neurology.* (2013) 80:747–53. doi: 10.1212/WNL.0b013e318283bb0a
30. Okoukoni C, McTyre ER, Ayala Peacock DN, Peiffer AM, Strowd R, Cramer C, et al. Hippocampal dose volume histogram predicts Hopkins Verbal Learning Test scores after brain irradiation. *Adv Radiat Oncol.* (2017) 2:624–9. doi: 10.1016/j.adro.2017.08.013

Conflict of Interest: The authors declare that the research was conducted in the absence of any commercial or financial relationships that could be construed as a potential conflict of interest.

frontiers in Oncology

ORIGINAL RESEARCH
published: 01 October 2019
doi: 10.3389/fonc.2019.00987

Individual Radiosensitivity in Oncological Patients: Linking Adverse Normal Tissue Reactions and Genetic Features

Elisa Palumbo[1†‡], Celeste Piotto[1†‡], Enrica Calura[2], Elena Fasanaro[1†], Elena Groff[1], Fabio Busato[1], Badr El Khouzai[1], Michele Rigo[1†], Laura Baggio[1], Chiara Romualdi[2], Demetre Zafiropoulos[3], Antonella Russo[4], Maddalena Mognato[2*] and Luigi Corti[1]*

[1] Department of Radiotherapy, Veneto Institute of Oncology IOV–IRCCS, Padua, Italy, [2] Department of Biology, University of Padua, Padua, Italy, [3] National Laboratories of Legnaro, Italian Institute of Nuclear Physics (LNL-INFN), Padua, Italy, [4] Department of Molecular Medicine, University of Padua, Padua, Italy

Introduction: Adverse effects of radiotherapy (RT) significantly affect patient's quality of life (QOL). The possibility to identify patient-related factors that are associated with individual radiosensitivity would optimize adjuvant RT treatment, limiting the severity of normal tissue reactions, and improving patient's QOL. In this study, we analyzed the relationships between genetic features and toxicity grading manifested by RT patients looking for possible biomarkers of individual radiosensitivity.

Methods: Early radiation toxicity was evaluated on 143 oncological patients according to the Common Terminology Criteria for Adverse Events (CTCAE). An individual radiosensitivity (IRS) index defining four classes of radiosensitivity (highly radiosensitive, radiosensitive, normal, and radioresistant) was determined by a G_2-chromosomal assay on *ex vivo* irradiated, patient-derived blood samples. The expression level of 15 radioresponsive genes has been measured by quantitative real-time PCR at 24 h after the first RT fraction, in blood samples of a subset of 57 patients, representing the four IRS classes.

Results: By applying univariate and multivariate statistical analyses, we found that fatigue was significantly associated with IRS index. Interestingly, associations were detected between clinical radiation toxicity and gene expression (*ATM*, *CDKN1A*, *FDXR*, *SESN1*, *XPC*, *ZMAT3*, and *BCL2/BAX* ratio) and between IRS index and gene expression (*BBC3*, *FDXR*, *GADD45A*, and *BCL2/BAX*).

Conclusions: In this prospective cohort study we found that associations exist between normal tissue reactions and genetic features in RT-treated patients. Overall, our findings can contribute to the identification of biological markers to predict RT toxicity in normal tissues.

Keywords: radiotherapy, adverse effects, chromosomal radiosensitivity, gene expression, association analysis

OPEN ACCESS

Edited by:
Tiziana Rancati, National Tumor Institute, Italy

Reviewed by:
Simeng Suy, Georgetown University, United States
Maria Carmen De Santis, National Tumor Institute, Italy

****Correspondence:***
Antonella Russo
antonella.russo@unipd.it
Maddalena Mognato
maddalena.mognato@unipd.it

†Present address:
Elisa Palumbo, Department of Molecular Medicine, University of Padua, Padua, Italy
Celeste Piotto, European Molecular Biology Laboratory Australia, Australian Regenerative Medicine Institute, Monash University, Melbourne, VIC, Australia
Elena Fasanaro, Otolaryngology Unit, Cittadella Hospital, Cittadella, Italy
Michele Rigo, IRCCS Sacro Cuore Don Calabria Hospital, Cancer Care Center, Verona, Italy

‡These authors have contributed equally to this work

Specialty section:
This article was submitted to Radiation Oncology, a section of the journal Frontiers in Oncology

Received: *24 June 2019*
Accepted: *16 September 2019*
Published: *01 October 2019*

INTRODUCTION

The development of radiation-induced complications following radiotherapy (RT) has a significant impact on treatment outcome and patient's quality of life (QOL). In the last decades the therapeutic ratio has improved due to advancements in RT technologies and use of radioprotectors, mitigators, and radiosensitizers (1). Nevertheless, radiation toxicity of normal tissues surrounding the tumor is a serious problem for ∼5–10% of patients, who are affected by high intrinsic radiosensitivity (2–4). Evidence of radiosensitivity *in vivo* is given by burns and radiodermitis in the irradiated body parts, together with bystander effect in neighboring area (5). Several factors, including cellular composition, differentiation, cell renewal capacity, as well as cellular radiosensitivity, determine the severity of radiation toxicity (6). Patient-related factors are deeply linked to the risk of manifesting radiation toxicity, and reliable biological markers are still not available to predict the onset of severe side-effects after RT. Human response to ionizing radiation (IR) is individual and variable, being influenced by age, smoking, diabetes, collagen vascular disease and genotype (7). Moreover, multiple genetic pathways such as DNA damage repair, oxidative stress, radiation fibrogenesis and endothelial cell damage are implicated in adverse tissue reactions following radiotherapy (8). However, the molecular basis of individual radiosensitivity remains poorly understood, and the relationship between different indicators of radiation sensitivity is elusive.

RT causes cancer cell death mainly by IR-induced DNA Double Strand Breaks (DSBs). Formation of DSBs, the most severe damage for genome integrity, triggers a cascade of cellular events, collectively termed DNA-damage response (DDR), which involves sensing the damage, signal transduction to the effectors of DNA repair, cell cycle arrest and apoptosis induction (9–11). Radiation-induced DSBs are efficiently repaired to ensure the maintenance of genome integrity but when DNA repair is hampered, unrepaired DSBs can originate chromosome aberrations (12). Following irradiation, unrepaired DSBs can be quantified in metaphase spreads by the yield of chromatid breaks formed at G_2-phase, which is inversely related to the efficiency of the G_2-phase checkpoint (13). Thus, the individual level of radiosensitivity can be assessed in *ex vivo* irradiated human peripheral blood lymphocytes (PBLs) by applying a "G_2-chromosomal assay" (14–17).

Increasing evidence supports the existence of individual response to IR-induced DNA damage, which can be related to mutations in key genes of DDR pathway or to individual capacity to modulate the expression of DDR genes after IR-exposure. In this regard, the expression of genes involved in DDR pathway may be variable between individuals and can impact on own radiation response.

Abbreviations: CTCAE, Common Terminology Criteria for Adverse Events; DDR, DNA-Damage Response; DSBs, Double-Strand Breaks; HNSCC, Head and Neck Squamous Cell Carcinoma; HRS, Highly Radiosensitive; IR, Ionizing Radiation; IRS, Individual Radiosensitivity; N, Normal; PBLs, Peripheral Blood Lymphocytes; QOL, Quality of Life; qRT-PCR, quantitative Real-Time PCR; RR, Radioresistant; RS, Radiosensitive; RT, Radiotherapy.

Several studies attempted to find biomarkers able to predict the onset of radiation toxicity in normal tissues after RT. Individual radiosensitivity evaluated by using *in vitro* irradiated patient-derived blood lymphocytes has been found to correlate with normal tissue reactions (13, 18, 19), and single nucleotide polymorphisms (SNPs) have been associated with acute and late radiation-induced normal tissue injury in RT patients (19–22). Data concerning the association between gene expression changes and normal tissue radiation toxicity refer to *in vitro* irradiation studies (4, 23–25) or to single gene analysis in oncological patients treated with RT (26). To date, a relationship between radio-induced normal tissue adverse effects, *in vitro* chromosomal radiosensitivity and *in vivo* expression of a set of radioresponsive genes is not available in the same cohort of RT patients. Since future clinical protocols aim at ameliorating patient's QOL it is demanding to identify patient-related factors that are associated with individual radiosensitivity before patients undergo RT (27, 28).

In this explorative study, the clinical features of early radiation toxicity have been associated with an Individual Radiosensitivity (IRS) index, defining four classes of radiosensitivity (highly radiosensitive, radiosensitive, normal and radioresistant) based on a G_2-chromosomal assay on patient-derived PBLs irradiated *in vitro* (15). The expression level of 15 selected radioresponsive genes belonging to DDR pathway has been measured in blood samples from a subgroup of patients, representing the different IRS classes, 24 h after the first RT fraction, as an additional variable of intrinsic radiosensitivity. Data of clinical and genetic features have been statistically analyzed to find possible genetic factors associated with individual radiation sensitivity.

MATERIALS AND METHODS

Outline of the Study

In this prospective study, breast cancer (BC) and head and neck squamous cell carcinoma (HNSCC) patients were enrolled as representative of patients experiencing normal tissue reactions after RT. Data of toxicity grading in normal tissues, *in vitro* chromosomal radiosensitivity and *in vivo* RT-induced gene expression changes, have been integrated to identify possible biomarkers of radiosensitivity in patients undergoing RT (**Figure 1**). Overall, 143 oncological patients were enrolled: 124 (all females) affected by BC, and 19 (6 females and 13 males) affected by HNSCC.

Patients

Patients with BC or HNSCC histological diagnosis undergoing RT were enrolled from 2015 to 2017 at the Department of Radiotherapy, Veneto Institute of Oncology IOV–IRCCS, Padua, Italy (IOV) upon evaluation and approval of the IOV-IRCCS Ethic Committee (CE IOV 2015/18; CE IOV 2016/04). Privacy rights of human subjects were observed; all the procedures were in accordance with relevant guidelines and regulations. All subjects gave written informed consent in accordance with the Declaration of Helsinki.

Patients were enrolled applying the following exclusion criteria: patients suffering from congenital syndromes

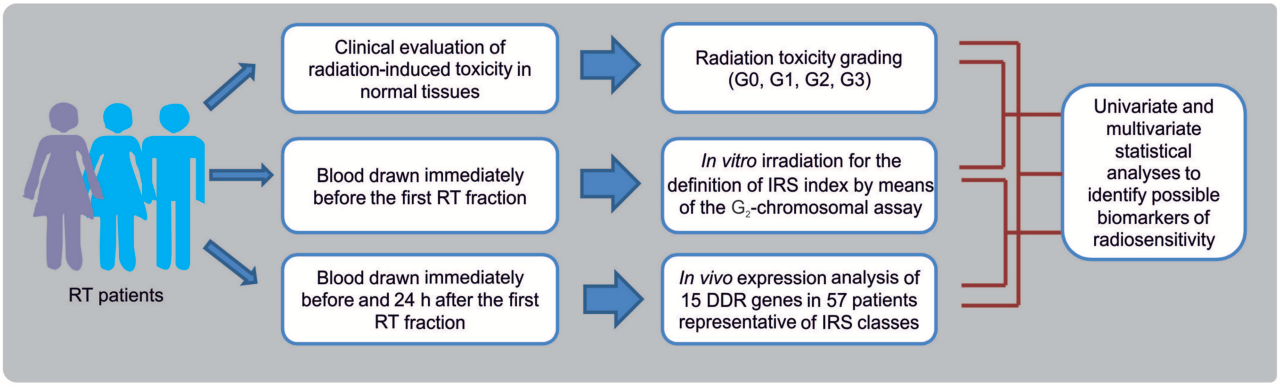

FIGURE 1 | Flow chart showing the experimental phases for the identification of biomarkers of individual radiosensitivity in patients undergoing radiotherapy (RT).

predisposing to radiosensitivity (such as Ataxia-Telangiectasia, Bloom syndrome, Down's syndrome, Gorlin syndrome, Klinefelter syndrome, Retinoblastoma, Wilm's tumor, Xeroderma pigmentosum, Rothmund-Thomson syndrome, Li-Fraumeni syndrome, Dyskeratosis congenita, Familial dysplastic nevus syndrome, Common variable immune deficiency, Nijmegen Breakage Syndrome, Fanconi Anemia, albinism), previous RT and/or chemotherapy treatment or ongoing chemotherapy treatment, previous anticancer drug employment, significant comorbidities, diabetic patients affected by breast cancer, age $\leq$ 18 years.

BC patients received by 3DCRT (42.40–50 Gy/16–25 fractions) plus a boost dose of 10 Gy in 5 fractions to the tumor bed. HNSCC patients received up to 70 Gy, daily fraction 1.8–2.12 Gy/day, for 5 days/week on primitive tumor by VMAT or IMRT.

Adverse tissue reactions (dermatitis radiation, pain, pruritus, fatigue) have been recorded at the completion of RT treatment (t_1) and 1 month later (t_2), using the Common Terminology Criteria for Adverse Events (CTCAE) (version 4.03, http://ctep.cancer.gov/protocolDevelopment/adverse_effects.htm). Adverse effects were classified as: grade 0 (G0, no adverse effects), grade 1 (G1, mild), grade 2 (G2, moderate), grade 3 (G3, severe). At the Department of Radiotherapy of the IOV-IRCCS management of acute toxicity followed a standardized procedure. All patients were clinically evaluated before starting RT and no significant side-effects were complained by patients.

Chromosome-Based Radiosensitivity Assay

The G_2-chromosomal assay was performed following a standardized protocol (15). Briefly, whole blood cultures were incubated for 72 h at 37°C, 5% CO_2 before being irradiated with 1 Gy of gamma rays in a Gamma Beam A15 ^{60}Co panoramic source at the National Laboratories of Legnaro (I.N.F.N., Padua, Italy; dose rate: 0.5 Gy/min).

Immediately after irradiation, each culture was split in two and one was treated with 4 mM caffeine. After 20 min at 37°C, both cultures were incubated with Colcemid at concentration of 0.1 μg/mL for 60 min, then chromosome spreads were prepared according to standard cytogenetic procedures. With few exceptions, chromatid aberration yields were obtained by scoring for chromatid breaks and gaps 50 metaphases per culture, under a Zeiss AxioImager Z2 microscope coupled with MSearch-AutoCapt software (Metasystems, Altlussheim Germany). Following calculation of the *in vitro* individual radiosensitivity index (IRS $= [1-(G_{2caf}-G_2)/G_{2caf}] \times 100\%$, simplified as IRS $= (G_2/G_{2caf}) \times 100\%$) patients were classified as: highly radiosensitive, HRS (IRS $>$ 70), radiosensitive, RS (50 $<$ IRS $\leq$ 70), normal, N (30 $\leq$ IRS $\leq$ 50), and radioresistant, RR (IRS $<$ 30) (15, 29).

Gene Expression Analysis

Fifty-seven over 143 patients were randomly selected within the four IRS classes (HRS, RS, N, RR) in order to have comparable numbers of patients in each group. This sample size guarantees a high statistical power (power = 0.83) in identifying as significant (alpha $<$ 0.1) genes with an effect equal to 1.1 among groups using either an ANOVA test or a Wilcoxon test. Two whole blood samples were collected from each patient: one immediately before the first fractionated RT dose and the second 24 h later. Samples were collected into PAXgene® Blood RNA tubes (PreAnalytiX GmbH, Qiagen, Venlo, The Netherlands) for immediate stabilization of intracellular RNA, and stored at −80°C. Total RNA was purified by using PAXgene® Blood RNA Kit 6 (PreAnalytiX GmbH, Qiagen, Venlo, The Netherlands) and quantified using the ND-1000 spectrophotometer (Nanodrop, Wilmington, DE, USA).

For mRNA detection, retrotranscription and quantitative real time-PCR (qRT-PCR) reactions were performed according to our established protocol (30, 31). The gene-specific primers for *ATM*, *BAX*, *BBC3*, *BCL2*, *CCNG1*, *cMYC*, *DDB2*, *FDXR*, *GADD45A*, *MDM2*, *CDKN1A*, *PCNA*, *SESN1*, *XPC*, and *ZMAT3* genes and for *GADPH* as reference, can be found in **Supplementary Table 1**. Real-time PCR was performed using an Applied Biosystems 7500 Fast Real-Time PCR System according to the following amplification protocol: 95°C for 10 min, 95°C for 15 sec, 60°C for 60 s (40 cycles). qRT-PCR reactions were always performed in triplicates. The relative expression levels of mRNAs between irradiated (2 Gy) and non-irradiated (0 Gy) blood samples of the same patients were calculated

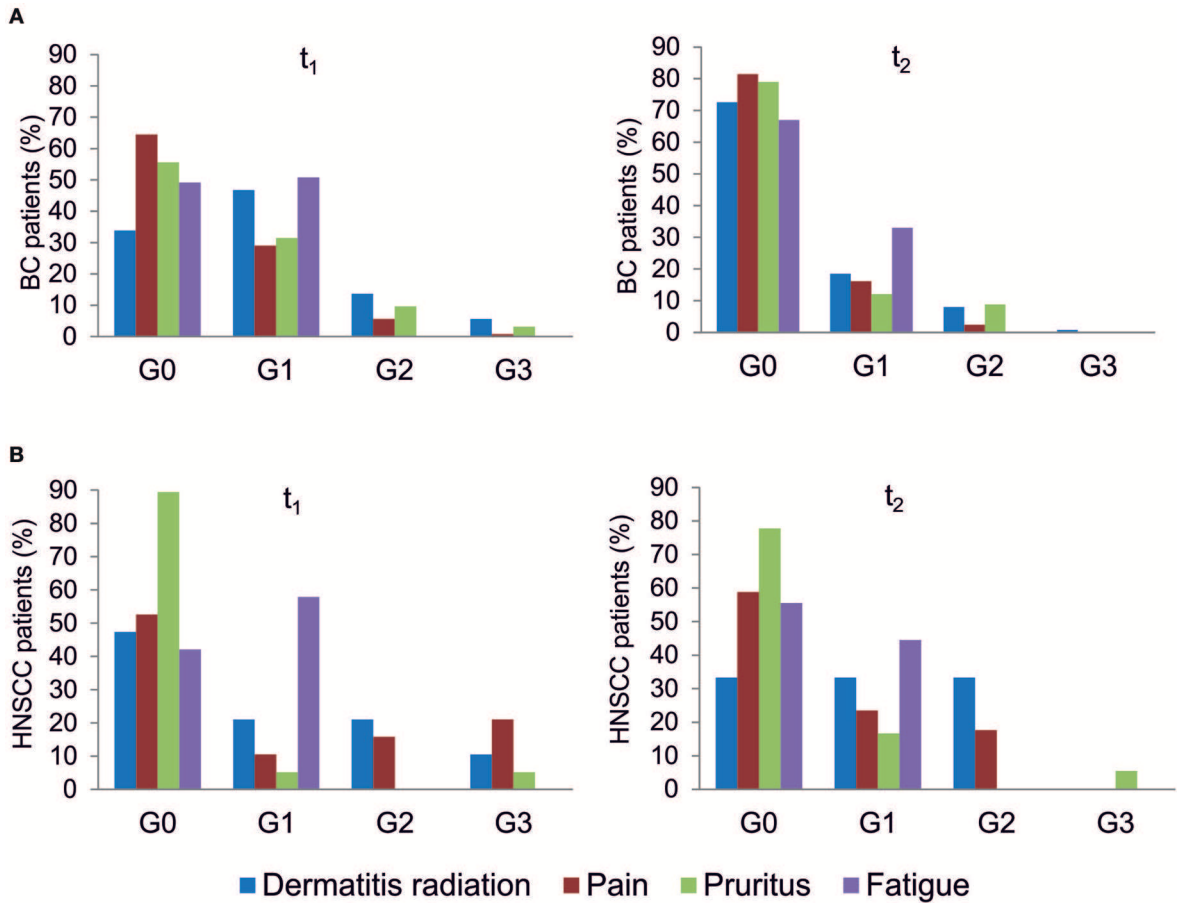

FIGURE 2 | Clinical variables of radiation toxicity in RT patients. RT-induced toxicity grading in breast cancer, BC **(A)** and in head and neck squamous cell carcinoma HNSSC **(B)** patients at completion of RT treatment (t_1) and 1 month later (t_2).

using the comparative delta CT (threshold cycle number) method ($2^{-\Delta\Delta CT}$) implemented in the 7500 Real Time System software (32).

Statistical Analysis

ANOVA and ANOVA *post-hoc* with Bonferroni correction was used to assess the gene expression mean differences among groups of patients defined using clinical and IRS annotations. In case of group size lower than 10 patients Kruskall-Wallis/Wilcoxon test was used. Multivariate regression analyses were used to test the association of clinical annotations (explanatory variables) with IRS value (dependent variable). Unsupervised cluster analysis of gene expression data was performed using hierarchical cluster analysis with Euclidean distance and complete linkage. All the analyses were performed using the R programming language (version 3.4), and the Bioconductor software suite (version 3.6).

RESULTS

Radiation-Induced Toxicity in RT-Treated Patients

All patients were evaluated for the onset of radiation toxicity at the completion of RT treatment (t_1) and 1 month later (t_2). The overall distribution of subjects suffering from dermatitis radiation, pain, pruritus and fatigue is reported in **Figure 2**; **Supplementary Table 2**. Moderate (G2) dermatitis radiation was recorded at t_1 in 13.7 and 21% of BC and HNSCC patients, respectively, whereas severe (G3) dermatitis radiation was observed in 5.6 and 10.5% of BC and HNSCC, respectively. At t_2, G2 dermatitis radiation was observed in 8% of BC patients and in 33% of HNSCC patients; G3 dermatitis radiation was manifested by 0.8% of BC patients. Pain of G2 grade was present in 5.6% of BC and in 15.8% of HNSCC patients at t_1; 1 month later (t_2), 2.4% of BC and 18% of HNSCC patients manifested G2 pain. At t_1, G3 pain was rarely recorded in BC patients but affected 21% of the HNSCC patients; at t_2 none of the BC and HNSCC patients suffered from pain of G3 grade. Pruritus of G2 and G3 grade was recorded at t_1 in 9.7 and 3.2% of BC patients, respectively, while at t_2, G2 pruritus was present in 8.9% of BC patients. Concerning HNSCC patients, 5.2 and 5.5% of them manifested G3 pruritus at t_1 and t_2, respectively. In summary, HNSCC patients manifested higher degrees of dermatitis radiation and pain at both t_1 and t_2, whereas pruritus appeared to be more pronounced in BC patients. Fatigue (G1 grade) was present in 50.8% (BC) and 57.8% (HNSCC) of patients, and at t_2 in 33.0 and 44.5%, respectively (**Figure 2**).

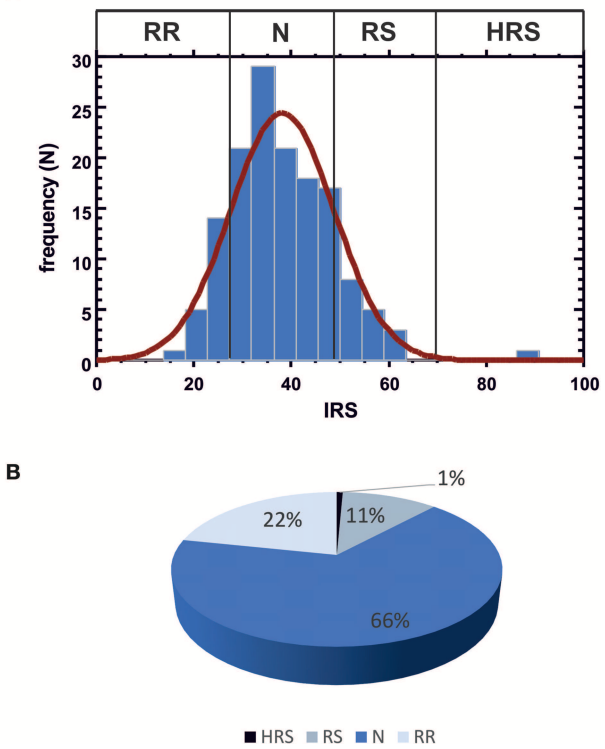

FIGURE 3 | (A) Data distribution for IRS values. Vertical lines indicate the observed thresholds for the 4 classes of individual radiosensitivity, calculated as: RR, mean - SD (IRS < 27.48); N, mean ± SD (27.48 ≤ IRS ≤ 48.72); RS, mean + SD (48.72 < IRS ≤ 69.96); HRS, mean + 3 SD (IRS > 69.96). **(B)** Patient distribution according to the four IRS classes.

G_2-Chromosomal Radiosensitivity in RT Patients

IRS values were determined in the complete patient cohort (143 subjects). In blood cultures exposed *in vitro* to 1 Gy [according to the standardized protocol developed by Pantelias and coworkers (15, 29)], the average yield of G_2 chromatid breaks was 2.5 (with standard deviation SD = 0.084 and coefficient of variation CV = 3%); the average IRS was 38.1 (SD = 10.62; CV = 27.8%). Based on the observed distribution of individual IRS values, the four classes of individual radiosensitivity should be, respectively: RR < 27.48 (mean – SD); 27.48 ≤ N ≤ 48.72 (mean ± SD); 48.72 < RS ≤ 69.96 (mean + SD); HRS > 69.96 (mean + 3×SD) (**Figure 3A**). As these values are in strict agreement with those proposed earlier (15), for further statistical analyses we used the published thresholds (see Materials and Methods). One patient resulted highly radiosensitive (HRS, 1%), 16 patients were classified as radiosensitive (RS, 11%), 95 patients as normal (N, 66%) and 31 as radioresistant (RR, 22%) (**Figure 3B**).

Gene Expression in Blood Samples of RT Patients

Fifteen radioresponsive genes belonging to DDR pathway (**Table 1**) were analyzed by qRT-PCR in blood samples from 57 patients, randomly selected from the whole cohort, in order to have comparable numbers of patients within the four IRS classes (HRS, RS, N, and RR). A summary of the clinical data of this group of patients is available in **Supplementary Table 3**.

Transcription of most genes was significantly induced after the first RT fraction (**Figure 4A**).

The unsupervised cluster analysis of gene expression profiles reported as a heatmap in **Figure 4B** did not reveal differences between the two types of cancer, although the response of DDR genes was variable across patients. Indeed, a group of patients is characterized by high expression values of *MDM2*, *SESN1*, *BCL2*, *ATM*, and *ZMAT3*, however this group did not show significant enrichment for any of the available clinical annotations. Finally, the heatmap did not show any association between IRS index and gene expression changes (**Figure 4B**).

TABLE 1 | Names and function of DDR genes evaluated by qRT-PCR in blood samples from RT patients.

Gene symbol	Gene name	Function
ATM	Ataxia Telangiectasia Mutated	DNA damage signal transduction; cell cycle checkpoint
BAX	BCL2-associated X protein	Apoptosis
BBC3	BCL2-binding component 3 (PUMA)	Apoptosis
BCL2	B-Cell CLL/Lymphoma 2	Apoptosis
CCNG1	Cyclin G1	Cell cycle progression/arrest
CDKN1A	Cyclin-dependent kinase inhibitor 1A (p21)	Cell cycle arrest
cMYC	MYC proto-oncogene, bHLH transcription factor	Cell cycle progression, apoptosis and cellular transformation
DDB2	Damage-specific DNA binding protein 2 (p48)	DNA repair
FDXR	Ferrodoxin reductase	DNA damage, apoptosis
GADD45A	Growth arrest and DNA-damage-inducible, alpha	Growth arrest; DNA repair; apoptosis
MDM2	Mdm2 p53 binding protein homolog	Inactivation of tumor protein p53
PCNA	Proliferating cell nuclear antigen	DNA repair
SESN1	Sestrin 1 (Sestrins)	Cell cycle arrest
XPC	Xeroderma pigmentosum, complementation group C	DNA repair
ZMAT3	Zinc finger, matrin type 3 (PAG608)	Cell growth; apoptosis

Identification of Biomarkers of Radiosensitivity

Univariate and multivariate statistical analyses were performed looking for association between (i) clinical variables of radiation toxicity and IRS index; (ii) clinical variables of radiation toxicity and expression level of DDR genes; (iii) IRS index and expression level of DDR genes.

Relationships between clinical variables of radiation toxicity and IRS classes are shown in **Figure 5.** At the completion of

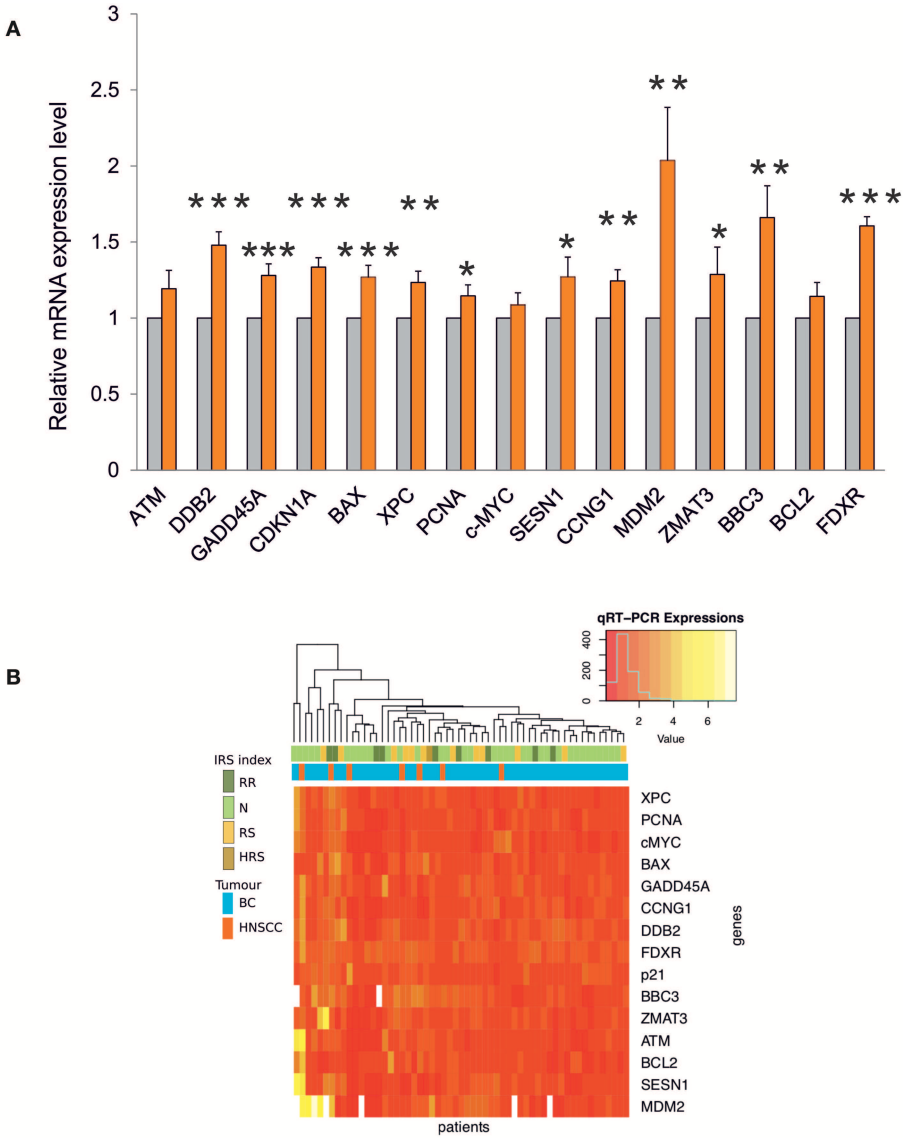

FIGURE 4 | (A) Gene expression analysis by qRT-PCR in blood samples from RT patients. The relative mRNA quantification was performed by comparing irradiated vs. non-irradiated blood samples derived from the same patient. Values are mean ± SE and expressed in fold-change. The value "1" of non-irradiated control (light gray bars) is arbitrarily given when no change is observed (***$p < 0.001$; **$p < 0.01$; *$p < 0.05$). **(B)** Heatmap and unsupervised cluster analysis on the expression profiles of DDR genes analyzed in 57 RT patients. The key color bar indicates standardized gene expression levels (low levels are in red, high levels are in yellow). The annotation bars (upper part of the heatmap) indicate the four classes of IRS index and tumor types.

RT treatment (t_1), patients experiencing adverse effects were distributed within the four IRS classes (HRS, RS, N, and RR), without any significant relationship and without differences between tumor types. Instead, for fatigue the IRS mean values significantly differed between patients with and without such adverse effect. Specifically, the estimated IRS mean values were, respectively, 40.44 and 36.17, with a decrease of 4.27 in patients with G1 fatigue at t_1 ($p = 0.015$, *t*-test). The significance was confirmed by multivariate linear regression model (adjusted for age and disease type) (**Table 2**). Neither the multivariate nor the univariate analyses showed significant association between IRS index and clinical variables of radiation toxicity at t_2.

Significant and moderately significant associations between gene expression and clinical radiation toxicity are shown in **Table 3**. Dermatitis radiation at t_1 was associated with a 1.88-fold change of *FDXR* expression in patients experiencing G3 toxicity vs. a 1.44-fold change in G2 patients. The presence of pain at t_1 was associated with a decrease of *SESN1* expression (0.92- vs. 1.36-fold change

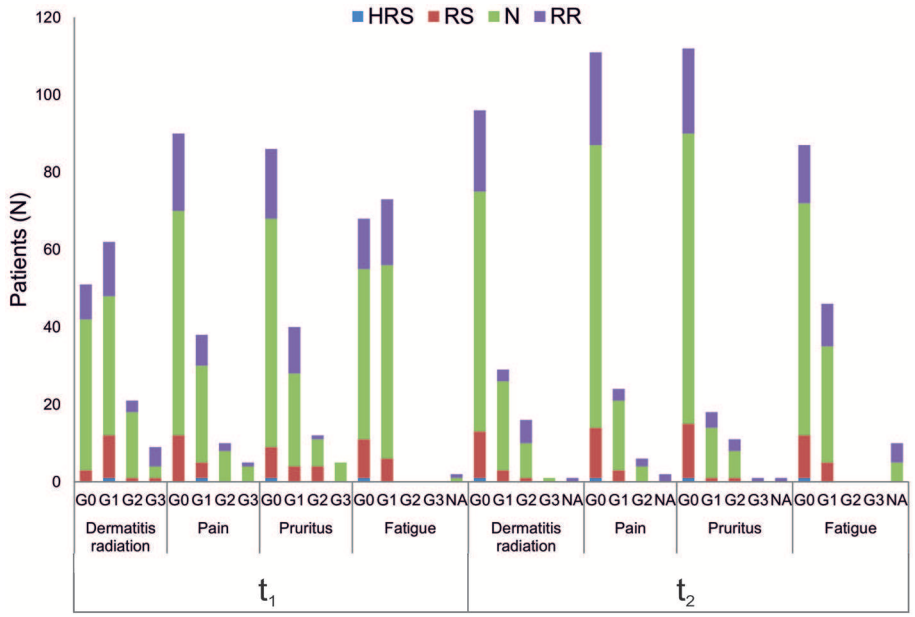

FIGURE 5 | Association analysis between clinical variables of radiation toxicity and IRS index. Number of patients in the four IRS classes (HRS, RS, N, RR) per grades of radiation-induced adverse effects (G0, G1, G2, G3), at the completion of RT treatment (t_1) and 1 month later (t_2). NA, data Not Available.

TABLE 2 | Multivariate linear regression model with IRS values and all clinical variables as covariates in 143 patients.

Coefficients	Estimate	Std. error	*t*-value	Pr(>|t|)	
(Intercept)	39.123	5.804	6.740	4.86e-10	***
Tumor type—HNSCC vs. breast cancer	−1.023	2.967	−0.345	0.730	
Age in years	0.005	0.087	0.060	0.952	
Dermatitis radiation—G1 vs. G0	3.761	2.216	1.697	0.092	□
Dermatitis radiation—G2 vs. G0	−0.072	3.328	−0.022	0.982	
Dermatitis radiation—G3 vs. G0	−4.401	4.623	−0.952	0.342	
Pain—G1 vs. G0	−0.317	2.177	−0.146	0.884	
Pain—G2 vs. G0	−2.143	3.836	−0.559	0.577	
Pain—G3 vs. G0	1.216	6.050	0.201	0.8410	
Pruritus—G1 vs. G0	−1.764	2.324	−0.759	0.449	
Pruritus—G2 vs. G0	2.994	3.558	0.841	0.401	
Pruritus—G3 vs. G0	6.988	5.370	1.301	0.195	
Fatigue–G1 vs. G0	−4.265	1.960	−2.176	0.03	*

IRS is considered as continuous value and clinical variables are those defined at the completion of RT treatment (t1). p-value of the model is 0.2217.
****p-value < 0.001, *p-value < 0.05, □p-value < 0.1.*

in the comparison presence-absence, and 0.97- vs. 1.36-fold change when comparing more specifically G1 vs. G0). Symptoms of pruritus resulted associated at t_1 with a 0.79-fold change of *XPC* and with a 1.01-fold change of *ZMAT3*; at t_2 pruritus was associated with a 0.87-fold change of *ATM*, and a lower *BCL2/BAX* ratio (respectively, 0.76- vs. 1.15-fold change). G1 fatigue resulted associated with a 1.19-fold change of *CDKN1A* (p21) at the second clinical evaluation.

TABLE 3 | DDR genes associated with clinical variables of radiation toxicity.

Clinical variable	Gene	Gene expression value[a]	Toxicity grade	Adjusted *p-value*	RT timing
Dermatitis radiation	*FDXR*	1.44	G2	0.096[c]	t_1
		1.88	G3		
Pain	*SESN1*	1.36	G0	0.043[b]	t_1
		0.97	G1		
	SESN1	1.36	Absent	0.020[b]	t_1
		0.92	Present		
Pruritus	*XPC*	1.49	G1	0.102[c]	t_1
		0.79	G2		
	ZMAT3	1.43	G0	0.046[b]	t_1
		1.01	G1		
	ATM	1.29	Absent	0.021[b]	t_2
		0.87	Present		
	BCL2/BAX	1.15	Absent	0.011[b]	t_2
		0.76	Present		
Fatigue	*CDKN1A*	1.42	G0	0.049[b]	t_2
		1.19	G1		

[a]Gene expression values are reported in irradiated relative to non-irradiated blood samples from RT patients and expressed in fold-change. [b]t-test; [c]Wilcoxon test. Bonferroni adjusted p-value is significant when <0.05, moderately significant when <0.10.

By univariate analyses (**Table 4**) we found a moderate significant association between the RS class and *BBC3* and *FDXR* expression (adjusted $p = 0.069$) and between RR class and *GADD45A* expression (adjusted $p = 0.096$). The *BCL2/BAX* ratio was also associated with the RS class (adjusted $p = 0.017$).

TABLE 4 | DDR genes associated with IRS classes in RT patients.

Gene	Gene expression value[a]	IRS class	Adjusted *p-value*
BBC3	1.28	N	0.069[b]
	1.90	RS	
FDXR	1.53	N	0.069[b]
	1.84	RS	
GADD45A	1.19	N	0.096[c]
	1.73	RR	
BCL2/BAX	1.15	N	0.017[b]
	0.73	RS	

[a]*Gene expression values are reported in irradiated relative to non-irradiated blood samples from RT patients and expressed in fold-change.* [b]*t-test;* [c]*Wilcoxon test. Bonferroni adjusted p-value is significant when <0.05, moderately significant when <0.10.*

DISCUSSION

Despite the advancements in understanding and preventing RT effects on normal tissue, injuries deriving from radiation therapy cannot be avoided (33–35). Inter-individual differences in radiosensitivity are due to different endogenous and exogenous factors (e.g., DNA repair capacity, age, diet, and life-style) as well as to the experimental endpoint (clinical radiation toxicity, chromosome aberrations, etc.) (15, 27, 36, 37). Assessing the intrinsic component of radiosensitivity before RT could predict toxicity risk and improve the QOL (27, 28). To this purpose, from a cohort of oncological patients we collected data concerning radiation toxicity in normal tissues, *in vitro* G_2-chromosomal radiosensitivity and *in vivo* expression level of 15 selected radioresponsive genes of DDR pathway, to find possible associations between genetic features and clinical radiosensitivity (**Figure 1**). By univariate and multivariate statistical models we have looked at significant associations between clinical and molecular data, controlling for potential confounders and for the multiplicity of the tests. Remarkably, no statistical differences have found between tumor types, allowing us to discuss our data as a whole.

To the best of our knowledge, this is the first study assessing the relationship between the three experimental endpoints in a cohort of RT-treated oncological patients. It is noteworthy that all patients have been enrolled in the same Radiotherapy Unit (IOV-IRCSS). Specifically, in this explorative study we considered breast and head and neck cancer patients as representative of patients experiencing radiation toxicity. Indeed, symptoms of grade 2 acute skin toxicity are observed in 15–24% of breast cancer patients at the completion of RT treatment (35, 38) whereas dermatitis radiation continues to be one of the most common side effects of RT in head and neck cancers (33, 39). In the present study, we considered dermatitis radiation, pain, pruritus and fatigue that are adverse effects commonly manifested in BC and HNSCC patients after RT, while tumor-specific adverse effects were excluded. Overall, HNSCC patients manifested higher degrees of dermatitis radiation and pain both at t_1 and t_2, whereas pruritus was more pronounced in BC patients at both t_1 and t_2 (**Figure 2**). For patients experiencing the highest level of dermatitis radiation we verified *ex post* the lack of relation with the phototype (Fitzpatrick scale). Fatigue induced by RT is a common symptom experienced by patients that deeply affects their QOL (40). In our cohort, all patients manifesting fatigue were evaluated as G1 grade, with overlapping proportions irrespective of cancer type: at t_1 50.8% (BC) and 57.8% (HNSCC), and at t_2 33.0 and 44.5%, respectively (**Figure 2**).

Previous studies showed that clinical radiation toxicity is related to G_2-chromosomal radiosensitivity of *in vitro* irradiated lymphocytes (13, 19, 41). Here, we followed the standardized G_2-assay developed by Pantelias and Terzoudi (15) in which the G_2-checkpoint efficiency is abrogated by caffeine (inhibitor of ATM kinase) to maximize the radio-induced chromosomal damage, i.e., simulating the condition of high radiosensitivity of AT (Ataxia Telangiectasia) patients. This leads to accurate estimations of the individual radiosensitivity (the IRS index) by calculating the percentage ratio between the yields of radio-induced chromatid breaks in presence or absence of the functional G_2-checkpoint (15, 29). IRS values obtained in the present study were distributed in strict agreement with previously published data (15, 29), confirming the reproducibility of the standardized G_2-assay for assessing individual radiosensitivity *in vitro*. Based on multivariate analyses, fatigue emerged as the only adverse effect strictly associated with IRS index. Interestingly, in patients displaying G1 vs. G0 fatigue but having same values of other predictors, the average IRS index differed for a value of 4.27. No other clinical reactions were found associated with IRS values in this statistical analysis (**Table 2**).

Clinical radiosensitivity can be associated with individual factors, such as abnormal transcriptional responses to DNA damage and with defects in DNA repair (42–44). In this regard, previous studies of gene expression profiling, carried out in patient-derived PBLs irradiated *in vitro*, succeeded to some extent in discriminating groups of patients with and without severe late radiotherapy toxicity (23). An association was also observed between early skin reaction and the transcriptional response of lymphoblastoid cells derived from patients with acute radiation toxicity (4). The candidate genes here analyzed, belonging to the DNA Damage Response (DDR) pathway, were chosen on the basis of our previous data showing significant changes in their expression level in human PBLs at 24 h after irradiation with 2 Gy of γ-rays (30, 31). Moreover, *GADD45A*, *CDKN1A*, *DDB2* and *XPC*, together with *FDXR* gene are well-known radio-responsive genes (4, 26, 30, 31, 45, 46). Gene expression analyses have been carried out in 57 patients randomly selected within the cohort of 143 patients, as representative of the four IRS classes (HRS, RS, N, and RR). This sample size is adequate to identify significant differences of gene expression among the four IRS classes (statistical power 0.83), either by ANOVA or Wilcoxon test. The expression of DDR genes was on the whole significantly induced at 24 h after the first fractionated dose (**Figure 4A**), in accordance with their radioresponsiveness. Notably, *FDXR* expression showed a 1.6-fold increase, that is very similar to the ∼1.7-fold increase reported at the same time point in four breast cancer and 8 HNSCC patients (26). In humans, *FDXR* expression is upregulated in a dose-dependent

manner after irradiation, both *ex vivo* and *in vivo*, indicating that *FDXR* is a good biomarker for radiation exposure and for estimating *in vivo* dose (46–48). Moreover, *FDXR* belongs to a genetic signature for the early prediction of hematological acute radiation syndrome (47, 49). Unlike those authors who have found no association between *FDXR* expression and the hematological acute radiation syndrome in subjects undergoing RT, our work associates *FDXR* expression level with dermatitis radiation at the completion of RT treatment (G2 vs. G3 grades, adjusted $p = 0.096$) (**Table 3**). While the expression level of *FDXR* gene increased in patients experiencing a high grade of dermatitis radiation, those of *SESN1*, *ATM*, *XPC*, *ZMAT3*, *CDKN1A* genes decreased when radiation toxicity was manifested (**Table 3**). Of course, these findings may be explained by a more complex radiation response than that determined by the DDR genes here analyzed. Indeed, additional genes belonging to different pathways are expected to participate in the whole cellular response to radiation. Emerging evidence suggests that the response to radiation is differently regulated in normal vs. cancer cells/tissues, and even within organism, where maintaining the overall homeostasis is a priority (50, 51). Interestingly, the tight interplay between DDR and immune response seems a key feature shared by systems that differ for higher levels of complexity (51).

By integrating the data of chromosomal radiosensitivity and gene expression we found that IRS classes were associated with the expression level of three DDR genes. In particular, the increased expression of *BBC3* and *FDXR* genes, involved in the apoptotic pathway, is associated with the RS class, whereas the increased expression of *GADD45A,* regulating cell growth and apoptosis, is associated with the RR class (**Table 4**). A role of apoptotic pathway in normal tissue radiation toxicity has been previously reported, indeed the T-lymphocyte apoptosis assay significantly predicted differences in late radiation toxicity (52). Also the balance between pro-apoptotic and anti-apoptotic members of the BCL-2 family has a clinical significance on chemotherapy sensitivity and survival (53, 54). In our cohort, the *BCL2/BAX* ratio resulted associated both with the presence of pruritus 1 month after the completion of RT treatment (**Table 3**), and with the class of patients classified as radiosensitive by means of IRS index (**Table 4**). This common function is reinforcing the predictive value of these genes, although further analyses are necessary to support that they are reliable biomarkers of radiation toxicity.

Given the exploratory and pilot nature of our work, we privileged a cohort of RT patients, enrolled, treated and clinically evaluated in the same clinical Institute, irrespective of the tumor site. However, despite our multivariate analysis shows no statistical differences between BC and HNSCC patients (**Table 2**; **Figure 4**) future studies would be desirable to validate our results in a new cohort, taking into account additional clinical variables such as breast size, body mass index, alcohol consumption, hypertension, smoking habit, which might be associated to acute skin toxicity (55–57). Moreover, dosimetric data, radiation treatment volumes and doses to specific organs at risk would be important information to be included in future studies. Clearly, since HNSCC patients are less frequent than BC patients and often must undergo chemotherapy either before or concomitant to RT, multicentric studies would be recommended to reach a large sample size for both diseases.

CONCLUSION

The possibility to identify patients that are sensitive to radiation and at risk of suffering adverse effects would help clinicians in tailoring the best RT protocol and improve patient's QOL. In this prospective cohort study, we found that symptoms of dermatitis radiation, pain, pruritus and fatigue were associated with the expression level of some genes of the DNA-damage response pathway (*FDXR*, *SESN1*, *XPC*, *ZMAT3*, *ATM*, *BCL2/BAX*, *and CDKN1A*). We also found that fatigue was significantly associated with IRS values; moreover, IRS classes resulted associated with the expression level of *BBC3*, *FDXR*, *GADD45A*, and *BCL2/BAX* genes.

Of course, radiation-induced side effects comprehend a complex cellular and tissue response that cannot be limited to the expression level of the DDR genes considered in this study, but it is rather regulated by a wide network of gene-interactions. The development of a reproducible and powerful assay to predict individual normal tissue radiosensitivity has been referred to as the "holy grail" of radiotherapy. Although several *in vitro* assays have been tested to identify reliable biomarkers able to predict normal tissue radiosensitivity, results obtained up to now are not informative enough. In this regard, our multidisciplinary approach can contribute to delineate the genetic features of patients manifesting different grades of radiation-induced toxicity.

DATA AVAILABILITY STATEMENT

The datasets analyzed during the current study are available from the corresponding authors on reasonable request.

ETHICS STATEMENT

The studies involving human participants were reviewed and approved by IOV-IRCCS Ethic Committee. The patients/participants provided their written informed consent to participate in this study.

AUTHOR CONTRIBUTIONS

LC, DZ, AR, and MM conceived and designed the study. EF, EG, FB, BE, and MR contributed in enrollment of patients, radiotherapy treatment, and clinical follow-up. EP and CP carried out the experiments of gene expression and participated in data evaluation. LB carried out the experiments of G2-chromosomal assay. EC and CR performed the statistical analyses and participated in data evaluation. MM and AR wrote the final manuscript. The definitive supervision of the paper was done by LC. All authors contributed to the initial draft, read, and approved the final manuscript.

FUNDING

This work was supported by the fund 5 × 1000 IOV- Demabio 1 Demabio 2 (Veneto Institute of Oncology IOV–IRCCS).

ACKNOWLEDGMENTS

We are grateful to Prof. Giuseppe Opocher (Veneto Institute of Oncology IOV–IRCCS) for scientific advice and support. We gratefully acknowledge Vito Barbieri (Department of Surgical, Oncological and Gastroenteric Sciences, University of Padova) for support with cell irradiation.

SUPPLEMENTARY MATERIAL

The Supplementary Material for this article can be found online at: https://www.frontiersin.org/articles/10.3389/fonc.2019.00987/full#supplementary-material

REFERENCES

1. De Ruysscher D, Niedermann G, Burnet NG, Siva S, Lee AWM, Hegi-Johnson F. Radiotherapy toxicity. *Nat Rev Dis Prim.* (2019) 5:13. doi: 10.1038/s41572-019-0064-5
2. Burnet NG, Johansen J, Turesson I, Nyman J, Peacock JH. Describing patients' normal tissue reactions: concerning the possibility of individualising radiotherapy dose prescriptions based on potential predictive assays of normal tissue radiosensitivity. *Int J Cancer.* (1998) 79:606–13. doi: 10.1002/(SICI)1097-0215(19981218)79:6<606::AID-IJC9>3.0.CO;2-Y
3. Azria D, Lapierre A, Gourgou S, De Ruysscher D, Colinge J, Lambin P, et al. Data-based radiation oncology: design of clinical trials in the toxicity biomarkers era. *Front Oncol.* (2017) 7:1–11. doi: 10.3389/fonc.2017.00083
4. Rieger KE, Hong W-J, Tusher VG, Tang J, Tibshirani R, Chu G. Toxicity from radiation therapy associated with abnormal transcriptional responses to DNA damage. *Proc Natl Acad Sci USA.* (2004) 101:6635–40. doi: 10.1073/pnas.0307761101
5. Foray N, Colin C, Bourguignon M. 100 years of individual radiosensitivity: how we have forgotten the evidence. *Radiology.* (2012) 264:627–31. doi: 10.1148/radiol.12112560
6. The 2007 recommendations of the International Commission on Radiological Protection. ICRP publication 103. *Ann ICRP.* (2007) 37:1–332. doi: 10.1016/j.icrp.2007.10.003
7. AGIR. *Human Radiosensitivity. Report of the Independent Advisory Group on Ionising Radiation.* Chilton, Doc HPA, RCE-21 (2013).
8. Barnett GC, West CML, Dunning AM, Elliott RM, Coles CE, iPharoah PDP, et al. Normal tissue reactions to radiotherapy: towards tailoring treatment dose by genotype. *Nat Rev Cancer.* (2009) 9:134–42. doi: 10.1038/nrc2587
9. Aparicio T, Baer R, Gautier J. DNA double-strand break repair pathway choice and cancer. *DNA Repair.* (2014) 19:169–75. doi: 10.1016/j.dnarep.2014.03.014
10. Harper JW, Elledge SJ. The DNA damage response: ten years after. *Mol Cell.* (2007) 28:739–45. doi: 10.1016/j.molcel.2007.11.015
11. Goldstein M, Kastan MB. The DNA damage response: implications for tumor responses to radiation and chemotherapy. *Annu Rev Med.* (2015) 66:129–43. doi: 10.1146/annurev-med-081313-121208
12. Durante M, Bedford JS, Chen DJ, Conrad S, Cornforth MN, Natarajan AT, et al. From DNA damage to chromosome aberrations: joining the break. *Mutat Res Toxicol Environ Mutagen.* (2013) 756:5–13. doi: 10.1016/j.mrgentox.2013.05.014
13. Borgmann K, Hoeller U, Nowack S, Bernhard M, Röper B, Brackrock S, et al. Individual radiosensitivity measured with lymphocytes may predict the risk of acute reaction after radiotherapy. *Int J Radiat Oncol.* (2008) 71:256–64. doi: 10.1016/j.ijrobp.2008.01.007
14. Barber JB., Burrill W, Spreadborough AR, Levine E, Warren C, Kiltie AE, et al. Relationship between *in vitro* chromosomal radiosensitivity of peripheral blood lymphocytes and the expression of normal tissue damage following radiotherapy for breast cancer. *Radiother Oncol.* (2000) 55:179–86. doi: 10.1016/S0167-8140(99)00158-9
15. Pantelias GE, Terzoudi GI. A standardized G2-assay for the prediction of individual radiosensitivity. *Radiother Oncol.* (2011) 101:28–34. doi: 10.1016/j.radonc.2011.09.021
16. Bryant PE, Gray L, Riches AC, Steel CM, Finnon P, Howe O, et al. The G2 chromosomal radiosensitivity assay. *Int J Radiat Biol.* (2002) 78:863–6. doi: 10.1080/09553000210144484
17. Scott D, Spreadborough AR, Jones LA, Roberts SA, Moore CJ. Chromosomal radiosensitivity in G2-phase lymphocytes as an indicator of cancer predisposition. *Radiat Res.* (1996) 145:3–16. doi: 10.2307/3579189
18. Lobachevsky P, Leong T, Daly P, Smith J, Best N, Tomaszewski J, et al. Compromized DNA repair as a basis for identification of cancer radiotherapy patients with extreme radiosensitivity. *Cancer Lett.* (2016) 383:212–9. doi: 10.1016/j.canlet.2016.09.010
19. De Ruyck K, Van Eijkeren M, Claes K, Morthier R, De Paepe A, Vral A, et al. Radiation-induced damage to normal tissues after radiotherapy in patients treated for gynecologic tumors: association with single nucleotide polymorphisms in XRCC1, XRCC3, and OGG1 genes and *in vitro* chromosomal radiosensitivity in lymphocytes. *Int J Radiat Oncol.* (2005) 62:1140–9. doi: 10.1016/j.ijrobp.2004.12.027
20. Alam A, Mukhopadhyay ND, Ning Y, Reshko LB, Cardnell RJG, Alam O, et al. A preliminary study on racial differences in HMOX1, NFE2L2, and TGFβ1 gene polymorphisms and radiation-induced late normal tissue toxicity. *Int J Radiat Oncol.* (2015) 93:436–43. doi: 10.1016/j.ijrobp.2015.05.049
21. Oliva D, Nilsson M, Strandéus M, Andersson B-Å, Sharp L, Laytragoon-Lewin N, et al. Individual genetic variation might predict acute skin reactions in women undergoing adjuvant breast cancer radiotherapy. *Anticancer Res.* (2018) 38:6763–70. doi: 10.21873/anticanres.13047
22. Borghini A, Vecoli C, Mercuri A, Petruzzelli MF, D'Errico MP, Portaluri M, et al. Genetic risk score and acute skin toxicity after breast radiation therapy. *Cancer Biother Radiopharm.* (2014) 29:267–72. doi: 10.1089/cbr.2014.1620
23. Svensson JP, Stalpers LJ, Esveldt-van Lange RE, Franken NA, Haveman J, Klein B, et al. Analysis of gene expression using gene sets discriminates cancer patients with and without late radiation toxicity. *PLoS Med.* (2006) 3:e422. doi: 10.1371/journal.pmed.0030422
24. Finnon P, Kabacik S, MacKay A, Raffy C, A'Hern R, Owen R, et al. Correlation of *in vitro* lymphocyte radiosensitivity and gene expression with late normal tissue reactions following curative radiotherapy for breast cancer. *Radiother Oncol.* (2012) 105:329–36. doi: 10.1016/j.radonc.2012.10.007
25. Badie C, Dziwura S, Raffy C, Tsigani T, Alsbeih G, Moody J, et al. Aberrant CDKN1A transcriptional response associates with abnormal sensitivity to radiation treatment. *Br J Cancer.* (2008) 98:1845–51. doi: 10.1038/sj.bjc.6604381
26. O'Brien G, Cruz-Garcia L, Majewski M, Grepl J, Abend M, Port M, et al. FDXR is a biomarker of radiation exposure *in vivo*. *Sci Rep.* (2018) 8:684. doi: 10.1038/s41598-017-19043-w
27. Herskind C, Talbot CJ, Kerns SL, Veldwijk MR, Rosenstein BS, West CML. Radiogenomics: a systems biology approach to understanding genetic risk factors for radiotherapy toxicity? *Cancer Lett.* (2016) 382:95–109. doi: 10.1016/j.canlet.2016.02.035
28. Pavlopoulou A, Bagos PG, Koutsandrea V, Georgakilas AG. Molecular determinants of radiosensitivity in normal and tumor tissue: a bioinformatic approach. *Cancer Lett.* (2017) 403:37–47. doi: 10.1016/j.canlet.2017.05.023
29. Terzoudi GI, Hatzi VI, Barszczewska K, Manola KN, Stavropoulou C, Angelakis P, et al. G2-checkpoint abrogation in irradiated lymphocytes: a new cytogenetic approach to assess individual radiosensitivity and predisposition to cancer. *Int J Oncol.* (2009) 35:1223–30. doi: 10.3892/ijo_00000439

30. Mognato M, Celotti L. Modeled microgravity affects cell survival and HPRT mutant frequency, but not the expression of DNA repair genes in human lymphocytes irradiated with ionising radiation. *Mutat Res.* (2005) 578:417–29. doi: 10.1016/j.mrfmmm.2005.06.011
31. Girardi C, De Pittà C, Casara S, Sales G, Lanfranchi G, Celotti L, et al. Analysis of miRNA and mRNA expression profiles highlights alterations in ionizing radiation response of human lymphocytes under modeled microgravity. *PLoS ONE.* (2012) 7:e31293. doi: 10.1371/journal.pone.0031293
32. Pfaffl MW. A new mathematical model for relative quantification in real-time RT-PCR. *Nucleic Acids Res.* (2001) 29:e45. doi: 10.1093/nar/29.9.e45
33. Trotti A, Bellm LA, Epstein JB, Frame D, Fuchs HJ, Gwede CK, et al. Mucositis incidence, severity and associated outcomes in patients with head and neck cancer receiving radiotherapy with or without chemotherapy: a systematic literature review. *Radiother Oncol.* (2003) 66:253–62. doi: 10.1016/S0167-8140(02)00404-8
34. Peponi E, Glanzmann C, Willi B, Huber G, Studer G. Dysphagia in head and neck cancer patients following intensity modulated radiotherapy (IMRT). *Radiat Oncol.* (2011) 6:1. doi: 10.1186/1748-717X-6-1
35. Ciammella P, Podgornii A, Galeandro M, Micera R, Ramundo D, Palmieri T, et al. Toxicity and cosmetic outcome of hypofractionated whole-breast radiotherapy: predictive clinical and dosimetric factors. *Radiat Oncol.* (2014) 9:1–10. doi: 10.1186/1748-717X-9-97
36. Smart V, Curwen GB, Whitehouse CA, Edwards A, Tawn EJ. Chromosomal radiosensitivity: a study of the chromosomal G2assay in human blood lymphocytes indicating significant inter-individual variability. *Mutat Res.* (2003) 528:105–10. doi: 10.1016/S0027-5107(03)00076-9
37. Vral A, Thierens H, Baeyens A, De Ridder L. Chromosomal aberrations and *in vitro* radiosensitivity: intra-individual versus inter-individual variability. *Toxicol Lett.* (2004) 149:345–52. doi: 10.1016/j.toxlet.2003.12.044
38. Valli M, Cima S, Gaudino D, Cartolari R, Deantonio L, Frapolli M, et al. Skin and lung toxicity in synchronous bilateral breast cancer treated with volumetric-modulated arc radiotherapy: a mono-institutional experience. *Clin Transl Oncol.* (2019). doi: 10.1007/s12094-019-02077-z. [Epub ahead of print].
39. Hegedus F, Mathew LM, Schwartz RA. Radiation dermatitis: an overview. *Int J Dermatol.* (2017) 56:909–14. doi: 10.1111/ijd.13371
40. Hopwood P, Haviland JS, Sumo G, Mills J, Bliss JM, Yarnold JR. Comparison of patient-reported breast, arm, and shoulder symptoms and body image after radiotherapy for early breast cancer: 5-year follow-up in the randomised Standardisation of Breast Radiotherapy (START) trials. *Lancet Oncol.* (2010) 11:231–40. doi: 10.1016/S1470-2045(09)70382-1
41. Guogyte K, Plieskiene A, Ladygiene R, Vaisiunas Ž, Sevriukova O, Janušonis V, et al. Assessment of correlation between chromosomal radiosensitivity of peripheral blood lymphocytes after *in vitro* irradiation and normal tissue side effects for cancer patients undergoing radiotherapy. *Genome Integr.* (2017) 8:2. doi: 10.4103/2041-9414.198907
42. Andreassen CN, Alsner J, Overgaard M, Sørensen FB, Overgaard J. Risk of radiation-induced subcutaneous fibrosis in relation to single nucleotide polymorphisms in TGFB1, SOD2, XRCC1, XRCC3, APEX and ATM–a study based on DNA from formalin fixed paraffin embedded tissue samples. *Int J Radiat Biol.* (2006) 82:577–86. doi: 10.1080/09553000600876637
43. Andreassen CN, Alsner J. Genetic variants and normal tissue toxicity after radiotherapy: a systematic review. *Radiother Oncol.* (2009) 92:299–309. doi: 10.1016/j.radonc.2009.06.015
44. Goodarzi AA, Jeggo PA. Irradiation induced foci (IRIF) as a biomarker for radiosensitivity. *Mutat Res Mol Mech Mutagen.* (2012) 736:39–47. doi: 10.1016/j.mrfmmm.2011.05.017
45. Amundson SA, Do KT, Shahab S, Bittner M, Meltzer P, Trent J, et al. Identification of potential mRNA biomarkers in peripheral blood lymphocytes for human exposure to ionizing radiation. *Radiat Res.* (2000) 154:342–6. doi: 10.1667/0033-7587(2000)154[0342:iopmbi]2.0.co;2
46. Manning G, Kabacik S, Finnon P, Bouffler S, Badie C. High and low dose responses of transcriptional biomarkers in *ex vivo* X-irradiated human blood. *Int J Radiat Biol.* (2013) 89:512–22. doi: 10.3109/09553002.2013.769694
47. Port M, Majewski M, Herodin F, Valente M, Drouet M, Forcheron F, et al. Validating baboon *ex vivo* and *in vivo* radiation-related gene expression with corresponding human data. *Radiat Res.* (2018) 189:389–98. doi: 10.1667/RR14958.1
48. Abend M, Badie C, Quintens R, Kriehuber R, Manning G, Macaeva E, et al. Examining radiation-induced *in vivo* and *in vitro* gene expression changes of the peripheral blood in different laboratories for biodosimetry purposes: first RENEB gene expression study. *Radiat Res.* (2016) 185:109–23. doi: 10.1667/RR14221.1
49. Port M, Herodin F, Valente M, Drouet M, Lamkowski A, Majewski M, et al. First generation gene expression signature for early prediction of late occurring hematological acute radiation syndrome in baboons. *Radiat Res.* (2016) 186:39–54. doi: 10.1667/RR14318.1
50. Georgakilas AG, Pavlopoulou A, Louka M, Nikitaki Z, Vorgias CE, Bagos PG. Michalopoulos I. Emerging molecular networks common in ionizing radiation, immune and inflammatory responses by employing bioinformatics approaches. *Cancer Lett.* (2015) 368:164–72. doi: 10.1016/j.canlet.2015.03.021
51. Pateras IS, Havaki S, Nikitopoulou X, Vougas K, Townsend PA, Panayiotidis MI, et al. The DNA damage response and immune signaling alliance: is it good or bad? Nature decides when and where. *Pharmacol Ther.* (2015) 154:36–56. doi: 10.1016/j.pharmthera.2015.06.011
52. Ozsahin M, Crompton NEA, Gourgou S, Kramar A, Li L, Shi Y, et al. CD4 and CD8 T-lymphocyte apoptosis can predict radiation-induced late toxicity: a prospective study in 399 patients. *Clin Cancer Res.* (2005) 11:7426–33. doi: 10.1158/1078-0432.CCR-04-2634
53. Avgeris M, Stamati L, Kontos CK, Piatopoulou D, Marmarinos A, Xagorari M, et al. BCL2L12 improves risk stratification and prediction of BFM-chemotherapy response in childhood acute lymphoblastic leukemia. *Clin Chem Lab Med.* (2018) 56:2104–18. doi: 10.1515/cclm-2018-0507
54. Del Principe MI, Bo MD, Bittolo T, Buccisano F, Rossi FM, Zucchetto A, et al. Clinical significance of bax/bcl-2 ratio in chronic lymphocytic leukemia. *Haematologica.* (2016) 101:77–85. doi: 10.3324/haematol.2015.131854
55. Kole AJ, Kole L, Moran MS. Acute radiation dermatitis in breast cancer patients: challenges and solutions. *Breast Cancer Targets Ther.* (2017) 9:313–23. doi: 10.2147/BCTT.S109763
56. Pignol JP, Olivotto I, Rakovitch E, Gardner S, Sixel K, Beckham W, et al. A multicenter randomized trial of breast intensity-modulated radiation therapy to reduce acute radiation dermatitis. *J Clin Oncol.* (2008) 26:2085–92. doi: 10.1200/JCO.2007.15.2488
57. Twardella D, Popanda O, Helmbold I, Ebbeler R, Benner A, Von Fournier D, et al. Personal characteristics, therapy modalities and individual DNA repair capacity as predictive factors of acute skin toxicity in an unselected cohort of breast cancer patients receiving radiotherapy. *Radiother Oncol.* (2003) 69:145–53. doi: 10.1016/S0167-8140(03)00166-X

Conflict of Interest: The authors declare that the research was conducted in the absence of any commercial or financial relationships that could be construed as a potential conflict of interest.

Citation: Palumbo E, Piotto C, Calura E, Fasanaro E, Groff E, Busato F, El Khouzai B, Rigo M, Baggio L, Romualdi C, Zafiropoulos D, Russo A, Mognato M and Corti L (2019) Individual Radiosensitivity in Oncological Patients: Linking Adverse Normal Tissue Reactions and Genetic Features. Front. Oncol. 9:987. doi: 10.3389/fonc.2019.00987

frontiers in Oncology

ORIGINAL RESEARCH
published: 16 December 2019
doi: 10.3389/fonc.2019.01411

External Validation of Radiation-Induced Dyspnea Models on Esophageal Cancer Radiotherapy Patients

Zhenwei Shi[1], Kieran G. Foley[2], Juan Pablo de Mey[3], Emiliano Spezi[4], Philip Whybra[4], Tom Crosby[2], Johan van Soest[1], Andre Dekker[1] and Leonard Wee[1]*

[1] Department of Radiation Oncology (MAASTRO), GROW School for Oncology and Developmental Biology, Maastricht University Medical Centre+, Maastricht, Netherlands, [2] Velindre Cancer Centre, Cardiff, United Kingdom, [3] Faculty of Health Medicine and Life Sciences (FHML), Maastricht University, Maastricht, Netherlands, [4] School of Engineering, Cardiff University, Cardiff, United Kingdom

Purpose: Radiation-induced lung disease (RILD), defined as dyspnea in this study, is a risk for patients receiving high-dose thoracic irradiation. This study is a TRIPOD (Transparent Reporting of A Multivariable Prediction Model for Individual Prognosis or Diagnosis) Type 4 validation of previously-published dyspnea models via secondary analysis of esophageal cancer SCOPE1 trial data. We quantify the predictive performance of these two models for predicting the maximal dyspnea grade $\geq$ 2 within 6 months after the end of high-dose chemo-radiotherapy for primary esophageal cancer.

Materials and methods: We tested the performance of two previously published dyspnea risk models using baseline, treatment and follow-up data on 258 esophageal cancer patients in the UK enrolled into the SCOPE1 multi-center trial. The tested models were developed from lung cancer patients treated at MAASTRO Clinic (The Netherlands) from the period 2002 to 2011. The adverse event of interest was dyspnea $\geq$ Grade 2 (CTCAE v3) within 6 months after the end of radiotherapy. As some variables were missing randomly and cannot be imputed, 212 patients in the SCOPE1 were used for validation of model 1 and 255 patients were used for validation of model 2. The model parameter Forced Expiratory Volume in 1 s (FEV_1), as a predictor to both validated models, was imputed using the WHO performance status. External validation was performed using an automated, decentralized approach, without exchange of individual patient data.

Results: Out of 258 patients with esophageal cancer in SCOPE1 trial data, 38 patients (14.7%) developed radiation-induced dyspnea ($\geq$ Grade 2) within 6 months after chemo-radiotherapy. The discrimination performance of the models in esophageal cancer patients treated with high-dose external beam radiotherapy was moderate, area under curve (AUC) of 0.68 (95% CI 0.55–0.76) and 0.70 (95% CI 0.58–0.77), respectively. The curves and AUCs derived by distributed learning were identical to the results from validation on a local host.

OPEN ACCESS

Edited by:
Claudio Fiorino, San Raffaele Hospital (IRCCS), Italy

Reviewed by:
Laura Cella, Italian National Research Council (CNR), Italy
Michele Avanzo, Centro di Riferimento Oncologico di Aviano (IRCCS), Italy

****Correspondence:***
Zhenwei Shi
zhenwei.shi@maastro.nl

Specialty section:
This article was submitted to Radiation Oncology, a section of the journal Frontiers in Oncology

Received: *27 August 2019*
Accepted: *28 November 2019*
Published: *16 December 2019*

Citation:
Shi Z, Foley KG, Pablo de Mey J, Spezi E, Whybra P, Crosby T, Soest Jv, Dekker A and Wee L (2019) External Validation of Radiation-Induced Dyspnea Models on Esophageal Cancer Radiotherapy Patients. Front. Oncol. 9:1411. doi: 10.3389/fonc.2019.01411

Conclusion: We have externally validated previously published dyspnea models using an esophageal cancer dataset. FEV_1 that is not routinely measured for esophageal cancer was imputed using WHO performance status. Prediction performance was not statistically different from previous training and validation sets. Risk estimates were dominated by WHO score in Model 1 and baseline dyspnea in Model 2. The distributed learning approach gave the same answer as local processing, and could be performed without accessing a validation site's individual patients-level data.

Keywords: radiation-induced dyspnea, esophageal cancer, chemo-radiotherapy, prognostic model, distributed learning

INTRODUCTION

In radiation therapy, radical radiation doses are expected to provide better local control than lower palliative doses, however the risk of radiation-induced adverse events is increased. Clinical symptoms of radiation-induced lung disease (RILD) include dyspnea, cough, and fever, which can have a serious effect on the patient's quality of life. Approximately 10–20% of patients with lung cancer who receive (chemo)-radiotherapy developing moderate to severe symptomatic RILD (1).

Radiation-induced dyspnea (RILD in this study) is a side-effect for patients treated with high-dose thoracic irradiation. Studies have reported the predictors for radiation-induced dyspnea for lung cancer patients treated with (chemo)radiotherapy (2, 3). The risk factors for RILD include dosimetric factors, clinical factors, pathological factors and blood biomarkers (2–16). In our knowledge, there is no published study reporting the risk factors of radiation-induced dyspnea for patients with primary esophageal cancer, which might be explained by the fact that dyspnea is not routinely assessed during follow-up of esophageal cancer treatment.

The current study conducted a TRIPOD (Transparent Reporting of A Multivariable Prediction Model for Individual Prognosis or Diagnosis) Type 4 validation (17) of previously-published dyspnea models M1 (2) and M2 (3) via secondary analysis of the SCOPE1 (18, 19) dataset. SCOPE1 was a randomized controlled trial investigating the effects of chemo-radiotherapy with and without additional cetuximab in patients with esophageal cancer, including follow-up assessments of dyspnea. We quantify the predictive performance of these two models for predicting the maximal dyspnea grade ≥ 2 within 6 months after the end of high-dose chemo-radiotherapy for primary esophageal cancer. The goal of this study is to verify two hypotheses: (I) that a common thoracic RILD model may be feasible for a different index tumor and (II) that it is feasible to perform an external validation of a toxicity model between two sites via a distributed learning approach without any exchange of patient-specific records.

METHODS AND MATERIALS

Model Development Cohorts

Patient characteristics in the development and validation cohorts are detailed in **Table 1.** The first radiation-induced dyspnea model (M1) (2) was developed from 438 patients with either non-small cell lung cancer (NSCLC) Stage I-IIIB or limited disease small cell lung cancer, treated with curatively-intended (chemo)radiotherapy between January 2002 till January 2007. Patients in this cohort were predominantly male (328/438, 74.8%) with confirmed NSCLC histology (292/438, 66.7%) and a spread of chemotherapy regimens (concurrent 70/438, 16%; sequential 203/438, 46%; no chemotherapy 159/438, 36%, unspecified 6/438, 1%). RILD, including dyspnea, was scored according to CTCAE (v3.0) (20) during radiotherapy (RT) and up to a maximum of 6 months after RT. A range of radiotherapy prescribed doses from 46.9 to 79.2 Gy were used, with fraction doses not exceeding 2 Gy.

A second radiation-induced dyspnea model was developed from 259 lung cancer patients treated with curatively intended chemo(radiotherapy) between 2008 and 2011, Stage I-IIIB and fractional dose ≤ 3 Gy were used to develop a second radiation-induced dyspnea model (M2) (3). These patients were treated in two hospitals, underwent PET/CT for radiotherapy treatment planning and had lung volumes delineated in the planning system. This cohort was drawn from an earlier iso-toxicity dose escalation radiotherapy trial (clinicaltrials.gov identifier NCT00572325 and NCT00573040) with maximum tumor dose not exceeding 69 Gy. This cohort was predominantly male (163/259, 62.9%) with confirmed NSCLC histology (198/259, 75.6%), received concurrent chemotherapy (148/259, 57.1%) and had no surgery prior to radiotherapy (236/259, 91.1%). Carboplatin and gemcitabine were given for sequential chemotherapy, and cisplatin and etoposide for concurrent chemotherapy. RILD, including dyspnea, was scored according to CTCAE (v3.0), by either thoracic physicians or radiation oncologists, at baseline and every 3 months following RT.

External Validation Cohort

Two hundred and 58 esophageal cancer patients were enrolled in the SCOPE1 (18, 19) trial from 36 UK centers between February 7, 2008 and February 22, 2012. The inclusion criteria were: non-metastatic, histologically confirmed carcinoma of the esophagus (adenocarcinoma, squamous-cell, or undifferentiated carcinoma) or gastro-esophageal junction (Siewert type 1 or 2 with <2 cm extension into the stomach); selected for definitive chemo-radiotherapy by a designated multidisciplinary team; aged 18 years or older; WHO performance status 0 or 1; stage I-III disease (TNM stage 6); and esophageal tumor length < 10 cm as measured by endoscopic ultrasound. The study protocol has been published (19) and the trial was coordinated by the Wales Cancer Trials Unit (WCTU). Recruitment in SCOPE1 was halted due to

TABLE 1 | Patient characteristics.

Variable	D1 Maastro clinic (*N* = 438)	D2 Maastro clinic (*N* = 259)	V1 SCOPE1 (*N* = 212)	V2 SCOPE1 (*N* = 255)
GENDER				
Male	328 (74.9%)	163 (62.9%)	120 (56.6%)	145 (56.2%)
Female	110 (25.1%)	96 (37.1%)	92 (43.4%)	113 (43.8%)
AGE (YEARS)				
	Mean 68 (SD 9)	Mean 67.5 (SD 10.1)	Mean 72.8 (SD 8.95)	Mean 72.9 (SD 9.02)
SMOKING STATUS				
Current smoker	77 (29.7%)	NA	NA	NA
WHO-PS				
0	119 (27.9%)	63 (24.3%)	110 (51.9%)	130 (50.9%)
1	223 (52.3%)	153 (59.1%)	102 (48.1%)	125 (49.1%)
≥2	84 (19.7%)	43 (16.6%)	0	0
CCI				
0	132 (30.9%)	No: 184 (71.0%)	NA	NA
1	128 (30.0%)	Yes: 75 (29%)		
2	95 (22.2%)			
≥3	72 (16.8%)			
Missing	0			
CARDIAC COMORBIDITY				
No	132(30.9%)	No: 184 (71.0%)	208 (98.1%)	252 (98.8%)
Yes	295 (69.0%)	Yes: 75 (29.0%)	2 (1.0%)	3 (1.2%)
Missing	1 (0.1%)		2 (1.0%)	None
BASELINE DYSPNEA SCORE				
0	NA	78 (30.1%)	197 (92.9%)	238 (93.3%)
1	NA	140 (54.1%)	10 (4.7%)	14 (5.5%)
≥2	NA	38 (14.7%)	3 (1.4%)	3 (1.2%)
Missing	NA	3 (1.1%)	2 (1.0%)	None
DYSPNEA SCORE AFTER RT				
0	NA	NA	135 (63.7%)	164 (64.3%)
1	NA	NA	46 (21.7%)	53 (20.8%)
≥2	NA	NA	31 (14.3%)	38 (14.9%)
Missing	NA	NA		
FEV_1 (%)				
	Mean 70.0 (SD 23)	Mean 76.0 (SD 21.86)	NA	NA
CHEMOTHERAPY				
No	159 (36.8%)	44 (17.0%)	0	0
Yes	273 (63.2%)	197 (76.1%)	212 (100%)	255 (100%)
Missing	0	18 (6.9%)	0	0
TUMOR LOCATION				
Lower/middle lobe	245 (56.3%)	76 (29.3%)	NA	NA
Upper lobe	190 (43.7%)	83 (32.1%)	NA	NA
MEAN LUNG DOSE (GRAY)				
	13.5 (SD 4.5)	15.7 (SD 4.44)	9.8 (SD 2.8)	9.83 (SD 2.8)
Min			0.01	0.01
Max			17.9	17.9
Median			10.0	9.9
Missing			None	45 (9.80%)
V_{20} (%)				
	Mean 21.0 (SD 7.3)	Mean 25.5 (SD 9.9)	NA	NA

WHO-PS, World Health Organization performance scale; CCI, Charlson comorbidity index; FEV_1, forced expiratory volume (1s); V_{20}, volume of the lung receiving ≥ 20 Gy, SD, standard deviation. D1 and D2 are development cohorts for the validated model 1(2) and model 2 (2). V1 and V2 are validation cohorts.

futility, but follow-up of at least 24 weeks on all recruited patients was available for secondary analysis.

All patients received four cycles of cisplatin and capecitabine; two cycles were given prior to commencement of RT, and two cycles were given concurrently with RT. This chemotherapy regimen was the most commonly used for esophageal cancer treatment in the UK. Chemotherapy dose was modulated for potential hematological toxicity (based on neutrophil and platelet counts) and kidney function (based on glomerular filtrate rate). Chemotherapy cycles were also withheld for serious non-hematological adverse events until resolution to grade 0 or 1. Half of these patients were randomized to additional cetuximab for their chemotherapy.

All 3D conformal RT plans were based on contrast CT 3 mm slices, for a prescribed dose of 50 Gy in 25 once-daily fractions. The esophageal clinical target volume (CTV) was manually delineated as a 2 cm distal and 2 cm proximal expansion along the esophagus from the gross primary tumor, and a 1 cm radial expansion. The planning target volume was an additional 1 cm proximal-distal expansion from the CTV and an extra 0.5 cm radially. Lung volume receiving 20 Gy or higher was constrained to be <25% of the total lung volume.

None of the SCOPE1 patients in the validation cohort received post-RT surgery. The majority of patients were male (145/258, 56%) with either mid- or lower-esophageal tumors (226/258, 87.6%) and mean endoscopy-defined tumor length of 5.6 cm. Toxicity scoring according to CTCAE (v3.0) was carried out at baseline, during each chemotherapy cycle, at 24 weeks and then every 3 months thereafter.

Previously Published Dyspnea Model Parameters

The model M1 (2) consisted of the following predictors: age, WHO performance status (WHO-PS) before start of RT, nicotine use (non-/ex-smoker vs. current smoker), FEV_1 at baseline and mean lung dose in Gy. The predictors used in model M2 (3) were dyspnea score before start of RT, cardiac comorbidity, FEV_1 at baseline, tumor location (upper vs. middle/lower lobes of lung) and sequential chemotherapy. Multivariate logistic regression analysis was performed to build M1 and M2. The coefficients used in the models are summarized in **Table 2**. Both models defined adverse outcomes as dyspnea grade 2 or higher within 6 months of the end of (chemo)-radiotherapy.

Model Assumptions and Missing-Values Imputation

The previous M1 and M2 had been developed on, and validated in, primary lung cancer patients. However, Forced Expiratory Volume (i.e., FEV_1), smoking status and lung tumor location (lobe) were uniformly absent from the esophageal SCOPE1 dataset. We assumed (based on the trial protocol) that all SCOPE1 patients received chemotherapy and we simulated different population scenarios for smoking status. For the model M2, we further assumed that unintended radiation dose for

TABLE 2 | Coefficients obtained from the multivariate logistic regression in the first (M1) (2) and second (M2) (3) dyspnea models.

Variable	Model coefficients (M1)	Model coefficients (M2)
Intercept	−2.2767	−1.512
PERFORMANCE STATUS		
WHO-PS = 1	0.28	–
WHO-PS ≥ 2	0.57	–
Current smoker	−0.45	–
Age	0.02	–
Mean lung dose	0.05	–
Baseline dyspnea	–	0.990
Cardiac comorbidity	–	0.826
Sequential chemotherapy	–	0.610
Tumor in middle/lower lung lobe	–	−0.290
Baseline FEV_1	−0.02	−0.007

esophageal cancers were most analogous to RT for lung tumors in lower and/or middle lung lobes.

Since FEV_1 was a predictor in both M1 and M2, we imputed the missing FEV_1 measurements of the SCOPE1 patients from available data in the model M1 development cohort while blinded to the dyspnea outcome. The imputation was based on categorical regression for WHO-PS = 0, WHO-PS = 1 and WHO-PS ≥2. A statistically significant fit for FEV1 (in % of total expired volume) was found using the model:

$$FEV1\ (in\ \%) = 82.0\ if\ WHO - PS = 0$$
$$FEV1\ (in\ \%) = 74.7\ if\ WHO - PS = 1$$
$$FEV1\ (in\ \%) = 67.3\ if\ WHO - PS\ \geq 2$$

Distributed Learning

External validation was performed using the same distributed methodology as published by Deist et al. (21), Jochems et al. (22) and Shi et al. (23) using the Varian Learning Portal (VLP, Varian Medical Systems, Palo Alto, CA) v1.0. A validation algorithm containing model coefficients of M1 and M2 were remotely distributed from the investigator site to the validation site via a secured http channel. The SCOPE1 data was parsed using a radiation oncology-specific semantic ontology into the Web 3.0-standard resource descriptor format (RDF). The distributed validation algorithm executes as a purely site-specific local computation by querying the local RDF repository. Only the summary classification results of validation on the SCOPE1 cohort was returned to the investigator site. Security and privacy settings within VLP blocked transfer and exposure of patient-level records from the validation site to the investigator. Previous studies (21–23) have proven that the algorithm converges to the same result as if all of the patient data was locally processed on site by an investigator. The workflow of the distributed learning approach is shown in **Figure 1**.

Statistical Analysis

The validation algorithm was deployed in MATLAB, version 9.0 (MathWorks, Natick, MA). Discrimination of predictive model was evaluated using the area under the receiver-operator curve (AUC) metric (24). The AUC metric was estimated by bootstrapping (1,000 resamples). Calibration of the predictive model was assessed using calibration plots. The logistic recalibration was performed through fitting a logistic regression model by the linear predictor as the only covariate, which leads to an updated model without changing discrimination performance (25, 26).

RESULTS

Out of 258 available validation cases in the SCOPE1 dataset, 46 and 3 patients, respectively, were excluded from the validation due to missing values of mean lung dose for validation of model M1 and baseline scores of cardiac comorbidity and dyspnea for validation of model M2. A total of 212 patients and 255 patients were available to externally validate model M1 and M2. In the validation cohort for M1 (V1), there were 31 patients (14.3%) manifesting dyspnea grade 2 or higher within 6 months of RT. In the validation cohort for M2 (V2), 38 patients (14.9%) manifested dyspnea at the equivalent time point.

To investigate the effect of smoking status on the performance of M1 in the external validation cohort, smoking status was assigned to (i) all smokers, (ii) non-smokers, and (iii) randomly and repeat 1,000 iterations. The test yielded the AUC of 0.68 ± 0.053, 0.68 ± 0.054, and 0.65 ± 0.04, respectively by bootstrap sampling. Although the smoking status a missing predictor for esophageal validation cohort, there was no statistically significant difference in performance observed based on a bootstrapped Wilcoxon test between the three scenarios ($p = 0.34$, $p = 0.17$, $p = 0.11$). Therefore, we set it randomly in the validation cohort.

The receiver operator curves (ROCs) of the models on external validation sets V1 and V2 are shown in **Figure 2**. The AUC of both models measured in the previous studies were 0.62 and 0.72 in internal validation and 0.61 and 0.67 in external validation. Compared to the previous studies, the AUC of the two models on V1 and V2 were 0.68 (95% CI: 0.55–0.76) and 0.70 (95% CI: 0.58–0.77), respectively. No statistically significant difference in performance was observed between M1 and M2 in the previous training cohorts and current external validation cohorts (AUC of M1 0.62 vs. 0.68, $p = 0.17$; AUC of M2 0.72 vs. 0.70, $p = 0.45$, Wilcoxon test). The detailed assessment of accuracy, sensitivity, specificity, positive predictive value and negative predictive value are shown in the **Supplementary Table 1**. Both prognostic models (M1 and M2) showed poor calibration performance and tended toward underestimation of dypsnea in the test population, which is shown in the calibration plots (**Figures 3i,iii**). Recalibration was performed to update the prognostic models (**Figures 3ii,iv**). As expected, the recalibration resulted in higher predicted

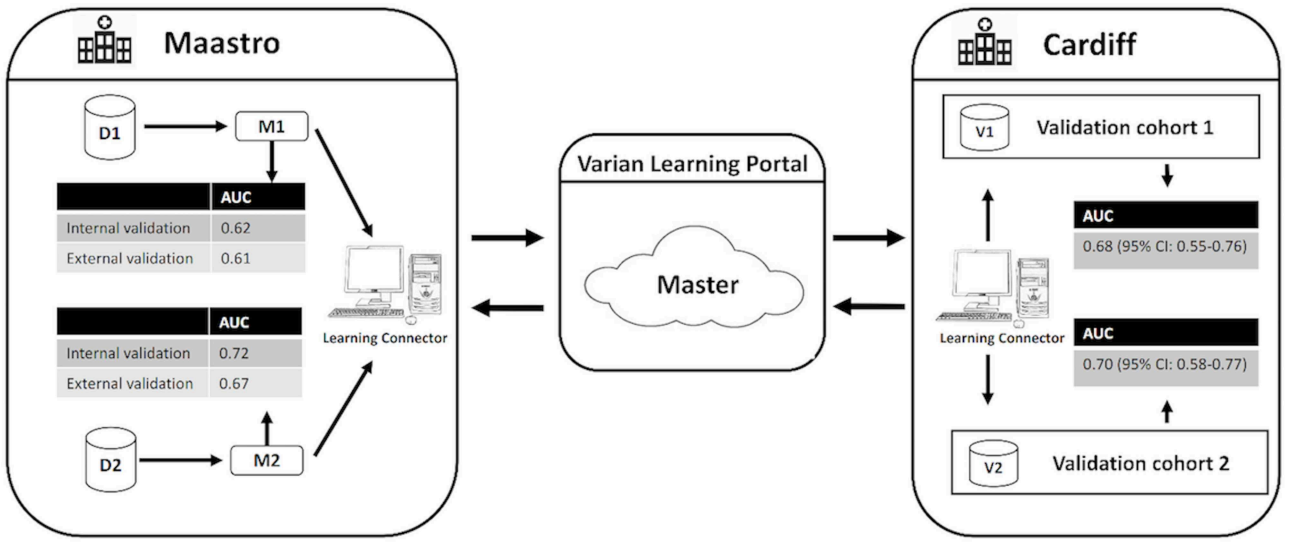

FIGURE 1 | Generalized workflow of the distributed learning approach used in this study. D1 and D2 indicate the development cohorts used to develop the original RILD models M1 and M2. V1 and V2 indicate the validation cohorts for M1 and M2, respectively. CI indicates confidence interval.

risks without changing the AUCs. The calibration line of the recalibrated M1 was shifted be closer to the ideal line, whereas the calibration line of M2 was not improved overall by the recalibration.

DISCUSSION

The current study has tested two previously-published RILD models M1 and M2 (2, 3) on the independent validation sets V1 and V2 of the SCOPE1 trial data (18, 19), which comprises esophageal cancer patients treated with chemo-radiotherapy. Moreover, external validation was successfully implemented using an automated and decentralized approach without exchange of individual patient data.

As is well known, high-dose of thoracic radiation can often provide better local tumor control and survival for patient with cancer. Previous studies have shown that additional radiation in an appropriate range can improve locoregional tumor control and increase survival of patients with lung cancer (27–29). However, the irradiation dose in the radiotherapy treatment of esophageal cancer can have an adverse effect on lung tissue resulting in RILD, such that it leads to disutility of care and have a serious negative impact on patients' quality of life. RILD usually manifests itself in the acute (<6 months) phase as radiation pneumonitis (RP) and in the later (>6 months) phase as chronic pulmonary fibrosis (30, 31). RP is the most common dose-limiting complication of thoracic radiation with clinical symptoms such as dyspnea, cough, and sometimes fever (32). Therefore, it is a trade-off between better tumor control (i.e., better survival or lower death rate) and RILD.

The prognostic models are regarded as the basis of clinical decision support systems (CDSS) (33) that can relieve clinicians from the pressure of analyzing the large volume of publications and data by applying discoveries from research into a data-analytics architecture (34, 35). However, it is difficult to apply the results of research in clinical practice to predict which patients with esophageal cancer will likely suffer from RILD. The first reason is that many studies have investigated the risk predictors of RILD including dosimetric, clinical, pathological factors or blood biomarkers (2–16), but results between studies are highly variable or even contradictory (1, 32). In the meantime, there is no standardized lung toxicity grading system and no standard data models (so-called umbrella protocols) to guide prospective collection on routine cases. On the other hand, few publications report the risk predictors of RILD (e.g., severe dyspnea), for patients with esophageal cancer. This difficulty might be explained by the fact that dyspnea is not routinely assessed during diagnosis and prognosis of esophageal cancer.

At present, it is widely acknowledged that a prognostic model cannot be applied in clinical practice before its feasibility and practicability have been certified via validation on different levels (17, 36). External validation of a prognostic model should be performed on an/some independent cohort(s), because most models present optimistic results in the development cohorts. Validation of prognostic models involves two aspects (37). First, generalizability of a prognostic model can be described by validation on similar (reproducibility) or different (transferability) cohorts. The similarity or difference between cohorts refer to temporal, geography, methodology or investigator, which aims to distinguish from the development cohort of the original model (17, 38, 39). One primary goal of the current study to investigate the transferability of two previously-published lung toxicity models M1 and M2 under these "different" situations.

Second, accuracy performance of a prognostic model shows the statistical validity (40). Discrimination and calibration, in general, measure the accuracy performance. (i) Discrimination

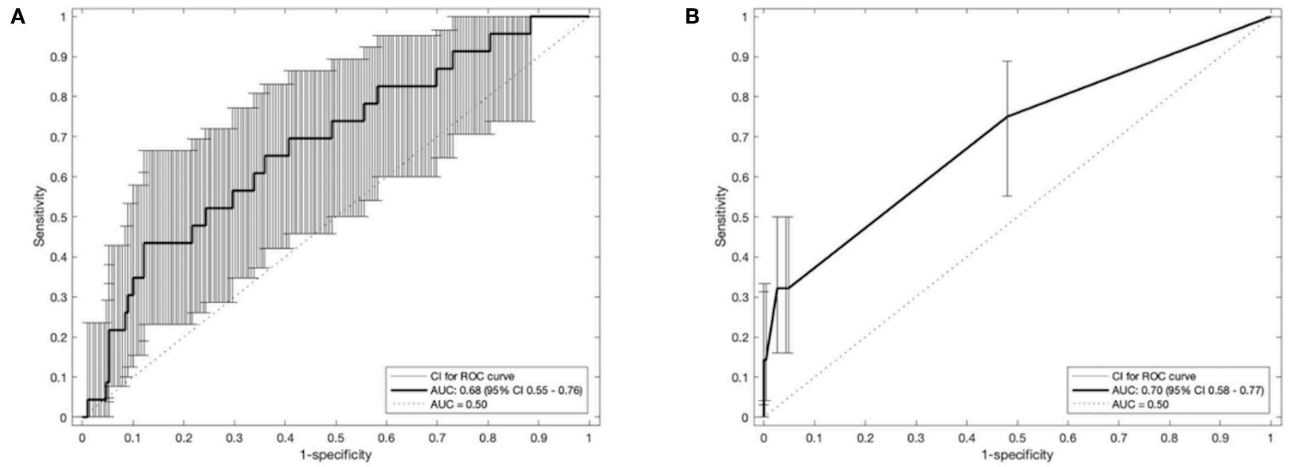

FIGURE 2 | Receiver operating characteristic curves of the prognostic models **(A)**: M1 and **(B)**: M2 with 95% CI of area under the receiver-operator curve (AUC). CI, confidence interval.

describes whether an individual with higher predictive probability is indeed experience RILD more often. Area under the receiver-operator curve (AUC) (24) was used to assess the discrimination performance, which is shown in **Figure 2**. The model M1 achieved a better discrimination performance (i.e., AUC) on V1 compared to the internal and external validation performed in the original study. The M2 obtained a better AUC on V2 than the AUC of the external validation but was consistently degraded in AUC from the internal validation of the original study. (ii) Calibration reflects the agreement between observed event and predicted risk. The calibration performance was assessed by calibration plots, which are shown in **Figure 3**. A perfectly calibrated model means that the predicted probabilities of RILD are identical to the observed frequencies of RILD for all patient groups. The calibration-in-the-large (i.e., intercept) of M1 and M2 were 3.79 ($p = 0.08$) and 0.42 ($p = 0.46$), and calibration slope were 2.60 ($p = 0.007$) and 1.99 ($p < 0.0001$), which indicates that predicted risks of M1 and M2 in SCOPE1 were systematically under-estimated and there was insufficient variation of covariates in V1 and V2 sets. A possible explanation may involve systematic under-reporting of clinical toxicity in the retrospectively-collected training sets. By testing different assumptions about smoking status in the test cohorts, there is no evidence to support an effect of smoking in either aggravating or protecting against dyspnea. It is also possible that the original models in lung cancer were improperly calibrated, but there was no additional information in the published articles to confirm this. However, a systematic underestimation of the dyspnea rate would be consistent with an offset error in the linear fit of FEV1 using the WHO performance score. This potential source of error could only be circumvented by measuring the FEV1 for the SCOPE1 test cases, which was not done. To correct poor calibration performance, recalibration can be performed through fitting a logistic regression model by the linear predictor as the only covariate, which leads to an updated model without changing discrimination performance (25, 26, 41). The calibration performance of M1 was moderate after conducting recalibration. The M2 model still had poor calibration performance even after recalibration, which means care should be taken applied in real clinical practice.

Strengths of the Analysis

The SCOPE1 trial data, as an independent validation cohort, satisfied the conditions of separation in terms of temporal (different treatment time of patients in SCOPE1 and previous training cohorts), geographic (different regions, Cardiff vs. Netherlands) and investigator (different people from different institutes) from the development cohort of lung cancer. It means that the SCOPE1 was a sufficiently challenging dataset to externally validate the transferability of a prediction model between different index cancers (38, 40). Second, we have shown the RILD models (e.g., M1) can be robustly transferred to other diseased sites (e.g., esophagus) that only having the incidentally irradiated normal tissues in common without losing accuracy performance. Thirdly, this study was implemented using an automated and distributed approach without exchanging any patient data. Due to the confidentiality of patient data, local laws and technical issues, it can be prohibitively difficult to exchange patient data among hospitals. Compared to the centralized learning approach, the distributed learning approach can avoid privacy-related issues by sending research questions among institutes. The distributed learning can be achieved by transferring a machine learning algorithm to a target site and returning the results back to the sender rather than transferring real data. This process means knowledge exchange occurs without important clinical data leaving hospitals and there is no loss of validation integrity when performed distributed learning.

Weakness of the Analysis

The current study has some limitations worthy of mention. First, some outcome data and predictor variables were missing in

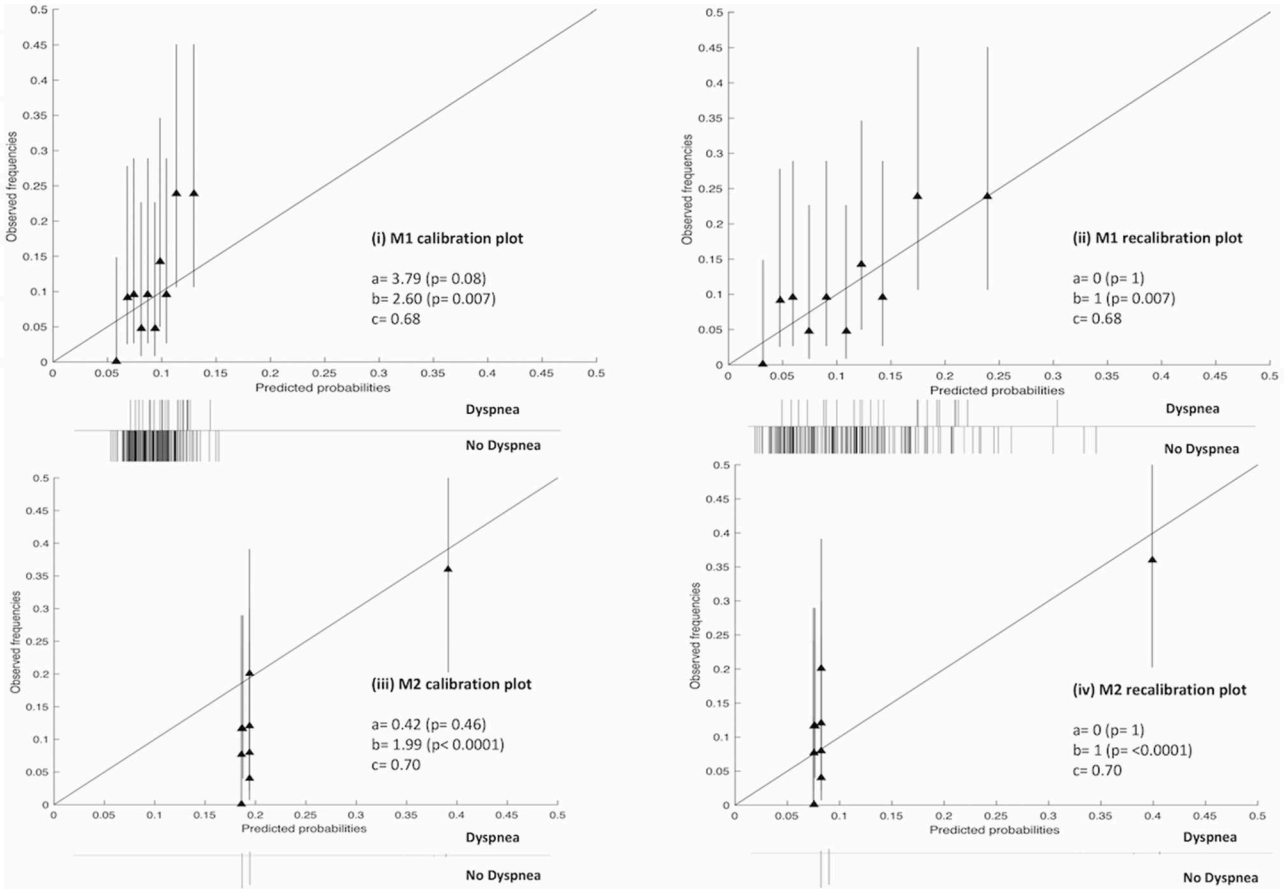

FIGURE 3 | Calibration and recalibration plots of M1 and M2 on the V1 and V2 cohorts, respectively. Perfect calibration is represented by the solid line through the origin with slope = 1. Ten quantile groups were used to compare the predicted probability and the corresponding observed frequencies with a triangle. Histogram of outcomes (i.e., dyspnea or no dyspnea) is shown below each plot. a, calibration-in-the large; b, calibration slop; c, area under the receiver-operator curve (AUC).

the validation cohorts, and data was not missing completely at random. If the missing data were compulsory predictors for the prognostic models (M1 and M2) and cannot be imputed, the corresponding patients had to be removed from the validation cohort. In addition to this, there are non-random missing data, which might be explained by the fact that the information about lung cancer were not be registered for patients with esophageal cancer in the SCOPE1 trial, such as tumor location, smoking status, and FEV_1. For tumor location, we assumed that all of these esophageal cancer patients treated with radiation were similar to lung patients with a tumor in the lower lung lobe. For the missing FEV_1, WHO-PS was used to impute as mentioned above. Second, there are some differences between the development (D1 and D2) and validation cohorts (V1 and V2), of which the effect on the model performance are the subject of future work. (i) SCOPE1 randomized half of the patients between cetuximab or not, whereas patients in D1 and D2 were not treated with cetuximab. (ii) All patients received chemo-radiotherapy in V1 and V2, while only 273 (63.2%) and 197 (76.1%) patients received chemotherapy in D1 and D2. (iii) The numbers of patients in D2 with baseline score 0, 1, $\geq$2 are 78 (30.1%), 140 (54.1%), and 48 (14.7%), whereas these numbers in V2 are 238 (93.33%), 14 (5.49%), and 3 (1.18%). It indicates that more patients had low-grade or no dyspnea overall in V2 compared with patients in D2. The effects of these uncertainties on the performance of prognostic models M1 and M2 remain unclear and are the subject of future studies.

Finally, another potential limitation is about the validated models' selection, that is the performance of M1 is moderate in terms of AUC and M2 does not include lung dose volume parameters. Although the discrimination performance of M1 is moderate, we found it achieved a similar and even better discrimination performance in the external validation cohort, which demonstrated that M1 has a good generalization. M2 was developed using multivariable regression approach. The original study (3) did evaluate mean lung dose and V20Gy as potential risk factors, but then dropped it from the final regression model because their contributions were small and/or could not be shown to be statistically significant.

Future Work

Future work would involve two aspects. First, the M1 could be tested on a similar dataset to validate the reproducibility. Second, we would like to re-train the lung toxicity model on D1 and D2 via combining different types of features, such as image, pathological or generic features.

CONCLUSION

In this study, we have externally validated previously published dyspnea models using an esophageal cancer dataset. First, the discrimination performance of the models in esophageal cancer patients treated with high-dose external beam radiotherapy are moderate, AUC of 0.68 (95% CI 0.55–0.76.) and 0.70 (95% CI 0.58–0.77), respectively. Second, risk estimates were strongly determined by WHO score in Model 1 and baseline dyspnea in Model 2. Third, the distributed learning approach gave the same answer as local validation but is feasible without accessing a validation site's patient-level data. Finally, the clinical contribution of the dyspnea prognostic model is that it would help doctors to identify patients who will likely suffer from severe dyspnea and who could therefore benefit from dose de-escalation in (chemo)-radiotherapy. Although we cannot conclude that a common thoracic RILD model is feasible for a different primary tumor, it can be deemed as a "benchmark" for further investigation of RILD prognostic models of thoracic tumor.

DATA AVAILABILITY STATEMENT

The datasets generated for this study will not be made publicly available. The data used in this study was generated in the external validate center. The corresponding author cannot see the data, which was the reason why we performed the distributed learning to avoid data sharing in this study.

ETHICS STATEMENT

The studies involving human participants were reviewed and approved by Velindre Cancer Centre, Cardiff, UK. Written informed consent for participation was not required for this study in accordance with the national legislation and the institutional requirements.

AUTHOR CONTRIBUTIONS

ZS implemented the distributed MATLAB code via VLP, converted clinical data of SCOPE1 to RDF format, performed analysis on the results using MATLAB, and made a major contribution to the writing of the manuscript as the first author. KF and TC were responsible for data preparation and quality check of SCOPE1 dataset. JP implemented the imputation analysis to deal with the missing data in SCOPE1 dataset. ES and PW were responsible for VLP setup in Cardiff for distributed learning. JS provided technical support for external validation analysis through VLP. AD and LW acted in the capacity of joint senior authors who motivated the study, set the general methodology and had overall scientific responsibility for this investigation. All co-authors contributed to proof-reading of the manuscript.

FUNDING

This work has been supported by a Dutch STW-Perspectief grant: Radiomics STRaTegy (file number 14930) and NWO grant: BIONIC (629.002. 205).

SUPPLEMENTARY MATERIAL

The Supplementary Material for this article can be found online at: https://www.frontiersin.org/articles/10.3389/fonc.2019.01411/full#supplementary-material

REFERENCES

1. Mehta V. Radiation pneumonitis and pulmonary fibrosis in non–small-cell lung cancer: pulmonary function, prediction, and prevention. *Int J Radiat Oncol Biol Phys.* (2005) 63:5–24. doi: 10.1016/j.ijrobp.2005.03.047
2. Dehing-Oberije C, De Ruysscher D, van Baardwijk A, Yu S, Rao B, Lambin P. The importance of patient characteristics for the prediction of radiation-induced lung toxicity. *Radiother Oncol.* (2009) 91:421–6. doi: 10.1016/j.radonc.2008.12.002
3. Nalbantov G, Kietselaer B, Vandecasteele K, Oberije C, Berbee M, Troost E, et al. Cardiac comorbidity is an independent risk factor for radiation-induced lung toxicity in lung cancer patients. *Radiother Oncol.* (2013) 109:100–6. doi: 10.1016/j.radonc.2013.08.035
4. Hope AJ, Lindsay PE, El Naqa I, Alaly JR, Vicic M, Bradley JD, et al. Modeling radiation pneumonitis risk with clinical, dosimetric, and spatial parameters. *Int J Radiat Oncol Biol Phys.* (2006) 65:112–24. doi: 10.1016/j.ijrobp.2005.11.046
5. Jenkins P, Watts J. An improved model for predicting radiation pneumonitis incorporating clinical and dosimetric variables. *Int J Radiat Oncol Biol Phys.* (2011) 80:1023–9. doi: 10.1016/j.ijrobp.2010.03.058
6. Kim M, Lee J, Ha B, Lee R, Lee KJ, Suh HS. Factors predicting radiation pneumonitis in locally advanced non-small cell lung cancer. *Radiat Oncol J.* (2011) 29:181–90. doi: 10.3857/roj.2011.29.3.181
7. Kwa SL, Theuws JC, Wagenaar A, Damen EM, Boersma LJ, Baas P, et al. Evaluation of two dose-volume histogram reduction models for the prediction of radiation pneumonitis. *Radiother Oncol.* (1998) 48:61–9. doi: 10.1016/S0167-8140(98)00020-6
8. Madani I, De Ruyck K, Goeminne H, De Neve W, Thierens H, Van Meerbeeck J. Predicting risk of radiation-induced lung injury. *J Thorac Oncol.* (2007) 2:864–74. doi: 10.1097/JTO.0b013e318145b2c6
9. Marks LB, Bentzen SM, Deasy JO, Kong FM, Bradley JD, Vogelius IS, et al. Radiation dose-volume effects in the lung. *Int J Radiat Oncol Biol Phys.* (2010) 76(3 Suppl.):S70–6. doi: 10.1016/j.ijrobp.2009.06.091
10. Palma DA, Senan S, Tsujino K, Barriger RB, Rengan R, Moreno M, et al. Predicting radiation pneumonitis after chemoradiation therapy for lung cancer: an international individual patient data meta-analysis. *Int J Radiat Oncol Biol Phys.* (2013) 85:444–50. doi: 10.1016/j.ijrobp.2012.04.043
11. Rancati T, Ceresoli GL, Gagliardi G, Schipani S, Cattaneo GM. Factors predicting radiation pneumonitis in lung cancer patients: a retrospective study. *Radiother Oncol.* (2003) 67:275–83. doi: 10.1016/S0167-8140(03)00119-1

12. Stenmark MH, Cai XW, Shedden K, Hayman JA, Yuan S, Ritter T, et al. Combining physical and biologic parameters to predict radiation-induced lung toxicity in patients with non-small-cell lung cancer treated with definitive radiation therapy. *Int J Radiat Oncol Biol Phys.* (2012) 84: e217–22. doi: 10.1016/j.ijrobp.2012.03.067
13. Vinogradskiy Y, Tucker SL, Liao Z, Martel MK. A novel method to incorporate the spatial location of the lung dose distribution into predictive radiation pneumonitis modeling. *Int J Radiat Oncol Biol Phys.* (2012) 82:1549–55. doi: 10.1016/j.ijrobp.2011.05.007
14. Iwata H, Shibamoto Y, Baba F, Sugie C, Ogino H, Murata R, et al. Correlation between the serum KL-6 level and the grade of radiation pneumonitis after stereotactic body radiotherapy for stage I lung cancer or small lung metastasis. *Radiother Oncol.* (2011) 101:267–70. doi: 10.1016/j.radonc.2011.05.031
15. Voets AM, Oberije C, Struijk RB, Reymen B, De Ruyck K, Thierens H, et al. No association between TGF-β1 polymorphisms and radiation-induced lung toxicity in a European cohort of lung cancer patients. *Radiother Oncol.* (2012) 105:296–8. doi: 10.1016/j.radonc.2012.09.016
16. Novakova-Jiresova A, Van Gameren MM, Coppes RP, Kampinga HH, Groen HJ. Transforming growth factor-β plasma dynamics and post-irradiation lung injury in lung cancer patients. *Radiother Oncol.* (2004) 71:183–9. doi: 10.1016/j.radonc.2004.01.019
17. Collins GS, Reitsma JB, Altman DG, Moons KG. Transparent reporting of a multivariable prediction model for individual prognosis or diagnosis (TRIPOD): the TRIPOD Statement. *BMC Med.* (2015) 13:1. doi: 10.1186/s12916-014-0241-z
18. Crosby T, Hurt CN, Falk S, Gollins S, Mukherjee S, Staffurth J, et al. Chemoradiotherapy with or without cetuximab in patients with oesophageal cancer (SCOPE1): a multicentre, phase 2/3 randomised trial. *Lancet Oncol.* (2013) 14:627–37. doi: 10.1016/S1470-2045(13)70136-0
19. Hurt CN, Nixon LS, Griffiths GO, Al-Mokhtar R, Gollins S, Staffurth JN, et al. SCOPE1: a randomised phase II/III multicentre clinical trial of definitive chemoradiation, with or without cetuximab, in carcinoma of the oesophagus. *BMC Cancer.* (2011) 11:466. doi: 10.1186/1471-2407-11-466
20. Trotti A, Colevas AD, Setser A, Rusch V, Jaques D, Budach V, et al. CTCAE v3. 0: development of a comprehensive grading system for the adverse effects of cancer treatment. *Semin Radiat Oncol.* (2003) 13:176–81. doi: 10.1016/S1053-4296(03)00031-6
21. Deist TM, Jochems A, van Soest J, Nalbantov G, Oberije C, Walsh S, et al. Infrastructure and distributed learning methodology for privacy-preserving multi-centric rapid learning health care: euroCAT. *Clin Transl Radiat Oncol.* (2017) 4:24–31. doi: 10.1016/j.ctro.2016.12.004
22. Jochems A, Deist TM, van Soest J, Eble M, Bulens P, Coucke P, et al. Distributed learning: developing a predictive model based on data from multiple hospitals without data leaving the hospital–a real life proof of concept. *Radiother Oncol.* (2016) 121:459–67. doi: 10.1016/j.radonc.2016.10.002
23. Shi Z, Zhovannik I, Traverso A, Dankers FJWM, Deist TM, Kalendralis P, et al. Distributed radiomics as a signature validation study using the Personal Health Train infrastructure. *Sci Data.* (2019) 6:1–8. doi: 10.1038/s41597-019-0241-0
24. Hanley JA, McNeil BJ. The meaning and use of the area under a receiver operating characteristic (ROC) curve. *Radiology.* (1982) 143:29–36. doi: 10.1148/radiology.143.1.7063747
25. Janssen KJ, Vergouwe Y, Kalkman CJ, Grobbee DE, Moons KG. A simple method to adjust clinical prediction models to local circumstances. *Can J Anaesth.* (2009) 56:194–201. doi: 10.1007/s12630-009-9041-x
26. Steyerberg EW, Borsboom GJ, van Houwelingen HC, Eijkemans MJ, Habbema JD. Validation and updating of predictive logistic regression models: a study on sample size and shrinkage. *Stat Med.* (2004) 23:2567–86. doi: 10.1002/sim.1844
27. Kong FM, Ten Haken RK, Schipper MJ, Sullivan MA, Chen M, Lopez C, et al. High-dose radiation improved local tumor control and overall survival in patients with inoperable/unresectable non–small-cell lung cancer: Long-term results of a radiation dose escalation study. *Int J Radiat Oncol Biol Phys.* (2005) 63:324–33. doi: 10.1016/j.ijrobp.2005.02.010
28. Pignon JP, Arriagada R, Ihde DC, Johnson DH, Perry MC, Souhami RL, et al. A meta-analysis of thoracic radiotherapy for small-cell lung cancer. *N Engl J Med.* (1992) 327:1618–24. doi: 10.1056/NEJM199212033272302
29. Warde P, Payne D. Does thoracic irradiation improve survival and local control in limited-stage small-cell carcinoma of the lung? A meta-analysis. *J Clin Oncol.* (1992) 10:890–5. doi: 10.1200/JCO.1992.10.6.890
30. Bernchou U, Schytte T, Bertelsen A, Bentzen SM, Hansen O, Brink C. Time evolution of regional CT density changes in normal lung after IMRT for NSCLC. *Radiother Oncol.* (2013) 109:89–94. doi: 10.1016/j.radonc.2013.08.041
31. Jiang ZQ, Yang K, Komaki R, Wei X, Tucker SL, Zhuang Y, et al. Long-term clinical outcome of intensity-modulated radiotherapy for inoperable non-small cell lung cancer: the MD Anderson experience. *Int J Radiat Oncol Biol Phys.* (2012) 83:332–9. doi: 10.1016/j.ijrobp.2011.06.1963
32. Rodrigues G, Lock M, D'Souza D, Yu E, Van Dyk J. Prediction of radiation pneumonitis by dose–volume histogram parameters in lung cancer—a systematic review. *Radiother Oncol.* (2004) 71:127–38. doi: 10.1016/j.radonc.2004.02.015
33. Lambin P, Zindler J, Vanneste BG, De Voorde LV, Eekers D, Compter I, et al. Decision support systems for personalized and participative radiation oncology. *Adv Drug Deliv Rev.* (2017) 109:131–53. doi: 10.1016/j.addr.2016.01.006
34. Abernethy AP, Etheredge LM, Ganz PA, Wallace P, German RR, Neti C, et al. Rapid-learning system for cancer care. *J Clin Oncol.* (2010) 28:4268–74. doi: 10.1200/JCO.2010.28.5478
35. Lambin P, Roelofs E, Reymen B, Velazquez ER, Buijsen J, Zegers CML, et al. Rapid Learning health care in oncology'–an approach towards decision support systems enabling customised radiotherapy. *Radiother Oncol.* (2013) 109:159–64. doi: 10.1016/j.radonc.2013.07.007
36. Steyerberg EW, Moons KG, van der Windt DA, Hayden JA, Perel P, Schroter S, et al. Prognosis Research Strategy (PROGRESS) 3: prognostic model research. *PLoS Med.* (2013) 10:e1001381. doi: 10.1371/journal.pmed.1001381
37. van Soest J, Meldolesi E, van Stiphout R, Gatta R, Damiani A, Valentini V, et al. Prospective validation of pathologic complete response models in rectal cancer: Transferability and reproducibility. *Med Phys.* (2017) 44:4961–7. doi: 10.1002/mp.12423
38. Justice AC, Covinsky KE, Berlin JA. Assessing the generalizability of prognostic information. *Ann Int Med.* (1999) 130:515–24. doi: 10.7326/0003-4819-130-6-199903160-00016
39. Moons KG, Kengne AP, Grobbee DE, Royston P, Vergouwe Y, Altman DG, et al. Risk prediction models: II. External validation, model updating, and impact assessment. *Heart.* (2012) 98:691–8. doi: 10.1136/heartjnl-2011-301247
40. Altman DG, Royston P. What do we mean by validating a prognostic model? *Stat Med.* (2000) 19:453–73. doi: 10.1002/(SICI)1097-0258(20000229)19:4<453::AID-SIM350>3.0.CO;2-5
41. Lamain-de Ruiter M, Kwee A, Naaktgeboren CA, de Groot I, Evers IM, Groenendaal F, et al. External validation of prognostic models to predict risk of gestational diabetes mellitus in one Dutch cohort: prospective multicentre cohort study. *BMJ.* (2016) 354:i4338. doi: 10.1136/bmj.i4338

Conflict of Interest: The authors declare that the research was conducted in the absence of any commercial or financial relationships that could be construed as a potential conflict of interest.

frontiers in Oncology

ORIGINAL RESEARCH
published: 14 January 2020
doi: 10.3389/fonc.2019.01504

Sub-acute Toxicity in Non-cancerous Tissue and Immune-Related Adverse Events of a Novel Combination Therapy for Cancer

Kelly J. McKelvey[1,2,3]*, *Amanda L. Hudson*[1,2,3], *Ramyashree Prasanna Kumar*[1,2], *Thomas Eade*[4], *Stephen J. Clarke*[1,2,4], *Helen R. Wheeler*[1,2,3,4], *Connie I. Diakos*[1,2,4] and *Viive M. Howell*[1,2,3]

[1] Bill Walsh Translational Cancer Research Laboratory, Kolling Institute, The University of Sydney Northern Clinical School and Northern Sydney Local Health District, St Leonards, NSW, Australia, [2] Sydney Vital Translational Cancer Research Centre, Royal North Shore Hospital, St Leonards, NSW, Australia, [3] The Brain Cancer Group, St Leonards, NSW, Australia, [4] Northern Sydney Cancer Centre, Royal North Shore Hospital, St Leonards, NSW, Australia

OPEN ACCESS

Edited by:
Ester Orlandi,
Fondazione IRCCS Istituto Nazionale dei Tumori, Italy

Reviewed by:
James William Jacobberger,
Case Western Reserve University, United States
Stefano Cavalieri,
Fondazione IRCCS Istituto Nazionale dei Tumori, Italy

***Correspondence:**
Kelly J. McKelvey
kelly.mckelvey@sydney.edu.au

Specialty section:
This article was submitted to Radiation Oncology, a section of the journal Frontiers in Oncology

Received: 29 August 2019
Accepted: 16 December 2019
Published: 14 January 2020

Citation:
McKelvey KJ, Hudson AL, Prasanna Kumar R, Eade T, Clarke SJ, Wheeler HR, Diakos CI and Howell VM (2020) Sub-acute Toxicity in Non-cancerous Tissue and Immune-Related Adverse Events of a Novel Combination Therapy for Cancer. Front. Oncol. 9:1504. doi: 10.3389/fonc.2019.01504

Brain, lung, and colon tissue experience deleterious immune-related adverse events when immune-oncological agents or radiation are administered. However, there is a paucity of information regarding whether the addition of radiation to immuno-oncological regimens exacerbates the tissue inflammatory response. We used a murine model to evaluate sub-acute tissue damage and the systemic immune response in C57Bl/6 mice when administered systemic anti-programmed cell death protein 1 (αPD-1) immunotherapy alone or in combination with stereotactic fractionated 10 gray/5 X-ray radiation to normal brain, lung or colon tissue. The model indicated that combinatorial αPD-1 immunotherapy and radiation may alter normal colon cell proliferation and cerebral blood vasculature, and induce systemic thrombocytopenia, lymphopenia, immune suppression, and altered immune repertoire (including interleukin-1β). Therein our data supports close monitoring of hematological and immune-related adverse events in patients receiving combination therapy.

Keywords: cancer, radiation, immunotherapy, inflammation, toxicity

INTRODUCTION

While immunotherapies have the potential to revolutionize therapy there is limited understanding of their interaction with radiation in healthy tissues. To date a number of factors have restricted the assessment of treatment efficacy of check point inhibitors in combination with radiation in cancer patients. These include treatment discontinuation in ∼10% of patients due to immune-related adverse events and unacceptable level of injury to healthy tissue (1). These factors sometimes stem from the complex immunostimulation arising from the combination of radiation and chemotherapy in these patients. As such it is not clear if patients may derive greater long-term benefit from combined use of radiotherapy (RT) and an immunotherapy checkpoint inhibitor.

Evidence demonstrating safety, i.e., minimal tissue damage and immune-related adverse events in normal/healthy tissue is lacking as it is unethical to administer RT to healthy tissue in people. Immunotherapy alone is reported to induce a range of side effects most commonly in skin, gastrointestinal tract, lung, and endocrine glands. While the majority of immune-related adverse

events are mild to moderate, serious and life threatening events have been reported (2). These led to the introduction of consensus recommendations from the Society for Immunotherapy of Cancer Toxicity Management Working Group (3), and the establishment of clinical practice guidelines for the management of toxicities from immunotherapy by the European and American Medical Societies (4, 5). A systematic review and meta-analysis of 13 studies of patients receiving the anti-programmed cell death protein 1 (αPD-1)/PD-L1 immunotherapies nivolumab, pembrolizumab, or atezolizumab—in combination with chemotherapy—identified increased odds ratios for the incidence of immune associated toxicities hypothyroidism, pneumonitis, colitis, hypophysitis (6), and acute interstitial nephritis (7). The immune-related adverse events associated with checkpoint inhibitors are thought to be linked to immunostimulation and reprogramming of the immune system, leading to a loss of immune tolerance (7). Such adverse events may be exacerbated by RT, where there is a rising paradigm of an immunostimulatory effect of RT in patients undergoing treatment with immune checkpoint inhibitors. Furthermore, the various checkpoint inhibitors differentially modulate T-cell responses leading to distinct toxicity patterns, kinetics, and dose–toxicity relationships. These need to be better understood before widely utilizing combinations of RT and immunotherapy in the clinical setting.

Radiation activates an interconnected network of inflammatory and immune response pathways inducing a host of changes to the tissue microenvironment (8). Lung and colon tissues display two of the most common immune-related adverse events in pneumonitis and colitis, while adverse events in brain tissue, such as encephalitis and neuropathy, are relatively rare (2–5). Due to the idiosyncratic nature of adverse events affected the brain, lung and colon tissues, we sought to pre-clinically model the subacute response to potentially predict future immune-related adverse events.

To understand whether the addition of RT to immuno-oncology agents exacerbates the immune response in normal brain lung and colon tissues, compared to immune-oncology agents alone, we used a murine model to characterize and quantify the sub-acute (day 28) tissue damage and local and systemic immune responses following combined fractionated stereotactic RT and αPD-1 immunotherapy. We hypothesized that this would identify systemic immune markers that could identify immune-mediated adverse events in brain, lung and colon tissues.

MATERIALS AND METHODS

Mice

The study was reviewed and approved by the Northern Sydney Local Heath District Animal Ethics Committee, Royal North Shore Hospital, St. Leonards, Australia (Approval #RESP/17/205). Eight week old male C57Bl/6.Kearn's mice were kept on 12 h day/night light cycles with standard chow and water provided *ad libitum*. Mice were randomly allocated into 6 mice per treatment group and monitored for well-being by trained animal house staff prior to being humanely killed by cardiac puncture under anesthesia at the pre-determined endpoint of 28 days. C57Bl/6 mice were used as this is the background strain to commonly used syngeneic cancer models.

Immunotherapy

Mice were treated with *InVivoMab* rat anti-mouse PD-1 (RMP1-14; 200 μg/dose; BE0146; BioXCell) or rat IgG2a isotype control, anti-trinitrophenol (2A3; 200 μg/dose; BE0089; BioXCell) in 100 mirolitres (μl) PBS by intraperitoneal injection every 3 days for 5 doses (day 8, 11, 14, 17, 20) alone or in combination with fractionated stereotactic RT.

Fractionated Stereotactic Radiotherapy

Cone beam computed tomography (CBCT)-guided stereotactic radiation was delivered to the brain (right hemisphere), lung (right) or colon (sigmoid colon) region at 10 Gray (Gy)/5 X-ray on days 1, 2, 3, 4, 5 using the Small Animal Radiation Research Platform (SARRP; Xstrahl Inc.), 5 × 5 millimeter (mm) collimator, 220 kV, 13 mA, 0.15 mm copper filter, 3.71 gray (Gy)/minute (min), 360° Arc (–180 to 180°) alone or in combination with immunotherapy. Dose output and half-value layer were verified by 0.6 cm^3 Waterproof Farmer® Chamber (PTW TN30013; −400 V) under reference conditions; 35 cm source to axis distance, 2 centimeter (cm) solid-state depth.

An additional 4 centigray (cGy) was delivered to each animal during CBCT imaging dose − 60 kV, 0.8 mA, 360 projections, fine focus as determined by MOSFET dosimetry MOSkin developed by the Center for Medical Radiation Physics of the University of Wollongong, Australia (9, 10) positioned in the center of a 3D printed modular CBCT cylindrical phantom (mass density $\rho = 1.17\ g/cm^3$) (11).

To estimate the radiation dose delivered to the targeted tissue region and non-targeted organs at risk, the SARRP Dose Volume Histogram (DVH) in the Treatment Planning Software (MuriPlan®; Xstrahl Inc.) was utilized. Tissues were contoured using the acquired CBCT images and Digimouse murine anatomy atlas (available at: https://neuroimage.usc.edu/neuro/Digimouse) (12, 13) (**Supplementary Figure 1**). Following application of the planned treatment beam, data indicated the mean dose per fraction delivered to the targeted brain region was 199.11 cGy at a volume of 0.02 cubic centimeters (cc), colon 169.57 cGy at 0.06 cc, and lung 158.39 cGy at 0.01 cc. Doses to non-targeted organs at risk were highest in tissues surrounding the brain—mean 84.88 cGy, anorectal region−60.95 cGy, and tissues surrounding the right lung−26.57 cGy (**Supplementary Table I**).

Histopathology

Brains were harvested and fixed in 10% v/v neutral buffered formalin for 24 h before embedding in paraffin wax. Four micrometer (4 μm) sections were rehydrated and microwave antigen retrieval performed in citrate buffer, pH 6.0. Next, sections were incubated with 2.5% v/v normal goat serum, followed by primary antibody for 1 h at room temperature. Primary antibodies were Ki67 (0.08 μg/ml; 12202; Cell Signaling Technologies), CD31 (0.013 μg/ml; 77699; Cell Signaling Technologies) and γ-H2AX (0.06 μg/ml; ab11174; Abcam).

Finally, sections were incubated with ImmPRESS™ HRP goat anti-rabbit IgG polymer (MP-7451; Vector Labs) for 30 min at room temperature and detected with NovaRed (SK-48000; VectorLabs).

Slides were scanned using the Aperio AT2 Digital Pathology Scanner and five digital images per section at 20x magnification captured using Aperio ImageScope (v12.3.2.8013; Leica Biosytems). Ki67 and γ-H2AX positive staining was quantified by ImmunoRatio ImageJ plugin (v1.0c, 14.2.2011; http://jvsmicroscope.uta.fi/immunoratio/). CD31 positive vessels were enumerated and measured using the Microvessel-Segmentation MATLAB plugin (14).

Hematology and Flow Cytometry

One milliliter (ml) of whole blood was collected via cardiac puncture into K_3EDTA tubes (Minicollect®; Greiner Bio-One) and assessed by a COULTER® Ac-T diff hematology analyzer with Vet App 1.06 (Beckman Coulter).

Using 100 μl whole blood, 1×10^6 splenocytes and 1×10^6 bone marrow-derived cells and red blood cells were lysed and leukocytes stained with a cocktail of antibodies—volume denoted per test; CD25-BV421 (1 μl; 564370), FV510-BV510 (1 μl; 564406), CD80-BV605 (1 μl; 563052), NK1.1-BV650 (1 μl; 564143), CD4-BV711 (0.25 μl; 563726), CD117-BV786 (1 μl; 564012), CD11b-BB515 (0.25 μl; 564454), CD19-PerCP/Cy5.5 (1 μl; 551001), CD115-PE (0.25 μl; 565249), Ly6G-PE/CF594 (0.06 μl; 562700), CD3-PE/Cy7 (1 μl; 552774), CD206-AF647 (1 μl; 565250), CD8a-AF700 (0.25 μl; 557959), Ly6C-APC/Cy7 (0.5 μl; 560596; all BD Biosciences). Acquired using a BD LSRFortessa™ and analyzed using BD FACSDiva™ Software version 6 (BD Biosciences).

Immune cell populations were defined as $CD3^+$ T cell, $CD3^+CD4^+$ helper T cell (Th), $CD3^+CD4^+CD25^+$ regulatory T cell (Treg), $CD3^+CD8$ cytotoxic T cell (Tc), $CD3^-NK1.1^+$ natural killer (NK) cells, $CD3^+NK1.1^+$ (NK/T), $CD115^+CD11b^+$ monocytes (Mono), $CD115^+CD11b^+CD80^+$ macrophage type 1 (M1), $CD115^+CD11b^+CD206^+$ macrophage type 2 (M2), $CD115^-CD11b^+$ dendritic cells (DC), $CD115^-CD11b^+Ly6C^{high}Ly6G^-$ monocytic-myeloid derived suppressor cells (M-MDSC), $CD115^-CD11b^+Ly6C^{low}Ly6G^{high}$ polymorphonuclear-myeloid derived suppressor cells (PMN-MDSC), $CD117^+$ hematopoietic stem cell (HSC), $CD19^+$ B cells and expressed as a percentage of the parent population.

Multiplex Immunoassays

Plasma was obtained by centrifugation of whole blood (500 × g, 5 min at room temperature). Mouse cytokine 23-plex immunoassay (Bio-Plex®; Bio-Rad Laboratories) and chromogenic sandwich enzyme-linked immunosorbent assay (ELISA) for transforming growth factor (TGF)-β1 (DY1679; R&D Systems) were performed as per the manufacturer's instructions.

Statistical Analyses

Animal weight between treatment groups was assessed by Two Way Repeated Measures Analysis of Variance (ANOVA) with Tukey's Multiple Comparison Test. Normality of the data was confirmed by the D'Agostino-Pearson omnibus test. Histological data are expressed as the mean of 5 high power fields ± standard error of the mean (SEM). Hematology, flow cytometry and chemokine/cytokine data are expressed as mean ± standard deviation (SD). Two Way Analysis of Variance (ANOVA) with Tukey's Multiple Comparison Test were performed to compare treatments groups for each cell phenotype or cytokine using Prism 7 for Windows (GraphPad Software, Inc.).

RESULTS

No Change in Animal Weight

Animal weights were not significantly altered by αPD-1 immunotherapy or RT of the brain, colon or right lung regions [$F_{(8, 45)} = 1.347$; $p = 0.25$; **Supplementary Figure 2**]. No animals demonstrated signs of poor body condition up to day 28; there was no skin irritation, hair loss, diarrhea or labored breathing. As expected, animal weight significantly increased with time [$F_{(9, 405)} = 292.5$; $p < 0.0001$].

Reduced $Ki67^+$ Proliferation and Blood Vasculature Following Combination Therapy

Quantification of $Ki67^+$ staining showed low levels of proliferation in normal brain glial cells and lung stromal cells, and high proliferation in the actively regenerating colon progenitor cells at the base of the intestinal crypts (**Figure 1A**). Combined RT and αPD-1 decreased $Ki67^+$ 45% in brain ($p = 0.09$; **Figure 1**) and 25% in colon tissue ($p = 0.0003$; **Figure 1**) compared to αPD-1 alone. Data indicate that normal brain and colon tissue is susceptible to radiation-induced changes in cellular proliferation.

To determine whether the combination therapy of fractionated stereotactic radiation and αPD-1 immunotherapy would impact blood vasculature, $CD31^+$ blood vessels were quantified at the targeted tissue region. In brain tissue, combined RT + αPD-1 reduced blood vasculature 3-fold ($p = 0.001$; **Figure 2**), while in lung tissue combined treatment increased blood vasculature 126% ($p = 0.06$; **Figure 2**) compared to RT + IgG2a. Other vasculature parameters assessed were vessel thickness, perimeter, area, luminal area, and vessel eccentricity—but did not differ significantly between the treatment groups (data not shown). Data show that RT + αPD-1 immunotherapy augments blood vasculature in normal brain tissue.

To determine whether RT-induced damage was prolonged at the sites of irradiation when αPD-1 immunotherapy is combined, γ-H2AX staining was performed to identify double stranded DNA breaks marked for repair (15). As expected, baseline $\gamma\text{-H2AX}^+$ staining was higher in colon tissue than brain and lung due to more rapid cell regeneration. Somewhat contradictory, $\gamma\text{-H2AX}^+$ staining was significantly reduced by 50% in irradiated colon tissue irrespective of αPD-1 immunotherapy (**Figure 3**). Data

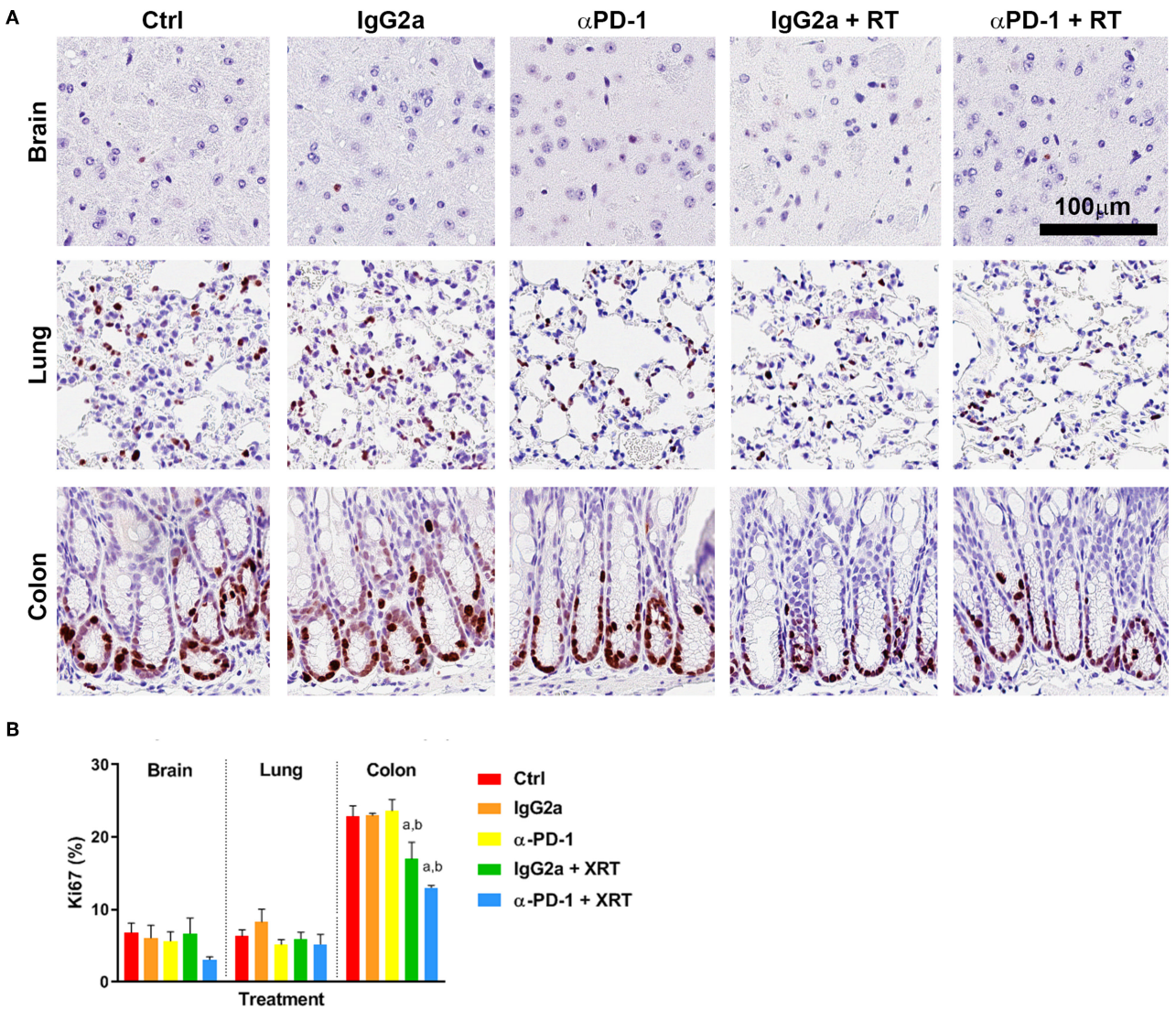

FIGURE 1 | Ki67^{+} staining at the irradiation sites of murine brain, lung and colon tissue **(A)**. Scale bar, 100 μm. Quantitation of five high power fields for each murine tissue ($N = 6$ per time point; **B**). Data are expressed as mean ± SEM per high power field. $^{a}p < 0.05$ vs. Ctrl, $^{b}p < 0.05$ vs. IgG2a by Tukey's multiple comparison test.

show that there is exacerbation of persistent radiation-induced DNA damage following combined radiation and αPD-1 treatment.

Combination therapy alters immune cell populations in systemic compartments. To assess the systemic immune response to combined stereotactic radiation and αPD-1 immunotherapy, hematological parameters and immune cell populations in the spleen, bone marrow and peripheral blood were quantified by flow cytometric analysis. Of the hematological parameters assessed, αPD-1 suppressed platelet numbers when compared to control (905.5 ± 86.8 vs. 1164.4 ± 26.6, $p = 0.0006$) but normalized in animals that received irradiation of the lung tissue (1087.3 ± 45.9 vs. 905.5 ± 86.8, $p = 0.034$; **Figure 4**).

Splenic CD4^{+} helper T (Th) cells increased 20%, while M-MDSC and M1 decreased 40–80% following combined treatment compared to αPD-1 alone ($p < 0.05$; **Figure 5**). In addition, splenic NK/T and monocytes were suppressed following irradiation irrespective of αPD-1 immunotherapy, though these did not reach significance.

In bone marrow, the most striking finding was the reduction in M1 macrophages with RT independent of immunotherapy ($p < 0.05$; **Figure 6**). These reductions closely mirrored the responses of splenic M1 macrophages (**Figure 5**). Furthermore, in bone marrow Th, Tc and DCs were increased while Tregs and B cells decreased following brain or lung RT + αPD-1 compared to monotherapies ($p < 0.05$; **Figure 6**). Data suggests that the addition of RT to αPD-1 monotherapy may enhance an immune response with increased Th, Tc and DCs. Additionally, a reduction of bone marrow Tregs following combination therapy in lung, may contribute to lymphopenia or immune suppression

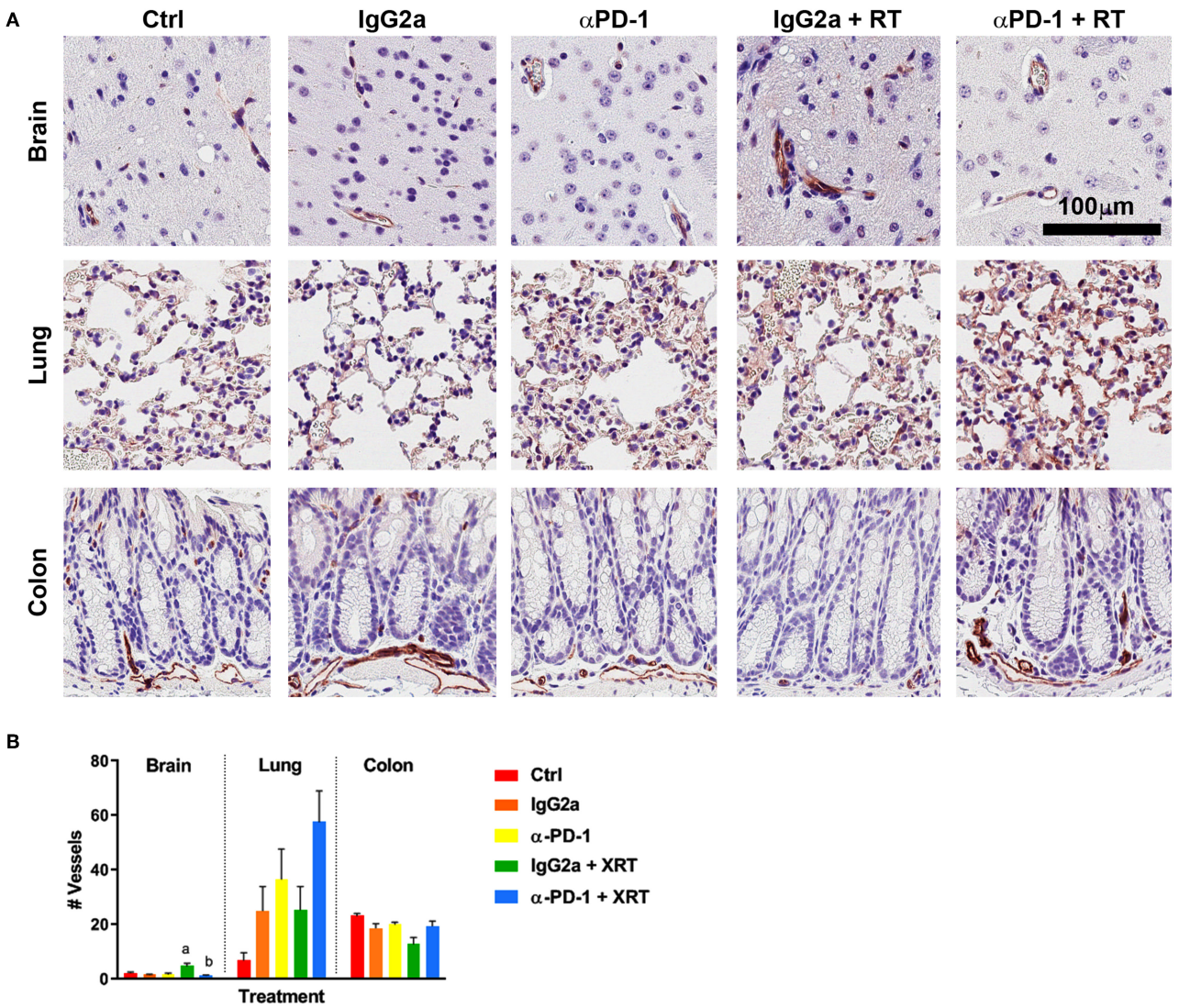

FIGURE 2 | CD31^{+} staining at the irradiation sites of murine brain, lung and colon tissue **(A)**. Scale bar, 100 μm. Quantitation of five high power fields for each murine tissue ($N = 6$ per time point; **B**). Data are expressed as mean ± SEM per high power field. $^{a}p < 0.05$ vs. IgGa, $^{b}p < 0.05$ vs. IgG2a + RT by Tukey's multiple comparison test.

due to the role of Tregs in B cell differentiation for HSCs (16). Notably, the proportion of HSCs was not altered by treatment (**Supplementary Figures 3–5**).

In peripheral blood, colon RT + αPD-1 increased B-cells 2.1-fold compared to αPD-1 alone ($p < 0.0001$; **Figure 7**). RT + IgG2a decreased DCs in brain and colon tissue compared to IgG2a alone ($p < 0.05$) and RT reduced PMN-MDSCs irrespective of immunotherapy. M2 were largely absent in peripheral blood but showed increases following brain RT + αPD-1, though this did not reach significance (**Figure 7**). Data show that the addition of brain or colon irradiation to αPD-1 immunotherapy may modulate in the peripheral immune response.

Plasma Cytokines, Chemokines, and Growth Factors Were Not Altered by Combination Therapy

To assess the cytokine and chemokine release following 10Gy/5 fractionated stereotactic radiation and αPD-1 immunotherapy plasma cytokine and chemokine levels were assessed by multiplex immunoassay. Irradiation of normal brain and lung tissue with or without αPD-1 decreased interleukin (IL)-1β levels 7 to 13-fold when compared to IgG2a or αPD-1 alone (**Figure 8**). Of note, TGF-β levels were below the level of detection in 17/48 (35%) of plasma samples (**Supplementary Figure 6**). Data suggest that at the sub-acute time point of 28 days post treatment commencement radiation-induced reduction of

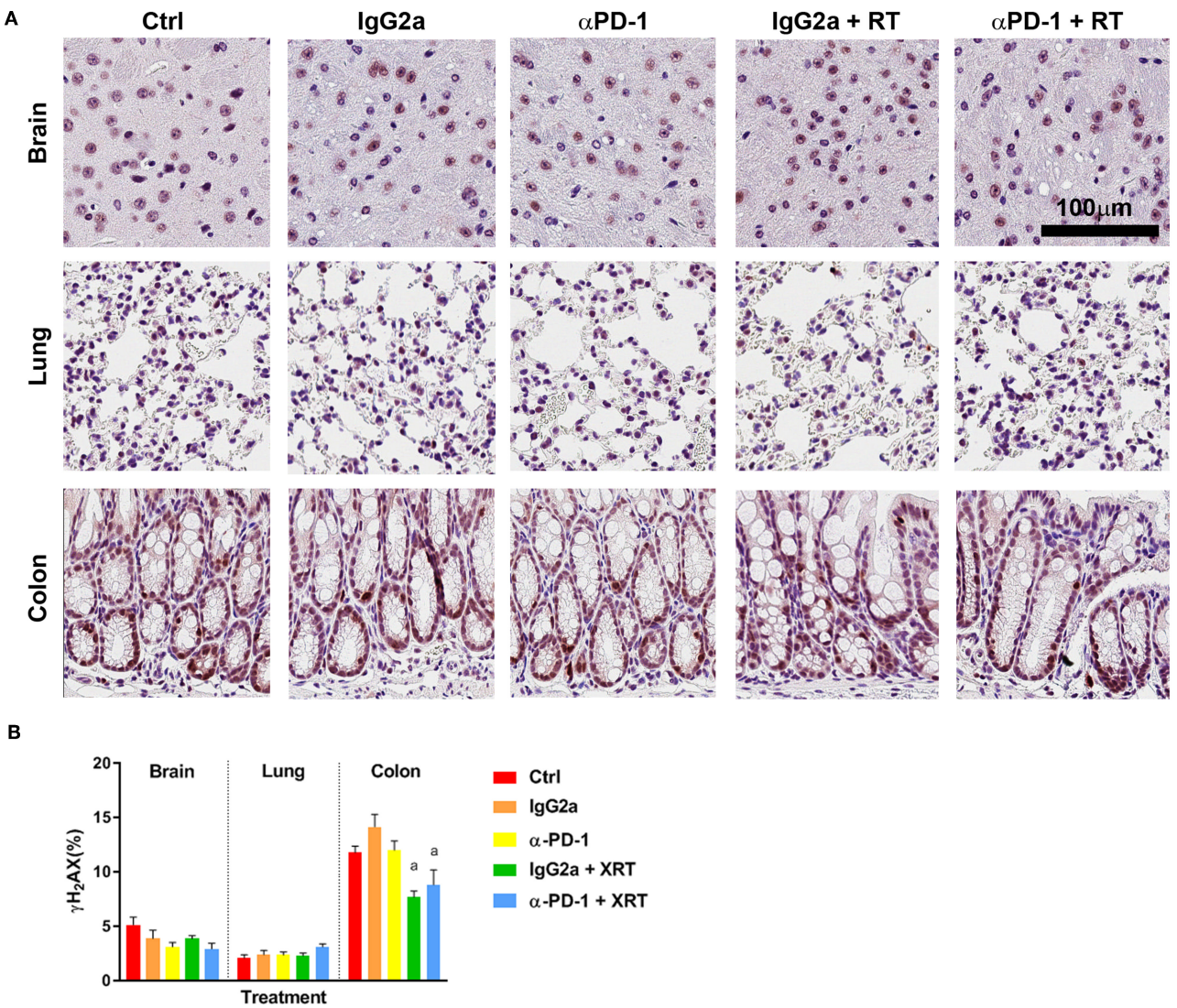

FIGURE 3 | γ-H2AX^{+} staining at the irradiation sites of murine brain, lung and colon tissue **(A)**. Scale bar, 100 μm. Quantitation of five high power fields for each murine tissue ($N = 6$ per time point; **B**). Data are expressed as mean ± SEM per high power field. $^{a}p < 0.05$ vs. Ctrl by Tukey's multiple comparison test.

IL-1β suppression is neither ameliorated nor exacerbated by αPD-1 immunotherapy.

DISCUSSION

Radiation induces DNA damage, cellular stress, apoptosis, cytokine release, and immune cell recruitment and activation (8). The effect of radiation on the tumor microenvironment is dependent on type, dose, field size, and fractionation (8). While this is known in the context of tumors, less is known regarding the systemic effect in response to local irradiation of normal tissues particularly when combined with immune-oncology agents. In this study the local tissue and systemic immune response of combined fractionated stereotaxic RT and αPD-1 immunotherapy was assessed in normal tissues that commonly (lung and colon) and infrequently (brain) experience immune-related toxicity. A schematic of the existing normal tissue response to radiation and immunotherapy, and the data summarized in this manuscript is provided in **Figure 9**.

The effect of combined radiation and αPD-1 immunotherapy on proliferative rates of normal tissues was assessed by Ki67^{+} staining. Ki67 is expressed during all active phases of the cell cycle (G1, S, G2, and M), but not resting cells (G0) allowing an assessment of the growth fraction of the irradiated cell populations. The mammalian intestinal epithelium rapidly renews itself, with the entire epithelium being replaced in 3–5 days. Additionally, it is known that following radiation injury, quiescent and/or radioresistant intestinal stem cells become active stem cells to regenerate the epithelium (17).

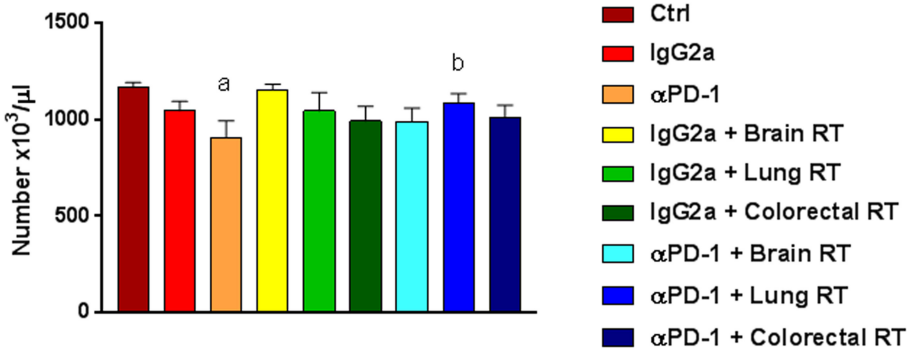

FIGURE 4 | Platelets in mice treated with αPD-1 and/or 10Gy/5 X-ray irradiation of brain, colon or right lung region. Blood was harvested at day 28 and quantitated by multi-color flow cytometry. Data are expressed as mean ± SD absolute count of platelets ($N = 6$ mice per treatment group). One Way ANOVA [a]$p < 0.05$ vs. Ctrl; [b]$p < 0.05$ vs. αPD-1 by Tukey's Multiple Comparison Test.

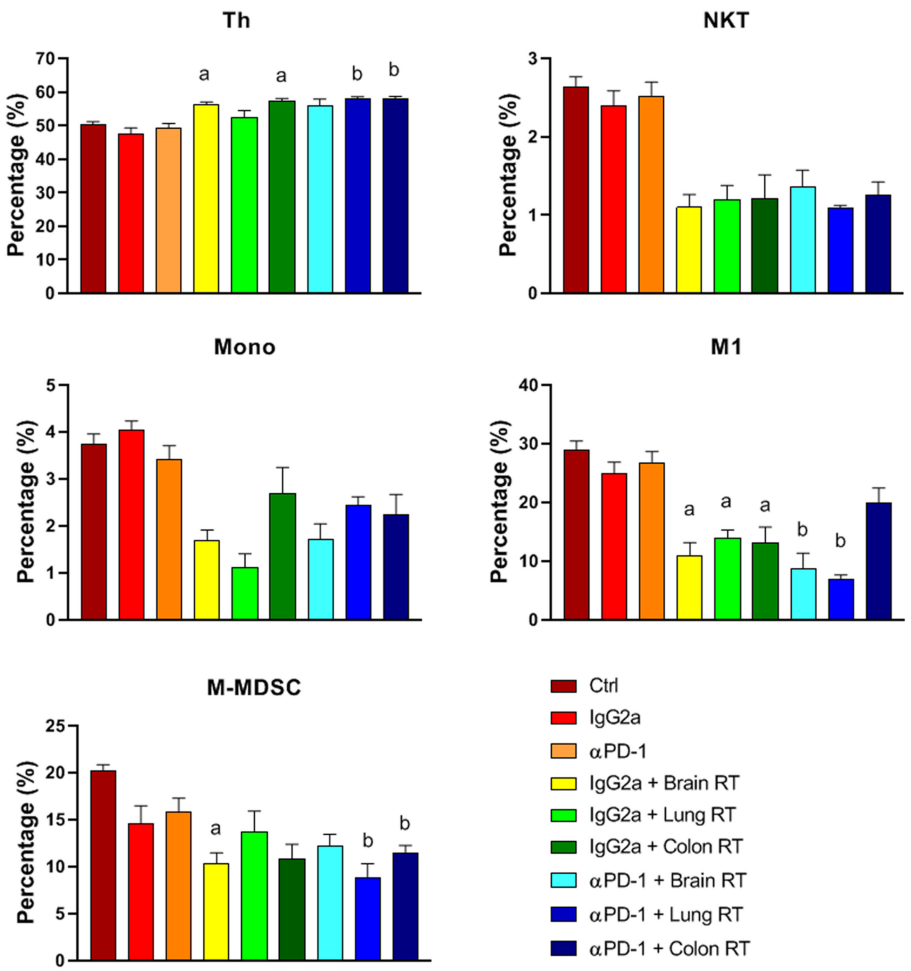

FIGURE 5 | Splenic immune cell populations from mice treated with αPD-1 and/or 10 Gy/5 X-ray irradiation of brain, lung and colon tissue. Cells were harvested at day 28 and quantitated by multi-color flow cytometry. Data are expressed as mean ± SD percentage of parent population (%; $N = 6$ mice per treatment group). Two Way ANOVA [a]$p < 0.05$ vs. IgG2a; [b]$p < 0.05$ vs. αPD-1 by Tukey's Multiple Comparison Test.

This process incorporates three phases; apoptotic phase (day 1–2), proliferative phase (days 3–7) and the normalization phase (days 7–14) (17). In spite of this 2-week restorative time line and fractionated 10Gy/5 radiation treatment regimen utilized in our study, the normal colon tissue showed reduced Ki67$^+$ 28 days post-irradiation of the intestinal epithelial cells.

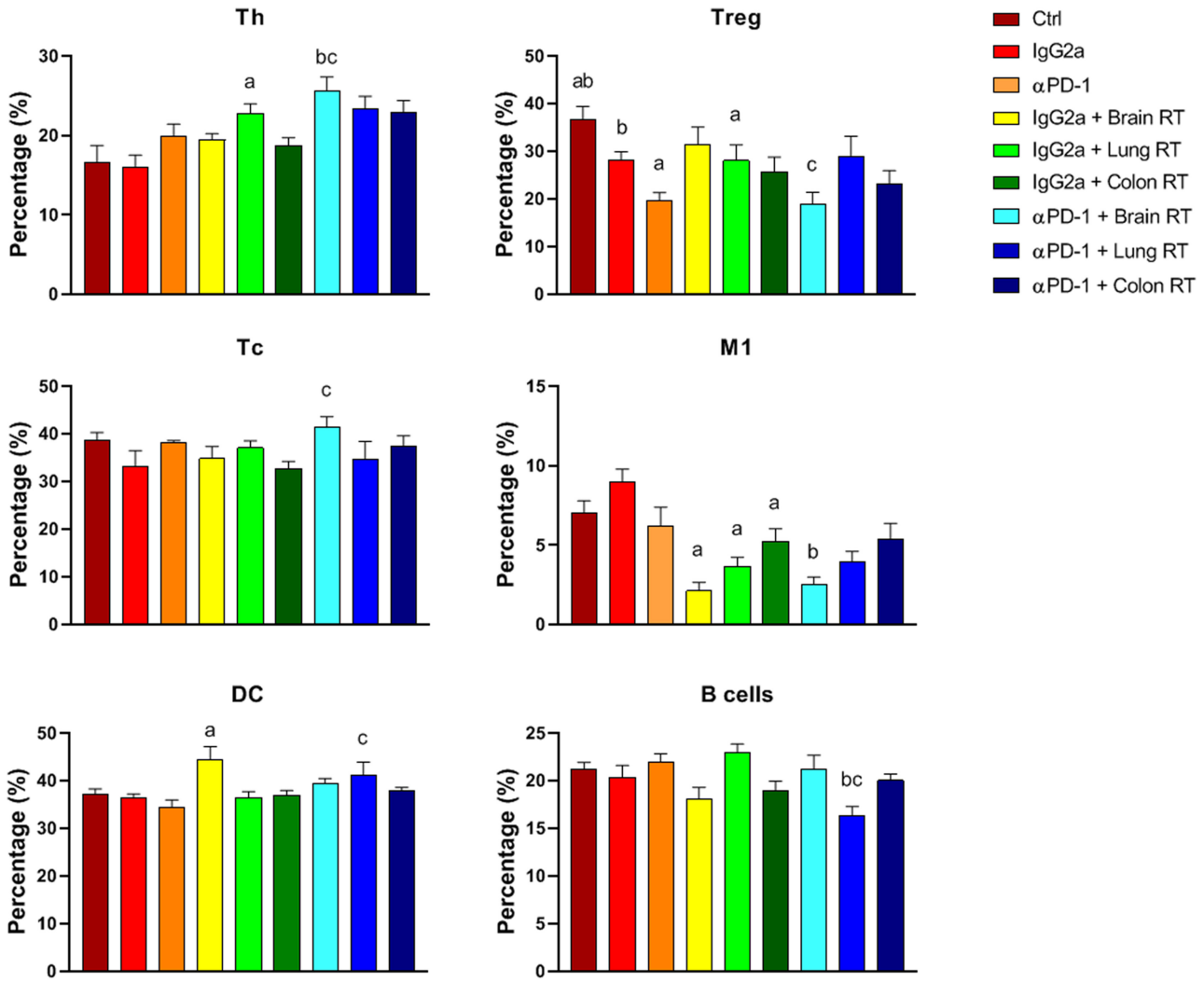

FIGURE 6 | Bone marrow immune cell populations from mice treated with αPD-1 and/or 10 Gy/5 X-ray irradiation of brain, lung, and colon tissue. Cells were harvested at day 28 and quantitated by multi-color flow cytometry. Data are expressed as mean ± SD percentage of parent population (%; $N = 6$ mice per treatment group). Two Way ANOVA $^{a}p < 0.05$ vs. IgG2a; $^{b}p < 0.05$ vs. αPD-1; $^{c}p < 0.05$ vs IgG2a + RT by Tukey's Multiple Comparison Test.

While this was not further exacerbated by the addition of αPD-1 immunotherapy, the data indicate that colon tissue is susceptible to persistent radiation-induced changes to cellular proliferation and attribute attributed to the development of colitis following radiotherapy.

The tumor vasculature and endothelial cells are some of the most studied components to assess radiobiological effects in the tumor microenvironment following radiation treatment. It is well-characterized that radiation induces endothelial cell dysfunction, including increased permeability, detachment from the underlying basement membrane, and endothelial cell senescence and/or apoptosis (18, 19). In normal brain tissue the αPD-1 immunotherapy alone increased blood vasculature while in combination with RT blood vasculature reduced. The latter was not significantly different to the number of blood vessels quantitated in IgG2a + RT brain tissue, indicating that this is consistent with the known effect of radiation on endothelial cells. A preclinical study using the same strain of mouse (C57Bl/6) to investigate cerebral permeability following 40Gy/20 fractionated radiation showed no significant difference in blood brain barrier permeability at day 30 post-irradiation; blood brain barrier permeability was not significantly increased until 90 days post-irradiation (20). Differences in the observance of alterations to blood vessel numbers and dynamics may be attributable to differences in radiation delivery and assessment methodologies. Notably, this study used whole brain irradiation and fluorescein-based intravital microscopy to assess blood permeability (which has a limitation of ∼1 mm in tissue depth), while our study assessed physical blood vasculature parameters by histopathology at the isocentre of our 5 × 5 mm stereotactic irradiation focused at the caudoputamen.

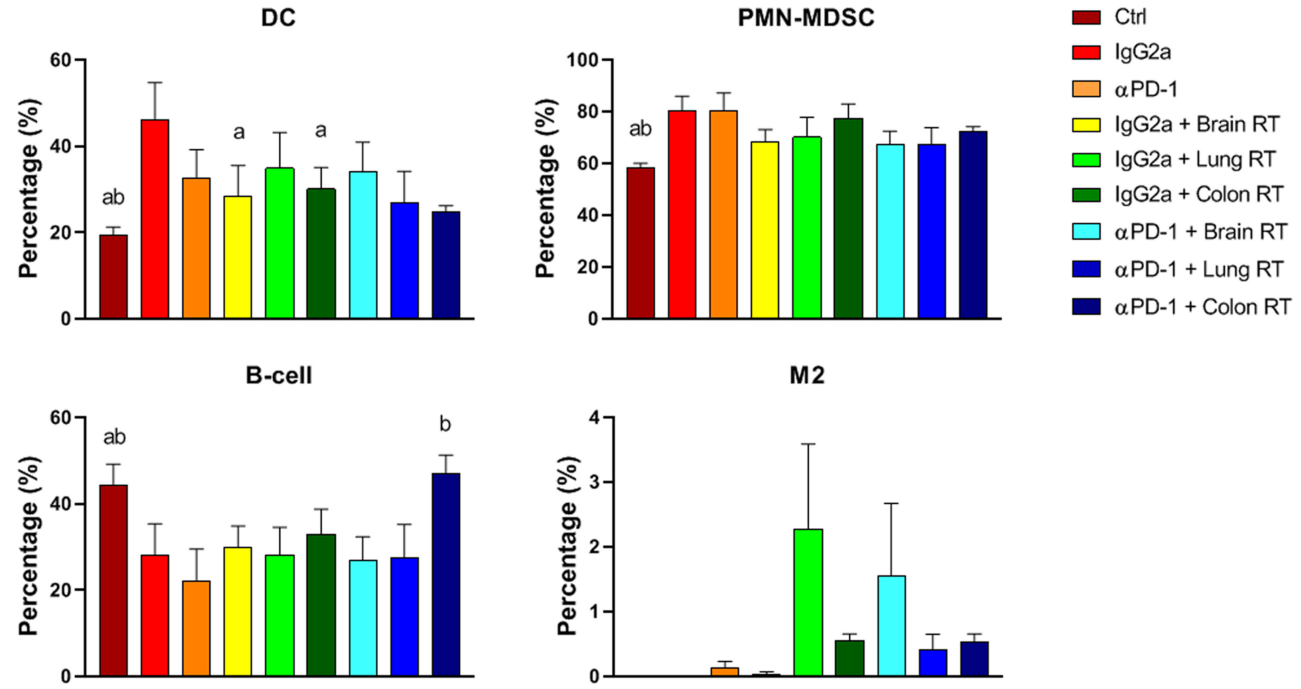

FIGURE 7 | Peripheral blood immune cell populations from mice treated with αPD-1 and/or 10 Gy/5 X-ray irradiation of brain, lung and colon tissue. Cells were harvested at day 28 and quantitated by multi-color flow cytometry. Data are expressed as mean ± SD percentage of parent population (%; $N = 6$ mice per treatment group). Two Way ANOVA [a]$p < 0.05$ vs. IgG2a; [b]$p < 0.05$ vs. αPD-1 by Tukey's Multiple Comparison Test.

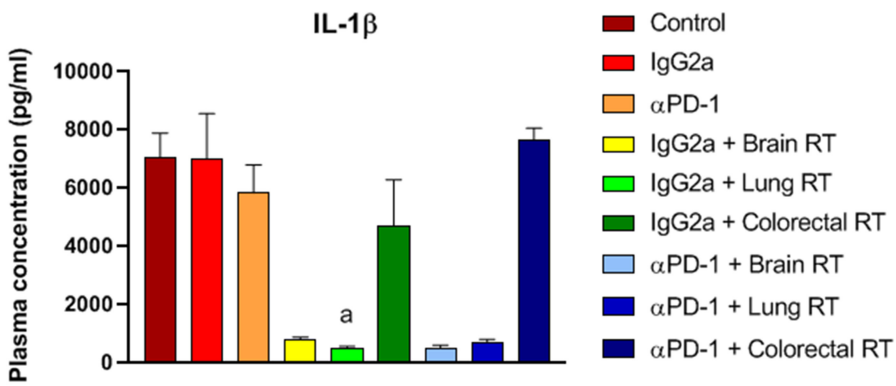

FIGURE 8 | IL-1β levels from mice treated with αPD-1 and RT. Plasma was harvested at day 28 and quantified by 23-plex immunoassay (additional cytokines are presented in **Supplementary Figure 6**). Data are expressed as mean ± SD observed concentration in pg/ml. $N = 6$ mice per treatment group. Two Way ANOVA [a]$p < 0.01$ vs. IgG2a by Tukey's Multiple Comparison Test.

Under fractionated treatment regimens (with comparatively low energy photons), radiation-induced DNA damage is principally evoked via the generation of reactive oxygen species and is mediated by H2AX (21). DNA damage to a variety of cell types in the tumor and within the surrounding healthy tissue can have a range of consequences, including microvascular endothelial cell apoptosis, crypt damage, organ failure and death (18). To investigate persistent radiation-induced DNA damage we quantified γ-H2AX staining. At the sub-acute time point γ-H2AX$^+$ staining was significantly reduced by 50% in irradiated colon tissue, but not when combined with αPD-1 immunotherapy. It is unclear why γ-H2AX staining was lower in αPD-1 treated tissue when compared to control and irradiated tissues. We speculate that repair of DNA damage may have occurred, but the normal proliferative rate of cells had been impacted out to the assessed 28-day post-treatment period. This has precedence with endogenous γ-H2AX being associated with cell cycle DNA replication mediated by the DNA-dependent

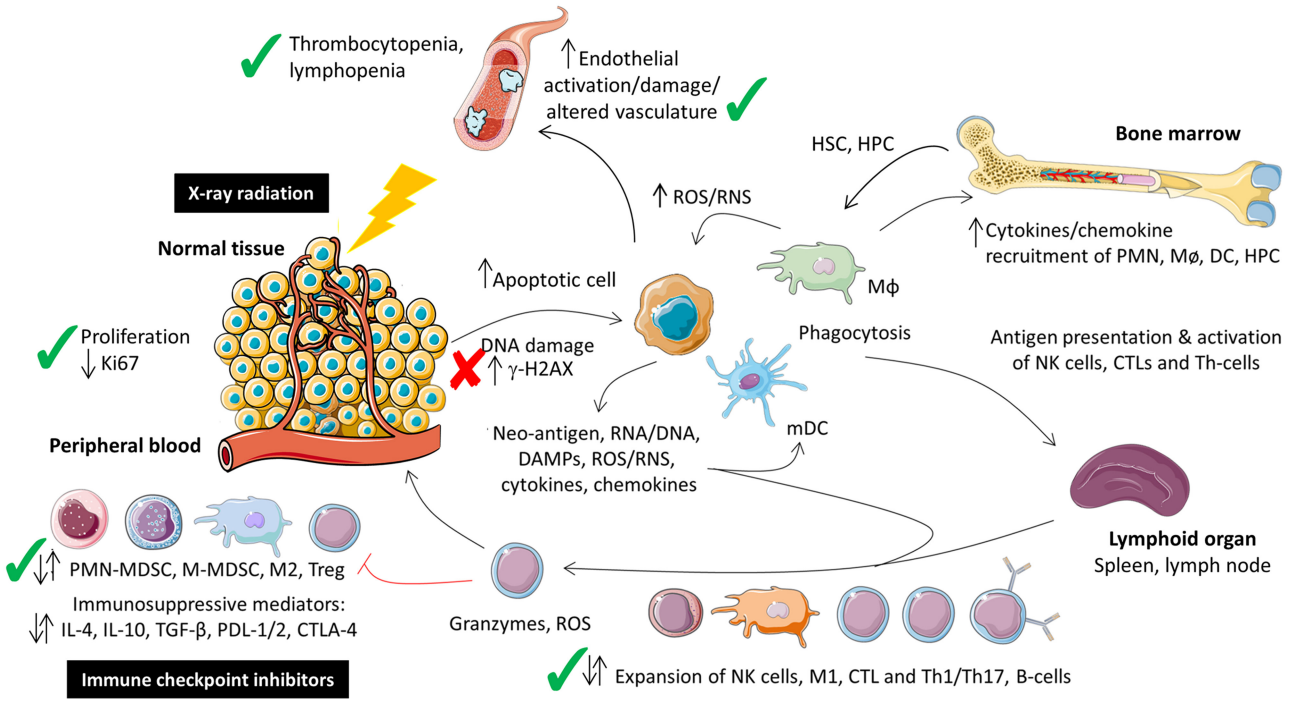

FIGURE 9 | Schematic representation of the local tissue and systemic immune response to combination fractionated stereotactic radiotherapy and αPD-1 immunotherapy at day 28 post-treatment. Figure modified from McKelvey et al. (8), Creative Commons Attribution 4.0 International License (http://creativecommons.org/licenses/by/4.0/) and prepared using Sevier Medical Art (https://smart.servier.com/). Check (✓) and cross marks (✗) indicate where the data was consistent with what has been described for monotherapeutic radiotherapy and immunotherapy monotherapy. Due to the paucity of data on the combination therapy it was unclear whether immune cell populations were expected to increase, decrease or remain unchanged at this acute time point, denoted by dual arrows. CTL, cytotoxic T-lymphocyte; HPC, haematopoietic progenitor cell; HSC, haematopoetic stem cell; Mø, monocyte; MΦ, macrophage; MDSC, myeloid-derived suppressor cell.

protein kinases/checkpoint kinase 2 pathway (22). However, γ-H2AX staining was present throughout the intestinal epithelial cells at not just the intestinal progenitor cells present at the base of intestinal crypts (as noted with Ki67 staining).

Thrombocytopenia is a hematological adverse event experienced by patients during immunotherapy treatment (23). αPD-1 administered alone suppressed platelet numbers, which normalized to control levels when radiation was added. In a descriptive observational study comprising three French pharmacovigilance databases, αPD-1 immunotherapy induced thrombocytopenia in the 0.5% of cancer patients who developed immune-related hematological adverse events (23). Surprisingly we did not observe an exacerbation of reduced platelet counts due to radiation in irradiated and animals despite bone marrow being included within our 360° Arc radiation treatment regimens.

Radiation-induced inflammasome activation and apoptosis has been noted in T cells, NK/T and monocytes with sustained caspase-1 cleavage until day 7 post-radiation (24) and is reflected in the splenic compartment (25). In our study, splenic M1 and M-MDSCs were suppressed in animals receiving combination therapy, when compared to αPD-1 monotherapy. Combined these data indicate that the addition of αPD-1 to RT significantly alters the immune repertoire of the splenic compartments. αPD-1 immunotherapy suppresses T cell function primarily by inactivating CD28 signaling (26). In the present study αPD-1 immunotherapy alone decreased Treg levels in bone marrow. Tregs play a critical role in B cell differentiation from HSCs (16) and coincided with decreased B-cells in the bone marrow compartment. Increased Th, Tc and DC cells in bone marrow were observed following combined therapy when compared to IgG2a + RT potentially indicating sequestration of pro-inflammatory immune cell types in the bone marrow. Alternatively the decreased Tregs may drive increased DCs via the PD-1-dependent bidirectional regulation of these two cell types. PD-1 is a critical homeostatic regulator for Tregs by modulating proliferation, survival and apoptosis mediated by IL-2 (27). Furthermore, the reciprocal modulation of Tregs and DC/MDSCs is dependent on chemokine CCL2 and TGF-β. PD-1 and TGF-β mediate the recruitment and bidirectional regulation of Treg cells and MDSCs (28–31) and remain elevated for up to 8 weeks post-radiation (32). While we observed an inverted Treg/DC relationship, the levels of IL-2, TGF-β and CCL2/MCP-1 were not altered in the present study.

Irradiation is known to evoke an inflammation response and is associated with increases in cytokine production. For example, irradiation of whole lung tissue with 12Gy elevates serum levels of G-CSF, IL-6, CXCL1/KC, CCL2/MCP-1, CXCL10/IP-10, and IL-1α (33) and the persistent elevation of inflammatory cytokines contributes to tissue injury and immune-related adverse events (32). In murine models of radiation-induced injury the serum

cytokine levels positively correlated with irradiated tissue levels, implicating blood as a surrogate marker for tissue cytokine levels (33). The only cytokine/chemokine modulated in our sub-acute study was plasma IL-1β which decreased in animals receiving irradiation to brain and lung tissue. While IL-1β is a pluripotent cytokine and plays a role in tumorigenesis and tumor progression, the role of IL-1β in radiation-induced normal tissue toxicity is unclear (32) but has been related to skin-related adverse events (34, 35). We did not observe skin irritation from the fractionated stereotactic radiation used in our study.

Immune toxicities from radiotherapy and immunotherapy alone have been extensively reported. These include the recent establishment of European and American clinical guidelines for the management of immune toxicities which varies with grade from continuation of immunotherapy with monitoring, withholding immunotherapy and administering immunosuppressant (prednisolone), to permanent discontinuation of the immunotherapy (4, 5). What remains comparatively unknown is whether combining radiation and immune check point immunotherapy will exacerbate these immune-related toxicities and whether these can be predicted at early time points during the treatment regimen. Overall our acute snapshot of this dynamic response showed that blood vasculature, cell proliferation, thrombocytopenia, lymphopenia, immune suppression and altered immune repertoire (including IL-1β) are observed when combination therapy of fractionated stereotactic radiotherapy and αPD-1 immunotherapy was used compared to either monotherapy. Consistent with low number of clinical studies on concurrent or sequential radiotherapy and immunotherapy there were no increases in serious acute toxicity from the combination therapy in our preclinical model when compared to monotherapy (36), but longer term studies are required. Akin to the clinical data, our report supports close monitoring of immune-related adverse events in patients who are to receive combination therapy. IL-1β and peripheral blood M2 could be further explored as potential biomarkers for immune toxicity.

DATA AVAILABILITY STATEMENT

The datasets generated for this study are available on request to the corresponding author.

ETHICS STATEMENT

The animal study was reviewed and approved by Northern Sydney Local Heath District Animal Ethics Committee, Royal North Shore Hospital, St Leonards, Australia (Approval #RESP/17/205).

AUTHOR CONTRIBUTIONS

KM, TE, SC, HW, CD, and VH contributed conception and design of the study. KM performed the animal experimentation, histopathology, hematology, flow cytometry, performed the statistical analyses, and wrote the first draft of the manuscript. RP contributed to the histopathology. AH performed the multiplex immunoassay. All authors contributed to manuscript revision, read, and approved the submitted version.

FUNDING

KM was supported by the Matt Callander 'Beanie for Brain Cancer' HMRI Fellowship (HMRI 17-25) funded by the Mark Hughes Foundation and AH by The Brain Cancer Group Fellowship. This project was supported by project grants from The Mark Hughes Foundation, The Brain Cancer Group, and Sydney Vital Translational Cancer Research Centre. The SARRP was funded by a Cancer Institute NSW Research Equipment Grant (2016/REG007 to VH).

ACKNOWLEDGMENTS

We thank the following groups for technical assistance; Histology Services, Hunter Medical Research Institute (histopathology). SARRP validation was performed with assistance from Cameron Stanton and Andrew Dipuglia, Department of Medical Physics, Royal North Shore Hospital, Northern Sydney Local Health District, NSW, Australia, and Michael Lerch, University of Wollongong, NSW, Australia.

SUPPLEMENTARY MATERIAL

The Supplementary Material for this article can be found online at: https://www.frontiersin.org/articles/10.3389/fonc.2019.01504/full#supplementary-material

REFERENCES

1. Carbone DP, Reck M, Paz-Ares L, Creelan B, Horn L, Steins M, et al. First-line nivolumab in stage IV or recurrent non-small-cell lung cancer. *N Engl J Med.* (2017) 376:2415–26. doi: 10.1056/NEJMoa1613493
2. Mantia CM, Buchbinder EI. Immunotherapy toxicity. *Hematol Oncol Clin N Am.* (2019) 33:275–90. doi: 10.1016/j.hoc.2018.12.008
3. Puzanov I, Diab A, Abdallah K, Bingham CO III, Brogdon C, Dadu R, et al. Managing toxicities associated with immune checkpoint inhibitors: consensus recommendations from the Society for Immunotherapy of Cancer (SITC) Toxicity Management Working Group. *J Immunother Cancer.* (2017) 5:95. doi: 10.1186/s40425-017-0300-z
4. Haanen J, Carbonnel F, Robert C, Kerr KM, Peters S, Larkin J, et al. Management of toxicities from immunotherapy: ESMO Clinical Practice Guidelines for diagnosis, treatment and follow-up. *Ann Oncol.* (2018) 29(Suppl 4):iv264–6. doi: 10.1093/annonc/mdy162
5. Brahmer JR, Lacchetti C, Schneider BJ, Atkins MB, Brassil KJ, Caterino JM, et al. Management of immune-related adverse events in patients treated with immune checkpoint inhibitor therapy: american society of clinical oncology clinical practice guideline. *J Clin Oncol.* (2018) 36:1714–68. doi: 10.1200/JCO.2017.77.6385
6. Baxi S, Yang A, Gennarelli RL, Khan N, Wang Z, Boyce L, et al. Immune-related adverse events for anti-PD-1 and anti-PD-L1 drugs: systematic review and meta-analysis. *BMJ.* (2018) 360:k793. doi: 10.1136/bmj.k793

7. Cortazar FB, Marrone KA, Troxell ML, Ralto KM, Hoenig MP, Brahmer JR, et al. Clinicopathological features of acute kidney injury associated with immune checkpoint inhibitors. *Kidney Int.* (2016) 90:638–47. doi: 10.1016/j.kint.2016.04.008
8. McKelvey KJ, Hudson AL, Back M, Eade T, Diakos CI. Radiation, inflammation and the immune response in cancer. *Mammal Genome.* (2018) 29:843–65. doi: 10.1007/s00335-018-9777-0
9. Qi ZY, Deng XW, Huang SM, Lu J, Lerch M, Cutajar D, et al. Verification of the plan dosimetry for high dose rate brachytherapy using metal-oxide-semiconductor field effect transistor detectors. *Med Phys.* (2007) 34:2007–13. doi: 10.1118/1.2736288
10. Kwan IS, Rosenfeld AB, Qi ZY, Wilkinson D, Lerch MLF, Cutajar DL, et al. Skin dosimetry with new MOSFET detectors. *Radiat Meas.* (2008) 43:929–32. doi: 10.1016/j.radmeas.2007.12.052
11. Breitkreutz DY, Bialek S, Vojnovic B, Kavanagh A, Johnstone CD, Rovner Z, et al. A 3D printed modular phantom for quality assurance of image-guided small animal irradiators: design, imaging experiments, and Monte Carlo simulations. *Med Phys.* (2019) 46:2015–24. doi: 10.1002/mp.13525
12. Dogdas B, Stout D, Chatziioannou AF, Leahy RM. Digimouse: a 3D whole body mouse atlas from CT and cryosection data. *Phys Med Biol.* (2007) 52:577–87. doi: 10.1088/0031-9155/52/3/003
13. Stout D, Chow P, Silverman R, Leahy RM, Lewis X, Gambhir S, et al. Creating a whole body digital mouse atlas with PET, CT and cryosection images. *Mol Imaging Biol.* (2002) 4:S27. Available online at: https://neuroimage.usc.edu/neuro/Digimouse
14. Reyes-Aldasoro CC, Williams LJ, Akerman S, Kanthou C, Tozer GM. An automatic algorithm for the segmentation and morphological analysis of microvessels in immunostained histological tumour sections. *J Microscopy.* (2011) 242:262–78. doi: 10.1111/j.1365-2818.2010.03464.x
15. Kuo LJ, Yang LX. γ-H2AX - a novel biomarker for DNA double-strand breaks. *In vivo.* (2008) 22:305–9. Available online at: http://iv.iiarjournals.org/content/22/3/305.long
16. Rajani KR, Carlstrom LP, Parney IF, Johnson AJ, Warrington AE, Burns TC. Harnessing radiation biology to augment immunotherapy for glioblastoma. *Front Oncol.* (2019) 8:656. doi: 10.3389/fonc.2018.00656
17. Kim C-K, Yang VW, Bialkowska AB. The role of intestinal stem cells in epithelial regeneration following radiation-induced gut injury. *Curr Stem Cell Rep.* (2017) 3:320–32. doi: 10.1007/s40778-017-0103-7
18. Paris F, Fuks Z, Kang A, Capodieci P, Juan G, Ehleiter D, et al. Endothelial apoptosis as the primary lesion initiating intestinal radiation damage in mice. *Science.* (2001) 293:293. doi: 10.1126/science.1060191
19. Venkatesulu BP, Mahadevan LS, Aliru ML, Yang X, Bodd MH, Singh PK, et al. Radiation-induced endothelial vascular injury: a review of possible mechanisms. *JACC Basic Transl Sci.* (2018) 3:563–72. doi: 10.1016/j.jacbts.2018.01.014
20. Yuan H, Gaber MW, Boyd K, Wilson CM, Kiani MF, Merchant TE. Effects of fractionated radiation on the brain vasculature in a murine model: blood-brain barrier permeability, astrocyte proliferation, and ultrastructural changes. *Int J Radiat Oncol Biol Phys.* (2006) 66:860–6. doi: 10.1016/j.ijrobp.2006.06.043
21. Kang MA, So EY, Simons AL, Spitz DR, Ouchi T. DNA damage induces reactive oxygen species generation through the H2AX-Nox1/Rac1 pathway. *Cell Death Dis.* (2012) 3:e249. doi: 10.1038/cddis.2011.134
22. Tu W-Z, Li B, Huang B, Wang Y, Liu X-D, Guan H, et al. γH2AX foci formation in the absence of DNA damage: mitotic H2AX phosphorylation is mediated by the DNA-PKcs/CHK2 pathway. *FEBS Lett.* (2013) 587:3437–43. doi: 10.1016/j.febslet.2013.08.028
23. Delanoy N, Michot JM, Comont T, Kramkimel N, Lazarovici J, Dupont R, et al. Haematological immune-related adverse events induced by anti-PD-1 or anti-PD-L1 immunotherapy: a descriptive observational study. *Lancet Haematol.* (2019) 6:e48–57. doi: 10.1016/S2352-3026(18)30175-3
24. Stoecklein VM, Osuka A, Ishikawa S, Lederer MR, Wanke-Jellinek L, Lederer JA. Radiation exposure induces inflammasome pathway activation in immune cells. *J Immunol.* (2015) 194:1178–89. doi: 10.4049/jimmunol.1303051
25. Balogh A, Persa E, Bogdándi EN, Benedek A, Hegyesi H, Sáfrány G, et al. The effect of ionizing radiation on the homeostasis and functional integrity of murine splenic regulatory T cells. *Inflammation Res.* (2013) 62:201–12. doi: 10.1007/s00011-012-0567-y
26. Hui E, Cheung J, Zhu J, Su X, Taylor MJ, Wallweber HA, et al. T cell costimulatory receptor CD28 is a primary target for PD-1-mediated inhibition. *Science.* (2017) 355:1428–33. doi: 10.1126/science.aaf1292
27. Asano T, Meguri Y, Yoshioka T, Kishi Y, Iwamoto M, Nakamura M, et al. PD-1 modulates regulatory T-cell homeostasis during low-dose interleukin-2 therapy. *Blood.* (2017) 129:2186–97. doi: 10.1182/blood-2016-09-741629
28. Lee CR, Kwak Y, Yang T, Han JH, Park SH, Ye MB, et al. Myeloid-derived suppressor cells are controlled by regulatory T cells via TGF-beta during murine colitis. *Cell Rep.* (2016) 17:3219–32. doi: 10.1016/j.celrep.2016.11.062
29. Zhang Y, Velez-Delgado A, Mathew E, Li D, Mendez FM, Flannagan K, et al. Myeloid cells are required for PD-1/PD-L1 checkpoint activation and the establishment of an immunosuppressive environment in pancreatic cancer. *Gut.* (2017) 66:124–36. doi: 10.1136/gutjnl-2016-312078
30. Shurin GV, Ma Y, Shurin MR. Immunosuppressive mechanisms of regulatory dendritic cells in cancer. *Cancer Microenviron.* (2013) 6:159–67. doi: 10.1007/s12307-013-0133-3
31. Chang AL, Miska J, Wainwright DA, Dey M, Rivetta CV, Yu D, et al. CCL2 produced by the glioma microenvironment is essential for the recruitment of regulatory T cells and myeloid-derived suppressor cells. *Cancer Res.* (2016) 76:5671–82. doi: 10.1158/0008-5472.CAN-16-0144
32. Rubin P, Johnston CJ, Williams JP, McDonald S, Finkelstein JN. A perpetual cascade of cytokines postirradiation leads to pulmonary fibrosis. *Int J Radiat Oncol Biol Phys.* (1995) 33:99–109. doi: 10.1016/0360-3016(95)00095-G
33. Ao X, Zhao L, Davis MA, Lubman DM, Lawrence TS, Kong FM. Radiation produces differential changes in cytokine profiles in radiation lung fibrosis sensitive and resistant mice. *J Hematol Oncol.* (2009) 2:6. doi: 10.1186/1756-8722-2-6
34. Liu W, Ding I, Chen K, Olschowka J, Xu J, Hu D, et al. Interleukin 1beta (IL1B) signaling is a critical component of radiation-induced skin fibrosis. *Radiat Res.* (2006) 165:181–91. doi: 10.1667/RR3478.1
35. Janko M, Ontiveros F, Fitzgerald TJ, Deng A, DeCicco M, Rock KL. IL-1 generated subsequent to radiation-induced tissue injury contributes to the pathogenesis of radiodermatitis. *Radiat Res.* (2012) 178:166–72. doi: 10.1667/RR3097.1
36. Verma V, Cushman TR, Tang C, Welsh JW. Toxicity of radiation and immunotherapy combinations. *Adv Radiat Oncol.* (2018) 3:506–11. doi: 10.1016/j.adro.2018.08.003

Conflict of Interest: The authors declare that the research was conducted in the absence of any commercial or financial relationships that could be construed as a potential conflict of interest.

frontiers in Oncology

ORIGINAL RESEARCH
published: 24 January 2020
doi: 10.3389/fonc.2019.01488

Prognosis and Risk Factors of Radiation-Induced Lymphopenia in Early-Stage Lung Cancer Treated With Stereotactic Body Radiation Therapy

Qianqian Zhao, Tingting Li, Gang Chen, Zhaochong Zeng and Jian He**

Department of Radiation Oncology, Zhongshan Hospital, Fudan University, Shanghai, China

Background: To investigate the role of stereotactic body RT (SBRT) in decreased total peripheral lymphocyte count (TLC) in patients with early-stage lung cancer and to explore possible risk factors for RT-induced lymphopenia.

Materials and Methods: We analyzed the TLCs and lymphocyte subsets of 76 patients in our prospective clinical database who received SBRT for early-stage lung cancer treatment. Relationships between clinical factors or dosimetric parameters and TLC were evaluated using Spearman's correlation analysis and Chi-square tests for continuous and categorical variables, respectively. Multivariate linear regression analysis was used to control for confounding factors. Kaplan–Meier analysis with a log-rank test and a multivariate Cox regression model were used for survival analysis.

Results: Most patients (64/76, 84.2%) experienced decreased absolute lymphocyte counts following SBRT, as well as shifts in lymphocyte subset distributions. Spearman's correlation coefficients between post-SBRT TLC and the percentage of the lung and heart receiving 5 to 50 Gy (in 5 Gy increments) shown that most lung DVH parameters [V(10)-V(50)] were significantly negatively correlated with post-SBRT TLC, while only heart V(5), V(20), V(25), V(30), and V(45) were significant. Univariate analyses revealed that a lower Pre-SBRT TLC level, higher mean lung dose, longer treatment duration, and longer TBT were significantly associated with a lower Post-SBRT TLC level (all $P < 0.05$). Stepwise multivariate linear regression, which incorporated all of the significantly clinical variables and SBRT-related parameters in univariate analysis, revealed that lower pre -SBRT TLC ($P < 0.001$), higher heart V5 ($P = 0.002$), and longer total beam-on time (TBT) ($P = 0.001$) were the independent risk factors for decrease in post-SBRT TLC. Patients with lower post-SBRT TLC and longer TBT exhibited significantly inferior progression-free survival (PFS) ($P < 0.001$ and $P = 0.013$) and overall survival ($P = 0.006$ and $P = 0.043$).

Conclusions: G2 and more severe lymphopenia after SBRT might be an independent prognostic factor for poorer outcome in early-stage lung cancer. Lowering heart V5 and TBT when designing SBRT plans may spare circulating lymphocytes and have the potential to further improve survival outcomes.

Keywords: radiation-induced lymphopenia, stereotactic body radiation therapy, early-stage lung cancer, prognosis, risk factors

OPEN ACCESS

Edited by:
Tiziana Rancati, Fondazione IRCCS Istituto Nazionale dei Tumori, Italy

Reviewed by:
Shahed Nicolas Badiyan, Washington University in St. Louis, United States
Bhanu Prasad Venkatesulu, Henry Ford Hospital, United States

****Correspondence:***
Zhaochong Zeng
zeng.zhaochong@zs-hospital.sh.cn
Jian He
hejian62@163.com

Specialty section:
This article was submitted to Radiation Oncology, a section of the journal Frontiers in Oncology

Received: *07 September 2019*
Accepted: *11 December 2019*
Published: *24 January 2020*

Citation:
Zhao Q, Li T, Chen G, Zeng Z and He J (2020) Prognosis and Risk Factors of Radiation-Induced Lymphopenia in Early-Stage Lung Cancer Treated With Stereotactic Body Radiation Therapy. Front. Oncol. 9:1488. doi: 10.3389/fonc.2019.01488

INTRODUCTION

The immunological side effects of radiation therapy (RT) for tumor treatment are complex and include both stimulatory and inhibitory activity (1, 2). The enhancement of anti-tumor immunity by RT is best exemplified by the observation that RT could promote the death of tumor immunogenicity through the generation of an analogous *in situ* cancer vaccine (1, 3). Unfortunately, this positive impact is often counteracted by RT-induced lymphopenia (RIL) (4). Circulating lymphocyte populations are highly radiosensitive and can undergo apoptosis or depletion due to radiation exposure. Ultimately, RIL suppresses anti-tumor immunity and is associated with inferior survival in patients with various tumors, including lung cancer (5–10). Moreover, previous work has shown that RIL would further compromise the therapeutic efficacy of immune checkpoint inhibitors through the loss of effector cells, which identify and destroy tumor cells (11, 12). This further emphasized the importance of preserving and maintaining circulating lymphocytes in the setting of the new therapeutic strategy of combining radiotherapy (RT) and immunotherapy in cancer patients.

The degree of RIL depends on the RT total dose, target volume, and number of fractions given (13–16), although many prior studies of RIL have focused on conventional fractionated radiotherapy (CFRT) (5). Anti-tumor immunity alterations caused by stereotactic body radiation therapy (SBRT) and CFRT differ distinctly (17, 18). Until recently, however, comparatively little attention has been paid to SBRT-induced lymphopenia. In clinical practice, the significant effects of SBRT on the total peripheral lymphocyte count (TLC) and corresponding risk factors in patients with lung cancer have yet to be established.

Thus, we evaluated the role of SBRT in the reduction of the TLC in patients with lung cancer and explored possible risk factors of RIL. Based on our findings, we then offer some strategies for sparing peripheral lymphocytes and further improving prognoses of these patients.

MATERIALS AND METHODS

Patient Eligibility and Clinical Characteristics

We analyzed our prospective clinical database of 171 patients who received definitive SBRT for lung cancer treatment between December 2014 and May 2018 at our institution. All patients underwent a comprehensive assessment before SBRT, including physical examination, laboratory analysis, chest computed tomography (CT) scans, abdominal CT or abdominal ultrasonography, brain magnetic resonance imaging, and bone scintigraphy. All patients with intrapulmonary tumors without pathological confirmation underwent ^{18}F-fluorodeoxyglucose-positron emission tomography/computed tomography (^{18}F-FDG PET/CT) scans. Diagnosis and treatment of these lesions were determined by a multidisciplinary lung cancer tumor team.

We applied the following study inclusion criteria for participant selection: (1) clinical early-stage lung cancer (tumor size < 5 cm) without regional lymph metastasis [N0] and distant metastasis [M0]; (2) ≥ 18 years of age; (3) Karnofsky performance status (KPS) ≥ 70; (4) fewer than three pulmonary lesions treated with SBRT; (5) complete blood cell counts within 1 week before SBRT and within 1 week after completion of SBRT available; (6) peripheral total white blood cells (WBCs) above 2,000 cells/μl, and did not receive prophylactic or remedial treatment for decreased WBCs during SBRT treatment. Patients were excluded if they were pathologically diagnosed with small-cell lung cancer, were missing dosimetry data, had a history of other malignancy within the last 5 years, had received prior thoracic irradiation, or had acute or chronic inflammatory, hematologic, or systemic immune disorders.

The detailed procedures of SBRT administration for lung cancer at our institution have been described previously (19, 20). All patients were treated with SBRT using the Helical TomoTherapy Hi-Art treatment system (Accuray; Madison, WI, USA). The study protocol was approved by the ethics board of Zhongshan Hospital, Fudan University (Approval Number: B2014-128). All participants signed an informed consent form prior to study inclusion.

Data Collection

The demographic and clinical information collected from participants included sex, age, KPS, smoking history, presence of respiratory system disease (chronic obstructive pulmonary disease, chronic bronchitis, or emphysema), tumor diameter, tumor location (central/peripheral), tumor histology, and total radiation dose. All laboratory values were measured using routine automated analyzers in the Clinical Laboratory of Zhongshan Hospital, Fudan University.

Venous blood samples were drawn from each patient at least twice: within 1 week before the start of SBRT (pre-SBRT) and within 1 week after completion of SBRT (post-SBRT) to quantify TLC and lymphocyte subset counts. Changes in the absolute counts and percentages of lymphocyte and lymphocyte subsets for each patient was calculated with the formula: Δvalue = post-SBRT value – pre-SBRT value. According to the National Cancer Institute Common Terminology Criteria for Adverse Events version 4.0, post-SBRT TLCs $<$ 1,000 cells/μL were considered to indicate lymphopenia, and post-SBRT TLCs $\geq$ 1,000 cells/μL (G0) were non-lymphopenia. Lymphopenia was further categorized into grade 1 (G1, $<$1,000 cells/μL), grade 2 (G2, $<$800 cells/μL), grade 3 (G3, $<$500 cells/μL), and grade 4 (G4, $<$200 cells/μL). For analysis of cell numbers in blood, peripheral venous blood was collected in lavender top K3EDTA (ethylenediaminetetraacetic acid) collection tubes and stained directly with fluorochrome-conjugated monoclonal antibodies for 30 min at +4°C within 4 h of collection. The monoclonal antibodies used in this study were: FITC-labeled CD3, clone SK7; PE-labeled CD16, clone B73.1, and CD56, clone NCAM16.2; PerCP-Cy^{TM}5.5†-labeled CD45, clone 2D1 (HLe-1); PE-Cy^{TM}7-labeled CD4, clone SK3; APC-labeled CD19, clone

Abbreviations: RIL, RT-induced lymphopenia; CFRT, conventional fractionated radiotherapy; TLC, total peripheral lymphocyte count; TBT, total beam-on time; MLD, mean lung dose; MHD, mean heart dose.

SJ25C1;25 and APC-Cy7‡-labeled CD8, clone SK1. Following staining, red blood cells were lysed using FACS Lysing solution (BD Biosciences) and analyzed on the BD FACSanto™ Flow Cytometer (BDBiosciences) within 6 h of staining.

Dosimetric parameters were also extracted from the treatment planning system, including treatment duration, total beam-on time (TBT), gross tumor volume (GTV), planning target volume (PTV), mean lung dose (MLD), mean heart dose (MHD), and a wide range of dose-volume histogram (DVH) parameters for total lung and heart volume: V5, V10, V15, V20, V25, V30, V35, V40, V45, and V50. V*n* (%) corresponds to the percentage of total lung or heart volume receiving at least *n* dose of radiation. The treatment duration (days) of SBRT was defined as the number of days from SBRT start to SBRT completion. TBT (seconds) of SBRT was defined as the length of time of circulating lymphocyte exposure to radiation, which was calculated by beam-on time per fraction multiplied by fraction number.

Patient Follow-Up and Outcomes

Follow-up duration and survival time were calculated from the start date of SBRT; the last follow-up date was May 30, 2019. Survival was censored if the patient was alive at the time of the last follow-up. Patients were generally evaluated weekly during SBRT, every 3 months following SBRT for the first 2 years, and every 6 months thereafter. PET/CT was performed only to distinguish recurrence from underlying SBRT-induced lung fibrosis. Progression-free survival (PFS) was calculated from the start date of SBRT to the date of any evidence of local or systemic cancer recurrence, death from any cause, or of the last follow-up. Overall survival (OS) was calculated from the start date of SBRT to the date of death from any cause or of the last follow-up.

Statistical Analysis

Continuous variables were summarized as means ± standard deviation or medians (ranges) and compared using the Wilcoxon rank-sum test. Categorical variables were summarized as proportions and compared using Chi-square analysis or Fisher's exact test. Optimal cut-off values of continuous variables for survival prediction were determined based on the receiver-operating characteristic (ROC) curve (21). Relationships between clinical factors or dosimetric parameters and peripheral lymphocyte levels were evaluated using Spearman's correlation analysis for continuous variables and Chi-square tests for categorical variables. Spearman correlation coefficients were obtained for the association among different dosimetric parameters, then stepwise backward elimination with a selection criterion of $p < 0.1$ was applied to find the best subset of variables. Linear regression with a backward-forward stepwise method was used to analyze the relationships of the clinical variables and dosimetric parameters with post-SBRT TLC. The survival of patients with more than a 6-month follow-up time was analyzed further. The Kaplan–Meier estimator with a log-rank test was used to calculate and compare PFS and OS by patient covariates. Multivariate Cox regression with a backward-forward stepwise method was used to assess the potential influence of clinical factors and dosimetric parameters on PFS and OS. For multivariate linear and Cox regression analyses, potential variables with $P < 0.1$ in the univariate analysis were then included as covariates to identify their independent effect. *P*-values of <0.05 were considered statistically significant and reported as two-sided. All analyses were conducted using IBM SPSS statistical software (version 23, SPSS Inc.; Chicago, IL, USA).

RESULTS

Patient Characteristics

A total of 76 eligible patients with 81 small lung tumor lesions were enrolled in our study (**Figure 1**). The detailed characteristics of all of the patients are shown in **Table 1**.

Changes in TLC and Lymphocyte Subset Counts Following SBRT

The gating strategy figures of one patient are shown in **Supplementary Figure 1**. Alterations of mean cell counts and percentages of total lymphocytes belonging to specific

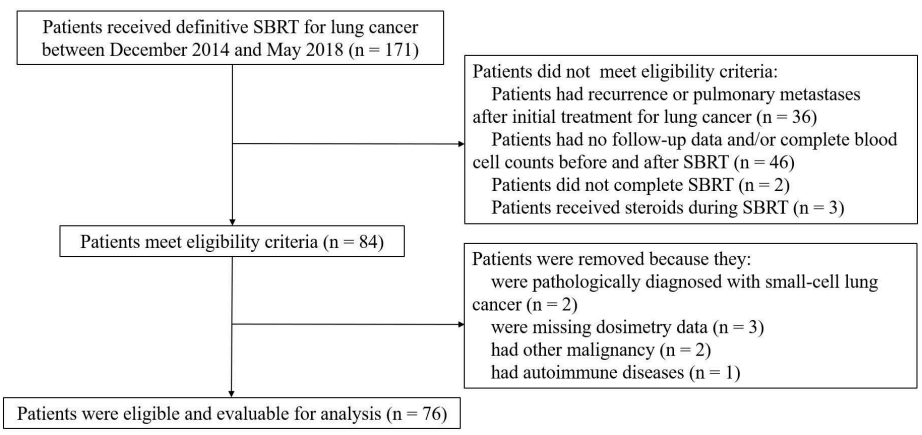

FIGURE 1 | Identification of included and excluded patients with early-stage lung cancer receiving stereotactic body radiation therapy.

lymphocyte subsets following SBRT. Fifty-five patients had data on lymphocyte subsets available for analysis. As expected, the majority of patients (64/76, 84.2%) experienced decreased absolute lymphocyte counts following SBRT. The mean alteration of the peripheral lymphocyte count after SBRT was −526.04 cells/μL. In total, 27 (35.53%) patients developed lymphopenia. Of these, 13 (17.10%) developed G1 lymphopenia, 11 (14.47%) developed G2, and 3 (3.95%) developed G3. No patient experienced G4 lymphopenia. The percentages of all of the lymphocyte subsets tested were affected post-SBRT (all $P < 0.05$), including $CD19^+$ B cells (fell by 53.88%), $CD3^+$ T cells (by 30.56%), $CD4^+$ T cells (by 34.64%), $CD8^+$ T cells (by 25.96%), and $CD56^+$ NK cells (by 13.28%). We observed a significant decrease in the $CD19^+$ B cell percentage following SBRT from mean 10.85% to 7.23% ($P < 0.001$) and the $CD4^+$ T cell percentage following SBRT from mean 37.95% to 36.27% ($P = 0.031$) and a significant increase in $CD56^+16$ T cells from mean 20.95% to 24.70% ($P < 0.001$). No statistically significant differences were noted in alterations of other lymphocyte subset percentages (**Table 2**).

TABLE 1 | Baseline characteristics ($n = 76$).

Characteristic	*n* (%) or median (range)
Sex	
Female	29 (38.16)
Male	47 (61.84)
Age at diagnosis (years)	72 (40–89)
Karnofsky performance status score	
≥80	55 (72.37)
<80	21 (27.63)
Smoking status	
Positive	32 (42.11)
Negative	44 (57.89)
Underlying respiratory system disease	
Yes	45 (59.21)
No	31 (40.79)
Tumor diameter (mm)	23.00 (9.00–48.00)
Gross tumor volume (cm^3)	10.61 (0.64–85.37)
Tumor location	
Central	20 (26.32)
Peripheral	56 (73.68)
SUV_{max}	5.10 (1.00–24.00)
Tumor histology	
Adenocarcinoma	39 (51.32)
Squamous	19 (25.00)
Unknown	18 (23.68)
SBRT dose and fractionation	
50 Gy in 5 fractions	26 (34.21)
60 Gy in 10 fractions	50 (65.79)

SUV_{max}, maximum standardized uptake value; SBRT, stereotactic body radiation therapy.

TABLE 2 | Mean ± standard deviation of peripheral lymphocyte count, lymphocyte subset counts, percentages of peripheral lymphocyte subsets, and $CD4^+/CD8^+$ before and after stereotactic body radiation therapy.

Parameters	*n*	Pre-SBRT	Post-SBRT	*P*
Total lymphocyte count (cells/μl)	76	1760.81 ± 649.06	1234.78 ± 528.82	< 0.001
$CD19^+$ B count (cells/μl)	55	206.42 ± 133.86	95.00 ± 59.18	< 0.001
$CD3^+$ T count (cells/μl)	55	1177.82 ± 522.81	818.00 ± 426.04	< 0.001
$CD4^+$ T count (cells/μl)	55	682.76 ± 327.47	446.24 ± 226.61	< 0.001
$CD8^+$ T count (cells/μl)	55	436.13 ± 238.54	322.91 ± 223.06	< 0.001
$CD56^+$ NK count (cells/μl)	55	361.20 ± 269.13	313.25 ± 290.30	0.030
$CD19^+$(%)	55	10.85 ± 4.70	7.23 ± 3.49	< 0.001
$CD3^+$(%)	55	66.62 ± 13.17	66.28 ± 14.78	0.681
$CD4^+$(%)	55	37.95 ± 9.60	36.27 ± 11.09	0.031
$CD8^+$(%)	55	25.42 ± 10.31	25.83 ± 10.37	0.392
$CD56^+16$(%)	55	20.95 ± 11.70	24.70 ± 14.58	< 0.001
$CD4^+/CD8^+$	55	1.81 ± 1.05	1.68 ± 0.96	0.017

SBRT, stereotactic body radiation therapy; $CD19^+$ B cells, B lymphocytes; $CD3^+$ T cells, T lymphocytes; $CD4^+$ T cells, T helper cells, $CD8^+$ T cells, T cytotoxic cells; $CD56^+$ NK cells, natural killer cells.

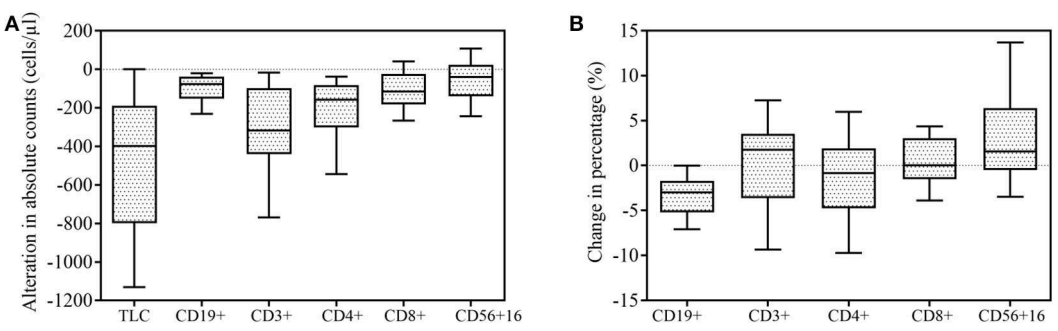

FIGURE 2 | Effect of stereotactic body radiation therapy (SBRT) on peripheral lymphocyte counts ($n = 76$) and lymphocyte subsets ($n = 55$). All box-and-whisker plots show median (middle horizontal line), 75th percentile (top horizontal line), 25th percentile (bottom horizontal line), 90th percentile (top whisker), and 10th percentile (bottom whisker) for change in lymphocyte and lymphocyte subsets following SBRT. **(A)** Alteration in absolute counts of lymphocytes and lymphocyte subsets. **(B)** Percentage change in lymphocyte subsets.

TABLE 3 | Correlation between post-SBRT total peripheral lymphocyte count and percentage of lung or heart dosed.

Characteristic	*n*	Spearman correlation coefficient (r)	*P*-value
Lung V5	76	−0.204	0.076
Lung V10	76	−0.276	0.016
Lung V15	76	−0.261	0.023
Lung V20	76	−0.278	0.015
Lung V25	76	−0.287	0.012
Lung V30	76	−0.293	0.010
Lung V35	76	−0.282	0.014
Lung V40	76	−0.331	0.004
Lung V45	76	−0.284	0.013
Lung V50	76	−0.337	0.003
Heart V5	72	−0.235	0.047
Heart V10	72	−0.170	0.152
Heart V15	72	−0.217	0.067
Heart V20	72	−0.271	0.021
Heart V25	72	−0.362	0.002
Heart V30	72	−0.287	0.015
Heart V35	72	−0.221	0.062
Heart V40	72	−0.229	0.053
Heart V45	72	−0.307	0.009
Heart V50	72	−0.212	0.073

SBRT, stereotactic body radiation therapy; Vn (%), the percentage of total lung or heart volume receiving at least n dose of radiation.

Correlations Between Post-SBRT TLC and Dosimetric Parameters

Spearman's correlation coefficients between post-SBRT TLC and the percentage of lung and heart receiving 5–50 Gy (in 5 Gy increments) are shown in **Table 3**. Most lung DVH parameters [V(10)-V(50) significantly negatively correlated with post-SBRT TLC, while only heart V(5), V(20), V(25), V(30), and V(45) were significant. Correlation coefficients remained greatest for lung V(50) ($r = -0.337$; $P = 0.003$) and heart V(25) ($r = -0.362$; $P = 0.002$). The correlation matrix among the different DVH parameters is presented in **Supplementary Table 1**.

Association of Post-SBRT TLC With Clinical Factors

Univariate and multivariate linear regression analysis between characteristics and post-SBRT TLC levels are shown in **Table 4**. Univariate analyses revealed that higher Pre-SBRT TLC level, higher mean lung dose, longer treatment duration, and longer TBT were significantly associated with a lower Post-SBRT TLC level. Stepwise multivariate linear regression, which incorporated all significantly clinical variables and SBRT-related parameters in univariate analysis, showed that lower pre-SBRT TLC ($P < 0.001$), longer TBT ($P = 0.001$), and higher heart V5 ($P = 0.002$) were independent risk factors for decreased post-SBRT TLC.

To evaluate if these associations existed pre-SBRT and were less likely to be SBRT-induced, we further assessed the relationships between pre-SBRT TLC and relevant patient characteristics (**Table 5**). Unlike post-SBRT TLC, we saw no significant differences in pre-SBRT TLC by sex, age, KPS, smoking status, underlying respiratory system disease, tumor diameter, tumor location, and SBRT-related parameters (all $P > 0.05$).

TABLE 4 | Univariate and multivariate linear regression analysis between characteristics and post-SBRT TLC.

Characteristic	Regression coefficient	95% CI	*P*
Univariate analysis			
Sex (female vs. male)	−32.517	−282.896 to 217.861	0.797
Age (year)	−3.266	−15.486 to 8.954	0.596
Karnofsky performance status (10%)	−3.030	−20.028 to 13.968	0.723
Smoker (smoker vs. never smoker)	−16.403	−231.169 to 263.976	0.895
Tumor diameter (mm)	−1.551	−14.304 to 11.203	0.809
Underlying respiratory system disease (yes vs. no)	97.891	−148.671 to 344.452	0.431
Pre-SBRT TLC (cells/μl)	0.528	0.385 to 0.672	<0.001
Dosimetric characteristics			
Gross tumor volume (cm^3)	−1.125	−8.857 to 6.608	0.773
Planning target volume (cm^3)	−1.995	−6.734 to 2.745	0.404
Mean lung dose (Gy)	−73.331	−139.641 to −7.021	0.031
Mean heart dose (Gy)	−34.819	−73.494 to 3.855	0.077
Radiation therapy			
Treatment duration (days)	−38.694	−69.801 to −7.587	0.015
Total beam-on time (seconds)	−0.129	−0.212 to −0.047	0.003
Fractionation (5 fractions vs. 10 fractions)	−215.285	−466.881 to 36.310	0.092
Multivariate analysis			
Pre-SBRT TLC (cells/μl)	0.524	0.393 to 0.656	< 0.001
Total beam-on time (seconds)	−0.103	−0.164 to −0.041	0.001
Heart V5	−5.452	−8.835 to −2.069	0.002

SBRT, stereotactic body radiation therapy; TLC, total peripheral lymphocyte count; CI, confidence interval; V_n, percentage of organ volume receiving n Gy.

Prognostic Value of Post-SBRT TLC

Survival analysis was performed to identify whether post-SBRT TLC exerted an independent prognostic influence on our patient population. Based on follow-up criteria, 63 patients were available for survival analysis. The median follow-up time was 22 months (range 6–55 months) for these patients, and at the end of the follow-up period, 53 (84.13%) patients were alive. In subgroup analysis, PFS and OS were not different between patients with G1 lymphopenia and those with G0 ($P = 0.466$ and $P = 0.449$, respectively). However, PFS and OS for G2-3 patients were significantly worse compared to G0-1 patients ($P < 0.001$ and $P = 0.006$, respectively). Considering this difference, we decided to classify patients into a G0-1 group and a G2-3 group to evaluate the prognostic value of post-SBRT TLC. In addition, we classified patients into a short TBT group (≤3,500 s) or high TBT group (>3,500 s) based on the ROC curve to evaluate the prognostic value of the beam-on time.

TABLE 5 | Relationships of Pre-SBRT TLC levels with baseline characteristics in patients with early-stage lung cancer.

Characteristic	Pre-SBRT lymphocyte count ≤ 1,600 ($n = 39$)	Pre-SBRT lymphocyte count > 1,600 ($n = 37$)	*P* value
Sex			
Male	27	20	
Female	12	17	0.173
Age (year)	74 (41–89)	70 (40–89)	0.189
Karnofsky performance status score			
≥80	29	26	
<80	10	11	0.690
Smoking status			
Positive	13	14	
Negative	26	18	0.368
Underlying respiratory system disease			
Yes	24	18	
No	15	19	0.259
Tumor diameter	23.00 (9.50–46.00)	23 (9.00–48)	0.686
Tumor location			
Central	7	13	
Peripheral	32	24	0.089
Dosimetric characteristics			
Gross tumor volume (cm^3)	12.95 (0.64–62.36)	10.40 (0.67–85.37)	0.776
Planning target volume (cm^3)	31.61 (4.14–105.35)	22.94 (3.82–116.20)	0.834
Mean lung dose (Gy)	4.38 (1.73–9.66)	4.27 (2.25–8.87)	0.719
Radiation therapy			
Treatment duration (days)	13 (5–16)	12 (5–20)	0.307
Irradiation time (seconds)	3599.00 (1921.50–8671.00)	3654.00 (1208.50–6384.00)	0.527
SBRT dose and fractionation			
50 Gy in 5 fractions	12	14	
60 Gy in 10 fractions	27	23	0.516

SBRT, stereotactic body radiation therapy; TLC, total peripheral lymphocyte count.

As shown in **Figure 3**, G0-1 and shorter TBT were significantly associated with improved PFS ($P < 0.001$ and $P = 0.013$) and OS ($P = 0.006$ and $P = 0.043$). **Table 6** presents univariate and multivariate analysis results for PFS and OS including relevant variables. Multivariate analysis showed that G0-1 was significantly associated with improved PFS (hazard ratio [HR]: 0.183; 95% CI: 0.076 to 0.441; $P < 0.001$) and OS (HR: 0.169; 95% CI: 0.043 to 0.665; $P = 0.011$) and longer TBT was significantly associated with inferior PFS (HR: 3.066; 95% CI: 1.186 to 7.929; $P = 0.021$) after controlling for confounding variables.

DISCUSSION

The key observations from the present study include the following findings. First, the paired analysis complete blood counts pre- and post-SBRT for lung cancer revealed that patients experienced a substantially reduced circulating TLC (1760.81 ± 649.06 vs. 1234.78 ± 528.82; $P < 0.001$), despite the small radiation field. This finding is in accordance with other studies (14, 22). Second, our multivariate linear regression showed that lower pre-SBRT TLC, higher heart V5, and longer TBT were independent risk factors of RIL. Third, multivariate Cox proportional hazard regression models further identified that post-SBRT TLC and TBT were independently correlated with PFS and OS in our patient population.

Figure 2 illustrates changes in the lymphocyte subset distribution following SBRT due to unequal decreases in various subsets. Peripheral lymphocyte homeostasis was disturbed by SBRT, as both the absolute number and percentage of $CD4^+$ T cells were significantly decreased after SBRT. Unlike $CD4^+$ T cells, the absolute number of $CD8^+$ T cells dropped less, and its relative percentage was nearly unchanged. Thus, the ratio of $CD4^+/CD8^+$ T cells decreased following SBRT ($P = 0.017$), which was also observed by Yang and colleagues in patients with head and neck cancer after receiving RT (23), although the radiosensitivities of $CD4^+$ T and $CD8^+$ T cells have been demonstrated to be similar (24). This result may be partially explained by SBRT's ability to promote priming and strong mobilization of $CD8^+$ T cells, therefore compensating for the reduced absolute number of $CD8^+$ T cells. This finding also supports the possibility that SBRT increases $CD8^+$ T cell accumulation in tumor sites because the therapeutic efficacy of local ablative radiation critically depends on the presence of effector $CD8^+$ T cells, but not $CD4^+$ T cells (25–27).

An effective anti-tumor immune response requires functional lymphocytes capable of detecting and destroying tumor cells. Given that the majority of our patients developed severe RIL following SBRT, which impedes anti-tumor immunity, determining possible risk factors for RIL is important. Accumulated data indicate that RIL depends on irradiation volume and fraction number (14, 15), although these two aspects of SBRT were not identified as independent risk factors for RIL in the present study. Perhaps the irradiation volumes of our patients were too small to achieve statistical significance, unlike the larger target volume of patients with advanced lung cancer. However, multivariate analyses of possible risk factors in previous studies did not incorporate treatment duration and TBT as variables. In contrast, we included clinical variables and SBRT-related parameters (lung and heart DVH parameters, treatment duration, and TBT) and only identified pre-SBRT TLC, heart V5, and TBT as independent risk factors for RIL. Thus, we inferred that higher heart V5 and longer TBT contribute to RIL in lung cancer patients and should be considered when designing SBRT regimens so as to maximize the number of circulating lymphocytes sustained during irradiation treatment. In addition, a positive correlation between tumor volume and beam-on time was observed ($r = 0.503$, $P < 0.001$) in our study. We also conducted univariate and multivariate Cox regression analyses

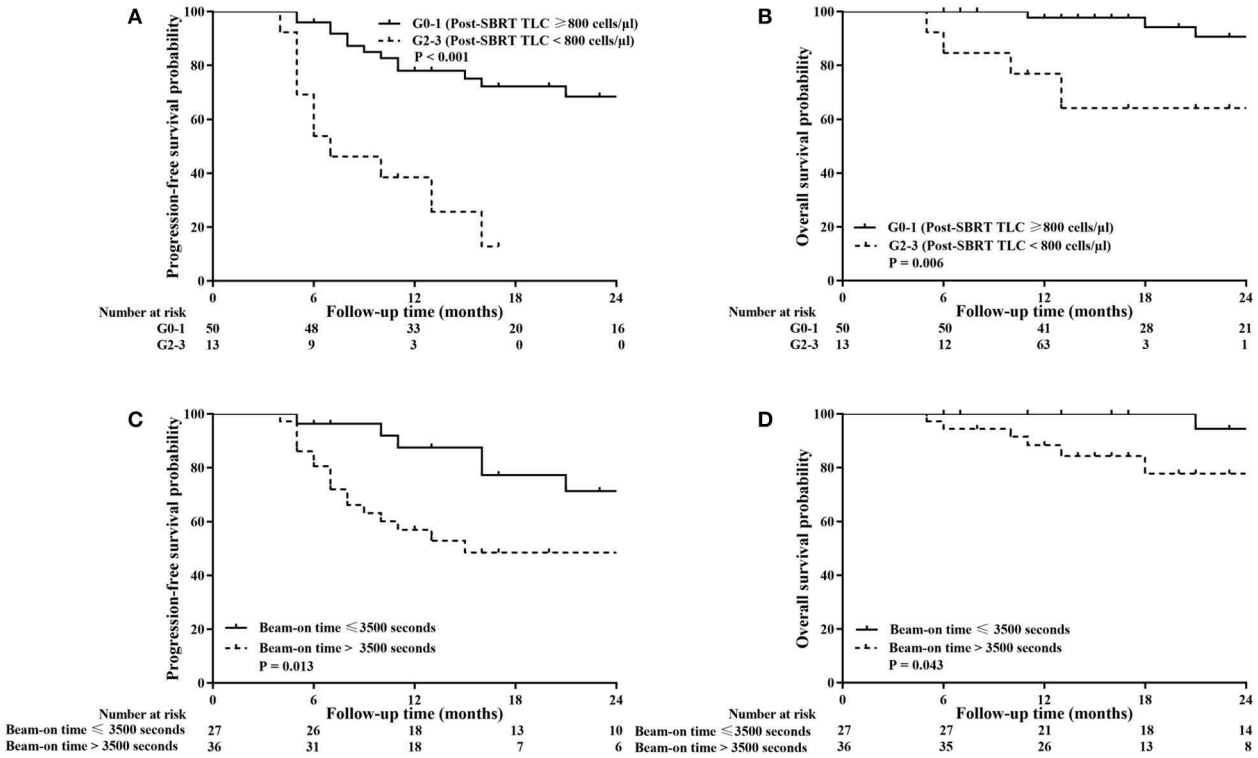

FIGURE 3 | Kaplan–Meier analysis of progression-free survival (PFS) and overall survival (OS) stratified by post-SBRT lymphocyte counts **(A,B)** and total beam-on time **(C,D)**. High total peripheral lymphocyte count (TLC) following SBRT and short total beam-on time were significantly associated with improved PFS ($P < 0.001$ and $P = 0.013$) and OS ($P = 0.006$ and $P = 0.043$).

to assess the correlation between survival outcomes and tumor volume as well as beam-on time. No significant correlation was found between tumor diameter and survival outcomes (*P*-value was 0.799 for PFS and 0.659 for OS), while the beam-on time had a negative effect on survival outcomes, as shown in **Table 6**. These results suggest that shortening the beam-on time may spare peripheral lymphocytes and ultimately improve patient prognosis. Of course, further large-scale validation studies are needed to confirm the impact of beam-on time on lymphocyte populations in patients with NSCLC who receive SBRT.

The mechanism of RIL is not completely understood, although circulating lymphocytes in peripheral vessels are directly killed as they pass through radiation treatment fields (28). Because larger radiation fields and longer TBT expose circulating lymphocytes to more radiation, the reduction in TLC should be proportional to the target volume and TBT (14, 16, 29), a supposition supported by our results. Irradiation of bone marrow or lymphatic tissue may also cause direct destruction of lymphocytes. Apart from direct toxicity, irradiation may indirectly affect circulating lymphocyte levels via cytokine modulation (15). For example, interleukin-7 (IL-7), a key cytokine involved in T-cell proliferation, is essential for maintaining circulating T-cell homeostasis. Although its circulating level negatively correlates with $CD4^+$ T cell counts (30), no compensatory rise in IL-7 levels in patients with severe RIL has been observed (31). Peiwen et al. reported an alternative cellular mechanism driving RIL related to the direct toxicity of radiation in SBRT-treated early-stage lung cancer. They considered that SBRT was delivered in a few fractions, thus limiting circulating lymphocyte exposure to ionizing irradiation as they pass through small radiation fields (32). However, SBRT was delivered with high ablative doses, as the biologically effective dose is often higher than 100 Gy. A negative correlation between the total radiation dose and post-RT TLC has also been demonstrated (29). Twelve patients in our study did not experience a decrease in peripheral lymphocytes. In this subset of our patient population, we speculate on whether the immune-stimulating effects of SBRT are greater than immunosuppressive effects or if their consistent TLC levels are driven by an unknown mechanism. Multiple questions and issues related to our observations remain unresolved: (1) the comprehensive effects of the target volume, fraction regimen, and total dose on RIL need to be explored; (2) the mechanism of lymphopenia development and its regulation needs to be characterized; (3) the optimal RT regimen to spare circulating lymphocytes need to be established. Given the clinical importance of this condition but the limited data regarding its nature and progression, additional research in this area is warranted. Several limitations should be considered in the interpretation of our findings. First, this study analyzed a single-centered dataset with limited patient numbers, so some useful predictors of RIL may have gone undetected. Second, several patients did not have pathological confirmation of pulmonary nodules because of the difficulty or perceived risk of obtaining small lesion specimens. However, all

TABLE 6 | Cox regression analysis for progression-free survival and overall survival.

Characteristic	Progression-free survival		Overall survival	
	HR (95% CI)	*P*	HR (95% CI)	*P*
Univariate associations				
Sex				
Female				
Male	0.932 (0.413–2.103)	0.866	0.552 (0.142–2.140)	0.390
Age (years)				
≤70				
>70	1.159 (0.495–2.713)	0.734	2.557 (0.540–12.104)	0.237
KPS score				
<80				
≥80	0.816 (0.321–2.073)	0.669	0.300 (0.079–1.130)	0.075
Smoking status				
Positive				
Negative	0.530 (0.197–1.425)	0.208	1.313 (0.329–5.239)	0.700
Underlying respiratory system disease				
Yes				
No	0.734 (0.328–1.641)	0.451	0.460 (0.129–1.641)	0.231
Tumor location				
Central				
Peripheral	1.830 (0.810–4.132)	0.146	2.421 (0.695–8.429)	0.165
Tumor diameter (mm)				
≤30				
>30	1.006 (0.961–1.053)	0.799	0.625 (0.078–5.036)	0.659
SBRT dose and fractionation				
50 Gy in 5 fractions				
60 Gy in 10 fractions	0.735 (0.304–1.774)	0.494	1.175 (0.878–1.572)	0.277
Treatment duration (days)				
≤7				
>7	1.819 (0.678–4.880)	0.235	43.621 (0.189–9616.973)	0.194
Beam-on time (seconds)				
≤3,500				
>3,500	3.034 (1.194–7.708)	0.020	4.402 (0.922–21.022)	0.063
Pre-SBRT lymphocytes (cells/μl)				
≤1,600				
>1,600	1.223 (0.547–2.733)	0.623	1.587 (0.447–5.642)	0.475
Post-SBRT lymphocytes (cells/μl)				
<800 (G2-3)				
≥800 (G0-1)	0.187 (0.080–0.439)	< 0.001	0.178 (0.046–0.695)	0.013
Multivariate associations				
KPS score				
<80				
≥80	NI		0.281 (0.074–1.068)	0.062
Beam-on time (seconds)				
≤3,500				
>3,500	3.066 (1.186–7.929)	0.021	NI	
Post-SBRT lymphocytes (cells/μl)				
<800 (G2-3)				
≥800 (G0-1)	0.183 (0.076–0.441)	<0.001	0.169 (0.043–0.665)	0.011

PFS, progression-free survival; OS, overall survival; HR, hazard ratio; CI, confidence interval; KPS, Karnofsky performance status; NI, not included in the multivariate model; SBRT, stereotactic body radiation therapy.

patients underwent ^{18}F-FDG PET/CT scans, and the diagnosis and treatment options for these lesions were determined by a multidisciplinary tumor board. Third, complete blood counts were measured at only two time points: before and after SBRT; our database did not document consecutive circulating lymphocyte count changes. We could not definitively determine when levels of circulating lymphocytes began to recover following SBRT, although we plan to further investigate this aspect of TLC development. Finally, the population in our study is a little heterogenous, in that patients with a central tumor or tumor close to the rib received 60 Gy in 10 fractions while patients with peripheral tumors received 50 Gy in 5 fractions. Therefore, these results require further investigations in larger prospective trials for validation.

Despite these limitations, we demonstrated that G2 and more severe lymphopenia after SBRT might be an independent prognostic factor for poorer outcome in early-stage lung cancer. The data further suggested that lowering heart V5 and reducing TBT may spare circulating lymphocytes in this patient population. Specifically, limiting the heart radiation dose and TBT when designing SBRT regimens may be crucial for reducing lymphocyte radiotoxicity and improving patient survival, especially in patients with a relatively low pre-SBRT TLC level.

DATA AVAILABILITY STATEMENT

The datasets generated for this study are available on request from the corresponding author.

ETHICS STATEMENT

The studies involving human participants were reviewed and approved by the ethics board of Zhongshan Hospital, Fudan University (B2014–128). The patients/participants provided their written informed consent to participate in this study.

AUTHOR CONTRIBUTIONS

ZZ and JH designed the study. QZ, TL, and GC contributed to the data collection. QZ analyzed the data and wrote the manuscript. All authors approved the version of the manuscript to be published.

FUNDING

This work was supported by the Clinical research projects of Zhongshan Hospital, Fudan University (No. 2018ZSLC26) and Medical Guidance Program of the Science and Technology Commission of Shanghai Municipality (No. 18411967900).

SUPPLEMENTARY MATERIAL

The Supplementary Material for this article can be found online at: https://www.frontiersin.org/articles/10.3389/fonc.2019.01488/full#supplementary-material

REFERENCES

1. Formenti SC, Demaria S. Combining radiotherapy and cancer immunotherapy: a paradigm shift. *J Natl Cancer Inst.* (2013) 105:256–65. doi: 10.1093/jnci/djs629
2. Dovedi SJ, Cheadle EJ, Popple A, Poon E, Morrow M, Stewart R, et al. Fractionated radiation therapy stimulates anti-tumor immunity mediated by both resident and infiltrating polyclonal T-cell populations when combined with PD1 blockade. *Clin Cancer Res.* (2017) 23:5514–26. doi: 10.1158/1078-0432.CCR-16-1673
3. Hatzi VI, Laskaratou DA, Mavragani IV, Nikitaki Z, Mangelis A, Panayiotidis MI, et al. Non-targeted radiation effects *in vivo*: a critical glance of the future in radiobiology. *Cancer Lett.* (2015) 356:34–42. doi: 10.1016/j.canlet.2013.11.018
4. Grossman SA, Ye X, Lesser G, Carraway H, Desideri S, Piantadosi S, et al. Immunosuppression in patients with high-grade gliomas treated with radiation and temozolomide. *Clin Cancer Res.* (2011) 17:5473–80 doi: 10.1158/1078-0432.CCR-11-0774
5. Grossman SA, Ellsworth S, Jian C, Campian J, Wild AT, Herman JM, et al. Survival in patients with severe lymphopenia following treatment with radiation and chemotherapy for newly diagnosed solid tumors. *J Natl Compr Canc Netw.* (2015) 13:1225–31. doi: 10.6004/jnccn.2015.0151
6. Campian JL, Ye X, Gladstone DE, Ambady P, Nirschl TR, Borrello I, et al. Pre-radiation lymphocyte harvesting and post-radiation reinfusion in patients with newly diagnosed high grade gliomas. *J Neurooncol.* (2015) 124:307–16. doi: 10.1007/s11060-015-1841-y
7. Balmanoukian A, Ye X, Herman J, Laheru D, Grossman SA. The association between treatment-related lymphopenia and survival in newly diagnosed patients with resected adenocarcinoma of the pancreas. *Cancer Invest.* (2012) 30:571–6. doi: 10.3109/07357907.2012.700987
8. Zhao Q, Xu X, Yue J, Zhu K, Feng R, Jiang S, et al. Minimum absolute lymphocyte counts during radiation are associated with a worse prognosis in patients with unresectable hepatocellular carcinoma. *Therap Adv Gastroenterol.* (2017) 10:231–41. doi: 10.1177/1756283X16685557
9. Liu LT, Chen QY, Tang LQ, Guo SS, Guo L, Mo HY, et al. The Prognostic Value of Treatment-related lymphopenia in nasopharyngeal carcinoma patients. *Cancer Res Treat.* (2017) 50:19–29. doi: 10.4143/crt.2016.595
10. Campian JL, Ye X, Brock M, Grossman SA. Treatment-related lymphopenia in patients with stage III non-small-cell lung cancer. *Cancer Invest.* (2013) 31:183–8. doi: 10.3109/07357907.2013.767342
11. Pike LRG, Bang A, Mahal BA, Taylor A, Krishnan M, Spektor A et al. The impact of radiation therapy on lymphocyte count and survival in metastatic cancer patients receiving PD-1 immune checkpoint inhibitors. *Int J Radiat Oncol Biol Phys.* (2019) 103:142–51. doi: 10.1016/j.ijrobp.2018.09.010
12. Schreiber RD, Old LJ, Smyth MJ. Cancer immunoediting: integrating immunity's roles in cancer suppression and promotion. *Science.* (2011) 331:1565–70. doi: 10.1126/science.1203486
13. Wild AT, Herman JM, Dholakia AS, Moningi S, Lu Y, Rosati LM, et al. Lymphocyte-Sparing Effect of stereotactic body radiation therapy in patients with unresectable pancreatic cancer. *Int J Radiat Oncol Biol Phys.* (2016) 94:571–9. doi: 10.1016/j.ijrobp.2015.11.026
14. Tang C, Liao Z, Gomez D, Levy L, Zhuang Y, Gebremichael RA, et al. Lymphopenia association with gross tumor volume and lung V5 and its effects on non-small cell lung cancer patient outcomes. *Int J Radiat Oncol Biol Phys.* (2014) 89:1084–91. doi: 10.1016/j.ijrobp.2014.04.025
15. Yuan C, Wang Q. Comparative analysis of the effect of different radiotherapy regimes on lymphocyte and its subpopulations in breast cancer patients. *Clin Transl Oncol.* (2018) 1219–25. doi: 10.1007/s12094-018-1851-2
16. Saito T, Toya R, Matsuyama T, Semba A, Oya N. Dosimetric predictors of treatment-related lymphopenia induced by palliative radiotherapy: predictive ability of dose-volume parameters based on body surface contour. *Radiol Oncol.* (2016) 51:228–34. doi: 10.1515/raon-2016-0050
17. Finkelstein SE, Timmerman R, Mcbride WH, Schaue D, Hoffe SE, Mantz CA, et al. The confluence of stereotactic ablative radiotherapy and tumor immunology. *Clin Dev Immunol.* (2011) 2011:439752. doi: 10.1155/2011/439752
18. Shi F, Wang X, Teng F, Kong L, Yu J. Abscopal effect of metastatic pancreatic cancer after local radiotherapy and granulocyte-macrophage colony-stimulating factor therapy. *Cancer Biol Ther.* (2017) 18:137–41. doi: 10.1080/15384047.2016.1276133
19. Ye L, Shi S, Zeng Z, Huang Y, Hu Y, He J. Nomograms for predicting disease progression in patients of Stage I non-small cell lung cancer treated with stereotactic body radiotherapy. *Jpn J Clin Oncol.* (2017) 48:160–6. doi: 10.1093/jjco/hyx179
20. He J, Huang Y, Shi S, Hu Y, Zeng Z. Comparison of effects between central and peripheral stage I lung cancer using image-guided stereotactic body radiotherapy via helical tomotherapy. *Technol Cancer Res Treat.* (2015) 14:701–7. doi: 10.1177/1533034615583206
21. Budczies J, Klauschen F, Sinn BV, Gyorffy B, Schmitt WD, Darb-Esfahani S, et al. Cutoff finder: a comprehensive and straightforward web application enabling rapid biomarker cutoff optimization. *PLoS ONE.* (2012) 7:e51862. doi: 10.1371/journal.pone.0051862
22. Maehata Y, Onishi H, Kuriyama K, Aoki S, Araya M, Saito R, et al. Immune responses following stereotactic body radiotherapy for stage I primary lung cancer. *Biomed Res Int.* (2013) 2013:731346. doi: 10.1155/2013/731346
23. Yang SJ, Rafla S, Youssef E, Selim H, Salloum N, Chuang JY. Changes in T-cell subsets after radiation therapy. *Radiology.* (1988) 168:537–40. doi: 10.1148/radiology.168.2.3260678
24. Nakamura N, Kusunoki Y and Akiyama M. Radiosensitivity of CD4 or CD8 positive human T-lymphocytes by an *in vitro* colony formation assay. *Radiat Res.* (1990) 123:224–7 doi: 10.2307/3577549
25. Lee Y, Auh SL, Wang Y, Burnette B, Wang Y, Meng Y, et al. Therapeutic effects of ablative radiation on local tumor require CD8+ T cells: changing strategies for cancer treatment. *Blood.* (2009) 114:589–95. doi: 10.1182/blood-2009-02-206870
26. Lugade AA, Moran JP, Gerber SA, Rose RC, Frelinger JG, Lord EM. Local radiation therapy of B16 melanoma tumors increases the generation of tumor antigen-specific effector cells that traffic to the tumor. *J Immunol.* (2005) 174:7516–23. doi: 10.4049/jimmunol.174.12.7516

27. Gupta A, Probst HC, Vuong V, Landshammer A, Muth S, Yagita H, et al. Radiotherapy promotes tumor-specific effector CD8+ T cells via dendritic cell activation. *J Immunol.* (2012) 189:558–66. doi: 10.4049/jimmunol.1200563
28. Sellins KS and Cohen JJ. Gene induction by gamma-irradiation leads to DNA fragmentation in lymphocytes. *J Immunol.* (1987) 139:3199–206.
29. Yovino S, Kleinberg L, Grossman SA, Narayanan M, Ford E. The etiology of treatment-related lymphopenia in patients with malignant gliomas: modeling radiation dose to circulating lymphocytes explains clinical observations and suggests methods of modifying the impact of radiation on immune cells. *Cancer Invest.* (2013) 31:140–4. doi: 10.3109/07357907.2012.762780
30. Mackall CL, Fry TJ, Gress RE. Harnessing the biology of IL-7 for therapeutic application. *Nat Rev Immunol.* (2011) 11:330–42. doi: 10.1038/nri2970
31. Susannah E, Ani B, Ferdynand K, Nirschl CJ, Nirschl TR, Grossman SA, et al. Sustained CD4+T cell-driven lymphopenia without a compensatory IL-7/IL-15 response among high-grade glioma patients treated with radiation and temozolomide. *Oncoimmunology.* (2014) 3:e27357. doi: 10.4161/onci.27357
32. Kuo P, Bratman SV, Shultz DB, von Eyben R, Chan C, Wang Z. Galectin-1 mediates radiation-related lymphopenia and attenuates NSCLC radiation response. *Clin Cancer Res.* (2014) 20:5558–69. doi: 10.1158/1078-0432.CCR-14-1138

Conflict of Interest: The authors declare that the research was conducted in the absence of any commercial or financial relationships that could be construed as a potential conflict of interest.

frontiers in Oncology

ORIGINAL RESEARCH
published: 11 February 2020
doi: 10.3389/fonc.2020.00124

Hypofractionated Radiotherapy Dose Scheme and Application of New Techniques Are Associated to a Lower Incidence of Radiation Pneumonitis in Breast Cancer Patients

*Byung Min Lee[1], Jee Suk Chang[1], Se Young Kim[1], Ki Chang Keum[1], Chang-Ok Suh[2] and Yong Bae Kim[1]**

[1] Department of Radiation Oncology, Yonsei University College of Medicine, Seoul, South Korea, [2] Department of Radiation Oncology, CHA Bundang Medical Center, CHA University, Bundang-gu, South Korea

OPEN ACCESS

Edited by:
Tiziana Rancati, National Cancer Institute Foundation (IRCCS), Italy

Reviewed by:
Gilles Defraene, KU Leuven, Belgium
Livia Marrazzo, Hospital Universitario Careggi, Italy

***Correspondence:**
Yong Bae Kim
ybkim3@yuhs.ac

Specialty section:
This article was submitted to Radiation Oncology, a section of the journal Frontiers in Oncology

Received: *18 October 2019*
Accepted: *23 January 2020*
Published: *11 February 2020*

Citation:
Lee BM, Chang JS, Kim SY, Keum KC, Suh C-O and Kim YB (2020) Hypofractionated Radiotherapy Dose Scheme and Application of New Techniques Are Associated to a Lower Incidence of Radiation Pneumonitis in Breast Cancer Patients. Front. Oncol. 10:124. doi: 10.3389/fonc.2020.00124

Purpose: Radiation pneumonitis (RP) is one of the most severe toxicities experienced by patients with breast cancer after radiotherapy (RT). RT fractionation schemes and techniques for breast cancer have undergone numerous changes over the past decades. This study aimed to investigate the incidence of RP as a function of such changes in patients with breast cancer undergoing RT and to identify dosimetric markers that predict the risk of this adverse event.

Methods and Materials: We identified 1,847 women with breast cancer who received adjuvant RT at our institution between 2015 and 2017. The RT technique was individually tailored based on each patient's clinicopathological features. Deep inspiration breath hold technique or prone positioning were used for patients who underwent left whole-breast irradiation for cardiac sparing, while those requiring regional lymph node irradiation underwent volumetric-modulated arc therapy (VMAT).

Results: Of 1,847 patients who received RT, 21.2% received the conventional dose scheme, while 78.8% received the hypofractionated dose scheme (mostly 40 Gy in 15 fractions). The median follow-up period was 14.5 months, and the overall RP rate was 2.1%. The irradiated organ at risk was corrected concerning biologically equivalent dose. The ipsilateral lung V_{30} in equivalent dose in 2 Gy (EQD2) was the most significant dosimetric factor associated with RP development. Administering RT using VMAT, and hypofractionated dose scheme significantly reduced ipsilateral lung V_{30}.

Conclusions: Application of new RT techniques and hypofractionated scheme significantly reduce the ipsilateral lung dose. Our data demonstrated that ipsilateral lung V_{30} in EQD2 is the most relevant dosimetric predictor of RP in patients with breast cancer.

Keywords: radiation pneumonitis, radiotherapy, breast cancer, hypofractionation, lung dosimetry

INTRODUCTION

Radiation pneumonitis (RP) is one of the most severe toxicities caused by radiotherapy (RT) in patients with breast cancer. Although sometimes fatal, particularly in elderly patients or those with medical comorbidities, most symptoms of RP can be resolved with steroid-based medications. In the era of two-dimensional conventional RT, the central lung distance, defined as the distance between the midpoint of the posterior field and the chest wall, was used as an indicator of RP (1, 2). After the introduction of treatment planning based on three-dimensional conformal RT (3D CRT), studies have aimed to identify the dosimetric parameters of the lung that predict RP following RT for breast cancer. However, such studies remain inadequate for clinical utility (3, 4).

There has been an important paradigm shift in RT for breast cancer over the past 20 years. First, hypofractionated dose scheme emerged as a new standard treatment for this disease. Several prospective randomized trials demonstrated that the hypofractionation RT is non-inferior to conventional fractionated RT with respect to treatment outcomes and toxicities after breast conserving surgery. Although hypofractionation RT after mastectomy is not standard of care yet, recent prospective trial has shown non-inferior results compared to conventional RT (5). More radiation oncologists have adopted such abbreviated RT methods because of their convenience and cost-effectiveness (6–9). Along with hypofractionated RT, some other techniques that have become available include volumetric-modulated arc therapy (VMAT), deep inspiration breath-hold (DIBH), and prone positioning.

In this study, we aimed to investigate the incidence of RP and identify the dosimetric markers that predict the risk of this adverse effect as a function of changes in hypofractionated dose schemes and application of new RT techniques used to treat breast cancer.

MATERIALS AND METHODS

Patients

We identified patients who underwent adjuvant RT following surgery for breast cancer at our institution between January 2015 and December 2017 using a prospectively collected registry ($n = 2{,}130$). We excluded patients who had distant metastases at the time of their diagnosis ($n = 42$), those who did not visit at regular follow-up ($n = 114$), and those who were followed at other hospitals ($n = 127$). Finally, 1,847 patients who met the eligibility criteria were included in our study cohort. We reviewed the medical charts of all patients to determine the incidence of RP. This study was approved by the institutional review board of Severance hospital (4-2018-0663).

Treatment

We performed computed tomography (CT) simulation (SOMATOM sensation; Siemens, Erlangen, Germany) with 3 mm-thick slices for all patients. For immobilization, patients positioned their ipsilateral arms in abduction and used a thermoplastic immobilization system (Type-S; Medtec, Alton, IA, USA). Per our institutional protocol, the irradiation technique was optimized for each individual to minimize the dose to the heart while maximizing target dose homogeneity. Patients with large, pendulous, or ptotic breasts were placed in the prone position to avoid skin reactions at the inframammary fold. For cancer of the left breast, the DIBH technique was applied to displace the heart from the chest wall, as described previously (10); patients were instructed to apply the Abches breathing monitoring device (APEX Medical, Tokyo, Japan) during DIBH. If the distance between the heart and chest wall was sufficient to lower the heart dose using DIBH by inflating the lung volume, we performed RT using the DIBH technique. Due to the setup uncertainties in prone positioning, we underwent daily cone beam CT during RT. However, if the heart was not sufficiently spared by DIBH or if internal mammary node (IMN) irradiation (IMNI) was required, we performed RT with VMAT for cardiac sparing.

For 3D CRT, target volumes were delineated based on palpating breast tissue and adding a margin; the border of the intact breast and treatment planning for 3D CRT was specified as described elsewhere (11). Regional lymph node irradiation (RNI), including that of the internal mammary, axillary, and supraclavicular lymph nodes, was recommended to patients with metastatic nodes or those with high-risk N0 breast cancer (i.e., tumor sizes larger than 2 cm, high-grade tumors, and estrogen receptor-negative tumors) based on two large scale randomized trials (12, 13). The partial wide tangent field technique was used to cover the entire breast as well as the IMNs. The supraclavicular and axillary lymph nodes were irradiated using a separate beam that did not overlap with that of the breast field. In patients who had undergone mastectomy, the chest wall and regional nodes were irradiated using the reverse hockey stick technique as described elsewhere (14). Since June 2015, we performed hypofractionation in patients who received mastectomy.

For VMAT, target volumes and organs at risk were contoured based on European Society for Radiotherapy and Oncology guidelines, which was validated using both single-center and multi-center datasets in Korea (15). For patients with T4 stage or N2-N3 stage, we followed the Radiation Therapy Oncology Group breast cancer target guidelines. For VMAT planning, two partial arcs were used limiting the unnecessary arc segments without compromising dose quality. Plan generation and dose calculation were performed using the RayStation treatment planning system (version 5.0, RaySearch, Stockholm, Sweden). For treatment, 6 MV photon beams emitted from a linear accelerator (Versa HD, Elekta, Stockholm, Sweden) were used. The 95% isodose encompassed the entire planning target volume, and volumes in target areas receiving over 107% of the prescribed dose were minimized. The planning requirements for organ at risk were as follows: ipsilateral lung V_5 <50%, V_{10} <35%, V_{20} <20% (V_χ defined as the percentage of the total volume exceeding χ Gy), mean heart dose <3 Gy, mean left coronary artery dose <6 Gy (maximum point dose [Dmax] <10 Gy), mean contralateral breast dose <2 Gy, esophagus Dmax <12 Gy, and mean thyroid dose <3 Gy. We concerned the esophagus and thyroid to reduce radiation induced esophagitis and hypothyroidism. Cone-beam CT images were obtained daily

TABLE 1 | Patient characteristics and treatment characteristics.

			CF group		HF group		
	No. of patients	**%**	**No. of patients**	**%**	**No. of patients**	**%**	***p***
Age (Year)							0.41
<51	908	49.2%	200	51.0%	708	48.7%	
≥51	939	50.8%	192	49.0%	747	51.3%	
Pathology							
Ductal carcinoma *in situ*	254	14.1%	59	15.1%	195	13.4%	0.56
Invasive ductal carcinoma	1,327	71.7%	283	72.2%	1,044	71.8%	
Invasive lobular carcinoma	85	4.6%	12	3.1%	71	4.9%	
Mucinous carcinoma	36	1.9%	15	3.8%	21	1.4%	
Tubular carcinoma	43	2.3%	10	2.6%	33	2.3%	
Stage							0.08
0	261	14.5%	55	14.0%	206	14.2%	
I	740	40.1%	171	43.6%	569	39.1%	
II	592	31.8%	110	28.1%	482	33.1%	
III	253	13.6%	56	14.3%	197	13.5%	
Surgery							0.01
Breast conserving mastectomy	1,485	80.4%	297	75.8%	1,188	81.6%	
Mastectomy	362	19.6%	95	24.2%	267	18.4%	
Lung disease*							0.94
Yes	9	0.5%	2	0.5%	7	0.5%	
No	1,838	99.5%	390	99.5%	1,488	99.5%	
Smoking history							0.45
Yes	73	4.2%	13	3.5%	60	4.4%	
No	1,728	95.8%	358	96.5%	1,370	95.6%	
Regional LN irradiation							0.08
Yes (SCL+IMN+AXL)	712	38.5%	166	42.3%	546	37.5%	
No	1135	61.5%	226	57.7%	909	62.5%	
Chemotherapy							0.52
Yes							
Neoadjuvant CTx	402	21.8%	89	22.7%	313	21.5%	
Adjuvant CTx	557	30.2%	109	27.8%	448	30.8%	
No	888	48.1%	194	49.5%	694	47.7%	
Hormone therapy							0.73
Yes	1,297	70.2%	278	70.9%	1,019	70.0%	
No	550	29.8%	114	29.1%	436	30.0%	
RT technique							<0.001
Free-breathing	1,258	68.1%					
FIF	226	12.2%	11	2.8%	215	14.8%	
Wedge	194	10.5%	178	45.4%	16	1.1%	
RHT	13	0.7%	13	3.3%	0	0.0%	
VMAT	825	44.7%	8	2.0%	817	56.2%	
DIBH	488	26.4%					
FIF	322	17.4%	22	5.6%	300	20.6%	
Wedge	164	8.9%	153	39.0%	11	0.8%	
RHT	2	0.1%	2	0.5%	0	0.0%	
Prone	101	5.5%					
FIF	97	5.3%	4	1.0%	93	6.4%	
Wedge	4	0.2%	1	0.3%	3	0.2%	

**COPD, ILD were included.*

CF, Conventional fractionation; HF, Hypofractionation; SCL, Supraclavicular lymph node; IMN, Internal mammary lymph node; AXL, Axillary lymph node; CTx, Chemotherapy; FIF, Field in field; RHT, Reverse hockey stick; VMAT, Volumetric-modulated arc therapy; BCS, Breast-conserving surgery.

to verify appropriate patient set-up and minimize positioning errors. During the study period, three different fractionation schedules were used: either 40.05 Gy in 15 fractions ($n = 1{,}055$, 57.1%), or 42.56 Gy in 16 fractions ($n = 400$, 21.7%) for hypofractionation and 50.4 Gy in 28 fractions ($n = 392$, 21.2%) schedule for conventional fractionation.

For tumor bed boost, 9 Gy in 5 fractions was applied in conventional fractionation ($n = 297$, 20.8%). The tumor bed boost in hypofractionated RT differed depending on RT modalities. In case that patients received RT using 3D CRT in hypofractionation, 10 Gy in 5 fractions was applied ($n = 541$, 37.9%). The electron beams were used for boost with 3D CRT. For patients treated by VMAT, the tumor bed boost was performed using simultaneous integrated boost. The simultaneous integrated boost dose was determined based on RTOG 1005 protocol. Total dose of 48 Gy in 15 fractions was applied to tumor bed while total dose of 40.05 Gy in 15 fractions was given to the whole breast or whole breast plus regional LN ($n = 373$, 26.2%).

Analysis

The primary endpoint was the occurrence of symptomatic RP, defined as respiratory symptoms (e.g., dyspnea, non-productive cough) with correlated radiologic images (e.g., chest radiography and CT). The RP was graded using common terminology criteria for adverse events version 5.0. Radiation oncologists prescribed oral prednisolone until symptoms were relieved. To evaluate the factors affecting the occurrence of RP, univariate and multivariate analyses using Cox proportional hazards models were performed. In multivariate analysis, the factors significant ($p < 0.05$) in univariate analysis were used. The factors related to RP in other studies were also included for multivariate analsysis. The receiver operating characteristic (ROC) and area under the curve analyses were used to identify the optimal cutoff values that best predict the occurrence of RP. The comparison between hypofractionation group and conventional fractionation group was performed using chi-squared test. The logistic regression analysis was used to evaluate the factors associated with the lung dose parameters.

For dosimetric analysis, the planning data of all the patients were transferred into the MIM software (version 6.7.14; Cleveland, OH, USA) for multiple-plan comparison. To analyze the ipsilateral lung dose parameter, we collected the ipsilateral mean lung dose, V_5, V_{10}, V_{15}, V_{20}, V_{30}, and V_{40}. The ipsilateral lung dose parameters were converted into equivalent dose in 2 Gy (EQD2) with α/β ratio of 3 Gy to correct for hypofractionation. All tests were conducted by using either the SPSS software version 20.0 (IBM Corp., Armonk, New York, USA) or R version 3.3.2 (R Foundation for Statistical Computing, Vienna, Austria).

TABLE 2 | Comparison of lung dose parameter depending on internal mammary node irradiation and radiotherapy technique.

	IMN (–)				IMN (+)		
	Free-breathing 3D CRT	**DIBH 3D CRT**	**Prone 3D CRT**	**Volumetric arc therapy**	**Free-breathing 3D CRT**	**DIBH 3D CRT**	**Volumetric arc therapy**
No. of patients	307	304	101	423	130	184	398
Mean lung dose							
Median	6.50	5.71	1.16	5.70	16.24	11.20	7.56
IQR	4.64–8.32	4.30–8.22	0.52–2.51	4.92–6.76	11.24–19.82	8.9–15.24	6.73–8.33
V_5							
Median	22.17	21.01	4.03	26.99	54.11	41.30	34.62
IQR	16.54–30.7	15.9–30.00	0.88–8.05	22.92–31.14	43.32–62.21	35.67–51.58	30.91–38.28
V_{10}							
Median	17.34	15.60	2.47	17.24	44.83	33.75	23.49
IQR	12.81–21.54	12.38–21.2	0.33–6.00	14.50–20.40	32.74–51.04	27.95–41.18	20.75–26.55
V_{15}							
Median	14.79	13.07	1.77	12.00	40.09	30.10	17.76
IQR	10.94–18.42	10.15–17.88	0.17–4.54	9.95–15.08	27.91–45.49	23.19–37.02	15.40–20.08
V_{20}							
Median	12.86	11.20	1.35	8.54	36.35	27.13	13.33
IQR	9.38–16.42	8.38–15.78	0.07–3.74	6.69–11.25	24.80–42.00	19.70–33.69	11.19–15.30
V_{30}							
Median	9.59	7.85	0.66	3.60	29.02	18.26	6.30
IQR	6.33–13.09	5.19–12.08	0.00–2.00	2.10–5.62	15.00–35.34	11.25–24.62	4.37–8.45
V_{40}							
Median	3.26	1.85	0.03	0.36	14.00	2.95	1.13
IQR	0.83–8.56	0.18–7.23	0.00–0.37	0.05–1.16	2.10–22.43	0.87–11.70	0.60–2.14

IMN, Internal mammary lymph node; 3D CRT, 3-Dimensional conformal radiation therapy; DIBH, Deep inspiration breath-hold; VMAT, Volumetric-modulated arc therapy; IQR, Interquartile range.

RESULTS

Patient Characteristics

The patient and tumor characteristics are summarized in **Table 1**. Approximately 85% of the patients had early breast cancer (stages 0–2). In total, 38.5% received RNI and 51.9% received either neoadjuvant or adjuvant chemotherapy. Adjuvant RT was performed either via the conventional dose scheme (21.2%) or the hypofractionated dose scheme (78.8%); 44.7% of patients underwent adjuvant RT using VMAT.

We also compared the patient and tumor characteristics between the conventional fractionation group and hypofractionation group (**Table 1**). Most of the variables were well-balanced between two groups except for the method of surgery and the techniques used for RT. More patients in the hypofractionated group received breast conserving surgery. Also, most of the patients treated with VMAT underwent hypofractionated RT.

RP Incidence

RP occurred in 40 patients (2.1%) within a median follow-up period of 14.5 months. The commonest symptom was a mild dry cough; few patients also experienced other symptoms such as shortness of breath. Patients experiencing RP symptoms were prescribed steroids, following which these symptoms resolved. None of the patients developed RP grade ≥3. Symptomatic RP

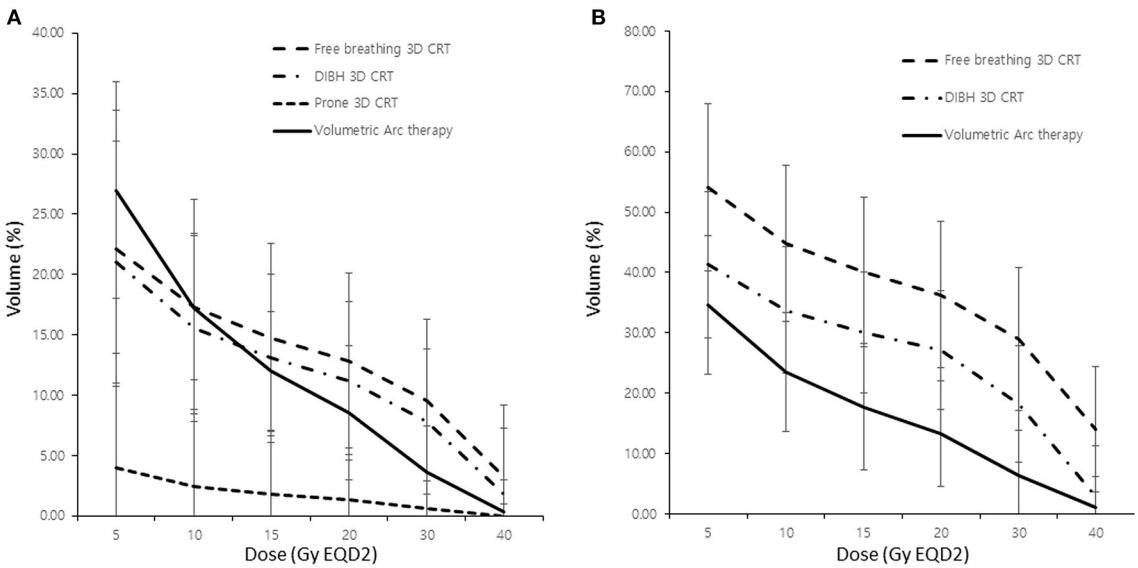

FIGURE 1 | Comparison of lung dose according to the radiotherapy modality without **(A)** and with **(B)** internal mammary lymph node irradiation. 3D CRT, three-dimensional conformal radiotherapy; DIBH, deep inspiration breath hold; V_{χ}, percentage of the total volume exceeding χ Gy.

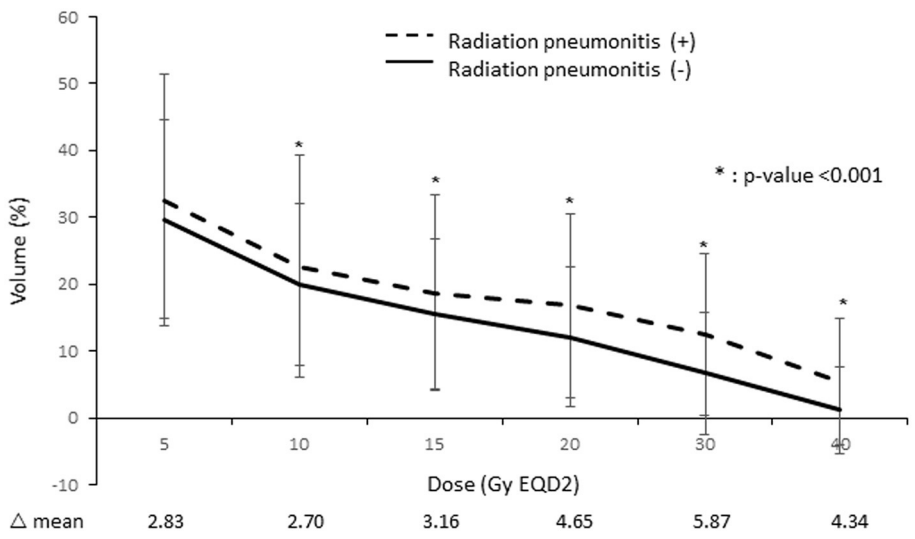

FIGURE 2 | Comparison of the lung dose-volume histogram between patients who developed radiation pneumonitis and those who did not.

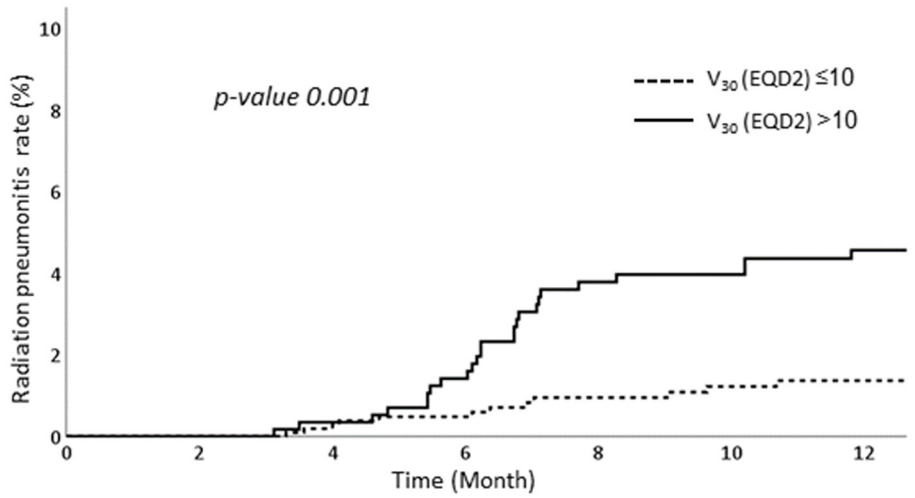

FIGURE 3 | Occurrence of radiation pneumonitis according to subgroups with V_{30} >10% and V_{30}≤10%.

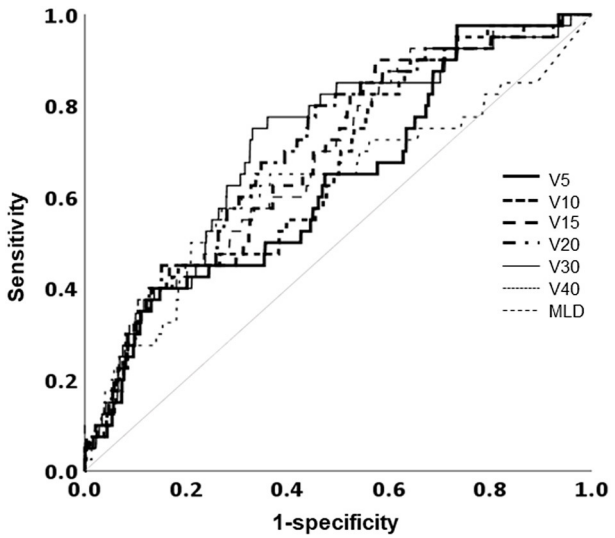

FIGURE 4 | Receiver operating characteristic curve analysis for the optimal cutoff value to predict the occurrence of radiation pneumonitis. MLD, mean lung dose; V_{χ}, percentage of the total volume exceeding χ Gy.

occurred no sooner than 3 months and no later than 12 months after commencing RT.

Comparison of Lung Dosimetry

The lung dosing parameters when using different RT techniques (i.e., free-breathing 3D-CRT, DIBH 3D-CRT, prone positioning RT, and VMAT) were compared (**Table 2**). Patients who underwent IMNI had higher doses to the lung than those who did not. The DIBH technique produced lower lung doses than the free-breathing technique especially when IMNI was performed. Among the various techniques, the lung doses in patients who used prone positioning techniques were significantly lower than that in patients using other techniques. In patients who did not undergo IMNI, the lung V_{30} and V_{40} were significantly lower in patients undergoing VMAT than in those in patients undergoing other techniques, while the lung V_5 was higher in patients undergoing VMAT (**Figure 1A**). For patients who did undergo IMNI, the VMAT group showed the lowest mean lung dose (**Figure 1B**).

Moreover, we found that patients with RP showed higher dose-volume histogram parameter values in all areas than those without RP. Among these individual parameters, ipsilateral lung V_{30} showed the largest difference between these two patient groups (**Figure 2**).

RPA

We performed RPA to determine the factors associated with RP. Among various dosimetric parameters, the ipsilateral lung V_{30} in EQD2 >10% was associated with significantly higher RP rates than those of ipsilateral lung V_{30} in EQD2 ≤ 10%. The RP occurred in 4.6% in patients with ipsilateral lung V_{30} more than 10% while only 1.4% of patients experienced RP when ipsilateral lung V_{30} was <10% (**Figure 3**).

Dosimetric Analysis

The mean lung dose, ipsilateral lung V_5, V_{10}, V_{15}, V_{20}, V_{30}, and V_{40} were all significantly associated with RP. The largest area under the ROC curve was that of the ipsilateral lung V_{30} (**Figure 4**). Univariate analysis showed that hormone treatment, fractionation schedule, RT technique, and the ipsilateral lung V_{30} significantly affected RP. On multivariate analysis, patients with ipsilateral lung V_{30} larger than 10% had a significantly higher rate of RP than those with ipsilateral lung V_{30} <10% (**Table 3**).

Among the RT techniques, fractionation schemes, and IMN irradiation, VMAT (odds ratio 0.12, 95% CI 0.08–0.17) was a major determinant of lowering ipsilateral lung V_{30} followed by hypofractionation (odds ratio 0.14, 95% CI 0.10–0.19). The IMN

TABLE 3 | Univariate and multivariate analysis of factors associated with symptomatic radiation pneumonitis.

	Univariate analysis			Multivariate analysis	
	Radiation pneumonitis rate	**HR (95% CI)**	***p***	**HR (95% CI)**	***p***
Age (≥51 vs. <51)	1.8 vs. 2.5%	0.69 (0.37–1.29)	0.25		
Lung disease (Yes vs. No)	11.1 vs. 2.1%	5.41 (0.74–39.45)	0.09	5.90 (0.79–43.55)	0.082
Smoking history (Yes vs. No)	0 vs. 2.1%	0.05 (0.00–86.13)	0.42		
Chemotherapy (Yes vs. No)	1.9 vs. 2.5%	0.90 (0.63–1.29)	0.58		
Chemotherapy regimen			0.09		
Taxane based vs. Adriamycin based	1.1 vs. 2.4%	0.52 (0.15–1.88)	0.32		
Herceptin based vs. Adriamycin based	6 vs. 2.4%	2.06 (0.83–5.13)	0.12		
Hormone therapy (Yes vs. No)	1.7 vs. 3.3%	0.50 (0.27–0.94)	0.03	0.53 (0.28–1.01)	0.053
Regional LN irradiation (Yes vs. No)	2.4 vs. 2.0%	1.12 (0.59–2.09)	0.73		
Fraction schedule (Hypofractionation vs. Conventional fractionation)	1.5 vs. 4.6%	0.43 (0.23–0.80)	<0.01	0.63 (0.31–1.28)	0.203
Ipsilateral lung dose (V_{30} > 10% vs. V_{30} ≤ 10%)	4.6 vs. 1.4%	2.93 (1.53–5.62)	<0.01	2.89 (1.51–5.54)	0.002
RT technique			0.007		
DIBH 3D CRT vs. Free-breathing 3D CRT	2.5 vs. 5.0%	0.47 (0.23–0.95)	0.04		
Prone 3D CRT vs. Free-breathing 3D CRT	0 vs. 5.0%	NR			
VMAT vs. Free-breathing 3D CRT	0.7 vs. 5.0%	0.22 (0.09–0.55)	0.001		

CI, Confidence interval; HR, Hazard ratio; LN, Lymph node; 3D CRT, 3-dimensional conformal radiotherapy; DIBH, Deep inspiration breath hold; VMAT, Volumetric modulated arc therapy; NR, Not reported.

TABLE 4 | Analysis the factor determining the lung V_{30}.

	Univariate analysis		Multivariate analysis	
	OR (95% CI)	***p***	**OR (95% CI)**	***p***
IMN irradiation (Yes vs. No)	2.63 (2.15–3.22)	<.001	6.59 (4.88–8.92)	<.001
Hypofractionation (Yes vs. No)	0.07 (0.06–0.10)	<.001	0.14 (0.10–0.19)	<.001
VMAT (Yes vs. No)	0.12 (0.10–0.16)	<.001	0.12 (0.08–0.17)	<.001
Prone (Yes vs. No)	NR	NR		
DIBH (Yes vs. No)	0.30 (0.24–0.38)	<.001	0.98 (0.73–1.33)	0.911

OR, Odds ratio; CI, Confidence interval; IMN, Internal mammary node; VMAT, Volumetric modulated arc therapy; DIBH, Deep inspiration breath hold; NR, Not reported.

irradiation was the only factor increasing the ipsilateral lung V_{30} (odds ratio 6.59, 95% CI 4.88–8.92) (**Table 4**).

DISCUSSION

This study investigated the incidence of RP in patients with breast cancer who underwent conventional and hypofractionation RT and identified dosimetric markers that predict the risk of RP. We demonstrated that ipsilateral lung V_{30} is the dosimetric predictor of RP that is the most relevant in patients with breast cancer. The change in RT techniques using VMAT and hypofractionation dose schemes reduce the ipsilateral lung V_{30}.

Several studies have shown that the occurrence of RP is affected by both patient-related and treatment-related factors. Patient-related factors that affect the incidence of RP include existing lung disease, poor pulmonary function, and smoking history (16, 17). Meanwhile, treatment-related factors known to affect RP development in patients with lung cancer include radiation dose, irradiated lung volume, schedule of fractionation, and usage of chemotherapy (18–21). However, as patients with breast cancer tend not to have underlying lung diseases or smoking histories with the same frequencies as those with lung cancer, our study revealed no association between patient-related factors and the occurrence of RP. However, treatment-related factors, particularly those related to RT, did affect RP development, as reported previously (11).

In this study, we showed that the hypofractionation dose scheme lowered the ipsilateral lung dose V_{30}. It was suggested that the α/β ratio for breast tissue ranges from 3 to 4 Gy, which is similar to that of normal tissues (6), and this was later confirmed in the START A, START B, and another Canadian study (8, 22, 23). Hence, hypofractionation has become the standard treatment for breast cancer. While hypofractionation did not significantly affect RP development in our study, the V_{30} of the ipsilateral lung were found to be strong predictors of RP.

We also demonstrated that advances in RT techniques have reduced the incidence rate of RP. Improvements that were designed to reduce the dose to the heart while maintaining RT safety and efficacy include intensity-modulated RT (IMRT), DIBH, and prone positioning; these techniques also significantly

decreased the dose to the lung by more than 50%. The DIBH can lower the dose to the heart, but the coverage of the ipsilateral whole breast planning target volume can be suboptimal. In case that the tumor was located at medial location of the breast, tangent fields are difficult to fully cover tumor bed and avoid the heart simultaneously. Even though the prone positioning for breast enables lowering the dose to the lung and heart, but setup uncertainties exist for prone positioning (24). By contrast, IMRT made it possible to protect the heart and ipsilateral lung without compromising target coverage and set up uncertainties.

Because landmark studies such as the MA 20 and EORTC 22922 trials demonstrated that RNI can reduce the risk of early breast cancer recurrence (12, 13), radiation oncologists increasingly consider its application but remain hesitant owing to the risk of toxicity to the heart and lung. While we perform DIBH and prone positioning for patients at our hospital who are not undergoing RNI, 3D CRT with partially wide tangent fields has been performed in patients requiring RNI, including IMNI. IMRT for breast cancer is widely used today after it became reimbursable by the national insurance program in our country in 2015. Our study showed that IMRT can sufficiently cover the whole breast and regional lymph nodes, particularly IMNs, while effectively reducing lung, and heart toxicity.

The chemotherapy regimen did not affect the incidence of RP in our study. As some chemotherapeutic agents act as sensitizers to radiation, the patients who received chemotherapy could be at higher risk to RP. The article showing that chemotherapy increased the risk of RP demonstrated that sequential chemotherapy diminished the risk of RP as compared to concurrent chemoradiotherapy (25). In our study, none of the patients underwent concurrent chemotherapy during RT. As sequential chemotherapy has minimal impact on development of RP, neither the chemotherapy regimen nor the use of chemotherapy increased the risk of RP in our study.

Sequential tumor bed boost was applied in patients treated with 3D CRT while simultaneous integrated boost was used in patients treated with VMAT. In this study, sequential tumor bed boost dose was not accounted for analysis. However, as electron beams were used for sequential tumor bed boost in case of patients treated with 3D CRT, we believed that the effect of tumor bed boost to the lung dose was negligible.

No significant parameters predicting the occurrence of RP in patients with breast cancer have been identified to date. The 3D CRT technique can reduce the areas receiving low irradiation doses (e.g., the V_5 and V_{10}) on the dose-volume histograms but not the areas receiving high doses. By contrast, the VMAT technique can reduce the areas of high RT dose while widening the areas of low irradiation (26). Previous studies in patients with breast cancer showed that V_{20} lung constraints could markedly reduce RP (27, 28). However, our results also demonstrated that V_{30} constraints were significantly associated with reduced RP rates in patients with breast cancer.

Our study was limited by its retrospective design and single-institution analysis. Some unbalance existed in patient characteristics between hypofractionated and conventional fractionated RT group, as the surgical method and RT techniques were significantly different between two groups. Also, the number of patients with RNI and without RNI differ largely. Although most of the factors were well-balanced between two groups, careful interpretation of results is needed. As such, external validation is necessary to confirm our findings.

In conclusion, our study demonstrated that the hypofractionation dose scheme and RT techniques such as VMAT can reduce the radiation dose and potentially the incidence of RP. Although external validation is still required, we clearly showed that ipsilateral lung V_{30} in EQD2 is reliable dosimetric predictors of RP in patients with breast cancer.

DATA AVAILABILITY STATEMENT

The datasets generated for this study are available on request to the corresponding author.

ETHICS STATEMENT

The studies involving human participants were reviewed and approved by institutional review board of Severance hospital (4-2018-0663). Written informed consent for participation was not required for this study in accordance with the national legislation and the institutional requirements.

AUTHOR'S NOTE

This study was presented at the 60th Annual meeting of the American Society for Radiation Oncology (ASTRO), October 21–24, 2018, San Antonio, Texas.

AUTHOR CONTRIBUTIONS

JC and YK: study concept and design. SK, KK, C-OS, and YK: data acquisition and quality control of data. BL, JC, and YK: data analysis and interpretation. BL and JC: manuscript preparation. JC and YK: manuscript review.

REFERENCES

1. Neal AJ, Yarnold JR. Estimating the volume of lung irradiated during tangential breast irradiation using the central lung distance. *Br J Radiol.* (1995) 68:1004–8. doi: 10.1259/0007-1285-68-813-1004
2. Das IJ, Cheng EC, Freedman G, Fowble B. Lung and heart dose volume analyses with CT simulator in radiation treatment of breast cancer. *Int J Radiat Oncol Biol Phys.* (1998) 42:11–9. doi: 10.1016/S0360-3016(98)00200-4
3. Kimsey FC, Mendenhall NP, Ewald LM, Coons TS, Layon AJ. Is radiation treatment volume a predictor for acute or late effect on pulmonary-function - a prospective-study of patients treated with breast-conserving surgery and postoperative irradiation. *Cancer.* (1994) 73:2549–55. doi: 10.1002/1097-0142(19940515)73:10<2549::AID-CNCR2820731016>3.0.CO;2-N
4. Marks LB, Bentzen SM, Deasy JO, Kong FM, Bradley JD, Vogelius IS, et al. Radiation dose-volume effects in the lung. *Int J Radiat Oncol Biol Phys.* (2010) 76(3 Suppl):S70–6. doi: 10.1016/j.ijrobp.2009.06.091

5. Wang SL, Fang H, Song YW, Wang WH, Hu C, Liu YP, et al. Hypofractionated versus conventional fractionated postmastectomy radiotherapy for patients with high-risk breast cancer: a randomised, non-inferiority, open-label, phase 3 trial. *Lancet Oncol*. (2019) 20:352–60. doi: 10.1016/S1470-2045(18)30813-1
6. Yarnold J, Ashton A, Bliss J, Homewood J, Harper C, Hanson J, et al. Fractionation sensitivity and dose response of late adverse effects in the breast after radiotherapy for early breast cancer: long-term results of a randomised trial. *Radiother Oncol.* (2005) 75:9–17. doi: 10.1016/j.radonc.2005.01.005
7. Owen JR, Ashton A, Bliss JM, Homewood J, Harper C, Hanson J, et al. Effect of radiotherapy fraction size on tumour control in patients with early-stage breast cancer after local tumour excision: long-term results of a randomised trial. *Lancet Oncol.* (2006) 7:467–71. doi: 10.1016/S1470-2045(06)70699-4
8. Group ST, Bentzen SM, Agrawal RK, Aird EG, Barrett JM, Barrett-Lee PJ, et al. The UK standardisation of breast radiotherapy. (START) Trial B of radiotherapy hypofractionation for treatment of early breast cancer: a randomised trial. *Lancet*. (2008) 371:1098–107. doi: 10.1016/S0140-6736(08)60348-7
9. Haviland JS, Owen JR, Dewar JA, Agrawal RK, Barrett J, Barrett-Lee PJ, et al. The UK standardisation of breast radiotherapy. (START) trials of radiotherapy hypofractionation for treatment of early breast cancer: 10-year follow-up results of two randomised controlled trials. *Lancet Oncol.* (2013) 14:1086–94. doi: 10.1016/S1470-2045(13)70386-3
10. Lee HY, Chang JS, Lee IJ, Park K, Kim YB, Suh CO, et al. The deep inspiration breath hold technique using Abches reduces cardiac dose in patients undergoing left-sided breast irradiation. *Radiat Oncol J.* (2013) 31:239–46. doi: 10.3857/roj.2013.31.4.239
11. Lee BM, Chang JS, Cho YU, Park S, Park HS, Kim JY, et al. External validation of IBTR! 2.0 nomogram for prediction of ipsilateral breast tumor recurrence. *Radiat Oncol J*. (2018) 36:139–46. doi: 10.3857/roj.2018.00059
12. Poortmans PM, Collette S, Kirkove C, Van Limbergen E, Budach V, Struikmans H, et al. Internal mammary and medial supraclavicular irradiation in breast cancer. *N Engl J Med.* (2015) 373:317–27. doi: 10.1056/NEJMoa1415369
13. Whelan TJ, Olivotto IA, Levine MN. Regional nodal irradiation in early-stage breast cancer. *N Engl J Med.* (2015) 373:1878–9. doi: 10.1056/NEJMc1510505
14. Chang JS, Park W, Kim YB, Lee IJ, Keum KC, Lee CG, et al. Long-term survival outcomes following internal mammary node irradiation in stage II-III breast cancer: results of a large retrospective study with 12-year follow-up. *Int J Radiat Oncol Biol Phys.* (2013) 86:867–72. doi: 10.1016/j.ijrobp.2013.02.037
15. Chang JS, Byun HK, Kim JW, Kim KH, Lee J, Cho Y, et al. Three-dimensional analysis of patterns of locoregional recurrence after treatment in breast cancer patients: validation of the ESTRO consensus guideline on target volume. *Radiother Oncol.* (2017) 122:24–9. doi: 10.1016/j.radonc.2016.10.016
16. Kong FM, Klein EE, Bradley JD, Mansur DB, Taylor ME, Perez CA, et al. The impact of central lung distance, maximal heart distance, and radiation technique on the volumetric dose of the lung and heart for intact breast radiation. *Int J Radiat Oncol Biol Phys.* (2002) 54:963–71. doi: 10.1016/S0360-3016(02)03741-0
17. Lind PA, Marks LB, Hardenbergh PH, Clough R, Fan M, Hollis D, et al. Technical factors associated with radiation pneumonitis after local +/- regional radiation therapy for breast cancer. *Int J Radiat Oncol Biol Phys.* (2002) 52:137–43. doi: 10.1016/S0360-3016(01)01715-1
18. Seppenwoolde Y, De Jaeger K, Boersma LJ, Belderbos JS, Lebesque JV. Regional differences in lung radiosensitivity after radiotherapy for non-small-cell lung cancer. *Int J Radiat Oncol Biol Phys.* (2004) 60:748–58. doi: 10.1016/j.ijrobp.2004.04.037
19. Khan MA, Van Dyk J, Yeung IW, Hill RP. Partial volume rat lung irradiation; assessment of early DNA damage in different lung regions and effect of radical scavengers. *Radiother Oncol.* (2003) 66:95–102. doi: 10.1016/S0167-8140(02)00325-0
20. Kahan Z, Csenki M, Varga Z, Szil E, Cserhati A, Balogh A, et al. The risk of early and late lung sequelae after conformal radiotherapy in breast cancer patients. *Int J Radiat Oncol Biol Phys.* (2007) 68:673–81. doi: 10.1016/j.ijrobp.2006.12.016
21. Tsujino K, Hirota S, Endo M, Obayashi K, Kotani Y, Satouchi M, et al. Predictive value of dose-volume histogram parameters for predicting radiation pneumonitis after concurrent chemoradiation for lung cancer. *Int J Radiat Oncol Biol Phys.* (2003) 55:110–5. doi: 10.1016/S0360-3016(02)03807-5
22. Group ST, Bentzen SM, Agrawal RK, Aird EG, Barrett JM, Barrett-Lee PJ, et al. The UK standardisation of breast radiotherapy. (START) Trial A of radiotherapy hypofractionation for treatment of early breast cancer: a randomised trial. *Lancet Oncol.* (2008) 9:331–41. doi: 10.1016/S1470-2045(08)70077-9
23. Whelan TJ, Pignol JP, Levine MN, Julian JA, MacKenzie R, Parpia S, et al. Long-term results of hypofractionated radiation therapy for breast cancer. *N Engl J Med.* (2010) 362:513–20. doi: 10.1056/NEJMoa0906260
24. Kawamura M, Maeda Y, Takamatsu S, Tamamura H, Yamamoto K, Tameshige Y, et al. Development of the breast immobilization system in prone setup: the effect of bra in prone position to eliminate the breast setup error. *Int J Radiat Oncol Biol Phys*. (2014) 90:S224–S. doi: 10.1016/j.ijrobp.2014.05.808
25. Vogelius IR, Bentzen SM. A literature-based meta-analysis of clinical risk factors for development of radiation induced pneumonitis. *Acta Oncol.* (2012) 51:975–83. doi: 10.3109/0284186X.2012.718093
26. Hall EJ, Wuu CS. Radiation-induced second cancers: the impact of 3D-CRT and IMRT. *Int J Radiat Oncol Biol Phys.* (2003) 56:83–8. doi: 10.1016/S0360-3016(03)00073-7
27. Blom Goldman U, Anderson M, Wennberg B, Lind P. Radiation pneumonitis and pulmonary function with lung dose-volume constraints in breast cancer irradiation. *J Radiother Pract.* (2014) 13:211–7. doi: 10.1017/S1460396913000228
28. Lingos TI, Recht A, Vicini F, Abner A, Silver B, Harris JR. Radiation pneumonitis in breast cancer patients treated with conservative surgery and radiation therapy. *Int J Radiat Oncol Biol Phys.* (1991) 21:355–60. doi: 10.1016/0360-3016(91)90782-Y

Conflict of Interest: The authors declare that the research was conducted in the absence of any commercial or financial relationships that could be construed as a potential conflict of interest.

frontiers in Oncology

ORIGINAL RESEARCH
published: 14 February 2020
doi: 10.3389/fonc.2019.01576

Senolytics (DQ) Mitigates Radiation Ulcers by Removing Senescent Cells

Huilan Wang[1,2†], Ziwen Wang[2†], Yu Huang[3], Yue Zhou[4], Xiaowu Sheng[4], Qingzhi Jiang[1,2], Yawei Wang[2], Peng Luo[2], Min Luo[3] and Chunmeng Shi[1,2*]*

[1] Department of Oncology, The Affiliated Hospital of Southwest Medical University, Luzhou, China, [2] State Key Laboratory of Trauma, Burns and Combined Injury, Institute of Rocket Force Medicine, Third Military Medical University, Chongqing, China, [3] Department of Toxicology, Key Laboratory of Environmental Pollution Monitoring and Disease Control, Ministry of Education, Guizhou Medical University, Guiyang, China, [4] Hunan Branch Center, National Tissue Engineering Center of China, Translational Medical Center, Central Laboratory, Hunan Cancer Hospital and The Affiliated Cancer Hospital of Xiangya School of Medicine, Central South University, Changsha, China

Radiation ulcers are a prevalent toxic side effect in patients receiving radiation therapy. At present, there is still no effective treatment for the complication. Senescent cells accumulate after radiation exposure, which can induce cell and tissue dysfunction. Here we demonstrate increased expression of p16 (a senescence biomarker) in human radiation ulcers after radiotherapy and radiation-induced persistent cell senescence in animal ulcer models. Furthermore, senescent cells secreted the senescence-associated secretory phenotype (SASP) and induced cell senescence in adjacent cells, which was alleviated by JAK inhibition. In addition, the clearance of senescent cells following treatment with a senolytics cocktail, Dasatinib plus Quercetin (DQ), mitigated radiation ulcers. Finally, DQ induced tumor cell apoptosis and enhanced radiosensitivity in representative CAL-27 and MCF-7 cell lines. Our results demonstrate that cell senescence is involved in the development of radiation ulcers and that elimination of senescent cells might be a viable strategy for patients with this condition.

Keywords: radiation ulcer, oral mucositis, skin ulcer, senescence, apoptosis, SASP

OPEN ACCESS

Edited by:
Tiziana Rancati, National Cancer Institute Foundation (IRCCS), Italy

Reviewed by:
Rihan El Bezawy, National Cancer Institute Foundation (IRCCS), Italy
Paolo Gandellini, University of Milan, Italy

***Correspondence:**
Chunmeng Shi
shicm@sina.com
Yue Zhou
yuezhoumed@outlook.com

† These authors have contributed equally to this work

Specialty section:
This article was submitted to Radiation Oncology, a section of the journal Frontiers in Oncology

Received: *06 November 2019*
Accepted: *31 December 2019*
Published: *14 February 2020*

Citation:
Wang H, Wang Z, Huang Y, Zhou Y, Sheng X, Jiang Q, Wang Y, Luo P, Luo M and Shi C (2020) Senolytics (DQ) Mitigates Radiation Ulcers by Removing Senescent Cells. Front. Oncol. 9:1576. doi: 10.3389/fonc.2019.01576

INTRODUCTION

Radiation therapy is a common and efficacious treatment for patients with solid cancers. About 50% of cancer patients receive radiation therapy, alone or in combination with other treatment methods such as surgery (1). Among them, radiotherapy is the main treatment method for patients with head and neck tumors and has varying success (2), but oral mucositis is a crucial dose-limiting toxic effect (3). Radiotherapy is an important adjuvant treatment after surgery for breast cancer and can reduce the metastasis and mortality rates (4), but high-dose radiation exposure to superficial tissue ultimately leads to intractable skin ulcers. Although advances in radiotherapy such as dynamic intensity-modulated radiotherapy achieve precise delivery of radiation to cancer cells, side effects to surrounding tissues are still inevitable and bring great pain and/or cost to patients (5).

Various precautionary methods and therapies such as anti-inflammatory agents, local anesthetics, and growth factors have been used to treat painful ulcerations, but the clinical effects are poor (2). Palifermin, a recombinant human form of keratinocyte growth factor (KGF), is the only U.S. Food & Drug Administration–approved agent that is used to prevent oral mucositis in patients with bone marrow transplantation, but fibroblast growth factor receptor 2b (FGFR2b) is often overexpressed in cancer cells and increases the risk of tumor growth (6). Although hyperbaric

oxygen therapy has been reported to reduce skin ulcers after radiation (7), the treatment duration is long. Therefore, the development of potential agents that mitigate radiation ulcers without accelerating tumor growth is intensively needed for oncological supportive care.

Cell senescence can be triggered by radiation-induced DNA damage and leads to delayed repair and regeneration of irradiated tissue (8). Persistent damage activates the cyclin-dependent kinase inhibitor $p16^{Ink4a}$ and causes cell cycle arrest (9). Cellular senescence is not just a state of proliferation inhibition and genetic alteration (10); senescent cells can secrete cytokines, called the senescence-associated secretory phenotype (SASP) including inflammatory factors (11, 12), tissue-reconstituted proteases, and growth factors, which can induce persistent chronic inflammation in the tissue microenvironment (13, 14) and promote cancer relapse (15). It has been reported that cordycepin and mammalian target of rapamycin inhibition can protect from radiation ulcers by inhibiting cell senescence (16, 17). These observations led us to explore if it is possible to mitigate radiation ulcers by eliminating senescent cells.

In this study, we show that senescent cells persist in radiation ulcers (clinical radiation ulcer samples and animal ulcer models), and clearance of senescent cells by the senolytics drug cocktail, dasatinib plus quercetin (DQ), can effectively mitigate radiation ulcers. Moreover, DQ treatment can enhance cancer cell radiosensitivity. Our findings suggest that cell senescence is involved in radiation ulcer development, and clearance of senescent cells can be a potential therapeutic method to mitigate radiation ulcers.

MATERIALS AND METHODS

Human Skin Samples

Skin tissues were obtained from healthy volunteers and patients with breast cancer receiving radiation therapy from 2016 to 2018 at Hunan Cancer Hospital (the Affiliated Hospital of Xiangya School of Medicine of Central South University). Skin ulcer samples were obtained from the chest wall at the time of surgery and were processed for further analysis. The studies involving human participants were approved by the ethics committee of Hunan Cancer Hospital; the patients/participants provided their written informed consent to participate in our study.

Cell Culture

Human oral keratinocytes (HOK ATCC, PCS-200-014) were cultured in an oral keratinocyte medium containing antibiotics at 37°C in 5% CO_2. Human fibroblasts, CAL27 (CRL-2095), and MCF-7 cells (ATCC, HTB-22) were cultured in Dulbecco's minimum essential medium with high sugar (Invitrogen) supplemented with 10% fetal bovine serum (Gibco) and 1% streptomycin/penicillin. The isolation protocol for human fibroblasts was described previously (18).

Conditioned Medium (CM)

CM was made by exposing young cells to a fresh medium for 24 h. SASP-CM was made by exposing senescent cells (7 days after radiation) to a fresh medium for 24 h. To collect (SASP+JAKi)-CM, senescent cells were treated with JAK inhibitor 1 (JAKi) or dimethyl sulfoxide (DMSO) for 72 h and cultured with a fresh medium containing JAKi or DMSO for another 24 h.

Animal Models

Female C3H mice (6–8 weeks) and male Sprague–Dawley rats (6–8 weeks) were purchased from Laboratory Animal Center of Army Medical University. To evaluate the effect of senolytics on radiation ulcers, animals were divided into non-radiation, radiation, and D+Q treatment groups. For local fractionated radiation, the head and neck area was exposed to irradiation at a dose of 6 Gy/day (X-RAD 160-225 instrument Precision X-Ray, 1.9 Gy/min) and treated with senolytics dasatinib (5 mg/kg) plus quercetin (50 mg/kg) (D+Q) (19, 20) by oral gavage every day for 5 days. Mice were sacrificed at days 3, 6, 8, and 10. For skin ulcer modeling, rats' right posterior limbs were exposed to a single dose of 40 Gy (0.9 Gy/min) radiation and treated with dasatinib (5 mg/kg) plus quercetin (50 mg/kg) (D+Q) by intraperitoneal injection every day for 5 days after irradiation. Rats were sacrificed at days 5, 8, 11, and 15 after irradiation.

Immunoanalysis and Histopathology

Tissues were fixed, embedded in paraffin, cut into 3-μm sections, and stained with hematoxylin and eosin (H&E). For p16 immunohistochemistry, slides were boiled in a citrate buffer for antigen retrieval after dehydration. Slides were then soaked in 10% hydrogen peroxide for 10 min to remove endogenous peroxidase and were washed. Slides were blocked in goat serum and incubated in primary antibody against p16 (Abcam, 1:100) at 4°C overnight. Washed slides were then incubated with secondary antibody for 40 min (biotinylated goat anti-rabbit IgG, BA-1000, Vector Labs), washed, and incubated in 3'-diaminobenzidine solution. For γ-H2AX and Ki67 immunofluorescence, antigen retrieval and blocking was performed as above, and primary antibody (γ-H2AX, Cell Signaling, 1:200; Ki67, Cell Signaling, 1:200) was applied and incubated at 4°C overnight. Slides were washed with phosphate-buffered saline and incubated with secondary antibody for 40 min (biotinylated goat antirabbit IgG, 594 nm) before adding an antifluorescence buffer containing 4′,6-diamidino-2-phenylindole for imaging.

Real-Time qPCR

Total RNA from tissues or cells was extracted using TRIzol (Life Technologies) and reverse-transcribed to cDNA using the Maxima First Strand cDNA Synthesis Kit (Thermo Scientific, K1671). Real-time PCR was performed by applying the SYBR Green (Takara) qPCR master mix following the manufacturer's protocol. ΔCt values were calculated as the following formula: ΔCt = Ct target – Ct actin. Values of sample reference to control were calculated using the ΔΔCT method; the difference of gene expression was calculated using the $2^{-(\Delta\Delta Ct)}$ formula. qRT-PCR

primer sequences are shown in **Supplementary Table 1**. Actin was used as an internal control.

SA-β-Gal Activity

Cells were seeded into 6-well plates and then either received 8-Gy (0.9 Gy/min) radiation or not. Cells were passed and assessed 7 days after radiation. SA-β-gal staining was done using a SA-β-gal staining kit (Cell Signaling) according to the manufacturer's instructions. First, 1 ml 4% paraformaldehyde was added to every plate to fix cells. Then, cells were incubated at 37°C for 24 h in a SA-β-gal staining solution (pH = 6.0, Cell Signaling). Blue-stained cells were senescent cells.

Flow Cytometry

Cells were seeded into 6-well plates at a density of 2×10^5 cells/well. Cells either exposed to radiation (8 Gy) or not were treated with DMSO or DQ (1 mM D+20 mM Q) for 24 h, digested with trypsin, and collected. Cells were then resuspended in a 100-μl binding buffer with 1-μl fluorescein isothiocyanate Annexin-V and 1-μl propidium iodine (PI; BD Biosciences, 556547). Finally, samples were analyzed by flow cytometry (C6, BD Biosciences, San Jose, CA). For cell cycle analysis, cells were fixed with Fixation/Permeabilization Diluent/Concentrate (eBioscience) for 30 min. Subsequently, intracellular Ki-67 (eBioscience) and Hoechst33342 (Sigma) staining were performed using PermWash solution (eBioscience). Cells were washed once prior to flow cytometry analysis.

Western Blot

Cells were extracted in a cell lysis buffer (Cell Signaling) with protease inhibitors (Sigma). Proteins were loaded into each lane on a 5–12% gradient sodium dodecyl sulfate/polyacrylamide gel and transferred to immunoblot polyvinylidene fluoride membranes (Bio-Rad). Membranes were blocked with 5% skim milk and probed with primary antibodies at 4°C overnight. Horseradish peroxidase-conjugated secondary antibodies (Beyotime) were applied for 1 h at room temperature. The band intensities were visualized and quantified using an enhanced chemiluminescence detection system (Bio-Rad Laboratories). Primary antibodies used were as follows: poly ADP-ribose polymerase (PARP, 1:1,000, abcam), caspase 3 (1:1,000, abcam), cleaved caspase 3 (1:1,000, abcam), p-JAK1(1:1,000, abcam), p-JAK2 (1:1,000, abcam), and β-actin (1:1,000, Beyotime).

Enzyme-Linked Immunosorbent Assay (ELISA)

The concentrations of human inflammatory cytokines from HOK and fibroblasts cell supernatant were measured with ELISA kits. IL-1α (KE00123), IL-6 (KE00139), IL-1β (KE00021), IL-8 (KE00006), and tumor necrosis factor (TNF)-α (KE00154) ELISA kits from ProteinTech were used following the manufacturer's protocols. Generating a linear standard curve based on the OD value of the standard, the expression of protein was calculated using the formula generated above.

Statistical Analysis

Comparisons between two groups were analyzed using unpaired Student's *t*-tests, and values are presented as mean with SD. Statistical significance was set as $^*P < 0.05$, $^{**}P < 0.01$, and $^{***}P < 0.001$. SPSS 13.0 statistical software was used to perform all statistical analyses, and GraphPad Prism 7.0 was used to generate graphs.

RESULTS

Senescence Biomarkers Accumulate in Human Radiation Ulcer After Radiotherapy

Senescence can be induced by multiple mechanisms such as DNA damage, reactive oxygen species (ROS) production, and oxidative stress (21), and DNA damage is a critical mediator of cellular alterations caused by radiation exposure (22). To explore the hypothesis that cell senescence and SASP are related to human radiation ulcers after radiotherapy, we first analyzed established senescence genes in the GSE103412 dataset (23) corresponding to mucositis in patients with tonsil squamous cell carcinoma (during and after radiation therapy) and control human cohorts (healthy mucosa and patients before radiotherapy). CDKN2A (p16) and TP53 were upregulated within oral mucosa samples of individuals with mucositis during and after radiation therapy (**Figure 1A**). In addition, HIST1H3B, HIST1H2BM, HIST1H3C, HIST1H3H, HIST1H1A, HIST1H4D, and HIST1H1B were downregulated (**Figure 1A**) in mucositis samples, especially at day 7 after radiation. This is notable since histone gene expression downregulation is a response to DNA damage (24). Ki67 (a marker of proliferation) was downregulated, indicating that radiation decreased the proliferative capacity of mucosa. Based on the hypothesis that senescent cells promote the development of radiation ulcers through the secretome, we analyzed the expression of SASP genes in human mucositis transcriptome datasets (GSE103412). Expression of pregnancy-associated plasma protein A (23), several matrix metalloproteinases (MMPs), and interleukin (IL) family members were also increased after radiation therapy (**Figure 1A**).

We also immunohistochemically detected p16 and γ-H2AX in skin tissue samples from healthy volunteers and patients with breast cancer receiving radiation therapy. As shown in **Figure 1B**, a lack of epithelium in the tissue was observed in ulcer tissue samples compared to normal skin. We also found a remarkable increase in the senescence marker p16 (**Figure 1C**) and the DNA damage marker γ-H2AX (**Figure 1D**). Collectively, our results indicate that senescence biomarkers accumulate in human radiation ulcers after radiotherapy, and senescence may play a critical role in promoting human radiation ulcers.

Radiation Induces Persistent Cell Senescence in Animal Ulcer Models

To further confirm the correlation between radiation ulcers and cell senescence, a mouse oral ulcer and rat skin ulcer model were established (**Figure 2A**). For radiation-induced oral ulcers, the head and neck of mice were treated with fractionated

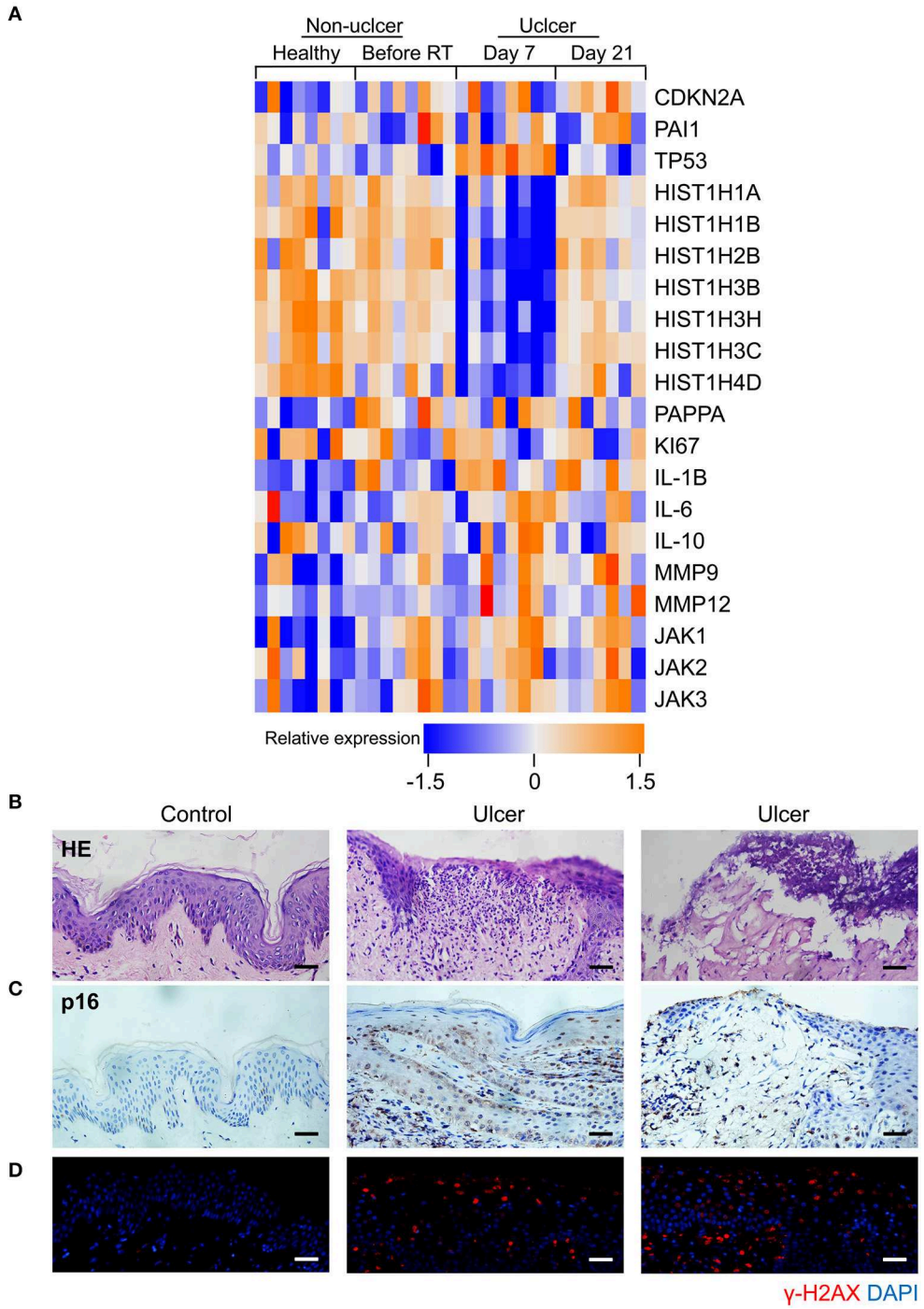

FIGURE 1 | Senescence biomarkers accumulate in human radiation ulcer after radiotherapy. **(A)** Heat map showed the expression of senescence, DNA damage, and SASP genes in mucositis in patients with tonsil squamous cell carcinoma (during and after radiation therapy) and control (healthy mucosa and patient before radiotherapy) human cohorts (healthy $n = 8$, before radiation $n = 8$, day 7 $n = 8$, day 21 $n = 7$). **(B)** Histological analysis of skin tissues from healthy volunteers and radiotherapy patients. **(C)** Immunohistochemistry staining of p16 of skin tissues from healthy volunteer and radiotherapy patients. **(D)** Immunofluorescence staining of γ-H2AX of skin tissues from healthy volunteer and radiotherapy patients. **(B–D)** Healthy $n = 1$, radiotherapy patients $n = 4$, skin tissue from the chest wall; scale bar, 50 μm.

radiation of a 6-Gy dose/day for 5 days (other body parts were covered with a lead board). Mice were euthanized at days 3, 6, 8, and 10, and the tongues were removed and analyzed. For radiation-induced skin ulcer, each rat's right posterior limb was exposed to a single 40-Gy radiation under anesthesia (25). As shown in **Figures 2B,C**, the irradiated tongues

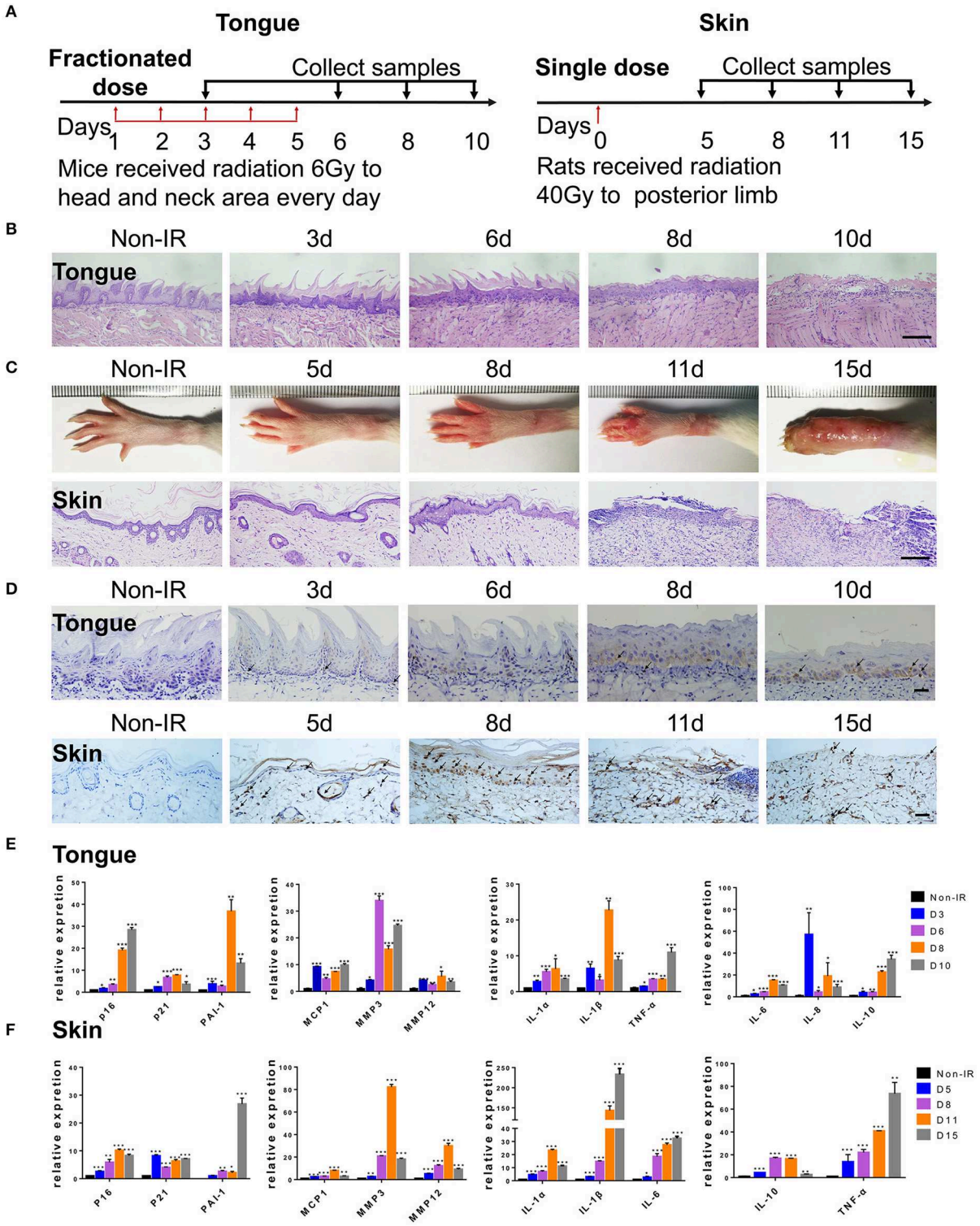

FIGURE 2 | Radiation induces persistent cell senescence in animal ulcer models. **(A)** Radiation and drug treatment scheme for mice (left) and rats (right). **(B)** Histological analysis of mouse tongue tissues 0–10 days postradiation ($n = 3$). **(C)** Representative images of hind limb 0–15 days postradiation (top); histological analysis of rat skin tissues 0–15 days postradiation (bottom) ($n = 3$). **(D)** Immunohistochemistry of p16 in mouse tongue and rat skin tissues ($n = 3$). As indicated by the arrow, brown represents positive cells. **(E,F)** The expressions of p16, p21, PAI-1, and SASP genes (IL-1α, IL-10, IL-1β, TNF-α, IL-6, MMP3, IL-8, MMP12, and MCP1) in different time points were quantified by qRT-PCR (mean with SD; $n = 3$, $^{*}P < 0.05$, $^{**}P < 0.01$, $^{***}P < 0.001$; Student's *t*-test). **(B,D)** Scale bar, 100 μm; **(C)** scale bar, 50 μm.

and skin exhibited severe destruction of the epithelial layer compared to normal epithelial morphology. Furthermore, both models showed increased immunohistochemical staining for the senescence marker p16 at different time points (**Figure 2D**). qRT-PCR showed that senescence markers p16, p21, and plasminogen activator inhibitor-1 (PAI-1) were increased in irradiated mice/rats (**Figures 2E,F**). We found that the SASP factors (26) [IL-1β, IL-6, IL-1α, IL-8, IL-10, TNF-α, MMP3, MMP12, and monocyte chemoattractant protein-1 (MCP1)] were all significantly upregulated in irradiated tongue and skin tissues compared to non-irradiated controls (**Figures 2E,F**). These results indicate that senescent cells and the SASP persist in radiation ulcer. These results are consistent with previously reported data for senescence-associated beta-galactosidase (SA-β-gal), a known marker of senescent cells (16). Therefore, eliminating senescent cells might be a viable strategy to alleviate radiation ulcers.

Senescent Cells Induce Cell Senescence and SASP in Adjacent Cells

Senescent cells acquire autocrine/paracrine abilities, and the cytokines they produce promote dysfunction and growth arrest in neighboring cells to maintain senescence by an autocrine positive-feedback loop (27). Next, we tested whether senescent HOK and human skin fibroblasts induce senescence and inflammation in adjacent healthy cells. We first established an *in vitro* HOK and skin fibroblast cell senescence model induced by radiation (**Figures 3A,B**), which were confirmed by SA-β-gal staining (28) and the expression of senescence mediators (p21 and p16) and SASP factors (MCP1 and IL-6) (29). Morphologically, senescent HOK are larger and rounder, with more vacuoles and fewer antennae compared with young HOK. Young fibroblasts are spindle-shaped or polygonal, whereas senescent cells become larger, flat, and overstretched, with elongated branches at the ends of extensions (**Figure 3A**). Notably, IL-1α, IL-8, IL-6, IL-1β, and TNF-α protein expression levels were increased in cell supernatant from irradiated cells compared with non-irradiated cells (**Figure 3C**). Then, CM from senescent cell supernatant (SASP-CM) and normal cell supernatant (Con-CM) were collected; we found that exposure of non-senescent HOK and skin fibroblasts to SASP-CM for 7 days induced SA-β-gal expression and senescent morphology compared with Con-CM (**Figure 3D**). Cells were also collected for qRT-PCR analysis, which showed that CM derived from senescent cells caused upregulation of senescence genes (p16, p21, PAI-1) and SASP genes (IL-1α, IL-10, IL-1β, TNF-α, IL-6, MMP3, IL-8, MMP12, and MCP1) relative to CM from non-senescent cells (**Figure 3E**). These results indicate that the SASP can induce cell senescence and inflammation in adjacent cells.

The JAK pathway is important in cytokine production, and JAK1 and 2 primarily regulate inflammatory signaling (30). The GSE103412 dataset showed increased JAK1/2 in ulcer patients after radiation therapy (**Figure 1A**). Similarly, we found significantly increased JAK expression after irradiating HOK and skin fibroblasts (**Figure 3F**). We then assessed the effect of JAKi, which can suppress SASP in senescent cells by inhibiting the JAK pathway. Senescent HOK and skin fibroblasts were incubated with vehicle and JAKi (1 μM) for 72 h; then CM from senescent cells (SASP-CM) and senescent cells incubated with JAKi [(SASP+JAKi)-CM] were collected. The results showed that JAKi (1 μM) downregulated the expression of crucial SASP genes in senescent cells (**Figure 3G**). Furthermore, after young HOK and skin fibroblasts were treated with SASP-CM and (SASP+JAKi)-CM for 24 h, respectively, SASP mRNA levels were lower in the (SASP+JAKi)-CM group relative to SASP-CM-treated young cells (**Figure 3H**). Therefore, SASP in senescent cells may promote SASP in adjacent cells. However, when young HOK and skin fibroblasts were treated with SASP-CM, followed by the addition of JAKi or vehicle for 24 h, we did not observe decreased levels of SASP (**Figure 3I**). Therefore, we hypothesize that JAKi mainly acts on senescent cells by suppressing the SASP to reduce inflammation, but it has no effect on non-senescent cells to prevent inflammation caused by SASP. These findings demonstrate that senescent cells can induce cell senescence and SASP in adjacent cells, and JAK inhibition alleviates SASP in senescent cells.

DQ Treatment Eliminates Senescent Cells by Inducing Apoptosis

The above observations suggest that senescent cells may be a viable target in preventing radiation ulcers. Therefore, we assessed the effect of DQ, which has been reported to selectively clear senescent cells (11, 19, 20). We found that a single dose of DQ (1 mM dasatinib+20 mM quercetin) eliminated 40–60% of senescent HOK and 10–20% skin fibroblasts within 24 h; nevertheless, DQ treatment had no observable effect on young HOK or skin fibroblasts (**Figure 4A**). Similarly, calcein AM/PI staining showed markedly higher cell death in senescent HOK and fibroblasts compared to young cells (**Figure 4B**). Moreover, DQ induced the expression of the apoptosis markers caspase 3, cleaved caspase 3, and PARP in senescent cells (**Figure 4C**). These results suggest that DQ selectively removed senescent cells through the intrinsic apoptotic pathway.

Senescent Cell Clearance Mitigates Radiation Ulcers

Next, we determined whether DQ could help heal radiation ulcers. DQ almost entirely prevented the appearance of mucositis in irradiated mice (**Figure 5A**). Histological analysis of the tongues showed complete and continuous epithelial layers in irradiated DQ-treated mice (**Figure 5B**). DQ also significantly decreased radiation-induced skin ulcers, desquamation, and edema and promoted epithelium repair (**Figures 5C,D**). In addition, we found reduced levels of the DNA damage response marker γ-H2AX in irradiated DQ-treated mice/rats (**Figure 6A**). Furthermore, DQ-treated mice/rats showed significantly increased levels of the proliferation marker Ki67 (31) (**Figure 6B**). As expected, DQ-treated mice/rats showed downregulation of the senescence marker p16 and SASP (**Figures 6C,D**). H&E staining showed that the heart, spleen, muscle, lung, intestine, kidney, and liver were not obviously affected by DQ treatment (**Supplementary Figure 1**),

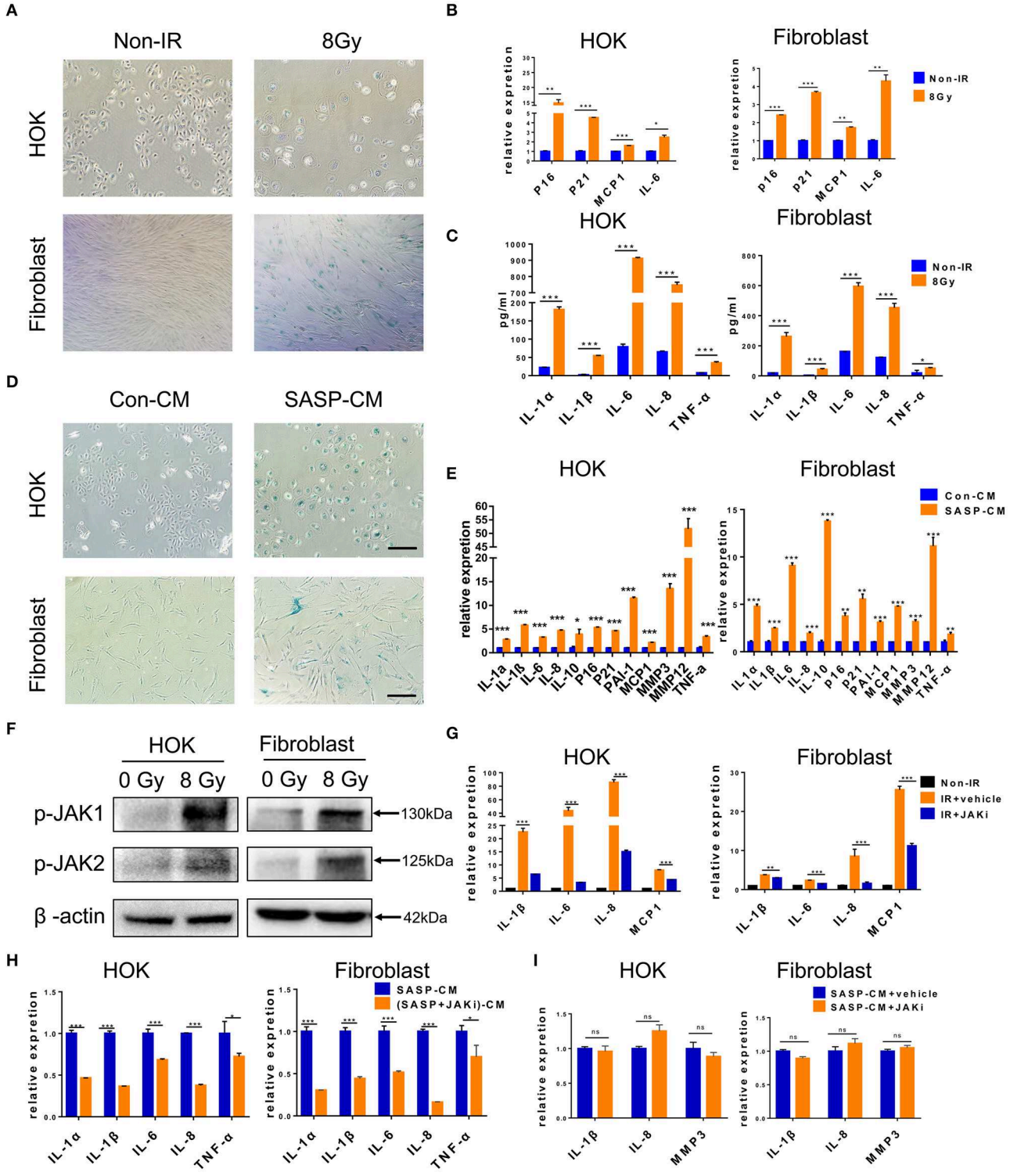

FIGURE 3 | Senescent cells induce cell senescence and SASP in adjacent cells. **(A)** SA-β-gal staining in HOK and skin fibroblasts at 7 days after radiation ($n = 3$). **(B)** mRNA expression levels for p16, p21, MCP1, and IL-6 in HOK and skin fibroblasts at 7 days after radiation ($n = 3$). **(C)** Protein expression levels for IL-1α, IL-8, IL-6, IL-1β, and TNF-α in HOK and skin fibroblast cell supernatant ($n = 3$). **(D)** HOK and skin fibroblasts were cultured in Con-CM and SASP-CM for 7 days and assessed by SA-β-gal staining ($n = 3$). **(E)** mRNA expression levels of p16, p21, PAI-1, and SASP genes (IL-1α, IL-10, IL-1β, TNF-α, IL-6, MMP3, IL-8, MMP12, and MCP1) in HOK and skin fibroblasts (cultured in Con-CM and SASP-CM for 7 days). **(F)** p-JAK1 and p-JAK2 expression levels in HOK and fibroblasts after radiation. Three

(Continued)

FIGURE 3 | independent experiments started with cell plating. **(G)** Irradiation-induced senescent HOK and fibroblast were treated with JAK inhibitor and vehicle for 72 h. Then RNA was collected, and qRT-PCR was performed ($n = 3$). **(H)** Young HOK and skin fibroblasts were treated with SASP-CM and (SASP+JAKi)-CM for 24 h, respectively; the mRNA levels of SASP were analyzed. **(I)** mRNA levels of SASP in young HOK and skin fibroblasts, which were treated with SASP-CM, followed by addition of JAK inhibitor 1 or vehicle for 24 h. **(E)** IR+vehicle group compared with IR+JAKi group. **(E,G–I)** Mean with SD. $n = 3$, $^{*}P < 0.05$, $^{**}P < 0.01$, $^{***}P < 0.001$; Student's *t*-test. **(A,D)** Scale bar, 100 μm.

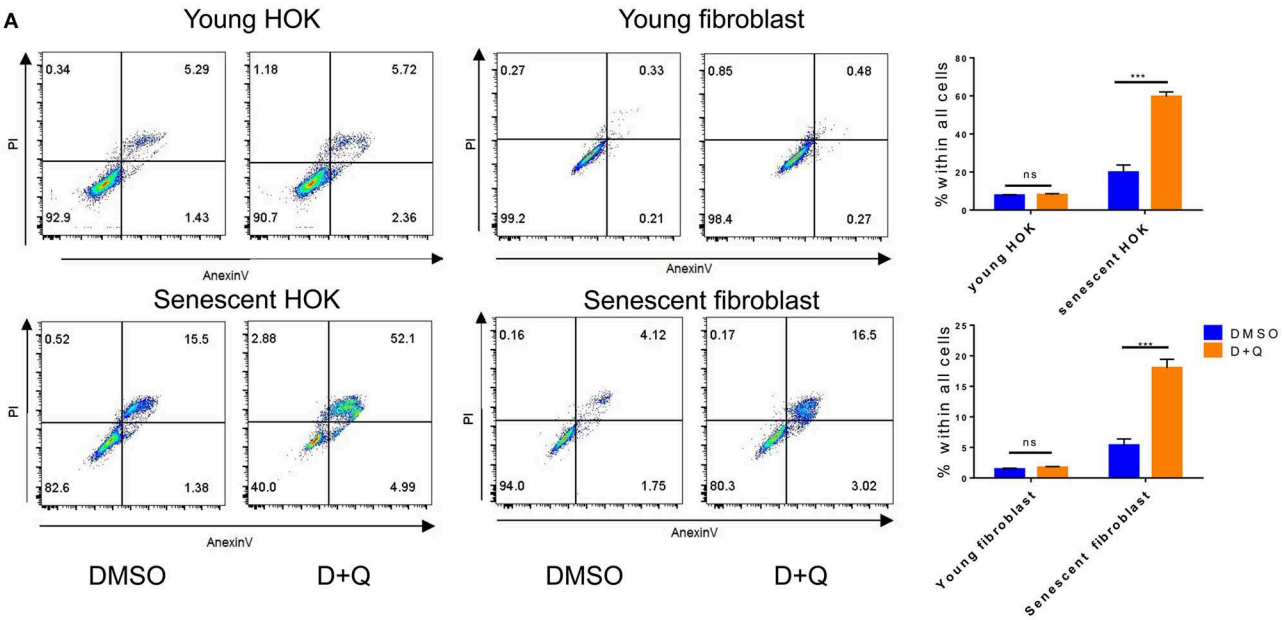

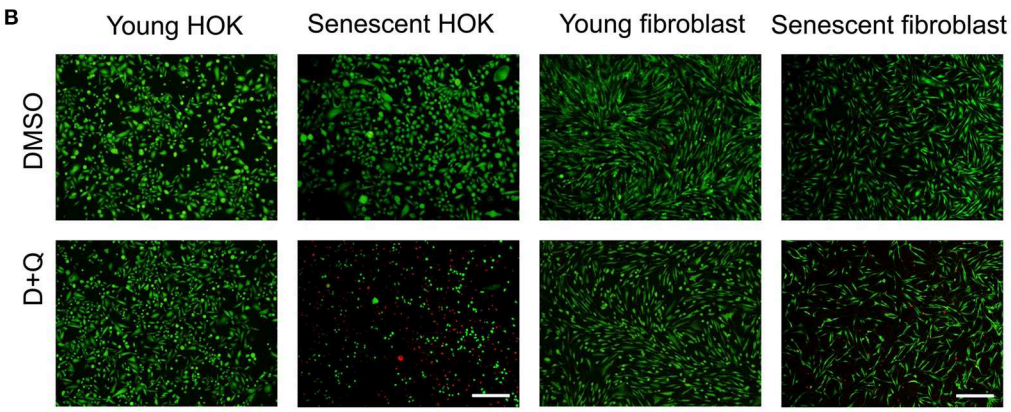

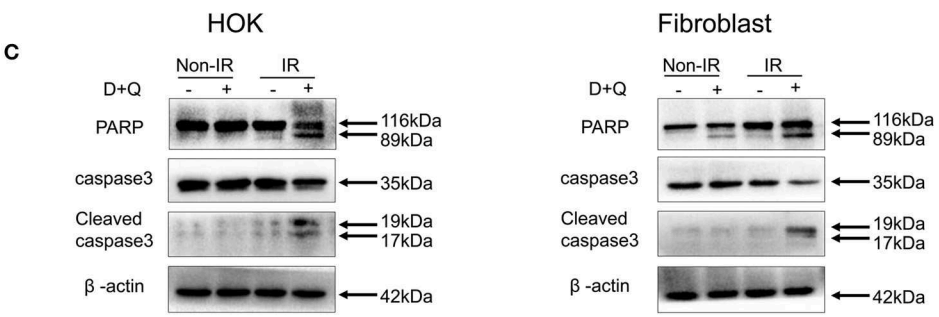

FIGURE 4 | Senescent cells are eliminated by DQ treatment. **(A)** Young/senescent HOK and skin fibroblasts were treated with DMSO or DQ for 24 h, and collected for apoptosis analysis using flow cytometry ($n = 3$), repeated three times independently (mean with SD. $n = 3$, $^{***}P < 0.001$; independent samples Student's *t*-test; ns, no significance). **(B)** HOK and skin fibroblasts were co-stained with calcein-AM (Invitrogen)/PI to visualize live cells (green fluorescence) and dead or late apoptotic cells (red fluorescence) ($n = 3$; scale bar, 100 μm). **(C)** Apoptosis markers PARP, caspase3, and cleaved caspase3 expression levels in young/senescent HOK and skin fibroblasts after being incubated with DMSO or DQ for 24 h. Three independent experiments started with cell plating.

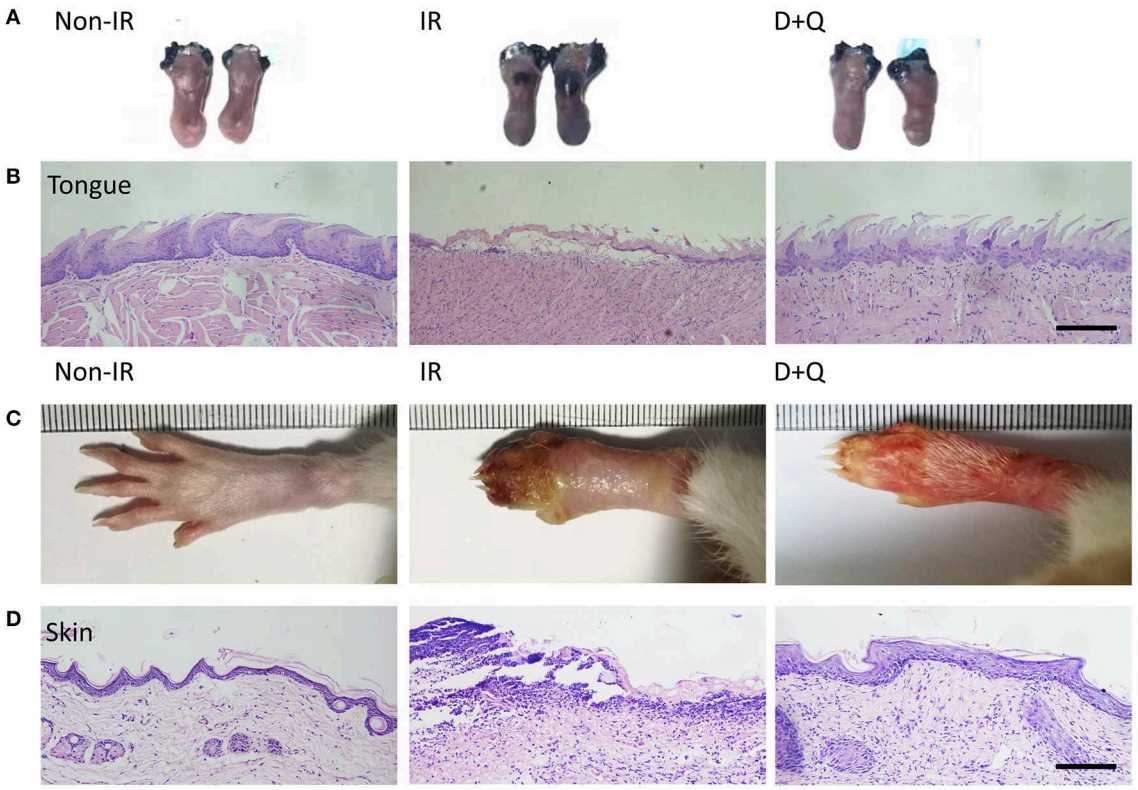

FIGURE 5 | Senescent cell clearance mitigates radiation ulcer. **(A)** Toluidine blue staining pictures of mouse tongues at day 10 from non-radiation, radiation, and DQ treatment mice. Lack of integrated epithelial barrier (ulcer) presents blue staining ($n = 5$). **(B)** Histological analysis of mouse tongues from non-radiation, radiation, and DQ treatment mice ($n = 5$). **(C)** Images of posterior limbs from SD rats (non-radiation, radiation, and DQ treatment mice) on day 15 ($n = 5$). **(D)** Histological analysis of skin tissues from non-radiation, radiation, and D+Q treatment rats at day 15 ($n = 5$). **(B,D)** Scale bar, 50 μm.

and there was no statistical difference in body weight between the DQ- and vehicle-treated groups after radiation (**Supplementary Figure 2**). These findings suggest the possibility that DQ treatment may alleviate DNA damage and maintain the proliferative capacity of tissue cells by eliminating senescent cells, thereby preventing the development of radiation ulcers.

DQ Enhances Cancer Cell Radiosensitivity

Senescence induced by ionizing radiation can contribute to tumor therapy via cell growth arrest (32) and autophagy (33). It can antagonize apoptosis and consequently shelter a population of dormant cells, and this anti-apoptotic effect ultimately leads to cancer radiotherapy resistance (34) and tumor recurrence (35). In our study, we assumed that senescent cells including senescent tumor cells (irradiated tumor cells) might be viable targets of DQ. CAL27 and MCF-7 cells are used as typical examples of head and neck squamous cell carcinomas and breast cancer, respectively. CAL27 and MCF-7 cells were exposed to 8-Gy irradiation and then incubated with DQ for 24 h. Flow cytometry result showed that a single dose of 1 mM D+20 mM Q induced apoptosis of CAL27 and MCF-7 and promoted radiosensitivity (**Figure 7A**). We next assessed cell-cycle percentages using flow cytometry and found that cells in the G1 phase were significantly increased in non-irradiated DQ-treated CAL27 and MCF-7 cells compared with the control group treated with DMSO (**Figure 7B**). This phenomenon was also evident in irradiated cells (**Figure 7B**), indicating that DQ treatment induces cell-cycle arrest at G1 and S/G2/M checkpoints in CAL27 and MCF-7 cells. Proliferation was measured by colony formation assays, which showed that DQ reduced the colony formation ability of both CAL27 and MCF-7 cells (**Figure 7C**). Our results suggest that DQ induced tumor cell apoptosis and also enhanced radiosensitivity and reduced proliferative capacity in CAL27 and MCF-7 cells.

DISCUSSION

Radiation therapy is an indispensable treatment for tumors that is applied to approximately half of cancer patients with different effects. It achieves good results in the treatment of head and neck and breast cancers. The radiation dose is determined by the sensitivity of the tumor and surrounding tissues (36). Oral mucositis is a crucial dose-limiting toxic effect in radiotherapy for head and neck cancers (37), and skin ulcers are a common side effect in patients with breast cancer (38, 39). Radiotherapy induces DNA strand breaks, ROS production, and oxidative stress that eventually trigger

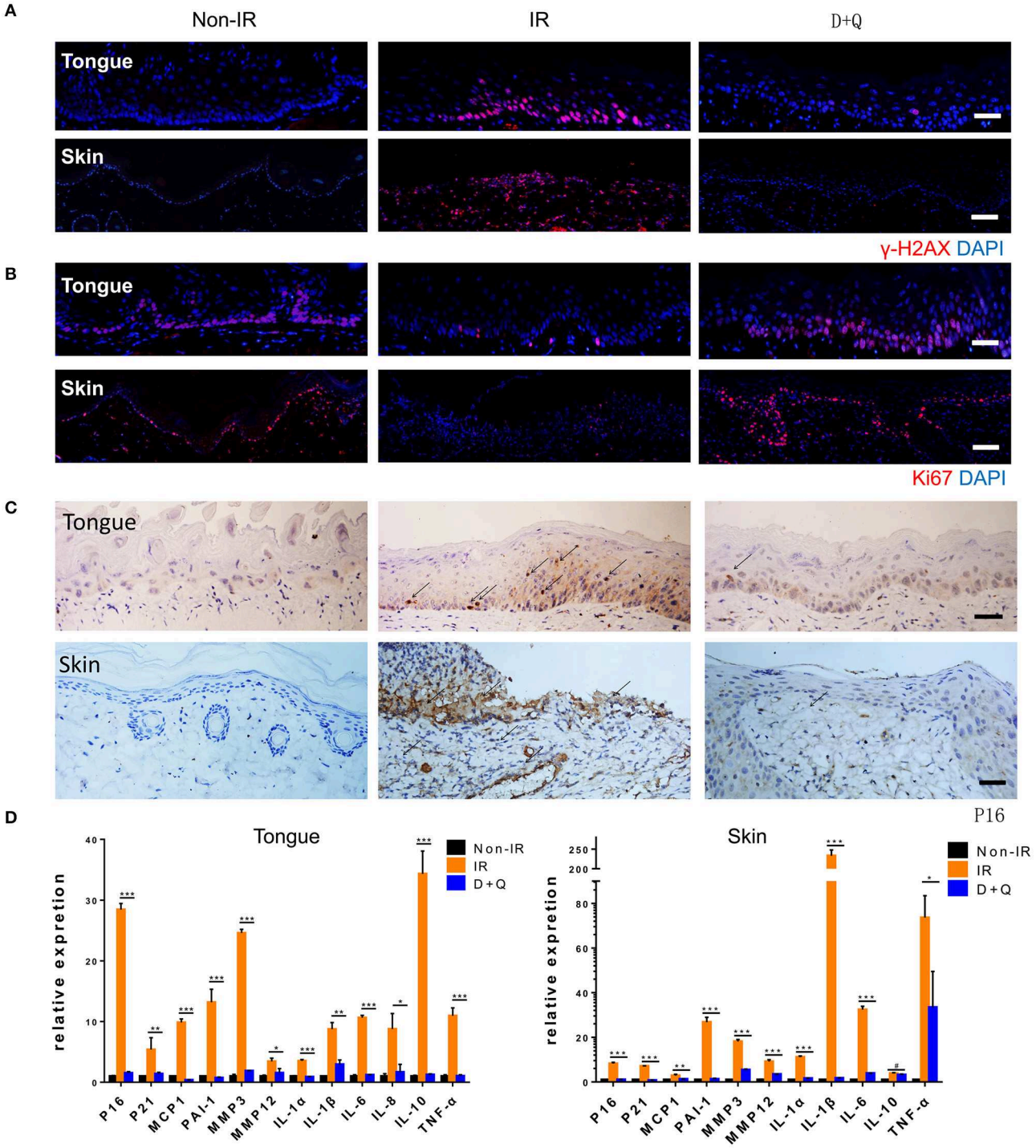

FIGURE 6 | Senescent cell clearance mitigates radiation ulcer. **(A,B)** Immunofluorescence staining of γ-H2AX and Ki67 in mouse tongue and rat skin tissues from non-radiation, radiation, and D+Q treatment groups ($n = 5$). **(C)** Immunohistochemistry staining of p16 in mouse tongue and rat skin tissue ($n = 5$). **(D)** Quantification of mRNA expression for p16, p21, and SASP in mouse tongue tissues and rat skin tissues. **(D)** Mean with SD. $n = 3$, $^{*}P < 0.05$, $^{**}P < 0.01$, $^{***}P < 0.001$, # means no significance; Student's *t*-test. **(A–C)** Scale bar, 25 μm.

cell senescence and amplify acute damage (9, 40, 41). Our results show that senescence biomarkers accumulate in human radiation ulcers after radiotherapy. Moreover, the expression of senescence-related genes and proteins was significantly increased after radiation and accumulated over time in radiation-induced ulcer models.

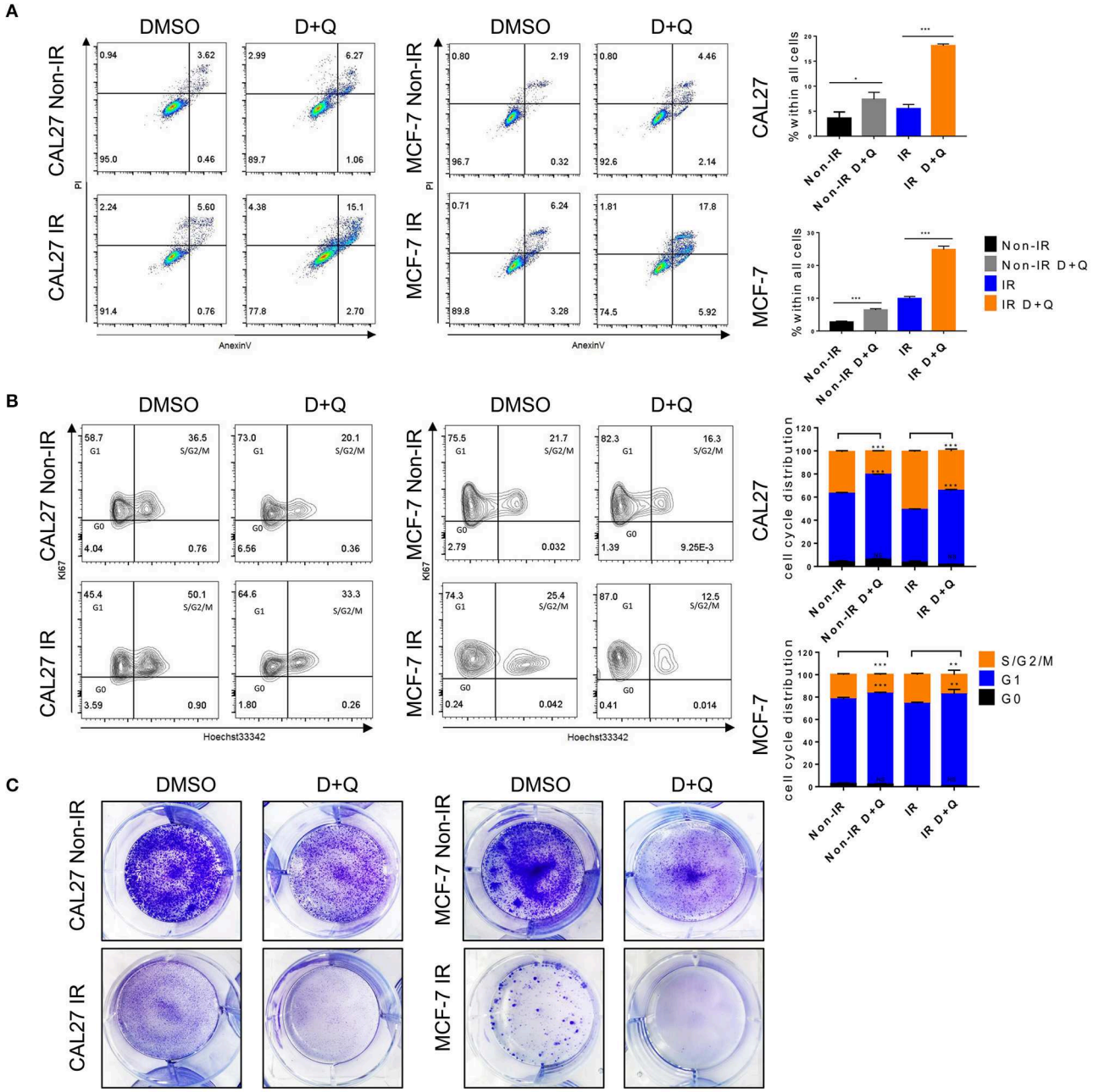

FIGURE 7 | DQ enhances radiosensitivity of cancer cells. **(A)** Irradiated or non-irradiated CAL27 and MCF-7 were incubated with DMSO or DQ for 24 h, then cells were collected for analysis of apoptosis using flow cytometry. **(B)** Irradiated or non-irradiated CAL27 and MCF-7 cells were incubated with DMSO or DQ for 24 h; cell cycle was analyzed by flow cytometry. **(C)** Representative colonies of irradiated or non-irradiated CAL27 and MCF-7. **(A–C)** $n = 3$; repeated three times independently (mean with SD. $n = 3$, $^{*}P < 0.05$, $^{**}P < 0.01$, $^{***}P < 0.001$; Student's *t*-test).

Cellular senescence is a cell-intrinsic program, and there is considerable evidence that senescent cells can affect neighboring cells and surrounding environment via their SASP (42, 43). In this study, senescent cells induced senescence and the SASP in adjacent cells, and JAK inhibition alleviated the SASP in senescent cells. Therefore, we reasoned that senescent cells may be a viable target in alleviating radiation ulcer. Furthermore, we found that DQ mitigated radiation ulcers via the removal of senescent cells. We previously reported that cordycepin prevented radiation ulcers by inhibiting cell senescence, and in this study, we showed that removal of senescent cells by DQ effectively ameliorated radiation ulcers. Therefore, inhibiting cell senescence or clearing senescent cells can be a therapeutic strategy in mitigating radiation-induced

ulcers. Plausibly, JAK inhibition can also be used to treat irradiation ulcers by alleviating the SASP; however, JAK inhibition needs to be continuously administered daily to maintain SASP inhibition. For this purpose, DQ would be administered several times (e.g., once monthly) to minimize senescent cells (19). Importantly, JAK inhibition causes severe side effects after discontinuation, including cardiogenic shock, tumor lysis syndrome, and even life-threatening events, but there are no obvious side effects after DQ treatment discontinuation (11, 44). Hence, DQ treatment is a better choice for mitigating radiation ulcers than JAKi, and there is great potential to treat radiation ulcers by developing safe and effective drugs that inhibit SASP.

A major challenge in treating radiation ulcers is repairing the ulcerated mucosa without promoting cancer, as KGF was shown to promote growth of human epithelial tumor cells (45). The development of potential agents that mitigate radiation ulcers without accelerating tumor growth is intensively needed in oncological supportive care. A related report concluded that Smad7 prevents radiotherapy-induced oral mucositis but does not prompt tumor growth (46). Here, we showed that DQ treatment alleviated radiation-induced ulcers by selectively eliminating senescent cells. Moreover, DQ also enhanced radiosensitivity and reduced proliferative capacity in representative CAL27 and MCF-7 cells.

In summary, we demonstrated that senescent cells persist in radiation ulcers, and clearance of senescent cells by DQ can effectively mitigate this painful side effect. Moreover, DQ treatment can enhance cancer cell radiosensitivity. Our results indicate that elimination of senescent cells is a potential therapeutic method to mitigate radiation ulcers.

DATA AVAILABILITY STATEMENT

The raw data supporting the conclusions of this article will be made available by the authors, without undue reservation, to any qualified researcher.

ETHICS STATEMENT

The animal study was reviewed and approved by the Ethics Committees of Army Medical University (AMU). The studies involving human participants were reviewed and approved by the ethics committee of Hunan Cancer Hospital. The patients/participants provided written informed consent for participation was required for this study in accordance with the national legislation and the institutional requirements.

AUTHOR CONTRIBUTIONS

CS, HW, and ZW designed, carried out, and analyzed data from most of the experiments and wrote the manuscript with input from all co-authors. CS conceived and supervised the study. YH, QJ, and ML performed experiments. YZ and XS collected clinical samples. YW and PL analyzed and interpreted data from experiments. All authors discussed the results and commented on the manuscript.

FUNDING

This work was supported by the National Key Research and Development Program (2016YFC1000805) and the University Innovation Team Building Program of Chongqing (CXTDG201602020), and intramural research project grants (AWS17J007 and 2018-JCJQ-ZQ-001).

ACKNOWLEDGMENTS

We thank Qing Zhou for the immunohistochemistry and immunofluorescence.

SUPPLEMENTARY MATERIAL

The Supplementary Material for this article can be found online at: https://www.frontiersin.org/articles/10.3389/fonc.2019.01576/full#supplementary-material

REFERENCES

1. Schaue D, McBride WH. Opportunities and challenges of radiotherapy for treating cancer. *Nat Rev Clin Oncol.* (2015) 12:527–40. doi: 10.1038/nrclinonc.2015.120
2. Mallick S, Benson R, Rath GK. Radiation induced oral mucositis: a review of current literature on prevention and management. *Eur Arch Otorhinolaryngol.* (2016) 273:2285–93. doi: 10.1007/s00405-015-3694-6
3. Saunders DP, Epstein JB, Elad S, Allemano J, Bossi P, van de Wetering MD, et al. Systematic review of antimicrobials, mucosal coating agents, anesthetics, and analgesics for the management of oral mucositis in cancer patients. *Support Care Cancer.* (2013) 21:3191–207. doi: 10.1007/s00520-013-1871-y
4. Senkus E, Kyriakides S, Ohno S, Penault-Llorca F, Poortmans P, Rutgers E, et al. Primary breast cancer: ESMO Clinical Practice Guidelines for diagnosis, treatment and follow-up. *Ann Oncol.* (2015) 26 (Suppl. 5):v8–30. doi: 10.1093/annonc/mdv298
5. Porceddu SV, Haddad RI. Management of elderly patients with locoregionally confined head and neck cancer. *Lancet Oncol.* (2017) 18:e274–83. doi: 10.1016/S1470-2045(17)30229-2
6. Finch PW, Rubin JS. Keratinocyte growth factor expression and activity in cancer: implications for use in patients with solid tumors. *J Natl Cancer Inst.* (2006) 98:812–24. doi: 10.1093/jnci/djj228
7. Enomoto M, Yagishita K, Okuma K, Oyaizu T, Kojima Y, Okubo A, et al. Hyperbaric oxygen therapy for a refractory skin ulcer after radical mastectomy and radiation therapy: a case report. *J Med Case Rep.* (2017) 11:5. doi: 10.1186/s13256-016-1168-0
8. Murphy CK, Fey EG, Watkins BA, Wong V, Rothstein D, Sonis ST. Efficacy of superoxide dismutase mimetic M40403 in attenuating radiation-induced oral mucositis in hamsters. *Clin Cancer Res.* (2008) 14:4292–7. doi: 10.1158/1078-0432.CCR-07-4669
9. van Deursen JM. The role of senescent cells in ageing. *Nature.* (2014) 509 (7501) 439–46. doi: 10.1038/nature13193
10. Campisi J. Aging, cellular senescence, and cancer. *Annu Rev Physiol.* (2013) 75:685–705. doi: 10.1146/annurev-physiol-030212-183653
11. Schafer MJ, White TA, Iijima K, Haak AJ, Ligresti G, Atkinson EJ, et al. Cellular senescence mediates fibrotic pulmonary disease. *Nat Commun.* (2017) 8:14532. doi: 10.1038/ncomms14532

12. Herranz N, Gil J. Mechanisms and functions of cellular senescence. *J Clin Invest.* (2018) 128:1238–46. doi: 10.1172/JCI95148
13. Dou Z, Ghosh K, Vizioli MG, Zhu J, Sen P, Wangensteen KJ, et al. Cytoplasmic chromatin triggers inflammation in senescence and cancer. *Nature.* (2017) 550:402–6. doi: 10.1038/nature24050
14. Coppe JP, Patil CK, Rodier F, Sun Y, Munoz DP, Goldstein J, et al. Senescence-associated secretory phenotypes reveal cell-nonautonomous functions of oncogenic RAS and the p53 tumor suppressor. *PLoS Biol.* (2008) 6:2853–68. doi: 10.1371/journal.pbio.0060301
15. Demaria M, O'Leary MN, Chang J, Shao L, Liu S, Alimirah F, et al. Cellular senescence promotes adverse effects of chemotherapy and cancer relapse. *Cancer Discov.* (2017) 7:165–76. doi: 10.1158/2159-8290.CD-16-0241
16. Wang Z, Chen Z, Jiang Z, Luo P, Liu L, Huang Y, et al. Cordycepin prevents radiation ulcer by inhibiting cell senescence via NRF2 and AMPK in rodents. *Nat Commun.* (2019) 10:2538. doi: 10.1038/s41467-019-10386-8
17. Iglesias-Bartolome R, Patel V, Cotrim A, Leelahavanichkul K, Molinolo AA, Mitchell JB, et al. mTOR inhibition prevents epithelial stem cell senescence and protects from radiation-induced mucositis. *Cell Stem Cell.* (2012) 11:401–14. doi: 10.1016/j.stem.2012.06.007
18. Chen Z, Wang X, Jin T, Wang Y, Hong CS, Tan L, et al. Increase in the radioresistance of normal skin fibroblasts but not tumor cells by mechanical injury. *Cell Death Dis.* (2017) 8:e2573. doi: 10.1038/cddis.2016.416
19. Farr JN, Xu M, Weivoda MM, Monroe DG, Fraser DG, Onken JL, et al. Targeting cellular senescence prevents age-related bone loss in mice. *Nat Med.* (2017) 23:1072–9. doi: 10.1038/nm.4385
20. Ogrodnik M, Miwa S, Tchkonia T, Tiniakos D, Wilson CL, Lahat A, et al. Cellular senescence drives age-dependent hepatic steatosis. *Nat Commun.* (2017) 8:15691. doi: 10.1038/ncomms15691
21. Treiber N, Maity P, Singh K, Kohn M, Keist AF, Ferchiu F, et al. Accelerated aging phenotype in mice with conditional deficiency for mitochondrial superoxide dismutase in the connective tissue. *Aging Cell.* (2011) 10:912. doi: 10.1111/j.1474-9726.2011.00739.x
22. Vijg J, Kennedy BK. The essence of aging. *Gerontology.* (2016) 62:381–5. doi: 10.1159/000439348
23. Marcussen M, Sonderkaer M, Bodker JS, Andersen M, Nielsen S, Vesteghem C, et al. Oral mucosa tissue gene expression profiling before, during, and after radiation therapy for tonsil squamous cell carcinoma. *PLoS ONE.* (2018) 13:e0190709. doi: 10.1371/journal.pone.0190709
24. Su C, Gao G, Schneider S, Helt C, Weiss C, O'Reilly MA, et al. DNA damage induces downregulation of histone gene expression through the G1 checkpoint pathway. *EMBO J.* (2004) 23:1133–43. doi: 10.1038/sj.emboj.7600120
25. Wang X, Chen Z, Luo S, Jin T, Wang Y, Chen F, et al. Development of therapeutic small-molecule fluorophore for cell transplantation. *Adv Funct Mater.* (2016) 26:8397–407. doi: 10.1002/adfm.201600996
26. Laberge RM, Sun Y, Orjalo AV, Patil CK, Freund A, Zhou L, et al. MTOR regulates the pro-tumorigenic senescence-associated secretory phenotype by promoting IL1A translation. *Nat Cell Biol.* (2015) 17:1049–61. doi: 10.1038/ncb3195
27. Acosta JC, O'Loghlen A, Banito A, Guijarro MV, Augert A, Raguz S, et al. Chemokine Signaling via the CXCR2 receptor reinforces senescence. *Cell.* (2008) 133:1006–18. doi: 10.1016/j.cell.2008.03.038
28. Storer M, Mas A, Robert-Moreno A, Pecoraro M, Ortells MC, Di Giacomo V, et al. Senescence is a developmental mechanism that contributes to embryonic growth and patterning. *Cell.* (2013) 155:1119–30. doi: 10.1016/j.cell.2013.10.041
29. Coppe JP, Desprez PY, Krtolica A, Campisi J. The senescence-associated secretory phenotype: the dark side of tumor suppression. *Annu Rev Pathol.* (2010) 5:99–118. doi: 10.1146/annurev-pathol-121808-102144
30. Meyer SC, Levine RL. Molecular pathways: molecular basis for sensitivity and resistance to JAK kinase inhibitors. *Clin Cancer Res.* (2014) 20:2051–9. doi: 10.1158/1078-0432.CCR-13-0279
31. Aragona M, Dekoninck S, Rulands S, Lenglez S, Mascre G, Simons BD, et al. Defining stem cell dynamics and migration during wound healing in mouse skin epidermis. *Nat Commun.* (2017) 8:14684. doi: 10.1038/ncomms14684
32. Gewirtz DA, Holt SE, Elmore LW. Accelerated senescence: an emerging role in tumor cell response to chemotherapy and radiation. *Biochem Pharmacol.* (2008) 76:947–57. doi: 10.1016/j.bcp.2008.06.024
33. Arthur CR, Gupton JT, Kellogg GE, Yeudall WA, Cabot MC, Newsham IF, et al. Autophagic cell death, polyploidy and senescence induced in breast tumor cells by the substituted pyrrole JG-03-14, a novel microtubule poison. *Biochem Pharmacol.* (2007) 74:981–91. doi: 10.1016/j.bcp.2007.07.003
34. Jain MV, Paczulla AM, Klonisch T, Dimgba FN, Rao SB, Roberg K, et al. Interconnections between apoptotic, autophagic and necrotic pathways: implications for cancer therapy development. *J Cell Mol Med.* (2013) 17:12–29. doi: 10.1111/jcmm.12001
35. Assani G, Zhou Y. Effect of modulation of epithelial-mesenchymal transition regulators Snail1 and Snail2 on cancer cell radiosensitivity by targeting of the cell cycle, cell apoptosis and cell migration/invasion. *Oncol Lett.* (2019) 17:23–30. doi: 10.3892/ol.2018.9636
36. Begg AC, Stewart FA, Vens C. Strategies to improve radiotherapy with targeted drugs. *Nat Rev Cancer.* (2011) 11:239–53. doi: 10.1038/nrc3007
37. Daugelaite G, Uzkuraityte K, Jagelaviciene E, Filipauskas A. Prevention and treatment of chemotherapy and radiotherapy induced oral mucositis. *Medicina.* (2019) 55:E25. doi: 10.3390/medicina55020025
38. Vindigni V, Kohlscheen E, Kraljic T, Bassetto F, Pavan C. Mammary malignant ulcer after radiotherapy: unpleasant surprise. *Plast Reconstr Surg Glob Open.* (2017) 5:e1312. doi: 10.1097/GOX.0000000000001312
39. Spalek M. Chronic radiation-induced dermatitis: challenges and solutions. *Clin Cosmet Investig Dermatol.* (2016) 9:473–82. doi: 10.2147/CCID.S94320
40. Rodier F, Coppe JP, Patil CK, Hoeijmakers WA, Munoz DP, Raza SR, et al. Persistent DNA damage signalling triggers senescence-associated inflammatory cytokine secretion. *Nat Cell Biol.* (2009) 11:973–9. doi: 10.1038/ncb1909
41. Passos JF, Nelson G, Wang C, Richter T, Simillion C, Proctor CJ, et al. Feedback between p21 and reactive oxygen production is necessary for cell senescence. *Mol Syst Biol.* (2010) 6:347. doi: 10.1038/msb.2010.5
42. Kuilman T, Peeper DS. Senescence-messaging secretome: SMS-ing cellular stress. *Nat Rev Cancer.* (2009) 9:81–94. doi: 10.1038/nrc2560
43. Biran A, Perelmutter M, Gal H, Burton DG, Ovadya Y, Vadai E, et al. Senescent cells communicate via intercellular protein transfer. *Genes Dev.* (2015) 29:791–802. doi: 10.1101/gad.259341.115
44. Ballinger TJ, Savani BN, Gupta V, Kroger N, Mohty M. How we manage JAK inhibition in allogeneic transplantation for myelofibrosis. *Eur J Haematol.* (2015) 94:115–9. doi: 10.1111/ejh.12455
45. Im KI, Nam YS, Kim N, Song Y, Lee ES, Lim JY, et al. Regulation of HMGB1 release protects chemoradiotherapy-associated mucositis. *Mucosal Immunol.* (2019) 12:1070–81. doi: 10.1158/1538-7445.AM2018-465
46. Han G, Bian L, Li F, Cotrim A, Wang D, Lu J, et al. Preventive and therapeutic effects of Smad7 on radiation-induced oral mucositis. *Nat Med.* (2013) 19:421–8. doi: 10.1038/nm.3118

Conflict of Interest: The authors declare that the research was conducted in the absence of any commercial or financial relationships that could be construed as a potential conflict of interest.

frontiers in Oncology

ORIGINAL RESEARCH
published: 17 March 2020
doi: 10.3389/fonc.2020.00344

NTCP Models for Severe Radiation Induced Dermatitis After IMRT or Proton Therapy for Thoracic Cancer Patients

Giuseppe Palma[1,2], *Serena Monti*[1], *Manuel Conson*[3], *Ting Xu*[4], *Stephen Hahn*[4], *Marco Durante*[5], *Radhe Mohan*[6], *Zhongxing Liao*[4] *and Laura Cella*[1,2]*

[1] *Institute of Biostructures and Bioimaging, National Research Council, Naples, Italy,* [2] *National Institute for Nuclear Physics, (INFN), Naples, Italy,* [3] *Department of Advanced Biomedical Sciences, Federico II University School of Medicine, Naples, Italy,* [4] *Department of Radiation Oncology, University of Texas MD Anderson Cancer Center, Houston, TX, United States,* [5] *GSI Helmholtz Centre for Heavy Ion Research, Department of Biophysics, Darmstadt, Germany,* [6] *Department of Radiation Physics, University of Texas MD Anderson Cancer Center, Houston, TX, United States*

Radiation therapy (RT) of thoracic cancers may cause severe radiation dermatitis (RD), which impacts on the quality of a patient's life. Aim of this study was to analyze the incidence of acute RD and develop normal tissue complication probability (NTCP) models for severe RD in thoracic cancer patients treated with Intensity-Modulated RT (IMRT) or Passive Scattering Proton Therapy (PSPT). We analyzed 166 Non-Small-Cell Lung Cancer (NSCLC) patients prospectively treated at a single institution with IMRT (103 patients) or PSPT (63 patients). All patients were treated to a prescribed dose of 60 to 74 Gy in conventional daily fractionation with concurrent chemotherapy. RD was scored according to CTCAE v3 scoring system. For each patient, the epidermis structure (skin) was automatically defined by an in house developed segmentation algorithm. The absolute dose-surface histogram (DSH) of the skin were extracted and normalized using the Body Surface Area (BSA) index as scaling factor. Patient and treatment-related characteristics were analyzed. The Lyman-Kutcher-Burman (LKB) NTCP model recast for DSH and the multivariable logistic model were adopted. Models were internally validated by Leave-One-Out method. Model performance was evaluated by the area under the receiver operator characteristic curve, and calibration plot parameters. Fifteen of 166 (9%) patients developed severe dermatitis (grade 3). RT technique did not impact RD incidence. Total gross tumor volume (GTV) size was the only non dosimetric variable significantly correlated with severe RD ($p = 0.027$). Multivariable logistic modeling resulted in a single variable model including S_{20Gy}, the relative skin surface receiving more than 20 Gy (OR = 31.4). The cut off for S_{20Gy} was 1.1% of the BSA. LKB model parameters were $TD_{50} = 9.5$ Gy, $m = 0.24$, $n = 0.62$. Both NTCP models showed comparably high prediction and calibration performances. Despite skin toxicity has long been considered a potential limiting factor in the clinical use of PSPT, no significant differences in RD incidence was found between RT modalities. Once externally validated, the availability of NTCP models for prediction of severe RD may advance treatment planning optimization.

Keywords: radiation dermatitis, dose-surface histogram, proton therapy, intensity modulated radiation therapy, NSCLC, NTCP

OPEN ACCESS

Edited by:
Claudio Fiorino,
San Raffaele Hospital (IRCCS), Italy

Reviewed by:
Michele Avanzo,
Centro di Riferimento Oncologico di Aviano (IRCCS), Italy
Sarah Gulliford,
University College London, United Kingdom

***Correspondence:**
Laura Cella
laura.cella@cnr.it

Specialty section:
This article was submitted to Radiation Oncology, a section of the journal Frontiers in Oncology

Received: *17 December 2019*
Accepted: *27 February 2020*
Published: *17 March 2020*

Citation:
Palma G, Monti S, Conson M, Xu T, Hahn S, Durante M, Mohan R, Liao Z and Cella L (2020) NTCP Models for Severe Radiation Induced Dermatitis After IMRT or Proton Therapy for Thoracic Cancer Patients. Front. Oncol. 10:344. doi: 10.3389/fonc.2020.00344

INTRODUCTION

The development of acute and chronic radiation-induced skin injuries is a common side effect of radiation therapy (RT). Acute radiation dermatitis (RD), with reactions evident one to four weeks after the beginning of RT, may limit the duration of treatment and the dose delivered (1, 2). The severity of adverse dermatologic events ranges from mild erythema to moist desquamation and ulceration, impacting on the quality of a patient's life (3). Acute RD occurs most frequently after RT of breast, pelvic (e.g., anal cancer, vulvar cancer) and head and neck malignancies, while lower incidence is reported for deeper tumors as lung cancers (4).

Thanks to the advent of high-energy photon RT, which provide more skin sparing treatments compared to older ones with lower energy treatment machines, a general reduction in RD incidence and severity has been achieved in the past decades. Still, RD remains one of the significant adverse effect of RT.

The introduction of most modern treatment modalities, such as intensity modulated RT (IMRT) or proton beam therapy, has nowadays changed the dose distribution patterns in the normal tissues surrounding the tumors (5, 6). Accordingly, advanced RT techniques have generally reduced the burden of radiation related risks, included skin toxicity (7, 8). The substantial sparing of organs-at-risk from proton beams compared to IMRT is expected to theoretically further reduce radiation-induced morbidity (9). However, the risk of a potential increase of skin toxicity has long been considered a peculiar drawback in the clinical use of protons. The higher beam entry dose of the spread-out Bragg peak represents a disadvantage for the skin; thus causing concern over a possible increase in skin adverse effects (10, 11).

The skin response to radiation has been studied since the discovery of X-rays (2, 12). Multiple patient-specific and dosimetric features have been identified as risk factors for acute skin toxicity after RT for diverse tumor locations, in particular breast (7, 13, 14), head and neck (15) or brain tumors (16). Notwithstanding this, normal tissue complication probability (NTCP) modeling of skin toxicity is still not fully explored. In addition, the available NTCP models are mostly designed for dose-volume histogram (DVH) from a target volume (e.g., breast) (17–20) or are based on DVH from a pseudo-skin structure defined as a layer of 2-5 mm inward from the body contour (15, 21, 22). A different approach could directly consider the surface phenomena connected to the actual organ at risk, i.e., the skin (23).

In the present study, we analyzed the incidence of acute RD in thoracic cancer patients treated with Intensity-Modulated RT (IMRT) or Passive Scattering Proton Therapy (PSPT) on a completed prospective randomized trial (24), and we developed NTCP models for severe acute RD. The model procedure was based on the introduction of a fully automated method for skin definition as a critical organ. Both the Lyman-Kutcher-Burman (LKB) and multivariable logistic regression modeling strategies were adopted.

METHODS AND MATERIAL

The study involved 225 patients with locally advanced Non-Small-Cell Lung Cancer (NSCLC) enrolled in the trial NCT00915005. One hundred sixty-six patients were eligible for the present analysis. The eligibility criteria included acute RD follow-up data and availability of dose maps. All patients were treated according to an IRB approved protocol (NCT00915005) with image-guided IMRT (103 patients) or PSPT (63 patients) to a prescribed dose of 66 or 74 Gy (RBE) in 33 or 37 conventional daily fractions delivered with concurrent chemotherapy (CHT). The typical three-field arrangement was used for all PSPT plans (24). Typically, a posterior and lateral beams plus an oblique beam that avoids lung parenchyma in its exit dose (25). In the IMRT plans, six to nine equidistant, coplanar, axial 6-MV beams were usually used (26).

Details of the protocol, patient and treatment characteristics are reported elsewhere (27, 28). All dose maps were obtained with a dose grid size of $2.0 \times 2.0 \times 2.5\,\text{mm}^3$.

For each patient, acute RD was assessed as the maximum score recorded during the treatment and within 90 days after RT. The RD was graded according to the National Cancer Institute's Common Toxicity Criteria for Adverse Events (CTCAE) version 3 into the following groups:

Grade 1: Faint erythema or dry desquamation
Grade 2: Moderate to brisk erythema; patchy moist desquamation, mostly confined to skin folds and creases; moderate edema
Grade 3: Moist desquamation in areas other than skin folds and creases; bleeding induced by minor trauma or abrasion
Grade 4: Life-threatening consequences; skin necrosis or ulceration of full thickness dermis; spontaneous bleeding from involved site; skin graft indicated.

Dosimetric Analysis

For each patient, individual DICOM RT plans (computed tomography (CT) scans, doses, and contoured organ structures) were converted into Matlab-readable format (MathWorks, Natick, MA, USA) using the CERR (Computational Environment for Radiotherapy Research) software (29).

The epidermis (skin) was automatically defined by an in-house segmentation algorithm developed on purpose. In detail, the body contour was first corrected applying a Hounsfield unit thresholding over a moving window to exclude possible contribution from treatment bed. The resulting structure Ω was then eroded by 3 mm [i.e., approximately the mean skin thickness (30)]; the skin was then obtained subtracting from Ω its erosion (**Figure 1**) according to the following equation

$$\text{skin}_r = [\Omega \setminus (\Omega \ominus B[r])]$$
$$\text{skin} = \text{skin}_{3\text{ mm}}$$

where $B[r]$ is a spherical structuring element of radius r, $\setminus$ represents the set difference, and $\ominus$ stands for morphological erosion (31).

The absolute dose-surface histograms (DSHs) of the skin thus extracted were computed by an in-house developed library for

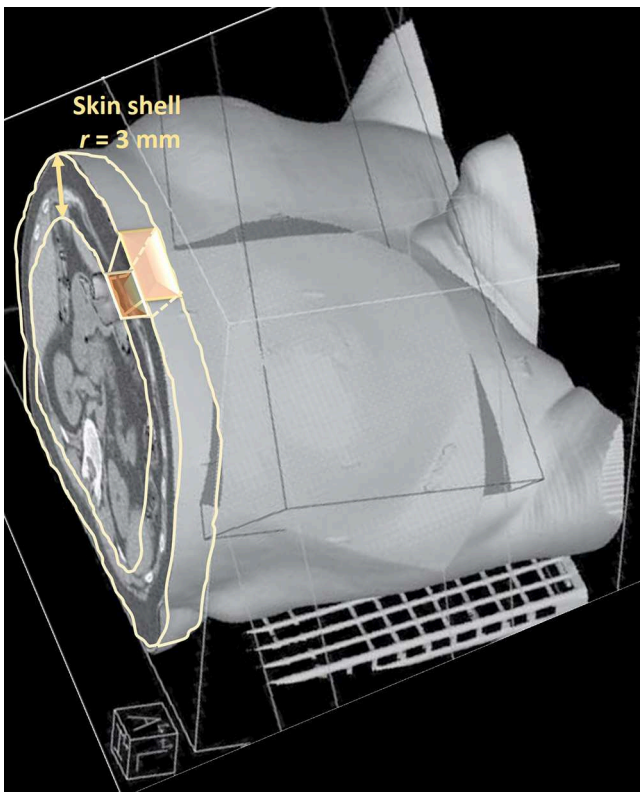

FIGURE 1 | Pictorial representation of the skin segmentation and dose-surface histogram extraction.

Matlab (23) according to

$$\mathrm{DSH}\,(x) = \lim_{r\to 0} \frac{\mathrm{DVH}(X)_{\mathrm{skin}_r}}{r}$$

The relative DSH were obtained using the Body Surface Area (BSA) index as scaling factor. The BSA index was calculated according to

$$\mathrm{BSA} = 7.184\,.\,\mathrm{cm}^2\ \left(W/\mathrm{kg}\right)^{0.425}.\ (H/\mathrm{cm})^{0.725}$$

Where W and H are patient's weight and height respectively (32).

The following DSH metrics were extracted: the relative skin surface receiving more than X Gy (S_x) in step of 1 Gy, the minimum dose given to the hottest x% skin surface in step of 5% (D_x), the skin near maximum dose ($D_{2\%}$) and the mean dose (D_{mean}).

Statistical Analysis

Acute RD was analyzed according to its severity, i.e., grade 3 (G3) RD vs. G0-G2 RD. All the extracted skin dose parameters along with patient-specific and treatment-related factors were analyzed by univariate statistical methods for the above defined grouping. Categorical variables were tested by Pearson's χ^2-test or Fisher's exact test when appropriate; continuous variables were tested by Mann-Whitney U-test.

Average relative DSHs stratified by treatment modality and toxicity endpoints were compared at each dose point by two-tailed t-test. A significance α-level of 0.05 corrected according to the Holm–Šidák method for multiple comparison was applied (33).

Normal Tissue Complication Probability Modeling

For the defined endpoint, two different NTCP modeling approaches were applied: the LKB model, built on generalized equivalent uniform dose (gEUD) (34, 35) and recast for DSHs (23), and the multivariable logistic model. The LKB model parameters (TD_{50}, m and n) and their 95% confidence intervals (CIs) were fitted as described in (36). TD_{50} is the value of the uniform dose given to the entire organ surface corresponding to the 50% probability to induce toxicity; m is inversely proportional to the slope of the dose-response curve; and n accounts, in this specific case, for the surface effect (n close to 0 meaning weak surface effect, n close to 1 strong surface effect). Briefly, the Maximum Likelihood method was used to find the best-fit values of the LKB parameters by maximizing the logarithm of the likelihood (LLH). The LLH function was numerically maximized by the Nelder-Mead Simplex Method using an in-house developed library for Matlab. Ninety-five percent confidence intervals for parameters estimates were obtained using the profile likelihood method.

In order to evaluate the possible impact of dosimetric and non-dosimetric factors, the multivariable stepwise logistic regression method for NTCP modeling was also applied (37, 38). In the multivariable analysis were included only the variables highly correlated with RD ($p < 0.1$ at the univariable analysis) that were not collinear (correlation $|\mathrm{Rs}|<0.75$) with variables more correlated with RD.

The Leave-One-Out (LOO) method was applied to the whole statistical pipelines to cross validate the models.

Model performance was evaluated by the area under the receiver operating characteristic (ROC) curve (AUC) and by balanced accuracy (39). Cut-off values on the ROC curve were determined by Youden's J statistic (40). Calibration plots were also generated for graphical assessment of the agreement between observed outcome and LOO prediction.

RESULTS

Of the 166 patients, 118 (71%) developed acute RD of any grade; fifteen of 166 (9%) patients developed G3 RD. In particular, 71 (69%) of IMRT patients developed a RD of any grade compared to 47 (75%) of PSPT patients; G3 RD occurred in 8 IMRT (8%) and 7 (11%) PSPT patients, respectively. The distribution of RD grades for each treatment modality is reported in **Figure 2**. There were no cases of grade 4 toxicity.

No significant differences were found in the distribution of clinical and disease factors between patients classified according to the treatment modality (**Table 1**). In addition, the univariate analysis did not show significant correlations between treatment modality and the incidence of RD categorized for any grade

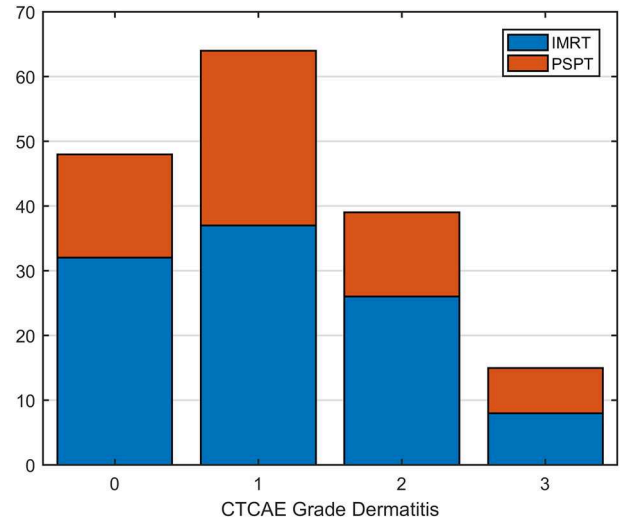

FIGURE 2 | Distribution of radiation dermatitis (RD) grades for patients categorized by treatment modality [Intensity Modulated Radiation Therapy (IMRT) vs. Passive Scattering Proton Therapy (PSPT)].

threshold (grade $\geq$ 1: $p = 0.48$; grade $\geq$ 2: $p = 0.19$; grade $\geq$ 3: $p = 0.58$).

The analysis of average skin DSH in patients stratified by treatment modality (**Figures 3A,C**) showed that PSPT, compared to IMRT, significantly reduced the skin surface receiving low doses (<12 Gy). An opposite behavior can be observed in the range from 25 to 55 Gy. Average skin DSHs of patients with and without G3-RD showed instead a significant separation between the two curves starting from the dose value of 5 Gy (**Figures 3B,D**).

At univariate analysis for patients stratified according to G3 RD (**Table 2**), all the S_x metrics for doses greater than 5 Gy were significantly correlated with G3-RD; among the clinical variables, total gross tumor volume (GTV) size was the only non dosimetric factor significantly correlated with severe RD ($p = 0.027$).

From NTCP model training, LKB model resulted in the following parameters: $TD_{50} = 9.5$ Gy (95% CI: [5.9, 18.4] Gy), $m = 0.24$ (95% CI: [0.17, 0.35]), $n = 0.62$ (95% CI: [0.36, 0.92]). Model performance metrics for both training and LOO cross validation were reported in **Table 3**.

Regarding the logistic modeling, after the variable selection procedure, multivariable modeling resulted in a single variable model including S_{20Gy} (OR = 31.4, 95% CI: [7.5, 131.7], constant= $-6.34\pm$ 1.03). The ROC analysis identified that the optimal cut-off for S_{20Gy} was 1.1% of the BSA.

Similarly, to the LKB model, the logistic model achieved high prediction performances as shown by the AUC values reported in **Table 3**. LOO cross validation confirmed good prediction and calibration performances (**Table 3** and **Figure 4**). Notably, the balanced accuracy demonstrated a good generalization score and a robust prediction capability despite data imbalance.

TABLE 1 | Comparison of clinical and disease characteristics between patients classified according to treatment modality.

	IMRT (103 patients)	PSPT (63 patients)	*P*-value*
Continuous variables	**Median (range)**	**Median (range)**	
Age at RT (yr.)	65 (30–85)	67 (39–80)	0.12
GTV Volume (cm^3)	80.5 (5.8–686.6)	71.0 (1.9–651.8)	0.92
Weight (Kg)	78.2 (48.0–131.4)	81.5 (47.2–122.5)	0.23
Height (cm)	176 (163–180)	176 (164–178)	0.82
BSA (m^2)	1.95 (1.50–2.43)	1.96 (1.48–5.43)	0.43
Categorical variables	**N (%)**	**N (%)**	
Gender			0.87
Female	46 (45)	27 (43)	
Male	57 (55)	36 (57)	
Tumor localization			0.49
Left lung	32 (33)	24 (40)	
Right lung	65 (67)	35 (60)	
Lower lobe	23 (24)	20 (34)	0.34
Middle lobe	5 (5)	3 (5)	
Upper lobe	69 (71)	35 (58)	
Prescribed dose			0.19
66 Gy	44 (43)	20 (32)	
74 Gy	59 (57)	43 (68)	
Smoking			0.37
No	10 (10)	3 (5)	
Yes	93 (90)	60 (95)	
Radiation Dermatitis			0.6
Grade 0	32 (31)	16 (25)	
Grade 1	37 (36)	27 (43)	
Grade 2	26 (25)	13 (21)	
Grade 3	8 (8)	7 (11)	

*RT, Radiation Therapy; GTV, Gross Tumor Volume; yr., year; BSA, Body Surface Area; IMRT, Intensity Modulated Radiation therapy; PSPT, Passive Scattering Proton Therapy. *Mann–Whitney U test for continuous variables and χ^2 test for categorical variables.*

DISCUSSION

The treatment of choice for many thoracic cancers, such as NSCLC, consists in RT given with either concurrent or sequential CHT (10, 41). Radiation induced morbidity to main organs at risk (heart, lungs, esophagus etc.) represents a major concern for radiation treatment. Advanced technologies may potentially reduce the risk of damaging normal tissue, and in particular the favorable physical characteristics of energy deposition in Hadron therapy make it a promising strategy for normal tissue dose sparing and for reducing the side effects of RT.

The skin, however, raises unique issues that deserve a separate discussion. Indeed, the initial dose build-up typical of photons is advantageous for skin sparing, compared to the higher entrance dose deriving from the pile-up of Bragg curves in the production of spread-out Bragg peaks. This effect may lead to an increase in incidence or severity of skin toxicity with a potential detrimental impact on both the RT course and the patient's quality of life. In addition, different amounts of dose may be delivered to the skin

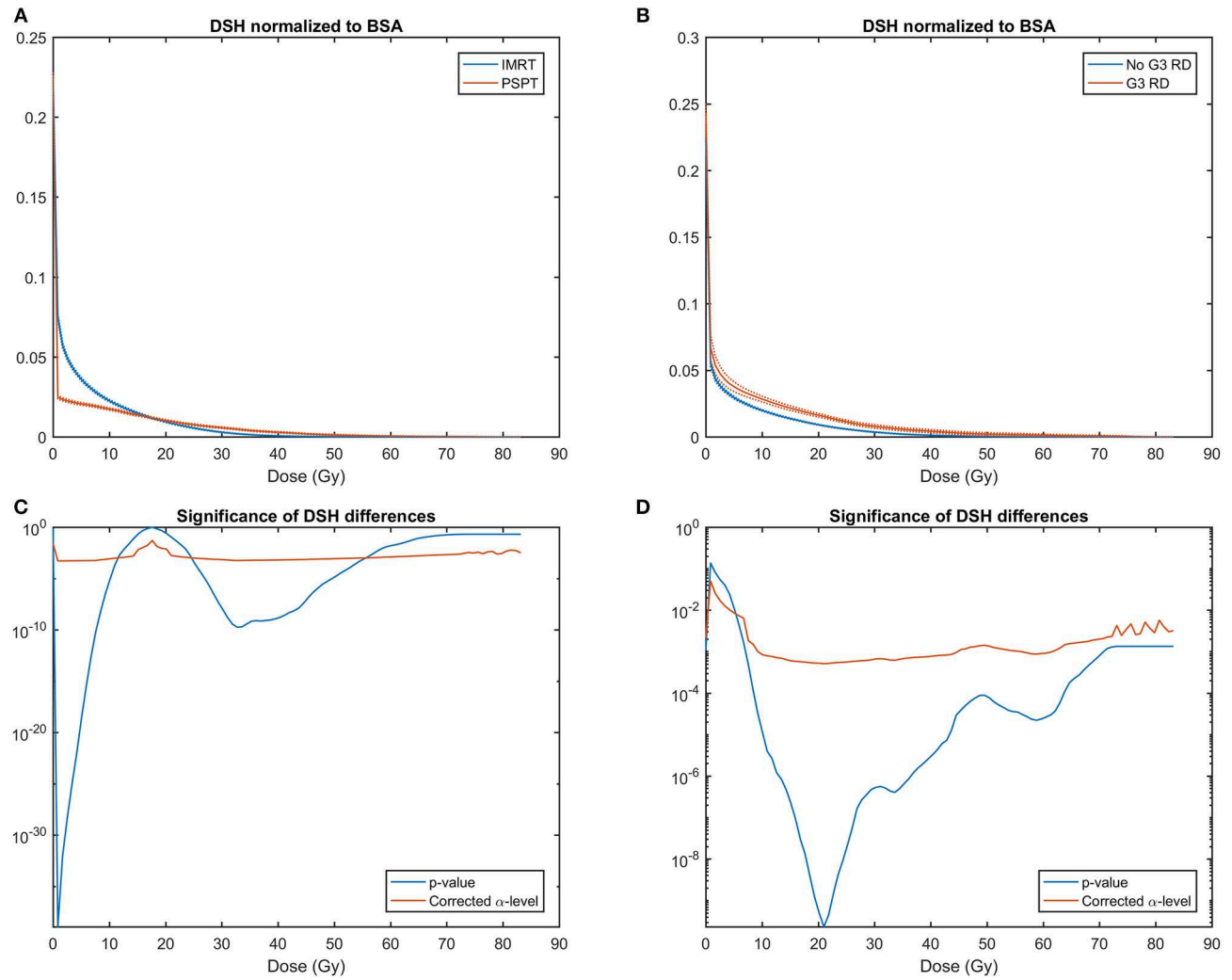

FIGURE 3 | (A) Average skin Dose Surface Histograms (DSHs) ± SEM (Standard Error of the Mean) normalized to Body Surface Area (BSA) in patients treated with Intensity Modulated Radiation Therapy (IMRT) and Passive Scattering Proton Therapy (PSPT); **(B)** Average skin DSHs ± SEM normalized to BSA in patients who developed severe (G3) radiation dermatitis (G3-RD) and who did not. SEM are plotted as dashed lines. **(C)** Semi-logarithmic plot for the two-tailed *t*-test between DSH values for PSPT and IMRT at each dose point; **(D)** Semi-logarithmic plot for the two-sample *t*-test between DSH values for G3-RD and unaffected patients. In **(C,D)** blue line for two-tailed *t*-test *p*-value, and red line for α-level of 0.05 corrected for multiple comparison according to Holm–Šidák method.

depending on the particular technology adopted to give proton therapy, which can rely on either passive scattering or active scanning techniques (42).

The domain of radiation-related skin side effects following proton beam therapy were recently investigated for brain tumor patients (16, 43). Erythema of grade 1-2 was found to be significantly correlated to skin (defined at 3 mm depth) dose volume parameters in the high dose region ($V_{35\text{Gy}}$) from both passive or active scanning proton beams. In a different study on severe RD following PSPT for breast cancer, the authors identified as prognostic factors the $V_{52.5\text{Gy}}$ or the $D_{10\text{cc}}$ of the skin structure defined as a layer of 5 mm inward from the body contour (21).

Few studies have performed a direct comparison on RD incidence following proton versus photon treatments. Acute side effects were compared in a retrospective study on a small cohort of patients after proton beam therapy (18 patients) and IMRT (23 patients) for head and neck cancer (44). Interestingly, in their study, the authors found a greater rate of G2 RD in the proton therapy group, but no difference in the rate of G3 RD between proton and IMRT. Recently, De Cesaris et al. (11) reported on RD after treatment of 86 breast cancer patients undergoing adjuvant proton or photon RT. They observed an increase in moderate (G2) toxicity associated to proton therapy; again, no significant difference between treatment modalities was found for severe RD.

In the present study, we analyzed the data from a randomized trial on PSPT vs. IMRT treatment for inoperable NSCLC patients, and we addressed different aspects related to radiation-induced skin reactions. This study has the unique characteristic of directly

TABLE 2 | Patient, treatment characteristics, dosimetric parameters and univariate analysis against acute grade 3 radiation dermatitis (G3 RD) status.

	No G3 RD	G3 RD	*P*-value*
Continuous variables	**Median (range)**	**Median (range)**	
Age at RT (yr)	66 (33–85)	62 (37-74)	0.13
GTV (cm^3)	71.9 (1.9–686.6)	139.3 (12.2–599.2)	0.03
Weight (Kg)	80 (47–129)	84 (59–131)	0.78
Height (cm)	176 (162–180)	176 (166–180)	0.38
BSA (m^2)	1.94 (1.48–2.41)	2.02 (1.63–2.43)	0.36
S_{5Gy} (%)	2.8 (0.7–6.0)	3.9 (1.7–6.6)	0.02
S_{10Gy} (%)	1.9 (0.3–3.9)	2.5 (1.5–4.4)	<0.001
S_{15Gy} (%)	1.3 (0.1–2.9)	2.3 (0.1–3.1)	<0.001
S_{20Gy} (%)	0.8 (0.0–2.2)	1.5 (0.7–2.4)	<0.001
S_{25Gy} (%)	0.5 (0.0–2.0)	1.0 (0.3–1.9)	<0.001
S_{30Gy} (%)	0.3 (0.0–1.1)	0.8 (0.3–1.8)	0.001
S_{35Gy} (%)	0.1 (0.0–0.1)	0.5 (0.0–1.7)	<0.001
S_{40Gy} (%)	0.02 (0.00–0.10)	0.3 (0.0–1.6)	<0.001
S_{45Gy} (%)	0.00 (0.00–0.01)	0.01 (0.00–1.50)	<0.001
Categorical variables	**N (%)**	**N (%)**	
Gender			0.43
Female	68 (45)	5 (33)	
Male	83 (55)	10 (67)	
Tumor localization			0.40
Left lung	48 (34)	7 (47)	
Right lung	92 (66)	8 (53)	
Lower lobe	39 (28)	4 (27)	0.32
Middle lobe	6 (4)	2 (13)	
Upper lobe	95 (68)	9 (60)	
RT modality			0.58
IMRT	95 (63)	8 (53)	
PSPT	56 (37)	7 (47)	
Smoking			1.00
No	12 (8)	1 (7)	
Yes	139 (92)	14 (93)	

*RT, Radiation Therapy; GTV, Gross Tumor Volume; yr., year; BSA, Body Surface Area; IMRT, Intensity Modulated Radiation therapy; PSPT, Passive Scattering Proton Therapy; S_X (%), percentage skin surface receiving more than X Gy. *Mann–Whitney U-test for continuous variables and $\chi 2$ test for categorical variables.*

TABLE 3 | Normal tissue complication probability (NTCP) model performances for acute grade 3 radiation dermatitis (G3-RD); 95% confidence interval are in brackets.

	G3-RD NTCP Model	
Performance	**LKB**	**MV Logistic**
AUC	0.82 [0.66, 0.90]	0.85 [0.72, 0.94]
Accuracy	0.67	0.93
Balanced accuracy	0.76	0.78
CV-AUC	0.78 [0.62, 0.88]	0.79 [0.60, 0.90]
CV-Accuracy	0.69	0.91
CV-Balanced accuracy	0.74	0.77
CV-calibration slope (±SE)	0.76 ± 0.19	1.03 ± 0.23
CV-calibration intercept (±SE)	0.008 ± 0.028	-0.003 ± 0.039

LKB, Lyman-Kutcher-Burman; M, Multivariable; SE, Standard Error; AUC, Area under the ROC curve; CV, cross-validation.

comparing acute skin toxicity in a quite large cohort of patients treated at the same institution with proton or photon RT.

First, we analyzed the differences of acute skin toxicity between patients treated with IMRT and PSPT. Both the depth of the lung tumor location within the body and the passive proton technique—used in the trial patients—were expected to increase the skin toxicity of the treatment. Despite this, a key finding of our investigation was that the RT technique did not impact neither incidence nor severity of acute RD (**Figure 2**).

Then, we evaluated the dose to the skin taking advantage of the DSHs expressly extracted for the epidermis. The DSHs were obtained by a fully automated algorithm that guarantees a high level of standardization. To account for the different patients' sizes, the absolute DSHs were normalized using the BSA (32) as scaling factor. The DSH differences between RT modalities showed that PSPT succeeded in lowering the skin surface receiving low dose (namely, <12 Gy), while the expected increase in entrance dose was evident for intermediate to high dose regime (i.e., higher than 25 Gy). Noteworthy, the switch in dose sparing effectiveness between PSPT and IMRT happens at a dose level in the range from 20 to 30 Gy. This range of doses is known to be strongly related to the probability of radiation-induced dermatological effects (12, 13, 16), as also confirmed in the current study by the comparison of average skin DSHs for patients grouped according to the development of severe RD (**Figure 3B**).

Since the treatment modality did not correlate with the considered outcome, the NTCP models for severe RD were derived from the whole cohort of patients. We focused on G3 toxicity due to its high clinical relevance. Two different approaches were applied: the traditional purely dosimetric LKB model and the multivariable logistic regression modeling scheme. Both models indeed are important and can find their application in clinical practice. The multivariate logistic model is more flexible when non-dosimetric variables needs to be considered and in order to build predictive tools for improving personalized patient follow-up care. On the other hand, the LKB scheme is more robust for treatment planning optimization (gEUD is a superior evaluator than multiple DSH cut-off points), since it controls the dose distribution over all dose range.

The LKB approach highlighted a relevant surface effect ($n = 0.62$) of the dose on RD development. While the LKB n and m parameter estimates were comparable with those obtained in previous published models on acute skin toxicity (1, 13), a TD_{50} of 10 Gy was a relatively low dose when compared to those previous studies. However, a direct comparison was hampered by the different modeling strategy (LKB recast on DSH) or the different normalization procedure (the BSA as scaling factor) adopted in the present analysis.

On the other hand, the multivariable logistic regression model highlighted that the most and only significantly independent toxicity predictor was the skin surface receiving more than 20 Gy. The robustness of those radiobiological hints is supported by

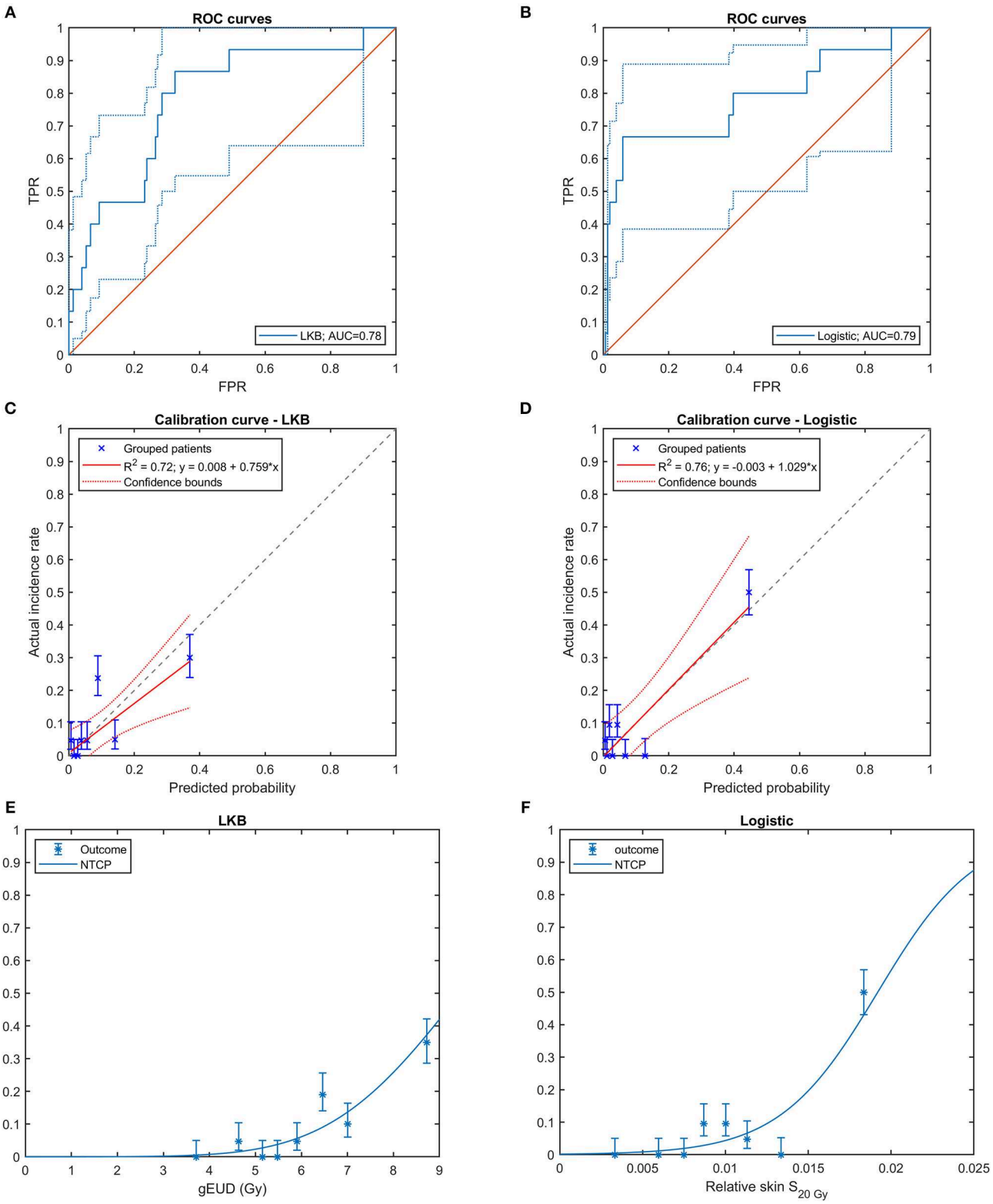

FIGURE 4 | Cross-validated ROC curves of **(A)** Lyman-Kutcher-Burman (LKB) model and **(B)** multivariable logistic regression model (FPR: False Positive Rate, TPR: True Positive Rate); cross-validated calibration plot of **(C)** LKB model and **(D)** logistic model; risk curves with the observed fraction of complications from the data grouped in bins for **(E)** LKB model and **(F)** logistic model. In **(C–F)** the error bars for the reported values represent the 68% confidence intervals.

the good performances of both predictive models, which showed cross-validated ROC-AUCs close to 0.8.

The current interest in the investigation on the patterns of dose-RD response is enhanced by the increasing attention to the quality of life of patients undergoing RT, in turn triggered by the substantially improved therapeutic ratio of the modern treatment techniques. Precise knowledge of the radiobiology of acute skin radiation effects constitutes the essential basis for the development of biology-based treatment strategies. In addition, severe acute skin reactions may be prodromal of consequential skin late effects (45), thus making their prediction and, possibly, prevention even more important.

The newest proton facilities have moved toward pencil beam scanning technology. A phantom dosimetric study investigating skin dose differences between spot scanning and passively scattered proton therapy beams indicated that, on average, a lower skin dose of about 12% was delivered when active spot scanning proton beams were used (42). Thanks to the higher flexibility with an enhanced modulation capability, the combined use of active scanning beams and the inclusion of skin specific model parameters in the planning strategies may result in further skin dose sparing to minimize the occurrence of cutaneous toxicity. In this respect, we focused on two classes of NTCP models that could be easily ported on the most common treatment planning systems used in the clinical practice. Indeed, the DSH formalism can be implemented following the procedure suggested in (23), thus directly allowing for the application of the dose constraints (e.g., S_{20Gy}) derived by the logistic approach. On the other side, the estimation of the n parameter of the LKB strategy can be exploited for treatment plan optimization by constraining the gEUD, which is a widespread empirical model available in several commercial systems.

In order to improve our understanding of the mechanisms underlying radiation-induced skin damage, future direction of the research is the inclusion of spatial information of dose distributions within the analysis of skin toxicity, as already performed for different toxicity endpoints after RT (46–50). The extraction of organ Dose-Surface Maps (51, 52) may allow for an enhanced prediction of RT toxicity based on the knowledge of the most radiosensitive skin areas.

Additional issues to be considered when modeling RD should be the impact of CHT treatments and of different RT dose fractionation schemes. Radiation-related skin side effects have been associated to different patient-related factors such as the use of radiosensitizing CHT and/or biologics (1). In particular, both incidence and severity of RD may be increased by concomitant CHT, although conflicting results are reported in the available literature. For example, a randomized comparison of patients treated for anal cancer by RT alone or combined with CHT found overall RD in 76% for radiation alone versus 93% for combined modality therapy (53). In contrast, a three-arm randomized trial in advanced larynx cancer found similar Grade 3–4 acute skin toxicities for patients receiving RT alone (9%), concurrent RT-CHT (10%), and sequential CHT-RT (7%) (54). Rates of acute and late skin toxicity were not significantly different also in a retrospective analysis of breast cancer patients undergoing lumpectomy with or without adjuvant CHT followed by hypofractionated RT (55). Recently, a multivariable NTCP analysis did not highlighted any effect of CHT on severe RD in breast cancer patients (13).

As regards to dose fractionation, greater dose per fraction are generally of concern to normal tissue toxicities. However, data on adverse skin reactions on patients who underwent Stereotactic Body Radiation Therapy (SBRT) is still limited (1). Suggested skin SBRT dose constraints (for toxicity grade ≥ 3) were $D_{10cc} <$ 23 Gy, for one single fraction of 34 Gy, and D_{10cc} <30-33 Gy for a total dose of 40-60 Gy in 4-5 fractions (56). Interestingly, these dose constraints are in the range of doses strongly related to the probability of RD (**Figure 3B**).

In the cohort analyzed in the current study, all patients received concurrent CHT and standard fractionation regimens. Future studies on large cohorts of patients undergoing RT with and without the use of CHT treatments and with different fractionation size are warranted in order to shed light on the possible CHT enhancement factor and fractionation effects.

A potential limitation of the study is related to the dose calculation uncertainties in the first few millimeters from body surface, which may be relatively large. However, in order to quantify their impact on the modeling results, Mori et al. (15) performed a sensitivity analysis showing that dose uncertainty has negligible impact on logistic regressions coefficients. Furthermore, the percentage differences between the measured dose to the skin and the estimate of the treatment planning system with passively scattered proton beams was evaluated in (42). The average measured doses resulted to be only 2% lower than the average calculated doses.

In conclusion, despite skin toxicity has long been considered a potential limiting factor in the clinical use of proton beam therapy, no significant differences in RD incidence was found between IMRT and PSPT in the analyzed trial. The developed NTCP models for the prediction of severe RD, once externally validated, may advance treatment planning optimization for the implementation of skin sparing techniques.

DATA AVAILABILITY STATEMENT

The datasets for this article are not publicly available because: Data Sharing Agreement does not include this option. Requests to access the datasets should be directed to Dr. Zhongxing Liao (zliao@mdanderson.org).

ETHICS STATEMENT

The studies involving human participants were reviewed and approved by MD Anderson Cancer Center IRB (protocol NCT00915005). The patients/participants provided their written informed consent to participate in this study.

AUTHOR CONTRIBUTIONS

GP and LC conceived and designed the study. ZL, TX, SH, and RM participated in patient recruitment and collected the clinical data. GP, SM, MC, and LC processed the data. GP and SM analyzed the results. GP and LC wrote the manuscript. All authors reviewed the final manuscript.

FUNDING

This work was funded in part by the Italian National Institute for Nuclear Physics CSN5 Call MoVe-IT and by National Cancer Institute, National Institutes of Health grants U19 CA021239 and P30 CA016672.

REFERENCES

1. Avanzo M, Stancanello J, Jena R. Adverse effects to the skin and subcutaneous tissue. In: Rancati T, Fiorino C, editors. *Modelling Radiotherapy Side Effects: Practical Applications For Planning Optimisation* CRC Press (2019). doi: 10.1201/b21956-12
2. Hymes SR, Strom EA, Fife C. Radiation dermatitis: clinical presentation, pathophysiology, and treatment 2006. *J Am Acad Dermatol.* (2006) 54:28–46. doi: 10.1016/j.jaad.2005.08.054
3. Decker RH, Strom EA, Wilson LD. Skin surface, dermis, and wound healing. In: Rubin P, Constine LS, Marks LB, editors. *ALERT-Adverse Late Effects of Cancer Treatment: Volume 2. Normal Tissue Specific Sites and Systems.* Springer (2013). p. 189. doi: 10.1007/978-3-540-75863-1_9
4. Jiang ZQ, Yang K, Komaki R, Wei X, Tucker SL, Zhuang Y, et al. Long-term clinical outcome of intensity-modulated radiotherapy for inoperable non-small cell lung cancer: the MD Anderson experience. *Int J Radiat Oncol Biol Phys.* (2012) 83:332–9. doi: 10.1016/j.ijrobp.2011.06.1963
5. Palm A, Johansson KA. A review of the impact of photon and proton external beam radiotherapy treatment modalities on the dose distribution in field and out-of-field; implications for the long-term morbidity of cancer survivors. *Acta Oncol.* (2007) 46:462–73. doi: 10.1080/02841860701218626
6. Pacelli R, Caroprese M, Palma G, Oliviero C, Clemente S, Cella L, et al. Technological evolution of radiation treatment: Implications for clinical applications. *Semin Oncol.* (2019) 46:193–201. doi: 10.1053/j.seminoncol.2019.07.004
7. Freedman GM, Anderson PR, Li J, Eisenberg DF, Hanlon AL, Wang L, et al. Intensity modulated radiation therapy (IMRT) decreases acute skin toxicity for women receiving radiation for breast cancer. *Am J Clin Oncol.* (2006) 29:66–70. doi: 10.1097/01.coc.0000197661.09628.03
8. Pignol JP, Olivotto I, Rakovitch E, Gardner S, Sixel K, Beckham W, et al. A multicenter randomized trial of breast intensity-modulated radiation therapy to reduce acute radiation dermatitis. *J Clin Oncol.* (2008) 26:2085–92. doi: 10.1200/JCO.2007.15.2488
9. Cella L, Lomax A, Miralbell R. New techniques in hadrontherapy: intensity modulated proton beams. *Phys Med.* (2001) 17(Suppl. 1):100–2.
10. Brooks ED, Ning MS, Verma V, Zhu XR, Chang JY. Proton therapy for non-small cell lung cancer: the road ahead. *Trans Lung Cancer Res.* (2019) 2019:S202–S12. doi: 10.21037/tlcr.2019.07.08
11. DeCesaris CM, Rice SR, Bentzen SM, Jatczak J, Mishra MV, Nichols EM. Quantification of acute skin toxicities in patients with breast cancer undergoing adjuvant proton versus photon radiation therapy: a single institutional experience. *Int J Radiat Oncol Biol Phys.* (2019) 104:1084–90. doi: 10.1016/j.ijrobp.2019.04.015
12. Turesson I, Thames HD. Repair capacity and kinetics of human skin during fractionated radiotherapy: erythema, desquamation, and telangiectasia after 3 and 5 year's follow-up. *Radiother Oncol.* (1989) 15:169–88. doi: 10.1016/0167-8140(89)90131-X
13. Pastore F, Conson M, D'Avino V, Palma G, Liuzzi R, Solla R, et al. Dose-surface analysis for prediction of severe acute radio-induced skin toxicity in breast cancer patients. *Acta Oncol.* (2016) 55:466–73. doi: 10.3109/0284186X.2015.1110253
14. Parekh A, Dholakia AD, Zabranksy DJ, Asrari F, Camp M, Habibi M, et al. Predictors of radiation-induced acute skin toxicity in breast cancer at a single institution: role of fractionation and treatment volume. *Adv Radiat Oncol.* (2018) 3:8–15. doi: 10.1016/j.adro.2017.10.007
15. Mori M, Cattaneo GM, Dell'Oca I, Foti S, Calandrino R, Di Muzio NG, et al. Skin DVHs predict cutaneous toxicity in Head and Neck Cancer patients treated with Tomotherapy. *Phys Med.* (2019) 59:133–41. doi: 10.1016/j.ejmp.2019.02.015
16. Dutz A, Luhr A, Agolli L, Troost EGC, Krause M, Baumann M, et al. Development and validation of NTCP models for acute side-effects resulting from proton beam therapy of brain tumours. *Radiother Oncol.* (2019) 130:164–71. doi: 10.1016/j.radonc.2018.06.036
17. Alexander MA, Brooks WA, Blake SW. Normal tissue complication probability modeling of tissue fibrosis following breast radiotherapy. *Phys Med Biol.* (2007) 52:1831–43. doi: 10.1088/0031-9155/52/7/005
18. Avanzo M, Stancanello J, Trovo M, Jena R, Roncadin M, Trovo MG, et al. Complication probability model for subcutaneous fibrosis based on published data of partial and whole breast irradiation. *Phys Med.* (2012) 28:296–306. doi: 10.1016/j.ejmp.2011.11.002
19. Mukesh MB, Harris E, Collette S, Coles CE, Bartelink H, Wilkinson J, et al. Normal tissue complication probability (NTCP) parameters for breast fibrosis: pooled results from two randomised trials. *Radiother Oncol.* (2013) 108:293–8. doi: 10.1016/j.radonc.2013.07.006
20. Kindts I, Defraene G, Laenen A, Petillion S, Van Limbergen E, Depuydt T, et al. Development of a normal tissue complication probability model for late unfavourable aesthetic outcome after breast-conserving therapy. *Acta Oncol.* (2018) 57:916–23. doi: 10.1080/0284186X.2018.1461926
21. Liang X, Bradley JA, Zheng D, Rutenberg M, Yeung D, Mendenhall N, et al. Prognostic factors of radiation dermatitis following passive-scattering proton therapy for breast cancer. *Radiat Oncol.* (2018) 13:72. doi: 10.1186/s13014-018-1004-3
22. Borm KJ, Loos M, Oechsner M, Mayinger MC, Paepke D, Kiechle MB, et al. Acute radiodermatitis in modern adjuvant 3D conformal radiotherapy for breast cancer - the impact of dose distribution and patient related factors. *Radiat Oncol.* (2018) 13:218. doi: 10.1186/s13014-018-1160-5
23. Palma G, Cella L. A new formalism of dose surface histograms for robust modeling of skin toxicity in radiation therapy. *Phys Med.* (2019) 59:75–8. doi: 10.1016/j.ejmp.2019.02.005
24. Zhang X, Li Y, Pan X, Xiaoqiang L, Mohan R, Komaki R, et al. Intensity-modulated proton therapy reduces the dose to normal tissue compared with intensity-modulated radiation therapy or passive scattering proton therapy and enables individualized radical radiotherapy for extensive stage IIIB non-small-cell lung cancer: a virtual clinical study. *Int J Radiat Oncol Biol Phys.* (2010) 77:357–66. doi: 10.1016/j.ijrobp.2009.04.028
25. Hui Z, Zhang X, Starkschall G, Li Y, Mohan R, Komaki R, et al. Effects of interfractional motion and anatomic changes on proton therapy dose distribution in lung cancer. *Int J Radiat Oncol Biol Phys.* (2008) 72:1385–95. doi: 10.1016/j.ijrobp.2008.03.007
26. Murshed H, Liu HH, Liao Z, Barker JL, Wang X, Tucker SL, et al. Dose and volume reduction for normal lung using intensity-modulated radiotherapy for advanced-stage non-small-cell lung cancer. *Int J Radiat Oncol Biol Phys.* (2004) 58:1258–67. doi: 10.1016/j.ijrobp.2003.09.086
27. Liao Z, Lee JJ, Komaki R, Gomez DR, O'Reilly MS, Fossella FV, et al. Bayesian adaptive randomization trial of passive scattering proton therapy and intensity-modulated photon radiotherapy for locally advanced non-small-cell lung cancer. *J Clin Oncol.* (2018) 36:1813–22. doi: 10.1200/JCO.2017.74.0720
28. Palma G, Monti S, Xu T, Scifoni E, Yang P, Hahn SM, et al. Spatial dose patterns associated with radiation pneumonitis in a randomized trial comparing intensity-modulated photon therapy with passive scattering proton therapy for locally advanced non-small cell lung cancer. *Int J Radiat Oncol Biol Phys.* (2019) 104:1124–32. doi: 10.1016/j.ijrobp.2019.02.039
29. Deasy JO, Blanco AI, Clark VH. CERR: a computational environment for radiotherapy research. *Med Phys.* (2003) 30:979–85. doi: 10.1118/1.1568978

30. Archambeau JO, Pezner R, Wasserman T. Pathophysiology of irradiated skin and breast. *Int J Rad Oncol*. (1995) 31:1171–85. doi: 10.1016/0360-3016(94)00423-I
31. Shih FY. *Image Processing and Mathematical Morphology: Fundamentals and Applications*. CRC Press (2017). doi: 10.1201/9781420089448
32. Du Bois D, Du Bois EF. Clinical calorimetry: tenth paper a formula to estimate the approximate surface area if height and weight be known. *Arch Inter Med*. (1916) 17:863–71. doi: 10.1001/archinte.1916.00080130010002
33. Holm S. A simple sequentially rejective multiple test procedure. *Scand J Stat*. (1979) 1979:65–70.
34. Luxton G, Hancock SL, Boyer AL. Dosimetry and radiobiologic model comparison of IMRT and 3D conformal radiotherapy in treatment of carcinoma of the prostate. *Int J Rad Oncol*. (2004) 59:267–84. doi: 10.1016/j.ijrobp.2004.01.024
35. Niemierko A. A generalized concept of equivalent uniform dose (EUD). *Med Phys*. (1999) 1999:26.
36. Cella L, Palma G, Deasy JO, Oh JH, Liuzzi R, D'Avino V, et al. Complication probability models for radiation-induced heart valvular dysfunction: do heart-lung interactions play a role? *PLoS ONE*. (2014) 9:e111753. doi: 10.1371/journal.pone.0111753
37. Cella L, D'Avino V, Liuzzi R, Conson M, Doria F, Faiella A, et al. Multivariate normal tissue complication probability modeling of gastrointestinal toxicity after external beam radiotherapy for localized prostate cancer. *Radiat Oncol*. (2013) 8:221. doi: 10.1186/1748-717X-8-221
38. Cella L, Liuzzi R, Conson M, D'Avino V, Salvatore M, Pacelli R. Multivariate normal tissue complication probability modeling of heart valve dysfunction in Hodgkin lymphoma survivors. *Int J Radiat Oncol Biol Phys*. (2013) 87:304–10. doi: 10.1016/j.ijrobp.2013.05.049
39. Brodersen KH, Ong CS, Stephan KE, Buhmann JM, editors. The balanced accuracy and its posterior distribution. In: *2010 20th International Conference on Pattern Recognition*. (2010). doi: 10.1109/ICPR.2010.764
40. Youden WJ. Index for rating diagnostic tests. *Cancer*. (1950) 3:32–5. doi: 10.1002/1097-0142(1950)3:1<32::AID-CNCR2820030106>3.0.CO;2-3
41. Liao Z, Simone CB, 2nd. Particle therapy in non-small cell lung cancer. *Transl Lung Cancer Res*. (2018) 7:141–52. doi: 10.21037/tlcr.2018.04.11
42. Arjomandy B, Sahoo N, Cox J, Lee A, Gillin M. Comparison of surface doses from spot scanning and passively scattered proton therapy beams. *Phys Med Biol*. (2009) 54:N295–302. doi: 10.1088/0031-9155/54/14/N02
43. Palma G, Taffelli A, Fellin F, D'Avino V, Scartoni D, Tommasino F, et al. Modelling the risk of radiation induced alopecia in brain tumor patients treated with scanned proton beams. *Radiother Oncol*. (2019) 144:127–34. doi: 10.1016/j.radonc.2019.11.013
44. Romesser PB, Cahlon O, Scher E, Zhou Y, Berry SL, Rybkin A, et al. Proton beam radiation therapy results in significantly reduced toxicity compared with intensity-modulated radiation therapy for head and neck tumors that require ipsilateral radiation. *Radiother Oncol*. (2016) 118:286–92. doi: 10.1016/j.radonc.2015.12.008
45. Dorr W, Hendry JH. Consequential late effects in normal tissues. *Radiother Oncol*. (2001) 61:223–31. doi: 10.1016/S0167-8140(01)00429-7
46. Monti S, Palma G, D'Avino V, Gerardi M, Marvaso G, Ciardo D, et al. Voxel-based analysis unveils regional dose differences associated with radiation-induced morbidity in head and neck cancer patients. *Sci Rep*. (2017) 7:7220. doi: 10.1038/s41598-017-07586-x
47. Mylona E, Acosta O, Lizee T, Lafond C, Crehange G, Magne N, et al. Voxel-based analysis for identification of urethrovesical subregions predicting urinary toxicity after prostate cancer radiation therapy. *Int J Radiat Oncol Biol Phys*. (2019)2019:88. doi: 10.1016/j.ijrobp.2019.01.088
48. Palma G, Monti S, Buonanno A, Pacelli R, Cella L. PACE: a probabilistic atlas for normal tissue complication estimation in radiation oncology. *Front Oncol*. (2019) 9:130. doi: 10.3389/fonc.2019.00130
49. Palma G, Monti S, D'Avino V, Conson M, Liuzzi R, Pressello MC, et al. A voxel-based approach to explore local dose differences associated with radiation-induced lung damage. *Int J Radiat Oncol Biol Phys*. (2016) 96:127–33. doi: 10.1016/j.ijrobp.2016.04.033
50. Yahya N, Ebert MA, House MJ, Kennedy A, Matthews J, Joseph DJ, et al. Modeling urinary dysfunction after external beam radiation therapy of the prostate using bladder dose-surface maps: evidence of spatially variable response of the bladder surface. *Int J Radiat Oncol Biol Phys*. (2017) 97:420–6. doi: 10.1016/j.ijrobp.2016.10.024
51. Buettner F, Gulliford SL, Webb S, Partridge M. Using dose-surface maps to predict radiation-induced rectal bleeding: a neural network approach. *Phys Med Biol*. (2009) 54:5139–53. doi: 10.1088/0031-9155/54/17/005
52. Dankers F, Wijsman R, Troost EG, Monshouwer R, Bussink J, Hoffmann AL. Esophageal wall dose-surface maps do not improve the predictive performance of a multivariable NTCP model for acute esophageal toxicity in advanced stage NSCLC patients treated with intensity-modulated (chemo-)radiotherapy. *Phys Med Biol*. (2017) 62:3668–81. doi: 10.1088/1361-6560/aa5e9e
53. Party UACTW. Epidermoid anal cancer: results from the UKCCCR randomised trial of radiotherapy alone versus radiotherapy, 5-fluorouracil, and mitomycin. *The Lancet*. (1996) 348:1049–54. doi: 10.1016/S0140-6736(96)03409-5
54. Forastiere AA, Goepfert H, Maor M, Pajak TF, Weber R, Morrison W, et al. Concurrent chemotherapy and radiotherapy for organ preservation in advanced laryngeal cancer. *N Engl J Med*. (2003) 349:2091–8. doi: 10.1056/NEJMoa031317
55. Hijal T, Al Hamad AA, Niazi T, Sultanem K, Bahoric B, Vuong T, et al. Hypofractionated radiotherapy and adjuvant chemotherapy do not increase radiation-induced dermatitis in breast cancer patients. *Curr Oncol*. (2010) 17:22–7. doi: 10.3747/co.v17i5.604
56. Benedict SH, Yenice KM, Followill D, Galvin JM, Hinson W, Kavanagh B, et al. Stereotactic body radiation therapy: the report of AAPM Task Group 101. *Med Phys*. (2010) 37:4078–101. doi: 10.1118/1.3438081

Conflict of Interest: The authors declare that the research was conducted in the absence of any commercial or financial relationships that could be construed as a potential conflict of interest.

frontiers in Oncology

ORIGINAL RESEARCH
published: 03 April 2020
doi: 10.3389/fonc.2020.00469

Local Dose Effects for Late Gastrointestinal Toxicity After Hypofractionated and Conventionally Fractionated Modern Radiotherapy for Prostate Cancer in the HYPRO Trial

Wilma D. Heemsbergen[1], Luca Incrocci[1], Floris J. Pos[2], Ben J. M. Heijmen[1] and Marnix G. Witte[2]*

[1] Department of Radiation Oncology, Erasmus Medical Center, Rotterdam, Netherlands, [2] Department of Radiation Oncology, The Netherlands Cancer Institute, Amsterdam, Netherlands

OPEN ACCESS

Edited by:
Tiziana Rancati, National Cancer Institute Foundation (IRCCS), Italy

Reviewed by:
Laura Cella, Italian National Research Council, Italy
Stephan Bodis, Kantonsspital Aarau, Switzerland
Barbara Avuzzi, National Cancer Institute Foundation (IRCCS), Italy

****Correspondence:***
Wilma D. Heemsbergen
w.heemsbergen@erasmusmc.nl

Specialty section:
This article was submitted to Radiation Oncology, a section of the journal Frontiers in Oncology

Received: *16 December 2019*
Accepted: *16 March 2020*
Published: *03 April 2020*

Citation:
Heemsbergen WD, Incrocci L, Pos FJ, Heijmen BJM and Witte MG (2020) Local Dose Effects for Late Gastrointestinal Toxicity After Hypofractionated and Conventionally Fractionated Modern Radiotherapy for Prostate Cancer in the HYPRO Trial. Front. Oncol. 10:469. doi: 10.3389/fonc.2020.00469

Purpose: Late gastrointestinal (GI) toxicity after radiotherapy for prostate cancer may have significant impact on the cancer survivor's quality of life. To date, little is known about local dose-effects after modern radiotherapy including hypofractionation. In the current study we related the local spatial distribution of radiation dose in the rectum to late patient-reported gastrointestinal (GI) toxicities for conventionally fractionated (CF) and hypofractionated (HF) modern radiotherapy in the randomized HYPRO trial.

Material and Methods: Patients treated to 78 Gy in 2 Gy fractions ($n = 298$) or 64.6 Gy in 3.4 Gy fractions ($n = 295$) with available late toxicity questionnaires ($n \geq 2$ within 1–5 years post-treatment) and available 3D planning data were eligible for this study. The majority received intensity modulated radiotherapy (IMRT). We calculated two types of dose surface maps: (1) the total delineated rectum with its central axis scaled to unity, and (2) the delineated rectum with a length of 7 cm along its central axis aligned on the prostate's half-height point (prostate-half). For each patient-reported GI symptom, dose difference maps were constructed by subtracting average co-registered EQD2 (equivalent dose in 2 Gy) dose maps of patients with and without the symptom of interest, separately for HF and CF. *P*-values were derived from permutation tests. We evaluated patient-reported moderate to severe GI symptoms.

Results: Observed incidences of rectal bleeding and increased stool frequency were significantly higher in the HF group. For rectal bleeding ($p = 0.016$), mucus discharge ($p = 0.015$), and fecal incontinence ($p = 0.001$), significant local dose-effects were observed in HF patients but not in CF patients. For rectal pain, similar local dose-effects ($p < 0.05$) were observed in both groups. No significant local dose-effects were observed for increased stool frequency. Total rectum mapping vs. prostate-half mapping showed similar results.

Conclusion: We demonstrated significant local dose-effect relationships for patient-reported late GI toxicity in patients treated with modern RT. HF patients were

at higher risk for increased stool frequency and rectal bleeding, and showed the most pronounced local dose-effects in intermediate-high dose regions. These findings suggest that improvement of current treatment optimization protocols could lead to clinical benefit, in particular for HF treatment.

Keywords: prostate cancer, hypofractionation, gastrointestinal toxicity, dose-surface maps, radiotherapy, NTCP

INTRODUCTION

Irradiation of tumors in the pelvic area through external beam radiotherapy comes inevitably with dose delivery to nearby organs at risk, such as the rectum. The potential permanent impact of late gastrointestinal (GI) toxicity after radiotherapy may have significant impact on the cancer survivor's quality of life (1). Preventing chronic late GI toxicity is therefore critical. For this purpose understanding how we should distribute radiation dose to surrounding normal tissues while keeping toxicity risks as low as possible is critical.

The QUANTEC project (quantitative analysis of normal tissue effects in the clinic) previously summarized the available clinical data and models on acute and late radiation-induced toxicities with the goal to improve patient care by providing useful tools (2). These models were mainly derived from traditionally fractionated 3D conformal radiotherapy (3DCRT). Shortcomings and open issues of the available models have broadly been recognized, including the uncertainty of fractionation effects, a lack of reliable models for modern radiotherapy with IMRT dose distributions and image-guidance, and a lack of knowledge concerning spatial effects (3). This causes a number of deficits in current strategies of treatment planning optimization in the current era of IMRT, image-guidance, and hypofractionated treatment.

With respect to the inhomogeneous dose distributions in the rectum, achieved with either radiation technique or fractionation schedule, we can theoretically translate physical dose distributions into (radio)biological dose parameters using mathematical models derived from radiobiology (4, 5). Altered fractionation schedules in recent hypofractionation trials in prostate cancer are based on such models (6–9). However, to achieve reliable biological NTCP models for late GI toxicity after modern RT, we first have to gain insight into local dose-effects and (hypo)fractionation effects in real patient populations rather than depending solely on theoretical models.

Historically, dose-response for normal tissues were evaluated taking dose-volume distributions to a whole single organ into consideration. It is nowadays recognized that function and radiosensitivity may vary within an organ, and that dose-shapes might be relevant. Therefore, local spatial dose evaluations beyond the boundaries of delineations and dose-volume may enhance our understanding of mechanisms causing radiation-induced damage (10). In particular voxel-based dose mapping procedures have been introduced to take into account the spatial dose distribution by co-registering dose distributions to a region of interest, often using a template patient. For hollow organs such as the rectum, a spatial 2D dose distribution of the rectal wall (i.e., virtual unfolding of the rectum to a 2D structure) is considered reasonably sufficient for this purpose (11–18). Evaluation of local rectal and anal dose distributions in relation to acute and late gastrointestinal toxicity endpoints by means of dose mapping have been previously performed by several research groups. This concerned mainly patients treated with conventional fractionation schedules, identifying local dose effects for various endpoints including rectal bleeding, fecal leakage, and increased stool frequency (11–18).

In the current study we explored local rectal dose distributions and their relation to GI toxicity endpoints, for both hypofractionated (HF) and conventionally fractionated (CF) treatment, using toxicity data and planning data from the HYPRO trial. In this trial patients were randomized between conventional and hypofractionated treatment, delivered with modern radiotherapy techniques including IMRT, image-guidance, and online prostate position verification.

MATERIALS AND METHODS

Patient Selection

The dataset of a recent Dutch randomized clinical trial (HYPRO) was analyzed in which patients were randomized to 78 Gy in conventional 2 Gy fractions (CF) or 64.4 Gy in hypofractionated 3.4 Gy fractions (HF) (19). Selected patients were eligible for the current study in case both late toxicity data ($n \geq 2$ questionnaires within the period 1–5 year post-treatment ($N = 633$, **Table 2**) and 3D planning data were available (which were not available for 40 patients), leaving 593 patients for the current study. Because planning of patient visits may vary from the study schedule, we accepted questionnaires up to 5.5 year post-treatment.

Treatment

Based on an estimated α/β for prostate cancer of 1.5 Gy, the EQD2 was 90.4 Gy for HF vs. 78.0 Gy for CF. For normal rectal tissue with an estimated α/β of 3 Gy, the EQD2 was 82.7 Gy for HF vs. 78.0 for CF. The clinical target volume was the prostate with or without the seminal vesicles (SV): based on the estimated risk of SV involvement according Partin tables (20), a SV dose of 0 Gy, 72.2 Gy, or 78 Gy was planned (19). The outer contours of the rectum were delineated on the planning CT scan from the anal verge to the bottom of the sacro-iliac joints. The HYPRO protocol prescribed that the rectal volume receiving 83% of the prescribed dose should be below 50% for the total rectal volume or below 60% for the rectal wall. Further treatment optimization was performed in accordance with local protocols at each participating center. The applied treatment technique for 99% of the patients was image-guided IMRT with daily online

positioning of the prostate. For this purpose, cone beam CT was used in 23% and portal imaging devices was used in 77% of the cases. A small proportion was treated with 3DCRT (1%). One center applied a rectal balloon, which pushes the posterior rectal wall out of the intermediate dose region (21). Further details of treatment planning have been previously reported (6, 19). CF patients received 5 fractions per week, and HF patients 3 fractions per week with 1 day intervals (Monday, Wednesday, Friday).

Toxicity Endpoints

The patient-reported GI symptoms were extracted from a patient-reported symptom list (questionnaire) distributed in the HYPRO trial at the late time points of 6 months, and yearly between 1 and 5 year (22). Evaluated GI symptoms were: rectal bleeding, fecal incontinence, pain/cramps with stools, mucus discharge (all had to be reported as moderate or severe to be scored), and increased stool frequency ≥ 4 per day. We identified from all available questionnaires the maximum score for each toxicity endpoint of interest.

Dose-Surface Maps

For the rectal wall the dose surface mapping was based on a central axis which was first computed as the maximum of a Euclidean distance transform. The average length of the delineated rectum along the central axis was 14.9 cm for both HF and CF. The intersections of equidistant slices perpendicular to this axis with the delineated rectum surfaces provided the corresponding locations between patients. We calculated two types of dose surface maps: (1) "total rectum mapping": the delineated rectum with its central axis scaled to unity, and (2) "prostate half mapping": the delineated rectum next to the prostate with a length of 7 cm along the central axis (plus 4 cm in cranial direction and minus 3 cm in caudal direction, measured from the half-height position of the prostate). These cutoffs were chosen to cover the dose range in the rectum of about 50–100% of the prescribed dose.

To correct a patient averaged dose-surface map for fractionation effects using the linear-quadratic model (i.e., equivalent dose in 2 Gy: EQD2), we applied a chosen α/β ratio of 3 Gy to the dose distribution of each patient. The resolution of the dose maps was chosen to effectively slightly exceed a 2 mm dose grid resolution. In the circumferential direction 90 pixels were taken, i.e., every 4 degrees. In the axis direction of rectum maps 100 pixels were taken, which would effectively cover a 15 cm long rectum at 1.5 mm resolution. As a final step, resulting dose-surface maps of individual patients (physical and biological) could be averaged and subtracted for each identified toxicity endpoint (yes vs. no). Further details have been previously reported (14).

Statistical Analysis

Distributions of baseline characteristics within the HF and CF group were calculated and tested for differences applying a Chisquare test for the ordinal and binary variables, and a *T*-test for age. Associations between clinical covariates and toxicity endpoints were tested univariate using binary logistic regression. For each evaluated GI symptom, dose difference maps were constructed by subtracting average EQD2 dose maps of patients with and without the toxicity of interest, separately for HF and CF. For the calculation of a *p*-value for each dose difference map, we used a permutation approach, randomly re-shuffling the patients among the subgroups (23). For the determination of significant differences within a dose-difference map, we calculated and evaluated the false discovery rates "q" as a realistic estimate of the local *p*-values, which is a practical and powerful approach to tackle the multiple testing issue (24, 25).

RESULTS

Baseline Characteristics

The baseline characteristics of the selected study patients are summarized in **Table 1** which shows that distribution of the characteristics are similar for HF and CF except for a history of TURp which was more common in the CF group (11 vs. 7%, $p = 0.07$, **Table 1**). A history of TURp was however not associated with any of the evaluated moderate to severe GI symptoms.

Reported GI Toxicities

In **Table 2**, the observed incidences of the late GI toxicities of interest are summarized per treatment group, both for all patients in the HYPRO trial who filled out ≥ 2 late questionnaires ($N = 633$) and for the selected group with available CT scans and dose distributions ($N = 593$). These are the result of accumulation over all available questionnaires between Year 1 and Year 5, taking maximum scores. The table shows that the selected population with available dose information, was a non-biased and representative selection of the patient group that filled out late questionnaires.

TABLE 1 | Patient and treatment characteristics ($N = 593$).

Variable	CF ($n = 298$)	HF ($n = 295$)	*p*-value[#]
Age (mean, sd) in years	70.1 (6.0)	69.5 (6.6)	0.2
TURp	11%	7%	0.07
Abdominal surgery	26%	25%	0.7
Diabetes mellitus	13%	14%	0.5
Adjuvant hormonal therapy	65%	63%	0.6
Fiducial markers	95%	95%	0.9
IMRT	98%	99%	0.3
T category			
T1-2	46%	48%	0.7
T3-4	54%	52%	
PTV margins prostate			
5-7 mm	89%	89%	0.9
8-10 mm	11%	11%	
Dose seminal vesicles			
0 Gy	23%	20%	0.4
72-78 Gy	77%	80%	

[#] *p-values calculated with Chisquare test, except for age (t-test).*

About 35% of CF and HF patients experienced one or more moderate to severe late symptoms after modern RT, accumulated over the evaluated late period (**Table 2**). Compared to CF, significantly higher incidences after HF treatment were observed for the late endpoints of rectal bleeding and increased stool frequency. More HF patients experienced multiple moderate to severe GI symptoms.

Among the late GI endpoints of study, all endpoints showed significant correlations with the other ones (i.e., if a patient reported 1 symptom it was likely that he also reports one or more of the other symptoms). Highest correlations were observed between fecal incontinence-increased stool frequency, and rectal bleeding-mucus discharge ($p < 0.001$).

Associations Between Clinical Covariates and Toxicity Endpoints

The results of assessing the associations between baseline covariates and the toxicity endpoints of interest are summarized in **Table 3**. Rectal incontinence was significantly associated with diabetes and age. Rectal bleeding and mucus discharge were significantly associated with T stage.

Dose-Surface Maps

Figure 1 shows the average EQD2 dose-surface maps and local standard deviations for both types of mapping and for both groups (CF and HF). Comparing the EQD2 dose distributions of CF and HF, we observed that the high-dose area is darker red for HF which can be explained by the somewhat higher prescription dose in EQD2 for HF (82.7 Gy vs. 78 Gy). Furthermore, the rectal surface receiving dose levels in the range of $\geq$ 1–$\geq$ 65 Gy EQD2 look very similar for HF and CF, whereas the rectal surface receiving dose levels in the range of $>$ 65–$\geq$ 80 Gy EQD2 were on average different with larger surfaces for HF. From previous calculations of "traditional" whole organ dose-surface histograms (DSH), it is known that indeed the average DSH of HF vs. CF only show a slightly unfavorable dose level in the range of $>$ 65–$\geq$ 80 Gy EQD2 (supporting DSH figure in **Supplementary File**). Furthermore, local standard deviations were larger for HF. The rectum adjacent to the prostate, as shown on the prostate-half maps, received dose levels in the range of 20–80 Gy, with the largest standard deviations (i.e., variation between patients) at the cranial and caudal side. The total rectum maps show dose levels in the range of 0–80 Gy, with 0–10 Gy in the most caudal 15% (the anal canal region) and the most cranial part close to the rectosigmoid region.

Dose-Difference Maps

For each toxicity endpoint, four dose difference maps were constructed: total rectum mapping and prostate-half mapping, and for each type of mapping the HF and CF version (**Figures 2**, **3**). In general, one or more significant dose difference maps were obtained for all GI endpoints except for increased stool frequency (lowest observed $p = 0.086$). All dose-difference maps were also generated with physical dose instead of EQD2 dose, to check whether this might change results. Since they were very similar to the EQD2 versions, we report here only results based on EQD2 dose maps.

For rectal bleeding, large local dose differences ($p = 0.016$) up to $\geq$10 Gy were observed between patients with and without this complaint (**Figures 2**, **3**), but only for HF patients. Remarkably, the prostate-half mapping (**Figure 3**) indicates significant differences in the region next to the prostate, whereas the total rectum mapping (**Figure 3**) indicates local dose-effects at a more cranial part of the rectum. Both locations are regions were on average ≈60 Gy (EQD2) is received by the rectal tissue (**Figure 1**).

For the late endpoint fecal incontinence, highly significant local dose-effects were found for the region receiving intermediate to high dose, i.e., in the neighborhood of the prostate (**Figures 2**, **3**), but again only for HF patients. For mucus discharge, we also observed local dose-effects for HF patients only, which were identified by the total rectum mapping (**Figure 2**). Pain/cramps with stools was associated with local

TABLE 2 | Incidence of late gastrointestinal toxicity endpoint (evaluated by the patient as "moderate—severe") on questionnaires in the period 1–5 year post-treatment.

	≥2 questionnaires ($N = 633$)			With available dose maps ($N = 593$)		
	CF	**HF**	**p**	**CF**	**HF**	**p**
	***n* = 310**	***n* = 323**		**n = 298**	**n = 295**	
Late GI endpoint						
Stool frequency ≥4/day	12.3%	19.5%	**0.013**	12.1%	19.7%	**0.011**
Rectal bleeding	11.0%	16.7%	**0.037**	10.7%	17.6%	**0.016**
Mucus discharge	5.2%	6.2%	0.6	5.0%	6.4%	0.5
Pain/cramps with stools	7.4%	9.9%	0.3	7.7%	10.2%	0.3
Fecal incontinence	10.6%	11.1%	0.8	10.7%	11.5%	0.8
≥1 symptom	30.3%	35.6%	0.16	30.2%	36.3%	0.12
≥2 symptoms	12.6%	18.0%	0.061	12.4%	19.3%	**0.020**
≥3 symptoms	3.2%	6.8%	**0.040**	3.4%	7.1%	**0.040**

P <0.05 are indicated in bold. GI, gastrointestinal; HF, hypofractionation; CF, conventional fractionation.

TABLE 3 | Association between clinical baseline covariates and toxicity endpoints.

	Stools ≥ 4/day		Rectal bleeding		Mucus discharge		Pain/cramps		Fecal incontinence	
	HR	***p***	**HR**	***p***	**HR**	***p***	**HR**	***p***	**HR**	***p***
Age > 70 vs. ≤ 70	0.87	0.5	0.89	0.6	0.61	0.2	0.63	0.1	2.67	**<0.01**
TURp yes vs. no	1.19	0.6	0.90	0.8	1.34	0.6	0.37	0.2	1.96	0.07
Previous abdominal surgery yes vs. no	0.76	0.3	1.23	0.4	0.47	0.1	1.14	0.7	1.26	0.4
Diabetes yes vs. no	1.21	0.05	0.84	0.6	no result		0.97	0.9	**2.05**	**0.024**
AHT yes vs. no	1.02	0.9	1.11	0.7	1.98	0.09	0.63	0.1	1.16	0.6
T3-4 vs. T1-2	1.00	1.0	**1.60**	**0.046**	**2.13**	**0.04**	1.00	1.0	0.87	0.6

P <0.05 are indicated in bold. Results from univariate logistic regression (N = 633). OR, Odds ratio; TURp, transurectal resection of prostate; AHT, adjuvant hormonal therapy; SV, seminal vesicles.

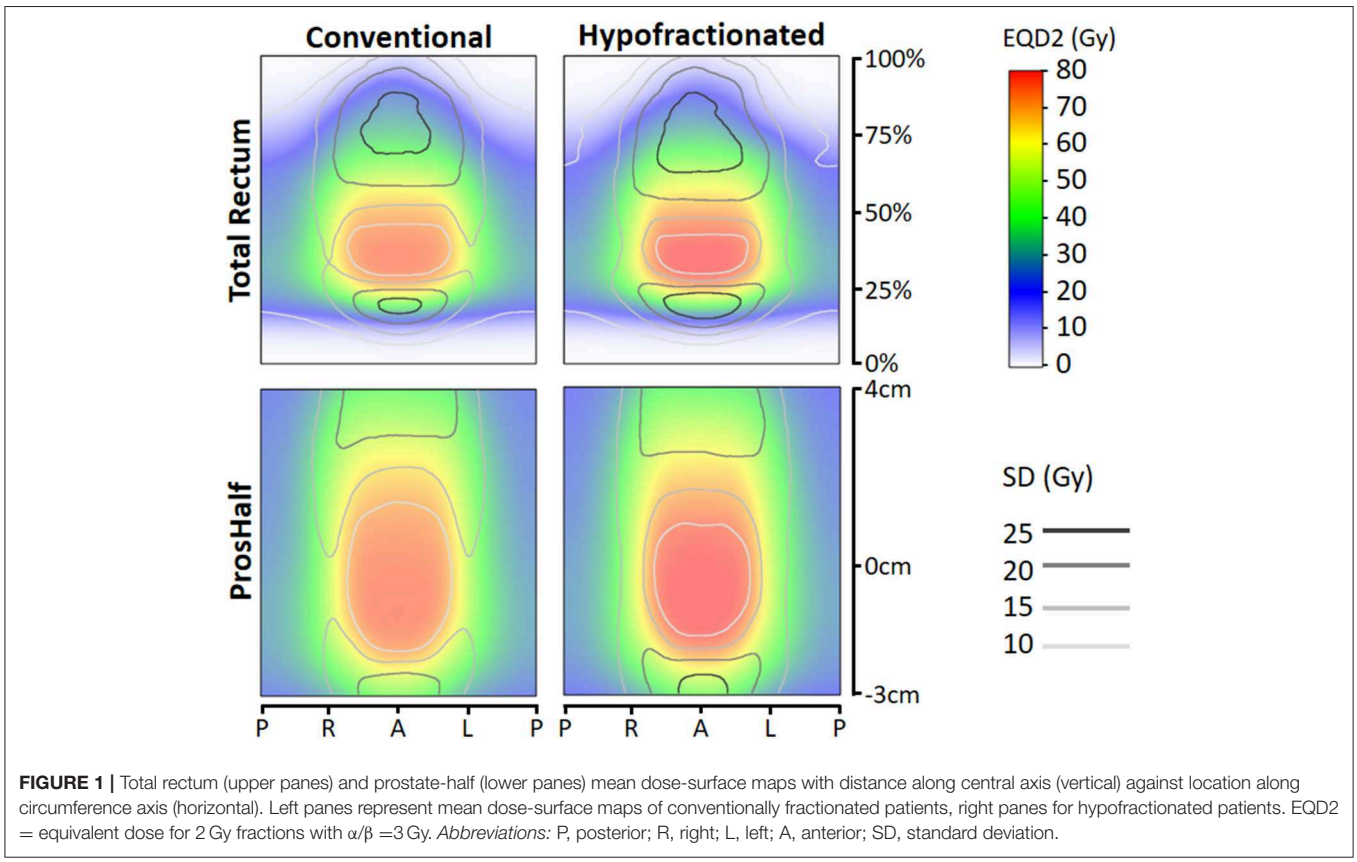

FIGURE 1 | Total rectum (upper panes) and prostate-half (lower panes) mean dose-surface maps with distance along central axis (vertical) against location along circumference axis (horizontal). Left panes represent mean dose-surface maps of conventionally fractionated patients, right panes for hypofractionated patients. EQD2 = equivalent dose for 2 Gy fractions with $\alpha/\beta = 3$ Gy. *Abbreviations:* P, posterior; R, right; L, left; A, anterior; SD, standard deviation.

dose distributions in CF patients; for HF patients no such effect was observed (**Figure 2**).

DISCUSSION

We explored local dose-effect relationships for GI toxicity in a study population treated with both conventionally fractionated and hypofractionated modern radiotherapy. Since both patient groups were treated within the same randomized trial, this is a unique dataset to study hypofractionation effects on rectal toxicity with a perfect internal reference group of CF patients. We observed significant local dose-effect relations for all studied GI endpoints, except for increased stool frequency. For the endpoints rectal bleeding, pain/cramps, and mucus discharge, we observed differences between HF and CF in the patterns and level of significance of local dose-effects, whereas for pain or cramps with stools, observed patterns and levels of significance were similar.

We evaluated two types of dose mapping. The "total rectum" mapping is more accurate in matching specific anatomical sub-locations within the rectum between different patients an also covers the most cranial and caudal part of the rectum, whereas the "prostate-half" mapping is more accurate in matching the intermediate-high dose areas behind the prostate from one patient to another. The identified local dose-effects for both types

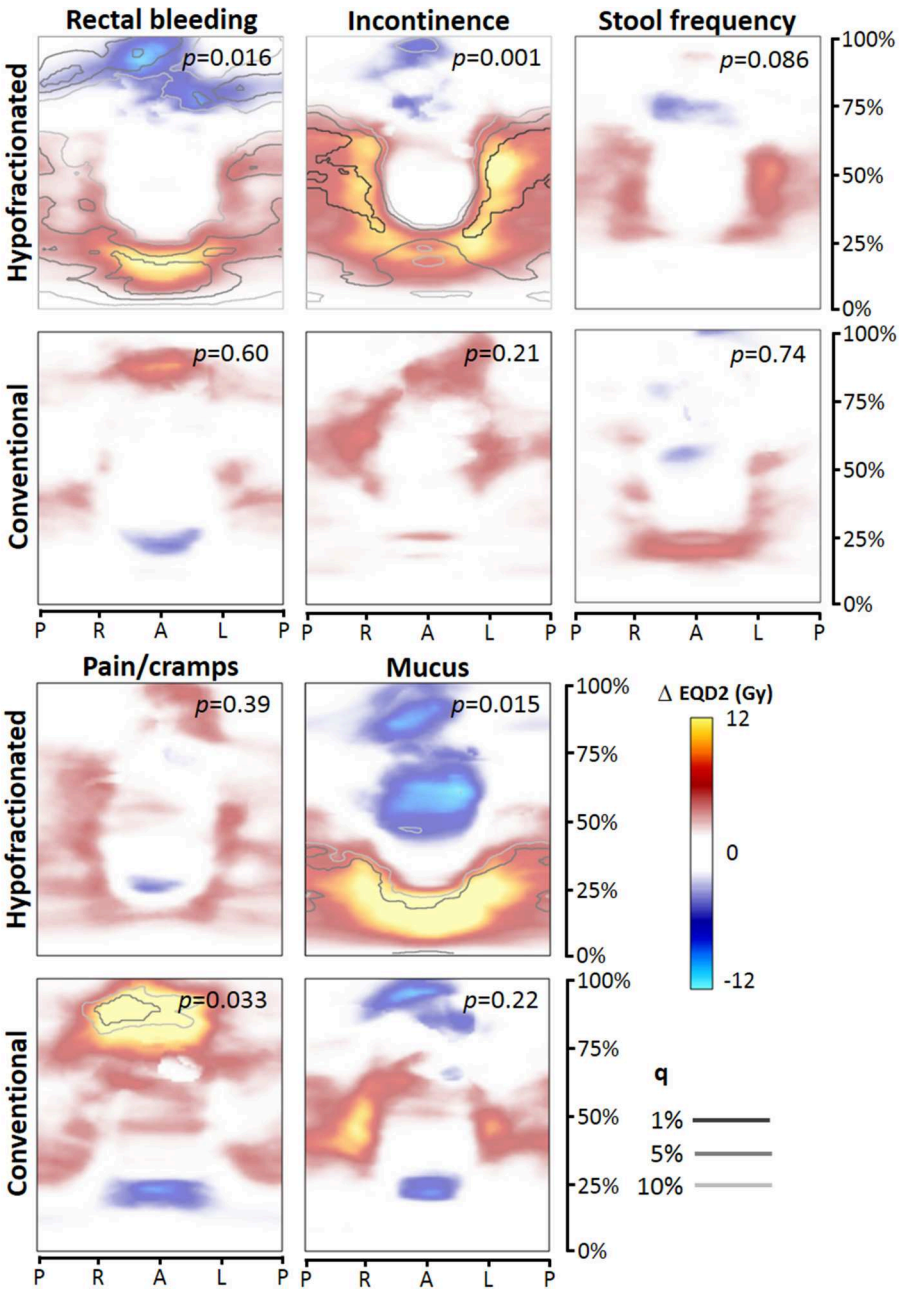

FIGURE 2 | Dose difference maps (ΔEQD2) based on total rectum dose mapping, for the toxicity endpoints (moderate to severe), for the hypofractionated and conventional group separately. EQD2 = equivalent dose for 2 Gy fractions with $\alpha/\beta = 3$ Gy, q = false discovery rate. *Abbreviations:* P, posterior; R, right; L, left; A, anterior.

of mapping were similar with comparable *p*-values. Theoretically, we expected that the prostate-half mapping would be more accurate in identifying risks associated with high-dose regions close to the prostate and is therefore of added value to the total rectum mapping which covers the whole anorectal tract, which was demonstrated in a previous study (14). However, we could not confirm this in the current study.

In the current study we used patient-reported toxicity from a prospective setting, accumulating the incidence over available questionnaires between year 1 and 5. As a result, 30% (CF) and 36% (HF) reported ≥1 moderate to severe complaint within this period. Previously, we reported that at 36 months of follow-up, 36% (CF), and 38% (HF) had a clinically relevant deterioration on the gastrointestinal subscale of the Prostate Cancer 25 Quality of Life module (26), which is in fair agreement with the current findings based on the symptom questionnaire. As discussed in this previous paper (26), reported toxicity incidences and differences between CF

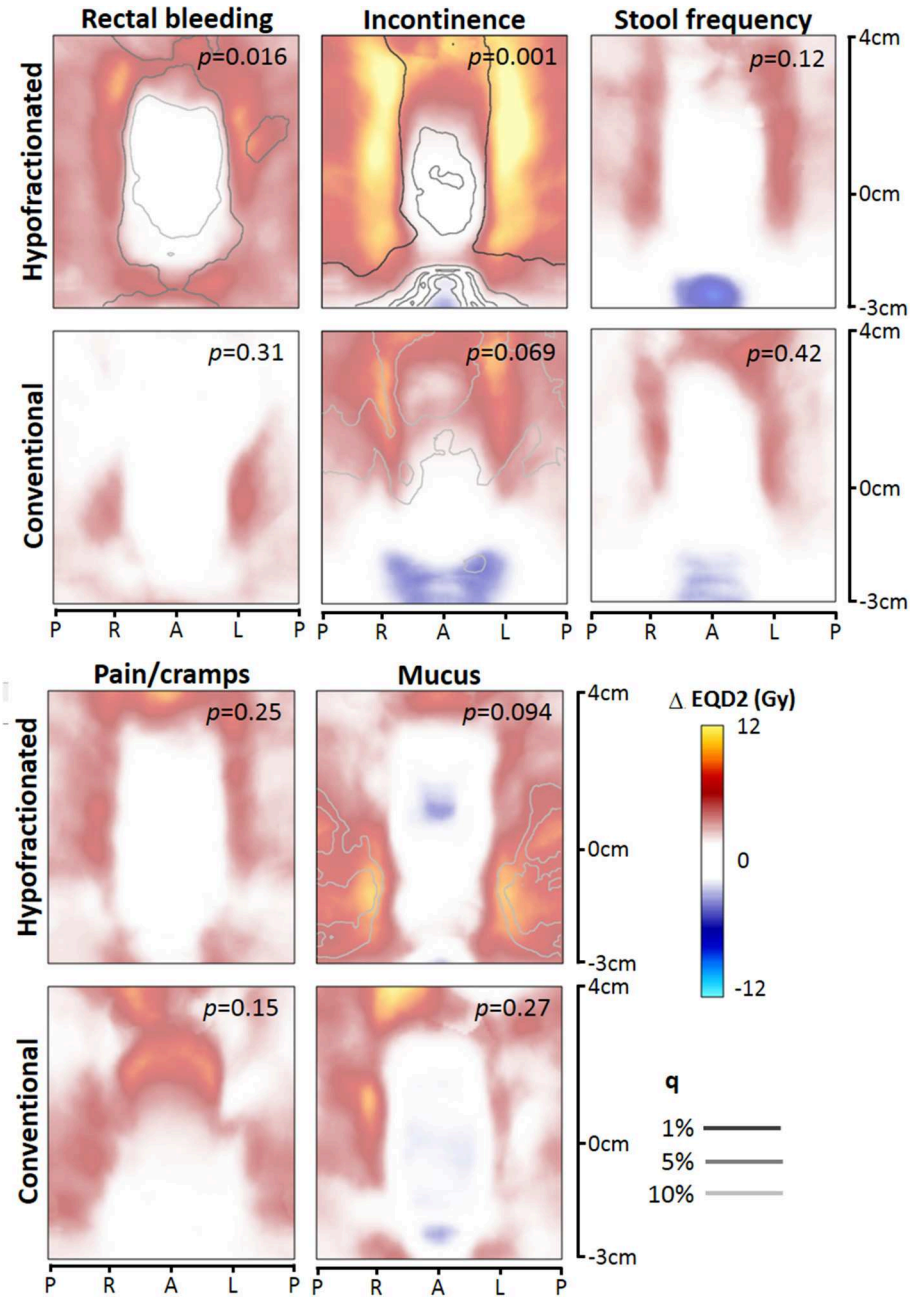

FIGURE 3 | Dose difference maps (ΔEQD2) based on prostate-half height dose mapping, for the toxicity endpoints (moderate to severe), for the hypofractionated and conventional group separately. EQD2 = equivalent dose for 2 Gy fractions with $\alpha/\beta = 3$ Gy, q = false discovery rate. *Abbreviations:* P, posterior; R, right; L, left; A, anterior.

and HF in the HYPRO trial are unfavorable compared to the CHHIP trial (7), which may have been caused by differences in target definition (for most HYPRO patients inclusion of the seminal vesicles), different patient population (HYPRO patients were mainly high-risk patients), and especially by a greater difference in EQD2 dose levels (with an α/β of 3 for normal tissue): 78 Gy (CF) vs. 82.7 Gy (HF) for the HYPRO trial, and 74 Gy (CF) vs. 72 Gy (HF – 20 × 3) for the CHHIP trial.

As reported by several previous studies, prospective registration translates in general into relatively high incidences of toxicity when compared to studies where only physician-reported toxicities are used, as we also previously demonstrated for the HYPRO trial (19). When we compare our patient-reported rates of rectal bleeding and fecal incontinence with the recent study of Onjukka et al. who also used patient-reported late toxicity in a modern IMRT setting with mainly conventional fractionation and partly mild hypofractionation, the reported

rates are very similar for both endpoints: about 10% in both studies (18).

We found that patient-reported GI toxicity incidences were higher for HF compared to CF with respect to the endpoints ≥3 symptoms, stool frequency, and rectal bleeding. Furthermore, we demonstrated that after converting both the HF and CF dose maps with the linear-quadratic model (with α/β of 3 Gy) to EQD2, we obtained very different dose-difference maps (**Figures 2**, **3**) where we would expect similar local dose-effects. This suggests that just by calculating EQD2 for a HF schedule, this might not completely capture the biological effect of a HF treatment. There are several differences between the HF and CF group which might have contributed to the observations of both higher incidences and different dose-difference maps: **(a)** applied dose constraints were based on earlier studies with CF; **(b)** the rectum dose for HF was on average somewhat higher because of the higher EQD2 prescription dose of 82.7 Gy with $\alpha/\beta = 3$; **(c)** local dose variations (standard deviations) were larger for the HF group; and **(d)** HF was delivered three times a week with 3.4 Gy fractions instead of 5 times a week 2 Gy fractions.

The symptom rectal bleeding was highly correlated with mucus discharge, which can be expected since both symptoms are the result of a radiation proctitis. In the literature, the endpoint of rectal bleeding has been extensively studied and modeled since it is regarded as a dose-limiting late toxicity (3). We observed a significantly higher incidence of patient-reported moderate to severe late rectal bleeding for HF compared to CF (17.6% vs. 10.7%). We previously reported the EORTC/RTOG grade ≥2 incidence of rectal bleeding (requiring clotting time), which was also higher for HF patients (5 vs. 2%, $p = 0.11$). (22). For rectal bleeding pronounced local dose-effects were observed in the dose-difference maps in the moderate to high-dose rectal regions close to the prostate, but only for HF patients. The location is in general in concordance with the literature based on conventional treatment, were high-dose regions above ≈60–70 Gy are found to be relevant for rectal bleeding. Applied dose constraints in the clinic are based on these published models (3). In the HYPRO trial, rectal volumes receiving ≥83% of the prescribed dose (i.e., ≥65 Gy for CF and ≥54 Gy for HF) had to be limited at treatment optimization to ≤50%. Our results suggest that for HF this planning criterion was suboptimal, resulting in increased risks of rectal bleeding. However, this observation might also be in part related to the higher EQD2 prescription dose of 82.7 Gy.

We observed similar fecal incontinence rates between CF and HF, but higher rates of increased stool frequency for HF (**Table 2**). At the same time, these complaints were highly correlated. In a recent study of Cicchetti et al. (27), comparing CF with mild HF (2.25–2.75 Gy per fraction), higher levels of fecal incontinence were observed for mild HF compared to CF. For the endpoints increased stool frequency and fecal incontinence, dose to other neighboring structures, such as pelvic floor muscles and nerves, might be relevant as well, as reported in several studies (28, 29). However, in other studies, similar rates of fecal incontinence were observed between 3DCRT and IMRT groups whereas the latter was associated with largely reduced dose levels to the anal canal region (27, 30) which is in the same region as the pelvic floor muscles.

As previously published, the results of the HYPRO trial were negative with respect to its hypothesis, i.e., non-inferiority with respect to Grade ≥2 toxicity and superiority with respect to freedom from failure could both not be demonstrated for the HF arm (6). Therefore, is this hypofractionation schedule of 19 times 3.4 Gy not recommendable or acceptable for clinical practice. However, for studying hypofractionation effects and dose-effect relationships these data are very useful. In current clinical practice, the hypofractionation schedule of the CCHIP trial (7) and the Widmark trial (9) have been adopted by centers worldwide, in which hypofractionated treatment is distributed over several weeks of treatment with intervals >24 h between fractions, similar to the HYPRO trial. To understand more about fractionation effects and effects of intervals between fractions on late (permanent) damage to normal tissues, additional modeling of the dose and outcome data from hypofractionation trials is essential. Recently, Wilkins et al. reported on dose-effect analyses from the CCHIP trial, derived from both conventional whole organ evaluation and from spatial dose mapping, aiming at formulating novel dose constraints for mild hypofractionation regimens in 3 Gy fractions (31). They report that different rectal dose constraints were obtained for different GI symptoms. In their study, spatial dose metrics did not improve prediction compared to dose-volume information.

Data from the hypofractionated trial arm of the HYPRO trial have been used for toxicity modeling using dose-volume data and additional features derived from texture analysis (32). They reported models for the GI symptoms of fecal incontinence and rectal modeling including clinical factors, dose-volume factors, and derived texture features. From other phase III randomized hypofractionation trials (6–9, 33), there are to our knowledge no publications yet on additional dose-effect modeling.

It is nowadays broadly recognized that incorporating spatial local dose information from voxel-based organ-at-risk calculations, in contrast to whole organ evaluations, has the potential to improve NTCP models and therefore improve the quality of derived planning constraints (10). Several studies have demonstrated that spatial local dose metrics are suitable for NTCP modeling of rectal toxicity compared to traditional dose-surface (DSH) and dose-volume histograms (DVH) (12–18). Recently, Casares et al. (34) reported on the superiority of spatial metric by comparing NTCP models; they concluded that predictability of patient-reported GI toxicity increased using spatial metrics compared to DSH/DVH metrics. The HYPRO data set is a very suitable dataset for bioeffect modeling of toxicity with the goal to obtain meaningful NTCP models and related dose constraints for optimized treatment planning with modern techniques including hypofractionation. An essential question to answer prior to the modeling is: how to summarize the inhomogeneous dose distributions into meaningful dose parameters for subsequent modeling. The dose maps resulting from this study clearly show that especially intermediate-high dose areas in the rectum are associated with a number of GI symptoms, especially for HF treatment. As previously described by Bentzen et al. (4), true equieffective dose levels (with the same bioeffect) result in identical toxicity risks. Further modeling of the HYPRO data, by constructing NTCP

models based on calculated EQD2 dose for each group, may demonstrate whether the calculated EQD2 levels are equieffective or whether other biological factors have to be taken into account to calculate the true biological equieffective dose. Furthermore, relevant clinical covariates have to be incorporated into such models as well to improve the predictive power of such models. As shown in **Table 3**, for the endpoint fecal leakage (age and diabetes) and for the endpoints rectal bleeding and mucus (T stage) predictive clinical covariates were identified. Our ultimate goal is to use the current findings to develop a biological NTCP model that correctly incorporates fractionation effects, modeling the GI toxicity as a function of biological dose. This could then theoretically be applied to all types of dose distributions including different fractionation schedules.

In conclusion, we demonstrated significant local dose-effect relationships for patient-reported late GI toxicity in patients treated with modern RT. HF patients were at higher risk for increased stool frequency and rectal bleeding, and showed the most pronounced local dose-effects in intermediate-high dose regions. These findings suggest that improvement of current treatment optimization protocols could lead to clinical benefit, in particular for HF treatment.

DATA AVAILABILITY STATEMENT

The datasets used in this study are available on request. The corresponding author can be contacted for this purpose.

ETHICS STATEMENT

This trial was approved by the Medical Ethics Committee of the Erasmus Medical Center in Rotterdam, the Netherlands (06-045). The patients/participants provided their written informed consent to participate in this study.

AUTHOR CONTRIBUTIONS

MW and WH contributed to the study design (patient selection, endpoint definitions, dose mapping procedures, statistical analyses) and writing of the drafts of the manuscript. LI and FP contributed to patient inclusion and follow-up. MW and BH contributed to data collection of dosimetric data. All authors contributed to critical reading, revision of the manuscript, and approval of the submitted version.

FUNDING

The HYPRO trial was financially supported by the Dutch Cancer Society (Grant No. CKTO 2006-08) which is a non-profit organization.

SUPPLEMENTARY MATERIAL

The Supplementary Material for this article can be found online at: https://www.frontiersin.org/articles/10.3389/fonc.2020.00469/full#supplementary-material

REFERENCES

1. Donovan JL, Hamdy FC, Lane JA, Mason M, Metcalfe C, Walsh E, et al. Patient reported outcomes after monitoring, surgery, or radiotherapy for prostate cancer. *N Engl J Med.* (2016) 375:1425–37. doi: 10.1056/NEJMoa1606221
2. Marks LB, Yorke ED, Jackson A, Ten Haken RK, Constine LS, Eisbruch A, et al. Use of normal tissue complication probability models in the clinic. *Int J Radiat Oncol Biol Phys.* (2010) 76(Suppl. 3):S10–9. doi: 10.1016/j.ijrobp.2009.07.1754
3. Landoni V, Fiorino C, Cozzarini C, Sanguinet G, Valdagni R, Rancati T. Predicting toxicity in radiotherapy for prostate cancer. *Phys Med.* (2016) 32:521–32. doi: 10.1016/j.ejmp.2016.03.003
4. Bentzen SM, Dörr W, Gahbauer R, Howell RW, Joiner MC, Jones B, et al. Bioeffect modeling and equieffective dose concepts in radiation oncology—terminology, quantities and units. *Radiother Oncol.* (2012) 105:266–8. doi: 10.1016/j.radonc.2012.10.006
5. Fowler JF. The radiobiology of prostate cancer including new aspects of fractionated radiotherapy. *Acta Oncol.* (2005) 44:265–76. doi: 10.1080/02841860410002824
6. Incrocci L, Wortel RC, Alemayehu WG, Aluwini S, Schimmel E, Krol S, et al. Hypofractionated versus conventionally fractionated radiotherapy for patients with localised prostate cancer (HYPRO): final efficacy results from a randomised, multicentre, open-label, phase 3 trial. *Lancet Oncol.* (2016) 17:1061–69. doi: 10.1016/S1470-2045(16)30070-5
7. Dearnaley D, Syndikus I, Mossop H, Khoo V, Birtle A, Bloomfield, D, et al. Conventional versus hypofractionated high-dose intensity-modulated radiotherapy for prostate cancer: 5-year outcomes of the randomised, non-inferiority, phase 3 CHHiP trial. *Lancet Oncol.* (2016) 17:1047–60. doi: 10.1016/S1470-2045(16)30102-4
8. Lee WR, Dignam JJ, Amin MB, Bruner DW, Low D, Swanson GP, et al. Randomized phase III noninferiority study comparing two radiotherapy fractionation schedules in patients with low-risk prostate cancer. *J Clin Oncol.* (2016) 34:2325–32. doi: 10.1200/JCO.2016.67.0448
9. Widmark A, Gunnlaugsson A, Beckman L, Thellenberg-Karlsson C, Hoyer M, Lagerlund M, et al. Ultra-hypofractionated versus conventionally fractionated radiotherapy for prostate cancer: 5-year outcomes of the HYPO-RT-PC randomised, non-inferiority, phase 3 trial. *Lancet.* (2019) 394:385–95. doi: 10.1016/S0140-6736(19)31131-6
10. Palma G, Monti S, Cella L. Voxel-based analysis in radiation oncology: a methodological cookbook. *Phys Med.* (2020) 69:192–204. doi: 10.1016/j.ejmp.2019.12.013
11. Heemsbergen WD, Hoogeman MS, Hart GA, Lebesque JV, Koper PC. Gastrointestinal toxicity and its relation to dose distributions in the anorectal region of prostate cancer patients treated with radiotherapy. *Int J Radiat Oncol Biol Phys.* (2005) 61:1011–8. doi: 10.1016/j.ijrobp.2004.07.724
12. Buettner F, Gulliford SL, Webb S, Sydes MR, Dearnaley DP, Partridge M. Assessing correlations between the spatial distribution of the dose to the rectal wall and late rectal toxicity after prostate radiotherapy: an analysis of data from the MRC RT01 trial (ISRCTN 47772397). *Phys Med Biol.* (2009) 54:6535–48. doi: 10.1088/0031-9155/54/21/006
13. Buettner F, Gulliford SL, Webb S, Sydes MR, Dearnaley DP, Partridge M. The dose-response of the anal sphincter region–an analysis of data from the MRC RT01 trial. *Radiother Oncol.* (2012) 103:347–52. doi: 10.1016/j.radonc.2012.03.002
14. Wortel RC, Witte MG, van der Heide UA, Pos FJ, Lebesque JV, van Herk M, et al. Dose-surface maps identifying local dose-effects for acute gastrointestinal toxicity after radiotherapy for prostate cancer. *Radiother Oncol.* (2015) 117:515–20. doi: 10.1016/j.radonc.2015.10.020
15. Acosta O, Drean G, Ospina JD, Simon A, Haigron P, Lafond C, de Crevoisier R. Voxel-based population analysis for correlating local dose and rectal toxicity in prostate cancer radiotherapy. *Phys Med Biol.* (2013) 58:2581–95. doi: 10.1088/0031-9155/58/8/2581

16. Munbodh R, Jackson A, Bauer J, Schmidtlein CR, Zelefsky MJ. Dosimetric and anatomic indicators of late rectal toxicity after high-dose intensity modulated radiation therapy for prostate cancer. *Med Phys*. (2008) 35:2137–50. doi: 10.1118/1.2907707
17. Moulton CR, House MJ, Lye V, Tang CI, Krawiec M, Joseph DJ, et al. Spatial features of dose-surface maps from deformably-registered plans correlate with late gastrointestinal complications. *Phys Med Biol*. (2017) 62:4118–39. doi: 10.1088/1361-6560/aa663d
18. Onjukka E, Fiorino C, Cicchetti A, Palorini F, Improta I, Gagliardi G, et al. Patterns in ano-rectal dose maps and the risk of late toxicity after prostate IMRT. *Acta Oncol*. (2019) 58:1757–64. doi: 10.1080/0284186X.2019.1635267
19. Aluwini S, Pos F, Schimmel E, van Lin E, Krol S, van der Toorn PP, et al. Hypofractionated versus conventionally fractionated radiotherapy for patients with prostate cancer (HYPRO): acute toxicity results from a randomised non-inferiority phase 3 trial. *Lancet Oncol*. (2015) 16:274–83. doi: 10.1016/S1470-2045(14)70482-6
20. Partin W, Mangold LA, Lamm DM, Walsh PC, Epstein JI, Pearson JD. Contemporary update of prostate cancer staging nomograms (partin tables) for the new millennium. *Urology*. (2001) 58:843–8. doi: 10.1016/s0090-4295(01)01441-8
21. Wortel RC, Heemsbergen WD, Smeenk RJ, Witte MG, Krol SDG, Pos FJ, et al. Local protocol variations for image guided radiation therapy in the multicenter dutch hypofractionation (HYPRO) trial: impact of rectal balloon and mri delineation on anorectal dose and gastrointestinal toxicity levels. *Int J Radiat Oncol Biol Phys*. (2017) 99:1243–52. doi: 10.1016/j.ijrobp.2017.07.044
22. Aluwini S, Pos F, Schimmel E, Krol S, van der Toorn PP, de Jager H, et al. Hypofractionated versus conventionally fractionated radiotherapy for patients with prostate cancer (HYPRO): late toxicity results from a randomised, non-inferiority, phase 3 trial. *Lancet Oncol*. (2016) 17:464–74. doi: 10.1016/S1470-2045(15)00567-7
23. Chen, C, Witte, M, Heemsbergen, W, van Herk, M, Multiple comparisons permutation test for image based data mining in radiotherapy. *Radiat Oncol*. (2013) 8:293. doi: 10.1186/1748-717X-8-293
24. Benjamini Y, Hochberg Y. Controlling the false discovery rate: a practical and powerful approach to multiple testing. *J R Statist Soc B*. (1995) 57:289–300.
25. Dréan G, Acosta O, Ospina JD, Fargeas A, Lafond C, Corrégé G, et al. Identification of a rectal subregion highly predictive of rectal bleeding in prostate cancer IMRT. *Radiother Oncol*. (2016) 119:388–97. doi: 10.1016/j.radonc.2016.04.023
26. Wortel RC, Oomen-de Hoop E, Heemsbergen WD, Pos FJ, Incrocci L. Moderate hypofractionation in intermediate- and high-risk, localized prostate cancer: health-related quality of life from the randomized, phase 3 hypro trial. *Int J Radiat Oncol Biol Phys*. (2019) 103:823–33. doi: 10.1016/j.ijrobp.2018.11.020
27. Cicchetti A, Avuzzi B, Palorini F, Ballarini F, Stucchi C, Fellin G, et al. Predicting late fecal incontinence risk after radiation therapy for prostate cancer: new insights from external independent validation. *Int J Radiat Oncol Biol Phys*. (2018) 102:127–36. doi: 10.1016/j.ijrobp.2018.05.013
28. Schaake W, van der Schaaf A, van Dijk LV, Bongaerts AH, van den Bergh AC, Langendijk JA. Normal tissue complication probability (NTCP) models for late rectal bleeding, stool frequency and fecal incontinence after radiotherapy in prostate cancer patients. *Radiother Oncol*. (2016) 119:381–7. doi: 10.1016/j.radonc.2016.04.005
29. Smeenk RJ, Hoffmann AL, Hopman WP, van Lin EN, Kaanders JH. Dose-effect relationships for individual pelvic floor muscles and anorectal complaints after prostate radiotherapy. *Int J Radiat Oncol Biol Phys*. (2012) 83:636–44. doi: 10.1016/j.ijrobp.2011.08.007
30. Wortel RC, Incrocci L, Pos FJ, van der Heide UA, Lebesque JV, Aluwini S, et al. Late side effects after image guided intensity modulated radiation therapy compared to 3D-conformal radiation therapy for prostate cancer: results from 2 prospective cohorts. *Int J Radiat Oncol Biol Phys*. (2016) 95:680–9. doi: 10.1016/j.ijrobp.2016.01.031
31. Wilkins A, Naismith O, Brand D, Fernandez K, Hall E, Dearnaley D, et al. Derivation of dose/volume constraints for the anorectum from clinician- and patient-reported outcomes in the chhip trial of radiation therapy fractionation. *Int J Radiat Oncol Biol Phys*. (2020) 106:928. doi: 10.1016/j.ijrobp.2020.01.003
32. Rossi L, Bijman R, Schillemans W, Aluwini S, Cavedon C, Witte M, et al. Texture analysis of 3D dose distributions for predictive modelling of toxicity rates in radiotherapy. *Radiother Oncol*. (2018) 129:548–53. doi: 10.1016/j.radonc.2018.07.027
33. Catton CN, Lukka H, Gu CS, Martin JM, Supiot S, Chung PWM, et al. Randomized trial of a hypofractionated radiation regimen for the treatment of localized prostate cancer. *J Clin Oncol*. (2017) 35:1884–90. doi: 10.1200/JCO.2016.71.7397
34. Casares-Magaz O, Muren LP, Moiseenko V, Petersen SE, Pettersson NJ, Høyer M, et al. Spatial rectal dose/volume metrics predict patient-reported gastro-intestinal symptoms after radiotherapy for prostate cancer. *Acta Oncol*. (2017) 56:1507–13. doi: 10.1080/0284186X.2017.1370130

Conflict of Interest: The authors declare that the research was conducted in the absence of any commercial or financial relationships that could be construed as a potential conflict of interest.

frontiers in Oncology

ORIGINAL RESEARCH
published: 08 April 2020
doi: 10.3389/fonc.2020.00467

Dosimetric Predictors of Acute and Chronic Alopecia in Primary Brain Cancer Patients Treated With Volumetric Modulated Arc Therapy

Silvia Scoccianti[1], Gabriele Simontacchi[1], Daniela Greto[1], Marco Perna[1], Francesca Terziani[1], Cinzia Talamonti[2], Maria Ausilia Teriaca[1], Giorgio Caramia[1], Monica Lo Russo[1], Emanuela Olmetto[1], Camilla Delli Paoli[1], Roberta Grassi[1], Vincenzo Carfora[1], Calogero Saieva[3], Pierluigi Bonomo[1], Beatrice Detti[1], Monica Mangoni[1], Isacco Desideri[1], Giulio Francolini[1], Vanessa Di Cataldo[1], Livia Marrazzo[2], Stefania Pallotta[2] and Lorenzo Livi[1]*

[1] Radiation Oncology Unit, Azienda Ospedaliera Universitaria Careggi, University of Florence, Florence, Italy, [2] Medical Physics Unit, Department of Experimental and Clinical Biomedical Sciences "Mario Serio," Azienda Ospedaliera Universitaria Careggi, University of Florence, Florence, Italy, [3] SC Epidemiology of Risk Factors and Lifestyles, Institute for Study, Prevention, and Oncology Network (ISPRO), Florence, Italy

OPEN ACCESS

Edited by:
Tiziana Rancati,
National Cancer Institute Foundation (IRCCS), Italy

Reviewed by:
Wilma Desiree Heemsbergen,
Erasmus University Rotterdam, Netherlands
Michele Avanzo,
Aviano Oncological Reference Center (CRO), Italy

***Correspondence:**
Silvia Scoccianti
silvia.scoccianti@unifi.it

Specialty section:
This article was submitted to Radiation Oncology, a section of the journal Frontiers in Oncology

Received: 27 November 2019
Accepted: 16 March 2020
Published: 08 April 2020

Citation:
Scoccianti S, Simontacchi G, Greto D, Perna M, Terziani F, Talamonti C, Teriaca MA, Caramia G, Lo Russo M, Olmetto E, Delli Paoli C, Grassi R, Carfora V, Saieva C, Bonomo P, Detti B, Mangoni M, Desideri I, Francolini G, Di Cataldo V, Marrazzo L, Pallotta S and Livi L (2020) Dosimetric Predictors of Acute and Chronic Alopecia in Primary Brain Cancer Patients Treated With Volumetric Modulated Arc Therapy. Front. Oncol. 10:467. doi: 10.3389/fonc.2020.00467

Purpose: To determine dose constraints that correlate with alopecia in patients treated with photon-based Volumetric Modulated Arc Therapy (VMAT) for primary brain tumors.

Methods: During the treatment planning process, the scalp was drawn as a region of interest. Dose received by 0.1 cc ($D_{0.1cc}$), mean dose (D_{mean}), absolute volumes receiving different doses (V_{16Gy}, V_{20Gy}, V_{25Gy}, V_{30Gy}, V_{35Gy}, V_{40Gy}, and V_{43Gy}) were registered for the scalp. Alopecia was assessed according to Common Terminology Criteria for Adverse Events (CTCAE) v4.0. Receiver operating characteristics (ROC) curve analysis was used to identify parameters associated with hair-loss.

Results: One-hundred and one patients were included in this observational study. At the end of radiotherapy (RT), 5 patients did not develop alopecia (D_{mean} scalp 3.1 Gy). The scalp of the patients with G1 ($n = 11$) and G2 ($n = 85$) alopecia received D_{mean} of 10.6 Gy and 11.8 Gy, respectively. At ROC analysis, $V_{16Gy20Gy} \geq 5.2$ cc were the strongest predictors of acute alopecia risk. Chronic hair-loss assessment was available for 74 patients: median time to recovery from G2 alopecia was 5, 9 months. The actuarial rate of hair regrowth was 98.1% at 18 months after the end of RT. At ROC analysis, $V_{40Gy43Gy} \geq 2.2$ cc were the strongest predictors of chronic G2-alopecia risk. V_{20Gy}, V_{40Gy}, and $D_{0,1cc}$ were shown to be independent variables according to correlation coefficient r.

Conclusions: V_{20Gy} and V_{40Gy} were the strongest predictors for acute and chronic G2 hair-loss, respectively. The low-dose bath typical of VMAT corresponds to large areas of acute but transient alopecia. However, the steep dose gradient of VMAT allows to reduce the areas of the scalp that receive higher doses, minimizing the risk of permanent alopecia.

The application of our dosimetric findings for the scalp may help in reducing the alopecia risk and also in estimating the probability of hair-loss during patient counseling before starting radiotherapy.

Keywords: alopecia, radiation-induced hair loss, scalp, constraints, predictors, VMAT, brain tumors, radiotherapy

INTRODUCTION

Due to the high radiosensitivity of hair follicles, radiotherapy (RT) may induce hair-loss with a huge psychological impact and, thus, negative effects on patient's quality of life, also in case of limited life expectancy (1–5).

In the treatment of brain tumors, the technology of IMRT and, most recently, rotating gantry IMRT techniques such as VMAT, can produce dose distributions that conform to the target volume and deliver a reduced dose to the critical organs (6).

Recently, due to the increased conformality of IMRT techniques, there has been considerable interest in sparing critical structures not classically included into the list of intracranial organs at risk, such as hippocampus (7) or dorsal vagal complex (8). Likewise, the inclusion of the scalp among the organs at risk may potentially reduce the incidence or the severity of hair loss.

In the present study we included a total of 101 patients whose scalp was drawn as a region of interest to spare during the treatment planning process. The present work reports a dosimetric analysis of the scalp describing the risk of acute and permanent hair-loss following cranial irradiation on limited volume, performed with a VMAT approach.

The primary objective is to define dosimetric predictors for hair-loss with the aim of using them as dose constraints during the inverse planning process. Secondary aims were to analyze the recovery time and to evaluate clinical factors possibly associated with permanent alopecia.

METHODS AND MATERIALS

Consecutive patients treated for a primary brain tumor in our Institute with a conventionally fractionated VMAT were included in this observational study. Eligibility criteria included the use of partial brain radiotherapy, conventional fractionation, total dose >50 Gy, life expectancy > 4 months. Exclusion criteria included previous radiation treatment on the brain; previous chemotherapy; the need for whole brain radiotherapy; any previously existing alopecia according to Basic and specific (BASP) classification (9). All patients signed a consent form before enrollment in this institutional review board-approved study. Factors that may have an impact on alopecia such as age, smoking history, use of antiepileptic drugs (AEDs) and chemotherapy were registered.

Scalp as a Region of Interest During the Treatment Planning Process

CT (Computed Tomography) image sets for radiation treatment planning were acquired using a Brilliance Big Bore CT (Philips Medical Systems). The slice thickness was 2 mm.

During the contouring process, a region of interest (ROI) was defined for the scalp.

At the moment of simulation CT, beyond the custom thermoplastic mask with the patient in the supine position (used as immobilization device during the treatment, as usual), for each patient a mask in prone position was molded (**Figure 1A**). With the aim of tracing the extension of the follicle-bearing scalp, the line between the hairy scalp and the hairless skin of the face and of the neck was defined with a wire (**Figures 1B,C**). CT scan of the mask in prone position without the patient was acquired for each case. These images were co-registered to the simulation CT of the corresponding patient, in order to avoid the hairless skin beyond the wire.

The scalp volume was defined as a ROI including the hair-bearing tissue between the skin and the outer table of the skull, up to a maximum thickness of 5 mm (4, 10–12) (**Figure 2**).

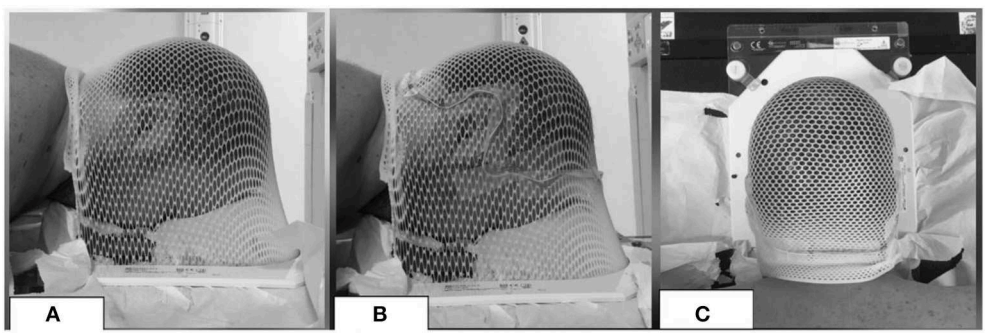

FIGURE 1 | Example of a mask in prone position **(A)** with a wire **(B,C)** to exclude the hairless skin from the ROI of the scalp.

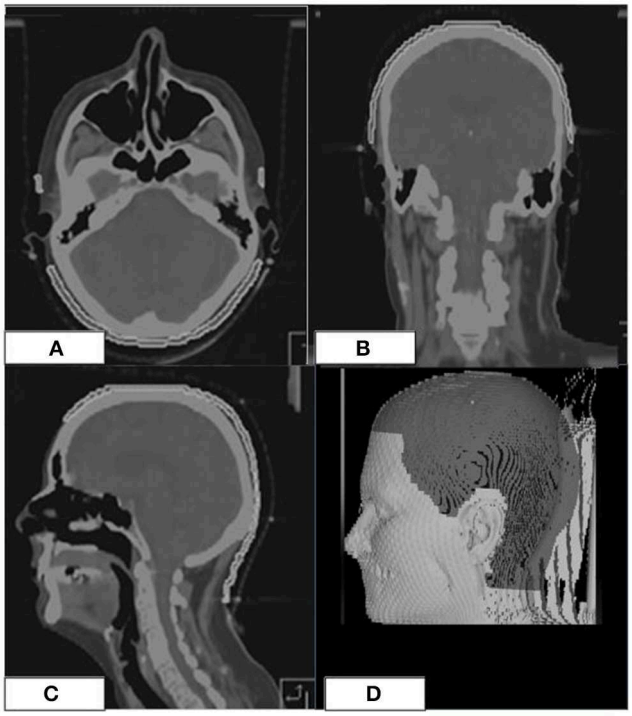

FIGURE 2 | Scalp ROI (white line) on the simulation CT of a patient **(A–C)**. 3D-view showing the scalp ROI **(D)**.

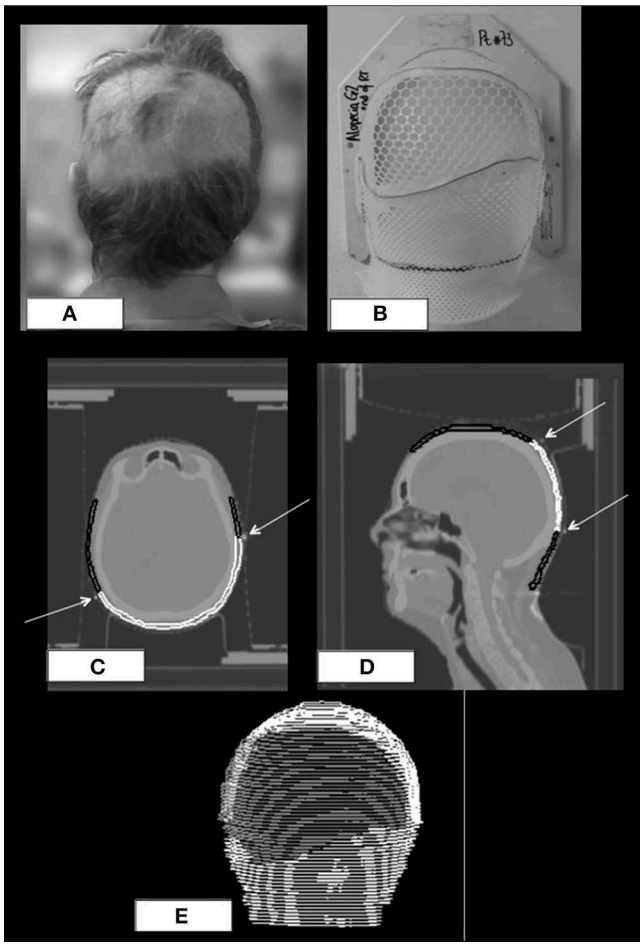

FIGURE 3 | Posterior view of a patient with a wide area of G2 alopecia **(A)** at the end of radiotherapy; prone mask with the wire defining the area of alopecia **(B)**; original CT simulation of the patient with coregistration of the wired prone mask **(C,D)**; scalp ROI is black colored, area of alopecia G2 is white colored, white arrows indicate the wire on the mask. 3D-view of the same patient at the treatment planning **(E)**.

The definition of the clinical target volume (CTV) varied according to the primary tumor. The planning target volume (PTV) was generated by adding a 3 mm isotropic margin to CTV.

VMAT plans were generated with Monaco (CMS-Elekta Ltd, UK) using a Monte-Carlo algorithm. Most of the cases were treated with a coplanar-partial arc technique. During the treatment planning, the scalp dose was kept as minimal as possible. Constraints to the other intracranial organs at risk [brainstem, optic chiasm and nerves, cochleas, pituitary (13)] had a higher priority than those of the scalp. The irradiation was delivered, using 6-MV photons with an Elekta Synergy machine equipped with a Beam Modulator multi-leaf collimator.

Hair Loss Assessment

Alopecia was assessed according to CTCAE version 4.0: G1 alopecia was defined as hair-loss of <50% of normal for that individual that is not obvious from a distance but only on close inspection; a different hairstyle may be required to cover the hair loss but it does not require a wig or hairpiece to camouflage; G2 alopecia was defined as hair-loss of ≥50% normal for that individual that is readily apparent to others; a wig or hairpiece was necessary if the patient desires to completely camouflage the hair loss; associated with psychosocial impact.

At the end of radiotherapy, in order to define the exact extension of the areas of acute alopecia, patients were required to wear the prone mask that had been molded during the simulation CT. Areas of alopecia were defined on the mask with a wire (**Figures 3A,B**); a new CT of the mask without the patient was acquired and, then, co-registered with the original simulation CT of the corresponding patient. Afterwards, areas of alopecia were contoured in order to obtain a treatment planning system-based dosimetric evaluation of the acute hair loss areas (**Figures 3C,E**).

For all the patients dose-volume histograms of the following ROIs were created: whole scalp, areas where G1 alopecia had developed during the treatment (G1-alopecia$_{endofRT}$), areas where G2 alopecia had developed during the treatment (G2-alopecia$_{endof\ RT}$).

Data regarding volumes in cc were collected both for the whole scalp and for the areas of acute alopecia. The following dosimetric parameters were collected: dose received by 0.1 cc of the ROI ($D_{0.1cc}$), mean dose (D_{mean}), absolute volumes that received 16, 20, 25, 30, 35, 40, and 43 Gy (V_{16Gy}, V_{20Gy}, V_{25Gy}, V_{30Gy}, V_{35Gy}, V_{40Gy}, and V_{43Gy}).

Patients were evaluated for hair loss at the end of radiotherapy and, then, every 3 months for the first 3 years of follow up.

G2 hair loss persisting for >9 months after the end of RT was defined as chronic alopecia.

Statistical Methods

A comparison between the dosimetric data was performed with the Mann–Whitney test.

The probability of developing acute G2 alopecia as a function of the $D_{0,1cc}$ was calculated using the maximal likelihood method according to the formula $P(D) = [1 + (D_{50}/D)^{4\gamma 50}]^{-1}$, where the D_{50} was $D_{0,1cc}$ at which 50% of the patients developed acute alopecia and $\gamma 50$ was the slope of the curve.

Receiver operating characteristics ROC analysis (14, 15), already adopted by other authors to identify dosimetric parameters associated with RT damage (16, 17), was used to identify the dosimetric parameters related to the risk of G2 alopecia. The maximum value of the Youden index (J) (18) was used for selecting the optimal cut-off point for each dosimetric variable.

Intercorrelation between dosimetric factors was analyzed: dosimetric variables with coefficient $r < 0.75$ were considered independent predictors.

Impact of clinical factors on incidence of acute alopecia was analyzed with chi-squared ($\chi 2$) test.

Kaplan–Meier survival analysis was carried out concerning alopecia recovery. The observation time was measured from the end of radiotherapy to complete recovery from alopecia or to the last follow-up for cases with the persistence of hair-loss. Differences between groups were evaluated by the log-rank test. Cox proportional regression analysis was used to determine the role of selected parameters on the risk of event occurrence by univariate models. Multivariate Cox proportional- hazards regression analysis was performed including only the variables that were shown to be not intercorrelated (coefficient $r < 0.75$).

All the statistical tests were performed using the IBM-SPSS Statistics software (Statistical Package for Social Science, version 22).

RESULTS

A total of 101 patients were included in the study. Characteristics of the patients are in **Table 1**.

Prescription doses ranged between 50.4 and 60 Gy in conventional fractionation. Mean scalp volume was 234.8 cc (SD 46.9).

Dosimetry of the whole scalp was available for all the patients. Of note, among the dosimetric parameters whose values were collected, V_{20Gy}, V_{40Gy}, and $D_{0,1cc}$ were shown to be independent variables according to correlation coefficient r.

Acute Alopecia

Clinical and dosimetric evaluation at the end of RT was available for all the patients.

TABLE 1 | Patients characteristics.

		n	Proportion (%)
Patients	All	101	100
Gender	Female	48	47.5
	Male	53	52.5
Age	Mean 51.7		
	Age <14	4	4.0
	Age ≥ 14	97	96.0
	Age < 50	38	37.6
	Age ≥ 50	63	62.4
Smoking history	no	68	67.3
	yes	33	32.7
Histology	High grade gliomas	68	67.3
	Low grade gliomas	12	11.9
	Meningioma	10	9.9
	Others	11	10.9
Antiepilectic drugs during radiotherapy	no	24	23.8
	yes	77	76.2
Concomitant chemotherapy	no	41	40.6
	Temozolomide	60	59.4
Chemotherapy after radiotherapy	no	34	33.7
	Temozolomide	59	58.4
	Procarbazine, vincristine, lomustine	8	7.9

Acute Alopecia: Dosimetry of the Whole Scalp

Five patients who were treated for deep tumors (pituitary adenomas $n = 4$; parasellar meningioma $n = 1$) did not develop any area of alopecia. The remaining 96 patients developed acute alopecia: 11 developed G1 alopecia only whereas 85 patients developed G2 alopecia (G2 only $n = 52$; G1+G2 $n = 33$). Significant differences in the dosimetric parameters were found between the scalp of the patients who did not develop alopecia and the scalp of patients who developed acute G1 alopecia and G2 alopecia (**Table 2**).

$D_{0,1cc}$ varied widely (**Figure 4**). D_{50}, i.e., $D_{0,1cc}$ at which 50% of the patients developed acute alopecia was found to be 33,0 ± 0,2 Gy. The slope of the curve ($\gamma 50$) was 1,58 ± 0,05 (**Figure 5**).

Acute Alopecia: Dosimetry of the Areas of Alopecia

Volumetric data regarding the areas of alopecia were collected in order to define the amount of hair loss in terms of percentage of the scalp volume at the end of radiotherapy (**Figure 6**). The mean volume of G1-alopecia$_{end-of-RT}$ and G2-alopecia$_{end-of-RT}$ was 26.6 and 66.1 cc, respectively. On average, G1-alopecia$_{end-of-RT}$ and G2-alopecia$_{end-of-RT}$ corresponded to 11.9% (SD 10.4) and 41.7% (SD 20.0) of the whole scalp volume, respectively. The

TABLE 2 | Dosimetric comparison between the scalp of the patients who did not develop alopecia and the scalp of the patients who developed G1 or G2 alopecia at the end of radiotherapy: mean values and standard deviations (in brackets) of dosimetric variables.

	n	Mean $D_{0.1cc}$ (Gy)	Mean D_{mean} (Gy)	Mean V_{16Gy} (cc)	Mean V_{20Gy} (cc)	Mean V_{25Gy} (cc)	Mean V_{30Gy} (cc)	Mean V_{35Gy} (cc)	Mean V_{40Gy} (cc)	Mean V_{43Gy} (cc)
$Scalp_{patients\ no\ alopecia}$	5	19.7 (± 12.6)	3.1 (± 1.5)	2.7 (± 3.7)	1.4 (± 1.9)	0.6 (± 1.1)	0.2 (± 0.5)	0.04 (± 0.09)	0	0
$Scalp_{patients\ with\ G1\ alopecia\ at\ the\ end\ of\ RT}$	11	40.2 (± 15.2)	10.6 (± 5.0)	45.2 (± 40.4)	31.0 (± 33.9)	22.2 (± 26.9)	15.6 (± 20.5)	10.8 (± 15.6)	7.4 (± 12.1)	5.8 (± 10.0)
p-value from Mann–Whitney Test		**0.02**	**0.001**	**0.002**	**0.02**	**0.03**	**0.04**	0.90	0.90	0.09
$Scalp_{patients\ with\ G2\ alopecia\ at\ the\ end\ of\ RT}$	85	47.3 (± 9.2)	11.8 (± 4.4)	68.8 (± 37.7)	50.6 (± 33.4)	34.8 (± 27.5)	23.1 (± 22.0)	14.3 (± 16.9)	8.4 (± 12.0)	5.9 (± 9.3)
p-value from Mann-Whitney Test		**0.0001**	**0.0001**	**0.0001**	**0.0001**	**0.0001**	**0.0001**	**0.001**	**0.004**	**0.005**

$D_{0.1cc}$, dose received by 0.1 cc; D_{mean}, mean dose; V_{xGy}, percentage of the scalp volume receiving ≥ x Gy.
Bold text indicates statistical significance.

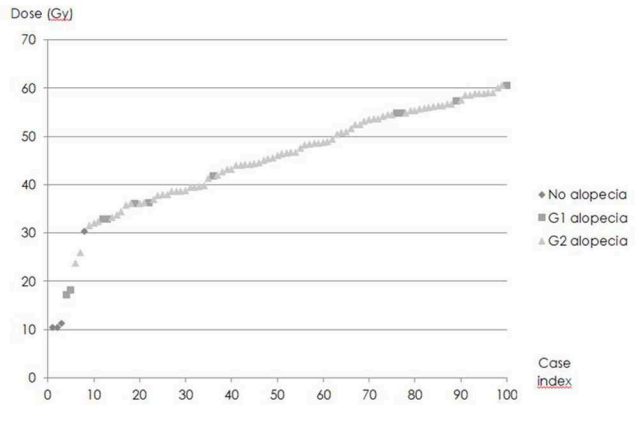

FIGURE 4 | Distribution of Maximum dose ($D_{0,1cc}$) in the series and grade of acute alopecia.

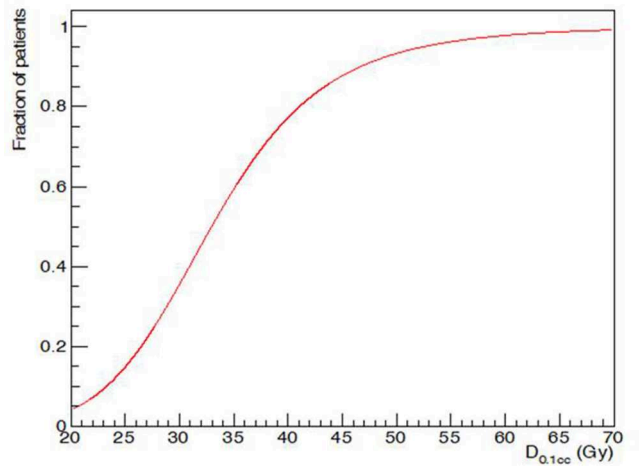

FIGURE 5 | Maximum dose ($D_{0,1cc}$) and acute G2 alopecia probability at the end of radiotherapy: dose-response relationship.

mean volume of alopecia of any grade was 70.7 cc (corresponding to 30.2% of the scalp, SD 20.7)

Significant differences in the dosimetric parameters were found when G1-$alopecia_{end-of-RT}$ were compared with alopecia $G2_{end-of-RT}$ (**Table 3**).

Acute Alopecia: ROC Analysis

At ROC analysis, all the dosimetric variables were found to be reliable parameters to distinguish patients at low-risk from those at high-risk of acute G2 alopecia (**Table 4**).

V_{16Gy} and V_{20Gy} were found to be the strongest predictors for acute alopecia (AUC 0.776 and 0.792, respectively). Cut-off values for high risk of development of alopecia at the end of radiation treatment were 16.7 cc and 5.2 cc for V_{16Gy} and V_{20Gy}, respectively.

Factors Impacting on Acute Alopecia

Gender ($\chi 2$ test: $p = 0.19$), age ($\chi 2$ test: $p = 0.37$), smoking history ($\chi 2$ test: $p = 0.65$), use of AEDs ($\chi 2$ test: $p = 0.09$), concomitant chemotherapy ($\chi 2$ test: $p = 0.17$) did not have any significant impact on acute hairloss incidence.

Chronic Alopecia

All the cases of persistent alopecia were an evolution of acute alopecia (i.e., all the patients who had chronic alopecia, had had previous acute alopecia in the same areas that did not recover; on the contrary, all the patients who had had no acute alopecia (n = 5) did not develop chronic alopecia).

Hair-loss assessment for G2-alopecia was available for 74 patients. The mean follow-up was 9.7 months. At the moment of analysis, 65/74 (87.8%) patients had a complete G2 recovery.

Late recovery from G2 hairloss was possible: 3 patients recovered between 12 and 18 months. Median time to recovery was 5.9 months (SD 2.8 months). Actuarial rate of G2 recovery was 49.2, 87.0, 92.2, and 98.1% at 6, 9, 12, and 18 months after the end of RT (**Figure 7**).

Chronic Alopecia: Dosimetry of the Whole Scalp

Dosimetric analysis of the whole scalp excluded patients with a follow-up shorter than 3 months ($n = 5$). Dosimetric parameters

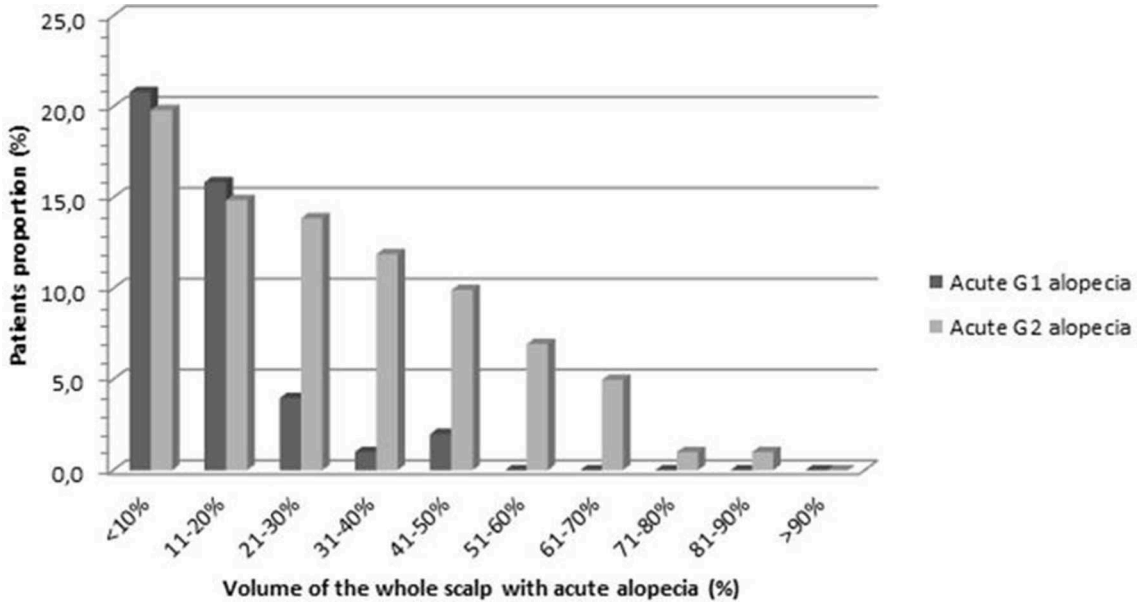

FIGURE 6 | Percentage of the volume of the scalp with G1 and G2 alopecia at the end of radiotherapy.

TABLE 3 | Dosimetric comparison between the areas of G1 alopecia and the areas of G2 alopecia at the end of radiotherapy: mean values and standard deviations (in brackets) of dosimetric variables.

	n	Mean $D_{0.1cc}$ (Gy)	Mean D_{mean} (Gy)	Mean V_{16Gy} (cc)	Mean V_{20Gy} (cc)	Mean V_{25Gy} (cc)	Mean V_{30Gy} (cc)	Mean V_{35Gy} (cc)	Mean V_{40Gy} (cc)	Mean V_{43Gy} (cc)
G1-Alopecia$_{end\ of\ RT}$	44	33.4 (± 14.3)	16.5 (± 8.3)	11.9 (± 14.6)	7.6 (± 9.6)	6.5 (± 11.8)	3.8 (± 7.9)	2.4 (± 6.4)	1.6 (± 5.4)	1.3 (± 4.8)
G2-Alopecia$_{end\ of\ RT}$	85	44.6 (± 11.2)	20.3 (± 6.4)	40.2 (± 35.4)	31.5 (± 30.5)	21.8 (± 24.3)	14.8 (± 18.9)	9.2 (± 14.3)	5.4 (± 10.2)	3.6 (± 7.7)
p-value from Mann-Whitney Test		**0.0001**	**0.002**	**0.0001**	**0.0001**	**0.0001**	**0.0001**	**0.001**	**0.0001**	**0.001**

$D_{0.1cc}$, dose received by 0.1 cc; D_{mean}, mean dose; V_{xGy}, percentage of the scalp volume receiving ≥ x Gy.
Bold text indicates statistical significance.

of the whole scalp of 8 patients who had a persistent alopecia (>9 months) were compared with the dosimetric data of 66 patients who had an intact scalp within 9 months after the end of RT (**Table 5**). Of note, patients who had not developed alopecia at the end of radiotherapy ($n = 5$) were included among these 66 patients. V_{40Gy} and V_{43Gy} were statistically different between these two groups (Mann–Whitney test $p = 0.028$ and $p = 0.036$).

Chronic Alopecia: ROC Analysis

At ROC analysis, several dosimetric variables were significantly related to the risk of permanent alopecia (**Table 6**). Among these, V_{40Gy} and V_{43Gy} were the strongest predictors for chronic G2-alopecia (AUC = 0.738 and 0.725, respectively): patients whose scalp ROI had $V_{40Gy43Gy}$.

Kaplan–Meier Analysis and Cox Regression for Recovery From Alopecia

All the dosimetric parameters that were found to be significant predictors of chronic G2-alopecia at the ROC analysis ($D_{0.1cc}$, D_{mean}, V_{30Gy}, V_{35Gy}, V_{40Gy}, and V_{43Gy}) and all the clinical variables were included in the Kaplan–Meier analysis (**Table 7**).

Patients were stratified according to the cut-off values defined at the ROC analysis for each dosimetric variable with the aim to have dichotomous variables. All the tested dosimetric parameters significantly impacted on recover probability.

Age had a significant impact on recover probability (age $>$ 14 = 97.9 vs. age $\leq$ 14 = 100%; log-rank test p = 0,01). No other clinical factors (gender, smoking history, use of AEDs, chemotherapy) significantly influenced the recover probability. Impact on recover probability due to different chemotherapy schedules was not tested because, among the cases with trichological follow-up, nearly all patients who had sequential chemotherapy received temozolomide (52 out of the 53).

Age and all the above mentioned dichotomous dosimetric variables were found to be significant at univariate Cox regression (**Table 8**). $D_{0,1cc}$ maintained significance also when tested as a continuous variable (p = 0,001) at the univariate analysis.

Among the dosimetric factors, only V_{40Gy} and $D_{0,1cc}$ were included in the multivariate Cox regression, because they were

TABLE 4 | Receiver operating characteristics (ROC) analysis for G2 alopecia at the end of radiotherapy.

Dosimetric variable	AUC	*p*-value for AUC	Cut-off value	Sensitivity, %	Specificity, %	Incidence of acute G2 alopecia		Fisher exact test *p*-value
						Low risk, %	High risk, %	
$D_{0.1cc}$	0.740	**0.008**	*36.2 Gy*	87.1	68.7	50.0%	93.7%	**0.0000**
Mean dose	0.714	**0.02**	*6.9 Gy*	87.1	56.2	55.0%	91.3%	**0.0006**
V_{16Gy}	0.776	**0.001**	*16.7 cc*	92.9	62.5	37.5%	92.9%	**0.0000**
V_{20Gy}	0.792	**0.0003**	*5.2 cc*	100.0	56.2	0%	91.4%	**0.0000**
V_{25Gy}	0.768	**0.002**	*5.5 cc*	85.9	68.7	52.2%	93.5%	**0.0000**
V_{30Gy}	0.756	**0.003**	*2.3 cc*	85.9	68.7	52.2%	93.6%	**0.0000**
V_{35Gy}	0.736	**0.005**	*0.7 cc*	82.4	68.7	57.7%	93.3%	**0.0005**
V_{40Gy}	0.685	**0.02**	*0.6 cc*	72.9	75.0	65.7%	93.9%	**0.0004**
V_{43Gy}	0.670	**0.04**	*0.1 cc*	70.6	68.7	69.4%	92.3%	**0.004**

$D_{0.1cc}$, Dose to 0.1 cc of the scalp volume; V_{xGy}, percentage of the scalp volume receiving ≥ x Gy; AUC, area under curve at ROC analysis.
Bold text indicates statistical significance.

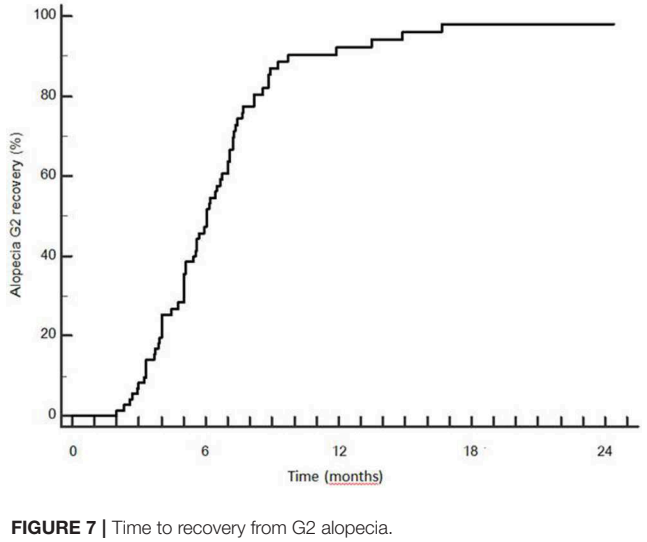

FIGURE 7 | Time to recovery from G2 alopecia.

shown to be independent predictors of chronic G2-alopecia according to correlation coefficient r. Multivariate analysis confirmed the predictive value of age ($p = 0.0002$) and V_{40Gy} ($p = 0.02$).

DISCUSSION

Hair loss, either temporary or permanent, is one of the most stressful side effects for patients undergoing oncologic treatment (1–5). Radiation-induced alopecia may permanently alter the self-perception of the neurooncological patients and have a significant impact on their quality of life (2, 5).

To our knowledge, this is the first study reporting a dose-volume analysis of the scalp describing the risk of hair-loss following a photon-based, conventionally fractionated VMAT treatment on a limited brain volume. Herein we reported a dosimetric analysis based on a TPS-based calculation to find a dose-response relationship for acute and chronic alopecia. Besides, although some authors reported about the possibility of hair regrowth within some months after irradiation (19, 20), to our knowledge, this is the first observational study focusing on the analysis of recovery time of the scalp damage.

Dose-Response Relationship for Acute Alopecia

On review of the available literature regarding photon-based radiotherapy, the doses that have been reported to cause hair-loss varied widely. Doses as low as 2 and 3 Gy in a single fraction might cause temporary alopecia according to some authors (4, 10, 21, 22). In a study regarding the use of VMAT for whole-brain irradiation (WBRT) in patients with multiple brain metastases (19), the authors hypothesized that the threshold dose for temporary alopecia is around 10 Gy in 5 fractions. By contrast, Archambeau et al. (23) described that acute epilation may be produced by a total dose of 20 Gy in conventional fractionation.

The risk of acute alopecia during IMRT has been explored also for patients with head and ncek cancer: Rosenthal et al. (24) provided recursive partitioning analysis in order to estimate dose thresholds associated with observed toxicities in a series of patients with oropharyngeal cancer treated with IMRT: they found that alopecia in the occipital region occurred more frequently when scalp maximum dose was >30 Gy (48% of cases) vs. <30 Gy (19% of cases).

Our experience confirmed that acute alopecia may be caused by very low doses: acute G2 alopecia developed also in areas where D_{mean} may be as low as 1.9 Gy.

However, the fact that we found significant differences regarding the dose received by the whole scalp between patients that did not develop alopecia and patients who presented acute hair-loss, demonstrated that a dose relationship with acute alopecia exists. That was also confirmed by the dosimetric analysis regarding the areas of alopecia: G2-alopecia$_{end-of-RT}$ received significantly higher doses than G1-alopecia$_{end-of-RT}$ (**Table 3**). Lastly, the relationship between dose and acute alopecia was also evidenced by the ROC analysis that showed that

TABLE 5 | Dosimetric comparison of the scalp of the patients who had persistent alopecia at 9 months compared with the scalp of the patients who had complete recover within 9 months: mean values and standard deviations (in brackets) of dosimetric variables.

ROI	*n*	Mean $D_{0.1cc}$ (Gy)	Mean D_{mean} (Gy)	Mean $V_{16\,Gy}$ (cc)	Mean $V_{20\,Gy}$ (cc)	Mean $V_{25\,Gy}$ (cc)	Mean $V_{30\,Gy}$ (cc)	Mean $V_{35\,Gy}$ (cc)	Mean $V_{40\,Gy}$ (cc)	Mean $V_{43\,Gy}$ (cc)
Scalp patients with alopecia at 9 month–follow up	8	53.2 (± 4.1)	14.1 (± 4.4)	78.7 (± 31.3)	57.8 (± 25.0)	40.1 (± 17.4)	28.4 (± 12.7)	19.6 (± 9.7)	12.6 (± 8.4)	8.7 (± 7.6)
Scalp patients with complete recovery from alopecia within 9 months after RT	66	46.7 (± 10.6)	11.6 (± 4.7)	66.8 (± 39.3)	49.5 (± 35.4)	34.7 (± 29.9)	23.4 (± 24.3)	14.8 (± 18.7)	8.9 (± 13.3)	6.4 (± 10.4)
p-value from Mann-Whitney Test		0.12	0.09	0.29	0.34	0.24	0.14	0.053	**0.028**	**0.036**

$D_{0.1cc}$, dose received by 0.1 cc; D_{mean}, mean dose; V_{xGy}, percentage of the scalp volume receiving ≥ x Gy.
Bold text indicates statistical significance.

TABLE 6 | Receiver operating characteristics (ROC) analysis for G2 alopecia at 9 months after the end of radiotherapy.

Dosimetric variable	AUC	*p*-value for AUC	Cut-off	Sensitivity, %	Specificity, %	Incidence of G2 alopecia at 9 months		Fisher exact test *p*-value
						Low risk, %	High risk, %	
$D_{0.1cc}$	0.684	**0.008**	*47.6 Gy*	100.00	51.5	0.0%	17.4%	**0.007**
Mean dose	0.669	**0.04**	*10.1 Gy*	100.00	43.9	0.0%	14.0%	**0.02**
V_{30Gy}	0.662	**0.04**	*11.4 cc*	100.00	39.4	0.0%	13.1%	**0.04**
V_{35Gy}	0.710	**0.001**	*9.3 cc*	100.00	54.5	0.0%	17.4%	**0.005**
V_{40Gy}	0.738	**<0.0001**	*5.4 cc*	100.00	63.64	0.0%	21.0%	**0.0000**
V_{43Gy}	0.725	**0.0002**	*2.2 cc*	100.00	59.1	0.0%	19.5%	**0.001**

$D_{0.1cc}$, Dose to 0.1 cc of the scalp volume;V_{xGy}, percentage of the scalp volume receiving ≥ x Gy; AUC, area under curve at ROC analysis.
Bold text indicates statistical significance.

the most important predictors of acute alopecia were V_{16Gy} and V_{20Gy} (**Table 4**).

Consequently, during the treatment planning process, the doses to the scalp should be kept as low as possible. However, by maintaining $V_{16Gy} < 16.7$ cc and $V_{20Gy} < 5.2$ cc, the risk of acute alopecia may be limited. Since these two variables were found to be interdependent, considering the better AUC and statistical significance at the ROC analysis, we would suggest to try to meet preferably the specified constraints for V20, with the aim of reducing the risk of acute alopecia.

Moreover, we also found that 50% of the patients who received $D_{0.1cc}$ of 33 Gy developed acute alopecia at the end of radiotherapy. All these data may be precious to predict the risk of acute hairloss when we talk with the patients about the toxicity of the radiation treatment.

Dose-Response Relationship for Chronic Alopecia

Our data showed that a dose-effect relationship exists for chronic alopecia as well: the scalp of patients who completely recovered from G2 alopecia received lower doses than the scalp of patients who had persistent alopecia at 9 months. Of note, the difference between these two groups of patients was significant only in terms of high doses (V_{40Gy}, V_{43Gy}) (**Table 6**). Noteworthy, at ROC analysis lower doses (<30 Gy) were not associated with chronic G2-alopecia, while the most important predictors of persistent alopecia were V_{40Gy} and V_{43Gy} (**Table 7**).

All these data taken together indicate that, although low doses (i.e., 16–20 Gy), are critical for acute alopecia (that is likely to recover within some months), higher doses (i.e., 40–43 Gy) are crucial for persistent alopecia.

To our knowledge, the only existing dosimetric study finding a dose-response relationship that described the probability of alopecia after photon-based radiotherapy has been reported in 2004 by Lawenda et al. (25). The authors retrospectively reviewed 26 patients and they concluded that follicle doses of 43 Gy are associated with a 50% risk of permanent alopecia. Their results are notably different from our findings due to two main reasons. First, the authors provided a very rough estimate of the follicle dose, based on the sum of the entrance and exit doses for each contributing radiation field, according to a formula that took into account the absolute dose delivered to the isocenter for the radiation field of interest; by contrast, the present study provided an accurate calculation of the dose to the scalp using a dose-volume histogram analysis calculated by the treatment planning system. Secondly and even more importantly, the patients included in the study from Lawenda et al. were treated with simple conventional photon techniques (typical field arrangements included parallel-opposed fields and right-angle field pairs). On the other hand, all the patients in our series were treated with VMAT-technique. The numerous beam angles and resultant highly conformal dose distributions of intensity-modulated treatments (IMRT and VMAT) make these modalities particularly suited to scalp dose reduction. The use of arcs, typical

TABLE 7 | Kaplan Meier analysis for factors impacting on the recovery probability from G2 alopecia.

Variable	pts	Events	%recovery	*p*-value log rank test
Sex				
F	33	28	–	0.99
M	41	37		
Age				
≤14	4	4	100.0	**0.01**
>14	70	61	97.9	0.70
≤50	30	28	–	
>50	44	37		
Smoking history				
No	51	46	–	0.54
Yes	23	19		
Antiepilectic drugs				
No	17	16	–	0.14
Yes	57	49		
Concomitant chemotherapy				
No	25	23	–	0.14
Yes	49	42		
Sequential chemotherapy				
No	21	19	–	0.17
Yes	53	46		
$D_{0.1\ cc}$				
<47.6 Gy	34	30	99.9	**0.001**
≥47.6 Gy	40	35	96.6	
D_{mean}				
<10.1 Gy	29	27	99.9	**0.002**
≥10.1 Gy	45	38	96.7	
$V_{30\ Gy}$				
<11.4 cc	26	24	99.9	**0.0001**
≥11.4 cc	48	41	97.0	
$V_{35\ Gy}$				
<9.3 cc	36	32	99.9	**0.0001**
≥9.3 cc	38	33	96.4	
$V_{40\ Gy}$				
<5.4 cc	42	38	99.9	**0.0001**
≥5.4 cc	32	27	95.6	
$V_{43\ Gy}$				
<2.2 cc	34	34	99.9	**0.0001**
≥2.2 cc	40	31	96.9	
Total	*74*	*65*		

Bold text indicates statistical significance.

TABLE 8 | Univariate Cox regression for variables impacting the recovery probability from G2 alopecia.

Variable	*p*-value	HR	95% CI
Age > 14 y	**0.017**	0.27	0.09–0.80
$D_{0.1cc}$ > 47.6 Gy	**0.001**	0.40	0.23–0.69
D_{mean} > 10.1 Gy	**0.003**	0.43	0.24–0.75
V_{30Gy} > 11.4 cc	**0.0001**	0.39	0.22–0.67
V_{35Gy} > 9.3 cc	**0.0001**	0.33	0.19–0.57
V_{40Gy} > 5.4 cc	**0.0001**	0.35	0.20–0.63
V_{43Gy} > 2.2 cc	**0.0001**	0.36	0.21–0.64

$D_{0.1cc}$, Dose to 0.1 cc of the scalp volume;V_{xGy}, percentage of the scalp volume receiving ≥ x Gy; HR, Hazard Ratio; CI, Confidence interval. Bold text indicates statistical significance.

of the VMAT technique, may further minimize the high doses to the scalp because the surface dose is distributed over the length of the arc (19). The investigation of Penoncello et al. (26) confirmed that VMAT may be superior in minimizing dose to the scalp than static-field IMRT.

The possibility to reduce the dose to the scalp with IMRT techniques has been extensively explored in patients treated WBRT for brain metastases (10–12, 19, 27). These studies differ from the present study for several reasons: firstly, the number of patients included was significantly lower (range 6(12)−17(27) patients) compared to our experience; secondly, the prescription dose for WBRT (EQD2 28–36 Gy) is significantly different than the one used for primary tumors (EQD2 50, 4–60 Gy). Thirdly, most of them did not include clinical data on alopecia: plans of patients who had been previously treated with conventional opposed lateral fields were simply replanned with IMRT to confirm the potential advantage of IMRT techniques in reducing scalp dose (10, 11, 28–30). Lastly, although some series including clinical evaluation of alopecia exist (12, 27, 28), their authors did not generate hypotheses about dose/permanent hair loss relationship and they did not provide clear dose constraints to minimize the risk of chronic alopecia.

Due to the very superficial location of the scalp, the existing uncertainty in the superficial dose calculation deserves some considerations. The accuracy of dose modeling in the build-up region mainly depends on the dose calculation algorithm used in a specific treatment planning system (TPS) (31). MC simulations have been used as a reference tool for superficial dosimetry evaluation of dose calculation algorithms in the commercially available TPS (32, 33) because they were shown to be consistent with measurements obtained by extrapolation chambers (34, 35). To our knowledge, there are no published studies specifically evaluating the accuracy of dose calculation in the build-up region for Monaco TPS. However, since Monaco TPS uses a MonteCarlo algorithm, we can assume that superficial dose is estimated by this TPS with reasonable accuracy.

In this clinical experience, the majority of patients (95%) presented acute alopecia in a wide area of the scalp (by average 30.2%). This phenomenon is due to the fact the highly conformal dose distribution achieved with VMAT comes with the cost of a larger volume of normal tissue receiving low radiation doses that are sufficient to cause an acute injury to the hair bulbs.

On the other hand, VMAT led to satisfying results in terms of hair regrowth (actuarial recovery rate = 98.1% at 18 months after the end of radiotherapy) because of the high conformality and rapid dose fall-off. We believe that the application of our dosimetric findings may further decrease the risk of radiation-induced hair-loss: maintaining V_{40Gy} < 5.4 and V_{43Gy} < 2.2 cc may help in reducing the risk of radiation-induced chronic alopecia. Since these two variables were found to be interdependent, considering the AUC and statistical significance at the ROC analysis, we would suggest to try to meet preferably the specified constraints for V40 in order to minimize the risk

of chronic alopecia. Noteworthy, the importance of V40 was confirmed also by the multivariate analysis.

Time to recovery was related to the dose, as shown by Kaplan–Meier analysis and Cox regression analysis that confirmed the significant impact of the dichotomous dosimetric variables on recovery probability during the follow-up. Furthermore, $D_{0,1cc}$ maintained significance also when tested as a continuous variable ($p = 0{,}001$) at the univariate Cox regression analysis.

Age $\leq$ 14 was the only clinical factor to be significantly associated with a greater probability of recovery. Younger age was identified as a positive factor also in the series of Rogers et al. (36).

In our experience, chemotherapy was not related to a higher risk of alopecia. Of note, the majority of chemotherapy-treated patients in the present series received temozolomide, whereas, in other experiences where this relationship was found, other drugs with a stronger alopecia-inducing power were used (10, 25). Notably, increased risk due to smoking history was not evidenced in our series.

Another point to mention is that the definition of dosimetric thresholds for chronic alopecia may also help in estimating the risk of this relevant side effect when discussing the toxicity of treatment with our patients. So far, indeed, the scarcity of available data about radiation-induced hair loss has led to great difficulties in providing risk estimates for given doses when radiation treatment is discussed with patients (37).

Keypoints and Pitfalls of the Study

Strengths of this study are the following: first, given the little literature on possible predictors of radiation induced alopecia in patients treated with photons, this study adds new information, especially considering the fact that it concerns VMAT technique. Secondly, to our knowledge, this is the first existing observational study with detailed measurements of the endpoint on patients treated with photons. On the other hand, our study has several limitations: the lack of a validation cohort to confirm our dosimetric results is probably the most important shortcoming. Secondly, a quality-of-life assessment or a patient-reported outcome data to describe how the patients psychologically experienced the hair loss would have added value to our research. Thirdly, an important drawback of our work is the lack of a more advanced modeling to robustly predict the risk of radiation induced alopecia. In this regard, a very recent study (38) provided normal tissue complication probability (NTCP) model for alopecia in patients treated with scanning beam protontherapy. Although it is necessary to take into account the different dose distribution in the superficial tissues for protons (which makes their results not applicable to photon-based radiotherapy), it is of interest to know that relative scalp surface receiving 21 Gy (S_{21Gy}) and age were selected as predictive factors for acute G2 alopecia whereas $D_{2\%}$ (near maximum scalp dose) was found to be related to permanent G2 alopecia.

CONCLUSIONS

We recommend contouring the scalp and including it into the organs at risk list.

According to our results, the steep gradient typical of VMAT gives the possibility to limit the volume of the scalp that receives higher doses that are associated with a greater risk of chronic G2-alopecia. At the same time, by using VMAT, a great proportion of the scalp volume will receive low doses that are sufficient to cause acute but transient alopecia in the majority of patients.

Our study provided new constraints for the scalp to use during the inverse planning process that may help in reducing the probability of hair-loss. Once a treatment is planned, these dose thresholds may help also in estimating the risk of alopecia for each single case. Future developments of our research may provide a validation cohort to confirm further improvement in terms of alopecia-free survival.

DATA AVAILABILITY STATEMENT

The datasets generated for this study are available on request to the corresponding author.

ETHICS STATEMENT

Ethical review and approval was not required for the study on human participants in accordance with the local legislation and institutional requirements. Written informed consent to participate in this study was provided by the participants' legal guardian/next of kin. Written informed consent was obtained from the individual(s) for the publication of any potentially identifiable images or data included in this article.

AUTHOR CONTRIBUTIONS

SS and GS conceived the study. SS was in charge of overall direction and planning. MP, FT, MT, GC, ML, EO, CD, RG, and VC performed the contouring of the cases at the treatment planning system and were responsible for the clinical evaluation of the alopecia at the end of the treatment and during the follow-up. CT, LM, and SP were responsible for the plans. SS processed the experimental data. CS performed the statistical analysis. SS wrote the manuscript with inputs from DG, PB, BD, MM, ID, GF, VD, CT, LM, SP, and LL. All authors discussed the results and contributed to final manuscript.

REFERENCES

1. Freites-Martinez A, Shapiro J, Goldfarb S, Nangia J, Jimenez JJ, Paus R, et al. Hair disorders in patients with cancer. *J Am Acad Dermatol*. (2019) 80:1179–96. doi: 10.1016/j.jaad.2018.03.055
2. Irvine L, Jodrell N. The distress associated with cranial irradiation: a comparison of patient and nurse perceptions. *Cancer Nurs*. (1999) 22:126–33 doi: 10.1097/00002820-199904000-00004
3. Steinmann D, Paelecke-Habermann Y, Geinitz H, Aschoff R, Bayerl A, Bölling T, et al. Prospective evaluation of quality of life effects in patients undergoing palliative radiotherapy for brain metastases. *BMC Cancer*. (2012) 12:283. doi: 10.1186/1471-2407-12-283
4. Haider M, Hamadah I, Almutawa A. Radiation- and chemotherapy-induced permanent alopecia: case series. *J Cutan Med Surg*. (2013) 17:55–61. doi: 10.2310/7750.2012.12033

5. Munro AJ, Biruls R, Griffin AV, Thomas H, Vallis KA. Distress associated with radiotherapy for malignant disease: a quantitative analysis based on patients perceptions. *Br J Cancer*. (1989) 60:370–4. doi: 10.1038/bjc.1989.287
6. Lee, NY, Terezakis SA. Intensity-modulated radiation therapy. *J Surg Oncol*. (2008) 97:691–6. doi: 10.1002/jso.21014
7. Gondi V, Tomé WA, Mehta MP. Why avoid the hippocampus? A comprehensive review. *Radiother Oncol*. (2010) 97:370–6 doi: 10.1016/j.radonc.2010.09.013
8. Beddok A, Faivre JC, Coutte A, Guévelou JL, Welmant J, Clavier JB, et al. Practical contouring guidelines with an MR-based atlas of brainstem structures involved in radiation-induced nausea and vomiting. *Radiother Oncol*. (2019) 130:113–20. doi: 10.1016/j.radonc.2018.08.003
9. Lee WS, Ro BI, Hong SP, Bak H, Sim WY, Kim DW, et al. A new classification of pattern hair loss that is universal for men and women: basic and specific (BASP) classification. *J Am Acad Dermatol*. (2007) 57:37–46. doi: 10.1016/j.jaad.2006.12.029
10. Roberge D, Parker W, Niazi TM, Olivares M. Treating the contents and not the container: dosimetric study of hair-sparing whole brain intensity modulated radiation therapy. *Technol Cancer Res Treat*. (2005) 4:567–70. doi: 10.1177/153303460500400510
11. Mancini BR, Wilkinson JB, Kim LH, Shaitelman SF, Yan D, Ionascu D, et al. Intensity-modulated radiation therapy or volumetric-modulated arc therapy to reduce alopecia, xerostomia, and otitis after whole brain radiation therapy for brain metastases: a planning analysis. *J Radiat Oncol*. (2013) 2:177–83. doi: 10.1007/s13566-013-0090-y
12. Mahadevan A, Sampson C, LaRosa S, Floyd SR, Wong ET, Uhlmann EJ, et al. Dosimetric analysis of the alopecia preventing effect of hippocampus sparing whole brain radiation therapy. *Radiat Oncol*. (2015) 10:245 doi: 10.1186/s13014-015-0555-9
13. Scoccianti S, Detti B, Gadda D, Greto D, Furfaro I, Meacci F, et al. Organs at risk in the brain and their dose-constraints in adults and in children: a radiation oncologist's guide for delineation in everyday practice. *Radiother Oncol*. (2015) 114:230–8. doi: 10.1016/j.radonc.2015.01.016
14. Metz CE. Basic principles of ROC analysis. *Semin Nucl Med*. (1978) 8:283–98. doi: 10.1016/S0001-2998(78)80014-2
15. Zweig MH, Campbell G. Receiver-operating characteristic (ROC) plots: a fundamental evaluation tool in clinical medicine. *Clin Chem*. (1993) 39:561–77. doi: 10.1093/clinchem/39.4.561
16. Pinnix CC, Cella L, Andraos TY, Ayoub Z, Milgrom SA, Gunther J, et al. Predictors of hypothyroidism in hodgkin lymphoma survivors after intensity modulated versus 3-dimensional radiation therapy. *Int J Radiat Oncol Biol Phys*. (2018) 101:530–40. doi: 10.1016/j.ijrobp.2018.03.003
17. Cella L, Conson M, Caterino M, De Rosa N, Liuzzi R, Picardi M, et al. Thyroid V30 predicts radiation-induced hypothyroidism in patients treated with sequential chemo-radiotherapy for hodgkin's lymphoma. *Int J Radiat Oncol Biol Phys*. (2012) 82:1802–8. doi: 10.1016/j.ijrobp.2010.09.054
18. Youden WJ. An index for rating diagnostic tests. *Cancer*. (1950) 3:32–5. doi: 10.1002/1097-0142
19. De Puysseleyr A, Van De Velde J, Speleers B, Vercauteren T, Goedgebeur A, Van Hoof T, et al. Hair-sparing whole brain radiotherapy with volumetric arc therapy in patients treated for brain metastases: dosimetric and clinical results of a phase II trial. *Radiat Oncol*. (2014) 9:170. doi: 10.1186/1748-717X-9-170
20. Olsen E. Anagen hair-loss: radiation. *In:* Olsen EA, editor. *Disorders of Hair Growth: Diagnosis and Treatment*. New York, NY: McGraw Hill; Libraries Australia (1994). p. 225–226
21. Vaccaro M, Guarneri F, Brianti P, Cannavò SP. Temporary radiation-induced alopecia after embolization of a cerebral arteriovenous malformation. *Clin Exp Dermatol*. (2015) 40:88–90. doi: 10.1111/ced.12472
22. Seol JE, Kim DH, Park SH, Cho GJ, Kim H. Three cases of radiation-induced temporary alopecia with hair microscopic examination: "coudability hair" might not be specific for alopecia areata. *Int J Trichology*. (2018) 10:40–3. doi: 10.4103/ijt.ijt_74_17
23. Archambeau JO, Pezner R, Wasserman T. Pathophysiology of irradiated skin and breast. *Int J Radiat Oncol Biol Phys*. (1995) 31:1171–85. doi: 10.1016/0360-3016(94)00423-I
24. Rosenthal DI, Chambers MS, Fuller CD, Rebueno NC, Garcia J, Kies MS, et al. Beam path toxicities to non-target structures during intensity-modulated radiation therapy for head and neck cancer. *Int J Radiat Oncol Biol Phys*. (2008) 72:747–55. doi: 10.1016/j.ijrobp.2008.01.012
25. Lawenda BD, Gagne HM, Gierga DP, Niemierko A, Wong WM, Tarbell NJ, et al. Permanent alopecia after cranial irradiation: dose-response relationship. *Int J Radiat Oncol Biol Phys*. (2004) 60:879–87. doi: 10.1016/j.ijrobp.2004.04.031
26. Penoncello GP, Ding GX. Skin dose differences between intensity-modulated radiation therapy and volumetric-modulated arc therapy and between boost and integrated treatment regimens for treating head and neck and other cancer sites in patients. *Med Dos*. (2016) 41:80–6. doi: 10.1016/j.meddos.2015.09.001
27. Kao J, Darakchiev B, Conboy L, Ogurek S, Sharma N, Ren X, et al. Tumor directed, scalp sparing intensity modulated whole brain radiotherapy for brain metastases. *Technol Cancer Res Treat*. (2015) 14:547–55. doi: 10.7785/tcrt.2012.500426
28. Ting J, Thomas CR, McClure JA, Scarbrough TJ. "Alopecia-less" whole brain radiotherapy (WBRT) via IMRT: preliminary experience and outcomes. *Int J Radiat Oncol Biol Phys*. (2005) 63(Suppl. 1):S263–4. doi: 10.1016/j.ijrobp.2005.07.451
29. Witek M, Vahknenko Y, Siglin J, Harrison A, Xiao Y, Lui H, et al. Dose reduction to the scalp with hippocampal sparing is achievable with intensity modulated radiotherapy. *Int J Med Phys Clin Eng Radiat Oncol*. (2014) 3:176–82. doi: 10.4236/ijmpcero.2014.33023
30. Pokhrel D, Sood S, Lominska C, Kumar P, Badkul R, Jiang H, et al. Potential for reduced radiation-induced toxicity using intensity-modulated arc therapy for whole-brain radiotherapy with hippocampal sparing. *J Appl Clin Med Phys*. (2015) 16:131–41. doi: 10.1120/jacmp.v16i5.5587
31. Panettieri V, Barsoum P, Westermark M, Brualla L, Lax I. AAA and PBC calculation accuracy in the surface build-up region in tangential beam treatments. Phantombreast case study with the MonteCarlo code PENELOPE. *Radiother Oncol*. (2009) 93:94–101. doi: 10.1016/j.radonc.2009.05.010
32. Cao Y, Yang X, Yang Z, Qiu X, Lv Z, Lei M, et al. Superficial dose evaluation of four dose calculation algorithms. *Radiat Phys and Chem*. (2017) 137:23–8. doi: 10.1016/j.radphyschem.2016.02.032
33. Wang L, Cmelak AJ, Ding GX. A simple technique to improve calculated skin dose accuracy in a commercial treatment planning system. *J Appl Clin Med Phys*. (2018) 19:191–7. doi: 10.1002/acm2.12275
34. Abdel-Rahman W, Seuntjens JP, Verhaegen F, Deblois F, Podgorsak EB. Validation of montecarlo calculated surface doses for megavoltage photon beams. *Med Phys*. (2005) 32:286–98. doi: 10.1118/1.1829401
35. Devic S, Seuntjens J, Abdel-Rahman W. Accurate skin dose measurements using radiochromic film in clinical applications. *Med Phys*. (2006) 33:1116–24. doi: 10.1118/1.2179169
36. Rogers S, Donachie P, Sugden E, Sharpe G, English M, Robinson K, et al. Comparison of permanent hair-loss in children with standard risk PNETS of the posterior fossa following radiotherapy alone or chemotherapy and radiotherapy after surgical resection. *Pediatr Blood Cancer*. (2011) 57:1074–6. doi: 10.1002/pbc.22992
37. Shakespeare TP, Dwyer M, Mukherjee R, Yeghiaian-Alvandi R, Gebski V. Estimating risks of radiotherapy complications as part of informed consent: the high degree of variability between radiation oncologists may be related to experience. *Int J Radiat Oncol Biol Phys*. (2002) 54:647–53. doi: 10.1016/S0360-3016(02)02996-6
38. Palma G, Taffelli A, Fellin F, D'Avino V, Scartoni D, Tommasino F, et al. Modelling the risk of radiation induced alopecia in brain tumor patients treated with scanned proton beams. *Radiother Oncol*. (2019) 144:127–34. doi: 10.1016/j.radonc.2019.11.013

Conflict of Interest: The authors declare that the research was conducted in the absence of any commercial or financial relationships that could be construed as a potential conflict of interest.

frontiers in Oncology

ORIGINAL RESEARCH
published: 15 April 2020
doi: 10.3389/fonc.2020.00430

Prognostic Significance of Baseline Neutrophil Count and Lactate Dehydrogenase Level in Patients With Esophageal Squamous Cell Cancer Treated With Radiotherapy

He-San Luo[1†], Hong-Yao Xu[1†], Ze-Sen Du[2], Xu-Yuan Li[3], Sheng-Xi Wu[1], He-Cheng Huang[1] and Lian-Xing Lin[1]*

[1] Department of Radiation Oncology, Shantou Central Hospital, Affiliated Shantou Hospital of Sun Yat-sen University, Shantou, China, [2] Department of Surgical Oncology, Shantou Central Hospital, Affiliated Shantou Hospital of Sun Yat-sen University, Shantou, China, [3] Department of Medical Oncology, Shantou Central Hospital, Affiliated Shantou Hospital of Sun Yat-sen University, Shantou, China

OPEN ACCESS

Edited by:
Giuseppe Sanguineti, Regina Elena National Cancer Institute, Italy

Reviewed by:
Sunyoung Jang, Princeton Radiation Oncology Center, United States
Vivek Verma, Allegheny General Hospital, United States

****Correspondence:***
He-San Luo
luohesan@163.com

[†] These authors have contributed equally to this work

Specialty section:
This article was submitted to Radiation Oncology, a section of the journal Frontiers in Oncology

Received: *22 September 2019*
Accepted: *10 March 2020*
Published: *15 April 2020*

Citation:
Luo H-S, Xu H-Y, Du Z-S, Li X-Y, Wu S-X, Huang H-C and Lin L-X (2020) Prognostic Significance of Baseline Neutrophil Count and Lactate Dehydrogenase Level in Patients With Esophageal Squamous Cell Cancer Treated With Radiotherapy. Front. Oncol. 10:430. doi: 10.3389/fonc.2020.00430

Background: This present study aimed to explore the prognostic value of pretreatment neutrophil and lactate dehydrogenase (LDH) and to develop a prognostic risk scoring model to predict prognosis in esophageal squamous cell cancer (ESCC) patients treated with definitive radiotherapy.

Methods: Retrospectively collected data of patients who received definitive radiotherapy for ESCC at Shantou Central Hospital between January 2009 and December 2015 were included for the analysis. The association between the level of LDH and neutrophil and clinicopathological characteristics were analyzed. We performed univariate and multivariate analyses to identify the prognostic predictors for patients with ESCC. Based on the results, we also developed a prognostic risk scoring model and assessed its predictive ability in the subgroups.

Results: A total of 567 patients who received definitive radiotherapy for ESCC were included in the present study. The optimal cutoff values were 4.5×10^9/L, 3.25, and 220 U/L for neutrophil, neutrophil-to-lymphocyte ratio (NLR), and LDH, respectively. A high level of LDH was significantly associated with advanced N stage ($p = 0.031$), and neutrophil count was significantly associated with gender ($p = 0.001$), T stage ($p < 0.001$), N stage ($p = 0.019$), clinical stage ($p < 0.001$), and NLR ($p < 0.001$). Multivariate survival analysis identified gender ($p = 0.006$), T stage ($p < 0.001$), N stage ($p = 0.008$), treatment modality ($p < 0.001$), LDH level ($p = 0.012$), and neutrophil count ($p = 0.038$) as independent prognostic factors for overall survival. Furthermore, a new prognostic risk scoring (PRS) model based on six prognostic factors was developed, in which the patients were divided into three groups with distinct prognosis ($\chi 2 = 67.94$, $p < 0.0001$).

Conclusions: Elevated baseline LDH level and neutrophil count predicted poor prognosis for ESCC patients treated with definitive radiotherapy. A PRS model comprised of LDH, neutrophil count, and other prognostic factors would help identify the patients who would benefit the most from definitive radiotherapy.

Keywords: prognosis, esophageal squamous cell cancer, definitive radiotherapy, LDH, neutrophil

INTRODUCTION

Esophageal cancer (EC) is one of the most common digestive malignant tumors, with high recurrence rate and poor overall survival (OS) (1). For patients with early EC, surgery is the mainstay of treatment (2). The majority of patients with locally advanced EC lost the opportunity for surgery at the time of diagnosis. Definitive concurrent chemoradiotherapy (dCRT) has been recommended as a standard treatment and plays important roles in these patients (1). However, the effectiveness of radiotherapy varies greatly among different patients, even patients at the same TNM stage and who received similar radiotherapy regimens, suggesting that there were some other factors affecting the effectiveness of radiotherapy, including patients' characteristics, tumor subsite, and hematological parameters (3–5). To our knowledge, no widely used prediction model about prognosis has been established in patients with esophageal squamous cell carcinoma (ESCC) treated with radiotherapy. Thus, it is critical to identify more accurate prognostic indicators and to develop a reliable prediction model for estimating the prognosis of patients with ESCC treated with radiotherapy.

The inflammation process has been proposed to be an important feature in patients with malignant tumors (6), which is involved in the progression of tumorigenesis, disease development, and patient prognosis (7, 8). Furthermore, some routinely tested blood parameters, such as neutrophil count, lymphocyte count, and lactate dehydrogenase (LDH) level, have been demonstrated as potential inflammatory biomarkers and have prognostic value in patients with cancers (9–11). Neutrophils are acknowledged as the first line of defense against inflammations and infections, as well as play an important role in the tumor microenvironment (TME) (12, 13). Previous studies have shown that tumor-associated neutrophil (TAN) was capable to suppress the immune system in the TME, which results in treatment resistance and promotes cancer development (14, 15). Patients with low neutrophil count were also found to exhibit better radiosensitivity (16). However, the predictive value of neutrophil count in the prognosis of ESCC patients treated with radiotherapy is still unclear. Recently, the prognostic value of LDH has been widely investigated in various cancers, such as metastatic renal cell carcinoma (17), breast cancer (18), nasopharyngeal carcinoma (19), prostate cancer (20), lymphoma (21), non–small cell lung cancer (22), and ESCC (23, 24). Although LDH and neutrophil count are reliable prognostic predictors, it is still not clear whether they can be combined together in a prognostic risk score model to predict the prognosis of ESCC patients treated with radiotherapy.

In this study, we aimed to explore the role of neutrophil count and LDH level in the prognosis of patients with ESCC treated with radiotherapy. We performed univariate and multivariate analyses to identify the prognostic factors for the ESCC patients. According to the results of the multivariate analysis, we devised a prognostic risk scoring model for estimating the prognosis of ESCC patients treated with radiotherapy.

Abbreviations: LDH, lactate dehydrogenase; ESCC, esophageal squamous cell cancer; dCRT, definitive chemoradiotherapy; PRS, prognostic risk scoring; EC, esophageal cancer; OS, overall survival; EAC, esophageal adenocarcinoma; GTV, gross tumor volume; GTVnd, nodal gross tumor volume; CTV, clinical target volume; CTVt, tumor clinical target volume; CTVnd, nodal clinical target volume; PTV, planning target volume; NLR, neutrophil-to-lymphocyte ratio; ROC, receiver operating characteristics; RFS, recurrence-free survival; CR, complete response.

PATIENTS AND METHODS

Study Design

We retrospectively reviewed the patients receiving definitive radiotherapy for EC at the Department of Radiation Oncology, Shantou Central Hospital during the period from January 2009 to December 2015. Only patients pathologically diagnosed as ESCC were included in this study. Patients with non-ESCC tumors were excluded from this study. The remaining patients were excluded if they met the following exclusion criteria: (1) patients with distant metastatic disease; (2) patients who received low-dose palliative radiotherapy (<50.4 Gy for patients treated with radiotherapy without chemotherapy and <60 Gy for patients treated with chemoradiotherapy); (3) patients who received preoperative or postoperative adjuvant radiotherapy; (4) patients who had recurrent disease and received radiotherapy for salvage purposes; (5) patients who failed to complete therapy; and (6) patients who had other primary tumor. This study was approved by the Institutional Committee of the Shantou Central Hospital on Human Rights. Disease of the patients was staged according to the sixth edition of AJCC TNM classification for EC.

Radiotherapy Protocols

Radiotherapy was delivered by three-dimensional conformal radiation therapy or intensity-modulated radiation therapy technique in this study. A Varian IX or Varian 23EX linear accelerator was used to deliver the radiotherapy treatment plan. The treatment planning approach has been reported in our previous study (25). Briefly, the gross tumor volume (GTV) includes the EC (GTVp) and the positive regional lymph nodes (GTVnd). The delineation of GTV was determined by CT, barium esophagogram, endoscopic examination, or PET imaging. The GTVp plus a 0.5–1cm radial margin and a 2.5–3 cm proximal and distal margin and the GTVnd plus a 0.5–0.8 cm margin were defined as CTV. The planning target volume (PTV) encompassed the CTV plus a 0.5–1 cm margin. All patients received simultaneous integrated boost (SIB) radiotherapy, which had been reported in a recent phase 1/2 trial conducted by Chen et al. (26). The prescribed dose was 60–66 Gy to GTV in 28–30 fractions, five fractions per week, and at least 50.4 Gy to CTV in 28 fractions, five fractions per week. Two cycles of platinum-based chemotherapy combined with 5-fluorouracil or a taxane (docetaxel or paclitaxel) were administered on the patients concurrently with radiotherapy.

Data of Hematological Index Collection

The pretreatment data of neutrophil count, lymphocyte count, and LDH level were collected from the test reports. The cutoff value for the LDH level was the upper limit of normal (ULN) values set (220 U/L) of the biochemical detector used in our

hospital. The neutrophil count divided by the lymphocyte count was defined as the neutrophil-to-lymphocyte ratio (NLR).

Follow-Up

All patients were assessed weekly during radiotherapy to monitor the treatment toxicities. Physical examination, blood routine, and biochemical test were done at a weekly visit. The first follow-up was 1 month after finishing radiotherapy, then continuing every 3 months for 2 years and every 6–12 months until disease progression or death. The last follow-up date was May 31, 2019. Physical examination, blood routine and biochemical test, barium esophagogram, and contrast-enhanced CT scan of the neck, chest, and abdomen were done at each follow-up visit. Information on patients' clinicopathological characteristics was retrospectively collected from their medical records.

Statistical Analysis

Recurrence-free survival (RFS) was defined as the interval from the date of definitive radiotherapy to either the first evidence of any recurrence (local or distant metastases) or death. OS was calculated from the date of treatment beginning to either the date of death from any cause or last follow-up. A chi-square test was performed to compare the differences of patients' clinicopathological characteristics. RFS and OS rates were estimated using the Kaplan–Meier method, and survival curve comparisons were performed using the log-rank test. Multivariate analysis was performed using a Cox regression model to identify prognostic factors associated with OS. The optimal cutoff value for NLR and neutrophil count to distinguish the difference of complete response (CR) rate was determined using the receiver operating characteristics (ROC) curve analysis. A two-sided $P < 0.05$ was considered statistically significant. All statistical analysis and data management were done with the statistical software IBM SPSS v22.0 (SPSS Inc., Chicago, IL, USA).

RESULTS

Patient Characteristics

A total of 567 ESCC patients who received definitive radiotherapy for ESCC in our hospital were included in this study, with 413 (72.8%) men and 154 (27.2%) women. The patient characteristics including age, gender, tumor location, T stage, N stage, TNM stage, and treatment modality are summarized in **Table 1**. All the patients received definitive radiotherapy, with a radiation dose ranging from 50 to 78 Gy. Two hundred and forty-seven (43.6%) patients received definitive radiotherapy alone, and 320 (56.4%) patients received definitive concurrent chemoradiotherapy. There were 209 (36.9%) patients who achieved CR after radiotherapy.

TABLE 1 | Baseline patient characteristics.

Characteristics	Number ($n = 567$)
Age (years), median	64 (40–95)
≦65y	298
>65y	269
Gender	
Female	154
Male	413
Location	
Cervical	37
Upper thoracic	125
Middle thoracic	336
Lower thoracic	69
T stage	
T1	9
T2	152
T3	146
T4	260
N stage	
N0	119
N1	448
TNM stage	
I+II	238
III+IV	329
Treatment	
RT	247
CCRT	320
RT dose (Gy), median	64 (50–78)
≦64 Gy	313
>64 Gy	254
Complete response	
Yes	209
No	358
NLR, median	2.64 (0.60–31.67)
LDH (U/L), median	208 (83.0–617.0)
Neutrophils (10^9/L), median	4.8 (1.1–15.8)

Baseline Serum LDH Level, Neutrophil Count, and Clinicopathological Characteristics

At baseline, the pretreatment blood routine and blood biochemical examination were performed in all 567 patients. The median LDH was 208.0 U/L, ranging from 83.0 to 617.0 U/L. The default normal range of LDH was 80–220 U/L according to the biochemical detector used in our hospital. The neutrophil count ranged from 1.1 to 15.8 $\times$ 10^9/L, with a median of 4.8 $\times$ 10^9/L. The pretreatment NLR was calculated by the formula of the neutrophil count divided by the lymphocyte count. The median pretreatment NLR was 2.64, ranging from 0.60 to 31.67. The ROC curve was used to determine the NLR and neutrophil count thresholds to predict CR. The optimal cutoff values to predict CR were 4.5 $\times$ 10^9/L and 3.25 for neutrophil count and NLR, respectively. The LDH threshold was determined to be 220 U/L according to the upper limit of normal. Using these cutoff values, we stratified the patients into different groups (LDH ≦ 220 U/L vs. LDH>220 U/L and neutrophil ≦ 4.5 $\times$ 10^9/L vs. neutrophil >4.5 $\times$ 10^9/L, respectively; as shown in **Table 2**). As a result, 347 patients had a low level of LDH (≦ 220 U/L), and 220 patients had a high level of LDH (>220 U/L). Two hundred and fifty-one patients had a low count of neutrophil (≦ 4.5 $\times$

TABLE 2 | The association between levels of LDH and neutrophil and clinicopathological characteristics in patients with ESCC.

Characteristics	LDH (U/L)				Neutrophil (10^9/L)			
	≦220	>220	χ2 /t	*p*	≦4.5	>4.5	χ2 /t	*p*
Age (years)			0.637	0.425			2.2812	0.131
≦65y	187 (53.9)	111 (50.5)			123 (49)	175 (55.4)		
>65y	160 (46.1)	109 (49.5)			128 (51)	141 (44.6)		
Gender			0.190	0.663			10.231	0.001
Female	92 (26.5)	62 (28.2)			85 (33.9)	69 (21.8)		
Male	255 (73.5)	158 (71.8)			166 (66.1)	247 (78.2)		
Location			1.919	0.589			2.172	0.538
Cervical	19 (5.5)	18 (8.2)			13 (5.2)	24 (7.6)		
Upper thoracic	79 (22.8)	46 (20.9)			60 (23.9)	65 (20.6)		
Middle thoracic	205 (59.1)	131 (59.5)			146 (58.2)	190 (59.3)		
Lower thoracic	44 (12.7)	25 (11.4)			32 (12.7)	37 (12.2)		
T stage			2.166	0.539			35.330	<0.001
T1	6 (1.7)	3 (1.4)			5 (2.0)	4 (1.3)		
T2	95 (27.4)	57 (25.9)			90 (35.9)	62 (19.6)		
T3	82 (23.6)	64 (29.1)			75 (29.9)	71 (22.5)		
T4	164 (47.3)	96 (43.6)			81 (32.3)	179 (56.6)		
N stage			4.635	0.031			5.525	0.019
N0	83 (23.9)	36 (16.4)			64 (25.8)	55 (28.7)		
N1	264 (76.1)	184 (83.6)			187 (74.2)	261 (71.3)		
TNM stage			0.004	0.952			17.822	<0.001
I+II	146 (42.1)	92 (19.4)			130 (51.8)	108 (34.2)		
III+IV	201 (57.9)	128 (45.2)			121 (48.2)	208 (65.8)		
NLR			0.920	0.337		59.839	<0.001	
≦3.25	239 (68.9)	143 (65.0)		212 (84.5)	170 (53.8)			
>3.25	108 (31.1)	77 (35.0)		39 (15.5)	146 (46.2)			

10^9/L), and 316 patients had a high count of neutrophil (>4.5 × 10^9/L). A high level of LDH was significantly associated with the advanced N stage ($p = 0.031$), and neutrophil count was significantly associated with gender ($p = 0.001$), T stage ($p < 0.001$), N stage ($p = 0.019$), clinical stage ($p < 0.001$), and NLR ($p < 0.001$).

The Association Between LDH Level, Neutrophil Count, and Treatment Outcome

Median follow-up was 67.4 months (95% CI, 56.6–73.4 months) in this study cohort. The median OS was 16.4 months (95% CI, 15.3–18.5 months). We performed univariate and multivariate analyses to identify the prognostic factors. Univariate analysis showed that gender ($p = 0.001$), tumor location ($p = 0.001$), T stage ($p < 0.001$), N stage ($p < 0.001$), treatment modality ($p = 0.002$), LDH level ($p = 0.010$), neutrophil count ($p < 0.001$), and NLR ($p = 0.001$) were associated with RFS. In the following multivariate analysis, gender ($p = 0.004$), T stage ($p < 0.001$), N stage ($p = 0.005$), treatment modality ($p < 0.001$), LDH level ($p = 0.007$), and neutrophil count ($p = 0.037$) were found to be independently associated with RFS (**Table 3**). Furthermore, in the univariate analysis, gender ($p = 0.001$), tumor location ($p < 0.001$), T stage ($p < 0.001$), N stage ($p < 0.001$), treatment modality ($p = 0.004$), LDH level ($p = 0.016$), neutrophil count ($p < 0.001$), and NLR ($p < 0.001$) were associated with overall survival. In the multivariate analysis, gender ($p = 0.006$), T stage ($p < 0.001$), N stage ($p = 0.008$), treatment modality ($p < 0.001$), LDH level ($p = 0.012$), and neutrophil count ($p = 0.038$) were still independently associated with overall survival (**Table 4**). The prognostic impacts on overall survival of gender ($p = 0.001$), treatment modality ($p = 0.0037$), T stage ($p < 0.0001$), N stage ($p = 0.0001$), LDH level ($p = 0.0158$), and neutrophil count ($p < 0.0001$) are shown in **Figures 1A–F**, respectively.

A New Prognostic Risk Scoring Model Based on LDH Level and Neutrophil Count

We devised a new prognostic risk scoring (PRS) model based on gender, treatment modality, T stage, N stage, LDH level, and neutrophil count, which were identified as independent prognostic factors in multivariate analysis for OS. In the PRS model, patients with none or one to two of these poor prognostic factors were scored as one (Group one), patients with three or four of these poor prognostic factors were scored as two (Group two), and patients with five or six of these poor prognostic factors were scored as three (Group three). According to this PRS model, patients were stratified into three groups with distinct prognosis,

TABLE 3 | Univariate and multivariate analysis of clinical factors associated with Recurrence-Free Survival among patients with ESCC.

Variates	Univariate analysis			Multivariate analysis		
	HR (95%CI)	χ2	*p*	HR (95%CI)	χ2	*p*
Gender	0.694(0.559–0.862)	10.870	0.001	0.717 (0.573–0.898)	8.444	0.004
Age	1.032 (0.857–1.243)	0.112	0.738			
Location	1.258 (1.104–1.433)	11.925	0.001		3.536	0.316
Cervical				Reference		
Upper thoracic				1.171 (0.750–1.830)	0.482	0.488
Middle thoracic				1.331 (0.880–2.013)	1.832	0.176
Lower thoracic				1.474 (0.919–2.364)	2.597	0.107
T stage	1.479 (1.320–1.657)	45.647	0.000		27.225	0.000
T4				Reference		
T1				0.386 (0.166–0.897)	4.890	0.027
T2				0.595 (0.462–0.765)	16.269	0.000
T3				0.563 (0.437–0.724)	20.028	0.000
N stage	1.799 (1.408–2.299)	22.011	0.000	1.449 (1.116–1.881)	7.755	0.005
RT dose	1.063 (0.883–1.280)	0.414	0.520			
Treatment	0.749 (0.622–0.901)	9.346	0.002	0.628 (0.518–0.762)	22.314	0.000
LDH	1.280 (1.060–1.546)	6.589	0.010	1.304 (1.076–1.580)	7.317	0.007
Neutrophils	1.427 (1.182–1.723)	13.668	0.000	1.242 (1.013–1.522)	4.352	0.037
NLR	1.389 (1.142–1.688)	10.873	0.001	1.021 (0.825–1.264)	0.037	0.848

TABLE 4 | Univariate and multivariate analysis of clinical factors associated with Overall Survival among patients with ESCC.

Variates	Univariate analysis			Multivariate analysis		
	HR (95%CI)	χ2	*p*	HR (95%CI)	χ2	*p*
Gender	0.695 (0.558–0.866)	10.536	0.001	0.727 (0.580–0.911)	7.648	0.006
Age	1.048 (0.868–1.265)	0.239	0.625			
LocationCervical	1.274 (1.116–1.454)	12.887	0.000	Reference	3.534	0.316
Upper thoracic				1.154 (0.733–1.819)	0.383	0.536
Middle thoracic				1.319 (0.865–2.011)	1.650	0.199
Lower thoracic				1.471 (0.910–2.379)	2.481	0.115
T stage	1.525 (1.358–1.713)	50.716	0.000		32.151	0.000
T4				Reference		
T1				0.367 (0.158–0.852)	5.443	0.020
T2				0.568 (0.439–0.735)	18.490	0.000
T3				0.527 (0.408–0.680)	24.268	0.000
N stage	1.799 (1.389–2.280)	20.741	0.000	1.430 (1.099–1.861)	7.077	0.008
RT dose	1.052 (0.871–1.270)	0.274	0.601			
Treatment	0.758 (0.628–0.914)	8.360	0.004	0.638 (0.524–0.776)	20.177	0.000
LDH	1.265 (1.044–1.531)	5.772	0.016	1.283 (1.076–1.580)	6.278	0.012
Neutrophils	1.462 (1.208–1.771)	15.158	0.000	1.245 (1.012–1.532)	4.308	0.038
NLR	1.426 (1.171–1.738)	12.439	0.000	1.014 (0.8175–1.259)	0.016	0.899

with 42 (7.4%) patients in Group one, 415 (73.2%) patients in Group two, and 110 (19.4%) patients in Group three. The median OS time was 101.2 months in Group one, which was significantly longer than 18 months in Group two and 10.05 months in Group three (shown in **Figure 2**, $\chi^2 = 67.94$, $p < 0.0001$). Moreover, the CR rate in Group one was significantly higher than that in Group two and Group three ($\chi^2 = 24.031$, $p < 0.0001$). Twenty-three (54.8%) patients achieved CR in Group one, 166 (40%) patients achieved CR in Group two, and 20 (18.2%) patients achieved CR in Group three.

DISCUSSION

For patients with ESCC treated with surgery, TNM stage classification acts as the most important prognostic factor for many years. However, TNM stage classification seemed

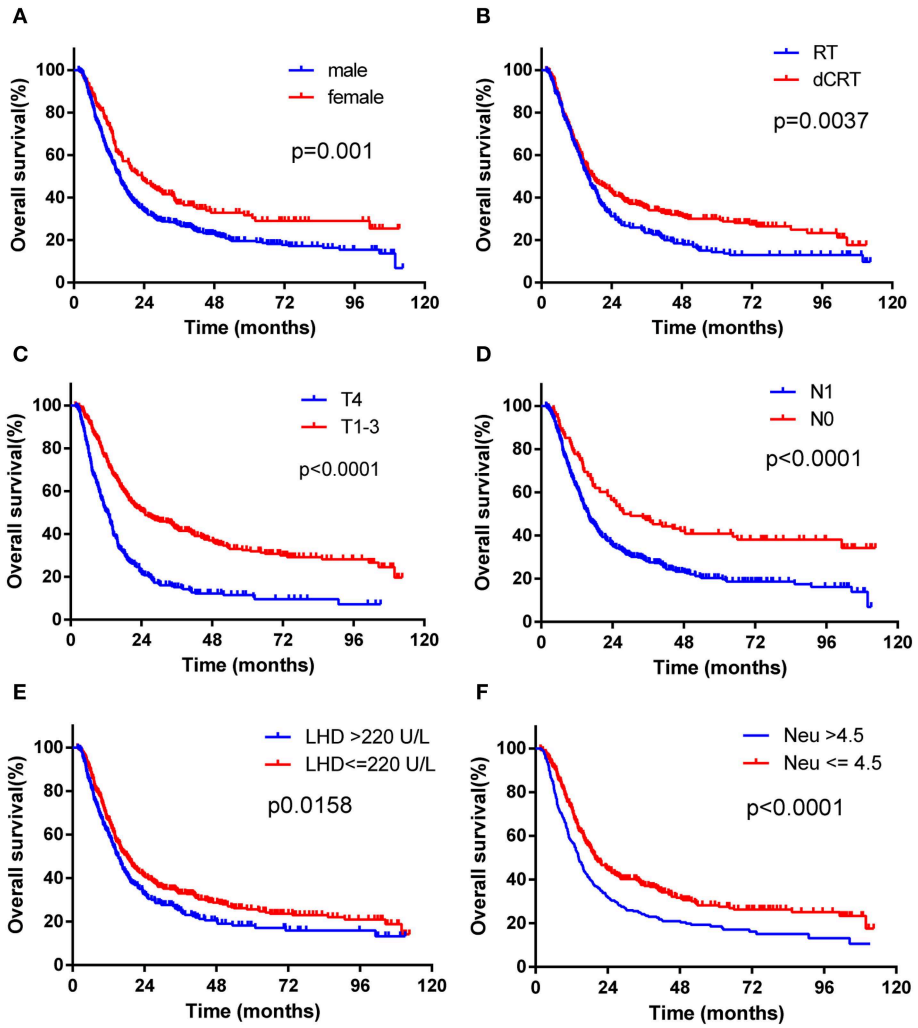

FIGURE 1 | Kaplan-Maier survival curves of overall survival of ESCC patients treated with radiotherapy stratified according to different prognostic factors. **(A)** Patients were stratified by gender. **(B)** Patients were stratified by treatment modality (RT vs. CCRT). **(C)** Patients were stratified by T stage (T4 stage vs. T1-3 stage). **(D)** Patients were stratified by N stage (N1 vs. N0 stage). **(E)** Patients were stratified by LDH level (LDH > 220 U/L vs. LDH _220 U/L). **(F)** Patients were stratified by neutrophil count (neutrophil >4.5G/L vs neutrophil ≤4.5G/L).

not sufficient to present enough prognostic information for patients treated with definitive radiotherapy (27). There could be some other factors impacted on the prognosis of patients who received definitive radiotherapy. Thus, identification of other new prognostic factors could allow a better prediction for treatment outcome. To further explore prognostic factors to identify patients with different prognosis, more easily available prognostic factors are warranted.

Neutrophil count and LDH both routinely detected the hematological index and were easily available in our clinical practice. Previous studies have investigated the prognostic value of LDH level, neutrophil count, and NLR in many solid tumors (10, 21, 24). However, there was no investigation about the role of the LDH level combined with neutrophil count or NLR in the prognosis of ESCC patients treated with radiotherapy. This study aimed to investigate the prognostic value of the LDH level, neutrophil count, and NLR in ESCC patients treated with radiotherapy. What is more, for the first time, we established a new risk prognostic scoring model based on the baseline LDH level and neutrophil count, which stratified patients into three groups with different prognosis.

According to previous studies, systemic inflammation was an enabling characteristic for cancer development and promoted tumor progression by affecting the response to systemic therapies (6, 28). NLR, determined by the neutrophil count and lymphocyte count, was suggested to reflect the systemic inflammatory responses (29). Previous study has reported that NLR could serve as a prognostic indicator for survival in EC (30). An investigation that enrolled a relatively large population of ESCC patients from Chen et al. (31) revealed

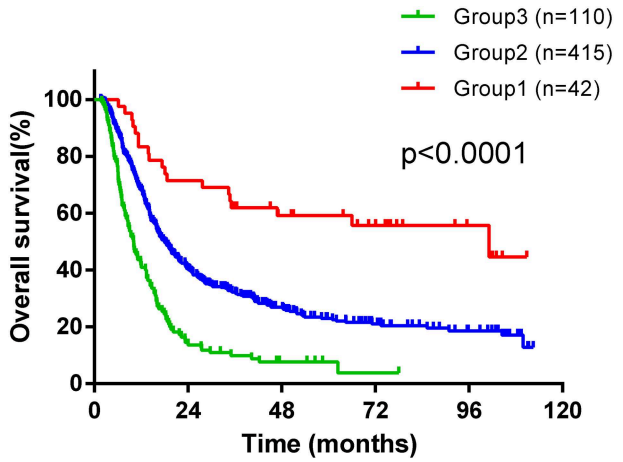

FIGURE 2 | Kaplan-Maier survival curves of overall survival of ESCC patients treated with radiotherapy stratified according to a new prognostic risk scoring (PRS) model.

that pretreatment elevated NLR was significantly associated with an advanced clinical stage and reduced OS. Moreover, elevated NLR was an independent prognostic indicator for OS in patients receiving chemoradiotherapy but not those receiving surgery. Interestingly, in this present study, multivariate analysis showed that NLR was not an independent prognostic indicator for RFS and OS in ESCC patients treated with radiotherapy. However, increased neutrophil was significantly associated with advanced T stage, N stage, clinical stage, and poor OS in ESCC patients treated with radiotherapy. One possible explanation is that tumor microenvironment is influenced by neutrophils themselves, but NLR is affected by lymphocyte count and couldn't reflect changes in the tumor microenvironment. Another possibility is that NLR and neutrophil count interact with each other in the modeling stats. When combined with other prognostic factors in multivariate analysis, neutrophil count had stronger predictive ability compared with NLR. Based on the results, pretreatment neutrophil count might be more appropriate to be used as a prognostic factor than NLR and could be a useful baseline indicator to predict the outcome for ESCC patients treated with radiotherapy.

Growing evidence has showed that neutrophilia can occur in cancer patients. Moreover, neutrophils are thought to promote angiogenesis and tumor growth, degrade the extracellular matrix, provide favorable conditions for metastasis, and potentiate genome instability and tumor evolution (29). Neutrophils can also be localized to the tumor to establish tumor-associated neutrophil (TAN), resulting in treatment resistance and cancer development (15). In this study, we explored the optimal cutoff value of neutrophil count using the ROC curve analysis to predict CR in ESCC patients treated with radiotherapy and found that patients with high neutrophil count had poor RFS and OS, indicating that increased neutrophil count may be a predictor for poor radiosensitivity.

According to previous studies, an elevated level of LDH isoforms is more common in malignant tumors than normal cells (32). The increased LDH level could promote tumor progression by regulating the tumor metabolism and microenvironment and acts as a poor prognostic indicator for cancer patients (32, 33). A meta-analysis investigating the prognostic value of the LDH level in solid tumors showed that a high LDH level is associated with poor survival in melanoma, gastric, lung cancer, prostate, and renal cell carcinomas (34). Recently, a high LDH level has been demonstrated to effectively predict the response to cancer treatment, such as chemotherapy (11), anti-angiogenetic agents (35), and checkpoint immunotherapy (22, 24) in various cancers. The prognostic role of the LDH level was also investigated in ESCC patients who underwent curative treatment in the study from Wei et al. (23). However, the study included patients treated with surgery or chemoradiotherapy, which led to treatment bias. In this present study, we only included the ESCC patients treated with radiotherapy and demonstrated that an elevated LDH level was an indicator for poor prognosis in the setting.

Several limitations were inevitable in our study. First, the retrospective nature of this study led to selection bias and potential confounding biases. Second, there were some other prognostic factors influencing the level of LDH and neutrophil count such as infectious diseases, which could not be stratified in our retrospective study, and thus the implication of the LDH level and neutrophil count on the prognosis of ESCC patients treated with radiotherapy should be further investigated in a carefully designed study. Third, some patients who cannot tolerate concurrent chemoradiotherapy were treated with radiotherapy only, leading to treatment selection bias. Thus, we performed multivariate analysis to identify independent prognostic factors. Finally, the conclusions were based on only a small number of 567 patients treated with radiotherapy. It is inappropriate to extrapolate to the patients in a trimodality setting.

In conclusion, we provided an investigation about the prognostic significance of the LDH level and neutrophil count in ESCC patients treated with radiotherapy and the optimal cutoff value to predict the response to radiotherapy. Furthermore, we demonstrated that a high level of LDH and neutrophil count were associated with poor prognosis in ESCC patients, and proposed a prognostic risk scoring model based on the LDH level and neutrophil count to help estimate the prognosis for ESCC patients for the first time.

DATA AVAILABILITY STATEMENT

The datasets used and/or analyzed during the current study are available from the corresponding author upon reasonable request.

ETHICS STATEMENT

The studies involving human participants were reviewed and approved by Ethics Committee of the Shantou Central Hospital.

Written informed consent for participation was not required for this study in accordance with the national legislation and the institutional requirements.

AUTHOR CONTRIBUTIONS

H-CH and L-XL designed the study. H-SL prepared figures and wrote the manuscript text. H-YX and S-XW collected the follow-up data. X-YL and Z-SD made statistical analysis. All authors reviewed the manuscript and approved the final manuscript.

ACKNOWLEDGMENTS

This study was registered in the Shantou City Science and Technology Plan Projects (2019), China.

REFERENCES

1. Lagergren J, Smyth E, Cunningham D, Lagergren P. Oesophageal cancer. *Lancet.* (2017) 390:2383–96. doi: 10.1016/S0140-6736(17)31462-9
2. Ajani JA, D'amico TA, Bentrem DJ, Chao J, Corvera C, Das P, et al. Esophageal and esophagogastric junction cancers, version 2.2019, NCCN clinical practice guidelines in oncology. *J Natl Compr Canc Netw.* (2019) 17:855–83. doi: 10.6004/jnccn.2019.0033
3. Chau I, Norman AR, Cunningham D, Waters JS, Oates J, Ross PJ. Multivariate prognostic factor analysis in locally advanced and metastatic esophago-gastric cancer–pooled analysis from three multicenter, randomized, controlled trials using individual patient data. *J Clin Oncol.* (2004) 22:2395–403. doi: 10.1200/JCO.2004.08.154
4. Gavin AT, Francisci S, Foschi R, Donnelly DW, Lemmens V, Brenner H, et al. Oesophageal cancer survival in Europe: a EUROCARE-4 study. *Cancer Epidemiol.* (2012) 36:505–12. doi: 10.1016/j.canep.2012.07.009
5. Huang FL, Yu SJ. Esophageal cancer: risk factors, genetic association, and treatment. *Asian J Surg.* (2018) 41:210–5. doi: 10.1016/j.asjsur.2016.10.005
6. Hanahan D, Weinberg RA. Hallmarks of cancer: the next generation. *Cell.* (2011) 144:646–74. doi: 10.1016/j.cell.2011.02.013
7. Grivennikov SI, Greten FR, Karin M. Immunity, inflammation, and cancer. *Cell.* (2010) 140:883–99. doi: 10.1016/j.cell.2010.01.025
8. Mcmillan DC. The systemic inflammation-based glasgow prognostic score: a decade of experience in patients with cancer. *Cancer Treat Rev.* (2013) 39:534–40. doi: 10.1016/j.ctrv.2012.08.003
9. Schmidt H, Bastholt L, Geertsen P, Christensen IJ, Larsen S, Gehl J, et al. Elevated neutrophil and monocyte counts in peripheral blood are associated with poor survival in patients with metastatic melanoma: a prognostic model. *Br J Cancer.* (2005) 93:273–8. doi: 10.1038/sj.bjc.6602702
10. Valpione S, Martinoli C, Fava P, Mocellin S, Campana LG, Quaglino P, et al. Personalised medicine: development and external validation of a prognostic model for metastatic melanoma patients treated with ipilimumab. *Eur J Cancer.* (2015) 51:2086–94. doi: 10.1016/j.ejca.2015.06.130
11. Namikawa T, Ishida N, Tsuda S, Fujisawa K, Munekage E, Iwabu J, et al. Prognostic significance of serum alkaline phosphatase and lactate dehydrogenase levels in patients with unresectable advanced gastric cancer. *Gastric Cancer.* (2019) 22:684–91. doi: 10.1007/s10120-018-0897-8
12. Pylaeva E, Lang S, Jablonska J. The essential role of Type I interferons in differentiation and activation of tumor-associated neutrophils. *Front Immunol.* (2016) 7:629. doi: 10.3389/fimmu.2016.00629
13. Matsumoto Y, Mabuchi S, Kozasa K, Kuroda H, Sasano T, Yokoi E, et al. The significance of tumor-associated neutrophil density in uterine cervical cancer treated with definitive radiotherapy. *Gynecol Oncol.* (2017) 145:469–75. doi: 10.1016/j.ygyno.2017.02.009
14. Chao T, Furth EE, Vonderheide RH. CXCR2-dependent accumulation of tumor-associated neutrophils regulates T-cell immunity in pancreatic ductal adenocarcinoma. *Cancer Immunol Res.* (2016) 4:968–82. doi: 10.1158/2326-6066.CIR-16-0188
15. Moses K, Brandau S. Human neutrophils: their role in cancer and relation to myeloid-derived suppressor cells. *Semin Immunol.* (2016) 28:187–96. doi: 10.1016/j.smim.2016.03.018
16. Hu P, Liu Q, Deng G, Zhang J, Liang N, Xie J, et al. Radiosensitivity nomogram based on circulating neutrophils in thoracic cancer. *Future Oncol.* (2019) 15:727–37. doi: 10.2217/fon-2018-0398
17. Armstrong AJ, George DJ, Halabi S. Serum lactate dehydrogenase predicts for overall survival benefit in patients with metastatic renal cell carcinoma treated with inhibition of mammalian target of rapamycin. *J Clin Oncol.* (2012) 30:3402–7. doi: 10.1200/JCO.2011.40.9631
18. Brown JE, Cook RJ, Lipton A, Coleman RE. Serum lactate dehydrogenase is prognostic for survival in patients with bone metastases from breast cancer: a retrospective analysis in bisphosphonate-treated patients. *Clin Cancer Res.* (2012) 18:6348–55. doi: 10.1158/1078-0432.CCR-12-1397
19. Wei Z, Zeng X, Xu J, Duan X, Xie Y. Prognostic value of pretreatment serum levels of lactate dehydrogenase in nonmetastatic nasopharyngeal carcinoma: single-site analysis of 601 patients in a highly endemic area. *Onco Targets Ther.* (2014) 7:739–49. doi: 10.2147/OTT.S59804
20. Hiew K, Hart CA, Ali A, Elliott T, Ramani V, Sangar V, et al. Primary mutational landscape linked with pre-docetaxel lactate dehydrogenase levels predicts docetaxel response in metastatic castrate-resistant prostate cancer. *Eur Urol Focus.* (2018) 5:831–41. doi: 10.1016/S1569-9056(18)30964-3
21. Kaito S, Kanemasa Y, Sasaki Y, Okuya T, Yamaguchi T, Funasaka C, et al. A new prognostic score comprising lactate dehydrogenase, albumin and neutrophil to lymphocyte ratio to predict sensitivity to first-line chemotherapy in patients with peripheral T-cell lymphomas. *Int J Hematol.* (2018) 107:451–9. doi: 10.1007/s12185-017-2362-6
22. Mezquita L, Auclin E, Ferrara R, Charrier M, Remon J, Planchard D, et al. Association of the lung immune prognostic index with immune checkpoint inhibitor outcomes in patients with advanced non-small cell lung cancer. *JAMA Oncol.* (2018) 4:351–7. doi: 10.1001/jamaoncol.2017.4771
23. Wei XL, Zhang DS, He MM, Jin Y, Wang DS, Zhou YX, et al. The predictive value of alkaline phosphatase and lactate dehydrogenase for overall survival in patients with esophageal squamous cell carcinoma. *Tumour Biol.* (2016) 37:1879–87. doi: 10.1007/s13277-015-3851-y
24. Wang X, Zhang B, Chen X, Mo H, Wu D, Lan B, et al. Lactate dehydrogenase and baseline markers associated with clinical outcomes of advanced esophageal squamous cell carcinoma patients treated with camrelizumab (SHR-1210), a novel anti-PD-1 antibody. *Thorac Cancer.* (2019) 10:1395–401. doi: 10.1111/1759-7714.13083
25. Luo HS, Xu HY, Du ZS, Li XY, Wu SX, Huang HC, et al. Impact of sex on the prognosis of patients with esophageal squamous cell cancer underwent definitive radiotherapy: a propensity score-matched analysis. *Radiat Oncol.* (2019) 14:74. doi: 10.1186/s13014-019-1278-0
26. Chen D, Menon H, Verma V, Seyedin SN, Ajani JA, Hofstetter WL, et al. Results of a phase 1/2 trial of chemoradiotherapy with simultaneous integrated boost of radiotherapy dose in unresectable locally advanced esophageal cancer. *JAMA Oncol.* (2019) 5:1597–604. doi: 10.1001/jamaoncol.2019.2809
27. Chen M, Li X, Chen Y, Liu P, Chen Z, Shen M, et al. Proposed revision of the 8th edition AJCC clinical staging system for esophageal squamous cell cancer treated with definitive chemo-IMRT based on CT imaging. *Radiat Oncol.* (2019) 14:54. doi: 10.1186/s13014-019-1258-4
28. Srivastava RM, Lee SC, Andrade Filho PA, Lord CA, Jie HB, Davidson HC, et al. Cetuximab-activated natural killer and dendritic cells collaborate to trigger tumor antigen-specific T-cell immunity in head and neck cancer patients. *Clin Cancer Res.* (2013) 19:1858–72. doi: 10.1158/1078-0432.CCR-12-2426
29. Treffers LW, Hiemstra IH, Kuijpers TW, Van Den Berg TK, Matlung HL. Neutrophils in cancer. *Immunol Rev.* (2016) 273:312–28. doi: 10.1111/imr.12444

30. Yodying H, Matsuda A, Miyashita M, Matsumoto S, Sakurazawa N, Yamada M, et al. Prognostic significance of neutrophil-to-Lymphocyte ratio and platelet-to-lymphocyte ratio in oncologic outcomes of esophageal cancer: a systematic review and meta-analysis. *Ann Surg Oncol.* (2016) 23:646–54. doi: 10.1245/s10434-015-4869-5
31. Chen MF, Chen PT, Kuan FC, Chen WC. The Predictive value of pretreatment neutrophil-to-lymphocyte ratio in esophageal squamous cell carcinoma. *Ann Surg Oncol.* (2019) 26:190–9. doi: 10.1245/s10434-018-6944-1
32. Urbanska K, Orzechowski A. Unappreciated role of LDHA and LDHB to control apoptosis and autophagy in tumor cells. *Int J Mol Sci.* (2019) 20. doi: 10.3390/ijms20092085
33. Doherty JR, Cleveland JL. Targeting lactate metabolism for cancer therapeutics. *J Clin Invest.* (2013) 123:3685–92. doi: 10.1172/JCI69741
34. Petrelli F, Cabiddu M, Coinu A, Borgonovo K, Ghilardi M, Lonati V, et al. Prognostic role of lactate dehydrogenase in solid tumors: a systematic review and meta-analysis of 76 studies. *Acta Oncol.* (2015) 54:961–70. doi: 10.3109/0284186X.2015.1043026
35. Faloppi L, Scartozzi M, Bianconi M, Svegliati Baroni G, Toniutto P, Giampieri R, et al. The role of LDH serum levels in predicting global outcome in HCC patients treated with sorafenib: implications for clinical management. *BMC Cancer.* (2014) 14:110. doi: 10.1186/1471-2407-14-110

Conflict of Interest: The authors declare that the research was conducted in the absence of any commercial or financial relationships that could be construed as a potential conflict of interest.

frontiers in Oncology

ORIGINAL RESEARCH
published: 21 April 2020
doi: 10.3389/fonc.2020.00490

Electron Density and Biologically Effective Dose (BED) Radiomics-Based Machine Learning Models to Predict Late Radiation-Induced Subcutaneous Fibrosis

Michele Avanzo[1], Giovanni Pirrone[1], Lorenzo Vinante[2], Angela Caroli[2], Joseph Stancanello[3], Annalisa Drigo[1], Samuele Massarut[4], Mario Mileto[4], Martina Urbani[5], Marco Trovo[6], Issam el Naqa[7], Antonino De Paoli[2] and Giovanna Sartor[1]*

[1] Department of Medical Physics, Centro di Riferimento Oncologico di Aviano (CRO) IRCCS, Aviano, Italy, [2] Department of Radiation Oncology, Centro di Riferimento Oncologico di Aviano (CRO) IRCCS, Aviano, Italy, [3] Guerbet SA, Villepinte, France, [4] Breast Surgery Unit, Centro di Riferimento Oncologico di Aviano (CRO) IRCCS, Aviano, Italy, [5] Department of Radiology, Centro di Riferimento Oncologico di Aviano (CRO) IRCCS, Aviano, Italy, [6] Department of Radiation Oncology, Udine General Hospital, Udine, Italy, [7] Department of Radiation Oncology, University of Michigan, Ann Arbor, MI, United States

OPEN ACCESS

Edited by:
Claudio Fiorino, San Raffaele Hospital (IRCCS), Italy

Reviewed by:
Laura Cella, Italian National Research Council, Italy
Carlo Cavedon, Integrated University Hospital Verona, Italy

***Correspondence:**
Michele Avanzo
mavanzo@cro.it

Specialty section:
This article was submitted to Radiation Oncology, a section of the journal Frontiers in Oncology

Received: *03 January 2020*
Accepted: *18 March 2020*
Published: *21 April 2020*

Citation:
Avanzo M, Pirrone G, Vinante L, Caroli A, Stancanello J, Drigo A, Massarut S, Mileto M, Urbani M, Trovo M, el Naqa I, De Paoli A and Sartor G (2020) Electron Density and Biologically Effective Dose (BED) Radiomics-Based Machine Learning Models to Predict Late Radiation-Induced Subcutaneous Fibrosis. Front. Oncol. 10:490. doi: 10.3389/fonc.2020.00490

Purpose: to predict the occurrence of late subcutaneous radiation induced fibrosis (RIF) after partial breast irradiation (PBI) for breast carcinoma by using machine learning (ML) models and radiomic features from 3D Biologically Effective Dose (3D-BED) and Relative Electron Density (3D-RED).

Methods: 165 patients underwent external PBI following a hypo-fractionation protocol consisting of 40 Gy/10 fractions, 35 Gy/7 fractions, and 28 Gy/4 fractions, for 73, 60, and 32 patients, respectively. Physicians evaluated toxicity at regular intervals by the Common Terminology Adverse Events (CTAE) version 4.0. RIF was assessed every 3 months after the completion of radiation course and scored prospectively. RIF was experienced by 41 (24.8%) patients after average 5 years of follow up.

The Hounsfield Units (HU) of the CT-images were converted into relative electron density (3D-RED) and Dose maps into Biologically Effective Dose (3D-BED), respectively. Shape, first-order and textural features of 3D-RED and 3D-BED were calculated in the planning target volume (PTV) and breast. Clinical and demographic variables were also considered (954 features in total). Imbalance of the dataset was addressed by data augmentation using ADASYN technique. A subset of non-redundant features that best predict the data was identified by sequential feature selection. Support Vector Machines (SVM), ensemble machine learning (EML) using various aggregation algorithms and Naive Bayes (NB) classifiers were trained on patient dataset to predict RIF occurrence. Models were assessed using sensitivity and specificity of the ML classifiers and the area under the receiver operator characteristic curve (AUC) of the score functions in repeated 5-fold cross validation on the augmented dataset.

Results: The SVM model with seven features was preferred for RIF prediction and scored sensitivity 0.83 (95% CI 0.80–0.86), specificity 0.75 (95% CI 0.71–0.77) and

AUC of the score function 0.86 (0.85–0.88) on cross-validation. The selected features included cluster shade and Run Length Non-uniformity of breast 3D-BED, kurtosis and cluster shade from PTV 3D-RED, and 10th percentile of PTV 3D-BED.

Conclusion: Textures extracted from 3D-BED and 3D-RED in the breast and PTV can predict late RIF and may help better select patient candidates to exclusive PBI.

Keywords: radiomics, radiotherapy, machine learning, breast cancer, fibrosis

INTRODUCTION

Subcutaneous radiation induced fibrosis (RIF) is characterized by a progressive induration and thickening of the subcutaneous tissues and is one of the late adverse effects of breast radiotherapy (RT) mostly affecting cosmesis. It is a dose dependent and slowly progressive side effect originating from a proliferative response of surviving fibrocytes to growth factors (e.g., the transforming growth factor β (TGF-β), released in response to tissue injury) (1).

The available tools to predict late subcutaneous fibrosis in patients treated with RT are of limited quality. Models to predict Normal Tissue Complication Probability (NTCP) for RIF after breast RT have been first fitted to published data of rates of incidence from whole breast irradiation (WBI) (2). Later, models for NTCP of RIF have been refined by including dose volume data from simulated dose distributions of WBI (3) and partial breast irradiations (PBI) (4).

Quantitative analysis of medical images could provide information about intensity, shape, size or volume, and texture of tumor or organs at risk that is distinct or complementary to that provided by other data sources (5). Recently, the combination of quantitative analysis of radiological images with Machine Learning (ML) methods, also known as "radiomics," has been applied also to predict side effects of RT such as lung-injury following Stereotactic Body RT (SBRT) for lung cancer (6), gastrointestinal and genitourinary toxicities (7) and xerostomia (8).

Other 3D information, as dose distribution delivered in RT calculated on pre-treatment Computer Tomography (CT), can be integrated in the radiomics analysis. The textural analysis of dose distribution could provide more detailed spatial information on the 3D dose distribution: it attempts to extract spatial features from dose distribution to predict RT response instead of dose-volume histogram (DVH) typically used in NTCP models. Dosiomics, or integration of dose features from the irradiated lung, has shown to be predictive of radiation pneumonitis with higher accuracy than DVH-based NTCP models (9).

The purpose of the present work is to develop a model to improve the accuracy of prediction of RIF by integrating data from pre-treatment CT, 3D dose distribution and clinical variables. For this purpose, we developed a ML classifier, that is, a predictive model assigning an unseen patient to one of two possible classes: patient with or without RIF during follow-up. Our study is the first, to the best of our knowledge, to derive a classifier for RIF which includes radiomic variables and individual dose data using ML algorithms.

METHODS

Patient Data

One hundred sixty-five patients treated with breast conservative surgery for an early stage ductal carcinoma who underwent external PBI were retrospectively analyzed. Patient characteristics, with results of univariate statistical tests to investigate correlation with RIF, are shown in **Table 1**. All patients underwent a complete free breathing pre-treatment planning CT to include all the organs at risk (OAR), according to the RTOG 0413 protocol (10). CTs were acquired with a GE Lightspeed RT (GE Medical Systems, Waukesha, WI) or a Toshiba Aquilion LB (Toshiba Medical Systems Europe, Zoetermeer, the Netherlands) using 120 kVp, 215–300 mAs 5 mm slice thickness, and voxel size ranging from 0.977 to 1.074 mm.

The clinical target volume (CTV) consisted of the lumpectomy cavity, identified by the post-surgery seroma or by the surgical clips, uniformly expanded by 15 mm, limited to 5 mm from the skin surface and 5 mm from the lung-chest wall interface. The planning target volume (PTV) was calculated from the CTV using uniform 3D expansion of 1 cm, then it was limited to exclude the part outside the ipsilateral breast, the first 5 mm of tissue under the skin and the expansion beyond the posterior extent of breast tissue. Breast tissue visible on the pre-treatment planning CT was outlined, according to the RTOG "Breast Cancer Atlas for Radiation therapy planning: consensus definition" (11).

Patients were treated following a hypo-fractionation protocol (12) designed using iso-effective doses for subcutaneous RIF based on NTCP models (4). The hypofractionation schemes consisted of 40 Gy in 10 fractions (73 patients), 35 Gy in 7 fractions (60) and 28 Gy in 4 fractions fractions. The RT technique consisted of "field-in-field" planning (forward-planned intensity modulated RT) (14) using multiple planar and non-coplanar 6-MV photon beams, and delivered by a Trilogy linear accelerator equipped with a kV on-board imager system and a 120-leaves Millennium multi-leaf collimator (Varian Medical Systems, Palo Alto, CA, US).

All treatments were developed using the Eclipse treatment planning system (Varian Medical), and dose calculations were carried out using the anisotropic analytical algorithm (AAA) with a grid resolution of 2.5 mm, taking into account heterogeneity correction. The CT scan, dose matrix and Region Of Interest (ROI) contours were exported in a DICOM format.

Physicians evaluated toxicity at regular intervals by the Common Terminology Criteria for Adverse Events (CTCAE)

TABLE 1 | Patients characteristics with statistical tests to investigate correlation with RIF.

Categorical variable	Patients (%)	*p*-value (Chi-square test)
Number of patients	165 (100)	
No RIF	124 (75.2)	
RIF Grade 1	26 (15.7)	
RIF Grade 2	12 (7.3)	
RIF Grade 3	3 (1.8)	
RIF any grade	41 (24.8)	
Tumor histology		
Ductal	155 (93.9)	0.540
Lobular	10 (6.1)	
Laterality		
Left	73 (44.2)	0.3651
Right	92 (55.8)	
Quadrant (cm)		
Upper, outer	80 (48.5.3)	0.056
Upper, inner	32 (19.4)	
Lower, outer	15 (9.1)	
Lower, inter	23 (13.9)	
Central	15 (9.1)	
Comorbidity		
No	112 (67.9)	0.658
Yes	53 (32.1)	
Fractionation regimen		
40 Gy/10 fx	73 (44.2)	0.5396
35 Gy/7 fx	60 (36.4)	
28 Gy/4 fx	32 (19.4)	
Chemotherapy		
No	152 (92.1)	0.064
Yes	13 (7.9)	
Hormone therapy		
No	51 (30.9)	0.793
Yes	114 (69.1)	
Continuous variable	**Average (95% CI)**	***p*-value (Wilcoxon test)**
Age (years)	69.8 (61.0–82.9)	0.611
Pathological tumor size (mm)	12.1 (4–25)	0.552
Follow-up (months)	60.2 (17.2–82.9)	0.384

(version 4.0). Clinical and demographic variables, age, presence of comorbidities (diabetes and rheumatological disorders), tumor histology, laterality and quadrant, administration of chemotherapy and hormone therapy, were considered (954 features in total). The presence of RIF of any grade (grade 1 or more) was assessed every 3 months after the completion of radiation course and scored in a prospective database. Forty-one (24.8%) patients experienced RIF after average 5 years of follow up. Fibrosis of grade 1, 2, and 3 occurred in 26, 12, and 3 patients, respectively. The maximum toxicity score (Grade 4) was not recorded during follow up.

Radiomic Analysis of BED and RED

Prior to the calculation of radiomic features, resampling to isotropic voxel size was applied to have standardized voxel spacing across the cohort (15). For example, all CT images were resampled to $3 \times 3 \times 3$ mm^3 (16). Voxel intensities were grouped into 64 equally spaced bins to reduce image noise and normalize intensities across all different patients.

In order to remove dependency on the Hounsfield scale used by the two scanners (17), the images were converted from Hounsfield Units to electron density relative to water (3D-RED) using the Hounsfield Units—RED conversion scales of the CTs (**Figure 1**) as measured on phantom on each CT scanner. Since patients were treated with different fractionation schemes, the 3D dose distributions were converted into 3D Biologically Effective Dose (3D-BED) using the number of fractions of the treatment, and an assumed value of α/β of 3Gy, typical of late-responding tissues as subcutaneous tissue, which has also been used to model RIF (2, 18). A total of 21 shapes, 57 radiomic and 57 dosimetric textural features were calculated from the PTV and breast volume in the 3D-RED and 3D-BED. The radiomic features were calculated following definitions and nomenclature from the Image Biomarker Standardization Initiative (IBSI) (19) using an in-house Matlab code. The in-house code had been previously validated by comparing its results with the Ibex open source software (20). The same features were also calculated after application of one between Gaussian, Laplacian of Gaussian (LoG), or Median filtering to 3D-RED and 3D-BED. The clinical variables follow up, age, tumor location, pathological tumor size, chemo and hormone therapy, were also collected and included in the analysis, so that the variables were 954 in total. A common problem in application of ML classifiers is that some classes have a significantly higher number of examples, a problem which is referred to as class imbalance. The effect of imbalanced datasets on ML performance is detrimental (21, 22), and there are two methods for overcoming this issue, namely under-sampling and over-sampling, of which the latter has been proven to be more effective in ML (21).

We then applied the Adaptive Synthetic Sampling Method for Imbalanced Data (ADASYN) over-sampling technique (23), an improved variant of the Synthetic Minority Over-sampling Technique (SMOTE), which generates synthetic data points by interpolating new feature values between the minority instance and its neighbors, according to the Euclidean distance, in the feature space. In ADASYN, the new minority samples are generated using a density distribution based on the number of out-of-class neighbors so that a minority instance surrounded by more out-of-class instances is considered hard-to-train, and is thus given a higher probability to be augmented (24).

ADASYN was applied to the level that the imbalance was completely eliminated, resulting in an augmented dataset of 252 patients, of which 50% had late RIF. All the analysis was performed using Matlab (Mathworks, Natick, MA).

ML Models

The occurrence of RIF in patients was converted into a binary outcome, positive for patients who experienced any grade (one or more) of RIF, and negative for patients who did not experience RIF during follow up.

The ML process includes two phases (5). First, to prevent overfitting, prior to applying ML classification, Stepwise forward feature selection was used to select a subset of variables best suited to predict late fibrosis. In Stepwise feature selection, terms from a generalized linear model are removed or added in order to find

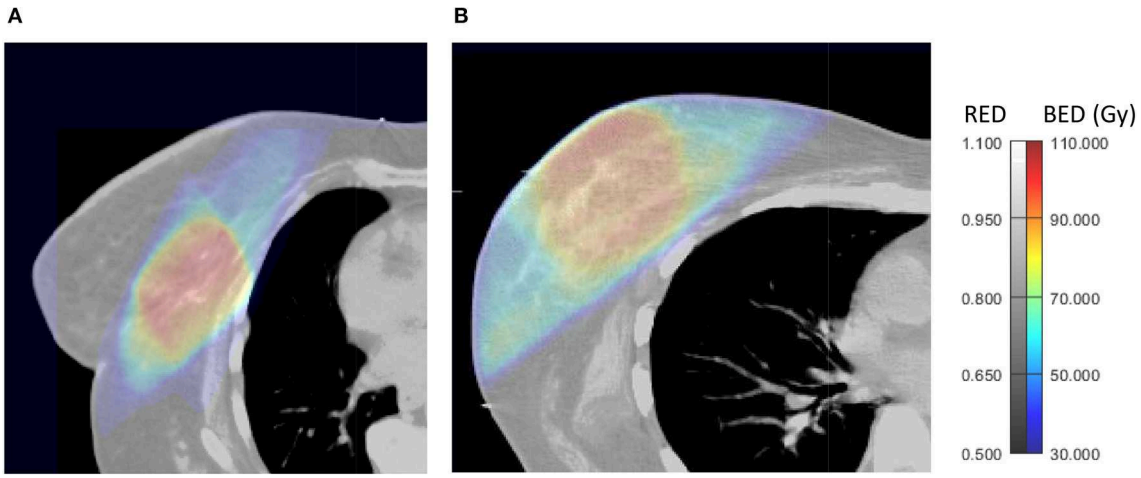

FIGURE 1 | Axial views of 3D-BED and 3D-RED in a patient who did not experience late RIF **(A)** and one who developed late RIF during follow up **(B)**.

the subset of variables in the data set resulting in the smallest model with lowest prediction error (25).

Forward stepwise selection is a wrapper method of feature selection, that is, a method which uses a learning technique, in our case a generalized linear model (GLM), to evaluate the importance of the features. Forward selection starts with an empty model. Then at each iteration, the single feature that best improves the fit of the GLM according to a specified criterion is determined (26). As a criterion we used the deviance of the values predicted by the GLM from the test data in a 5-fold cross validation. This is repeated until a best subset predictors (features) are selected.

In order to choose a proper number of variables, the process was initially performed with 4 variables allowed in the feature selection, then repeated with increasing number of variables.

After feature selection, the following binary ML classifiers were applied to the dataset to predict RIF:

1) SVM, which, by means of a kernel function, projects the data into a higher-dimensional feature space and determine a hyperplane in this feature space which separates data points into two categories (27). During the optimization, the proper box constraint level and kernel scale are chosen.
2) Ensemble machine learning (EML) which aggregates multiple learners into a single learner. Decision Trees were used as weak learners (5). During training, the best ensemble EML algorithm is selected between Random forests, Adaptive Logistic Regression and various boosting algorithms: Adaptive, Gentle, and Random Undersampling boosting (28) as well as the optimal number of learning cycles, learning rate, and minimum leaf size.
3) Naïve-Bayesian (NB) classifier which calculates the probability of each class assuming the conditional independence of the attributes using the Naive Bayes formula. A new instance is classified into the class with maximum calculated probability (29, 30). The optimizer also searches the best type of probability distribution (Gaussian or Kernel) and width of the kernel function.

TABLE 2 | Features selected to predict late fibrosis.

Image (3D-RED/ 3D-BED)	Filter	ROI	Variables	Wilcoxon-Mann–Whitney test *p*
3D-BED	LoG	Breast	Cluster shade	0.1389
3D-BED	LoG	Breast	RLN	0.0084
3D-RED	None	PTV	Kurtosis	0.0238
3D-RED	Gaussian	PTV	Range	0.1021
3D-RED	Gaussian	PTV	Cluster shade	0.6687
3D-BED	Gaussian	PTV	10th Percentile	0.0054
3D-BED	LoG	PTV	Variance	0.1624

LoG, Laplacian of Gaussian filter; RLN, run length non-uniformity.

The model to predict the occurrence of RIF was chosen according to the following criteria. First, the performance of the models was evaluated by calculating the average and 95% confidence intervals of sensitivity and specificity of the classifier and the AUC of the score function used by the classifiers in a 5-fold cross validation repeated 500 times in the augmented dataset. Finally, the sensitivity, specificity, and AUC were recalculated on the original, non-augmented dataset.

The models were required to have at least sensitivity and specificity of 0.75, and AUC of the model score of 0.85. Second, models were required to provide a realistic description of occurrence of RIF vs. BED variables. For this purpose, the score used by the best performing models to predict RIF was calculated vs. variables from 3D-BED variables. For biological consistency, models were required to have a continuously monotonic response to increasing dose. Models with non-monotonically increasing dose response were discarded, as this would imply that two different doses can lead to the same risk of side effects and that increasing dose could reduce the risk (31).

TABLE 3 | Performances of different models as a function of increasing number of variables allowed.

Model	Number of variables	Cross-validation in the augmented dataset, with 95% CI			Original (non-augmented) dataset		
		Sensitivity	Specificity	AUC	Sensitivity	Specificity	AUC
SVM	4	0.77 (0.74–0.80)	0.69 (0.66–0.71)	0.80 (0.79–0.81)	0.68	0.70	0.78
	5	0.82 (0.79–0.84)	0.68 (0.65–0.71)	0.83 (0.82–0.84)	0.73	0.66	0.81
	6	0.85 (0.83–0.87)	0.71 (0.68–0.73)	0.85 (0.84–0.86)	0.81	0.73	0.84
	7	0.83 (0.80–0.86)	0.75 (0.71–0.77)	0.86 (0.85–0.88)	0.81	0.77	0.86
	8	0.84 (0.81- 0.87)	0.76 (0.73–0.78)	0.88 (0.87–0.88)	0.83	0.81	0.89
EML	4	0.78 (0.73–0.84	0.73 (0.68–0.78)	0.83 (0.80–0.85)	1.00	1.00	1.00
	5	0.84 (0.79–0.88)	0.73 (0.69–0.78)	0.87 (0.84–0.90)	1.00	1.00	1.00
	6	0.86 (0.81–0.89)	0.77 (0.73–0.82)	0.87 (0.85–0.90)	1.00	1.00	1.00
	7	0.87 (0.82–0.91)	0.78 (0.73–0.84)	0.91 (0.88–0.93)	1.00	1.00	1.00
	8	0.89 (0.84–0.94)	0.78 (0.73–0.81)	0.92 (0.90–0.94)	1.00	1.00	1.00
NB	4	0.88 (0.84–0.91)	0.44 (0.41–0.47)	0.65 (0.63–0.68)	0.90	0.46	0.71
	5	0.92 (0.90–0.93)	0.44 (0.42–0.47)	0.82 (0.81–0.83)	0.90	0.45	0.71
	6	0.91 (0.88–0.92)	0.47 (0.45–0.49)	0.82 (0.81–0.83)	0.90	0.46	0.71
	7	0.89 (0.86–0.91)	0.40 (0.35–0.43)	0.78 (0.76–0.81)	0.90	0.45	0.71
	8	0.95 (0.94–0.95)	0.36 (0.34–0.38)	0.80 (0.78–0.82)	0.90	0.45	0.71

For each model and number of variables, the specificity and sensitivity of the classifier and the AUC with 95% CI calculated in repeated cross-validation are reported, as well as the specificity, sensitivity and AUC in the original (non-augmented) dataset.

RESULTS

The variables selected for ML are shown in **Table 2**. Two were textural variables of 3D-BED from the breast, cluster shade and Run Length Non-uniformity (RLN) after application of LoG filter, two were histogram (kurtosis and range) and one textural (Gray Level Co-occurrence Matrix Cluster shade) features (19) from the 3D-RED in the PTV and two histogram (10th percentile and inverse variance) variables of 3D-BED in the PTV. Among these, three variables (RLN of 3D-BED in breast, kurtosis of 3D-RED in PTV, 10th percentile of 3D-RED in PTV) were significantly correlated with occurrence of RIF according to the Wilcoxon-Mann-Whitney test for independent samples. No clinical variable was selected in the model.

EML with Adaptive Boosting was the best performing model for any number of variables, and it scored an AUC of the radiomic signature of 0.87 (0.85–0.90) with only 6 variables. SVM was the second best performing classifier as it achieved acceptable scores with 7 variables, while Native Bayes gave generally poor performance in terms of specificity (**Table 3**).

To interpret the features, their values were investigated in the two subsets of patients having extreme values of the function score. These patients were chosen as the 5% with the lowest score function among those without RIF, and the 5% with the highest score function of those who had RIF. Their features are shown in **Table 4**.

The score functions of the SVM and EML classifiers, were plotted against the 10th percentile of 3D-BED in the PTV for two values of kurtosis, that is, the average values of the patients at low and high risk of RIF, with the other features fixed at their average values among all the patients (**Figure 2**). The EML model was then discarded, as it showed a non-monotonically increasing dose-score function. The 7 variables SVM, scoring sensitivity 0.83 (95% CI 0.80–0.86), specificity 0.75 (95% CI 0.71–0.77) and AUC of the score function 0.86 (0.85–0.88) on cross-validation, was chosen as the preferred model. The model had sensitivity, specificity and AUC of 0.81, 0.77, and 0.86 respectively in the original dataset.

DISCUSSION

Supervised ML methods have been increasingly used in medicine, especially in the field of radiomics (32) to identify patients as responders or not responders but also to predict side effects in OARs (13, 13, 27). They are prone to overfitting, an event in which the model will better reflect noise in the image than the data themselves (33). Hence, careful feature selection and validation must be performed to tackle this limitation. In our results, EML is an example of ML models which overfitted the data, as it provided the best performance on repeated cross-validation for any number of variables, but produced unrealistic dose-response (**Figure 2A**) which was not monotonic. It was then discarded in favor of the SVM, whose score was monotonically increasing as a function of dose (**Figure 2B**). SVM models are more robust to overfitting than other ML methods such as decision trees (34), because they tolerate some points on the wrong side of the hyperplane, thus improving model robustness and generalization (5). Because the AUC of the SVM model of 0.86 on the non-augmented dataset is considered excellent (35) and, as the sum of sensitivity and specificity is 1.58, larger than 1.5, the model fulfills the rule of thumb for being useful of a clinical test (36), it can be used to stratify patients according to the risk of subcutaneous RIF.

To the best of our knowledge, this is the first study using radiomic features extracted from dose distribution after conversion to 3D-BED, which was necessary since our patients

TABLE 4 | Values of radiomic variables of the patients with low **(A)** and high **(B)** risk of RIF.

Image:	**3D-BED**	**3D-BED**	**3D-RED**	**3D-RED**	**3D-BED**	**3D-BED**	**3D-BED**
Filter:	Log	LoG	None	Gaussian	Gaussian	Gaussian	LoG
ROI:	Breast	Breast	PTV	PTV	PTV	PTV	PTV
Feature:	Cluster shade	RLN	Kurtosis	Range	Cluster shade	Percentile area 10	Variance
(A)							
Patient:							
1	−22517	0.58	441.8	3.6	15.2	91.0	0.31
2	−8696.7	0.55	50.7	0.47	−2250.1	74.8	0.43
3	−4993.3	0.62	320.5	1.64	410.6	87.3	0.42
4	−32445.8	0.59	64.2	0.66	−714.9	80.4	0.38
5	−17231.7	0.60	176.7	1.83	400.1	88.4	0.43
6	−10022.4	0.47	15.7	0.90	−2546.9	65.6	0.41
7	35401.4	0.63	92.4	0.64	131.1	90.4	0.39
8	−5332.1	0.54	19.8	0.52	−9583.5	52.41	0.41
Average:	−8229.7	0.57	147.7	1.28	−1767.3	78.8	0.40
(B)							
Patient:							
1	−18557.7	0.62	19.9	0.75	−3129.0	82.2	0.44
2	−3426.54	0.60	23.4	0.71	−2300.7	84.7	0.48
3	−53664.9	0.70	13.5	0.65	−3202.5	82.3	0.43
4	−80106.7	0.51	1.9	0.19	539.1	94.0	0.47
5	−29002.7	0.57	15.9	0.56	−6021.6	84.8	0.44
6	−29432.7	0.58	18.1	0.70	−1762.5	81.0	0.46
7	−10230.9	0.63	17.1	0.71	−2367.8	88.7	0.47
Average	−32060.3	0.60	15.7	0.61	−2606.4	85.4	0.46

These were defined as the 5% patients without RIF and with the lowest function score and the 5% patients with RIF with the highest function score, respectively.

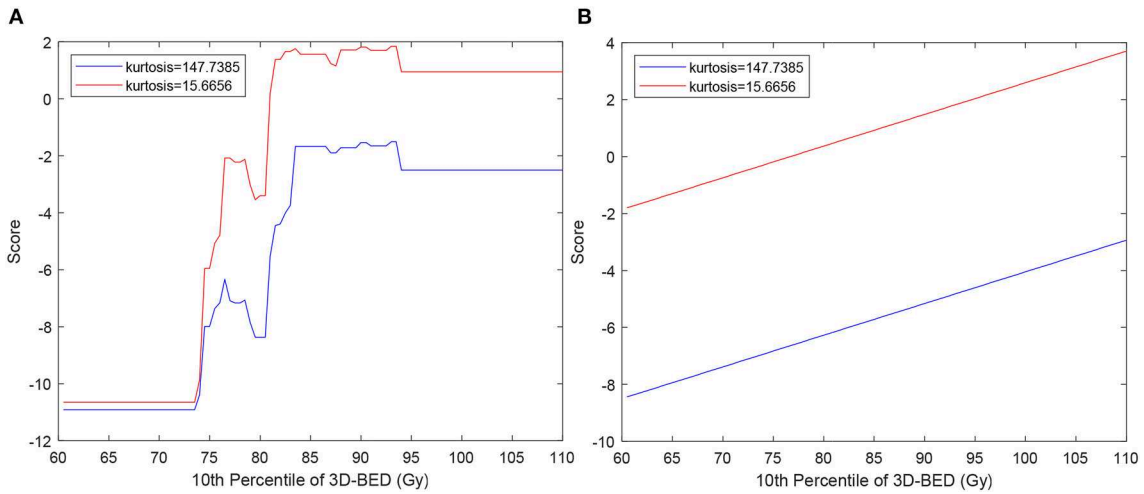

FIGURE 2 | Score function of EML **(A)** and SVM **(B)** used to classify patients vs. 10th percentile of 3D-BED in the PTV. The curves are calculated for values of kurtosis typical of patients at low and high risk of RIF, chosen as average of kurtosis in the 10 patients without RIF with lowest score (blue lines) and in 10 patients with RIF with highest score (red lines).

had different fractionation schemes. As the BED variables were the most correlated with RIF, our analysis confirms that radiation-induced RIF is governed by BED calculated with $\alpha/\beta = 3$ Gy to the whole breast and to the high dose region, the PTV. This result is in agreement with previous clinical findings showing that fibrosis is related to dose and dose per fraction (18). On the other hand, a correlation between RIF and maximum dose has been observed in clinical data for both WBI (37) and

PBI (38). RIF after PBI has been related to minimum PTV dose (39).

The features that were most correlated with RIF were BED features10th percentile and variance in the PTV and RLN of the breast, cluster shade to both PTV and breast.

Among the BED features, the 10th percentile in PTV is a descriptor of the minimum BED to the PTV, and describes the dependency of fibrosis on the lowest fractionation-corrected dose covering at least 90% of PTV. Cluster shade of BED in the PTV describes asymmetry of the GLCM. A larger module of cluster shade implies large GLCM asymmetry (19), which means that there are regions in the PTV with large differences in BED from their neighbors and may be related to the presence of hot spots in the PTV. Of note, if a PTV is close to the patient's surface, like in **Figure 1B**, there is a sudden change of dose in the build-up region which may increase cluster shade of BED. These associations are confirmed by larger variance of BED to the PTV in patients with RIF (**Table 4**).

RLN of BED in the breast describes the similarity among run lengths, defined as the lengths of consecutive voxels having the same dose value in a specified direction, in number of voxels (19) throughout the breast. RLN is related to homogeneity of dose, and lower values indicate more homogeneity among run lengths in the image. In our results patients without RIF had lower RLN of BED (more inhomogeneity). This may be due to larger "out-of-field" areas of the breast in patients less at risk of fibrosis (**Figure 1A**) that, being irradiated with low, uniform doses from scattered radiation, tend to have larger runs of voxels with the same values of dose from scattered radiation. An example of this situation can be observed in **Figure 1A**, and suggests that a steep dose gradient outside of the PTV may be beneficial to prevent fibrosis.

These findings indicate that the radiomic BED variables show that higher BED and presence of hot spots of BED in the PTV, as well as higher volumes receiving intermediate doses out of the PTV, as in **Figure 1B**, are related to occurrence of fibrosis.

The hypothesis underlying the application of radiomics to predict side effects in OARs is that a patient who is more at risk of side effect has a particular appearance of the organ at risk in pretreatment CT from the patient at lower risk. Often, these models are still perceived as "black boxes," meaning that it is difficult to determine how they arrive at their predictions, which impairs their use by clinicians as part of their clinical practice (40, 41). To address this issue, we provide interpretation of the radiomic features that are selected by the models. In our results, it was found that 3D-RED kurtosis in the PTV was correlated with a higher risk for RIF. Because kurtosis describes inhomogeneity of the electron density of the breast, the patients with more inhomogeneous breast (small kurtosis) are more sensitive, that is, have higher function score for all dose values (**Figure 2**). Fat, which is radiolucent, appears dark on a CT, while epithelial and stromal tissue appear radiodense and may represent connective tissues (42, 43). Senescence may in the human mammary epithelium be at the origin of RIF (44) and RT may have a more pronounced effect on stroma (42). Thus, an already dense breast could be more prone to developing fibrosis. As younger patients have more inhomogeneous breast, this result seems in agreement with studies reporting worse cosmetic results in young patients [e.g., (45)], who typically have a denser breast. In our results, however, fibrosis was not correlated with age, neither kurtosis (Pearson correlation $p = 0.28$). This lack of correlations with age could be due to the limited range of age of our patients (95%CI 61.0–82.9 years), that do not include younger (<50) patients. The relationship of fibrosis and radiomic features from CT of the breast with age therefore could be the subject of future investigation.

CONCLUSION

The models implemented show that radiomic and dose textural variables extracted from the breast and PTV volumes after correction for fractionation and CT density scale can predict RIF and may help better select patients candidate to exclusive PBI.

DATA AVAILABILITY STATEMENT

The datasets generated for this study are available on request to the corresponding author.

ETHICS STATEMENT

The studies involving human participants were reviewed and approved by Comitato Etico Unico Regionale—CEUR Friuli Venezia Giulia. Azienda Regionale di Coordinamento per la Salute (ARCS), via Pozzuolo n. 330 – 33100 Udine (palazzina B). The patients/participants provided their written informed consent to participate in this study.

AUTHOR CONTRIBUTIONS

MA and LV conceived the study. LV and AC performed the contouring of the cases and were responsible for the clinical evaluation of side effects during the follow-up. GP and ADr extracted the imaging and dose data. GP processed the data and performed radiomics analysis. MA performed the machine learning and statistical analysis and wrote the manuscript with inputs from JS, IN, MT, ADP, MU, SM, MM, and GS. All the authors discussed the results and contributed to final manuscript.

REFERENCES

1. Avanzo M, Stancanello J, Jena R. Adverse effects to the skin and subcutaneous tissue. In: Rancati T, Fiorino C, editors. *Modelling Radiotherapy Side Effects: Practical Applications for Planning Optimisation.* Boca Raton, FL: CRC Press, Taylor & Francis Group (2019). p. 291–307. doi: 10.1201/b21956-12
2. Alexander MA, Brooks WA, Blake SW. Normal tissue complication probability modelling of tissue fibrosis following breast radiotherapy. *Phys Med Biol.* (2007) 52:1831–43. doi: 10.1088/0031-9155/52/7/005
3. Mukesh MB, Harris E, Collette S, Coles CE, Bartelink H, Wilkinson J, et al. Normal tissue complication probability (NTCP) parameters for breast fibrosis:

pooled results from two randomised trials. *Radiother Oncol.* (2013) 108:293–8. doi: 10.1016/j.radonc.2013.07.006
4. Avanzo M, Stancanello J, Trovo M, Jena R, Roncadin M, Trovo MG, et al. Complication probability model for subcutaneous fibrosis based on published data of partial and whole breast irradiation. *Phys Med.* (2012) 28:296–306. doi: 10.1016/j.ejmp.2011.11.002
5. Avanzo M, Stancanello J, El Naqa I. Beyond imaging: the promise of radiomics. *Phys Med.* (2017) 38:122–39. doi: 10.1016/j.ejmp.2017.05.071
6. Moran A, Daly ME, Yip SSF, Yamamoto T. Radiomics-based assessment of radiation-induced lung injury after stereotactic body radiotherapy. *Clin Lung Cancer.* (2017) 18:e425–31. doi: 10.1016/j.cllc.2017.05.014
7. Rossi L, Bijman R, Schillemans W, Aluwini S, Cavedon C, Witte M, et al. Texture analysis of 3D dose distributions for predictive modelling of toxicity rates in radiotherapy. *Radiotherap Oncol.* (2018) 129:548–53. doi: 10.1016/j.radonc.2018.07.027
8. Gabryś HS, Buettner F, Sterzing F, Hauswald H, Bangert M. Design and selection of machine learning methods using radiomics and dosiomics for normal tissue complication probability modeling of xerostomia. *Front Oncol.* (2018) 8:35. doi: 10.3389/fonc.2018.00035
9. Liang B, Yan H, Tian Y, Chen X, Yan L, Zhang T, et al. Dosiomics: extracting 3D spatial features from dose distribution to predict incidence of radiation pneumonitis. *Front Oncol.* (2019) 9:269. doi: 10.3389/fonc.2019.00269
10. Trovo M, Avanzo M, Vinante L, Furlan C, Fiorica F, Perin T, et al. Seven fractions to deliver partial breast irradiation: the toxicity is low. *Radiat Oncol.* (2017) 12:86. doi: 10.1186/s13014-017-0825-9
11. *The Radiation Therapy Oncology Group (RTOG) Contouring Atlases*. Available online at: https://www.rtog.org/CoreLab/ContouringAtlases.aspx
12. Avanzo M, Trovo M, Stancanello J, Jena R, Roncadin M, Toffoli G, et al. Hypofractionation of partial breast irradiation using radiobiological models. *Phys Med.* (2015) 31:1022–8. doi: 10.1016/j.ejmp.2015.08.016
13. Ospina JD, Zhu J, Chira C, Bossi A, Delobel JB, Beckendorf V, et al. Random forests to predict rectal toxicity following prostate cancer radiation therapy. *Int J Radiat Oncol Biol Phys.* (2014) 89:1024–31. doi: 10.1016/j.ijrobp.2014.04.027
14. Haciislamoglu E, Colak F, Canyilmaz E, Dirican B, Gurdalli S, Yilmaz AH, et al. Dosimetric comparison of left-sided whole-breast irradiation with 3DCRT, forward-planned IMRT, inverse-planned IMRT, helical tomotherapy, and volumetric arc therapy. *Phys Med.* (2015) 31:360–7. doi: 10.1016/j.ejmp.2015.02.005
15. Vallières M, Freeman CR, Skamene SR, El Naqa I. A radiomics model from joint FDG-PET and MRI texture features for the prediction of lung metastases in soft-tissue sarcomas of the extremities. *Phys Med Biol.* (2015) 60:5471–96. doi: 10.1088/0031-9155/60/14/5471
16. Coroller TP, Agrawal V, Narayan V, Hou Y, Grossmann P, Lee SW, et al. Radiomic phenotype features predict pathological response in non-small cell lung cancer. *Radiother Oncol.* (2016) 119:480–6. doi: 10.1016/j.radonc.2016.04.004
17. Lamba R, McGahan JP, Corwin MT, Li C, Tran T, Seibert JA, et al. CT hounsfield numbers of soft tissues on unenhanced abdominal CT scans: variability between two different manufacturersâ€™ MDCT scanners. *Am J Roentgenol.* (2014) 203:1013–20. doi: 10.2214/AJR.12.10037
18. Johansson S, Svensson H, Denekamp J. Dose response and latency for radiation-induced fibrosis, edema, and neuropathy in breast cancer patients. *Int J Radiat Oncol Biol Phys.* (2002) 52:1207–19. doi: 10.1016/S0360-3016(01)02743-2
19. Zwanenburg A, Leger S, Vallières M, Lock S. The Image Biomarker Standardisation Initiative for. Image biomarker standardisation initiative. *arXiv e-prints.* arXiv:1612.07003v11 (2016).
20. Zhang L, Fried DV, Fave XJ, Hunter LA, Yang J, Court LE. IBEX: an open infrastructure software platform to facilitate collaborative work in radiomics. *Med Phys.* (2015) 42:1341–53. doi: 10.1118/1.4908210
21. Buda M, Maki A, Mazurowski MA. A systematic study of the class imbalance problem in convolutional neural networks. *arXiv e-prints.* arXiv:1710.05381 (2017). doi: 10.1016/j.neunet.2018.07.011
22. Lemaitre G, Nogueira F, Aridas CK. Imbalanced-learn: a python toolbox to tackle the curse of imbalanced datasets in machine learning. *arXiv e-prints.* arXiv:1609.06570 (2016) .
23. Haibo He, Yang Bai, E. A. Garcia, Shutao Li. ADASYN: Adaptive synthetic sampling approach for imbalanced learning. In: *2008 IEEE International Joint Conference on Neural Networks (IEEE World Congress on Computational Intelligence*) Hong Kong (2008). doi: 10.1109/IJCNN.2008.4633969
24. Yung M, Brown ET, Rasin A, Furst JD, Raicu DS. Synthetic sampling for multi-class malignancy prediction. *arXiv e-prints.* arXiv:1807.02608 (2018).
25. Franke GR. Stepwise Regression. In: Sheth J, Malhotra N, editors. *Wiley International Encyclopedia of Marketing.* Hoboken, NJ: American Cancer Society (2010). doi: 10.1002/9781444316568.wiem02071
26. Thu N. Faster feature selection with a dropping forward-backward algorithm. *arXiv e-prints.* arXiv:1910.08007 (2019).
27. Chen S, Zhou S, Yin FF, Marks LB, Das SK. Investigation of the support vector machine algorithm to predict lung radiation-induced pneumonitis. *Med Phys.* (2007) 34:3808–14. doi: 10.1118/1.2776669
28. Galar M, Fernandez A, Barrenechea E, Bustince H, Herrera F. A review on ensembles for the class imbalance problem: bagging-, boosting-, and hybrid-based approaches. *IEEE Trans Syst Man Cybernet.* (2012) 42:463–84. doi: 10.1109/TSMCC.2011.2161285
29. Ben-Bassat M, Klove KL, Weil MH. Sensitivity analysis in bayesian classification models: multiplicative deviations. *IEEE Trans Pattern Analysis Mach Intellig.* (1980) 2:261–6. doi: 10.1109/TPAMI.1980.4767015
30. Kukar M, Kononenko I, Silvester T. Machine learning in prognosis of the femoral neck fracture recovery. *Artif Intellig Med.* (1996) 8:431–51. doi: 10.1016/S0933-3657(96)00351-X
31. Massari E, Rancati T, Giandini T, Cicchetti A, Vavassori V, Fellin G, et al. PO-0851: Artificial neural networks for toxicity prediction in RT: a method to validate their "intelligence". *Radiother Oncol.* (2017) 123:S461–2. doi: 10.1016/S0167-8140(17)31288-4
32. Parmar C, Grossmann P, Bussink J, Lambin P, Aerts HJ. Machine learning methods for quantitative radiomic biomarkers. *Sci Rep.* (2015) 5:13087. doi: 10.3389/fonc.2015.00272
33. Parekh V, Jacobs MA. Radiomics: a new application from established techniques. *Expert Rev Precis Med Drug Dev.* (2016) 1:207–26. doi: 10.1080/23808993.2016.1164013
34. Castiglioni I, Gallivanone F, Soda P, Avanzo M, Stancanello J, Aiello M, et al. AI-based applications in hybrid imaging: how to build smart and truly multi-parametric decision models for radiomics. *Eur J Nucl Med Mol Imaging.* (2019) 46:2673–99. doi: 10.1007/s00259-019-04414-4
35. Mandrekar JN. Receiver operating characteristic curve in diagnostic test assessment. *J Thorac Oncol.* (2010) 5:1315–6. doi: 10.1097/JTO.0b013e3181ec173d
36. Power M, Fell G, Wright M. Principles for high-quality, high-value testing. *Evid Based Med.* (2013) 18:5–10. doi: 10.1136/eb-2012-100645
37. Collette S, Collette L, Budiharto T, Horiot JC, Poortmans PM, Struikmans H, et al. Predictors of the risk of fibrosis at 10 years after breast conserving therapy for early breast cancer: a study based on the EORTC Trial 22881–10882 'boost versus no boost'. *Eur J Cancer.* (2008) 44:2587–99. doi: 10.1016/j.ejca.2008.07.032
38. Hepel JT, Tokita M, MacAusland SG, Evans SB, Hiatt JR, Price LL, et al. Toxicity of three-dimensional conformal radiotherapy for accelerated partial breast irradiation. *Int J Radiat Oncol Biol Phys.* (2009) 75:1290–6. doi: 10.1016/j.ijrobp.2009.01.009
39. Lozza L, Fariselli L, Sandri M, Rampa M, Pinzi V, De Santis MC, et al. Partial breast irradiation with CyberKnife after breast conserving surgery: a pilot study in early breast cancer. *Radiat Oncol.* (2018) 13:49. doi: 10.1186/s13014-018-0991-4
40. Yosinski J, Clune J, Nguyen A, Fuchs T, Lipson H. Understanding neural networks through deep visualization. *arXiv e-prints.* arXiv:1506.06579 (2015).
41. Sankar V, Kumar D, Clausi DA, Taylor GW, Wong A. SISC: End-to-end interpretable discovery radiomics-driven lung cancer prediction via

stacked interpretable sequencing cells. *arXiv e-prints.* arXiv:1901.04641 (2019).
42. Maskarinec G, Woolcott CG, Kolonel LN. Mammographic density as a predictor of breast cancer outcome. *Future Oncol.* (2010) 6:351–4. doi: 10.2217/fon.10.3
43. Alowami S, Troup S, Al-Haddad S, Kirkpatrick I, Watson PH. Mammographic density is related to stroma and stromal proteoglycan expression. *Breast Cancer Res.* (2003) 5:R129–35. doi: 10.1186/bcr622
44. Nguyen HQ, To NH, Zadigue P, Kerbrat S, De La Taille A, Le Gouvello S, et al. Ionizing radiation-induced cellular senescence promotes tissue fibrosis after radiotherapy. A review. *Crit Rev Oncol Hematol.* (2018) 129:13–26. doi: 10.1016/j.critrevonc.2018.06.012
45. Vargas L, Sole S, Sole CV. Cosmesis after early stage breast cancer treatment with surgery and radiation therapy: experience of patients treated in a Chilean radiotherapy centre. *Ecancermedicalscience.* (2018) 12:819. doi: 10.3332/ecancer.2018.819

Conflict of Interest: JS is employed by the company Guerbet SA, Villepinte, France.

The remaining authors declare that the research was conducted in the absence of any commercial or financial relationships that could be construed as a potential conflict of interest.

The handling editor declared a past collaboration with two of the authors MA and IN.

frontiers in Oncology

REVIEW
published: 05 June 2020
doi: 10.3389/fonc.2020.00790

Machine Learning-Based Models for Prediction of Toxicity Outcomes in Radiotherapy

Lars J. Isaksson[1†], Matteo Pepa[1†], Mattia Zaffaroni[1†], Giulia Marvaso[1,2], Daniela Alterio[1], Stefania Volpe[1], Giulia Corrao[1,2], Matteo Augugliaro[1], Anna Starzyńska[3], Maria C. Leonardi[1], Roberto Orecchia[4] and Barbara A. Jereczek-Fossa[1,2]*

[1] Division of Radiotherapy, IEO European Institute of Oncology IRCCS, Milan, Italy, [2] Department of Oncology and Hemato-Oncology, University of Milan, Milan, Italy, [3] Department of Oral Surgery, Medical University of Gdańsk, Gdańsk, Poland, [4] Scientific Directorate, IEO European Institute of Oncology IRCCS, Milan, Italy

In order to limit radiotherapy (RT)-related side effects, effective toxicity prediction and assessment schemes are essential. In recent years, the growing interest toward artificial intelligence and machine learning (ML) within the science community has led to the implementation of innovative tools in RT. Several researchers have demonstrated the high performance of ML-based models in predicting toxicity, but the application of these approaches in clinics is still lagging, partly due to their low interpretability. Therefore, an overview of contemporary research is needed in order to familiarize practitioners with common methods and strategies. Here, we present a review of ML-based models for predicting and classifying RT-induced complications from both a methodological and a clinical standpoint, focusing on the type of features considered, the ML methods used, and the main results achieved. Our work overviews published research in multiple cancer sites, including brain, breast, esophagus, gynecological, head and neck, liver, lung, and prostate cancers. The aim is to define the current state of the art and main achievements within the field for both researchers and clinicians.

Keywords: radiotherapy, toxicity, predictive models, machine-learning, radiomics

OPEN ACCESS

Edited by:
Claudio Fiorino,
San Raffaele Hospital (IRCCS), Italy

Reviewed by:
Jung Hun Oh,
Cornell University, United States
Alexander F. I. Osman,
Al-Neelain University, Sudan

****Correspondence:***
Giulia Marvaso
giulia.marvaso@ieo.it

[†]These authors have contributed equally to this work

Specialty section:
This article was submitted to Radiation Oncology, a section of the journal Frontiers in Oncology

Received: *30 January 2020*
Accepted: *22 April 2020*
Published: *05 June 2020*

Citation:
Isaksson LJ, Pepa M, Zaffaroni M, Marvaso G, Alterio D, Volpe S, Corrao G, Augugliaro M, Starzyńska A, Leonardi MC, Orecchia R and Jereczek-Fossa BA (2020) Machine Learning-Based Models for Prediction of Toxicity Outcomes in Radiotherapy. Front. Oncol. 10:790. doi: 10.3389/fonc.2020.00790

INTRODUCTION

It is estimated that as many as half of the cancer patients in the world are eligible for radiotherapy (RT), either with curative or palliative intent (1). Ultimate generation linear accelerators and modern techniques, such as intensity-modulated RT (IMRT), stereotactic body RT (SBRT), and proton therapy (PT), offer high conformity and submillimetric levels of precision. However, normal tissues close to the target region, defined as organs at risk (OARs), can also be affected, leading to RT-induced toxicity. Short-term or acute toxicity occurs during treatment or within 3 months after its completion, and generally, full recovery occurs within weeks to months. Conversely, late effects, such as fibrosis or RT-induced oncogenesis, are generally considered as irreversible and progressive over time. It follows that, when planning any RT treatment, its potential benefits have to be weighed against the possibilities of damage to healthy organs and tissues, with the final aim of maximizing curative response while minimizing the probability of normal tissue complications. On the other hand, when RT is delivered with curative intent, target coverage should not be jeopardized in favor of sparing OARs (2). However, different RT-induced side effects vary in their clinical significance, so an accurate estimate of risks is mandatory, especially when alternatives such as surgery or

chemotherapy are available. The physiopathology of toxicity is not only related to the radiation dose but also depends on genetic factors and tumor microenvironment. Therefore, identifying the main factors that predispose for a specific type of toxicity can help to improve treatment planning and inform patients and clinicians about expected treatment tolerance.

Radiosensitivity is generally studied with the so-called normal tissue complication probability (NTCP) models, which can be classified into mechanistic (or analytical) and data-driven [or (semi)empirical] (3). The former category is based on a simplified characterization of the interaction between radiation and biological tissues and seeks to explain the underlying mechanisms with explicit algorithms. The most common analytical models are the Lyman–Kutcher–Burman models, which are often included into treatment planning systems to allow for a biological optimization of the delivered dose among competing treatment strategies (4). These algorithms are based on handcrafted rules with intricate exceptions that often fail to predict the actual complications induced by RT. On the other hand, data-driven approaches are based on the assumption that the interaction between radiation and normal tissue is complex and cannot be properly represented deterministically. Therefore, such approaches aim to identify the model that best fits the input data (also termed features or independent variables) and output data (also termed response or dependent variables). Predictors of toxicity can be roughly classified into "dosimetric," which directly concerns the delivery of radiation (e.g., dose-volume histogram (DVH) points), "clinical," which includes patient- and disease-related variables (e.g., gender and tumor histology), and "image-based" or "radiomic," which can be extracted from various medical images (e.g., the mean, variance, and skewness of image intensity histograms). In general, these approaches can be further distinguished into well-known traditional statistical techniques, such as regression-based techniques, and approaches based on artificial intelligence (AI) and machine learning (ML) (5).

Abbreviations: 3D-CRT, 3D conformal RT; ADC, apparent diffusion coefficient; AI, artificial intelligence; ANN, artificial neural network; AUC, area under the curve; BMI, body mass index; BRT, brachytherapy; CNN, convolutional neural networks; CP-DMA, canonical polyadic decomposition–deterministic multi-way analysis; CT, computed tomography; CTCAE, common terminology criteria for adverse events; Dmax, dose max; DV, dose-volume; DVH, dose-volume histogram; EBRT, external beam RT; ED, erectile disfunction; EORTC, European Organization for Research and Treatment of Cancer; FDG PET, [^{18}F]-fluorodeoxyglucose PET; GEC-ESTRO, Groupe Européen de Curiethérapie-European SocieTy for Radiotherapy & Oncology; GI, gastrointestinal; GLCM, gray level co-occurrence matrix; GU, genitourinary; H&N, head and neck; IBM, image biomarker; IBDM, image-based data mining; ICA, independent component analysis; IMRT, intensity-modulated RT; kNN, k-nearest neighbors; LASSO, Least Absolute Selection and Shrinkage Operator; LR, logistic regression; MARS, multivariate adaptive regression splines; ML, machine learning; MRI, magnetic resonance imaging; NSCLC, non-small-cell lung cancer; NTCP, normal tissue complication probability; NTR, non-treatment related; OAR, organ at risk; PCa, prostate cancer; PCA, principal component analysis; PET, positron emission tomography; PLR, penalized logistic regression; PRFR, pre-conditioned random forest regression; PSA, prostate-specific antigen; PT, proton therapy; PTV, planning target volume; RB, rectal bleeding; RF, random forest; RSDM, rectum surface dose maps; RT, radiotherapy; RUS, random under-sampling; SBRT, stereotactic body RT; SNP, single nucleotide polymorphism; SVM, support vector machine; TPS, treatment planning system. TRIPOD, Transparent Reporting of a multivariable prediction model for Individual Prognosis Or Diagnosis; V20, volume receiving 20% of dose.

ML-Based Models of Toxicity

The theoretical framework for artificially intelligent ML models was laid down already in the 1950s (6), but it was not until recently that advances in technology have allowed for the integration of these tools into the experimental and clinical practice of health sciences. AI, in its broadest sense, denotes an artificial system able to perform a certain task to some success. ML, typically considered a subset of AI, generally refers to some set of algorithms that can "learn" to perform a specific task without explicit implementation of the solution (although the terms AI and ML are often used interchangeably). For instance, ML algorithms are able to produce predictions on new and unseen data after being trained on a finite learning data set and are especially useful for tasks that involve a large amount of data or variables (**Figure 1**). With the plethora of possible variables that can lead to toxicity, ML approaches are particularly well suited to model the relationship between treatment-induced side effects and related covariates. An ML model that is able to predict an outcome from a set of inputs, after tuning the best set of parameters on a number of training cases, is referred to as a classifier. Some common classifiers are naïve Bayes, logistic regression (LR), k-nearest neighbors (kNN), random forests (RF), support vector machine (SVM), and artificial neural networks (ANN).

Since the ML model will learn the parameters from the available data, it follows that the characteristics of the data set are absolutely crucial. If the training data set is sparse, the model typically fails to learn a representative set of parameters that can be generalized to instances outside of the data set. This problem, which generally arises when a model has been trained to encompass a particular set of data too closely, is known as overfitting or overtraining. Overfitting can occur for a variety of reasons and should always be a major concern when constructing an ML model.

Since the performance of any ML model depends on the particular problem and data set it is applied to, it is intractable to generally rank different methods. Nevertheless, an acceptable approximation of a model's performance is given by the so-called AUC (which is defined as the area under the receiver operating characteristic curve) applied to an independent validation set. The AUC value of a model ranges between 1, corresponding to perfect classification of the validation set, and 0.5, corresponding to a purely random classification. It is important to note, however, that the AUC can be severely misleading in case of flaws in the model design, such as heavily imbalanced data sets or misused validation procedures.

Successful ML models have the potential to aid clinical facilities and practitioners in minimizing side effects and increasing the likelihood of positive outcomes. Despite a good amount of research in ML methods for toxicity assessment, to the best of our knowledge, this is the first effort to summarize the current state of the field. Previous publications have focused either on specific anatomical districts (5) or exclusively on methodologies and theory (7, 8). Therefore, the aim of this review is to present an overview of current achievements in the field as well as main areas of debate and possible future directions, both from a methodological and a clinical perspective.

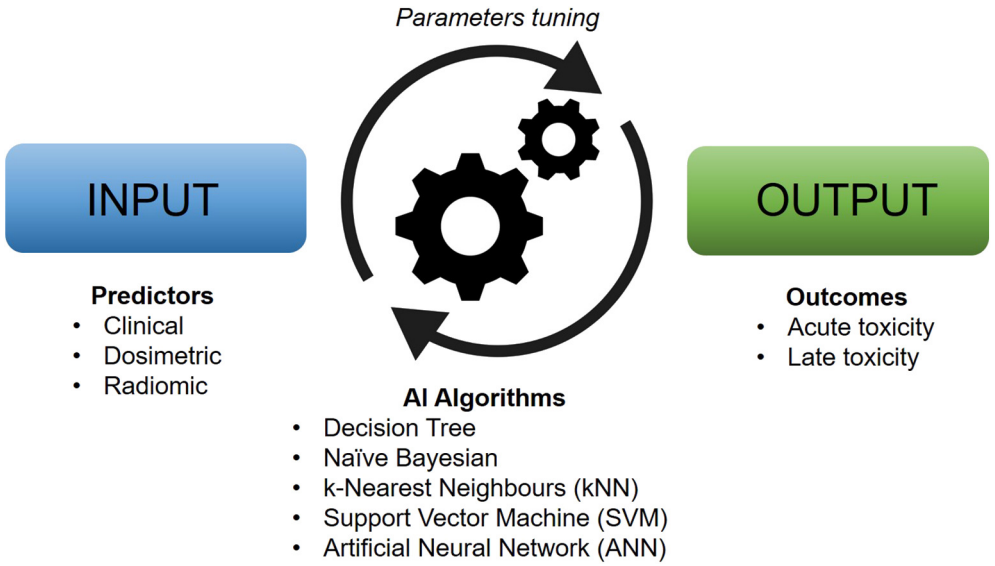

FIGURE 1 | Typical workflow of artificial intelligence-based models for clinical toxicity prediction. Machine learning algorithms work by tuning their characteristic parameters by modeling the relationship between input and output data in an automatic manner.

SEARCH STRATEGY AND SELECTION CRITERIA

A comprehensive literature review was performed through the use of a search string (see **Supplementary Materials S1**) built by an experienced medical librarian with input from the study investigators. Different combinations of database-specific terms were used, supplemented by keywords in order to cover all the areas related to RT toxicity, ML, and toxicity prediction. The literature review was conducted using the PubMed/Medline databases in order to identify publications to be synthetized into an exhaustive overview of the state of the art of ML application for the prediction of RT-induced toxicity. The search resulted in 864 hits. Reference lists of selected articles were hand searched for further potential relevant papers and also using the Snowballing technique (9). Studies with no focus on cancer, radiation therapy, toxicity, or any kind of ML (in its broadest sense) were excluded, together with articles dealing with pediatric patients. All publications in languages other than English were also excluded. In the end, 53 studies were included in this narrative review. The search was conducted in March 2020 (see **Supplementary Materials S2**).

OVERVIEW OF CONTEMPORARY RESEARCH

Many studies were found that employ ML-based models to predict RT-related side effects. Most of them concern head and neck (H&N) (13 studies), lung (15 studies), and prostate (16 studies) cancers, while a minor portion focused on brain (1 study), breast (3 studies), esophagus (1 study), gynecology (3 studies), and liver (1 study) cancers (**Table 1**). The presented literature is divided into different sections according to the anatomical district. Focus was put into presenting both methodological and clinical aspects of the papers.

Brain

A single study on ML-based toxicity modeling was found related to brain cancer (4). In the study, the authors conducted a comprehensive comparison of the performance of different ML classifiers on multiple data sets including patients with brain, lung, and H&N primaries. Their models included decision trees, RF, neural network, SVM, elastic net LR, and Logit-Boost classifiers and were tested on 12 distinct data sets for a total of 3496 patients. Both dosimetric and blood marker data from meningioma as well as (non)-small-cell lung cancer (NSCLC) and H&N cancer patients were considered. No single classifier was found to be ideal across all data sets, but RF and net LR performed comparably (best in six and four data sets, respectively). Based on these results, the authors also investigated methods of preselecting a classifier, concluding that empirical selection of the classifier is advantageous, leading to an average AUC increase of 0.02.

Breast

Current available literature includes only one abstract (11) and two full papers (10, 12). In the study by Saednia et al., they proposed an innovative approach based on the detection of body-surface temperature increase induced by radiation dermatitis. Thermal images of the irradiated breast were taken from a pool of 90 patients at four consecutive time points: pre-RT and after 5, 10, and 15 fractions, respectively (with a total dose of 42.50 Gy in 16 fractions). Skin toxicity was assessed at the end of RT with the Common Terminology Criteria for Adverse Events (CTCAE) guidelines. On the independent testing data set, the RF classifier

TABLE 1 | Summary of reviewed literature.

Cancer type	References	No. of pts	Type of RT	Type of predicted toxicity	Features type	Classifier	Results*
Breast	(10)	90	RT	Dermatitis	R	RF	Acc = 0.87 (test)
	(11)	2277		Moist desquamation, dermatitis, chest pain, fatigue	D, C	LR, RF, gradient boosting	0.56–0.85
	(12)	827	RT	Telangiectasia	D, C	LASSO	
Esophagus	(13)	101	IMRT or 3D-CRT	Pneumonitis	D, C	LR	Acc = 0.63
Gyneco	(14)	42	EBRT+BRT	Rectal toxicity	D	SVM	0.82–0.91
	(15)	42	EBRT+BRT	Rectal toxicity	D	CNN (transfer learning)	1.29
	(16)	35	BRT	Fistula formation	D, C	SVM	1.30
H&N	(17)	437	RT (397) PT (40)	Toxicity (grade ≥3)	C	LR, RF, XGBoost	0.63–0.65
	(18)	2121	RT	Unplanned hospitalizations, Feeding tube placement, Weight loss	D, C	LR, gradient boosting, RF	0.64–0.76
	(19)	153	RT	Xerostomia	D, R, C	6 ML algotithms	Best SVM and extra-trees 0.74–0.89
	(20)	86	RT	Trismus	D	IBDM	Identification of a cluster of voxel related with toxicity
	(21)	427	RT	Xerostomia	D, C	LR, LASSO, RF	Best LR (0.70)
	(22)	173	RT	Acute dysphagia	D, C	SVM, RF	0.82
	(23)	297	IMRT	Xerostomia (grade ≥2)	D, C	LR	Model updating is beneficial
	(24)	134	IMRT and PT	Esophagitis	R, D	LASSO	0.75
	(25)	47	3D-CRT	Sensorineural hearing loss	R, C	Decision stump, Hoeffding	76.08% accurarcy 75.9% precision
	(26)	37	IMRT	Parotid shrinkge Xerostomia	D, C	Fuzzy logic Naïve Bayes	Acc = 0.79–0.86
	(27)	249	IMRT	Xerostomia, sticky saliva	R, D	Multivariate LR	0.77
	(28)	351	IMRT	Mucositis	D, C	LR, SVM, RF	0.71 (RF)
	(29)	1 (H&N) 1 (Prostate)	IMRT	Xerostomia (H&N), Rectal bleeding (prostate)	D	Decision tree, SVM	0.42% MAE (H&N) 97% acc (prostate)
Liver	(30)	125	SBRT	Hepatobiliary toxicity	D, C	CNN (transfer learning)	1.25
Lung	(31)	110	SBRT	LC, DFS, OS, and fibrosis	R	Cox regression	
	(32)	203	IMRT or PT	Pneumonitis	C	RF	1.06
	(33)	192	IMRT and 3D-CRT	Radiation pneumonitis	R, D, C	LASSO	0.68
	(34)	197	SBRT	Chest wall syndrome	D, C	Descision tree RF	n/a
	(4)	3496 (lung+brain +H&N)	RT	Classifiers comparison	D, C	Decision tree, RF, ANN, SVM, elastic net, logit-boost	Best: elastic net LR and RF
	(35)	14	SBRT	Lung injuries	R, D	LR	0.64–0.78
	(36)	201	SBRT	Pneumonitis	D, C	Decision trees, RF, RUSBoost	
	(37)	115	RT	Esophagitis	D, C	LASSO	0.78
	(38)	54	3D-CRT	Pneumonitis	D, C	Bayesian network LR Single variable	0.66–0.83
	(39)	748	RT	Esophagitis	D, C	LR	0.83
	(40)	219	3D-CRT	Pneumonitis	D, C	SVM	1.16

(Continued)

TABLE 1 | Continued

Cancer type	References	No. of pts	Type of RT	Type of predicted toxicity	Features type	Classifier	Results*
	(41)	55 (H&N) 219+166 (Lung)	3D-CRT	Xerostomia, Pneumonitis (166) Esophagitis (216)	D, C	LR, SVM, ANN	Best: modified SVM
	(42)	219	RT	Radiation pneumonitis	D, C	Decision tree, ANN, SVM, self-organizing maps	0.79
	(43)	234	RT	Radiation pneumonitis	D, C	Decision tree	0.72
	(44)	166	EBRT	Esophagitis xerostomia	D	LR	
	(45)	142	3D-CRT	Pneumonitis	D	ANN	0.61–0.85
Prostate	(46)	64	IMRT (52 pts), 3D-CRT (12 pts)	Urinary toxicity Gastro-intestinal toxicity	R, D, C	LR	0.65–0.77
	(47)	33	IMRT	Cystitis	R	LR	0.62–0.75
	(48)	33	IMRT	Rectal wall changes	R	LR	0.46–0.81
	(49)	351	RT	Rectal bleeding Fecal incontinence Urinary incontinence Nocturia	R, D, C	LR	0.58–0.73
	(50)	598	RT	Late fecal incontinence	D, C	ANN	0.78
	(51)	593	RT	Rectal bleeding	D, C	ICA	0.83, 0.80, 0.78
	(52)	324	BRT+-EBRT	GU toxicity symptoms	D, C, G	RF	0.7
	(53)	118	EBRT, BRT	GI toxicities	D	LR	Identification of spatial constraint for toxicity reduction
	(54)	368	RT	Rectal bleeding, Erectile dysfunction	C, G	RF, LR	0.71 (rectal bleeding) 0.68 (erectile dysfunction)
	(55)	79	IMRT	Rectal toxicity (grade $\geq$2)	D, C	LR	1.28
	(56)	754	EBRT	Dysuria, hematuria, incontinence, frequency	D, C	LR, Elastic-net, SVM, RF, ANN, MARS	Best: LR, MARS AUC = 0.65
	(57)	99	EBRT	Rectal bleeding	D	LDA, SVM, k-means, kNN, PCA, CP-DMA	Best: CP-DMA
	(58)	261	3D-CRT	Rectal toxicity, rectal bleeding	D, C	RF NTCP, NTCP	0.76, 0.66
	(59)	718	RT	Rectal bleeding		LR, ANN	0.655, 0.704
	(60)	321	RT	Acute bladder and rectal toxicity	D, C	ANN, SVM	0.7
	(61)	119	RT	Rectal bleeding Nocturia	D	ANN	Sensitivity and specificity >55%

*3D-CRT, 3D conformal RT; Acc, accuracy; ANN, artificial neural network; AUC, area under the curve; BRT, brachytherapy; CNN, convolutional neural network; CP-DMA, canonical polyadic decomposition–deterministic multi-way analysis; DFS, disease free-survival; EBRT, external beam RT; GI, gastrointestinal; GU, genitourinary; H&N, head and neck; IBDM, image-based data mining; ICA, indipendent component analysis; IMRT, intensity-modulated RT; kNN, k-nearest neighbors; LASSO, Least Absolute Selection and Shrinkage Operator; LC, local control; LDA, linear discriminant analysis; LR, logistic regression; MAE, mean absolute error; MARS, multivariate adaptive regression splines; ML, machine learning; NTCP, normal tissue complication probability; n/a, not applicable; OS, overall survival; PCA, principal component analysis; pt, patient; PT, proton therapy; RF, random forest; RT, radiotherapy; RUSBoost, random under-sampling Boost; SBRT, stereotactic body RT; SVM, support vector machine. Features were classified as clinical (C), dosimetric (D), genomic (G), or radiomic (R). *If not specified, AUC values are reported.*

showed a good accuracy (87%) at the fifth fraction in predicting the skin toxicity at the end of RT.

The authors in the study by Reddy et al. trained three different classifiers, namely, RF, gradient boosted decision tree, and LR, on a large population of 2277 patients to predict the occurrence of common radiation toxicities, such as moist desquamation, radiation dermatitis, breast/chest wall pain, and fatigue. Validation performances reached AUC values of 0.85, 0.82, 0.77, and 0.56 for the respective endpoints. According to the authors, it was the first demonstration of the ability to accurately predict acute RT toxicities in a prospective validation data set.

Finally, Mbah et al. set out to highlight the main failure causes for models predicting RT-induced toxicity. Data from two different German cohorts were used for a total of 827 breast cancer patients who received RT. The Least Absolute Selection and Shrinkage Operator (LASSO) LR model was used to predict

telangiectasia within each individual data set separately. Each model was also externally tested on the other data set. To their surprise, they found that one predictive variable (hypertension) had a positive coefficient on one data set, and a negative coefficient on the other. Some variables were also exclusive to a specific model, thus suggesting that overcoming overfitting does not completely solve the problem of generalization.

Esophagus

An ML-based model for toxicity prediction in esophagus cancer patients was published by Hart et al. (13). In their work, the authors investigated the relationship between clinical symptoms of radiation pneumonitis and the pulmonary metabolic activity on post-treatment [^{18}F]-fluorodeoxyglucose positron emission tomography (FDG PET). Their study included a cohort of 101 patients who underwent restaging FDG PET/computed tomography (CT) imaging between 3 and 12 weeks after completing thoracic RT for esophageal cancer. Several LR models were built with different combinations of treatment and dosimetric variables, obtaining a peak accuracy of 0.63 with $p \leq 0.032$ when combining pulmonary metabolic radiation response with the mean lung dose, thus indicating a significant relationship between pulmonary metabolic radiation response and radiation pneumonitis.

Gynecological Cancers

The three studies in this section analyze toxicity outcomes prediction following brachytherapy alone or in combination with external beam RT (EBRT) in gynecological cancers. All the models were trained with limited data sets, ranging between 35 and 42 patients, and with SVM or convolutional neural network (CNN) classifiers.

Tian et al. (16) developed a model for fistula formation prediction with an SVM classifier. Thirty-one different features were used as predictor variables from a relatively small sample of 35 patients treated with interstitial brachytherapy. Their model reached a high accuracy of 0.901, but the authors rightfully point out the strong limitation deriving from the usage of the small data set.

One study by Chen et al. (14) investigated the relationship between rectal toxicity (CTCAE grade $\geq$2) and dosimetric features. In detail, the feature calculation was performed on both the 3D rectum surface and the 2D deformed accumulated rectal surface dose map. The models, for which they used SVM classifiers, achieved AUC values of 0.82 and 0.91 for different feature selection procedures (and 42 patients). The authors also demonstrated that the ML model outperformed classification based on the conventional Groupe Européen de Curiethérapie-European SocieTy for Radiotherapy & Oncology (GEC-ESTRO) dosimetric parameters Dose to 0.1, 1 and 2 cm^3, which achieved an AUC of 0.71.

Zhen et al. (15) tested the feasibility of a CNN for rectum toxicity prediction through a transfer learning approach. The network itself, originally developed by the visual geometry group at the University of Oxford, had been pretrained on the ImageNet data set. The fine-tuning step was then performed on unfolded rectum surface dose maps (RSDM). By using the gradient-weighted class activation maps, the authors were also able to identify the existence of discriminative regions on the RSDM. Their results demonstrate than the CNN can outperform conventional dosimetric parameters with top AUC values of 0.89 as compared to a meager 0.58 for the one-dimensional dose-volume (DV) parameters (or 0.7 for 2D RSDM features). The authors also presented comparisons between the transfer learned network and a network trained from scratch.

Head and Neck

The size of the training data sets in published works on H&N cancers ranges from 37 to 2121 patients. Predicted toxicity outcomes included late xerostomia, acute mucositis, parotid shrinkage, unplanned hospitalization, and weight loss. Applied classifiers included LR, RF, gradient boosting, and one based on fuzzy logic. In addition, one study (4) made a comparison of the performance of different classifiers on different data sets (please refer to the Brain section for further details).

The two most recent articles (17, 18) both applied three different classifiers (RF, gradient boosting, and LR models) to predict unplanned hospitalizations, feeding tube placement, and significant weight loss (Reddy) and grade $\geq$3 toxicity (Wojcieszynski). Reddy et al. considered a large data set of 2,121 patients, comparing over 700 treatment-related and clinical variables, and achieved AUC values of up to 0.640, 0.755, and 0.751 for RF, gradient boosting, and LR, respectively. Wojcieszynski et al. achieved a moderate success in predicting grade $\geq$3 toxicity for 437 patients after 90 and 180 days (*c*-statistic 0.65 and 0.63, respectively) using 47 different patient covariates. Among them, planning target volume (PTV) integral dose, body mass index (BMI), integral dose to regions outside the PTV, and age were most statistically impactful ones.

By retrospectively comparing updating strategies, Nakatsugawa et al. (23) demonstrated the importance of continuous model revising. On their data set, they concluded that the best strategy was to update the model yearly, keeping only the two most recent years of data. The method they used was LR classifying grade $\geq$2 late xerostomia with clinical and dosimetric variables from 297 patients.

The aim of the study by Beasley et al. (20) was to identify specific CT image regions with a dose–toxicity association to identify radiation-induced trismus in H&N patients treated with RT. To achieve this objective, an image-based data mining (IBDM) framework was applied to a cohort of 86 patients. The IBDM approach allowed for the identification of a cluster of voxels associated with trismus; this cluster was internally validated using a DVH-based approach and externally on a cohort of 35 patients. As stated by the authors, this study represents the first clinical application of IBDM with a continuous outcome variable.

Jiang et al. (21) utilized a data set of 427 H&N cancer patients treated with RT to predict xerostomia. Ridge LR, LASSO LR, and RF classifiers were trained with planned radiation dose data and non-dosimetric features to investigate the influence of dose patterns on xerostomia. Among the three different ML methods explored, ridge LR showed the best predictive power

with an AUC of 0.70, although the difference in performance was not statistically significant. The study highlighted how radio-morphology combined with ML methods can indicate the patterns of dose which are most influential on xerostomia, potentially improving radiation treatment planning.

Dean et al. (22) developed a model to predict severe acute dysphagia in H&N cancer patients treated with RT. Penalized LR (PLR), SVM, and RF models were trained using dosimetric and clinical data and then internally and externally validated on 173 and 90 patients, respectively. Results showed that PLR model performances were comparable with the more complex models with an AUC of 0.82 and that dose to the pharyngeal mucosa was an important predictor of dysphagia.

In another study, Gabryś et al. (19) investigated whether xerostomia risk assessment can be amended by ML with dosimetric, radiomic, and demographic features, rather than only using a NTCP model. The authors compared predictive performance of seven classification algorithms, six feature selection methods, and 10 data cleaning/class balancing techniques using the Friedman test and the Nemenyi *post-hoc* analysis. A cohort of 153 H&N cancer patients was used to predict xerostomia at different time stages. Their multivariate models achieved AUC values ranging from 0.74 to 0.88, with SVM and "extra-trees" having the top performances. The authors also pointed out that LR was preferred for univariate feature selection, and that data cleaning/class balancing had no advantage. Their NTCP models, on the other hand, failed to predict xerostomia (AUC < 0.6).

The study of Abdollahi et al. (48) aimed to predict sensorineural hearing loss in radiochemotherapy-treated H&N cancer patients. From a cohort of 47 patients, 490 image features of 94 cochlea were derived from CT images. To perform feature selection, classification, and prediction, 10 different ML approaches were tested. The predictive power (AUC, accuracy, and precision) of the ML algorithms was over 0.70 in all cases; the best was obtained by Decision Stump and Hoeffding modeling with 76.08% and 75.9% accuracy and precision, respectively. In conclusion, CT radiomic analysis, both with and without clinical and dosimetric variables, could help with chemoradiation-induced hearing loss.

On a small data set of 37 patients treated with IMRT, Pota et al. (26) applied a fuzzy logic-based classifier in order to predict the occurrence of parotid shrinkage and 12-month xerostomia. To do this, they used clinical features, dosimetric parameters, CT-based radiomic features, and combinations thereof as predictor variables. They achieved high respective accuracies of up to 0.86 (parotid shrinkage) and 0.79 (xerostomia). Their developed model is easily interpretable and have comparable performance to a naïve Bayes classifier.

The goal of the study by Van Dijk et al. (27) was to build a predictive model for xerostomia and sticky saliva in H&N cancer patients using CT image biomarkers (IBMs). The planning CT scans of 249 H&N cancer patients were collected to extract IBMs in order to create multivariable LR models, which were then internally validated by bootstrapping. In total, 26 features correlated with xerostomia and 24 correlated with sticky saliva were selected. The results showed how the addition of IBMs of the parotid and submandibular glands to dosimetric data improved the mean AUC from 0.74 to 0.77. The authors found that the IBM "short run emphasis" was the most important for xerostomia prediction, and "maximum CT intensity" was the most important for sticky saliva prediction. These features represented heterogeneity and density within the salivary glands, respectively.

Dean et al. (28) compared LR, SVM, and RF classifiers in a framework to predict severe acute mucositis on a cohort of 351 patients. Their variables included dose-volume (DV) parameters, spatial dose metrics, and clinical data. Although model performances were comparable, the best performance was obtained with the RF classifier, with an AUC value of 0.71. The authors also confirmed that reducing the volumes of oral cavity receiving intermediate/high doses may reduce mucositis incidence.

Zhang et al. (29) developed decision tree and SVM models for a single H&N patient. The model was supposed to predict saliva flow rate with DV constraints and tailored plan properties as input variables. The mean absolute error of predicting saliva flow rate was 0.42%. Their results suggest that "ML tools can be used to guide planners to select DV constraint settings corresponding to all involved OARs in a knowledge-driven manner."

El Naqa et al. (41) investigated several types of linear and non-linear kernels[1] to generate interaction terms and approximate the treatment-response function in order to capture the potential complexity of heterogeneous variable interactions more accurately. This study investigated xerostomia on a data set with 55 H&N cancer patients as well as two data sets with prostate cancer (PCa) patients. By first analyzing patient distributions with principal component analysis (PCA), they concluded that SVM outperformed both LR and an ANN.

Liver

Ibragimov et al. (30) employed a pre-trained CNN model on 3D dose maps in order to predict liver toxicity after SBRT. They also included non-dosimetric patient variables as additional inputs to the network. By using the saliency maps of the network, they were able to identify anatomical regions that are critical to spare during SBRT. On their data set of 125 patients, their model managed to predict hepatobiliary toxicity with an AUC of 0.85. In addition, their deep learning model also predicted almost two times fewer false-positive toxicity cases compared to DVH-based predictions. The authors also observed that irradiation of the proximal portal vein was associated with two times higher toxicity risks than irradiation of the left portal vein.

Lung

For lung cancers, the size of the data sets ranged between 54 and 235 patients. The majority of the studies dealt with radiation-induced pneumonitis, whereas some studies dealt with esophagitis, xerostomia, sticky saliva, and chest pain. Lung cancer RT may cause chest pain due to rib fracture, radiation-induced

[1] In this context, kernels are mathematical transformation functions that allow an implicit embedding of data in another feature space. For the purpose of this article, different kernels can be thought of as different types of SVMs.

neuropathy of the intercostal nerves or nerve branches, chest wall edema, or chest wall fibrosis. However, the only study we found that specifically investigated chest pain is the one by (34). The authors utilized decision tree and RF methods to identify robust features predictive of chest wall pain in a cohort of 197 patients. Both univariate and multivariate analyses confirmed the role of rib dose to 1 cc, chest wall dose to 30 cc, and rib dose max (D_{max}) as relevant variables. Based on these findings, efforts should be directed at lowering the rib dose to 1 cc <4000 cGy, chest wall dose to 30 cc <900 cGy, and rib D_{max} < 5100 cGy in order to mitigate chest wall syndrome.

Das et al. performed two studies (42, 43) for pneumonitis prediction in a data set of 219 lung cancer patients treated with RT. In both studies, the final model derived from a fusion of two or more single models. In the study dated 2007, starting from a data set of 234 lung cancer patients treated with RT, they trained a model for lung radiation-induced grade 2+ pneumonitis. The model consisted of a parametric dose-based Lyman NTCP model in conjunction with weighted non-parametric decision trees. The combined models' predictive power resulted in an AUC of 0.72—an improvement compared to the 0.62 AUC of the Lyman NTCP alone. In particular, the information about non-dose variables provided by the decision trees could add interpretability and aid in dissemination. In the study dated 2008, the authors constructed a consensus model by fusing four different non-linear multivariate models: decision trees, neural networks, SVMs, and self-organizing maps. Consensus was achieved by simply averaging the predictions for each patient from all four individual models (in an ensemble-wise manner, i.e., with several predictions for each individual model). This achieved an average AUC value of 0.79 with lower variance than the individual component models.

Esophagitis is another common side effect in lung cancer RT, but only two studies researched this topic (41, 44). In the former, the authors explored model building and variable selection methods for multivariate dose-response assessment, considering a data set of 166 NSCLC patients. Using a LR classifier, the authors concluded that performance can be improved by mixing clinical and DV factors as input parameters. In the second paper, they investigated several types of linear and non-linear kernels to approximate the treatment-response function and capture the potential complexity of heterogeneous variable interactions. This was done with a data set of 219 lung cancer patients. In the same article, the authors also investigated pneumonitis on a data set of 166 patients and xerostomia on a data set of 55 patients. After applying PCA to analyze variable distributions, they concluded that SVM outperformed both LR and an ANN.

Niedzielski et al. (24) explored a novel method for using CT imaging biomarkers to quantify patients' radiosensitivity and subsequently predict esophagitis risk. Patients with high response to radiation, despite lower radiation dose, were labeled as radiosensitive. This information was extracted through K-means clustering (an automatic clustering algorithm) with three nodes. The authors concluded that inclusion of the radiosensitive variable improved LASSO LR model performance (mean AUC, 0.75) compared to models without this information (mean AUC, 0.69). Their predictive model was built with a cohort of 134 NSCLC patients treated with IMRT (85 pts) or passive-scatter PT (49 pts).

Valdes et al. (36) developed a patient-specific "big data" clinical decision tool in order to predict radiation-induced pneumonitis in stage I NSCLC patients who received SBRT. In the study, the performance of three different algorithms [Decision Trees, RF, random under-sampling (RUS) Boost] was evaluated on a cohort of 201 lung cancer patients. The feature selection highlighted that the most important features for pneumonitis prediction were the diffusion capacity of the lung for carbon monoxide and the dose to the heart, trachea, and bronchus. The authors also stated that at least 800 patients are needed to keep the error below 10% for pneumonitis prediction.

Huang et al. performed two studies for prediction of esophagitis. In the first one (39), a model for the assessment of severe acute esophagitis for NSCLC patients treated with RT was constructed. Correlation analysis and LR models with clinical and dosimetric variables were tested on three different Washington University data sets including a total of 748 patients. Their most successful bivariate model (using the variables mean esophagus dose and concurrent chemotherapy) achieved an AUC of 0.83. In the second one (37), they tested the previously published model to predict the risk of severe acute esophagitis on a new independent data set of 115 NSCLC patients. The model used a logistic function with the same two predictor variables: mean esophageal dose and concurrent chemotherapy. When comparing the model with a new model built solely on the independent data set, the authors concluded that the former was almost as predictive as the latter (although the same variables were selected), being AUC = 0.78.

Most of the published studies concern radiation-induced pneumonitis as the target variable, as it represents one of the principal dose-limiting toxicities associated with thoracic RT (40). Of these studies, Lee et al. (38) developed a Bayesian network approach in a cohort of 54 NSCLC patients treated with 3D conformal RT (3D-CRT). For inference, they included DV, clinical, and blood biomarker data. They also compared the Bayesian network ensemble approach, which managed to achieve an AUC of 0.83, with a LR classifier (AUC = 0.77), and univariate predictors (AUC $\leq$ 0.69). Valdes et al. (36) considered a larger data set of 201 stage I NSCLC patients to construct different models with decision trees, RF, and RUSBoost, concluding that RUSBoost had the best performance. They found that the three most important predictive features were the dose to 15 cc of the heart, dose to 4 cc of the trachea or bronchus, and race. However, rather than developing a model for clinical use, the article focused on the power of using learning curves and comparisons of testing and training error to guide the discovery process.

Su et al. (45) investigated an approach to build an ANN, comparing three different validation methods. The ANN was built as a fully connected three-layered feed forward network, and achieved peak AUC values of 0.85. As input to the network, they used DV data from a data set of 142 patients treated with 3D-CRT. Chen et al. (40) tested an SVM model in a data set of 219 patients and compared two models: one including only dose variables (AUC = 0.71), while the other used dose as well as non-dose variables (AUC = 0.76). They concluded that it is

indeed beneficial to include non-dose factors in prediction. The two most predictive variables in their model were generalized equivalent uniform doses close to the mean lung dose, and chemotherapy prior to RT. Luna et al. (32) used a RF approach in a cohort of 203 patients treated with stage II–III locally advanced NSCLC. They evaluated 32 clinical features at both univariate and multivariate analysis and confirmed the importance of lung volume receiving 20% of dose (V20), lung mean, and pack-year as predictors of radiation pneumonitis. They also identified esophagus max as a new possible indicator.

Beside dosimetric- and clinical-based predictors, image-based variable models have also been employed to predict RT-related toxicity outcomes in lung cancer patients. Bousabarah et al. (31) used CT-based radiomic features to predict radiation-induced lung injuries. The study analyzed 110 patients with primary stage I/IIa NSCLC treated with stereotactic body RT for predicting various outcomes, including local lung injury up to fibrosis. Interestingly, for this classification task, only first-order features from gray-level histogram were found to be predictive. Overall, the work suggested that radiomic analysis of planning CT images may help to predict local lung injury up to fibrosis, together with disease-free survival and overall survival in lung cancer patients treated with SBRT. The derived features can be regarded as imaging biomarkers that could support the clinical decision process to the benefit of the patients and oncologist.

Moran et al. (35) investigated the potential of CT-based radiomic features to characterize post-SBRT lung injury. They also investigated the relationship between changes of radiomic feature values and accumulated dose by constructing dose–response curves. The ability to assess lung injury was tested by using a logistic regression classifier, which achieved AUC values in the 0.64–0.75 range using only gray level co-occurrence matrix (GLCM) features. Their results showed that eight out of nine features demonstrated a significant dose–response relationship, suggesting a potential objective measurement of post-SBRT lung injury.

Krafft et al. (33) developed a predictive model for radiation pneumonitis using CT-extracted radiomic features in combination with clinical and dosimetric parameters from a cohort of 192 NSCLC patients. Of the 192 patients, 80% (152) were treated with IMRT while the remainder with 3D-CRT. A LASSO logistic regression classifier was built, resulting in an average AUC of 0.68, showing an increased performance compared to models not including image features (AUC = 0.51).

Prostate

The most common toxicity outcomes in PCa RT are erectile dysfunction (ED), gastrointestinal (GI) disorders, rectal toxicity, and genitourinary (GU) side effects. To predict these unwanted outcomes, the reviewed studies trained several different ML classifiers including SVM, ANN, RF, and multivariate adaptive regression splines (MARS) with data sets of sizes between 79 and 754. Lee et al. (52) also took a gene ontology analysis into account to identify biological processes related to radiation-induced toxicity and predicted late GU toxicity symptoms in a cohort of 324 PCa patients. In this study, the only clinically valid model, which achieved an AUC of 0.7, was for predicting weak stream with RFs. The genetic analysis they conducted highlighted neurogenesis and ion transport as key biological processes related to urinary tract functions.

The study by Carrara et al. (50) was designed to predict late fecal incontinence in PCa patients treated with RT, using ANN classification methods. A population of 598 PCa patients was tested, recording information about comorbidities, previous abdominal surgeries, drug treatments, and dose distribution. In order to identify the best-performing ANNs, the authors varied the number of inputs and neurons and simulated a great amount of ANN configurations. Finally, the best ANN model was selected, showing an 80.8% sensitivity and 63.7% specificity in late fecal incontinence prediction, with an AUC of 0.78.

Fargeas et al. (51) applied an independent component analysis (ICA) model to predict RB in a cohort of 593 PCa patients treated with RT. Two subspaces from the rectal DVHs (with and without RB) were identified and integrated with dosimetric and clinical parameters in a Cox proportional hazards model for RB prediction. The model was tested for 3, 5, and 8 years RB prediction, with AUCs of 0.68, 0.66, and 0.64, respectively. Interestingly, when ICA parameters were included the model, performances increased with new AUCs of 0.83, 0.80, and 0.78.

In their paper, Oh et al. (54) developed a novel classification algorithm that they call pre-conditioned random forest regression (PRFR). The algorithm was tailored for genome-wide association studies based on single-nucleotide polymorphisms (SNPs). On their cohort of 368 PCa patients treated with RT, the aim was to construct a predictive model of two post-RT clinical endpoints: rectal bleeding and ED. After generating a SNP importance score, they included the top 50% most relevant SNPs in their model. This procedure achieved AUC values of 0.71 and 0.68 for rectal bleeding and ED, respectively, outperforming traditional classification algorithms such as RF and logistic regression. The authors also concluded that the model performance could be further improved by incorporating clinical variables.

Moulton et al. (53) investigated the relationship between spatial dose distribution and GI toxicities including rectal bleeding, stool frequency, diarrhea, and tenesmus. Their study contained data from 118 patients treated with a combined EBRT/high-dose-rate brachytherapy treatment. By building models with logistic regression and the Wilcoxon signed rank test, they were able to investigate the association between dose surface map-related features and toxicities. Their findings indicated that spatial constraints on doses to certain sections of the rectum may be important for reducing toxicities and optimizing the dose.

Both Liu and Li (55) and Pella et al. (60) modeled acute grade rectal toxicity for PCa patients using dosimetry and patient clinical characteristics after treatments with IMRT and 3D-CRT, respectively. The model by Liu achieved a significatively better AUC (0.88) when clinical and dosimetric variables were combined, as compared to a model considering only dosimetric features (0.67). In particular, the use of statin drugs and prostate-specific antigen (PSA) level prior to IMRT was found to be strongly related to the toxicity outcome. Pella et al. instead compared an ANN model with an SVM model trained

with dosimetric and clinical data from 321 patients treated with conformal RT. The results obtained showed comparable performances of up to 0.7 AUC for the two compared models.

Yahya et al. (56) conducted a classifier comparison for different urinary symptoms on a cohort of 754 PCa patients. With dose-surface data, comorbidities, and medication intake as input parameters, they analyzed the clinical endpoints dysuria, hematuria, incontinence, and frequency. The following classifiers were compared: LR, elastic-net, SVM, RF, neural network, and MARS. They pointed out that the predictive power is endpoint-dependent and modest at best (AUC = 0.65). Best performance was found for LR and MARS, although elastic-net and RF gave comparable results.

Fargeas et al. (57) developed a novel approach that they call CP-DMA to predict patients presenting rectal bleeding. The name CP-DMA comes from *canonical polyadic decomposition*, an alternative name for tensor rank decomposition, and *deterministic multi-way analysis*. The model uses tensor rank decomposition of the fourth-order tensors created by 3D dose distributions concatenated for different patients (in the fourth dimension) in order to find two separate vector subspaces (one subspace for each outcome, with or without rectal bleeding). Patients are then classified according to their distance to the respective subspaces. Results were compared to linear discriminant analysis, SVM, K-means, kNN, a PCA-based unsupervised algorithm, unsupervised multidimensional classification, and an NTCP model. Their model achieved an AUC of 0.85, outperforming the alternative methods.

Ospina et al. (58) compared the performances of a classical NTCP model with a RF NTCP model for late rectal toxicity prediction on a cohort of 261 patients with PCa treated with 3D-CRT. Both clinical and dosimetric features were collected to train three RF models in order to predict three different 5-year rectal toxicity endpoints: grade 2 overall rectal toxicity and grade 1 and 2 rectal bleeding. Performance of the model ranged between 0.66 and 0.76 depending on the toxicity endpoint. Authors highlighted that the most suitable parameters to be considered in rectal toxicity prediction include dose to the rectum, age, and anticoagulant treatment of the patients.

Zhang et al. (29) developed decision tree and SVM models for one PCa patient (as well as a H&N cancer case), predicting rectal bleeding (RB) with DV constraints and tailored plan properties as input variables. The RB prediction had an average accuracy of 97.04%, indicating that the selection of DV constraint setting can be guided with ML methods.

The study by Tomatis et al. (59) aimed to compare the performances in predicting late RB in a cohort of 718 PCa patients of an LR model and an ANN one using clinical and DVH-based parameters. Overall, the ANN model outperformed the other, with AUCs of 0.704 vs. 0.655, respectively. Authors suggested how the integration of gene expression profiles and surface dose mapping could help to improve the predictive performances of the model.

Gulliford et al. (61) were early adopters of ANN for predicting biological outcomes following PCa RT. They used the treatment plan prescription and dose distribution data in order to predict rectal bleeding and nocturia on a data set with 119 patients. Analysis was made on different discretization levels of the outcomes, and an attempt was made to "look inside" the ANN at a basic level. Their results showed sensitivities and specificities of roughly 0.55.

Several studies aiming to correlate radiomic features with toxicity outcomes are present in the literature. In the study by Mostafaei et al. (46), the potential role of CT radiomics to predict prostate RT toxicities, including acute bladder and rectal injuries, was investigated. Sixty-four PCa patients were studied. The findings highlighted the feasibility and good performance of pre-treatment CT image features as new markers to predict radiation toxicities. The results also showed that, for cystitis, the combination of radiomic features with clinical and dosimetric features could enhance the predictive performance: from AUC values of 0.71 and 0.67 for radiomic and clinical models alone, to AUC = 0.77 when the features were combined. However, for proctitis modeling, the performance was lower in the combined setup compared to the radiomics-only model (AUCs for clinical, radiomic, and clinical–radiomic models were 0.66, 0.71, and 0.65, respectively). These results suggest that integration of radiomics with clinical and dosimetric features may improve the performance of predictive models.

Abdollahi et al. (47) analyzed magnetic resonance imaging (MRI) images from a pool of 33 patients in order to predict urinary toxicity in PCa patients. Different radiomics features (S5.0SumVarnc, S2.2SumVarnc, S1.0AngScMom, S0.4SumAverg, and S5.5InvDfMom) were tested, resulting in AUC values between 0.62 and 0.75 and showing a major dependence of radiomic features on radiation dose. Overall, feature changes resulted to have a good correlation with radiation dose and radiation-induced urinary toxicity. These radiomic features can be identified as being potentially important imaging biomarkers which can also allow to assess mechanisms of radiation-induced bladder injuries.

Abdollahi et al. (25) applied radiomic feature analysis on pre/post IMRT MRI images to find imaging biomarkers for rectal toxicity prediction. Feature extraction was made on both T2-weighted and apparent diffusion coefficient (ADC) images (two different MRI scanning protocols). Pre-IMRT T2-weighted radiomic image features could predict rectal toxicity with a fairly good performance (AUC mean: 0.68), showing a better predicting power in relation to ADC image features (AUC mean: 0.58). The AUC reached 0.81 when all features were combined, suggesting that pre-treatment MRI features may be a feasible approach to predict radiation-induced early rectal toxicity.

Finally, Rossi L. et al. (49) applied DVH parameters, texture features of patients' 3D dose distributions, and non-treatment-related (NTR) predictors to develop predictive models for GI and GU toxicities. Multivariate LR models were trained using the NTR features alone as well as in combination with the other variables. RB, fecal incontinence, nocturia, and urinary incontinence were considered. For RB, fecal incontinence, and urinary incontinence, AUC values increased when adding DVH and texture features to NTR features (from 0.58, 0.63, and 0.68 to 0.73, 0.73, and 0.73, respectively). In the case

of nocturia, inclusion of DVH parameters resulted in a marginal improvement (0.64 vs. 0.66). Overall, the inclusion of more features improved prediction performance for GI and GU toxicity.

DISCUSSION

In recent years, the growing interest toward AI in all fields of science has led to the development of innovative tools in RT (62), including several toxicity prediction models. Some of them have demonstrated high performance on very large and diverse data sets, making them potential candidates for clinical integration. Other ones have highlighted cases where ML prediction seems to fail, such as in predicting unplanned hospitalizations or fatigue. Interestingly, almost half of the 53 reviewed papers were published in the last 3 years, with the earliest publication dating back to 2004, making it a rather young area of interest with much potential for future research.

Our overview indicates that the amount of research on ML-based models for prediction of toxicity is not balanced across districts, as some of them, such as lung, prostate, and H&N have been receiving more attention than others such as brain, skin, blood, and breast. Regarding brain cancer, the lack of ML models is potentially ascribable to the scarcity of literature in general concerning radio-induced toxicity within the brain. This may be explained by the fact that acute and late complications of brain tumor patients prevalently manifest themselves as neurological disorders that are difficult to assess. On the other hand, H&N studies are common mainly because these kinds of cancers, albeit not as common as PCa or lung cancer, are very often associated with clinically relevant toxicity, with a well-documented impact on patients' quality of life. Additionally, accurate prediction of RT toxicity in H&N cancer may help physicians to identify the best treatment option whenever equally effective approaches (i.e., surgery) are available. Furthermore, integration of genetic information in the modeling approaches, despite being desirable, appears almost completely absent, being treated only in two studies (52, 54).

The large variety of variables, features, and models, as well as the lack of standardization in the development of predictive tools, accounts for the scarce comparability of the existing works. As previously pointed out, performance measures such as the AUC are not the be-all and end-all of model assessment and should be taken with a grain of salt. The AUC measure has even been criticized as an indicator of performance altogether (63) and can sometimes be misleading. For instance, out of all the selected papers, the best results (AUC $>$ 0.85) were achieved in small- or medium-sized data sets ($<$150 patients). This implies that further validation of the current best-performing models on larger and/or more diverse data sets is mandatory.

Since the principal aim of ML models for toxicity prediction is clinical integration, critical efforts are required to make the relevant research understandable, transparent, and accessible to an audience with little or no specific computational background. As a matter of fact, considering the specific case of this review, the studies did not always accurately report clinical information concerning pathology, RT treatment (technique, dose, fractionation scheme), the kind of developed toxicity (late or acute), as well as methodological details (feature selection procedures and employed models). Therefore, a rigorous method for communicating characteristics and results of prediction models, which would foster the synthesis and critical appraisal of the relevant information, is of paramount importance. One of them was proposed by the Transparent Reporting of a multivariable prediction model for Individual Prognosis Or Diagnosis (TRIPOD) initiative (64), which consists of a checklist that encompasses a minimum set of details that authors should fulfill to provide essential and clear information about their work. In particular, the key points should include a summary of objectives, study design, setting, participants, sample size, predictors, outcomes, statistical analysis, results, and conclusions. This would ensure that proper assessment of usefulness, potential biases, and possible drawbacks of published research can be made.

Other open issues are the importance of data sharing among centers, the need for continuous model updates, and the need for prospective studies to support the clinical applicability of the developed models. More research and effort in these areas will alleviate the issue of clinical integration, which represents both the primary driver and the ultimate goal of these efforts.

CONCLUSION

Despite the loose ends about the clinical applicability of RT-induced toxicity models, our overall findings show that ML-based solutions for toxicity prediction in RT could represent a valid tool in research settings. In order to maximize the therapeutic index of RT and to guide the clinical selection of patients, an effective toxicity prediction scheme is essential. Application of such models can be a valuable asset in many different aspects for both patients and clinicians.

AUTHOR CONTRIBUTIONS

LI, MP, MZ, GM, and BJ-F were responsible for conception and design of the study and wrote the first draft of the manuscript. SV was responsible for data acquisition and wrote sections of the manuscript. MA, DA, GC, AS, ML, and RO wrote sections of the manuscript. All authors contributed to manuscript revision, and read and approved the submitted version.

FUNDING

This study was partially supported by a research grant from the Associazione Italiana per la Ricerca sul Cancro (AIRC) entitled "Radioablation ± hormonotherapy for prostate cancer oligorecurrences (RADIOSA trial): potential of imaging and biology" registered at ClinicalTrials.gov NCT03940235, approved by the Ethics Committee of IRCCS Istituto Europeo di Oncologia and Centro Cardiologico Monzino (IEO-997), by the Italian Ministry of Health with Ricerca Corrente and 5x1000 funds and by a research grant from Accuray Inc. entitled "Data collection andanalysis of Tomotherapy and CyberKnife breast clinical studies, breast physics studies and prostate study". Accuracy

Inc. was not involved in the study design, collection, analysis, interpretation of data, the writing of this article or the decision to submit it for publication.

ACKNOWLEDGMENTS

Many thanks to William Samuel Russell-Edu for his precious help in the papers search. L. J. Isaksson and S. Volpe are Ph.D. students within the European School of Molecular Medicine (SEMM), Milan, Italy.

SUPPLEMENTARY MATERIAL

The Supplementary Material for this article can be found online at: https://www.frontiersin.org/articles/10.3389/fonc.2020.00790/full#supplementary-material

REFERENCES

1. Citrin DE. Recent developments in radiotherapy. *N Engl J Med.* (2017) 377:1065–75. doi: 10.1056/NEJMra1608986
2. Marks LB, Yorke ED, Jackson A, Haken RK, Constine LS, Eisbruch A, et al. Use of normal tissue complication probability models in the clinic. *Int J Radiat Oncol Biol Phys.* (2010) 76:S10–9. doi: 10.1016/j.ijrobp.2009.07.1754
3. D'Andrea M, Benassi M, Strigari L. Modeling radiotherapy induced normal tissue complications: an overview beyond phenomenological models. *Comput Math Methods Med.* (2016) 2016:2796186. doi: 10.1155/2016/2796186
4. Deist TM, Dankers FJ, Valdes G, Wijsman R, Hsu I, Oberije C, et al. Erratum: "Machine learning algorithms for outcome prediction in (chemo)radiotherapy: An empirical comparison of classifiers". *Med Phys.* (2019) 46:1080–7. doi: 10.1002/mp.12967
5. Coates J, El Naqa I. Outcome modeling techniques for prostate cancer radiotherapy: data, models, and validation. *Physica Medica.* (2016) 32:512–20. doi: 10.1016/j.ejmp.2016.02.014
6. Turing IBA. Computing machinery and intelligence-AM Turing. *Mind.* (1950) 59:433. doi: 10.1093/mind/LIX.236.433
7. Bibault J, Giraud P, Burgun A. Big data and machine learning in radiation oncology: state of the art and future prospects. *Cancer Lett.* (2016) 382:110–7. doi: 10.1016/j.canlet.2016.05.033
8. Kang J, Schwartz R, Flickinger J, Beriwal S. Machine learning approaches for predicting radiation therapy outcomes: a clinician's perspective. *Int J Radiat Oncol Biol Phys.* (2015) 93:1127–35. doi: 10.1016/j.ijrobp.2015.07.2286
9. Wohlin C. Guidelines for snowballing in systematic literature studies and a replication in software engineering. In: *Proceedings of the 18th International Conference on Evaluation and Assessment in Software Engineering*. New York, NY: Association for Computing Machinery (2014), Article 38, p. 1-10. doi: 10.1145/2601248.2601268
10. Saednia K, Tabbarah S, Lagree A, Wu T, Klein J, Garcia E, et al. Quantitative thermal imaging biomarkers to detect acute skin toxicity from breast radiotherapy using supervised machine learning. *Int J Radiat Oncol Biol Phys.* (2020) 106:1071–83. doi: 10.1016/j.ijrobp.2019.12.032
11. Reddy J, Lindsay WD, Berlind CG, Ahern CA, Smith BD. Applying a machine learning approach to predict acute toxicities during radiation for breast cancer patients. *Int J Radiat Oncol Biol Phys.* (2018) 102:S59. doi: 10.1016/j.ijrobp.2018.06.167
12. Mbah C, Thierens H, Thas O, Neve JD, Chang-Claude J, Seibold P, et al. Pitfalls in prediction modeling for normal tissue toxicity in radiation therapy: an illustration with the individual radiation sensitivity and mammary carcinoma risk factor investigation cohorts. *Int J Radiat Oncol Biol Phys.* (2016) 95:1466–76. doi: 10.1016/j.ijrobp.2016.03.034
13. Hart JP, Mccurdy MR, Ezhil M, Wei W, Khan M, Luo D, et al. Radiation pneumonitis: correlation of toxicity with pulmonary metabolic radiation response. *Int J Radiat Oncol Biol Phys.* (2008) 71:967–71. doi: 10.1016/j.ijrobp.2008.04.002
14. Chen J, Chen H, Zhong Z, Wang Z, Hrycushko B, Zhou L, et al. Investigating rectal toxicity associated dosimetric features with deformable accumulated rectal surface dose maps for cervical cancer radiotherapy. *Radiat Oncol.* (2018) 13:125. doi: 10.1186/s13014-018-1068-0
15. Zhen X, Chen J, Zhong Z, Hrycushko B, Zhou L, Jiang S, et al. Deep convolutional neural network with transfer learning for rectum toxicity prediction in cervical cancer radiotherapy: a feasibility study. *Phys Med Biol.* (2017) 62:8246–63. doi: 10.1088/1361-6560/aa8d09
16. Tian Z, Yen A, Zhou Z, Shen C, Albuquerque K, Hrycushko B. A machine-learning–based prediction model of fistula formation after interstitial brachytherapy for locally advanced gynecological malignancies. *Brachytherapy.* (2019) 18:530–8. doi: 10.1016/j.brachy.2019.04.004
17. Wojcieszynski A, Cava WL, Baumann B, Lukens J, Ghiam AF, Urbanowicz R, et al. Machine learning to predict toxicity in head and neck cancer patients treated with definitive chemoradiation. *Int J Radiat Oncol Biol Phys.* (2019) 105:E139–40. doi: 10.1016/j.ijrobp.2019.06.2182
18. Reddy J, Lindsay W, Berlind C, Ahern C, Holmes A, Smith B, et al. Applying a machine learning approach to predict acute radiation toxicities for head and neck cancer patients. *Int J Radiat Oncol Biol Phys.* (2019) 105:S69. doi: 10.1016/j.ijrobp.2019.06.520
19. Gabryś HS, Buettner F, Sterzing F, Hauswald H, Bangert M. Design and selection of machine learning methods using radiomics and dosiomics for normal tissue complication probability modeling of xerostomia. *Front Oncol.* (2018) 8:35. doi: 10.3389/fonc.2018.00035
20. Beasley W, Thor M, McWilliam A, Green A, Mackay R, Slevin N, et al. Image-based data mining to probe dosimetric correlates of radiation-induced trismus. *Int J Radiat Oncol Biol Phys.* (2018) 102:1330–8. doi: 10.1016/j.ijrobp.2018.05.054
21. Jiang W, Lakshminarayanan P, Hui X, Han P, Cheng Z, Bowers M, et al. Machine learning methods uncover radiomorphologic dose patterns in salivary glands that predict xerostomia in patients with head and neck cancer. *Adv Radiat Oncol.* (2019) 4:401–12. doi: 10.1016/j.adro.2018.11.008
22. Dean J, Wong K, Gay H, Welsh L, Jones AB, Schick U, et al. Incorporating spatial dose metrics in machine learning-based normal tissue complication probability (NTCP) models of severe acute dysphagia resulting from head and neck radiotherapy. *Clin Transl Radiat Oncol.* (2018) 8:27–39. doi: 10.1016/j.ctro.2017.11.009
23. Nakatsugawa M, Cheng Z, Kiess A, Choflet A, Bowers M, Utsunomiya K, et al. The needs and benefits of continuous model updates on the accuracy of RT-induced toxicity prediction models within a learning health system. *Int J Radiat Oncol Biol Phys.* (2019) 103:460–7. doi: 10.1016/j.ijrobp.2018.09.038
24. Niedzielski JS, Yang J, Stingo F, Liao Z, Gomez D, Mohan R, et al. A novel methodology using CT imaging biomarkers to quantify radiation sensitivity in the esophagus with application to clinical trials. *Sci Rep.* (2017) 7:6034. doi: 10.1038/s41598-017-05003-x
25. Abdollahi H, Mostafaei S, Cheraghi S, Shiri I, Mahdavi SR, Kazemnejad A. Cochlea CT radiomics predicts chemoradiotherapy induced sensorineural hearing loss in head and neck cancer patients: a machine learning and multi-variable modelling study. *Physica Medica.* (2018) 45:192–7. doi: 10.1016/j.ejmp.2017.10.008
26. Pota M, Scalco E, Sanguineti G, Farneti A, Cattaneo GM, Rizzo G, et al. Early prediction of radiotherapy-induced parotid shrinkage and toxicity based on CT radiomics and fuzzy classification. *Artif Intell Med.* (2017) 81:41–53. doi: 10.1016/j.artmed.2017.03.004
27. Dijk L, Brouwer CL, Schaaf AV, Burgerhof JG, Beukinga RJ, Langendijk JA, et al. CT image biomarkers to improve patient-specific prediction of radiation-induced xerostomia and sticky saliva. *Radiother Oncol.* (2017) 122:185–91. doi: 10.1016/j.radonc.2016.07.007
28. Dean JA, Wong KH, Welsh LC, Jones A, Schick U, Newbold KL, et al. Normal tissue complication probability (NTCP) modelling using spatial dose metrics and machine learning methods for severe acute oral mucositis

resulting from head and neck radiotherapy. *Radiother Oncol.* (2016) 120:21–7. doi: 10.1016/j.radonc.2016.05.015
29. Zhang HH, D'souza WD, Shi L, Meyer RR. Modeling plan-related clinical complications using machine learning tools in a multiplan IMRT framework. *Int J Radiat Oncol Biol Phys.* (2009) 74:1617–26. doi: 10.1016/j.ijrobp.2009.02.065
30. Ibragimov B, Toesca D, Chang D, Yuan Y, Koong A, Xing L. Development of deep neural network for individualized hepatobiliary toxicity prediction after liver SBRT. *Med Phys.* (2018) 45:4763–74. doi: 10.1002/mp.13122
31. Bousabarah K, Temming S, Hoevels M, Borggrefe J, Baus WW, Ruess D, et al. Radiomic analysis of planning computed tomograms for predicting radiation-induced lung injury and outcome in lung cancer patients treated with robotic stereotactic body radiation therapy. *Strahlenther Und Onkol.* (2019) 195:830–42. doi: 10.1007/s00066-019-01452-7
32. Luna JM, Chao H, Diffenderfer ES, Valdes G, Chinniah C, Ma G, et al. Predicting radiation pneumonitis in locally advanced stage II–III non-small cell lung cancer using machine learning. *Radiother Oncol.* (2019) 133:106–12. doi: 10.1016/j.radonc.2019.01.003
33. Krafft SP, Rao A, Stingo F, Briere TM, Court LE, Liao Z, et al. The utility of quantitative CT radiomics features for improved prediction of radiation pneumonitis. *Med Phys.* (2018) 45:5317–24. doi: 10.1002/mp.13150
34. Chao HH, Valdes G, Luna JM, et al. Exploratory analysis using machine learning to predict for chest wall pain in patients with stage I non-small-cell lung cancer treated with stereotactic body radiation therapy. *J Appl Clin Med Phys.* (2018) 19:539–546. doi: 10.1002/acm2.12415
35. Moran A, Daly ME, Yip SS, Yamamoto T. Radiomics-based assessment of radiation-induced lung injury after stereotactic body radiotherapy. *Clin Lung Cancer.* (2017) 18:e425–31. doi: 10.1016/j.cllc.2017.05.014
36. Valdes G, Solberg TD, Heskel M, Ungar L, Simone CB. Using machine learning to predict radiation pneumonitis in patients with stage I non-small cell lung cancer treated with stereotactic body radiation therapy. *Phys Med Biol.* (2016) 61:6105–20. doi: 10.1088/0031-9155/61/16/6105
37. Huang EX, Robinson CG, Molotievschi A, Bradley JD, Deasy JO, Oh JH. Independent test of a model to predict severe acute esophagitis. *Adv Radiat Oncol.* (2017) 2:37–43. doi: 10.1016/j.adro.2016.11.003
38. Lee S, Ybarra N, Jeyaseelan K, Faria S, Kopek N, Brisebois P, et al. Bayesian network ensemble as a multivariate strategy to predict radiation pneumonitis risk. *Med Phys.* (2015) 42:2421–30. doi: 10.1118/1.4915284
39. Huang EX, Bradley JD, Naqa IE, Hope AJ, Lindsay PE, Bosch WR, et al. Modeling the risk of radiation-induced acute esophagitis for combined washington university and RTOG trial 93-11 lung cancer patients. *Int J Radiat Oncol Biol Phys.* (2012) 82:1674–9. doi: 10.1016/j.ijrobp.2011.02.052
40. Chen S, Zhou S, Yin F, Marks LB, Das SK. Investigation of the support vector machine algorithm to predict lung radiation-induced pneumonitis. *Med Phys.* (2007) 34:3808–14. doi: 10.1118/1.2776669
41. El Naqa IE, Bradley JD, Lindsay PE, Hope AJ, Deasy JO. Predicting radiotherapy outcomes using statistical learning techniques. *Phys Med Biol.* (2009) 54:S9. doi: 10.1088/0031-9155/54/18/S02
42. Das SK, Chen S, Deasy JO, Zhou S, Yin F, Marks LB. Combining multiple models to generate consensus: application to radiation-induced pneumonitis prediction. *Med Phys.* (2008) 35:5098–109. doi: 10.1118/1.2996012
43. Das SK, Zhou S, Zhang J, Yin F, Dewhirst MW, Marks LB. Predicting lung radiotherapy-induced pneumonitis using a model combining parametric lyman probit with nonparametric decision trees. *Int J Radiat Oncol Biol Phys.* (2007) 68:1212–21. doi: 10.1016/j.ijrobp.2007.03.064
44. El Naqa IE, Bradley J, Blanco AI, Lindsay PE, Vicic M, Hope A, et al. Multivariable modeling of radiotherapy outcomes, including dose–volume and clinical factors. *Int J Radiat Oncol Biol Phys.* (2006) 64:1275–86. doi: 10.1016/j.ijrobp.2005.11.022
45. Su M, Miften M, Whiddon C, Sun X, Light K, Marks L. An artificial neural network for predicting the incidence of radiation pneumonitis. *Med Phys.* (2005) 32:318–25. doi: 10.1118/1.1835611
46. Mostafaei S, Abdollahi H, Dehkordi SK, Shiri I, Razzaghdoust A, Moghaddam SH, et al. CT imaging markers to improve radiation toxicity prediction in prostate cancer radiotherapy by stacking regression algorithm. *La Radiologia Medica.* (2019) 125:87–97. doi: 10.1007/s11547-019-01082-0
47. Abdollahi H, Tanha K, Mofid B, Razzaghdoust A, Saadipoor A, Khalafi L, et al. MRI radiomic analysis of IMRT-induced bladder wall changes in prostate cancer patients: a relationship with radiation dose and toxicity. *J Med Imaging Radiat Sci.* (2019) 50:252–60. doi: 10.1016/j.jmir.2018.12.002
48. Abdollahi H, Mahdavi SR, Mofid B, Bakhshandeh M, Razzaghdoust A, Saadipoor A, et al. Rectal wall MRI radiomics in prostate cancer patients: Prediction of and correlation with early rectal toxicity. *Int J Radiat Biol.* (2018) 94:829–37. doi: 10.1080/09553002.2018.1492756
49. Rossi L, Bijman R, Schillemans W, Aluwini S, Cavedon C, Witte M, et al. Texture analysis of 3D dose distributions for predictive modelling of toxicity rates in radiotherapy. *Radiother Oncol.* (2018) 129:548–53. doi: 10.1016/j.radonc.2018.07.027
50. Carrara M, Massari E, Cicchetti A, Giandini T, Avuzzi B, Palorini F, et al. Development of a ready-to-use graphical tool based on artificial neural network classification: application for the prediction of late fecal incontinence after prostate cancer radiation therapy. *Int J Radiat Oncol Biol Phys.* (2018) 102:1533–42. doi: 10.1016/j.ijrobp.2018.07.2014
51. Fargeas A, Acosta O, Arrango JDO, Ferhat A, Costet N, Albera L, et al. Independent component analysis for rectal bleeding prediction following prostate cancer radiotherapy. *Radiother Oncol.* (2018) 126:263–9. doi: 10.1016/j.radonc.2017.11.011
52. Lee S, Kerns S, Ostrer H, Rosenstein B, Deasy JO, Oh JH. Machine learning on a genome-wide association study to predict late genitourinary toxicity after prostate radiation therapy. *Int J Radiat Oncol Biol Phys.* (2018) 101:128–35. doi: 10.1016/j.ijrobp.2018.01.054
53. Moulton CR, House MJ, Lye V, Tang CI, Krawiec M, Joseph DJ, et al. Spatial features of dose–surface maps from deformably-registered plans correlate with late gastrointestinal complications. *Phys Med Biol.* (2017) 62:4118–39. doi: 10.1088/1361-6560/aa663d
54. Oh JH, Kerns S, Ostrer H, Powell SN, Rosenstein B, Deasy JO. Computational methods using genome-wide association studies to predict radiotherapy complications and to identify correlative molecular processes. *Sci Rep.* (2017) 7:43381. doi: 10.1038/srep43381
55. Liu X, Li J. Patient specific characteristics are an important factor that determines the risk of acute grade $\geq$ 2 rectal toxicity in patients treated for prostate cancer with IMRT and daily image guidance based on implanted gold markers. *OMICS J Radiol.* (2016) 5:255. doi: 10.4172/2167-7964.1000225
56. Yahya N, Ebert MA, Bulsara M, House MJ, Kennedy A, Joseph DJ, et al. Statistical-learning strategies generate only modestly performing predictive models for urinary symptoms following external beam radiotherapy of the prostate: a comparison of conventional and machine-learning methods. *Med Phys.* (2016) 43:2040–52. doi: 10.1118/1.4944738
57. Fargeas A, Albera L, Kachenoura A, Dréan G, Ospina J, Coloigner J, et al. On feature extraction and classification in prostate cancer radiotherapy using tensor decompositions. *Med Eng Phys.* (2015) 37:126–31. doi: 10.1016/j.medengphy.2014.08.009
58. Ospina JD, Zhu J, Chira C, Bossi A, Delobel JB, Beckendorf V, et al. Random forests to predict rectal toxicity following prostate cancer radiation therapy. *Int J Radiat Oncol Biol Phys.* (2014) 89:1024–31. doi: 10.1016/j.ijrobp.2014.04.027
59. Tomatis S, Rancati T, Fiorino C, Vavassori V, Fellin G, Cagna E, et al. Late rectal bleeding after 3D-CRT for prostate cancer: development of a neural-network-based predictive model. *Phys Med Biol.* (2012) 57:1399. doi: 10.1088/0031-9155/57/5/1399
60. Pella A, Cambria R, Riboldi M, Jereczek-Fossa BA, Fodor C, Zerini D, et al. Use of machine learning methods for prediction of acute toxicity in organs at risk following prostate radiotherapy. *Med Phys.* (2011) 38:2859–67. doi: 10.1118/1.3582947
61. Gulliford SL, Webb S, Rowbottom CG, Corne DW, Dearnaley DP. Use of artificial neural networks to predict biological outcomes for patients receiving radical radiotherapy of the prostate. *Radiother Oncol.* (2004) 71:3–12. doi: 10.1016/j.radonc.2003.03.001

62. Boldrini L, Bibault J, Masciocchi C, Shen Y, Bittner M. Deep learning: a review for the radiation oncologist. *Front Oncol.* (2019) 9:977. doi: 10.3389/fonc.2019.00977
63. Lobo JM, Jiménez-Valverde A, Real R. AUC: a misleading measure of the performance of predictive distribution models. *Global Ecol Biogeogr*. (2008) 17:145–51. doi: 10.1111/j.1466-8238.2007.00358.x
64. Collins GS, Reitsma JB, Altman DG, Moons KG. Transparent reporting of a multivariable prediction model for individual prognosis or diagnosis (TRIPOD): The TRIPOD statement. *BMJ*. (2015) 350:g7594. doi: 10.1136/bmj.g7594

Conflict of Interest: The authors declare that the research was conducted in the absence of any commercial or financial relationships that could be construed as a potential conflict of interest.

frontiers in Oncology

ORIGINAL RESEARCH
published: 11 June 2020
doi: 10.3389/fonc.2020.00910

External Validation of a Predictive Model of Urethral Strictures for Prostate Patients Treated With HDR Brachytherapy Boost

Vanessa Panettieri[1,2], Tiziana Rancati[3], Eva Onjukka[4], Martin A. Ebert[5,6,7], David J. Joseph[7,8,9], James W. Denham[10], Allison Steigler[10] and Jeremy L. Millar[1,11]*

[1] Alfred Health Radiation Oncology, Alfred Hospital, Melbourne, VIC, Australia, [2] Medical Imaging and Radiation Sciences, Monash University, Clayton, VIC, Australia, [3] Prostate Cancer Program, Scientific Directorate, Fondazione IRCCS Istituto Nazionale dei Tumori, Milan, Italy, [4] Medical Radiation Physics and Nuclear Medicine, Karolinska University Hospital, Stockholm, Sweden, [5] Radiation Oncology, Sir Charles Gairdner Hospital, Perth, WA, Australia, [6] School of Physics, Mathematics and Computing, University of Western Australia, Perth, WA, Australia, [7] 5D Clinics, Claremont, WA, Australia, [8] GenesisCare, Subiaco, WA, Australia, [9] School of Surgery, University of Western Australia, WA, Australia, [10] School of Medicine and Public Health, University of Newcastle, Newcastle, NSW, Australia, [11] Central Clinical School, Monash University, Melbourne, VIC, Australia

OPEN ACCESS

Edited by:
Brian James Davis, Mayo Clinic College of Medicine and Science, United States

Reviewed by:
Sarah O. S. Osman, Queen's University Belfast, United Kingdom
Susanne Rogers, Kantonsspital Aarau, Switzerland
Xinglei Shen, University of Kansas Medical Center, United States

***Correspondence:**
Vanessa Panettieri
V.Panettieri@alfred.org.au

Specialty section:
This article was submitted to Radiation Oncology, a section of the journal Frontiers in Oncology

Received: *15 January 2020*
Accepted: *11 May 2020*
Published: *11 June 2020*

Citation:
Panettieri V, Rancati T, Onjukka E, Ebert MA, Joseph DJ, Denham JW, Steigler A and Millar JL (2020) External Validation of a Predictive Model of Urethral Strictures for Prostate Patients Treated With HDR Brachytherapy Boost. Front. Oncol. 10:910. doi: 10.3389/fonc.2020.00910

Purpose: For prostate cancer treatment, comparable or superior biochemical control was reported when using External-Beam-Radiotherapy (EBRT) with High-Dose-Rate-Brachytherapy (HDRB)-boost, compared to dose-escalation with EBRT alone. The conformal doses produced by HDRB could allow further beneficial prostate dose-escalation, but increase in dose is limited by normal tissue toxicity. Previous works showed correlation between urethral dose and incidence of urinary toxicity, but there is a lack of established guidelines on the dose constraints to this organ. This work aimed at fitting a Normal-Tissue-Complication-Probability model to urethral stricture data collected at one institution and validating it with an external cohort, looking at neo-adjuvant androgen deprivation as dose-modifying factor.

Materials and Methods: Clinical and dosimetric data of 258 patients, with a toxicity rate of 12.8%, treated at a single institution with a variety of prescription doses, were collected to fit the Lyman–Kutcher–Burman (LKB) model using the maximum likelihood method. Due to the different fractionations, doses were converted into 2 Gy-equivalent doses ($\alpha/\beta = 5$ Gy), and urethral stricture was used as an end-point. For validation, an external cohort of 187 patients treated as part of the TROG (Trans Tasman Radiation Oncology Group) 03.04 RADAR trial with a toxicity rate of 8.7%, was used. The goodness of fit was assessed using calibration plots. The effect of neo-adjuvant androgen deprivation (AD) was analyzed separating patients who had received it prior to treatment from those who did not receive it.

Results: The obtained LKB parameters were TD50 = 116.7 Gy and $m = 0.23$; n was fixed to 0.3, based on numerical optimization of the likelihood. The calibration plot showed a good agreement between the observed toxicity and the probability predicted by the model, confirmed by bootstrapping. For the external validation, the calibration

plot showed that the observed toxicity obtained with the RADAR patients was well-represented by the fitted LKB model parameters. When patients were stratified by the use of AD TD50 decreased when AD was not present.

Conclusions: Lyman–Kutcher–Burman model parameters were fitted to the risk of urethral stricture and externally validated with an independent cohort, to provide guidance on urethral tolerance doses for patients treated with a HDRB boost. For patients that did not receive AD, model fitting provided a lower TD50 suggesting a protective effect on urethra toxicity.

Keywords: NTCP, HDR brachytherapy, urethra, predictive modeling, prostate cancer

INTRODUCTION

In the treatment of unfavorable prostate cancer, several studies have shown that the use of High-Dose-Rate Brachytherapy (HDRB) as a boost in combination with External Beam Radiotherapy (EBRT) provides biochemical control and prostate-cancer specific survival comparable or superior to dose-escalation with EBRT alone (1–6). These results are in line with findings suggesting that prostate cancer tends to respond similarly to late reacting tissues to dose fractionation schedules, consistent with lower α/β ratio (7, 8). The conformal doses provided by HDRB could potentially allow further beneficial dose-escalation due to their excellent organs-at-risk (OARs) sparing. However, concerns have been raised regarding the potential risk of acute and late urethral toxicity, in particular urethral stricture, which has been reported by several authors in rates up to 30% (9–11). Causes for urethral strictures have been investigated and contradictory findings are reported in the literature with reports showing correlation between urethral dose and incidence of urinary toxicity (10, 12), and others instead reporting no significant correlations (2, 13, 14).

Due to the variety of fractionation regimens used for HDRB boost treatments in different centers, ranging from multiple fractions to monotherapy (9), it is still hard to compare practices and related toxicity results. Additionally, follow-up time tends to vary ranging between 2 and over 5 years (2, 10, 13). For this reason, there is no consensus on the dose constraints for urethral doses (15–17), and often limits are decided in each institution based on experience of the practitioners. In-depth analyses of the dose-effect relationships have been performed for the bladder and urethral toxicity mainly in the context of EBRT to gain understanding of the potential effect of increasing dose per fraction on the main OARs, following the increase in the use of hypofractionation in prostate radiotherapy treatments (18–20). A small number of studies have also looked at Normal Tissue Complication Probability (NTCP) for the urethra, but in all cases, they have highlighted that parameters for the most used NTCP models, such as the relative seriality or the Lyman–Kutcher–Burman model, were not available, and have assumed that the urethra had a similar response as organs such the esophagus (21, 22).

Using the long term data and experience accumulated in our department in treating prostate cancer patients with HDRB boost the purpose of this work has been to establish NTCP model parameters specific for the urethra by fitting a normal tissue toxicity curve on urethral stricture data recorded in our institution. This curve has then been validated with an independent external cohort, in order to provide general applicability and a tool to guide treatment design and fractionation selection criteria.

MATERIALS AND METHODS

Model Fitting

Patients and Clinical Data

Clinical and three dimensional (3D) treatment planning data of 258 patients treated at Alfred Health Radiation Oncology (AHRO) from 2001 to 2013 were retrospectively collected for this analysis. These 258 patients were selected as a subset of a larger group of more than 500 patients treated at our institution, receiving a curative regimen that included a boost of HDRB, in combination with EBRT, since they had complete retrievable 3D planning and associated toxicity information with at least 4 years of follow-up. Most patients were classified in the intermediate and high risk group, and details of the CT-planning based treatment technique are presented in previous publications (10, 23). In summary, for patients treated before 2006 metal needles, replaced by plastic needles for patients treated after 2006, were inserted transperineally using ultrasound guidance. Before 2005, patients were not replanned in subsequent days, then until 2008 only if a second CT-simulator scan showed a superior-inferior displacement of the needles of more than 1 cm. As of 2008 for all patients, a new CT scan and plan is performed on the second day. All patients received an EBRT dose of 46–50 Gy in 2 Gy per fraction. For the HDRB boost, a variety of fractionations regimens were used to treat the patients over the years (**Table 1**), but all patients were treated in 2 consecutive days, with the patients treated with three fractions having two fractions on the 2nd day.

For all patients, clinical, demographic, and toxicity data were extracted from our institutional prospective brachytherapy database BrachyNET. All patients had a review after 6, 12, 24 months and every year until 10 years after the HDRB implant, and no patient was lost to follow-up. At each review, patients completed the Expanded Prostate Cancer Index Composite

TABLE 1 | AHRO HDRB boost patients' characteristics including number of patients (no. of patients), HDRB physical, and biological prescription dose (respectively, Brachytherapy Prescription dose-physical and equivalent), toxicity rate, mean, and median time to stricture (%), patient who had received Neo-Adjuvant Androgen Deprivation and age.

	Group 1	Group 2	Group 3	Group 4	Total
No of patients	131	117	8	2	258
Brachytherapy Prescription dose (physical dose, Gy)	18 Gy in 3 fractions	19 Gy in 2 fractions	17 Gy in 2 fractions	10 and 6 Gy in 2 fractions	
External Beam Prescription dose (physical dose, Gy)	46 Gy in 23 fractions	46 Gy in 23 fractions	46 Gy in 23 fractions	46 Gy in 23 fractions	
Brachytherapy Prescription dose (2 Gy equivalent dose, $\alpha/\beta = 5$ Gy)	28.3 Gy	39.4 Gy	32.8 Gy	30.8 Gy	
Total dose EBRT + HDRB (2 Gy equivalent dose, $\alpha/\beta = 5$ Gy)	74.3 Gy	85.4 Gy	78.8 Gy	76.8 Gy	
Toxicity rate at 4 years (%)	6.9%	20.5%	0%	0%	12.8%
Mean time to stricture (years)	3.6	2.1	Not applicable	Not applicable	
Median time to stricture (years)	3.0	1.4	Not applicable	Not applicable	
Adjuvant androgen deprivation (no of patients)	118	113	8	2	241
Mean age (years)	65.4	66.3	66.1	65	65.7

For EBRT the 46 in 2 Gy per fraction prescription is shown as only 1 patient in the whole cohort had 50 in 2 Gy per fraction.

(EPIC-26) form (24), and rectal and urethral toxicity information was collected. In terms of urethral toxicity, a stricture was recorded if the patient underwent a surgical procedure for a stricture (dilatation or urethrotomy). In this work, the end-point was chosen to be the time of the first urethrotomy, with a follow-up cut off time of 4 years, and the average stricture rate was 12.8%. Among the clinical parameters, age, and the use of neo-adjuvant androgen deprivation (AD) were also collected (**Table 1**). In the HDRB plan, the urethra was contoured by the Radiation Oncologist (RO) around the external diameter of a 22-Fr gauge three-way indwelling urinary catheter as a solid structure from typically 1 cm below the apex to the bladder base (**Figure 1a**) considering the specific anatomy of each patient to include the mucosal wall. OAR doses were limited using departmental guidelines based mainly on the GEC-ESTRO recommendations (15). For the Planning Target Volume (PTV): $D_{90\%} > 100\%$ (at least 100% of prescribed dose covering 90% of PTV), $V_{100\%} > 95\%$ (i.e., 95% of PTV receiving at least 100% of the prescription dose), $V_{150\%} = 15$–32% (i.e., 150% of the prescription dose to 15–32% of the PTV), $V_{200\%} = 5$–9% (i.e., 200% of the prescription dose to 5–9% of the PTV). For the OARs: urethra $D_{10\%} < 110\%$ (i.e., 10% of urethra receiving no more than 110% of the prescription dose), and rectal wall $D_{2cc} < 66\%$ (i.e., 2 cc of rectal wall receiving no more than 66% of the prescription dose).

Dosimetric Data

Due to the long time period for patient treatment included in this study the AHRO HDRB patient treatment plans were originally calculated either in the Plato (Nucletron) or in Oncentra treatment planning system (Elekta). In order to limit differences due to different Dose Volume Histogram (DVH) estimates, all plans were de-identified and re-imported in Oncentra, and DVHs were recalculated and exported. Since the patients were treated with four different fractionation regimens, and due to the inhomogeneous dose in the urethra, each fraction's physical doses were converted into equivalent doses in 2 Gy per fraction (EQD_2) considering an α/β ratio of 5 Gy, as previously used by Gloi and Buchanan (22) (of note equivalent doses for late effects to normal tissues are of interest in the frame of this work). Due to the conformal nature of the EBRT plan, it was assumed that for all patients the urethra had received the full EBRT prescription dose of 46–50 Gy in 2 Gy per fraction. Converted prescription doses for the brachytherapy boost are shown in **Table 1**.

Determination of the Model Parameters

The Lyman–Kutcher–Burman model (LKB) was used in this analysis (25, 26), and the dose-response curve plotted as a function of the equivalent uniform dose (EUD). The determination of the best estimate of the model parameters was done by fitting clinical and dosimetric data using the maximum likelihood method as previously described (27, 28), using MatlabR2018 (Mathworks). Due to the small urethral volumes involved, initially a numerical optimization of the likelihood function was performed to establish a volume effect parameter (n) value descriptive of the relationship between urethral "architecture" and the considered toxicity endpoint in the available dataset. Then this value was fixed, and TD50 (Gy) (EUD that causes 50% probability of toxicity) and m (slope of the response curve at TD50) were fitted. As the most recent patients were rescanned and replanned on the 2nd day of treatment, EUD from day 1 and 2 were considered in the model.

Internal validation was performed by bootstrapping the original dataset 1,000 times as previously described (29), and recalculating the model parameters. Results from the bootstrap procedure were also used to define confidence intervals for best-fit parameters: a 68% confidence interval was calculated as the range 16th−84th percentiles of the distribution of the parameter

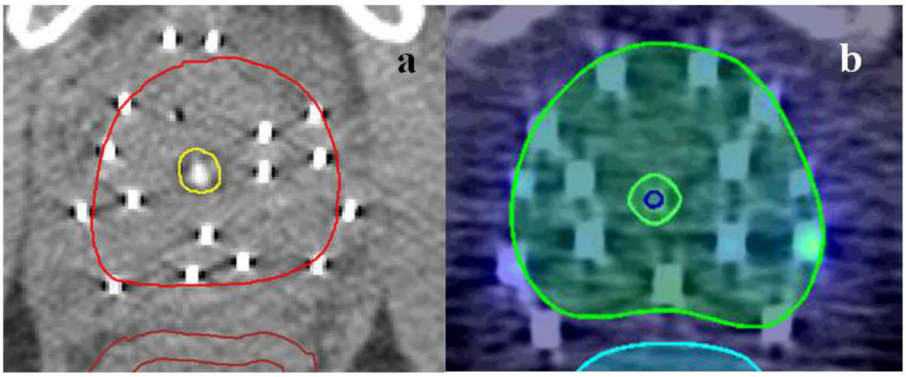

FIGURE 1 | Urethra contouring characteristics for AHRO **(a)** and RADAR **(b)** patient.

values obtained through bootstrap, while a 95% confidence interval was calculated as the range 2.5th−97.5th percentiles of the same distribution.

Goodness of fit was determined by using a model calibration plot to establish the relationship between the observed and predicted probability. Due to the binary nature of the stricture data (yes/no) the observed probabilities were obtained by dividing the 258 patients studied into four dose-bin groups and determining the corresponding rate of toxicity of each group. These observed rates were then plotted against those predicted by the model and a trend line derived. This line was then compared against the identity line which represents a perfect prediction (30). Calibration plot was established for the model fitted with the original AHRO data (apparent calibration line). Bootstrapping was employed to determine optimism and optimism-corrected performance (calibration line after correction for optimism) was then calculated as described by Steyerberg (31).

The discriminative ability of the model, that is, the ability to distinguish patients with different outcomes, was also evaluated with the area under the receiver operating characteristic curve (AUC).

External Model Validation

Data from a second cohort of 187 patients from a different institution treated as part of the TROG (Trans Tasman Radiation Oncology Group) 03.04 RADAR trial (32) were collected. For this group of patients, the HDRB prescription dose was 19.5 Gy in three fractions [corresponding to EQD_2 ($\alpha/\beta = 5$ Gy)], the stricture rate at 8.6% was comparable to AHRO patients, and all patients had ∼5 months of AD prior to radiotherapy, as part of a randomized total of 6 or 18 months of AD. The urethral toxicity end-point was considered to be equivalent to the one chosen for the AHRO patients, as the time of the first urethrotomy. The RADAR cohort was also treated with EBRT doses of 46 in 2 Gy fractions. For this group urethral structures were initially contoured by the RO as the visible lumen of the urinary catheter (**Figure 1b**, blue contour) and, then, these original contours were expanded on average 2 mm in the anterior-posterior and left-right direction and modified in the superior-inferior direction to be similar to the AHRO contours (**Figure 1b**, yellow contour). An expansion was chosen in order to preserve the variability in contours due to the RO outlines and provided urethral volumes on average equivalent to those obtained in the AHRO patients (respectively, expanded RADAR 1.5 cm^3 and AHRO 1.4 cm^3).

Both structures' DVHs (RADAR original and expanded) and associated clinical data were used to externally validate the LKB parameters obtained with the AHRO cohort. Model calibration, as described above, was used to establish agreement between the AHRO model estimated probabilities and RADAR observed stricture rates.

Effect of Clinical Covariates As Dose-Modifying Factors

For the AHRO patients, the effect of using AD on the model parameters was also investigated. The n and m value of the LKB model parameters were fixed and the fit was re-done separating the patients with (241/258) and without AD (17/258) to obtain two different TD50s as proposed by Peeters et al. (33).

RESULTS

LKB Model Parameters

For the AHRO patients, the urethral stricture prediction for the complete treatment (HDRB + EBRT) was modeled by means of a sigmoid function of EUD (**Figure 2A**). The numerical optimization of the likelihood showed a maximum for $n = 0.3$. The remaining best fitted parameters were found to be TD50 = 116.7 Gy (68% confidence interval, 108.3–134.1 Gy), $m = 0.23$ (68% confidence interval, 0.17–0.31; **Table 2**). The AUC of the development population was 0.64. **Figure 3** reports the distribution of TD50 (Gy) and m parameters obtained with bootstrapping.

The LKB NTCP curve was obtained and compared with the AHRO observed data (**Figure 2A**). The calibration plot confirmed the agreement between the observed probability of the outcome and the probability predicted by the model, as the trend line between the data was close to the identity line (**Figure 2B**), with calibration in the large = 0.007 and slope = 0.92, $R^2 = 0.71$

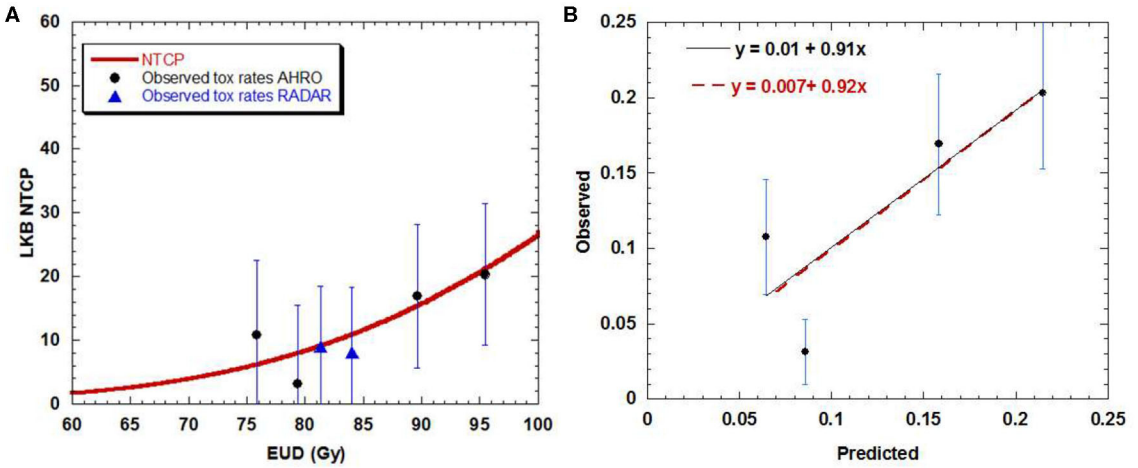

FIGURE 2 | (A) Dose-volume response curve obtained with the best estimated parameters for the LKB model for urethral stricture. Solid black circles represent the AHRO observed toxicity rates with corresponding error. The blues triangles represent the RADAR patients. **(B)** Calibration (predicted vs. observed) curves obtained by using the AHRO LKB model and data (red dotted line, apparent calibration line; black continuous line, calibration line after correction for optimism).

TABLE 2 | LKB model parameters obtained fitting the original AHRO data (all cohort), with bootstrapping, corresponding Confidence Intervals (CI) and when the cohort was separated by the use or not of Androgen Deprivation (AD).

	TD50 (Gy)	m	n
AHRO best fit	116.7	0.23	0.3
AHRO Bootstrapping median	116.5	0.23	0.3
AHRO Bootstrapping 68% CI	108.2–134	0.17–0.31	
AHRO Bootstrapping 95% CI	104.2–218.7	0.14–0.51	
AHRO with AD	118.2	0.23	0.3
AHRO without AD	104.9	0.23	0.3

for apparent calibration and calibration in the large = 0.01 and slope = 0.91 after correction for optimism.

External Validation of the Model

The external validation performed using the urethra data exported from the RADAR cohort gave the best agreement with the AHRO prediction model when the urethra contours were expanded to be similar to AHRO's contours (calibration in the large = −0.04 and calibration slope = 1.3, R^2 = 0.94). As shown in **Figure 4B**, poorer calibration was found when using the original contours (calibration in the large = −1.5 and calibration slope = 18.5, R^2 = 0.93; **Figure 4A**).

Looking at the dose-response curve (**Figure 2A**), consistency was found between the RADAR observed toxicity rates and the AHRO LKB model, confirming that the RADAR toxicity was well-represented by the estimated LKB model parameters.

Effect of Using Neo-Adjuvant Androgen Deprivation

When separating AHRO patients that received AD from those that did not receive it, results showed a decrease of around 13 Gy in the TD50 (Gy) for patients who did not receive AD, suggesting a protective effect of AD (**Table 2**, **Figure 5**).

DISCUSSION

Interest in understanding the nature of long term side effects in OARs produced by prostate radiotherapy has grown due to the increase in utilization of hypofractionated regimens in EBRT (34–36). Of particular concern is the risk of urethral stricture which generally requires surgical intervention to be resolved. Guidelines for urethral dose constraints are still sparse due to the fact that urethra contouring has only recently being considered for such techniques and correlation with dose, and clinical data follow-up and collection is lacking (17, 18, 30). HDRB boost techniques, which have been used for decades due to the introduction of afterloaders (9) instead provide the potential for analysis of toxicity and dosimetric data specific for the urethral side effects due to the routine inclusion of the urethral contour in the planning process.

This work has focused on fitting the LKB model parameters of urethral stricture data collected on a large cohort of patients treated with HDRB boost at one single institution for a time-period of 12 years. This NTCP model was created by considering urethrotomy recorded in the first 4 years after the treatment as an end-point. All toxicity data were prospectively recorded in a database and the follow-up was meticulously done by reviewing the patients at well set time intervals. Additionally, any correspondence with the treating doctors after brachytherapy was analyzed in order to look for additional urethrotomy recorded.

The predictive model fitted in this work showed a clear dose-effect relationship between the incidence of urethral stricture and the dose delivered to the urethra (**Figure 2A**), and it was obtained by using the DVH as opposed to a single representative dose parameter (for example, D10%). As shown in **Table 1** by increasing the dose from 18 Gy in three fractions to 19 Gy in two

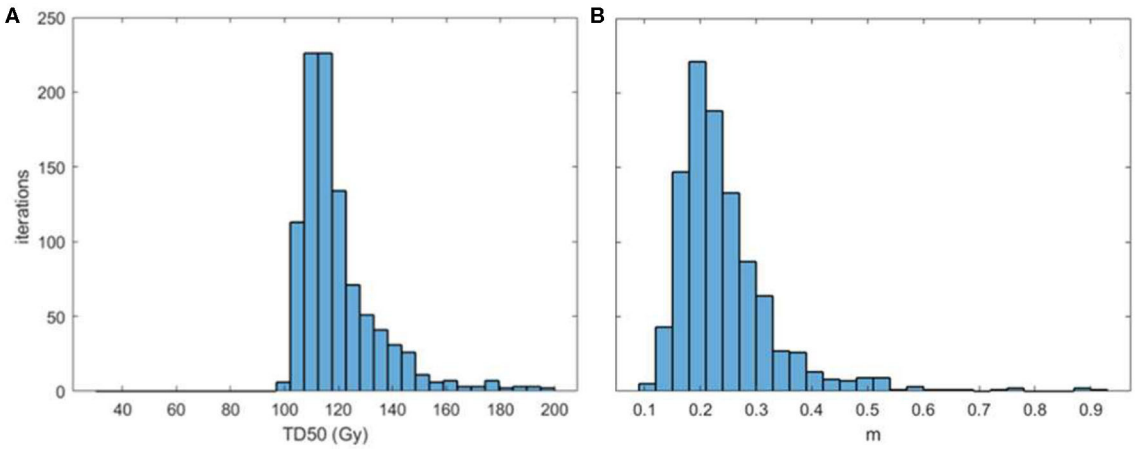

FIGURE 3 | Distribution of TD50 (Gy) **(A)** and *m* **(B)** parameters obtained with bootstrapping.

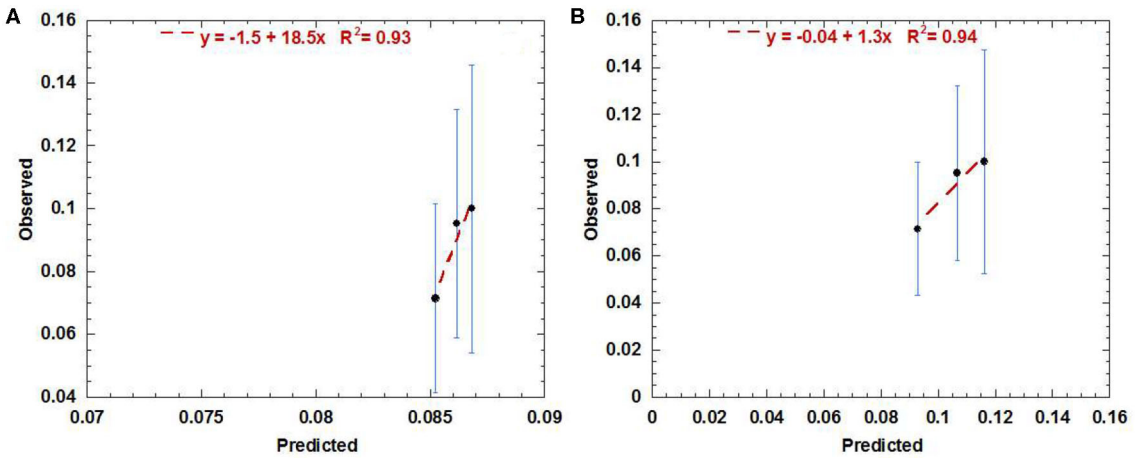

FIGURE 4 | Calibration (predicted vs. observed) curve obtained by using the AHRO LKB model for the RADAR data with original contours **(A)** and the expanded contours **(B)**.

fractions in a 2-day treatment schedule the incidence of strictures was increased by almost three times from an average rate of 6.9–20.5% for an identical cut-off time of 4 years of follow-up. This finding was previously documented by Hindson et al. (10) for a similar cohort of patients treated in the same institution, and it is here confirmed by means of a sigmoidal relationship. The fitted dose-response relationship showed that to ensure a toxicity rate to below 10% the urethral EUD should be limited to 85 Gy (with $\alpha/\beta = 5$ Gy). Similar dose correlation was documented by other groups, with toxicity rates equivalent to the AHRO cohort for similar fractionation regimens (37, 38), and comparable follow-up time (5–6 years on average), however, comparisons were mainly performed by considering the prescription doses and not the planned dose to the urethra. In contrast, several publications reported no significant correlation in doses between the group that had toxicity and the group that did not have it (39, 40). For example, in the case of HDRB monotherapy, more recently in an analysis of 178 patients with a median follow-up time of 28.2 months, Tsang et al. (41) only reported 3% rate of urethral stricture and could not identify significant correlation with the toxicity and the urethral dose, identifying instead potential radiomics features that could predict the risk of developing toxicity on the pre-treatment MRI. This conclusion is similar to the work by Diez et al. (2) which instead considered a median follow-up time of 55 months for all groups. However, by fixing the follow-up time at 4 years the same authors reported an increase from 3 to 7% of the Kaplan–Meier estimates from the patients that were treated with 34 Gy in four fractions to the patients that were treated with 31.5 Gy in three fractions (14). Patients' follow-up time seems to represent an important variable in all of these studies, with large variations between groups and most works not considering a fixed time at which to

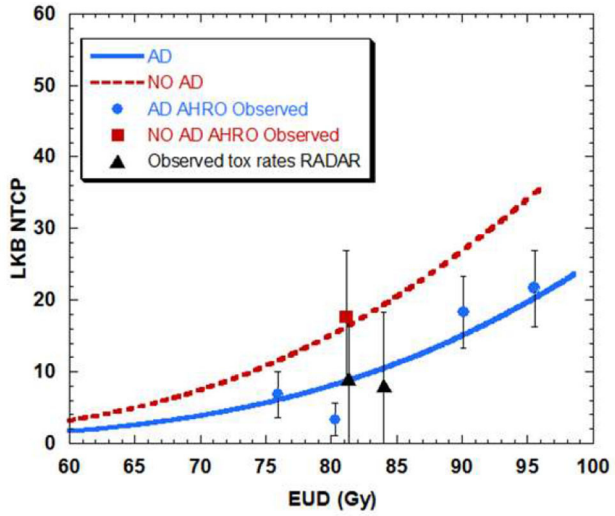

FIGURE 5 | Dose-volume response curve obtained with the best estimated parameters for the LKB model for urethral stricture for patients that had neo-adjuvant androgen deprivation (AD-blue) as opposed to patient that did not have AD (NO AD-red).

compare different dose groups. For example, in a large cohort, Bece et al. (13) reported a decrease in toxicity rate from 12.8 to 3% by moving from 18 to 19 Gy in two fractions, however, the first group was followed for 4 years as opposed to 2 years for the second group limiting the information collected and the analysis. As shown in **Table 1**, in our group for a follow-up of 4 years the time to toxicity on-set decreased with increasing overall dose (from an average time of 3.6–2.1 years). So, a short follow-up time could potentially underestimate the recorded stricture rates.

The fitted model parameters (**Table 2**) well-represented the AHRO observed data, as shown by the calibration plot (**Figure 2B**), and internal calibration bootstrapped results (**Figure 3**). The AUC was of the order of 0.64, which is of the order of values obtained for most models based on dose features alone (42). An outlier was observed in the 80 Gy EUD dose group, believed to be associated with the little variability of urethral doses for patients in this dose group (**Figures 2A,B**). Notably, the volume parameter n was larger than expected (0.3), suggesting that the architecture of the urethra could be more parallel than generally believed, due to its shape and similarity to structures such as the spinal cord or the esophagus. However, this result could be related to the small volumes involved (ranging from 0.02 to 3.6 cm^3 for the AHRO cohort), and the limitation in fitting the parameter with the data available. Additional studies have been undertaken in order to analyze surface or voxelized dose maps (18) of this organ, as opposed to the 2D representation provided by the DVH, to identify spatial and volumetric correlations with toxicity. In this work an $\alpha/\beta = 5$ Gy was used in order to convert the physical doses into EQD_2, and EUD. This value was chosen in accordance to work by Gloi and Buchanan (22) as representative of the urethral late effects, however, more dedicated studies are in progress in order to confirm the validity of this assumption, making it a limitation of this work.

The LKB model parameters were also tested by using data from a completely independent cohort treated with comparable HDRB boost doses to establish the generality of its predictive value. The external cohort was part of a large group of patients treated as part of the RADAR clinical trial (32) so all patients were planned by following a well-defined protocol for dose constraints and contouring guidelines. An interesting finding was the importance of urethra contouring in the assessment of NTCP dose-volume relationship. The RADAR patients' whole urethras were all initially contoured by the clinician as the lumen of the urinary catheter (here defined as original-**Figure 1b**, blue contour). The DVH extracted from this contour did not correlate with the initial model as shown in the calibration plot (**Figure 4A**). When re-outlined to match the AHRO contours (**Figure 1a**, yellow contour) the goodness of fit was confirmed. This result highlights that in order to understand the relationship between dose and toxicity, and compare the data of different groups, consensus for the outlining of the urethral volume is advisable, and contour practices should be clearly documented. It also suggests that in order to establish a dose-volume correlation the urethra should be contoured in order to include the urethral mucosal wall, and at least 10–20 mm of urethra distally to the prostate apex in order to include the bulbomembranous portion as previously highlighted (43). In this work for both AHRO and RADAR patients, the urethral dose provided by the external beam portion of the treatment was considered uniform and equivalent to the EBRT prescription dose. This method was followed due to the fact that for both cohorts the urethral structures were not contoured and considered at the time of treatment planning, and the plan was performed to achieve uniform PTV coverage (between 95 and 107% of the prescription dose). Due to the introduction of external beam hypofractionated treatments, and of routine urethral contouring this assumption might need to be modified in order to account for the available calculated urethral DVH information (35, 36).

In this work, the whole urethra was considered, as opposed to other studies (2, 41) in which the volume was divided in membranous and prostatic urethra.

Among the patients' clinical parameters, the effect of the use of neo-adjuvant androgen deprivation was investigated in the model fitting. Despite the modeling limitation that a small number of AHRO patients did not receive AD (**Table 1**), when LKB was fitted with and without AD, the TD50 (Gy) showed an absolute TD50 reduction of 13.3 Gy without AD, suggesting that AD could act as dose-modifier and a protective effect on urethral toxicity. A similar result was previously documented by Palorini et al. (30) for a large multicenter group of patients treated with EBRT, and it could be due to the known effect of tumor shrinkage and reduction of the irradiation volume, and potentially a cytoreductive effect (30, 44).

All DVHs used in this study were extracted from the treatment planning system and so they are representative of the planned dose. This is a known limitation as experience and previous works (10, 13) have shown the potential for prostate swelling and needle movement with respect to the anatomy, which could

potentially under or overestimate the dose-toxicity correlation found. As of 2017, our group has started performing on-line verification between CT and treatment and re-scanning and planning the patients when the movement exceeds our clinical tolerances (45), and data will be analyzed when mature.

CONCLUSION

Urethral toxicity is a limiting factor in providing additional dose escalation in radiotherapy of the prostate. For HDRB of prostate cancer clear urethral dose guidelines are still not available due to the variety of dose prescription used and the variety of contouring protocols. In this work, an LKB model was fitted to the risk of urethral stricture for a large single center cohort. The model was then externally validated with independent patients' clinical and dosimetric data, showing a clear and reproducible relationship between dose delivered to the whole organ and urethral toxicity. When clinical factors were included findings showed that for patients that did not receive neo-adjuvant androgen deprivation, model fitting provided a lower TD50 (Gy) suggesting a protective effect on urethral toxicity, as previously highlighted for EBRT studies.

DATA AVAILABILITY STATEMENT

The datasets generated for this study will not be made publicly available due to the ethics considerations.

ETHICS STATEMENT

The studies involving human participants were reviewed and approved by Alfred Hospital Ethics Committee (Project 323/14). Use of RADAR data was approved by the TROG Publications Committee. Written informed consent for participation was not required for this study in accordance with the national legislation and the institutional requirements.

AUTHOR CONTRIBUTIONS

VP has designed the study, collected the data, performed the MATLAB calculations described in the methods, and has written the draft of the manuscript. TR has provided extensive technical advice on the implementation of the work, model building, and validation and has revised several versions of both calculations and manuscript. EO has provided the MATLAB code used in the study and has provided advice on the technical component. ME, JD, DJ, and AS have provided the RADAR data used for the external validation and JM has provided advice and patients data used for model building. All co-authors contributed to proof-reading of the manuscript.

ACKNOWLEDGMENTS

The authors would like to acknowledge Ms. Karen Scott for the accurate and comprehensive AHRO data collection. Dr. Ryan Smith is also kindly acknowledged for advice on historical data extraction, and Dr. Angel Kennedy for the support in extracting the RADAR patient data. We thank the Trans Tasman Radiation Oncology Group for making the TROG 03.04 RADAR data available for this project.

REFERENCES

1. Morton GC. High-dose-rate brachytherapy boost for prostate cancer: rationale and technique. *J Contemp Brachytherapy.* (2014) 6:323–30. doi: 10.5114/jcb.2014.45759
2. Diez P, Mullassery V, Dankulchai P, Ostler P, Hughes R, Alonzi R, et al. Dosimetric analysis of urethral strictures following HDR (192)Ir brachytherapy as monotherapy for intermediate- and high-risk prostate cancer. *Radiother Oncol.* (2014) 113:410–3. doi: 10.1016/j.radonc.2014.10.007
3. Kent AR, Matheson B, Millar JL. Improved survival for patients with prostate cancer receiving high-dose-rate brachytherapy boost to EBRT compared with EBRT alone. *Brachytherapy.* (2019) 18:313–21. doi: 10.1016/j.brachy.2019.01.013
4. Ong WL, Evans SM, Millar JL. Under-utilisation of high-dose-rate brachytherapy boost in men with intermediate-high risk prostate cancer treated with external beam radiotherapy. *J Med Imaging Radiat Oncol.* (2018) 62:256–61. doi: 10.1111/1754-9485.12699
5. Hoskin PJ, Rojas AM, Bownes PJ, Lowe GJ, Ostler PJ, Bryant L. Randomised trial of external beam radiotherapy alone or combined with high-dose-rate brachytherapy boost for localised prostate cancer. *Radiother Oncol.* (2012) 103:217–22. doi: 10.1016/j.radonc.2012.01.007
6. Martell K, Mendez LC, Chung HT, Tseng CL, Alayed Y, Cheung P, et al. Results of 15Gy HDR-BT boost plus EBRT in intermediate-risk prostate cancer: analysis of over 500 patients. *Radiother Oncol.* (2019) 141:149–55. doi: 10.1016/j.radonc.2019.08.017
7. Martinez AA, Gonzalez J, Ye H, Ghilezan M, Shetty S, Kernen K, et al. Dose escalation improves cancer-related events at 10 years for intermediate- and high-risk prostate cancer patients treated with hypofractionated high-dose-rate boost and external beam radiotherapy. *Int J Radiat Oncol Biol Phys.* (2011) 79:363–70. doi: 10.1016/j.ijrobp.2009.10.035
8. Fowler J, Chappell R, Ritter M. Is α/β for prostate tumors really low? *Int J Radiat Oncol Biol Phys.* (2001) 50:1021–31. doi: 10.1016/S0360-3016(01)01607-8
9. Crook J, Marban M, Batchelar D. HDR prostate brachytherapy. *Semin Radiat Oncol.* (2020) 30:49–60. doi: 10.1016/j.semradonc.2019.08.003
10. Hindson BR, Millar JL, Matheson B. Urethral strictures following high-dose-rate brachytherapy for prostate cancer: analysis of risk factors. *Brachytherapy.* (2013) 12:50–5. doi: 10.1016/j.brachy.2012.03.004
11. Yaxley JW, Lah K, Yaxley JP, Gardiner RA, Samaratunga H, MacKean J. Long-term outcomes of high-dose-rate brachytherapy for intermediate- and high-risk prostate cancer with a median follow-up of 10 years. *BJU Int.* (2017) 120:56–60. doi: 10.1111/bju.13659
12. Ishiyama H, Kitano M, Satoh T, Kotani S, Uemae M, Matsumoto K, et al. Genitourinary toxicity after high-dose-rate (HDR) brachytherapy combined with Hypofractionated External beam radiotherapy for localized prostate cancer: an analysis to determine the correlation between dose-volume histogram parameters in HDR brachytherapy and severity of toxicity. *Int J Radiat Oncol Biol Phys.* (2009) 75:23–8. doi: 10.1016/j.ijrobp.2008.11.006
13. Bece A, Patanjali N, Jackson M, Whitaker M, Hruby G. High-dose-rate brachytherapy boost for prostate cancer: outcomes and genitourinary

toxicity. *Brachytherapy*. (2015) 14:670–6. doi: 10.1016/j.brachy.2015.04.004
14. Hoskin P, Rojas A, Lowe G, Bryant L, Ostler P, Hughes R, et al. High-dose-rate brachytherapy alone for localized prostate cancer in patients at moderate or high risk of biochemical recurrence. *Int J Radiat Oncol Biol Phys.* (2012) 82:1376–84. doi: 10.1016/j.ijrobp.2011.04.031
15. Hoskin PJ, Colombo A, Henry A, Niehoff P, Paulsen Hellebust T, Siebert FA, et al. GEC/ESTRO recommendations on high dose rate afterloading brachytherapy for localised prostate cancer: an update. *Radiother Oncol.* (2013) 107:325–32. doi: 10.1016/j.radonc.2013.05.002
16. Yamada Y, Rogers L, Demanes DJ, Morton G, Prestidge BR, Pouliot J, et al. American Brachytherapy Society consensus guidelines for high-dose-rate prostate brachytherapy. *Brachytherapy*. (2012) 11:20–32. doi: 10.1016/j.brachy.2011.09.008
17. Olsson CE, Jackson A, Deasy JO, Thor M. A Systematic post-QUANTEC review of tolerance doses for late toxicity after prostate cancer radiation therapy. *Int J Radiat Oncol Biol Phys.* (2018) 102:1514–32. doi: 10.1016/j.ijrobp.2018.08.015
18. Mylona E, Acosta O, Lizee T, Lafond C, Crehange G, Magne N, et al. Voxel-based analysis for identification of urethrovesical subregions predicting urinary toxicity after prostate cancer radiation therapy. *Int J Radiat Oncol Biol Phys.* (2019) 104:343–54. doi: 10.1016/j.ijrobp.2019.01.088
19. Yahya N, Ebert MA, House MJ, Kennedy A, Matthews J, Joseph DJ, et al. Modeling urinary dysfunction after external beam radiation therapy of the prostate using bladder dose-surface maps: evidence of spatially variable response of the bladder surface. *Int J Radiat Oncol Biol Phys.* (2017) 97:420–6. doi: 10.1016/j.ijrobp.2016.10.024
20. Carillo V, Cozzarini C, Rancati T, Avuzzi B, Botti A, Borca VC, et al. Relationships between bladder dose-volume/surface histograms and acute urinary toxicity after radiotherapy for prostate cancer. *Radiother Oncol.* (2014) 111:100–5. doi: 10.1016/j.radonc.2014.02.006
21. Takam R, Bezak E, Yeoh EE, Marcu L. Assessment of normal tissue complications following prostate cancer irradiation: comparison of radiation treatment modalities using NTCP models. *Med Phys.* (2010) 37:5126–37. doi: 10.1118/1.3481514
22. Gloi AM, Buchanan R. Dosimetric assessment of prostate cancer patients through principal component analysis (PCA). *J Appl Clin Med Phys.* (2013) 14:40–9. doi: 10.1120/jacmp.v14i1.3882
23. Zwahlen DR, Andrianopoulos N, Matheson B, Duchesne GM, Millar JL. High-dose-rate brachytherapy in combination with conformal external beam radiotherapy in the treatment of prostate cancer. *Brachytherapy.* (2010) 9:27–35. doi: 10.1016/j.brachy.2009.04.007
24. Szymanski KM, Wei JT, Dunn RL, Sanda MG. Development and validation of an abbreviated version of the expanded prostate cancer index composite instrument for measuring health-related quality of life among prostate cancer survivors. *Urology.* (2010) 76:1245–50. doi: 10.1016/j.urology.2010.01.027
25. Kutcher GJ, Burman C. Calculation of complication probability factors for non-uniform normal tissue irradiation: the effective volume method gerald. *Int J Radiat Oncol Biol Phys.* (1989) 16:1623–30. doi: 10.1016/0360-3016(89)90972-3
26. Lyman JT. Complication probability as assessed from dose-volume histograms. *Radiat Res.* (1985) 104:S13–S9. doi: 10.2307/3576626
27. Onjukka E, Baker C, Nahum A. The performance of normal-tissue complication probability models in the presence of confounding factors. *Med Phys.* (2015) 42:2326–41. doi: 10.1118/1.4917219
28. Rancati T, Fiorino C, Gagliardi G, Cattaneo GM, Sanguineti G, Borca VC, et al. Fitting late rectal bleeding data using different NTCP models: results from an Italian multi-centric study (AIROPROS0101). *Radiother Oncol.* (2004) 73:21–32. doi: 10.1016/j.radonc.2004.08.013
29. El Naqa I, Bradley J, Blanco AI, Lindsay PE, Vicic M, Hope A, et al. Multivariable modeling of radiotherapy outcomes, including dose-volume and clinical factors. *Int J Radiat Oncol Biol Phys.* (2006) 64:1275–86. doi: 10.1016/j.ijrobp.2005.11.022
30. Palorini F, Rancati T, Cozzarini C, Improta I, Carillo V, Avuzzi B, et al. Multi-variable models of large International Prostate Symptom Score worsening at the end of therapy in prostate cancer radiotherapy. *Radiother Oncol.* (2016) 118:92–8. doi: 10.1016/j.radonc.2015.11.036
31. Steyerberg EW. *Clinical Prediction Models A Practical Approach to Development, Validation, and Updating*. New York, NY: Springer (2009).
32. Denham JW, Steigler A, Joseph D, Lamb DS, Spry NA, Duchesne G, et al. Radiation dose escalation or longer androgen suppression for locally advanced prostate cancer? Data from the TROG 03.04 RADAR trial. *Radiother Oncol.* (2015) 115:301–7. doi: 10.1016/j.radonc.2015.05.016
33. Peeters STH, Hoogeman MS, Heemsbergen WD, Hart AAM, Koper PCM, Lebesque JV. Rectal bleeding, fecal incontinence, and high stool frequency after conformal radiotherapy for prostate cancer: normal tissue complication probability modeling. *Int J Radiat Oncol Biol Phys.* (2006) 66:11–9. doi: 10.1016/j.ijrobp.2006.03.034
34. McDonald AM, Baker CB, Popple RA, Cardan RA, Fiveash JB. Increased radiation dose heterogeneity within the prostate predisposes to urethral strictures in patients receiving moderately hypofractionated prostate radiation therapy. *Pract Radiat Oncol.* (2015) 5:338–42. doi: 10.1016/j.prro.2015.02.010
35. Dearnaley D, Syndikus I, Mossop H, Khoo V, Birtle A, Bloomfield D, et al. Conventional versus hypofractionated high-dose intensity-modulated radiotherapy for prostate cancer: 5-year outcomes of the randomised, non-inferiority, phase 3 CHHiP trial. *Lancet Oncol.* (2016) 17:1047–60. doi: 10.1016/S1470-2045(16)30102-4
36. Martin JM, Rosewall T, Bayley A, Bristow R, Chung P, Crook J, et al. Phase II trial of hypofractionated image-guided intensity-modulated radiotherapy for localized prostate adenocarcinoma. *Int J Radiat Oncol Biol Phys.* (2007) 69:1084–9. doi: 10.1016/j.ijrobp.2007.04.049
37. Mohammed N, Kestin L, Ghilezan M, Krauss D, Vicini F, Brabbins D, et al. Comparison of acute and late toxicities for three modern high-dose radiation treatment techniques for localized prostate cancer. *Int J Radiat Oncol Biol Phys.* (2012) 82:204–12. doi: 10.1016/j.ijrobp.2010.10.009
38. Sullivan L, Williams SG, Tai KH, Foroudi F, Cleeve L, Duchesne GM. Urethral stricture following high dose rate brachytherapy for prostate cancer. *Radiother Oncol.* (2009) 91:232–6. doi: 10.1016/j.radonc.2008.11.013
39. Hsu IC, Bae K, Shinohara K, Pouliot J, Purdy J, Ibbott G, et al. Phase II trial of combined high-dose-rate brachytherapy and external beam radiotherapy for adenocarcinoma of the prostate: preliminary results of RTOG 0321. *Int J Radiat Oncol Biol Phys.* (2010) 78:751–8. doi: 10.1016/j.ijrobp.2009.08.048
40. Konishi K, Yoshioka Y, Isohashi F, Sumida I, Kawaguchi Y, Kotsuma T, et al. Correlation between dosimetric parameters and late rectal and urinary toxicities in patients treated with high-dose-rate brachytherapy used as monotherapy for prostate cancer. *Int J Radiat Oncol Biol Phys.* (2009) 75:1003–7. doi: 10.1016/j.ijrobp.2008.12.051
41. Tsang YM, Vignarajah D, McWilliam A, Tharmalingam H, Lowe G, Choudhury A, et al. A pilot study on dosimetric and radiomics analysis of urethral strictures following HDR brachytherapy as monotherapy for localized prostate cancer. *Br J Radiol.* (2019) 93:20190760. doi: 10.1259/bjr.20190760
42. Yahya N, Ebert MA, Bulsara M, Kennedy A, Joseph DJ, Denham JW. Independent external validation of predictive models for urinary dysfunction following external beam radiotherapy of the prostate: issues in model development and reporting. *Radiother Oncol.* (2016) 120:339–45. doi: 10.1016/j.radonc.2016.05.010
43. Moltzahn F, Dal Pra A, Furrer M, Thalmann G, Spahn M. Urethral strictures after radiation therapy for prostate cancer. *Investig Clin Urol.* (2016) 57:309–15. doi: 10.4111/icu.2016.57.5.309
44. Datta NR, Stutz E, Rogers S, Bodis S. Clinical estimation of α/β values for prostate cancer from isoeffective phase III randomized trials with

moderately hypofractionated radiotherapy. *Acta Oncol.* (2018) 57:883–94. doi: 10.1080/0284186X.2018.1433874

45. Smith RL, Hanlon M, Panettieri V, Millar JL, Matheson B, Haworth A, et al. An integrated system for clinical treatment verification of HDR prostate brachytherapy combining source tracking with pretreatment imaging. *Brachytherapy*. (2018) 17:111–21. doi: 10.1016/j.brachy.2017.08.004

Conflict of Interest: DJ was employed by GenesisCare and 5D Clinics. ME has an honorary position at 5D Clinics. DJ and ME each have a financial shareholding in 5D Clinics.

The remaining authors declare that the research was conducted in the absence of any commercial or financial relationships that could be construed as a potential conflict of interest.

frontiers in Oncology

PERSPECTIVE
published: 24 June 2020
doi: 10.3389/fonc.2020.00978

Registering Study Analysis Plans (SAPs) Before Dissecting Your Data—Updating and Standardizing Outcome Modeling

Maria Thor, Jung Hun Oh, Aditya P. Apte and Joseph O. Deasy*

Department of Medical Physics, Memorial Sloan Kettering Cancer Center, New York, NY, United States

Public preregistration of study analysis plans (SAPs) is widely recognized for clinical trials, but adopted to a much lesser extent in observational studies. Registration of SAPs prior to analysis is encouraged to not only increase transparency and exactness but also to avoid positive finding bias and better standardize outcome modeling. Efforts to generally standardize outcome modeling, which can be based on clinical trial and/or observational data, have recently spurred. We suggest a three-step SAP concept in which investigators are encouraged to (1) Design the SAP and circulate it among the co-investigators, (2) Log the SAP with a public repository, which recognizes the SAP with a digital object identifier (DOI), and (3) Cite (using the DOI), briefly summarize and motivate any deviations from the SAP in the associated manuscript. More specifically, the SAP should include the *scope* (brief data and study description, co-investigators, hypotheses, primary outcome measure, study title), in addition to step-by-step details of the *analysis* (handling of missing data, resampling, defined significance level, statistical function, validation, and variables and parameterization).

Keywords: cancer, clinical trial, observational study, outcome modeling, preregistration, public repository, radiotherapy, study plan

OPEN ACCESS

Edited by:
Tiziana Rancati, Istituto Nazionale dei Tumori (IRCCS), Italy

Reviewed by:
Alexander F. I. Osman, Al-Neelain University, Sudan
Wilma Desiree Heemsbergen, Erasmus University Rotterdam, Netherlands

****Correspondence:***
Maria Thor
thorm@mskcc.org

Specialty section:
This article was submitted to Radiation Oncology, a section of the journal Frontiers in Oncology

Received: *20 January 2020*
Accepted: *18 May 2020*
Published: *24 June 2020*

Citation:
Thor M, Oh JH, Apte AP and Deasy JO (2020) Registering Study Analysis Plans (SAPs) Before Dissecting Your Data—Updating and Standardizing Outcome Modeling. Front. Oncol. 10:978. doi: 10.3389/fonc.2020.00978

INTRODUCTION

Starting from 1997, the Food and Drug Administration Modernization Act (FDAMA) mandated the National Institute of Health (NIH) to design a platform in which information about FDA regulated clinical trials would become publicly available[1]. As a result, NIH launched ClinicalTrials.gov shortly thereafter (1). Public pre-registration of clinical trials has since become a general publication requirement (2), and fast forwarded to two decades after FDAMA was introduced, ClinicalTrials.gov hosts 341 988 (as of June 11, 2020) registered studies conducted worldwide[2].

[1]Food and Drug Administration Modernization Act of 1997: https://www.govinfo.gov/content/pkg/PLAW-105publ115/pdf/PLAW-105publ115.pdf#page=16

[2]https://clinicaltrials.gov/ct2/resources/trends

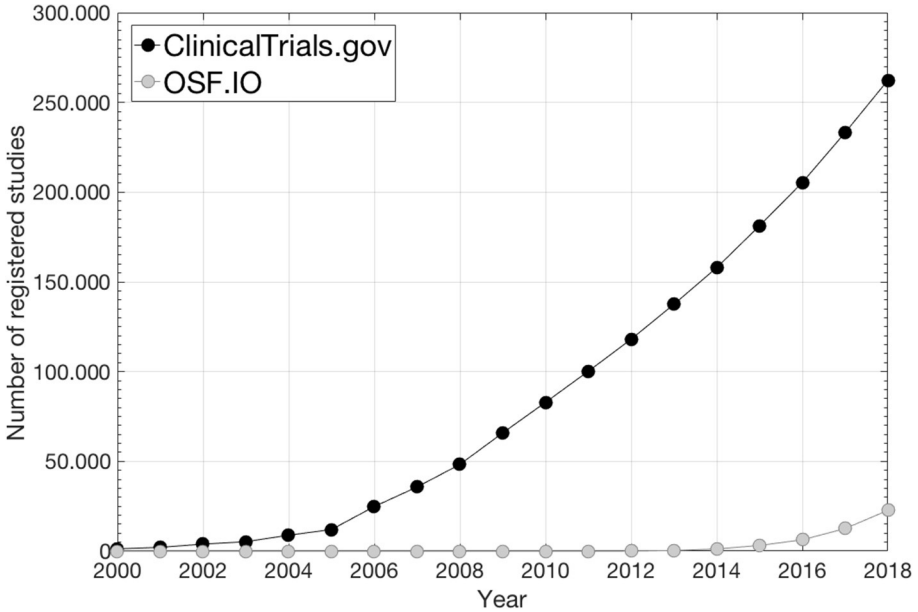

FIGURE 1 | The number of preregistered SAPs during the last two decades under ClinicalTrials.gov[2] and under OSF[3] (data from ClinicalTrials.gov is taken from[2]; data from OSF is taken from https://cos.io/our-products/osf-registries/).

This site primarily focuses on interventional studies/clinical trials while study analysis plans (SAPs) and associated results from observational studies are scarce (1)[2] as also illustrated in **Figure 1** where the number of preregistrations from ClinicalTrials.gov and from the Open Science Foundation (OSF)[3], which mainly holds SAPs from observational studies, is given over time. Consequently, for observational exploratory research it is often unclear as to the number of analyses undertaken, which further feeds into what is referred to as "*p-hacking*," i.e., a positive finding publication bias since the vast majority of published studies that report *p*-values disclose positive/significant findings (3, 4). Further, SAP pre-registration is likely to facilitate researchers to better distinguish between confirmatory research (hypothesis-testing in which *p*-values retain diagnostic value) and exploratory research (hypothesis-generating in which *p*-values loose diagnostic value) in order to avoid overconfidence in *post-hoc* explanations in a finding that has not been proven, which could limit reproducibility (5).

The Transparent Reporting of a multivariate prediction model for Individual Prognosis Or Diagnosis (TRIPOD) statement has encouraged to better standardize outcome modeling (6). Outcome modeling can be based on data generated from clinical trials or observational studies. Here we propose to pre-register SAPs under public repositories for any outcome modeling study to further promote standardization, transparency and exactness and to mitigate the false positive inflation of published results.

[3]https://osf.io/

METHODS AND MATERIALS

Public pre-registration of SAPs could be thought of as committing to an analytical path but without advancing knowledge of the research outcome (4). To date, the two most commonly used public SAP repositories, which both provide SAP unique digital object identifiers (DOIs), are located under ClinicalTrials.gov (1) and under the OSF[3]. As previously pointed out, ClinicalTrials.gov has primarily been used to register clinical trials, while under OSF a larger extent of SAPs from observational studies can be found.

THE SAP CONCEPT

The suggested SAP concept consists of three steps: (1) Designing the SAP and circulating it among the co-investigators; (2) Logging the SAP with a public repository, which recognizes the SAP with a DOI, and (3) Citing (using the DOI), briefly summarizing and motivating any deviations from the SAP in the associated manuscript (*Note: any new major post-SAP analysis should only be considered hypothesis-generating/exploratory*). The three-step SAP concept is summarized in **Figure 2**.

The outcome modeling pipeline in the SAP should adhere to the modeling procedures defined in the TRIPOD landmark paper on how to model outcomes (6). This refers to description of data, outcomes and input variables and parameterization in addition to detailed step-by-step lay-out of the analysis. Below we list more specifically what the SAP should include (at a minimum) inspired by OSF's preregistration template, which is available as a GoogleDoc here: https://docs.google.com/document/d/1DaNmJEtBy04bq1l5OxS4JAscdZEkUGATURWwnBKLYxk/

FIGURE 2 | A flow chart of the suggested three-step SAP concept: (1) Design SAP and distribute to co-investigators (left); (2) Log SAP (middle), and (3) Cite (using the DOI), summarize and motivate any deviations from the SAP in the associated manuscript (right).

edit?pli=1, but more directed toward outcome modeling assuming an observational study design. An associated example SAP template for the purpose of outcome modeling is provided in the **Supplementary Material**.

Scope (Description of Data and Study)

The study scope should include title, co-investigators, and a brief study description, and the underlying study hypothesis/hypotheses. The brief study description should be accompanied by a description of data/patient population (inclusion criteria, number of patients, primary tumor site, treatment era, etc.) and primary outcome measure with range and minimum follow-up time and censoring defined if applicable. The study type should also be clearly stated (e.g., validation, exploration, and/or prediction).

Analysis (Description of the Analysis)

All variables considered for analysis should be described in detail along with their parameterization (binary, categorical and continuous; specify increments if applicable). Handling of missing data (if excluding data then describe how this will be accounted for) should be disclosed, and if applicable data transformation (or normalization) as well as definition of variable interaction terms should be given. The exact definition of the studied outcome, e.g., timing and scoring of radiation-induced toxicity and how pre-treatment status was taken into account, should be given. Although this SAP concept work focuses on outcome modeling in general, the expected minimum level of detail on reported variables is exemplified for RT dose, which is central for outcome modeling following RT: Specify if dose was parameterized as 2D dose-volume histograms (denote metrics, interval investigated and sampling), and/or summary measures such as the mean dose or the generalized equivalent uniform dose, and/or if being represented spatially (denote metrics and describe method) and if dose originated from the planned dose distribution, if being accumulated (plus type of dose accumulation), and/or if during treatment dose was used (applies possibly only for acute toxicity). Denote if and how fractionation effects were handled, and give the exact anatomical definition of the investigated organ(s) along with the associated segmentation approach. Please refer to the Results section for a practical example of the level of detail in describing dose.

The statistical functions/methods of analysis (e.g., regression (and type), time to event, competing risk, etc.) should be explained in detail along with a description of risk groups and defined errors/confidence intervals (if valid), any considered resampling (e.g., iterated cross-validation hold-out or bootstrapping; number of iterations, etc.), validation (external/internal), and if and how univariate and/or multivariate analysis will be performed. Any considered level of significance/model quality should be specified and the associated performance metric described. If investigating more than one variable authors should denote how multiple testing will be corrected for.

Lastly, the SAP should include the statistical software tools (and version) that are being considered.

LITERATURE RESOURCES FOR OUTCOME MODELING IN RADIOTHERAPY

Aside from advocating the use of TRIPOD (6) as a guideline for outcome modeling in general, we below provide a short introduction to relevant literature for outcome modeling in radiotherapy (RT) with a particular emphasis on standardization.

To obtain reliable information about toxicities that influence patient's quality of life, normal tissue toxicities are likely best represented by patient-reported outcomes (PROs) (7). Using clinical decision-support tools (8, 9) and keeping the number of items/questions as few as possible (10) are necessary for actionability to patient-reported complaints. Dose-volume histogram (DVH) metrics of interest depend on a large variety of factors as pointed out within the 21 papers by the QUANTEC effort (11). Gathering published DVH metrics to better understand the reliability and generalizability of such metrics was first initiated by QUANTEC and is, as illustrated in their offspring efforts [pediatric RT (12) and hypo fractionated RT (13)] and work by other groups (14), a continuous process. These and related efforts (ideally multi-institutional) in which

models have been validated (6, 15, 16) probably hold the most reliable DVH findings. Also, incorporation of additional sources of data is likely to shed much further light on the complex mechanisms of both tumor response and normal tissue toxicity following RT. Examples are shown in studies focusing on genome-wide assays (17) and immune status (18) as well as medical imaging within associated standardization efforts (19).

RESULTS

A SAP Pre-registration Example

The authors recent experience in depositing an outcome modeling SAP with a public repository (15) will be used as an example of the SAP pipeline and content for outcome modeling.

After circulating the SAP among co-investigators, the SAP was logged with the OSF on July 23rd 2018 (15), and the analysis was, thereafter, initiated [the associated full-length manuscript was recently accepted for publication (16)].

As stated under the study *scope* (15), data were generated from a clinical trial (20) but the trial was not part of the outcome modeling itself. The *primary outcome measure* was overall survival defined from the start date of randomization and right-censoring was applied if alive at the last follow-up. For *Input data* related to disease, patient and treatment characteristics (the latter included 2D DVH parameterizations of the atria, lung, pericardium, and ventricles [please see (16) for exact anatomical definitions and parameterization of the remaining input data] structures: the minimum dose to the hottest 5–95% volume in steps of 5%, mean dose, minimum dose, max dose and the mean of the hottest 5–100% volume in steps of 5%, all metrics were corrected for fractionation effects assuming $\alpha/\beta = 3\,\mathrm{Gy}$), significance was denoted at a 5% Bonferroni-corrected level. *Validation* was considered using a holdout subset on which performance would be assessed after settling the final model. The validation procedures were directly adopted from a previously published study (21). The main *statistical function* was Cox Proportional Hazard regression. Both univariate and multivariate analyses, with a clear advancement criterion ($p < 0.05$ of the log-likelihood statistics), were undertaken, and re-sampling was considered using Bootstrapping with 1,000 iterations. Lastly, arriving at the final model, two alternative approaches were explored—the $\geq$10% most frequently selected multivariate models or the ensemble thereof.

CONCLUSION

We have suggested a SAP pre-registration pipeline to be used for outcome modeling studies, which typically use observational data. An example of an already submitted SAP and cited for outcome modeling is given along with an outcome modeling directed SAP template. The ambition of the authors is that pre-registration of SAPs, using the suggested layout and pipeline, is becoming standard, like it has for clinical trials, also in outcome modeling.

AUTHOR CONTRIBUTIONS

MT and JD contributed to the conception and design of the study. MT drafted the manuscript. All authors contributed to manuscript revision, read, and approved the submitted version.

FUNDING

This research was funded in part through the NIH/NCI Cancer Center Support Grant P30 CA008748.

SUPPLEMENTARY MATERIAL

The Supplementary Material for this article can be found online at: https://www.frontiersin.org/articles/10.3389/fonc.2020.00978/full#supplementary-material

REFERENCES

1. McCray AT. Better access to information about clinical trials. *Ann Intern Med.* (2000) 133:609–14. doi: 10.7326/0003-4819-133-8-200010170-00013
2. De Angelis C, Drazen JM, Frizelle FA, Haug C, Hoey J, Horton R, et al. Clinical trials registration: a statement from the International committee of medical journal editors. *N Engl J Med.* (2004) 351:1250–1. doi: 10.1056/NEJMe048225
3. Ioannidis JPA. The proposal to lower p value thresholds to.005. *JAMA.* (2018) 319:1429–30. doi: 10.1001/jama.2018.1536
4. Kaplan RM, Irvin VL. Likelihood of null effects of large NHLBI clinical trials has increased over time. *PLoS ONE.* (2015) 10:e0132382. doi: 10.1371/journal.pone.0132382
5. Nosek BA, Ebersole CR, DeHaven AC, Mellor DT. The preregistration revolution. *PNAS.* (2017) 115:2600–06. doi: 10.1073/pnas.1708274114
6. Moons KG, Altman DG, Reitsma JB, Ioannidis JPA, Macaskill P, Steyerberget EW, et al. Transparent reporting of a multivariate prediction model for individual prognosis or diagnosis (TRIPOD): explanation and elaboration. *Ann Intern Med.* (2015) 162:1–73. doi: 10.7326/M14-0698
7. Yeung AR, Pugh SL, Klopp AH, Gil KM, Wenzel L, Westin SN, et al. Improvement in patient-reported outcomes with intensity-modulated radiotherapy (RT) compared with standard RT: a report from the NRG Oncology RTOG 1203 study. *J Clin Oncol.* (2020) 38:1685–92. doi: 10.1200/JCO.19.02381
8. Salz T, Schnall RB, McCabe MS, Oeffinger KC, Corcoran S, Vickers AJ, et al. Incorporating multiple perspectives into the development of an electronic survivorship platform for head and neck cancer. *JCO Clin Cancer Inform.* (2018) 2: CCI.17.00105 doi: 10.1200/CCI.17.00105
9. Kildea J, Battista J, Cabral B, Hendren L, Herrera D, Hijal T, et al. Design and development of a person-centered patient portal using participatory stakeholder co-design. *J Med Internet Res.* (2019) 21:e11371 doi: 10.2196/11371
10. Young Afat DA, Gibbons C, Klassen AF, Vickers AJ, Cano SJ, Pusic AL. Introducing BREAST_Q computerized adaptive testing - short and individualized patient-reported outcome assessment following reconstructive breast surgery. *Last Reconstr Surg.* (2019) 143:679–84. doi: 10.1097/PRS.0000000000005314
11. Bentzen SM, Constine LS, Deasy JO, Eisbruch A, Jackson A, Marks LB, et al. Quantitative analyses of normal tissue effects in the clinic (QUANTEC): an

introduction to the scientific issues. *Int J Radiat Oncol Biol Phys.* (2010) 76 (3 Suppl.):3–9. doi: 10.1016/j.ijrobp.2009.09.040
12. Constine LS, Ronckers CM, Hua CH, Olch A, Kremer LCM, Jackson A, et al. Pediatric normal tissue effects in the clinic (PENTEC): an international collaboration to analyze normal tissue radiation dose-dose-volume response relationships for paediatric cancer patients. *Clin Oncol.* (2019) 31:199–207. doi: 10.1016/j.clon.2019.01.002
13. Ohri N, Tomé WA, Méndez Romero A, Miften M, Haken RKT, Dawson LA, et al. Local control after stereotactic body radiation therapy for liver tumors. *Int J Radiat Oncol Biol Phys.* (in press). doi: 10.1016/j.ijrobp.2017.12.288
14. Olsson CE, Jackson A, Deasy JO, Thor M. A systematic post-quantec review of tolerance doses for late toxicity after prostate cancer radiation therapy. *Int J Radiat Oncol Biol Phys.* (2018) 102:1514–32. doi: 10.1016/j.ijrobp.2018.08.015
15. Lee S, Kerns S, Ostrer H, Rosenstein B, Deasy JO, Oh JH. Machine learning on a genome-wide association study to predict late genitourinary toxicity after prostate radiation therapy. *Int J Radiat Oncol Biol Phys.* (2018) 101:128–35. doi: 10.1016/j.ijrobp.2018.01.054
16. Thor M, Montovano M, Hotca A, Luo L, Jackson A, Wu AJ, et al. Are unsatisfactory outcomes after concurrent chemoradiotherapy for locally advanced non-small cell lung cancer due to treatment-related immunosuppression? *Radiother Oncol.* (2020) 143:51–7. doi: 10.1016/j.radonc.2019.07.016
17. Zwanenburg A, Vallières M, Abdalah MA, Aerts HJWL, Andrearczyk V, Apte A, et al. The image biomarker standardization initiative: standardized quantitative radionics for high-throughput image-based phenotyping. *Radiology.* (2020) 295:328–38. doi: 10.1148/radiol.2020191145
18. Thor M, Deasy JO. The role of heart-related dose-volume metrics on overall survival in the RTOG 0617 clinical trial. *OSF.* (2018). doi: 10.17605/OSF.IO/HZSVA
19. Thor M, Deasy JO, Hu C, Gore E, Bar-Ad V, Robinson C, et al. Modeling the impact of cardio-pulmonary irradiation on overall survival in NRG Oncology trial RTOG 0617. *Clin Can Res.* doi: 10.1158/1078-0432.CCR-19-2627
20. Bradley JD, Paulus R, Komaki R, Masters G, Blumenschein G, Schildet S, et al. Standard-dose versus high-dose conformal radiotherapy with concurrent and consolidation carboplatin plus paclitaxel with or without cetuximab for patients with stage IIIA or IIIB non-small cell lung cancer (RTOG 0617): a randomized, two-by-two factorial phase 2 study. *Lancet Oncol.* (2015) 16:187–99. doi: 10.1016/S1470-2045(14)71207-0
21. Royston P, Altman DG. External validation of a Cox prognostic model: principles and methods. *BMC Med Res Methodol.* (2013) 33:1–15. doi: 10.1186/1471-2288-13-33

Conflict of Interest: The authors declare that the research was conducted in the absence of any commercial or financial relationships that could be construed as a potential conflict of interest.

frontiers in Oncology

ORIGINAL RESEARCH
published: 30 June 2020
doi: 10.3389/fonc.2020.00943

Automated Radiotherapy Planning for Patient-Specific Exploration of the Trade-Off Between Tumor Dose Coverage and Predicted Radiation-Induced Toxicity—A Proof of Principle Study for Prostate Cancer

Rik Bijman, Linda Rossi, Abdul Wahab Sharfo, Wilma Heemsbergen, Luca Incrocci, Sebastiaan Breedveld and Ben Heijmen*

Department of Radiation Oncology, Erasmus MC Cancer Institute, Rotterdam, Netherlands

OPEN ACCESS

Edited by:
Tiziana Rancati, Istituto Nazionale dei Tumori (IRCCS), Italy

Reviewed by:
Emanuele Scifoni, Ministry of Education, University and Research, Italy
Angelia Landers, Thomas Jefferson University, United States
Alessandro Scaggion, Istituto Oncologico Veneto (IRCCS), Italy

****Correspondence:***
Rik Bijman
r.bijman@erasmusmc.nl

Specialty section:
This article was submitted to Radiation Oncology, a section of the journal Frontiers in Oncology

Received: *15 January 2020*
Accepted: *13 May 2020*
Published: *30 June 2020*

Citation:
Bijman R, Rossi L, Sharfo AW, Heemsbergen W, Incrocci L, Breedveld S and Heijmen B (2020) Automated Radiotherapy Planning for Patient-Specific Exploration of the Trade-Off Between Tumor Dose Coverage and Predicted Radiation-Induced Toxicity—A Proof of Principle Study for Prostate Cancer. Front. Oncol. 10:943. doi: 10.3389/fonc.2020.00943

Background: Currently, radiation-oncologists generally evaluate a single treatment plan for each patient that is possibly adapted by the planner prior to final approval. There is no systematic exploration of patient-specific trade-offs between planning aims, using a set of treatment plans with a-priori defined (slightly) different balances. To this purpose, we developed an automated workflow and explored its use for prostate cancer.

Materials and Methods: For each of the 50 study patients, seven plans were generated, including the so-called clinical plan, with currently clinically desired ≥99% dose coverage for the low-dose planning target volume (PTV_{Low}). The six other plans were generated with different, reduced levels of PTV_{Low} coverage, aiming at reductions in rectum dose and consequently in predicted grade≥2 late gastro-intestinal (GI) normal tissue complication probabilities (NTCPs), while keeping other dosimetric differences small. The applied NTCP model included diabetes as a non-dosimetric predictor. All plans were generated with a clinically applied, in-house developed algorithm for automated multi-criterial plan generation.

Results: With diabetes, the average NTCP reduced from 24.9 ± 4.5% for ≥99% PTV_{Low} coverage to 17.3 ± 2.6% for 90%, approaching the NTCP (15.4 ± 3.0%) without diabetes and full PTV_{Low} coverage. Apart from intended differences in PTV_{Low} coverage and rectum dose, other differences between the clinical plan and the six alternatives were indeed minor. Obtained NTCP reductions were highly patient-specific (ranging from 14.4 to 0.1%), depending on patient anatomy. Even for patients with equal NTCPs in the clinical plan, large differences were found in NTCP reductions.

Conclusions: A clinically feasible workflow has been proposed for systematic exploration of patient-specific trade-offs between various treatment aims. For each patient, automated planning is used to generate a limited set of treatment plans with

well-defined variations in the balances between the aims. For prostate cancer, trade-offs between PTV_{Low} coverage and predicted GI NTCP were explored. With relatively small coverage reductions, significant NTCP reductions could be obtained, strongly depending on patient anatomy. Coverage reductions could also make up for enhanced NTCPs related to diabetes as co-morbidity, again dependent on the patient. The proposed system can play an important role in further personalization of patient care.

Keywords: personalized radiotherapy, automated multi-criterial treatment planning, normal tissue complication probability (NTCP), prostate cancer, gastro-intestinal

INTRODUCTION

The aim of radiotherapy treatment planning is to define a treatment that provides adequate tumor volume irradiation with the highest expected therapeutic ratio. To this purpose, doses in organs at risk (OARs) are minimized based on known risks for radiation-induced toxicity (1). Technical developments in external beam radiotherapy (EBRT), e.g., replacement of 3D-conformal radiotherapy (3DCRT) by intensity modulated radiation therapy (IMRT) and volumetric modulated arc therapy (VMAT) (2–4), and improvements in image guidance (5–7), have significantly improved treatment outcome and/or reduced radiation induced side effects in a variety of treatment sites. Recently, developments in automation of treatment planning have further enhanced opportunities for generation of high quality treatment plans (8–10).

Ideally, toxicity risks to be used in planning are modeled with normal tissue complication probabilities (NTCPs). There is an active field of research developing these predictive models (1, 11–15). More and more, published NTCP models include non-dosimetric parameters that modulate the radiation-induced toxicity risk (16). For example, Cozzarini et al. (14) used multivariate logistic regression to include both dosimetric parameters, extracted from the clinical plans, and patient characteristics (e.g., smoking status, age, application and duration of hormonal therapy) in the toxicity prediction models. Pre-selection of a relevant predictor subset was performed using univariate logistic regression. A similar approach was performed in previous work by Sharfo et al. (17) who developed a multivariate logistic regression model predicting radiation induced gastro intestinal (GI) toxicity.

Current practice in radiation therapy treatment planning is based on treatment site specific clinical protocols, containing hard constraints, and planning aims. Evidence based medicine recommends the definition of clinical protocols, based on findings in prospective clinical trials and dose escalation studies (18). Generally, the planning protocol is used by a planner to generate for each patient a single treatment plan that may or may not be adjusted after discussion with the treating physician prior to final approval. There is no systematic exploration of patient-specific trade-offs between the various planning aims by generation of a set of treatment plans for each patient with (slightly) different trade-offs.

We hypothesized that generation of a limited set of well-designed treatment plans per patient, instead of a single plan, can help to better identify plans with optimal patient-specific trade-offs. For example, for some patients with specific anatomies, a slight decrease in coverage might result in a relatively large NTCP gain. For patients with non-dosimetric conditions that result in a significantly enhanced predicted NTCP, a lower PTV coverage or a somewhat enhanced NTCP for a different side-effect might be accepted to counter-act the enhancement. We also hypothesized that automated planning can be used to effectively generate the required treatment plans.

In this paper we have investigated these hypotheses for treatment of prostate cancer. An automated planning algorithm was used to generate for each patient a set of plans to explore the trade-off between the dose coverage of the large planning target volume to be irradiated with reduced dose (PTV_{Low}) and the predicted NTCP for grade $\geq$2 GI toxicity for otherwise similar dose distributions. In particular, measures were taken to maintain clinical target volume (CTV) coverage at 100% and to keep the coverage of the (smaller) PTV_{High} at the requested $\geq$99% level. Deterioration of bladder dose was also to be avoided. We also investigated to what extent reduction in PTV_{Low} coverage could compensate for significantly enhanced toxicity risks caused by diabetes.

MATERIALS AND METHODS

Patients and Clinical Protocol

Fifty arbitrarily selected prostate cancer patients, previously treated in our center in the context of the randomized HYPRO trial (19) with a simultaneously integrated boost technique, were included in the study. PTV_{High} consisted of the prostate (CTV_{High}) expanded with a 5–6 mm isotropic margin, but avoiding overlap with the rectum. PTV_{Low} was defined by applying a 8–10 mm isotropic margin around the prostate + seminal vesicles (CTV_{Low}). All patients were treated in the hypofractionation arm with prescribed total doses for PTV_{High} and PTV_{Low} of 64.6 Gy and 57.76 Gy, delivered in 19 fractions. For both PTVs, the planning aim was to have $\geq$99% of the volume covered by 95% of the prescription dose, with full coverage of the CTVs. Contoured organs at risks (OARs) were rectum, bladder, anus, and hips. Reduction of rectum dose was the highest OAR priority.

System for Automated Plan Generation

In this study, all treatment plans were generated with the in-house developed Erasmus-iCycle system for fully-automated

multi-criterial plan generation, which has been extensively described in the literature (8, 20–22). Generated plans are Pareto-optimal and often superior to manually generated plans (10, 23, 24). Here a short description of the system provided. Plans are generated using a so-called wish-list (described in more detail in section Wish-Lists) that defines the protocol for automated plan generation, based on a set of cost functions that are either defined as hard constraints or planning objectives with assigned priorities and goal values. In plan generation, planning constraints are never violated. On the other hand, goal values of objective functions are met as well as possible or possibly superseded, taking into account the constraints and ascribed priorities. Planning objectives are sequentially optimized according to their priorities while always adhering to all imposed constraints. After each objective function optimization, a new constraint is added to the optimization problem to ensure that the previously obtained function value is maintained while minimizing lower priority objectives. Wish-lists are treatment site specific and are constructed in an iterative tuning process, together with the treating physician. Although clinically delivered manual plans serve as an initial reference for wish-list generation, the final goal is always to supersede the manual plan quality.

Exploration of Patient-Specific Trade-Offs Between Target Coverage and Radiation-Induced Toxicity

In a recent study, Sharfo et al. (17) used automated treatment planning to investigate the quality of dose distributions delivered in the HYPRO trial (19). To that purpose, logistic regression analyses was used to develop an NTCP model (Equation 1) for grade ≥ 2 GI toxicity, based on scored toxicities, delivered doses and non-dosimetric predictive parameters.

$$NTCP = \frac{1}{1 + e^{-6.362 + B \cdot 2.083 + D \cdot 0.608 + T \cdot 0.406 + E \cdot 0.084}} \quad (1)$$

B = Baseline GI toxicity (yes/no), D = Diabetes (yes/no), T = High risk treatment group (yes/no) (19), and E = rectum $gEUD_{EQD2Gy}(7.7)$.

Here we used this model to systematically investigate patient-specific trade-offs between predicted GI toxicity and PTV_{Low} coverage. Seven plans were generated for each patient to quantify risk reductions associated with reductions in coverage from the clinical ≥99% to as low as 90% for otherwise highly similar dose distributions.

A sub-group of the patients in the study cohort had diabetes as a co-morbidity. However, to systematically explore diabetes as a co-morbidity, analyses were performed both assuming that all patients had diabetes or none of them had.

Generated Treatment Plans

Erasmus-iCycle was used to automatically generate VMAT plans with 10 MV photon beams. Starting point for the plan generations was a slightly modified version of the wish-list developed by Sharfo et al. (17) for automated generation of plans with ≥99% coverage for both PTVs, in line with the HYPRO protocol. In this study, this wish-list was used to generate for each patient the so-called 'clinical plan' which is a high-quality Pareto-optimal plan with the currently required ≥99% coverage for both PTVs. (Note: these are not the clinically delivered plans, which were manually generated and of lower quality (17). The six alternative plans with various PTV_{Low} coverages in the range 99%−90% were generated with modified versions of this wish-list (as specified in section Wish-Lists) aiming for increased rectum sparing while guaranteeing high similarity with the clinical plan for other dose parameters.

Wish-Lists

The applied wish-lists are described in **Table 1** with some explanations in the following text. In Erasmus-iCycle, target coverage is generally optimized by minimizing a logarithmic tumor control probability (LTCP) cost function (Equation 2) (25),

$$LTCP = \frac{1}{m} \sum_{j=1}^{m} e^{(-\alpha(d_j - PD)} \quad (2)$$

where m is the number of voxels in the target, PD the prescribed dose, d_j the dose in voxel j, and α the cell sensitivity parameter (26). A ≥99% coverage for PTV_{High} was for all generated plans achieved using a goal value of 0.8. Minimum dose constraints for CTV_{High} and CTV_{Low} guaranteed that CTV coverage was always maintained when reducing PTV_{Low} coverage.

For generation of the clinical plan, the priority 2 cost function was disabled and a goal value of X = 0.4 was used in priority 3 to always acquire >99% coverage for PTV_{Low} (the LTCP cost function was applied to the entire PTV_{Low}, including the overlapping area with the rectum). Rectum sparing was obtained by optimizing a gEUD(k) with k equal to 7.7, in line with the NTCP model (Equation 1). Conformality of the dose outside the PTVs was controlled by a set of maximum dose objectives (priorities 5 and 8), assigned to concentric shells around PTV_{Low}.

For generation of the six plans with reduced PTV_{Low} coverage, modifications in the wish-list were made at the level of the bold/italic lines in **Table 1**. The aim was always to have PTV_{Low} underdosages in the most promising regions for GI NTCP reduction, i.e., where rectum was overlapping with the PTV_{Low} and its surroundings, without compromising the CTV doses and while keeping the remainder of the dose distribution as similar as possible to the clinical one. To this purpose, the priority 2 objective was introduced for dose optimization in the PTV_{Low}-RectumPRV structure in which the overlapping rectum expanded by a margin was subtracted from the PTV_{Low}. The applied PRV margins were 25, 20, 15, or 10 mm for patient-specific PTV_{Low} and rectum overlapping areas of <4, <6, <7, or >7%, respectively. An LTCP cost function with a goal value of 0.4 was used to always cover >99% of PTV_{Low}-RectumPRV.

To obtain plans with various PTV_{Low} coverages <99%, the LTCP in priority 3 was now used for partial recoveries of the PTV_{Low} coverage in a controlled way. This was performed by using well-selected (patient-independent) X-values in priority 3 that were different for each of the six plans generated with reduced PTV_{Low} coverage. For generation of the plans with reduced PTV_{Low} coverage, the bladder D_{Mean} objective in priority 9 was removed, while a bladder D_{Mean} constraint was

TABLE 1 | Wish-lists used for automated plan generations in this study.

CONSTRAINTS			
	Structure	**Constraint function**	**Limit**
	PTV_{High}	Maximum dose	<105% of PD_{High}
	PTV_{High}	Mean dose	<100.5% of PD_{High}
	PTV_{Low}-(PTV_{High} exp by 2.5mm)	Maximum dose	<95% of PD_{High}
	PTV Shell 50	Maximum dose	<50% of PD_{High}
	Rectum	Maximum dose	<102% of PD_{High}
	Anus	Maximum dose	<102% of PD_{High}
	Patient	Maximum dose	<105% of PD_{High}
	CTV_{High}	Minimum dose	>95% of PD_{High}
	CTV_{Low}	Minimum dose	>95% of PD_{Low}
OBJECTIVES			
Priority	**Structure**	**Aim & objective function**	**Goal value (Sufficient)**
1	PTV_{High}	↓ LTCP(99.5% of PD_{High},α =0.8)	0.8 (0.8)
2	***PTV_{Low}-RectumPRV***	***↓ LTCP(PD_{Low},α=1.4)***	***0.4 (0.4)***
3	***PTV_{Low}***	***↓ LTCP(PD_{Low},α=1.4)***	***X (X)***
4	Rectum	↓ gEUD(7.7)	0
5	Entrance Dose	↓ Maximum dose	<20% PD_{Low}
5	PTV Shell 5	↓ Maximum dose	<80% PD_{Low}
6	Rectum	↓ Mean dose	5
7	Anus	↓ Mean dose	5
8	PTV Shell 15	↓ Maximum dose	<50% PD_{Low}
8	PTV Shell 25	↓ Maximum dose	<30% PD_{Low}
9	***Bladder***	***↓ Mean dose***	***5***
10	Hip left	↓ Maximum dose	40
10	Hip right	↓ Maximum dose	40

Bold/italic lines are different for the clinical plans and alternative plans (see text). Minimum values to CTVs were set 2 Gy higher to account for voxel sampling in the optimizations. PD_{High}, prescribed dose for PTV_{High} (64.6 Gy); PD_{Low}, prescribed dose for PTV_{Low} (57.76 Gy); gEUD(k), generalized equivalent uniform dose; k, volume parameter; LTCP(PD,α), logarithmic tumor control probability (25); with α, cell sensitivity; OAR, organ at risk; ↓, minimization; ↑, maximization.

added with a limit value equal to the patient-specific bladder D_{Mean} obtained in the clinical plan. This was done in order to avoid dose being pushed away from the rectum toward the bladder.

Creation of the appropriate wish-lists was performed in a tuning process involving CT-scans of a set of 10 patients.

RESULTS

Figures 1, **2** show NTCP reductions for the 50 study patients as a function of the loss in PTV_{Low} dose coverage. **Figure 1** is valid in case of diabetes, while for **Figure 2** we assumed that there was no diabetes. As explained in the M&M section, reductions in PTV_{Low} coverage in the six alternative plans for each patient were obtained with (convex) LTCP cost functions. Convexity avoids getting trapped in local minima, but with the LTCP cost function, obtained PTV_{Low} coverage values vary somewhat between patients. For generation of **Figures 1**, **2**, NTCPs for the defined coverage reductions were for each patient obtained by piecewise linear interpolations between the generated plans. The different colors show the impact of incremental underdosage steps of 1% in PTV_{Low} on obtained NTCP. For some patients (e.g., patient 13), reducing the coverage to as low as 90% was not possible, possibly due to not sufficiently large PRV margins or conflicting constraints on the PTV_{High} and the CTVs dose requirements. For patient 50, accepting lower PTV_{Low} coverage did not result in any NTCP reduction because of lack in overlap between PTV_{Low} and rectum (see also **Figure 6**).

Following Equation 1, NTCP values were indeed higher in case patients had diabetes (compare upper panels of **Figures 1**, **2**). On the other hand, NTCP reductions were also larger in case of diabetes. For a PTV_{Low} coverage of 95%, average NTCP reductions of 4.3% (0.3–8.0%) and 2.9% (0.2–5.5%) were obtained with or without diabetes, respectively. For 90% coverage, the obtained NTCP reductions increased to 8.3% (0.3–14.4%) and 5.6% (2.0–10.1%), respectively. Both with and without diabetes, there was an overall trend toward enhanced NTCP reductions for patients with the highest clinical NTCPs (lower panels **Figures 1**, **2**). On the other hand, large inter-patient variations were observed. For example, patients 1 and 3 had similar clinical NTCPs, but a large difference in achievable NTCP reductions. Moreover, similar NTCP reductions were observed for different costs in PTV_{Low} coverage. For example, patients 12 and 14 have similar NTCP reductions of ∼10% accepting 94% or 91% PTV_{Low} coverage instead of 99% (**Figure 1**). Observed maximum NTCP reductions ranged from > 14% (patient 1) to <1% for patient 50, depending on differences in anatomy (see **Figure 6**).

Figures 3, **4** show the differences between clinical and alternative plans on a per patient base and in population DVHs, respectively. They demonstrate that the enforced PTV_{Low} coverage reductions mainly had an impact on rectum sparing while having a clinically insignificant dosimetric impact on PTV_{High}, CTV_{High}, CTV_{Low}, bladder, anus and hips, as intended (section Generated Treatment Plans). **Figure 5** shows for an example patient highly similar dose distributions, except for the region of overlap between rectum and PTV_{Low}.

In **Figure 6** we investigated the extent of feasible NTCP reduction as a function of overlap between rectum and PTV_{Low}. Although, there is an overall trend toward more reduction with larger overlap, there are inter-patient variations with R^2 equal to 0.6 and 0.7, for 95 and 90% PTV_{Low} coverage, respectively.

For the 50 patients in this study, presence of diabetes resulted in an average increase in clinical NTCP from 15.4 ± 3.0% (1SD) to 24.9 ± 4.5% (1SD) (compare also the upper panels of **Figures 1**, **2**). **Figure 7** explores opportunities for mitigation of enhanced toxicity risk due to diabetes by reducing required PTV_{Low} coverage. Clearly, depending on the allowed coverage reduction and the patient anatomy, NTCP enhancements due to diabetes could be largely compensated. For some patients, (e.g.,

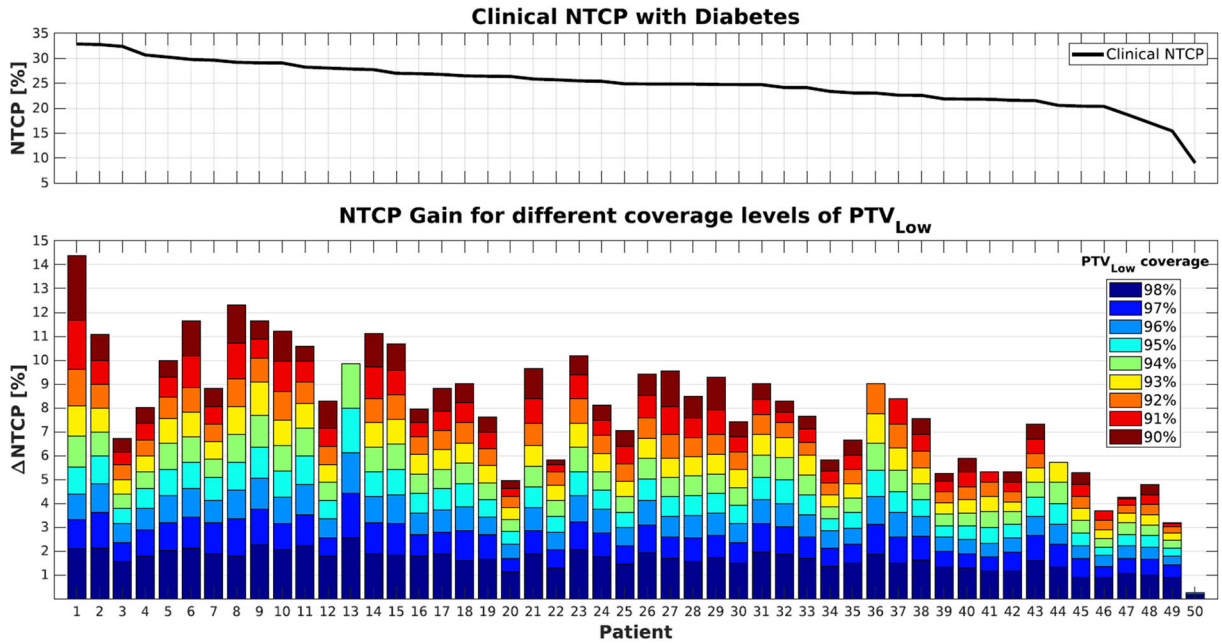

FIGURE 1 | (Top) NTCP values for the clinical plans (PTV_{Low} coverage ≥99%) in case of diabetes as a co-morbidity. **(Bottom)** Cumulative NTCP reductions for decreasing levels of PTV_{Low} coverage. Patients were sorted according to their clinical NTCP as visualized in the top panel.

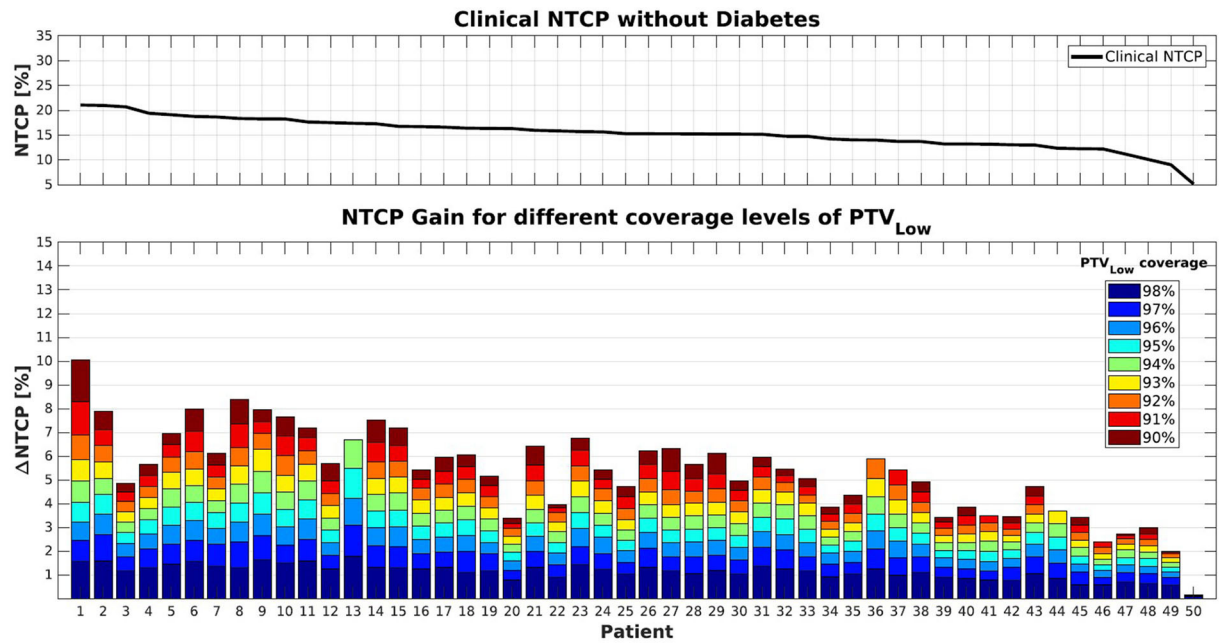

FIGURE 2 | (Top) NTCP values for the clinical plans (PTV_{Low} coverage ≥99%). **(Bottom)** Cumulative NTCP reductions for decreasing levels of PTV_{Low} coverage. Patients were supposed not to have diabetes. Patient sorting along the x-axis was the same as for **Figure 1**.

1, 6, and 8) the impact of diabetes could be completely canceled when using a coverage of 90–91%. Other patients (e.g., 3 and 20) demonstrate quite large residual differences in NTCP with and without diabetes, for reduced PTV_{Low} coverages.

DISCUSSION

In this study, we have used prostate cancer radiotherapy as a model for development of a clinically feasible workflow for

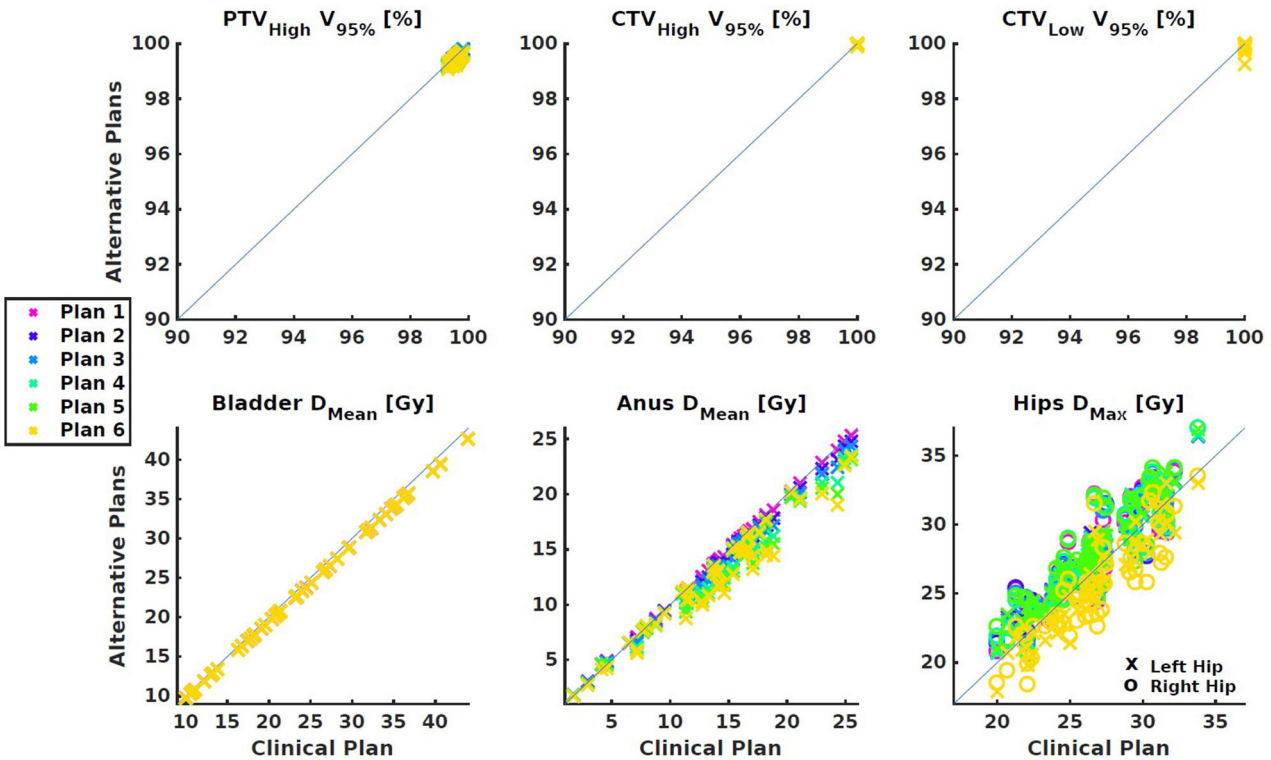

FIGURE 3 | Dose parameter differences between the clinical plan and the alternative plans with reduced PTV_{Low} coverages. **(Top)** Targets. **(Bottom)** OARs. All differences were small and within clinically acceptable limits.

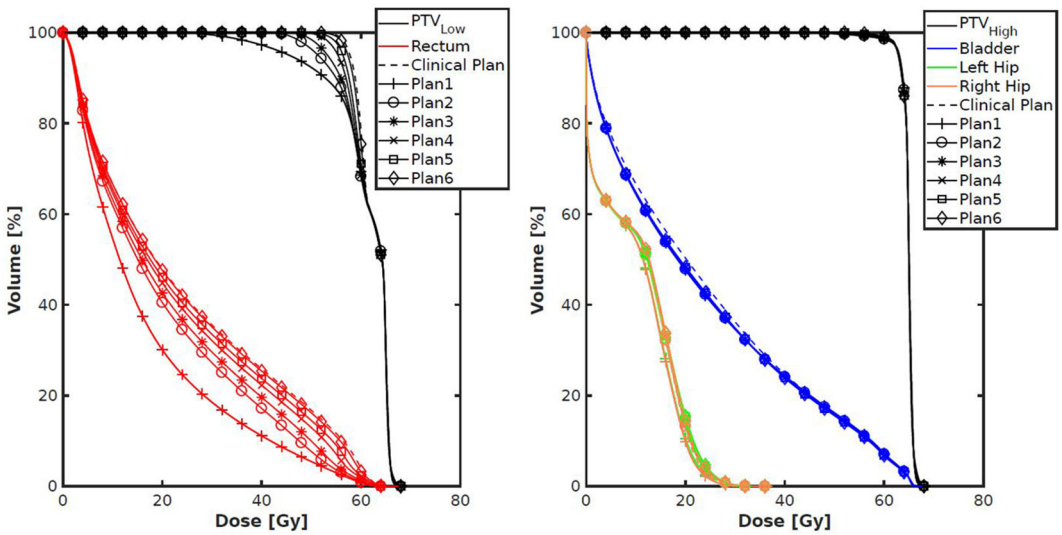

FIGURE 4 | Population average DVHs for each of the seven plans generated per patient. The left panel shows a clear (intended) trade-off between rectum dose and coverage of PTV_{Low}. The right panel shows very small differences for other structures.

application of automated planning for assessment of patient-specific trade-offs between treatment goals. All plans were generated fully automatically, i.e., without any manual fine-tuning. With carefully designed, patient-independent variations in the autoplanning configuration (i.e., wish-list), the PTV_{Low} coverage could be varied in a controlled way in the range 99–90% to reduce the predicted NTCP, without significant further changes in the dose distributions. In particular, CTV coverage

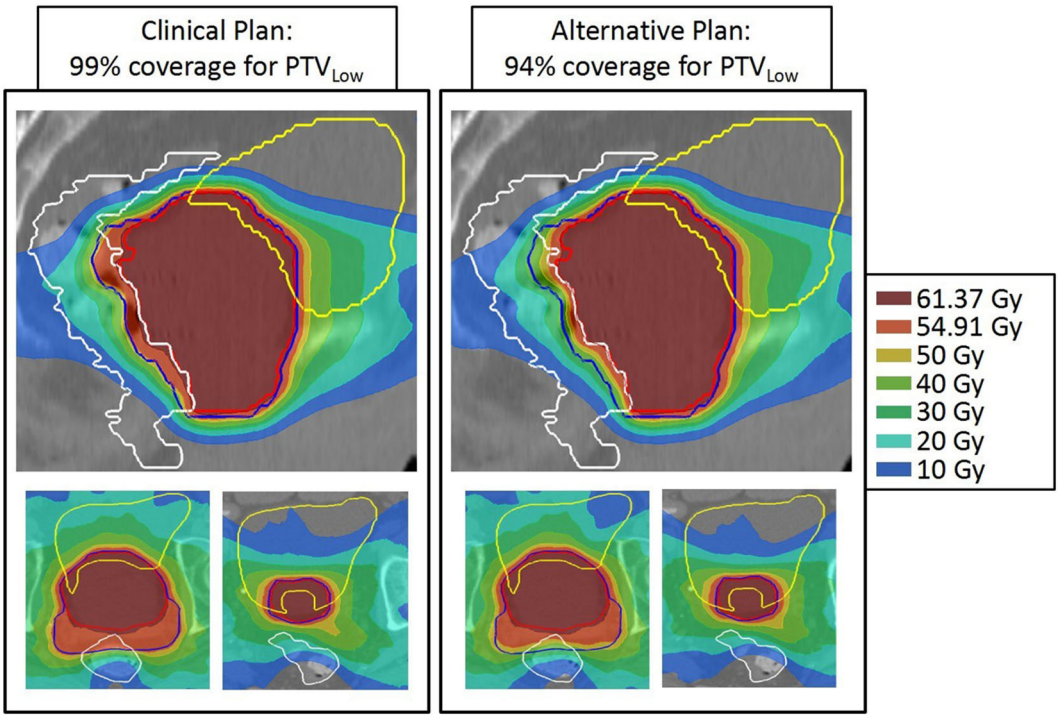

FIGURE 5 | Dose distributions of patient 13 for 99% (left) and 94% PTV_{Low} dose coverage. For both patients, **top**: sagittal view through isoc., **bottom**: axial views at two levels. Structures: red = PTV_{High}, blue = PTV_{Low}, white = rectum, and yellow = bladder. Apart from the dose in the posterior part of PTV_{Low}, dose distributions are highly similar.

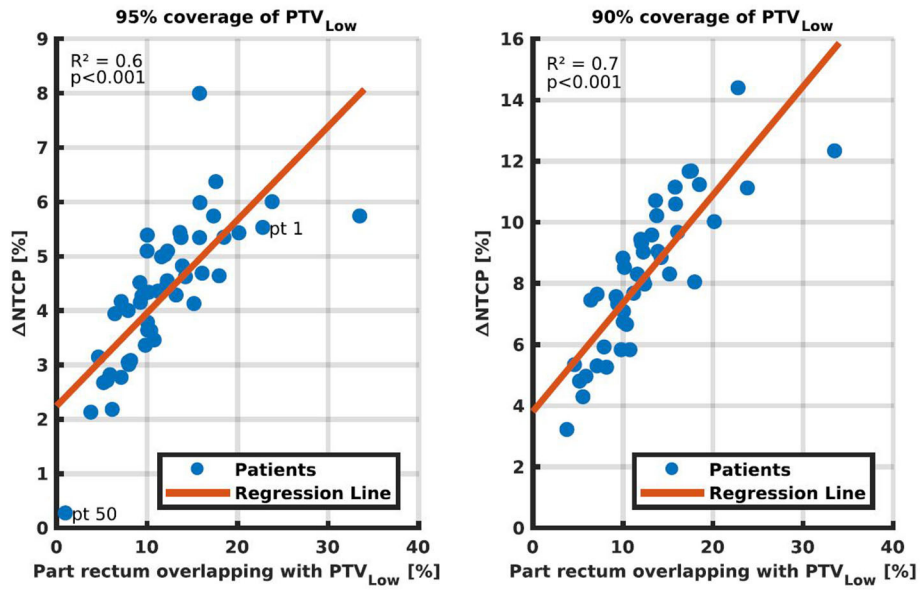

FIGURE 6 | NTCP reductions by going from ≥99% coverage for PTV_{Low} to 95% **(Left)** and 95% **(Right)**, as a function of the percentage of rectum overlapping with PTV_{Low}. Each dot represents one of the fifty study patients. In the left panel, patients 1 and 50 are marked for discussions in the text.

remained 100%, PTV_{High} coverage was kept at ≥99%, and bladder dose did also not significantly change. For each patient, the obtained bladder D_{Mean} in the clinical plan (PTV_{Low} coverage ≥99%) was used as constraint in the generation of the six other plans with reduced PTV_{Low} coverage. It was demonstrated that large, but highly patient-specific NTCP reductions could

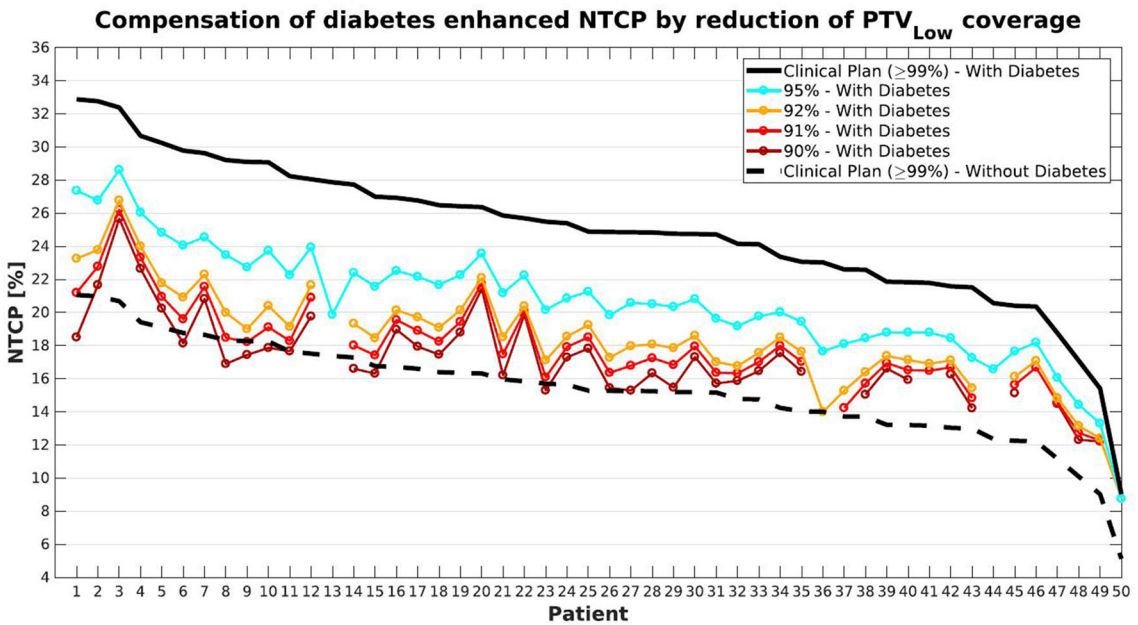

FIGURE 7 | Compensation for diabetes induced-enhancement of predicted NTCPs (compare black solid and dashed lines) by reducing PTV_{Low} coverage levels. With gradual decreases in coverage, NTCPs with diabetes gradually approach the dashed curve for NTCPs without diabetes. Patient sorting along the x-axis was the same as for **Figure 1**.

be obtained. For a PTV_{Low} coverage of 90%, observed NTCP reductions ranged from 14.4 to 0.1%, compared to 99% coverage, depending on the patient anatomy. Reductions in required PTV_{Low} coverage could to a large extent make up for diabetes as a co-morbidity, again depending on patient anatomy. To the best of our knowledge, this is the first study that proposes the use of automated planning for patient-specific exploration of opportunities for dosimetric compensation of non-dosimetric toxicity risk factors.

Automated treatment plan generation required about 1–2 h per treatment plan. No manual interaction was required at any step of the procedure. Therefore, multiple plans could be run, sequentially or in parallel, over the night. Generation of a wish-list generally takes several weeks. This is a one-time effort and should be seen as an upfront time-investment, which saves a lot of manual planning time at a later stage. Specifically for this project, the wish-list was already developed in a previous study (17).

Observed NTCP reductions correlated to some extent with the volume of rectum overlapping with PTV_{Low} (**Figure 6**, $R^2 = 0.6$–07). Once a correlation model is built based on the plans generated with the proposed method, the regression lines might be of use as a tool for selection of the PTV_{Low} coverage region of interest, or for selection of patients. That is, the proposed method could be applied only to patients and/or to PTV_{Low} levels that show to be more promising in NTCP reduction. However, even in the relatively easy treatment site of prostate cancer, a not too strong correlation was found. Different parameters may be investigated, but for more challenging treatment sites finding predictors for NTCP reduction may be even more complex. The presented method, on the other hand, only requires computation time once the procedure is defined.

In the wish-lists applied in this study, concentric shells at distances of 5, 15, 25, and 50 mm from the PTV edge were used to control plan conformality (**Table 1**). The limit and goal values were the same for all patients and all plans. Initially, we did however try to get further NTCP reductions by loosening conformality goal values. This was not successful; conformality worsened but NTCPs remained practically unchanged.

Equation 1 was used for NTCP prediction in this study, as our patients were treated in the context of the HYPRO trial, and Equation 1 was derived for these patients. Important to note is that various alternative predictive models exist (11, 15), which could possibly have resulted in different conclusions, or could have resulted in different approaches for lowering NTCPs. Direct use of Equation 1 in this study was limited to plan evaluations, i.e., Equation 1 was not used in the wish-list for plan generations (see **Table 1**). For planning, we generally prefer to use convex cost functions to avoid getting trapped in local minima, and the NTCP expression in Equation 1 is not convex. Alternatively, the (convex) rectum gEUD (7.7), as used in Equation 1, was directly applied as an objective function (priority 4 in **Table 1**).

The proposed method to explore trade-offs in planning goals has some similarities with the well-known Pareto navigation, using a graphical user interface with sliders to find a clinically favorable plan (8, 26–31). Also in that method, multiple plans are automatically generated for manual plan selection. There are, however, important differences. The most important difference is that for each patient, we first generate a high-quality, Pareto optimal plan ("wish-point") with clinically most desired PTV_{Low}

coverage (≥99%). For each patient, this plan is then used as anchor point for patient-specific generation of the plans with slightly reduced PTV_{Low} coverage, using the bladder dose obtained in the wish-point plan as constraint. In the proposed workflow, only plans are generated that are useful for the desired analyses. In conventional generation of plans for Pareto navigation, there is no knowledge of the "wish-point," and generation of plans is less focused. Due to our highly focused plan generation, only few plans are needed for the analyses. In this study we used seven plans per patient. This number was not optimized in terms of finding the minimum number of required plans. The aim was to include for all patients, the full range of PTV_{Low} coverages from 99 to 90%. If a clinical protocol has more precise directions for reductions in PTV_{Low} coverage, for sure even fewer plans need to be generated.

PTV margins are generally used to minimize risk in CTV miss. In this paper, we kept all margins unchanged, but allowed doses in the overlap area of PTV_{Low} with rectum to get lower than in the clinical plan. Coverages in PTV_{High} and CTV were always maintained. With this approach, the risk of CTV miss was minimized, but still (at least potentially) enhanced compared to regular clinical planning. Therefore, clinical introduction of this type of workflow is not trivial. Extensive computer simulations could be performed to assess the true risks, taking into account the clinically applied image-guided approach. Clinical introduction could well be performed in a formal study. Anyway, it seems that patient selection could be important, with patients with a high clinical NTCP (e.g., related to an unfavorable anatomy or diabetes) and a large potential for NTCP reductions, as best candidates. It is important to realize that we used in this study our clinically required PTV coverage level of 99%. In many studies, coverages of 95% were reported (32).

We have investigated trade-offs between PTV coverage and GI NTCP for prostate cancer but believe that the proposed methodology could also be applied for other tumor sites. The system could also be used to explore patient-specific trade-offs between various toxicities for fixed PTV coverage. Focusing on balances between toxicities instead of toxicity vs. PTV coverage could ease clinical implementation. The developed workflow could potentially also be used in shared decision making studies.

CONCLUSION

A novel, clinically feasible workflow has been proposed for the use of automated planning to systematically explore patient-specific trade-offs between various treatment aims. For prostate cancer, the patient-specific balance between PTV coverage and predicted GI toxicity risk was explored. Opportunities for compensating significantly enhanced predicted toxicity risk related to diabetes by reducing the PTV coverage were investigated as well. Large variations in potential benefit were observed in the fifty study patients. The proposed system could play an important role in further high-precision personalization of patient care.

DATA AVAILABILITY STATEMENT

The datasets generated for this study are available on request to the corresponding author.

ETHICS STATEMENT

Ethical review and approval was not required for the study on human participants in accordance with the local legislation and institutional requirements. Written informed consent for participation was not required for this study in accordance with the national legislation and the institutional requirements.

AUTHOR CONTRIBUTIONS

RB: conducting main research and writing manuscript. LR and BH: supervision of research and writing manuscript. AS: brainstorming about research and writing manuscript. SB: developing code and writing manuscript. WH: data collection and writing manuscript. LI: PI of Data collection and writing manuscript. All authors contributed to the article and approved the submitted version.

FUNDING

This work was in part funded by a research grant of Elekta AB (Stockholm, Sweden). Erasmus MC Cancer Institute also has a research collaboration with Accuray Inc., Sunnyvale, USA.

REFERENCES

1. Rancati T, Fiorino C. *Modelling Radiotherapy Side Effects*. Boca Raton, FL: CRC Press. (2019).
2. Wortel RC, Incrocci L, Pos FJ, Lebesque JV, Witte MG, van der Heide UA, et al. Acute toxicity after image-guided intensity modulated radiation therapy compared to 3D conformal radiation therapy in prostate cancer patients. *Int J Radiat Oncol Biol Phys.* (2015) 91:737–44. doi: 10.1016/j.ijrobp.2014.12.017
3. Wortel RC, Incrocci L, Pos FJ, van der Heide UA, Lebesque JV, Aluwini S, et al. Late side effects after image guided intensity modulated radiation therapy compared to 3D-conformal radiation therapy for prostate cancer: results from 2 prospective cohorts. *Int J Radiat Oncol Biol Phys.* (2016) 95:680–9. doi: 10.1016/j.ijrobp.2016.01.031
4. Rana S. Intensity modulated radiation therapy versus volumetric intensity modulated arc therapy. *J Med Radiat Sci.* (2013) 60:81–3. doi: 10.1002/jmrs.19
5. Dang A, Kupelian PA, Cao M, Agazaryan N, Kishan AU. Image-guided radiotherapy for prostate cancer. *Transl Androl Urol.* (2018) 7:308–20. doi: 10.21037/tau.2017.12.37
6. Nguyen NP, Kratz S, Lemanski C, Vock J, Vinh-Hung V, Olena G, et al. Image-guided radiotherapy for locally advanced head and neck cancer. *Front Oncol.* (2013) 3:172. doi: 10.3389/fonc.2013.00172
7. Korreman SS. Image-guided radiotherapy and motion management in lung cancer. *Br J Radiol.* (2015) 88:20150100. doi: 10.1259/bjr.20150100
8. Hussein M, Heijmen BJM, Verellen D, Nisbet A. Automation in intensity modulated radiotherapy treatment planning-a review of recent innovations. *Br J Radiol.* (2018) 91:20180270. doi: 10.1259/bjr.20180270

9. Cozzi L, Heijmen, B.J.M., Muren, L.P. Advanced treatment planning strategies to enhance quality and efficiency of radiotherapy (Editorial). *Phys. Imaging Radiat Oncol.* (2019) 11:69–70. doi: 10.1016/j.phro.2019.09.002
10. Heijmen B, Voet P, Fransen D, Penninkhof J, Milder M, Akhiat H, et al. Fully automated, multi-criterial planning for Volumetric Modulated Arc Therapy - An international multi-center validation for prostate cancer. *Radiother Oncol.* (2018) 128:343–8. doi: 10.1016/j.radonc.2018.06.023
11. Rancati T, Fiorino C, Fellin G, Vavassori V, Cagna E, Casanova Borca V, et al. Inclusion of clinical risk factors into NTCP modelling of late rectal toxicity after high dose radiotherapy for prostate cancer. *Radiother Oncol.* (2011) 100:124–30. doi: 10.1016/j.radonc.2011.06.032
12. Fiorino C, Rancati T, Fellin G, Vavassori V, Cagna E, Casanova Borca V, et al. Late fecal incontinence after high-dose radiotherapy for prostate cancer: better prediction using longitudinal definitions. *Int J Radiat Oncol Biol Phys.* (2012) 83:38–45. doi: 10.1016/j.ijrobp.2011.06.1953
13. Heemsbergen WD, Peeters ST, Koper PC, Hoogeman MS, Lebesque JV. Acute and late gastrointestinal toxicity after radiotherapy in prostate cancer patients: consequential late damage. *Int J Radiat Oncol Biol Phys.* (2006) 66:3–10. doi: 10.1016/j.ijrobp.2006.03.055
14. Cozzarini C, Rancati T, Carillo V, Civardi F, Garibaldi E, Franco P, et al. Multivariable models predicting specific patient-reported acute urinary symptoms after radiotherapy for prostate cancer: Results of a cohort study. *Radiother Oncol.* (2015) 116:185–91. doi: 10.1016/j.radonc.2015.07.048
15. Fiorino C, Valdagni R, Rancati T, Sanguineti G. Dose-volume effects for normal tissues in external radiotherapy: pelvis. *Radiother Oncol.* (2009) 93:153–67. doi: 10.1016/j.radonc.2009.08.004
16. Defraene G, Van den Bergh L, Al-Mamgani A, Haustermans K, Heemsbergen W, Van den Heuvel F, et al. The benefits of including clinical factors in rectal normal tissue complication probability modeling after radiotherapy for prostate cancer. *Int J Radiat Oncol Biol Phys.* (2012) 82:1233–42. doi: 10.1016/j.ijrobp.2011.03.056
17. Sharfo AWM, Dirkx MLP, Bijman RG, Schillemans W, Breedveld S, Aluwini S, et al. Late toxicity in the randomized multicenter HYPRO trial for prostate cancer analyzed with automated treatment planning. *Radiother Oncol.* (2018) 128:349–56. doi: 10.1016/j.radonc.2018.05.028
18. Bentzen SM. Towards evidence based radiation oncology: improving the design, analysis, and reporting of clinical outcome studies in radiotherapy. *Radiother Oncol.* (1998) 46:5–18. doi: 10.1016/S0167–8140(97)00226–0
19. Incrocci L, Wortel RC, Alemayehu WG, Aluwini S, Schimmel E, Krol S, et al. Hypofractionated versus conventionally fractionated radiotherapy for patients with localised prostate cancer (HYPRO): final efficacy results from a randomised, multicentre, open-label, phase 3 trial. *Lancet Oncol.* (2016) 17:1061–9. doi: 10.1016/S1470–2045(16)30070–5
20. Breedveld S, Storchi PR, Heijmen BJ. The equivalence of multi-criteria methods for radiotherapy plan optimization. *Phys Med Biol.* (2009) 54:7199–209. doi: 10.1088/0031–9155/54/23/011
21. Breedveld S, Storchi PR, Voet PW, Heijmen BJ. iCycle: Integrated, multicriterial beam angle, and profile optimization for generation of coplanar and noncoplanar IMRT plans. *Med Phys.* (2012) 39:951–63. doi: 10.1118/1.3676689
22. Heijmen B, Schwarz M. Radiobiological models in (automated) treatment planning. In: Rancati T, Fiorino C, editors. *Modelling Radiotherapy Side Effects*. Boca Raton, FL: CRC Press (2019). p. 441–54. doi: 10.1201/b21956–18
23. Voet PW, Dirkx ML, Breedveld S, Fransen D, Levendag PC, Heijmen BJ. Toward fully automated multicriterial plan generation: a prospective clinical study. *Int J Radiat Oncol Biol Phys.* (2013) 85:866–72. doi: 10.1016/j.ijrobp.2012.04.015
24. Sharfo AW, Voet PW, Breedveld S, Mens JW, Hoogeman MS, Heijmen BJ. Comparison of VMAT and IMRT strategies for cervical cancer patients using automated planning. *Radiother Oncol.* (2015) 114:395–401. doi: 10.1016/j.radonc.2015.02.006
25. Alber M, Reemtsen R. Intensity modulated radiotherapy treatment planning by use of a barrier-penalty multiplier method. *Optim Methods Softw.* (2007) 22:391–411. doi: 10.1080/10556780600604940
26. Craft DL, Hong TS, Shih HA, Bortfeld TR. Improved planning time and plan quality through multicriteria optimization for intensity-modulated radiotherapy. *Int J Radiat Oncol Biol Phys.* (2012) 82:e83–90. doi: 10.1016/j.ijrobp.2010.12.007
27. Craft D, Halabi T, Shih HA, Bortfeld T. An approach for practical multiobjective IMRT treatment planning. *Int J Radiat Oncol Biol Phys.* (2007) 69:1600–7. doi: 10.1016/j.ijrobp.2007.08.019
28. Wheeler PA, Chu M, Holmes R, Woodley OW, Jones CS, Maggs R, et al. Evaluating the application of Pareto navigation guided automated radiotherapy treatment planning to prostate cancer. *Radiother Oncol.* (2019). doi: 10.1016/j.radonc.2019.08.001
29. Thieke C, Kufer KH, Monz M, Scherrer A, Alonso F, Oelfke U, et al. A new concept for interactive radiotherapy planning with multicriteria optimization: first clinical evaluation. *Radiother Oncol.* (2007) 85:292–8. doi: 10.1016/j.radonc.2007.06.020
30. Kamran SC, Mueller BS, Paetzold P, Dunlap J, Niemierko A, Bortfeld T, et al. Multi-criteria optimization achieves superior normal tissue sparing in a planning study of intensity-modulated radiation therapy for RTOG 1308-eligible non-small cell lung cancer patients. *Radiother Oncol.* (2016) 118:515–20. doi: 10.1016/j.radonc.2015.12.028
31. Miguel-Chumacero E, Currie G, Johnston A, Currie S. Effectiveness of Multi-Criteria Optimization-based Trade-Off exploration in combination with RapidPlan for head & neck radiotherapy planning. *Radiat Oncol.* (2018) 13:229. doi: 10.1186/s13014–018-1175-y
32. Viani GA, Viana BS, Martin JE, Rossi BT, Zuliani G, Stefano EJ. Intensity-modulated radiotherapy reduces toxicity with similar biochemical control compared with 3-dimensional conformal radiotherapy for prostate cancer: a randomized clinical trial. *Cancer.* (2016) 122:2004–11. doi: 10.1002/cncr.29983

Conflict of Interest: The authors declare that the research was conducted in the absence of any commercial or financial relationships that could be construed as a potential conflict of interest.

frontiers in Oncology

ORIGINAL RESEARCH
published: 07 July 2020
doi: 10.3389/fonc.2020.00989

Secondary Malignancy Risk Following Proton vs. X-ray Treatment of Mediastinal Malignant Lymphoma: A Comparative Modeling Study of Thoracic Organ-Specific Cancer Risk

Laila König[1,2,3,4,5]*, *Peter Haering*[6,7], *Clemens Lang*[6,7], *Mona Splinter*[6,7], *Bastian von Nettelbladt*[1,2,3,4,5], *Fabian Weykamp*[1,2,3,4,5], *Philipp Hoegen*[1,2,3,4,5], *Jonathan W. Lischalk*[8], *Klaus Herfarth*[1,2,3,4,5], *Jürgen Debus*[1,2,3,4,5,6,7] *and Juliane Hörner-Rieber*[1,2,3,4,5,6]

[1] Department of Radiation Oncology, Heidelberg University Hospital, Heidelberg, Germany, [2] Heidelberg Institute of Radiation Oncology (HIRO), Heidelberg, Germany, [3] National Center for Tumor Diseases (NCT), Heidelberg, Germany, [4] Department of Radiation Oncology, Heidelberg Ion-Beam Therapy Center (HIT), Heidelberg University Hospital, Heidelberg, Germany, [5] Clinical Cooperation Unit Radiation Oncology, German Cancer Research Center (DKFZ), Heidelberg, Germany, [6] Department for Medical Physics in Radiation Oncology, German Cancer Research Center (DKFZ), Heidelberg, Germany, [7] German Cancer Consortium (DKTK), Heidelberg, Germany, [8] Department of Radiation Medicine, Georgetown University School of Medicine, Washington, DC, United States

OPEN ACCESS

Edited by:
Tiziana Rancati, Istituto Nazionale dei Tumori (IRCCS), Italy

Reviewed by:
William F. Hartsell, Northwestern University, United States
Yaacov Lawrence, Sheba Medical Center, Israel

***Correspondence:**
Laila König
laila.koenig@med.uni-heidelberg.de

Specialty section:
This article was submitted to Radiation Oncology, a section of the journal Frontiers in Oncology

Received: *11 February 2020*
Accepted: *19 May 2020*
Published: *07 July 2020*

Citation:
König L, Haering P, Lang C, Splinter M, von Nettelbladt B, Weykamp F, Hoegen P, Lischalk JW, Herfarth K, Debus J and Hörner-Rieber J (2020) Secondary Malignancy Risk Following Proton vs. X-ray Treatment of Mediastinal Malignant Lymphoma: A Comparative Modeling Study of Thoracic Organ-Specific Cancer Risk. Front. Oncol. 10:989. doi: 10.3389/fonc.2020.00989

Purpose: Proton radiotherapy (PRT) is potentially associated with a lower risk for secondary malignancies due to a decreased integral dose to the surrounding organs at risk (OARs). Prospective trials confirming this are lacking due to the need for long-term follow-up and the ethical complexities of randomizing patients between modalities. The objective of the current study is to calculate the risk for secondary malignancies following PRT and photon-based intensity-modulated radiotherapy (IMRT).

Materials and Methods: Twenty-three patients (16 female and seven male), previously treated with active scanning PRT for malignant mediastinal lymphoma at Heidelberg Ion Beam Therapy Center, were retrospectively re-planned using helical photon IMRT. The risk for radiation-induced secondary malignancies was estimated and evaluated using two distinct prediction models (1–4).

Results: According to the Dasu model, the median absolute total risk for tumor induction following IMRT was 4.4% (range, 3.3–5.8%), 9.9% (range, 2.0–27.6%), and 1.0% (range, 0.5–1.5%) for lung, breast, and esophageal cancer, respectively. For PRT, it was significantly lower for the aforementioned organs at 1.6% (range, 0.7–2.1%), 4.5% (range, 0.0–15.5), and 0.8% (range, 0.0–1.6%), respectively ($p \leq 0.01$). The mortality risk from secondary malignancies was also significantly reduced for PRT relative to IMRT at 1.1 vs. 3.1% ($p \leq 0.001$), 0.9 vs. 1.9% ($p \leq 0.001$), and 0.7 vs. 1.0% ($p \leq 0.001$) for lung, breast, and esophageal tumors, respectively. Using the Schneider model, a significant risk reduction of 54.4% (range, 32.2–84.0%), 56.4% (range, 16.0–99.4%), and 24.4% (range, 0.0–99.0%) was seen for secondary lung, breast, and esophageal malignancies, favoring PRT vs. X-ray-based IMRT ($p \leq 0.01$).

Conclusion: Based on the two prediction models, PRT for malignant mediastinal lymphoma is expected to reduce the risk for radiation-induced secondary malignancies compared with the X-ray-based IMRT. The young age and the long natural history of patients diagnosed with mediastinal lymphoma predisposes them to a high risk of secondary malignancies following curative radiotherapy treatment and, as a consequence, potentially reducing this risk by utilizing advanced radiation therapy techniques such as PRT should be considered.

Keywords: mediastinal lymphoma, proton radiotherapy, intensity modulated radiotherapy, photon radiotherapy, secondary malignancies, risk

INTRODUCTION

Over the last few decades, significant improvements in combined modality therapy consisting of multi-agent chemotherapy and consolidation radiotherapy (RT) have resulted in high cure rates in patients diagnosed with lymphoma. Furthermore, due to their young age and excellent survival rates, the mediastinal lymphoma patients are at a significant risk for late toxicity from their oncologic therapy. Notable improvements in oncologic outcomes have prompted a new focus on the reduction of treatment-related morbidity *via* de-escalation in both the chemotherapy and the radiation realms. A reduction in RT treatment doses and field sizes, as well as the utilization of modern highly conformal RT techniques [e.g., intensity-modulated RT (IMRT), in contrast to conventional 3D-conformal radiotherapy], has led to a further reduction in radiation doses to organs at risk (OARs) (5–8). Thoracic radiotherapy to the mediastinum poses notable challenges due to the close proximity of target volumes to OARs including the heart, breast, and esophagus, making dose reductions to these organs difficult despite using the most advanced X-ray-based radiotherapy techniques such as IMRT. Multiple comparative dosimetric studies have demonstrated radiation dose reductions to healthy surrounding tissues due to the superior physics of proton therapy *vis-à-vis* the Bragg Peak (9–12). Radiobiologically, these dose reductions can not only result in reduced deterministic side effects leading to lower acute toxicity rates but also in reduced stochastic side effects and, consequently, reduced risk for secondary malignancies (SM). Due to the stochastic nature of the risks, even small doses delivered to OARs may induce a long-term SM induction after RT. However, prospective trials confirming this are lacking due to the need for an extremely long-term follow-up and the ethical complexities of randomizing patients between these two modalities. Although the risk for development of SM is small, it is statistically significant, particularly for long-term survivors of treatment, e.g., lymphoma patients (7, 8). One study conducted with extended follow-up, published by Sethi et al., reported statistically significant reductions in secondary malignancy risk in pediatric patients treated for retinoblastoma (0 vs. 14%, $p = 0.015$) (13). The frequency of radiation-induced cancers after total body exposures with very low doses of ionizing radiation has been determined in different epidemiological studies (14, 15). However, these epidemiologic data involve doses (<100 mSv) which are dramatically lower than those used for RT. Hence, different dose–response models, valid for all dose levels, have been proposed using mechanistic models for predicting cancer induction after fractionated radiotherapy, which are based upon the linear–quadratic model:

(1) The Dasu model (1) explores several methods for estimating the risk of cancer following RT in order to investigate the influences of fractionation and non-uniformity of dose to the irradiated volume. This model takes into consideration the competition between cell killing and the induction of carcinogenic mutations for a more realistic risk estimate.
(2) The Schneider model introduced the concept of organ equivalent dose (OED) to estimate organ-specific radiation-induced cancer incidence rates (4). The OED concept assumes that any two dose distributions in an organ are equivalent if they cause the same radiation-induced cancer incidence. The two operational parameters of the OED concept are the organ-specific cancer incidence rate at low doses, which was taken from the data of atomic bomb survivors, and cell sterilization at higher doses. For the OED concept, the effect of cell sterilization in various organs was estimated by analyzing the historical secondary cancer incidence data of patients treated with RT due to Hodgkin's disease. Using these two model parameters, the OED concept can be applied to any three-dimensional dose distribution for estimating radiation-induced secondary malignancy incidence.

The aim of the present study was to use these two radiobiological models to investigate the potential improvement of PT vs. X-ray irradiation relative to the risk of radiation-related secondary malignancies using actual proton dosimetric data from patients who were previously treated with mediastinal RT for malignant lymphoma.

MATERIALS AND METHODS

Patient Selection and Treatment Planning

Twenty-three (16 female and seven male) patients with histologically proven lymphoma with mediastinal involvement and treated with consolidative proton radiotherapy were included in the present study. The patients received PT due to their young age (<30 years), in female patients with an expected high dose to breast tissue ($D_{\text{mean}} > 4.5$ Gy) and/or in patients

TABLE 1 | Patient, treatment, and disease-specific characteristics of 23 patients with mediastinal lymphoma.

Number of patients	23
Median age (range)	30 years (18-54 years)
Sex (m/f)	7/16
HL/NHL	13/10
Ann Arbor staging	
I	3 (13%)
II	13 (57%)
III	0 (0%)
IV	7 (30%)
Median total dose (range)	36 Gy(RBE) [20-39.6 Gy(RBE)]
Median no. of fractions (range)	18 (10-22)
Median dose per fraction (range)	2 Gy(RBE) [1.8-2 Gy(RBE)]
Median PTV	494 ml (120-886 ml)
Mediastinal involvement	
Only superior	10 (43%)
Superior and inferior	13 (57%)
Laterality	
Left	8 (35%)
Right	9 (39%)
Middle	6 (26%)
Additional cervical involvement	8 (35%)

Gy(RBE), Gray (Relative Biological Effectiveness); PTV, Planning target volume.

with particularly high expected radiation dose to the heart ($D_{\mathrm{mean}} > 5$ Gy) if treated with conventional photon irradiation. In summary, 10 patients with bulky disease (>7.5 cm) non-Hodgkin lymphoma (NHL) received consolidation RT following induction chemotherapy consisting of R-CHOP+/−MTX (16–18). Thirteen Hodgkin lymphoma (HL) patients were treated according to the German Hodgkin Study Group criteria, depending on the stage and the risk factors (2, 19, 20). Treatment technique and clinical outcomes have recently been described in detail (12). The patient, treatment, and disease-specific characteristics are presented in **Table 1**.

For treatment planning, the patients were immobilized with the help of either individually shaped thermoplastic masks with shoulder fixation or the WingSTEP system (IT V, Innsbruck). A planning computed tomography (CT) scan with 3-mm slice thickness as well as a 4D CT scan under free breathing were acquired using Siemens' either Somtom or Confidence (Siemens Healthnears, Erlangen Germany). The aim of the 4D CT was to qualitatively analyze the impact of respiratory motion on tumor movement. Particle therapy planning was performed using Siemens Syngo PT Software (Siemens, Erlangen, Germany) that applies pencil beam algorithm for dose calculation (21–23). The prescribed dose was optimized with proton beams of spot size of 8–25 mm full width at half maximum, and with 2–3 mm of overlap in lateral (dx, dy) and longitudinal (dz) directions. Both single-beam optimization and multi-beam optimization (IMPT) were applied, depending on the different tumor locations. If IMPT was applied, generation of high-dose gradients per field was avoided. Due to the location of the clinical tumor volumes (CTV)s in close proximity to the lungs, a maximum of two anterior beams with gantry angles between ± 20° was selected. CTV coverage with D95% to 95% of the prescribed dose was aimed while respecting known OAR dose constraints (24). The final proton dose was scaled with a constant radiobiological effectiveness (RBE) factor of 1.1. An active beam application with raster-scanning technique (25) under daily image guidance was used.

Comparative photon plans were calculated for all patients using the TomoTherapy® Treatment Planning System (Tomotherapy, Accuray® Incorporated, Sunnyvale, USA). Whenever possible, directional or complete blocks for breast tissue were used for optimization, resulting in a "butterfly" IMRT beam arrangement approach [weighted anteriorly and posteriorly oblique beam entry angles (26)]. The planning goals were the same for the proton and the IMRT plans, with the aim to keep the dose to the surrounding OAR as low as reasonably achievable and not only according to QUANTEC and Emami constraints, which can be easily achieved in moderate-dose prescriptions like lymphoma treatments. Since this young patient cohort was treated on a solely curative basis, main priority was always given to optimal target coverage. Further prioritization depended on the anatomical localization (upper vs. lower mediastinal region with precardial involvement) and the gender of the patient, but with a generally higher priority to breast and heart tissue compared to the lung and the esophagus.

Risk Estimation for Radiation-Induced Secondary Cancers

Two distinct radiobiological models proposed by Dasu et al. (1) and Schneider et al. (4) were applied for the risk estimation of radiation-induced secondary cancers as previously described by Mondlane et al. (27). Data extracted from the dose–volume histograms from both the proton and the X-ray plans were used for the risk calculation of radiation-induced secondary malignancies.

Dasu Model

The Dasu model is a linear–quadratic (LQ)-based model (Equation 1):

$$Total risk_{organ} = \frac{1}{\sum_i v_i} \sum_i v_i \times \left\{ \left(\alpha_1 D_i + \frac{\beta_1 D_i^2}{n} \right) \times exp\left[- \left(\alpha_2 D_i + \frac{\beta_2 D_i^2}{n} \right) \right] \right\}$$

where v_i is the volume of tissue receiving dose D_i given in n fractions. The first term in the parenthesis describes the induction of DNA mutations, while the second term models cell survival in the irradiated organs. Calculations of the parameter α_1 were performed with the risk coefficients for fatal and total risk of cancer induction derived according to the recommendations of ICRP Publication 103 as previously described (1, 27, 28) (see **Table 2**). The term "total risk" defines the mere risk for development of cancer, while the term "fatal risk" describes the risk of induced secondary cancer leading to death. An α/β ratio

TABLE 2 | Risk coefficients (α_1, second and third column) and the linear quadratic model parameter (last column) used for risk assessment for the different organs at risk.

Organ	α_1 (Gy $^{-1}$) fatal risk	α_1 (Gy $^{-1}$) total risk	α_2 (Gy $^{-1}$)
Lung	0.0101	0.0144	0.129
Breast	0.0028	0.0144	0.008
Esophagus	0.0014	0.0015	0.274

The risk coefficients were taken from ICRP 103, the linear LQ-model parameters were adapted from Schneider et al. (4).

of 3 was taken for the lungs, esophagus, and breasts. Nominal risk coefficients are derived by averaging sex and age at exposure lifetime risk estimates in representative populations.

Schneider-Model

The risks for inducing secondary malignancies were also estimated using the Schneider model, which is based on determination of the OED (Equation 2):

$$OED = \frac{1}{\sum_i v_i} \sum_i v_i \times RED(D_i)$$

where v_i and D_i are defined as in the Dasu model and RED (D_i) is the selected dose–response relationship.

As described by Mondlane et al. (27), three distinct dose–response relationship scenarios (linear, linear–exponential, and plateau) were applied for estimating the risk of SM. The linear model assumes a direct increase in risk with increasing doses. The linear–exponential dose relationship completely neglects the repopulation/repair effect, while the plateau model expects complete repopulation/repair to take place. The aforementioned three equations modeling the dose–response relationship for linear, linear–exponential, and plateau models are depicted in Equation (3).

$$RED\,(D_i) = \begin{cases} D_i \\ D_i e^{-\alpha' D_i} \\ \frac{1-e^{-\alpha' D_i}}{\alpha'} \end{cases}$$

According to Mondlane et al. (27), α' is defined by applying the LQ model and is proportional to the number of cells which are reduced by cell killing:

$$\alpha' = \alpha + \beta \frac{D_i}{n}$$

in which n is the number of fractions used. The values of α in Equation (4) are shown in the last column of **Table 2** as α_2. Analogously to the Dasu model, an α/β ratio of 3 was taken for the lungs, esophagus, and breasts. The relative risks for SMs were calculated as the ratio of the OEDs obtained for specific OARs (the PT dose relative to the photon dose). Therefore, a value <1 stands a lower risk for SM induction following PT.

Follow-Up

Following the completion of thoracic proton radiotherapy, the patients received regular follow-up visits including clinical examinations and CT or MR imaging. Response to treatment was assessed using the revised response criteria for lymphoma (29).

Statistical Analysis

Statistical comparisons were performed using the non-parametric Wilcoxon signed-rank test. Significance was noted for two-tailed p-values of $\leq$0.05. Survival analyses for overall (OS) as well as progression-free survival (PFS) following radiotherapy were performed using the Kaplan–Meier method. A p-value $\leq$0.05 was considered as statistically significant. All statistical analyses were performed using the software SPSS 24.0 (IBM Corporation, Armonk, NY, USA).

Ethical Approval

Ethical approval was obtained from the local Ethics Committee of Heidelberg University Hospital (S-201/2017).

RESULTS

Patient and Treatment Characteristics

Twenty-three patients with a median age of 30 years (range, 18–54 years) and diagnosed with mediastinal lymphoma were treated with consolidation radiotherapy using PT. Fifty-seven percent (n = 13) of the patients suffered from HL, whereas 43% (n = 10) of the patients had aggressive NHL. Most patients presented in Ann Arbor stages I–II (70%) with involvement of the superior and the inferior mediastinal regions (57%). Additional cervical involvement was present in one third of the patients. Median treatment volume (planning target volume) was 494 ml (range, 120–886 ml). Complete patient-, treatment-, and disease specific characteristics are shown in **Table 1**.

Planning and Dosimetric Characteristics

The Dasu model was applied to estimate both the total risk as well as the fatal risk. **Figure 1** depicts the calculated risks for total and fatal SM induction for relevant thoracic organs for each patient. For X-ray irradiation, the median total risk for tumor induction was calculated to be 2.2% (range, 1.6–3.1%), 2.1% (range, 1.7–2.9%), and 1.0% (range, 0.5–1.5%) for the right lung, the left lung, and the esophagus, while for proton irradiation the risk was significantly reduced to 0.8% (range, 0.1–1.2%), 0.8% (range, 0.3–1.4%), and 0.8% (range, 0.0–1.6%), respectively ($p \leq$ 0.001). The fatal risk for secondary malignancies also significantly decreased to 0.5% (range, 0.1–0.9%), 0.6% (range, 0.2–1.0%), and 0.7% (range, 0.0–1.5%) in the right lung, the left lung, and the esophagus when applying PT, compared to 1.5% (range, 0.7–2.2%), 1.5% (range, 0.6–2.0%), and 1.0% (range, 0.5–1.4%) with photon irradiation ($p \leq$ 0.001). For female patients treated with PT, the risk of total and fatal cancer induction was 1.5% (range, 0–10.1%) and 0.3% (range, 0–2.0%) for the right breast as well as 2.4% (range, 0–9.7%) and 0.5% (range, 0–1.9%) for the left breast, respectively. A significant increase in both total cancer and fatal cancer induction was calculated in the corresponding photon plans with 3.5% (range, 0.8–10.4%) and 0.7% (range, 0.2–2.0%)

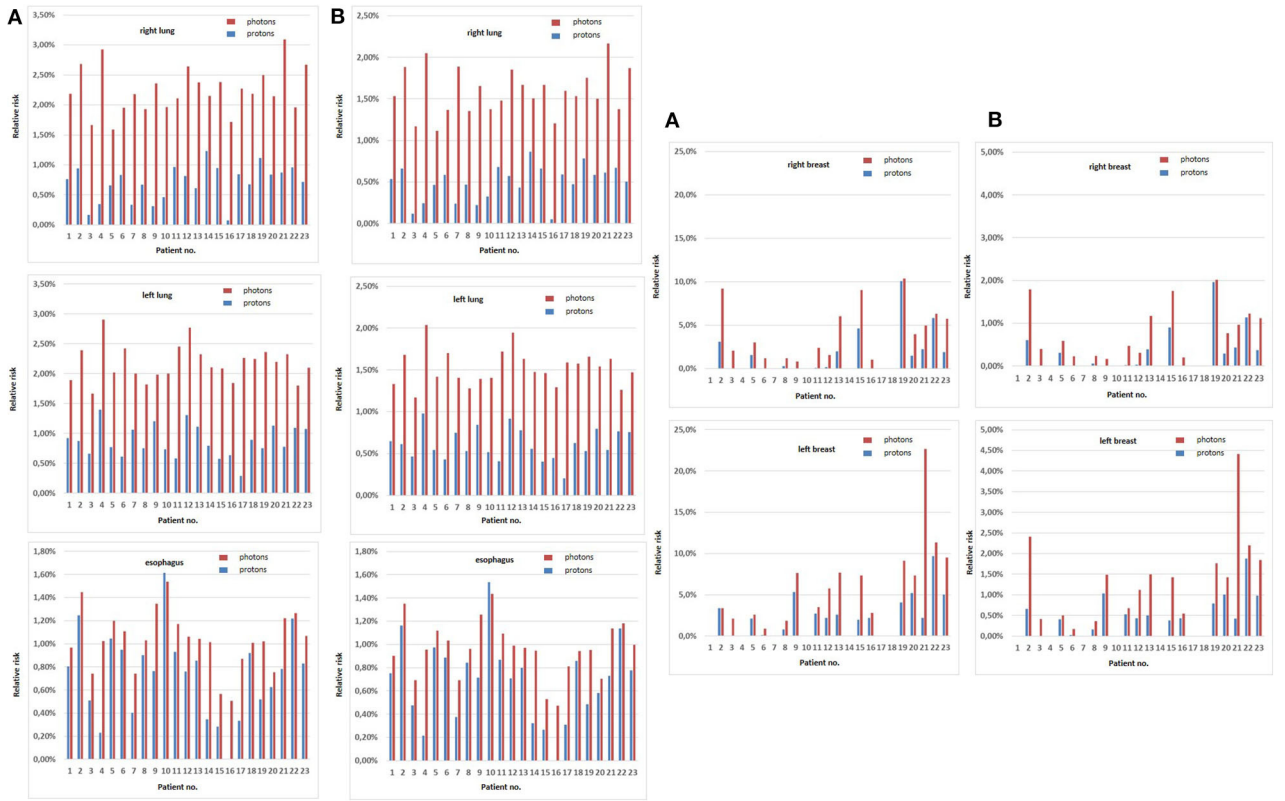

FIGURE 1 | Total **(A)** and fatal **(B)** secondary malignancy risks according to the Dasu model for relevant thoracic organs (right and left lung, esophagus, right and left breast) for each patient. Total and fatal secondary malignancy risks for photons are depicted in red, for protons in blue.

for the right breast and 6.6% (range, 0.9–22.7%) and 1.4% (range, 0.2–4.4%) for the left breast, respectively ($p \leq 0.001$). However, one patient showed a slightly increased risk for both total and fatal esophagus cancer induction when PT was applied compared to photon irradiation (patient 10, **Figure 1**).

Utilizing the Schneider model to estimate the risk for carcinoma induction, the ratios of the OED values derived from the PT and the X-ray therapy plans were calculated and the relative risk reduction using the linear, the linear–exponential, and the plateau model was derived. According to all three models, PT statistically significantly reduced the risk of radiation-induced lung, esophagus, and breast carcinoma for female patients (at least $p \leq 0.008$) when compared to X-ray irradiation (**Table 3**). For each patient, the calculated relative risks for tumor induction in bilateral lungs, esophagus, and bilateral breasts for female patients are presented in **Figure 2** for the three distinct dose–response relationship models. However, two patients (patients 10 and 18) were calculated to have an increased relative risk for esophageal cancer and two female patients showed a higher relative risk for right-sided breast cancer (patients 2 and 20) for PT compared to X-ray radiotherapy.

Clinical and oncologic outcomes have been reported in detail elsewhere (12). At the time of this analysis, median follow-up was 49.5 months (range, 34.7–68.8 months), and 5-year OS and 5-year PFS were 100 and 91.3%, respectively. No SM have been documented during follow-up.

DISCUSSION

As oncologic outcomes for mediastinal lymphoma have improved over time, there has been a renewed focus on treatment-related side effects. This is all the more important in a patient population who are typically diagnosed at a younger median age and have a more extended cancer natural history. Multiple dosimetric studies have provided evidence that PT offers a superior dose distribution in patients with mediastinal lymphoma relative to X-ray irradiation (12, 30, 31), which may lead to reduced acute and long-term toxicity. Of undisputed importance is the induction of SM, particularly lung and breast cancer. Majority of the applications are retrospective in nature and prospective trials are pending and oftentimes not feasible due to ethical complexities. Furthermore, for patients that have already been treated with PT, long-term data are still lacking, given the very long-term follow-up periods acquired to identify chronic toxicity including cardiovascular diseases or SM induction.

The bulk of clinical data comes from the X-ray era and partially from the 2D RT era and are therefore of limited applicability to modern RT techniques such as IMRT. One Dutch retrospective cohort study enrolled 3,905 HL patients treated with RT (primarily large-field irradiation techniques) and who had survived HL. In this cohort, 1,055 SM were diagnosed, resulting in a standardized incidence ratio of 4.6

TABLE 3 | Median values (range) of the relative risks for observing carcinomas at OAR (lung, breast, esophagus) assessed using the Schneider-model.

	Proton/Photon relative risk of cancer					
	Linear	***p*-value**	**Exponential**	***p*-value**	**Plateau**	***p*-value**
Lung right	0.38 (0.08-0.60)	<0.001	0.34 (0.04-0.60)	<0.001	0.35 (0.05-0.50)	<0.001
Lung left	0.46 (0.16-0.68)	<0.001	0.39 (0.13-0.63)	<0.001	0.41 (0.13-0.58)	<0.001
Breast right	0.33 (0.00-2.68)	0.008	0.33 (0.00-2.14)	0.008	0.33 (0.00-2.4)	0.008
Breast left	0.44 (0.01-0.84)	<0.001	0.42 (0.01-0.81)	<0.001	0.43 (0.01-0.83)	<0.001
Esophagus	0.72 (0.01-2.77)	0.002	0.70 (0.01-1.63)	<0.001	0.76 (0.01-2.24)	0.001

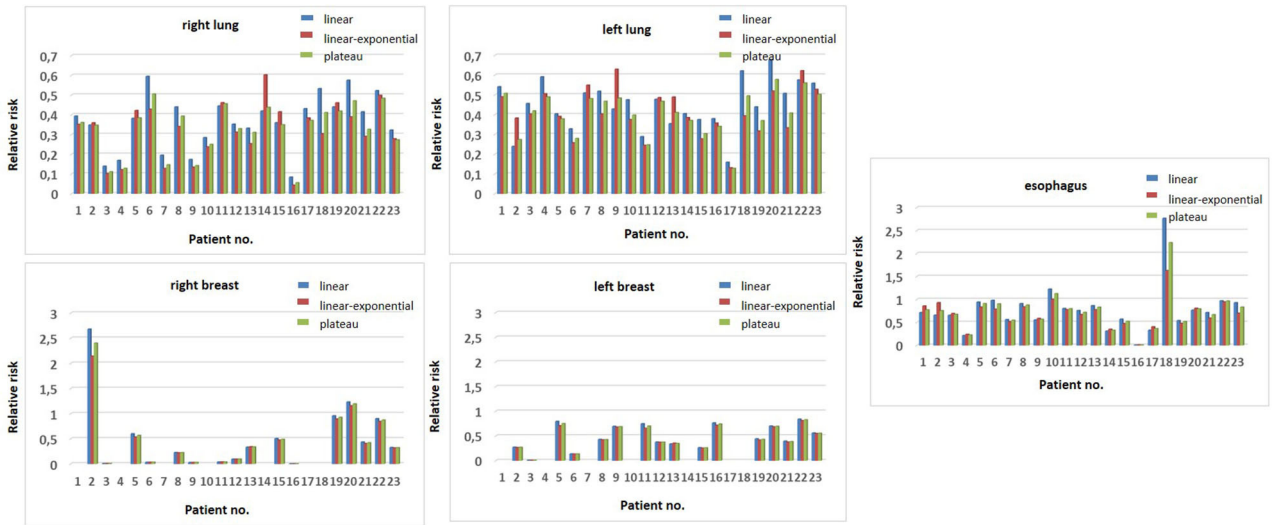

FIGURE 2 | Relative risk reduction for the three distinct dose-response relationship models (linear in blue, the linear-exponential in red and the plateau model in green) according to the Schneider model. Calculated relative risks for tumor induction are shown for relevant thoracic organs (right and left lung, esophagus, right, and left breast) for each patient.

compared to the general population, with the cumulative incidence of SM being 48.5% at 40 years after treatment vs. 19% in the general population. In this series, breast and lung cancer contributed the bulk of overall absolute excess risk increase (each 20%) (32). Furthermore, Moskowitz reported that the cumulative incidence of breast cancer by the age of 50 is comparable with the risk of BRCA1 mutation carriers for childhood HL survivors (33). Although data have to be interpreted with caution when extrapolating older studies using less advanced radiation techniques with current RT technology, these clinical data emphasize the importance of dose reduction, especially in young patients where the risk is even higher (34).

Regarding PT, clinical data are even more limited; however, in a retrospective matched-pair analysis of 558 patients, SM occurred in 7.5% after X-ray irradiation vs. 5.2 % after PT (35). Although the median follow-up is short (6.7 years), the extrapolated incidence rate of SM after X-ray irradiation was 10.3 cancers per 1,000 person-years compared to 6.9 cancers per 1,000 person-years following PT. Moreover, the interpretation of these results is also complicated by the heterogeneity of tumor and histologies, variations in combined modality approach, heterogeneity of radiation dose, and fractionation schemes used which may bias the results.

In an effort to evaluate the risk for SM induction following RT with modern techniques, we performed a pairwise comparison of the estimated individual risks for radiation-induced SMs after PT vs. X-ray irradiation for relevant organs in patients with mediastinal lymphoma using two different, well-established mechanistic calculation models. We showed that the calculated risks were significantly lower after PT compared to X-ray irradiation for all OARs investigated in this study (i.e., lungs, esophagus, and breast). Of note is that the risks in the aforementioned publications (32–34) may be higher, owing to the older radiation techniques, younger patient age, and consideration of the cumulative risk for all secondary malignancies, compared to an organ-, sex-, and age-specific risk estimation like our analysis. Several publications already confirmed a strong dependency of developing cancer at the age of exposure, including Hancock et al. who reported over three times of elevated risk for breast cancer when a patient below the age of 20 years was compared to older patients aged 20–29 years (36).

A retrospective comparative analysis of HL patients demonstrated that PT decreased the avoidable cancer incidence

compared to X-rays by a factor of about 2 (3), using the IRCP-60 method. Similarly, our results show comparable values for risk reduction when using protons of 2.75–3.0 for lung cancer, 2.75–2.33 for breast cancer, and 1.25 for esophageal cancer (total risk according to Dasu), confirming previously reported results with a larger patient cohort. Another valuable metric, investigated by Rechner et al. (37), is the calculation of life years lost (LYL) attributable to the late effects after RT. This publication evaluated the risk for 22 patients and found that the use of PT significantly reduced LYL compared to IMRT. The primary drivers for LYL were heart failure, myocardial infarction, valvular heart disease, and breast and lung cancer, which again emphasize the importance of dose reduction to these OARs.

In two patients (nos. 2 and 20), the risk ratio (RR) according to the Schneider model for breast cancer on the right side was >1 and therefore higher with PT. Of note is that both patients were diagnosed with more right-lateralized mediastinal involvement and beam application was weighted more from this side, resulting in a lower dose to the left side (see **Figure 2**) and especially a lower dose to the heart. In both patients, for example, this was considered more important since these patients had already suffered from grade 2 chronic heart failure after chemotherapy. In general, this demonstrates that relative risks are associated not only with treatment planning and technique factors but also with patient-specific geometry and tumor location. Nevertheless, these two patients were treated with PT due to the significant improvement in other thoracic OARs. Finally, the two patients (nos. 10 and 18) with a higher RR for esophageal cancer induction were both patients with cervical and upper mediastinal involvement, where the dose to the esophagus was higher with PT, owing to the beam arrangements. Nevertheless, PT was chosen in these patients due to better sparing of other OARs (breast and heart), where risk for SM or long-term toxicity is more relevant.

Overall, most organs at risk demonstrated significant dosimetric improvements across the cohort analyzed. However, tumor location and patient geometry, on rare occasions, led to improvements in dose to certain organs. As a result, clinician judgment must be used on a case-by-case basis when deciding between radiation modalities that may have variable improvements between OAR doses, that is, if a given proton plan yields reduction in heart and lung dose but higher breast dose relative to a comparative IMRT plan, clinical factors will need to be weighed by the radiation oncologist to choose the plan most likely to optimize patient clinical outcome. Notably, there are several limitations for modeling radiation-induced carcinogenesis: Firstly, both models applied in this analysis use data derived from epidemiological studies which *per se* have uncertainties: factors like whole-body exposure in atomic bomb survivors vs. local dose exposure in radiotherapy might reduce comparability (38). Moreover, RBE may vary in PT, and this effect is currently not considered in these models but is also not taken into consideration in standard clinical PT (use of constant RBE of 1.1).

Nevertheless, the strength of the two models is the inclusion of factors for cell killing as well as repair and repopulation, which reflect the non-linear dose–response relationship that is well known for SM induction (39).

Apart from all these factors, real patient data (that need decades to be collected) will also suffer from variables that influence certainty, e.g., variation of target size and tumor location between patients, as well as the use of different planning/optimization techniques and constraints. In this context, using risk ratios in a pairwise comparison of different modalities may be very useful when ranking RT modalities like proton and photon irradiation in a given patient cohort.

As proposed by a current guideline of the ILROG (40), PT is an attractive treatment option which should be discussed for lymphoma patients, especially if mediastinal involvement is present. Nevertheless, the potential benefit is variable and dependent on many factors including age, gender, tumor location, and patient-specific comorbidities. This specific radiation modality should be discussed on a "case-by-case" basis and, if found to be warranted, patients should be treated at PT facilities with sufficient expertise (41). At our facility, all lymphoma patients treated with PT are placed on a prospective registry study with long follow-up to investigate long-term toxicities like cardiac events or SM.

Furthermore, the American Cancer Society, the American College of Radiology, and the Society of Breast Imaging recommend annual screening by breast magnetic resonance imaging as an intensified screening for breast cancer, especially for patients treated at an age <30 years, similar to the already established screening for high-risk patients with a BRCA1 mutation (42, 43).

CONCLUSION

Proton therapy for patients diagnosed with mediastinal lymphoma offers a dramatic dose reduction to surrounding thoracic OARs. Based on the multiple radiobiological models utilized in the present study, PT is estimated to reduce SM risk for lung and breast tissue. Future research will include a long-term follow-up of patients treated at experienced facilities to identify the "real" risk of secondary malignancies in this patient population.

DATA AVAILABILITY STATEMENT

The datasets generated for this study are available on request to the corresponding author.

ETHICS STATEMENT

The studies involving human participants were reviewed and approved by Ethikkommission Universität Heidelberg. Written informed consent for participation was not required for this study in accordance with the national legislation and the institutional requirements.

AUTHOR CONTRIBUTIONS

LK, PHa, CL, and MS performed the data collection. LK, JL, and JH-R were responsible for writing of the original

draft preparation. LK, BN, FW, PHo, JD, and KH performed patient treatment and clinical assessments and were responsible for radiooncological follow-up documentation. LK, PHa, and JH-R performed the statistical analysis. LK and JH-R conceived the study and participated in its design and coordination. All the authors were responsible for data interpretation, participated in the manuscript revisions, and approved the final manuscript.

ACKNOWLEDGMENTS

This work was supported by a Heidelberg University young investigator grant to LK. We acknowledge the financial support by Deutsche Forschungsgemeinschaft within the funding program Open Access Publishing, by the Baden-Württemberg Ministry of Science, Research, and the Arts, and by Ruprecht-Karls-Universität Heidelberg.

REFERENCES

1. Dasu A, Toma-Dasu I, Olofsson J, Karlsson M. The use of risk estimation models for the induction of secondary cancers following radiotherapy. *Acta Oncol.* (2005) 44:339–47. doi: 10.1080/02841860510029833
2. Engert A, Haverkamp H, Kobe C, Markova J, Renner C, Ho A, et al. Reduced-intensity chemotherapy and PET-guided radiotherapy in patients with advanced stage Hodgkin's lymphoma (HD15 trial): a randomised, open-label, phase 3 non-inferiority trial. *Lancet.* (2012) 379:1791–9. doi: 10.1016/S0140-6736(11)61940-5
3. Schneider U, Lomax A, Lombriser N. Comparative risk assessment of secondary cancer incidence after treatment of Hodgkin's disease with photon and proton radiation. *Radiat Res.* (2000) 154:382–8. doi: 10.1667/0033-7587(2000)154(0382:craosc)2.0.co;2
4. Schneider U, Zwahlen D, Ross D, Kaser-Hotz B. Estimation of radiation-induced cancer from three-dimensional dose distributions: concept of organ equivalent dose. *Int J Radiat Oncol Biol Phys.* (2005) 61:1510–5. doi: 10.1016/j.ijrobp.2004.12.040
5. Girinsky T, Pichenot C, Beaudre A, Ghalibafian M, Lefkopoulos D. Is intensity-modulated radiotherapy better than conventional radiation treatment and three-dimensional conformal radiotherapy for mediastinal masses in patients with Hodgkin's disease, and is there a role for beam orientation optimization and dose constraints assigned to virtual volumes? *Int J Radi Oncol Biol Phys.* (2006) 64:218–26. doi: 10.1016/j.ijrobp.2005.06.004
6. Goodman KA, Toner S, Hunt M, Wu EJ, Yahalom J. Intensity-modulated radiotherapy for lymphoma involving the mediastinum. *Int J Radi Oncol Biol Phys.* (2005) 62:198–206. doi: 10.1016/j.ijrobp.2004.08.048
7. Hall EJ. Intensity-modulated radiation therapy, protons, and the risk of second cancers. *Int J Radi Oncol Biol Phys.* (2006) 65:1–7. doi: 10.1016/j.ijrobp.2006.01.027
8. Maraldo MV, Jorgensen M, Brodin NP, Aznar MC, Vogelius IR, Petersen PM, et al. The impact of involved node, involved field and mantle field radiotherapy on estimated radiation doses and risk of late effects for pediatric patients with Hodgkin lymphoma. *Pediatr Blood Cancer.* (2014) 61:717–22. doi: 10.1002/pbc.24861
9. Andolino DL, Hoene T, Xiao L, Buchsbaum J, Chang AL. Dosimetric comparison of involved-field three-dimensional conformal photon radiotherapy and breast-sparing proton therapy for the treatment of Hodgkin's lymphoma in female pediatric patients. *Int J Radi Oncol Biol Phys.* (2011) 81:e667–71. doi: 10.1016/j.ijrobp.2011.01.061
10. Chera BS, Rodriguez C, Morris CG, Louis D, Yeung D, Li Z, et al. Dosimetric comparison of three different involved nodal irradiation techniques for stage II Hodgkin's lymphoma patients: conventional radiotherapy, intensity-modulated radiotherapy, and three-dimensional proton radiotherapy. *Int J Radi Oncol Biol Phys.* (2009) 75:1173–80. doi: 10.1016/j.ijrobp.2008.12.048
11. Hoppe BS, Flampouri S, Su Z, Morris CG, Latif N, Dang NH, et al. Consolidative involved-node proton therapy for Stage IA-IIIB mediastinal Hodgkin lymphoma: preliminary dosimetric outcomes from a Phase II study. *Int J Radi Oncol Biol Phys.* (2012) 83:260–7. doi: 10.1016/j.ijrobp.2011.06.1959
12. Konig L, Bougatf N, Horner-Rieber J, Chaudhri N, Mielke T, Kluter S, et al. Consolidative mediastinal irradiation of malignant lymphoma using active scanning proton beams: clinical outcome and dosimetric comparison. *Strahlentherapie und Onkol.* (2019) 195:677–687. doi: 10.1007/s00066-019-01460-7
13. Sethi RV, Shih HA, Yeap BY, Mouw KW, Petersen R, Kim DY, et al. Second nonocular tumors among survivors of retinoblastoma treated with contemporary photon and proton radiotherapy. *Cancer.* (2014) 120:126–33. doi: 10.1002/cncr.28387
14. Li CI, Nishi N, McDougall JA, Semmens EO, Sugiyama H, Soda M, et al. Relationship between radiation exposure and risk of second primary cancers among atomic bomb survivors. *Cancer Res.* (2010) 70:7187–98. doi: 10.1158/0008-5472.CAN-10-0276
15. Preston DL, Ron E, Tokuoka S, Funamoto S, Nishi N, Soda M, et al. Solid cancer incidence in atomic bomb survivors: 1958-1998. *Radiat Res.* (2007) 168:1–64. doi: 10.1667/RR0763.1
16. Held G, Murawski N, Ziepert M, Fleckenstein J, Poschel V, Zwick C, et al. Role of radiotherapy to bulky disease in elderly patients with aggressive B-cell lymphoma. *J Clin Oncol.* (2014) 32:1112–8. doi: 10.1200/JCO.2013.51.4505
17. Ng AK, Dabaja BS, Hoppe RT, Illidge T, Yahalom J. Re-Examining the role of radiation therapy for diffuse large b-cell lymphoma in the modern era. *J Clin Oncol.* (2016) 34:1443–7. doi: 10.1200/JCO.2015.64.9418
18. Pfreundschuh M, Kuhnt E, Trumper L, Osterborg A, Trneny M, Shepherd L, et al. CHOP-like chemotherapy with or without rituximab in young patients with good-prognosis diffuse large-B-cell lymphoma: 6-year results of an open-label randomised study of the MabThera International Trial (MInT) Group. *Lancet Oncol.* (2011) 12:1013–22. doi: 10.1016/S1470-2045(11)70235-2
19. Engert A, Plutschow A, Eich HT, Lohri A, Dorken B, Borchmann P, et al. Reduced treatment intensity in patients with early-stage Hodgkin's lymphoma. *N Engl J Med.* (2010) 363:640–52. doi: 10.1056/NEJMoa1000067
20. von Tresckow B, Plutschow A, Fuchs M, Klimm B, Markova J, Lohri A, et al. Dose-intensification in early unfavorable Hodgkin's lymphoma: final analysis of the German Hodgkin Study Group HD14 trial. *J Clin Oncol.* (2012) 30:907–13. doi: 10.1200/jco.2011.38.5807
21. Kramer M, Jakel O, Haberer T, Kraft G, Schardt D, Weber U. Treatment planning for heavy-ion radiotherapy: physical beam model and dose optimization. *Phys Med Biol.* (2000) 45:3299–317. doi: 10.1088/0031-9155/45/11/313
22. Kramer M, Jakel O, Haberer T, Rietzel E, Schardt D, Scholz M, et al. Treatment planning for scanned ion beams. *Radiother Oncol.* (2004) 2(73 Suppl.):S80–5. doi: 10.1016/s0167-8140(04)80021-5
23. Kramer M, Scholz M. Treatment planning for heavy-ion radiotherapy: calculation and optimization of biologically effective dose. *Phys Med Biol.* (2000) 45:3319–30. doi: 10.1088/0031-9155/45/11/314
24. Emami B, Lyman J, Brown A, Coia L, Goitein M, Munzenrider JE, et al. Tolerance of normal tissue to therapeutic irradiation. *Int J Radi Oncol Biol Phys.* (1991) 21:109–22.
25. Haberer T, Becher W, Schardt D, Kraft G. Magnetic scanning system for heavy ion therapy. *Nucl Instr Methods Phys Res.* (1993) 330:296–305. doi: 10.1016/0168-9002(93)91335-K
26. Voong KR, McSpadden K, Pinnix CC, Shihadeh F, Reed V, Salehpour MR, et al. Dosimetric advantages of a "butterfly" technique for intensity-modulated radiation therapy for young female patients with mediastinal Hodgkin's lymphoma. *Radiat Oncol.* (2014) 9:94. doi: 10.1186/1748-717X-9-94
27. Mondlane G, Gubanski M, Lind PA, Ureba A, Siegbahn A. Comparative study of the calculated risk of radiation-induced cancer after photon- and proton-beam based radiosurgery of liver metastases. *Phys Med.* (2017) 42:263–270. doi: 10.1016/j.ejmp.2017.03.019
28. Nenot J-C, Brenot J, Laurier D, Rannou A, Thierry D. *ICRP Publication 103. The 2007 Recommendations of the International Commission on Radiological*

Protection. Ottawa, ON (2009). Available online at: https://inis.iaea.org/search/search.aspx?orig_q=RN:49042116
29. Cheson BD, Pfistner B, Juweid ME, Gascoyne RD, Specht L, Horning SJ, et al. Revised response criteria for malignant lymphoma. *J Clin Oncol.* (2007) 25:579–86. doi: 10.1200/JCO.2006.09.2403
30. Hoppe BS, Flampouri S, Su Z, Latif N, Dang NH, Lynch J, et al. Effective dose reduction to cardiac structures using protons compared with 3DCRT and IMRT in mediastinal Hodgkin lymphoma. *Int J Radi Oncol Biol Phys.* (2012) 84:449–55. doi: 10.1016/j.ijrobp.2011.12.034
31. Lautenschlaeger S, Iancu G, Flatten V, Baumann K, Thiemer M, Dumke C, et al. Advantage of proton-radiotherapy for pediatric patients and adolescents with Hodgkin's disease. *Radi Oncol.* (2019) 14:157. doi: 10.1186/s13014-019-1360-7
32. Schaapveld M, Aleman BM, van Eggermond AM, Janus CP, Krol AD, van der Maazen RW, et al. Second cancer risk up to 40 years after treatment for Hodgkin's lymphoma. *N Engl J Med.* (2015) 373:2499–511. doi: 10.1056/NEJMoa1505949
33. Moskowitz CS, Chou JF, Wolden SL, Bernstein JL, Malhotra J, Novetsky Friedman D, et al. Breast cancer after chest radiation therapy for childhood cancer. *J Clin Oncol.* (2014) 32:2217–23. doi: 10.1200/JCO.2013.54.4601
34. De Bruin ML, Sparidans J, van't Veer MB, Noordijk EM, Louwman MW, Zijlstra JM, et al. Breast cancer risk in female survivors of Hodgkin's lymphoma: lower risk after smaller radiation volumes. *J Clin Oncol.* (2009) 27:4239–46. doi: 10.1200/JCO.2008.19.9174
35. Chung CS, Yock TI, Nelson K, Xu Y, Keating NL, Tarbell NJ. Incidence of second malignancies among patients treated with proton versus photon radiation. *Int J Radi Oncol Biol Phys.* (2013) 87:46–52. doi: 10.1016/j.ijrobp.2013.04.030
36. Hancock SL, Tucker MA, Hoppe RT. Breast cancer after treatment of Hodgkin's disease. *J Natl Cancer Inst.* (1993) 85:25–31. doi: 10.1093/jnci/85.1.25
37. Rechner LA, Maraldo MV, Vogelius IR, Zhu XR, Dabaja BS, Brodin NP, et al. Life years lost attributable to late effects after radiotherapy for early stage Hodgkin lymphoma: The impact of proton therapy and/or deep inspiration breath hold. *Radiother Oncol.* (2017) 125:41–7. doi: 10.1016/j.radonc.2017.07.033
38. Kry SF, Followill D, White RA, Stovall M, Kuban DA, Salehpour M. Uncertainty of calculated risk estimates for secondary malignancies after radiotherapy. *Int J Radi Oncol Biol Phys.* (2007) 68:1265–71. doi: 10.1016/j.ijrobp.2007.04.014
39. Hall EJ, Wuu CS. Radiation-induced second cancers: the impact of 3D-CRT and IMRT. *Int J Radi Oncol Biol Phys.* (2003) 56:83–8. doi: 10.1016/s0360-3016(03)00073-7
40. Dabaja BS, Hoppe BS, Plastaras JP, Newhauser W, Rosolova K, Flampouri S, et al. Proton therapy for adults with mediastinal lymphomas: the International Lymphoma Radiation Oncology Group guidelines. *Blood.* (2018) 132:1635–46. doi: 10.1182/blood-2018-03-837633
41. Ricardi U, Maraldo MV, Levis M, Parikh RR. Proton Therapy For Lymphomas: Current State Of The Art. *Onco Targets Ther.* (2019) 12:8033–46. doi: 10.2147/OTT.S220730
42. Lee CH, Dershaw DD, Kopans D, Evans P, Monsees B, Monticciolo D, et al. Breast cancer screening with imaging: recommendations from the Society of Breast Imaging and the ACR on the use of mammography, breast MRI, breast ultrasound, and other technologies for the detection of clinically occult breast cancer. *J Am Coll Radiol.* (2010) 7:18–27. doi: 10.1016/j.jacr.2009.09.022
43. Saslow D, Boetes C, Burke W, Harms S, Leach MO, Lehman CD, et al. American Cancer Society guidelines for breast screening with MRI as an adjunct to mammography. *CA Cancer J Clin.* (2007) 57:75–89. doi: 10.3322/canjclin.57.2.75

Conflict of Interest: The authors declare that the research was conducted in the absence of any commercial or financial relationships that could be construed as a potential conflict of interest.

frontiers in Oncology

ORIGINAL RESEARCH
published: 21 July 2020
doi: 10.3389/fonc.2020.01058

Evaluating the Propagation of Uncertainties in Biologically Based Treatment Planning Parameters

Miriam A. Barry[1]*, *Mohammad Hussein*[1] and *Giuseppe Schettino*[1,2]

[1] National Physical Laboratory, Metrology for Medical Physics Department, Teddington, United Kingdom, [2] Department of Physics, University of Surrey, Guildford, United Kingdom

Biologically based treatment planning is a broad term used to cover any instance in radiotherapy treatment planning where some form of biological input has been used. This is wide ranging, and the simpler forms (e.g., fractionation modification/optimization) have been in use for many years. However, there is a reluctance to use more sophisticated methods that incorporate biological models either for plan evaluation purposes or for driving plan optimizations. This is due to limited data available regarding the uncertainties in these model parameters and what impact these have clinically. This work aims to address some of these issues and to explore the role that uncertainties in individual model parameters have on the overall tumor control probability (TCP)/normal tissue complication probability (NTCP) calculated, those parameters that have the largest influence and situations where extra care must be taken. In order to achieve this, a software tool was developed, which can import individual clinical DVH's for analysis using a range of different TCP/NTCP models. On inputting individual model parameters, an uncertainty can be applied. Using a normally distributed random number generator, distributions of parameters can be generated, from which TCP/NTCP values can be calculated for each parameter set for the DVH in question. These represent the spread in TCP/NTCP parameters that would be observed for a simulated population of patients all being treated with that particular dose distribution. A selection of clinical DVHs was assessed using published parameters and their associated uncertainties. A range of studies was carried out to determine the impact of individual parameter uncertainties including reduction of uncertainties and assessment of what impact fractionation and dose have on these probabilities.

Keywords: normal tissue complication probability (NTCP), tumor control probability (TCP), uncertainty, biologically based treatment planning, biological optimization

OPEN ACCESS

Edited by:
Ester Orlandi,
Istituto Nazionale dei Tumori (IRCCS), Italy

Reviewed by:
Emanuele Scifoni,
Ministry of Education, Universities and Research, Italy
Sarah O. S. Osman,
Queen's University Belfast, United Kingdom

***Correspondence:**
Miriam A. Barry
Miriam.Barry@npl.co.uk

Specialty section:
This article was submitted to Radiation Oncology, a section of the journal Frontiers in Oncology

Received: *17 December 2019*
Accepted: *27 May 2020*
Published: *21 July 2020*

Citation:
Barry MA, Hussein M and Schettino G (2020) Evaluating the Propagation of Uncertainties in Biologically Based Treatment Planning Parameters. Front. Oncol. 10:1058. doi: 10.3389/fonc.2020.01058

INTRODUCTION

Radiobiology has played a critical role in clinical radiotherapy for many years, and it is common practice to use radiobiological methods, for example, to account for different fractionation regimes and modalities in combined treatment (such as combined external beam radiotherapy and brachytherapy in gynecological treatments) (1) and to account for interruptions in treatment (2). Following the significant technological development of the last decade, which has resulted in a variety of methods for the delivery of precise radiation doses, there is now a drive

to implement radiobiological methods in either the evaluation of treatment plans (for plan comparison for an individual patient) or for triaging patients who would benefit from more advanced radiotherapy techniques, e.g., protons (3) or the actual optimization of plans. Moreover, the use of radiobiological models for treatment plan optimization is an important first step for the development of truly personalized radiotherapy. This would allow full exploitation of the therapeutic power of radiation and the advances in genomic testing while safeguarding the more radiosensitive individuals.

The Task Group document from the AAPM, report 166 (4, 5) provides an outline describing biologically based treatment planning including descriptions of commonly used models and how different treatment planning systems (TPS) implement these. They also provide guidelines for implementation and quality assurance (QA) of such systems and vision for the future. A coherent explanation of the different levels of biological optimization was described by Nahum et al. (6). They outlined the different levels, which ranged from very simple methods (level 1) included in trials, such as IDEAL-CRT and I-Start, which individualize/escalate prescription levels based on organ at risk dose, to level 5, where they envisage such techniques being employed that would take into account a patient's individual (*not* based on population data) biology. The different levels coined by Nahum et al. are paraphrased from the original publication (6) below. The reader is directed to their publication for further details on this subject.

Level 0: no biological optimization.
Level I: individualization of prescription dose for specified level of toxicity [i.e., dose escalated in plans where possible using fixed normal tissue complication probability (NTCP) level for the organ at risk (OAR)].
Level II: the same as above, but the number of fractions is adjusted as well as the prescription dose based on an isotoxic basis.
Level III: biological cost functions used in the actual optimization of the dose distribution. Equivalent uniform dose (EUD), TCP, and NTCP parameters are used alongside conventional DVH parameters used in the optimization (e.g., Dmax, D99, V50%, mean).
Level IV: individual patient-specific data is used in the optimization of the patient's plan (e.g., use of functional imaging to highlight areas of hypoxia and other areas of increased radio-resistance).
Level V: using individual patient biology to optimize dose prescriptions in conjunction with any of the other levels.

We are currently at, or are approaching, level III where TPS are now incorporating biological models for either evaluation or optimization purposes. One of the benefits in using TCP or NTCP models is that a single value can be used in place of an array of dosimetric parameters describing points along a DVH curve. However, it is critical to assess the uncertainty affecting such values and what the key elements underpinning such uncertainty are. Different companies and TPS systems employ different formalisms and algorithms despite adopting the same radiobiological models, resulting in fundamental differences for the final calculations of the TCP/NTCP values and related uncertainties. An accurate understanding of how the uncertainties associated with the input parameters impact the final NTCP or TCP values is paramount and will support the increasing use of such approaches in planning radiotherapy treatments. Moreover, understanding how uncertainties are propagated in the TCP and NTCP calculations will identify the input parameters, which will need to be better defined along with their acceptable level of uncertainty to guide pre-clinical research efforts.

The aim of this study was to assess the impact of uncertainties in individual parameters used in TCP/NTCP calculations. This was achieved using in-house software developed in MATLAB™ vR2017a (The MathWorks Inc., MA, USA) that generates a simulated population of parameters within the constraints of the input parameters and their uncertainties, from which TCP or NTCP values and their uncertainties can be calculated. Dose is supplied using the 1D dose distribution as described by the planning DVH for the structures in question. The simulated data is generated using MatLab™'s normally distributed random number generator. A set of values are generated that are normally distributed with a mean, standard deviation, and size as specified by the user. The impact from single-parameter and multiple-parameter uncertainties was assessed for a range of clinically acceptable prostate plans, focusing on both survival probability and the probability of rectal complications. A similar approach was taken by Zhang et al. (7) for epithelial pleural mesothelioma where they applied an uncertainty to either the alpha term for the TCP model used (8) or the D_{50} parameter of the NTCP model used, the Lyman Kutcher Burman (LKB) model (9–12). This was to simulate heterogeneity in radiosensitivity of a population over a set dose range and focusing on therapeutic ratio for the prescription dose set. Our approach used uncertainties in all model input parameters and was focused not on a prescription dose but the planned organ doses (physical and biological) from clinical plans. No uncertainty was applied to the dose; however, there was a natural variation in doses as a result of the uncertainties applied to those parameters used in the biological dose calculation. The resulting dose (for the rectum especially) was very specific to the individual anatomy and the resulting plan generated. Plans were selected to represent the full range of possible doses that might be encountered.

The data reported show how the proposed approach can quickly generate uncertainty levels for TCP and NTCP models (for individual dose distributions as calculated by a treatment planning system for clinically acceptable plans) taking into consideration the uncertainties in the input parameters. The approach was tested for the specific case of prostate treatment and using the Lind (13) and LKB (9–12) models for TCP and NTCP, respectively, and highlighted the key role that the D_{50} parameter plays in the overall uncertainties. The study also indicates a strong synergy between the input parameters with small uncertainties on a single parameter having an overall large effect on the variation in the TCP/NTCP values generated when combined with uncertainties from the other parameters. The approach can be considered a first step in the

robustness validation of radiotherapy treatment planning based on biological optimization.

METHODS

Software

Software was developed in MATLAB, which allowed the import of dose volume histograms from clinical plans from different TPS. Different input formats available were for DVHs from BioSuite© (13), Eclipse™, Pinnacle™, and Raystation™. Dose and volume data were processed to allow the visualization of both cumulative and probability density histograms of the data. Using the linear quadratic formula, dose was converted into the equivalent dose if the treatment was given in 2 Gy fractions (LQED2) (14, 15) using the alpha/beta ratio (α/β) and the number of fractions as supplied by the user (see Equation 1). The α/β ratio is from the linear-quadratic relationship between cell survival and irradiated dose, D_i is the total dose per DVH dose-bin, and n is the number of fractions.

$$LQED2_i = D_i \cdot \frac{1 + \frac{D_i/n}{\alpha/\beta}}{1 + \frac{2}{\alpha/\beta}} \tag{1}$$

It is possible, in the software, to incorporate an uncertainty on the α/β value entered. This is used to generate a normally distributed virtual distribution of alpha and beta parameters. This is done using the normally distributed random number generator in MatLab™, which generates a distribution of values of size n. The values are generated such that they have a mean and standard deviation that matches that supplied by the user. Using these parameters, simulated variations in the LQED2 are calculated. After calculation of the LQED2 variations for a DVH, the required radiobiological models can be selected for the TCP and NTCP analysis.

The TCP model used for this study was Lind's model (16). Equation (2) shows the model formula as displayed in AAPM report 166 (4) for use with doses converted into LQED2 using Equation (1). The γ parameter is the slope parameter, D_{50} is the dose at which there is a 50% probability of tumor control occurring, and D_i and v_i are dose-bin values and corresponding fractional volume obtained from the DVH, respectively.

$$P(D_i) = exp\left(-exp\left(e\gamma - \frac{D_i}{D_{50}}\left(e\gamma - ln\left(ln2\right)\right)\right)\right)$$
$$TCP = \prod_{i=1}^{M} P(D_i)^{v_i} \tag{2}$$

The NTCP model used in this study was the LKB model (9–12) (see Equations 3–5), where effective dose (D_{eff}) is the uniform dose, which gives the equivalent biological effect to the structure in question as the planned inhomogeneous dose distribution from the DVH. The volume parameter n describes how serial or parallel an organ is. D_i and v_i are dose-bin values and corresponding fractional volume obtained from the DVH. The m parameter describes the slope of the NTCP vs. dose relationship, and D_{50} is the dose at which 50% chance of complications occur. Similar to what was described for the α/β uncertainty, uncertainties in all the above user input parameters (i.e., D_{50}, m, n) can be provided and are propagated to the final NTCP value calculated. TCP/NTCP values are collected for each simulation and the standard deviation calculated as a measure of the propagated uncertainty.

$$NTCP = \frac{1}{\sqrt{2\pi}} \int_{-\infty}^{t} e^{\frac{x^2}{2}} dx \tag{3}$$
$$t = \frac{D_{eff} - D_{50}}{mD_{50}} \tag{4}$$
$$D_{eff} = \left(\sum_i v_i D_i^{1/n}\right)^n \tag{5}$$

Input Parameters

DVHs from a selection of clinically acceptable prostate plans were used for this study. The conventional vs. hypofractionated high-dose intensity-modulated radiotherapy for prostate cancer (CHHIP) trial (17) planning constraints were used, and the prescription was either 74 or 78 Gy to allow a range of doses (and, therefore, positions on the TCP curve) to be evaluated. The input parameters investigated were taken from the literature. Initial study parameters for rectal toxicity were from Lyman et al. (10): D_{50} = 7,500 cGy, m = 0.1, n = 0.1, and α/β = 300 cGy. A study from Marzi et al. (18) was used for the later analysis as this study provided uncertainty values with its published parameters. Parameters used were for the prediction of greater than, or equal to, G2 late toxicity of the rectum; D_{50} = 7,600 ± 190 cGy, α/β = 230±60 cGy, n = 0.12, and m = 0.15 (no uncertainties were provided for the n and m parameters). The TCP values used for the prostate PTV analysis were from Okunieff et al. (19) for T2 multi-institute macroscopic disease; the slope parameter γ was used for the slope parameter γ in the Lind formulism, γ = 1.16 and D_{50} = 4,518 cGy. Data from the CHHIP trial (17) was used for the prostate α/β parameter: α/β = 180 cGy.

Analysis 1

For the first analysis, the uncertainty in each parameter was progressively increased to determine its specific impact on the final probability calculated. The analysis was performed by varying the uncertainty on one parameter at a time while assuming no error on the other parameters. This was carried out for both NTCP and TCP models investigating the rectum and for the prostate PTV. Analysis was performed using Lyman and Okunieff parameters for the NTCP and TCP calculation, respectively. For each model, in turn, and for each associated parameter, in turn, the MatLab code allowed simulated sets of parameters to be generated. These sets of input parameters were simulated such that the mean and standard deviation were as specified by the user. Using each value, in turn, from the simulated parameter set, an NTCP or TCP value was then calculated. Finally, a mean and standard deviation was calculated over the probabilities (either NTCP or TCP)

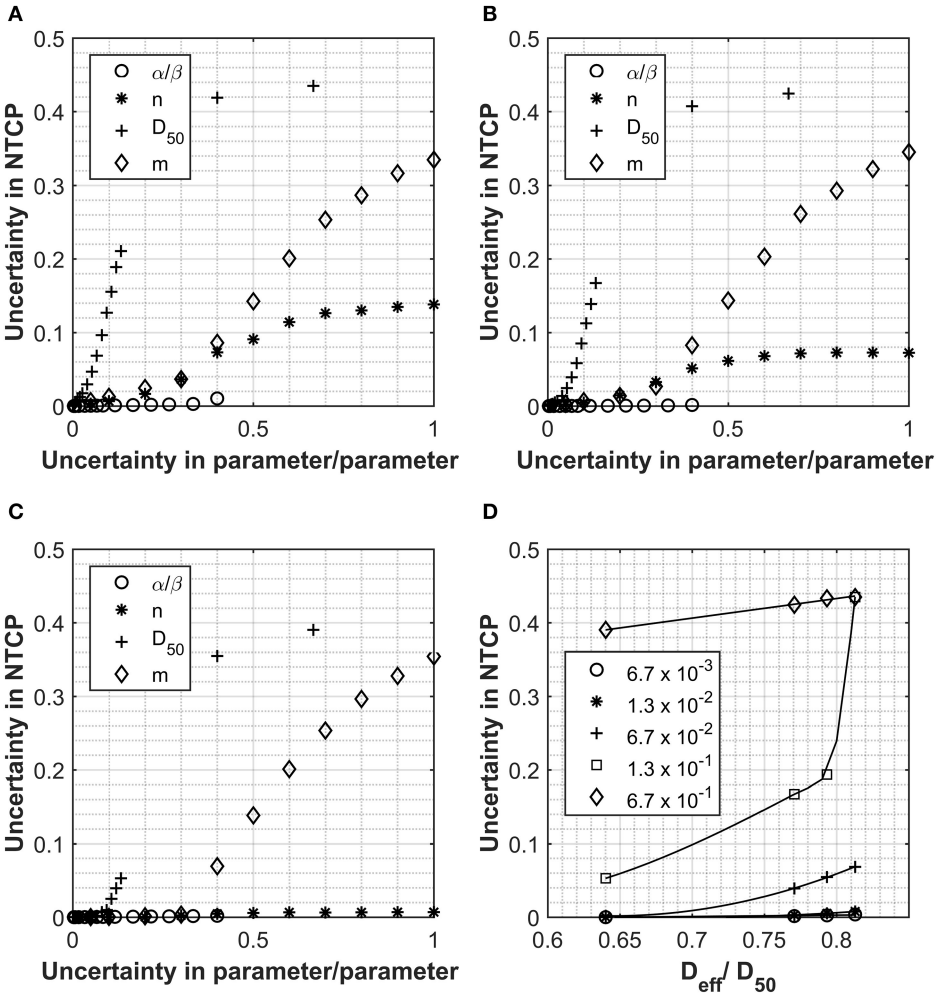

FIGURE 1 | Data collected for Analysis 1, normal tissue complication probability (NTCP) calculations using the Lyman Kutcher Burman (LKB) model for the rectum. **(A–C)** The impact on the overall NTCP uncertainties as a result of increasing uncertainty in the individual parameters. Values used for α/β, n, D_{50}, and m were 300 cGy, 0.1, 7,500 cGy, and 0.1, respectively, and the uncertainties applied are expressed as a fraction of each parameter. **(D)** shows the relationship between D_{eff} (as a fraction of the D_{50}) and the uncertainty in the final NTCP calculated for different levels of uncertainty in the D_{50} parameter; lines are for guiding the eye only.

calculated for an individual user-defined set of parameters and associated uncertainties.

Analysis 2

The second analysis involved using the Marzi parameters and uncertainties for calculating the NTCP for late rectal toxicity with the aim of determining the impact of such clinically acceptable values in the final probability calculated. For this analysis, all the reported uncertainties were simultaneously considered.

RESULTS

Figures 1A–C report how the uncertainties in the calculated NTCP values varies as a function of the uncertainties of the input parameters for three clinically approved treatment cases with different D_{eff} doses. **Figure 1D** shows how the D_{eff} as a percentage of the D_{50} parameter varies with uncertainty in NTCP for the four patient cases investigated. The different curves represent different levels of uncertainty applied to the D_{50}-simulated parameter sets. For all cases, the uncertainty in the NTCP calculation is dominated by the uncertainty in the D_{50} parameter, and it follows a similar trend with its value initially increasing exponentially to then reaching a plateau (NTCP uncertainty ∼42%) for D_{50} uncertainties >40%. There is an almost immediate increase in NTCP uncertainty for the patients with the higher D_{eff}, while a slight lag is observed for the lowest D_{eff} patient. A similar trend is observed for the NTCP uncertainty as a function of the m parameter, although the impact is much smaller than for the D_{50} parameter. Interestingly, the other parameters (including the α/β ratio) play a much smaller role contributing at most 15% of the NTCP uncertainty for 100% uncertainty in the input parameter. The uncertainty in the α/β ratio had the least impact on the overall uncertainty in NTCP. Only the patient with the very highest D_{eff} showed a significant increase in NTCP uncertainty

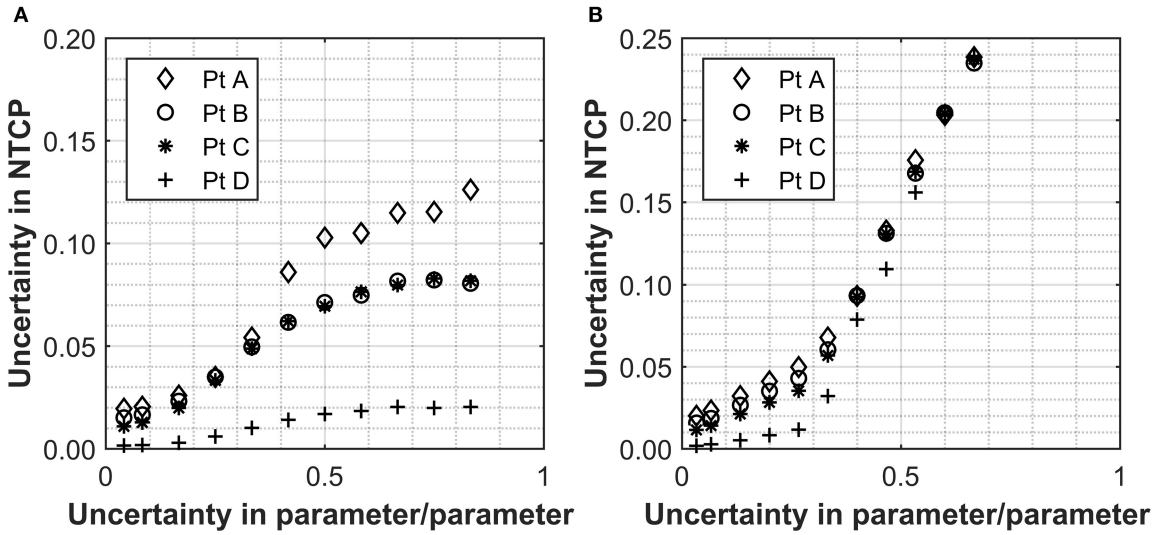

FIGURE 2 | The relationship between the uncertainty in n **(A)** and m **(B)** with the overall uncertainty in the NTCP calculated for a selection of patients with ranging values of rectum Deff. Values used for α/β, n, D_{50}, and m were 230 ± 60 cGy, 0.12, 7,600 ± 190 cGy, and 0.15, respectively (18). The uncertainties applied are expressed as a fraction in question and uncertainties are applied to either n or m individually with an uncertainty of zero used for the parameter not being assessed.

but that was small and not observed until the uncertainty in α/β reached 40%.

Considering the critical effect of D_{eff}, the uncertainties in the NTCP have been reported as a function of the D_{eff}/D_{50} ratio for different D_{50} uncertainties in **Figure 1D**. The data highlight how, for low D_{eff} plans, the uncertainty in NTCP are quite small irrelevant of the uncertainty in all the input parameters. However, as D_{eff} approaches 80% of the D_{50} value, the inaccuracy in determining the D_{50} has a major impact on the NTCP uncertainty. From **Figure 1**, it also emerges that an uncertainty of $D_{50} < 6.7\%$ would be required to maintain the NTCP uncertainty <5% irrespective of the D_{eff} values. The only exception is patient A (uncertainty in NTCP of 6.9%); however, this patient is at the upper limit of what would be accepted clinically for rectal doses.

In order to appreciate the level of uncertainties, which commonly affect clinically relevant NTCP estimations, the data set from Marzi et al. was used on the four patient cases highlighted above. This data set was selected as it investigated NTCP for a relevant biological endpoint and was one of the fewer studies quoting uncertainties on input parameters, 2.5 and 26% for D_{50} and α/β, respectively. Without further uncertainty considerations for the other parameters, the overall NTCP uncertainties calculated through the simulation approach are of the order of 2% for all cases investigated (**Figure 2**). This is significantly lower than the uncertainty that would result from a simple relative error propagation (i.e., square root of the sum of the individual relative errors squared), which would be dominated by the error in the α/β resulting in the overall uncertainty for the NTCP values of ∼26%. Moreover, the impact of uncertainties in the n or m parameters (the former in particular) become quickly significant pushing the NTCP uncertainty up to ∼10% for an input parameter error of 40% [**Figures 2A** (n), **B** (m)]. The effect was again more pronounced for patients with high D_{eff}. For small uncertainties in m or n, the uncertainty in NTCP derives mainly from the D_{50} uncertainty, and the differences in the uncertainties between the patients are a consequence of the different D_{eff} values.

As expected, the uncertainties in the input parameters combine for the overall NTCP calculations. For the patient with the highest D_{eff}, a D_{50} uncertainty alone of 2.5% (as for the Marzi data set) would result in an NTCP uncertainty of 1.9%, which remains the same when combined with the uncertainty in α/β (up to ∼26%). With a 26% uncertainty in the α/β alone, the uncertainty in the final NTCP parameter is 0.3% confirming that D_{50} is the dominant source of uncertainty where the fractionation regime is at, or close to, 2 Gy/fraction. This clearly shows that impact of the individual parameters is not linear with regard to uncertainty propagation.

In order to better appreciate the interlink between the input parameter uncertainties, variation in the NTCP values have been simulated for the four different clinical cases assuming uncertainties on all the parameters simultaneously. The Marzi data set was again used as starting point, and errors of ∼7 or ∼20% were added to both the n and m parameters. Data in **Figure 3A** (no uncertainty on m or n) clearly show the impact of uncertainty in the D_{50} and α/β on the NTCP values with minimum effect on the D_{eff}. It is also interesting to notice how the NTCP values are not symmetrically distributed around the NTCP curve but stretched toward the high NTCP values. This would have strong consequences for the setting of NTCP acceptance levels for a population case. The addition of uncertainties in the n and m parameters (see **Figures 3B,C**) increases the D_{eff} values moving the calculations toward the steeper part of the NTCP curve resulting, therefore, in higher NTCP values. While an individual ∼20% uncertainty in the n or

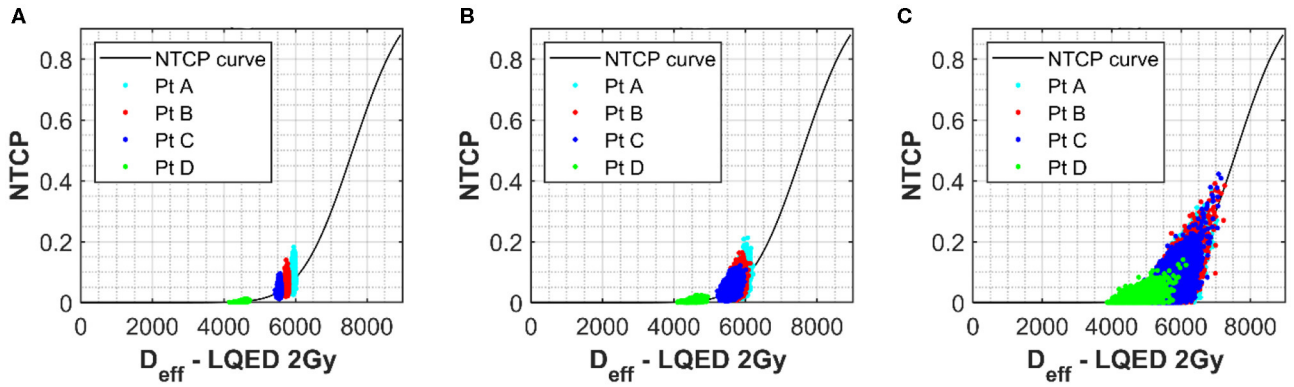

FIGURE 3 | (A) The NTCP vs. D_{eff} curve for grade 2 late toxicity of the rectum (18). Values used for α/β, n, D_{50}, and m were 230 cGy, 0.12, 7,600 cGy, and 0.15, respectively. Simulated rectum NTCP values for a selection of patients with uncertainties of 60 and 190 cGy applied to α/β and D_{50} parameters, respectively, have been plotted onto the curve for a selection of patients with different D_{eff}. Each point represents one simulation. **(B,C)** The simulated results when an additional uncertainty is applied to both m and n of 0.1 **(B)** and 0.3 **(C)**.

m parameters had only a small effect on the NTCP uncertainty when D_{50} ∼2.5% (**Figures 3A,B**), their combined effect pushes the NTCP values from <15% up to 40% despite a still low D_{50} uncertainty (**Figure 3C**). Therefore, when considering the combined uncertainties, it is important to keep the uncertainty in the m and n parameters below 0.3 for both parameters.

For a greater understanding of the overall picture, the range in the NTCP values calculated was also evaluated. The NTCP range without uncertainties applied to the m and n parameter was 0.03–0.21. This range increases to 0.01–0.21 for an uncertainty of 0.1 in m and n and then to 0–0.37 for an uncertainty of 0.3. This demonstrates a clear benefit in keeping the uncertainty for such parameters in the lower range (around the 0.1 mark) where the influence of these parameters is low.

Interestingly, a conventional error propagation approach would result in an average NTCP uncertainty of ∼28% for the input parameter set: D_{50} = 7,600 ± 190, α/β = 230 ± 60, n = 0.12 ± 0.01 and m = 0.15 ± 0.01, while the simulation approach estimates an uncertainty of ∼40% for the selected patients. The average NTCP values also change when accounting for uncertainties using the simulation approach due to the low-level boundary of NTCP = 0 and the data spread, which pushes the NTCP values up. **Table 1** shows the difference in the NTCP values and their related uncertainties comparing a conventional error propagation method to the simulation approach.

A similar approach has been also used to investigate the impact of the input parameter uncertainties on the TCP calculations (see **Figures 4A–D**). Each input parameter was individually considered for the four cases used so far and the relationship between uncertainty in TCP plotted against the uncertainties applied to the individual input parameters. The PTV was used as opposed to the prostate volume due the availability of data. For the one patient data set where both PTV and prostate volume were present, an analysis was performed with both structures, and data were very similar (see **Figures 4A,B**). D_{50} again appeared to be the most critical parameter, however, following a more linear response than for the NTCP investigations. The relationship between TCP and uncertainty in parameter appeared to be almost linear for all parameters and almost identical for all D_{eff} analyzed. The relationship D_{eff}/D_{50} vs. TCP uncertainty showed a slight benefit for the higher dose structures (see **Figure 4D**). From the limited range of cases investigated, uncertainty levels <10% for D_{50} would be required to achieve TCP uncertainties <5%. This could also be of importance when considering co-factors, e.g., clinical factors such as age, concurrent chemo, prior surgery, etc. A study on the impact of co-factors (20) dealt with differences in response through the D_{50} parameter. Using an uncertainty analysis such as described could be used clinically to define a level (uncertainty in D_{50}) at which it is appropriate to separate sub-groups out of a main group.

Uncertainties in the α/β parameter appear to have a negligible impact on the TCP uncertainty for the Lind model. This is due to the fractionation regime used and the fact that the influence of the α/β ratio is in converting from physical dose into LQED2. Owing to the fact that most of the voxels in the PTV will be receiving a fractionation of very close to 2 Gy per fraction, physical dose is almost identical to LQED2, which means that the parameter has very little impact on the structure dose being evaluated with this model. The only response observed were for patients B and C (**Figure 4C**), where there was a small impact on TCP uncertainty after an uncertainty in the parameter of greater than 0.5. These

TABLE 1 | Table showing the differences in both mean and uncertainty (standard deviation expressed as a percentage of the mean) for different methods of error propagation calculation, the conventional numerical method, and the simulated method discussed in this manuscript.

	Conventional error propagation		Simulation approach	
	NTCP	Error [%]	NTCP	Error [%]
Patient A	0.0733	28	0.0761	32
Patient B	0.0535	28	0.0557	36
Patient C	0.0367	28	0.0391	41
Patient D	0.0040	28	0.0046	63

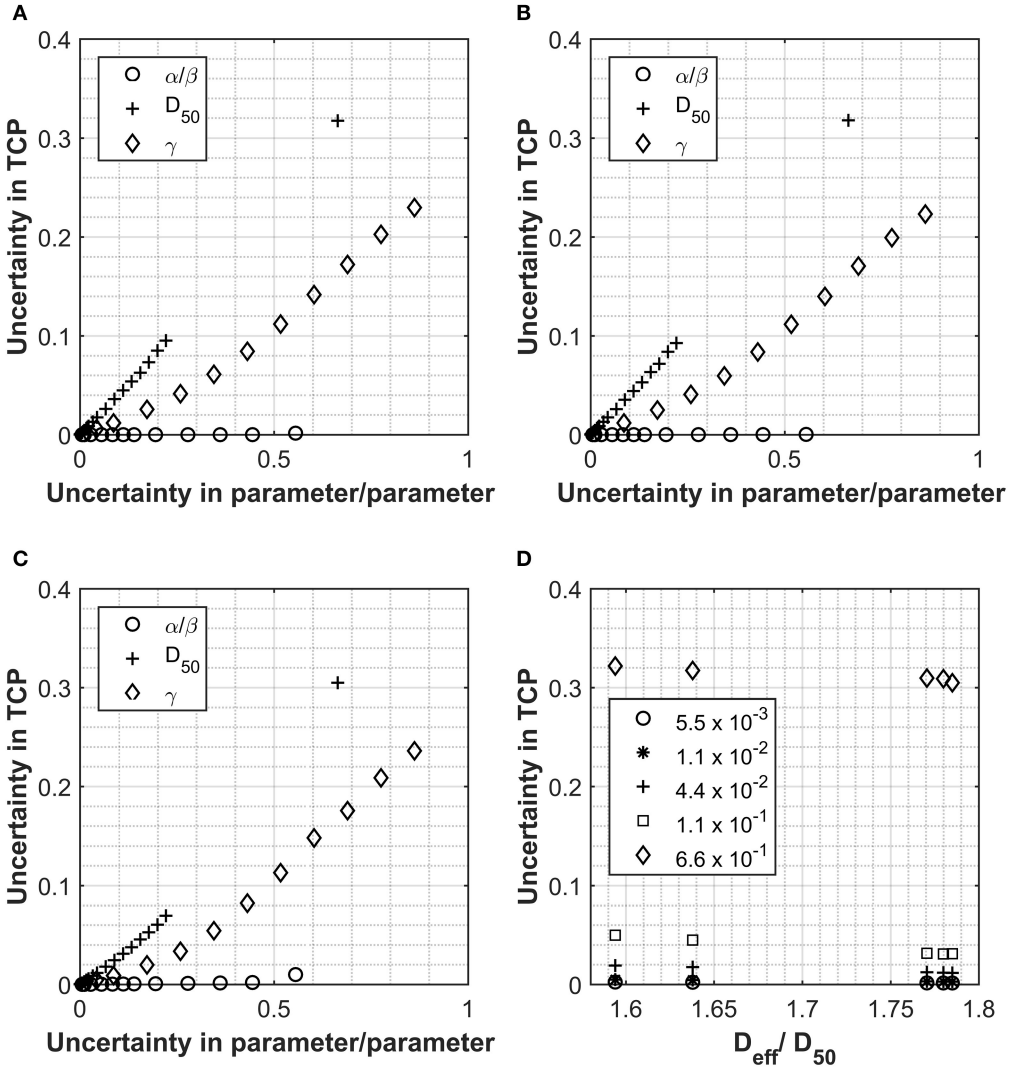

FIGURE 4 | Data collected for Analysis 1, tumor control probability (TCP) calculations using the Lind model for the prostate and prostate PTV. PTV and prostate data displayed in Panel **(A, B)** respectively for Pt A. Patient B PTV data displayed in Panel **(C)**. Panels show the impact on the overall TCP value as a result of increasing individual parameters. Values used for α/β, D_{50} and γ were 180 cGy, 4518 cGy and 1.16 respectively and the uncertainties applied are expressed as a fraction of each parameter. Panel **(D)** shows the relationship between D_{eff} (as a fraction of the D_{50}) and the uncertainty in the final TCP calculated for different levels of uncertainty in the D_{50} parameter.

patients had the highest Deff and, therefore, the highest dose per fraction (∼2.2 Gy/fraction), which is the farthest dose/fraction from 2 Gy, which is the fractionation that LQED2 is referenced to. While the behavior observed with these test cases would hold true for a large majority of treatments, it would not be the case for all. With the move toward more biologically driven treatments [e.g., use of biological treatment volume (BTV) and also dose escalation to parts of the tumor] (21), far less homogenous treatments are used with large variations in dose across the PTV; these could exceed 130%. In such cases, not all voxels within the PTV will have doses at, or around, 2 Gy/#, and this will influence the impact of alpha-beta ratio uncertainty.

Figures 5A–C show the shape of the TCP curve using prostate tumor parameters from Okunieff et al. (19). Similar to the NTCP analysis, uncertainties of 2.5 and 26% were applied to D_{50} and α/β, respectively, and the simulated data were plotted on the graph. Uncertainties of 0, 0.1, and 0.3 were applied to the γ parameter and are shown in **Figures 5A–C**, respectively. A value of −10 was selected for the "a" parameter to convert the DVH dose into an equivalent uniform dose (EUD), which is identical to D_{eff}, with n = 1/a. This value is widely used for tumor structures, and due to the fact that the variation in the dose distribution (from the DVH) for the structure is low (1% variation), it was thought to be an appropriate choice (22). Of course, in cases where there is dose escalation in the PTV, an appropriate value for the parameter "a" would have to be considered more carefully. There is little spread in the x-direction axis due to the fact that the only parameter with influence on dose is the α/β. As mentioned

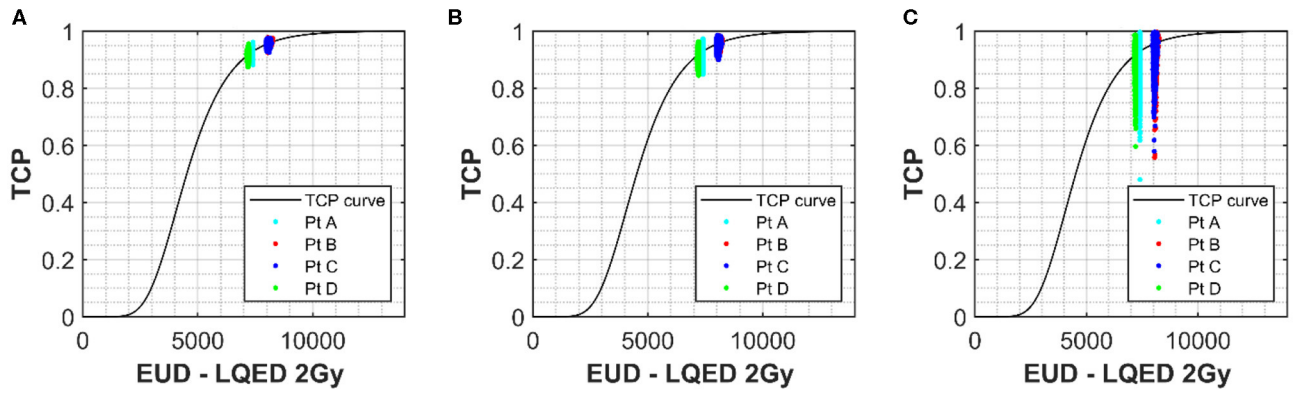

FIGURE 5 | The solid line shows the TCP vs. D_{eff} curve for the prostate PTV using values of 180 cGy, 4,518 cGy, and 1.16 for α/β, D_{50}, and γ respectively (18). Simulated prostate TCP values for a selection of patients with uncertainties of 47 cGy (26%) and 113 cGy (2.5%) applied to α/β and D_{50} parameters, respectively, have been plotted onto the curve for a selection of patients with different D_{eff}. **(A)** Shows no uncertainty applied to m for the simulated patients and **(B,C)** show uncertainties in γ of 0.1 and 0.3 respectively. D_{eff} for each simulation was calculated using the generalized equivalent uniform dose (EUD) formula, with parameter a set to −10.

earlier, where the fractionation regime is close to a standard one delivering 2 Gy/fraction, the α/β has little impact on the resulting LQED2 Gy calculated. Patients B and C have the largest spread because their dose/fraction is farthest away from the standard 2 Gy/fraction. However, while their x-axis uncertainty is larger, the overall uncertainty in the TCP is lower (e.g. 3.5% for Patient C (less standard dose/fraction) compared with 4.4% for Patient D (standard dose/fraction) for an uncertainty in γ of 30%), which is in keeping with the relationship shown in **Figure 4D**, where the higher-dose PTVs benefit from slightly improved uncertainties in TCP for different levels of uncertainty in the D_{50} parameter. As for the NTCP data, the combined effect of uncertainties in the input parameters quickly results in a significant increase in the TCP range. The TCP value range using an uncertainty in γ of 30% is high (∼48 to 99%) compared to a range of 88 to 96% for 0 uncertainty in γ, which increases to 85 to 97% for uncertainty in γ of 10%. While the actual TCP uncertainty (calculated as standard deviation of the probability data collected) is under 5% for all patients, the spreading of the range data shows a clear benefit (similar to the LKB for the NTCP data) of keeping uncertainties in the γ below 10%.

There was a dose effect with structures having D_{eff} or EUD at the periphery of the slope, having smaller uncertainty than those nearer the center of the curve. This is due to the fact that positions on the curve that are at the start or end of the curve are on a shallower gradient and, therefore, less impacted by changes in the slope. This software can be used as a tool to highlight where models maybe susceptible to steep increases in uncertainty size, e.g., for LKB, there are certain boundaries around which you may need to be especially careful; however, for the Lind model, there seems to be an almost linear increase in uncertainty in TCP for increasing uncertainty of the input parameters. The analysis also indicates the desired level of uncertainty for the input biological parameters in order to obtain TCP/NTCP values with reasonable confidence intervals. Such information can be used to focus future research efforts and improve estimation of biological parameters, which play a key role in TCP/NTCP models.

CONCLUSION

We have developed software, which allows an estimation of the uncertainty associated with TCP/NTCP predictions. The approach can provide insight on the uncertainty associated with TCP and NTCP calculations as a function of the uncertainty for the biological input parameters, the patient specific anatomy and the treatment dose. The software has been used to identify the dominant parameters (D_{50} for both models tested) with respect to uncertainty propagation. A conventional basic error propagation approach was also carried out, and it appeared to underestimate the error in the final NTCP/TCP values suggesting that different approaches should be considered. Owing to the fractionation regime of the treatment plans used for the study, there was little impact from the α/β parameter. For future work, there is a need to evaluate the impact for cases where the fractionation regime is significantly different, e.g., CHHIP trial and also in cases where inhomogeneous dose distributions are delivered to the PTV. This could soon be the norm especially now that imaging modalities are in place to identify such areas within the PTV with, e.g., increased radiosensitivity, increased clonogen density, and areas of increased hypoxia that would benefit from escalated doses. As we are moving into an era of highly conformal treatment planning, dose escalation, and novel approaches, such as dose painting, including radiobiological guidance as part of the optimization process, has been proposed to help inform the evaluation of the trade-off between tumor control and normal tissue toxicity (21, 23–25). Including uncertainty will allow evaluation and optimization of the robustness of plans to biological variations. Similarly, the algorithm can be used as a useful tool to compare radiobiological models both in terms of sensitivity and, through application to clinical studies, accuracy and guide further developments. The present approach estimates the errors on the NTCP/TCP values by simulating a random population of input parameters uncorrelated but each with constrains of their individual uncertainties. Future work will look at the inter-dependency of input parameter errors

using Bayesian approaches. An additional useful feature to include in this software would be to incorporate an uncertainty in the dose itself. Currently, the software only looks at the probability in input parameters; however, there is an uncertainty on dose from many contributing factors. It would be useful to be able to characterize the uncertainty in the DVH and incorporate dose uncertainties in the TCP/NTCP uncertainties. Finally, the study will also be extended to allow analysis of data from other TCP and NTCP calculations that incorporate the α/β directly into the models to a greater extent and not just through converting physical dose to LQED2, e.g., the Webb model (22).

DATA AVAILABILITY STATEMENT

The datasets generated for this study are available on request to the corresponding author.

AUTHOR CONTRIBUTIONS

GS, MB, and MH contributed to the conception and design of the study. MatLab software was written by MB. Implementation of the model was checked by MH and GS. Eclipse and Raystation plans and DVHs were prepared by MH. Simulations and data preparation for the manuscript were carried out by MB. Content discussion, writing/revision of the manuscript was carried out by MB, GS, and MH. All authors contributed to the article and approved the submitted version.

FUNDING

This work was funded by the UK Government's Department for Business, Energy and Industrial Strategy (BEIS) through the UK's National Measurement System programs.

ACKNOWLEDGMENTS

The authors would like to thank the UK Government's Department for Business, Energy and Industrial Strategy (BEIS) for funding this work.

SUPPLEMENTARY MATERIAL

The Supplementary Material for this article can be found online at: https://www.frontiersin.org/articles/10.3389/fonc.2020.01058/full#supplementary-material

REFERENCES

1. Report 89. *J Int Comm Radiat Units Meas.* (2016) 13:1–2. doi: 10.1093/jicru/ndw042
2. Radiologists TRC. *The Timely Delivery of Radical Radiotherapy: Standards and Guidelines for the Management of Unscheduled Treatment Interruptions*. 3rd ed. London: Royal College of Radiologists (2008).
3. Bijman RG, Breedveld S, Arts T, Astreinidou E, de Jong MA, Granton PV, et al. Impact of model and dose uncertainty on model-based selection of oropharyngeal cancer patients for proton therapy. *Acta Oncol.* (2017) 56:1444–50. doi: 10.1080/0284186X.2017.1355113
4. AAPM Task Group 166 TPC. *The Use and QA of Biologically Related Models for Treatment Planning Report of AAPM Task Group 166*. New York, NY (2012). p. 7–10.
5. Allen Li X, Alber M, Deasy JO, Jackson A, Ken Jee K-W, Marks LB, et al. The use and QA of biologically related models for treatment planning: short report of the TG-166 of the therapy physics committee of the AAPM. *Med Phys.* (2012) 39:1386–409. doi: 10.1118/1.3685447
6. Nahum AE, Uzan J. (Radio)biological optimization of external-beam radiotherapy. *Comput Math Methods Med.* (2012) 2012:329214. doi: 10.1155/2012/329214
7. Zhang L, Hub M, Thieke C, Floca RO, Karger CP. A method to visualize the uncertainty of the prediction of radiobiological models. *Phys Med.* (2013) 29:556–61. doi: 10.1016/j.ejmp.2012.11.004
8. Nahum AE, Sanchez-Nieto B. Tumour control probability modelling: basic principles and applications in treatment planning. *Phys Medica.* (2001) 17:13–23.
9. Lyman JT, Wolbarst B. Optimization of radiation therapy, III: a method of assessing complication probabilities from dose-volume histograms. *Int J Radiat Oncol Biol Phys.* (1987) 13:103–9. doi: 10.1016/0360-3016(87)90266-5
10. Lyman JT. Complication probability as assessed from dose-volume histograms. *Radiat Res.* (1985) 104:S13–9.
11. Lyman JT, Wolbarst AB. Optimization of radiation therapy, IV: a dose-volume histogram reduction algorithm. *Int J Radiat Oncol.* (1989) 17:433–6.
12. Kutcher GJ, Burman C. Calculation of complication probability factors for non-uniform normal tissue irradiation: the effective volume method gerald. *Int J Radiat Oncol.* (1989) 16:1623–30.
13. Uzan J, EswarVee C, Malik Z, Nahum AE. BioSuite, New software for radiobiological customisation of dose and fraction size in EBRT. *Radiother Oncol.* (2009) 92:S239. doi: 10.1016/S0167-8140(12)73231-0
14. Wheldon TE, Deehan C, Wheldon EG, Barrett A. The linear-quadratic transformation of dose – volume histograms in fractionated radiotherapy. *Radiat Oncol.* (1998) 46:285–95.
15. Yorke ED. Modeling the effects of inhomogeneous dose distributions in normal tissues. *Semin Radiat Oncol.* (2001) 11:197–209. doi: 10.1053/srao.2001.23478
16. Bengt K. Lind, Panayiotis Mavroidis B. Optimization of the dose level for a given treatment plan to maximize the complication-free tumor cure. *Acta Oncol.* (1999) 38:787–98. doi: 10.1080/028418699432950
17. Dearnaley D, Syndikus I, Mossop H, Khoo V, Birtle A, Bloomfi D, et al. Conventional versus hypofractionated high-dose intensity-modulated radiotherapy for prostate cancer : 5-year outcomes of the randomised, non-inferiority, phase 3 CHHiP trial. *Lancet Oncol.* (2016) 17:1047–60. doi: 10.1016/S1470-2045(16)30102-4
18. Marzi S, Saracino B, Petrongari MG, Arcangeli S, Gomellini S, Arcangeli G, et al. Modeling of α / β for late rectal toxicity from a randomized phase II study : conventional versus hypofractionated scheme for localized prostate cancer. J *Exp Clin Cancer Res.* (2009) 28:117. doi: 10.1186/1756-9966-28-117
19. Okunieff P, Morgan D, Niemierko A, Suit HD. Radiation dose-response of human tumors. *Int J Radiat Oncol Biol Phys.* (1995) 32:1227–37.
20. Peeters STH, Hoogeman MS, Heemsbergen WD, Hart AAM, Koper PCM, Lebesque J V. Rectal bleeding, fecal incontinence, and high stool frequency after conformal radiotherapy for prostate cancer: normal tissue complication probability modeling. *Int J Radiat Oncol Biol Phys.* (2006) 66:11–9. doi: 10.1016/j.ijrobp.2006.03.034
21. Tommasino F, Nahum A, Cella L. Increasing the power of tumour control and normal tissue complication probability modelling in radiotherapy: recent trends and current issues. *Transl Cancer Res.* (2017) 6:S807–21. doi: 10.21037/tcr.2017.06.03
22. Søvik Å, Ovrum J, Olsen DR, Malinen E. On the parameter describing the generalised equivalent uniform dose (gEUD) for tumours. *Phys Med.* (2007) 23:100–6. doi: 10.1016/j.ejmp.2007.09.001

23. Uzan J, Nahum AE, Syndikus I. Prostate dose-painting radiotherapy and radiobiological guided optimisation enhances the therapeutic ratio. *Clin Oncol*. (2016) 28:165–70. doi: 10.1016/j.clon.2015.09.006
24. van Leeuwen CM, Crezee J, Oei AL, Franken NAP, Stalpers LJA, Bel A, et al. 3D radiobiological evaluation of combined radiotherapy and hyperthermia treatments. *Int J Hyperthermia*. (2017) 33:160–9. doi: 10.1080/02656736.2016.1241431
25. Toma-Dasu I, Dasu A. Towards multidimensional radiotherapy: key challenges for treatment individualisation. *Comput Math Methods Med*. (2015) 2015:1–8. doi: 10.1155/2015/934380

Conflict of Interest: The authors declare that the research was conducted in the absence of any commercial or financial relationships that could be construed as a potential conflict of interest.

frontiers in Oncology

ORIGINAL RESEARCH
published: 22 July 2020
doi: 10.3389/fonc.2020.01174

Increased Dose to Organs in Urinary Tract Associates With Measures of Genitourinary Toxicity in Pooled Voxel-Based Analysis of 3 Randomized Phase III Trials

Marco Marcello[1,2], James W. Denham[3], Angel Kennedy[1], Annette Haworth[4], Allison Steigler[5], Peter B. Greer[6,7], Lois C. Holloway[8,9,10], Jason A. Dowling[6,11], Michael G. Jameson[8,9,10,12], Dale Roach[8,9,12], David J. Joseph[13,14,15], Sarah L. Gulliford[16,17], David P. Dearnaley[18], Matthew R. Sydes[19], Emma Hall[20] and Martin A. Ebert[1,2,14]*

[1] Department of Radiation Oncology, Sir Charles Gairdner Hospital, Nedlands, WA, Australia, [2] Department of Physics, University of Western Australia, Perth, WA, Australia, [3] School of Medicine and Public Health, University of Newcastle, Callaghan, NSW, Australia, [4] School of Physics, University of Sydney, Sydney, NSW, Australia, [5] Prostate Cancer Trials Group, School of Medicine and Public Health, University of Newcastle, Callaghan, NSW, Australia, [6] School of Mathematical and Physical Sciences, University of Newcastle, Callaghan, NSW, Australia, [7] Department of Radiation Oncology, Calvary Mater Newcastle, Waratah, NSW, Australia, [8] Department of Medical Physics, Liverpool Cancer Centre, Liverpool, NSW, Australia, [9] South Western Sydney Clinical School, University of New South Wales, Kensington, NSW, Australia, [10] Centre for Medical Radiation Physics, University of Wollongong, Wollongong, NSW, Australia, [11] CSIRO, St Lucia, QLD, Australia, [12] Cancer Research Team, Ingham Institute for Applied Medical Research, Liverpool, NSW, Australia, [13] School of Surgery, University of Western Australia, Perth, WA, Australia, [14] 5D Clinics, Claremont, WA, Australia, [15] GenesisCare WA, Wembley, WA, Australia, [16] Radiotherapy Department, University College London Hospitals NHS Foundation Trust, London, United Kingdom, [17] Department of Medical Physics and Biomedical Engineering, University College London, London, United Kingdom, [18] Academic UroOncology Unit, The Institute of Cancer Research and the Royal Marsden NHS Trust, London, United Kingdom, [19] MRC Clinical Trials Unit, Medical Research Council, London, United Kingdom, [20] Clinical Trials and Statistics Unit, The Institute of Cancer Research, London, United Kingdom

OPEN ACCESS

Edited by:
Giuseppe Sanguineti, Regina Elena National Cancer Institute (IRCCS), Italy

Reviewed by:
Mack Roach III, University of California, San Francisco, United States
Young Kwok, University of Maryland Medical Center, United States
Leila Evelyn Aitken Shelley, Western General Hospital, United Kingdom

***Correspondence:**
Marco Marcello
20739859@student.uwa.edu.au

Specialty section:
This article was submitted to Radiation Oncology, a section of the journal Frontiers in Oncology

Received: *01 January 2020*
Accepted: *09 June 2020*
Published: *22 July 2020*

Citation:
Marcello M, Denham JW, Kennedy A, Haworth A, Steigler A, Greer PB, Holloway LC, Dowling JA, Jameson MG, Roach D, Joseph DJ, Gulliford SL, Dearnaley DP, Sydes MR, Hall E and Ebert MA (2020) Increased Dose to Organs in Urinary Tract Associates With Measures of Genitourinary Toxicity in Pooled Voxel-Based Analysis of 3 Randomized Phase III Trials. Front. Oncol. 10:1174. doi: 10.3389/fonc.2020.01174

Purpose: Dose information from organ sub-regions has been shown to be more predictive of genitourinary toxicity than whole organ dose volume histogram information. This study aimed to identify anatomically-localized regions where 3D dose is associated with genitourinary toxicities in healthy tissues throughout the pelvic anatomy.

Methods and Materials: Dose distributions for up to 656 patients of the Trans-Tasman Radiation Oncology Group 03.04 RADAR trial were deformably registered onto a single exemplar CT dataset. Voxel- based multiple comparison permutation dose difference testing, Cox regression modeling and LASSO feature selection were used to identify regions where 3D dose-increase was associated with late grade $\geq$ 2 genitourinary dysuria, incontinence and frequency, and late grade $\geq$ 1 haematuria. This was externally validated by registering dose distributions from the RT01 (up to $n = 388$) and CHHiP (up to $n = 247$) trials onto the same exemplar and repeating the voxel-based tests on each of these data sets. All three datasets were then combined, and the tests repeated.

Results: Voxel-based Cox regression and multiple comparison permutation dose difference testing revealed regions where increased dose was correlated with genitourinary toxicity. Increased dose in the vicinity of the membranous and spongy

urethra was associated with dysuria for all datasets. Haematuria was similarly correlated with increased dose at the membranous and spongy urethra, for the RADAR, CHHiP, and combined datasets. Some evidence was found for the association between incontinence and increased dose at the internal and external urethral sphincter for RADAR and the internal sphincter alone for the combined dataset. Incontinence was also strongly correlated with dose from posterior oblique beams. Patients with fields extending inferiorly and posteriorly to the CTV, adjacent to the membranous and spongy urethra, were found to experience increased frequency.

Conclusions: Anatomically-localized dose-toxicity relationships were determined for late genitourinary symptoms in the urethra and urinary sphincters. Low-intermediate doses to the extraprostatic urethra were associated with risk of late dysuria and haematuria, while dose to the urinary sphincters was associated with incontinence.

Keywords: external beam radiotherapy, prostate cancer, urinary toxicity, voxel-based analysis, dose-toxicity relationships

INTRODUCTION

External beam radiotherapy (EBRT) is a prominent treatment option for prostate cancer patients (1), resulting in genitourinary (GU) toxicity with an even higher incidence than rectal toxicity (2). Relationships between treatment and patient specific risk factors, and GU toxicity have been established (3–5). More evidence of GU dose-toxicity relationships is required as more conformal techniques (6, 7) have introduced dose-escalated treatments.

Risk estimation used in establishing dose constraints for healthy organs at risk (OARs) associated with GU toxicity, such as the bladder and urethra, is typically based on considering the planned dose to the whole organ according to dose volume histogram (DVH) or dose surface histogram (DSH) information. This is problematic, however, as it ignores potential spatially varied intra-organ radio-sensitivity. Intuitively, planned dose to symptom related sub-regions (SRSs) of the urethra and bladder has been shown to be more predictive of GU symptoms than information derived from whole-organ DVHs (8). Further understanding of the relationship between dose and urinary toxicity at the voxel level could assist in identifying new SRSs, confirm established SRSs, and help provide these SRS with optimal dose constraints. This would restrict dose to healthy tissues with more spatial specificity, and thus help reduce GU toxicity in patients while maintaining tumor control.

Evidence is accumulating for the establishment of relationships between acute and late GU toxicity and spatial dose variance, particularly within the prostatic urethra (8), at various regions on the surface of the bladder (9, 10), the bladder trigone (11–13), the bladder neck (14) and at subregions within the bladder volume (8). No study to date, however, has performed a voxel-based analysis searching for correlation between dose variation and GU toxicity throughout the entire pelvic anatomy without the assumption that dose-toxicity relationships are limited to within OAR volumes or surfaces. This would enable the identification of dose-toxicity relationships in a broader range of the urinary tract, beyond the prostatic urethra to the membranous and spongy urethra. This extended naïve analysis may also improve understanding of how broader dose patterns, such as those representative of treatment technique (e.g., beam arrangement), relate to toxicity.

In this study, multiple voxel-based statistical methods were employed to investigate the association between 3D planned dose and measures of late GU toxicity in the entire pelvic anatomy. Many shortcomings have typically hindered previous voxel-based analyses (15, 16), including misregistration of planned 3D dose distributions, false positive rates due to the large number of voxels being statistically compared, not using time-to-event data, or not controlling for patient baseline characteristics. This study performed a combination of statistical tests to compensate for these shortcomings. High quality planned dose data from three prospective multi-center prostate radiotherapy clinical trials was utilized in order to assess the consistency of derived associations across cohorts, participating centers, employed radiotherapy techniques and overall treatment approach. "Validation" was defined as applying the same voxel-based tests to datasets from two other trials, with one trial providing a cohort similar to that of the primary dataset and the other substantially different (primarily in terms of treatment technique). This validation determined whether the emergent dose-toxicity patterns within the primary dataset were generalizable to these (similar and different) external datasets. This validation also had an exploratory element, in that it enabled the identification of new emergent patterns in the external datasets regardless of whether they matched the patterns in the primary datasets.

METHODS AND MATERIALS

RADAR Trial

Coordinated by the Trans-Tasman Radiation Oncology Group (TROG), the Randomized Androgen Deprivation and Radiotherapy (RADAR) phase 3 factorial trial (TROG 03.04) compared 6 months of androgen deprivation therapy (ADT) plus radiotherapy with 18 months of ADT with the same

radiotherapy, with and without bisphosphonates (17, 18). Accruing a total of 1071 men between October 2003 and August 2007, trial patients had T2 – T4 prostate cancer, undergoing dose-escalated 3D conformal EBRT with prescribed doses of 66, 70 or 74 Gy, or 46 Gy EBRT combined with a brachytherapy boost. Plans could be generated with any preferred combination of 3 or more conformal beams. 3D planned dose distributions with corresponding CT images including delineated CTV, rectum and bladder were collected and utilized as the primary dataset for this study. RADAR was the first TROG trial to incorporate full electronic review of the treatment planning data of accrued patients, facilitated by use of the SWAN system (19). See **Table 1** for information on each trial summarized for direct comparison.

RT01 Trial

The RT01 phase 3, international, superiority, randomized controlled trial compared dose-escalated conformal radiotherapy with standard-dose conformal radiotherapy (20, 21). Accruing a total of 843 men between January 1998 and December 2001, patients had confirmed T1b – T3a prostate cancer. The patients underwent 3D conformal EBRT with either a conventional prescribed dose of 64 Gy using prescribed arrangements of either 3 or 4 beams, or the same with an additional 4 or 6 beam boost to 74 Gy. ADT was recommended for 6 months. Similar 3D planned dose distributions, CT and delineation data were collected and utilized as the first external validation dataset of this study. The trial was managed by the Medical Research Council Clinical Trials Unit at University College, London.

CHHiP Trial

The CHHiP randomized phase 3 non-inferiority trial compared conventional and hypofractionated prostate Intensity Modulated Radiotherapy (IMRT) (22, 23). 3,216 men with T1b–T3a localized prostate cancer were accrued to the trial between October 2002 and June 2011. These underwent IMRT with a conventional prescribed dose of 74 Gy in 2 Gy fractions or hypofractionated courses of 60 Gy or 57 Gy in 3 Gy fractions, all with optional IGRT. ADT was recommended for 6 months, but was optional for patients with low risk disease. Similar 3D planned data was utilized as the second external validation data set for this study. Data was limited to an early cohort of CHHiP patients with processed DICOM information available at the time of acquisition. This trial was managed by the Clinical Trials and Statistics Unit at The Institute of Cancer Research, UK.

3D Data Preparation

Three CT image templates were chosen from an independent cohort of 39 prostate EBRT patients (26). Pairwise registrations of CT images within this cohort along with registrations between this cohort and the RADAR CT dataset were used to generate a normalized cross correlation similarity matrix. This matrix was used to perform clustering by affinity propagation to select the single most representative patient CT as an exemplar from the initial cohort. This exemplar was the first registration template (T1). Next, an anti-exemplar, most-different from T1, was chosen as a template on which the impact of registration and reference geometry could be tested (T2). Finally, a similar process was used to select a cropped exemplar, enabling analysis to be restricted to a small region including the prostate and immediate surrounding organs (T3). Dose distributions were then deformed onto these templates through application of deformation vector fields obtained from the image-based registrations above. All registration and dose deformation were performed in 3D. See **Appendix Section 2** for images of templates and registration pipelines. The 3D dose distributions from all phases of radiotherapy were summed together according to biologically isoeffective 2 Gy per fraction dose (EQD2) (27), using a spatially invariant alpha/beta ratio of 3, resulting in a single distribution for each patient registered onto each template. The number of voxels and dimensions of the CT image of each registration template and corresponding dose distributions are as follows:

T1: $332 \times 249 \times 64$ voxels
voxel size: $1.17 \times 1.17 \times 2$ mm

T2: $327 \times 178 \times 76$ voxels
voxel size: $1.17 \times 1.17 \times 2.5$ mm

T3: $132 \times 130 \times 129$ voxels
voxel size: $1.24 \times 1.24 \times 1$ mm

Dose distributions used in this analysis were uniformly sampled 1 in 2 voxels for T1 and T2 (due to the large number of total voxels). For T3, every voxel was used.

Genitourinary Toxicity Endpoints

Four time-to-event GU toxicity endpoints were included for analysis: urinary dysuria, haematuria, incontinence and frequency. For each endpoint, an event consisted of the first peak grade ≥ 2 occurrence during follow-up. For haematuria, however, grade ≥ 1 events were considered instead, due to the rarity of grade ≥ 2 events in the RADAR cohort. All toxicity events were late (> 3 months). All patients who experienced baseline toxicity of grade ≥ 1 were removed from analysis, apart from potential baseline dysuria and haematuria patients from the RT01 dataset, as this information was not available. Physician assisted toxicity grading was performed according to the Late Effects on Normal Tissue, Subjective, Objective, Management, Analytic (LENT/SOMA) questionnaire (28). For RADAR, patients were routinely followed up, post-treatment, approximately every 3 months for 18 months, every 6 months to 5 years, and annually thereafter. RT01 patients were assessed for toxicities at 6, 12, 18, and 24 months after commencing radiotherapy, and annually thereafter. CHHiP patients were assessed for late side-effects beginning 26 weeks after the start of radiotherapy and every 6 months for 2 years, and then annually thereafter.

Note that all voxel-based tests were repeated for all four endpoints, on all three trial datasets (RADAR, RT01 and CHHiP), as well as on a dataset combining patients from all trials ("Combined"). All three registration templates were used for RADAR for exploration of dose-toxicity associations, but only T1 for RT01, CHHiP and Combined for validation. The permutation and uni-voxel tests were performed using MATLAB R2016b

TABLE 1 | Clinical trials information.

	RADAR	RT01	CHHiP
Full name	Randomized Androgen Deprivation and Radiotherapy (TROG 03.04) Trial (17, 18)	A Randomized Trial of High Dose Therapy in Localized Cancer of the Prostate using Conformal Radiotherapy Techniques (20, 21)	Conventional or Hypofractionated High Dose Intensity Modulated Radiotherapy for Prostate Cancer Trial (22, 23)
Descriptors	• Randomized • Phase 3 • Factorial	• Randomized • Phase 3 • Superiority	• Randomized • Phase 3 • Non-inferiority
Goal	Comparison of 6 months of androgen deprivation therapy (ADT) plus radiotherapy with 18 months of ADT with the same radiotherapy	Comparison of 64 Gy standard-dose and 74 Gy dose-escalated conformal radiotherapy	Comparison of conventional and hypofractionated IMRT
Countries	Australia and New Zealand	United Kingdom, New Zealand, Australia	United Kingdom, New Zealand, Rep. of Ireland, Switzerland
Accrual years	Oct 2003 – Aug 2007	Jan 1998 – Dec 2001	Oct 2002 – Jun 2011
Total accrued patients	1071	843	3216
Date data was frozen	June 2015	Aug 2013	Oct 2017
Patients	Intermediate-risk (T2a) or high-risk (T2b+) prostate cancer	T1b – T3a prostate cancer	T1b – T3a prostate cancer
Radiotherapy type	Dose escalated 3D conformal EBRT	Standard or dose escalated 3D conformal EBRT	Dose escalated IMRT
Prescribed dose groups (dose per fraction)	66 Gy (2 Gy), 70 Gy (2 Gy), 74 Gy (2 Gy)	64 Gy (2 Gy), 74 Gy (2 Gy)	57 Gy (3 Gy), 60 Gy (3 Gy), 74 Gy (2 Gy)
Beam arrangements	Any preferred combination of 3 or more conformal beams	3 or 4 beams (anterior/lateral/posterior) for first 64 Gy, with additional 4 or 6 beam boost to 74 Gy	3 or 4 beams (anterior/lateral/posterior) or 5 beams or more if inverse planning utilized
Electronic review of treatment planning data	Full retrospectve review for all patients (19)	No electronic individual plan review (24)	Full prospective case reviews for the first 2 or 3 patients at each center (25)
Manager	TROG Cancer Research, NSW, Australia	Medical Research Clinical Trials Unit, London, UK	Clinical Trials and Statistics Unit, the Institute of Cancer Research, London, UK
Trial registration number	ISRCTN90298520	ISRCTN47772397	ISRCTN97182923
Ethics approval number	Approved by Hunter New England Human Research Ethics Committee Trial ID 03/06/11/3.02	North Thames Multi-center Research Ethics Committee number MREC/97/2/16	Approved by the London Multi-center Research Ethics Committee number 04/MRE02/10

and later versions (MathWorks, Natick MA), while the multi-voxel LASSO test was performed on R 3.6.1 (The R Foundation, Vienna). All 3D results were displayed using ITK-SNAP version 3.8.0 (29).

Voxel-Based Dose Difference Permutation Test

It is recommended that **Figure 1** is closely followed while reading through the following descriptions of the voxel-based tests. This test was performed according to the method outlined by Chen et al. (16). Following (**Figure 1A**), for each given toxicity endpoint, patients were divided according to whether they experienced a toxicity event at any time during follow-up. The mean dose distributions of each group were then compared to each other, voxel-by-voxel, to reveal regions of statistically significant dose difference. This method utilizes a non-parametric permutation-based test in which the group labels (for the with and without toxicity groups) are randomly swapped (permuted) and the dose-comparison repeated for each permutation. 1,000 permutations were performed generating a distribution of test statistics. Each test statistic was calculated as the maximum value across all voxels of the locally normalized dose difference in each voxel for both the true labeling sample and all random permuted samples. The null hypothesis was that the mean of the distribution of dose values in a given voxel for the with toxicity group is not different to the without toxicity group. To find voxels of significant dose-difference between the with and without toxicity groups at any given p-value α, a test statistic T was calculated as the $(1 - \alpha)$ percentile of the test statistics distribution from the random permuted samples. Voxels where the locally normalized dose difference values for the true labeling sample were greater than T are voxels where the dose difference between the with and without toxicity groups is statistically significant at the $p = \alpha$ level. In this study, thresholds of $p < 0.05$, $p < 0.1$, $p < 0.2$, and $p < 0.3$ were applied. Multiple p-value thresholds were applied in an attempt to thoroughly explore the dose difference, accounting for the conservative nature of the permutation test (see section discussion for further explanation). This test accounts for the multiple statistical testing problem arising from comparing a vast number of voxels (see **Appendix A** of Chen et al. for more detail). As shown in **Figure 1**, the mean dose difference map was imposed on the registration template,

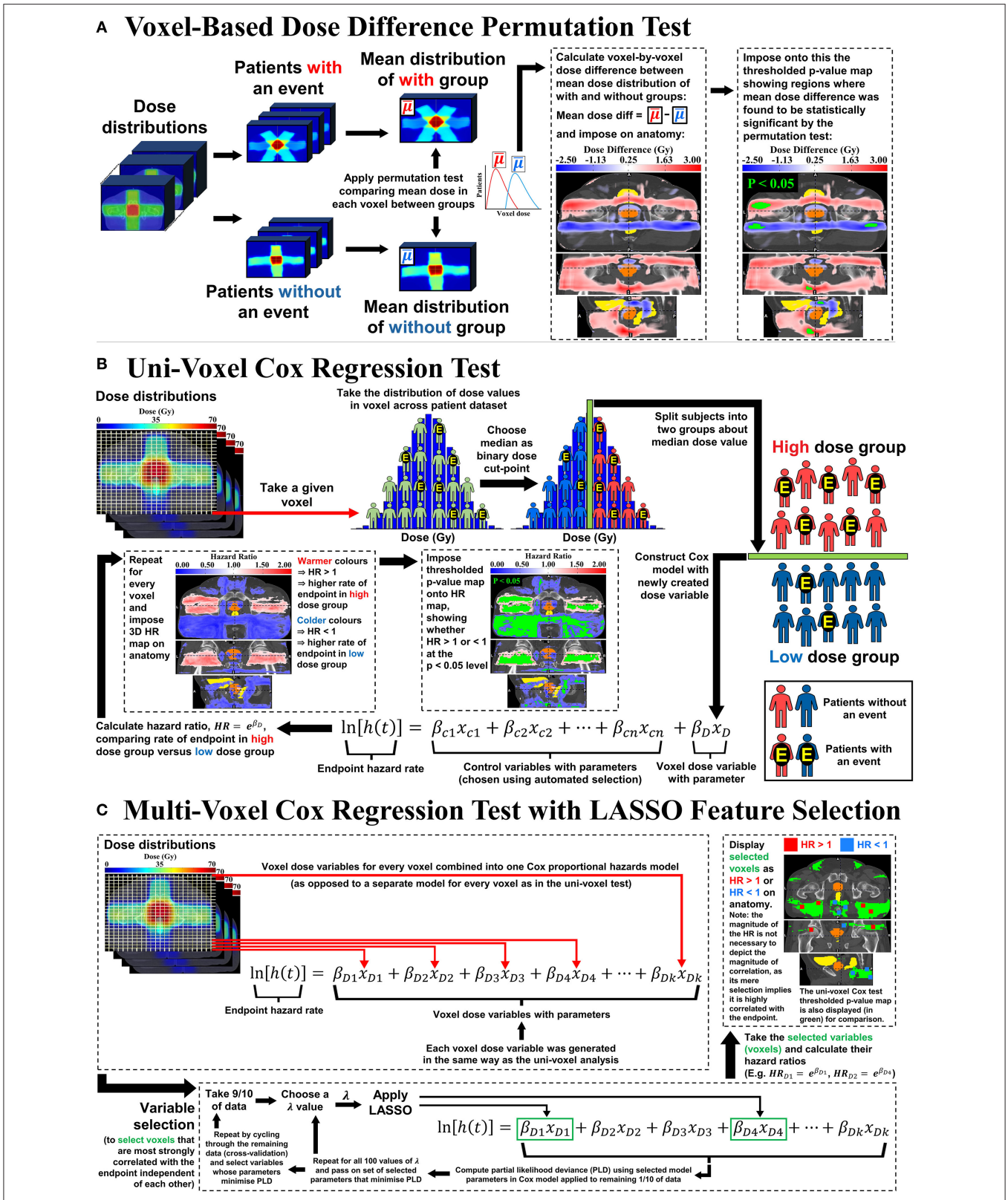

FIGURE 1 | Visual representation of the **(A)** Voxel-Based Dose Difference Permutation Test, **(B)** Uni-Voxel Cox Regression test and **(C)** Multi-Voxel Cox Regression Test with LASSO Feature Selection.

including the delineated CTV, bladder and rectum. If the dose difference reached statistical significance at one of the given *p*-value thresholds, then the voxels corresponding to this difference (the thresholded *p*-value map) were highlighted in green and imposed onto the dose difference map.

Uni-Voxel Cox Regression Test

This test generates a separate Cox proportional hazards model for each voxel (hence, "uni"-voxel), testing for association between dose in that voxel and incidence of the toxicity endpoint. Taking a given voxel, patients were divided into two groups about the median of the combined distribution of dose values, as in **Figure 1B**). The hazard ratio (HR) of the incidence of the endpoint between the high dose value group and low dose value group was then calculated, including a corresponding *p*-value determining whether the HR was significantly greater than or <1 at the $p < 0.05$ level. This HR therefore compares the incidence of toxicity between each dose group, indicating the dose-toxicity relationship at the given voxel. Age, prescribed dose, disease risk, cancer stage, baseline PSA concentration and number of treatment beams were patient baseline characteristics investigated as potential control variables in each model, attempting to eliminate their confounding influence at each voxel (30, 31). These were chosen through an automated selection procedure (see **Appendix Section 1** for details). Repeating this entire process for every voxel produced a 3D HR map and corresponding p-value map revealing the relationship between dose and the given toxicity endpoint across the pelvic anatomy. The continuous HR map was first imposed on the anatomical template. Following this, the thresholded p-value map was imposed onto the HR map, showing (in green) voxels where $HR < 1$ or $HR > 1$ at the $p < 0.05$ level.

Multi-Voxel Cox Regression Test With LASSO Feature Selection

This test is represented in **Figure 1C**). In contrast to the uni-voxel Cox regression test, this test combined all voxel-dose variables across the pelvic anatomy into a single multivariate Cox regression model (hence, "multi"-voxel). The LASSO [Least Absolute Shrinkage Selection Operator (32)] was then applied to select voxels (voxel-dose variables) that did not correlate with each other in the model, while still correlating strongly with the toxicity endpoint. The LASSO requires a pre-specified variable, λ, that determines the threshold by which features or variables (voxels) in the Cox model are selected. As λ increases, more features are excluded, until none are selected. 100 values of λ were pre-specified, equally spaced from that which selected all voxels to that which selected none. For each value of λ, one-in-ten cross validation was used to test the predictive ability of the resulting Cox model – the model comprised of the voxels selected by the LASSO. The final value of λ was that which maximized the given model's ability to predict the toxicity endpoint hazard rate by minimizing the partial likelihood deviance. The selected voxels were then imposed on the anatomical template, indicating whether $HR > 1$ or $HR < 1$ in each case. As with the univoxel Cox regression test, HRs in this test compared the incidence of the endpoint (e.g., dysuria) between the high dose group and low dose group at a given voxel, with the cut-point for dose determined in the same way. The LASSO enabled selection of voxels strongly correlated with the endpoint while accounting for inter-voxel dose correlation and the multiple testing problem.

RESULTS

Trial Datasets

Tables 2, **3** show the number of patients from each trial included for each endpoint's respective analysis, with corresponding patient variable and endpoint follow-up information, after patients were excluded due to loss of follow-up, missing data, and considering only patients receiving EBRT alone.

Voxel-Based Tests Results

The tests identified voxel clusters (VCs) and individual voxels within the pelvic anatomy where increased dose was associated with the four genitourinary toxicity endpoints. Several anatomical landmarks (different urethral regions, sphincters etc.) are mentioned in the following descriptions. These structures are not directly visible on the registration template CT images. Their locations are assumed based on their anatomical proximity to (or within) the prostate and the penile shaft, both visible on the registration template CT images. I.e., it is assumed the spongy urethra runs along the central axis of the visible penile shaft (extending approximately 10.2 cm anteriorly from the base of the penile shaft toward the surface of the patient on the T1 template), the membranous urethra is located between the apex of the prostate and the base of the penile shaft (extending approximately 3.4 cm inferiorly from the prostatic apex to the base of the penile shaft on the T1 template), the bladder neck is located where the bladder and prostate delineations meet (near the superior prostate boundary), and the external and internal sphincters are located immediately inferior to the prostatic apex and immediately superior to the central superior boundary of the prostate. **Figure 2** shows the visibility of the penile shaft on the T1 registration template CT image. It must be noted that these structures have not been delineated and therefore references to their location are approximate.

The following dose-toxicity patterns from all RADAR datasets on T1 were generally reproduced on the other registration templates (T2 and T3). The patterns were distorted according to the anatomical difference between the templates, but otherwise were similar, suggesting the revealed dose-toxicity association patterns are largely independent of choice of registration template (see **Appendix Section 3** for these results).

Dysuria

The pelvic dose associations for dysuria are shown in **Figure 3**. The consistent pattern is an association between a higher incidence of dysuria and increased dose in the membranous urethra and spongy urethra. This is particularly evident in the uni-voxel HR maps, revealing VCs with $HR > 1$ ($p < 0.05$) in the spongy urethra for RADAR, RT01 and Combined, and VCs with

TABLE 2 | The number of patients in each trial dataset, broken down by endpoint and baseline variables, including follow-up information, for dysuria and haematuria.

RADAR				RT01			CHHiP			COMBINED		
		Dysuria (grade ≥ 2)	**Haematuria (grade ≥ 1)**		**Dysuria (grade ≥ 2)**	**Haematuria (grade ≥ 1)**		**Dysuria (grade ≥ 2)**	**Haematuria (grade ≥ 1)**		**Dysuria (grade ≥ 2)**	**Haematuria (grade ≥ 1)**
Total number of patients		595	619	Total number of patients	388	388	Total number of patients	242	247	Total number of patients	1225	1254
Events		79 (13.3%)	86 (13.9%)	Events	36 (9.3%)	52 (13.4%)	Events	11 (4.5%)	21 (8.5%)	Events	126 (10.3%)	159 (12.7%)
Follow-up in months (min, max, med, IQR)		(12, 84, 54, 30)	(5, 95, 53, 30)	Follow-up in months (min, max, med, IQR)	(6, 158, 105, 57)	(6, 158, 102, 55)	Follow-up in months (min, max, med, IQR)	(6, 68, 60, 2)	(6, 68, 60, 2)	Follow-up in months (min, max, med, IQR)	(6, 158, 60, 30)	(5, 158, 61, 30)
Variables	Definitions			Definitions			Definitions			Definitions		
Age[1]	Median	69.4 yrs	69.4 yrs	Median	67.9 yrs	67.9 yrs	Median	67.4 yrs	67.4 yrs	Median	68.4 yrs	68.4 yrs
Prescribed dose	[66 Gy]	78	81	[64 Gy]	204	204	[57 Gy]	82	87	[66 Gy (RADAR), 64 Gy (RT01), 57 Gy and 60 Gy (CHHiP)]	467	455
	[70 Gy]	328	343	[74 Gy]	184	184	[60 Gy]	82	83			
	[74 Gy]	189	195				[74 Gy]	78	77	[70 Gy and 74 Gy (RADAR), 74 Gy (RT01), 74 Gy (CHHiP)]	857	799
Disease risk	[GS ≤ 7]	418	436	[T1b/c or T2a with (PSA + (GS - 6)*10) < 15]	110	110	[T1b/c or T2a with PSA ≤ 10 and GS ≤ 6]	57	59	[Lower risk group patients from each respective dataset]	648	605
	[GS > 7]	177	183	[T1b/c or T2a with (PSA + (GS - 6)*10) ≥ 15 or T2b/T3a]	278	278	[Any of the following: Stage ≥ T2b, 10 < PSA ≤ 20, GS > 6]	185	188	[Higher risk group patients from each respective dataset]	676	649
Cancer stage	[T2]	427	448	[≤ T2a (T1b, T1c, T2a)]	235	235	[≤ T2a (T1a, T1b, T1c, T2a)]	177	179	[Lower cancer stage group patients from each respective dataset]	839	862
	[T3/T4]	168	171	[> T2a (T2b, T3a)]	153	153	[> T2a (T2b, T2c, T3a)]	65	68	[Higher cancer stage group patients from each respective dataset]	386	392
Baseline PSA[a]	Median	14.04 ng/ml	14.00 ng/ml	Median	13.80 ng/ml	13.80 ng/ml	Median	11.70 ng/ml	11.70 ng/ml	Median	13.60 ng/ml	13.50 ng/ml
Number of beams	[3 beams]	65	65	[3 beams for phase 1 of treament]	228	228	[≤ 4 beams]	212	217	[≤ 4 beams (RADAR), 3 beams (RT01), ≤ 4 beams (CHHiP)]	816	841
	[4 beams]	311	331				[> 4 beams]	30	35			
	[5 beams]	79	81	[4 beams for phase 1 of treament]	160	160						
	[6 beams]	84	87							[> 4 beams (RADAR), 4 beams (RT01), > 4 beams (CHHiP)]	409	413
	[≥ 7 beams]	56	55									

[a] *This variable was divided into two approximately equal subgroups split about the median value.*

TABLE 3 | The number of patients in each trial dataset, broken down by endpoint and baseline variables, including follow-up information, for incontinence and frequency.

RADAR				RT01			CHHiP			COMBINED		
		Incontinence (grade ≥ 2)	**Frequency (grade ≥ 2)**		**Incontinence (grade ≥ 2)**	**Frequency (grade ≥ 2)**		**Incontinence (grade ≥ 2)**	**Frequency (grade ≥ 2)**		**Incontinence (grade ≥ 2)**	**Frequency (grade ≥ 2)**
Total number of patients		647	416	Total number of patients	354	264	Total number of patients	242	206	Total number of patients	1243	886
Events		24 (3.7%)	125 (30.0%)	Events	26 (7.3%)	131 (49.6%)	Events	6 (2.5%)	33 (16.0%)	Events	56 (4.5%)	289 (32.6%)
Follow-up in months (min, max, med, IQR)		(12, 84, 54, 36)	(12, 84, 18, 36)	Follow-up in months (min, max, med, IQR)	(6, 152, 103, 48)	(12, 158, 60, 90)	Follow-up in months (min, max, med, IQR)	(6, 68, 60, 2)	(6, 67, 60, 3)	Follow-up in months (min, max, med, IQR)	(6, 158, 60, 30)	(6, 158, 48, 46)
Variables	Definitions			Definitions			Definitions			Definitions		
Age[a]	Median	69.5 yrs	69.1 yrs	Median	67.6 yrs	68.6 yrs	Median	67.3 yrs	67.3 yrs	Median	68.4 yrs	68.4 yrs
Prescribed dose	[66 Gy]	82	43	[64 Gy]	186	141	[57 Gy]	84	72	[66 Gy (RADAR), 64 Gy (RT01), 57 Gy and 60 Gy (CHHiP)]	433	326
	[70 Gy]	358	230	[74 Gy]	168	123	[60 Gy]	81	70			
	[74 Gy]	207	143				[74 Gy]	77	64	[70 Gy and 74 Gy (RADAR), 74 Gy (RT01), 74 Gy (CHHiP)]	810	560
Disease risk	[GS ≤ 7]	457	288	[T1b/c or T2a with (PSA + (GS - 6)*10) < 15]	101	74	[T1b/c or T2a with PSA ≤ 10 and GS ≤ 6]	58	51	[Lower risk group patients from each respective dataset]	616	413
	[GS > 7]	190	128	[T1b/c or T2a with (PSA + (GS - 6)*10) ≥ 15 or T2b/T3a]	253	190	[Any of the following: Stage ≥ T2b, 10 < PSA ≤ 20, GS > 6]	184	155	[Higher risk group patients from each respective dataset]	627	473
Cancer stage	[T2]	465	305	[≤ T2a (T1b, T1c, T2a)]	216	156	[≤ T2a (T1a, T1b, T1c, T2a)]	176	152	[Lower cancer stage group patients from each respective dataset]	857	613
	[T3/T4]	182	111	[> T2a (T2b, T3a)]	138	108	[> T2a (T2b, T2c, T3a)]	66	53	[Higher cancer stage group patients from each respective dataset]	386	273
Baseline PSA[a]	Median	14.04 ng/ml	14.25 ng/ml	Median	13.40 ng/ml	14.00 ng/ml	Median	11.70 ng/ml	11.85 ng/ml	Median	13.45 ng/ml	13.60 ng/ml
Number of beams	[3 beams]	69	44	[3 beams for phase 1 of treament]	212 142	159 105	[≤ 4 beams]	212	181	[≤ 4 beams (RADAR), 3 beams (RT01), ≤ 4 beams (CHHiP)]	838	607
	[4 beams]	345	223	[4 beams for phase 1 of treament]			[> 4 beams]	30	25		405	279
	[5 beams]	85	58							[> 4 beams (RADAR), 4 beams (RT01), > 4 beams (CHHiP)]		
	[6 beams]	89	52									
	[≥ 7 beams]	59	39									

[a] *This variable was divided into two approximately equal subgroups split about the median value.*

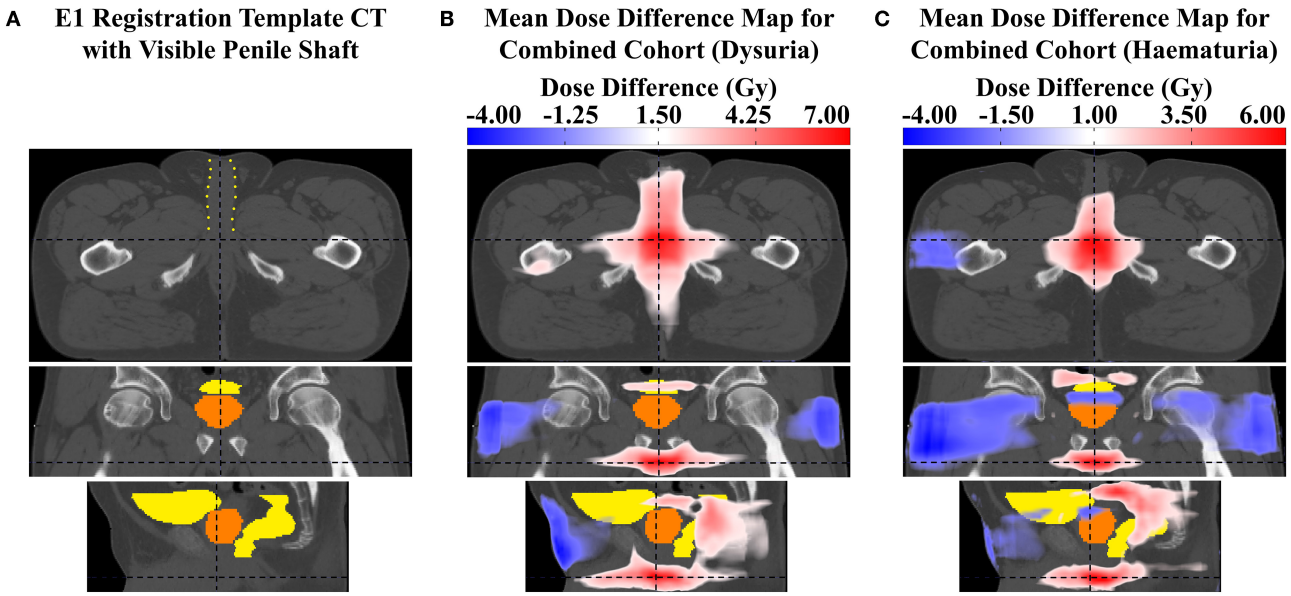

FIGURE 2 | (A) slices of the T1 registration template CT image with the penile shaft (containing the spongy urethra) visible despite not being delineated, outlined in yellow dots. Mean dose difference maps between patients with and without **(B)** grade ≥ 2 dysuria and **(C)** grade ≥ 1 haematuria, on approximately the same urethral slice as the image in **(A)** for comparison. It is evident that maximum dose difference is most likely occurring at the urethra.

HR > 1 ($p > 0.05$) here for CHHiP. These are most evident in the axial and sagittal planes. For Combined, VCs with HR > 1 ($p < 0.05$) are also present in the vicinity of the membranous urethra. For RT01, HR > 1 ($p < 0.05$) VCs are also found surrounding the extraprostatic urethra, particularly laterally and in the posterior beam region adjacent to the extraprostatic urethra (seen in the axial plane). Although the permutation test found no significant mean dose difference up to the $p < 0.3$ level, the corresponding mean dose difference maps are generally consistent with these associations. Patients who experienced dysuria had up to 7 Gy more planned dose on average in the corresponding associated regions for RADAR, RT01 and Combined, and 4 Gy for CHHiP. **Figure 7** shows that patients with and without dysuria in the combined dataset had total doses of 48.2 and 42.2 Gy, respectively at a point near the membranous urethra, and 19.7 and 16.2 Gy at a point near the spongy urethra. It is also noteworthy that patients experiencing dysuria had up to 7 Gy more dose near the bladder neck region for RADAR and RT01, with patients in each cohort having mean total doses here of approximately 44 and 51 Gy, respectively (see **Appendix Section 4** for mean dose distributions). For Combined, the dominant spongy and membranous urethral dose-association is confirmed by the corresponding multi-voxel results, as the LASSO selected voxels with HR > 1 in the same regions as the HR > 1 ($p < 0.05$) VCs found in the uni-voxel map. The RADAR uni-voxel maps on the T3 template (see **Appendix Section 3**) confirm the membranous and spongy urethra correlation and reveal some correlated voxels in the prostatic urethra also. In conclusion, patients with increased dose in the vicinity of the membranous and spongy urethra experienced a higher incidence of late grade ≥ 2 dysuria.

Haematuria

Figure 4 shows the results for haematuria. Similar to dysuria, the major association is between increased dose in the membranous and spongy urethra and increased haematuria. The uni-voxel HR maps show VCs with HR > 1 ($p < 0.05$) in these regions for RADAR (including for T3), CHHiP and Combined. RT01 results are not consistent with these findings, revealing VCs with HR > 1 ($p < 0.05$) in the posterior oblique beam regions. Reduced dose in the lateral beam regions is also correlated with increased haematuria, evident in the HR > 1 ($p < 0.05$) VCs found in these regions for RADAR and Combined, particularly visible on the coronal planes. Although the permutation test found no regions of significant dose difference, the corresponding mean dose difference maps confirm these dominant associations for all datasets. For example, these reveal that patients who experienced haematuria had up to 8, 5, and 6 Gy more dose on average in the vicinity of the membranous and spongy urethra for RADAR, CHHiP and Combined respectively. **Figure 7** shows that patients with and without haematuria in the combined dataset had total doses of 47.4 and 42.3 Gy, respectively at a point near the membranous urethra, and 18.6 and 16.5 Gy at a point near the spongy urethra. The dose difference maps also show that patients with haematuria had up to 5, 8 and 4 Gy more dose on average near the bladder neck/trigone region for RT01, CHHiP and Combined, respectively. The LASSO selected a voxel with HR > 1 directly posterior to the spongy/membranous urethra region for Combined. It also selected HR < 1 voxels in the lateral beam region. In conclusion, patients with increased dose in the vicinity of the spongy and membranous urethra experienced a higher incidence of late grade ≥ 1 haematuria. **Figure 2** shows how the maximum dose difference for both dysuria and haematuria was

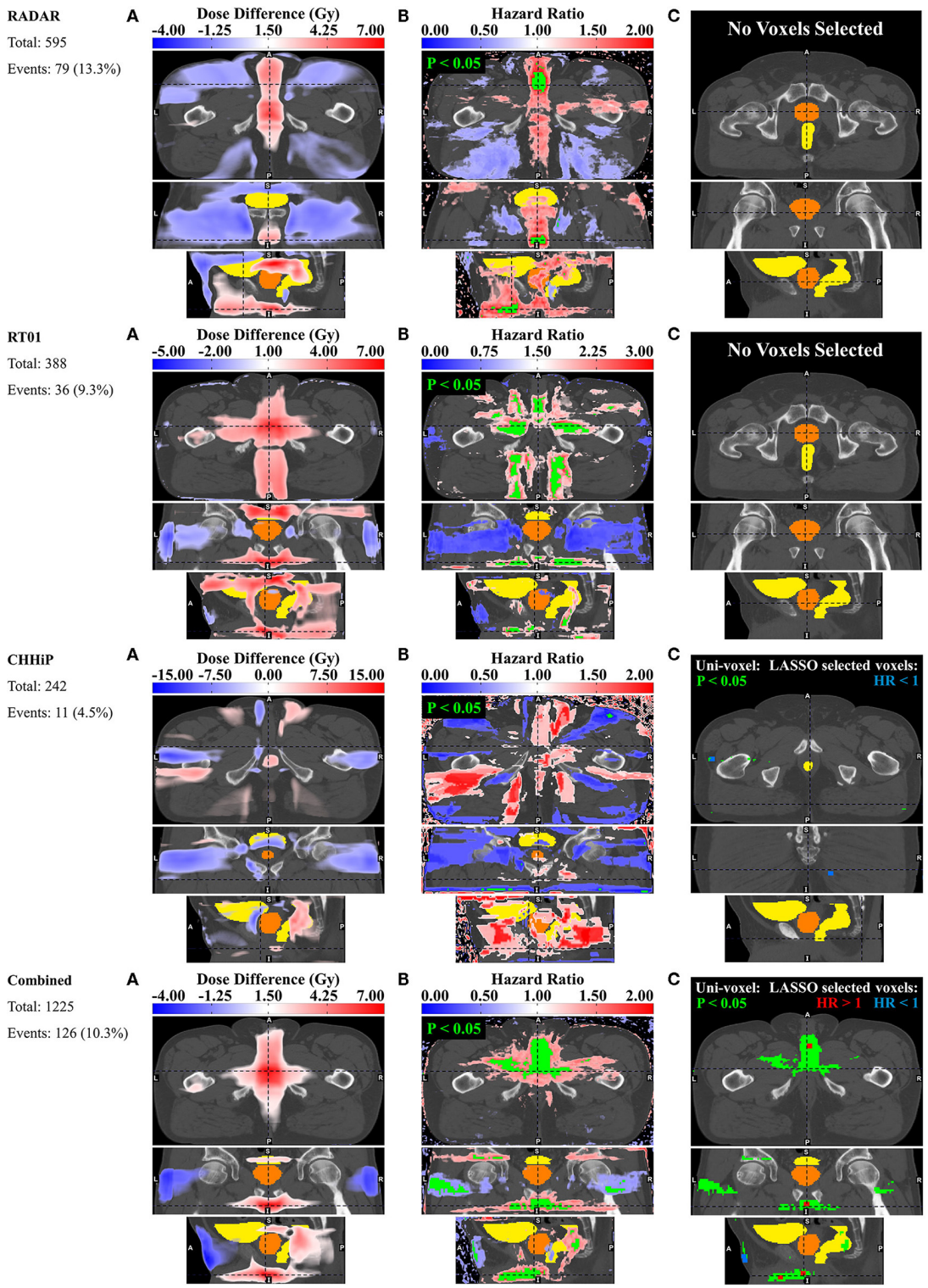

FIGURE 3 | Results for dysuria. Corresponding axial, coronal and sagittal slices (top to bottom) of **(A)** mean dose difference maps, **(B)** uni-voxel Cox regression HR and *p*-value maps and **(C)** multi-voxel Cox regression LASSO HR maps (with uni-voxel *p*-values for comparison), for respective data sets. "No Voxels Selected" implies the LASSO selected no voxels of significant correlation with the endpoint within the patient region. The slices chosen for display are those which coincide with the most dominant emergent dose-endpoint patterns, indicated in corresponding planes with dashed lines. Tones of red correspond to regions where increased dose is associated with incidence of dysuria (HR > 1), while tones of blues correspond to regions where reduced dose is associated with incidence of dysuria (HR < 1). The CTV is delineated in orange while the bladder and rectum are delineated in yellow. Anatomical directions left (L), right (R), superior (S), inferior (I), anterior (A), and posterior (P) are also indicated.

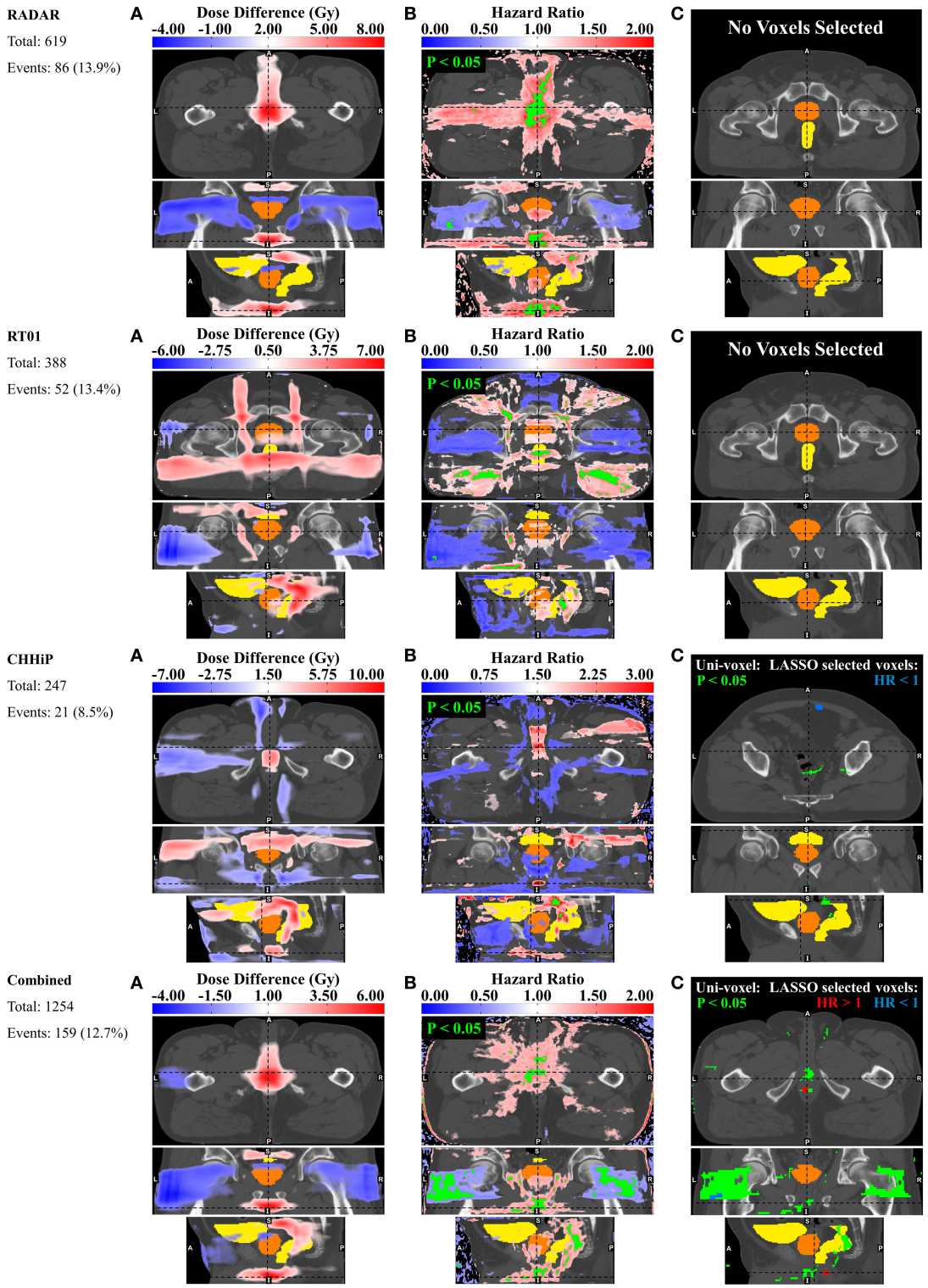

FIGURE 4 | Results for haematuria. Corresponding axial, coronal and sagittal slices (top to bottom) of **(A)** mean dose difference maps, **(B)** uni-voxel Cox regression HR and *p*-value maps and **(C)** multi-voxel Cox regression LASSO HR maps (with uni-voxel *p*-values for comparison), for respective data sets. "No Voxels Selected" implies the LASSO selected no voxels of significant correlation with the endpoint within the patient region. The slices chosen for display are those which coincide with the most dominant emergent dose-endpoint patterns, indicated in corresponding planes with dashed lines. Tones of red correspond to regions where increased dose is associated with incidence of haematuria (HR > 1), while tones of blues correspond to regions where reduced dose is associated with incidence of haematuria (HR < 1). The CTV is delineated in orange while the bladder and rectum are delineated in yellow. Anatomical directions left (L), right (R), superior (S), inferior (I), anterior (A), and posterior (P) are also indicated.

located in the extraprostatic urethra (using the visibility of the penile shaft).

Incontinence

Figure 5 shows the results for incontinence. There is some evidence of an association between incontinence and increased dose at the urethral sphincters, while the dominant association is between incontinence and patients treated with posterior oblique beams and posteriorly extended lateral beams. The uni-voxel HR maps show VCs with HR > 1 ($p < 0.05$) in the vicinity of the internal and external urethral sphincters for RADAR, while a smaller HR > 1 ($p < 0.05$) VC is present near the internal sphincter for Combined, most clearly visible in the coronal plane. Larger VCs with HR > 1 ($p < 0.05$) are present in the vicinity of the internal and external sphincters for RADAR on the T3 template, with the LASSO confirming this internal sphincter association by selecting HR > 1 voxels near the internal sphincter. The permutation test found no VCs of dose difference up to $p < 0.3$, but the corresponding dose difference maps did show that patients with incontinence had up to 10 Gy more dose on average than patients without incontinence near both sphincters for RADAR (more clearly seen on the T3 template), and up to 5 Gy more for Combined. RADAR patients had a mean total dose of ∼69 Gy near the internal sphincter and 65 Gy at the external sphincter, reading off the mean dose distribution on the T3 template in **Appendix Section 4**. Larger VCs with HR > 1 ($p < 0.05$) were present in the posterior oblique beam regions for RADAR, RT01 and Combined, and in the posterior extension of the lateral beams for Combined and RT01. The dose difference maps show patients with incontinence had up to 10 Gy more dose in the lateral beam posterior extension region than patients without incontinence for RT01 and CHHiP, and 9 Gy more for Combined. The LASSO selected HR > 1 voxels in the posterior oblique beam lateral beam posterior lateral beam extension regions for Combined. Only 6 grade ≥ 2 incontinence events were present for CHHiP, thus all voxel HRs were at $p > 0.05$. In summary, patients with increased dose in the vicinity of urethral sphincters and in posterior oblique beam and lateral beam posterior extension regions had a higher incidence of late grade ≥ 2 incontinence.

Frequency

Figure 6 shows the results for frequency. The uni-voxel HR maps in this figure reveal the presence of VCs with HR > 1 ($p < 0.05$) in anterior and posterior beam regions inferior to the prostate for RADAR, the left lateral beam for RT01, and (like RADAR) the posterior beam region extending inferiority to the prostate for CHHiP and Combined. Combined showed VCs in the posterior beam region extending inferiorly to the prostate. The permutation test revealed VCs of significant dose difference ($p < 0.05$) in this same region for Combined, where patients with frequency experienced up to 6 Gy more planned dose on average than patients without frequency. RADAR patients with frequency experienced up to 10 Gy more average dose in the same posterior beam region. The LASSO generally selected voxels with HR > 1 in the same regions as the significant HR > 1 VCs found in the uni-voxel maps, for RT01 and Combined, further confirming these associations. In summary, the dominant association revealed was the relationship between patients experiencing more dose in regions extending inferiorly and posteriorly to the prostate and a higher incidence of late grade ≥ 2 frequency.

DISCUSSION

In this study, quality-assured and reviewed planning data collected in multi-center clinical trials with extensive follow-up was used to derive independent datasets for analysis. Deformable registration of planned dose distributions onto common templates enabled identification of associations between voxel-dose and measures of GU toxicity across the pelvic anatomy. This is the first study to generate dose-GU toxicity relationships of this nature without the assumption that these necessarily occur on or within OARs.

Although no individual voxel-based test in this study addressed every typical shortcoming of voxel- based analyses, each test did address specific problems such that a consistent result across all techniques could be considered independent of these issues. Late genitourinary toxicity differs from late gastrointestinal (GI) toxicity in that the occurrence of late GI toxicity generally reaches a plateau after 3 years post-RT, while late GU toxicity more frequently extends past 3 years (33). This suggests extended follow-up is necessary for the accurate estimation of late GU toxicity. The uni-voxel and multi-voxel Cox regression tests utilized post-treatment time-to-event endpoints with follow-up times extending from approximately 6 to 13 years, enabling an accurate accounting of late GU symptoms. The uni-voxel test controlled for patient baseline characteristics, attempting to remove their confounding influence upon discovered dose-toxicity correlations. The LASSO regression ensured selected voxels, which strongly correlated with GU endpoints, were independent of correlation with other voxels. Incorporating all voxels in the model together accounted for the multiple comparisons problem. The permutation dose difference test similarly accounted for the multiple comparisons problem, while also being the only method of the three that excluded noisy extraneous voxels.

Late grade ≥ 2 dysuria was consistently associated with increased dose to the spongy and membranous urethra regions in this study. Mylona et al. discovered a subregion in the posterior bladder, partially in the trigone, where increased dose was correlated with late grade ≥ 1 dysuria (8). Their study was limited to the bladder and prostatic urethra. Utilizing bladder dose-surface maps, Yahya et al. discovered a similar correlation between late grade ≥ 2 dysuria and increased dose at the posterosuperior bladder surface, near the bladder trigone, however concluded that dysuria was not associated with dose received directly by the trigone (10). The authors predicted, rather, that dose in this region "might also correlate with dose to other organs in the genitourinary system outside the bladder," alluding to further studies "anticipated to properly investigate this possibility, including the dose to the posterior prostatic

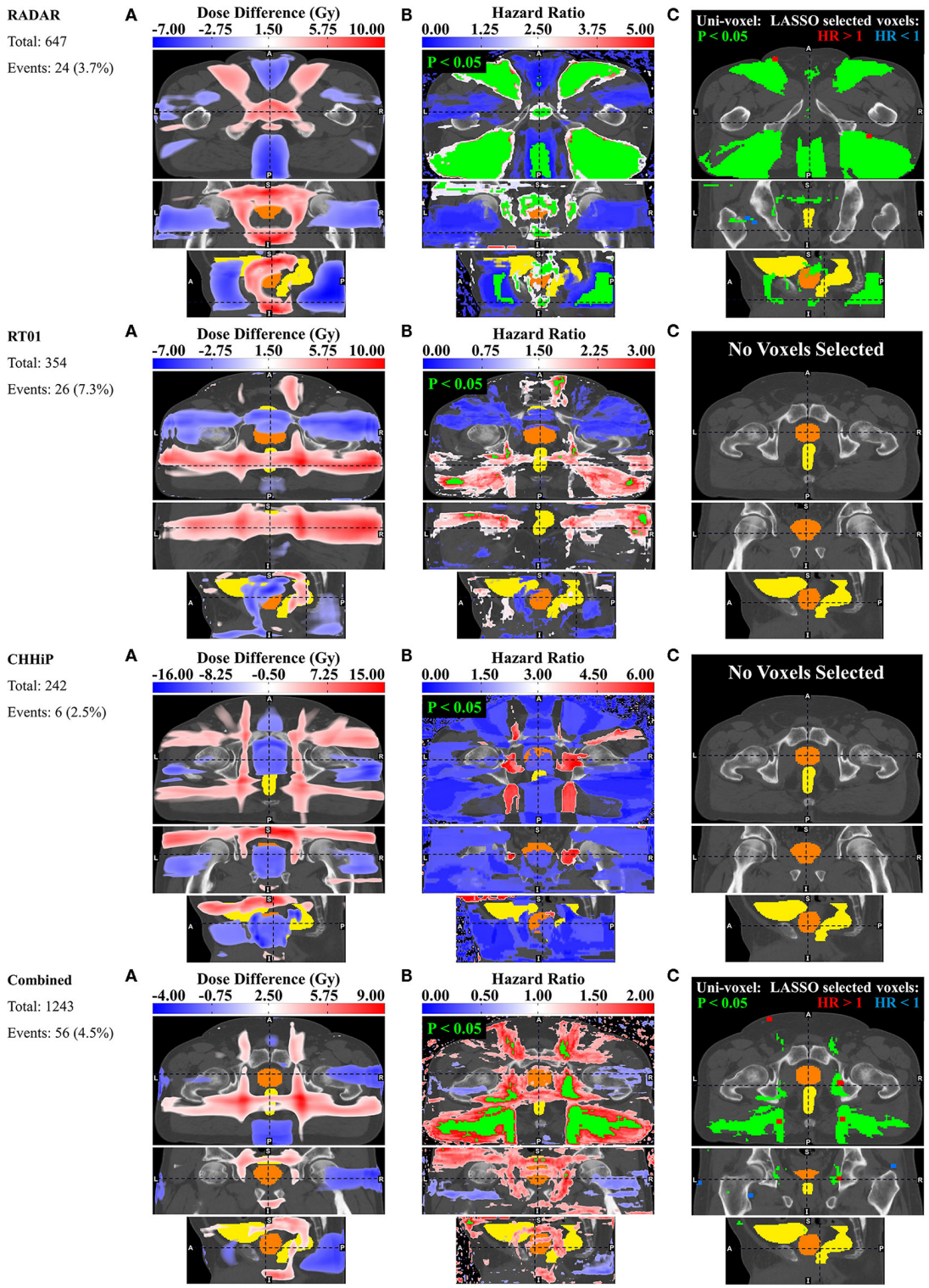

FIGURE 5 | Results for incontinence. Corresponding axial, coronal and sagittal slices (top to bottom) of **(A)** mean dose difference maps, **(B)** uni-voxel Cox regression HR and *p*-value maps and **(C)** multi-voxel Cox regression LASSO HR maps (with uni-voxel *p*-values for comparison), for respective data sets. "No Voxels Selected" implies the LASSO selected no voxels of significant correlation with the endpoint within the patient region. The slices chosen for display are those which coincide with the most dominant emergent dose-endpoint patterns, indicated in corresponding planes with dashed lines. Tones of red correspond to regions where increased dose is associated with incidence of incontinence (HR > 1), while tones of blues correspond to regions where reduced dose is associated with incidence of incontinence (HR < 1). The CTV is delineated in orange while the bladder and rectum are delineated in yellow. Anatomical directions left (L), right (R), superior (S), inferior (I), anterior (A), and posterior (P) are also indicated.

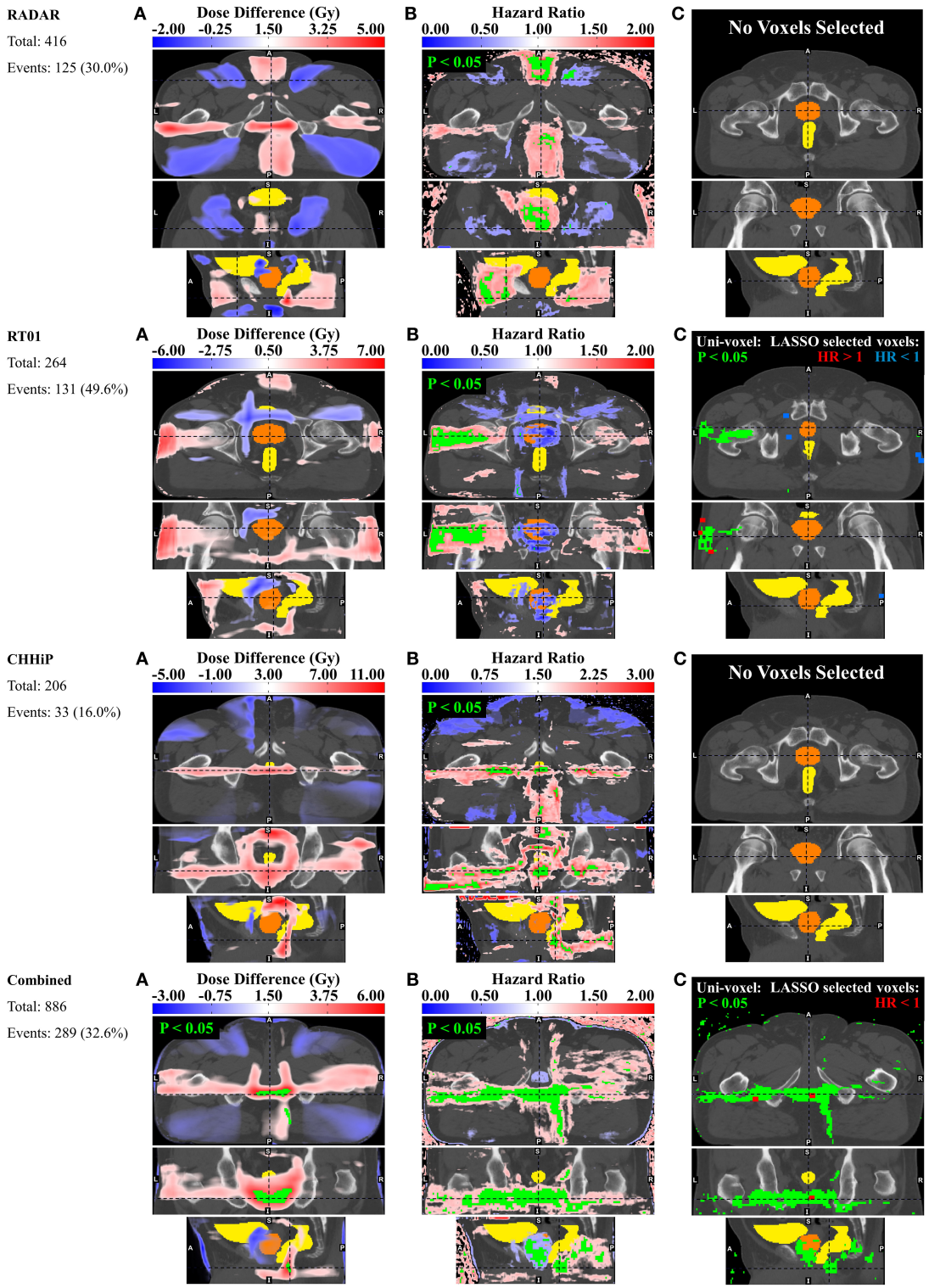

FIGURE 6 | Results for frequency. Corresponding axial, coronal and sagittal slices (top to bottom) of **(A)** mean dose difference maps and regions of significant dose difference determined by permutation test, **(B)** uni-voxel Cox regression HR and *p*-value maps and **(C)** multi-voxel Cox regression LASSO HR maps (with uni-voxel or permutation test *p*-values for comparison), for respective data sets. The slices chosen for display are those which coincide with the most dominant emergent dose-endpoint patterns, indicated in corresponding planes with dashed lines. Tones of red correspond to regions where increased dose is associated with incidence of frequency (HR > 1), while tones of blues correspond to regions where reduced dose is associated with incidence of frequency (HR < 1). The CTV is delineated in orange while the bladder and rectum are delineated in yellow. Anatomical directions left (L), right (R), superior (S), inferior (I), anterior (A), and posterior (P) are also indicated.

urethra and anterior urethra, which includes the membranous and bulbous urethra." This study has investigated the dose-dysuria relationship in these regions and has indeed found correlation primarily in the membranous and spongy/bulbous urethra and not primarily in the prostatic urethra. The RADAR T3 result did, however, expose some correlation in the prostatic urethra. Thirteen patients in the RADAR cohort included in the dysuria analysis in this study had reported strictures. It is noteworthy that one stricture was found in the prostatic urethra with the rest found in the membranous/spongy urethra. While only 5 of the 13 patients with strictures presented with grade $\geq$2 dysuria, 8 of the 13 presented with grade $\geq$ 1 dysuria. Perhaps the membranous/spongy urethra is particularly susceptible to the radiation damage capable of inducing dysuria, such as stricture formation. Dose escalation has been shown to increase urethral strictures in the RADAR cohort (18).

However, upon examination of the standard deviation dose distributions (see **Appendix Section 4** or **Figure 7** for just the combined cohort), the maximum dose variation occurs in the membranous/spongy urethra region with minimum variation in the prostatic urethra region, for all trial datasets. This is particularly evident in the T3 standard deviation dose distribution. Therefore, this anterior urethral correlation may have been exposed through sufficient intra-cohort dose-variance in this region, while a potential prostatic urethral correlation may be hidden due to lack of dose variation in the CTV. **Figure 7** contains mean dose distributions for the combined cohort displaying dose values in the vicinity of the spongy and membranous urethra, for patients with and without grade $\geq$ 2 dysuria. Patients with dysuria have a mean dose of 19.7 and 48.2 Gy near the spongy and membranous urethra, respectively. Therefore, this dose-toxicity relationship is occurring in the low dose range at the spongy urethra and intermediate dose range at the membranous urethra. It should be noted that doses <20 Gy are associated with this effect at the spongy urethra. One further hypothesis is that the low dose bath at the distal spongy urethra may reduce the capacity of stem cells to migrate back to the more heavily irradiated prostatic (or even membranous) urethra where they would facilitate urethral healing (34, 35). In conclusion, there is strong evidence that radiation dose to the urethra is associated with resulting dysuria. The membranous and spongy urethra may be particularly susceptible, however dose to the prostatic urethra is likely to be related to dysuria as well. Limiting dose to the spongy urethra may be more realistic as the prostatic urethra resides in the high dose region. Future studies delineating the prostatic/membranous/spongy urethra and investigating the dose-volume-dysuria relationship in these regions may further characterize urethral dose sensitivity.

Late grade $\geq$ 1 haematuria was similarly associated with increased dose to the spongy and membranous urethra regions. Urinary bleeding has typically related to the high dose region of the bladder (14, 36–38) where the bladder neck and trigone reside, and has been observed in the bladder neck and trigone at cystoscopy (8). Yahya et al. (10), however, in agreement with the superior bladder subregion found by Mylona et al. (8), determined that late haematuria was associated with dose to the anterosuperior regions of the bladder, and concluded that haematuria was not a result of dose to the trigone or bladder neck, but rather to tissue damage in the bladder wall. Although Inokuchi et al. investigated and found no dose-volume association with haematuria at the prostatic urethra (14), no study to date has investigated dose-haematuria association at the membranous or spongy urethra. To the best of the author's knowledge this is the first study to have included these regions of the urethra in localized dose-toxicity analysis. As a result, an association with haematuria has been found in the extra-prostatic urethra, contrary to the general pattern. This is not beyond the scope of current evidence, however, as haematuria can be caused by urinary tract infection and strictures (39). As previously discussed, urethral strictures were present in the cohort and can result from urethral radiation damage. Considering patients in the subset of the RADAR cohort included in the haematuria analysis, 9 out of the 12 patients with reported spongy/membranous urethral strictures also had grade $\geq$ 1 haematuria. It is also plausible that radiation damage to the anterior urethra can cause inflammation leading to urinary tract infection. As demonstrated for dysuria, **Figure 7** shows that this haematuria effect is associated with doses lower than 20 Gy at the spongy urethra. Therefore, reduced stem cell migration in response to the low dose bath at the spongy urethra may also be contributing to this effect. Due to these considerations and the similar association found with dysuria, limiting dose to the anterior urethra may substantially reduce the incidence of these two prominent urinary toxicities. Spongy urethral dose could be reduced by taping down the penis to the thigh. Or perhaps by using two anterior oblique beams instead of a single anterior beam.

It should also be acknowledged that the above dysuria and haematuria dose relationships were found in 3D-CRT patients (from the RADAR and RT01 trials). In the current era, almost all patients are treated with IMRT or VMAT which result in more conformal dose distributions in comparison to 3D-CRT. It is therefore very likely that the majority of contemporary patients would receive less spongy urethral dose, perhaps eliminating the need for the application of dose constraints or any dose reduction scheme. This is even evident in the current study, with CHHiP patients (treated with IMRT) experiencing less urethral dose correlation and less events corresponding to both dysuria and haematuria. It is also noteworthy that applying dose constraints to the membranous urethra, which begins proximally at the prostatic apex, may not be feasible due to its proximity to the high dose PTV region. The reader is reminded that the primary purpose of this study was not to discover dose constraints but to explore the underlying causal relationships between localized dose and toxicity without the assumption that these relationships necessarily occurred at OAR sites (from which future analyses may derive dose constraints if appropriate—see the third final paragraph of this discussion).

Increased dose in the external and internal urethral sphincter and in the posterior oblique beams was shown to correlate with late grade $\geq$ 2 incontinence. It is established that urinary incontinence can (40), and most commonly does (41), result from urethral sphincter malfunctioning. Although both the internal and external sphincters are involved in maintaining continence,

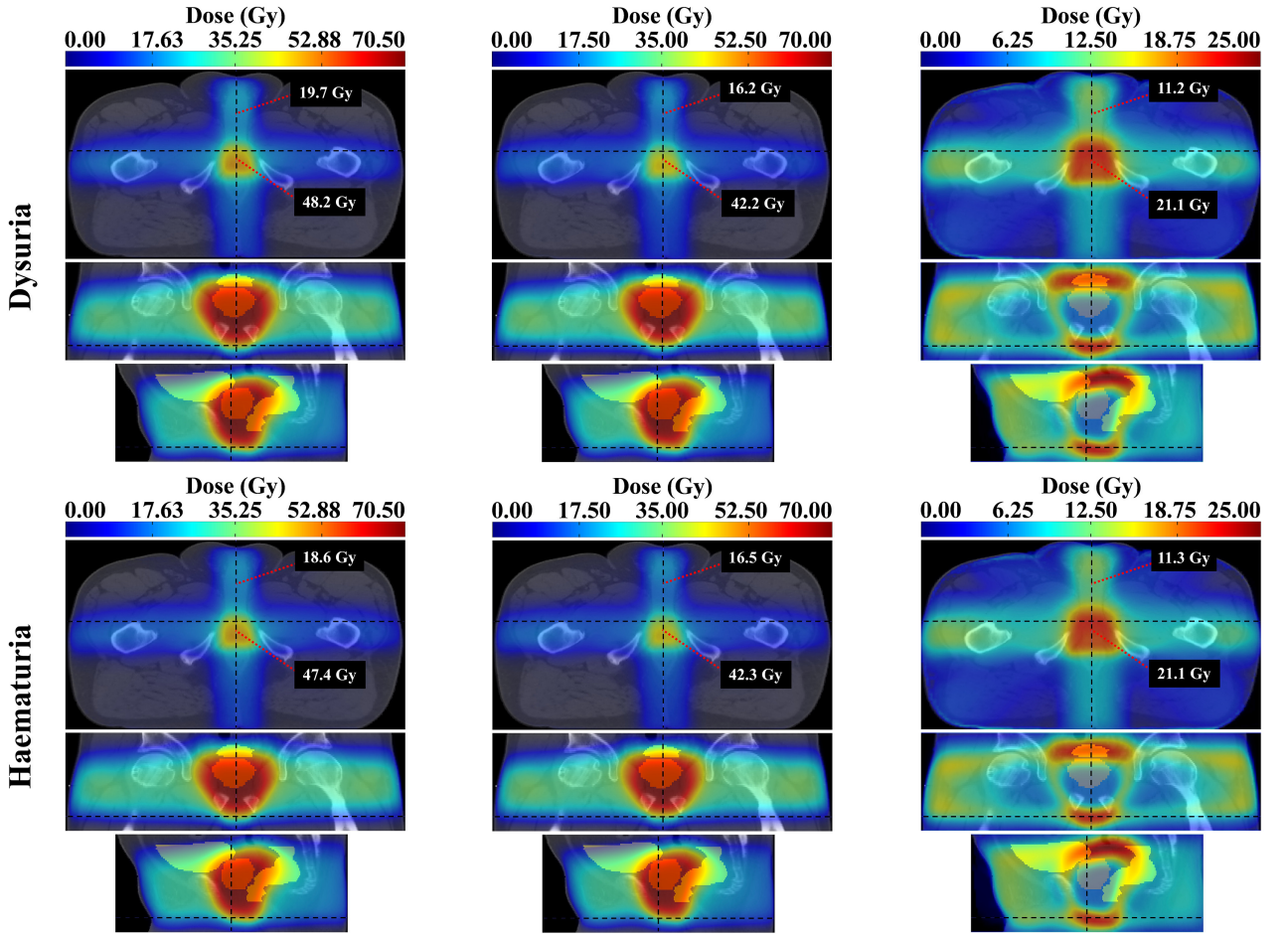

FIGURE 7 | (A) Mean dose distributions for patients with the given toxicity in the combined cohort, **(B)** mean dose distributions for patients without the given toxicity in the combined cohort, and **(C)** standard deviation dose distributions maps for patients in the combined cohort dataset for the given toxicity. Each map displays the dose value at a point in the vicinity of the distal spongy urethra (above) and membranous urethra (below). The top row represents the grade ≥2 dysuria dataset and the bottom row the grade ≥1 haematuria dataset.

the internal sphincter is of primary importance (42). Mylona et al. found a predictive subregion in the prostatic urethra for incontinence, concluding this was related to damage to the urethral sphincter (8). Yahya et al. found an association between incontinence and dose to the posteroinferior bladder at the trigone, suggesting this was likely related to dose received by the internal sphincter (10). The sphincter muscles may be scarred by irradiation, or dose to the nearby bladder neck may increase ischemia and fibrosis and thus incontinence due to internal sphincter damage (10). The association with the posterior oblique beams may be a surrogate for dose directly to the sphincters, although no direct evidence for this has been discovered. It is recommended that clinicians be aware of the potential radiation damage to the sphincters, while recognizing they do coincide with the high dose region, and that a large scale clinical trial did not reveal increasing incidence of incontinence with dose escalation (43).

Late grade ≥ 2 frequency was associated with dose extending inferiorly and posteriorly to the prostate and rectum. This may indicate that patients treated with a posterior beam extending inferiorly beyond the rectum had a higher incidence of frequency. This result is largely unintuitive and difficult to rationalize. It is noteworthy that Mylona et al. could not demonstrate a dosimetric association with urinary frequency (8).

The relationships presented here are correlations that may or may not represent anatomically-localized physiological dose-toxicity associations. The low number of toxicity events, namely <10% of the cohort for 7 of the 16 datasets, should reinforce this suspicion. Only the uni-voxel Cox regression accounted for intrinsic patient factors, and these represent only a sample of possible patient cofactors that could confound the associations. To ensure dose-toxicity relationships are independent of a given patient factor, separating the cohort into this factor's subgroups prior to analysis is necessary. This, however, would

reduce power, requiring a larger cohort to establish statically meaningful associations. Furthermore, these relationships must be interpreted in light of the differences in dosemaps from the three trials. For example, the mean dose distributions from respective trials (see **Appendix Section 4**) indicate that the average CHHiP distribution is more conformal than that of RADAR or RT01. This is consistent with the fact that CHHiP patients received IMRT instead of 3D-CRT for RADAR and RT01, and may explain why the number of toxicity events were lower and correlation patterns were much weaker in CHHiP datasets. It must also be noted that the follow-up times were not identical between the datasets derived from the three trials. For example, datasets from the RADAR trial included follow-up data at 9 and 15 months post-treatment while the datasets from the RT01 and CHHiP trails did. Defining the endpoints differently in this way may bias the comparison and therefore it is that data from the same timepoints are used in generating endpoints when comparing applying analysis to different trials with the goal of comparing results. Finally, it is recognized that the results from the combined cohort (for all toxicity endpoints) are biased toward the RADAR dataset as RADAR patients comprise a higher proportion of this dataset than patients from the other two trials. The goal of the combined analysis was to maximize the statistical power available for each toxicity endpoint and observe the resulting dose-toxicity patterns. The aforementioned bias was therefore accepted as necessary to achieve this goal. Although, in future analyses, if an adequate number of patients are available, it is recommended that, in addition to combining all patients together, an equal number of patients from each trial be included in the combined dataset (or a form of normalization employed) to remove bias from any individual trial dataset. Comparing results from a combined cohort with those from a balanced (or normalized cohort) would be useful in discerning the bias introduced from the dominant dataset.

The permutation test is quite conservative. In the dose difference comparison between patients with and without an event pertaining to a given endpoint, it applies a global threshold that cannot identify local maxima of dose difference. Also, due to the large number of voxels compared, in order to adequately account for the multiple statistical testing problem this threshold can be quite high, and therefore may exclude not only local regions of significant dose difference but also global regions. Hence only large and statistically strong global dose differences can be identified (and therefore p-value thresholds up to $p < 0.3$ were used). This could explain why, across all datasets and endpoints, only in one dataset (Combined for frequency) was a region of statistically significant dose difference discovered by this test. A test more sensitive in identifying local maxima, such as a threshold-free cluster enhancement test (44), may be appropriate for further voxel-based analyses. Palorini et al. (12) outline further reasons for being wary of a straightforward application of the permutation test in the context of bladder dose surface maps. These include (1) the distribution of t-scores obtained in each pixel being significantly different from the null distribution (invalidating the test's assumption of a universal null hypothesis), and (2) macro regions of heterogenous voxel dose skewness reducing the probability of regions with less skewness of registering a significant dose difference. Point (1) implies that the test be overly restrictive, while (2) indicates the need for possibly dividing the dose distribution into regions of relatively uniform skewness and repeating the test on each region separately. This may be an appropriate future directive for using this test in the context of voxel-based analysis.

The assumption that planned dose is equivalent to delivered dose, which differ in reality (45), is a major limitation of this study. It has been shown that delivered dose can be a better predictor of rectal toxicity than planned dose (46). As the agreement between planned and delivered dose improves, or delivered dose becomes more easily measurable, voxel-based dose analyses will be more effective in identifying anatomically localized dose-toxicity relationships. Cone beam CT daily imaging, for example, could be used to measure cumulative delivered dose across the course of treatment (47). Furthermore, all voxel-based tests in this analysis were applied throughout the entire pelvic region, including a broad range of late-responding normal tissues. An alpha/beta value of 3 was chosen as it has been regarded as generally representative of all late responding normal tissues (48). It is acknowledged, however, that different normal tissues respond differently with respect to different toxicities, thus resulting in different alpha/beta values. Therefore, an appropriate future direction would be to test the sensitivity of results to different alpha/beta values, particularly with respect to the different urinary toxicities. Another limitation could be the registration accuracy and the suitability of the choice of exemplar and anti-exemplar. The anatomical localization of the emergent dose-toxicity patterns is directly dependent on registration accuracy. A perfect registration would ensure the identified patterns are in fact occurring at the presumed anatomical sites. Diversity in the distribution of dose across each cohort is also limiting, as the mean dose distributions are approximately 3 or 4 field treatments in all datasets (see **Appendix Section 4** for mean and standard deviation dose distributions). Greater diversity in technique will enable more generalizable feature selection. Differences in diversity between trials may also account for lack of consistency in results across trials. For example, RADAR treatments were allowed any combination of 3 or more beams, while RT01 treatments were restricted to 3 or 4 beams in the anterior/lateral/posterior directions. This has led to differences in the spatial distribution of dose variation between trial cohorts, resulting in different potential sites with sufficient variation for exposing dose-toxicity associations.

Incorporating the voxel-based evidence into normal tissue complication probability (NTCP) models may facilitate translation of these results into clinical practice. Palma et al. have derived a new NTCP philosophy to include voxel-based evidence of OAR radio-sensitivity (49). Incorporating the evidence of OAR sensitivity from this study into a model like this could result in reduced toxicity for patients when applied to treatment planning. It is also acknowledged that the majority of evidence discovered in this study was from 3D-CRT patients. Therefore, the methods here may need to be applied to a larger cohort of patients treated with contemporary techniques before translation is made to the clinic.

This study focused on urinary specific and not toxicities related to sexual function. An exploration of the relationship between erectile dysfunction (ED) and dose in a voxel-based

manner is recommend for future analyses. Additionally, the relationship between ED and dose to the penile bulb was studied elsewhere for the RT01 and CHHiP patients (50, 51). Finally, the study of the relationship between ED and dose is problematic in cohorts that use additional ADT due to the impact of ADT on various measures of sexual function including ED (52–54). The RADAR trial, from which our primary dataset was derived, is one such cohort. Additionally, it has previously been shown that ADT did not increase urinary dysfunction (including dysuria, haematuria, frequency and incontinence) in the RADAR cohort (55). Similar studies have not been performed for the RT01 and CHHiP cohorts, however, as trial arms did not vary in terms of ADT duration. The impact of ADT may therefore be a confound in the datasets derived from RT01 and CHHiP.

This was the first study performing a full voxel-based analysis of dose-urinary toxicity relationships in the entire pelvic anatomy, without the assumption that these occurred exclusively at OAR sites. Associations between late dysuria and haematuria and dose to the spongy and membranous urethra have been newly identified, while dose to the urinary sphincters and resulting incontinence has confirmed the idea that radiation damage at the sphincter can cause incontinence.

DATA AVAILABILITY STATEMENT

The datasets for this article are not publicly available because of ethical restrictions placed on patient data derived from clinical trials. Requests to access the datasets should be directed to Marco Marcello, 20739859@student.uwa.edu.au.

ETHICS STATEMENT

The studies involving human participants were reviewed and approved by the Hunter New England Human Research Ethics Committee Trial ID 03/06/11/3.02 for the RADAR trial, the North Thames Multi-center Research Ethics Committee number MREC/97/2/16 for the RT01 trial, and the London Multi-center Research Ethics Committee number 04/MRE02/10 for the CHHiP trial. The patients/participants provided their written informed consent to participate in this study.

AUTHOR CONTRIBUTIONS

All contributors met the criteria required to be considered a qualified author. All authors approved of the final submitted version of the manuscript and agree to be accountable for all aspects of the work. MM performed all statistical analyses, processed the results, and was the primary author of the manuscript and supplementary material. JD, AH, and ME provided expert information on the RADAR trial and contributed to the editing of the manuscript. They also assisted in acquisition of the RADAR trial data. MS did all of the above, however for the RT01 trial data. DD and SG did the same for both the RT01 and CHHiP trial data. EH for just the CHHiP trial data. AK performed the dose distribution registrations and provided technical support in displaying the results on CT templates. AS provided expert information assisting with aspects of the statistical analysis. PG, LH, MJ, and DR provided expert information in regards to the methodology and interpretation of results, and contributed to the editing of the manuscript. JD provided expert information in regards to the registration process and interpretation of results, and contributed to the editing of the manuscript. DJ assisted in acquisition of the RADAR trial data.

FUNDING

We acknowledge funding from the Australian National Health and Medical Research Council (Grants nos. 300705, 455521, 1006447, and 1077788), the Hunter Medical Research Institute, the Health Research Council (New Zealand), the University of Newcastle, the Calvary Mater Newcastle, the Medical Research Council Clinical Trials Unit at University College London, Abbott Laboratories and Novartis Pharmaceuticals. These funders (Abbott Laboratories and Novartis Pharmaceuticals) were not involved in the study design, collection, analysis, interpretation of data, the writing of this article or the decision to submit it for publication. We acknowledge funding from the Medical Research Council UK (grant MC_UU_12023/28) for the MRC RT01 trial. DD, EH, and SG acknowledge NHS funding to the National Institute for Health Research (NIHR) Biomedical Research Center at the Royal Marsden NHS Foundation Trust and The Institute of Cancer Research, London. We acknowledge support of Cancer Research UK (C8262/A7253, C1491/A9895, C1491/A15955, SP2312/021), the Department of Health, the NIHR Cancer Research Network for the CHHiP trial.

ACKNOWLEDGMENTS

We acknowledge all trial investigators and patients who've made this study possible. We gratefully acknowledge the support of the Sir Charles Gairdner Hospital, Rachel Kearvell, the Elvis study team including Kristie Harrison, participating RADAR centers, the Trans-Tasman Radiation Oncology Group, Ben Hooton and Elizabeth van der Wath. We are also grateful for the contributions of Oscar Acosta, Renaud de Crevoisier, and Eugenia Mylona.

SUPPLEMENTARY MATERIAL

The Supplementary Material for this article can be found online at: https://www.frontiersin.org/articles/10.3389/fonc.2020.01174/full#supplementary-material

REFERENCES

1. Barton MB, Jacob S, Shafiq J, Wong K, Thompson SR, Hanna TP, et al. Estimating the demand for radiotherapy from the evidence : a review of changes from 2003 to 2012. *Radiother Oncol.* (2014) 112:140–4. doi: 10.1016/j.radonc.2014.03.024
2. Zelefsky MJ, Levin EJ, Hunt M, Yamada Y, Shippy AM, Jackson A, et al. Incidence of late rectal and urinary toxicities after three-dimensional

conformal radiotherapy and intensity-modulated radiotherapy for localized prostate cancer. *Int J Radiat Oncol Biol Phys.* (2008) 70:1124–9. doi: 10.1016/j.ijrobp.2007.11.044
3. Barnett GC, De Meerleer G, Gulliford SL, Sydes MR, Elliott RM, Dearnaley DP. The impact of clinical factors on the development of late radiation toxicity : results from the medical research council RT01 trial (ISRCTN47772397). *Clin Oncol*. (2011) 23:613–24. doi: 10.1016/j.clon.2011.03.001
4. Rancati T, Cozzarini C, Improta I, Palorini F, Garibaldi E, Franco P, et al. Multivariable models predicting specific patient-reported acute urinary symptoms after radiation therapy for prostate cancer: results of a cohort study. *Int J Radiat Oncol Biol Phys.* (2015) 93:E240–1. doi: 10.1016/j.ijrobp.2015.07.1153
5. Yahya N, Ebert MA, Bulsara M, Haworth A, Kennedy A, Joseph DJ, et al. Dosimetry, clinical factors and medication intake influencing urinary symptoms after prostate radiotherapy: an analysis of data from the RADAR prostate radiotherapy trial. *Radiother Oncol*. (2015) 116:112–8. doi: 10.1016/j.radonc.2015.06.011
6. Luxton G, Hancock SL, Boyer AL. Dosimetry and radiobiologic model comparison of IMRT and 3D conformal radiotherapy in treatment of carcinoma of the prostate. *Int J Radiat Oncol Biol Phys.* (2004) 59:267–84. doi: 10.1016/j.ijrobp.2004.01.024
7. De Crevoisier R, Pommier P, Bachaud J, Crehange G, Boutry C, Chauvet B, et al. Image-Guided Radiation Therapy (IGRT) in prostate cancer: preliminary results in prostate registration and acute toxicity of a randomized study. *Radiat Oncol Biol*. (2009) 75:S99. doi: 10.1016/j.ijrobp.2009.07.242
8. Mylona E, Acosta O, Lizee T, Lafond C, Crehange G, Chiavassa S, et al. Voxel-based analysis for identification of urethrovesical subregions predicting urinary toxicity after prostate cancer radiation therapy. *Int J Radiat Oncol Biol Phys.* (2019) 104:343–54. doi: 10.1016/j.ijrobp.2019.01.088
9. Improta I, Palorini F, Cozzarini C, Rancati T, Avuzzi B, Franco P, et al. Bladder spatial-dose descriptors correlate with acute urinary toxicity after radiation therapy for prostate cancer. *Phys Medica*. (2016) 32:1681–9. doi: 10.1016/j.ejmp.2016.08.013
10. Yahya N, Ebert MA, House MJ, Kennedy A, Matthews J, Joseph DJ, et al. Modeling urinary dysfunction after external beam radiation therapy of the prostate using bladder dose-surface maps: evidence of spatially variable response of the bladder surface. *Radiat Oncol Biol*. (2018) 97:420–6. doi: 10.1016/j.ijrobp.2016.10.024
11. Ghadjar P, Zelefsky MJ, Spratt DE, Munck Af Rosenschöld P, Oh JH, Hunt M, et al. Impact of dose to the bladder trigone on long-term urinary function after high-dose intensity modulated radiation therapy for localized prostate cancer. *Int J Radiat Oncol Biol Phys.* (2014) 88:339–44. doi: 10.1016/j.ijrobp.2013.10.042
12. Palorini F, Cozzarini C, Gianolini S, Botti A, Carillo V, Iotti C, et al. First application of a pixel-wise analysis on bladder dose – surface maps in prostate cancer radiotherapy. *Radiother Oncol*. (2016) 119:123–8. doi: 10.1016/j.radonc.2016.02.025
13. Henderson DR, Murray JR, Gulliford SL, Tree AC, Harrington KJ, Van As NJ. An investigation of dosimetric correlates of acute toxicity in prostate stereotactic body radiotherapy: dose to urinary trigone is associated with acute urinary toxicity. *Clin Oncol.* (2018) 30:539–47. doi: 10.1016/j.clon.2018.05.001
14. Inokuchi H, Mizowaki T, Norihisa Y, Takayama K, Ikeda I, Nakamura K, et al. Correlation between urinary dose and delayed radiation cystitis after 78 Gy intensity-modulated radiotherapy for high-risk prostate cancer: a 10-year follow-up study of genitourinary toxicity in clinical practice. *Clin Transl Radiat Oncol*. (2017) 6:31–6. doi: 10.1016/j.ctro.2017.09.005
15. Ospina JD, Acosta O, Dréan G, Cazoulat G, Simon A, Correa JCC, et al. Spatial nonparametric mixed-effects model with spatial-varying coefficients for analysis of populations. In: Suzuki K, Wang F, Shen D, Yan P, editors. *Machine Learning in Medical Imaging. MLMI 2011. Lecture Notes in Computer Science,* Vol. 7009. Berlin; Heidelberg: Springer (2011). Available online at: https://link.springer.com/chapter/10.1007%2F978-3-642-24319-6_18
16. Chen C, Witte M, Heemsbergen W, van Herk M. Multiple comparisons permutation test for image based data mining in radiotherapy. *Radiat Oncol*. (2013) 8:293. doi: 10.1186/1748-717X-8-293
17. Denham JW, Joseph D, Lamb DS, Spry NA, Duchesne G, Matthews J, et al. Short-term androgen suppression and radiotherapy versus intermediate-term androgen suppression and radiotherapy, with or without zoledronic acid, in men with locally advanced prostate cancer (TROG 03.04 RADAR): an open-label, randomised, phase 3 factorial. *Lancet Oncol*. (2014) 15:1076–89. doi: 10.1016/S1470-2045(14)70328-6
18. Denham JW, Steigler A, Joseph D, Lamb DS, Spry NA, Duchesne G, et al. Radiation dose escalation or longer androgen suppression for locally advanced prostate cancer? Data from the TROG 03.04 RADAR trial. *Radiother Oncol*. (2015) 115:301–7. doi: 10.1016/j.radonc.2015.05.016
19. Ebert MA, Haworth A, Kearvell R, Hooton B, Coleman R, Spry N, et al. Detailed review and analysis of complex radiotherapy clinical trial planning data: evaluation and initial experience with the SWAN software system. *Radiother Oncol.* (2008) 86:200–10. doi: 10.1016/j.radonc.2007.11.013
20. Dearnaley DP, Sydes MR, Graham JD, Aird EG, Bottomley D, Cowan RA, et al. Escalated-dose versus standard-dose conformal radiotherapy in prostate cancer: first results from the MRC RT01 randomised controlled trial. *Lancet Oncol.* (2007) 8:475–87. doi: 10.1016/S1470-2045(07)70143-2
21. Dearnaley DP, Jovic G, Syndikus I, Khoo V, Cowan RA, Graham JD, et al. Escalated-dose versus control-dose conformal radiotherapy for prostate cancer : long-term results from the MRC RT01 randomised controlled trial. *Lancet Oncol*. (2014) 15:464–73. doi: 10.1016/S1470-2045(14)70040-3
22. Dearnaley D, Syndikus I, Sumo G, Bidmead M, Bloomfield D, Clark C, et al. Conventional versus hypofractionated high-dose intensity-modulated radiotherapy for prostate cancer: preliminary safety results from the CHHiP randomised controlled trial. *Lancet Oncol.* (2012) 13:43–54. doi: 10.1016/S1470-2045(11)70293-5
23. Dearnaley D, Syndikus I, Mossop H, Khoo V, Birtle A, Bloomfield D, et al. Conventional versus hypofractionated high-dose intensity-modulated radiotherapy for prostate cancer: 5-year outcomes of the randomised, non-inferiority, phase 3 CHHiP trial. *Lancet Oncol*. (2016)17:1840–50. doi: 10.1016/S1470-2045(16)30102-4
24. Sydes MR, Stephens RJ, Moore AR, Aird EG, Bidmead AM, Fallowfield LJ, et al. Implementing the UK Medical Research Council (MRC) RT01 trial (ISRCTN 47772397): methods and practicalities of a randomised controlled trial of conformal radiotherapy in men with localised prostate cancer. *Radiother Oncol.* (2004) 72:199–211. doi: 10.1016/j.radonc.2004.04.007
25. Naismith O, Mayles H, Bidmead M, Clark CH, Gulliford S, Hassan S, et al. Radiotherapy quality assurance for the CHHiP trial: conventional versus hypofractionated high-dose intensity-modulated radiotherapy in prostate cancer. *Clin Oncol.* (2019) 31:611–20. doi: 10.1016/j.clon.2019.05.009
26. Kennedy A, Dowling JA, Greer PB, Holloway L, Jameson MG, Roach D, et al. Similarity clustering based atlas selection for pelvic CT image segmentation. *Med Phys*. (2019) 46:2246–50. doi: 10.1002/mp.13494
27. Bentzen SM, Dorr W, Gahbauer R, Howell RW, Joiner MC, Jones B, et al. Bioeffect modeling and equieffective dose concepts in radiation oncology-Terminology, quantities and units. *Radiother Oncol.* (2012) 105:266–8. doi: 10.1016/j.radonc.2012.10.006
28. Pavi J, Denekamp J, Letschert J. LENT-SOMA scales for all anatomic sites. *Int J Radiat Oncol Biol Phys.* (1995) 31:1049–91. doi: 10.1016/0360-3016(95)90159-0
29. Yushkevich PA, Piven J, Hazlett HC, Smith RG, Ho S, Gee JC, et al. User-guided 3D active contour segmentation of anatomical structures: significantly improved efficiency and reliability. *Neuroimage.* (2006) 31:1116–28. doi: 10.1016/j.neuroimage.2006.01.015
30. VanderWeele TJ, Shpitser I. On the definition of a confounder. *Ann Stat*. (2013) 41:196–220. doi: 10.1214/12-AOS1058
31. Marcello M, Ebert M, Haworth A, Steigler A, Kennedy A, Joseph D, et al. Association between treatment planning and delivery factors and disease progression in prostate cancer radiotherapy: results from the TROG 03.04 RADAR trial. *Radiother Oncol*. (2018) 126:249–56. doi: 10.1016/j.radonc.2017.10.021
32. Tibshiranit BR. Regression shrinkage and selection via the lasso. *J R Stat Soc Ser B.* (1996) 58:267–88. doi: 10.1111/j.2510-17-6161.1996.tb02080.x
33. Mathieu R, Arango JDO, Beckendorf V, Delobel J-B, Messai T, Chira C, et al. Nomograms to predict late urinary toxicity after prostate cancer radiotherapy. *World J Urol.* (2014) 32:743–51. doi: 10.1007/s00345-013-1146-8
34. Cao Y, Luo G-H, Luo L, Yang X-S, Hu J-X, Shi H, et al. Re-epithelialization resulted from prostate basal cells in canine prostatic urethra may represent the ideal healing method after two-micron laser resection of the prostate. *Asian J Androl.* (2015) 17:831. doi: 10.4103/1008-682X.146972

35. Castiglione F, Dewulf K, Hakim L, Weyne E, Montorsi F, Russo A, et al. Adipose-derived stem cells counteract urethral stricture formation in rats. *Eur Urol.* (2016) 70:1032–41. doi: 10.1016/j.eururo.2016.04.022
36. De Langhe S, De Meerleer G, De Ruyck K, Ost P, Fonteyne V, De Neve W, et al. Integrated models for the prediction of late genitourinary complaints after high-dose intensity modulated radiotherapy for prostate cancer: making informed decisions. *Radiother Oncol.* (2014) 112:95–9. doi: 10.1016/j.radonc.2014.04.005
37. Olsson CE, Jackson A, Deasy JO, Thor M. A systematic post-QUANTEC review of tolerance doses for late toxicity after prostate cancer radiation therapy. *Int J Radiat Oncol Biol Phys.* (2018) 102:1514–32. doi: 10.1016/j.ijrobp.2018.08.015
38. Yahya N, Ebert MA, Bulsara M, House MJ, Kennedy A, Joseph DJ, et al. Urinary symptoms following external beam radiotherapy of the prostate :dose – symptom correlates with multiple-event and event-count models. *Radiother Oncol.* (2015) 117:277–82. doi: 10.1016/j.radonc.2015.10.003
39. Yeoh M, Lai NK, Anderson D, Appadurai V. Macroscopic haematuria: a urological approach. *Aust Fam Physician.* (2013) 42:123. Available online at: https://search.informit.com.au/documentSummary;dn=181208201500871;res=IELHEA
40. Nitti VW. The prevalence of urinary incontinence. *Rev Urol.* (2001) 3(Suppl 1):S2.
41. Jung J, Ahn HK, Huh Y. Clinical and functional anatomy of the urethral sphincter. *Int Neurourol J.* (2012) 16:102–6. doi: 10.5213/inj.2012.16.3.102
42. Shah AP, Mevcha A, Wilby D, Alatsatianos A, Hardman JC, Jacques S, et al. Continence and micturition: an anatomical basis. *Clin Anat.* (2014) 27:1275–83. doi: 10.1002/ca.22388
43. Al-Mamgani A, van Putten WLJ, Heemsbergen WD, van Leenders GJLH, Slot A, Dielwart MFH, et al. Update of Dutch multicenter dose-escalation trial of radiotherapy for localized prostate cancer. *Int J Radiat Oncol Biol Phys.* (2008) 72:980–8. doi: 10.1016/j.ijrobp.2008.02.073
44. Smith SM, Nichols TE. Threshold-free cluster enhancement: addressing problems of smoothing, threshold dependence and localisation in cluster inference. *Neuroimage.* (2009) 44:83–98. doi: 10.1016/j.neuroimage.2008.03.061
45. Colvill E, Booth JT, Brien RTO, Eade TN, Kneebone AB, Poulsen PR, et al. Multileaf collimator tracking improves dose delivery for prostate cancer radiation therapy : results of the first clinical trial. *Radiat Oncol Biol.* (2015) 92:1141–7. doi: 10.1016/j.ijrobp.2015.04.024
46. Shelley LEA, Scaife JE, Romanchikova M, Harrison K, Forman JR, Bates AM, et al. Delivered dose can be a better predictor of rectal toxicity than planned dose in prostate radiotherapy. *Radiother Oncol.* (2017) 123:466–71. doi: 10.1016/j.radonc.2017.04.008
47. Delobel J-B, Gnep K, Ospina JD, Beckendorf V, Chira C, Zhu J, et al. Nomogram to predict rectal toxicity following prostate cancer radiotherapy. *PLoS ONE.* (2017) 12:e0179845. doi: 10.1371/journal.pone.0179845
48. Emami B, Woloschak G, Small W Jr. Beyond the linear quadratic model: intraoperative radiotherapy and normal tissue tolerance. *Transl Cancer Res.* (2015) 4:140–7. doi: 10.3978/j.issn.2218-676X.2015.04.06
49. Palma G, Monti S, Buonanno A, Pacelli R, Cella L. PACE: a probabilistic atlas for normal tissue complication estimation in radiation oncology. *Front Oncol.* (2019) 9:130. doi: 10.3389/fonc.2019.00130
50. Mangar SA, Sydes MR, Tucker HL, Coffey J, Sohaib SA, Gianolini S, et al. Evaluating the relationship between erectile dysfunction and dose received by the penile bulb: using data from a randomised controlled trial of conformal radiotherapy in prostate cancer (MRC RT01, ISRCTN47772397). *Radiother Oncol.* (2006) 80:355–62. doi: 10.1016/j.radonc.2006.07.037
51. Murray J, Gulliford S, Griffin C, Wilkins A, Syndikus I, Staffurth J, et al. Evaluation of erectile potency and radiation dose to the penile bulb using image guided radiotherapy in the CHHiP trial. *Clin Transl Radiat Oncol.* (2020) 21:77–84. doi: 10.1016/j.ctro.2019.12.006
52. Higano CS. Side effects of androgen deprivation therapy: monitoring and minimizing toxicity. *Urology.* (2003) 61:32–8. doi: 10.1016/S0090-4295(02)02397-X
53. DiBlasio CJ, Malcolm JB, Derweesh IH, Womack JH, Kincade MC, Mancini JG, et al. Patterns of sexual and erectile dysfunction and response to treatment in patients receiving androgen deprivation therapy for prostate cancer. *BJU Int.* (2008) 102:39–43. doi: 10.1111/j.1464-410X.2008.07505.x
54. Bruner DW, James JL, Bryan CJ, Pisansky TM, Rotman M, Corbett T, et al. Randomized, double-blinded, placebo-controlled crossover trial of treating erectile dysfunction with sildenafil after radiotherapy and short-term androgen deprivation therapy: results of RTOG 0215. *J Sex Med.* (2011) 8:1228–38. doi: 10.1111/j.1743-6109.2010.02164.x
55. Denham JW, Wilcox C, Lamb DS, Spry NA, Duchesne G, Atkinson C, et al. Rectal and urinary dysfunction in the TROG 03.04 RADAR trial for locally advanced prostate cancer. *Radiother Oncol.* (2012) 105:184–92. doi: 10.1016/j.radonc.2012.09.018

Conflict of Interest: DD discloses that his employer, the Institute of Cancer Research, receives royalty income from Abiraterone and receives a share of this income through the ICR's Rewards to Discoverers Scheme. MS reports grants from Health Data Research UK, during the conduct of the study; personal fees from Lilly Oncology and Janssen, grants and non-financial support from Astellas, Clovis Oncology, Janssen, Novartis, Pfizer, and Sanofi-Aventis, outside the submitted work. EH reports grants from Cancer Research UK, during the conduct of the study; grants from Accuray Inc., outside the submitted work. ME reports grants from Australian National Health and Medical Research Council, during the conduct of the study.

The remaining authors declare that the research was conducted in the absence of any commercial or financial relationships that could be construed as a potential conflict of interest.

frontiers in Oncology

ORIGINAL RESEARCH
published: 23 July 2020
doi: 10.3389/fonc.2020.01207

Predictors of 2-Year Incidence of Patient-Reported Urinary Incontinence After Post-prostatectomy Radiotherapy: Evidence of Dose and Fractionation Effects

Andrea Bresolin[1,2], Elisabetta Garibaldi[3], Adriana Faiella[4], Domenico Cante[5], Vittorio Vavassori[6], Justina Magdalena Waskiewicz[7], Giuseppe Girelli[8], Barbara Avuzzi[9], Elisa Villa[6], Alessandro Magli[10], Barbara Noris Chiorda[9], Fernando Munoz[11], Giuseppe Sanguineti[4], Pietro Gabriele[3], Marco Gatti[3], Tiziana Rancati[12], Riccardo Valdagni[9,12,13], Nadia Di Muzio[14,15], Claudio Fiorino[1] and Cesare Cozzarini[14]*

[1] IRCCS Istituto Scientifico Ospedale San Raffaele, Medical Physics, Milan, Italy, [2] Fondazione Centro San Raffaele, Milan, Italy, [3] Istituto di Candiolo—Fondazione del Piemonte per l'Oncologia IRCCS, Radiotherapy, Turin, Italy, [4] IRCCS Istituto Nazionale dei Tumori "Regina Elena," Radiotherapy, Rome, Italy, [5] Ospedale di Ivrea, Radiotherapy, Ivrea, Italy, [6] Cliniche Gavazzeni-Humanitas, Radiotherapy, Bergamo, Italy, [7] Comprensorio Sanitario di Bolzano, Radiotherapy, Bolzano, Italy, [8] Ospedale degli Infermi, Radiotherapy, Biella, Italy, [9] Fondazione IRCCS Istituto Nazionale dei Tumori, Radiotherapy, Milan, Italy, [10] Azienda Ospedaliero Universitaria S. Maria della Misericordia, Radiotherapy, Udine, Italy, [11] Ospedale Regionale Parini-AUSL Valle d'Aosta, Radiotherapy, Aosta, Italy, [12] Fondazione IRCCS Istituto Nazionale dei Tumori, Prostate Cancer Program, Milan, Italy, [13] Department of Oncology and Hemato-Oncology, University of Milan, Milan, Italy, [14] Istituto Scientifico Ospedale San Raffaele, Radiotherapy, Milan, Italy, [15] University Vita-Salute San Raffaele, Milan, Italy

OPEN ACCESS

Edited by:
Sean P. Collins,
Georgetown University, United States

Reviewed by:
Young Kwok,
University of Maryland Medical Center, United States
Nima Aghdam,
MedStar Georgetown University Hospital, United States

***Correspondence:**
Claudio Fiorino
fiorino.claudio@hsr.it

Specialty section:
This article was submitted to Radiation Oncology, a section of the journal Frontiers in Oncology

Received: 15 January 2020
Accepted: 15 June 2020
Published: 23 July 2020

Citation:
Bresolin A, Garibaldi E, Faiella A, Cante D, Vavassori V, Waskiewicz JM, Girelli G, Avuzzi B, Villa E, Magli A, Noris Chiorda B, Munoz F, Sanguineti G, Gabriele P, Gatti M, Rancati T, Valdagni R, Di Muzio N, Fiorino C and Cozzarini C (2020) Predictors of 2-Year Incidence of Patient-Reported Urinary Incontinence After Post-prostatectomy Radiotherapy: Evidence of Dose and Fractionation Effects. Front. Oncol. 10:1207. doi: 10.3389/fonc.2020.01207

Objective: To investigate predictors of patient-reported urinary incontinence (PRUI) in the first 2 years after post-prostatectomy radiotherapy (PORT) with particular emphasis on possible dose-effect relationships.

Patients and Methods: Two-hundred-thirteen patients, whose clinical and dosimetric data were prospectively collected within a registered multi-institutional cohort study, underwent PORT with adjuvant ($n = 106$) or salvage ($n = 107$) intent with conventional ($n = 123$, prescribed dose to the prostatic bed: 66.6–79.8Gy in 1.8–2.0Gy/fr) or moderately hypo- ($n = 90$, 65.8–76.8Gy in 2.1–2.7Gy/fr) fractionation during the period 2011–2017. PRUI was evaluated through the ICIQ-SF questionnaire filled in at baseline and every 6 months thereafter. The analysis focused on three ICIQ-based clinically relevant endpoints: (a) very frequent leakage (FREQUENCY, ICIQ3 score >3), (b) moderate to severe amount of urine loss (AMOUNT, ICIQ4>2) (c) objective severe symptoms (OBJECTIVE, ICIQ3+4>5). Predictors of the incidence within 2 years for the three endpoints were investigated focusing only on patients without endpoint symptoms at baseline. A uni-variable logistic regression analysis was performed in order to determine the best dose metrics describing PRUI risk in terms of 2-Gy equivalent dose (EQD2) calculated with different α/β values reported in the literature (0.8, 3, 5Gy), and to identify the most significant clinical variables. Variables showing $p < 0.20$ at uni-variable analysis

were entered into a backward stepwise multi-variable logistic regression analysis. Lastly, the goodness of fit and model calibration were evaluated and internally validated.

Results: Patients without symptoms at baseline experienced (a), (b), and/or (c) within 2 years in 41/130 (32%), 40/192 (21%), and 41/129 (32%) of the cases, respectively. EQD2 for $\alpha/\beta = 0.8$Gy was the best dose metric associated with PRUI. Multi-variable analysis identified baseline incontinence levels as the strongest predictor for all endpoints ($p < 0.006$). Both FREQUENCY and OBJECTIVE were significantly influenced also by EQD2($\alpha/\beta = 0.8$Gy). The goodness of fit was excellent, as was the calibration; internal calibration confirmed apparent performance.

Conclusion: Baseline mild urinary incontinence symptoms strongly modulate the 2-year risk of PRUI. In addition, FREQUENCY is characterized by a marked dose-effect relationship also influencing the trend of OBJECTIVE, with results more reliable than AMOUNT as an objective index. A strong impact of fractionation on severe PRUI after post-prostatectomy radiotherapy also emerged.

Keywords: urinary incontinence, predictive models, prostatectomy, radiotherapy, prostate cancer

INTRODUCTION

Urinary toxicity is a common side effect of radiotherapy for prostate cancer (PCa), despite the modern intensity-modulated (IMRT) delivery techniques and image-guidance technologies currently available (1, 2). Amongst the wide variety of symptoms included in the term "urinary toxicity," urinary incontinence (UI) plays an important role in the deterioration of patient quality of life.

The reported incidence of severe late incontinence after radical radiotherapy for PCa at 3–5 years ranges between 1 and 5%, but increases up to more than 20% in the post-operative setting (3–5). In general, since prostatectomy may negatively impact the urinary outcome *per se* (6), the actual detrimental impact on urinary function deriving from post-operative radiotherapy (PORT) is difficult to quantify.

The difficulty in sparing the bladder, owing to its proximity to the target, but especially the substantial lack of adequate knowledge concerning predictive factors of radiation-induced urinary incontinence represent the most significant limitations to further reducing both the rate and the severity of urinary complications. High-quality individually and prospectively collected data relative to a large number of patients followed for a sufficient long time are therefore eagerly awaited in order to develop reliable models in this field.

In addition, the optimal dose in the adjuvant (ART) and salvage (SRT) settings remains controversial. The radiation dose delivered after radical prostatectomy is typically 20–25% lower than that recommended in the case of radical radiotherapy (∼60–64 *vs.* 76–80 Gy). More recently, the community of radiation oncologists has demonstrated a growing interest, supported both by elegant radiobiological models (7, 8) and retrospective analyses (7, 9, 10), in dose escalation in the setting of post-prostatectomy radiotherapy. The evidence of a relationship between radiation dose and clinical outcome has in fact been highlighted by several studies (8–12), supporting the hypothesis of a dose-response effect for PORT not significantly different from that observed for radical irradiation. The possible benefit deriving from escalating the radiation dose from 64 to 70 Gy in the salvage setting is currently under investigation by the randomized, multi-centric, Phase III trial SAKK 09/10 (13), whose preliminary results indicate that dose intensification of SRT had no impact on early urinary continence recovery or prevalence of *de novo* incontinence. Nevertheless, to date no robust data on a possible independent relationship between dose-escalation and effects of fractionation in the post-prostatectomy setting and an increased risk of mid-term risk of persistence/worsening of post-prostatectomy urinary incontinence are available, especially in the setting of patient-reported toxicity.

The main objectives of the current research were therefore:

1) the quantification of the dose-effect relationship of 2-year patient-reported urinary incontinence (PRUI) in the setting of post-prostatectomy irradiation;
2) the identification of clinically significant predictors of 2-year PRUI incidence after ART and SRT.

Urinary incontinence was assessed using patient-reported data prospectively collected within a prospective and registered multi-Institute observational study.

PATIENTS AND METHODS

The IHU-WPRT TOX Study

The IHU-WPRT TOX (Intestinal Hematologic Urinary Toxicity from Whole-Pelvis Radiotherapy) is a registered multi-Institutional cohort study (ClinicalTrials.gov identifier #NCT02803086) aimed at developing predictive models of toxicity after WPRT for PCa (14–16). Before the activation of the IHU-WPRT TOX trial in February 2014, a Review Board approved pilot study had been performed at the Coordinating

Institute (San Raffaele Scientific Institute, Milan, Italy) (14, 15). The IHU-WPRT TOX was approved by the Institutional Review Board of each of the participating Institutes and is still enrolling patients (16).

Prophylactic WPRT, always at the discretion of the referring radiation oncologist, is usually advised for patients with seminal vesicle invasion, Gleason score ≥ 7, pre-surgical PSA >10 ng/mL and/or histologically positive lymph-nodes at prostatectomy, or in the case of PSA ≥ 0.50 ng/mL in the salvage setting.

According to the protocol requirements (14–16), the validated Italian versions of the IBDQ (Inflammatory Bowel Disease Questionnaire) (17), ICIQ-SF (International Consultation on Incontinence Questionnaire-Short Form) (18) and IPSS (International Prostatic Symptom Score) (19) are to be prospectively collected for the patient-reported evaluation of WPRT-induced intestinal and urinary toxicity. All the questionnaires are to be filled in by the enrolled patients at baseline, at radiation treatment mid-point and end, at 3 and 6 months after radiotherapy conclusion, and thereafter every 6 months, up to 5 years. At identical time intervals a blood sample is to be collected for the evaluation of WPRT-induced hematologic toxicity (14, 15). In addition to clinical and dosimetric data (see below section Dose-Effect Quantification, Uni- and Multivariable Models and **Tables 3**, **4** for the list of the variables analyzed), patient personality and its possible impact on self-reported radiation-induced toxicities was considered by means of the abbreviated 24-item version of the revised Eysenck Personality Questionnaire (EPQ-R) (20) filled in by patients at baseline. Four personality traits are measured using four scales, each scored from 0 (no presence of the trait) to 6 (maximal presence of the trait): Extraversion (sociability, impulsiveness, but also some tendency to aggressiveness), Neuroticism (emotional instability, nervousness, and general anxiety), Psychoticism (tough-mindedness, but also a measurement of hostility) and Lie (a control scale introduced into personality measures in order to detect the "faking good" of scores on other scales; the Lie scale is reconstructed from items listing behaviors that are either socially desirable but infrequently practiced or frequently practiced but socially undesirable). When only one answer for each personality trait was missing ($n = 12$), imputation of EPQ-R scores was accomplished using the most frequent value reported by those patients who answered similarly.

The ICIQ-SF Questionnaire

The ICIQ-SF consists of six items, three of which do not generate a score as they concern personal patient data (questions 1 and 2) or descriptive features (question 6). The quantitative items are represented by questions 3 (hereafter ICIQ3, score 0–5) and 4 (ICIQ4, score 0–6) pertaining to the frequency and amount of urine loss, respectively, and question 5 (ICIQ5, score 0–10) quantifying the subjective patient-perceived impairment of quality of life attributable to PRUI. The sum of these scores is used to quantify both the "objective" component (ICIQ3 + 4) and the "total" detriment (ICIQ3 + 4 + 5) of PRUI. Higher scores indicate worse symptoms.

Patient Population

At the time of analysis, 2-year data were available for 213 patients. The population selected for the current work is composed of 71 patients from the pilot study (14, 15) and 142 from the observational protocol (16), with the requirements for the two studies being identical, according to the following criteria:

(i) patient underwent post-prostatectomy radiotherapy with either adjuvant or salvage intent.
(ii) ICIQ-SF was completed both at baseline and at 24 months.
(iii) at least two questionnaires were available between 6 and 24 months after radiotherapy end.

ICIQ-Based Endpoints

The analysis focused on three clinically significant endpoints based on the quantitative and objective questions of the ICIQ-SF. In particular, endpoints were selected *a priori*, subsequent to a thorough discussion within the Institutes involved in the protocol, as those deemed to be "clinically significant" for patients, as follows:

(a) very frequent leakage (FREQUENCY), defined as an ICIQ3 score $>$ 3 at least once between 6 and 24 months after PORT end;
(b) moderate to severe amount of urine loss (AMOUNT), defined as an ICIQ4 score >2 at least once between 6 and 24 months after PORT conclusion (the choice of this endpoint, somewhat "weaker" as compared to that selected for FREQUENCY, was deemed necessary owing to the markedly lower number of events, see below);
(c) objective severe symptoms (OBJECTIVE), defined as the sum of ICIQ3 + 4 scores >5 at least once between 6 and 24 months following PORT end.

Incidentally, all of the three scores corresponded to the highest tertile in the considered population. For each endpoint only patients who did not exhibit an already impaired situation at baseline were considered, and therefore patients with ICQ3 $>$ 3 or ICQ4 $>$ 2 or ICQ3 + 4 $>$ 5 at baseline were excluded when defining the corresponding endpoint.

A longitudinal analysis of the symptom trend across the 24 months post-radiotherapy was performed in order to characterize and compare the final sample group of patients and the part of population that was excluded from the statistical analyses.

Dose-Effect Quantification, Uni-, and Multivariable Models

Firstly, a univariable logistic regression analysis was performed in order to select the best dose metrics associated to an increased risk of the ICIQ-based endpoints in terms of EQD2 doses calculated according to the different α/β values most commonly reported by the available literature for the bladder (i.e., 0.8, 3, and 5 Gy). The prescribed EQD2 to PBPTV was considered here as a surrogate for the high dose received by the normal bladder adjacent to the PBPTV. The dose metric corresponding to the model with the maximum log-likelihood was selected to be used for further analysis.

TABLE 1 | Summary of patient characteristics.

Variables	Overall ($n = 213$)	Adjuvant ($n = 106$)	Salvage ($n = 107$)
PATIENT DATA			
Age (yr)	67 (62–71)	67.5 (63–72)	67 (62–71)
BMI (kg/m2)	25.9 (15.9–27.7)	26.4 (24.4–28.1)	25.5 (24.1–27.3)
Hypertension (yes)	99 (47%)	49 (47%)	50 (47%)
Smoke (yes)	36 (17%)	21 (21%)	15 (14%)
Diabetes (yes)	15 (7%)	8 (8%)	7 (7%)
SURGERY DATA			
Type of Surgery			
Open	131 (63%)	74 (70%)	57 (55%)
Robotic	56 (27%)	23 (22%)	33 (32%)
Laparoscopic	22 (10%)	8 (8%)	14 (13%)
PSA (ng/ml)			
Pre-RP	8.01 (5.63–12.93)	8.68 (6.00–15.45)	7.60 (5.40–10.08)
Post-RP	0.04 (0.01–0.12)	0.07 (0.02–0.27)	0.03 (0.01–0.05)
No of removed lymph nodes	12 (6–20)	15 (8–22)	10 (3–18)
RADIOTHERAPY DATA			
PSA pre-RT (ng/ml)	0.24 (0.05–0.48)	0.06 (0.02–0.32)	0.33 (0.21–0.54)
Time to RT (mo)	8.3 (4–26.7)	4.0 (3.2–5.5)	26.7 (16.1–56.1)
Fractionation			
CONV (1.8–2.0 Gy/fr)	123 (58%)	55 (52%)	68 (64%)
HYPO (2.1–2.7 Gy/fr)	90 (42%)	51 (48%)	39 (36%)
Dose to PBPTV (Gy)			
Prescribed dose	71 (69–74)	70 (67–72)	73 (70–74)
EQD2($\alpha/\beta = 0.8$ Gy)	74 (70–76)	74 (70–74)	74 (70–76)
Irradiation technique			
SF-IMRT	20 (9%)	6 (6%)	14 (13%)
VMAT	106 (50%)	52 (49%)	54 (50%)
Tomotherapy	87 (41%)	48 (45%)	39 (37%)
Gleason score			
ISUP Groups 1–3	58 (27%)	17 (16%)	41 (39%)
ISUP Groups 4–5	154 (73%)	89 (84%)	65 (61%)
Stage T			
pT2	67 (32%)	11 (11%)	56 (52%)
pT3a	72 (34%)	36 (34%)	36 (34%)
pT3b & pT4	73 (34%)	58 (55%)	15 (14%)
ANDROGEN DEPRIVATION THERAPY DATA			
No ADT	116 (57%)	45 (45%)	71 (68%)
Bicalutamide monotherapy	25 (12%)	14 (14%)	11 (11%)
LH-RH	51 (25%)	35 (35%)	16 (16%)
CAB	12 (6%)	7 (7%)	5 (5%)
PATIENT-REPORTED DATA			
EPQ-R			
Extraversion	4 (3–5)	4 (3–5)	4 (3–5)
Neuroticism	1 (0–3)	1 (1–3)	1 (0–2)
Psychoticism	1 (0–1)	1 (0–1)	1 (0–2)
Lie	5 (4–6)	6 (5–6)	5 (4–6)
ICIQ-SF at baseline pre-RT			
ICIQ3			
Median	2	3	1
Quartiles (25–75%)	(0–4)	(1–4)	(0–3)
Tertiles (33–66%)	(1–3)	(2–4)	(0–2)
ICIQ4			
Median	2	2	2
Quartiles (25–75%)	(0–2)	(2–2)	(0–2)
Tertiles (33–66%)	(2–2)	(2–2)	(0–2)
ICIQ34			
Median	4	5	3
Quartiles (25–75%)	(0–6)	(3–6)	(0–5)
Tertiles (33–66%)	(3–5)	(4–6)	(0–4)

Data are presented as counts (percentages in brackets) for categorical variables and as median values (inter-quartile ranges in bracket) for continuous variables. CONV, conventionally fractionated; HYPO, hypofractionated; BMI, body mass index; RP, radical prostatectomy; RT, radiotherapy; PBPTV, prostatic bed planning target volume; EQD2, 2-Gy equivalent dose; ADT, androgen deprivation therapy; CAB, combined androgen blockade; EPQ-R, eysenck personality questionnaire revised; ICIQ-SF, International Consultation On Incontinence Modular Questionnaire Short Form.

Univariable analyses were also performed in order to identify, for each endpoint, the most significant clinical variables, including age, body mass index (BMI, kg/m^2), comorbidities such as diabetes and hypertension, smoking (yes *vs.* no/stopped at least 5 years before radiotherapy start), type of surgery, preoperative PSA, pathologic stage and Gleason score at prostatectomy, type and length of androgen deprivation therapy delivered concomitantly and after radiotherapy, months elapsed from prostatectomy to irradiation (time to radiotherapy), as well as ICIQ-SF scores at baseline.

Variables with a $p < 0.2$ at univariable analysis and without cross-correlations (Pearson or Spearman coefficient $\in [-0.25, 0.25]$) were entered into a backward stepwise multivariable logistic regression. Lastly, each model was reprocessed using only the variables retained by the backward multivariable analysis with a p-value threshold ≤ 0.05.

Goodness of fit was assessed by means of the Hosmer and Lemeshow test and the calibration plot (slope and R^2). Brier scores were used to measure accuracy. Internal validation was performed by 1,000 bootstrap resamplings, and optimism determined. Analyses were performed with MedCalc® version 12.1.4.0 (MedCalc Software, Mariakerke Brussels, Belgium) and the R software version 3.2.4 (©The R Foundation for Statistical Computing, Vienna, Austria).

RESULTS

The patients were treated from 2011–2017 in 11 Italian Institutes with either conventionally-fractionated radiotherapy ($n = 123$, prescribed dose to PBPTV: 66.6–79.8 Gy in 1.8–2.0 Gy/fr.) or

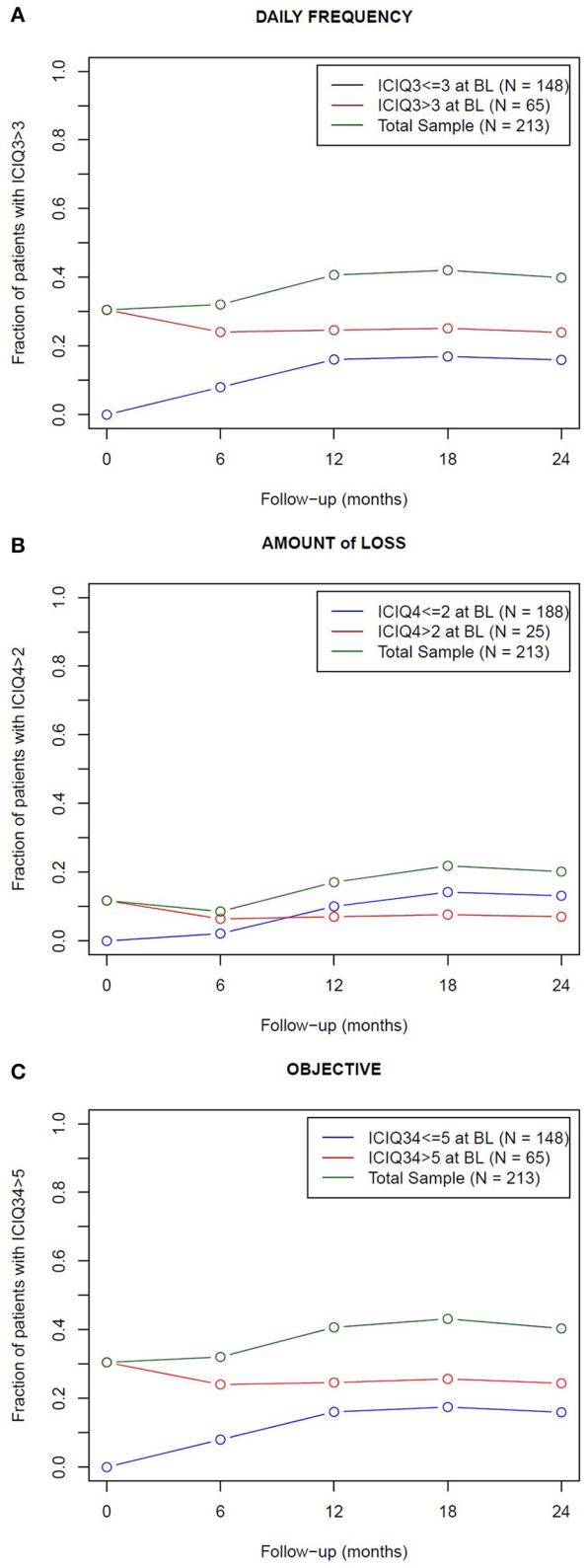

FIGURE 1 | Fraction of patients who experienced endpoint symptoms (green curve) across the 24 months following post-prostatectomy radiotherapy. The *(Continued)*

FIGURE 1 | total sample was dichotomized in patients who experienced (red curve) and did not experience (blue curve) the endpoint symptoms at baseline (BL): a not negligible fraction of patients with good baseline scores became incontinent (15–20%, according to the end-point definitions): inversely, the fraction of incontinent patients after radiotherapy slightly reduced in the group of patients incontinent at baseline. The endpoints are related to the frequency **(A)** and amount **(B)** of urine leakage and to the objective component **(C)** of urinary incontinence, as reported in the ICIQ-SF questionnaire.

moderately hypo-fractionated regimens ($n = 90$, prescribed dose to PBPTV: 65.8–76.8 Gy in 2.1–2.7 Gy/fr.) with either adjuvant ($n = 106$) or salvage ($n = 107$) intent. Patient and treatment characteristics of the two subpopulations are detailed in **Table 1**.

The prescribed doses to PBPTV (D) were converted into 2-Gy equivalent doses (EQD2) according to the linear-quadratic model (21):

$$EQD2\,(\alpha/\beta) = D\frac{(\alpha/\beta + d)}{(\alpha/\beta + 2)}$$

where d is the daily dose and α/β was set at 0.8, 3 and 5 Gy (hence EQD2(0.8), EQD2(3), EQD2(5), respectively), as reported in the literature (21, 22).

An impaired situation at baseline, according to the definition of the ICIQ-based endpoints (see ICIQ-Based Endpoints) was present in 31, 12, and 31% of patients for FREQUENCY, AMOUNT, and OBJECTIVE, respectively. As a consequence, the size of the final sample groups was: 148 patients for FREQUENCY, 188 for AMOUNT, and 148 for OBJECTIVE. It is noteworthy to underline that 31% of the entire population (67/213) was found to be "completely dry" (ICIQ3 + 4 = 0) before radiotherapy start.

The evolution of the fraction of patients experiencing (or not) the endpoint symptoms at baseline is shown in **Figure 1**, while the longitudinal trend of their mean ICIQ score is plotted in **Figure 2**. The Mann-Whitney-Wilcoxon test clearly indicated that the median values of the ICIQ score distributions in **Figure 2** were always significantly different between the two sample groups ($p < 0.001$).

When looking to the differences from baseline scores, patients with good baseline scores (< ICIQ-based endpoints) showed a significant worsening 12 months after radiotherapy end and thereafter; patients with higher (= worse) baseline scores improved with the best recovery achieved 6 months after radiotherapy conclusion, then usually returned to the baseline incontinence level at 24 months (**Table S1** of the Supplementary Material reports the p-values of the corresponding Mann-Whitney-Wilcoxon tests). In addition, the distribution of the changes between baseline and the 2-year scores confirmed an unbalanced distribution toward positive delta, i.e., worse symptoms in the group with good baseline score, as shown in **Figure S1** of the Supplementary Material.

The results of univariable analyses are summarized in **Tables 2**, **3**: an association with the dose was found for both the FREQUENCY and OBJECTIVE endpoints, while AMOUNT showed no dose-dependent trend (**Table 2**). The log likelihood

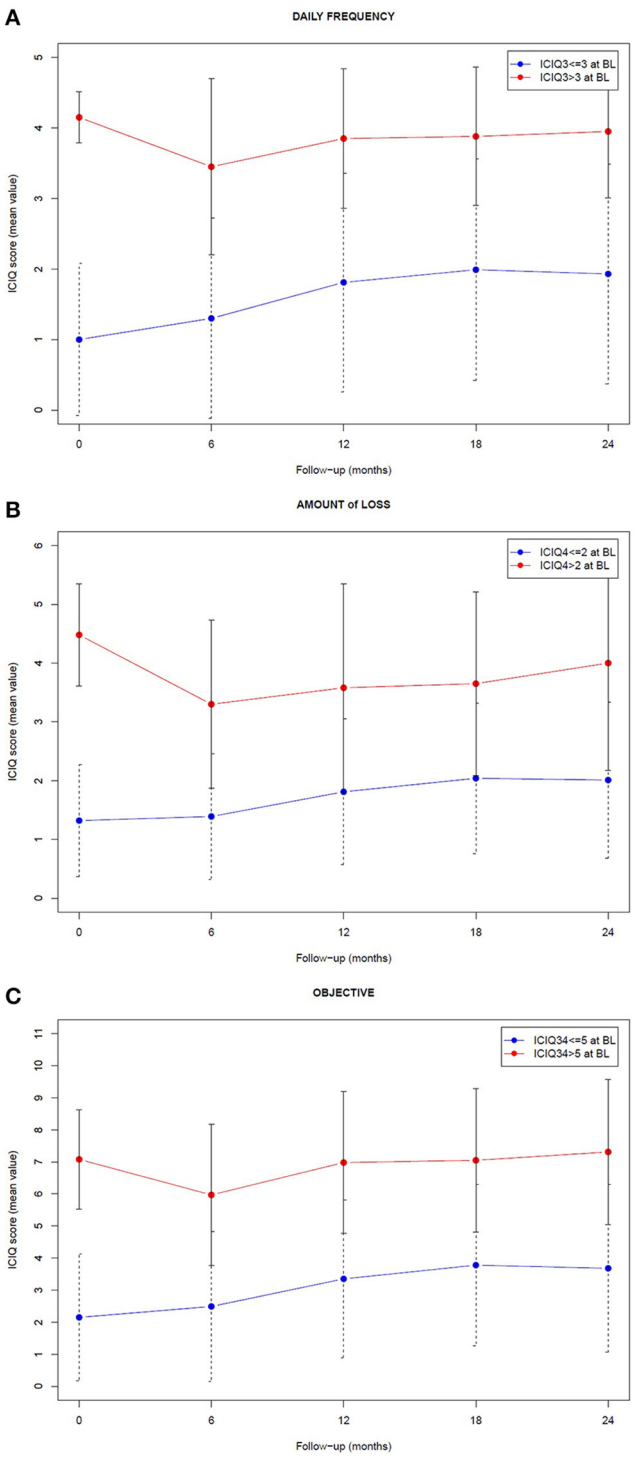

FIGURE 2 | Longitudinal trend of the mean ICIQ score associated with the sample group of patients who experienced (red) and did not experience (blue) the endpoint symptoms at baseline (BL). The endpoints are related to frequency **(A)**, amount **(B)**, and objective component **(C)** of urinary incontinence, as reported in ICIQ-SF questionnaire. Error bars represent the standard deviation associated with the score distribution at each time.

TABLE 2 | Results of the univariable logistic regression analysis: association between the 2 Gy equivalent dose at different $\frac{\alpha}{\beta}$ values (0.8, 3, and 5 Gy) and the endpoints related to frequency, amount, and objective component of urinary incontinence, as reported in ICIQ-SF.

Variables	*EQD2* (α/β)		
	$\alpha/\beta = 0.8$ Gy	$\alpha/\beta = 3$ Gy	$\alpha/\beta = 5$ Gy
FREQUENCY endpoint (ICIQ3>3)			
p-value	0.08	0.1	0.18
OR	1.06	1.09	1.09
CI (95%)	1.00–1.12	0.98–1.21	0.96–1.23
Log Likelihood	−94.32	−94.59	−95.02
AMOUNTT endpoint (ICIQ4>2)			
p-value	0.98	0.62	0.44
OR	1.00	1.03	1.05
CI (95%)	0.94–1.06	0.92–1.14	0.93–1.19
Log Likelihood	−97.31	−97.19	−97.02
OBJECTIVE endpoint (ICIQ3+4>5)			
p-value	0.08	0.1	0.18
OR	1.06	1.09	1.09
CI (95%)	1.00–1.12	0.98–1.21	0.96–1.23
Log Likelihood	−94.32	−94.59	−95.02

ICIQ-SF, International Consultation On Incontinence Modular Questionnaire Short Form.

of EQD2 (0.8) was higher with respect to those of EQD2 (3) and EQD2 (5); thus, EQD2 (0.8) was chosen as the dosimetric variable to be entered in the multi-variable analysis. For both FREQUENCY and OBJECTIVE endpoints, the *p*-values relative to EQD2 (0.8), age, smoking, and Gleason score were always $p < 0.2$, and the corresponding baseline ICIQ score emerged as the most significant variable ($p < 0.001$). The univariable analysis pertaining to the "amount of urine loss" endpoint (ICIQ4) confirmed baseline ICIQ as the most significant variable indicating, in addition, some role for age, robot surgery, and Extraversion (**Table 3**).

Table 4 outlines the resulting multi-variable models. Patients reporting none to mild symptoms at baseline experienced the pre-specified FREQUENCY, AMOUNT, and OBJECTIVE endpoints within 2 years from post-operative irradiation in 52/148 (35%), 40/188 (21%), and 52/148 (35%) of the cases, respectively. The corresponding baseline score was the most significant predictor for all endpoints ($p < 0.006$). Both FREQUENCY and OBJECTIVE were largely modulated by EQD2 (0.8), as illustrated in **Figure 3**.

The goodness of fit was always satisfactory (Hosmer and Lemeshow test > 0.78), as was the calibration (see **Figure 4**), with slopes and R^2 ranging between 1.0–1.1 and 0.82–1.00, respectively. Internal validation resulted in optimism of 0.005–0.01 on the Brier score, confirming the robustness of the results.

DISCUSSION

This is the first analysis focused on the identification of the main predictors of mid-term patient-reported UI and on the dose-effect quantification in a cohort of patients treated

TABLE 3 | Results of the univariable logistic regression analysis (*p*-value and Odds-Ratio).

	Frequency (ICIQ3>3)		Amount (ICIQ4>2)		Objective (ICIQ3+4>5)	
Variables	***p*-value**	**OR**	***p*-value**	**OR**	***p*-value**	**OR**
PATIENT VARIABLES						
Age (yr)	**0.186**	1.04	**0.036**	1.06	**0.186**	1.04
BMI (kg/m2)	0.806	1.01	0.694	1.02	0.806	1.01
Hypertension						
No		Ref.		Ref.		Ref.
Yes	0.550	1.23	0.712	1.14	0.550	1.23
Smoke						
No		Ref.		Ref.		Ref.
Yes	**0.139**	1.95	0.855	0.91	**0.139**	1.95
Diabetes						
No		Ref.		Ref.		Ref.
Yes	0.752	1.24	0.878	1.11	0.752	1.24
SURGERY VARIABLES						
Type of Surgery						
Open		Ref.		Ref.		Ref.
Robotic	0.963	1.02	**0.186**	0.56	0.963	1.02
Laparoscopic	0.859	0.89	0.510	0.64	0.859	0.89
PSA (ng/ml)						
pre-RP	0.463	1.01	1.000	1.00	0.463	1.01
post-RP	0.846	0.97	0.928	1.02	0.846	0.97
No of removed lymph nodes	0.317	0.98	0.371	0.98	0.317	0.98
RADIOTHERAPY VARIABLES						
PSA pre-RT (ng/ml)	0.879	1.01	0.698	1.02	0.879	1.01
Time to RT (mo)						
$\leq$ 8 months		Ref.		Ref.		Ref.
> 8 months	0.319	0.71	0.243	0.66	0.319	0.71
EQD2($\alpha/\beta = 0.8$Gy)	**0.076**	1.06	0.975	1.00	**0.076**	1.06
Gleason score						
ISUP Groups 1–3		Ref.		Ref.		Ref.
ISUP Groups 4–5	**0.159**	0.59	0.568	0.80	**0.159**	0.59
Stage T						
pT2		Ref.		Ref.		Ref.
pT3a	0.673	1.20	0.572	0.79	0.673	1.20
pT3b & pT4	0.294	1.55	0.221	0.57	0.294	1.55
ANDROGEN DEPRIVATION THERAPY VARIABLES						
ADT						
No		Ref.		Ref.		Ref.
Yes	0.714	0.88	0.440	1.32	0.714	0.88
PATIENT-REPORTED VARIABLES						
EPQ-R						
Extraversion	0.944	1.01	**0.089**	0.83	0.944	1.01
Neuroticism	0.762	1.03	0.205	1.15	0.762	1.03
Psychoticism	0.344	0.84	0.436	0.86	0.344	0.84
Lie	0.433	0.89	**0.145**	1.30	0.433	0.89
ICIQ-SF at baseline	**<0.001**	1.81	**0.006**	1.91	**<0.001**	1.39

The endpoints are related to frequency, amount and objective component of urinary incontinence, as reported in ICIQ-SF. Significant values accepted for inclusion in subsequent multivariable analyses ($p < 0.2$) are in bold. BMI, body mass index; RP, radical prostatectomy; RT, radiotherapy; ADT, androgen deprivation therapy; CAB, combined androgen blockade; EPQ-R, eysenck personality questionnaire revised; ICIQ-SF, International Consultation On Incontinence Modular Questionnaire Short Form.

TABLE 4 | Results of the multi-variable logistic regression analysis.

Predictors	Coeff ± dev.std.	*p*-value	OR	CI (95%)
FREQUENCY—Frequency of urine loss				
Endpoint: ICIQ3 >3, *N* = 52/148 (35%), excluded: ICIQ3 >3 at baseline				
Baseline score	0.655 ± 0.174	<0.001	1.93	1.38–2.74
EQD2(0.8) [Gy]	0.075 ± 0.033	0.024	1.08	1.01–1.15
Intercept	−6.964			
H&L = 0.78	**Slope** = 1.06	R^2 = 0.82	**Brier score** = 0.198 (optimism = 0.01)	
AMOUNT—Amount of Urine Loss				
Endpoint: ICIQ4 >2, *N* = 40/188 (21%), excluded: ICIQ4 >2 at baseline				
Baseline score	0.648 ± 0.237	0.006	1. 91	1.24–3.19
Intercept	−2.269			
H&L = 1.00	**Slope** = 1.00	R^2 = 1.00	**Brier score** = 0.160 (optimism = 0.005)	
OBJECTIVE—Objective				
Endpoint: ICIQ3+4 >5, *N* = 52/148 (35%), excluded: ICIQ3+4 >5 at baseline				
Baseline score	0.371 ± 0.099	<0.001	1.45	1.20–1.77
EQD2(0.8) [Gy]	0.077 ± 0.033	0.022	1.08	1.01–1.16
Intercept	−7.220			
H&L = 0.97	**Slope** = 1.11	R^2 = 0.92	**Brier score** = 0.199 (optimism = 0.009)	

The endpoints are related to frequency, amount and objective component of urinary incontinence, as reported in ICIQ-SF.
H&L, Hosmer and Lemeshow test; ICIQ-SF, International Consultation on Incontinence Modular Questionnaire Short Form.

with post-prostatectomy irradiation. Owing to previous surgical injury, the urinary outcome of these patients could occasionally be somewhat worse than those undergoing radiotherapy with radical intent (23, 24); moreover, the growing evidence of a beneficial dose-effect relative to the risk of biochemical relapse (12) is gradually translating into the delivery of higher doses than in the past. The interplay between urinary recovery after surgery and the role of the timing of delivery of post-operative radiotherapy on baseline PRUI also contributes to further jeopardize the picture. Hence the necessity of a thorough analysis based upon both accurate endpoint definition and sufficiently large cohorts of patients treated at different dose levels in order to separately analyze the possible independent detrimental role of both previous surgery and dose-escalation in the post-prostatectomy setting.

The fine tuning of ICIQ-based endpoints allowed a focus on patients with none or only relatively mild symptoms after prostatectomy, corresponding to the most clinically significant subgroup, who exhibited a modulation and a worsening of patient-reported urinary incontinence across the 24 months following post-prostatectomy radiotherapy, as shown in **Figures 1**, **2**. On the contrary, the mean ICIQ score of the remaining patients who began with severe symptoms did not increase (worsen) following post-surgical irradiation (**Figure 2**): interestingly, a significant improvement was observed at 6 months after radiotherapy ($p < 0.002$), probably as the result of a predominant recovery from surgical damage independent from radiotherapy. Furthermore, the difference between the ICIQ score distributions related to the groups with and without symptoms according to the different endpoint definition at baseline was always significant ($p < 0.001$), supporting the hypothesis that pre-radiotherapy baseline urinary incontinence is the strongest predictor of long-term post-prostatectomy patient-reported UI recovery, regardless of the subsequent delivery of adjuvant or salvage irradiation.

As baseline UI is expected to impact post-radiotherapy UI recovery, our results are also consistent with those of van Stam et al. (25), who observed that patients starting SRT seven months or more after RP were more likely to recover urinary function after irradiation (25). Both studies lend support to the growing trend to spare as many men as possible immediate adjuvant radiotherapy in order to permit full recovery of their post-prostatectomy UI, also taking into account the possibility of treating them safely with early salvage irradiation at the first sign of a PSA rise. The first results of the multicenter, randomized Phase III trials RADICALS, to be confirmed in a longer follow-up, indicate no difference in terms of 5-year biochemical relapse-free survival and freedom from salvage hormonal therapy between patients managed with immediate ART or early SRT. On the contrary, the incidence of 1-year patient-reported UI worsening with respect to baseline was slightly but significantly higher (5.3 vs. 2.7%, $p = 0.008$) in the cohort treated with immediate ART (26).

The high quality data of the IHU WPRT TOX database and the heterogeneous range of prescribed doses delivered with both conventional and moderately hypo-fractionated regimens allowed a thorough quantification of the dose effect. An independent correlation between the analyzed endpoints and EQD2 was found for FREQUENCY and OBJECTIVE, and the best fit was achieved using $\alpha/\beta = 0.8$ Gy. These findings are strongly suggestive of an independent detrimental effect of both fractionation and higher doses on the risk of severe urinary incontinence following both adjuvant or salvage radiotherapy, consistent with the previously reported results of a large retrospective study (22).

Interestingly, the "amount" of urine leakage showed no relationship with the radiation doses, whereas it was found to be slightly correlated to one personality trait, Extraversion ($p = 0.089$) though at univariable analysis only. The apparent lack of dose-effect relationship for this endpoint could depend on the weak level of "objectivity" of the answers to the ICIQ4 item (the patient's perception of the "amount" of urine leakage is undoubtedly more "subjective" than that of "frequency"), as well as, at least in part, on the relatively "mild" end-point selected (ICIQ4 score >2 out of 6), a choice deemed necessary by the low frequency (21%) of more severe events. Consequently, the trend for frequency of urine loss (ICIQ3) also dominated the objective component of PRUI (ICIQ3 + 4) at both uni- and multivariable analyses.

The current analysis clearly highlighted that the probability of severe mid-term (2 years) PRUI was dramatically higher in patients with higher urinary incontinence baseline levels even when including only patients with none/mild symptoms

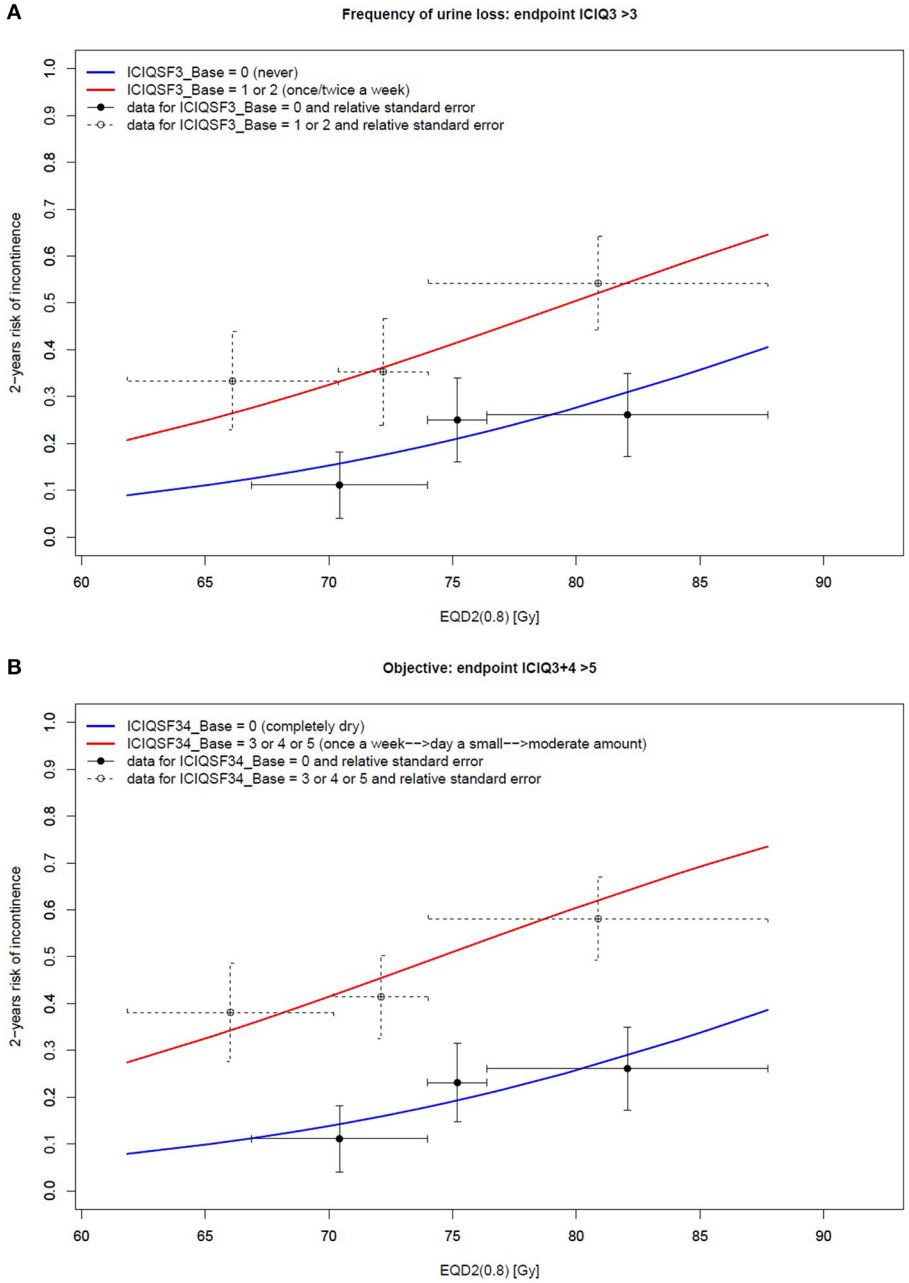

FIGURE 3 | Two-variable model of the 2-year risk of urinary incontinence according to **(A)** the frequency of urine loss and **(B)** objective endpoints: the relationship between the dose and the ICIQ-SF score. Vertical bars represent the standard error, while horizontal bars represent the size of each tertile.

at baseline, as in the current study. As shown in **Figure 3**, the 2-year risk of severe PRUI for patients with even only mild symptoms at baseline is much higher than that of the "completely dry" patients: when considering the range of doses typically delivered in the post-prostatectomy setting (65–75 Gy), this risk is in the range of 25–40% and 10–20%, respectively.

As recently reported, the 3-year risk for the same/slightly milder endpoints was around 5–10% for EQD2 (0.8) >80–85 Gy in the radical setting (3). This rate is dramatically lower than that found in this cohort of patients treated with post-prostatectomy radiotherapy, typically delivered at doses $\leq$ 75 Gy, even in the "completely dry" subset (as shown by the blue slope in **Figure 3**). These results suggest that, from the point of view of urinary incontinence, even in the case of an optimal baseline recovery at adjuvant or salvage radiotherapy start (i.e., "completely dry" patients) the clinical scenario is largely influenced by the "memory" of surgical injury, which is likely to negatively affect the repair capacity of the radiation-induced effects to the bladder and urethra.

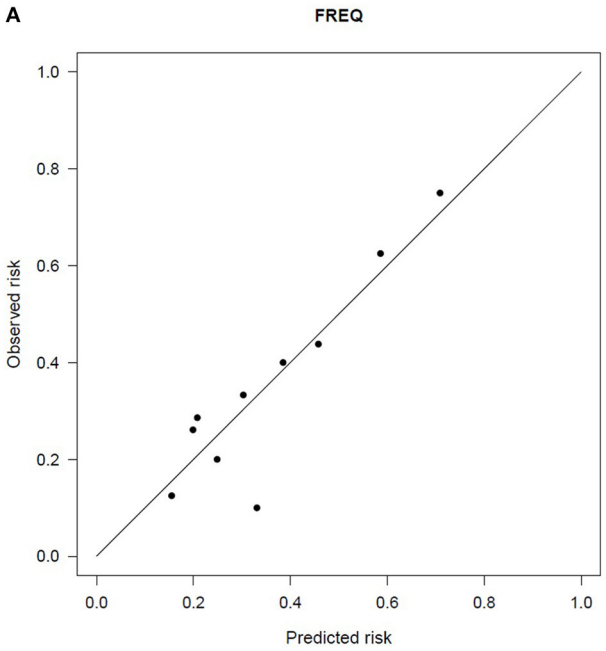

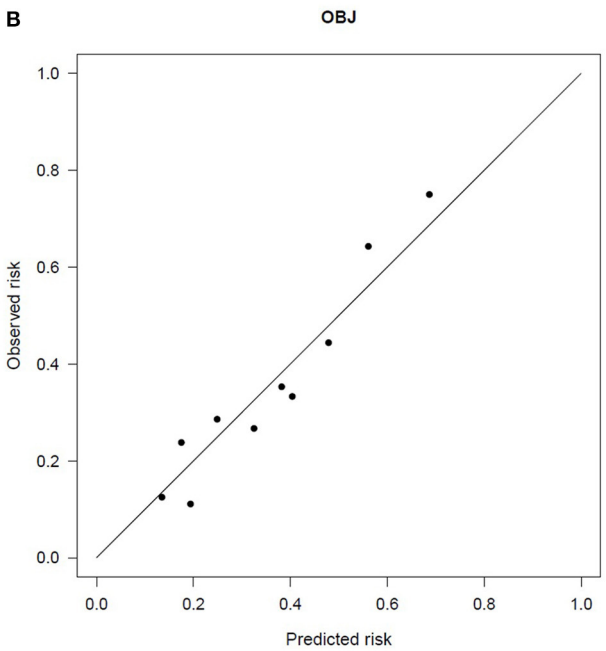

FIGURE 4 | Calibration plot of the two-variable model of the 2-year risk of urinary incontinence according to **(A)** the frequency of urine loss and **(B)** the objective endpoints.

CONCLUSIONS

The most predictive factor of the 2-year risk of severe patient-reported urinary incontinence for patients treated with post-prostatectomy radiotherapy showing none to mild baseline symptoms was found to be the baseline level of urinary incontinence, showing that even mild incontinence symptoms are associated to an increased risk of 2-year severe incontinence. In addition, the frequency of urine loss was characterized by a marked dose-effect relationship that predominantly influenced the trend of the "objective" component (frequency + amount) of urinary incontinence; on this issue, the patient's perception of the "frequency" of urine loss seemed to be more reliable as an objective index than that of the "amount." The identification of $\alpha/\beta = 0.8$ Gy as the best fitting value confirmed previously reported findings from retrospective studies (22) and clearly highlighted the marked impact of fractionation on the risk of late severe urinary incontinence after post-prostatectomy radiotherapy.

DATA AVAILABILITY STATEMENT

The datasets generated for this study will not be made publicly available for privacy reasons.

ETHICS STATEMENT

The studies involving human participants were reviewed and approved by San Raffaele Scientific Institute. The patients/participants provided their written informed consent to participate in this study.

AUTHOR CONTRIBUTIONS

CF and CC contributed to conception and design of the study. AB performed the statistical analysis and the interpretation of data under the supervision of CF and CC and wrote the first draft of the manuscript. All authors contributed to acquisition of data and to manuscript revision and approved the submitted version.

FUNDING

This study was supported by grant from AIRC (Associazione Italiana Ricerca Cancro)—Investigational Grants #14603 and #230150.

ACKNOWLEDGMENTS

Cinzia Bianconi and Fabio Badenchini are to be acknowledged for data-managing. The authors thank Dr. Frank Bagg for the linguistic revision of the manuscript.

SUPPLEMENTARY MATERIAL

The Supplementary Material for this article can be found online at: https://www.frontiersin.org/articles/10.3389/fonc.2020.01207/full#supplementary-material

REFERENCES

1. Rancati T, Palorini F, Cozzarini C, Fiorino C, Valdagni R. Understanding urinary toxicity after radiotherapy for prostate cancer: first steps forward. *Tumori.* (2017) 103:395–404. doi: 10.5301/tj.5000681
2. Landoni V, Fiorino C, Cozzarini C, Sanguineti G, Valdagni R, Rancati T. Predicting toxicity in radiotherapy for prostate cancer. *Phys Med.* (2016) 32:521–32. doi: 10.1016/j.ejmp.2016.03.003
3. Cozzarini C, Rancati T, Palorini F, Avuzzi B, Garibaldi E, Balestrini D, et al. Patient-reported urinary incontinence after radiotherapy for prostate cancer: quantifying the dose–effect. *Radiother Oncol.* (2017) 125:101–6. doi: 10.1016/j.radonc.2017.07.029
4. Ghadjar P, Zelefsky MJ, Spratt DE, Munck Af Rosenschöld P, Oh JH, Hunt M, et al. Impact of dose to the bladder trigone on long-term urinary function after high-dose intensity modulated radiation therapy for localized prostate cancer. *Int J Radiat Oncol Biol Phys.* (2014) 88:339–44. doi: 10.1016/j.ijrobp.2013.10.042
5. Cozzarini C, Fiorino C, Deantoni C, Briganti A, Fodor A, La Macchia M, et al. Higher-than-expected Severe (Grade 3-4) late urinary toxicity after postprostatectomy hypofractionated radiotherapy: a single-institution analysis of 1176 patients. *Eur Urol.* (2014) 66:1024–30. doi: 10.1016/j.eururo.2014.06.012
6. Taneja SS. Re: patient-reported outcomes after monitoring, surgery, or radiotherapy for prostate cancer. *J Urol.* (2017) 197:1265–6. doi: 10.1016/j.juro.2017.02.004
7. King CR, Kapp DS. Radiotherapy after prostatectomy: is the evidence for dose escalation out there? *Int J Radiat Oncol Biol Phys.* (2008) 71:346–50. doi: 10.1016/j.ijrobp.2007.10.008
8. King CR. The dose–response of salvage radiotherapy following radical prostatectomy: a systematic review and meta-analysis. *Radiother Oncol.* (2016) 121:199–203. doi: 10.1016/j.radonc.2016.10.026
9. Bernard JR, Buskirk SJ, Heckman MG, Diehl NN, Ko SJ, Macdonald OK, et al. Salvage radiotherapy for rising prostate-specific antigen levels after radical prostatectomy for prostate cancer: dose-response analysis. *Int J Radiat Oncol Biol Phys.* (2010) 76:735–40. doi: 10.1016/j.ijrobp.2009.02.049
10. Cozzarini C, Montorsi F, Fiorino C, Alongi F, Bolognesi A, Da Pozzo LF, et al. Need for high radiation dose (≥70 Gy) in early postoperative irradiation after radical prostatectomy: a single-institution analysis of 334 high-risk, node-negative patients. *Int J Radiat Oncol Biol Phys.* (2009) 75:966–74. doi: 10.1016/j.ijrobp.2008.12.059
11. Fiorino C, Broggi S, Di Muzio NG, Fossati N, Briganti A, Cozzarini C. Salvage radiation therapy after prostatectomy: understanding the dose–response effect. *Radiother Oncol.* (2017) 123:486–7. doi: 10.1016/j.radonc.2017.02.020
12. Fiorino C, Broggi S, Fossati N, Cozzarini C, Goldner G, Wiegel T, et al. Predicting the 5-year risk of biochemical relapse after postprostatectomy radiation therapy in ≥PT2, pN0 patients with a comprehensive tumor control probability model. *Int J Radiat Oncol Biol Phys.* (2016) 96:333–40. doi: 10.1016/j.ijrobp.2016.06.014
13. Ghadjar P, Hayoz S, Bernhard J, Zwahlen DR, Stein J, Hölscher T, et al. Impact of dose intensified salvage radiation therapy on urinary continence recovery after radical prostatectomy: results of the randomized trial SAKK 09/10. *Radiother Oncol.* (2018) 126:257–62. doi: 10.1016/j.radonc.2017.10.025
14. Sini C, Fiorino C, Perna L, Noris Chiorda B, Deantoni CL, Bianchi M, et al. Dose-volume effects for pelvic bone marrow in predicting hematological toxicity in prostate cancer radiotherapy with pelvic node irradiation. *Radiother Oncol.* (2016) 118:79–84. doi: 10.1016/j.radonc.2015.11.020
15. Cozzarini C, Chiorda BN, Sini C, Fiorino C, Briganti A, Montorsi F, et al. Hematologic toxicity in patients treated with postprostatectomy whole-pelvis irradiation with different intensity modulated radiation therapy techniques is not negligible and is prolonged: preliminary results of a longitudinal, observational study. *Int J Radiat Oncol Biol Phys.* (2016) 95:690–5. doi: 10.1016/j.ijrobp.2016.01.022
16. Sini C, Noris Chiorda B, Gabriele P, Sanguineti G, Morlino S, Badenchini F, et al. Patient-reported intestinal toxicity from whole pelvis intensity-modulated radiotherapy: first quantification of bowel dose–volume effects. *Radiother Oncol.* (2017) 124:296–301. doi: 10.1016/j.radonc.2017.07.005
17. Ciccocioppo R, Klersy C, Russo ML, Valli M, Boccaccio V, Imbesi V, et al. Validation of the italian translation of the inflammatory bowel disease questionnaire. *Dig Liver Dis.* (2011) 43:535–41. doi: 10.1016/j.dld.2010.12.014
18. Avery K, Donovan J, Peters TJ, Shaw C, Gotoh M, Abrams P. ICIQ: a brief and robust measure for evaluating the symptoms and impact of urinary incontinence. *Neurourol Urodyn.* (2004) 23:322–30. doi: 10.1002/nau.20041
19. Barry MJ, Fowler FJ, O'Leary MP, Bruskewitz RC, Holtgrewe HL, Mebust WK, et al. The American urological association symptom index for benign prostatic hyperplasia. the measurement committee of the American urological association. *J Urol.* (1992) 148:1549–57. doi: 10.1016/S0022-5347(17)36966-5
20. Francis LJ, Brown LB, Philipchalk R. The development of an abbreviated form of the revised Eysenck personality questionnaire (EPQR-A): its use among students in England, Canada, the USA and Australia. *Pers Individ Dif.* (1992) 13:443–9. doi: 10.1016/0191-8869(92)90073-X
21. Fowler JF. The radiobiology of prostate cancer including new aspects of fractionated radiotherapy. *Acta Oncol.* (2005) 44:265–76. doi: 10.1080/02841860410002824
22. Fiorino C, Cozzarini C, Rancati T, Briganti A, Cattaneo GM, Mangili P, et al. Modelling the impact of fractionation on late urinary toxicity after postprostatectomy radiation therapy. *Int J Radiat Oncol Biol Phys.* (2014) 90:1250–7. doi: 10.1016/j.ijrobp.2014.08.347
23. Budäus L, Bolla M, Bossi A, Cozzarini C, Crook J, Widmark A, et al. Functional outcomes and complications following radiation therapy for prostate cancer: a critical analysis of the literature. *Eur Urol.* (2012) 61:112–27. doi: 10.1016/j.eururo.2011.09.027
24. Cozzarini C, Fiorino C, Da Pozzo LF, Alongi F, Berardi G, Bolognesi A, et al. Clinical factors predicting late severe urinary toxicity after postoperative radiotherapy for prostate carcinoma: a single-institute analysis of 742 patients. *Int J Radiat Oncol Biol Phys.* (2012) 82:191–9. doi: 10.1016/j.ijrobp.2010.09.027
25. van Stam MA, Aaronson NK, Pos FJ, Bosch JLHR, Kieffer JM, Tillier CN, et al. The effect of salvage radiotherapy and its timing on the health-related quality of life of prostate cancer patients. *Eur Urol.* (2016) 70:751–7. doi: 10.1016/j.eururo.2016.03.010
26. Parker C, Clarke NV, Cook A, Kynaston HG, Meidahl Petersen P, Cross W, et al. Timing of radiotherapy (RT) after radical prostatectomy (RP): first results from the RADICALS RT randomised controlled trial (RCT) [NCT00541047]. *Ann Oncol.* (2019) 30(Suppl. 5):v851–934. doi: 10.1093/annonc/mdz394.042

Conflict of Interest: The authors declare that the research was conducted in the absence of any commercial or financial relationships that could be construed as a potential conflict of interest.

frontiers in Oncology

ORIGINAL RESEARCH
published: 06 August 2020
doi: 10.3389/fonc.2020.01395

Predictive Modeling of Thoracic Radiotherapy Toxicity and the Potential Role of Serum Alpha-2-Macroglobulin

Donata von Reibnitz[1], Ellen D. Yorke[2], Jung Hun Oh[2], Aditya P. Apte[2], Jie Yang[2], Hai Pham[2], Maria Thor[2], Abraham J. Wu[1], Martin Fleisher[3], Emily Gelb[1], Joseph O. Deasy[2] and Andreas Rimner[1]*

[1] Department of Radiation Oncology, Memorial Sloan Kettering Cancer Center, New York, NY, United States, [2] Department of Medical Physics, Memorial Sloan Kettering Cancer Center, New York, NY, United States, [3] Department of Laboratory Medicine, Memorial Sloan Kettering Cancer Center, New York, NY, United States

Background: To investigate the impact of alpha-2-macroglobulin (A2M), a suspected intrinsic radioprotectant, on radiation pneumonitis and esophagitis using multifactorial predictive models.

Materials and Methods: Baseline A2M levels were obtained for 258 patients prior to thoracic radiotherapy (RT). Dose-volume characteristics were extracted from treatment plans. Spearman's correlation (Rs) test was used to correlate clinical and dosimetric variables with toxicities. Toxicity prediction models were built using least absolute shrinkage and selection operator (LASSO) logistic regression on 1,000 bootstrapped datasets.

Results: Grade ≥2 esophagitis and pneumonitis developed in 61 (23.6%) and 36 (14.0%) patients, respectively. The median A2M level was 191 mg/dL (range: 94–511). Never/former/current smoker status was 47 (18.2%)/179 (69.4%)/32 (12.4%). We found a significant negative univariate correlation between baseline A2M levels and esophagitis ($Rs = -0.18/p = 0.003$) and between A2M and smoking status ($Rs = 0.13/p = 0.04$). Further significant parameters for grade ≥2 esophagitis included age ($Rs = -0.32/p < 0.0001$), chemotherapy use ($Rs = 0.56/p < 0.0001$), dose per fraction ($Rs = -0.57/p < 0.0001$), total dose ($Rs = 0.35/p < 0.0001$), and several other dosimetric variables with $Rs > 0.5$ ($p < 0.0001$). The only significant non-dosimetric parameter for grade ≥2 pneumonitis was sex ($Rs = -0.32/p = 0.037$) with higher risk for women. For pneumonitis D15 (lung) ($Rs = 0.19/p = 0.006$) and D45 (heart) ($Rs = 0.16/p = 0.016$) had the highest correlation. LASSO models applied on the validation data were statistically significant and resulted in areas under the receiver operating characteristic curve of 0.84 (esophagitis) and 0.78 (pneumonitis). Multivariate predictive models did not require A2M to reach maximum predictive power.

Conclusion: This is the first study showing a likely association of higher baseline A2M values with lower risk of radiation esophagitis and with smoking status. However, the baseline A2M level was not a significant risk factor for radiation pneumonitis.

Keywords: alpha-2-macroglobulin (A2M), thoracic radiation, toxicity, radioprotection, predictive modeling

OPEN ACCESS

Edited by:
Claudio Fiorino, San Raffaele Hospital (IRCCS), Italy

Reviewed by:
Francesco Tommasino, University of Trento, Italy
Joseph Stancanello, Guerbet, France

***Correspondence:**
Jung Hun Oh
OhJ@mskcc.org

Specialty section:
This article was submitted to Radiation Oncology, a section of the journal Frontiers in Oncology

Received: *15 January 2020*
Accepted: *02 July 2020*
Published: *06 August 2020*

Citation:
von Reibnitz D, Yorke ED, Oh JH, Apte AP, Yang J, Pham H, Thor M, Wu AJ, Fleisher M, Gelb E, Deasy JO and Rimner A (2020) Predictive Modeling of Thoracic Radiotherapy Toxicity and the Potential Role of Serum Alpha-2-Macroglobulin. Front. Oncol. 10:1395. doi: 10.3389/fonc.2020.01395

INTRODUCTION

Advances in radiation technology like intensity modulated radiation therapy (IMRT) and image guided RT (IGRT) have facilitated improved sparing of healthy surrounding tissues and organs. Nonetheless, radiation pneumonitis and esophagitis remain the most common dose-limiting toxicities in thoracic RT (1–6). Concurrent chemoradiation significantly increases the risk of developing pneumonitis or esophagitis compared to radiation alone (7, 8).

The reported incidence of pneumonitis after definitive thoracic RT ranges from 10 to 20%, although figures can vary greatly (3, 9–13). This is partly because pneumonitis remains a clinical diagnosis; there are no biomarkers or radiological findings that unequivocally confirm its presence. Medical intervention is required for patients with grade two or higher radiation pneumonitis, and severe cases can lead to fatal outcomes [Common Terminology Criteria for Adverse Events (CTCAE) v4.03, **Supplementary Material 1**]. Significant esophageal toxicity (grade 3–5) occurs in around 4% of patients with sequential chemotherapy and RT and in 18–22% of patients with concurrent chemoradiation (5, 14). Most patients experience mild symptoms like dysphagia and odynophagia while still undergoing radiation. Commonly opioids are used to control symptoms, but in severe cases, tube feeding or surgical intervention can be necessary (**Supplementary Material 1**).

To reduce dose-limiting toxicity in thoracic radiation, efforts have been made to adhere to normal tissue constraints derived from dose volume correlations with clinical toxicities (15). However, dose volume histograms do not fully predict clinical toxicities, as great interindividual variation remains. Intrinsic predictors of normal tissue radiation response may explain the variation and should be further analyzed.

Radioprotective agents, both natural and synthetic, can present an alternative method to prevent radiation-induced toxicity. Although this has been an active field of research for decades, only two compounds, amifostine and palifermine, are FDA-approved for the use in radiation therapy and neither is commonly used in routine thoracic RT (16–19). Another compound under investigation is alpha-2-Macroglobulin (A2M), a postulated intrinsic radioprotector. Human A2M is a glycoprotein and the largest non-immunoglobulin serum protein. In animal studies, A2M has exhibited radioprotective effects in healthy irradiated tissue. In studies with rats that underwent full body irradiation to 6.7 Gy, rats with endo- or exogenously increased levels of A2M had a higher rate of survival, regained their baseline body weight and lymphocyte count faster, and displayed normal proliferative ability of the liver tissue compared to the control groups with normal A2M levels (20–22). Suggested key mechanisms supporting the potential of A2M as a radioprotector include promoting expression of antioxidant enzymes, inhibiting fibroblast activation thus preventing fibrosis, deactivating pro-inflammatory cytokines, and enhancing DNA and cell repair mechanisms (23). Our previous study in a small cohort showed a correlation of A2M with radiation pneumonitis (9). Smoking can potentially increase A2M levels. However, literature specifically on A2M in smokers remains rare. Some studies confirmed higher A2M levels in smokers compared to non-smokers (24–26).

We investigated whether pre-treatment serum A2M levels are an independent predictive variable for the development of post-radiation toxicity in the lung and esophagus in a large cohort of patients receiving thoracic RT.

MATERIALS AND METHODS

Patients

Clinical, laboratory, treatment and toxicity data were systematically collected in a series of thoracic RT patients between 2012 and 2016 during standard treatment and follow-up procedures. Patients were treated with either conventionally fractionated RT using 3D conformal RT (3DCRT) or intensity-modulated RT (IMRT), or with stereotactic body RT (SBRT). Patients with any prior thoracic RT were excluded. Serum samples for A2M analysis were collected at baseline prior to fraction #1 of RT. We obtained a retrospective institutional review board waiver to analyze the data. Toxicity data consist of radiation pneumonitis and esophagitis rates graded per CTCAE v4.03. Data were obtained at baseline and at routine follow-up visits every 3 months for the first 2 years.

Alpha-2-Macroglobulin

Serum samples were taken $\leq$30 days prior to RT start, typically at the time of simulation. The mean and standard deviation between A2M measurement date and RT start date were 14 and 6 days, respectively. CLIA (Clinical Laboratory Improvement Amendments) approved A2M testing was performed at Quest Diagnostics Nichols Institute (San Juan Capistrano, CA). A2M levels were given in mg/dL; the normal range was defined as 100–280 mg/dL.

Treatment Plans

For patients treated before 2014, treatment plans were retrieved from our in-house planning system (27). From 2014 onwards, treatments were planned in the Eclipse treatment planning system (Varian Medical Systems, Palo Alto, CA). To analyze dosimetric data, treatment plans were imported to the research platform CERR (Computational Environment for Radiological Research) for computing dosimetric variables (28). Dosimetric variables were extracted from target structures: complete esophagus for esophagitis and "lung minus gross tumor volume (GTV)" and heart for pneumonitis. Before that, plan doses were converted to equivalent dose in 2 Gy fractions (EQD2) with α/β ratio of 10 for esophagus and 3 for lung minus GTV and heart (29). As radiation esophagitis tends to develop acutely during radiotherapy, one more set of dosimetric variables for esophagus was extracted in addition to the planned doses. For these fractional variables (denoted by the prefix "f," e.g., fmax dose) we divided the dose volume histogram (DVH) bins by the number of treatment days between the start of RT and the end of RT including weekends.

Statistical Methods

Univariate and multivariate analyses were performed to investigate associations between toxicity (esophagitis and pneumonitis) and A2M levels, clinical, and dosimetric variables. Patients were categorized into two groups for each endpoint: non-toxicity (grade <2) and clinically significant toxicity (grade ≥2).

A Wilcoxon rank-sum test was used to find a difference in A2M expression between the two groups. Spearman's correlation (Rs) test was used to assess associations between endpoints, Dx values (minimum dose to the volume with the x% hottest dose in the organ of interest), computed from $x = 5\%$ to $x = 100\%$ in intervals of 5%, mean dose, max dose, clinical variables, and A2M. For this test CTCAE grades 0–5 were used instead of dichotomized values (grade <2 and grade ≥2).

Multivariate analysis using the least absolute shrinkage and selection operator (LASSO) logistic regression was performed using features with $p < 0.1$ that resulted from the univariate Spearman's correlation test. To avoid variable instability due to high collinearity, Pearson's correlation test was conducted among all dosimetric variables before the multivariate analysis. A cutoff of Pearson's correlation coefficient >0.75 was used to determine a relatively small group of variables for further LASSO modeling, by selecting a single variable that has the best correlation with the endpoint among a set of correlated variables after hierarchical clustering.

To rigorously verify model validity, the data were split into two groups (training data with 2/3 and validation data with 1/3 of samples). The training and validation data were balanced with cancer subtypes and outcomes. This split was performed separately for pneumonitis and esophagitis. The model building process was carried out using only the training data. Furthermore, to examine the stability of LASSO variable selection, the model building process was conducted using a bootstrapped dataset generated from the training data. Finally, the validation data were tested on the resulting model, quantified by the area under the receiver operating characteristic curve (AUC) as a function of true positive rate (sensitivity) and false positive rate (1-specificity). The final reported results represent the average performance on the validation data for predictive models built using 1,000 bootstrapped datasets.

For statistical analyses, R language (version 3.2.4), MATLAB (version 8.6.0; MathWorks. Natick, MA) and SPSS (version 24; IBM. Armonk, NY) were used.

RESULTS

Patient Characteristics

In total, 258 patients were eligible for analysis. Most patients were former ($n = 179$, 69.4%) or current smokers ($n = 32$, 12.4%). One hundred and thirty-four patients (51.9%) underwent chemotherapy in addition to RT and the median total RT dose was 54 Gy (range: 27–74 Gy) for conventional fractionation and 50 Gy (range: 30–70 Gy) for SBRT. The median A2M level was 191 mg/dL (range: 94–511 mg/dL). The median follow-up was 8.9 months (range: 0.2–40.2; calculated from the start of RT). More details are available in **Table 1**.

TABLE 1 | Patient characteristics.

Factor	*N*	%
Age [median, range]	69 (25–93) years	
Sex		
Male	122	47.3
Female	136	52.7
KPS [median, range]	90 (50–100) %	
Subgroups		
NSCLC	202	78.3
SCLC	17	6.6
Thymoma	8	3.1
Mesothelioma	25	9.7
Lung metastases (other primary)	6	2.3
Smoking history		
Never	47	18.2
Former	179	69.4
Current	32	12.4
Pack-years (former/current smokers) [median, range]	37 (1–204) years	
Alpha-2-macroglobulin [median, range]	191 (94–511) mg/dL	
Chemotherapy timing		
Concurrent	60	23.2
Sequential	74	28.7
No chemotherapy	124	48.1
RT total dose [median, range]		
Conventional RT	54 (27–74) Gy	
SBRT	50 (30–70) Gy	
Follow-up time (from start of RT) [median, range]	8.9 (0.2–40.2) months	
Time to toxicity [median]	1.0 months (esophagitis), 3.6 months (pneumonitis)	

Toxicities

Fifty-third patients (20.5%) experienced grade two and eight (3.1%) grade three radiation esophagitis. No grade four or five esophagitis was observed. Median time to development of esophagitis was 0.85 months after the start of RT (range: 0.2–6.47 months). Grade two radiation pneumonitis developed in 26 patients (10.1%), grade three in nine (3.5%) and grade four in one patient (0.4%). No grade five pneumonitis was observed. Median time to development of pneumonitis was 4.7 months after the start of RT (range: 1.3–8.1 months).

Of the patients who developed grade ≥2 esophagitis, 8 (13.1%) were never, 43 (70.5%) former and 10 (16.4%) current smokers whereas in pneumonitis 9 (25%) were never, 24 (66.7%) former and 3 (8.3%) current smokers.

Univariate Analysis

Alpha-2-Macroglobulin

A significant correlation between baseline A2M values and esophagitis was found ($Rs = -0.18/p = 0.003$). Using a Wilcoxon rank-sum test, we found that patients with grade <2 had significantly higher baseline serum A2M levels than patients with grade ≥2 esophagitis ($p = 0.015$) as shown in **Table 2**.

No statistically significant difference was found between baseline A2M levels and grade ≥2 pneumonitis ($p = 0.84$).

A trend between smoking status and A2M levels was observed. Current smokers had higher levels (217.3 mg/dl) compared to former (207.3 mg/dl) and never smokers (185.4 mg/dl), and former smokers had higher levels compared to never smokers. The A2M level had a significant correlation with a status of former/current smoker when compared to never smokers (Rs = 0.13/$p = 0.04$).

Clinical Factors

Among standard clinical variables, the following variables showed significant correlations with grade ≥2 esophagitis: age (Rs = −0.32/$p < 0.0001$), fraction number (Rs = 0.64/$p < 0.0001$), treatment days (Rs = 0.60/$p < 0.0001$), chemotherapy use (Rs = 0.56/$p < 0.0001$), dose per fraction (Rs = −0.57/$p < 0.0001$), and total dose (Rs = 0.35/$p < 0.0001$), whereas for grade ≥2 pneumonitis, the only significant clinical variable was sex (Rs = −0.32/$p = 0.037$) with a higher risk for women.

Dosimetric Factors

Spearman's correlation test between dosimetric variables in esophagus and esophagitis showed that all variables had Rs > 0.60 ($p < 0.0001$) as shown in **Figure 1A**. For the fractional dose, fD40 was the highest correlated variable (Rs = 0.58/$p < 0.0001$) as shown in **Figure 1B**.

D15 (Rs = 0.19/$p = 0.006$) in lung and D45 (Rs = 0.16/$p = 0.016$) in heart were assessed as the highest correlated variables with pneumonitis for each organ (**Figure 1C**). Maximum dose in heart was also significantly correlated with Rs = 0.14 ($p = 0.043$).

TABLE 2 | Comparison of mean A2M serum levels [mg/dL] between grade <2 and ≥2 esophagitis and pneumonitis.

Toxicity		Grade 0 or 1	Grade 2+	*p*-value
Esophagitis	*N*	197	61	0.015
	Mean A2M	208.9	190.4	
Pneumonitis	*N*	222	36	0.837
	Mean A2M	204.1	207.0	

P-value was calculated using Wilcoxon rank-sum test.

Multivariate Analysis and Validation Testing

Hierarchical clustering coupled with Pearson's correlation test using training data was performed on dosimetric variables of each organ to measure variable similarity. Many dosimetric variables were highly correlated (**Supplementary Material 2**). Using a threshold of 0.75 in Pearson's correlation the variable with the highest Rs value for the endpoint among the variables in each cluster was selected. Clinical variables with $p < 0.1$ in the univariate analysis and dosimetric variables left after the clustering test were used in the LASSO logistic regression: D25, D40, D50, D65, D85, fD10, fD25, fD35 in esophagus, age, total dose, and A2M for esophagitis; D10, D15, D65, D95 in lung, D20, D45, max dose in heart and sex for pneumonitis. For both endpoints, treatment days, SBRT (yes/no) and chemotherapy (yes/no) were used. Two variables including dose per fraction and number of fractions were excluded due to their high correlation with the number of treatment days.

LASSO logistic regression models were trained using bootstrapped datasets generated from training data and were tested on the validation data, resulting in an average AUC of 0.84 (standard deviation [SD] = 0.03) and 0.78 (SD = 0.06) for esophagitis and pneumonitis, respectively. Additional modeling was performed for esophagitis without A2M resulting in the same average AUC (0.84). This appears to be due to more significant dosimetric and clinical variables used in the modeling. To assess the importance of features, the frequency of occurrence of each feature during the model building process was counted (**Figure 2**). For the esophagitis model, chemotherapy and treatment days were most frequently selected with 770 and 758 times from 1,000 different models, respectively. It is worth noting that A2M was selected 610 times, implying its likely association with esophagitis. For the pneumonitis model, D65 in lung and max dose in heart were most frequently selected with 865 and 798 times, respectively. Patients were sorted based on predicted outcomes on the validation data and grouped into six equal bins with one being the lowest risk group and six being the highest risk group. When comparing observed and predicted

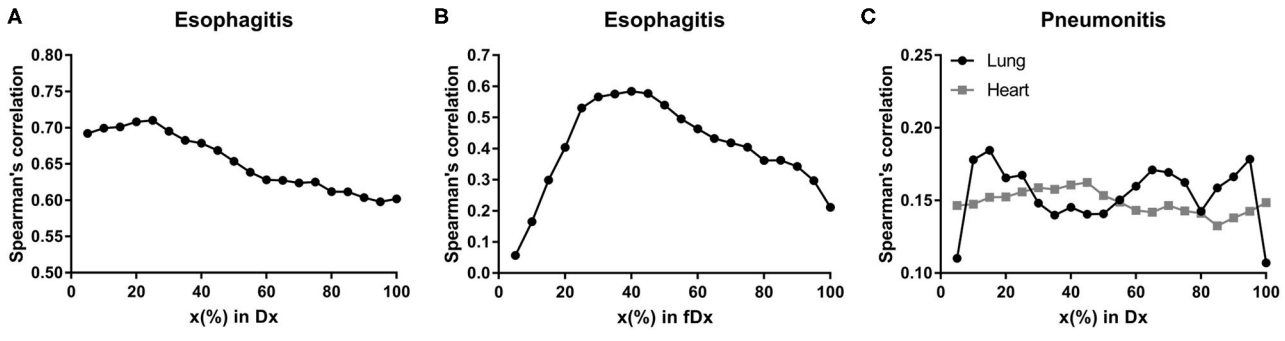

FIGURE 1 | Spearman's correlation coefficients. Spearman's correlation coefficients between radiation-induced injuries (≥ grade 2) and Dx in esophagus for **(A)** esophagitis, fDx in esophagus for **(B)** esophagitis, and Dx in lung and heart for **(C)** pneumonitis.

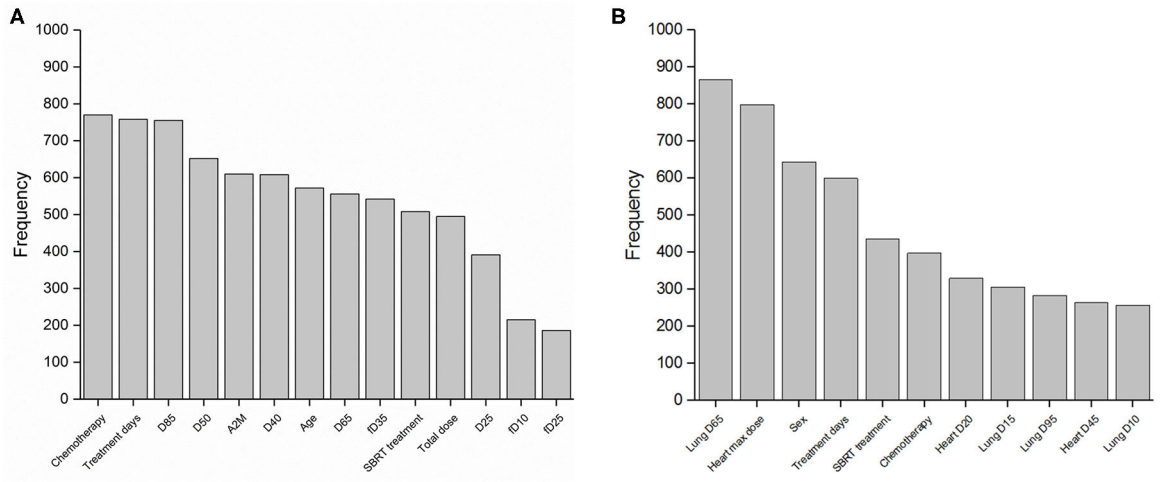

FIGURE 2 | Features in predictive models. Frequency of occurrence of each feature used in 1,000 predictive models for **(A)** esophagitis and **(B)** pneumonitis.

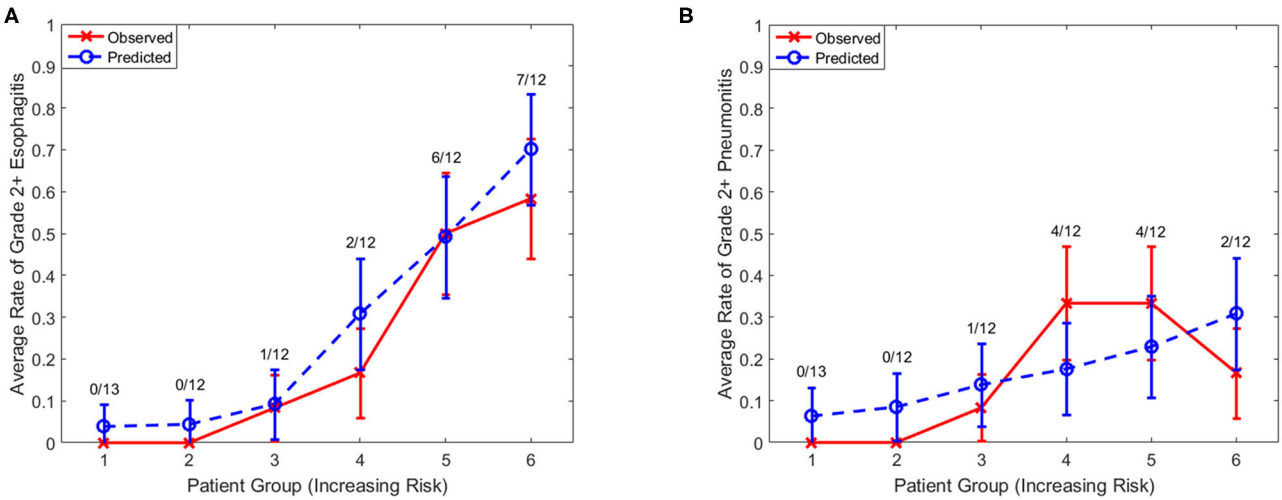

FIGURE 3 | Observed and predicted incidence. Comparison of observed and predicted incidence on validation data (1/3 of samples) for **(A)** esophagitis and **(B)** pneumonitis. Numerator, number of events in each bin; Denominator, number of samples in each bin.

incidence, we found a high conformity of both endpoints, meaning that the predictive models are highly robust (**Figure 3**). Final predictive models built using all training data are shown in **Table 3**. Interestingly, a variable of treatment days (between the start of RT and the end of RT including weekends) was selected in both models.

In addition, the frequency of occurrence of each pair of features used in the LASSO logistic regression model was investigated (**Figure 4**), which provides the information of interaction effects of features in the predictive model.

DISCUSSION

Taking into account the multifactorial etiology of radiation toxicity (30), it is essential to look at different predictive factors in the development of lung and esophageal injury after RT. Dosimetric parameters are most commonly included in predictive models but biological and genetic determinants are also under investigation (9, 11, 30–37). In our analysis, we focused on dose-volume metrics, age, chemotherapy, and other clinical variables in addition to the intrinsic radioprotectant A2M.

As we identified in our correlative analysis, baseline serum A2M levels appear to be influenced by patients' smoking status. Former and current smokers displayed higher A2M values than patients that had never smoked. Active and former smoking has been associated with lower rates of grade $\geq$3 radiation pneumonitis compared to never smokers in patients with NSCLC after 3DCRT or IMRT (38). The effect of smoking on the immune system has been studied extensively. Paradoxically,

smoking results in immunosuppression as well as aggravated autoimmunity. Altered levels of inflammatory cytokines like TNF-α, IFN-γ, IL-1β, IL-6, IL-8, IL-10, and others have been reported in healthy smokers (39–42). A possible explanation for the connection between active smoking and a lower risk for esophagitis or pneumonitis is that long-term cigarette smoking leads to an increased immune response in the lung and surrounding tissues due to the damage it inflicts on the lung parenchyma. Although the mechanisms resulting in normal tissue injury after RT are still under investigation, the release of reactive oxygen species (ROS) as well as proinflammatory and profibrotic cytokines is thought to have a central role in the process (30). Higher baseline levels of acute-phase proteins like A2M may have a protective effect on the irradiated tissue by binding proinflammatory and profibrotic cytokines, thus reducing the acute cytokine toxicity, and inducing an upregulation of antioxidant enzymes like manganese superoxide dismutase (MnSOD) (23, 30).

Our study suggests that there may be an association between natural pre-treatment baseline levels of the intrinsic radioprotectant serum A2M in patients with thoracic malignancies and an increased risk of developing radiation esophagitis. This association reached univariate statistical significance for esophagitis, but not for the pneumonitis endpoint. This finding indicates that higher levels of A2M may have a protective effect in patients undergoing thoracic RT. The high selection frequency of A2M in the model building process confirms our primary univariate analyses implying a likely correlation of A2M levels with esophagitis rates. Factors that have repeatedly shown significant correlation with esophagitis include V40–V60 (6, 43–46) (Vx: percentage volume receiving at least x Gy), mean esophageal dose (47–49), as well as sequential and especially concurrent chemoradiation in comparison to RT alone (5, 6, 50–53).

For pneumonitis, we validated the correlation with radiation dose received by the heart. Different lung dose volumes (V5–V40 and mean dose in lung) have been found to predict the development of pneumonitis (7, 10, 54). In addition, the dose received by the heart during thoracic radiation seems to be an accurate predictor (55, 56). The best fitting predictive model reported by Huang et al. included D10 (heart), D35 (lung) and max dose (lung), and had an AUC of 0.72 (55). Although the ideal dosimetric variable(s) for predicting pneumonitis across all patient subgroups may not yet be known, it is evident that heart doses are an essential part of any model built for this cause. Though we could not confirm the impact of A2M on pneumonitis with our data, a correlation between them has been previously described (9, 56). We may have been limited by the

TABLE 3 | Final predictive models for esophagitis and pneumonitis.

Variable	Coefficient	STD	Odds ratio	95% CI	
Esophagitis model					
D25	0.012	0.026	1.012	0.962	1.064
D40	0.036	0.022	1.037	0.993	1.083
Treatment days	0.048	0.026	1.049	0.997	1.105
Constant	−3.880	0.725	0.021	0.005	0.086
Pneumonitis model					
D65 in lung	0.252	0.146	1.286	0.967	1.711
Max dose in heart	0.015	0.008	1.015	0.999	1.032
Treatment days	0.024	0.020	1.024	0.986	1.064
Constant	−3.824	0.793	0.022	0.005	0.103

CI, confidence interval; STD, standard deviation.

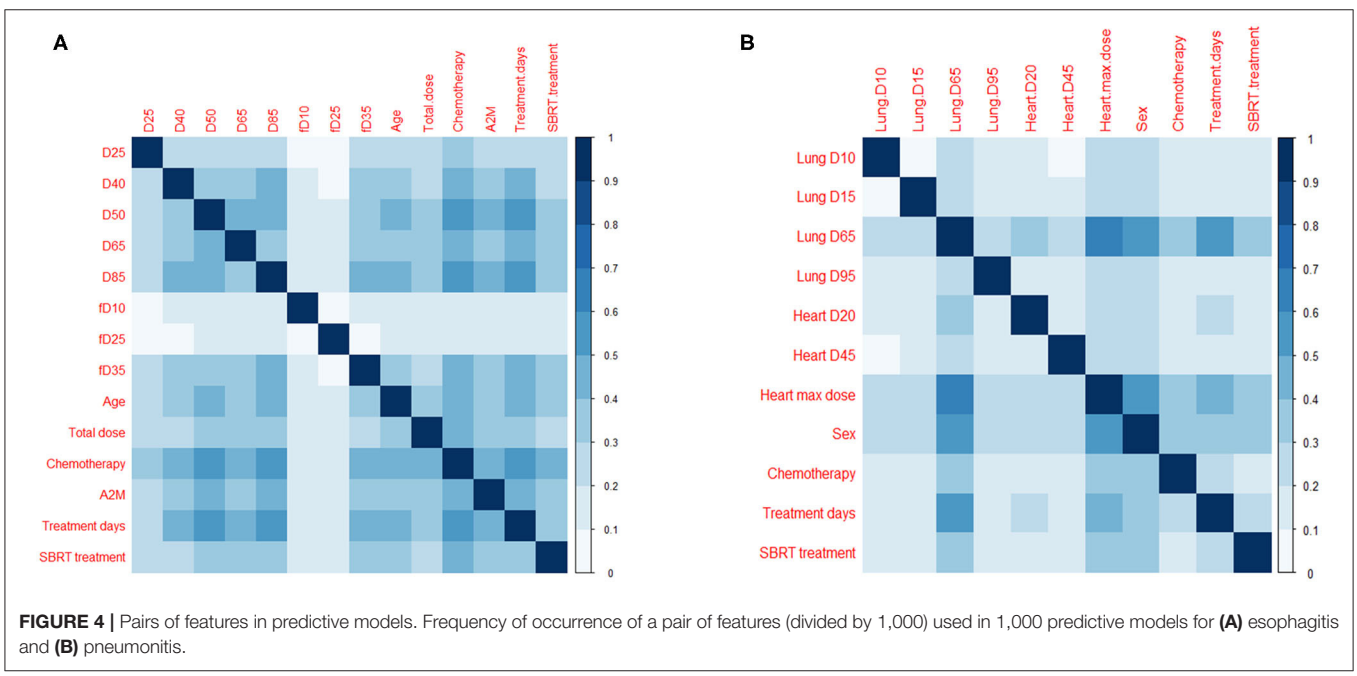

FIGURE 4 | Pairs of features in predictive models. Frequency of occurrence of a pair of features (divided by 1,000) used in 1,000 predictive models for **(A)** esophagitis and **(B)** pneumonitis.

lower incidence of grade ≥2 pneumonitis (14.0%) and the low rate of current smokers in our patient cohort. In the previously published study on A2M and pneumonitis, pneumonitis rates were between 19 and 35%. The variable of sex was found to be correlated with pneumonitis in univariate analysis and had the third-highest frequency in 1,000 model runs (**Figure 2B**), consistent with another study (57). However, its role as a risk factor for pneumonitis is controversial (58).

While all patients had A2M collected within 30 days prior to the start of RT and toxicity data were systematically prospectively graded per our clinical standard, caution is warranted regarding the interpretation of these results. In particular, including a factor like chemotherapy in predictive models should be considered carefully as different regimens, doses and timings, depending on the patient population, make it a very heterogeneous variable. Similarly, the patient cohort we studied was diverse regarding diagnosis and treatment. Although requirements for eligibility included no prior RT, patients underwent different modes of RT (3DCRT/SBRT/IMRT) which may have an impact on the toxicity profile. Furthermore, smoking status as a variable was not evenly distributed. Given its proposed link to serum A2M levels, this could be a cause for certain discrepancies in our results. A2M levels in humans reported in previous studies range on average between 100 and 450 mg/dL with a mean of around 215 mg/dL. Age and gender are known to influence this value with females generally showing around 20% higher levels than same-aged males (59, 60). Given the lack of data thus far concerning other factors that may influence intrinsic A2M levels, further analyses with serum levels recorded immediately prior to and while receiving RT are necessary.

In summary, the analysis of our institutional dataset has produced predictive models for both esophagitis and pneumonitis. Although the addition of A2M did not increase the predictive power of multivariate predictive models, this is the first report on the possible association of higher levels of A2M with a lower risk of radiation esophagitis and with smoking, warranting further investigation and independent validation.

DATA AVAILABILITY STATEMENT

The datasets generated for this study are available on request to the corresponding author.

ETHICS STATEMENT

The studies involving human participants were reviewed and approved by Memorial Sloan Kettering Cancer Center. The patients/participants provided their written informed consent to participate in this study.

AUTHOR CONTRIBUTIONS

JD, JO, AR, DR, AW, and EY contributed to conception and design of the study. MF, EG, AR, and DR acquired and organized the data. AA, JD, JO, HP, MT, and JY analyzed the data and performed the statistical analysis. JO, AR, and DR drafted the manuscript. All authors contributed to the critical revision and approved the submission of the manuscript.

FUNDING

This research was funded in part through the NIH/NCI Cancer Center Support Grant Nos. P30 CA008748 and R21 CA234752.

SUPPLEMENTARY MATERIAL

The Supplementary Material for this article can be found online at: https://www.frontiersin.org/articles/10.3389/fonc.2020.01395/full#supplementary-material

REFERENCES

1. Marks L, Yu X, Vujaskovic Z, Smalljr W, Folz R, Anscher M. Radiation-induced lung injury. *Semin Radiat Oncol.* (2003) 13:333–45. doi: 10.1016/S1053-4296(03)00034-1
2. Bradley J, Movsas B. Radiation esophagitis: predictive factors and preventive strategies. *Semin Radiat Oncol.* (2004) 14:280–6. doi: 10.1016/j.semradonc.2004.06.003
3. Kocak Z, Evans ES, Zhou SM, Miller KL, Folz RJ, Shafman TD, et al. Challenges in defining radiation pneumonitis in patients with lung cancer. *Int J Radiat Oncol Biol Phys.* (2005) 62:635–8. doi: 10.1016/j.ijrobp.2004.12.023
4. Mehta V. Radiation pneumonitis and pulmonary fibrosis in non-small-cell lung cancer: pulmonary function, prediction, and prevention. *Int J Radiat Oncol Biol Phys.* (2005) 63:5–24. doi: 10.1016/j.ijrobp.2005.03.047
5. Werner-Wasik M, Paulus R, Curran WJ, JR, Byhardt R. Acute esophagitis and late lung toxicity in concurrent chemoradiotherapy trials in patients with locally advanced non-small-cell lung cancer: analysis of the radiation therapy oncology group (RTOG) database. *Clin Lung Cancer.* (2011) 12:245–51. doi: 10.1016/j.cllc.2011.03.026
6. Kwint M, Uyterlinde W, Nijkamp J, Chen C, Bois J de, Sonke JJ, et al. Acute esophagus toxicity in lung cancer patients after intensity modulated radiation therapy and concurrent chemotherapy. *Int J Radiat Oncol Biol Phys.* (2012) 84:e223–8. doi: 10.1016/j.ijrobp.2012.03.027
7. Palma DA, Senan S, Tsujino K, Barriger RB, Rengan R, Moreno M, et al. Predicting radiation pneumonitis after chemoradiation therapy for lung cancer: an international individual patient data meta-analysis. *Int J Radiat Oncol Biol Phys.* (2013) 85:444–50. doi: 10.1016/j.ijrobp.2012.04.043
8. Palma DA, Senan S, Oberije C, Belderbos J, Dios NR de, Bradley JD, et al. Predicting esophagitis after chemoradiation therapy for non-small cell lung cancer: an individual patient data meta-analysis. *Int J Radiat Oncol Biol Phys.* (2013) 87:690–6. doi: 10.1016/j.ijrobp.2013.07.029
9. Oh JH, Craft JM, Townsend R, Deasy JO, Bradley JD, El Naqa I. A bioinformatics approach for biomarker identification in radiation-induced lung inflammation from limited proteomics data. *J Proteome Res.* (2011) 10:1406–15. doi: 10.1021/pr101226q
10. Rodrigues G, Lock M, D'souza D, Yu E, van Dyk J. Prediction of radiation pneumonitis by dose - volume histogram parameters in lung cancer–a systematic review. *Radiother Oncol.* (2004) 71:127–38. doi: 10.1016/j.radonc.2004.02.015
11. Tsujino K, Hirota S, Endo M, Obayashi K, Kotani Y, Satouchi M, et al. Predictive value of dose-volume histogram parameters for predicting

radiation pneumonitis after concurrent chemoradiation for lung cancer. *Int J Radiat Oncol Biol Phys.* (2003) 55:110–5. doi: 10.1016/S0360-3016(02)03807-5
12. Wang JY, Chen KY, Wang JT, Chen JH, Lin JW, Wang HC, et al. Outcome and prognostic factors for patients with non-small-cell lung cancer and severe radiation pneumonitis. *Int J Radiat Oncol Biol Phys.* (2002) 54:735–41. doi: 10.1016/S0360-3016(02)02994-2
13. Kong F-M, Haken RT, Eisbruch A, Lawrence TS. Non-small cell lung cancer therapy-related pulmonary toxicity: an update on radiation pneumonitis and fibrosis. *Semin Oncol.* (2005) 32:42–54. doi: 10.1053/j.seminoncol.2005.03.009
14. Auperin A, Le Pechoux C, Rolland E, Curran WJ, Furuse K, Fournel P, et al. Meta-analysis of concomitant versus sequential radiochemotherapy in locally advanced non-small-cell lung cancer. *J Clin Oncol.* (2010) 28:2181–90. doi: 10.1200/JCO.2009.26.2543
15. Bentzen SM, Constine LS, Deasy JO, Eisbruch A, Jackson A, Marks LB, et al. Quantitative Analyses of Normal Tissue Effects in the Clinic (QUANTEC): an introduction to the scientific issues. *Int J Radiat Oncol Biol Phys.* (2010) 76:S3–9. doi: 10.1016/j.ijrobp.2009.09.040
16. Movsas B, Scott C, Langer C, Werner-Wasik M, Nicolaou N, Komaki R, et al. Randomized trial of amifostine in locally advanced non–small-cell lung cancer patients receiving chemotherapy and hyperfractionated radiation: radiation therapy oncology group trial 98-01. *J Clin Oncol.* (2005) 23:2145–54. doi: 10.1200/JCO.2005.07.167
17. Hensley ML, Hagerty KL, Kewalramani T, Green DM, Meropol NJ, Wasserman TH, et al. American Society of Clinical Oncology 2008 clinical practice guideline update: use of chemotherapy and radiation therapy protectants. *J Clin Oncol.* (2009) 27:127–45. doi: 10.1200/JCO.2008.17.2627
18. Buentzel J, Micke O, Adamietz IA, Monnier A, Glatzel M, de Vries A. Intravenous amifostine during chemoradiotherapy for head-and-neck cancer: a randomized placebo-controlled phase III study. *Int J Radiat Oncol Biol Phys.* (2006) 64:684–91. doi: 10.1016/j.ijrobp.2005.08.005
19. Spielberger R, Stiff P, Bensinger W, Gentile T, Weisdorf D, Kewalramani T, et al. Palifermin for oral mucositis after intensive therapy for hematologic cancers. *N Engl J Med.* (2004) 351:2590–8. doi: 10.1056/NEJMoa040125
20. Mihailovic M, Dobric S, Poznanovic G, Petrovic M, Uskokovic A, Arambasic J, et al. The acute-phase protein alpha2-macroglobulin plays an important role in radioprotection in the rat. *Shock.* (2009) 31:607–14. doi: 10.1097/SHK.0b013e31818bb625
21. Mihailović M, Poznanović G, Grdović N, Vidaković M, Dinić S, Grigorov I, et al. The rat acute-phase protein α 2 -macroglobulin plays a central role in amifostine-mediated radioprotection. *J Radiol Prot.* (2010) 30:567–83. doi: 10.1088/0952-4746/30/3/011
22. Bogojevic D, Poznanovic G, Grdovic N, Grigorov I, Vidakovic M, Dinic S, et al. Administration of rat acute-phase protein alpha(2)-macroglobulin before total-body irradiation initiates cytoprotective mechanisms in the liver. *Radiat Environ Biophys.* (2011) 50:167–79. doi: 10.1007/s00411-010-0331-z
23. Chen X, Kong X, Zhang Z, Chen W, Chen J, Li H, et al. Alpha-2-macroglobulin as a radioprotective agent: a review. *Chin J Cancer Res.* (2014) 26:611–21. doi: 10.3978/j.issn.1000-9604.2014.09.04
24. Tappia PS, Troughton KL, Langley-Evans SC, Grimble RF. Cigarette smoking influences cytokine production and antioxidant defences. *Clin Sci.* (1995) 88:485–9. doi: 10.1042/cs0880485
25. Suriyaprom K, Harnroongroj T, Namjuntra P, Chantaranipapong Y, Tungtrongchitr R. Effects of tobacco smoking on alpha-2-macroglobulin and some biochemical parameters in Thai males. *Southeast Asian J Trop Med Public Health.* (2007) 38:918–26.
26. Mocchegiani E, Giacconi R, Costarelli L. Metalloproteases/anti-metalloproteases imbalance in chronic obstructive pulmonary disease: genetic factors and treatment implications. *Curr Opin Pulm Med.* (2011) 17(Suppl. 1):S11–9. doi: 10.1097/01.mcp.0000410743.98087.12
27. Mohan R, Barest G, Brewster LJ, Chui CS, Kutcher GJ, Laughlin JS, et al. A comprehensive three-dimensional radiation treatment planning system. *Int J Radiat Oncol Biol Phys.* (1988) 15:481–95. doi: 10.1016/S0360-3016(98)90033-5
28. Deasy JO, Blanco AI, Clark VH. CERR: a computational environment for radiotherapy research. *Med Phys.* (2003) 30:979–85. doi: 10.1118/1.1568978
29. Duijm M, van der Voort van Zyp NC, Granton PV, van de Vaart P, Mast ME, Oomen-de Hoop E, et al. Predicting high-grade esophagus toxicity after treating central lung tumors with stereotactic radiation therapy using a normal tissue complication probability model. *Int J Radiat Oncol Biol Phys.* (2020) 106:73–81. doi: 10.1016/j.ijrobp.2019.08.059
30. Anscher MS, Chen L, Rabbani Z, Kang S, Larrier N, Huang H, et al. Recent progress in defining mechanisms and potential targets for prevention of normal tissue injury after radiation therapy. *Int J Radiat Oncol Biol Phys.* (2005) 62:255–9. doi: 10.1016/j.ijrobp.2005.01.040
31. Zhao L, Pu X, Ye Y, Lu C, Chang JY, Wu X. Association between genetic variants in DNA double-strand break repair pathways and risk of radiation therapy-induced pneumonitis and esophagitis in non-small cell lung cancer. *Cancers.* (2016) 8:23. doi: 10.3390/cancers8020023
32. Kim KS, Jeon SU, Lee CJ, Kim YE, Bok S, Hong BJ, et al. Radiation-induced esophagitis *in vivo* and *in vitro* reveals that epidermal growth factor is a potential candidate for therapeutic intervention strategy. *Int J Radiat Oncol Biol Phys.* (2016) 95:1032–41. doi: 10.1016/j.ijrobp.2016.02.051
33. Sprung CN, Forrester HB, Siva S, Martin OA. Immunological markers that predict radiation toxicity. *Cancer Lett.* (2015) 368:191–7. doi: 10.1016/j.canlet.2015.01.045
34. Kerns SL, Kundu S, Oh JH, Singhal SK, Janelsins M, Travis LB, et al. The prediction of radiotherapy toxicity using single nucleotide polymorphism-based models: a step toward prevention. *Semin Radiat Oncol.* (2015) 25:281–91. doi: 10.1016/j.semradonc.2015.05.006
35. Bradley J, Deasy JO, Bentzen S, El-Naqa I. Dosimetric correlates for acute esophagitis in patients treated with radiotherapy for lung carcinoma. *Int J Radiat Oncol Biol Phys.* (2004) 58:1106–13. doi: 10.1016/j.ijrobp.2003.09.080
36. Seppenwoolde Y, Lebesque JV, Jaeger K de, Belderbos JS, Boersma LJ, Schilstra C, et al. Comparing different NTCP models that predict the incidence of radiation pneumonitis. Normal tissue complication probability. *Int J Radiat Oncol Biol Phys.* (2003) 55:724–35. doi: 10.1016/S0360-3016(02)03986-X
37. Yorke ED, Jackson A, Rosenzweig KE, Merrick SA, Gabrys D, Venkatraman ES, et al. Dose-volume factors contributing to the incidence of radiation pneumonitis in non-small-cell lung cancer patients treated with three-dimensional conformal radiation therapy. *Int J Radiat Oncol Biol Phys.* (2002) 54:329–39. doi: 10.1016/S0360-3016(02)02929-2
38. Jin H, Tucker SL, Liu HH, Wei X, Yom SS, Wang S, et al. Dose-volume thresholds and smoking status for the risk of treatment-related pneumonitis in inoperable non-small cell lung cancer treated with definitive radiotherapy. *Radiother Oncol.* (2009) 91:427–32. doi: 10.1016/j.radonc.2008.09.009
39. van Keulen HV, Gomes AS, Toffolo MC, Oliveira EE, Silva LC, Alves CC, et al. Serum levels of nitric oxide and cytokines in smokers at the beginning and after 4 months of treatment for smoking cessation. *Int J Cardiol.* (2017) 230:327–31. doi: 10.1016/j.ijcard.2016.12.111
40. Shiels MS, Katki HA, Freedman ND, Purdue MP, Wentzensen N, Trabert B, et al. Cigarette smoking and variations in systemic immune and inflammation markers. *J Natl Cancer Inst.* (2014) 106:dju294. doi: 10.1093/jnci/dju294
41. Arnson Y, Shoenfeld Y, Amital H. Effects of tobacco smoke on immunity, inflammation and autoimmunity. *J Autoimmun.* (2010) 34:J258–65. doi: 10.1016/j.jaut.2009.12.003
42. Levitzky YS, Guo CY, Rong J, Larson MG, Walter RE, Keaney JF, et al. Relation of smoking status to a panel of inflammatory markers: the framingham offspring. *Atherosclerosis.* (2008) 201:217–24. doi: 10.1016/j.atherosclerosis.2007.12.058
43. Rodriguez N, Algara M, Foro P, Lacruz M, Reig A, Membrive I, et al. Predictors of acute esophagitis in lung cancer patients treated with concurrent three-dimensional conformal radiotherapy and chemotherapy. *Int J Radiat Oncol Biol Phys.* (2009) 73:810–7. doi: 10.1016/j.ijrobp.2008.04.064
44. Zhu J, Zhang Z-C, Li B-S, Liu M, Yin Y, Yu J-M, et al. Analysis of acute radiation-induced esophagitis in non-small-cell lung cancer patients using the Lyman NTCP model. *Radiother Oncol.* (2010) 97:449–54. doi: 10.1016/j.radonc.2010.09.025
45. Zhang Z, Xu J, Zhou T, Yi Y, Li H, Sun H, et al. Risk factors of radiation-induced acute esophagitis in non-small cell lung cancer patients treated with concomitant chemoradiotherapy. *Radiat Oncol.* (2014) 9:54. doi: 10.1186/1748-717X-9-54
46. Caglar HB, Othus M, Allen AM. Esophagus in-field: a new predictor for esophagitis. *Radiother Oncol.* (2010) 97:48–53. doi: 10.1016/j.radonc.2010.07.024
47. Watkins JM, Wahlquist AE, Shirai K, Garrett-Mayer E, Aguero EG, Fortney JA, et al. Factors associated with severe acute esophagitis from

hyperfractionated radiotherapy with concurrent chemotherapy for limited-stage small-cell lung cancer. *Int J Radiat Oncol Biol Phys.* (2009) 74:1108–13. doi: 10.1016/j.ijrobp.2008.09.013
48. Ozgen A, Hayran M, Kahraman F. Mean esophageal radiation dose is predictive of the grade of acute esophagitis in lung cancer patients treated with concurrent radiotherapy and chemotherapy. *J Radiat Res.* (2012) 53:916–22. doi: 10.1093/jrr/rrs056
49. Grant JD, Shirvani SM, Tang C, Juloori A, Rebueno NC, Allen PK, et al. Incidence and predictors of severe acute esophagitis and subsequent esophageal stricture in patients treated with accelerated hyperfractionated chemoradiation for limited-stage small cell lung cancer. *Pract Radiat Oncol.* (2015) 5:e383–91. doi: 10.1016/j.prro.2015.01.005
50. Singh AK, Lockett MA, Bradley JD. Predictors of radiation-induced esophageal toxicity in patients with non-small-cell lung cancer treated with three-dimensional conformal radiotherapy. *Int J Radiat Oncol Biol Phys.* (2003) 55:337–41. doi: 10.1016/S0360-3016(02)03937-8
51. Ahn S-J, Kahn D, Zhou S, Yu X, Hollis D, Shafman TD, et al. Dosimetric and clinical predictors for radiation-induced esophageal injury. *Int J Radiat Oncol Biol Phys.* (2005) 61:335–47. doi: 10.1016/j.ijrobp.2004.06.014
52. Huang EX, Bradley JD, El Naqa I, Hope AJ, Lindsay PE, Bosch WR, et al. Modeling the risk of radiation-induced acute esophagitis for combined Washington University and RTOG trial 93-11 lung cancer patients. *Int J Radiat Oncol Biol Phys.* (2012) 82:1674–9. doi: 10.1016/j.ijrobp.2011.02.052
53. Huang EX, Robinson CG, Molotievschi A, Bradley JD, Deasy JO, Oh JH. Independent test of a model to predict severe acute esophagitis. *Adv Radiat Oncol.* (2017) 2:37–43. doi: 10.1016/j.adro.2016.11.003
54. Zhang XJ, Sun JG, Sun J, Ming H, Wang XX, Wu L, et al. Prediction of radiation pneumonitis in lung cancer patients: a systematic review. *J Cancer Res Clin Oncol.* (2012) 138:2103–16. doi: 10.1007/s00432-012-1284-1
55. Huang EX, Hope AJ, Lindsay PE, Trovo M, El Naqa I, Deasy JO, et al. Heart irradiation as a risk factor for radiation pneumonitis. *Acta Oncol.* (2011) 50:51–60. doi: 10.3109/0284186X.2010.521192
56. Lee S, Ybarra N, Jeyaseelan K, Faria S, Kopek N, Brisebois P, et al. Bayesian network ensemble as a multivariate strategy to predict radiation pneumonitis risk. *J Med Phys.* (2015) 42:2421–30. doi: 10.1118/1.4915284
57. Das SK, Zhou S, Zhang J, Yin FF, Dewhirst MW, Marks LB. Predicting lung radiotherapy-induced pneumonitis using a model combining parametric Lyman probit with nonparametric decision trees. *Int J Radiat Oncol Biol Phys.* (2007) 68:1212–21. doi: 10.1016/j.ijrobp.2007.03.064
58. Kong F-M, Wang S. Non-dosimetric risk factors for radiation-induced lung toxicity. *Semin Radiat Oncol.* (2014) 25:100–9. doi: 10.1016/j.semradonc.2014.12.003
59. Ritchie RF, Palomaki GE, Neveux LM, Navolotskaia O, Ledue TB, Craig WY. Reference distributions for alpha2-macroglobulin: a practical, simple and clinically relevant approach in a large cohort. *J Clin Lab Anal.* (2004) 18:139–47. doi: 10.1002/jcla.20012
60. Jespersen MH, Jensen J, Rasmussen LH, Ejlersen E, Møller-Petersen J, Sperling-Petersen HU. The reference range for complexed α2-macroglobulin human plasma: development of a new enzyme linked in immunosorbent assay (ELISA) for quantitation of complexed α2-macroglobulin. *Scand J Clin Lab Invest.* (1993) 53:639–48. doi: 10.3109/00365519309092565

Conflict of Interest: JD has research contracts with Varian Medical Systems and Philips. AR has grants from Varian Medical Systems, Boehringer Ingelheim, Pfizer, Astrazeneca, Merck, and personal fees from Astrazeneca, Merck, Cybrexa, MoreHealth, and ResearchtoPractice as well as non-financial support from Philips/Elekta. AW has a grant from CivaTech Oncology, personal fees from AstraZeneca, and a travel grant from AlphaTau Medical.

The remaining authors declare that the research was conducted in the absence of any commercial or financial relationships that could be construed as a potential conflict of interest.

The handling editor declared a past collaboration with two of the authors MT and JD.

frontiers in Oncology

ORIGINAL RESEARCH
published: 11 August 2020
doi: 10.3389/fonc.2020.01577

Significant Correlation Between Overall Survival and Mean Lung Dose in Lung Stereotactic Body Radiation Therapy (SBRT)

Guillaume Dupic[1], Julian Biau[1], Ioana Molnar[2,3], Vincent Chassin[4], Véronique Dedieu[4], Michel Lapeyre[1] and Aurélie Bellière-Calandry[1]*

[1] Department of Radiation Oncology, University of Clermont Auvergne, Jean Perrin Center, Clermont-Ferrand, France, [2] INSERM U1240 IMoST, University of Clermont Auvergne, Clermont-Ferrand, France, [3] Department of Clinical Research UMR 501, Jean Perrin Center, Clermont-Ferrand, France, [4] Department of Medical Physics, University of Clermont Auvergne, Jean Perrin Center, Clermont-Ferrand, France

Background: After stereotactic body radiation therapy (SBRT) for medically inoperable stage I non-small-cell lung cancer (NSCLC), more patients die of comorbidities, particularly severe pulmonary insufficiency, than of tumor progression. The aim of this study was to evaluate correlation between lung biologically effective dose (BED) with an α/β ratio of 3 Gy (BED_3) and overall survival (OS) for these patients.

Methods: From 2012 to 2017, we have developed a prospectively updated institutional database for all first 100 consecutively treated patients with inoperable Stage 1 (T1T2N0M0) NSCLC. All SBRT were conducted on a Novalis Tx® LINAC with two coplanar dynamic conformal arcs (84%) or with coplanar volumetric modulated arc therapy (VMAT) (16%). Mean GTV and PTV were 8.6 cc and 50.8 cc, respectively. The marginal dose prescribed to the PTV was the 80% isodose line (IDL), i.e., 54 Gy in 3 fractions for 76 patients (BED_{10} = 126 Gy) and 50 Gy in 5 fractions for 24 patients (BED_{10} = 83.3 Gy). Pulmonary heterogeneity has been taken into account by using Monte Carlo or AAA algorithms. Median follow-up was 25 months.

Results: At 1, 2, 3 and 5 years, local control (LC) was respectively 100, 98.2, 98.2, and 77.7%, and OS was respectively 83, 71.2, 58.1, and 33.2% (median OS was 49 months). Significant OS prognostic factors in univariate and multivariate analysis were mean lung BED_3 (HR = 1.14, p = 0.01) and PTV volume (HR = 1.01, p = 0.004). A mean lung $BED_3 \leq 5$ Gy was significantly associated with a doubling of median OS from 29 months to more than 60 months (not achieved, p = 0.0068). For patients with a forced expiratory volume in 1 second (FEV1) ≤ 40%, a mean lung $BED_3 \leq 4$ Gy was significantly associated with a doubling of median OS from 23 to 46 months (p = 0.019).

Conclusion: Mean lung BED_3 is strongly and significantly associated with OS in SBRT for inoperable Stage I NSCLC. For all treated patients, a mean lung $BED_3 \leq 5$ Gy lead to a doubling of median OS. This threshold value should be reduced to 4 Gy for patients with FEV1 ≤ 40%.

Keywords: lung, stereotactic radiotherapy, prognostic factor, mean lung dose, toxicity

OPEN ACCESS

Edited by:
Claudio Fiorino,
San Raffaele Hospital (IRCCS), Italy

Reviewed by:
Jian-Guo Zhou,
University of Erlangen Nuremberg, Germany
Dalong Pang,
Georgetown University, United States

****Correspondence:***
Guillaume Dupic
guillaume.dupic@clermont.unicancer.fr

Specialty section:
This article was submitted to Radiation Oncology, a section of the journal Frontiers in Oncology

Received: *15 November 2019*
Accepted: *21 July 2020*
Published: *11 August 2020*

Citation:
Dupic G, Biau J, Molnar I, Chassin V, Dedieu V, Lapeyre M and Bellière-Calandry A (2020) Significant Correlation Between Overall Survival and Mean Lung Dose in Lung Stereotactic Body Radiation Therapy (SBRT). Front. Oncol. 10:1577. doi: 10.3389/fonc.2020.01577

HIGHLIGHTS

- Grade 5 radiation pneumonitis after lung SBRT is probably under-evaluated because of poor baseline pulmonary function of treated patients.
- Mean lung BED_3 is a strong and significant prognostic factor of overall survival after lung SBRT.
- Mean lung $BED_3 \leq 5$ Gy (i.e., 3.6 Gy in 3 fractions or 4.3 Gy in 5 fractions) is significantly associated with higher overall survival after lung SBRT with a doubling in median overall survival.
- For patients with poor baseline pulmonary function (FEV1 or DLCO $\leq 40\%$), this threshold should be reduced to 4 Gy (i.e., 3 Gy in 3 fractions or 3.5 Gy in 5 fractions).

INTRODUCTION

Stereotactic body radiation therapy (SBRT) is the standard treatment for medically inoperable stage I non-small-cell lung cancer (NSCLC) (1). Generally, overall survival (OS) for these patients in prospective studies is around 81–100, 65–70, 39–68, and 30–65%, respectively at 1, 2, 3 and 5 years. Local control (LC) is high, around 86–100 and 79–85%, respectively at 3 and 5 years (1–3). It is widely agreed that more NSCLC patients treated with SBRT die of comorbidities than of tumor progression. Significant prognostic factors are age (4), gender (5), performance status (4, 6), histologic type (4), tumor volume (5–7), pretreatment maximum standardized uptake value (SUV_{max}) (6, 8, 9), platelet-to-lymphocyte ratio (8, 10), pretreatment immune parameters (neutrophil-to-lymphocyte ratio, neutrophil and lymphocyte counts) (10) and prescribed dose (11). The role of lung dosimetric parameters as prognostic factors remains unknown. After lung SBRT, many patients died from severe pulmonary insufficiency attributed to their previous medical history [OS at 5 years is 30–65% after SBRT vs. 60–80% after surgery (12)], which makes severe radiation-induced pneumonitis (RP) difficult to interpret (2, 13).

RP is the most frequent complication after lung SBRT (14). Clinically symptomatic RP seems to develop mostly in 10–20% of patients (range: 0–49% among published studies) with most patients having asymptomatic Grade 1 pneumonitis (2, 15–17). Pre-treatment pulmonary function tests have not been shown to be predictive for RP. Therefore, patients with NSCLC with a poor baseline pulmonary function are not excluded from treatment with SBRT (18). Mean lung dose (MLD) seems to be a strong and reproducible dosimetric parameter of RP, with a significant cut-off at 4–4.7 Gy in three fractions, and is often correlated to the volume of PTV (15, 17, 19–21). Many factors may have confounded the reported MLD because of inadequate heterogeneity correction algorithms, various dose prescriptions and fractionations and probably a lack of lung volume definitions (whole or ipsilateral lung volume minus GTV or PTV) (17, 22, 23). In this way, the biologically effective dose (BED) determined with adequate heterogeneity correction algorithms may be used for estimating toxicity probabilities. For high fraction doses, the linear-quadratic model with an α/β ratio of 3 Gy is the best method for converting the physical lung dose to predict RP (24).

Our study aimed to evaluate the correlation between lung BED_3 and OS in a prospectively updated institutional cohort of 100 consecutively treated patients with stage I NSCLC. The secondary objective was to study the impact of lung dosimetric parameters in a population with a poor baseline pulmonary function.

PATIENTS AND METHODS

Patients' Selection and Characteristics

From October 2012 to August 2017, we have developed a prospectively updated institutional database for all patients consecutively treated with SBRT for inoperable Stage 1 (T1T2N0M0) NSCLC in our institution. This database has been approved by our local ethics committee and a regional ethics committee (CECIC Rhône-Alpes-Auvergne, Grenoble, IRB 5921), and developed according to the French law regulating clinical research (Loi Huriet). Thus, our study is an observational cohort study from all first 100 patients recorded in this prospectively updated institutional database. All treated patients fulfilled inclusion criteria of those first described by Timmerman et al. in the analysis of RTOG 0236 (25): performance status (PS) ≤ 2, age ≥ 18 years, stages T1T2N0M0, peripherally located NSCLC at least 2 cm from the proximal bronchial tree, and medical inoperability (baseline forced expiratory volume in one second (FEV1) $\leq 40\%$, predictive postoperative FEV1 $\leq 30\%$, diffusing capacity for carbon monoxide (DLCO) $\leq 40\%$, severe cerebral, pulmonary or cardiovascular disease or patient refusal).

All patients were required to have a complete imaging screening performed less than 1 month prior to lung SBRT: a high-resolution contrast-enhanced lung computed tomography (CT), a 18F-fluorodeoxyglucose positron emission tomography (18F-FDG PET) and a cerebral magnetic resonance imaging (MRI) to exclude regional or distant metastases. A flexible bronchoscopy was needed to exclude an endobronchial location or infectious disease such as lung tuberculosis. A cytologically or histologically proven NSCLC was strongly

Abbreviations: 18F-FDG PET, 18-F FluoroDeoxyGlucose Positron Emission Tomography; BED, biologically effective dose; CBCT, cone beam CT; CI, conformality index, ratio of 80% prescription isodose volume to the PTV; CT, computed tomography; CTV, clinical target volume; D2cm, maximum dose 2 cm from the PTV in any direction; DCA, dynamic conformal arcs; DLCO, diffusing lung capacity for carbon monoxide; FEV1, forced expiratory volume in 1 second; GTV, gross tumor volume; Gy, Gray; ITV, internal target volume; LC, local control; LINAC, LINear ACcelator; MLD, mean lung dose; MRI, magnetic resonance imaging; NCI-CTCAE, National Cancer Institute's Common Toxicity Criteria for Adverse Events; NSCLC, non-small-cell lung cancer; NYHA, New York Heart Association; OS, overall survival; PFS, progression-free survival; PS, performance status; PTV, planning target volume; R50, ratio of 50% prescription isodose volume to the PTV; RECIST, Response Evaluation Criteria in Solid Tumors; ROC, receiver operating characteristics; RP, radiation-induced pneumonitis; RTOG, Radiation Therapy Oncology Group; SBRT, stereotactic body radiation therapy; SUVmax, maximum standardized uptake value; TPS, treatment planning systems; VMAT, volumetric modulated arc therapy.

recommended but not mandatory in case of contraindications. If this proof was not obtained, a tumor growth observed with an interval at least 3 months between two CT or a maximum standardized uptake value (SUV_{max}) in 18F-FDG PET above 2.5–3 was necessary to include patients. Exclusion criteria were small-cell lung cancer, mediastinal location and no meeting of normal tissue dose constraints. Pre-treatment pulmonary function tests were performed for all patients.

All pre-treatment characteristics of the 100 included patients are reported in **Table 1**. Most patients were elderly [median age = 70 years (range: 47–90)] and male (79%) with a good general status (93% PS $\leq$ 1) and no history of lung surgery (78%) or radiotherapy (93%), but with poor baseline pulmonary function [57% NYHA (New York Heart Association) class $\geq$ 2 dyspnea, median FEV1 was 62% (20–100%) and median DLCO was 48% (8–100%)]. Fifty-six percent of patients had no histologically or cytologically proven NSCLC. Mean GTV was 8.6 cc (0.2–61.5 cc), i.e., about 2 cm in diameter.

SBRT Specifications

The gross tumor volume (GTV) was contoured on 2.5-mm-thick lung CT windows. Intrafraction tumor motion due to breathing was limited by an abdominal compression and taken into account by creating an internal target volume (ITV) obtained with a four-dimensional (4D) CT scan at the time of CT simulation. An additional margin of 8 mm for adenocarcinoma and 6 mm for other histologic types was added for microscopic tumor extension to create the clinical target volume (CTV) (26, 27). Finally, the planning target volume (PTV) was obtained with a uniform 3 mm CTV expansion, according to our defined geometric stereotactic conditions.

All SBRT treatment characteristics are reported in **Table 1**. The isocenter prescription dose was 67.5 Gy in 3 fractions and reduced to 62.5 Gy in 5 fractions for central lung tumors to meet normal tissue dose contraints. The marginal isodose line prescribed to the edge of PTV was the 80% isodose: respectively, 54 Gy in 3 fractions and 50 Gy in 5 fractions (BED_{10} = 126 Gy and 83.3 Gy). Each fraction was separated by at least 40 h (25).

All treatments used 6-MV photons. Dose distributions were performed with two coplanar dynamic conformal arcs (DCA) in 84% of cases and with volumetric modulated arc therapy (VMAT) in 16%. Treatment planning systems (TPS) were Iplan® v4.1 (Brainlab, Feldkirchen, Germany) for DCA plans and Eclipse® v13.5 (Varian Medical Systems, Palo Alto, CA, United States) for VMAT plans. Pulmonary heterogeneity has been taken into account by using the Monte Carlo algorithm for DCA plans and the AAA algorithm for VMAT plans. Target coverage was adequate when at least 95% of the PTV was covered by 80% of the prescribed isodose. Treatment quality was verified by calculating the conformality index (CI) (a ratio of 80% prescription isodose volume to the PTV), a ratio of 50% prescription isodose volume to the PTV (R50) and the maximum dose 2 cm from the PTV

TABLE 1 | Patients and SBRT characteristics.

Characteristics	Number
Patients' characteristics	
Total	100 (100%)
Gender	
Female	21 (21%)
Male	79 (79%)
Age (years)	
Mean	71 (47.1–90.4)
Performance status	
0	54 (54%)
1	39 (39%)
2	7 (7%)
≥3	0 (0%)
Medical history	
Surgery	
Pneumonectomy	4 (4%)
Lobectomy	18 (18%)
None	78 (78%)
Lung radiotherapy	
Yes	7 (7%)
No	93 (93%)
Pre-treatment dyspnea (NYHA)	
0	18 (18%)
1	25 (25%)
2	18 (18%)
3	30 (30%)
4	9 (9%)
Pre-treatment pulmonary function	
FEV1(%)	
Mean	64.1 (20–100)
DLCO (%)	
Mean	49.2 (8.0–100)
Characteristics of pulmonary nodules	
Histological/cytological proof	
None	56 (56%)
Adenocarcinoma	32 (32%)
Squamous cell carcinoma	9 (9%)
Undifferentiated carcinoma	1 (1%)
Neuroendocrine carcinoma	2 (2%)
RTOG localization	
Central	7 (7%)
Peripheral	93 (93%)
Pulmonary localization	
Right upper lobe	36 (36%)
Right middle lobe	5 (5%)
Right lower lobe	14 (14%)
Left upper lobe	31 (31%)
Left lower lobe	14 (14%)
Pre-treatment SUVmax	
Mean	7.5 (1.2–19.5)
Tumor volume	
Longest diameter (mm)	
Mean	23.4 (7.8–53.9)

(Continued)

TABLE 1 | Continued

Characteristics	Number
GTV (cc)	
Mean	8.6 (0.2–61.5)
PTV (cc)	
Mean	50.8 (3.8–223.1)
SBRT characteristics	
Technique	
DCA	84 (84%)
VMAT	16 (16%)
Fractionation	
3	76 (76%)
5	24 (24%)
Overall treatment time (days)	
Mean	8 (4–35)
Isocenter prescribed BED_{10} (Gy)	
Mean	196 (100–219)
Received PTV BED_{10} (Gy)	
D_{max}	198 (87–252)
$D_{2\ \%}$	194 (87–246)
$D_{98\ \%}$	137 (111–165)
D_{min}	110 (27–166)
80% prescription isodose volume (%)	79 (39.8–100)
Treatment quality	
Conformality index (CI)	1.19 (1.0–1.64)
R50	1.8 (0.46–5.72)
D2cm (Gy)	36.6 (22.7–57.5)
Follow-up (months)	
Mean	27 (0.6–64)
Median	25 (0.6–64)

NHYA: New York Heart Association, SUVmax: maximum Standardized Uptake Value, FEV1: Forced Expiratory Volume in 1 second, DLCO: Diffusing Lung capacity for Carbon Monoxide, DCA: Dynamic Conformal Arcs, VMAT: volumetric modulated arc therapy, BED10 = biologically effective dose with an α/β ratio of 10 Gy, Conformality Index (CI): ratio of 80% prescription isodose volume to the PTV, R50: ratio of 50% prescription isodose volume to the PTV, D2cm: maximum dose 2 cm from the PTV in any direction.

in any direction (D2cm), as seen in **Table 1** (28). Lung SBRT was performed using a Novalis Tx® (Varian Medical Systems, Palo Alto, CA, United States) linear accelator (LINAC) with an integrated Exactrac X-ray 6D system® (Brainlab AG, Feldkirchen, Germany). This system enabled a pre-treatment positioning which was then adjusted daily with a Cone Beam CT (CBCT).

Follow-Up

Follow-up included prospective clinical examination and CT scans every 3 months during the first two years post-SBRT and every 6 months afterward. Follow-up PET scans were required only in cases of progressive soft tissue abnormalities observed on CT. Efficacy was assessed with the Response Evaluation Criteria in Solid Tumors (RECIST) (29). A complete response was defined as the disappearance of the target lesion, a partial response as a decrease of at least 30% of the tumor's longest diameter and a progressive disease as an increase of at least 20% of the longest diameter. LC was defined as the absence of local failure. Local failure was characterized as the combination of a RECIST progressive disease and evidence of tumor viability as shown by biopsy or SUV_{max} in 18F-FDG PET above the pre-treatment SUV_{max} or above a value of 5 (30). Progression-free survival (PFS) was defined as the period of time from the end of SBRT to the date of local-regional failure, disseminated (visceral or lymph-node) recurrence or the patient's death. OS was defined as the time between the end of SBRT and the patient's death. Toxicity was evaluated with the National Cancer Institute's Common Toxicity Criteria for Adverse Events version 4.0 (NCI-CTCAE).

Mean and median follow-up were respectively 27 and 25 months (range: 0.6–64). Only one patient was lost to follow-up after 10 months (**Table 1**).

Statistical Analysis

No patient included in the prospectively updated institutional database of all first 100 patients consecutively treated with SBRT in our institution was excluded from the study or from the statistical analysis (**Figure 1**). LC, PFS, and OS were calculated using the Kaplan–Meier method. The Cox proportional hazards model was performed to identify predictive factors of LC and prognostic factors of PFS and OS. A two-sided p-value < 0.05 was considered significant. The following factors were included in the univariate analysis for LC: histological type, pre-treatment SUV_{max}, conformality index, R50, GTV, PTV, an 80% prescription isodose volume (%), and maximum and minimum PTV BED_{10} (D_{max}, $D_{98\ \%}$, $D_{2\ \%}$, D_{min}). Concerning PFS and OS, the following factors were included in the univariate analysis in addition to the previously studied LC predictive factors: gender, age, performance status, history of lung surgery, pre-treatment FEV1, pre-treatment DLCO, baseline pulmonary function, and mean lung BED_3 (whole lungs, ipsilateral lung, whole lungs minus PTV, ipsilateral lung minus PTV), The Benjamini–Hochberg method was used to adjust p-values to limit false positives, considering the large number of tests. The Spearman correlation enabled the identification of strongly correlated factors between them that were not included in the multivariate analysis (Spearman's rank correlation coefficient of 0.75). Factors associated with a p-value < 0.25 in the univariate analysis were included in the multivariate analysis if they were also selected by the LASSO method. The Wald test and the Likelihood ratio test were performed to calculate and verify the p-value for each coefficient in multivariate analyses.

Linear correlation between OS and significant prognostic factors was then verified with a Pearson or Spearman correlation coefficient, depending on the cases, especially for patients with a poor pre-treatment pulmonary function (i.e., FEV1 or DLCO $\leq 40\%$). For each significant linear correlation observed, a ROC (Receiver Operating Characteristics) curve was performed to identify the best threshold. Finally, comparisons of OS curves with obtained thresholds were conducted using the log-rank test.

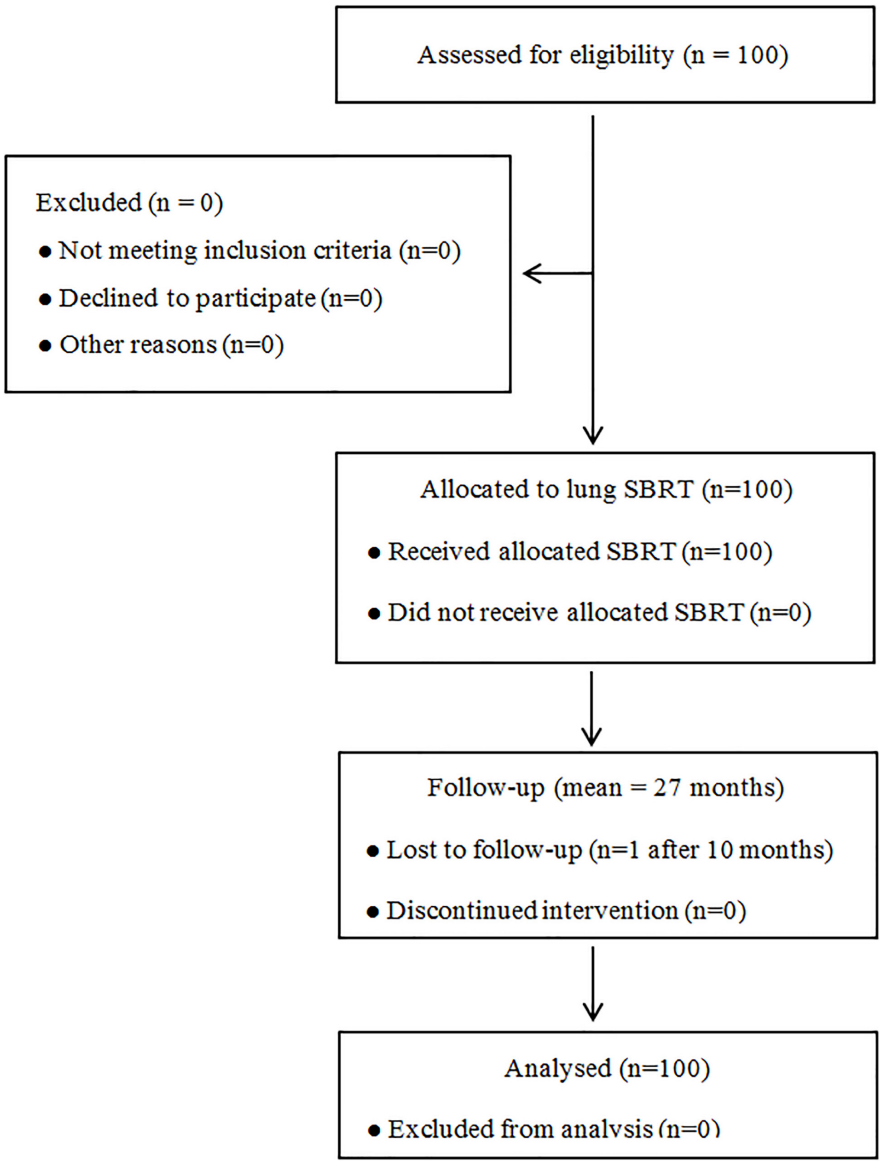

FIGURE 1 | Flowchart of the patient enrollment process of study cohort.

RESULTS

Local Control and Progression-Free Survival

Local control at 1, 2, 3, and 5 years was respectively 100, 98.2, 98.2, and 77.7% (**Figure 2**). Three local failures were observed. No statistically significant predictive factor of LC was found (**Table 2**). PFS at 1, 2, 3, and 5 years was respectively 80, 55.1, 43.7, and 19.7% (**Figure 2**). Median PFS was 28 months (CI95%: 22–51 months). PFS after lung SBRT was significantly correlated to tumor volume (GTV) in univariate analysis (HR = 1.065, 95%CI = 1.040–1.091, $p < 0.001$) and in multivariate analysis (HR = 1.060, 95%CI = 1.033–1.087, $p < 0.001$), as shown in **Table 2**. There was a strong trend for significance when we studied mean ipsilateral lung BED_3 (p-value of 0.063; HR = 2.035, 95%CI = 1.000–1.072).

Overall Survival

Overall survival at 1, 2, 3, and 5 years was respectively 83, 71.2, 58.1, and 33.2% (**Figure 2**). Median OS was 49 months. In univariate analysis, significant prognostic factors of OS were GTV (HR = 1.074, 95%CI = 1.047–1.102, $p < 0.001$), PTV (HR = 1.016, 95%CI = 1.010–1.022,$p < 0.001$), mean lung BED_3 (HR = 1.125, 95%CI = 1.033–1.225, $p = 0.04$), mean ipsilateral lung BED_3 (HR = 1.060, 95%CI = 1.020–1.103, $p = 0.04$) and mean ipsilateral lung minus PTV BED_3 (HR = 1.087, 95%CI = 1.023–1.156, $p = 0.04$). Prognostic factors of OS that remained significant in multivariate analysis were mean lung BED_3 (HR = 1.14,

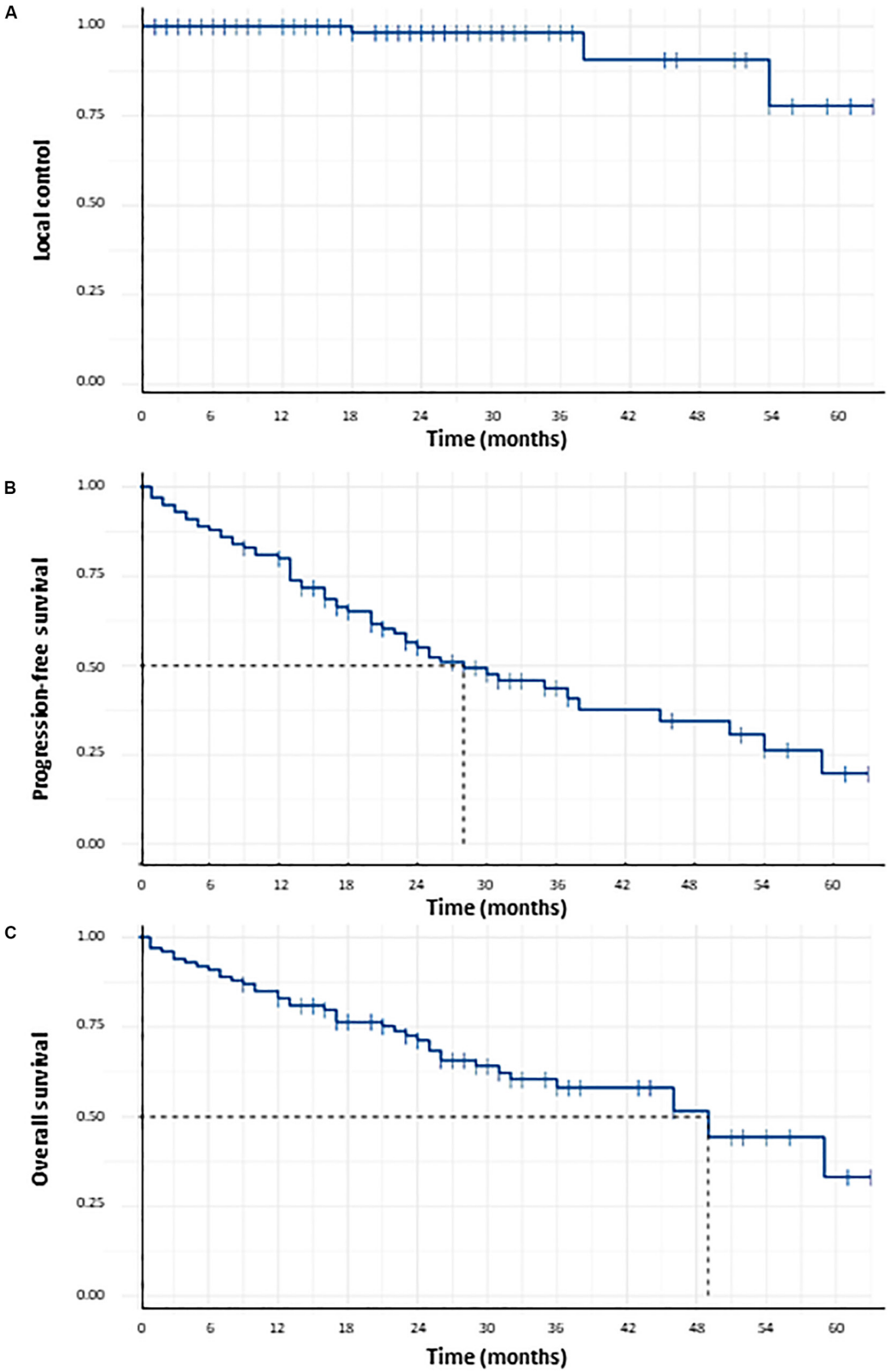

FIGURE 2 | Probability of local control **(A)**, probability of progression-free survival **(B)** and probability of overall survival **(C)** for the 100 patients receiving lung SBRT for Stage I NSCLC.

TABLE 2 | Results of univariate and multivariate analyses for local control, progression-free survival, overall survival and radiation pneumonitis incidence.

	Univariate analysis (LR p BH)				Multivariate analysis (W p)			
	LC	**PFS**	**OS**	**RP**	**LC**	**PFS**	**OS**	**RP**
Histological type	0.92	0.21	0.18	–	–	–	0.38	–
Pre-treatment SUVmax	0.92	0.96	0.79	–	–	–	–	–
Conformality index	0.92	0.21	0.32	–	–	–	–	–
R50	0.92	0.95	0.85	–	–	–	–	–
GTV	0.92	**<0.001**	**<0.001**	0.91	–	–	–	–
PTV	0.92	**0.003**	**<0.001**	0.89	–	**<0.001**	**0.004**	–
80% prescription isodose volume	0.92	0.21	0.14	–	–	–	–	–
PTV BED_{10}								
D_{max}	0.92	0.51	0.66	–	–	–	–	–
$D_{2\%}$	0.92	0.56	0.66	–	–	–	–	–
$D_{98\%}$	0.92	0.80	0.79	–	–	–	–	–
D_{min}	0.92	0.80	0.79	–	–	–	–	–
Gender	–	0.86	0.84	–	–	–	–	–
Age	–	0.96	0.46	**0.10**	–	–	–	0.45
Performans status	–	0.56	0.38	–	–	–	–	–
Past medical history of								
Lung surgery	–	0.95	0.79	–	–	–	–	–
Lung radiotherapy	–	0.80	0.66	–	–	–	–	–
Pre-treatment								
FEV1	–	0.80	0.58	**<0.001**	–	–	–	**0.003**
DLCO	–	0.49	0.18	**<0.001**	–	–	0.07	**0.015**
Level of dyspnea (NYHA)	–	0.80	0.65	–	–	–	–	–
Mean lung BED_3								
Whole lungs	–	0.32	**0.04**	0.09	–	–	**0.01**	–
Ipsilateral lung	–	0.23	**0.04**	**0.04**	–	–	–	–
Whole lungs minus PTV	–	0.32	0.14	**0.02**	–	–	–	0.29
Ipsilateral lung minus PTV	–	0.31	**0.04**	**0.03**	–	–	–	–

LR p BH: p-value with Likelihood ratio adjusted by Benjamini–Hochberg method, W p: p-value with Wald test, SUVmax: maximum standardized uptake value, R50: ratio of 50% prescription isodose volume to the PTV, BEDx = biologically effective dose with an α/β ratio of × Gy, FEV1: forced expiratory volume in 1 second, DLCO: diffusing lung capacity for carbon monoxide, NHYA: New York Heart Association. Bold values are those that are statistically significant.

CI95% = 1.03–1.25, $p = 0.01$) and PTV (HR = 1.01, CI95% = 1.0–1.02, $p = 0.004$), as shown in **Table 2**. Subgroup analysis has been done to study the prognostic role of mean lung BED_3 in OS. Concerning subgroup analysis of FEV_1, mean lung BED_3 remained significantly correlated to OS in multivariate analysis whether for patients with $FEV_1 \leq 40\%$ (HR = 1.55, 95%CI = 1.12–2.14, $p = 0.008$) or with $FEV_1 > 40\%$ (HR = 1.14, 95%CI = 1.02–1.28, $p = 0.021$). Concerning subgroup analysis of GTV, mean lung BED_3 remained significantly correlated to OS in multivariate analysis for patients with GTV < mean GTV, i.e., 8.6 cc (HR = 1.34, 95%CI = 1.06–1.69, $p = 0.015$) but not for patients with GTV ≥ mean GTV (HR = 1.02, 95%CI = 0.88–1.18, $p = 0.78$).

Concerning subgroup analysis for frailty patients with poor baseline pulmonary function, significant negative correlations were observed between OS and mean lung BED_3 in cases of FEV1 ≤ 40% ($r = -0.6$, $p = 0.005$) and DLCO ≤ 40% ($r = -0.36$, $p = 0.033$) (**Figure 3**). The best prognostic mean lung BED_3 threshold identified on the ROC curve in terms of sensitivity and specificity for OS was 5 Gy for the entire population (i.e., 3.6 Gy in 3 fractions or 4.3 Gy in 5 fractions) and reduced to 4 Gy for patients with FEV1 ≤ 40% (i.e., 3 Gy in 3 fractions or 3.5 Gy in 5 fractions). Concerning all the 100 treated patients, a mean lung $BED_3 \leq 5$ Gy was significantly associated with a higher OS ($p = 0.0068$) with a doubling of median OS from 29 months to more than 60 months (not achieved). OS at 1, 2, 3, 4, and 5 years was respectively 89.1, 78.8, 71.8, 65.2, and 58% for a mean lung $BED_3 \leq 5$ Gy rather than 75.6, 61.8, 42, 36, and 19.2% for a mean lung $BED_3 > 5$ Gy (**Figure 4**). Similarly, in patients with poor baseline pulmonary function (i.e., FEV1 ≤ 40%), a mean lung $BED_3 \leq 4$ Gy was significantly associated with a higher OS ($p = 0.019$) with a doubling of median OS from 23 months to 46 months. OS at 1, 2 and 3 years was respectively 90, 90, and 67.5% for a mean lung $BED_3 \leq 4$ Gy rather than 70, 46.7, and 23.3% for a mean lung $BED_3 > 4$ Gy (**Figure 3**).

Clinical Follow-Up and Toxicities

At the end of follow up, lung SBRT led to 31% Grade ≤ 2 clinically symptomatic radiation pneumonitis (RP), 14% G1 chest wall pain, 7% transient G ≤ 2 radiation dermatitis (4 G1 and 3 G2), 4% rib fractures after a mean period of 28 months (range: 12–45), and 14% G1 chest wall pain. At least 22 patients (22%)

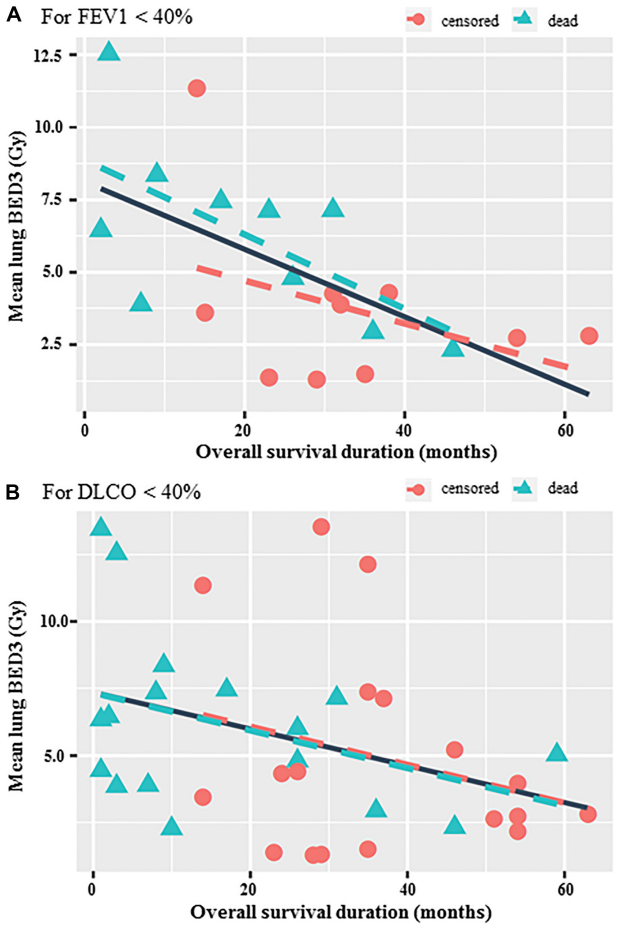

FIGURE 3 | Correlation between OS and mean lung BED3 for patients with FEV1 < 40% (r = –0.6, p = 0.005) **(A)** and with DLCO < 40% (r = –0.36, p = 0.033) **(B)**. The solid line shows correlation independently of the censored or dead patients.

died from severe pulmonary insufficiency. Significant predictive factors of clinically symptomatic G ≥ 1 RP were in univariate analysis FEV1 (OR = 0.630, 95%CI = 0.550–0.780, p < 0.001), DLCO (OR = 0.750, 95%CI = 0.660–0.859, p < 0.001) and mean ipsilateral lung BED_3 (OR = 0.956, 95%CI = 0.923–0.999, p = 0.043). There was a trend towards mean lung BED_3 (OR = 0.986, 95%CI = 0.998–0.967, p = 0.086). In multivariate analysis, FEV1 (OR = 0.929, 95%CI = 0.878–0.971, p = 0.003) and DLCO (OR = 0.939, 95%CI = 0.886–0.984, p = 0.015) remained significant (**Table 2**). No significant predictive factor of radiation dermatitis, rib fractures or chest wall pain was found. No other toxicity was observed.

DISCUSSION

To date, the present study is the first to demonstrate a significant correlation between OS and MLD after Stage I NSCLC SBRT. Moreover, this finding leads us to propose reducing published lung constraints with thresholds of 5 and 4 Gy in mean lung BED_3 respectively for patients with FEV1 > 40% and FEV1 ≤ 40%.

Our lung SBRT characteristics are in agreement with international guidelines about Stage I NSCLC, especially with Timmerman et al. in the analysis of RTOG 0236 (25). Marginal prescribed dose to the edge of PTV was 54 Gy in three fractions if it met dose constraints. Concerning target volume delineation, we no longer create a CTV since it is not recommended (31). When we started to treat patients in 2012, guidelines were less clear and CTV creation was debated (26). In our study, LC and OS were respectively over 95% and about 60% at the three-year point, which is consistent with previously published studies (1–3, 25). No significant predictive factor of LC was found, probably because only three local failures were observed and adequate BED_{10} was prescribed to the tumor.

Likewise, this study found toxicity in the same proportions as previous reports: 31% clinically symptomatic RP [about 10–20% of patients in literature (range: 0–49% among published studies)] with most patients having asymptomatic Grade 1 pneumonitis (2, 15–17), 14% G1 chest wall pain [10–40% in literature (32)], 7% transient G ≤ 2 radiation dermatitis [12–38% in literature (33)], and 4% rib fractures [0–23% in literature (34)] without other toxicity. No significant predictive factor of chest wall pain, radiation dermatitis or rib fractures was found, probably due to meeting dose constraints (35). Significant predictive factors of RP reported in our study are in agreement with published studies concerning MLD, which is frequently mentioned (15, 17, 19–21). In contrast, baseline pulmonary function (FEV1 and DLCO) was strongly and significantly correlated to RP in univariate and multivariate analyses (18). Thus, the results reported in the present study are demonstrated to be reproducible and may be applied to other studies. As compared to normo-fractionated radiotherapy, MLD corresponds to the most used parameter in predictive risk models pulmonary toxicity due to its simplicity and effectiveness (36, 37). Dose constraint for MLD is often ≤ 15–20, i.e., mean lung BED_3 ≤ 16–21 Gy (38, 39). Estimated risk of symptomatic RP is 5, 10, 20, 30, and 40% for thresholds of 7, 13, 20, 24, and 27 Gy in MLD, i.e., thresholds of 7, 13, 21, 27, and 30 Gy in mean lung BED_3 (39).

Radiation pneumonitis is a known important dose-limiting factor in lung cancer radiation therapy. RP is categorized into two interdependent stages: acute RP and late RP (a chronic injury stage known as pulmonary fibrosis) which can theoretically be fatal, especially if pulmonary function is already impaired. The summarized sequence of classic RP is as follows: cellular injury leads to cytokine release, cytokine recruitment of the inflammatory infiltrate causes acute pneumonitis, and the body's attempt to repair the injury results in pulmonary fibrosis (13). It is accepted that recognition of sporadic RP can be particularly difficult for clinicians because it is rare (≈ 10%) and patients often present with severe dyspnea and/or "out-of-field" radiographic findings that may raise the possibility of other disease process (13). So we can think that RP are probably underestimated in published studies, and especially their exact relationship with the death of patients. This might be one of the explanations of why MLD was a significant prognostic factor of OS in our study.

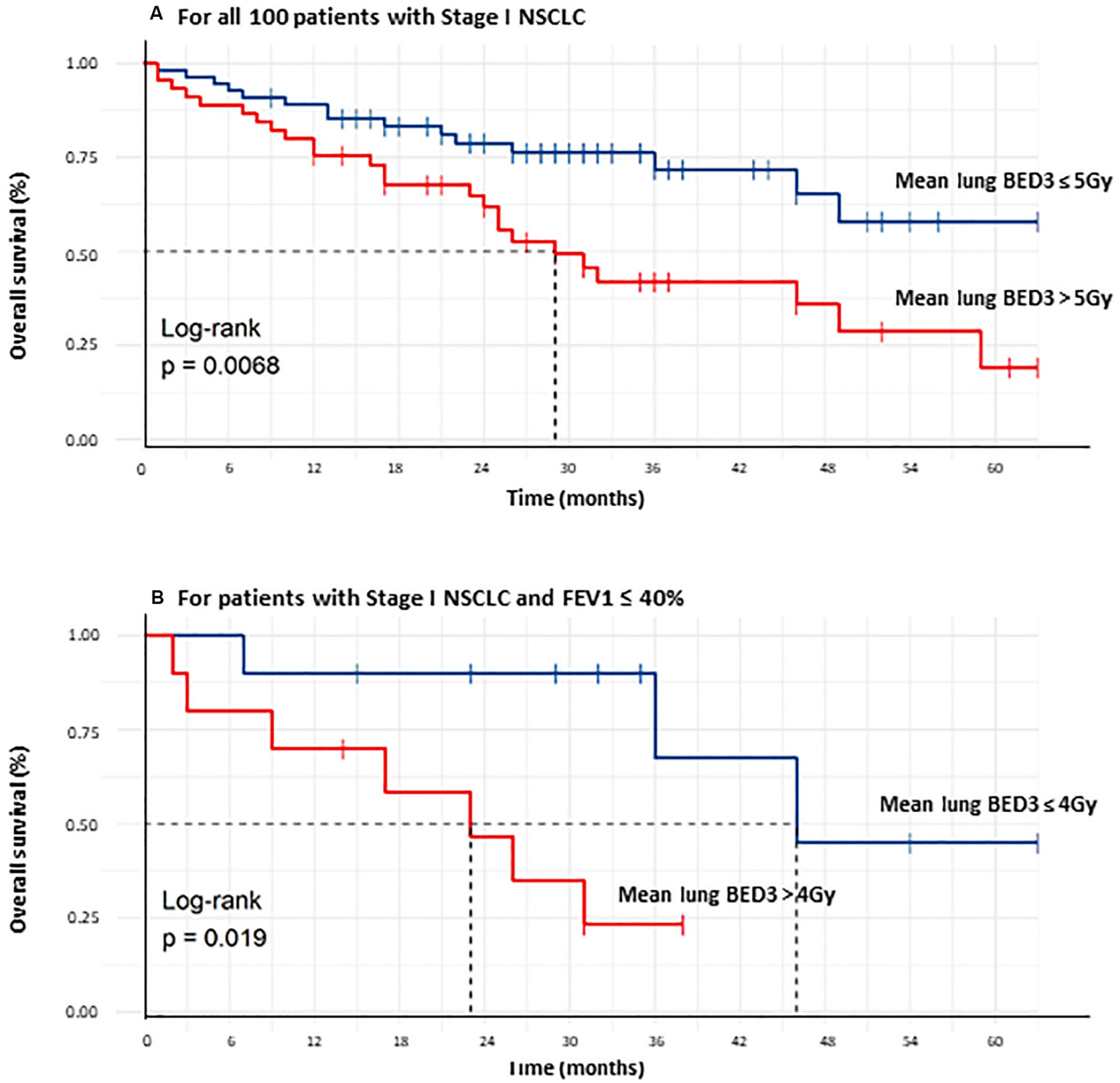

FIGURE 4 | Comparison of overall survival curves of all 100 Stage I NSCLC treated patients between those receiving a mean lung $BED_3 \leq 5$ Gy and those > 5 Gy **(A)**, comparison of overall survival curves of all Stage I NSCLC treated patients with FEV1 $\leq 40\%$ between those receiving a mean lung $BED_3 \leq 4$ Gy and those > 4 Gy **(B)**.

Limitations of the study were in link with the difficulty to recognize RP particularly in patients with a poor baseline pulmonary function and frequent flares of acute pulmonary insufficiency. It was very difficult to know from what patients were dying and the cause of their pulmonary insufficiency: natural and classic outcome of their comorbidities or especially related to RP? Other limitations were that study was mono institutional and not multicentric, only 100 patients were included which could have led to a lack of power for statistical analyses and data were retrospectively analyzed even if they were prospectively updated. Statistical analysis was robust and there was only one patient lost to follow-up after a period of 10 months after SBRT. Pulmonary heterogeneity, which may be a reason for false interpretation, has been taken into account by using the Monte Carlo algorithm for DCA plans and the AAA algorithm for VMAT plans. Various dose prescriptions and fractionations have been studied with the linear-quadratic model with an α/β ratio of 3 Gy which was the best method for converting the physical lung dose to predict RP (24).

Concerning PFS, PFS after lung SBRT was significantly correlated to tumor volume (GTV) in univariate and in multivariate analysis. We did not find mean lung BED_3 as a

significant prognostic factor of PFS in univariate analysis. One of the explanations might be a lack of power of our study because the lower threshold value of the 95%CI was very close to 1 (0.988). Interestingly, there was therefore a strong trend for significance when we studied mean ipsilateral lung BED_3 (p-value of 0.063; HR = 2.035, 95%CI = 1.000–1.072).

Concerning OS, it is widely agreed that more patients die of comorbidities than of tumor progression since LC is excellent, over 95% at three years. Therefore, significant published prognostic factors to date mostly relate to comorbidities [age (4), gender (5), performance status (4, 6), platelet-to-lymphocyte ratio (8, 10), and pretreatment immune parameters (10)] if the prescribed dose is sufficiently high (11). However, no relationship between toxicity and OS is demonstrated to date. Many patients treated with lung SBRT die from severe pulmonary insufficiency, but it is not easy to distinguish whether the main cause is the natural course of pulmonary or cardiovascular disease or if SBRT lung toxicity might have worsened the situation. Severe RP is probably under-evaluated in literature. It is the main toxicity factor after lung SBRT; furthermore, MLD seems to be the strongest and most reproducible dosimetric parameter of RP (15, 17, 19–21). In addition, tumor volume is a reproducible and frequently reported significant prognostic factor of OS (5–7). We can also surmise that tumor volume is linked to MLD and that patients could die from a higher received MLD than GTV because LC is high. For this reason, we have made the choice to study the correlation between OS and MLD, which we have demonstrated to be significant in multivariate analysis for all patients (HR = 1.14, CI95% = 1.03–1.25, p = 0.01) and in subgroup multivariate analysis, whether for patients with $FEV_1 \leq 40\%$ (HR = 1.55, 95%CI = 1.12–2.14, p = 0.008) or with $FEV_1 > 40\%$ (HR = 1.14, 95%CI = 1.02–1.28, p = 0.021) or with GTV < mean GTV, i.e., 8.6 cc (HR = 1.34, 95%CI = 1.06–1.69, p = 0.015). GTV and FEV_1 cannot be modified while the prescribed dose can be adjusted.

Moreover, we showed in our study a significant correlation between OS and MLD with a significant threshold value of 5 Gy for BED_3, i.e., 3.6 Gy in three fractions. A significant cut-off at 4–4.7 Gy in three fractions is reported in literature concerning the probability of RP after lung SBRT (17, 19). So our threshold value of 3.6 Gy in three fractions is not very different from that published for symptomatic RP, which enables us to assume that the threshold value of 5 Gy for OS may be related to RP. Thresholds values may have to be reduced to 5 Gy (i.e., 3.6 Gy in 3 fractions or 4.3 Gy in 5 fractions) and 4 Gy (i.e., 3 Gy in 3 fractions or 3.5 Gy in 5 fractions) in mean lung BED_3 respectively for patients with $FEV1 > 40\%$ and $FEV1 \leq 40\%$, as our study suggests, to have an impact on OS. These two thresholds values are totally in agreement because we may have to be more careful to treat frailty patients and probably we may have to reduce prescribed dose for these patients. We therefore recommend using effective algorithms that take into account pulmonary heterogeneity and limiting PTV irradiated volume to a minimum by reducing margins (not creating a CTV or using gating or tracking techniques). This is particularly crucial for frailty patients with poor baseline pulmonary function ($FEV1 \leq 40\%$).

CONCLUSION

In summary, our study demonstrates a significant and strong correlation between OS and mean lung BED_3, confirmed in univariate and multivariate analysis in all patients, in subgroup analysis and in survival curves analysis. Higher mean lung BED_3 is always strongly and significantly associated with a poorer OS. Moreover, significant mean lung BED_3 threshold values have here been shown to correlate with OS: 5 Gy for the entire population (i.e., 3.6 Gy in 3 fractions or 4.3 Gy in 5 fractions) and 4 Gy for patients with $FEV1 \leq 40\%$ (i.e., 3 Gy in 3 fractions or 3.5. Gy in 5 fractions). Stay below these threshold values significantly enabled a doubling of median OS.

DATA AVAILABILITY STATEMENT

The datasets generated for this study are available on request to the corresponding author.

ETHICS STATEMENT

Study ethics approval was obtained on 06 December 2019 (CECIC Rhône-Alpes-Auvergne, Grenoble, IRB 5921).

AUTHOR CONTRIBUTIONS

GD and IM analyzed the data. GD wrote and revised the manuscript. JB, VC, VD, ML, and AB-C also revised the manuscript. All authors have actively participated in the data acquisition, commented, and approved the final version of the manuscript.

REFERENCES

1. Baumann P, Nyman J, Hoyer M, Wennberg B, Gagliardi G, Lax I, et al. Outcome in a prospective phase II trial of medically inoperable stage I non-small-cell lung cancer patients treated with stereotactic body radiotherapy. *J Clin Oncol Off J Am Soc Clin Oncol.* (2009) 27:3290–6. doi: 10.1200/JCO.2008.21.5681
2. Abel S, Hasan S, Horne ZD, Colonias A, Wegner RE. Stereotactic body radiation therapy in early-stage NSCLC: historical review, contemporary evidence and future implications. *Lung Cancer Manag.* (2019) 8:LMT09. doi: 10.2217/lmt-2018-0013
3. Prezzano KM, Ma SJ, Hermann GM, Rivers CI, Gomez-Suescun JA, Singh AK. Stereotactic body radiation therapy for non-small cell lung cancer: A review. *World J Clin Oncol.* (2019) 10:14–27. doi: 10.5306/wjco.v10.i1.14
4. Spratt DE, Wu AJ, Adeseye V, Din SU, Shaikh F, Woo KM, et al. Recurrence patterns and second primary lung cancers after stereotactic body radiation therapy for early-stage non-small-cell lung cancer: implications for surveillance. *Clin Lung Cancer.* (2015) 17:177–83.e2. doi: 10.1016/j.cllc.2015.09.006
5. Matsuo Y, Shibuya K, Nagata Y, Takayama K, Norihisa Y, Mizowaki T, et al. Prognostic factors in stereotactic body radiotherapy for non–small-cell lung

cancer. *Int J Radiat Oncol.* (2011) 79:1104–11. doi: 10.1016/j.ijrobp.2009.12.022
6. Kohutek ZA, Wu AJ, Zhang Z, Foster A, Din SU, Yorke ED, et al. FDG-PET maximum standardized uptake value is prognostic for recurrence and survival after stereotactic body radiotherapy for non-small cell lung cancer. *Lung Cancer Amst Neth.* (2015) 89:115–20. doi: 10.1016/j.lungcan.2015.05.019
7. Chi A, Liao Z, Nguyen NP, Xu J, Stea B, Komaki R. Systemic review of the patterns of failure following stereotactic body radiation therapy in early-stage non-small-cell lung cancer: clinical implications. *Radiother Oncol.* (2010) 94:1–11. doi: 10.1016/j.radonc.2009.12.008
8. Shi S, Ye L, Zhao Q, Hu Y, Huang Y, Chen G, et al. Prognostic index score predicts outcome of patients with Stage I non-small cell lung cancer after stereotactic body radiation therapy. *Jpn J Clin Oncol.* (2019) 49:367–72. doi: 10.1093/jjco/hyy205
9. Chang JY, Liu H, Balter P, Komaki R, Liao Z, Welsh J, et al. Clinical outcome and predictors of survival and pneumonitis after stereotactic ablative radiotherapy for stage I non-small cell lung cancer. *Radiat Oncol.* (2012) 7:152. doi: 10.1186/1748-717X-7-152
10. Shaverdian N, Veruttipong D, Wang J, Schaue D, Kupelian P, Lee P. Pretreatment immune parameters predict for overall survival and toxicity in early-stage non-small-cell lung cancer patients treated with stereotactic body radiation therapy. *Clin Lung Cancer.* (2016) 17:39–46. doi: 10.1016/j.cllc.2015.07.007
11. Stahl JM, Ross R, Harder EM, Mancini BR, Soulos PR, Finkelstein SE, et al. The effect of biologically effective dose and radiation treatment schedule on overall survival in stage I non-small cell lung cancer patients treated with stereotactic body radiation therapy. *Int J Radiat Oncol Biol Phys.* (2016) 96:1011–20. doi: 10.1016/j.ijrobp.2016.08.033
12. Martin A, Gaya A. Stereotactic body radiotherapy: a review. *Clin Oncol.* (2010) 22:157–72. doi: 10.1016/j.clon.2009.12.003
13. Hanania AN, Mainwaring W, Ghebre YT, Hanania NA, Ludwig M. Radiation-induced lung injury: assessment and management. *Chest.* (2019) 156:150–62. doi: 10.1016/j.chest.2019.03.033
14. Haasbeek CJA, Lagerwaard FJ, Slotman BJ, Senan S. Outcomes of stereotactic ablative radiotherapy for centrally located early-stage lung cancer. *J Thorac Oncol Off Publ Int Assoc Study Lung Cancer.* (2011) 6:2036–43. doi: 10.1097/JTO.0b013e31822e71d8
15. Matsuo Y, Shibuya K, Nakamura M, Narabayashi M, Sakanaka K, Ueki N, et al. Dose–volume metrics associated with radiation pneumonitis after stereotactic body radiation therapy for lung cancer. *Int J Radiat Oncol Biol Phys.* (2012) 83:e545–9. doi: 10.1016/j.ijrobp.2012.01.018
16. Baker R, Han G, Sarangkasiri S, DeMarco M, Turke C, Stevens CW, et al. Clinical and dosimetric predictors of radiation pneumonitis in a large series of patients treated with stereotactic body radiation therapy to the lung. *Int J Radiat Oncol Biol Phys.* (2013) 85:190–5. doi: 10.1016/j.ijrobp.2012.03.041
17. Zhao J, Yorke ED, Li L, Kavanagh BD, Li XA, Das S, et al. Simple factors associated with radiation-induced lung toxicity after stereotactic body radiation therapy of the thorax: a pooled analysis of 88 studies. *Int J Radiat Oncol Biol Phys.* (2016) 95:1357–66. doi: 10.1016/j.ijrobp.2016.03.024
18. Henderson M, McGarry R, Yiannoutsos C, Fakiris A, Hoopes D, Williams M, et al. Baseline pulmonary function as a predictor for survival and decline in pulmonary function over time in patients undergoing stereotactic body radiotherapy for the treatment of stage I non-small-cell lung cancer. *Int J Radiat Oncol Biol Phys.* (2008) 72:404–9. doi: 10.1016/j.ijrobp.2007.12.051
19. Barriger RB, Forquer JA, Brabham JG, Andolino DL, Shapiro RH, Henderson MA, et al. A dose-volume analysis of radiation pneumonitis in non-small cell lung cancer patients treated with stereotactic body radiation therapy. *Int J Radiat Oncol Biol Phys.* (2012) 82:457–62. doi: 10.1016/j.ijrobp.2010.08.056
20. Lu C, Lei Z, Wu H, Lu H. Evaluating risk factors of radiation pneumonitis after stereotactic body radiation therapy in lung tumor: meta-analysis of 9 observational studies. *PLoS One.* (2018) 13:e0208637. doi: 10.1371/journal.pone.0208637
21. Parker SM, Siochi RA, Wen S, Mattes MD. Impact of tumor size on local control and pneumonitis after stereotactic body radiation therapy for lung tumors. *Pract Radiat Oncol.* (2019) 9:e90–7. doi: 10.1016/j.prro.2018.09.003
22. Yamashita H, Takahashi W, Haga A, Nakagawa K. Radiation pneumonitis after stereotactic radiation therapy for lung cancer. *World J Radiol.* (2014) 6:708–15. doi: 10.4329/wjr.v6.i9.708
23. Biau J, Bellière A, Verrelle P, Lapeyre M. Excluding either gross tumor volume or planning target volume from the normal lung volume in lung cancer irradiation: evaluation of the dosimetric impact. *Pract Radiat Oncol.* (2013) 3:e79–85. doi: 10.1016/j.prro.2012.06.001
24. Borst GR, Ishikawa M, Nijkamp J, Hauptmann M, Shirato H, Bengua G, et al. Radiation pneumonitis after hypofractionated radiotherapy: evaluation of the LQ(L) model and different dose parameters. *Int J Radiat Oncol Biol Phys.* (2010) 77:1596–603. doi: 10.1016/j.ijrobp.2009.10.015
25. Timmerman R, Paulus R, Galvin J, Michalski J, Straube W, Bradley J, et al. STereotactic body radiation therapy for inoperable early stage lung cancer. *JAMA.* (2010) 303:1070–6. doi: 10.1001/jama.2010.261
26. De Ruysscher D, Faivre-Finn C, Nestle U, Hurkmans CW, Le Péchoux C, Price A, et al. European organisation for research and treatment of cancer recommendations for planning and delivery of high-dose, high-precision radiotherapy for lung cancer. *J Clin Oncol Off J Am Soc Clin Oncol.* (2010) 28:5301–10. doi: 10.1200/JCO.2010.30.3271
27. Giraud P, Antoine M, Larrouy A, Milleron B, Callard P, De Rycke Y, et al. Evaluation of microscopic tumor extension in non–small-cell lung cancer for three-dimensional conformal radiotherapy planning. *Int J Radiat Oncol.* (2000) 48:1015–24. doi: 10.1016/S0360-3016(00)00750-1
28. Xiao Y, Papiez L, Paulus R, Timmerman R, Straube WL, Bosch WR, et al. Dosimetric evaluation of heterogeneity corrections for RTOG 0236: stereotactic body radiotherapy of inoperable stage I-II non-small-cell lung cancer. *Int J Radiat Oncol Biol Phys.* (2009) 73:1235–42. doi: 10.1016/j.ijrobp.2008.11.019
29. Therasse P, Arbuck SG, Eisenhauer EA, Wanders J, Kaplan RS, Rubinstein L, et al. New guidelines to evaluate the response to treatment in solid tumors. European Organization for Research and Treatment of Cancer, National Cancer Institute of the United States, National Cancer Institute of Canada. *J Natl Cancer Inst.* (2000) 92:205–16. doi: 10.1093/jnci/92.3.205
30. Bollineni VR, Widder J, Pruim J, Langendijk JA, Wiegman EM. Residual ^{18}F-FDG-PET uptake 12 weeks after stereotactic ablative radiotherapy for stage I non-small-cell lung cancer predicts local control. *Int J Radiat Oncol Biol Phys.* (2012) 83:e551–5. doi: 10.1016/j.ijrobp.2012.01.012
31. Timmerman RD, Paulus R, Pass HI, Gore EM, Edelman MJ, Galvin J, et al. Stereotactic body radiation therapy for operable early-stage lung cancer. *JAMA Oncol.* (2018) 4:1263–6. doi: 10.1001/jamaoncol.2018.1251
32. Din SU, Williams EL, Jackson A, Rosenzweig KE, Wu AJ, Foster A, et al. Impact of fractionation and dose in a multivariate model for radiation-induced chest wall pain. *Int J Radiat Oncol Biol Phys.* (2015) 93:418–24. doi: 10.1016/j.ijrobp.2015.06.014
33. Hoppe BS, Laser B, Kowalski AV, Fontenla SC, Pena-Greenberg E, Yorke ED, et al. Acute skin toxicity following stereotactic body radiation therapy for stage I non-small-cell lung cancer: who's at risk? *Int J Radiat Oncol Biol Phys.* (2008) 72:1283–6. doi: 10.1016/j.ijrobp.2008.08.036
34. Nambu A, Onishi H, Aoki S, Tominaga L, Kuriyama K, Araya M, et al. Rib fracture after stereotactic radiotherapy for primary lung cancer: prevalence, degree of clinical symptoms, and risk factors. *BMC Cancer.* (2013) 13:68. doi: 10.1186/1471-2407-13-68
35. Timmerman RD. An overview of hypofractionation and introduction to this issue of seminars in radiation oncology. *Semin Radiat Oncol.* (2008) 18:215–22. doi: 10.1016/j.semradonc.2008.04.001
36. Seppenwoolde Y, Lebesque JV, de Jaeger K, Belderbos JSA, Boersma LJ, Schilstra C, et al. Comparing different NTCP models that predict the incidence of radiation pneumonitis. Normal tissue complication probability. *Int J Radiat Oncol Biol Phys.* (2003) 55:724–35. doi: 10.1016/s0360-3016(02)03986-x
37. Jain V, Niezink AGH, Frick M, Doucette A, Mendes A, Simone CB, et al. Updating photon-based normal tissue complication probability

models for pneumonitis in lung cancer patients treated with proton beam therapy. *Pract Radiat Oncol.* (2020) 102:S223–4. doi: 10.1016/j.prro.2020.04.005

38. Kong F-M, Hayman JA, Griffith KA, Kalemkerian GP, Arenberg D, Lyons S, et al. Final toxicity results of a radiation-dose escalation study in patients with non-small-cell lung cancer (NSCLC): predictors for radiation pneumonitis and fibrosis. *Int J Radiat Oncol Biol Phys.* (2006) 65:1075–86. doi: 10.1016/j.ijrobp.2006.01.051
39. Marks LB, Bentzen SM, Deasy JO, Kong F-MS, Bradley JD, Vogelius IS, et al. Radiation dose-volume effects in the lung. *Int J Radiat Oncol Biol Phys.* (2010) 76:S70–6. doi: 10.1016/j.ijrobp.2009.06.091

Conflict of Interest: The authors declare that the research was conducted in the absence of any commercial or financial relationships that could be construed as a potential conflict of interest.

frontiers in Oncology

ORIGINAL RESEARCH
published: 14 August 2020
doi: 10.3389/fonc.2020.01647

Modeling of Xerostomia After Radiotherapy for Head and Neck Cancer: A Registry Study

Eva Onjukka[1,2], Claes Mercke[2,3], Einar Björgvinsson[3], Anna Embring[2,3], Anders Berglund[4], Gabriella Alexandersson von Döbeln[3], Signe Friesland[2,3], Giovanna Gagliardi[1], Clara Lenneby Helleday[3], Helena Sjödin[3] and Ingmar Lax[1]*

[1] Medical Radiation Physics and Nuclear Medicine, Karolinska University Hospital, Stockholm, Sweden, [2] Department of Oncology-Pathology, Karolinska Institute, Stockholm, Sweden, [3] Department of Oncology, Karolinska University Hospital, Stockholm, Sweden, [4] Epistat Epidemiology and Statistics Consulting, Uppsala, Sweden

OPEN ACCESS

Edited by:
Ester Orlandi, Istituto Nazionale dei Tumori (IRCCS), Italy

Reviewed by:
Jon Cacicedo, Cruces University Hospital, Spain
Giuseppe Magro, National Center of Oncological Hadrontherapy, Italy

***Correspondence:**
Eva Onjukka
eva.onjukka@sll.se

Specialty section:
This article was submitted to Radiation Oncology, a section of the journal Frontiers in Oncology

Received: *30 January 2020*
Accepted: *27 July 2020*
Published: *14 August 2020*

Citation:
Onjukka E, Mercke C, Björgvinsson E, Embring A, Berglund A, Alexandersson von Döbeln G, Friesland S, Gagliardi G, Lenneby Helleday C, Sjödin H and Lax I (2020) Modeling of Xerostomia After Radiotherapy for Head and Neck Cancer: A Registry Study. Front. Oncol. 10:1647. doi: 10.3389/fonc.2020.01647

Aim: Data from a local quality registry are used to model the risk of late xerostomia after radiotherapy for head and neck cancer (HNC), based on dosimetric- and clinical variables. Strengths and weaknesses of using quality registry data are explored.

Methods: HNC patients treated with radiotherapy at the Karolinska University hospital are entered into a quality registry at routine follow up, recording morbidity according to a modified RTOG/LENT-SOMA scale. Other recorded parameters are performance status, age, gender, tumor location, tumor stage, smoking status, chemotherapy and radiotherapy data, including prescribed dose and organ-at-risk (OAR) dose. Most patients are entered at several time points, but at variable times after treatment. Xerostomia was modeled based on follow-up data from January 2014 to October 2018, resulting in 753 patients. Two endpoints were considered: maximum grade ≥2 ($XER_{G\geq2}$) or grade ≥3 ($XER_{G\geq3}$) late xerostomia. Univariate Cox regression was used to select variables for two multivariate models for each endpoint, one based on the mean dose to the total parotid volume (D_{tot}) and one based on the mean dose to the contralateral parotid (D_{contra}). Cox regression allows the estimation of the risk of xerostomia at different time points; models were presented visually as nomograms estimating the risk at 9, 12, and 24 months respectively.

Results: The toxicity rates were 366/753 (49%) for $XER_{G\geq2}$ and 40/753 (5.3%) for $XER_{G\geq3}$. The multivariate models included several variables for $XER_{G\geq2}$, and dose, concomitant chemotherapy and age were included for $XER_{G\geq3}$. Induction chemotherapy and an increased number of fractions per week were associated with a lower risk of $XER_{G\geq2}$. However, since the causality of these relationships have limited support from previous studies, alternative models without these variables were also presented. The models based on the mean dose to the total parotid volume and the contralateral parotid alone were very similar.

Conclusion: Late xerostomia after radiotherapy can be modeled with reasonable predictive power based on registry data; models are presented for different endpoints highly relevant in clinical practice. However, the risk of modeling indirect relationships, given the unavoidably heterogeneous registry data, needs to be carefully considered in the interpretation of the results.

Keywords: xerostomia, head and neck cancer, cox regression, nomogram, registry analysis

INTRODUCTION

Radiotherapy contributes to favorable control of disease in the great majority of patients with head and neck cancer (HNC) and will certainly remain one of the prominent integral components in the multidisciplinary management of this disease. Approximately 80% of the patients receive radiotherapy at least once during the course of their disease (1). Even with great advances in radiotherapy planning facilitating a tailored delivery of radiation dose, some damage will be inflicted on normal cells in tissues adjacent to the tumor. The treatment of HNC is associated with clinically significant radiation-induced toxicity, especially in combination with concurrent systemic agents, chemotherapy or biomodulators (2, 3).

One of the most frequently reported side effects is hyposalivation, and subsequent xerostomia, due to co-irradiation of the salivary glands. Chronic xerostomia is a multifactorial process which can affect quality of life profoundly. The process includes reduced salivary output, decreased salivary pH and increased viscosity of the saliva (4, 5). This may result in the unpleasant sensation of dry mouth, altered taste, dysfunction of mastication, swallowing dysfunction and difficulties with speech (6–8). Xerostomia is also associated with changes in the normal flora of the mouth, which increases the risk of oral infections including dental caries (9). The reported prevalence of xerostomia in the normal population ranges from 5.5 to 46% (10). It increases with age, partly due to the frequent use of multiple medications by the elderly (11, 12). In a retrospective study including over 12,000 dental patients, predictors for patient-reported xerostomia were intake of more medications, recreational drug use, rheumatic diseases, psychiatric diseases, eating disorders and radiotherapy (10). Thus, the risk of xerostomia in patients undergoing radiotherapy for HNC is dependent on clinical factors as well as the radiation dose.

The incidence of HNC is currently on the rise as more patients suffer from an HPV-related tumor, predominantly in the oropharynx. These patients have a good prognosis with respect to tumor control and will have to live a long life with potential treatment-related side effects. It is therefore of utmost importance to clarify further the dose/volume-response relationship, also for lower grades of radiation-induced xerostomia. The introduction of new, more conformal, techniques such as intensity-modulated radiotherapy (IMRT) has reduced the rate of xerostomia both with respect to measurement of saliva flow and quality of life. There is a consensus that xerostomia is sufficiently limited by keeping the mean dose to the total parotid volume below 26 Gy as a planning criterion (13). However, as this criterion is frequently violated in order to achieve adequate tumor coverage, the rate of xerostomia in HNC patients is still a concern (14). Also, the relative importance of each parotid gland for preserved salivary function is unclear (15).

Evidence-based radiotherapy requires models which can be used for treatment planning, based on representative datasets. It has been recognized that such models need to be continuously validated and updated (16, 17) as treatment protocols and patient populations evolve (16). For this purpose, registries of outcome data need to be implemented, maintained and analyzed; the limited size of datasets historically used for model fitting, and the homogeneous nature of the data provided by controlled clinical trials, put into question the applicability of these models as decision-support tools in clinical practice. Also, one or a few fixed follow-up times are considered, not considering the risk of toxicity as a function of time. In the current study, Cox regression, where the endpoint is time to event, is used and thus the risk of xerostomia at any time point after treatment can be estimated. To the best of our knowledge, this is the first model of this type developed for xerostomia.

In this registry study, a multivariate model of xerostomia is fitted using clinical-, patient-, and treatment-related parameters in an effort to better predict both more severe but also moderate grades of xerostomia in the individual patient. The real-world nature of the collected data, and the size of the dataset, are favorable for the application of the model as a decision-support tool when treating HNC patients. The risk of modeling indirect relationships, given the unavoidably heterogeneous registry data, is carefully considered in the choice of model, variable selection method and interpretation of the results.

MATERIALS AND METHODS

Quality Registry

Head and neck cancer patients who are treated with radiotherapy at the Karolinska University Hospital, either radically or postoperatively with or without chemotherapy, are followed up after their therapy according to local protocols every third to fourth month during the first 2 years and thereafter every 6 months for an additional 3 years. Since 2013, clinical follow-up data, as well as patient- and treatment-related parameters are entered into a quality-registry database for all patients. A modified Radiation Therapy Oncology Group (RTOG)/LENT-SOMA scale is used for skin-, mucosa-, larynx- and mandible toxicity as well as xerostomia, dysphagia and trismus. Morbidity appearing within 3 months of completed radiotherapy is categorized as acute while morbidity appearing

later is categorized as late. Performance status evaluated according to WHO/ECOG/ZUBROD is also registered at every follow-up visit. Patient-related parameters collected are: gender, age, tumor location, tumor stage, HPV association (for patients with cancer in the oropharynx) and smoking status at the time of treatment. The treatment parameters collected are: data on induction chemotherapy, concomitant drug therapy as well as prescribed dose and organ-at-risk (OAR) dose.

Informed consent regarding participation in the quality registry, including in the publication of analyzed data, is obtained from each patient. The study was approved by the regional ethics committee (2016/268-31/1).

Patients

The patients included in this study had histologically confirmed HNC originating in and categorized as cancer of the oral cavity, oropharynx or other (epipharynx, hypopharynx, nasal cavity, paranasal sinuses or metastases in the neck with an unknown primary). Patients with a tumor location associated with very low parotid dose were excluded (larynx, lip and basalioma) and tumors in the parotid were excluded since these patients can only be considered to have one single parotid as OAR.

None of the included patients had previous head and neck radiotherapy or previous malignancy except non-melanoma skin cancer. Radiotherapy was prescribed curatively, alone or with induction chemotherapy and/or concomitant cisplatin or cetuximab. Cisplatin was prescribed according to the estimated surface area of the patient as follows: 40 mg/m^2 (maximum 70 mg) once weekly, or 80 mg/m^2 (maximum 160 mg) every third week, for the duration of the radiotherapy course. Cetuximab was prescribed with the first dose (400 mg/m^2, maximum 800 mg) one week before the start of radiotherapy and thereafter a weekly dose of 250 mg/m^2 (maximum 500 mg) for the duration of the radiotherapy course, i.e., typically six additional doses. Follow-up data in this study are from January 2014 to October 2018, relating to radiotherapy mainly from 2010 to May 2018, though a few records in the registry relate to even earlier treatments. The compliance in the registration of follow-up data for patients in this study was about 70%, resulting in 753 patients.

Xerostomia was assessed by oncologists specialized in treating HNC. The assessment was based both on visual inspection of the oral cavity and on the description of symptoms described by the patient. The endpoints of this study were late xerostomia of grade 2–4 (moderately dry, completely dry and fibrosis) and grade 3 to 4 late xerostomia (completely dry and fibrosis), respectively; the maximum grade registered for each patient was considered. The two endpoints will hereafter be referred to as $XER_{G\geq2}$ and $XER_{G\geq3}$.

Baseline (before radiotherapy) xerostomia scores were not available in this study. Thus, all endpoints reflect the overall xerostomia status after treatment, not exclusively relating to the treatment.

Treatment

External-beam radiotherapy was delivered with a linear accelerator using 6 MV photons. Twenty-five percent of the patients were treated with a combination of external-beam and brachy radiotherapy. The majority of the external-beam treatments were delivered with IMRT but 7% received 3D-conformal radiotherapy. During treatment planning the parotid glands and larynx were considered the primary OAR followed by swallowing structures; target coverage had the highest priority. Target volumes for primary tumor and regional nodal groups at risk of harboring occult metastatic disease, as well as OAR, were delineated according to departmental guidelines, which also include dose constraints. Specifically, the parotids were delineated as the entire gland as visible in the CT images, including both the deep lobe and the superficial lobe.

Prescribed dose to the primary target volume was; >73 Gy in 12%, 68 Gy in 69%, 66 Gy in 8%, and 50 Gy in 9%. The dose per fraction was 2.2 Gy for the highest dose group and 2.0 Gy for the other groups. Fifty-one percent of the patients were treated with six fractions per week and 45% received five fractions per week. The dose per fraction to elective volumes was 2.0 Gy or 1.52 Gy when treating with a sequential- and simultaneous-integrated boost, respectively.

In this study, the mean dose to ipsilateral- and contralateral parotid glands separately, as well as the mean dose for the two glands together was considered, from the external-beam radiotherapy only. A separate investigation, made on a limited number of patients, showed that the contribution to the parotid mean dose from brachytherapy was negligible for modeling purposes (95%-percentile: 1.5 Gy).

Modeling

Since the time to the registered score varied from patient to patient, multivariate Cox regression models were developed. For each endpoint, the time to event was defined as the interval between the end of radiotherapy and the first score exceeding the respective threshold. Hazard ratios and nomograms were produced for each model. A bootstrap validation with 1000 samples was performed and the mean C-statistic over the bootstrap samples was used as a measure of model performance. Calibration was performed using bootstrap cross validation with 100 bootstrap samples, as described in (18), using Harrell's R packages. All analyses were performed in R.

The candidate explanatory variables were: mean dose to the total parotid volume (D_{tot}), mean dose to the contralateral parotid (D_{contra}), mean dose to the ipsilateral parotid (D_{ipsi}), number of treatment fractions per week, tumor location, T stage, N stage, smoking status, induction chemotherapy, concomitant chemotherapy, gender and age. Two alternative models, based on D_{tot} and D_{contra}, respectively, were considered. This dose variable was forced into the model, irrespective of the univariate significance for the endpoint, and D_{ipsi} was only a candidate variable for the D_{contra} model, to avoid direct dependence between variables. For each model, the candidate variables with $p \leq 0.2$ in a univariate analysis were considered in the multivariate analysis, while an alpha value of 0.05 was used in the multivariate analysis. Categorical variables were considered significant if at least half of the groups passed the alpha value.

Given the lack of register-data analyses available for comparison, and that only internal validation was possible, an alternative selection of variables was made following the

univariate analysis, excluding any variables with no/limited support in the literature with regard to their contribution to the risk of xerostomia. These variables were induction chemotherapy and the number of treatment fractions per week.

RESULTS

Patients

Out of the 753 patients included in the analysis, there were 366 (49%) with grade ≥ 2 late xerostomia and 40 (5.3%) with grade ≥3 late xerostomia. The median follow-up was 363 days and 292 days for $XER_{G\geq2}$ and $XER_{G\geq3}$ respectively. **Table 1** lists the descriptive statistics.

TABLE 1 | Patient- and treatment characteristics.

	Patients	%
Mean parotid dose		
D_{tot} (Gy); mean (SD)	26.2 (8.2)	
D_{contra} (Gy); mean (SD)	17.7 (7.2)	
D_{ipsi} (Gy); mean (SD)	34.8 (13)	
Fractions per week		
5	294	39
6	437	58
10	22	2.9
Age (years); mean (SD)	61.4 (11.4)	
Gender		
Female	249	33
Male	504	67
Tumor location		
Oral cavity	172	23
Oropharynx	443	59
Other	138	18
T stage		
0	40	5.3
1	174	23
2	289	38
3	108	14
4	142	19
N stage		
0	252	34
1	85	11
2a/b	348	46
2c	61	8.1
3	7	0.9
Smoking		
No/never	299	40
Smoker	152	20
Previous	302	40
Concomitant chemotherapy		
Cisplatin	254	34
ERBIT	206	27
No	293	39
Induction chemotherapy		
Yes	203	27
No	550	73

Univariate Analysis

The results from the univariate analysis (hazard ratios and *p*-values) are listed in **Supplementary Table A1** in the **Supplementary Material**, where the variables considered in the multivariate analysis are highlighted in bold. The main dose variable (D_{tot} or D_{contra}) did not consistently obtain low *p*-values but according to the chosen model selection strategy, this variable was still included in the multivariate model. More variables were significant for grade ≥2 xerostomia than for ≥3 xerostomia. This might be due to the fewer events of high-grade xerostomia in the population.

Radiotherapy technique (3D-conformal vs. IMRT) was not considered as an explanatory variable since any effect would be indirect, through cross-correlation with the volume of exposed parotid. However, it's association with xerostomia was nonetheless tested in the univariate analysis. Surprisingly, as seen in **Supplementary Table A1**, the risk of xerostomia was significantly reduced in the small group of patients with 3D-conformal radiotherapy; these patients were typically treated for unilateral targets and received a lower target dose, as well as a lower D_{tot}.

Multivariate Analysis

Two multivariate models were fitted to each endpoint, one based on D_{tot} and one on D_{contra}; in a second step the models were refitted to only the variables associated with $p < 0.05$ in the initial multivariate model – see **Table 2**. The models are well calibrated – see calibration plots in **Figure 1**.

$XER_{G\geq3}$ showed a positive dependence on dose, as opposed to $XER_{G\geq2}$, and the performance of this model was better. The dose variable was not statistically significant in all models but many non-dosimetric variables were significant, especially in the models for $XER_{G\geq2}$. The models based on D_{tot} and D_{contra} were very similar.

Given the explorative nature of the above analysis, an alternative variable selection method was also applied for the multivariate analysis by excluding any non-consensus variables. While in **Table 2** the models revealed a lower risk of $XER_{G\geq2}$ for patients with an accelerated treatment schedule and induction chemotherapy, the causality in these relationships might be controversial. Thus, the $XER_{G\geq2}$ models were refitted, excluding the number of fractions per week and induction chemotherapy – see **Table 3**. As two variables were excluded the performance of the models reduced somewhat. The calibration plots are shown in **Figure 2**.

Since the models for $XER_{G\geq2}$ had an inverse dose-response these are not suitable as decision support tools. Instead, **Figure 3** shows a nomogram where dose was not forced into the model (for model specifics and the calibration plot, see **Supplementary Table A2** and **Supplementary Figure A1** in the **Supplementary Material**). **Figure 4** shows the nomogram for $XER_{G\geq3}$ corresponding to the model listed in **Table 2**. Please refer to the **Supplementary Material** for an example of how to read the nomograms.

TABLE 2 | Hazard ratios and corresponding *p*-values (in brackets) for the Cox regression multivariate analysis.

Endpoint	Included variables	Hazard ratio (*p*-value)	
		Model: D_{tot}	**Model: D_{contra}**
$XER_{G\geq2}$	Mean parotid dose (D_{tot} or D_{contra})	0.98 (0.033)	1.004 (0.65)
	D_{ipsi}	–	0.99 (<0.01)
	Fractions per week; reference = 5		
	6	1.02 (0.86)	0.997 (0.99)
	10	0.33 (<0.01)	0.32 (<0.01)
	Tumor location; reference = oral cavity		
	Oropharynx	1.12 (0.50)	1.14 (0.44)
	Other	0.60 (<0.01)	0.62 (0.016)
	N stage; reference = 2c		
	0	0.45 (<0.01)	0.50 (<0.01)
	1	0.43 (<0.01)	0.49 (<0.01)
	2a/b	0.59 (<0.01)	0.65 (0.017)
	3	0.24 (0.018)	0.27 (0.031)
	Concomitant chemotherapy; reference = no		
	Cisplatin	1.73 (<0.01)	1.66 (<0.01)
	Erbitux	1.37 (0.50)	1.32 (0.088)
	Induction chemotherapy; reference = no		
	Yes	0.62 (<0.01)	0.62 (<0.01)
	Age	1.01 (0.023)	1.011 (0.023)
	C-statistic (SE)	**0.64 (0.057)**	**0.64 (0.057)**
$XER_{G\geq3}$	Mean parotid dose (D_{tot} or D_{contra})	1.01 (0.054)	1.02 (0.26)
	Concomitant chemotherapy; reference = no		
	Cisplatin	2.57 (0.012)	2.46 (0.017)
	Erbitux	0.96 (0.94)	0.92 (0.87)
	Age	1.06 (<0.01)	1.06 (<0.01)
	C-statistic (SE)	**0.67 (0.017)**	**0.68 (0.017)**

The xerostomia endpoints were grade ≥ 2 ($XER_{G\geq2}$) and grade ≥ 3 ($XER_{G\geq3}$). The bootstrap-validation C-statistic is listed below the included variables.

DISCUSSION

While the rate of xerostomia is reduced by sparing the parotid glands, a probable contributor to persistent xerostomia could be radiation-induced damage to other salivary glands such as the submandibular glands, sublingual glands and minor salivary glands in the oral cavity. Studies have shown a correlation between the dose to submandibular glands and sticky saliva (19). Some studies have also demonstrated that in selected patients it is safe to try to spare the submandibular glands with IMRT; however, this approach should be used with caution in patients with a significant risk of recurrence, relating to tumor location (20). The impact on xerostomia from minor salivary glands in the oral cavity and oropharynx is difficult to study because of their anatomical dispersion and their poor anatomical definition in the planning image. Data are conflicting regarding the benefit of reducing the dose to these glands (19, 21) but delineation of the oral cavity as an OAR with respect to xerostomia has been recommended in some institutions. In the present analysis, the only OAR considered was the parotid gland since other salivary glands had not been consistently delineated and the corresponding dose is not recorded in the registry. Also, the series of studies by Beetz et al. (19, 22, 23) suggest that the parotid is the main OAR for xerostomia (although using a slightly different definition compared to the present study), by showing that only the dose to the parotids, among the different salivary glands, was a significant predictor of patient-rated xerostomia.

The dose to the *contralateral* parotid has been studied as a predictor for patient-rated xerostomia (19) and salivary function is largely preserved if at least one parotid receives less than 25 Gy of mean dose (24). Still, there seems to be a benefit of limiting the dose to both parotids (25). Given the uncertainty of the definition of the OAR, both the total parotid volume and the contralateral parotid volume were considered, in different models. These models were very similar but applying the model for the contralateral parotid only, to optimize treatment plans, could be expected to lead to an increase in *ipsilateral* parotid dose. Such a strategy is not supported by the current study; all patient plans were optimized to spare both parotids as much as the target coverage allowed.

Baseline xerostomia is not uncommon in HNC patients and is predictive of xerostomia after radiotherapy (19, 26). Therefore, patients with baseline xerostomia are often excluded from studies of purely radiation-induced xerostomia. In contrast, the aim of the current study was to develop a model based on real-world data, predicting the risk of xerostomia for the greater population of HNC patients receiving radiotherapy. Therefore, it was not considered appropriate to exclude patients with baseline xerostomia. Baseline scores were also not available for all patients as this assessment has only recently been included in the registry. In future analyses, baseline xerostomia will be considered as a variable in the model. Notably, older age was highly significant in all models, likely as a surrogate for baseline xerostomia, as this is related to age in general and increased medication in particular (8).

Xerostomia is typically assessed by direct measurement of salivary-flow rate, by self-reported questionnaires or by scoring methods, as in the present study. Salivary-flow rates provide important information about salivary gland function and can be performed from each major gland or from a mixed sample of the oral fluids, often termed whole saliva. However, xerostomia is experienced differently by individuals (14) and is not identical to hyposalivation since it also depends on changes in the quality of saliva even with unchanged salivary-flow rate. Therefore patients may complain of dry mouth despite adequate salivation (27). In the current study, the oncologists perceived grade-2 xerostomia (moderately dry) to be less specific than grade 3 and 4 (completely dry and fibrosis, respectively). This may have

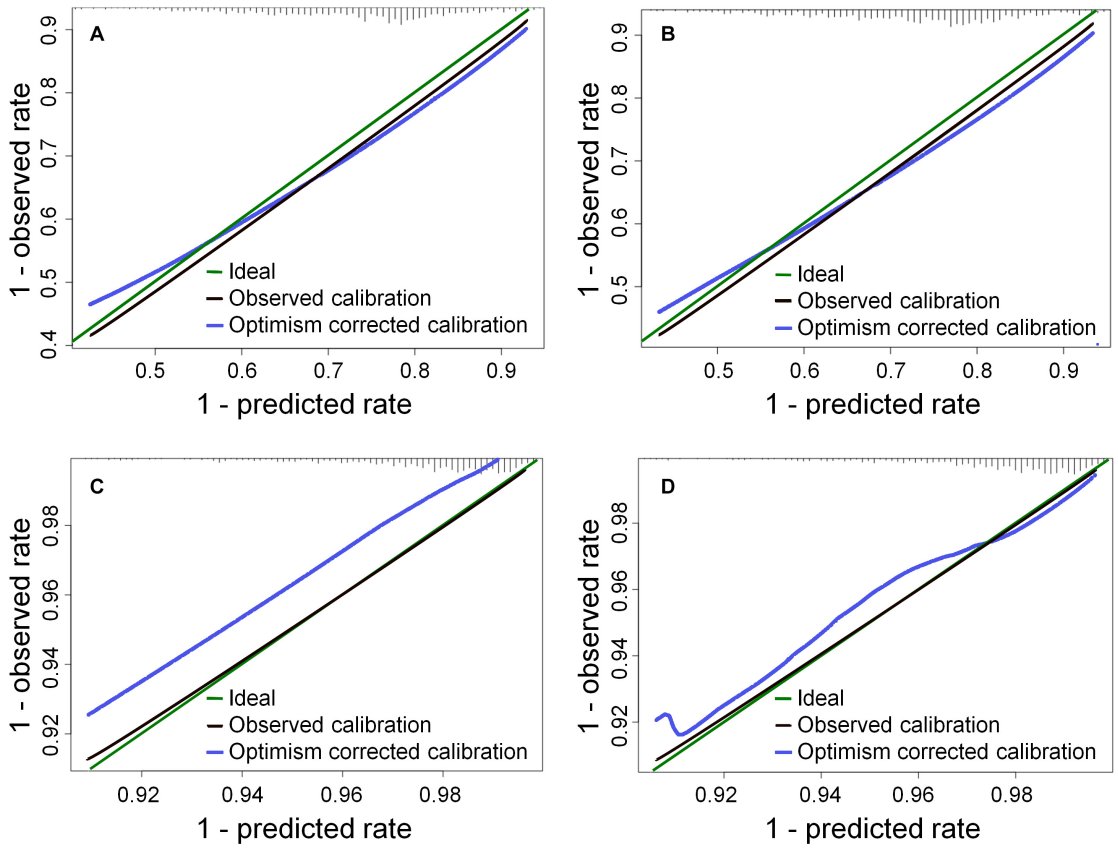

FIGURE 1 | Calibration plots for the models in **Table 2** at 1 year: **(A)** the D_{tot} model for $XER_{G\geq2}$, **(B)** the D_{contra} model for $XER_{G\geq2}$, **(C)** the D_{tot} model for $XER_{G\geq3}$, **(D)** the D_{contra} model for $XER_{G\geq3}$. The histogram on the upper × axis represents the frequency distribution of 1 minus the predicted probabilities (c.f. a survival analysis).

contributed to the lower predictive power of the low-grade models; predictions made using the high-grade models are more reliable. However, since grade ≥2 xerostomia is problematic for the patients and relatively prevalent it is important to avoid also grade 2, if possible.

Another factor possibly contributing to the modest predictive power of the models is the variability in the time between radiotherapy and registered follow-up in the cohort. While focusing on a fixed time after treatment was not possible for our data set, this might have improved the performance of the model since there is a time dependence of incidence of xerostomia after treatment (15). As future work we plan to fit a model to a subset of the patients with follow-up data in a limited time interval. As well as revealing the importance of the follow-up time, this will also facilitate comparisons with studies using a fixed follow-up time. Future work will also explore the significance of HPV status for the risk of xerostomia after radiotherapy. Further, the predictive power may have been limited by the omission of HPV status, the patient-specific chemotherapy dose and alcohol consumption as explanatory variables; the two latter variables were not recorded in the registry and were not available for analysis.

IMRT has been shown to be associated with a lower incidence of severe xerostomia compared to 3D-conformal radiotherapy (14). Still, treatment with IMRT was not selected as an inclusion criterion in the current study since any relationship is expected to be indirect, through its impact on the mean parotid dose. Moreover, it was found that it would have made a very small difference to the model if non-IMRT patients had been excluded. Only age was not included in the $XER_{G\geq2}$ models; for all other variables, hazard ratios and *p*-values remained similar to those in the presented models. The value of the C statistic reflected a lower model performance when limiting the size of the cohort accordingly.

The *physical* mean parotid dose was used in this study, i.e., without correcting for fraction size per voxel or different fractionation schedules, since dose-volume histograms were not available for conversion to BED. The sensitivity of the results to this limitation was explored by converting the mean dose values to BED; this differs from the actual mean BED by around 1–15% (according to a comparison for a limited number of patients) since each dose bin was not converted before calculating the mean. It was seen, however, that while the predictive power of the models did not consistently improve they were somewhat sensitive to the representation of dose. Future work is planned to collect dose-volume histograms and refit the model with the dose variables in BED. Other sources of uncertainty in the dose variables are, as mentioned previously, that the small contribution from brachytherapy for 25% of the

TABLE 3 | Hazard ratios and corresponding *p*-values (in brackets) for the Cox regression multivariate analysis excluding non-consensus variables for the $XER_{G\geq2}$ models.

Endpoint	Included variables	Hazard ratio (*p*-value)	
		Model: D_{tot}	**Model: D_{contra}**
$XER_{G\geq2}$	Mean parotid dose (D_{tot} or D_{contra})	0.98 (<0.01)	0.997 (0.68)
	D_{ipsi}	–	0.99 (<0.01)
	Tumor location; reference = oral cavity		
	Oropharynx	1.07 (0.67)	1.07 (0.67)
	Other	0.57 (<0.01)	0.58 (<0.01)
	N stage; reference = 2c		
	0	0.58 (<0.01)	0.62 (0.020)
	1	0.57 (0.014)	0.61 (0.042)
	2a/b	0.69 (0.027)	0.73 (0.080)
	3	0.31 (0.052)	0.33 (0.067)
	Concomitant chemotherapy; reference = no		
	Cisplatin	2.02 (<0.01)	1.98 (<0.01)
	Erbitux	1.46 (0.011)	1.42 (0.019)
	Age	1.02 (<0.01)	1.02 (<0.01)
	C-statistic (SE)	**0.60 (0.057)**	**0.60 (0.057)**

The bootstrap-validation C-statistic is listed below the included variables.

patients was ignored, but also the difference between planned and delivered dose. It has been shown that the actual mean dose to the parotids can increase by 10% or more compared to the planned dose, due to a gradual migration of the gland toward the high-dose volume over the course of treatment (28, 29). Furthermore, the identification of the parotid tissue in the CT images can be difficult, resulting in an uncertainty even in the planned dose.

The registry includes follow-up data for about 70% of the HNC patients treated with radiotherapy. However, since the missing data is mainly explained by a logistical failing in the data collection, patients were likely excluded without bias and thus the lack of full compliance should have a negligible impact on the results.

The fact that the current study included a large number of patients treated consecutively in our institution made it possible to develop a model more representative for the population it will be applied to, compared to models from controlled clinical trials. The diversity naturally occurring in the population is present in the sample and many relevant variables were candidates for inclusion in the models. By using Cox regression the time factor in the follow-up data was naturally accounted for and the risk of xerostomia can be predicted for different times after treatment. However, as a result of the inherent diversity in the dataset, it was found that the fitted model was very sensitive to small adjustments to the patients included in the analysis, despite the great size of the dataset. It was of particular interest to study the risk of xerostomia as a function of OAR dose, but these relationships were relatively weak, and in the case of grade ≥2 xerostomia an *inverse* dose-response relationship was found. The latter was unexpected but probably a result of indirect correlations or bias, which are more likely to appear in a dataset from a registry compared to a clinical trial. In line with our results, there are some indications that when patients have been treated with IMRT, resulting in lower parotid dose and steeper dose gradients compared to 3D-conformal radiotherapy, the strong association between xerostomia and mean parotid dose observed historically (22, 30) can be expected to be weaker or completely absent (31, 32). In the current analysis, the inverse dose-response found when forcing the dose variable into the multivariate models for $XER_{G\geq2}$ made the model unsuitable as a decision support tool and a nomogram was instead produced for a model which did not contain dose. Thus, unlike the nomogram for $XER_{G\geq3}$, this cannot be used to guide radiotherapy treatment planning but is nonetheless useful for managing the risk of moderate xerostomia.

Models developed based on real-world data are a valuable complement to controlled clinical trials and are particularly suitable as decision-support tools in a learning healthcare system (16). The analysis of registry data needs to be performed carefully, taking advantage of the heterogeneity of the population while

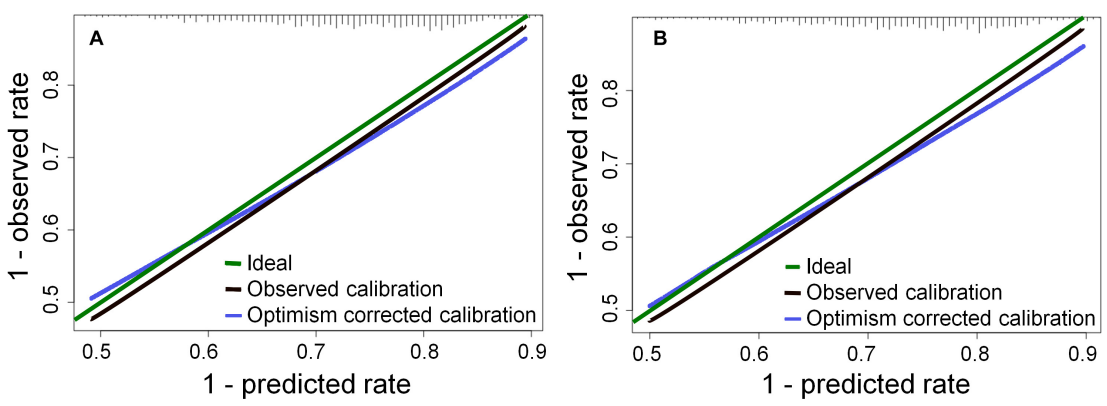

FIGURE 2 | Calibration plots for the models in **Table 3** at 1 year: **(A)** the D_{tot} model for $XER_{G\geq2}$, **(B)** the D_{contra} model for $XER_{G\geq2}$, The histogram on the upper × axis represents the frequency distribution of 1 minus the predicted probabilities (c.f. a survival analysis).

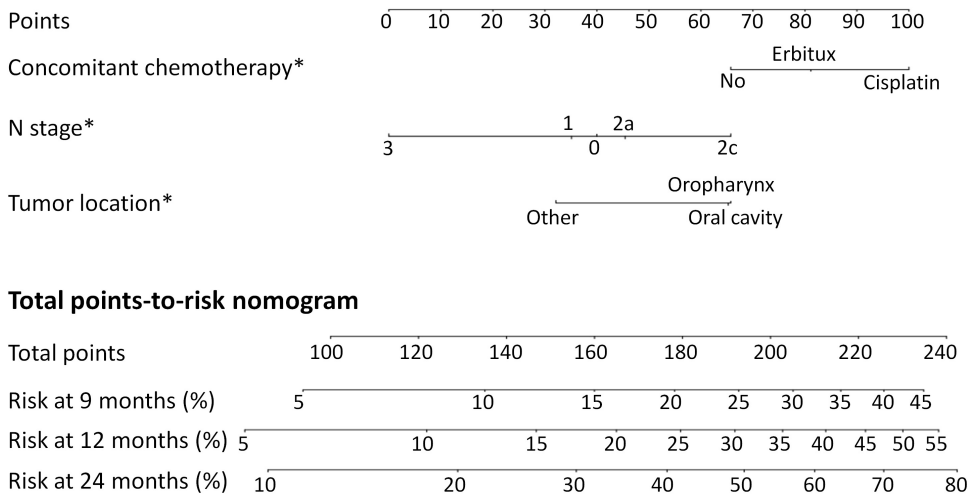

FIGURE 3 | The predicted risk of grade ≥2 xerostomia at 9, 12, and 24 months after radiotherapy, not including dose, due to the inverse dose-response relationship. Model specifics are listed in **Supplementary Table A2** in the **Supplementary Material**. *Note that the model does not imply significant differences between all categories with respect to the endpoint – the *p*-value only refers to the difference from the reference category (see **Supplementary Table A2** for *p*-values). "No" was reference for concomitant chemotherapy and Erbitux was not significantly different from the reference. "N2c" was reference for N stage and N3 was not statistically different. Note that the model does not establish whether there is a difference between N0 and N1. "Oral cavity" was reference for tumor location and oropharynx was not statistically different.

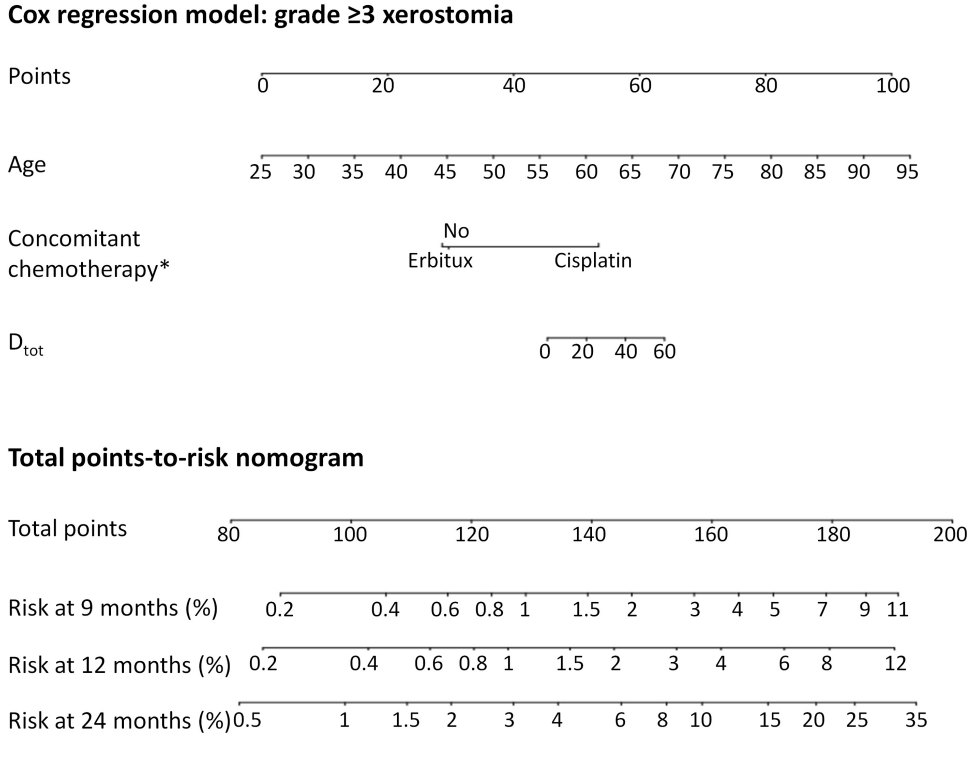

FIGURE 4 | The predicted risk of grade ≥3 xerostomia at 9, 12, and 24 months after radiotherapy, using the D_{tot} dose variable. *Note that not all categories are significantly different from each other with respect to the endpoint – the *p*-value only refers to the difference from the reference category (see **Table 2** for *p*-values). **"**No**"** was reference for concomitant chemotherapy and Erbitux was not significantly different.

selecting endpoints, variables and variable parameterization to obtain a useful model. For example, 2c was selected as reference for N stage since it was discovered that this disease stage was associated with a higher risk of xerostomia, even compared to stage 3 (although the prediction for stage 3 could be uncertain, given the few cases included in the dataset and that N3 was not statistically different from N2c as shown by the *p*-value in **Supplementary Table A2**). It was speculated that this is related to the bilateral location of involved lymph nodes with N2c. It is also important to not overinterpret the nomogram and assume that all aspects are statistically significant. For example, the model behind the nomogram in **Figure 3** does not establish the relationship between N0 and N1, only each category's difference from the reference category, N2c. There is no reason to suppose that N0 implies a higher risk compared to N1, and the small difference seen in the nomogram is unlikely to result in misleading predictions.

If the model is developed to improve future treatment plans it is important to consider possible mechanisms behind observed relationships, i.e., causality. In the current analysis it was felt that external validation would be required to confirm the lower risk associated with hyperfractionated/accelerated treatment schedules and induction chemotherapy, to rule out false correlations. The only support in the literature for the former is weak given the few patients studied and limited dose-volume information (33). It is hoped that future studies can confirm or dement the causality of these relationships.

CONCLUSION

Late xerostomia after radiotherapy can be modeled with reasonable predictive power based on registry data, providing valuable alternatives to models developed on cohorts with stricter inclusion criteria. Similarities with similar models were observed but as the first Cox regression model for xerostomia, some important lessons were learned. The variables included and the performance of the model depend strongly on the grade of the endpoint, the patient selection and the candidate variables considered. The role of the parotid dose may be of lower importance compared to some clinical variables in a heterogeneous population. The results also suggest that an accelerated treatment schedule or induction chemotherapy may be associated with a lower risk of xerostomia, but until this has been confirmed a model excluding these variables can be used. The risk of modeling indirect relationships, given the unavoidably heterogeneous registry data, needs to be carefully considered in the interpretation of the results.

DATA AVAILABILITY STATEMENT

The datasets generated for this study will not be made publicly available. The patients participating in the study have not consented to their data being publicly available.

ETHICS STATEMENT

The studies involving human participants were reviewed and approved by the Stockholm Regional Ethics Committee. The patients/participants provided their written informed consent to participate in this study.

AUTHOR CONTRIBUTIONS

EO, IL, and CM contributed to the conception and design of the study and interpreted the results together with EB and AE. AB was also involved in the design and interpretation of the statistical methodology and performed the analysis. CM, EB, AE, GA, SF, CL, and HS contributed to the data collection and IL to the registry design and management. GG and SF facilitated the development of the registry and advised on the scientific contents of the study. EO compiled and presented the results. The manuscript was written by EO, IL, and CM. All authors reviewed and approved the manuscript.

FUNDING

This study was partly funded by a grant (number 164082) from the King Gustaf V Jubilee Fund (Stockholm, Sweden).

ACKNOWLEDGMENTS

The authors are grateful to Dr. Tiziana Rancati (Fondazione IRCCS Istituto Nazionale dei Tumori, Milan, Italy) for her advice on outcome modeling techniques.

SUPPLEMENTARY MATERIAL

The Supplementary Material for this article can be found online at: https://www.frontiersin.org/articles/10.3389/fonc.2020.01647/full#supplementary-material

REFERENCES

1. Borras JM, Barton M, Grau C, Corral J, Verhoeven R, Lemmens V, et al. The impact of cancer incidence and stage on optimal utilization of radiotherapy: methodology of a population based analysis by the ESTRO-HERO project. *Radiother Oncol.* (2015) 116:45–50. doi: 10.1016/j.radonc.2015.04.021
2. Barnett GC, West CM, Dunning AM, Elliott RM, Coles CE, Pharoah PD, et al. Normal tissue reactions to radiotherapy: towards tailoring treatment dose by genotype. *Nat Rev Cancer.* (2009) 9:134–42.
3. Langendijk JA, Doornaert P, Verdonck-de Leeuw IM, Leemans CR, Aaronson NK, Slotman BJ. Impact of late treatment-related toxicity on quality of life among patients with head and neck cancer treated with radiotherapy. *J Clin Oncol.* (2008) 26:3770–6.

4. Dirix P, Nuyts S. Evidence-based organ-sparing radiotherapy in head and neck cancer. *Lancet Oncol.* (2010) 11:85–91. doi: 10.1016/s1470-2045(09)70231-1
5. Dirix P, Nuyts S, Van den Bogaert W. Radiation-induced xerostomia in patients with head and neck cancer: a literature review. *Cancer.* (2006) 107:2525–34.
6. Hamlet S, Faull J, Klein B, Aref A, Fontanesi J, Stachler R, et al. Mastication and swallowing in patients with postirradiation xerostomia. *Int J Radiat Oncol Biol Phys.* (1997) 37:789–96.
7. Logemann JA, Pauloski BR, Rademaker AW, Lazarus CL, Mittal B, Gaziano J, et al. Xerostomia: 12-month changes in saliva production and its relationship to perception and performance of swallow function, oral intake, and diet after chemoradiation. *Head Neck.* (2003) 25:432–7.
8. Roh JL, Kim AY, Cho MJ. Xerostomia following radiotherapy of the head and neck affects vocal function. *J Clin Oncol.* (2005) 23:3016–23.
9. Epstein JB, Chin EA, Jacobson JJ, Rishiraj B, Le N. The relationships among fluoride, cariogenic oral flora, and salivary flow rate during radiation therapy. *Oral Surg Oral Med Oral Pathol Oral Radiol Endod.* (1998) 86:286–92.
10. Villa A, Nordio F, Gohel A. A risk prediction model for xerostomia: a retrospective cohort study. *Gerodontology.* (2016) 33:562–8.
11. Astor FC, Hanft KL, Ciocon JO. Xerostomia: a prevalent condition in the elderly. *Ear Nose Throat J.* (1999) 78:476–9.
12. Thorselius I, Emilson CG, Osterberg T. Salivary conditions and drug consumption in older age groups of elderly Swedish individuals. *Gerodontics.* (1988) 4:66–70.
13. Chambers MS, Garden AS, Rosenthal D, Ahamad A, Schwartz DL, Blanco AI, et al. Intensity-modulated radiotherapy: is xerostomia still prevalent? *Curr Oncol Rep.* (2005) 7:131–6.
14. Nutting CM, Morden JP, Harrington KJ, Urbano TG, Bhide SA, Clark C, et al. Parotid-sparing intensity modulated versus conventional radiotherapy in head and neck cancer (PARSPORT): a phase 3 multicentre randomised controlled trial. *Lancet Oncol.* (2011) 12:127–36.
15. Brodin NP, Tome WA. Revisiting the dose constraints for head and neck OARs in the current era of IMRT. *Oral Oncol.* (2018) 86:8–18. doi: 10.1016/j.oraloncology.2018.08.018
16. Nakatsugawa M, Cheng Z, Kiess A, Choflet A, Bowers M, Utsunomiya K, et al. The needs and benefits of continuous model updates on the accuracy of rt-induced toxicity prediction models within a learning health system. *Int J Radiat Oncol Biol Phys.* (2019) 103:460–7.
17. van der Schaaf A, Langendijk JA, Fiorino C, Rancati T. Embracing phenomenological approaches to normal tissue complication probability modeling: a question of method. *Int J Radiat Oncol Biol Phys.* (2015) 91:468–71.
18. Frank E, Harrell J. *Regression Modeling Strategies, With Applications to Linear Models, Logistic and Ordinal Regression, and Survival Analysis*. 2 ed. New York, NY: Springer Science+Business Media (2015).
19. Beetz I, Schilstra C, van der Schaaf A, van den Heuvel ER, Doornaert P, van Luijk P, et al. NTCP models for patient-rated xerostomia and sticky saliva after treatment with intensity modulated radiotherapy for head and neck cancer: the role of dosimetric and clinical factors. *Radiother Oncol.* (2012) 105:101–6.
20. Jang JW, Parambi RJ, Liliana LS, Liebsch NJ, Chan AW. Intensity Modulated radiation therapy and level 1B nodal coverage for oropharyngeal carcinoma. *Int J Radiat Oncol.* (2012) 84:S22–3.
21. Hawkins PG, Lee JY, Mao YP, Li P, Green M, Worden FP, et al. Sparing all salivary glands with IMRT for head and neck cancer: Longitudinal study of patient-reported xerostomia and head-and-neck quality of life. *Radiother Oncol.* (2018) 126:68–74. doi: 10.1016/j.radonc.2017.08.002
22. Beetz I, Schilstra C, Burlage FR, Koken PW, Doornaert P, Bijl HP, et al. Development of NTCP models for head and neck cancer patients treated with three-dimensional conformal radiotherapy for xerostomia and sticky saliva: the role of dosimetric and clinical factors. *Radiother Oncol.* (2012) 105:86–93. doi: 10.1016/j.radonc.2011.05.010
23. Beetz I, Schilstra C, van Luijk P, Christianen ME, Doornaert P, Bijl HP, et al. External validation of three dimensional conformal radiotherapy based NTCP models for patient-rated xerostomia and sticky saliva among patients treated with intensity modulated radiotherapy. *Radiother Oncol.* (2012) 105:94–100. doi: 10.1016/j.radonc.2011.11.006
24. Blanco AI, Chao KS, El Naqa I, Franklin GE, Zakarian K, Vicic M, et al. Dose-volume modeling of salivary function in patients with head-and-neck cancer receiving radiotherapy. *Int J Radiat Oncol Biol Phys.* (2005) 62:1055–69.
25. Deasy JO, Moiseenko V, Marks L, Chao KS, Nam J, Eisbruch A. Radiotherapy dose-volume effects on salivary gland function. *Int J Radiat Oncol Biol Phys.* (2010) 76(Suppl. 3):S58–63.
26. Eneroth CM, Henrikson CO, Jakobsson PA. Pre-irradiation qualities of a parotid gland predicting the grade of functional disturbance by radiotherapy. *Acta Otolaryngol.* (1972) 74:436–44.
27. Ship JA, Fox PC, Baum BJ. How much saliva is enough–normal function defined. *J Am Dental Associat.* (1991) 122:63–9.
28. Lee C, Langen KM, Lu WG, Haimerl J, Schnarr E, Ruchala KJ, et al. Assessment of parotid gland dose changes during head and neck cancer radiotherapy using daily megavoltage computed tomography and deformable image registration. *Int J Radiat Oncol.* (2008) 71:1563–71.
29. Wu QW, Chi YW, Chen PY, Krauss DJ, Yan D, Martinez A. Adaptive replanning strategies accounting for shrinkage in head and neck imrt. *Int J Radiat Oncol.* (2009) 75:924–32.
30. Jellema AP, Doornaert P, Slotman BJ, Leemans CR, Langendijk JA. Does radiation dose to the salivary glands and oral cavity predict patient-rated xerostomia and sticky saliva in head and neck cancer patients treated with curative radiotherapy? *Radiother Oncol.* (2005) 77:164–71.
31. Gabrys HS, Buettner F, Sterzing F, Hauswald H, Bangert M. Design and selection of machine learning methods using radiomics and dosiomics for normal tissue complication probability modeling of xerostomia. *Front Oncol.* (2018) 8:35.
32. Kaae JK, Johnsen L, Hansen CR, Kristensen MH, Brink C, Eriksen JG. Relationship between patient and physician-rated xerostomia and dose distribution to the oral cavity and salivary glands for head and neck cancer patients after radiotherapy. *Acta Oncol.* (2019) 58:1366–72.
33. Leslie MD, Dische S. Parotid gland function following accelerated and conventionally fractionated radiotherapy. *Radiother Oncol.* (1991) 22:133–9.

Conflict of Interest: The authors declare that the research was conducted in the absence of any commercial or financial relationships that could be construed as a potential conflict of interest.

frontiers in Oncology

ORIGINAL RESEARCH
published: 11 September 2020
doi: 10.3389/fonc.2020.01597

Planning With Patient-Specific Rectal Sub-Region Constraints Decreases Probability of Toxicity in Prostate Cancer Radiotherapy

Caroline Lafond, Anaïs Barateau, Joël N'Guessan, Nicolas Perichon, Nolwenn Delaby, Antoine Simon, Pascal Haigron, Eugenia Mylona, Oscar Acosta and Renaud de Crevoisier*

Univ Rennes, CLCC Eugène Marquis, INSERM, LTSI - UMR 1099, Rennes, France

Background: A rectal sub-region (SRR) has been previously identified by voxel-wise analysis in the inferior-anterior part of the rectum as highly predictive of rectal bleeding (RB) in prostate cancer radiotherapy. Translating the SRR to patient-specific radiotherapy planning is challenging as new constraints have to be defined. A recent geometry-based model proposed to optimize the planning by determining the achievable mean doses (AMDs) to the organs at risk (OARs), taking into account the overlap between the planning target volume (PTV) and OAR. The aim of this study was to quantify the SRR dose sparing by using the AMD model in the planning, while preserving the dose to the prostate.

Material and Methods: Three-dimensional volumetric modulated arc therapy (VMAT) planning dose distributions for 60 patients were computed following four different strategies, delivering 78 Gy to the prostate, while meeting the genitourinary group dose constraints to the OAR: (i) a standard plan corresponding to the standard practice for rectum sparing (STD_{pl}), (ii) a plan adding constraints to SRR (SRR_{pl}), (iii) a plan using the AMD model applied to the rectum only (AMD_RECT_{pl}), and (iv) a final plan using the AMD model applied to both the rectum and the SRR ($AMD\_RECT\_SRR_{pl}$). After PTV dose normalization, plans were compared with regard to dose distributions, quality, and estimated risk of RB using a normal tissue complication probability model.

Results: $AMD\_RECT\_SRR_{pl}$ showed the largest SRR dose sparing, with significant mean dose reductions of 7.7, 3, and 2.3 Gy, with respect to the STD_{pl}, SRR_{pl}, and AMD_RECT_{pl}, respectively. $AMD\_RECT\_SRR_{pl}$ also decreased the mean rectal dose by 3.6 Gy relative to STD_{pl} and by 3.3 Gy relative to SRR_{pl}. The absolute risk of grade $\geq$1 RB decreased from 22.8% using STD_{pl} planning to 17.6% using $AMD\_RECT\_SRR_{pl}$ considering SRR volume. $AMD\_RECT\_SRR_{pl}$ plans, however, showed slightly less dose homogeneity and significant increase of the number of monitor units, compared to the three other strategies.

Conclusion: Compared to a standard prostate planning, applying dose constraints to a patient-specific SRR by using the achievable mean dose model decreased the mean dose by 7.7 Gy to the SRR and may decrease the relative risk of RB by 22%.

Keywords: prostate cancer radiotherapy, rectal bleeding, toxicity, plan optimization, organ-at-risk sparing, voxel-wise analysis

OPEN ACCESS

Edited by:
Tiziana Rancati, Istituto Nazionale dei Tumori (IRCCS), Italy

Reviewed by:
Michele Avanzo, Centro di Riferimento Oncologico di Aviano (IRCCS), Italy
Sarah O. S. Osman, Queen's University Belfast, United Kingdom
Leila Evelyn Aitken Shelley, Western General Hospital, United Kingdom

****Correspondence:***
Oscar Acosta
oscar.acosta@univ-rennes1.fr

Specialty section:
This article was submitted to Radiation Oncology, a section of the journal Frontiers in Oncology

Received: *16 January 2020*
Accepted: *23 July 2020*
Published: *11 September 2020*

Citation:
Lafond C, Barateau A, N'Guessan J, Perichon N, Delaby N, Simon A, Haigron P, Mylona E, Acosta O and de Crevoisier R (2020) Planning With Patient-Specific Rectal Sub-Region Constraints Decreases Probability of Toxicity in Prostate Cancer Radiotherapy. Front. Oncol. 10:1597. doi: 10.3389/fonc.2020.01597

INTRODUCTION

Rectal toxicity is one of the main side effects arising when treating prostate cancer with radiotherapy. Five-year grade ≥1 and ≥2 rectal bleeding (RB) rates have been reported to be around 30 and 10%, respectively, when combining intensity-modulated radiation therapy (IMRT) with image-guided radiotherapy (IGRT) (1, 2). Several strategies may be implemented in order to spare the rectum and therefore decrease toxicity. For instance, by increasing mechanically the anterior perirectal space, using hydrogel spacer, has been shown to significantly reduce rectal irradiation (3–5). Such an approach is, however, invasive and expensive. A more appealing approach, in the context of dose escalation, would be to intervene at the planning step by adding dosimetric constraints to particular portions of the rectum which may be highly radiosensitive. This requires, however, a robust technique for identifying patient-specific rectal sub-regions (SRR) that should be spared in the treatment planning.

In response to this question, voxel-based methods have already been applied for unveiling spatially variable dose–effect patterns, thereby allowing the identification of sub-regions at risk in several anatomical locations such as the lungs (6), the heart (7), head and neck (H&N) (8), and the bladder (9). Overall, the principles of voxel-based methods rely on the analysis of the local dose–toxicity relationship at fine spatial scales, through (i) non-rigid registration (8), (ii) dose resampling to a common space, and (iii) voxel-wise comparisons between patients with and without toxicity (10, 11). The methodology and pitfalls of voxel-wise analysis are discussed in detail in (12). With respect to rectal toxicity in case of prostate IMRT, a sub-region in the inferoanterior hemianorectum, which will be considered in this study as SRR, was identified by voxel-based analysis as highly predictive of RB (10).

Once a sub-region is identified as predictive for toxicity, the addition of dosimetric constraints to be applied during the planning is, however, challenging. There are no specific recommendations on dose optimization for these original sub-regions as they can be considered as independent structures at risk. A possible strategy to solve this issue is the application of the model proposed by Moore et al. (13) aimed to determine, at the inverse planning step, an achievable mean dose (AMD) in the organs at risk (OARs). Indeed, they showed that, compared to standard dose volume constraints, the mean dose in various OARs could be decreased by using a geometry-based population model relying on volume overlap between the planning target volume (PTV) and OAR. The concept of AMD can be extended to a specific sub-region to be spared (instead of considering the whole OAR) while preserving target coverage.

In the case of prostate cancer IMRT/IGRT, the objectives of this study were to compare four inverse planning strategies: (i) a standard planning (STD_{pl}); (ii) a planning with specific SRR constraints without using the AMD model (SRR_{pl}); (iii) a strategy using the AMD model applied only to the rectum (AMD_RECT_{pl}); (iv) a combined strategy using the AMD model applied to both the rectum and the SRR ($AMD\_RECT\_SRR_{pl}$). The comparisons were performed via dosimetric, planning quality parameters, and a normal tissue complication probability (NTCP) model. The workflow of the study is depicted in **Figure 1**.

METHODS AND MATERIALS

A total of 60 patients were included in this study. All of them were treated for localized prostate cancer between 2012 and 2015 in the same institution with a volumetric modulated arc therapy (VMAT) technique (1 full-clockwise arc of 18 MV) combined with daily IGRT, using a Synergy/Elekta linac with Agility MLC. A sequential treatment was proposed, delivering first a dose of 50 Gy in 5 weeks to the prostate and seminal vesicles, followed by a boost of 28 Gy in 2.8 weeks to the prostate only. The total number of fractions was therefore 39 fractions, and the dose per fraction was 2 Gy.

Volumes of Interest on the Planning Computed Tomography

Planning computed tomography (CT) images were acquired on a BigBore (Philips, the Netherlands) scanner, with 2-mm slice thickness. The clinical target volume (CTV) included the prostate and seminal vesicles. The CTV and the OARs (bladder, rectum, and femoral heads) were manually delineated on CT slices according to the French Genitourinary Group (GETUG) recommendations (14, 15). Rectal length was defined as to 2 cm above and below the CTV. The rectal wall was generated with a thickness of 0.5 cm from the external manually delineated rectal contour. The bladder wall was generated with a thickness of 0.7 cm from the external manually delineated bladder contour. PTVs were generated from the CTVs by adding a 0.5-cm margin in all directions.

The definition of the SRR was based on the voxel-wise population study presented in Dréan et al. (10). In summary, repeated voxel-wise analyses (16) were performed on 118 different patients in a leave-one-out scheme. Each patient served iteratively as template of reference to non-rigidly register (17) the remaining 117 patients and propagate the three-dimensional (3D) dose distributions allowing for spatially meaningful dosimetric comparisons. Thus, for each template, voxel-wise analysis (with Wilcoxon test and false discovery rate correction for multiple comparisons) produced a single region where significant dose differences between patients with and without RB appear. These sub-regions were then propagated to a single rectum template, which was divided in 64 subsections, eight sections in both the anteroposterior and axial directions (**Figure A1**). The generic SRR was finally defined by generating a probability map of presence of the 118 sub-regions within this anatomy. Each one of the 64 subsections with a probability of presence of ≥50% was selected as belonging to the SRR. The rectal sub-region was located close to the prostate (1 cm) and represented 15% of the absolute rectal volume. By construction, the SRR can be easily transferred to a patient-specific anatomy by splitting the rectum in the same 64 subsections, without requiring any registration method. This last step was implemented in an in-house toolbox (RedTox®), which, automatically and in a few seconds, produces a DICOM RTstructure file to be imported in a treatment planning system (TPS) (**Figure 1**).

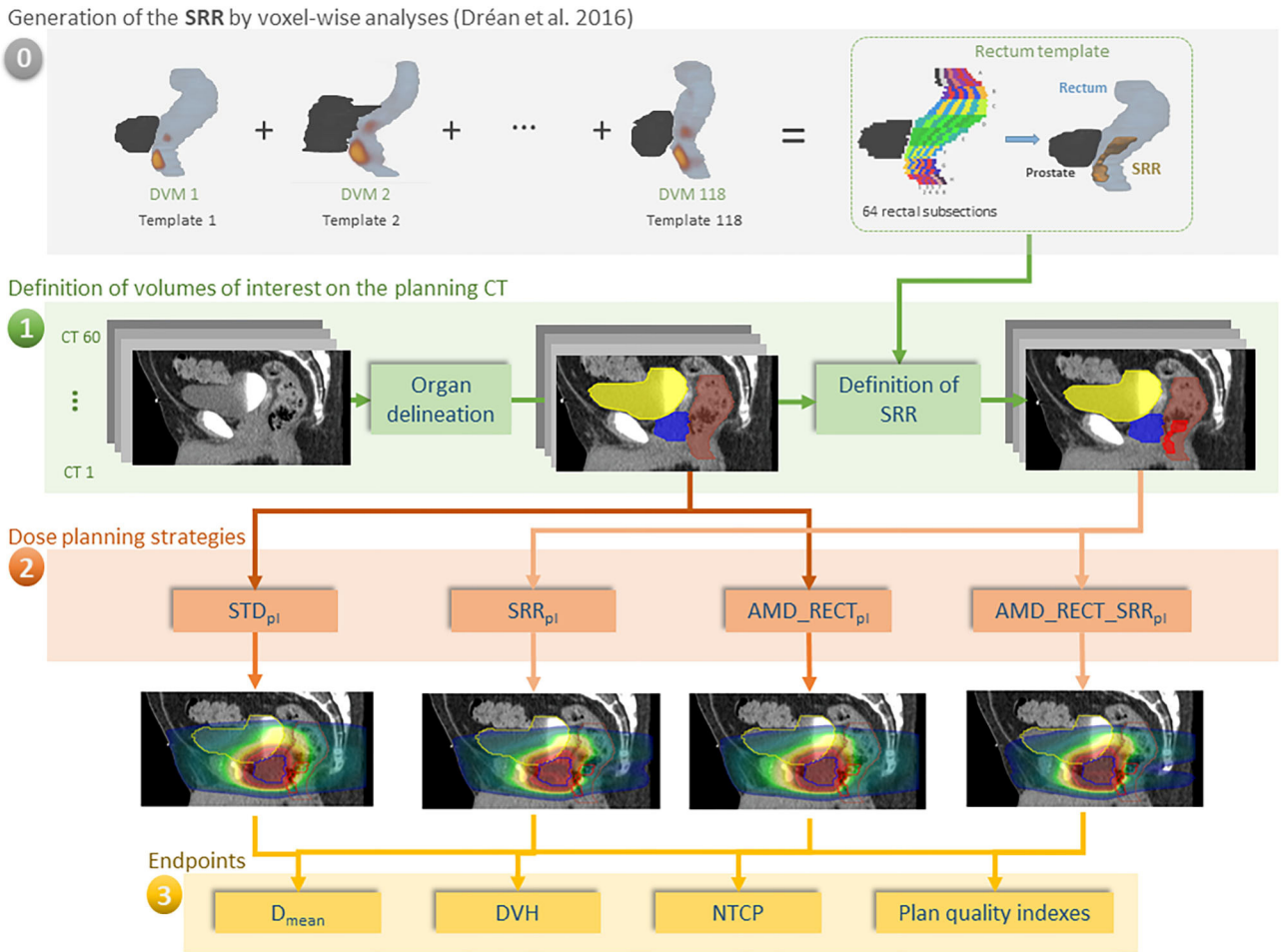

FIGURE 1 | Workflow of our study for 60 individuals. (0) The rectal subregion (SRR) was obtained after averaging results of voxel-wise analysis, using the dose volume maps (DVMs) on 118 different templates in Dréan et al. (10); (1) delineation of OARs and SRR; (2) planning according to four different strategies; (3) endpoint comparisons. In order for the SRR to be generic, the rectum was split in 64 subsections as depicted in **Figure A1**. The subsections were labeled as belonging to the SRR as a function of the probability (threshold at 50%) of the voxel-wise sub-regions to overlap with the squared subsections. The transfer of the SRR to the TPS was straightforward, following a chess squared mapping of 64 subsections to the 3D volume implemented in RedTox®. Once the organs and sub-regions were segmented, the four planning strategies were implemented, and the dosimetric endpoints were compared.

Additionally, a volume of the rectum excluding the SRR ("rectum without SRR") was generated. In the dosimetric study, we considered only the wall for the rectum and the bladder. Thus, we used herein the term *rectum* to refer to the rectal wall; likewise, the term *bladder* to refer to the bladder wall.

Dose Planning Strategies

Dose planning was performed with Pinnacle v.9.10 (Philips) TPS. The collapsed cone convolution algorithm and a dose grid size of $3 \times 3 \times 3$ mm^3 were used for dose calculation. Four different VMAT dose planning strategies were applied for each of the 60 patients: STD$_{pl}$, SRR$_{pl}$, AMD_RECT$_{pl}$, and AMD_RECT_SRR$_{pl}$. These four strategies are described below for each planning strategy. The minimum PTV coverage by the 95% prescribed isodose was 95%.

Standard Planning (STD$_{pl}$)

Treatment plans were generated for each CT according to the GETUG recommendations. GETUG dose–volume constraints were observed throughout: $V_{70Gy} \leq 50\%$ and $D_{max} \leq 80$ Gy for the bladder wall, and $V_{50Gy} \leq 50\%$, $V_{72Gy} \leq 25\%$, and $D_{max} \leq 76$ Gy for the rectum wall. The main dose constraints used during inverse optimization derived from clinical dose limits and are displayed in **Additional Table 1** for the four planning strategies.

Planning With SRR Constraints (SRR$_{pl}$)

Four SRR dose constraints were applied in addition to STD$_{pl}$ dose constraints: $D_{max} = 0.8 * D$prescription (weight = 10), $D15\% = 0.75 * D$prescription (weight = 1), $D25\% = 0.60 * D$prescription (weight = 1), and $D_{40\%} = 0.40 * D$prescription (weight = 1).

Moore's Model and Optimization of Achievable Mean Dose Model

Moore et al. (13) defined a mathematical model allowing for prediction of a radiation plan to achieve the lowest possible mean dose to an OAR overlapping with PTV. This model considers the prescribed dose to the PTV and the overlap volume between the PTV and the considered OAR (13). The general equation of the model was the following:

$$D_{achievable\_mean} = D_{prescribed}\left(\mathbf{A} + \mathbf{B}(\mathbf{C} - e^{-\mathrm{D}xV_{overlap}/V_{OAR}})\right)$$

where V_{overlap} is the intersection between the PTV and OAR.

This model was created from 17 H&N patients (overlap between parotid glands and PTV) and 8 prostate patients (overlap between rectum and prostate) static IMRT plans, with $A = 0.2$, $B = 0.8$, $C = 1$, $D = 3$. For our study, an adapted Moore's model was fitted based on 15 prostate standard treatment plans from our institution, following the same method as we already published for the H&N case (18). The ratio of the OAR D_{mean} to the prescription dose to PTV ($D_{\text{prescribed}}$) was plotted against the ratio of the overlap volume between PTV and OAR (V_{overlap}) to the OAR volume (V_{OAR}), for each patient. Moore's equation coefficients (A, B, C, and D) were modified by dichotomy, thereby fitting the curve of the model with the lower bound of our local data, which represents the optimal average OAR dose achievable in our selected cohort of patients ($N = 15$).

Planning With Achievable Mean Dose Model Applied to the Rectum ($\text{AMD\_RECT}_{\text{pl}}$)

The dose constraints used for the standard strategy were applied, as well as additional use of the AMD for the rectum. Our adaptation of the Moore's model provided the following equation for the rectum AMD ($\text{AMD}_{\text{rectum}}$):

$$AMD_{rectum} = Prescribed\ dose\left(0.22 + 0.8(1 - e^{-2V_{overlap}/V_R})\right)$$

with V_{overlap} = overlap between PTV and rectum, and V_{R} = rectum volume.

Planning With Achievable Mean Dose Models Applied to the Rectum and the SRR ($\text{AMD\_RECT\_SRR}_{\text{pl}}$)

The dose constraints used for the $\text{AMD\_RECT}_{\text{pl}}$ strategy were applied, as well as additional use of the AMD for the SRR. Our adaptation of the Moore's model provided the following equation for the SRR AMD (AMD_{SRR}):

$$AMD_{SRR} = Prescribed\ dose\left(\mathbf{0.34} + \mathbf{0.8}(\mathbf{1} - e^{-2V_{overlap}/V_{SRR}})\right)$$

with V_{overlap} = overlap between PTV and SRR, and V_{SRR} = SRR volume.

ENDPOINTS AND STATISTICAL ANALYSES

The four planning strategies were evaluated with respect to dosimetric parameters and predicted toxicity endpoints, as well as planning quality indexes.

The dosimetric parameters were as follows: the mean dose for the rectum and for the SRR, and the dose volume histogram (DVH) for the PTV and the OARs. In particular, the following reference RTOG/GETUG points have been reported: volume receiving at least 50 Gy ($V_{50\text{Gy}}$) and volume receiving at least 70 Gy ($V_{70\text{Gy}}$) for the SRR and the rectum, $V_{50\text{Gy}}$ and $V_{70\text{Gy}}$ for the bladder, and $V_{95\%}$ for the PTV. The ratio between the D_{mean} and the prescribed dose to the PTV (78 Gy) (D_{mean} /Dprescription$_{\text{PTV}}$) was also indicated.

The benefit of each strategy to spare the SRR was quantitatively assessed as the difference in the SRR mean dose achieved with respect to the STD_{pl}. The risk of toxicity was calculated using the Lyman–Kutcher–Burman NTCP model considering the SRR DVHs. The three parameters (TD50, n, and m) have been previously identified specifically for the SRR with the maximum likelihood method (19). Thus, our NCTP model predicted the risk of 3-year grade >1 RB with $n = 0.21$, $m = 0.28$, and $\text{TD}_{50} = 72$ (10).

The planning quality parameters were as follows: number of monitor units, irregularity index, and modulation index (20, 21). The irregularity index quantified the non-circularity of the aperture (equal to 1 in case of circular aperture). The modulation index takes into account aperture area and MU number associated to each segment (equal to 0 with a treatment plan without modulation). Conformal and homogeneity indexes were also calculated. The conformal index was defined as the ratio of the volume of PTV receiving 95% of prescribed dose to the volume of PTV. The homogeneity index was defined as the ratio $D_{2\%}$-$D_{98\%}$ to the $D_{50\%}$ of the PTV.

Paired Wilcoxon tests were used to compare the endpoints between the standard planning and each of the three other planning strategies. Correlation tests were used to identify parameters related with the dosimetric benefit of the $\text{AMD\_RECT\_SRR}_{\text{pl}}$ strategy. The correlation between the mean dose or the mean dose decrease to the SRR and V_{SRR} or $V_{\text{overlap(PTV}\bigcap\text{SRR)}}$ was tested for each planning strategy. Spearman coefficients (r_{S}) were computed.

Ethics Statement

The research has been approved by the institutional review board of the Eugene Marquis Cancer Center, and the patients have been informed of the research.

RESULTS

Dosimetric Comparison Between the Four Planning Strategies

Table 1 displays the dosimetric values in the SRR, rectum, the whole rectum without SRR, bladder, and PTV for the four planning strategies. Compared to STD_{pl}, $\text{AMD\_RECT\_SRR}_{\text{pl}}$ decreased significantly the dosimetric parameters for the rectum (D_{mean}, $V_{50\text{Gy}}$, $V_{70\text{Gy}}$) and for the SRR (D_{mean}, $V_{50\text{Gy}}$, $V_{70\text{Gy}}$), while preserving the PTV coverage. Although the PTV coverage ($V_{95\%}$) was statistically different between STD_{pl} and SRR_{pl}, or $\text{AMD\_RECT}_{\text{pl}}$, the 95% dose coverage constraint was achievable. Compared to STD_{pl}, $\text{AMD\_RECT}_{\text{pl}}$ significantly decreased the rectum mean dose from 37.3–33.2 Gy. Compared to STD_{pl},

TABLE 1 | Volumes, dosimetric endpoints, and NTCP parameters in the subrectal region (SRR), rectum, rectum without SRR, bladder, and PTV by the four planning strategies.

		Planning strategies			
		STD_{pl}	**SRR_{pl}**	**AMD_RECT$_{pl}$**	**AMD_RECT_SRR$_{pl}$**
SRR (whole volume)	*D*mean (Gy)	50.6 ± 5.9	45.9 ± 7.1*	45.2 ± 5.8*	42.9 ± 6.1*
	$V50_{Gy}$ (%)	50.4 ± 17.0	40.4 ± 16.7*	37.6 ± 14.3*	34.6 ± 13.3*
	$V70_{Gy}$ (%)	12.8 ± 8.8	10.5 ± 7.1*	9.7 ± 7.1*	9.7 ± 6.3*
	NTCP# (%)	22.8 ± 6.8	19.4 ±6.6**	18.4 ± 6.2**	17.6 ± 5.7**
	Volume (cm^3) [range]			9.9 ± 4.3 [4.0; 21.3]	
Rectum (wall)	*D*mean (Gy)	37.3 ± 3.0	37.0 ± 3.4	33.2 ± 3.3*	33.7 ± 3.6*
	$V50_{Gy}$ (%)	29.0 ± 5.3	28.7 ± 6.1	24.3 ± 5.1*	25.0 ± 5.6*
	$V70_{Gy}$ (%)	12.4 ± 3.3	11.9 ± 3.6*	10.4 ± 3.1*	10.8 ± 3.4*
	Volume (cm^3) [range]			32.4 ± 7.8 [48.7; 18.4]	
Rectum volume without SRR (whole volume)	*D*mean (Gy)	34.6 ± 3.7	34.6 ± 4.0	30.0 ± 3.8*	30.5 ± 4.2*
	$V50_{Gy}$ (%)	23.0 ± 6.8	23.5 ± 7.5	17.5 ± 6.0*	18.5 ± 6.4*
	$V70_{Gy}$ (%)	7.2 ± 2.5	6.5 ± 2.5*	5.7 ± 2.2*	5.5 ± 2.2*
	Volume (cm^3) [range]			59.8 ± 24.5 [23.9; 113.9]	
Bladder (wall)	$V50_{Gy}$ (%)	30.4 ± 12.4	29.8 ± 12.0*	29.7 ± 12.0*	29.4 ± 12.5*
	$V70_{Gy}$ (%)	14.2 ± 6.1	14.0 ± 6.0	14.2 ± 6.0	14.2 ± 6.2
	Volume (cm^3) [range]			67.8 ± 26.8 [124.3; 24.4]	
PTV	D95% (%)	96.2 ± 0.6	95.8 ± 0.5*	96.5 ± 0.5*	96.1 ± 0.7
	Homogeneity index	0.08 ± 0.01	0.10 ± 0.01*	0.08 ± 0.01*	0.10 ± 0.02*
	Conformal index	0.98 ± 0.01	0.97 ± 0.01*	0.98 ± 0.01	0.97 ± 0.02*
	Volume (cm^3) [range]			109.7 ± 36.1 [41.4; 260.3]	
Overlap between SRR and PTV	Volume (cm^3) [range]			0.9 ± 0.5 [0.1; 2.4]	
Overlap between rectum and PTV	Volume (cm^3) [range]			3.2 ± 1.3 [0.9; 6.9]	

AMD, achievable mean dose; STD_{pl}, standard planning; SRR_{pl}, planning with specific SRR constraints without using AMD model; AMD_RECT$_{pl}$, planning using the AMD model applied to the rectum only; AMD_RECT_SRR$_{pl}$, combined strategy using the AMD model applied to both the rectum and the SRR.

Values are mean ± standard deviation.

The NTCP# values have been calculated by using the following parameters: n = 0.21, m = 0.28, and TD_{50} = 72. The NTCP evaluates the risk of 3-year grade ≥1 rectal bleeding (10).

**p < 0.05 (assuming significance level) of the Wilcoxon test comparing the standard strategy (STD_{pl}) to each of the tested strategy.*

***p < 0.001.*

the AMD_RECT_SRR$_{pl}$ strategy significantly decreased the rectum mean dose from 37.3 Gy to 33.7 Gy and the SRR mean dose from 50.6 to 42.9 Gy. **Figure 2** shows the impact of adding constraints on SRR (SRR_{pl}) compared to a STD_{pl} (**Figure 2A**), using the AMD model to decrease the mean dose to the SRR (AMD_RECT_SRR$_{pl}$) compared to the SRR_{pl} (**Figure 2B**) and using the AMD model to decrease the mean dose to the rectum (AMD_RECT$_{pl}$) compared to a STD_{pl} (**Figure 2C**).

Figure 3 shows the average DVH of the PTV, rectum, and SRR for the four strategies. Compared to STD_{pl}, AMD_RECT_SRR$_{pl}$ reduced significantly the volume of the rectum and the SRR receiving a dose between 4 and 75 Gy and between 10 and 74 Gy, respectively.

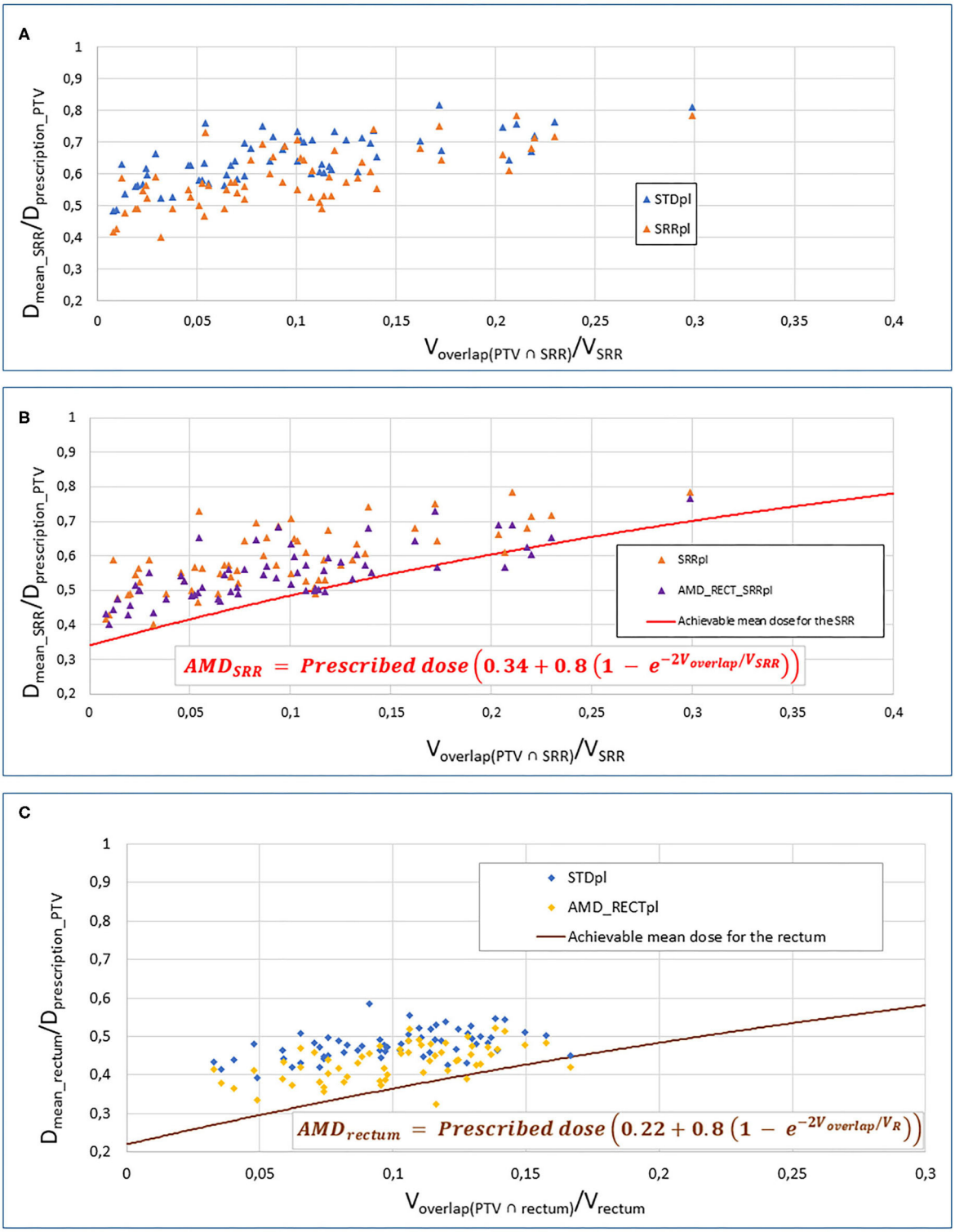

FIGURE 2 | Impact of adding constraints to SRR (SRR_{pl}) compared to a STD_{pl} **(A)**, using the AMD model to decrease the mean dose to the SRR ($AMD\_RECT\_SRR_{pl}$) compared to the SRR_{pl} **(B)** and using the AMD model to decrease the mean dose to the rectum (AMD_RECT_{pl}) compared to a STD_{pl}. **(C)** AMD, achievable mean dose; STD_{pl}, standard planning; SRR_{pl}, planning with specific SRR constraints without using AMD model; AMD_RECT_{pl}, planning using the AMD model applied to the rectum only; $AMD\_RECT\_SRR_{pl}$, combined strategy using the AMD model applied to both the rectum and the SRR. The mean doses (D_{mean}) to the SRR **(A,B)** or rectum **(C)** or "normalized" to the PTV prescribed dose (D_{mean_rectum} or $SRR/D_{prescription\_PTV}$). This ratio is plotted against the percentage of overlap between the SRR **(A,B)** or the rectum **(C)** and the PTV ($V_{overlap(PTV \cap rectum\ or\ SRR)}/V_{SRR}$). The curves display the AMD generated from the equation presented in the figure. The prescription dose to the PTV (Dprescription$_{PTV}$) was 78 Gy.

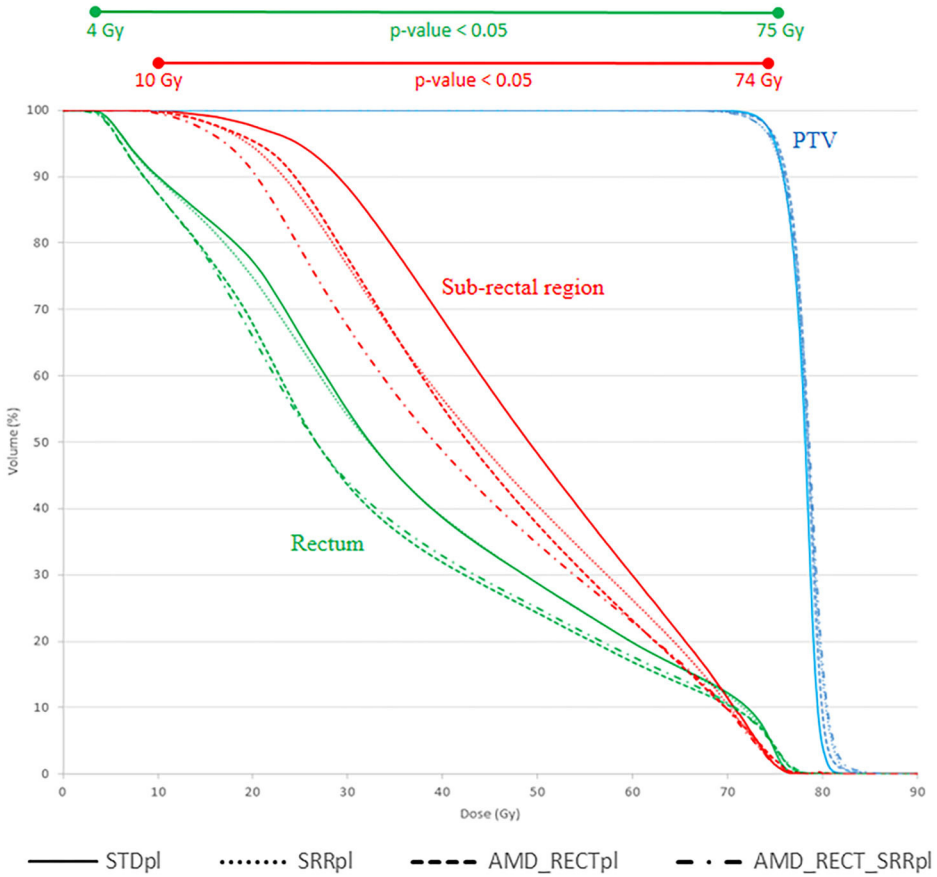

FIGURE 3 | Mean DVH corresponding to each of the four planning strategies. AMD, achievable mean dose; STD_{pl}, standard planning; SRR_{pl}, planning with specific SRR constraints without using AMD model; AMD_RECT_{pl}, planning using the AMD model applied to the rectum only; $AMD\_RECT\_SRR_{pl}$, combined strategy using the AMD model applied to both the rectum and the SRR. The prescription dose was 78 Gy. Wilcoxon tests were used to compare the DVHs from the standard strategy (STD_{pl}) to those of each planning strategy. Significant differences ($p < 0.05$) are displayed at the top of the graphic.

Figure 4 depicts the mean dose to the SRR for each planning strategy (**Figures 4A,B**) to the SRR between STD_{pl} and each tested planning (SRR_{pl}, AMD_RECT_{pl}, and $AMD\_RECT\_SRR_{pl}$). Compared to STD_{pl}, $AMD\_RECT\_SRR_{pl}$ decreased the mean dose to the SRR up to 16.2 Gy. The median SRR mean dose reduction, compared to STD_{pl}, was 4.6 Gy when using SRR_{pl}, 5.1 Gy when using AMD_RECT_{pl}, and 7.9 Gy when using $AMD\_RECT\_SRR_{pl}$. **Figure 5** illustrates the dose distribution corresponding to each of the four planning strategies for a given patient.

No correlation ($|r_S| < 0.21$) was found between the mean dose or the mean dose decrease to the SRR and *V*SRR or the *V*overlap(PTV $_n$ SRR).

NTCP Comparison Between the Four Strategies

Table 1 displays the NCTP values computed from the SRR when considering the four planning strategies. Compared to STD_{pl}, the $AMD\_RECT\_SRR_{pl}$ strategy significantly decreased the estimated risk of RB. The NTCP values decreased from 22.8 to 17.6% when considering the SRR DVH.

Quality Comparison of the Planning Between the Four Strategies

Table 1 displays the homogeneity and conformal indexes in the PTV by the four planning strategies. The homogeneity index significantly increased for $AMD\_RECT\_SRR_{pl}$ with respect to STD_{pl}. The conformal index significantly decreased for the $AMD\_RECT\_SRR_{pl}$ with respect to STD_{pl}. **Table 2** displays the planning quality parameters for each strategy. The MU significantly increased from 372 for STD_{pl} to 454 MU for $AMD\_RECT\_SRR_{pl}$. The irregularity and the modulation indexes significantly increased for the $AMD\_RECT\_SRR_{pl}$ with respect to STD_{pl}.

DISCUSSION

This paper proposed a methodology for decreasing rectal toxicity by adding a patient-specific sub-region in the prostate inverse radiotherapy planning and by using a specific achievable mean dose model. We compared four different inverse planning strategies in terms of

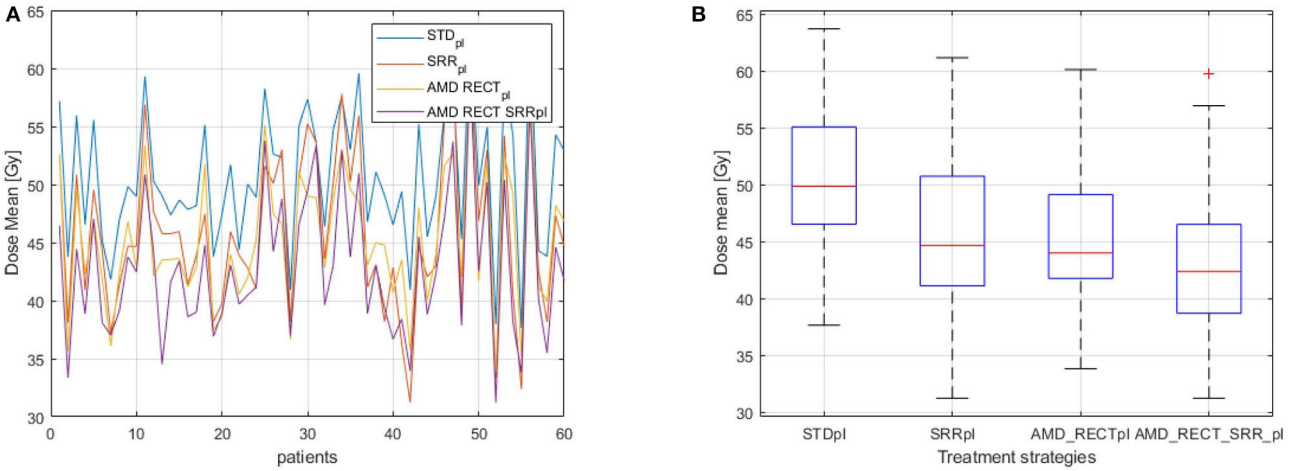

FIGURE 4 | (A) D_{mean} to the SRR for the 60 patients; **(B)** Distribution of D_{mean} to the SRR according to the planning strategies. Mean dose (D_{mean}) to the subrectal region (SRR) for the four planning strategies (STD_{pl}, SRR_{pl}, AMD_RECT_{pl}, and $AMD\_RECT\_SRR_{pl}$). AMD, achievable mean dose; STD_{pl}, standard planning; SRR_{pl}, planning with specific SRR constraints without using the AMD model; AMD_RECT_{pl}, planning using the AMD model applied to the rectum only; $AMD\_RECT\_SRR_{pl}$, combined strategy using the AMD model applied to both the rectum and the SRR.

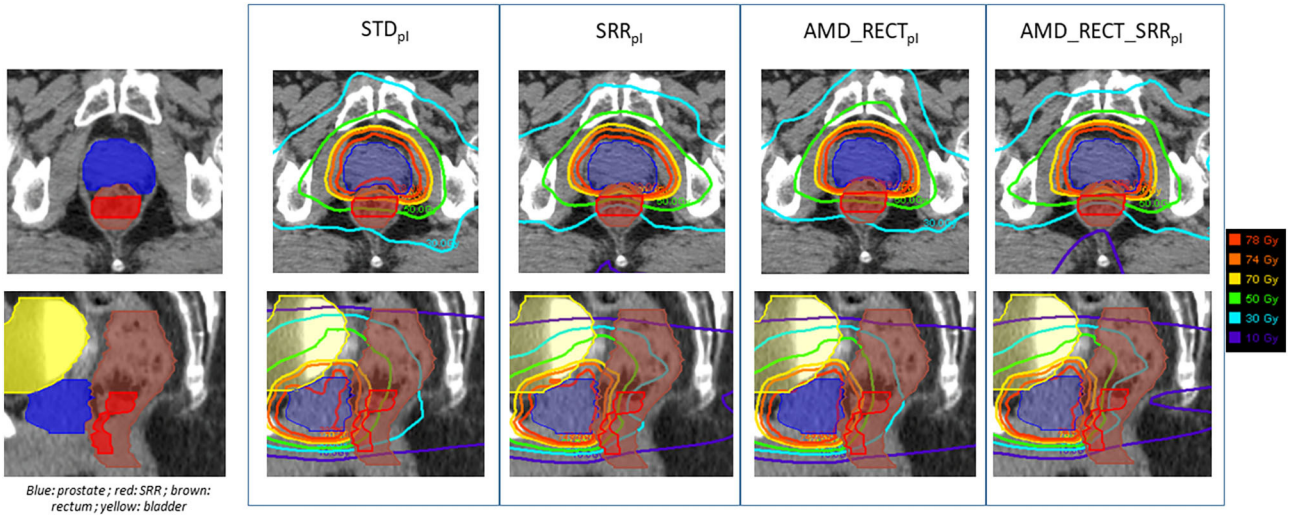

FIGURE 5 | Illustration of the dose distributions corresponding to each of the four planning strategies for a given patient. AMD, achievable mean dose; STD_{pl}, standard planning; SRR_{pl}, planning with specific SRR constraints without using the AMD model; AMD_RECT_{pl}, planning using the AMD model applied to the rectum only; $AMD\_RECT\_SRR_{pl}$, combined strategy using the AMD model applied to both the rectum and the SRR. The prescribed dose is 78 Gy.

dosimetric benefit, planning quality parameters, and NTCP prediction.

A considerable dose reduction can be achieved to both the rectum and the SRR with the combined approach ($AMD\_RECT\_SRR_{pl}$) compared to the standard planning (**Table 1**). This planning strategy appears particularly appealing because it is not invasive, can be easily customized, does not increase the treatment workload, and offers improved OAR sparing while preserving PTV coverage. Furthermore, the application of the NTCP model ratifies a reduction in rectal toxicity. It must be pointed out that decreasing the dose in the SRR via the SRR_{pl}, did not have any impact on dose increase elsewhere in the rectum (**Table 1**, rectum without SRR). On the contrary, a diminution on SRR mean dose was accompanied by a global diminution of dose in the rectum (D_{mean} and V_{70Gy}).

For the dose planning step, the rectal and bladder walls were used in order to meet the French GETUG recommendations. However, both the whole 3D organ and the wall can be considered either for planning dose constraints or for toxicity prediction. As shown in the literature and confirmed in the clinical routine, the recta DVH and rectal wall DVHs are highly

TABLE 2 | Planning quality parameters for each planning strategy.

Planning optimization	STD_{pl}	SRR_{pl}	AMD_RECT_{pl}	$AMD\_RECT\_SRR_{pl}$
Monitor units (MU)	372 ± 25	396 ± 29*	441 ± 35*	454 ± 42*
Irregularity index (ideal value → 1)	4.35 ± 1.25	5.24 ± 1.08*	5.92 ± 1.62*	6.86 ± 1.8*
Modulation index (ideal value → 0)	0.63 ± 0.04	0.65 ± 0.04*	0.69 ± 0.03*	0.69 ± 0.04*

AMD, achievable mean dose; STD_{pl}, standard planning; SRR_{pl}, planning with specific SRR constraints without using AMD model; AMD_RECT_{pl}, planning using the AMD model applied to the rectum only; $AMD\_RECT\_SRR_{pl}$, combined strategy using the AMD model applied to both the rectum and the SRR.

Values are mean ± standard deviation.

**$p < 0.05$ (assuming significance level) of the Wilcoxon test comparing the standard strategy to each of the tested strategy.*

correlated (22). Moreover, rectal wall DVH provides a moderate improvement when fitting NTCP models (23).

Concerning the dose constraints in the TPS, we implemented a version of the AMD model proposed by Moore et al. (13) to decrease the dose in the rectum and the SRR. This model was first introduced in a dosimetric quality control context with the aim of improving the planner's experience in the case of inverse planning. They proposed a simple tool using a generic model to predict OAR mean dose taking into account the PTV and OAR volume overlap. Their results showed a significant reduction to the mean dose for both rectum and parotid glands, compared to a standard planning approach. However, the application of the AMD model requires a customization to each clinical center and to each tumor location, as shown by Powis et al. (24) and Delaby et al. (18). Powis et al. (24) improved plan quality for prostate cancer. With their customized AMD model, the rectum mean dose was significantly decreased from 41.6 to 36 Gy, for a prescribed dose of 74 Gy to the prostate. Delaby et al. (18) showed a dose reduction of 6.1 Gy to the parotid glands using their own adaptation of AMD model for H&N. In our study, the dosimetric benefit on rectal mean dose was 4.1 Gy (**Table 1**, STD_{pl} minus AMD_RECT_{pl}) for a prescribed dose of 78 Gy to the prostate.

Voxel-wise analysis by non-rigid registration has become a well-established methodology able to unveil the likely heterogeneous radiosensitivity across the organs, which may be helpful in the identification of sub-regions to be spared at the planning step. One of the major advantages of the voxel-wise analysis is its ability to explore the full 3D anatomy without prior assumptions regarding the location of regions correlating with toxicity (25). As compared with dose surface maps, which have also been used for this purpose, the voxel-based methods present the advantage of generating 3D volumes that can be transferred to the clinical practice in a straightforward way.

The rectal SRR, considered in this study, was previously identified through voxel-based analysis as predictive of RB in a series of 118 prostate cancer patients treated with IMRT/IGRT and validated on a testing data set of 53 patients (10). This SRR represented the 15% of the absolute rectal volume and was located in the inferior–anterior rectal region. If the benefit of using the SRR was shown in the previous study for toxicity prediction (10), the present work additionally explores the potential advantage of sparing this SRR during the planning. The same workflow can be applied in other locations such as lung, bladder, or H&N, where sub-regions have been previously identified.

Our study presents several limitations. The main issue is the lack of clinical data to demonstrate the real improvement of combining the SRR with the AMD strategies in toxicity reduction. Furthermore, we were not able to correlate geometric characteristics (overlap volume between the PTV and SRR) with the dose reduction within the SRR. As mentioned before, one of the issues that may arise in voxel-wise analysis, stemming from the interindividual variability, is the reproducibility of the SRRs in different templates and the reliability of non-rigid registration (26). The SRR used in this study was, however, previously generated through repeated voxel-wise analyses on 118 different templates in a leave-one-out strategy (10) using a validated non-rigid registration method (17), confirming the robustness to the computed SRR. Because of the deformable nature of organs and soft tissues, another potential issue is that the planning dose may not be representative of the true delivered dose. Indeed, considering the mean dose to the rectum, the dose difference between the planned dose and the estimated cumulated dose by elastic registration has been quantified to be around 2 Gy (27). Because organs are moving and deforming between fractions, new models should include this information either by quantifying daily deformations with MVCT (28) or by estimating cumulative dose with statistical methods as in Rios et al. (29). Other image modalities such as cone-beam CT or magnetic resonance imaging can also provide daily images helping to quantify anatomical changes.

Although very useful for indicating achievable doses, the use of the AMD model presents geometric and dosimetric limitations. For instance, it only considers the global overlap (OAR $\bigcap$ PTV) volume, without taking into account the OAR shape, orientation, or geometric irregularities. Wu et al. (30) pointed out this issue by showing similar OAR $\bigcap$ PTV overlap configurations but with different OAR shapes. Hence, two different configurations would yield equivalent AMD. They also introduced the concept of overlap volume histogram (OVH) to describe the fractional volume of the structure of an OAR but with respect to a specified distance to the target volume. The OVH is a shape relationship descriptor, measuring the proximity of the OAR to the target, which also provides a way to infer the likely DVH of an OAR. A relation between DVH and OVH could be computed near the target volume in order to refine the achievable DVH. Wall et al. (31) investigated DVH-OVH (rectum and bladder volumes) correlations in a series of 124 prostate patients. By replanning 31 randomly selected patients, the rectum mean dose decreased by 9.4 Gy, compared to the initial planning. Another limitation of the AMD model is the use of the mean dose as a constraint. The mean dose is rarely considered for dose–toxicity prediction in the rectum as are rather the higher doses, which are correlated to rectal toxicity (27).

A practical limitation also exists regarding the generalization of the proposed workflow in a clinical setup. This stems from the fact that transferring the SRR to a specific patient anatomy requires the use of nonintegrated tools in the TPS for the time being. Nevertheless, the algorithm for the SRR generation (10) has been implemented in an in-house toolbox (RedTox®), which produces a DICOM-RT structure of the SRR in a few seconds, which can be imported within any TPS. This workflow provides therefore a way forward on the implementation of personalized treatments.

CONCLUSION

In case of prostate cancer radiotherapy, a sub-region highly predictive of RB, determined by voxel-wise analyses, was transferred to patient-specific anatomies for dose planning. The integration of this SRR into the TPS allows tailoring a personalized planning with dose constraints based on an AMD model. Compared to the standard planning approach, the proposed AMD strategy decreases the rectal and the SRR mean doses by 3.6 and 7.7 Gy, respectively, while preserving PTV coverage. This dosimetric benefit may be translated into a relative reduction in probability of RB by 22%. Following this workflow, a reduced-toxicity personalized treatment can be achieved. Nevertheless, such clinical benefit on IMRT/IGRT needs to be confirmed in prospective clinical trials.

DATA AVAILABILITY STATEMENT

The datasets generated for this study are available on request to the corresponding author.

AUTHOR CONTRIBUTIONS

All authors listed have made a substantial, direct and intellectual contribution to the work, and approved it for publication.

FUNDING

This work was supported by the French Institut National du Cancer for the STIC, IGRT-P, and PROFIT trials, and by the French National Research Agency (ANR) in the framework of the Investing for the future Program through Labex CAMI (ANR-11-LABX-0004) and Labex CominLabs ANR-10-LABX-07-01.

SUPPLEMENTARY MATERIAL

The Supplementary Material for this article can be found online at: https://www.frontiersin.org/articles/10.3389/fonc.2020.01597/full#supplementary-material

REFERENCES

1. de Crevoisier R, Bayar MA, Pommier P, Muracciole X, Pêne F, Dudouet P, et al. Daily vs. weekly prostate cancer image guided radiation therapy: phase 3 multicenter randomized trial. *Int J Radiat Oncol.* (2018) 102:1420–9. doi: 10.1016/j.ijrobp.2018.07.2006
2. Holch P, Henry AM, Davidson S, Gilbert A, Routledge J, Shearsmith L, et al. Acute and late adverse events associated with radical radiation therapy prostate cancer treatment: a systematic review of clinician and patient toxicity reporting in randomized controlled trials. *Int J Radiat Oncol.* (2017) 97:495–510. doi: 10.1016/j.ijrobp.2016.11.008
3. Karsh LI, Gross ET, Pieczonka CM, Aliotta PJ, Skomra CJ, Ponsky LE, et al. Absorbable hydrogel spacer use in prostate radiotherapy: a comprehensive review of phase 3 clinical trial published data. *Urology.* (2018) 115:39–44. doi: 10.1016/j.urology.2017.11.016
4. Hamstra DA, Mariados N, Sylvester J, Shah D, Karsh L, Hudes R, et al. Continued benefit to rectal separation for prostate radiation therapy: final results of a phase III trial. *Int J Radiat Oncol.* (2017) 97:976–85. doi: 10.1016/j.ijrobp.2016.12.024
5. Chao M, Lim Joon D, Khoo V, Lawrentschuk N, Ho H, Spencer S, et al. The use of hydrogel spacer in men undergoing high-dose prostate cancer radiotherapy: results of a prospective phase 2 clinical trial. *World J Urol.* (2019) 37:1111–6. doi: 10.1007/s00345-018-2502-5
6. Palma G, Monti S, D'Avino V, Conson M, Liuzzi R, Pressello MC, et al. A voxel-based approach to explore local dose differences associated with radiation-induced lung damage. *Int J Radiat Oncol.* (2016) 96:127–33. doi: 10.1016/j.ijrobp.2016.04.033
7. McWilliam A, Kennedy J, Hodgson C, Vasquez Osorio E, Faivre-Finn C, van Herk M. Radiation dose to heart base linked with poorer survival in lung cancer patients. *Eur J Cancer.* (2017) 85:106–13. doi: 10.1016/j.ejca.2017.07.053
8. Monti S, Palma G, D'Avino V, Gerardi M, Marvaso G, Ciardo D, et al. Voxel-based analysis unveils regional dose differences associated with radiation-induced morbidity in head and neck cancer patients. *Sci Rep.* (2017) 7:7220. doi: 10.1038/s41598-017-07586-x
9. Mylona E, Acosta O, Lizee T, Lafond C, Crehange G, Magné N, et al. Voxel-based analysis for identification of urethrovesical subregions predicting urinary toxicity after prostate cancer radiation therapy. *Int J Radiat Oncol.* (2019) 104:343–54. doi: 10.1016/j.ijrobp.2019.01.088
10. Dréan G, Acosta O, Ospina JD, Fargeas A, Lafond C, Corrégé G, et al. Identification of a rectal subregion highly predictive of rectal bleeding in prostate cancer IMRT. *Radiother Oncol.* (2016) 119:388–97. doi: 10.1016/j.radonc.2016.04.023
11. Rigaud B, Simon A, Castelli J, Lafond C, Acosta O, Haigron P, et al. Deformable image registration for radiation therapy: principle, methods, applications and evaluation. *Acta Oncol.* (2019) 58:1225–37. doi: 10.1080/0284186X.2019.1620331
12. Acosta O, De Crevoisier R. Beyond DVH: 2D/3D based dose comparison to assess predictors of toxicity. In Rancati T, Fiorino C, editors. *Modelling Radiotherapy Side Effects: Practical Application for Planning Optimisation*. Boca Raton, FL: CRC Press Taylor & Francis Group (2019). p. 415–40. doi: 10.1201/b21956
13. Moore KL, Brame RS, Low DA, Mutic S. Experience-based quality control of clinical intensity-modulated radiotherapy planning. *Int J Radiat Oncol.* (2011) 81:545–51. doi: 10.1016/j.ijrobp.2010.11.030
14. Beckendorf V, Guerif S, Prisé EL, Cosset J-M, Bougnoux A, Chauvet B, et al. 70 Gy vs. 80 Gy in localized prostate cancer: 5-year results of GETUG 06 randomized Trial. *Int J Radiat Oncol Biol Phys.* (2011) 80:1056–63. doi: 10.1016/j.ijrobp.2010.03.049
15. de Crevoisier R, Pommier P, Latorzeff I, Chapet O, Chauvet B, Hennequin C. Radiothérapie externe des cancers prostatiques. *Cancer Radiothérapie.* (2016) 20:S200–9. doi: 10.1016/j.canrad.2016.07.037
16. Acosta O, Drean G, Ospina JD, Simon A, Haigron P, Lafond C, et al. Voxelbased population analysis for correlating local dose and rectal

toxicity in prostate cancer radiotherapy. *Phys Med Biol.* (2013) 58:2581–95. doi: 10.1088/0031-9155/58/8/2581
17. Dréan G, Acosta O, Lafond C, Simon A, de Crevoisier R, Haigron P. Interindividual registration and dose mapping for voxelwise population analysis of rectal toxicity in prostate cancer radiotherapy. *Med Phys.* (2016) 43:2721–30. doi: 10.1118/1.4948501
18. Delaby N, Martin S, Barateau A, Henry O, Perichon N, De Crevoisier R, et al. Implementation of an optimization method for parotid gland sparing during inverse planning for head and neck cancer radiotherapy. *Cancer Radiothérapie*. (2020) 24:28–37. doi: 10.1016/j.canrad.2019.09.006
19. Lyman JT. Complication probability as assessed from dose-volume histograms. *Radiat Res.* (1985) 104:S13. doi: 10.2307/3576626
20. Senthi S, Gill SS, Haworth A, Kron T, Cramb J, Rolfo A, et al. Benchmarking dosimetric quality assessment of prostate intensity-modulated radiotherapy. *Int J Radiat Oncol.* (2012) 82:998–1005. doi: 10.1016/j.ijrobp.2010.12.016
21. Du W, Cho SH, Zhang X, Hoffman KE, Kudchadker RJ. Quantification of beam complexity in intensity-modulated radiation therapy treatment plans: IMRT beam complexity. *Med Phys.* (2014) 41:021716. doi: 10.1118/1.4861821
22. Fiorino C, Gianolini S, Nahum AE. A cylindrical model of the rectum: comparing dose– volume, dose–surface and dose–wall histograms in the radiotherapy of prostate cancer. *Phys Med Biol.* (2003) 48:2603–16. doi: 10.1088/0031-9155/48/16/303
23. Tucker SL, Dong L, Cheung R, Johnson J, Mohan R, Huang EH, et al. Comparison of rectal dose–wall histogram vs. dose–volume histogram for modeling the incidence of late rectal bleeding after radiotherapy. *Int J Radiat Oncol.* (2004) 60:1589–601. doi: 10.1016/j.ijrobp.2004.07.712
24. Powis R, Bird A, Brennan M, Hinks S, Newman H, Reed K, et al. Clinical implementation of a knowledge based planning tool for prostate VMAT. *Radiat Oncol.* (2017) 12:81. doi: 10.1186/s13014-017-0814-z
25. Mylona E, Cicchetti A, Rancati T, Palorini F, Fiorino C, Supiot S, et al. Local dose analysis to predict acute and late urinary toxicities after prostate cancer radiotherapy: Assessment of cohort and method effects. *Radiother Oncol.* (2020) 147:40–9. doi: 10.1016/j.radonc.2020.02.028
26. Dréan G, Acosta O, Ospina JD, Voisin C, Rigaud B, Simon A, et al. How to identify rectal sub-regions likely involved in rectal bleeding in prostate cancer radiotherapy. In: Brieva J, Escalante-Ramírez B, editors. *Proceedings SPIE 8922, IX International Seminar on Medical Information Processing and Analysis*. Mexico City (2013). doi: 10.1117/12.2035238
27. Nassef M, Simon A, Cazoulat G, Duménil A, Blay C, Lafond C, et al. Quantification of dose uncertainties in cumulated dose estimation compared to planned dose in prostate IMRT. *Radiother Oncol.* (2016) 119:129–36. doi: 10.1016/j.radonc.2016.03.007
28. Shelley LEA, Scaife JE, Romanchikova M, Harrison K, Forman JR, Bates AM, et al. Delivered dose can be a better predictor of rectal toxicity than planned dose in prostate radiotherapy. *Radiother Oncol.* (2017) 123:466–71. doi: 10.1016/j.radonc.2017.04.008
29. Rios R, De Crevoisier R, Ospina JD, Commandeur F, Lafond C, Simon A, et al. Population model of bladder motion and deformation based on dominant eigenmodes and mixed-effects models in prostate cancer radiotherapy. *Med Image Anal.* (2017) 38:133–49. doi: 10.1016/j.media.2017.03.001
30. Wu B, Ricchetti F, Sanguineti G, Kazhdan M, Simari P, Chuang M, et al. Patient geometry-driven information retrieval for IMRT treatment plan quality control: Geometry-driven information retrieval for IMRT plan quality control. *Med Phys.* (2009) 36:5497–505. doi: 10.1118/1.3253464
31. Wall PDH, Carver RL, Fontenot JD. An improved distance-to-dose correlation for predicting bladder and rectum dose-volumes in knowledge-based VMAT planning for prostate cancer. *Phys Med Biol.* (2018) 63:015035. doi: 10.1088/1361-6560/aa9a30

Conflict of Interest: The authors declare that the research was conducted in the absence of any commercial or financial relationships that could be construed as a potential conflict of interest.

The handling editor declared a past co-authorship with several of the authors EM, OA, and RC.

frontiers in Oncology

ORIGINAL RESEARCH
published: 15 September 2020
doi: 10.3389/fonc.2020.528686

Aerosolized Thyroid Hormone Prevents Radiation Induced Lung Fibrosis

*Long Li, Xiaoqi Nie, Minxiao Yi, Wan Qin, Fang Li, Bili Wu and Xianglin Yuan**

Department of Oncology, Tongji Hospital, Huazhong University of Science and Technology, Wuhan, China

Radiation induced lung fibrosis (RILF) is a common late complication after radiotherapy without effective treatment. Thyroid hormone (TH) is known to reverse bleomycin-induced pulmonary fibrosis in recent study. We therefore sought to examine TH effect in RILF. Aerosolized TH delivery prevented pulmonary fibrosis according to either micro-computed tomography scans or histological evaluations, without significant changes in serum THs in a murine model of RILF by attenuating TGF-β1 and phosphorylated Smad2/3 expressions and reducing the accumulation of M2-like macrophages. Furthermore, hypothyroidism was significantly correlated with RILF in a retrospectively analyzed data from nasopharyngeal carcinoma patients treated by intensity-modulated radiation therapy with a median follow-up time of 25.5 months. Together, aerosolized TH may prevent RILF by inhibiting the TGF-β1/SMADs signaling pathway.

Keywords: radiation induced lung fibrosis, aerosolized, thyroid hormone, TGF-β1, macrophage, hypothyroidism

OPEN ACCESS

Edited by:
Timothy James Kinsella, Warren Alpert Medical School of Brown University, United States

Reviewed by:
Rihan El Bezawy, Istituto Nazionale dei Tumori (IRCCS), Italy
Tiziana Rancati, Istituto Nazionale dei Tumori (IRCCS), Italy

***Correspondence:**
Xianglin Yuan
yuanxianglin@hust.edu.cn

Specialty section:
This article was submitted to Radiation Oncology, a section of the journal Frontiers in Oncology

Received: *21 January 2020*
Accepted: *20 August 2020*
Published: *15 September 2020*

Citation:
Li L, Nie X, Yi M, Qin W, Li F, Wu B and Yuan X (2020) Aerosolized Thyroid Hormone Prevents Radiation Induced Lung Fibrosis. Front. Oncol. 10:528686. doi: 10.3389/fonc.2020.528686

INTRODUCTION

Radiotherapy is widely used in tumor treatment. More than 50 percent of malignant cancer patients require radiation therapy for both curative and palliative purposes (1). However, the application of radiotherapy is limited by the radiation-induced lung injury (RILI), which is a common complication after radiotherapy of thoracic malignant tumors. RILI often causes early radiation pneumonitis and late-onset radiation induced lung fibrosis (RILF) usually occurs in 1 year after radiotherapy (2). The incidence of symptomatic RILF in patients receiving thoracic radiotherapy is about 5–24%, and higher in patients with subclinical damage (3). Because effective treatments are lacking, RILF has an adverse impact on the quality of life of suffering patients, causing cough, shortness of breath, fever, progressive respiratory dysfunction, or even death (4–6). Currently, corticosteroids are commonly used in the clinic for radiation induced lung injury. Several prevention strategies have shown certain promising effects in murine models of RILF, including treatments with amifostine, ACE inhibitors, angiotensin II receptor inhibitors, pentoxifylline as well as with inhibitors of PDGF, VEGF, FGF, TGF-β1, and Cox-2, but firm clinical evidence is lacking (7–9).

Thyroid hormone is one of the most important hormones that regulate energy metabolism. The levels of active triiodothyronine and its precursor thyroxine (T4) are mainly regulated by DIO2 in cells and tissues (10). There is growing evidence of the correlation between thyroid function and fibrosis disease in patients. Grazinao (11) found that patients with idiopathic retroperitoneal fibrosis (IRF) had a higher risk of hypothyroidism than controls (OR = 3.56, 95%CI 1.48–8.59,

and P = 0.004). Nearly a quarter of IRF patients received L-thyroxine at the end of the follow-up (median, 45 month), but only 3% of controls needed treatment in the same period. The incidence of hypothyroidism in idiopathic pulmonary fibrosis (IPF) was 16.8%, compared with 7.1% in control group; multivariate analysis showed that hypothyroidism was an independent predictor of death risk in IPF patients (12). Clinical data from a large sample showed that hypothyroidism significantly correlated with non-alcoholic fatty liver fibrosis (OR = 2.23, 95%CI 1.18–4.23, and P = 0.014) (13). Hypothyroidism also plays an important role in myocardial fibrosis (14) and diabetic nephropathy (15).

Furthermore, recent studies have shown that TH may have a therapeutic effect in acute lung injury (16, 17). Yu et al. (18) demonstrated that TH significantly attenuated adverse signs in a mouse model of bleomycin-induced pulmonary fibrosis by restoring epithelial mitochondrial function. TH efficacy was higher than that of pirfenidone and nintedanib, which are currently approved for IPF by the US Food and Drug Administration. That study suggested that in contrast to the expensive drugs mentioned above, TH may have broad application prospects in IPF. However, the role of TH in RILF has not been investigated so far.

It is generally accepted that TGF-β1 (19, 20) and the polarization of M2 phenotype macrophages (21, 22) play critical roles in multiple organ fibrosis as well as in RILF. Therefore, inhibition of the TGF-β1 signaling pathway may be a plausible strategy to alleviate RILF. It has been reported that TH significantly reduced liver fibrosis and skin fibrosis in mice by inhibiting transcriptional activation evoked by TGF-β/SMAD (23). Based on this evidence, we explored potential protective effects of TH in RILF in the present study.

MATERIALS AND METHODS

Animals and Radiation

Prednisone (PDN, HY-B0214) and 3,3′,5-triiodo-L-thyronine (T3, HY-A0070A) were purchased from MedChemExpress (Monmouth Junction, NJ, United States) and formulated in dimethyl sulfoxide solution. RILF was modeled in female C57BL/6 mice because they were likely to develop lung fibrosis (24). A total of 60 female C57BL/6J mice (Experimental Animal Center of Hubei province, China) aged 6–8 weeks were randomly assigned to five groups: control group (n = 12), aerosolized T3 group (n = 12), radiation treatment (RT) group (n = 12), RT + T3 group (n = 12), and RT + PDN (n = 12). Drug delivery of T3 or PDN was started on the first day of RT and continued daily for 1 month after RT. Each time, six mice were simultaneously exposed to a nebulizer chamber where T3 suspension was aerosolized at a dose of 40 μg/kg in 6 mL of phosphate buffered saline by an ordinary aerosol nebulizer (Omron) until atomization stopped (18). PDN was given intraperitoneally at 5 mg/kg. Mice developed pulmonary fibrosis after RT at a single dose of 16 Gy, as previously described (25). Mice were maintained in the specific pathogen-free animal facility of the Huazhong University of Science and Technology.

Micro-CT Scan

At weeks 6, 16, and 25 after radiation, three mice per group were randomly selected and sacrificed for thorax CT with a micro-CT scanner (Skyscan 1176, Bruker Inc, Billerica, MA, United States). The obtained CT images were imported into RadiAnt DICOM Viewer 3.4.1[1]. Lung slice image analysis was performed in the most typical slice that exhibited pulmonary fibrosis features. Four regions per slice were selected as measurement points: anterior and posterior in right and left lungs. Quantitative lung density of one mouse was represented as the mean Hounsfield unit (HU) value ± standard error of the mean (SEM).

Lung Histology and Fibrosis Score

Lung histological analysis was conducted as previously described (25). Briefly, three mice per group were euthanized for histology on the days of micro-CT chest scans. 25 weeks post RT, all remaining mice were killed by cervical dislocation. The left lungs were fixed in 4% paraformaldehyde for 24 h, embedded in paraffin, then cut into 5 μm thick slices and stained with hematoxylin-eosin stain and Masson's trichrome stain for collagen deposition.

The degree of pulmonary fibrosis was assessed by the modified Ashcroft score (26) on a range from 0 to 8 by examining five random microscopic fields at 200 × magnification. The final fibrosis degree was determined by an average score of all fields.

Expression of proteins was examined by immunohistochemistry (IHC) using staining with antibodies against αSMA (1:100, 14395-1-AP, Proteintech, Wuhan, China), F4/80 (1:400, ab111101, Abcam, United Kingdom), CD163 (1:200, ab182422, Abcam), iNOS (1:400, ab15323, Abcam), CD206 (1:200, ab64693, Abcam), and DIO2 (1:200, 26513-1-AP, Proteintech) according to previously described standard procedures (25). IHC results were semi-quantitatively analyzed. In brief, each sample was scored by combining immunoreactive signal intensity (negative = 0, weak = 1, moderate = 2, and strong = 3) and the percentage of positively stained cells (<10% positive cells = 0, 10%–30% positive cells = 1, 30%–50% positive cells = 2, and >50% positive cells = 3). All slides were individually analyzed by two pathologists, using a light microscope. All histological samples were randomly numbered in a blinded fashion to avoid observer bias.

Human Tissue Samples

Human lung samples were collected from the Department of Pathology of the Tongji Hospital, guided by Ethics Board at the hospital without the need for specific consent. Lung samples were obtained from pulmonary malignancy patients who underwent surgery more than 6 months after radiotherapy. Surgical lung specimens from patients that did not receive radiotherapy at the same period were included as control. All patients were operated at the Department of Thoracic Surgery in our hospital.

Patient Population and Follow-Up

In order to explore the role of hypothyroidism in RILF, we retrospectively analyzed data from nasopharyngeal carcinoma

[1]http://www.radiantviewer.com/

patients (NPC) treated by intensity-modulated radiation therapy (IMRT) at the Tongji Hospital of the Huazhong University of Science and Technology between January 2010 and December 2018, for thyroid dysfunction is prevalent after radiotherapy in NPC. The bilateral upper lungs were delineated on computed tomography (CT) scans, and lung doses were calculated. Eligible cases had to meet the following inclusion criteria: confirmed NPC without lung metastasis was present before radiotherapy; IMRT was conducted in our hospital, thus complete information was available; thyroid function was examined before and after IMRT; patients with hypothyroidism before IMRT were also included in the analysis; patients had a series of chest CT scans in the follow-up every 2–3 months within 2 years after treatment, and every 3–6 months later, finally annually after 5 years. We excluded subjects who had no irradiation dose in lungs, were diagnosed with connective tissue diseases, or were followed for less than 3 months. We restaged all patients using the 7th American Joint Committee on Cancer staging system. RILI was confirmed according to Common Terminology Criteria for Adverse Events (version 4.0).

Serum TH Assay

Total serum TH in NPC patients, including thyroid-stimulating hormone (TSH), free triiodothyronine (fT3), and free thyroxine (fT4) were measured in the Laboratory Department of our hospital by using the electrochemiluminescence immunoassay. The normal values for TSH, fT3, and fT4 were considered to be 0.35–4.94 μIU/mL, 1.71–3.71 pg/mL, and 0.7–1.48 ng/dL, respectively. The presence of abnormally elevated TSH in the serum was defined as hypothyroidism, with or without decreases in fT4.

Serum samples were prepared from mouse blood collected from eyelids using BD vacutainers on the days of micro-CT chest scans. In the remaining mice, serum was obtained at week 25 after RT using the same method. Total serum T3, T4, and TSH levels were measured using a T3 (ELK1339, ELK Biotechnology, Wuhan, China), T4 (ELK1204, ELK Biotechnology), and TSH (ELK2284, ELK Biotechnology) ELISA kits, following the manufacturers' protocols.

Hydroxyproline Assay

Right lung hydroxyproline level was analyzed with a hydroxyproline colorimetric assay kit (A030-2, Nanjing Jiancheng Bioengineering Institute, Nanjing, China) to assess collagen content as previously described (25).

Western Blot Analysis

Total protein was extracted from mouse left lung tissue, and its concentration was determined using the bicinchoninic acid assay. Then the constituent proteins were separated by electrophoresis in a 10% sodium dodecyl sulfate polyacrylamide gel, transferred to polyvinylidene fluoride membranes (Millipore, Billerica, MA, United States), covered with 5% milk at room temperature for 1 h, and incubated overnight with appropriate primary antibodies diluted in 0.1% Tween 20 (TBST) at 4°C. Primary antibodies against the following proteins were used: SMAD2/3 (8685T, Cell Signaling Technology, Beverly, MA, United States), p-SMAD2/3 (8828S, Cell Signaling Technology), TGF-β1 (3711S, Cell Signaling Technology); GAPDH (AC002, Abclonal, Wuhan, China); αSMA (14395-1-AP, Proteintech), collagen I (14695-1-AP, Proteintech), and PAI-1 (TA504056S, Origene, Maryland). After washing with TBST, the membranes were incubated with anti-rabbit or anti-mouse IgG horseradish peroxidase conjugated antibody (Cell Signaling Technology) for 1 h at room temperature. The protein bands were visualized using SuperSignale West Pico plus Chemiluminescent Substrate (Thermo Fisher Scientifice, Waltham, MA, United States).

Statistics

For the analysis of patient data, univariate analysis was performed by the chi-square test, Fisher's exact test, or Student's *t*-test to find possible risk factors associated with RILF. One-way analysis of variance (ANOVA) was used to reveal whether the grouping factor (treatment) differentially affected the results in more than three groups. Significant variables in univariate analysis were included into multivariate analysis with binary logistic regression model. Comparisons between the experimental groups for lung density, hydroxyproline content, fibrosis score, and protein expression levels were performed by ANOVA or Student's *t*-test using Prism 6.01 (GraphPad Software, San Diego, CA, United States) or SPSS 19.0 (IBM Corp, Armonk, NY, United States). All statistical analyses were conducted with a significance level of $\alpha = 0.05$ ($P < 0.05$).

RESULTS

Pulmonary Fibrosis Development in RT Treated Murine Model

Micro-CT scans performed at three time points after RT revealed increased number of diffuse and patchy shadows in the RT group. A trend of increase in lung density was observed after RT, which turned to be significantly consolidated at week 16 and gradually stabilized over 6 months, suggesting the development of RILF (**Figures 1A,B**). The irradiated field of mouse hair slowly turned gray during the post-irradiation period (**Figure 1C**). This indicated that our irradiated area coincided with the lungs of the mice. The western blot assay indicated that α-SMA, a myofibroblast activation marker that indicates fibrosis severity, and PAI-1 expressions increased significantly in lung tissue at week 16 after RT (**Figures 1D,E**). All these results suggested obvious fibrotic changes in lung tissues by week 16 post RT.

Attenuation of RILF Development in Mouse Lungs by TH

To test the potential radioprotective effect of TH in RILF, micro-CT and histological analyses of lung samples were performed under the light microscope at 6 months post RT in each experimental group. Manifestations such as the presence of alveolar wall thickening, fibrotic nodules, and destruction of alveolar structures after irradiation were less pronounced in the RT + T3 group but not in the RT + PDN group, as compared

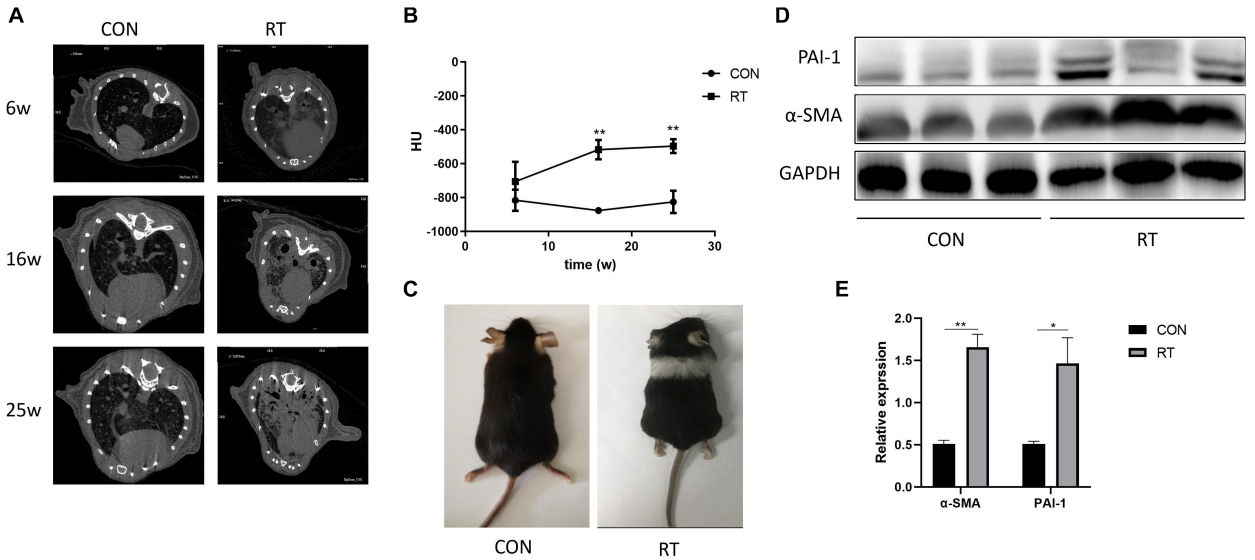

FIGURE 1 | Establishment and confirmation of radiation-induced lung fibrosis in a murine model. **(A)** Representative images of micro-CT scan for lung density at weeks (W) 6, 16, and 25 after irradiation in control or RT group. **(B)** Lung density evaluated by Hounsfield units (HU) presented as the mean ± SEM in radiation-treated and control C57BL/6J mice over time (n = 3); $^{*}P < 0.05$. **(C)** Photograph of a representative mouse at week 16 after radiation treatment. **(D,E)** The expression levels of α-SMA and PAI-1 in treated or control groups at week 16 was determined by western blotting. $^{**}P < 0.01$.

to the parameters in RT group according to hematoxylin and eosin staining (**Figure 2A**) and modified Ashcroft scale ($P < 0.01$, **Figure 2E**). No specific reduction of blue collagen deposition was observed by using Masson's trichrome stain (**Figure 2B**) at the end point of the experiment in RT + PDN group compared to the level of blue collagen in RT group. In contrast, we found that lung hydroxyproline content was dramatically decreased in RT + T3 group (**Figure 2B**; $P < 0.05$, **Figure 2H**) and α-SMA expression was markedly reduced (**Figure 2D**; $P < 0.01$, **Figure 2G**) compared to the values in RT group. Additionally, we observed appearance of abnormal morphological changes of patchy shadows, ground-glass opacity, and consolidation of large areas of lung tissues (**Figure 2C**) in RT and RT + PDN groups. However, the treatment of PDN could not inhibit the formation of pulmonary fibrosis caused by RT. We further quantitatively evaluated pulmonary fibrosis by estimating lung density using HU values. A reduction of approximately 324 HU (**Figure 2F**) was observed in RT + T3 group compared to the value in RT group at 25 weeks post RT.

Lack of Change in Serum TH Levels After Pulmonary Aerosolized T3 Delivery

In order to improve drug absorption in the lungs, aerosolized T3 (40 μg/kg) was administered to treated mice. We sought to verify whether this method of administration affected serum thyroid function levels and/or had possible side effects. Serum thyroid function tests were performed at 6, 16, and 25 weeks after radiation scheduled on micro-CT chest scans. There were no significant differences in serum T3, T4, and TSH levels among these groups at those three experimental points (**Figures 3A–C**). These results suggested that there was no obvious correlation between the improvement of RILF by aerosolized T3 and possible changes in serum TH levels.

Increased Risk of RILF in Patients With Hypothyroidism

Next, we conducted a single-center retrospective clinical case study. NPC patients that were regularly examined for serum TH and had chest CT scans before and after IMRT were included in this investigation. Dosimetric parameters of patients' lungs were calculated by a physicist. A total of 82 patients from January 2010 to August 2018 met the inclusion criteria. Two patients had already suffered from decreased thyroid function at the beginning of radiotherapy. Hypothyroidism is mainly caused by significantly elevated TSH. Of the 82 subjects, 61 males and 21 females, 38.75% of the patients developed hypothyroidism (**Figure 4A**) and 22.0% (18 patients) had mild RILF (**Figure 4B**) during the median follow-up time of 25.5 months (2–79 months).

In the univariate analysis, V50 Gy was 16.11 ± 13.59 cm^3 in the RILI group and 4.29 ± 5.77 cm^3 in the non-RILI group ($P = 0.002$). At the same time, hypothyroidism [odds ratio (OR) 4.095, 95% confidence interval (CI) 1.349–12.429, $P = 0.01$] and N stage ($P = 0.018$) were also significantly correlated with RILI, respectively, (**Table 1**). For the N stage, chi-square test showed that N3 stage was significantly associated with RILI (N3/N1: OR 6.60, 95%CI 1.515–28.747, $P = 0.014$; N3/N2: OR 5.20, 95%CI 1.181–22.891, $P = 0.047$), while N2 had no statistical significance compared with N1 (OR 1.269, 95%CI 0.366–4.398, $P = 0.707$). Finally, multivariate logistic regression analysis model found that V50 Gy (OR 1.173, 95% CI 1.077–1.278, $P < 0.001$) and hypothyroidism (OR 6.137, 95%CI 1.448–26.002, $P = 0.014$) were significantly associated with RILI (**Table 2**).

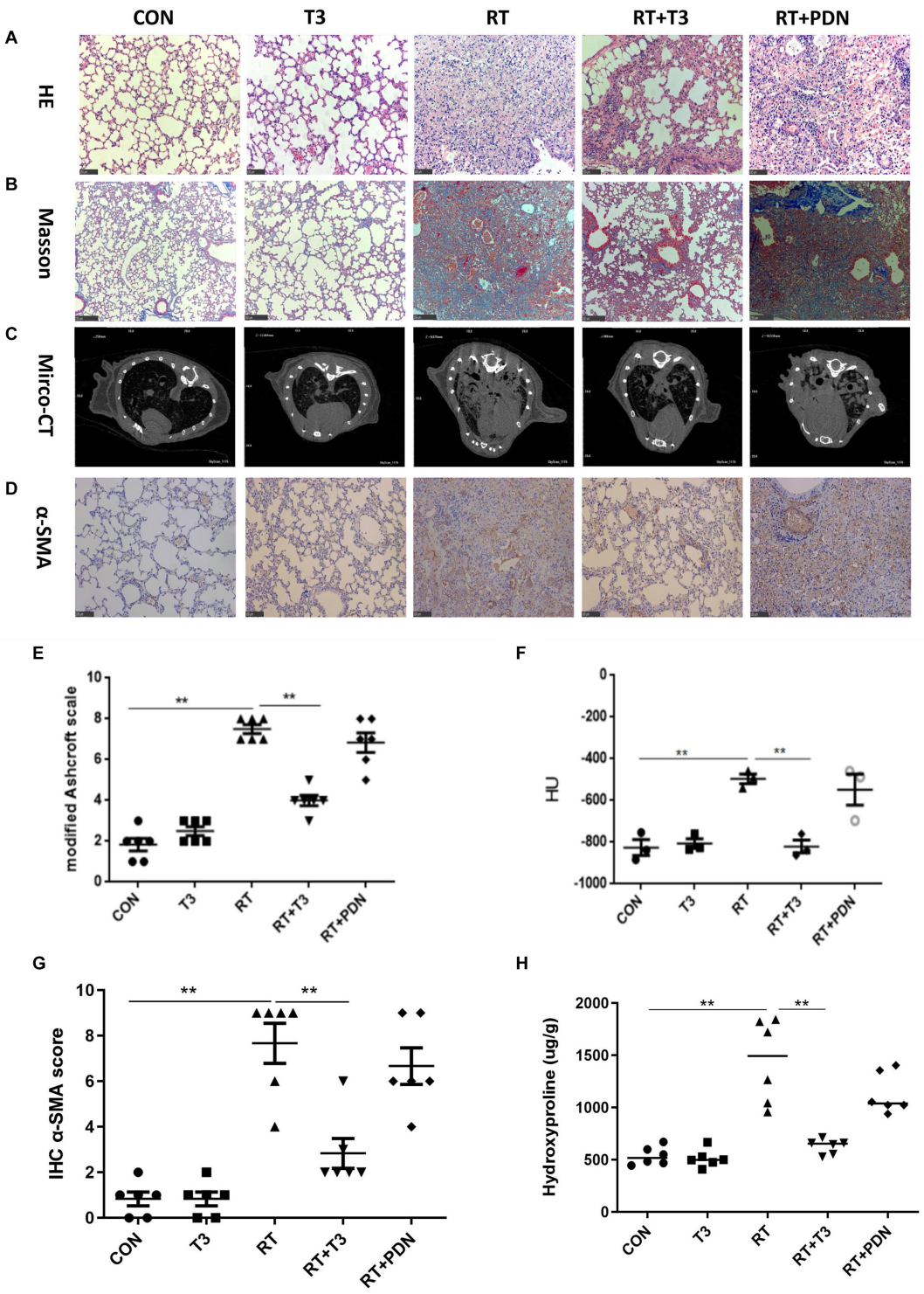

FIGURE 2 | Aerosolized T3 prevents pulmonary fibrosis post radiation treatment in mice. **(A,B)** Representative images of hematoxylin/eosin (200×; scale bar = 100 μm) and Masson's trichrome staining (100×; scale bar = 250 μm) from each group at 25 weeks after radiation treatment. **(C)** Images of representative micro-CT scans obtained at week 25 post radiation treatment in each group. **(D)** Representative immunohistochemistry staining images with α-SMA protein expression (200×; scale bar = 100 μm) in lung tissues in each group at the end of the experiment. **(E)** Grading of pulmonary fibrosis evaluated blindly by the modified previously described Ashcroft Scale at week 25 post radiation treatment. **(F)** Lung density values evaluated quantitatively by Hounsfield units derived from micro-CT scans at week 25 post irradiation (n = 3 for each individual group). **(G)** Immunohistochemistry scores for lung histopathological changes calculated using a semi-quantitative scoring system. **(H)** Collagen deposition in mouse right lung tissue assessed by measuring hydroxyproline content in each group at the end of the experiment. Data are expressed as the mean ± SEM, $^{*}P < 0.05$, $^{**}P < 0.01$. There were six mice in each group, except where indicated otherwise.

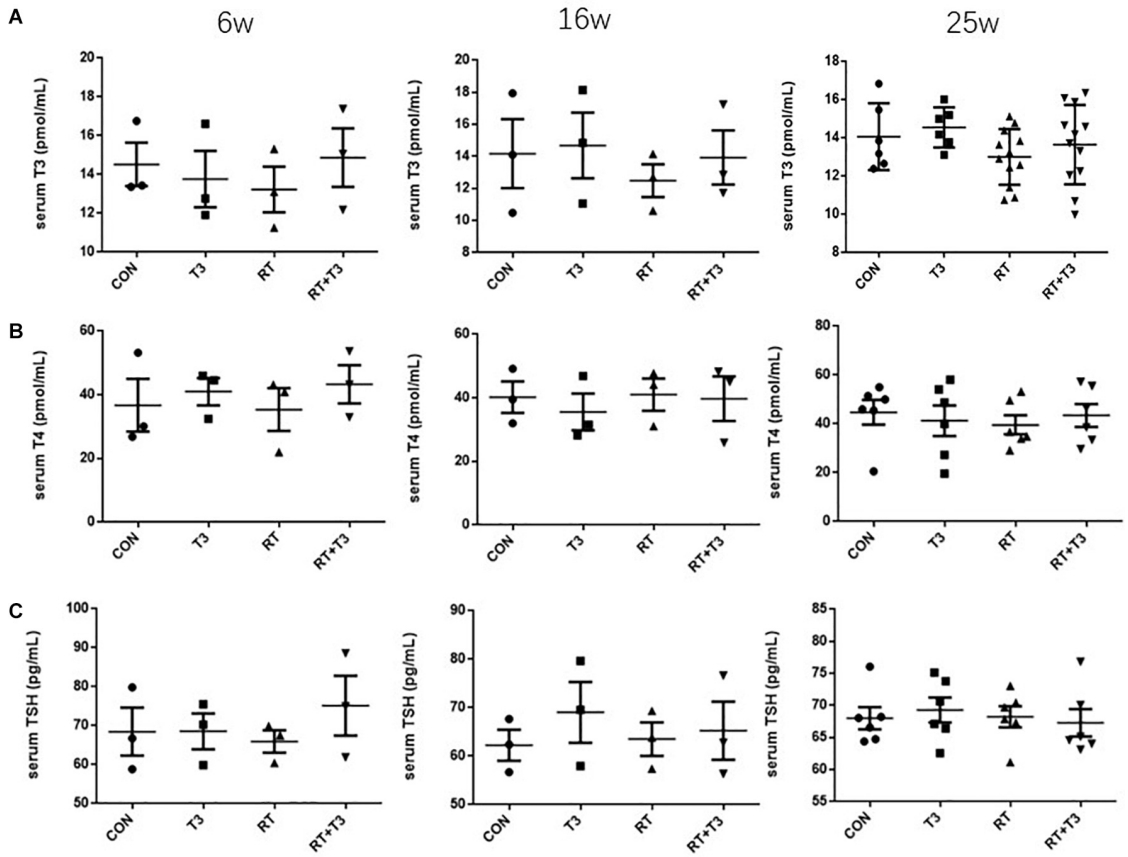

FIGURE 3 | Serum levels of thyroid hormones in mice at different time points. **(A–C)** Serum T3 (pmol/mL), T4 (pmol/mL), and TSH (pg/mL) levels in each experimental group at weeks 6, 16, and 25 after radiation treatment. No significant effect of time on concentrations was observed. Data are presented as the mean ± SEM. Weeks 6 and 16: $n = 3$; week 25: $n = 6$.

Higher Expression of DIO2 in Human RILF Tissues and Inhibition of TGF-β1 Signaling in the Lung by TH

Irradiated lung tissue was acquired from the surgical samples of five patients treated between 2011 and 2018 in our hospital. They were four squamous lung cancers and one lung metastases from colon carcinoma, who had relapsed *in situ* after radiation therapy. They all had received preoperative radiation treatment with a total dose ranging from 50 to 66 Gy between year 2008 and 2017. Untreated control lung samples were obtained from another five patients that did not receive any radiotherapy. In contrast to control samples, samples from patients with RILF displayed thickening of the alveolar septum or loss of alveolar structure and deposition of collagen fibers (**Figure 5A**). Considering the established role of iodothyronine deiodinase in T4 to active T3 conversion in tissues, we investigated the expression of DIO2 gene in order to verify the relationship between TH and RILF. Interestingly, DIO2 was highly expressed in epithelial cells within fibrotic regions of irradiated human lung tissue compared to its low-level control group (**Figures 5B,C**), suggesting that locally increased T3 concentration may improve energy metabolism of alveolar epithelial cells in the stressed fibrotic lung. Given the very limited number of human RILF tissue samples, this result implies a potentially protective role of TH on RILF.

In order to investigate the mechanisms whereby T3 exerts a protective effect on RILF, we evaluated the expression of pro-fibrotic growth factors in the lung tissues of mice using western blotting. Collagen I and TGF-β1 were found to be highly expressed in the lungs of RT and RT + PDN groups. In contrast, the expression of the principal pro-fibrotic factor TGF-β1 was decreased in sham RT and RT + T3 groups. In addition, western blotting also demonstrated that phosphorylated Smad2/3 levels were reduced in RT + T3 group (**Figures 5D,E**). These results suggested that T3 likely mitigated RILF by inhibiting expression of TGF-β1 and its downstream signaling molecules.

M2 but Not M1-Like Macrophages Accumulate in RILF

We explored the role of macrophages in clinical and preclinical animal levels. Compared with the control group, scattered macrophages could be found in the pulmonary fibrosis area of mice at 25 weeks after irradiation, which had the morphological characteristics of nuclear deviation and relatively large cell volume (**Figure 6A**). F4/80 (macrophage marker) positive

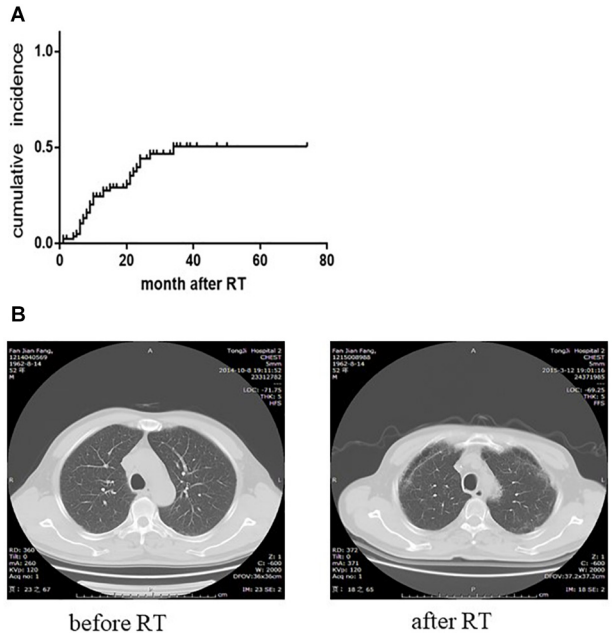

FIGURE 4 | Changes of serum thyroid function and bilateral pulmonary apex in patients with nasopharyngeal carcinoma after radiotherapy. **(A)** The cumulative incidence curve of radiation-induced hypothyroidism (two patients had already suffered from hypothyroidism before radiotherapy). The cumulative incidence was 49.58% at 3 years after radiotherapy. **(B)** CT images of patients before and after radiotherapy. Increased density of apex or superior lobe of lungs is seen on the follow-up CT examination after radiotherapy. Such changes without serious clinical symptoms could be classified as grade 1 radiation-induced lung injury.

TABLE 1 | Univariate analysis of radiation-induced lung injury risk factors.

Variable	RILI	non-RILI	*P* value
Gender			0.709
Male	14	47	
Female	4	17	
Year	48.6 ± 8.10	46.1 ± 9.60	0.333
T stage			0.481
T1-2	6	16	
T3-4	12	48	
N stage			**0.018**
N1	6	33	
N2	6	26	
N3	6	5	
M stage			0.22
M0	17	64	
M1	1	0	
V50 Gy, cm^3	16.11 ± 13.59	4.29 ± 5.77	**0.002**
Induction chemotherapy			0.108
NO	0	10	
YES	18	54	
Concurrent chemotherapy			0.678
NO	1	7	
YES	17	57	
Hypothyroidism			**0.01**
NO	6	43	
YES	12	21	

Values are expressed as number or mean ± SD. Variables that were significantly altered (P < 0.05) are highlighted. RILI, radiation induced lung injury; V50 Gy, normal lung volume that received radiation dose > 50 Gy.

TABLE 2 | Multivariate analysis of radiation-induced lung injury risk factors.

Variable	OR	95%CI	*P* value
Hypothyroidism	6.137	1.448–26.002	0.014
V50	1.173	1.077–1.278	<0.001

OR, odds ratio and CI, confidence interval.

cells were observed in pulmonary fibrosis tissues induced by irradiation than that of sham irradiation controls ($P < 0.01$, **Figures 6B,E**). Notably, in the lung tissues of RT + T3 group, but not RT + PDN group, the decrease of F4/80 positive macrophage proportion was detected along with the remission of pulmonary fibrosis ($P < 0.05$, **Figures 6B,E**). An obvious increase of M2-like macrophages (CD206 positive cells) were predominantly located in lung fibrosis tissues. Moreover, M2-like macrophages were significantly reduced in RT + T3 group ($P < 0.05$, **Figure 6E**). In contrast, there was no significant change in the proportion of M1-like macrophages (iNOS positive cells) in each group (**Figure 6E**). We then also assessed the accumulation of M2-like macrophages in irradiated human lung tissues. Compared to non-irradiated control lung tissues, M2-like macrophages (CD163 positive cells) were significantly increased in human pulmonary fibrotic area ($P < 0.05$, **Figures 6C,D**). These results suggest that M2 rather than M1-like macrophages are associated with RILF, and that aerosolized T3 attenuates RILF in mice accompanied by a decrease in M2-like macrophages in the fibrosis tissue.

DISCUSSION

Radiation induced lung fibrosis is a common complication in the management of radiotherapy and it seriously affects patients' quality of life. To date, however, there is still no viable therapeutic strategy for RILF, and its mechanism remains unclear. With the growing incidence and mortality rate of lung cancer worldwide (27), therapies that prevent RILF represent an unmet clinical need. In the current study, we have demonstrated a therapeutic effect of aerosolized T3 treatment in a rodent experiment model during the post RT phase. Secondly, we showed that the antifibrotic effect of T3 does not require increased serum levels of T3, T4, or TSH, suggesting that aerosolized delivery may be effective without side effects of iatrogenically elevated thyroid hormones. Thirdly, we found that hypothyroidism increases the risk of RILF in NPC patients; moreover, M2-like macrophages were associated with RILF. Considering these results, we suggest the delivery of aerosolized T3 as a new potential treatment strategy for RILF attenuation.

Thyroid hormone regulates diverse biological processes, from growth to metabolism, and is critically important for nearly all tissues (28–30). Both T4 and T3 can be deiodinated either into

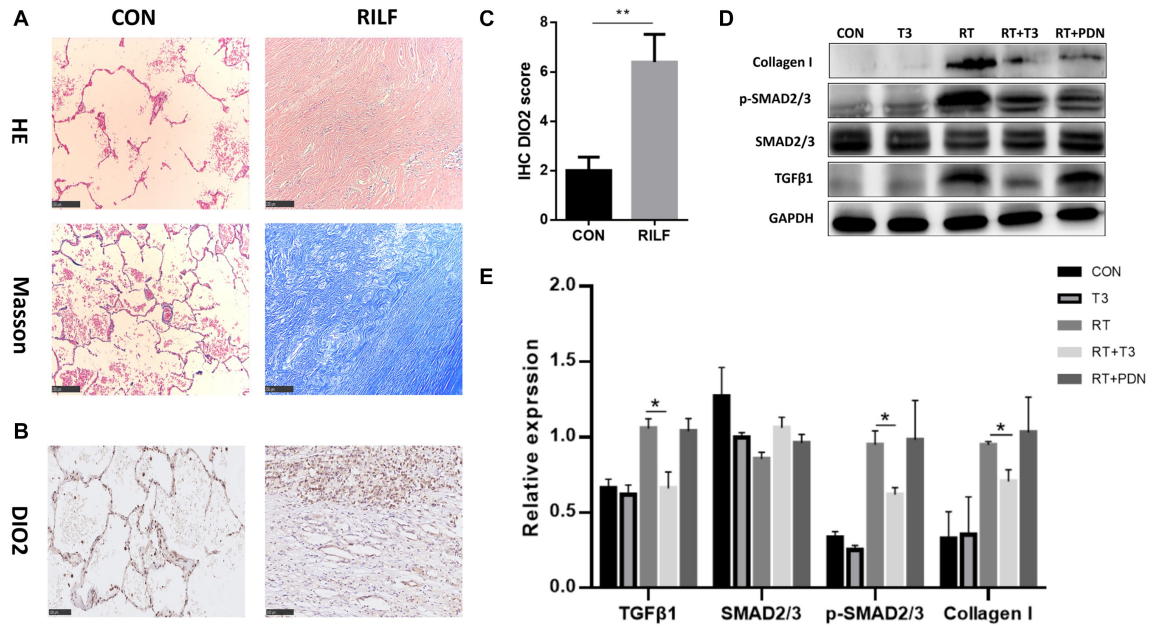

FIGURE 5 | Increased DIO2 expression in lung tissue after radiation treatment and inhibition of the TGF-β1 signaling pathway by thyroid hormone. **(A)** Representative images of hematoxylin/eosin and Masson's trichrome staining (100×; scale bar = 250 μm) from treated (n = 5) and control (n = 5) patients. Absence of alveolar structures and apparent collagen deposition can be seen in the irradiated lung tissue. Representative immunohistochemistry staining **(B)** and immunohistochemistry scores **(C)** for DIO2 (200×; scale bar = 100 μm) in human lung tissue samples (n = 5) showing DIO2 expression in the lung affected by radiation-induced lung fibrosis (left) and in control lung (right). **(D,E)** Western blots of profibrotic growth proteins (collagen I, TGF-β1) and p-Smad2/3, a downstream protein in the TGF-β1 signaling pathway, in mouse lung tissues of each group at 25 weeks post radiation treatment are shown. *P < 0.05; **P < 0.01.

the active form by DIO1 and DIO2 or into the inactive form — by DIO3 (31). DIO2 plays a major role in the synthesis of biologically active TH. Increased expression of DIO2 in tissues may reflect either a lack of TH or the need for increased metabolism. Previous studies have shown that hypothyroidism is associated with poor prognosis in many critical diseases, including heart failure (32), non-alcoholic fatty liver disease (33), chronic kidney disease (34), and lung disease (28). Hypothyroid mice suffered more severe lung injury than those with normal serum TH levels in a mouse model of ventilator-induced lung injury, and administration of T3 reduced chemokine and cytokine levels in *Dio2* knockout mice (16).

Our results showed that the relationship between both the expression of DIO2 protein as well as TH levels and RILF was consistent with the above results, indicating that there is a correlation between RILF and TH. It is common to find pulmonary shadows in follow-up CT image examinations in some NPC patients due to upper lungs being exposed to the radiation field, which could also be classified as RILI. According to two population-based studies, the incidence of radiation-induced hypothyroidism varied from 27 to 70% in patients that received a dose of 7.5–40 Gy (35, 36). The incidence of hypothyroidism induced by radiation was 38.75% during the follow-up in our study. All patients observed in this cohort had subclinical hypothyroidism. The reasons for this finding likely include insufficient follow-up duration in a small sample and wide use of IMRT in our hospital (37, 38). Bhandare's study (39) reported that the median latency of clinical hypothyroidism was 4.8 years. RILF occurred in 18 (22.0%) of 82 patients from our cohort during a median follow-up of 25.5 months (range 2–79 months). The proportion of RILF in subjects with hypothyroidism was obviously higher than that in subjects with normal thyroid function, and hypothyroidism was significantly associated with RILF in multivariate logistic regression analysis model. This finding may help understanding the mechanisms of RILF occurrence.

The pathological mechanism of hypothyroidism leading to RILF remains unclear. One possible link may lie in thyroid transcription factor-1 (TTF-1). It plays an important role in the differentiation and formation of both thyroid and lung. Increased expression of TTF-1 was found in some thyroiditis patients (40). In the lung, TTF-1 regulates the differentiation of alveolar epithelial cells and the expression of alveolar surfactant protein, which is very important to maintain alveolar ventilation function and repair lung injury (41). Another possible link maybe related to the biological functions of thyroid hormone, which is not only an important in regulating human endocrine metabolism, but also affects mitochondrial function and transformation. Mitochondrial damage contributes to the development of RILF.

Treatment with TH, an old but probably underused drug, may be utilized in cases with pathologies other than thyroid dysfunction. Some synthetic TH mimetics have shown encouraging results in the experimental treatment of obesity, dyslipidemia, and liver cancer (42). T3 also could alleviate the pulmonary fibrosis in TGF transgenic mice, but the mechanism is not fully explained (18). Recent studies showed that TH

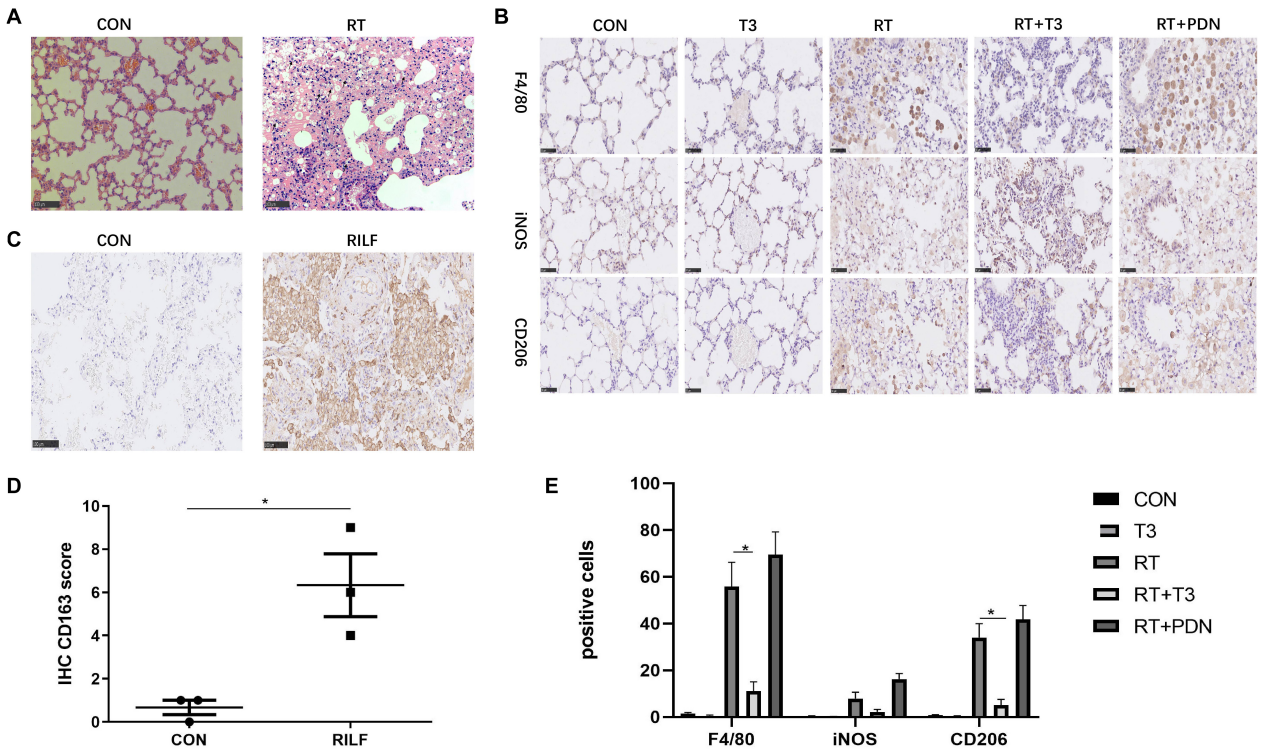

FIGURE 6 | Macrophage accumulation in the lungs of mice and humans after thoracic radiotherapy. **(A)** Representative images of macrophage in mice lung 25 weeks post irradiation compared to controls in HE staining. arrows indicated macrophages (200×; scale bar = 100 μm). **(B)** Representative images of total, M1 and M2 macrophages in lung tissues of each group identified by F4/80, iNOS, and CD206, respectively, using immunohistochemistry (400×; scale bar = 50 μm). **(C)** Representative immunohistochemistry images of CD163 positive macrophage in lung tissues (200×; scale bar = 100 μm). **(D)** Imimmunohistochemistry assessment for macrophage quantification in lungs of control and irradiation patients (n = 3 per group). **(E)** The numbers of F4/80, iNOS, and CD206 positive macrophages were counted at high magnification field and take the average of three times (n = 3 per group), data are expressed as the mean ± SEM, $^*P < 0.05$.

attenuated skin and pulmonary fibrosis induced by bleomycin and liver fibrosis caused by carbon tetrachloride in mouse models. These actions may be explained by TH effects on mitochondrial biogenesis and inhibition of TGF-β1-dependent transcription (18, 23). TGF-β1 plays a critical role in profibrotic signals: about 80% of the proteins encoded by genes dysregulated in pulmonary tissues from IPF patients have been reported to be associated with TGF-β1 signaling pathway (43). RILF is similar to other forms of lung fibrosis, especially IPF. Aerosolized TH treatment significantly reduced expression of profibrotic growth proteins, including collagen I, PAI-1 and TGF-β1, whereas no such down-regulation was observed in the RT + PDN group in our study. We concluded that PDN did not inhibit the elevation of TGF-β1 and thus had no anti-fibrotic effect previously suggested by Arata et al. (44). Furthermore, we also consistently found that expression level of phosphorylated Smad2/3, an important transcription factor downstream of the TGF-β1 pathway, was significantly decreased in TH treatment group.

A recent study showed that M2-like tissue-infiltrating macrophages played an important role in RILF (21), but the relationship between local or recruited alveolar macrophages and RILF is still worthy of further study (45). Alveolar macrophages are highly heterogeneous. M1 like macrophages mediate resistance to pathogens, while M2 like macrophages have anti-inflammatory and repair functions (46). T3 can promote the polarization of mouse bone marrow-derived monocytes to M1 macrophages phenotype and inhibit activated M2 macrophage phenotype (47). Tumor infiltrating myeloid-derived cells secrete high levels of TGFβ, and up-regulate CD206 expression (48). In the pulmonary fibrosis model induced by TGF-β1, reduced pulmonary M2 macrophages had a significant anti-fibrosis effect (49). A study suggested that the development of RILF may depend on TGFβ to promote the transformation of macrophages into M2 phenotype (50). However, glucocorticoids can reduce the number of M1 phenotype differentiation of macrophages (51) and have the ability to promote the activation of M2 phenotype macrophages (52). In our study, we also found that the M2 macrophages in lung tissues did not decrease, and even showed a trend of increasing in RT + PDN group. This may partly explain the role of thyroid hormone in alleviating RILF, which may be associated with TGFβ1 and macrophages.

Our study had some limitations. First, our clinical data were obtained from a retrospective analysis of a small size cohort that did not have very long follow-up. Secondly, we included into the analysis the patients that did not receive thoracic radiotherapy and had no advanced RILF. Thirdly, several

questions related to the mechanism of TH involvement were not studied. For example, we mainly focused on the DIO2, whereas other deiodinases were not detected, and the mechanism of the role of DIO2 in the development of fibrosis after irradiation need to be further explored. Furthermore, the mechanism underlying inhibitory effects of TH on TGF-β1/SMAD signaling pathway and M2-like macrophage has to be elucidated.

In conclusion, despite recent advances in radiation treatment planning and image-guide radiation therapy, RILF still remains a limiting factor for local tumor control by radiotherapy. To the best of our knowledge, our study for the first time demonstrated that hypothyroidism maybe associated with an increased risk of RILF in patients and provided the first evidence that T3 may be a safe therapeutic option to prevent RILF.

DATA AVAILABILITY STATEMENT

All datasets generated for this study are included in the article/supplementary material.

ETHICS STATEMENT

The studies involving human participants were reviewed and approved by Ethics committee of Tongji hospital, Huazhong University of Science and Technology. The patients/participants provided their written informed consent to participate in this study. The animal study was reviewed and approved by Institutional Animal Care and Use Committee of the Tongji Medical College at the Huazhong University of Science and Technology. Written informed consent was obtained from the individual(s) for the publication of any potentially identifiable images or data included in this manuscript.

AUTHOR CONTRIBUTIONS

LL, XN, and MY carried out experiments. LL and XN analyzed data. WQ and XY designed the experiments. LL, FL, and BW wrote the manuscript. All authors had final approval of the submitted and published versions.

FUNDING

This work was supported by the National Natural Science Foundation of China (Grant No. 81472921).

ACKNOWLEDGMENTS

We thank the members of our laboratory. We would also like to thank Editage (www.editage.cn) for English language editing.

REFERENCES

1. De Ruysscher D, Niedermann G, Burnet NG, Siva S, Lee A, Hegi-Johnson F. Radiotherapy toxicity. *Nat Rev Dis Primers*. (2019) 5:13. doi: 10.1038/s41572-019-0064-5
2. Giuranno L, Ient J, De Ruysscher D, Vooijs MA. Radiation-induced lung injury (RILI). *Front Oncol*. (2019) 9:877. doi: 10.3389/fonc.2019.00877
3. Xiong S, Pan X, Xu L, Yang Z, Guo R, Gu Y, et al. Regulatory T cells promote beta-catenin–mediated epithelium-to-mesenchyme transition during radiation-induced pulmonary fibrosis. *Int J Radiat Oncol Biol Phys*. (2015) 93:425–35. doi: 10.1016/j.ijrobp.2015.05.043
4. Rajan RR, Chandrasekharan G. Pulmonary injury associated with radiation therapy – assessment, complications and therapeutic targets. *Biomed Pharmacother*. (2017) 89:1092–104. doi: 10.1016/j.biopha.2017.02.106
5. Simone CN. Thoracic radiation normal tissue injury. *Semin Radiat Oncol*. (2017) 27:370–7. doi: 10.1016/j.semradonc.2017.04.009
6. Beach TA, Groves AM, Williams JP, Finkelstein JN. Modeling radiation-induced lung injury: lessons learned from whole thorax irradiation. *Int J Radiat Biol*. (2018) 96:129–44. doi: 10.1080/09553002.2018.1532619
7. Bickelhaupt S, Erbel C, Timke C, Wirkner U, Dadrich M, Flechsig P, et al. Effects of CTGF blockade on attenuation and reversal of radiation-induced pulmonary fibrosis. *J Natl Cancer Inst*. (2017) 109:djw339. doi: 10.1093/jnci/djw339
8. Choi SH, Hong ZY, Nam JK, Lee HJ, Jang J, Yoo RJ, et al. A hypoxia-induced vascular endothelial-to-mesenchymal transition in development of radiation-induced pulmonary fibrosis. *Clin Cancer Res*. (2015) 21:3716–26. doi: 10.1158/1078-0432.CCR-14-3193
9. Flechsig P, Dadrich M, Bickelhaupt S, Jenne J, Hauser K, Timke C, et al. LY2109761 attenuates radiation-induced pulmonary murine fibrosis via reversal of TGF-beta and BMP-associated proinflammatory and proangiogenic signals. *Clin Cancer Res*. (2012) 18:3616–27. doi: 10.1158/1078-0432.CCR-11-2855
10. Biondi B, Wartofsky L. Treatment with thyroid hormone. *Endocr Rev*. (2014) 35:433–512. doi: 10.1210/er.2013-1083
11. Ceresini G, Urban ML, Corradi D, Lauretani F, Marina M, Usberti E, et al. Association between idiopathic retroperitoneal fibrosis and autoimmune thyroiditis: a case-control study. *Autoimmun Rev*. (2015) 14:16–22. doi: 10.1016/j.autrev.2014.08.006
12. Oldham JM, Kumar D, Lee C, Patel SB, Takahashi-Manns S, Demchuk C, et al. Thyroid disease is prevalent and predicts survival in patients with idiopathic pulmonary fibrosis. *Chest*. (2015) 148:692–700. doi: 10.1378/chest.14-2714
13. Kim D, Kim W, Joo SK, Bae JM, Kim JH, Ahmed A. Subclinical hypothyroidism and low-normal thyroid function are associated with nonalcoholic steatohepatitis and fibrosis. *Clin Gastroenterol Hepatol*. (2018) 16:123–31.e1. doi: 10.1016/j.cgh.2017.08.014
14. Razvi S, Jabbar A, Pingitore A, Danzi S, Biondi B, Klein I, et al. Thyroid hormones and cardiovascular function and diseases. *J Am Coll Cardiol*. (2018) 71:1781–96. doi: 10.1016/j.jacc.2018.02.045
15. Hataya Y, Igarashi S, Yamashita T, Komatsu Y. Thyroid hormone replacement therapy for primary hypothyroidism leads to significant improvement of renal function in chronic kidney disease patients. *Clin Exp Nephrol*. (2013) 17:525–31. doi: 10.1007/s10157-012-0727-y
16. Barca-Mayo O, Liao XH, DiCosmo C, Dumitrescu A, Moreno-Vinasco L, Wade MS, et al. Role of type 2 deiodinase in response to acute lung injury (ALI) in mice. *Proc Natl Acad Sci USA*. (2011) 108:E1321–9. doi: 10.1073/pnas.1109926108
17. Ma SF, Xie L, Pino-Yanes M, Sammani S, Wade MS, Letsiou E, et al. Type 2 deiodinase and host responses of sepsis and acute lung injury. *Am J Respir Cell Mol Biol*. (2011) 45:1203–11. doi: 10.1165/rcmb.2011-0179OC
18. Yu G, Tzouvelekis A, Wang R, Herazo-Maya JD, Ibarra GH, Srivastava A, et al. Thyroid hormone inhibits lung fibrosis in mice by improving epithelial mitochondrial function. *Nat Med*. (2018) 24:39–49. doi: 10.1038/nm.4447
19. Stewart AG, Thomas B, Koff J. TGF-beta: master regulator of inflammation and fibrosis. *Respirology*. (2018) 23:1096–7. doi: 10.1111/resp.13415
20. Yuan X, Liao Z, Liu Z, Wang LE, Tucker SL, Mao L, et al. Single nucleotide polymorphism at rs1982073:T869C of the TGFbeta 1 gene is associated with the risk of radiation pneumonitis in patients with non-small-cell lung cancer

treated with definitive radiotherapy. *J Clin Oncol*. (2009) 27:3370–8. doi: 10.1200/JCO.2008.20.6763
21. Meziani L, Mondini M, Petit B, Boissonnas A, Thomas DMV, Mercier O, et al. CSF1R inhibition prevents radiation pulmonary fibrosis by depletion of interstitial macrophages. *Eur Respir J*. (2018) 51:1702120. doi: 10.1183/13993003.02120-2017
22. Wynn TA, Vannella KM. Macrophages in tissue repair, regeneration, and fibrosis. *Immunity*. (2016) 44:450–62. doi: 10.1016/j.immuni.2016.02.015
23. Alonso-Merino E, Martin OR, Ruiz-Llorente L, Martinez-Iglesias OA, Velasco-Martin JP, Montero-Pedrazuela A, et al. Thyroid hormones inhibit TGF-beta signaling and attenuate fibrotic responses. *Proc Natl Acad Sci USA*. (2016) 113:E3451–60. doi: 10.1073/pnas.1506113113
24. Dabjan MB, Buck CM, Jackson IL, Vujaskovic Z, Marples B, Down JD. A survey of changing trends in modelling radiation lung injury in mice: bringing out the good, the bad, and the uncertain. *Lab Invest*. (2016) 96:936–49. doi: 10.1038/labinvest.2016.76
25. Qin W, Liu B, Yi M, Li L, Tang Y, Wu B, et al. Antifibrotic agent pirfenidone protects against development of radiation-induced pulmonary fibrosis in a murine model. *Radiat Res*. (2018) 190:396–403. doi: 10.1667/RR15017.1
26. Hubner RH, Gitter W, El MN, Mathiak M, Both M, Bolte H, et al. Standardized quantification of pulmonary fibrosis in histological samples. *Biotechniques*. (2008) 44:507–11, 514–7. doi: 10.2144/000112729
27. Bray F, Ferlay J, Soerjomataram I, Siegel RL, Torre LA, Jemal A. Global cancer statistics 2018: GLOBOCAN estimates of incidence and mortality worldwide for 36 cancers in 185 countries. *CA Cancer J Clin*. (2018) 68:394–424. doi: 10.3322/caac.21492
28. Breitzig MT, Alleyn MD, Lockey RF, Kolliputi N. Thyroid hormone: a resurgent treatment for an emergent concern. *Am J Physiol Lung Cell Mol Physiol*. (2018) 315:L945–50. doi: 10.1152/ajplung.00336.2018
29. Mullur R, Liu YY, Brent GA. Thyroid hormone regulation of metabolism. *Physiol Rev*. (2014) 94:355–82. doi: 10.1152/physrev.00030.2013
30. Yen PM. Physiological and molecular basis of thyroid hormone action. *Physiol Rev*. (2001) 81:1097–142. doi: 10.1152/physrev.2001.81.3.1097
31. Gereben B, McAninch EA, Ribeiro MO, Bianco AC. Scope and limitations of iodothyronine deiodinases in hypothyroidism. *Nat Rev Endocrinol*. (2015) 11:642–52. doi: 10.1038/nrendo.2015.155
32. Mitchell JE, Hellkamp AS, Mark DB, Anderson J, Johnson GW, Poole JE, et al. Thyroid function in heart failure and impact on mortality. *Jacc Heart Fail*. (2013) 1:48–55. doi: 10.1016/j.jchf.2012.10.004
33. Ferrandino G, Kaspari RR, Spadaro O, Reyna-Neyra A, Perry RJ, Cardone R, et al. Pathogenesis of hypothyroidism-induced NAFLD is driven by intra- and extrahepatic mechanisms. *Proc Natl Acad Sci USA*. (2017) 114:E9172–80. doi: 10.1073/pnas.1707797114
34. Zhang Y, Chang Y, Ryu S, Cho J, Lee WY, Rhee EJ, et al. Thyroid hormone levels and incident chronic kidney disease in euthyroid individuals: the Kangbuk Samsung Health Study. *Int J Epidemiol*. (2014) 43:1624–32. doi: 10.1093/ije/dyu126
35. Colevas AD, Read R, Thornhill J, Adak S, Tishler R, Busse P, et al. Hypothyroidism incidence after multimodality treatment for stage III and IV squamous cell carcinomas of the head and neck. *Int J Radiat Oncol Biol Phys*. (2001) 51:599–604. doi: 10.1016/s0360-3016(01)01688-1
36. Kumpulainen EJ, Hirvikoski PP, Virtaniemi JA, Johansson RT, Simonen PM, Terava MT, et al. Hypothyroidism after radiotherapy for laryngeal cancer. *Radiother Oncol*. (2000) 57:97–101. doi: 10.1016/s0167-8140(00)00276-0
37. Lin Z, Chen L, Fang Y, Cai A, Zhang T, Wu VW. Longitudinal study on the correlations of thyroid antibody and thyroid hormone levels after radiotherapy in patients with nasopharyngeal carcinoma with radiation-induced hypothyroidism. *Head Neck*. (2014) 36:171–5. doi: 10.1002/hed.23285
38. Wu YH, Wang HM, Chen HH, Lin CY, Chen EY, Fan KH, et al. Hypothyroidism after radiotherapy for nasopharyngeal cancer patients. *Int J Radiat Oncol Biol Phys*. (2010) 76:1133–9. doi: 10.1016/j.ijrobp.2009.03.011
39. Bhandare N, Kennedy L, Malyapa RS, Morris CG, Mendenhall WM. Primary and central hypothyroidism after radiotherapy for head-and-neck tumors. *Int J Radiat Oncol Biol Phys*. (2007) 68:1131–9. doi: 10.1016/j.ijrobp.2007.01.029
40. Huang H, Li X, Lin L, Shi Y, Lin X, Li L, et al. Upregulation of thyroid transcription factor-1 and human leukocyte antigen class I in Hashimoto's disease providing a clinical evidence for possible triggering autoimmune reaction. *Eur J Endocrinol*. (2011) 164:795–800. doi: 10.1530/EJE-10-0960
41. Boggaram V. Thyroid transcription factor-1 (TTF-1/Nkx2.1/TITF1) gene regulation in the lung. *Clin Sci*. (2009) 116:27–35. doi: 10.1042/CS20080068
42. Kowalik MA, Columbano A, Perra A. Thyroid Hormones, Thyromimetics and their metabolites in the treatment of liver disease. *Front Endocrinol*. (2018) 9:382. doi: 10.3389/fendo.2018.00382
43. Kaminski N, Allard JD, Pittet JF, Zuo F, Griffiths MJ, Morris D, et al. Global analysis of gene expression in pulmonary fibrosis reveals distinct programs regulating lung inflammation and fibrosis. *Proc Natl Acad Sci USA*. (2000) 97:1778–83. doi: 10.1073/pnas.97.4.1778
44. Azuma A. Pirfenidone treatment of idiopathic pulmonary fibrosis. *Ther Adv Respir Dis*. (2012) 6:107–14. doi: 10.1177/1753465812436663
45. Zhou X, Moore BB. Location or origin? What is critical for macrophage propagation of lung fibrosis? *Eur Respir J*. (2018) 51:1800103. doi: 10.1183/13993003.00103-2018
46. Byrne AJ, Mathie SA, Gregory LG, Lloyd CM. Pulmonary macrophages: key players in the innate defence of the airways. *Thorax*. (2015) 70:1189–96. doi: 10.1136/thoraxjnl-2015-207020
47. Perrotta C, Buldorini M, Assi E, Cazzato D, De Palma C, Clementi E, et al. The thyroid hormone triiodothyronine controls macrophage maturation and functions: protective role during inflammation. *Am J Pathol*. (2014) 184:230–47. doi: 10.1016/j.ajpath.2013.10.006
48. Flavell RA, Sanjabi S, Wrzesinski SH, Licona-Limón P. The polarization of immune cells in the tumour environment by TGFbeta. *Nat Rev Immunol*. (2010) 10:554–67. doi: 10.1038/nri2808
49. Murray LA, Chen Q, Kramer MS, Hesson DP, Argentieri RL, Peng X, et al. TGF-beta driven lung fibrosis is macrophage dependent and blocked by serum amyloid P. *Int J Biochem Cell Biol*. (2011) 43:154–62. doi: 10.1016/j.biocel.2010.10.013
50. Park HR, Jo SK, Jung U. Ionizing radiation promotes epithelial-to-mesenchymal transition in lung epithelial cells by TGF-β-producing M2 macrophages. *In Vivo*. (2019) 33:1773–84. doi: 10.21873/invivo.11668
51. Xie Y, Tolmeijer S, Oskam JM, Tonkens T, Meijer AH, Schaaf MJM. Glucocorticoids inhibit macrophage differentiation towards a pro-inflammatory phenotype upon wounding without affecting their migration. *Dis Model Mech*. (2019) 12:dmm037887. doi: 10.1242/dmm.037887
52. Heideveld E, Hampton-O'Neil LA, Cross SJ, van Alphen FPJ, van den Biggelaar M, Toye AM, et al. Glucocorticoids induce differentiation of monocytes towards macrophages that share functional and phenotypical aspects with erythroblastic island macrophages. *Haematologica*. (2018) 103:395–405. doi: 10.3324/haematol.2017.179341

Conflict of Interest: The authors declare that the research was conducted in the absence of any commercial or financial relationships that could be construed as a potential conflict of interest.

frontiers in Oncology

MINI REVIEW
published: 06 October 2020
doi: 10.3389/fonc.2020.01708

Application of Radiomics for the Prediction of Radiation-Induced Toxicity in the IMRT Era: Current State-of-the-Art

*Isacco Desideri, Mauro Loi, Giulio Francolini, Carlotta Becherini, Lorenzo Livi and Pierluigi Bonomo**

Radiation Oncology, Azienda Ospedaliero-Universitaria Careggi, University of Florence, Florence, Italy

Normal tissue complication probability (NTCP) models that were formulated in the Quantitative Analyses of Normal Tissue Effects in the Clinic (QUANTEC) are one of the pillars in support of everyday's clinical radiation oncology. Because of steady therapeutic refinements and the availability of cutting-edge technical solutions, the ceiling of organs-at-risk-sparing has been reached for photon-based intensity modulated radiotherapy (IMRT). The possibility to capture heterogeneity of patients and tissues in the prediction of toxicity is still an unmet need in modern radiation therapy. Potentially, a major step towards a wider therapeutic index could be obtained from refined assessment of radiation-induced morbidity at an individual level. The rising integration of quantitative imaging and machine learning applications into radiation oncology workflow offers an unprecedented opportunity to further explore the biologic interplay underlying the normal tissue response to radiation. Based on these premises, in this review we focused on the current-state-of-the-art on the use of radiomics for the prediction of toxicity in the field of head and neck, lung, breast and prostate radiotherapy.

Keywords: Radiomics, Intensity modulated radiotherapy, xerostomia, radiation induced lung injury, cardiac toxicity, lower gastro-intestinal toxicity

OPEN ACCESS

Edited by:
Tiziana Rancati,
Istituto Nazionale dei Tumori (IRCCS), Italy

Reviewed by:
Arjen Van Der Schaaf,
University Medical Center Groningen, Netherlands
Elisa Scalco,
Italian National Research Council, Italy

***Correspondence:**
Pierluigi Bonomo
bonomop@aou-careggi.toscana.it
orcid.org/0000-0001-8999-5208

Specialty section:
This article was submitted to Radiation Oncology, a section of the journal Frontiers in Oncology

Received: *13 February 2020*
Accepted: *30 July 2020*
Published: *06 October 2020*

Citation:
Desideri I, Loi M, Francolini G, Becherini C, Livi L and Bonomo P (2020) Application of Radiomics for the Prediction of Radiation-Induced Toxicity in the IMRT Era: Current State-of-the-Art. Front. Oncol. 10:1708. doi: 10.3389/fonc.2020.01708

INTRODUCTION

The seminal QUANTEC collection (1) provided a comprehensive set of recommendations for the estimation of normal tissue complication probability (NTCP) that were largely based on empirical data, whereas the earlier influential paper by Emami (2) was mainly based on a consensus of experts. Leveraging the available published evidence into definitions of dose-volume relationships for most organs at risk epitomized the paradigm shift of QUANTEC.

However, its analyses relied on data from a time when predominantly 3D-conformal radiotherapy (3DCRT) was used with relatively uniform dose distributions. The advent of intensity modulated radiotherapy (IMRT) led to an unprecedented improvement in radiation ballistics (3), allowing for exquisite precision in dose distribution. Over the years, through constant optimization of IMRT techniques (4), the ceiling of organ-at-risk sparing has been reached: in the frame of photon therapy delivery, incremental advances in the reduction of radiation-induced toxicity are unlikely to occur, mainly due to limits dictated by physics. Ideally, further improvement must

come from better shaping the dose distribution, which can only be personally optimized if precise knowledge (5) of dose-effect relationships is used. The current state-of-the-art of relying exclusively on NTCP models from QUANTEC has its own caveats (6): above all, the lack of integration of biologic heterogeneity and patients' individual factors such as age, comorbidities, pre-existing organ dysfunction, and use of systemic agents represent the most limiting factors. In addition, an overarching issue is represented by the paucity of external validation studies (7, 8) for most NTCP models.

Overall, the absence of predictive biomarkers for radiation-related morbidity is a major unmet need in modern radiation therapy. Within the last 10 years (9, 10), the advent of radiomics has reshaped the approach to medical images, based on the hypothesis that they are inherently able to convey information on the underlying physiopathology. Standardization in image acquisition, high-throughput generation of objective descriptors and extensive data-mining characterized the transition from purely qualitative to quantitative imaging (11). As outlined in the pivotal CRUK-EORTC consensus review (12), distinct features can be envisaged in the re-thinking of imaging as a biomarker: non-invasiveness, serial assessment, comprehensive tumor mapping, repeatability, and cost-effectiveness. In the perspective of personalized oncology (13) as currently implemented in the clinic, the use of quantitative imaging may allow us to overcome the known limits associated with molecular profiling. Several applications of radiomics in the field of precision radiation oncology have been identified, providing insights in terms of stage discrimination (14, 15), molecular stratification (16–18), prognostic impact (19, 20), and prediction of response to treatment (21–23). With imaging, the possibility to capture intrinsic tumor and organ-specific heterogeneity could be leveraged to evaluate the individual predisposition to radiation-induced toxicity (24). Thus, radiomics-based analyses have the potential to enrich standard NTCP models for the definition of individualized risk profiling, ultimately aiming for a personalized patient management and optimized therapeutic ratio. At present, such efforts must still be considered investigational and not ready for prime time (25). The aim of our mini-review was to provide an overview on the evidence pertaining to the role of radiomics in the prediction of radiation-induced toxicity for parotid glands, lungs, heart, and rectum. Based on the aforementioned premises, in each of the following sections an introduction on the traditional QUANTEC-based NTCP models is followed by the description of the most relevant data thus far available on radiomics-analyses and their potential in improving the predictive ability of side effects.

HEAD AND NECK RADIOTHERAPY: PAROTID GLANDS

Xerostomia represents a well known side-effect in head and neck cancer (HNC) radiotherapy (RT), accounting for significant impairment in patients' quality of life due to its impact on taste, swallowing, and speech (26). The major determinant of xerostomia is radiation-induced damage of the parotid and submandibular glands, which globally release over 80% of saliva (27). The QUANTEC consortium (6, 28) identified a mean parotid gland dose of 26 Gy as a critical threshold for the preservation of salivary function. However, in IMRT clinical practice, it is often challenging to comply with this recommendation, since a detrimental impact on target coverage can't be completely minimized (29). Furthermore, it has been demonstrated that a late recovery of salivary function is feasible, even in cases of overt xerostomia shortly after RT (30). These considerations led to the assumption that the dose-response relationship of parotid glands is more complex than initially hypothesized in QUANTEC, and that within this context, the use of quantitative imaging could lead to a better understanding of this issue. In an effort to better elucidate radiation-induced xerostomia pathogenesis, van Lujk et al. (31) postulated the existence of stem cell regions in the context of parotid glands involved in the regeneration of salivary function. As the distribution of stem cells within the parotid gland was shown to be inhomogeneous, with the highest concentration located near the dorsal edge of the mandible (where the first branching of the Stensen duct is located), it has been theorized that intentionally sparing these sub-regions would yield better results rather than attempting to spare the whole gland. The validity of this approach was further confirmed by a *post hoc* analysis of the PARSPORT trial performed by Buettner et al. (32). In fact, by taking into account the spatial information of dose distribution within parotid glands, the authors demonstrated that a significantly better prediction of patient-reported xerostomia could be obtained in respect to a model solely based on standard mean dose. Further efforts in unraveling the complex relationship between dose distribution within the parotid and NTCP led to the concept that different thresholds for xerostomia injury and recovery exist. Recently, Guo et al. (33) assessed the spatial radiation dose-based importance pattern in the major salivary glands in relation to late and acute xerostomia in a retrospective population of 146 HNC patients. The authors identified the superior portion of the two parotid glands (low dose region) as the most influential on xerostomia recovery, and demonstrated a different voxel hierarchy pattern for injury and recovery. In a retrospective analysis on 258 patients, Han and colleagues (34) showed an inverse correlation between the pattern of dose-volume histograms and clinical outcomes: a relatively high dose to small portions of a glandular sub-volume (between 10 and 40%) may be more harmful than a low-dose bath effect. Hence, in terms of function preservation, limiting the dose to specific sub-volumes such as the superior-posterior region of the ipsilateral parotid gland may be more useful (nested cross-validation area under the curve (AUC) – values of 0.78 and 0.70 for prediction of injury and recovery, respectively). In this perspective, the identification of quantitative imaging parameters correlated with both acute and late xerostomia is of paramount importance. Changes over time of radiomics features (delta-radiomics) have been extensively evaluated both in terms of acute and late xerostomia prediction (35–38). In an effort to better elucidate the relationship between parotid gland shrinkage after RT and late xerostomia, van Dijk et al. (37) recently demonstrated a correlation between delta radiomics

surface changes in contralateral parotid gland and late xerostomia in 68 patients (AUC 0.93 in test cohort). This association was significant during the whole course of RT, but performed best for mid-treatment (week 3). This finding may have profound clinical implications, allowing an early identification of patients at risk for developing late side effects and prompting adaptive re-planning or even switching to other forms of radiation (e.g., proton therapy). A similar approach was performed by Rosen and colleagues (38), who retrospectively analyzed serial cone-beam CTs (CBCT) of 119 HNC cancer patients undergoing RT. The authors concluded that the rate of CBCT-measured parotid gland image feature changes improved NTCP modeling over dose alone for late xerostomia prediction (AUC 0.77). In the context of late xerostomia prediction, baseline evaluation of changes in magnetic resonance (MR) and 18F-fluorodeoxyglucose (FDG) positron emission tomography/computed tomography (PET-CT)-based parotid gland features was also shown to be a promising field of application (39–43). In particular, parotid glands with low metabolic activity and a low fat-to-functional parenchymal ratio were matched by more heterogeneous intensity and texture imaging features: overall, these hypothesis-generating studies showed that pre-treatment radiomics-based prediction outperformed conventional NTCP models. Finally, a machine-learning approach integrating dosiomics, radiomics, and morphological data in predicting both acute and late injury to salivary glands has recently shown promising results (44, 45). Interestingly, by applying a novel artificial intelligence methodology ("likelihood-fuzzy analysis"), Pota et al. (46) identified quantitative predictors of 12-month toxicity through a longitudinal assessment of parotid glands in a dual institution experience. Taking all data together, radiomics-based analyses proved to be reliable tools to assess the risk for xerostomia in HNC patients, warranting further validation in larger prospective cohorts.

THORACIC RADIOTHERAPY: LUNG

Radiation-induced lung injury (RILI) is at the same time a complex radiobiological entity with a multi-faceted physiopathology and a serious challenge for the clinician, representing an important source of morbidity in 15–40% (47, 48) of patients receiving radiation or chemoradiation as definitive treatment for non-small cell lung cancer (NSCLC). In the IMRT era, a stringent trade-off between dose delivery to locoregional disease and adequate sparing of healthy lung tissue is advocated. This assumption was corroborated by a secondary analysis of the controversial RTOG 0617 trial, suggesting that the lack of benefit of dose escalation may have resulted from an increase in cardio-pulmonary mortality in patients receiving more aggressive dose regimens (49, 50). It is well known that RILI is a dose-limiting toxicity in the management of esophageal cancer (51, 52) and lymphoma (53, 54) patients, as well. In view of the usually lower total dose delivered for these malignancies in current practice, the most compelling evidence on radiation-induced lung toxicity can be extrapolated from NSCLC. Hence, it is of primary importance to unravel the intricate network of technical, clinical, and treatment-related factors implicated in the onset of RILI in order to develop models that allow us to accurately predict the risk of serious adverse events. The use of dose estimates to the lung as a predictor of RILI risk is well established (55), while the role of other factors, in particular dose to the heart, is controversial (56–58). Currently, dose-volume parameters, namely the mean lung dose (MLD) and the volume of lungs receiving at least 20 Gy (V20Gy), have been integrated in the QUANTEC (59) as partially reliable surrogates for the risk of radiation pneumonitis. Taking into account the known low dose bath-effect of IMRT, lower dose-volume thresholds have also been suggested, such as V13Gy (60, 61) and V5Gy (54, 62) In comparison with the historical standard Lyman model, the development of the "generalized Lyman-model" (GLM) (63) led to the introduction of a new radiobiological parameter (the effective dose, or D_{eff}, corresponding to the equivalent uniform dose, EUD), allowing for exposed volumes of the organ at risk to be weighted differently. However, dose-volume parameters do not ultimately allow us to take into account the functional heterogeneity within different lung regions and among individuals. On the other hand, data extraction from pre-treatment imaging may provide information for a tailored strategy. Thus far, a few reports are available on the potential added value of radiomics in the context of RILI prediction. In a single-center, retrospective experience on 96 patients who received curative RT for esophageal cancer, Anthony et al. (64) evaluated the correlation between the development of symptomatic radiation pneumonitis and pre-treatment analysis of FDG PET/CT and diagnostic CT scans. In a logistic regression model, the addition of the standard uptake value (SUV) standard deviation to 18 lung CT texture feature changes in the low-dose area (0–10 Gy) improved by 0.08 the mean AUC value in discriminating the diagnosis of RILI. In a larger experience on 192 patients treated for NSCLC in the same institution, Krafft et al. (65) extracted 6851 features from planning CT scans, as candidate predictors for RILI. Compared with standard clinical and dosimetric factors, at least absolute shrinkage and selection operator (LASSO) logistic regression, a final 449-feature set of the total lung volume yielded a higher average cross-validated AUC, demonstrating improved discrimination (0.51 and 0.68, respectively). The existence of a strict relationship between the dose distribution, a change of CT texture features before and after RT, and the risk of RILI development was firstly demonstrated by Cunliffe et al. (66). Recently, this dosiomic approach was replicated through a convolutional deep-neural network analysis (67, 68) in a cohort of 70 NSCLC patients treated with volumetric modulated arc therapy (VMAT), providing a high discriminative power (AUC of 0.84) over standard logistic regression models for the prediction of radiation pneumonitis. Taking into account the much less clinically relevant impact of radiation pneumonitis in the context of stereotactic body RT, limited data are available (69, 70) in this context in comparison to conventionally-fractionated regimens. Overall, in parallel to robust prognostic value in the context of stereotactic body RT (71) and chemoradiation (72), the reported data promisingly support the relevance of radiomics in the prediction of lung toxicity. However, to take into account the complexity of RILI, optimal models should integrate, in

addition to dosimetric variables, other individual risk factors such as age (73), genetic polymorphysms (74), pre-existing functional impairment of the lung (48), chemotherapy regimens (75), and, curiously, a paradoxical protective effect of smoking as a possible result of functional exhaustion of the inflammatory microenvironment in current smokers (73). In summary, RILI is a multi-faceted phenomenon resulting from complex processes that depend on biologic, dosimetric, and treatment-related variables that need to be integrated in a comprehensive model (76, 77), beyond a mechanicistic dose-response relationship.

BREAST RADIOTHERAPY: HEART

Radiotherapy plays a crucial role in the curative management of non-metastatic breast cancer, with well-established benefits in terms of loco-regional control and survival for node-positive patients (78, 79). In 2005, the Early Breast Cancer Trialists' Collaborative Group (EBCTCG) meta-analysis on individual patient data epitomized the known potential correlation of radiation and cardiac damage, showing a significant excess of non-breast cancer mortality from heart disease (rate ratio 1.27, SE 0.07, 2p = 0.0001) (80). Notably, the high cure rate of radiation for Hodgkin lymphoma (HL) has been historically offset by late heart dysfunction in long survivors (81). In the QUANTEC publication (82) it was recommended that the heart volume receiving up to 25 Gy (V25) should be below 10%. In current practice, the "ALARA" ("as low as reasonably achievable") principle is usually applied to left-sided breast cancer patients, aiming for a mean heart dose (MHD) below 2 Gy whenever possible. However, the NTCP model does not take into account other dosimetric factors, such as the possible interaction between cardiac and lung dose-volume parameters (83), as suggested by Cella et al. in an institutional analysis on 90 HL patients (84). Abnormalities in myocardial perfusion and echocardiography have been reported (85) when larger than average heart volumes were inadvertently irradiated. In particular, a mean dose to the left ventricle of 9 $\pm$4 Gy was significantly correlated with a reduced anterior wall strain (-16.8% at 14 months after RT), an early surrogate marker of myocardial function detectable with doppler echocardiographic imaging. Conversely, in patients with relatively low MHD (< 4 Gy), Bian et al. found no association between cardiac dosimetry and left ventricular ejection fraction (LVEF) (86). Multiple heart dose parameters have been associated with clinically relevant cardiotoxicity in breast cancer (87). At a median follow-up of 12 years, Correa et al. found an increased incidence of coronary artery disease and chronic heart failure (CHF) rates for increasing heart dose (85). Likewise, Saiki et al. found a significant association between MHD and the risk of heart failure with preserved ejection fraction (OR: 16.9, 95% CI: 3.9–73.7) (88). In a pivotal study, Darby et al. were able to demonstrate the existence of a linear relationship between the occurrence of major coronary events and MHD, with a 7.4% increase in the risk per Gy (95% CI: 2.9–14.5; $p < 0.001$). Nonetheless, a distinct dose threshold could not be identified (89). In a large cohort of 910 patients, Van den Bogaard et al. confirmed these findings, reporting a 16.5% increase per Gy in the cumulative incidence of acute coronary events (90), although they were not able to detect a correlation between RT dose and LVEF (91). Overall, the inter-individual heterogeneity in cardiac exposure to radiation has been an unresolved issue in cardiotoxicity studies. The inter-observer reproducibility in delineation of heart substructures and their dosimetric evaluation (82) are critical factors for a prospective, personalized risk assessment. Indeed, contouring standardization may have a significant role in minimizing differences in dose reporting (92–95). Patients enrolled in the prospective BACCARAT study (96) underwent a coronary computed tomography angiography (CCTA) before irradiation. By analyzing the dose distribution to the whole heart and its substructures in 89 left-sided subjects, the authors highlighted that MHD is a poor dosimetric surrogate parameter for the left ventricle and coronary arteries (in particular the left anterior descending artery). A machine learning approach based on CCTA-derived radiomics may have potential for a better prediction of atherosclerotic plaques over visual assessment (AUC of 0.73 vs 0.65, $p = 0.04$) (97). Taking all clinical observations together, no NTCP modeling provides conclusive evidence on late heart toxicity based on MHD analysis. To the best of our knowledge, no radiomics applications have been reported for the prediction of radiation-induced heart damage. Interestingly, Currie et al. (98) performed an explorative study based on automated feature extraction from single-photon emission computed tomography (SPECT) imaging in 22 non-cancer patients with cardiomyopathy to evaluate the most potent prognostic index for future cardiac events. With an artificial neural network approach, the authors showed that a ^{23}iodine meta-iodobenzylguanidine (^{123}I-mIBG) planar global washout higher than 30% was the best indicator for risk of cardiac events when accompanied by a decline in LVEF of more than 10%. In summary, in spite of technical capability of modern IMRT techniques to tightly refine the dose distribution within the thorax, the definition of dose-volume relationships and specific NTCP modeling for myocardial sub-volumes lags behind. Taking into account that the risk of future cardiac events after RT is strongly related to persistent smoking, age, prior cardiac events, and pre-existing cardiovascular risk factors, big data applications (99) may lend support to clinical decision making.

PROSTATE RADIOTHERAPY: RECTUM

Definitive RT represents one of the main treatment options for localized prostate cancer (100). Thanks to the availability of long-term data on clinical outcome and adverse events, radiation-induced lower gastro-intestinal toxicity remains one of the most relevant factors known to have a detrimental impact on patients' quality of life (101). The relationship between increased late rectal toxicity and high radiation dose is well known for 3DCRT (102) and conventional fractionation up to 78 Gy, with increasing rates of bleeding with rectal volumes receiving 50, 60, 65, 70, and 75 Gy greater than 50, 35, 25, 20, and 15%, respectively (V50Gy > 50%, V60Gy > 35%, V65Gy > 25%, V70Gy > 20%, and V75Gy > 15%) (103,

104). When externally validated in patients treated with 3DCRT, the QUANTEC-based EUD model had relatively low predictive power (AUC 0.61) for late rectal bleeding (105). Further, the NTCP cross-applicability to IMRT for chronic gastrointestinal toxicity was assessed in a large single-institution cohort study (106). Indeed, debilitating symptoms such as fecal incontinence or rectal urgency were mostly reported when large volumes of the rectum were exposed to intermediate doses, as confirmed by the Medical Research Council RT01 randomized phase 3 trial (107) and the long-term follow-up of the AIROPROS 0102 study (108). In recent years, the implementation of moderate hypo-fractionated regimens in clinical practice prompted the development of dose-volume constraints adapted to different treatment schedules (109). Unlike what happens for moderate hypo-fractionated IMRT, high rather than low-dose regions in the rectum predict toxicity after an ultra hypo-fractionated regimen. Of note, V35Gy was shown to be a strong predictor of rectal bleeding (110) and a recent pooled analysis of patients treated within four different trials demonstrated that late toxicity and quality of life were significantly related to V38Gy after the delivery of 35-40 Gy in five fractions (111). Overall, prospectively defined dosimetric predictors of lower gastro-intestinal toxicity can be adapted according to different techniques and fractionations used in the context of definitive treatment for localized prostate cancer.

In view of the available spectrum of NTCP models and of the clinical variability of late rectal side effects, extracting mineable data from imaging would facilitate a personalized treatment prescription. Few radiomics analyses allow us to refine the toxicity prediction in the current scenario. In a single-center prospective study on 33 patients treated with moderately accelerated IMRT (70.2 Gy in 26 fractions), Abdollahi et al. (112) performed a machine learning approach on pre- and post-treatment T2-weighted MR scans of the rectal wall. Out of a total of 1096 features, a 37-set of descriptors extracted from baseline T2-weighted images was more accurate (mean AUC of 0.68) than post-treatment T2-weighted apparent diffusion coefficient (ADC) and delta values. Of note, a broad clinical endpoint was chosen by the authors (G1 rectal toxicity, occurring in 54% of the cohort). Similar pilot analyses from the same group focused on the bladder wall (113) and femoral head changes (114). In a secondary analysis of the multi-institutional randomized HYPRO trial, Rossi et al. (115) evaluated the correlation of late gastrointestinal and genitourinary toxicity with non-treatment related characteristics (age, baseline PSA, Gleason score, comorbidities), DVH parameters, and radiomics features. Of the 820 patients with intermediate and high risk prostate cancer enrolled in the trial, 351 had dose distributions to rectum and bladder available for 3D texture analysis. For both rectal bleeding and fecal incontinence, logistic NTCP models showed that the addition of texture features led to a statistically significant improvement in the predictive ability (AUC of 0.73 for both; $p < 0.04$), higher than what was obtained with clinical and DVH parameters. In a smaller prospective study on 64 patients, Mostafaei et al. came to similar results by analyzing baseline CT markers with a stacking regression algorithm (116). Interestingly, an explorative approach focused on four patients irradiated on a 1.5 Tesla MR-Linear Accelerator within a prospective observational trial. Delta-radiomics assessed with a longitudinal T2-weighted intensity histogram of prostate and surrounding organs at risk showed early significant variations of the rectal wall, with change in mean, median, and standard deviation metrics values at the second week of treatment. A longitudinal radiomic data acquisition process was deemed feasible on the hybrid machine (117). To summarize, in the modern context of prostate RT, the prediction of gastrointestinal toxicity based only on NTCP models may be misleading, given the current trend for dose-escalated IMRT and the establishment of hypo-fractionated and ultra hypo-fractionated regimens as standards of care. Early prospective data on the integration of radiomics analyses are available. Potentially, these features may represent a valuable tool for clinical decision in the future. Further refinement could be provided by applying machine learning methods and bioinformatics tools to genome-wide data to identify patients with a greater congenital risk of toxicity before treatment (118).

ASSESSING THE QUALITY OF RADIOMICS INVESTIGATIONS: A WORD OF CAUTION

In the previous sections, the potential of radiomics for the prediction of radiation-induced toxicity for parotid glands, lung, heart, and rectum was highlighted. Promisingly, quantitative imaging represents an area of active research under the light of precision oncology (25). Nonetheless, when evaluating the investigations thus far published on radiomics, some caveats need to be taken into account. In view of the complexity of the radiomic workflow, Lambin and colleagues (11) introduced a radiomics quality score (RQS) tool. Based on a set of 16 well-defined criteria addressing several aspects such as image protocol quality, segmentation method, feature reduction, presence of biologic correlates, and extent of validation, the authors proposed to define an objective ranking of quality for radiomics studies. In particular, a score of 36 corresponds to the highest value achievable, whereby the prospective validation of a radiomics signature in a registered trial confers the largest contribution (7 points). Through a systematic review of the literature focusing on the link between radiomic biomarkers and tumor biology, Sanduleanu et al. (119) applied the RQS in 41 studies. Unsurprisingly, most studies (30/41) were of poor quality, with an average score of 30% or less, mainly because of a lack of robust segmentation, external validation, and discrimination based on cut-off values. In addition, interobserver variability among authors in terms of scoring was significant, suggesting that the proposed scale requires further refinement. When applying the RQS to evaluate the methodological quality of the most relevant radiomics analyses thus far published for the prediction of xerostomia, RILI, and late rectal toxicity, the overall outlook (**Tables 1**, **2**) is unsatisfactory. Although all studies performed well in terms of describing feature reduction methods (all used measures to decrease the risk of overfitting), multivariable analyses with non-radiomic factors, and reporting cut-off analyses, the weaknesses

TABLE 1 | Most consolidated data in radiomics-based approaches in predicting radiotherapy-induced xerostomia.

Reference	Patient population	Study design	Imaging biomarker	Main outcome	Main finding	Prediction measure	RQS
Van Dijk (37)	68	Retrospective (training and test cohort)	CT	Late Xerostomia	Contralateral PG surface change @ 3 wks	AUCtrain = 0.92; AUCtest = 0.93	50%
Rosen (38)	119	Retrospective (single cohort)	CBCT	Late Xerostomia	Contralateral PG shrinkage	AUC = 0.77	38.8%
Guo (33)	146	Retrospective (Single cohort)	CT	Late xerostomia	Low dose region to superior portion of the 2 PGs	AUC = 0.68	36.1%
Han (34)	589 (258 assessable for late xerostomia)	Prospective (multicentric)	CT	Late Xerostomia	Low dose bath to whole gland	AUC = 0.70	50%
Van Dijk (41)	68 (25 patients for external cohort)	Retrospective (+ validation cohort)	MR	Late Xerostomia	High intensity MR P90 values	AUC = 0.83	50%
Wilkie (42)	47	Prospective (single cohort)	PET	Late Xerostomia	Pre-treatment PET P90 values	AUC = 0.78	44.4%

CT, computed tomography; PG, parotid gland, AUC: area under the curve; CBCT, cone-beam CT; MR, magnetic resonance; P90, 90th percentile; PET, positron-emission tomography; RQS, radiomics quality score.

TABLE 2 | Most promising data in radiomics-based approaches in predicting radiotherapy-induced toxicity in the treatment of solid tumors.

Reference	Patient population	Study design	Imaging biomarker	Main outcome	Main finding	Prediction measure	RQS
Krafft (65)	192 (NSCLC)	Retrospective (single cohort)	CT	RILI	449-feature set of the total lung volume	AUC = 0.68	44.4%
Liang (67)	70 (NSCLC)	Retrospective (single cohort)	CT	RILI	GLCM of ipsilateral lung	AUC = 0.78	41.6%
Rossi (115)	351 (PCA)	Prospective	CT	Late Rectal toxicity	42 Texture features (LRHGE most selected	AUC = 0.73	80.5%
Abdollahi (112)	33 (PCA)	Prospective	MR	Late Rectal toxicity	Pre-treatment T2 MRI features	AUC = 0.68	25%

NSCLC, non-small cell lung cancer; CT, computed tomography; RILI, radiation-induced lung injury; AUC, area under the curve; GLCM, gray level co-occurrence matrix; PCA, prostate cancer; LRHGE, long run high Gaey level emphasis; MR, magnetic resonance; RQS, radiomics quality score.

are represented by the limited validation (typically, on a dataset from the same institution), the retrospective study design, the infrequent discussion of biological correlates, and the lack of cost-effectiveness. A notable exception is represented by the work of Rossi et al. (112) with a RQS of 80.5% (29/36): the high score can be justified due to the fact that the radiomics signature in this study was prospectively validated in a large, multi-institutional randomized trial with a resulting potential direct clinical utility. In view of the suboptimal methodological quality frequently observed in the radiomics studies we evaluated, caution is advised in the interpretation of the reported findings. Another relevant limit to bear in mind is the lack of standardization in regards to imaging features definition and interpretation. In this perspective, the recently published Image Biomarker Standardization Initiative (IBSI) position paper (120) should be viewed as a relevant step ahead, fostering homogeneity in radiomics analyses across different research platforms.

CONCLUSION

In comparison to efficacy outcomes, the current state-of-the-art on radiomics prediction of radiation-induced toxicity is still relatively limited, with the notable exception of xerostomia prognostication (**Tables 1**, **2**). Taking all data together, the vast majority of reviewed studies suggested that indeed radiomics applications may increase the predictive ability of organ-specific side effects over standard clinical and dosimetric factors. For further progress, four major areas of improvement can be envisaged. Firstly, the need for standardization is a critical, well-recognized major step for further development (120, 121). Secondly, in view of the frequent single-center retrospective design and the generally low number of enrolled patients and of clinical endpoints (i.e., side effects), the robustness of data is questionable for most studies (122). In this perspective, the lack of or very limited external validation in independent datasets is a point of weakness for both conventional NTCP models

(123) and radiomics applications (119). Thirdly, progress in the field of radio-genomics is eagerly awaited (124), in order to improve the understanding of underlying biological processes, such as intrinsic radio-sensitivity. Lastly, controlled randomized clinical trials testing radiomics-based interventions in adequately powered studies are still yet to be published. At present, no single radiomics finding is readily applicable to patient management in clinical practice. Nonetheless, the available body of evidence is encouraging and warrants further investigation, given the size of benefit demonstrated in terms of high predictive ability of common toxicities. In conclusion, building on established NTCP models, the so far available hypothesis-generating data underline the potential of radiomics for improved clinical decision making in precision radiation oncology.

AUTHOR CONTRIBUTIONS

All authors listed have made a substantial, direct and intellectual contribution to the work, and approved it for publication.

REFERENCES

1. Marks LB, Ten Haken RK, Martel MK. Guest editor's introduction to QUANTEC: a users guide. *Int J Radiat Oncol Biol Phys*. (2010) 76(3 Suppl.):S1–2. doi: 10.1016/j.ijrobp.2009.08.075
2. Emami B, Lyman J, Brown A, Coia L, Goitein M, Munzenrider JE, et al. Tolerance of normal tissue to therapeutic irradiation. *Int J Radiat Oncol Biol Phys*. (1991) 21:109–22.
3. Ling CC, Yorke E, Fuks Z. From IMRT to IGRT: frontierland or neverland?. *Radiother Oncol*. (2006) 78:119–22. doi: 10.1016/j.radonc.2005.12.005
4. Bentzen SM. Theragnostic imaging for radiation oncology: dose-painting by numbers. *Lancet Oncol*. (2005) 6:112–7. doi: 10.1016/S1470-2045(05)01737-7
5. Baumann M, Krause M, Overgaard J, Debus J, Bentzen SM, Daartz J, et al. Radiation oncology in the era of precision medicine. *Nat Rev Cancer*. (2016) 16:234–49. doi: 10.1038/nrc.2016.18
6. Bentzen SM, Constine LS, Deasy JO, Eisbruch A, Jackson A, Marks LB, et al. Quantitative analyses of normal tissue effects in the clinic(QUANTEC): an introduction to the scientific issues. *Int J Radiat Oncol Biol Phys*. (2010) 76(3 Suppl.):S3–9. doi: 10.1016/j.ijrobp.2009.09.040
7. Collins GS, De Groot JA, Dutton S, Omar O, Shanyinde M, Tajar A, et al. External validation of multivariable prediction models: a systematic review of methodological conduct and reporting. *BMC Med Res Methodol*. (2014) 14:40. doi: 10.1186/1471-2288-14-40
8. Collins GS, Reitsma JB, Altman DG, Moons KG. Transparent reporting of a multivariable prediction model for individual prognosis or diagnosis (TRIPOD): the TRIPOD statement. *Br J Cancer*. (2015) 112:251–9. doi: 10.1038/bjc.2014.639
9. Lambin P, Rios-Velazquez E, Leijenaar R, Carvalho S, van Stiphout RG, Granton P, et al. Radiomics: extracting more information from medical images using advanced feature analysis. *Eur J Cancer*. (2012) 48:441–6. doi: 10.1016/j.ejca.2011.11.036
10. Gillies RJ, Kinahan PE, Hricak H. Radiomics: images are more than pictures,they are data. *Radiology*. (2016) 278:563–77. doi: 10.1148/radiol.2015151169
11. Lambin P, Leijenaar RTH, Deist TM, Peerlings J, de Jong EEC, van Timmeren J, et al. Radiomics: the bridge between medical imaging and personalized medicine. *Nat Rev Clin Oncol*. (2017) 14:749–62. doi: 10.10138/nrclinonc.2017.141
12. O'Connor JP, Aboagye EO, Adams JE, Aerts HJWL, Barrington SF, Beer AJ, et al. Imaging biomarker roadmap for cancer studies. *Nat Rev Clin Oncol*. (2017) 14:169–86. doi: 10.1038/nrclinonc.2016.162
13. Tannock IF, Hickman JA. Limits to personalized cancer medicine. *N Engl J Med*. (2016) 375:1289–94. doi: 10.1056/NEJMsb1607705
14. Liang C, Huang Y, He L, Chen X, Ma X, Dong D, et al. The development and validation of a CT-based radiomics signature for the preoperative discrimination of stage I-II and stage III-IV colorectal cancer. *Oncotarget*. (2016) 7:31401–12. doi: 10.18632/oncotarget.8919
15. Ren J, Tian J, Yuan Y, Dong D, Li X, Shi Y, et al. Magnetic resonance imaging based radiomics signature for the preoperative discrimination of stage I-II and III-IV head and neck squamous cell carcinoma. *Eur J Radiol*. (2018) 106:1–6. doi: 10.1016/j.ejrad.2018.07.002
16. Kniep HC, Madesta F, Schneider T, Hanning U, Schoenfeld MH, Schoen G, et al. Radiomics of brain MRI: utility in prediction of metastatic tumor type. *Radiology*. (2019) 290:479–87. doi: 10.1148/radiol.2018180946
17. Peeken JC, Bernhofer M, Spraker MB, Pfeiffer D, Devecka M, Thamer A, et al. CT-based radiomic features predict tumor grading and have prognostic value in patients with soft tissue sarcomas treated with neoadjuvant radiation therapy. *Radiother Oncol*. (2019) 135:187–96. doi: 10.1016/j.radonc.2019.01.004
18. Bogowicz M, Jochems A, Deist TM, Tanadini-Lang S, Huang SH, Chan B, et al. Privacy-preserving distributed learning of radiomics to predict overall survival and HPV status in head and neck cancer. *Sci Rep*. (2020) 10:4542. doi: 10.1038/s41598020-61297-4
19. Aerts HJ, Velazquez ER, Leijenaar RT, Parmar C, Grossmann P, Carvalho S, et al. Decoding tumour phenotype by noninvasive imaging using a quantitative radiomics approach. *Nat Commun*. (2014) 5:4006. doi: 10.1038/ncomms5006
20. Krarup MMK, Nygård L, Vogelius IR, Andersen FL, Cook G, Goh V, et al. Heterogeneity in tumours: validating the use of radiomic features on 18F-FDG PET/CT scans of lung cancer patients as a prognostic tool. *Radiother Oncol*. (2020) 144:72–8. doi: 10.1016/j.radonc.2019.10.012
21. Sun R, Limkin EJ, Vakalopoulou M, Dercle L, Champiat S, Han SR, et al. A radiomics approach to assess tumour-infiltrating CD8 cells and response to anti-PD-1 or anti-PD-L1 immunotherapy: an imaging biomarker, retrospective multicohort study. *Lancet Oncol*. (2018) 19:1180–91. doi: 10.1016/S1470-2045(18)30413-3
22. Bulens P, Couwenberg A, Intven M, Debucquoy A, Vandecaveye V, Van Cutsem E, et al. Predicting the tumor response to chemoradiotherapy for rectal cancer: model development and external validation using MRI radiomics. *Radiother Oncol*. (2020) 142:246–52. doi: 10.1016/j.radonc.2019.07.033
23. Cao Q, Li Y, Li Z, An D, Lin Q. Development and validation of a radiomics signature on differentially expressed features of 18F-FDG PET to predict treatment response of concurrent chemoradiotherapy in thoracic esophagus squamous cell carcinoma. *Radiother Oncol*. (2020) 146:9–15. doi: 10.1016/j.radonc.2020.01.027
24. Gardin I, Gregoire V, Gibon D, Kirisli H, Pasquier D, Thariat J, et al. Radiomics: principles and radiotherapy applications. *Crit Rev Oncol Hematol*. (2019) 138:44–50. doi: 10.1016/j.critrevonc.2019.03.015
25. Jaffray DA, Das S, Jacobs PM, Jerai R, Lambin P. How advances in imaging will affect precision radiation oncology. *Int J Radiat Oncol Biol Phys*. (2018) 101:292–8. doi: 10.1016/j.ijrobp.2018.01.047
26. Jellema AP, Slotman BJ, Doornaert P, Leemans CR, Langendijk JA. Impact of radiation-induced xerostomia on quality of life after primary radiotherapy among patients with head and neck cancer. *Int J Radiat Oncol Biol Phys*. (2007) 69:751–60.
27. Ortholan C, Benezery K, Bensadoun RJ. Normal tissue tolerance to external beam radiation therapy: salivary glands. *Cancer Radiother*. (2010) 14:290–4. doi: 10.1016/j.canrad.2010.03.007
28. Deasy JO, Moiseenko V, Marks L, Chao KS, Nam J, Eisbruch A. Radiotherapy dose-volume effects on salivary gland function. *Int J Radiat Oncol Biol Phys*. (2010) 76(3 Suppl.):S58–63. doi: 10.1016/j.ijrobp.2009.06.090
29. Kreps S, Berges O, Belin L, Zefkili S, Petras S, Giraud P. Salivary gland-sparing helical tomotherapy for head and neck cancer: preserved salivary function on quantitative salivary gland scintigraphy after tomotherapy. *Eur*

Ann Otorhinolaryngol Head Neck Dis. (2016) 133:257–62. doi: 10.1016/j.anorl.2016.05.003

30. Owosho AA, Thor M, Oh JH, Riaz N, Tsai CJ, Rosenberg H, et al. The role of parotid gland irradiation in the development of severe hyposalivation (xerostomia) after intensity-modulated radiation therapy for head and neck cancer: temporal patterns, risk factors, and testing the QUANTEC guidelines. *J Craniomaxillofac Surg*. (2017) 45:595–600. doi: 10.1016/j.jcms.2017.01.020
31. van Luijk P, Pringle S, Deasy JO, Moiseenko VV, Faber H, Hovan A, et al. Sparing the region of the salivary gland containing stem cells preserves saliva production after radiotherapy for head and neck cancer. *Sci Transl Med*. (2015) 7:305ra147. doi: 10.1126/scitranslmed.aac4441
32. Buettner F, Miah AB, Gulliford SL, Hall M, Harrington KJ, Webb S, et al. Novel approaches to improve the therapeutic index of head and neck radiotherapy: an analysis of data from the PARSPORT randomised phase III trial. *Radiother Oncol*. (2012) 103:82–7. doi: 10.1016/j.radonc.2012.02.006
33. Guo Y, Jiang W, Lakshminarayanan P, Han P, Cheng Z, Bowers M, et al. Spatial radiation dose influence on xerostomia recovery and its comparison to acute incidence in patients with head and neck cancer. *Adv Radiat Oncol*. (2019) 5:221–30. doi: 10.1016/j.adro.2019.08.009
34. Han P, Lakshminarayanan P, Jiang W, Shpitser I, Hui X, Lee SH, et al. Dose/Volume histogram patterns in salivary gland subvolumes influence xerostomia injury and recovery. *Sci Rep*. (2019) 9:3616. doi: 10.1038/s41598-019-40228-y
35. Wu H, Chen X, Yang X, Tao Y, Xia Y, Deng X, et al. Early prediction of acute xerostomia during radiation therapy for head and neck cancer based on texture analysis of daily CT. *Int J Radiat Oncol Biol Phys*. (2018) 102:1308–18. doi: 10.1016/j.ijrobp.2018.04.059
36. Liu Y, Shi H, Huang S, Chen X, Zhou H, Chang H, et al. Early prediction of acute xerostomia during radiation therapy for nasopharyngeal cancer based on delta radiomics from CT images. *Quant Imaging Med Surg*. (2019) 9:1288–302. doi: 10.21037/qims.2019.07.08
37. van Dijk LV, Langendijk JA, Zhai TT, Vedelaar TA, Noordzij W, Steenbakkers RJHM, et al. Delta-radiomics features during radiotherapy improve the prediction of late xerostomia. *Sci Rep*. (2019) 9:12483. doi: 10.1038/s41598-019-48184-3
38. Rosen BS, Hawkins PG, Polan DF, Balter JM, Brock KK, Kamp JD, et al. Early changes in serial CBCT-measured parotid gland biomarkers predict chronic xerostomia after head and neck radiation therapy. *Int J Radiat Oncol Biol Phys*. (2018) 102:1319–29. doi: 10.1016/j.ijrobp.2018.06.048
39. Sheikh K, Lee SH, Cheng Z, Lakshminarayanan P, Peng L, Han P, et al. Predicting acute radiation induced xerostomia in head and neck Cancer using MR and CT radiomics of parotid and submandibular glands. *Radiat Oncol*. (2019) 14:131. doi: 10.1186/s13014-019-1339-4
40. Van Dijk LV, Noordzij W, Brouwer CL, Boellard R, Burgerhof JGM, Langendijk JA, et al. 18F-FDG PET image biomarkers improve prediction of late radiation-induced xerostomia. *Radiother Oncol*. (2018) 126:89–95. doi: 10.1016/j.radonc.2017.08.024
41. van Dijk LV, Thor M, Steenbakkers RJHM, Apte A, Zhai TT, Borra R, et al. Parotid gland fat related magnetic resonance image biomarkers improve prediction of late radiation-induced xerostomia. *Radiother Oncol*. (2018) 128:459–66. doi: 10.1016/j.radonc.2018.06.012
42. Wilkie JR, Mierzwa ML, Casper KA, Mayo CS, Schipper MJ, Eisbruch A, et al. Predicting late radiation-induced xerostomia with parotid gland PET biomarkers and dose metrics. *Radiother Oncol*. (2020) 148:30–7. doi: 10.1016/j.radonc.2020.03.037
43. Klein Nulent TJW, Valstar MH, de Keizer B, Willems S, Smit LA, Al-Mamgani A, et al. Physiologic distribution of PSMA-ligand in salivary glands and seromucous glands of the head and neck on PET/CT. *Oral Surg Oral Med Oral Pathol Oral Radiol*. (2018) 125:478–86. doi: 10.1016/j.oooo.2018.01.011
44. Gabryś HS, Buettner F, Sterzing F, Hauswald H, Bangert M. Design and selection of machine learning methods using radiomics and dosiomics for normal tissue complication probability modeling of xerostomia. *Front Oncol*. (2018) 8:35. doi: 10.3389/fonc.2018.00035
45. Jiang W, Lakshminarayanan P, Hui X, Han P, Cheng Z, Bowers M, et al. Machine learning methods uncover radiomorphologic dose patterns in salivary glands that predict xerostomia in patients with head and neck cancer. *Adv Radiat Oncol*. (2018) 4:401–12. doi: 10.1016/j.adro.2018.11.008
46. Pota M, Scalco E, Sanguineti G, Farneti A, Cattaneo GM, Rizzo G, et al. Early prediciton of radiotherapy-induced parotid shrinkage and toxicity based on CT radiomics and fuzzy classification. *Artif Intell Med*. (2017) 81:41–53. doi: 10.1016/j.artmed.2017.03.004
47. Madani I, De Ruyck K, Goeminne H, De Neve W, Thierens H, Van Meerbeeck J. Predicting risk of radiation-induced lung injury. *J Thorac Oncol*. (2007) 2:864–74. doi: 10.1097/JTO.0b013e318145b2c6
48. Palma DA, Senan S, Tsujino K, Barriger RB, Rengan R, Moreno M, et al. Predicting radiation pneumonitis after chemoradiation therapy for lung cancer: an international individual patient data meta-analysis. *Int J Radiat Oncol Biol Phys*. (2013) 85:444–50. doi: 10.1016/j.ijrobp.2012.04.043
49. Hong JC, Salama JK. Dose escalation for unresectable locally advanced non-small cell lung cancer: end of the line? *Transl Lung Cancer Res*. (2016) 5:126–33. doi: 10.3978/j.issn.2218-6751.2016.01.07
50. Chun SG, Hu C, Choy H, Komaki RU, Timmerman RD, Schild SE, et al. Impact of intensity-modulated radiation therapy technique for locally advanced non-small-cell lung cancer: a secondary analysis of the NRG Oncology RTOG 0617 randomized clinical trial. *J Clin Oncol*. (2017) 35:56–62. doi: 10.1200/JCO.2016.69.1378
51. Nguyen NP, Krafft SP, Vin-Hung V, Vos P, Almeida F, Jang S, et al. Feasibility of tomotherapy to reduce normal lung and cardiac toxicity for distal esophageal cancer compared to three-dimensional radiotherapy. *Radiother Oncol*. (2011) 101:438–42. doi: 10.1016/j.radonc.2011.07.015
52. Niezink AGH, de Jong RA, Muijs CT, Langendijk JA, Widder J. Pulmonary function changes after radiotherapy for lung or esophageal cancer: a systematic review focusing on dose-volume parameters. *Oncologist*. (2017) 22:1257–64. doi: 10.1634/theoncologist.2016.0324
53. Koh ES, Sun A, Tran TH, Tsang R, Pintilie M, Hodgson DC, et al. Clinical dose-volume histogram analysis in predicting radiation pneumonitis in Hodgkin's lymphoma. *Int J Radiat Oncol Biol Phys*. (2006) 66:223–8.
54. Pinnix CC, Smith GL, Milgrom S, Osborne EM, Reddy JP, Akhtari M, et al. Predictors of radiation pneumonitis in patients receiving intensity modulated radiation therapy for Hodgkin and non-Hodgkin lymphoma. *Int J Radiat Oncol Biol Phys*. (2015) 92:175–82. doi: 10.1016/j.ijrobp.2015.02.010
55. Barriger RB, Fakiris AJ, Hanna N, Yu M, Mantravadi P, McGarry RC. Dose-volume analysis of radiation pneumonitis in non-small-cell lung cancer patients treated with concurrent cisplatinum and etoposide with or without consolidation paclitaxel. *Int J Radiat Oncol Biol Phys*. (2010) 78:1381–6. doi: 10.1016/j.ijrobp.2009.09.030
56. Huang EX, Hope AJ, Lindsay PE, Trovo M, El Naqa I, Deasy O, et al. Heart irradiation as a risk factor for radiation pneumonitis. *Acta Oncol*. (2011) 50:51–60. doi: 10.3109/0284186X.2010.521192
57. Tucker SL, Liao Z, Dinh J, Bian SX, Mohan R, Martel MK, et al. Is there an impact of heart exposure on the incidence of radiation pneumonitis? Analysis of data from a large clinical cohort. *Acta Oncol*. (2014) 53:590–6. doi: 10.3109/0284186X.2013.831185
58. Wijsman R, Dankers FJWM, Troost EGC, Hoffmann A, van der Heijden EHFM, de Geus-Oei LF, et al. Inclusion of incidental radiation dose to the cardiac atria and ventricles does not improve the prediction of radiation pneumonitis in advanced-stage non-small cell lung cancer patients treated with intensity modulated radiation therapy. *Int J Radiat Oncol Biol Phys*. (2017) 99:434–41. doi: 10.1016/j.ijrobp.2017.04.011
59. Marks LB, Bentzen SM, Deasy JO, Spring Kong FM, Bradley JD, Vogelius IS, et al. Radiation dose-volume effects in the lung. *Int J Radiat Oncol Biol Phys*. (2010) 76(3 Suppl.):S70–6. doi: 10.1016/j.ijrobp.2009.06.091
60. Seppenwoolde Y, Lebesque JV, de Jaeger K, Belderbos JSA, Boersma LJ, Schilstra C, et al. Comparing different NTCP models that predict the incidence of radiation pneumonitis. Normal tissue complication probability. *Int J Radiat Oncol Biol Phys*. (2003) 55:724–35.
61. Schallenkamp JM, Miller RC, Brinkmann DH, Foote T, Garces Y. Incidence of radiation pneumonitis after thoracic irradiation: dose-volume correlates. *Int J Radiat Oncol Biol Phys*. (2007) 1:724–35.
62. Wang D, Li B, Wang Z, Zhu J, Sun H, Zhang J, et al. Functional dose-volume histograms for predicting radiation pneumonitis in locally advanced non-small cell lung cancer treated with late-course accelerated hyperfractionated radiotherapy. *Exp Ther Med*. (2011) 2:1017–22.
63. Tucker SL, Liu HH, Liao Z, Wei X, Wang S, Jin H, et al. Analysis of radiation pneumonitis risk using a generalized Lyman model [published correction

appears in Int J Radiat Oncol Biol Phys. 2010 Sep 1;78(1):316-7. Dosage error in article text]. *Int J Radiat Oncol Biol Phys*. (2008) 72:568–74. doi: 10.1016/j.ijrobp.2008.04.053

64. Anthony GJ, Cunliffe A, Castillo R, Pham N, Guerrero T, Armato SG, et al. Incorporation of pre-therapy $_{18}$ F-FDG uptake data with CT texture features into a radiomics model for radiation pneumonitis diagnosis. *Med Phys*. (2017) 44:3686–94. doi: 10.1002/mp.12282
65. Krafft SP, Rao A, Stingo F, Briere TM, Court LE, Liao Z, et al. The utility of quantitative CT radiomics features for improved prediction of radiation pneumonitis. *Med Phys*. (2018) 45:5317–24. doi: 10.1002/mp.13150
66. Cunliffe A, Armato SG, Castillo R, Pham N, Guerrero T, Al-Hallaq HA. Lung texture in serial thoracic computed tomography scans: correlation of radiomics-based features with radiation therapy dose and radiation pneumonitis development. *Int J Radiat Oncol Biol Phys*. (2015) 91:1048–56. doi: 10.1016/j.ijrobp.2014.11.030
67. Liang B, Yan H, Tian Y, Chen X, Yan L, Zhang T, et al. Dosiomics: extracting 3D spatial features from dose distribution to predict incidence of radiation pneumonitis. *Front Oncol*. (2019) 9:269. doi: 10.3389/fonc.2019.00269
68. Liang B, Tian Y, Chen X, Yan H, Yan L, Zhang T, et al. Prediction of radiation pneumonitis with dose distribution: a convolutional neural network (CNN) based model. *Front Oncol*. (2020) 9:1500. doi: 10.3389/fonc.2019.01500
69. Moran A, Daly ME, Yip SF, Yamamoto T. Radiomics-based assessment of radiation-induced lung injury after stereotactic body radiotherapy. *Clin Lung Cancer*. (2017) 18:e425–31. doi: 10.1016/j.cllc.2017.05.014
70. Bousabarah K, Temming S, Hoevels M, Borggrefe J, Baus WW, Ruess D, et al. Radiomic analysis of planning computed tomograms for predicting radiation-induced lung injury and outcome in lung cancer patients treated with robotic stereotactic body radiation therapy. *Strahlenther Onkol*. (2019) 195:830–42. doi: 10.1007/s00066-019-01452-7
71. Starkov P, Aguilera TA, Golden DI, Shultz DB, Trakul N, Maxim PG, et al. The use of texture-based radiomics CT analysis to predict outcomes in early-stage non-small cell lung cancer treated with stereotactic ablative radiotherapy. *Br J Radiol*. (2019) 92:20180228. doi: 10.1259/bjr.20180228
72. van Timmeren JE, van Elmpt W, Leijenaar RTH, Reymen B, Monshouwer R, Bussink J, et al. Longitudinal radiomics of cone-beam CT images from non-small cell lung cancer patients: Evaluation of the added prognostic value for overall survival and locoregional recurrence. *Radiother Oncol*. (2019) 136:78–85. doi: 10.1016/j.radonc.2019.03.032
73. Vogelius IR, Bentzen SM. A literature-based meta-analysis of clinical risk factors for development of radiation induced pneumonitis. *Acta Oncol*. (2012) 51:975–83. doi: 10.3109/0284186X.2012.718093
74. De Ruysscher D, Jin J, Lautenschlaeger T, She JX, Liao Z, Kong FS. Blood-based biomarkers for precision medicine in lung cancer: precision radiation therapy. *Transl Lung Cancer Res*. (2017) 6:661–9. doi: 10.21037/tlcr.2017.09.12
75. Liu T, He Z, Dang J, Li G. Comparative efficacy and safety for different chemotherapy regimens used concurrently with thoracic radiation for locally advanced non-small cell lung cancer: a systematic review and network meta-analysis. *Radiat Oncol*. (2019) 14:55. doi: 10.1186/s13014-019-1239-7
76. Lee S, Ybarra N, Jeyaseelan K, Faria S, Kopek N, Brisebois P, et al. Bayesan network ensemble as a multivariate strategy to predict radiation pneumonitis risk. *Med Phys*. (2015) 42:2421–30. doi: 10.1118/1.4915284
77. Luna JM, Chao HH, Diffenderfer ES, Valdes G, Chinniah C, Ma G, et al. Predicting radiation pneumonitis in locally advanced stage II-III non-small cell lung cancer using machine learning. *Radiother Oncol*. (2019) 133:106–12. doi: 10.1016/j.radonc.2019.01.003
78. Clarke M, Collins R, Darby S, Davies C, Elphinstone P, Evans V, et al. Effects of radiotherapy and of differences in the extent of surgery for early breast cancer on local recurrence and 15-year survival: an overview of the randomised trials. *Lancet*. (2005) 366:2087–106. doi: 10.1016/S0140-6736(05)67887-7
79. Cserni G. Effects of radiotherapy and surgery for early breast cancer. *Lancet*. (2006) 367:1652–3. doi: 10.1016/S0140-6736(06)68724-2
80. EBCTCG (Early Breast Cancer Trialists' Collaborative Group), McGale P, Taylor C, Correa C, Cutter D, Duane F, et al. Effect of radiotherapy after mastectomy and axillary surgery on 10-year recurrence and 20-year breast cancer mortality: meta-analysis of individual patient data for 8135 women in 22 randomised trials. *Lancet*. (2014) 383:2127–35. doi: 10.1016/S0140-6736(14)60488-8
81. Galper SL, Yu JB, Mauch PM, Strasser JF, Silver B, Lacasce A, et al. Clinically significant cardiac disease in patients with Hodgkin lymphoma treated with mediastinal irradiation. *Blood*. (2011) 117:412–8. doi: 10.1182/blood-2010-06-291328
82. Gagliardi G, Constine LS, Moiseenko V, Correa C, Pierce LJ, Allen AM, et al. Radiation dose-volume effects in the heart. *Int J Radiat Oncol Biol Phys*. (2010) 76(3 Suppl.):S77–85. doi: 10.1016/j.ijrobp.2009.04.093
83. Ghobadi G, van der Veen S, Bartelds B, de Boer RA, Dickinson MG, de Jong JR, et al. Physiological interaction of heart and lung in thoracic irradiation. *Int J Radiat Oncol Biol Phys*. (2012) 84:e639–46. doi: 10.1016/j.ijrobp.2012.07.2362
84. Cella L, Palma G, Deasy JO, Oh JH, Liuzzi R, D'Avino V, et al. Complication probability models for radiation-induced heart valvular dysfunction: do heart-lung interactions play a role? *PLoS One*. (2014) 9:e111753. doi: 10.1371/journal.pone.0111753
85. Correa CR, Das IJ, Litt HI, Ferrari V, Hwang WT, Solin LJ, et al. Association between tangential beam treatment parameters and cardiac abnormalities after definitive radiation treatment for left-sided breast cancer. *Int J Radiat Oncol Biol Phys*. (2008) 72:508–16. doi: 10.1016/j.ijrobp.2007.12.037
86. Bian SX, Korah MP, Whitaker TR, Ji L, Groshen S, Chung E. No acute changes in LVEF observed with concurrent trastuzumab and breast radiation with low heart doses. *Clin Breast Cancer*. (2017) 17:510–5. doi: 10.1016/j.clbc.2017.03.011
87. Cao L, Cai G, Chang C, Yang ZZ, Feng Y, Yu XL, et al. Early cardiac toxicity following adjuvant radiotherapy of left-sided breast cancer with or without concurrent trastuzumab. *Oncotarget*. (2016) 7:1042–54. doi: 10.18632/oncotarget.6053
88. Saiki H, Petersen IA, Scott CG, Bailey KR, Dunlay SM, Finley RR, et al. Risk of heart failure with preserved ejection fraction in older women after contemporary radiotherapy for breast cancer. *Circulation*. (2017) 135:1388–96. doi: 10.1161/CIRCULATIONAHA.116.025434
89. Darby SC, Ewertz M, McGale P, Bennet AM, Goldman-Blom U, Brønnum D, et al. Risk of ischemic heart disease in women after radiotherapy for breast cancer. *N Engl J Med*. (2013) 368:987–98. doi: 10.1056/NEJMoa1209825
90. van den Bogaard VA, Ta BD, van der Schaaf A, Bouma AB, Middag AMH, Bantema-Joppe EJ, et al. Validation and modification of a prediction model for acute cardiac events in patients with breast cancer treated with radiotherapy based on three-dimensional dose distributions to cardiac substructures. *J Clin Oncol*. (2017) 35:1171–8. doi: 10.1200/JCO.2016.69.8480
91. van den Bogaard VAB, van Luijk P, Hummel YM, van der Meer P, Schuit E, Boerman LM, et al. Cardiac function after radiation therapy for breast cancer. *Int J Radiat Oncol Biol Phys*. (2019) 104:392–400. doi: 10.1016/j.ijrobp.2019.02.003
92. Lorenzen EL, Taylor CW, Maraldo M, Nielsen MH, Offersen BV, Andersen MR, et al. Inter-observer variation in delineation of the heart and left anterior descending coronary artery in radiotherapy for breast cancer: a multi-centre study from Denmark and the UK. *Radiother Oncol*. (2013) 108:254–8. doi: 10.1016/j.radonc.2013.06.025
93. Feng M, Moran JM, Koelling T, Chugtai A, Chan JL, Freedman L, et al. Development and validation of a heart atlas to study cardiac exposure to radiation following treatment for breast cancer. *Int J Radiat Oncol Biol Phys*. (2011) 79:10–8. doi: 10.1016/j.ijrobp.2009.10.058
94. Lee J, Hua KL, Hsu SM, Lin JB, Lee CH, Lu KW, et al. Development of delineation for the left anterior descending coronary artery region in left breast cancer radiotherapy: an optimized organ at risk. *Radiother Oncol*. (2017) 122:423–30. doi: 10.106/j.radonc.2016.12.029
95. Francolini G, Desideri I, Meattini I, Becherini C, Terziani F, Olmetto E, et al. Assessment of a guideline-based heart substructures delineation in left-sided breast cancer patients undergoing adjuvant radiotherapy : Quality assessment within a randomized phase III trial testing a cardioprotective treatment strategy (SAFE-2014). *Strahlenther Onkol*. (2019) 195:43–51. doi: 10.1007/s00066-018-1388-x
96. Jacob S, Camilleri J, Derreumaux S, Walker V, Lairez O, Lapeyre M, et al. Is mean heart dose a relevant surrogate parameter of left ventricle and coronary arteries exposure during breast cancer radiotherapy: a dosimetric

evaluation based on individually-determined radiation dose (BACCARAT study). *Radiat Oncol*. (2019) 14:29. doi: 10.1186/s13014-019-1234-z
97. Kolossváry M, Karády J, Kikuchi Y, Ivanov A, Schlett CL, Lu MT, et al. Radiomics versus visual and histogram-based assessment to identify atheromatous lesions at coronary CT angiography: an ex vivo study. *Radiology*. (2019) 293:89–96. doi: 10.1148/radiol.2019190407
98. Currie G, Iqbal B, Kiat H. Intelligent imaging: radiomics and artificial neural networks in heart failure. *J Med Imaging Radiat Sci*. (2019) 50:571–4. doi: 10.1016/j.jmir.2019.08.006
99. Lustberg T, van Soest J, Jochems A, Deist T, van Wijk Y, Walsh S, et al. Big data in radiation therapy: challenges and opportunities. *Br J Radiol*. (2017) 90:20160689. doi: 10.1259/bjr.20160689
100. Mottet N, Bellmunt J, Bolla M, Briers E, Cumberbatch MG, De Santis M, et al. EAU-ESTRO-SIOG guidelines on prostate cancer. part 1: screening, diagnosis, and local treatment with curative intent. *Eur Urol*. (2017) 71:618–29. doi: 10.1016/j.eururo.2016.08.003
101. Davis KM, Kelly SP, Luta G, Tomko C, Miller AB, Taylor KL. The association of long-term treatment-related side effects with cancer-specific and general quality of life among prostate cancer survivors. *Urology*. (2014) 84:300–6. doi: 10.1016/j.urology.2014.04.036
102. Viani GA, Stefano EJ, Afonso SL. Higher-than-conventional radiation doses in localized prostate cancer treatment: a meta-analysis of randomized, controlled trials. *Int J Radiat Oncol Biol Phys*. (2009) 74:1405–18. doi: 10.1016/j.ijrobp.2008.10.091
103. Fiorino C, Fellin G, Rancati T, Vavassori V, Bianchi C, Borca Casanova V, et al. Clinical and dosimetric predictors of late rectal syndrome after 3D-CRT for localized prostate cancer: preliminary results of a multicenter prospective study. *Int J Radiat Oncol Biol Phys*. (2008) 70:1130–7. doi: 10.1016/j.ijrobp.2007.07.2354
104. Michalski JM, Yan Y, Watkins-Bruner D, Bosch WR, Winter K, Galvin JM, et al. Preliminary toxicity analysis of 3-dimensional conformal radiation therapy versus intensity modulated radiation therapy on the high-dose arm of the Radiation Therapy Oncology Group 0126 prostate cancer trial. *Int J Radiat Oncol Biol Phys*. (2013) 87:932–8. doi: 10.1016/j.ijrobp.2013.07.041
105. Liu M, Moiseenko V, Agranovich A, Karvat A, Kwan W, Saleh ZH, et al. Normal tissue complication probability (NTCP) modeling of late rectal bleeding following external beam radiotherapy for prostate cancer: a test of the QUANTEC-recommended NTCP model. *Acta Oncol*. (2010) 49:1040–4. doi: 10.3109/0284186X.2010.509736
106. Troeller A, Yan D, Marina O, Schulze D, Alber M, Parodi K, et al. Comparison and limitations of DVH-based NTCP models derived from 3D-CRT and IMRT data for prediction of gastrointestinal toxicities in prostate cancer patients by using propensity score matched pair analysis. *Int J Radiat Oncol Biol Phys*. (2015) 91:435–43. doi: 10.1016/j.ijrobp.2014.09.046
107. Gulliford SL, Foo K, Morgan RC, Aird EG, Bidmead AM, Critchley HC, et al. Dose-volume constraints to reduce rectal side effects from prostate radiotherapy: evidence from MRC RT01 Trial ISRCTN 47772397. *Int J Radiat Oncol Biol Phys*. (2010) 76:747–54. doi: 10.1016/j.ijrobp.2009.02.025
108. Fellin G, Rancati T, Fiorino C, Vavassori V, Antognoni P, Baccolini M, et al. Long term rectal function after high-dose prostatecancer radiotherapy: results from a prospective cohort study. *Radiother Oncol*. (2014) 110:272–7. doi: 10.1016/j.radonc.2013.09.028
109. Morgan SC, Hoffman K, Loblaw DA, Buyyounouski MK, Patton C, Barocas D, et al. Hypofractionated radiation therapy for localized prostate cancer: an ASTRO, ASCO, and AUA evidence-based guideline. *J Clin Oncol*. (2018) 36:JCO1801097. doi: 10.1200/JCO.18.01097
110. Musunuru HB, Davidson M, Cheung P, Vesprini D, Liu S, Chung H, et al. Predictive parameters of symptomatic hematochezia following 5-fraction gantry-based SABR in prostate cancer. *Int J Radiat Oncol Biol Phys*. (2016) 94:1043–51. doi: 10.1016/j.ijrobp.2015.12.010
111. Alayed Y, Davidson M, Quon H, Cheung P, Chu W, Chung HT, et al. Dosimetric predictors of toxicity and quality of life following prostate stereotactic ablative radiotherapy. *Radiother Oncol*. (2019) 144:135–40. doi: 10.1016/j.radonc.2019.11.017
112. Abdollahi H, Mahdavi SR, Mofid B, Bakhshandeh M, Razzaghdoust A, Saadipoor A, et al. Rectal wall MRI radiomics in prostate cancer patients: prediction of and correlation with early rectal toxicity. *Int J Radiat Biol*. (2018) 94:829–37. doi: 10.1080/09553002.2018
113. Abdollahi H, Tanha K, Mofid B, Razzaghdoust A, Saadipoor A, Khalafi L, et al. MRI radiomic analysis of IMRT-induced bladder wall changes in prostate cancer patients: a relationship with radiation dose and toxicity. *J Med Imaging Radiat Sci*. (2019) 50:252–60. doi: 10.1016/j.jmir.2018.12.002
114. Abdollahi H, Mahdavi SR, Shiri I, Mofid B, Bakhshandeh M, Rahmani K. Magnetic resonance imaging radiomic feature analysis of radiation-induced femoral head changes in prostate cancer radiotherapy. *J Cancer Res Ther*. (2019) 15(Supplement):S11–9. doi: 10.4103/jcrt.JCRT_172_18
115. Rossi L, Bijman R, Schillemans W, Aluwini S, Cavedon C, Witte M, et al. Texture analysis of 3D dose distribution for predictive modelling of toxicity rates in radiotherapy. *Radiother Oncol*. (2018) 129:548–53. doi: 10.1016/j.radonc.2018.07.027
116. Mostafaei S, Abdollahi H, Kazempour Dehkordi S, Shiri I, Razzaghdoust A, Moghaddam SHZ, et al. CT imaging markers to improve radiation toxicity prediction in prostate cancer radiotherapy by stacking regression algorithm. *Radiol Med*. (2020) 125:87–97. doi: 10.1007/s11547-019-01082-0
117. Lorenz JW, Schott D, Rein L, Mostafaei F, Noid G, Lawton C, et al. Serial T2-weighted magnetic resonance images acquired on a 1.5 tesla magnetic resonance linear accelerator reveal radiomic feature variation in organs at risk: an exploratory analysis of novel metrics of tissue response in prostate cancer. *Cureus*. (2019) 11:e4510. doi: 10.7759/cureus.4510
118. Lee S, Kerns S, Ostrer H, Rosenstein B, Deasy JO, Oh JH. Machine learning on a genome-wide association study to predict late genitourinary toxicity after prostate radiation therapy. *Int J Radiat Oncol Biol Phys*. (2018) 101:128–35. doi: 10.1016/j.ijrobp.2018.01.054
119. Sanduleanu S, Woodruff HC, de Jong EEC, van Timmeren JE, Jochems A, Dubois L, et al. Tracking tumor biology with radiomics: a systematic review utilizing a radiomics quality score. *Radiother Oncol*. (2018) 127:349–60. doi: 10.1016/j.radonc.2018.03.033
120. Zwanenburg A, Vallieres M, Abdalah MA, Aerts HJWL, Andrearczyk V, Apte A, et al. The image biomarker standardization initiative: standardized quantitative radiomics for high-throughput image-based phenotyping. *Radiology*. (2020) 295:328–38. doi: 10.1148/radiol.2020191145
121. Traverso A, Wee L, Dekker A, Gillies R. Repeatability and reproducibility of radiomic features: a systematic review. *Int J Radiat Oncol Biol Phys*. (2018) 102:1143–58. doi: 10.1016/j.ijrobp.2018.05.053
122. Welch ML, McIntosh C, Haibe-Kains B, Milosevic MF, Wee L, Dekker A, et al. Vulnerabilities of radiomic signature development: the need of safeguards. *Radiother Oncol*. (2019) 130:2–9. doi: 10.1016/j.radonc.2018.10.027
123. Sharabiani M, Clementel E, Andratschke N, Hurkmans C. Generalizability assessment of head and neck cancer NTCP models based on the TRIPOD criteria. *Radiother Oncol*. (2020) 146:143–50. doi: 10.1016/j.radonc.2020.02.013
124. El Naqa I, Pandey G, Aerts H, Chien JT, Andreassen CN, Niemierko A, et al. Radiation therapy outcomes models in the era of radiomics and radiogenomics: uncertainties and validation. *Int J Radiat Oncol Biol Phys*. (2018) 102:1070–3. doi: 10.1016/j.ijrobp.2018.08.022

Conflict of Interest: The authors declare that the research was conducted in the absence of any commercial or financial relationships that could be construed as a potential conflict of interest.

frontiers in Oncology

ORIGINAL RESEARCH
published: 15 October 2020
doi: 10.3389/fonc.2020.584756

Intermediate Dose-Volume Parameters, Not Low-Dose Bath, Is Superior to Predict Radiation Pneumonitis for Lung Cancer Treated With Intensity-Modulated Radiotherapy

*Yinnan Meng[1,2], Wei Luo[3], Wei Wang[1,2], Chao Zhou[1,2], Suna Zhou[1,2], Xingni Tang[1,2], Liqiao Hou[1,2], Feng-Ming Spring Kong[1,4,5] and Haihua Yang[1,2]**

[1] Laboratory of Cellular and Molecular Radiation Oncology, Radiation Oncology Institute of Enze Medical Health Academy, Affiliated Taizhou Hospital of Wenzhou Medical University, Taizhou, China, [2] Department of Radiation Oncology, Affiliated Taizhou Hospital of Wenzhou Medical University, Taizhou, China, [3]Department of Radiation Medicine, University of Kentucky, Lexington, KY, United States, [4] Department of Clinical Oncology, Hong Kong University Shenzhen Hospital and Queen Mary Hospital, Hong Kong University Li Ka Shing Medical School, Hong Kong, China, [5] Department of Radiation Oncology, University Hospitals/Seidman Cancer Center and Case Comprehensive Cancer Center, Case Western Reserve University, Cleveland, OH, United States

OPEN ACCESS

Edited by:
Tiziana Rancati,
Istituto Nazionale dei Tumori (IRCCS), Italy

Reviewed by:
Gilles Defraene,
KU Leuven, Belgium
Zachary D Horne,
Allegheny Health Network, United States

***Correspondence:**
Haihua Yang
yhh93181@hotmail.com

Specialty section:
This article was submitted to Radiation Oncology, a section of the journal Frontiers in Oncology

Received: 18 July 2020
Accepted: 22 September 2020
Published: 15 October 2020

Citation:
Meng Y, Luo W, Wang W, Zhou C, Zhou S, Tang X, Hou L, Kong FS and Yang H (2020) Intermediate Dose-Volume Parameters, Not Low-Dose Bath, Is Superior to Predict Radiation Pneumonitis for Lung Cancer Treated With Intensity-Modulated Radiotherapy. Front. Oncol. 10:584756. doi: 10.3389/fonc.2020.584756

Purpose: Although intensity-modulated radiotherapy (IMRT) is now a preferred option for conventionally fractionated RT in lung cancer, the commonly used cutoff values of the dosimetric constraints are still mainly derived from the data using three-dimensional conformal radiotherapy (3D-CRT). We aimed to compare the prediction performance among different dosimetric parameters for acute radiation pneumonitis (RP) in patients with lung cancer received IMRT.

Methods: A total of 236 patients treated with IMRT were retrospectively reviewed in two independent groups of lung cancer from January 2014 to August 2018. The primary endpoint was grade 2 or higher acute RP (RP2). Dose metrics were generated from the bilateral lung volume outside GTV ($Vdose_G$) and PTV ($Vdose_P$). The associations of RP2 with clinical variables, dose-volume parameters and mean lung dose (MLD) were analyzed by univariate and multivariate logistic regression. The power of discrimination among each predictor was assessed by employing the bootstrapped area under the receiver operating characteristic curve (AUC), net reclassification improvement (NRI), and the integrated discrimination improvement (IDI).

Results: Thirty-four (14.4%) out of 236 patients developed acute RP2 after the end of IMRT. The clinical parameters were identified as less important predictors for RP2 based on univariate and multivariate analysis. In both studied groups, the significance of association was more convincing in $V20_P$, $V30_P$, and MLD_P (smaller Ps) than $V5_G$ and $V5_P$. The largest bootstrapped AUC was identified for the $V30_P$. We found a trend of better

discriminating performance for the $V20_P$ and $V30_P$, and MLD_P than the $V5_G$ and $V5_P$ according to the higher values in AUC, IDI, and NRI analysis. To limit RP2 incidence less than 20%, the $V30_P$ cutoff was 14.5%.

Conclusions: This study identified the intermediate dose-volume parameters $V20_P$ and $V30_P$ with better prediction performance for acute RP2 than low-dose metrics $V5_G$ and $V5_P$. Among all studied predictors, the $V30_P$ had the best discriminating power, and should be considered as a supplement to the traditional dose constraints in lung cancer treated with IMRT.

Keywords: lung cancer, intensity modulated radiotherapy (IMRT), radiation pneumonitis (RP), dosimetric parameters, prediction model

INTRODUCTION

Acute radiation pneumonitis (RP), a challenging dose-limiting toxicity, commonly occurs within 1 to 6 months (most often within 12 weeks) after the completion of thoracic radiotherapy (RT) (1, 2). It is also the main reason to preclude the initiation of consolidative immunotherapy for local-advanced unresectable non-small cell lung cancer (3).

The quantitative analyses of normal tissue effects in the clinic (QUANTEC) lung project reviewed over 70 articles published before 2010 and provided the most reliable dose-RP relationship models to overcome the inconsistency (4). Accordingly the guidelines recommend the cutoff values of lung dose constraints to be the bilateral lung volume exceeding 20 Gy (V20) ≤35% and mean lung dose (MLD) ≤20 Gy (5, 6). However, the majority of evidence in the QUANTEC was based on three-dimensional conformal radiation therapy (3D-CRT), which may not well represent the dose distributions delivered by the more advanced techniques, such as intensity-modulated radiotherapy (IMRT). Ten years have passed since the QUANTEC, and there is a need to investigate more accurate dose predictors based on new data emerging from IMRT.

In a secondary analysis of the Radiation Therapy Oncology Group (RTOG) 0617, the IMRT group had a significantly larger V5 (61.6% vs. 58.4%), similar V20 and MLD compared to the 3D-CRT group. However, on the contrary, the severe RP was found to be significantly lower in the IMRT group (3.5% vs. 7.9%) (7). The commonly used dose constraints, especially V5, could not provide a sufficient explanation of why the severe RP was much lower in the IMRT group.

We hypothesized that the dose distribution differences between 3D-CRT and IMRT might impact the plan optimization strategy. This study aimed to analyze the prediction performance for symptomatic RP using various dosimetric parameters in two independent groups of lung cancer treated with IMRT.

MATERIALS AND METHODS

Study Population

In this study, we retrospectively reviewed a total of 236 patients treated with IMRT between January 2014 and August 2018. The primary IMRT group included 183 consecutive patients with lung cancer treated before September 2017. The key inclusion criteria were pathologically confirmed lung cancer, available dosimetric data, follow-up records of at least three months, conventional daily fraction, first time receiving thoracic RT, and only thoracic IMRT. Patients receiving a prescription dose of less than 50 Gy were excluded from this study.

Starting from November 2017, we prescribed a higher dose for definitive radiotherapy to patients with unresectable stage III NSCLC. In addition, we routinely acquired a mid-treatment computed tomography (CT) and planned a new adaptive radiotherapy (ART). An independent group of 53 consecutive patients treated with IMRT-ART were selected using the same inclusion criteria as for the primary IMRT group.

The bilateral lung volumes were delineated according to the RTOG 1106 atlas of organs at risk under the revision and supervision of a senior physician (8). An additional lung definition was created for each patient by excluding the PTV from the bilateral lung volume. For all included patients, the collected clinical variables included age, gender, smoking status, tumor histology and stage, chemotherapy, and surgery. Dose metrics generated from dose-volume histograms (DVHs) in this study were including $V5_G$, $V10_G$, $V20_G$, $V30_G$, $V40_G$, $V50_G$, and MLD_G from the bilateral lung volume minus GTV, and $V5_P$, $V10_P$, $V20_P$, $V30_P$, $V40_P$, $V50_P$, and MLD_P from the lung minus PTV. The absolute lung volumes spared from certain dose levels were collected, including 5, 10, 20, 30, 40, and 50 Gy ($AV5\text{-}50_{Spared}$). The total dose metrics for adaptative plans were summed up by using rigid registration and slightly manual adjustment with initial plans.

The institutional review board in our medical center waived the requirement of written informed consent because of the retrospective design in this study.

Radiotherapy

Conventional or four-dimensional (4D) computed tomography (CT) was performed for the radiotherapy simulations. The patients were immobilized in the supine position with their arms above their head. The CT scans were performed with 5 mm or less slice thickness and included the entire neck and lung. Pre-treatment positron emission tomography (PET)/CT was not routinely used in staging and tumor volume delineation.

All of the patients were treated with conventionally fractionated simultaneous integrated boost IMRT. The gross tumor volume (GTV) was defined as the visible primary tumor and positive mediastinal lymph node on the treatment planning CT or pre-treatment PET scan. The clinical target volume (CTV) was defined as GTV with a 0.5 cm to 1 cm margin and the region at high risk for lymph node involvement. Another 5 mm uniform expansion was delineated from the GTV and CTV to create the planning gross tumor volume (PGTV) and planning target volume (PTV). Image guidance was performed with an orthogonal megavoltage electronic portal imaging device (EPID) or a kilovoltage cone beam computed tomography (CBCT) for inter-fractional geometric assurance.

The prescriptions of conventionally fractionated IMRT were 54 to 66 Gy to the PGTV and 45 to 54 Gy to the PTV in 25 to 30 fractions for curative intent. The prescription dose was 50 Gy to the PTV for the patients receiving postoperative RT with negative margins or local palliative purposes. All treatment plans were designed with the goal of delivering the prescribed dose to at least 95% of the PGTV and PTV.

Endpoints and Follow-Ups

The primary endpoint was grade 2 or above acute radiation pneumonitis (RP2) within three months after radiotherapy. We graded RP according to the system described by Kong et al., which combines the considerations of SWOG, RTOG criteria, and CTCAE to provide an accurate assessment. The toxicities were prospectively evaluated during RT, and at 1 and 3 months of follow-up after the completion of IMRT. The diagnosis of acute RP was required to be distinguished from other causes, such as fibrosis, infection, or tumor recurrence.

Statistical Analysis

For a description of the population, we used the median and range for continuous variables and the percentage for categorical variables. Univariate and multivariate logistic regression were performed to analyze the correlation between predictors and RP2. The age and location factors will be included in the multivariate analysis since they were found associated with a higher risk of pneumonitis from several previous reports (9, 10). All factors with a P value less than 0.20 in the univariate analysis will be included in a multivariate analysis. Because the multicollinearity among dose metrics, only one parameter at a time will be put in each multivariate model with set clinical factors. The patients who died before a diagnosis of RP2 were not censored, since only the acute phase of RP after radiotherapy was considered. The Akaike information criterion (AIC) and Bayesian information criterion (BIC) were applied to assess the relative goodness of fit for each dose prediction model. We employed the area under the receiver operating characteristic curve (AUC) of the receiver operating characteristic curve (ROC) to assess the RP2 discrimination performance, with the 1000-sample bootstrap method to internal validate the stability of the predictors. The RP2 risk predictors were further compared by the integrated discrimination improvement (IDI) and net reclassification improvement (NRI) analysis. A positive value of NRI or IDI indicates a preferred model over the reference in discriminating of the events and non-events (11, 12). Differences were considered significant at $P<0.05$ (2-sided). GraphPad Prism, version 8.02 (GraphPad Software, San Diego, California) and R (R Foundation for Statistical Computing, Vienna, Austria) were used in this study.

RESULTS

Baseline Characteristics and RP2 Association Analysis

A total of 236 patients were retrospectively reviewed in this study. The clinical characteristics and their association with RP2 are shown in **Table 1**. RP2 was found in 34 patients (14.4%); 26 out of 183 (14.2%) in the IMRT group, and 8 out of 53 (15.1%) in the IMRT-ART group. In the univariate logistic regression, none of the clinical factors was significantly associated with RP2, although the female gender (P=0.101) and the use of chemotherapy (P=0.107) had a trend of higher RP2 risk.

In the primary IMRT group, a significant association with RP2 was found for V5, V10, V20, V30, and MLD from two lung definitions. The significance was more convincing in $V20_P$ (P= 0.005, OR=1.204), $V30_P$ (P=0.003, OR=1.302) and MLD_P (0.004, OR=1.421) than in the other parameters (**Figure 1A**). In the IMRT-ART group, only the parameters of V20, V30, and MLD from both lung volumes were confirmed to be significantly associated with RP2 (**Figure 1B**).

In the multivariate analysis, age, tumor location, and chemotherapy did not reach significance (All Ps> 0.05). All of the dosimetric factors remained as independent predictors of RP2 in each of their multivariate models. Female gender was found significantly associated with RP2 in the models including $V20_G$ and $V20_P$, but not had a significant association in those including other dosimetric parameters (**Table S1**). Given a very limited number of female patients were included in this study (9.7%), the gender factor will not be considered in the direct comparison of the prediction performance for RP2 using different dosimetric factors. Discrimination performance for RP2

We employed the bootstrapped area under the ROC (AUC) to evaluate the discrimination performance for RP2 using each dosimetric parameter in 236 patients. The $V30_P$ had the best prediction performance among all dose metrics (AUC=0.683). We found that the V5, V20, V30 and MLD from the bilateral lung volume minus PTV with larger AUCs than the ones from the lung minus GTV. The V20, V30 and MLD from both lung volumes showed a trend of better discriminating values than V5, even their confidence intervals of AUCs overlapped. The absolute volume of spared lung parameters showed lower prediction values for RP2 (All AUCs smaller than 0.55) compared with the dose-volume predictors (**Table 2**).

The $V20_P$, $V30_P$, and MLD_P displayed a trend towards larger values of NRI and IDI than the most commonly used parameter, MLD_G, in both the primary IMRT and IMRT-ART groups. The V5 and V10 from two lung volumes compared with the MLD_G had less reliable prediction performance in IMRT-ART group, while V40 and V50 were significantly inferior in discrimination based on the primary IMRT data. Details of NRI and IDI analysis for each dose metrics are shown in **Figure 2**.

TABLE 1 | Correlation of clinical characteristics with grade ≥2 acute radiation pneumonitis.

Characteristics	No. of Patients(N=236) (%)	No. of Grade ≥2 RP(N=34) (%)	Odds Ratio	95% CI	P Value*
Age					
≤64 (Median)	125 (53)	17 (50.0)	1.00		
>64 (Median)	111 (47)	17 (50.0)	1.15	0.56–2.38	0.708
Gender					
Male	213 (90.3)	28 (82.0)	1.00		
Female	23 (9.7)	6 (18.0)	2.33	0.85–6.42	0.101
Smoking					
Non-smoker	47 (19.9)	7 (21.0)	1.00		
Smoker	189 (80.1)	27 (79.0)	0.95	0.39–2.34	0.915
Pathology					
Squamous	158 (66.9)	25 (74.0)	1.00		
Adenocarcinoma	36 (15.3)	5 (15.0)	0.86	0.30–2.42	0.772
Small Cell	36 (15.3)	3 (9.0)	0.48	0.14–1.70	0.257
Others	6 (2.5)	1 (3.0)	1.06	0.12–9.50	0.956
Stage					
I/II	14 (5.9)	0 (0)	0		0.999
III	168 (71.2)	28 (82)	1.60	0.63–4.10	0.327
IV	54 (22.9)	6 (18)	1.00		
Tumor location					
Upper	109 (46.2)	14 (41.2)	1.00		
Middle or lower	127 (53.8)	20 (58.8)	1.27	0.61–2.65	0.527
Chemo					
No	29 (12.3)	1 (3.0)	1.00		
Yes	207 (87.7)	33 (97.0)	5.31	0.70–40.40	0.107
Surgery					
No	181 (76.7)	28 (82.4)	1.00		
Yes	55 (23.3)	6 (17.6)	0.67	0.26–1.71	0.401

RP, radiation pneumonitis; CI, confidence interval.
**By univariate logistic regression analysis.*

Evaluation of the Goodness of Fit for Prediction Models

The Akaike information criterion (AIC) and Bayesian information criterion (BIC) were used to evaluate the relative values of the goodness of fit for RP2 prediction models in two independent groups. Among all candidate models, better data fitness with the smallest values of AIC and BIC were found in the model with $V30_P$ in both IMRT and IMRT-ART groups. The models with $V20_P$, $V30_P$, and MLD_P had relatively smaller values of AIC and BIC than $V5_G$ and $V5_P$ in both groups of patients (**Figure 3**).

Prediction Model With $V30_P$

The probability of RP2 from 236 included patients can be estimated from $V30_P$ by a fitted logistic formula: Logit(P) = −4.84+0.238X; P (% of RP2) =1/[1+exp (−0.238*$V30_P$ + 4.84)]. The prediction curve was plotted in **Figure 4**. The Hosmer-Lemeshow test showed no significant departure from a well-fitted model (P=0.968). To limit the probability of RP2 less than 20%, the $V30_P$ should be controlled to under 14.5%. According to current data, when the $V30_P$ <14.5%, the RP2 incidence was 11.2%; and when the $V30_P$ >14.5%, the RP2 incidence was 26.5%.

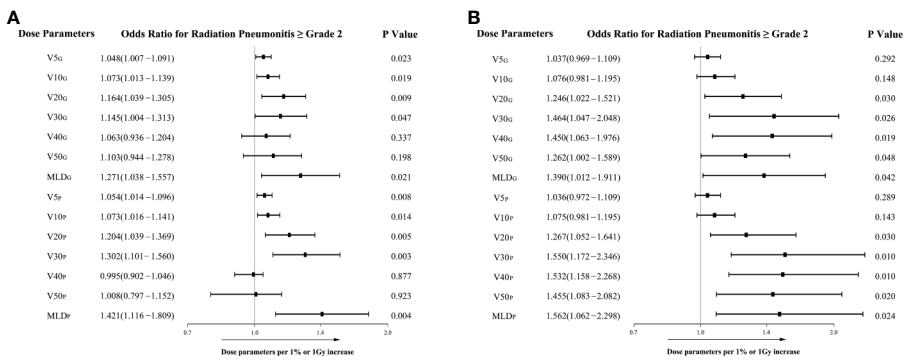

FIGURE 1 | The associations of dosimetric parameters with grade ≥2 radiation pneumonitis in the univariate logistic regression analysis. **(A)** The associations in the primary IMRT group; **(B)** The associations in the IMRT-ART group.

TABLE 2 | Bootstrapped AUC and 95% CI for dosimetric parameters.

Parameters	AUC	Lower CI	Upper CI
$V5_G$	0.603	0.538	0.666
$V10_G$	0.634	0.550	0.678
$V20_G$	0.650	0.585	0.711
$V30_G$	0.623	0.558	0.685
$V40_G$	0.596	0.530	0.659
$V50_G$	0.579	0.513	0.643
MLD_G	0.638	0.573	0.699
$V5_P$	0.615	0.550	0.678
$V10_P$	0.643	0.578	0.704
$V20_P$	0.650	0.585	0.710
$V30_P$	0.683	0.620	0.742
$V40_P$	0.619	0.553	0.681
$V50_P$	0.579	0.513	0.643
MLD_P	0.677	0.613	0.736
$AV5_{Spared}$	0.513	0.447	0.578
$AV10_{Spared}$	0.506	0.440	0.571
$AV20_{Spared}$	0.522	0.456	0.587
$AV30_{Spared}$	0.535	0.469	0.600
$AV40_{Spared}$	0.539	0.474	0.604
$AV50_{Spared}$	0.550	0.484	0.614

AUC, the area under the receiver operating curves; RT, radiotherapy; $Vdose_G$, MLD_G, dosimetric parameters from lung volume excluding gross tumor volume; $Vdose_P$, MLD_P, dosimetric parameters from lung volume excluding planning treatment volume; $AVdose_{spared}$, Absolute volume of lung spared above certain threshold of dose; V5–50, volume of lung receiving a dose≥5–50Gy; MLD, mean lung dose; CI, confidential interval.

DISCUSSION

This study demonstrated that the $V30_P$ had the best RP2 prediction performance among all dosimetric parameters in two independent groups. None of the clinical factors showed a significant correlation with RP2 in univariate and multivariate analysis. The best prediction performance for RP2 was found with $V30_P$, based on better goodness of fit in AIC and BIC, the largest bootstrapped AUC, and an upward trend towards higher NRI and IDI compared to other dosimetric predictors.

To the best of our knowledge, when using IMRT, this is one of the first studies to compare the prediction performance for RP2 among dosimetric factors from two lung definitions. The results showed that putting a higher priority on the $V30_P$ over V5 in planning optimization may better shape the DVHs, which may lead to a lower RP2 probability.

The normal lung volume definition currently recommended by both the RTOG and EORTC guidelines is total bilateral lung volume minus GTV (5, 8). QUANTEC also recommended using the definition of excluding GTV for the consideration of inconsistent delineation of the PTV from one institution to another (4). Therefore, most studies using IMRT from the past several years only report dose data from the lung volume minus GTV (13–15). However, our previous studies demonstrated that the dosimetric parameters from the lung minus PTV are not inferior to those in the lung minus GTV for RP2 prediction (16). In this study, we further demonstrated that $V30_P$ might be the best predictor among all parameters. Reducing the lung dose inside the PTV may not be reasonable during the optimization process. The conflict between getting 95% of the PTV covered with prescription and simultaneously reducing the dose to the lung in the PTV may complicate the optimization process.

Various dosimetric parameters are highly correlated with each other (17–19). The relative priority of reducing one dose parameter at the expense of increasing another is still unknown. However, with IMRT and VMAT, we have more freedom to optimize the shape of the DVH by reducing the volume of the intermediate dose region by irradiating a more substantial volume with a low dose bath. A few studies discussed the question of whether to deliver a low dose to a larger volume ("a little to a lot") or a high dose to a smaller volume ("a lot to a little") to further reduce the symptomatic RP probability. Willner et al. concluded that a small dose to a large volume was preferable to a large dose to a small lung volume (20). Multiple studies, on the other hand, highlighted the importance of the V5 or other low dose predictors. Metha et al. argued that "a little to a lot"

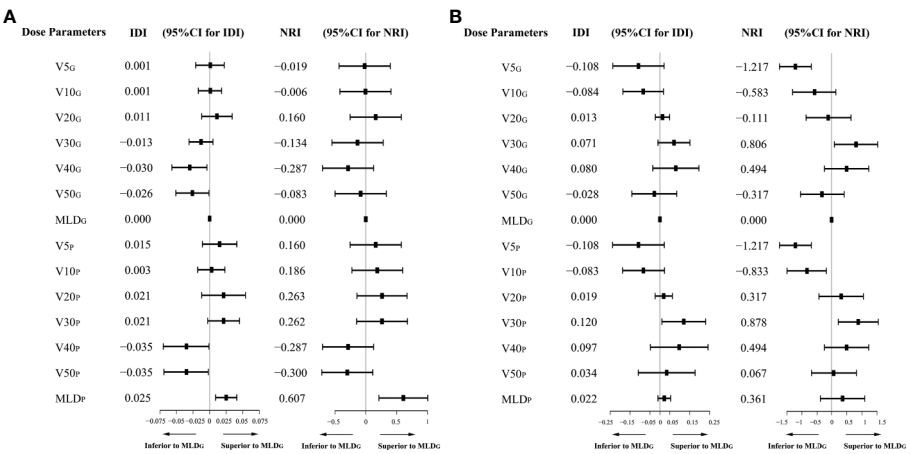

FIGURE 2 | Integrated discrimination improvement (IDI) and net reclassification improvement (NRI) analysis for each dosimetric predictor compared with the MLD_G. **(A)** IDI and NRI values in the primary IMRT group; **(B)** IDI and NRI values in the IMRT-ART group.

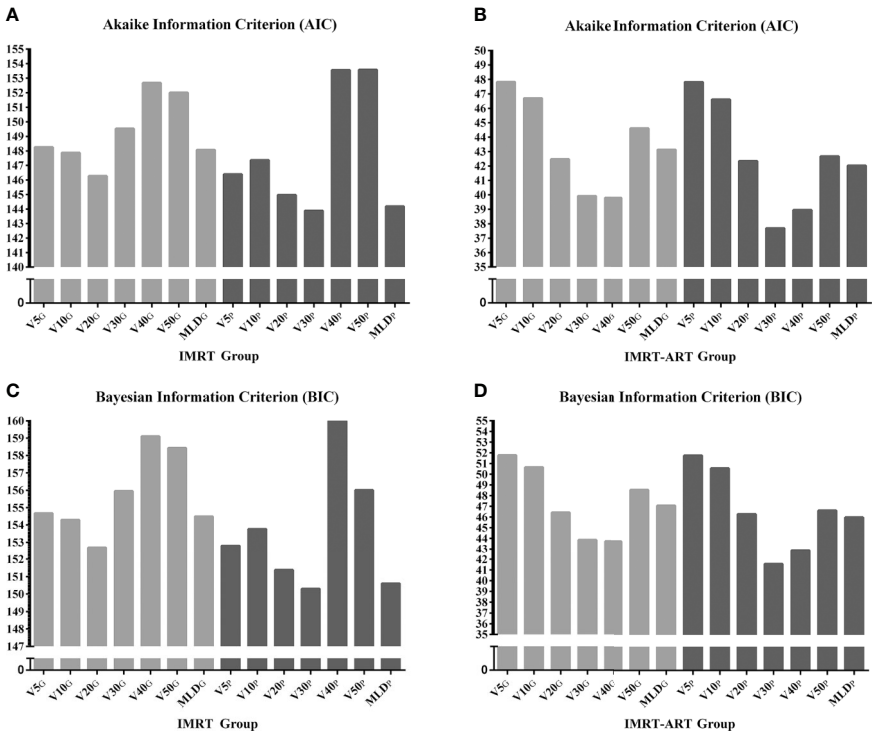

FIGURE 3 | The relative evaluation of goodness of fit test for a model selection using Akaike information criterion (AIC) and Bayesian information criterion (BIC). **(A)** The relative values of the AIC in the IMRT group; **(B)** The relative values of the AIC in the IMRT-ART group; **(C)** The relative values of the BIC in the IMRT group; **(D)** The relative values of the BIC in the IMRT-ART group.

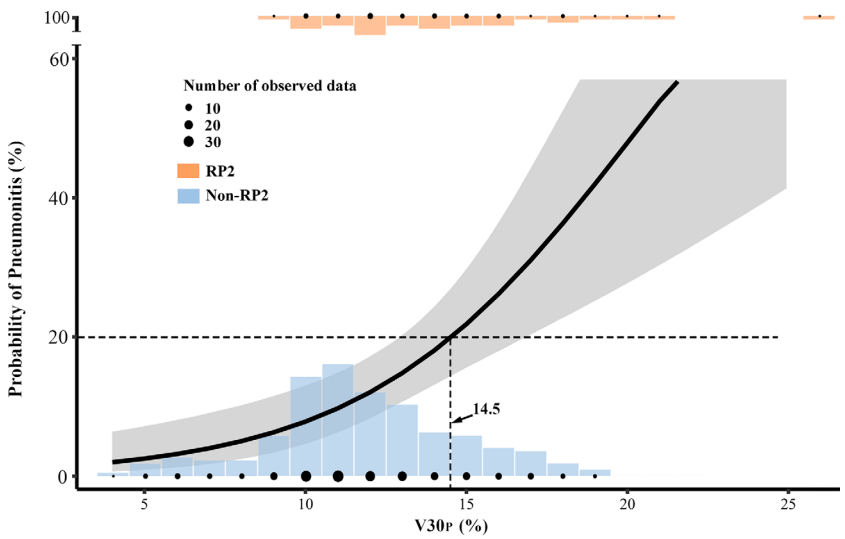

FIGURE 4 | The prediction model with $V30_P$ was plotted in a solid curve with a 95% confidential interval for the probability of grade≥2 acute radiation pneumonitis (RP2). The $V30_P$ cutoff was 14.5% for limiting 20% RP2. The plotted dots and columns represented the number of observed data at each dose level.

could be worse than "a lot to a little" because the loss of carbon monoxide diffusing capacity occurs at 13 Gy (21). Wang et al. analyzed 223 patients treated with 3D-CRT and found a cutoff point of 42% in the V5 to have the best discrimination power for severe RP (18). Yorke et al. concluded that the low dose from V5 to V13 in the total and ipsilateral lung volume were more strongly correlated with severe RP than the V20 and higher dose parameters (19). In the IMRT era, however, the lung V5 did

not show a higher priority than other dose metrics for lung toxicity prevention based on most studies (7, 22). Tucker et al. analyzed the differences in RP risk for patients receiving the same MLD but with different shapes of the DVHs. They suggested that the high dose region plays a more important role than the mean lung dose in the risk of severe RP; "a lot to a little" is associated with a higher risk of severe RP than "a little to a lot." (23) These findings were also confirmed in their later validation study (24). Our results found an inferior predictive value for the V5, which was consistent with the IMRT studies above. We further demonstrated a better RP2 prediction performance with the V30 in the lung region outside the PTV. Adding $V30_P$ along with the traditional $V20_G$ and MLD_G constraints in treatment planning optimization may better shape the DVH to further reduce the RP2 probability.

We recognized that this study is limited in several aspects. First, the patients in the IMRT- ART group had a mid-treatment CT scan and a treatment replanning. The difference in dose calculation methods between non-adaptive and adaptive RT could have resulted in variation in the overall lung dose estimation. However, the prediction performance for each dose parameter was always directly compared in a single patient. Different approaches could have impacted the exact cutoff value, but they would not have changed the relative predictive power regarding which predictor is better. Second, this was a single-institution retrospective study; 236 patients were still a small sample size considering that only 34 patients developed acute RP2. Third, immunotherapy after definitive concurrent chemoradiotherapy is considered a standard routine practice for unresectable locally advanced NSCLC (25). However, during the time of this study, our patients did not have access to PD-1 or PD-L1 inhibitors. The influence of immunotherapy on RP toxicity was not considered in this study.

Ideally, the individual sensitivity to RP2 should be identified before determining the RT prescription. Some investigators have focused on the impact of clinical factors on RP (9, 26, 27). In the current study, only the gender and chemotherapy showed a trend of association with RP2. The older age and lower lobe location were not identified as high-risk factors, and they may not significantly impact the comparison results of dosimetric predictors. Correlations between biological markers and an increased risk of RP have also been found in several studies (28–30). However, none of these risk predictors has been applied and proved in a prospective clinical trial yet. The conventionally fractionated definitive RT for lung cancer is generally prescribed at 60 to 70 Gy with no further escalation in routine practice (31, 32). The most important tool to prevent symptomatic RP is not only to keep it under "safety" criteria, but also to optimize the lung dose as low as reasonably. Our results suggested that the $V30_P$ should be weighted as a higher priority dose constraint in the treatment planning optimization in order to lower the RP2 risk further. A large external dataset from other institutions is needed in the future to further validate the superior RP2 predictive value of the V30 from the lung volume outside the PTV.

DATA AVAILABILITY STATEMENT

The raw data supporting the conclusions of this article will be made available by the authors, without undue reservation.

ETHICS STATEMENT

The studies involving human participants were reviewed and approved by the institutional review board of Taizhou Hospital. Written informed consent for participation was not required for this study in accordance with the national legislation and the institutional requirements.

AUTHOR CONTRIBUTIONS

HY, F-MSK, and WL had the ideas and contributed to the study design. YM, WW, HY, and LH carried out the statistical analysis. YM, CZ, SZ, WL, and WW contributed to the literature search. YM, LH, and XT contributed to the treatment planning and dosimetry data. CZ, SZ, and HY contributed to the evaluation of radiation pneumonitis and clinical data. YM, WL, F-MSK, and HY were major contributors to the writing of the manuscript. All authors contributed to the article and approved the submitted version.

FUNDING

This work was funded by the National Natural Science Foundation of China (81874221), and Taizhou Science and Technology Bureau (20ywa09 and 1802ky07).

SUPPLEMENTARY MATERIAL

The Supplementary Material for this article can be found online at: https://www.frontiersin.org/articles/10.3389/fonc.2020.584756/full#supplementary-material

REFERENCES

1. Kim TH, Cho KH, Pyo HR, Lee JS, Zo JI, Lee DH, et al. Dose-volumetric parameters for predicting severe radiation pneumonitis after three-dimensional conformal radiation therapy for lung cancer. *Radiology* (2005) 235(1):208–15. doi: 10.1148/radiol.2351040248
2. Hanania AN, Mainwaring W, Ghebre YT, Hanania NA, Ludwig M. Radiation-Induced Lung Injury: Assessment and Management. *Chest* (2019) 156(1):150–62. doi: 10.1016/j.chest.2019.03.033
3. Shaverdian N, Offin MD, Rimner A, Shepherd AF, Wu AJ, Rudin CM, et al. Utilization and factors precluding the initiation of consolidative durvalumab in unresectable stage III non-small cell lung cancer. *Radiother Oncol* (2020) 144:101–4. doi: 10.1016/j.radonc.2019.11.015
4. Marks LB, Bentzen SM, Deasy JO, Kong FM, Bradley JD, Vogelius IS, et al. Radiation dose-volume effects in the lung. *Int J Radiat Oncol Biol Phys* (2010) 76(3 Suppl):S70–76. doi: 10.1016/j.ijrobp.2009.06.091
5. De Ruysscher D, Faivre-Finn C, Moeller D, Nestle U, Hurkmans CW, Le Péchoux C, et al. European Organization for Research and Treatment of

Cancer (EORTC) recommendations for planning and delivery of high-dose, high precision radiotherapy for lung cancer. *Radiother Oncol* (2017) 124(1): S0167814017304036. doi: 10.1016/j.radonc.2017.06.003
6. National Comprehensive Cancer Network. *Non-small cell lung Cancer. Version 1*. (2020). Available at: http://www.nccn.org.
7. Chun SG, Hu C, Choy H, Komaki RU, Timmerman RD, Schild SE, et al. Impact of Intensity-Modulated Radiation Therapy Technique for Locally Advanced Non-Small-Cell Lung Cancer: A Secondary Analysis of the NRG Oncology RTOG 0617 Randomized Clinical Trial. *J Clin Oncol* (2017) 35 (1):56–62. doi: 10.1200/JCO.2016.69.1378
8. Kong FM, Ritter T, Quint DJ, Senan S, Gaspar LE, Komaki RU, et al. Consideration of dose limits for organs at risk of thoracic radiotherapy: atlas for lung, proximal bronchial tree, esophagus, spinal cord, ribs, and brachial plexus. *Int J Radiat Oncol Biol Phys* (2011) 81(5):1442–57. doi: 10.1016/j.ijrobp.2010.07.1977
9. Vogelius IR, Bentzen SRM. A literature-based meta-analysis of clinical risk factors for development of radiation induced pneumonitis. *Acta Oncol* (2012) 51(8):975–83. doi: 10.3109/0284186X.2012.718093
10. Kong FM, Wang S. Nondosimetric risk factors for radiation-induced lung toxicity. *Semin Radiat Oncol* (2015) 25(2):100–9. doi: 10.1016/j.semradonc.2014.12.003
11. Pencina MJ, D' Agostino RB Sr., D' Agostino RB Jr., Vasan RS. Evaluating the added predictive ability of a new marker: From area under the ROC curve to reclassification and beyond. *Stat Med* (2008) 27(2):157–72. doi: 10.1002/sim.2929
12. Pencina MJ, D'Agostino RB, Vasan RS. Statistical methods for assessment of added usefulness of new biomarkers. *Clin Chem Lab Med* (2010) 48(12):1703–11. doi: 10.1515/CCLM.2010.340
13. Khalil AA, Hoffmann L, Moeller DS, Farr KP, Knap MM. New dose constraint reduces radiation-induced fatal pneumonitis in locally advanced non-small cell lung cancer patients treated with intensity-modulated radiotherapy. *Acta Oncol* (2015) 54(9):1343–9. doi: 10.3109/0284186X.2015.1061216
14. Wijsman R, Dankers F, Troost EGC, Hoffmann AL, van der Heijden EHFM, de Geus-Oei L-F, et al. Comparison of toxicity and outcome in advanced stage non-small cell lung cancer patients treated with intensity-modulated (chemo-) radiotherapy using IMRT or VMAT. *Radiother Oncol* (2017) 122(2):295–9. doi: 10.1016/j.radonc.2016.11.015
15. Wijsman R, Dankers FJWM, Troost EGC, Hoffmann AL, van der Heijden EHFM, de Geus-Oei L-F, et al. Inclusion of Incidental Radiation Dose to the Cardiac Atria and Ventricles Does Not Improve the Prediction of Radiation Pneumonitis in Advanced-Stage Non-Small Cell Lung Cancer Patients Treated With Intensity Modulated Radiation Therapy. *Int J Radiat Oncol Biol Physics* (2017) 99(2):434–41. doi: 10.1016/j.ijrobp.2017.04.011
16. Meng Y, Yang H, Wang W, Tang X, Jiang C, Shen Y, et al. Excluding PTV from lung volume may better predict radiation pneumonitis for intensity modulated radiation therapy in lung cancer patients. *Radiat Oncol* (2019) 14 (1):7. doi: 10.1186/s13014-018-1204-x
17. Kong FM, Hayman JA, Griffith KA, Kalemkerian GP, Arenberg D, Lyons S, et al. Final toxicity results of a radiation-dose escalation study in patients with non-small-cell lung cancer (NSCLC): predictors for radiation pneumonitis and fibrosis. *Int J Radiat Oncol Biol Phys* (2006) 65(4):1075–86. doi: 10.1016/j.ijrobp.2006.01.051
18. Wang S, Liao Z, Wei X, Liu HH, Tucker SL, Hu C-S, et al. Analysis of clinical and dosimetric factors associated with treatment-related pneumonitis (TRP) in patients with non–small-cell lung cancer (NSCLC) treated with concurrent chemotherapy and three-dimensional conformal radiotherapy (3D-CRT). *Int J Radiat Oncol Biol Phys* (2006) 66(5):1399–407. doi: 10.1016/j.ijrobp.2006.07.1337
19. Yorke ED, Jackson A, Rosenzweig KE, Braban L, Leibel SA, Ling CC. Correlation of dosimetric factors and radiation pneumonitis for non-small-cell lung cancer patients in a recently completed dose escalation study. *Int J Radiat Oncol Biol Physics* (2004) 63(3):672–82. doi: 10.1016/j.ijrobp.2005.03.026
20. Willner J, Jost A, Baier K, Flentje M. A Little to a Lot or a Lot to a Little? *Strahlenther Und Onkol* (2003) 179(8):548–56. doi: 10.1007/s00066-003-1078-0
21. Mehta V. Radiation pneumonitis and pulmonary fibrosis in non–small-cell lung cancer: Pulmonary function, prediction, and prevention. *Int J Radiat Oncol Biol Phys* (2005) 63(1):5–24. doi: 10.1016/j.ijrobp.2005.03.047
22. Yom SS, Liao Z, Liu HH, Tucker SL, Hu CS, Wei X, et al. Initial evaluation of treatment-related pneumonitis in advanced-stage non-small-cell lung cancer patients treated with concurrent chemotherapy and intensity-modulated radiotherapy. *Int J Radiat Oncol Biol Phys* (2007) 68(1):94–102. doi: 10.1016/j.ijrobp.2006.12.031
23. Tucker SL, Liu HH, Liao Z, Wei X, Wang S, Jin H, et al. Analysis of radiation pneumonitis risk using a generalized Lyman model. *Int J Radiat Oncol Biol Phys* (2008) 72(2):568–74. doi: 10.1016/j.ijrobp.2008.04.053
24. Tucker SL, Xu T, Paganetti H, Deist T, Verma V, Choi N, et al. Validation of Effective Dose as a Better Predictor of Radiation Pneumonitis Risk Than Mean Lung Dose: Secondary Analysis of a Randomized Trial. *Int J Radiat Oncol Biol Phys* (2019) 103(2):403–10. doi: 10.1016/j.ijrobp.2018.09.029
25. Antonia SJ, Villegas A, Daniel D, Vicente D, Murakami S, Hui R, et al. Overall Survival with Durvalumab after Chemoradiotherapy in Stage III NSCLC. *N Engl J Med* (2018) 379(24):2342–50. doi: 10.1056/NEJMoa1809697
26. Palma DA, Senan S, Tsujino K, Barriger RB, Rengan R, Moreno M, et al. Predicting Radiation Pneumonitis After Chemoradiation Therapy for Lung Cancer: An International Individual Patient Data Meta-analysis. *Int J Radiat Oncol Biol Phys* (2013) 85(2):444–50. doi: 10.1016/j.ijrobp.2012.04.043
27. Appelt AL, Bentzen SM, Farr KP, Khalil AA, Vogelius IR. OC-0077: Towards individualized dose constraints: The QUANTEC radiation pneumonitis model with clinical risk factors. *Radiother Oncol* (2013) 106(5):605. doi: 10.1016/S0167-8140(15)32383-5
28. Stenmark MH, Cai X-W, Shedden K, Hayman JA, Yuan S, Ritter T, et al. Combining Physical and Biologic Parameters to Predict Radiation-Induced Lung Toxicity in Patients With Non-Small-Cell Lung Cancer Treated With Definitive Radiation Therapy. *Int J Radiat Oncol Biol Phys* (2012) 84(2):e217–22. doi: 10.1016/j.ijrobp.2012.03.067
29. Hawkins PG, Boonstra PS, Hobson ST, Jwd H, Hayman JA, Ten Haken RK, et al. Radiation-induced lung toxicity in non-small-cell lung cancer: Understanding the interactions of clinical factors and cytokines with the dose-toxicity relationship. *Radiother Oncol J Eur Soc Ther Radiol Oncol* (2017) 125(1):66. doi: 10.1016/j.radonc.2017.09.005
30. Wang S, Campbell J, Stenmark MH, Zhao J, Stanton P, Matuszak MM, et al. Plasma Levels of IL-8 and TGF-β1 Predict Radiation Induced Lung Toxicity in Non-Small Cell Lung Cancer Patients: A Validation Study. *Int J Radiat Oncol Biol Phys* (2017) 98(3):615. doi: 10.1016/j.ijrobp.2017.03.011
31. Bezjak A, Temin S, Franklin G, Giaccone G, Govindan R, Johnson ML, et al. Definitive and Adjuvant Radiotherapy in Locally Advanced Non-Small-Cell Lung Cancer: American Society of Clinical Oncology Clinical Practice Guideline Endorsement of the American Society for Radiation Oncology Evidence-Based Clinical Practice Guideline. *J Clin Oncol* (2015) 33(18):2100–5. doi: 10.1200/JCO.2014.59.2360
32. Bradley PJD, Rebecca Paulus BS, Komaki PR, Gregory Masters MD, MD PHC. Standard-dose versus high-dose conformal radiotherapy with concurrent and consolidation carboplatin plus paclitaxel with or without cetuximab for patients with stage IIIA or IIIB non-small-cell lung cancer (RTOG 0617): a randomised, two-by-two factorial ph. *Lancet Oncol* (2015) 16(2):187–99. doi: 10.1016/S1470-2045(14)71207-0

Conflict of Interest: The authors declare that the research was conducted in the absence of any commercial or financial relationships that could be construed as a potential conflict of interest.

frontiers in Oncology

ORIGINAL RESEARCH
published: 15 October 2020
doi: 10.3389/fonc.2020.541281

A Deep Learning Approach Validates Genetic Risk Factors for Late Toxicity After Prostate Cancer Radiotherapy in a REQUITE Multi-National Cohort

Michela Carlotta Massi[1,2], Francesca Gasperoni[3], Francesca Ieva[1,2,4], Anna Maria Paganoni[1,2,4], Paolo Zunino[1], Andrea Manzoni[1], Nicola Rares Franco[1], Liv Veldeman[5,6], Piet Ost[5,6], Valérie Fonteyne[5,6], Christopher J. Talbot[7], Tim Rattay[7], Adam Webb[7], Paul R. Symonds[7], Kerstie Johnson[7], Maarten Lambrecht[8], Karin Haustermans[8], Gert De Meerleer[8], Dirk de Ruysscher[9,10], Ben Vanneste[10], Evert Van Limbergen[9,10], Ananya Choudhury[11], Rebecca M. Elliott[11], Elena Sperk[12], Carsten Herskind[12], Marlon R. Veldwijk[12], Barbara Avuzzi[13], Tommaso Giandini[14], Riccardo Valdagni[13,15,16], Alessandro Cicchetti[16], David Azria[17], Marie-Pierre Farcy Jacquet[18], Barry S. Rosenstein[19,20], Richard G. Stock[19], Kayla Collado[19], Ana Vega[21,22,23], Miguel Elías Aguado-Barrera[21,22], Patricia Calvo[22,24], Alison M. Dunning[25], Laura Fachal[25,26], Sarah L. Kerns[27], Debbie Payne[28], Jenny Chang-Claude[29,30], Petra Seibold[29], Catharine M. L. West[11†], Tiziana Rancati[16†] and on behalf of the REQUITE Consortium*

[1] Modelling and Scientific Computing Laboratory, Math Department, Politecnico di Milano, Milan, Italy, [2] Center for Analysis, Decisions and Society, Human Technopole, Milan, Italy, [3] Medical Research Council-Biostatistic Unit, University of Cambridge, Cambridge, United Kingdom, [4] CHRP-National Center for Healthcare Research and Pharmacoepidemiology, University of Milano-Bicocca, Milan, Italy, [5] Department of Human Structure and Repair, Ghent University, Ghent, Belgium, [6] Department of Radiation Oncology, Ghent University Hospital, Ghent, Belgium, [7] Leicester Cancer Research Centre, Department of Genetics and Genome Biology, University of Leicester, Leicester, United Kingdom, [8] Department of Radiation Oncology, University Hospitals Leuven, Leuven, Belgium, [9] Maastricht University Medical Center, Maastricht, Netherlands, [10] Department of Radiation Oncology (Maastro), GROW Institute for Oncology and Developmental Biology, Maastricht, Netherlands, [11] Translational Radiobiology Group, Division of Cancer Sciences, Manchester Academic Health Science Centre, Christie Hospital, University of Manchester, Manchester, United Kingdom, [12] Department of Radiation Oncology, Universitätsmedizin Mannheim, Medical Faculty Mannheim, Heidelberg University, Mannheim, Germany, [13] Department of Radiation Oncology 1, Fondazione IRCCS Istituto Nazionale dei Tumori, Milan, Italy, [14] Department of Medical Physics, Fondazione IRCCS Istituto Nazionale dei Tumori, Milan, Italy, [15] Department of Oncology and Haemato-Oncology, University of Milan, Milan, Italy, [16] Prostate Cancer Program, Fondazione IRCCS Istituto Nazionale dei Tumori, Milan, Italy, [17] Department of Radiation Oncology, University Federation of Radiation Oncology, Montpellier Cancer Institute, Univ Montpellier MUSE, Grant INCa_Inserm_DGOS_12553, Inserm U1194, Montpellier, France, [18] Department of Radiation Oncology, University Federation of Radiation Oncology, CHU Caremeau, Nîmes, France, [19] Department of Radiation Oncology, Icahn School of Medicine at Mount Sinai, New York, NY, United States, [20] Department of Genetics and Genomic Sciences, Icahn School of Medicine at Mount Sinai, New York, NY, United States, [21] Fundación Pública Galega de Medicina Xenómica, Grupo de Medicina Xenómica (USC), Santiago de Compostela, Spain, [22] Instituto de Investigación Sanitaria de Santiago de Compostela, Santiago de Compostela, Spain, [23] Biomedical Network on Rare Diseases (CIBERER), Madrid, Spain, [24] Department of Radiation Oncology, Complexo Hospitalario Universitario de Santiago, SERGAS, Santiago de Compostela, Spain, [25] Strangeways Research Labs, Department of Oncology, Centre for Cancer Genetic Epidemiology, University of Cambridge, Cambridge, United Kingdom, [26] Wellcome Sanger Institute, Wellcome Genome Campus, Hinxton, United Kingdom, [27] Departments of Radiation Oncology and Surgery, University of Rochester Medical Center, Rochester, New York, NY, United States, [28] Centre for Integrated Genomic Medical Research (CIGMR), University of Manchester, Manchester, United Kingdom, [29] Division of Cancer Epidemiology, German Cancer Research Center (DKFZ), Heidelberg, Germany, [30] University Cancer Center Hamburg, University Medical Center Hamburg-Eppendorf, Hamburg, Germany

Background: REQUITE (validating pREdictive models and biomarkers of radiotherapy toxicity to reduce side effects and improve QUalITy of lifE in cancer survivors) is an international prospective cohort study. The purpose of this project was to analyse a cohort of patients recruited into REQUITE using a deep learning algorithm to identify

OPEN ACCESS

Edited by:
Timothy James Kinsella, Warren Alpert Medical School of Brown University, United States

Reviewed by:
Wei Zhao, Stanford University, United States
Sean P. Collins, Georgetown University, United States

***Correspondence:**
Francesca Ieva
francesca.ieva@polimi.it

[†] These authors have contributed equally to this work

Specialty section:
This article was submitted to Radiation Oncology, a section of the journal Frontiers in Oncology

Received: 08 March 2020
Accepted: 02 September 2020
Published: 15 October 2020

Citation:
Massi MC, Gasperoni F, Ieva F, Paganoni AM, Zunino P, Manzoni A, Franco NR, Veldeman L, Ost P, Fonteyne V, Talbot CJ, Rattay T, Webb A, Symonds PR, Johnson K, Lambrecht M, Haustermans K, De Meerleer G, de Ruysscher D, Vanneste B, Van Limbergen E, Choudhury A, Elliott RM, Sperk E, Herskind C, Veldwijk MR, Avuzzi B, Giandini T, Valdagni R, Cicchetti A, Azria D, Jacquet M-P, Rosenstein BS, Stock RG, Collado K, Vega A, Aguado-Barrera ME, Calvo P, Dunning AM, Fachal L, Kerns SL, Payne D, Chang-Claude J, Seibold P, West CML and Rancati T (2020) A Deep Learning Approach Validates Genetic Risk Factors for Late Toxicity After Prostate Cancer Radiotherapy in a REQUITE Multi-National Cohort. Front. Oncol. 10:541281. doi: 10.3389/fonc.2020.541281

patient-specific features associated with the development of toxicity, and test the approach by attempting to validate previously published genetic risk factors.

Methods: The study involved REQUITE prostate cancer patients treated with external beam radiotherapy who had complete 2-year follow-up. We used five separate late toxicity endpoints: ≥grade 1 late rectal bleeding, ≥grade 2 urinary frequency, ≥grade 1 haematuria, ≥ grade 2 nocturia, ≥ grade 1 decreased urinary stream. Forty-three single nucleotide polymorphisms (SNPs) already reported in the literature to be associated with the toxicity endpoints were included in the analysis. No SNP had been studied before in the REQUITE cohort. Deep Sparse AutoEncoders (DSAE) were trained to recognize features (SNPs) identifying patients with no toxicity and tested on a different independent mixed population including patients without and with toxicity.

Results: One thousand, four hundred and one patients were included, and toxicity rates were: rectal bleeding 11.7%, urinary frequency 4%, haematuria 5.5%, nocturia 7.8%, decreased urinary stream 17.1%. Twenty-four of the 43 SNPs that were associated with the toxicity endpoints were validated as identifying patients with toxicity. Twenty of the 24 SNPs were associated with the same toxicity endpoint as reported in the literature: 9 SNPs for urinary symptoms and 11 SNPs for overall toxicity. The other 4 SNPs were associated with a different endpoint.

Conclusion: Deep learning algorithms can validate SNPs associated with toxicity after radiotherapy for prostate cancer. The method should be studied further to identify polygenic SNP risk signatures for radiotherapy toxicity. The signatures could then be included in integrated normal tissue complication probability models and tested for their ability to personalize radiotherapy treatment planning.

Keywords: prostate cancer, late toxicity, snps, deep learning, autoencoder, validation

INTRODUCTION

Radiotherapy represents the most effective non-surgical modality for the potentially curative treatment of prostate cancer. Around a half of survivors underwent radiotherapy as part of their curative care (1), either as single curative treatment or as adjuvant/salvage treatment after radical prostatectomy.

Despite the fact that prognosis is very good in terms of patients' survival rates, it is widely acknowledged that long-term side-effects after radiotherapy can affect a patient's quality-of-life (2–4). A tool able to identify patients likely to develop toxicity could be a crucial step toward personalized radiotherapy with modification of the dose, fractionation, techniques and supportive care. The ultimate goal is to reduce morbidity and improve quality-of-life.

Radiation toxicity is a multifactorial problem, related not only to the cumulative delivered dose, but also to an intrinsic process within tissues responding to cellular injury. Individual genetic background and biological expression pattern, premorbid conditions, concomitant oncological therapies, as well as the cellular microenvironment, could be important factors in the development of side-effects, although their exact contributions are unknown.

With increased interest in this field and relevant data collection on this topic, predictive models have been developed to identify patients likely to develop side effects during radiotherapy (3).

The identification of genetic factors associated with susceptibility to radiation toxicity represents an emerging research area in oncology. A number of different approaches have been explored (5–13), however, the developed models and biomarkers have failed to progress to routine clinical use due to the lack of thorough independent validation.

REQUITE (validating pREdictive models and biomarkers of radiotherapy toxicity to reduce side effects and improve QUalITy of lifE in cancer survivors) was established with the aim of validating models and biomarkers for the prediction of adverse effects following radiotherapy (14–16). In order to address previous limitations in pooling data, in using common toxicity scoring systems and in collecting standardized data, REQUITE carried out an international, multi-center, prospective observational study. A centralized biobank was also established to store blood samples and genome-wide genotyping of single nucleotide polymorphisms (SNPs) was carried out.

The specific purpose of the present study was to attempt to validate genetic risk factors for late toxicity (rectal bleeding and late urinary symptoms) after prostate cancer radiotherapy in the REQUITE population using a deep learning algorithm. This technique aims to identify patient-specific features that define patients with toxicity ("unhealthy") as outliers with respect to the population of irradiated patients without toxicity ("healthy").

Deep learning has the potential to overcome the difficulties in replication of results faced by the widespread single-SNP association methods used by genome wide association studies (GWAS). The statistical power of GWAS is limited by a combination of the large number of hypotheses being tested simultaneously and the inherently small effect size of the single SNP (17).

Deep learning approaches, with their intrinsic hierarchical structure (where each layer performs a combination of the outcomes of the previous layers), seem particularly adapt at mimicking complex dependencies within data. The method addresses effectively the following issues: (i) unstable selections of correlated variables and inconsistent selections of linearly dependent genetic variables (18); (ii) strong imbalance between positive and negative outcomes which is usually encountered in studies of radiation toxicity.

MATERIALS AND METHODS

Population

REQUITE prostate cancer patients treated with external beam radiotherapy (with/without hormonal therapy, with/without a previous prostatectomy, no brachytherapy) and complete 2-year follow-up were included. Details on the REQUITE population are given in Seibold et al. (14).

Prostate cancer patients were recruited prior to radiotherapy between April 2014 and October 2016. Recruitment was at ten main sites in eight countries (Belgium, France, Germany, Italy, the Netherlands, Spain, UK, US). Conventionally fractionated or hypo-fractionated radiotherapy was prescribed according to local standard-of-care regimens. The patients were followed prospectively for at least 24 months, with longer follow-up encouraged where possible. All patients gave written informed consent. The study was approved by local Ethical Committees and is registered at www.controlled-trials.com (ID ISRCTN98496463).

Demographic, co-morbidity, treatment, physics, longitudinal toxicity (CTCAE v4.0 healthcare professional and patient reported), quality-of-life, and treatment outcome data were collected prospectively using standardized case report forms. CTCAE v4.0 based questionnaires developed to collect patient reported outcomes were adapted from those published elsewhere for the male pelvis (19) and updated to fit with CTCAE v4.0 items.

All patients donated at least two blood samples prior to the start of radiotherapy: an EDTA sample for SNP genotyping plus a PAXgene sample. Genotyping data were generated using the Illumina Infinium OncoArray-500K beadchip. Following standard quality control procedures (20), genotype data were imputed using the 1,000 Genomes Project (version 3) as a reference panel.

Selection of Genetic Risk Factors

We undertook a comprehensive search of Medline and PubMed databases using the keywords "prostate," "prostatic," "radiotherapy," "radiation," "irradiation," "toxicity," "adverse effects," "side-effects," "morbidity," "injury," "genetic variation," "SNP," "GWAS," and "polymorphism." This search identified 60 SNPs published (up to May 31st, 2019) in GWAS patient studies with $p < 1.0{\cdot}10^{-5}$ and where findings were adjusted for multiple comparisons OR in studies including a controlled number of SNPs ($\sim 10^2$) and using multivariable regularization methods coupled to internal validation to control overfitting.

Forty-three of 60 SNPs were available for the REQUITE population (either directly determined or after imputation) and were included in the analysis. These SNPs were identified in five papers (5, 11, 21–23) and the full list is reported in **Table 1**.

Outcome Endpoints

Toxicity endpoints were defined using CTCAE v4.0 scoring reported by health professionals or Patient Reported Outcomes, as detailed for each single endpoint. As the frame of the DSAE is to identify SNPs who would tag a patient as exceptionally "sensitive" to radiation (an "outlier"), patients with other possible known intrinsic higher risk of exhibiting radiation toxicity were always excluded, in particularly patients who had systemic lupus erythematosus, rheumatoid arthritis and other collagen vascular diseases.

The following endpoints were considered:

1. Late rectal bleeding grade≥1 (CTCAE v4.0 scoring): patients exhibiting at least mild bleeding (even requiring no intervention) at 12 or at 24 months. Patients with grade≥1 at baseline and grade≤1 during follow-up were considered as not bleeders; patients with hemorrhoids before radiotherapy treatment were excluded.
2. Late urinary frequency grade≥2 (CTCAE v4.0 scoring): patients with urinary frequency limiting instrumental activities of daily living or if urinary frequency requiting medical management at 12 or at 24 months. Patients with urinary frequency grade≥2 at baseline and grade≤2 during follow-up were considered as not exhibiting this endpoint.
3. Late haematuria grade ≥1 (CTCAE scoring): patients with asymptomatic haematuria (clinical or diagnostic observations only, no intervention indicated) at 12 or 24 months. Patients with haematuria grade≥1 at baseline and grade≤1 during follow-up were considered as not exhibiting the endpoint.
4. Late nocturia grade ≥2 (Patient Reported Outcome): patients declaring need to urinate at least two-three times per night at 12 or 24 months. Patients with nocturia grade≥2 at baseline and grade≤2 during follow-up were considered as not exhibiting the endpoint.
5. Late grade≥1 (Patient Reported Outcome): patients scored with hesitant or dripping stream at 12 or 24 months. Patients with decreased urinary stream grade≥1 at baseline and grade≤1 during follow-up were considered as not exhibiting the endpoint.

Patients who underwent transurethral resection of the bladder and patients on anti-muscarinic drugs (factors which could

TABLE 1 | Full list of SNPs selected from the literature for validation and associated toxicity endpoint following prostate radiotherapy.

SNP	OR	*p*-value	References
Rectal bleeding			
rs10519410	3.7	1.3×10^{-6}	(21)
rs17055178	1.95[#]	6.2×10^{-10}	(23)
Urinary frequency			
rs17599026	3.12	4.16×10^{-8}	(5)
rs342442	0.51	3.86×10^{-7}	(5)
rs8098701	2.41	2.11×10^{-6}	(5)
rs7366282	3.2	2.03×10^{-6}	(5)
rs10209697	2.66	2.27×10^{-6}	(5)
rs4997823	0.49	2.35×10^{-6}	(5)
rs7356945	1.74	3.71×10^{-6}	(5)
rs6003982	0.51	4.28×10^{-6}	(5)
rs10101158	1.8	4.39×10^{-6}	(5)
Decreased urinary stream			
rs7720298	2.71	3.21×10^{-8}	(5)
rs17362923	2.7	6.79×10^{-7}	(5)
rs76273496	3.68	2.71×10^{-6}	(5)
rs144596911	3.6	2.94×10^{-6}	(5)
rs62091368	4.36	3.95×10^{-6}	(5)
rs141342719	3.5	3.97×10^{-6}	(5)
rs673783	2.49	4.33×10^{-6}	(5)
rs10969913	3.92[#]	2.9×10^{-10}	(23)
Haematuria			
rs11122573	1.92[#]	1.8×10^{-8}	(23)
rs708498	0.24	n.a.[§]	(22)
rs845552	0.95	n.a.[§]	(22)
Nocturia			
rs1799983	0.19	n.a.[§]	(22)
rs1045485	0.27	n.a.[§]	(22)
Overall toxicity (STAT[#] score)			
rs10497203*	1.48	8.84×10^{-11}	(11)
rs7582141*	1.45	4.64×10^{-11}	(11)
rs6432512*	1.42	1.97×10^{-10}	(11)
rs264651*	1.49	1.48×10^{-7}	(11)
rs264588*	1.45	3.08×10^{-10}	(11)
rs264631*	1.43	6.4×10^{-10}	(11)
rs147596965	1.95	6.19×10^{-8}	(5)
rs77530448	1.43	7.36×10^{-8}	(5)
rs4906759	1.73	1.55×10^{-7}	(5)
rs71610881	1.82	5.41×10^{-7}	(5)
rs141799618	1.55	1.22×10^{-6}	(5)
rs2842169	1.32	1.45×10^{-6}	(5)
rs11219068	1.32	1.74×10^{-6}	(5)
rs8075565	1.32	2.20×10^{-6}	(5)
rs6535028	1.34	2.70×10^{-6}	(5)
rs4775602	1.26	3.20×10^{-6}	(5)
rs7829759	1.39	3.84×10^{-6}	(5)
rs79604958	1.60	4.33×10^{-6}	(5)
rs12591436	1.20	5.66×10^{-6}	(5)

[#]*overall toxicity as defined by calculating the Standardized Total Average Toxicity (STAT) score (24).*

All these variants are highly correlated in European populations and represent the same association signal. See also correlation matrix as determined in the REQUITE population in the* ***Supplementary Figure 1**.*

[#]*Hazard Ratio.*

§SNPs were selected using Least Absolute Shrinkage and Selection Operator (LASSO) multivariable regression out of a panel of 384 previous identified SNPs, p-value not available.

constitute a confounding factor in the scoring of urinary toxicity) were excluded when considering all urinary endpoints.

Deep Sparse AutoEncoder for SNPs Validation

The methodology described in Massi et al. (25) was considered. This method proposes a novel feature selection algorithm for the minority class in an imbalanced dataset, i.e., in cases like this dataset, where there is a strong imbalance between the number of patients that are scored as healthy (without side effects) vs. unhealthy (with side effects). The approach uses a representation learning technique, specifically a Deep Sparse AutoEncoder, to obtain the best representation of the majority class (healthy patients in this dataset) and to consequently identify which features (SNPs) distinguish the minority class (unhealthy patients) with respect to the majority class.

An AutoEncoder (AE) is a neural network with an output that reconstructs the input (26). In its simplest version an AE is composed of the input, the output and only a single hidden layer. The input layer in our case is composed of J nodes, one per feature (one per SNP), and we consider a data matrix X, in which each row $\mathbf{x}_i$ is the vector of SNPs recorded for the patient i, $i \in \{1, .., N\}$. The input layer is connected to the hidden layer, $\mathbf{h}_i$, through the *encoder* function, f, such that $\mathbf{h}_i = f(\mathbf{W}\mathbf{x}_i + \mathbf{b})$; here $\mathbf{W} \in \mathrm{R}^{H \times J}$ denotes the weight matrix and $\mathbf{b} \in \mathrm{R}^{H \times 1}$ the bias vector. Then, the output is the result of the application of a *decoder* function, g, to the hidden layer $\mathbf{h}_i$, such that $\hat{\mathbf{x}}_i = g(\mathbf{W'}\mathbf{h}_i + \mathbf{b'})$, where $\mathbf{W'} \in \mathrm{R}^{J \times H}$ is the weight matrix and $\mathbf{b} \in \mathrm{R}^{J \times 1}$ is the bias vector. Having fixed the functions f and g, the training of the network consists in estimating the corresponding optimal parameters ($\mathbf{W}$, $\mathbf{b}$, $\mathbf{W'}$, $\mathbf{b'}$), by minimizing the loss function $L(\mathbf{x}_i, \hat{\mathbf{x}}_i)$, which is a function that gives a measure of the similarity between the input and the reconstructed output. In this work, we considered the Euclidean distance as loss function L.

A more sophisticated version of AE (named Deep AE) has *multiple* hidden layers in which the output of a layer is the input of the next one. **Figure 1** depicts a simplified scheme of a Deep AutoEncoder.

In order to get an *effective reconstruction* of the input, that allows selection of features that best characterize the input data, we included a penalization term in the loss function. AE algorithms of this type are known as Deep Sparse AEs. Given this framework and with the final goal of validating the SNPs effect on the long-term radiation toxicity, we applied the previously described Deep Sparse AE as follows:

(i) *sampling*: we sampled S *healthy* patients (those without toxicity) where S equals the total number of *unhealthy* patients (those with toxicity). All the unhealthy patients and the S sampled healthy patients form the *test set*. All the remaining healthy patients constitute the *training set*.

(ii) *training*: we trained the network only on the previously specified training set. The idea here was to *learn* how to best represent healthy patients. The result of this step is the estimate of the neural network characteristics (weight and bias vectors, encoder and decoder functions).

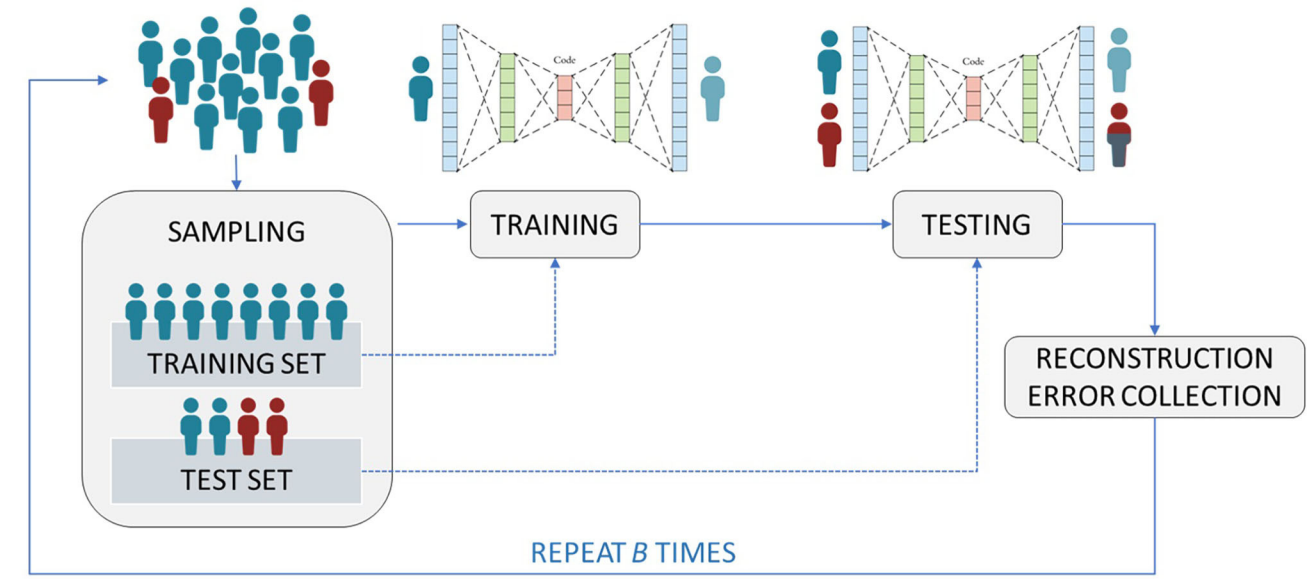

FIGURE 1 | Simplified scheme of a Deep AutoEncoder.

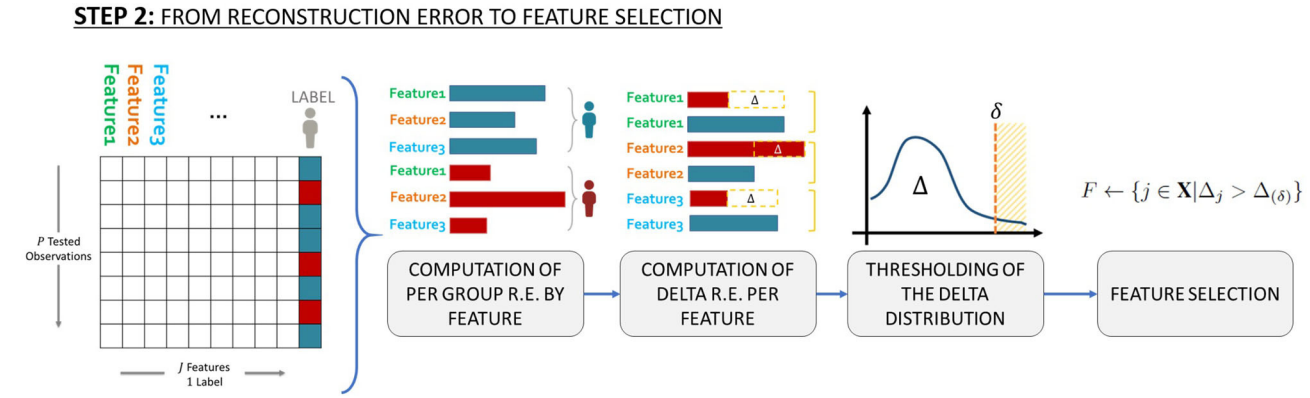

FIGURE 2 | Schematic representation of the workflow used to identify which features to select to characterize the minority class (i.e., patients with toxicity) with respect to the majority class (patients without toxicity).

(iii) *testing*: we tested the estimated network on the previously specified test set. The result of this step is a matrix of Reconstruction Errors, $R \in \mathrm{R}^{(2S)\times J}$. Considering the previous step and the fact that unhealthy patients are the minority class, the rows of R which are related to unhealthy patients should contain higher values with respect to those rows of R associated to healthy patients.

(iv) *SNP identification*: we identified which SNPs are associated with the *highest* Reconstruction Error. Further details on this step are given at the end of this section.

The steps (i)-(iii) are repeated 50 times in order to reduce a possible selection bias induced by the sampling step (i), thus obtaining 50 R matrices.

In order to identify which features should be selected for characterizing the minority class with respect to the majority class, in step (iv) the average Reconstruction Error per feature per class is computed according to that proposed in Massi et al. (25), which means computing two vectors (one for the unhealthy patients and one for the healthy patients), both made by J elements. Then, we investigated the distribution of the difference, Δ, between the average Reconstruction Errors related to unhealthy patients and the average Reconstruction Errors related to healthy patients. See **Figure 2** for a schematic representation of the above described workflow.

Finally, to define which SNPs are associated with late toxicity endpoints, we set possible thresholds equal to the 70-th, 80-th, the 90-th and the 95-th percentiles of the distribution of the Reconstruction Error differences, Δ. This means that we investigated the SNPs associated with the top 30%, the top

20%, the top 10% and the top 5% differences. These thresholds identity the effect size of identified SNPs, a large effect size (Odds Ratio>2) for SNPs in the 90-th/95-th percentiles, a moderate (Odds Ratio∼2) and small (Odds Ratio<2) effect size for SNPs in the 80-th and 70-th percentiles, respectively.

Architectural and Implementation Details

For the interested reader, in this section we provide some more specific details regarding the development and specific implementation of the DSAE for the applications described in this paper. For more details on the methodology, its strenghts

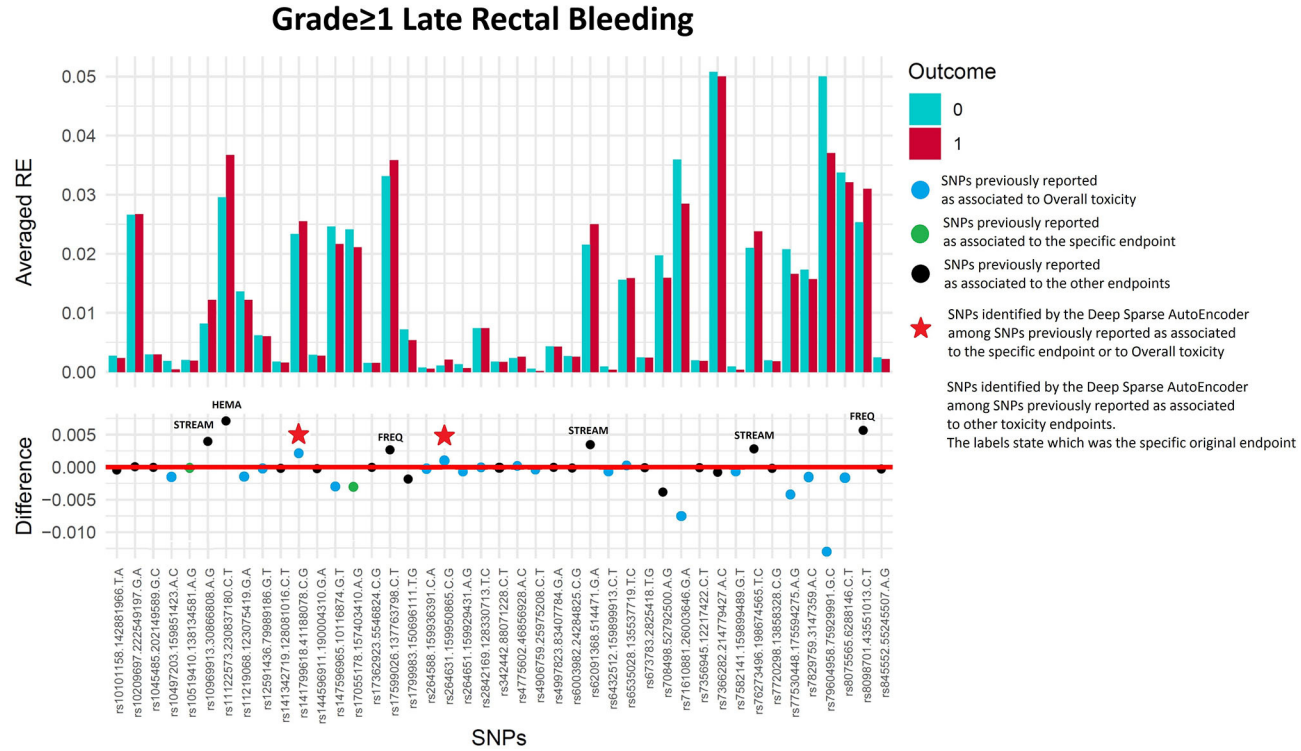

FIGURE 3 | Results for late rectal bleeding grade≥1 from the Deep Sparse AutoEncoder. The 43 considered SNPs are reported in the x-axis and the averaged Reconstruction Errors (RE) are reported in the y-axis (top panel), red columns refer to patients with toxicity, while blue columns refer to patients without toxicity. In the lower panel the difference between averaged Reconstruction Errors between the two classes are represented for each SNP (i.e., differences between red and blue columns). For most SNPs, the difference is close to zero (red line in the bottom panel of the figure). The chosen thresholds in this difference (i.e., highest 30, 20, 10, and 5% differences) are selecting SNPs associated to the toxicity outcome. Green circles refer to SNPs that were previously identified as associated with late rectal bleeding, while blue circles refer to SNPs that were previously associated with overall toxicity as defined by calculation of the Standardized Total Average Toxicity (STAT) score (24). Red stars indicate SNPs (either specific for this endpoint or related to overall toxicity) defining patients with toxicity as outliers with respect to the characteristics of patients without toxicity. Labels show SNPs that not directly associated with late rectal bleeding/overall toxicity, but contributing to their identification. The label states for which toxicity endpoint the SNPs were originally associated with in the literature: FREQ=urinary frequency, HEMA=haematuria, NOCT=nocturia, STREAM=decreased urinary stream.

TABLE 2 | Deep Sparse AutoEncoder testing of SNPs associated with Late Rectal Bleeding*.

SNP	References	70-th percentile small effect size	80-th percentile moderate effect size	90-th percentile large effect size	95-th percentile large effect size
SNPs previously associated with late rectal bleeding					
rs10519410	(21)	Not validated	Not validated	Not validated	Not validated
rs17055178	(23)	Not validated	Not validated	Not validated	Not validated
SNPs previously associated with overall toxicity (STAT score)					
rs264631	(11)	**Identified**	**Identified**	Not validated	Not validated
rs141799618	(5)	**Identified**	**Identified**	Not validated	Not validated

**grade≥1 (all considered SNPs reported in the table) and to overall toxicity as defined by calculation of the Standardized Total Average Toxicity (STAT) score (24) (in this case only "Identified" SNPs were reported in the table). The SNPs that were correctly identified by the algorithm are flagged as "Identified".*

and all model's hyperparameters mentioned below, refer to the description in Massi et al. (25).

The experiments were implemented and carried out using Python Keras framework for Deep Learning with Tensorflow as backend.

For better comparability of results in the experiments we structured the DSAEs included in the *sampling-training-testing* procedure with the same architecture and hyperparameters for all five endpoints. In particular, all the encoders of the DSAEs were composed of an input layer with $J = 43$ nodes (one per SNP), followed by a sequence of hidden layers of 40, 30 (with hyperbolic tangent activation function) and 20 nodes, respectively. To the 20 nodes of the innermost hidden layer we applied a sigmoidal activation function to foster the sparsity induced by the penalization term (weighted with λ =10e-5). The decoder architecture of all DSAEs was specular to the encoder, with a sequence of layers with 30 and 40 nodes, followed by an output layer of $J = 43$ nodes. The training of the DSAE for each of the B = 50 iterations was performed for 400 epochs, exploiting the Adam optimization algorithm with its default parameters (*learning rate* equal to 0.001).

RESULTS

Cohort

REQUITE enrolled 1,681 prostate cancer patients who were treated with external beam radiotherapy without brachytherapy. One thousand four hundred and fifty patients with complete 2-year follow-up were available for analysis. Forty-nine patients were excluded because of an intrinsic higher risk of exhibiting radiation toxicity, due to their co-morbidities (patients with a diagnosis of systemic lupus erythematosus, rheumatoid arthritis and other collagen vascular diseases). Details on the clinical characteristics of the cohorts selected for each toxicity endpoint are given in **Supplementary Tables 1,2**.

Validation of SNPs Associated With Late Toxicity Endpoints Through a Deep Sparse AutoEncoder

Late Rectal Bleeding grade≥1

One hundred and sixty of 1,366 available patients (11.7%) had late rectal bleeding grade≥1. **Figure 3** shows the differences between averaged Reconstruction Errors between the two classes

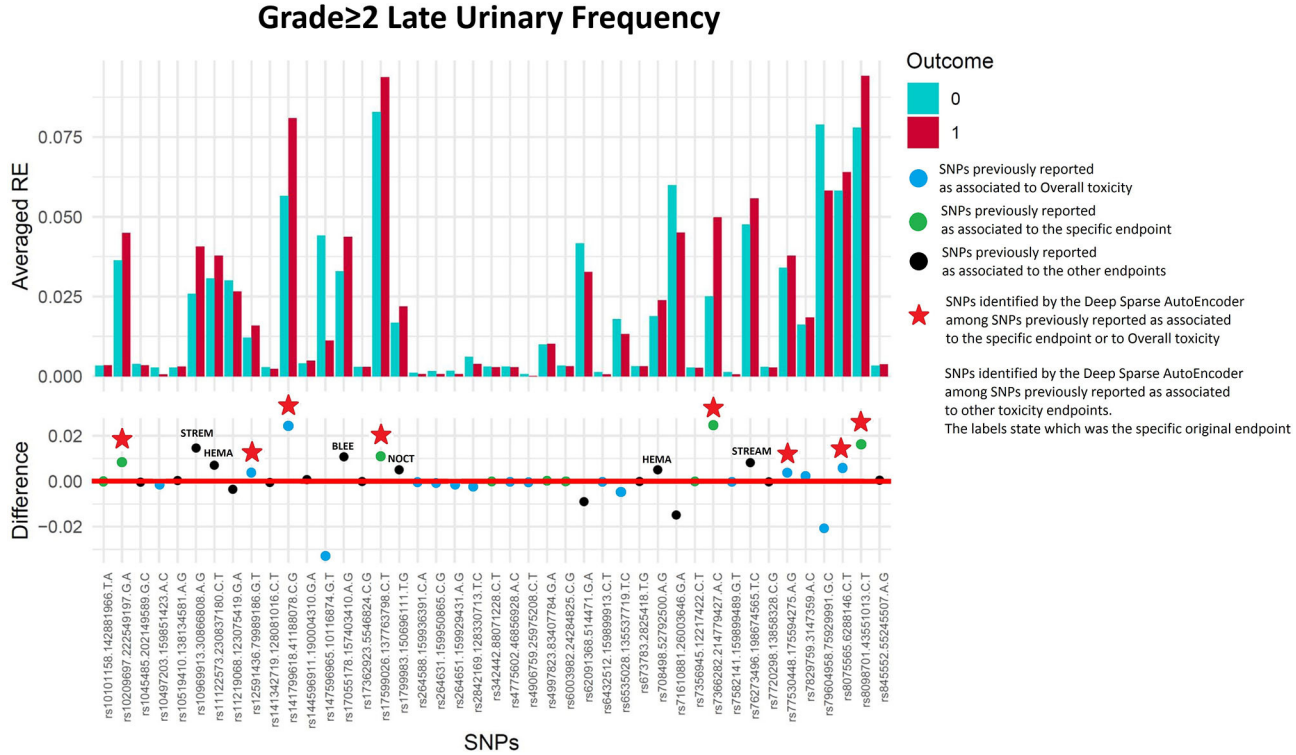

FIGURE 4 | Results for late urinary frequency grade≥2 from the Deep Sparse AutoEncoder. The 43 considered SNPs are reported in the x-axis and the averaged Reconstruction Errors (RE) are reported in the y-axis (top panel), red columns refer to patients with toxicity, while blue columns refer to patients without toxicity. In the lower panel the difference between averaged Reconstruction Errors between the two classes are represented for each SNP (i.e., differences between red and blue columns). For most SNPs, the difference is close to zero (red line in the bottom panel of the figure). The chosen thresholds in this difference (i.e., highest 30, 20, 10, and 5% differences) are selecting SNPs associated to the toxicity outcome. Green circles refer to SNPs that were previously identified as associated with late urinary frequency, while blue circles refer to SNPs that were previously associated with overall toxicity as defined by calculation of the Standardized Total Average Toxicity (STAT) score (24). Red stars indicate SNPs (either specific for this endpoint or related to overall toxicity) defining patients with toxicity as outliers with respect to the characteristics of patients without toxicity. Labels show SNPs that not directly associated with late urinary frequency/overall toxicity, but contributing to their identification. The label states for which toxicity endpoint the SNPs were originally associated with in the literature: BLEE=rectal bleeding, HEMA=haematuria, NOCT=nocturia, STREAM=decreased urinary stream.

(i.e., differences between red and blue columns). The largest part of the differences is close to zero (red line in the bottom panel of **Figure 3**). The chosen thresholds in this difference (i.e., highest 30, 20, 10, and 5% differences) select SNPs associated with the toxicity outcome with different effect size. **Table 2** lists results for the SNPs previously reported to be associated with late rectal bleeding and overall toxicity in comparison with SNPs selected by the DSAE in the REQUITE cohort. For late rectal bleeding eight SNPs were identified, two SNPs previously associated with overall toxicity (red stars in **Figure 3**) and six SNPs previously found to be associated with urinary toxicity.

Late Urinary Frequency Grade≥2

Fifty-six of 1,334 available patients (4.2%) experienced late urinary frequency grade≥2. Patients were excluded from the analysis if they had urinary frequency grade≥2 at baseline ($n = 26$), they underwent transurethral resection of the bladder ($n = 31$) or were using anti-muscarinic drugs ($n = 10$). **Figure 4** and **Table 3** show that the DSAE analysis identified 14 SNPs: four already reported as associated with urinary frequency (*rs17599026, rs8098701, rs7366282, rs10209697*), four associated with overall toxicity, one previously associated with bleeding and five with other urinary symptoms.

Late Haematuria Grade≥1

Seventy-four of 1,343 available patients (5.5%) experienced late haematuria grade≥1. Seventeen patients were excluded from the analysis because they had haematuria at baseline grade≥1, while 41 were excluded because underwent transurethral resection of the bladder or were using anti-muscarinic drugs. **Figure 5** and **Table 4** report DSAE results for this endpoint: 10 SNPs were identified. Two SNPs already associated with haematuria (*rs708498* and *rs845552*), five SNPs associated with overall toxicity, and three SNPs with other urinary symptoms.

Late Nocturia Grade≥2

Two hundred and twenty-three patients out of 1,250 available patients (17.8%) experienced late nocturia grade≥2. One hundred and ten patients were excluded from analysis because they had nocturia grade≥2 at baseline, while 41 were excluded because underwent transurethral resection of the bladder or were using anti-muscarinic drugs. **Figure 6** and **Table 5** report results for the validation through DSAE in the REQUITE population. Eleven SNPs were identified: one SNP already found to be associated with nocturia, four with overall toxicity, one with bleeding and five with other urinary symptoms.

Late Decreased Urinary Stream Grade≥1

Two hundred and eleven out of 1,234 available patients (17.1%) experienced late decreased stream grade≥1. One hundred and twenty-six patients were excluded from analysis because they had decreased stream grade≥1 at baseline, while 41 were excluded because underwent transurethral resection of the bladder or were using anti-muscarinic drugs. Eleven SNPs were selected: two SNPs previously identified for decreased urinary stream (*rs76273496* and *rs673783*), two for overall toxicity, six for other urinary symptoms and one for bleeding (**Figure 7** and **Table 6**).

Classical Validation Approach Using Univariate Analysis

A simple validation approach, using univariate logistic analysis, identified eight SNPs with $p < 0.05$ (range 0.01–0.05), none of them is validated when considering the Bonferroni correction for multiple testing, which would require $p < 0.0011$ in this case. Detailed results are presented in **Supplementary Table 4**.

TABLE 3 | Results from Deep Sparse AutoEncoder testing of SNPs associated with Urinary Frequency*.

SNP	References	70-th percentile small effect size	80-th percentile moderate effect size	90-th percentile large effect size	95-th percentile large effect size
SNPs previously associated with late urinary frequency					
rs17599026	(5)	**Identified**	**Identified**	**Identified**	Not validated
rs342442	(5)	Not validated	Not validated	Not validated	Not validated
rs8098701	(5)	**Identified**	**Identified**	**Identified**	**Identified**
rs7366282	(5)	**Identified**	**Identified**	**Identified**	**Identified**
rs10209697	(5)	**Identified**	**Identified**	Not validated	Not validated
rs4997823	(5)	Not validated	Not validated	Not validated	Not validated
rs7356945	(5)	Not validated	Not validated	Not validated	Not validated
rs6003982	(5)	Not validated	Not validated	Not validated	Not validated
rs10101158	(5)	Not validated	Not validated	Not validated	Not validated
SNPs previously associated with overall toxicity (STAT score)					
rs147596965	(5)	**Identified**	Not validated	Not validated	Not validated
rs77530448	(5)	**Identified**	**Identified**	**Identified**	**Identified**
rs8075565	(5)	**Identified**	Not validated	Not validated	Not validated
rs12591436	(5)	**Identified**	Not validated	Not validated	Not validated

**Late Urinary Frequency grade≥2 (all considered SNPs reported in the table) and to overall toxicity as defined by calculation of the Standardized Total Average Toxicity (STAT) score (24) (in this case only "Identified" SNPs were reported in the table). The SNPs that were correctly identified by the algorithm are flagged as "Identified."*

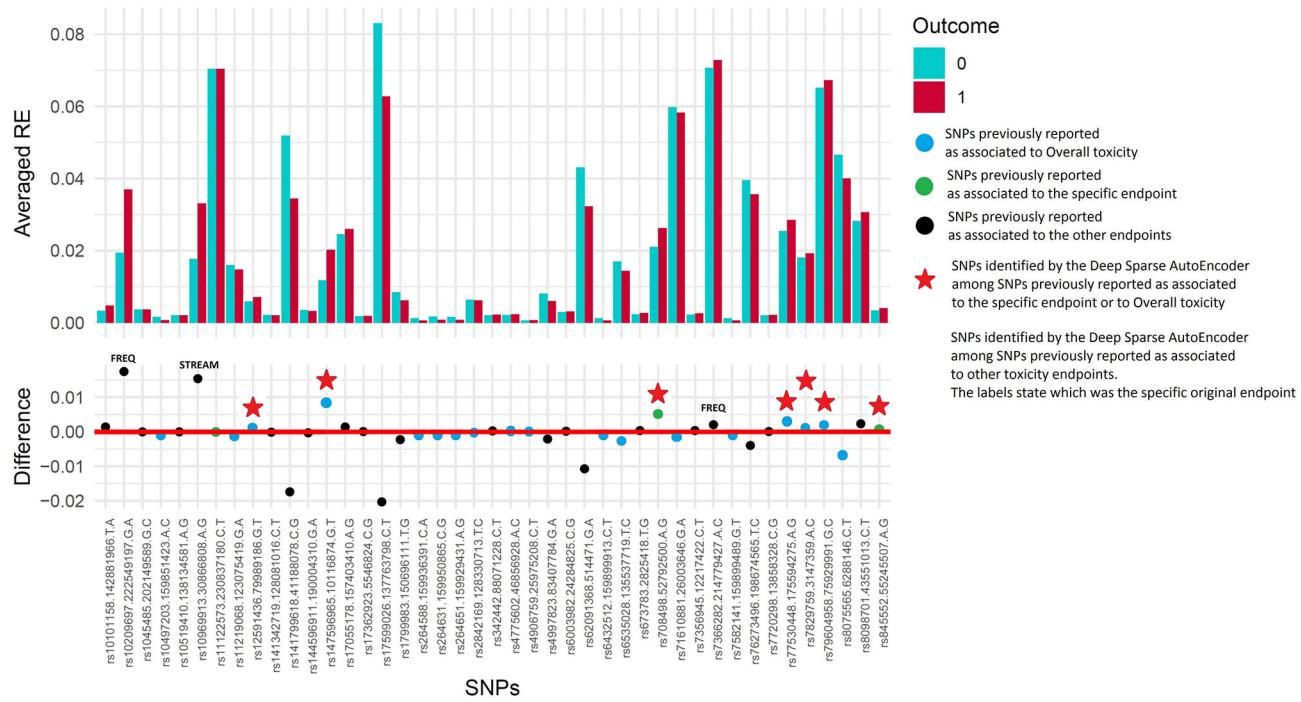

FIGURE 5 | Results for late haematuria grade≥1 from the Deep Sparse AutoEncoder. The 43 considered SNPs are reported in the x-axis and the averaged Reconstruction Errors (RE) are reported in the y-axis (top panel), red columns refer to patients with toxicity, while blue columns refer to patients without toxicity. In the lower panel the difference between averaged Reconstruction Errors between the two classes are represented for each SNP (i.e., differences between red and blue columns). For most SNPs, the difference is close to zero (red line in the bottom panel of the figure). The chosen thresholds in this difference (i.e., highest 30, 20, 10, and 5% differences) are selecting SNPs associated to the toxicity outcome. Green circles refer to SNPs that were previously identified as associated with late haematuria, while blue circles refer to SNPs that were previously associated with overall toxicity as defined by calculation of the Standardized Total Average Toxicity (STAT) score (24). Red stars indicate SNPs (either specific for this endpoint or related to overall toxicity) defining patients with toxicity as outliers with respect to the characteristics of patients without toxicity. Labels show SNPs that not directly associated with late haematuria/overall toxicity, but contributing to their identification. The label states for which toxicity endpoint the SNPs were originally associated with in the literature: BLEE=rectal bleeding, FREQ=urinary frequency, NOCT=nocturia, STREAM=decreased urinary stream.

TABLE 4 | Results from Deep Sparse AutoEncoder testing of SNPs associated with Late Haematuria*.

SNP	References	70-th percentile small effect size	80-th percentile moderate effect size	90-th percentile large effect size	95-th percentile large effect size
SNPs previously identified as associated to late haematuria					
rs11122573	(23)	Not validated	Not validated	Not validated	Not validated
rs708498	(22)	**Identified**	**Identified**	**Identified**	Not validated
rs845552	(22)	**Identified**	**Identified**	Not validated	Not validated
SNPs previously identified as associated to overall toxicity (STAT score)					
rs147596965	(5)	**Identified**	**Identified**	**Identified**	Not validated
rs77530448	(5)	**Identified**	**Identified**	Not validated	Not validated
rs7829759	(5)	**Identified**	**Identified**	Not validated	Not validated
rs79604958	(5)	**Identified**	**Identified**	Not validated	Not validated
rs12591436	(5)	**Identified**	**Identified**	Not validated	Not validated

**Late Haematuria grade≥1 (all considered SNPs reported in the table) and to overall toxicity as defined by calculation of the Standardized Total Average Toxicity (STAT) score (24) (in this case only "Identified" SNPs were reported in the table). The SNPs that were correctly identified by the algorithm are flagged as "Identified".*

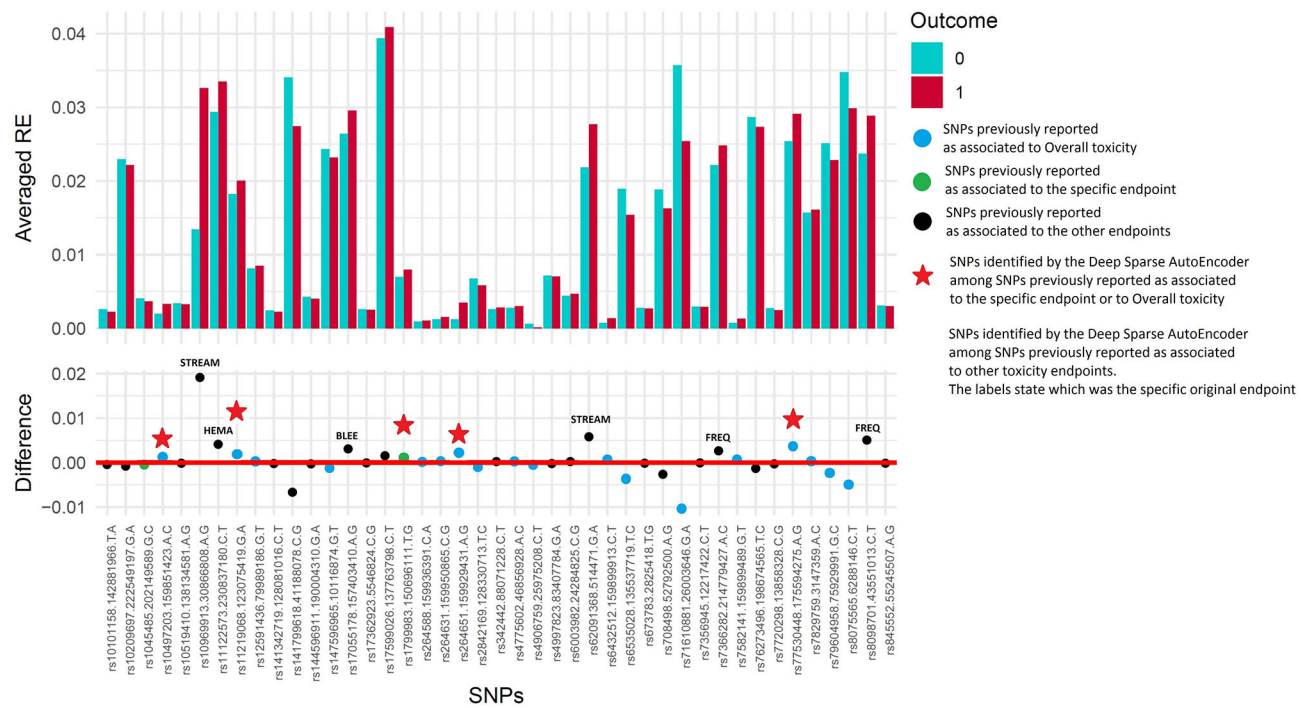

FIGURE 6 | Results for late nocturia grade≥2 from the Deep Sparse AutoEncoder. The 43 considered SNPs are reported in the x-axis and the averaged Reconstruction Errors (RE) are reported in the y-axis (top panel), red columns refer to patients with toxicity, while blue columns refer to patients without toxicity. In the lower panel the difference between averaged Reconstruction Errors between the two classes are represented for each SNP (i.e., differences between red and blue columns). For most SNPs, the difference is close to zero (red line in the bottom panel of the figure). The chosen thresholds in this difference (i.e., highest 30, 20, 10, and 5% differences) are selecting SNPs associated to the toxicity outcome. Green circles refer to SNPs that were previously identified as associated with late nocturia, while blue circles refer to SNPs that were previously associated with overall toxicity as defined by calculation of the Standardized Total Average Toxicity (STAT) score (24). Red stars indicate SNPs (either specific for this endpoint or related to overall toxicity) defining patients with toxicity as outliers with respect to the characteristics of patients without toxicity. Labels show SNPs that not directly associated with late nocturia/overall toxicity, but contributing to their identification. The label states for which toxicity endpoint the SNPs were originally associated with in the literature: BLEE=rectal bleeding, FREQ=urinary frequency, HEMA=haematuria, STREAM=decreased urinary stream.

TABLE 5 | Results from Deep Sparse AutoEncoder testing of SNPs associated with Late Nocturia*.

SNP	References	70-th percentile small effect size	80-th percentile moderate effect size	90-th percentile large effect size	95-th percentile large effect size
SNPs previously identified as associated to late nocturia					
rs1799983	(22)	**Identified**	Not validated	Not validated	Not validated
rs1045485	(22)	Not validated	Not validated	Not validated	Not validated
SNPs previously identified as associated to overall toxicity (STAT score)					
rs10497203	(11)	**Identified**	**Identified**	Not validated	Not validated
rs264651	(11)	**Identified**	**Identified**	Not validated	Not validated
rs77530448	(5)	**Identified**	**Identified**	Not validated	Not validated
rs11219068	(5)	**Identified**	**Identified**	Not validated	Not validated

**Late Nocturia grade≥2 (all considered SNPs reported in the table) and to overall toxicity as defined by calculation of the Standardized Total Average Toxicity (STAT) score (24) (in this case only "Identified" SNPs were reported in the table). The SNPs that were correctly identified by the algorithm are flagged as "Identified".*

DISCUSSION

In recent years Normal Tissue Complication Probability (NTCP) models have been developed to attempt to predict before the start of treatment patients at risk of long-term radiation toxicity. These recent developments were also characterized by the shift from NTCP dose-based modeling to the wider field of more "comprehensive" predictive models. In the speculative case that two patients receive exactly the "same dose distribution," the risk of toxicity is always modulated by the single individual profile.

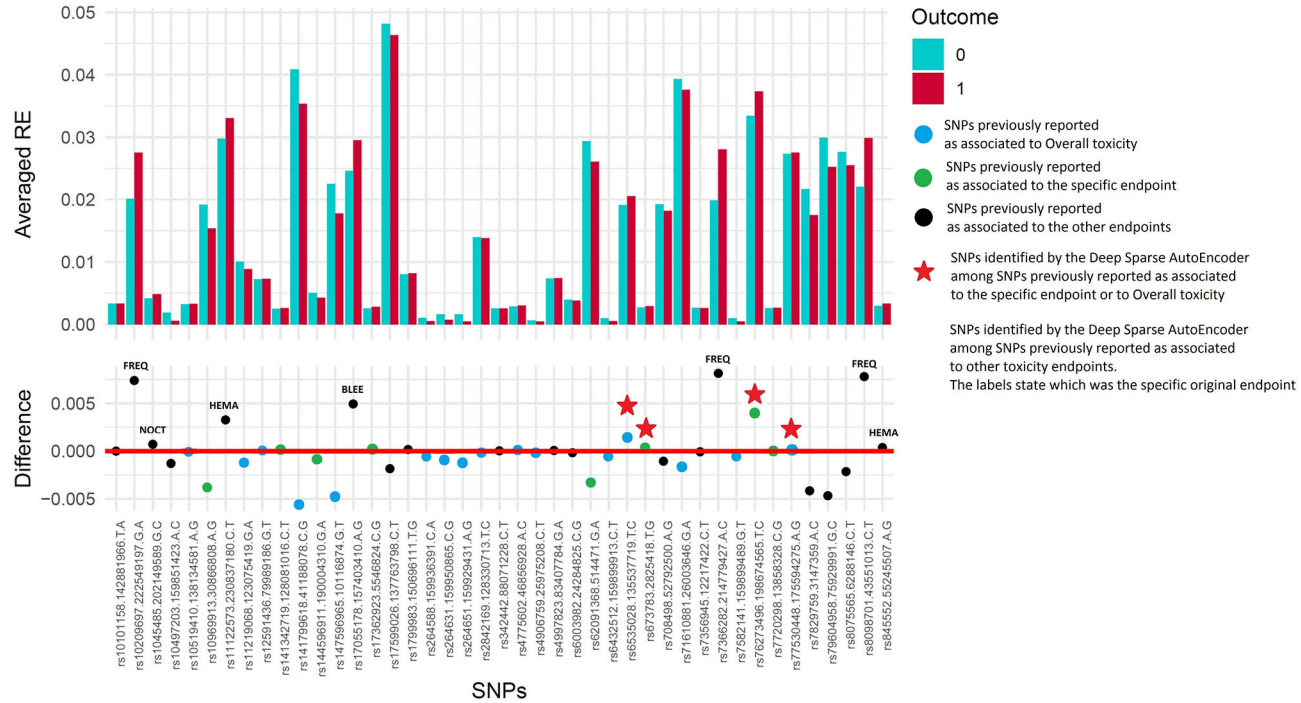

FIGURE 7 | Results for late decreased urinary stream grade≥1 from the Deep Sparse AutoEncoder. The 43 considered SNPs are reported in the x-axis and the averaged Reconstruction Errors (RE) are reported in the y-axis (top panel), red columns refer to patients with toxicity, while blue columns refer to patients without toxicity. In the lower panel the difference between averaged Reconstruction Errors between the two classes are represented for each SNP (i.e., differences between red and blue columns). For most SNPs, the difference is close to zero (red line in the bottom panel of the figure). The chosen thresholds in this difference (i.e., highest 30, 20, 10, and 5% differences) are selecting SNPs associated to the toxicity outcome. Green circles refer to SNPs that were previously identified as associated with late decreased urinary stream, while blue circles refer to SNPs that were previously associated with overall toxicity as defined by calculation of the Standardized Total Average Toxicity (STAT) score (24). Red stars indicate SNPs (either specific for this endpoint or related to overall toxicity) defining patients with toxicity as outliers with respect to the characteristics of patients without toxicity. Labels show SNPs that not directly associated with late decreased urinary stream /overall toxicity, but contributing to their identification. The label states for which toxicity endpoint the SNPs were originally associated with in the literature: BLEE=rectal bleeding FREQ=urinary frequency, HEMA=haematuria, NOCT=nocturia.

The fact that "dose is not enough" was clear from the early days of radiobiology but is receiving constantly growing attention in the current "omics" epoch (Bentzen, 2006): the availability of individual information characterizing patients and potentially influencing their reactions to radiation is increasingly important, especially in the era of image-guided radiotherapy that can spare the organs at risk in most patients.

The purpose of any predictive model in oncology is to provide valid outcome predictions for new patients. Essentially, the main interest of a dataset used to develop a model is to learn for the future. Systematic validation in multi-center collaborative settings hence is a crucial aspect in the process of predictive modeling. REQUITE is the largest multi-center observational study in this field to date, collecting standardized data longitudinally. The study was specifically designed to enable validation of models and biomarkers that predict a patient's risk of developing long-term side-effects following radiotherapy.

The present work focused on the validation of findings from previous GWAS of radiation toxicity after radiotherapy for prostate cancer. To the best of our knowledge, few validation studies in this frame have been conducted so far. Barnett et al. (13) performed an independent validation study of 92 SNPs in 46 genes in a large cohort of breast (976 patients) and prostate (637 patients) cancer patients who received radiotherapy. They focused on five rectal (bleeding, proctitis, sphincter control, stool frequency, tenesmus) and four urinary endpoints (frequency, nocturia, incontinence, and decreased stream) reported by patients 2 years after radiotherapy. An additional endpoint of overall toxicity as measured by the STAT score was also considered. None of the investigated associations was confirmed after adjustment for multiple comparisons.

Genome-wide radiogenomic studies are identifying and validating SNPs. However, to date these studies have relied on the classical single marker association test (both in the discovery and validation setting), which is hampered by the need for multiple-testing corrections. For typical study sizes, this method can detect only relatively large effect size and has limited power to identify reliably modest effects from the many SNPs that are likely to contribute to a polygenic risk profile associated with radiation

TABLE 6 | Results from Deep Sparse AutoEncoder testing of SNPs associated with Late Decreased Urinary Stream*.

SNP	References	70-th percentile small effect size	80-th percentile moderate effect size	90-th percentile large effect size	95-th percentile large effect size
SNPs previously identified as associated to late decreased urinary stream					
rs7720298	(5)	Not validated	Not validated	Not validated	Not validated
rs17362923	(5)	Not validated	Not validated	Not validated	Not validated
rs76273496	(5)	**Identified**	**Identified**	**Identified**	Not validated
rs144596911	(5)	Not validated	Not validated	Not validated	Not validated
rs62091368	(5)	Not validated	Not validated	Not validated	Not validated
rs141342719	(5)	Not validated	Not validated	Not validated	Not validated
rs673783	(5)	**Identified**	Not validated	Not validated	Not validated
rs10969913	(23)	Not validated	Not validated	Not validated	Not validated
SNPs previously identified as associated to overall toxicity (STAT score)					
rs77530448	(5)	**Identified**	Not validated	Not validated	Not validated
rs6535028	(5)	**Identified**	Not validated	Not validated	Not validated

**Late Decreased Urinary Stream grade≥1 (all considered SNPs reported in the table) and to overall toxicity as defined by calculation of the Standardized Total Average Toxicity (STAT) score (24) (in this case only "Identified" SNPs were reported in the table). The SNPs that were correctly identified by the algorithm are flagged as "Identified".*

toxicity. Genome-wide studies miss SNPs that make small but real contributions to risk.

Machine learning has already been proposed as a promising alternative approach to estimate overall genetic risk (27). The approach can identify multiple SNPs with small effects that together but not individually reach genome-wide significance. Two studies have already proposed machine learning methods to identify SNP-based signatures associated with late toxicity after radiotherapy for prostate cancer (27, 28).

Here, we extended the use of machine learning methods by using a method that addresses an important limitation of studies on radiation toxicity: the imbalance of classes, with a lower frequency of patients *with* vs. *without* late toxicity. This imbalance is important because it can lead to sub-optimal solutions (29), even when datasets are used for validation. As a first step in testing our approach, we attempted to and were successful in validating previously reported associations identified in studies based on classical single marker association tests. The next step will be a *de novo* analysis to identify SNPs with smaller individual effects.

Dealing with imbalance requires non-classical statistical solutions. Here, we explore novel methods for feature selection that come from the Deep Learning research field (25). Indeed, deep learning approaches, with their intrinsic hierarchical structure (where each layer realizing a combination of the previous layer), seem particularly adept at mimicking complex dependencies within data. Deep learning has already been applied and shown to have potential in similar bioinformatics research areas, such as for modeling the competition between splice sites (30) and in predicting RNA- and DNA-binding specificity (31).

We used DSAE to obtain the best possible representation of the majority class (without toxicity) and so to identify which features (SNPs) distinguish the minority class (with toxicity). The encoder and decoder functions are usually non-linear (i.e., sigmoid, hyperbolic tangent, rectified linear unit etc.), which enables a better reconstruction of the input by the capture of complex non-linear relationships among SNPs. Training on healthy patients allows the overall SNP pattern of normal radio-sensitivity to be established. Testing measures the "distance" between each new patient and the pattern of normal radio-sensitivity to identify SNPs associated with the highest reconstruction errors (i.e., highest distances) between the pattern of normality and the SNP profile of patients scored with toxicity (i.e., radio-sensitive patients). The distribution of the reconstructed errors allows identification and classification of SNPs with very large/large effect (SNPs associated with the top 95th percentile and 90th percentile of the distribution of reconstructed errors) and with moderate/small effects (SNPs associated with the top 80th percentile and 70th percentile of the distribution of reconstructed errors).

The DSAE successfully validated multiple SNPs contributing to an increased risk of toxicity. Some SNPs were already associated with the specific considered endpoint, others were previously associated with overall toxicity, and some were previously associated with other toxicities.

As common in GWAS, many significant SNPs lie in non-coding regions, and it is premature to speculate on their functional significance. We refer readers to the original publications which discuss possible gene functions (5, 11, 23), but give an example to illustrate likely clinical relevance. DSAE validated two SNPs previously associated with haematuria, *rs708498* and *rs845552*, which are located in the *PTGER2* and *EGFR* genes, respectively. *PTGER2* (widely distributed in humans) encodes Prostaglandin E2 receptor 2. Irradiation causes hypermethylation of this antifibrotic gene (32). *EGFR* has been shown to play a critical role in TGF-β1 dependent fibroblast to myofibroblast differentiation (33). These two SNPs

were also identified for urinary stream (*rs845552*) and urinary frequency (*rs708498*).

The main strength of our study is use of a large international prospective multi-center cohort of patients treated with modern radiotherapy techniques and fractionation schemes. The patients were specifically enrolled to validate models and biomarkers for predicting radiation toxicity, and the study design involved a standardized data collection scheme for collecting healthcare professional and patient-reported outcomes. The extensive role of data management also allowed for quality assurance of data collected, and we used "real world" data coming from "data-farming" (34).

A possible limitation of our study was use of 2-year follow-up toxicity data. The REQUITE study is still maturing, normal tissue reactions in the intestinal and urinary tract develop gradually from 6 months after radiotherapy till to around 3 years for the intestinal syndrome and to 5 years for the urinary syndrome. Recent additional funding is allowing extension of the REQUITE study with the aim of reaching standardized collection of follow-up data till year 5.

The use of grade 1 and grade 2 events is another possible limitation of this study. As the application of deep learning techniques requires a suitable number of events, the choice of mild or moderate (when possible) toxicity was forced by the number of morbidity events registered in the REQUITE population. The low number of severe toxicity is for sure a reflection of modern radiotherapy techniques which allow a substantial sparing of normal tissues, at least for the case of prostate cancer irradiation. Yet, some grade 1 and grade 2 toxicity can assume a chronic behavior, with substantial impact on the quality of life of long term survivors, for example, this could happen, for grade 2 urinary frequency and nocturia which are impairing daily activities and the quality of sleep for many years (35). A further point, more associated to research rather to clinical activity, is related to the possibility that the same genes/variants predispose to severe toxicity that predispose to low-grade toxicity. A realistic hypothesis is that some genes/variants will be common and others will be unique to severe toxicities. For example, ATM seems to be important for both mild and severe toxicity, though the particular variants differ with common SNPs associated with any toxicity, but rare mutations associated with severe toxicity. We think we can make a good case that genes identified via GWAS of mild toxicity represent good candidates for subsequent sequencing studies to identify rare mutations that may be associated with severe toxicities. Probably there are at least some biologic mechanisms common to both mild and severe toxicity, though the optimal genomic signature for each may differ. Our work still adds value by pointing to the candidate genes or loci that are likely important for both.

We have shown our approach is worth studying further and the next step would be to use it to identify patterns of SNPs to define polygenic risk scores that can be included into integrated normal tissue complication probability models, together with validated dosimetric and clinical risk factors.

The DSAE methodology underlines that, within the current RT, experiencing no toxicity could be considered as the "normal" situation, with patients with mild/moderate toxicity being outliers. The possible knowledge of the single patient intrinsic radiosensitivity and the identification of these outlier subjects could help in tailoring decision making. This should not entail changing the probability of tumor control to avoid mild/moderate side-effects, yet it should be focused on maximizing uncomplicated tumor control, even considering the patient inclination toward the different side-effects. The availability of such models would be relevant for the clinic, allowing the single patient optimization, thus constituting an important step toward the implementation of predictive modeling in the clinic. This approach would allow tailoring of therapeutic approach (i.e., active surveillance vs. prostatectomy vs. brachytherapy vs. external beam radiotherapy) and of doses (both to tumor and organs at risk) to the specific patient anatomy, clinical situation and individual biology. Combining biological stratification with toxicity reducing techniques (such as imaging fusion, image guidance, fractionation and reduced margins for Planning Target Volume) could further decrease treatment related toxicity rates and allow for dose escalation to enhance tumor control. Integrated predictive models will also be an essential tool in the design of interventional trials to modify the radiotherapy strategies. A detailed discussion of the potential ways in which biomarker/SNP assays might be implemented in routine clinical practice can be found in Azria et al. (7).

Other future work could study the possibility of "scaling" the use of DSEAs to the discovery of new genetic signatures using the whole GWAS information available in the REQUITE population, thus achieving the possibility of considering millions of features to detect outliers.

CONCLUSION

A deep learning approach can validate SNPs associated with toxicity after radiotherapy. The method can identify complex SNP signatures for multiple toxicity endpoints and should be studied further to extract polygenic risk scores to include in integrated normal tissue complication probability models that could be used to personalize radiotherapy planning.

DATA AVAILABILITY STATEMENT

Funding for the five year REQUITE project ended on 30th September 2018. REQUITE does not benefit financially from supplying data and/or samples to researchers, but does make a charge to cover its costs and support continued maintenance of the database and biobank beyond the ending of the funding period. To facilitate this continued access to researchers, the REQUITE Steering Committee approved a tiered cost recovery model for access to data and/ or samples. Contact REQUITE (requite@manchester.ac.uk) for more information on pricing.

ETHICS STATEMENT

The REQUITE study was reviewed and approved by North West - Great Manchester East Ethics Committee (UK,

reference 14 NW 0035) and by the local Ethics Committees of all participating centers. The patients provided their written informed consent to participate in this study and for the publication of the data included in this article.

AUTHOR CONTRIBUTIONS

MM, AP, FG, TRan, and CW: study design. MM, FG, and TRan: study development. AP, FI, AM, PZ, RE, and JC-C: coordination/supervision of the study. LV, PO, VF, TRat, PRS, KJ, ML, KH, GdM, DdR, BV, EvL, ACh, ES, CH, MV, BA, RV, DA, M-PJ, RS, KC, and PC: patient enrolment and follow-up. CT, TG, ACi, BR, AV, and MA-B: collection of the data. LF, AD, SK, and DP: SNP assay. JC-C, PS, AW, and RE: trial and data management. MM, FG, NF, FI, AP, AM, and TRan: statistical analysis. MM, FG, NF, TRan, and CW: draft of the paper. All authors: critical revision of the manuscript/final approval.

FUNDING

REQUITE received funding from the European Union's Seventh Framework Programme for research, technological development and demonstration under grant agreement no. 601826. FG was supported by MRC unit programme MC_UU_00002/5. ACh, RE, and CW were supported by the NIHR Manchester Biomedical Research Center. LF was supported by the European Union's Horizon 2020 Research and Innovation Programme under Marie Sklodowska-Curie grant agreement number 656144. TRan was supported by Fondazione Italo Monzino. ACi was supported by AIRC IG 21479. AV was supported by Spanish Instituto de Salud Carlos III (ISCIII) funding, an initiative of the Spanish Ministry of Economy and Innovation partially supported by European Regional Development FEDER Funds (INT15/00070; INT16/00154; INT17/00133; PI19/01424; PI16/00046; PI13/02030; PI10/00164), and through the Autonomous Government of Galicia (Consolidation and structuring program: IN607B). TRat is currently an NIHR Clinical Lecturer. He was previously funded by a National Institute of Health Research (NIHR) Doctoral Research Fellowship (DRF 2014-07-079). This publication represents independent research. The views expressed are those of the authors and not necessarily those of the NHS, the NIHR, or the Department of Health. SK was supported by grant K07CA187546 from the National Cancer Institute (NCI).

SUPPLEMENTARY MATERIAL

The Supplementary Material for this article can be found online at: https://www.frontiersin.org/articles/10.3389/fonc.2020.541281/full#supplementary-material

REFERENCES

1. Cooperberg MR, Carroll PR. Trends in management for patients with localized prostate cancer, 1990-2013. *JAMA.* (2015) 314:80–2. doi: 10.1001/jama.2015.6036
2. Zelefsky MJ, Poon BY, Eastham J, Vickers A, Pei X, Scardino PT. Longitudinal assessment of quality of life after surgery, conformal brachytherapy, and intensity-modulated radiation therapy for prostate cancer. *Radiother Oncol.* (2016) 118:85–91. doi: 10.1016/j.radonc.2015.11.035
3. Landoni V, Fiorino C, Cozzarini C, Sanguineti G, Valdagni R, Rancati T. Predicting toxicity in radiotherapy for prostate cancer. *Phys Med.* (2016) 32:521–32. doi: 10.1016/j.ejmp.2016.03.003
4. Rancati T, Palorini F, Cozzarini C, Fiorino C, Valdagni R. Understanding urinary toxicity after radiotherapy for prostate cancer: first steps forward. *Tumori.* (2017) 103:395–404. doi: 10.5301/tj.5000681
5. Kerns SL, Dorling L, Fachal L, Bentzen S, Pharoah PD, Barnes DR, et al. Meta-analysis of genome wide association studies identifies genetic markers of late toxicity following radiotherapy for prostate cancer. *EBioMedicine.* (2016) 10:150–63. doi: 10.1016/j.ebiom.2016.07.022
6. El Naqa I, Kerns SL, Coates J, Luo Y, Speers C, West CML, et al. Radiogenomics and radiotherapy response modeling. *Phys Med Biol.* (2017) 62:R179–206. doi: 10.1088/1361-6560/aa7c55
7. Azria D, Lapierre A, Gourgou S, De Ruysscher D, Colinge J, Lambin P, et al. Data-based radiation oncology: design of clinical trials in the toxicity biomarkers era. *Front Oncol.* (2017) 7:83. doi: 10.3389/fonc.2017.00083
8. Herskind C, Talbot CJ, Kerns SL, Veldwijk MR, Rosenstein BS, West CM. Radiogenomics: a systems biology approach to understanding genetic risk factors for radiotherapy toxicity? *Cancer Lett.* (2016) 382:95–109. doi: 10.1016/j.canlet.2016.02.035
9. Andreassen CN, Rosenstein BS, Kerns SL, Ostrer H, De Ruysscher D, Cesaretti JA, et al. Individual patient data meta-analysis shows a significant association between the ATM rs1801516 SNP and toxicity after radiotherapy in 5456 breast and prostate cancer patients. *Radiother Oncol.* (2016) 121:431–9. doi: 10.1016/j.radonc.2016.06.017
10. Kerns SL, West CM, Andreassen CN, Barnett GC, Bentzen SM, Burnet NG, et al. Radiogenomics: the search for genetic predictors of radiotherapy response. *Future Oncol.* (2014) 10:2391–406. doi: 10.2217/fon.14.173
11. Fachal L, Gómez-Caamaño A, Barnett GC, Peleteiro P, Carballo AM, Calvo-Crespo P, et al. A three-stage genome-wide association study identifies a susceptibility locus for late radiotherapy toxicity at 2q24.1. *Nat Genet.* (2014) 46:891–84. doi: 10.1038/ng.3020
12. Barnett GC, Thompson D, Fachal L, Kerns S, Talbot C, Elliott RM, et al. A genome wide association study (GWAS) providing evidence of an association between common genetic variants and late radiotherapy toxicity. *Radiother Oncol.* (2014) 111:178–85. doi: 10.1016/j.radonc.2014.02.012
13. Barnett GC, Coles CE, Elliott RM, Baynes C, Luccarini C, Conroy D, et al. Independent validation of genes and polymorphisms reported to be associated with radiation toxicity: a prospective analysis study. *Lancet Oncol.* (2012) 13:65–77. doi: 10.1016/S1470-2045(11)70302-3
14. Seibold P, Webb A, Aguado-Barrera ME, Azria D, Bourgier C, Brengues M, et al. REQUITE: a prospective multicentre cohort study of patients undergoing radiotherapy for breast, lung or prostate cancer. *Radiother Oncol.* (2019) 138:59–67. doi: 10.1016/j.radonc.2019.04.034
15. De Ruysscher D, Defraene G, Ramaekers BLT, Lambin P, Briers E, Stobart H, et al. Optimal design and patient selection for interventional trials using radiogenomic biomarkers: a REQUITE and radiogenomics consortium statement. *Radiother Oncol.* (2016) 121:440–6. doi: 10.1016/j.radonc.2016.11.003
16. West C, Azria D, Chang-Claude J, Davidson S, Lambin P, Rosenstein B, et al. The REQUITE project: validating predictive models and biomarkers of radiotherapy toxicity to reduce side-effects and improve quality of life in cancer survivors. *Clin Oncol.* (2014) 26:739–42. doi: 10.1016/j.clon.2014.09.008

17. Ioannidis JP, Trikalinos TA, Khoury MJ. Implications of small effect sizes of individual genetic variants on the design and interpretation of genetic association studies of complex diseases. *Am J Epidemiol.* (2006) 164:609–14. doi: 10.1093/aje/kwj259
18. Michalopoulos I, Pavlopoulos GA, Malatras A, Karelas A, Kostadima MA, et al. Human gene correlation analysis (HGCA): a tool for the identification of transcriptionally co-expressed genes. *BMC Res Notes*. (2012) 5:265. doi: 10.1186/1756-0500-5-265
19. Farnell DJ, Mandall P, Anandadas C, Routledge J, Burns MP, Logue JP, et al. Development of a patient-reported questionnaire for collecting toxicity data following prostate brachytherapy. *Radiother Oncol.* (2010) 97:136–42. doi: 10.1016/j.radonc.2010.05.011
20. Amos CI, Dennis J, Wang Z, Byun J, Schumacher FR, Gayther SA, et al. The oncoarray consortium: a network for understanding the genetic architecture of common cancers. *Cancer Epidemiol Biomarkers Prev.* (2017) 26:126–35. doi: 10.1158/1055-9965.EPI-16-0106
21. Kerns SL, Stock RG, Stone NN, Blacksburg SR, Rath L, Vega A, et al. Genome-wide association study identifies a region on chromosome 11q14.3 associated with late rectal bleeding following radiation therapy for prostate cancer. *Radiother Oncol*. (2013) 107:372–6. doi: 10.1016/j.ijrobp.2013.06.343
22. De Langhe S, De Meerleer G, De Ruyck K, Ost P, Fonteyne V, De Neve W, et al. Integrated models for the prediction of late genitourinary complaints after high-dose intensity modulated radiotherapy for prostate cancer: making informed decisions. *Radiother Oncol.* (2014) 112:95–9. doi: 10.1016/j.radonc.2014.04.005
23. Kerns SL, Fachal L, Dorling L, Barnett GC, Baran A, Peterson DR, et al. Radiogenomics consortium genome-wide association study meta-analysis of late toxicity after prostate cancer radiotherapy. *J Natl Cancer Inst.* (2020) 112:179–90. doi: 10.1093/jnci/djz075
24. Barnett GC, West CM, Coles CE, Pharoah PD, Talbot CJ, Elliott RM, et al. Standardized total average toxicity score: a scale- and grade-independent measure of late radiotherapy toxicity to facilitate pooling of data from different studies. *Int J Radiat Oncol Biol Phys.* (2012) 82:1065–74. doi: 10.1016/j.ijrobp.2011.03.015
25. Massi M, Ieva F, Gasperoni F, Paganoni AM. *Minority class feature selection through semi-supervised deep sparse autoencoders*. Milano: Mox Report - Politecnico di Milano (2019)
26. Hinton GE, Salakhutdinov RR. Reducing the dimensionality of data with neural networks. *Science.* (2006) 313:504–7. doi: 10.1126/science.1127647
27. Oh JH, Kerns S, Ostrer H, Powell SN, Rosenstein B, Deasy JO. Computational methods using genome-wide association studies to predict radiotherapy complications and to identify correlative molecular processes. *Sci Rep.* (2017) 7:43381. doi: 10.1038/srep43381
28. Lee S, Kerns S, Ostrer H, Rosenstein B, Deasy JO, Oh JH. Machine learning on a genome-wide association study to predict late genitourinary toxicity after prostate radiation therapy. *Int J Radiat Oncol Biol Phys.* (2018) 101:128–35. doi: 10.1016/j.ijrobp.2018.01.054
29. Yin L, Ge Y, Xiao K, Wang X, Quan X. Feature selection for high-dimensional imbalanced data. *Neurocomputing*. (2013) 105:3–11. doi: 10.1016/j.neucom.2012.04.039
30. Xiong HY, Alipanahi B, Lee LJ, Bretschneider H, Merico D, Yuen RK, et al. RNA splicing. The human splicing code reveals new insights into the genetic determinants of disease. *Science.* (2015) 347:1254806. doi: 10.1126/science.1254806
31. Alipanahi B, Delong A, Weirauch MT, Frey BDNA- J, and RNA-binding proteins by deep learning. *Nat Biotechnol.* (2015) 33:831–8. doi: 10.1038/nbt.3300
32. Huang SK, Fisher AS, Scruggs AM, White ES, Hogaboam CM, Richardson BC, et al. Hypermethylation of PTGER2 confers prostaglandin E2 resistance in fibrotic fibroblasts from humans and mice. *Am J Pathol.* (2010) 177:2245–55. doi: 10.2353/ajpath.2010.100446
33. Midgley AC, Rogers M, Hallett MB, Clayton A, Bowen T, Phillips AO, et al. Transforming growth factor-β1 (TGF-β1)-stimulated fibroblast to myofibroblast differentiation is mediated by hyaluronan (HA)-facilitated epidermal growth factor receptor (EGFR) and CD44 co-localization in lipid rafts. *J Biol Chem.* (2013) 288:14824–38. doi: 10.1074/jbc.M113.451336
34. Mayo CS, Kessler ML, Eisbruch A, Weyburne G, Feng M, Hayman JA, et al. The big data effort in radiation oncology: data mining or data farming? *Adv Radiat Oncol.* (2016) 1:260–71. doi: 10.1016/j.adro.2016.10.001
35. Choi EPH, Wan EYF, Kwok JYY, Chin WY, Lam CLK The mediating role of sleep quality in the association between nocturia and health-related quality of life. *Health Qual Life Outcomes.* (2019)17:181. doi: 10.1186/s12955-019-1251-5

Conflict of Interest: The authors declare that the research was conducted in the absence of any commercial or financial relationships that could be construed as a potential conflict of interest.

frontiers in Oncology

REVIEW
published: 22 October 2020
doi: 10.3389/fonc.2020.527121

Pre-clinical Research on Bladder Toxicity After Radiotherapy for Pelvic Cancers: State-of-the Art and Challenges

Stefania Zuppone[1,2†], Andrea Bresolin[2,3†], Antonello E. Spinelli[4], Giuseppe Fallara[1], Roberta Lucianò[5], Federico Scarfò[5], Fabio Benigni[1‡], Nadia Di Muzio[6,7], Claudio Fiorino[3], Alberto Briganti[1,7], Andrea Salonia[1,7], Francesco Montorsi[1,7], Riccardo Vago[1,7] and Cesare Cozzarini[6]*

[1] Division of Experimental Oncology, Urological Research Institute, IRCCS San Raffaele Scientific Institute, Milan, Italy, [2] Fondazione Centro San Raffaele, Milan, Italy, [3] Department of Medical Physics, IRCCS San Raffaele Scientific Institute, Milan, Italy, [4] Experimental Imaging Center, IRCCS San Raffaele Scientific Institute, Milan, Italy, [5] Unit of Pathology, IRCCS San Raffaele Scientific Institute, Milan, Italy, [6] Department of Radiotherapy, IRCCS San Raffaele Scientific Institute, Milan, Italy, [7] University Vita-Salute San Raffaele, Milan, Italy

Despite the dramatic advancements in pelvic radiotherapy, urinary toxicity remains a significant side-effect. The assessment of clinico-dosimetric predictors of radiation cystitis (RC) based on clinical data has improved substantially over the last decade; however, a thorough understanding of the physiopathogenetic mechanisms underlying the onset of RC, with its variegated acute and late urinary symptoms, is still largely lacking, and data from pre-clinical research is still limited. The aim of this review is to provide an overview of the main open issues and, ideally, to help investigators in orienting future research. First, anatomy and physiology of bladder, as well as the current knowledge of dose and dose-volume effects in humans, are briefly summarized. Subsequently, pre-clinical radiobiology aspects of RC are discussed. The findings suggest that pre-clinical research on RC in animal models is a lively field of research with growing interest in the development of new radioprotective agents. The availability of new high precision micro-irradiators and the rapid advances in small animal imaging might lead to big improvement into this field. In particular, studies focusing on the definition of dose and fractionation are warranted, especially considering the growing interest in hypo-fractionation and ablative therapies for prostate cancer treatment. Moreover, improvement in radiotherapy plans optimization by selectively reducing radiation dose to more radiosensitive substructures close to the bladder would be of paramount importance. Finally, thanks to new pre-clinical imaging platforms, reliable and reproducible methods to assess the severity of RC in animal models are expected to be developed.

Keywords: small animal, pre-clinical research, urinary bladder toxicity, micro-irradiator, animal model

OPEN ACCESS

Edited by:
Timothy James Kinsella, Warren Alpert Medical School of Brown University, United States

Reviewed by:
Luca Nicosia, Sacro Cuore Don Calabria Hospital, Italy
Sean P. Collins, Georgetown University, United States

***Correspondence:**
Antonello E. Spinelli
spinelli.antonello@hsr.it

†These authors have contributed equally to this work

‡Present address:
Fabio Benigni, HuMabs Biomed, a Subsidiary of Vir Biotechnology, Bellinzona, Switzerland

Specialty section:
This article was submitted to Radiation Oncology, a section of the journal Frontiers in Oncology

Received: *15 January 2020*
Accepted: *31 August 2020*
Published: *22 October 2020*

Citation:
Zuppone S, Bresolin A, Spinelli AE, Fallara G, Lucianò R, Scarfò F, Benigni F, Di Muzio N, Fiorino C, Briganti A, Salonia A, Montorsi F, Vago R and Cozzarini C (2020) Pre-clinical Research on Bladder Toxicity After Radiotherapy for Pelvic Cancers: State-of-the Art and Challenges. Front. Oncol. 10:527121. doi: 10.3389/fonc.2020.527121

INTRODUCTION

Despite dramatic advance in pelvic radiotherapy, mainly due to the implementation of image-guided intensity-modulated (IMRT) techniques, acute and late urinary toxicity (radiation cystitis [RC] or actinic cystitis) remains a significant side-effect, especially in the case of high-dose schedules such as those used for prostate and gynecological cancer treatment (1, 2). The assessment of clinical, molecular and/or genetic predictors of urinary toxicity has improved substantially over the last decade, also by use of data from large cohorts of prospectively monitored patients treated with external beams or brachytherapy (3–7). Nevertheless, a thorough understanding of the pathophysiology at the base of acute and late radiation-induced urinary symptoms, such as urgency, nocturia, urethral stenosis, incontinence, hematuria, etc., is still largely lacking, as well as robust pre-clinical data based on animal models. The advent of micro-irradiators, capable of delivering radiotherapy even to small animals with micrometric resolution, and the simultaneous rapid advancement of imaging methods, might lead to big advancements into this field. Animal models of radiation-induced bladder toxicity might improve the current understanding of physio-pathogenetic mechanisms at the base of radiation induced cystitis and expedite the detection and testing of possible radioprotective agents aimed at reducing such damage.

The aim of the current paper is therefore to review this suboptimally explored field of research, with the aim of providing both basic researchers and radiation oncologists an overview of the main open issues and, ideally, to assist them in orienting future research. First, normal bladder anatomy and physiology, radiation dose and dose-volume effects are briefly summarized. Then, the potential of modern radiobiology "tools" and the realization of robust and reproducible animal models of radiation-induced cystitis, are described. The most promising approaches aimed at preventing/minimizing RC are then discussed, by systemically reviewing both historical and recent findings on animal experiments. Finally, suggestions for future research will be explored.

Anatomical Features

The urinary bladder collects urine from the ureters and, when sufficiently filled, empties through the urethra. Two different parts can be distinguished: the bladder body, located above the inter-ureteric crest, and the base, composed of the trigone, the bladder neck and the urethro-vesical junction (8).

The urinary bladder is a hollow smooth muscle organ made up of 4-folds. The most external one is the adventitia, a serous layer. Below, the detrusor muscle, a thick muscular layer made up of smooth muscle cells and extracellular matrix, rich in collagen and elastin, allows bladder emptying. Three layers of muscular cells, differently distributed between bladder body and neck, exists: outer longitudinal, circular medial and inner longitudinal (8, 9). The submucosa is the smooth connective tissue laying between the detrusor muscle and the inner mucosal layer. It is rich in elastin and collagen, mostly types 1 and 3, mixed with a proteoglycan matrix which attracts water, giving the tissue high elasticity (8). Finally, the most internal layer, the mucosa is structured in three parts from the outer to the inner: muscolaris mucosae, a thin muscular layer dividing the submucosa from the mucosa; lamina propria, a connective layer, rich in blood vessels and nerve endings, which structurally and functionally supports the urothelium; and urothelium, a pseudostratified epithelium where basal, intermediate and umbrella cells can be identified (8). Each umbrella cell covers many intermediate cells, and their shape resembles an umbrella; they are in direct contact with urine and flatten when the bladder fills (10). Most of their membrane apical surface (almost 80%) is covered with protein plaque whose precise composition is unclear, but a main component seems to be protein called Uroplakin (9). Together with the glycosaminoglycan (GAG) layer over the urothelium and the tight junctions between umbrella cells, the protein plaque creates the urine-plasma barrier and probably hampers bacterial adherence (9, 11). Another function of urothelial cells seems the detection of bladder volumes and strain, through a direct signaling on afferent nerves or indirect communication with interstitial cells (9).

Physiology and Mechanical Features

Storage of urine and voiding represent the two most important functions of the urinary bladder, involving extremely complex interactions between its structural components and the nervous system.

Urine storage occurs at low pressure, and the bladder behaves passively (8, 9). During filling, the smooth muscle cells have to relax, elongate and rearrange. Laplace's law, assuming spherical shape, incompressible wall and an isotropic homogeneous stretch, accurately describes the bladder mechanics during filling: wall tension, intravesical pressure and bladder size are directly related (8, 9). During bladder filling, intravesical pressure is relatively constant, avoiding urine outflow to the upper urinary tract, and bladder is slowly stretched while volume increases (8, 9, 11, 12). A small increase in bladder pressure during filling is caused by a small increase in bladder wall tension, due to the viscoelastic response of the extracellular matrix when collagen fibers, initially folded, begin to stretch (12, 13). The viscoelastic property of the bladder wall is directly reflected in bladder compliance (C), defined as the change in volume (V) relative to the corresponding change in intravesical pressure (P). High compliance indicates that bladder volume could increase during filling without a significant pressure surge (9).

During the active micturition phase, smooth cells contract rapidly and synchronously throughout the bladder (8, 9). Immediately prior to voiding, after parasympathetic nerve system activation, the sphincters relax, the detrusor contracts and internal pressure increases (9, 12, 14). Contraction of muscle cells occurs with the interaction of α-myosin and actin molecules, triggered by intracellular calcium concentration increase and calmodulin activation. Thanks activation of muscarinic M3 receptor by acetylcholine, intracellular calcium is released by the opening of membrane nifedipine-sensitive L-type Ca2+

channels, by the increase in inositol 1,4,5-trisphosphate (IP3) production with consequent release of calcium from the sarcoplasmic reticulum, and by the activation of ryanodine receptors (9).

In addition, cellular framework and membrane attachments are provided by other cytoskeletal proteins, such as non-muscle β- and γ-actins, filamin, calponin and intermediate filaments (8, 9, 11).

All of these mechanisms can be significantly altered and impaired by irradiation (See below 2.5.2 Radiation damage and bladder dysfunction).

Clinical Doses and Thresholds in Humans

Although both state-of-the-art imaging guidance and intensity modulated techniques have been developed to allow better radiation dose distribution and improve treatment safety, when radiation is delivered to pelvic organs, the involvement of healthy portions of the bladder is inevitable. Therefore, a significant fraction of irradiated patients experience bladder radiation-induced side effects. The onset of RC significantly affects patients' quality of life, as there are no recommended standard management treatments (15). Radiation dose, fraction, and field size, as well as age at radiation treatment, genetic variations, concurrent therapies and comorbidities such as diabetes and immunodeficiency are considered risk factors for developing RC (16).

In particular, several recent reviews (17–20) have outlined how radiation dose correlates to the risk of urinary toxicity. Evidence of a quite rapid increase of the risk of Grade 3 urinary toxicity according to the Common Toxicity Criteria for Adverse Events (CTCAE, e.g., urethral stenosis and/or bladder neck stricture requiring surgical intervention, gross hematuria requiring blood transfusion and/or hyperbaric oxygen therapy, urinary incontinence requiring treatments such as invasive treatment) (21) for 2-Gy equivalent doses (EQD2) to the whole bladder above 50–55 Gy have been demonstrated (22). Segments of the urinary tract can receive much higher doses of radiation during bladder, prostate and gynecologic cancer radiotherapy, and dose-volume effects for several urinary symptoms have been demonstrated (23). The bladder shows the behavior of a prevalently serial organ, being extremely sensitive to even small volumes receiving high doses, such that any procedure leading to a reduction of bladder volumes receiving EQD2 doses $\geq$75–78 Gy or $\geq$8–12 Gy/week may significantly decrease the risk of toxicity (18). Here, image-guided radiotherapy (IMRT) reduced bladder areas overlaying the planning target volume (PTV) and hence lowered urinary toxicity risk. A spatial effect was also highlighted in the trigone, the most radiosensitive bladder substructure, for which the mean dose delivered was proven to be strongly associated to a higher risk of severe acute and late urinary damage (19). More recently, growing evidence of bladder sensitivity to fractionation suggested an $\frac{\alpha}{\beta}$ value (a parameter of the sensitivity of both tumor and healthy tissues to fractionation) significantly lower than previously hypothesized, in the range of 1 Gy. The prevalent dose-effect in hypofractionated protocols is consistently associated with the risk of severe late toxicities such as gross hematuria, urethral stenosis and severe incontinence (21), a risk which rises considerably for prescribed EQD2 radiation doses to the PTV above 80–85 Gy (calculated for an $\frac{\alpha}{\beta}$ ratio of 1 Gy).

Image-Guided Small Animal Irradiation Systems

The use of image-guided small animal irradiation systems is rapidly increasing in preclinical and translational radiotherapy research (24, 25). Recent technological developments allow the possibility of mimicking *in vivo* the main steps of clinical image-guided radiotherapy, from CT images to treatments, and the evaluation of the effects of radiation on tumor and healthy tissues. The main difference with respect to the clinical setting is that the entire procedure, comprising CT imaging, dose planning and delivery, is performed within about 20 min, while the animal is under anesthesia. This strict time limitation is necessary to reduce the effect of hypothermia, as well as to increase the number of animals that can be treated in a single experimental session.

Considering the size of the animals and the small volumes to be treated, lower photon energy beams generated using a conventional x-ray tube working at a tension up to about 200–250 kVp (instead of MV energies needed for treating humans) are used. The same x-ray tube is normally employed to acquire CT images of the animal, with a tension range between 40 and 80 kVp.

Two small animal image guided irradiators are currently commercially available: SARRP (Xstrahl, Atlanta, GA, USA) and XRAD225Cx SmART (PXI North Branford, CT, USA). The two systems are similar in terms of x-ray energy and differ mainly in terms of the geometry of CT acquisition. There are also home-made solutions and prototypes developed by several research groups (26–29). An exhaustive description of these prototypes is beyond the scope of this review.

Given the size of mice and rats, the downscaling of the imaging, planning and dose delivery procedures on such small animals is not a trivial issue. As mentioned in a recent ESTRO ACROP guideline (30), challenges include how to perform accurate and precise small field dosimetry and how to verify dose distributions on such small fields.

With regard to the two available commercial systems, the dose is calculated using dedicated treatment planning systems (TPS) based on Superposition–Convolution (31) and Monte Carlo simulation (25). An example of a planned treatment to the entire rat bladder is shown in **Figure 1**. Here, the TPS allows the calculation of dose volume histogram (DVH), visualization of the beams, dose distributions etc., as in clinical TPS.

In order to obtain a better delineation of the target volume it is also possible to merge the planning CT image with images acquired with different modalities, such as Magnetic Resonance (MR) (32), Positron emission tomography (PET) (33), single photon emission tomography (SPECT) (34) and bioluminescence imaging (35, 36). Importantly, the use of multimodal imaging can significantly increase planning time, while reducing system throughput.

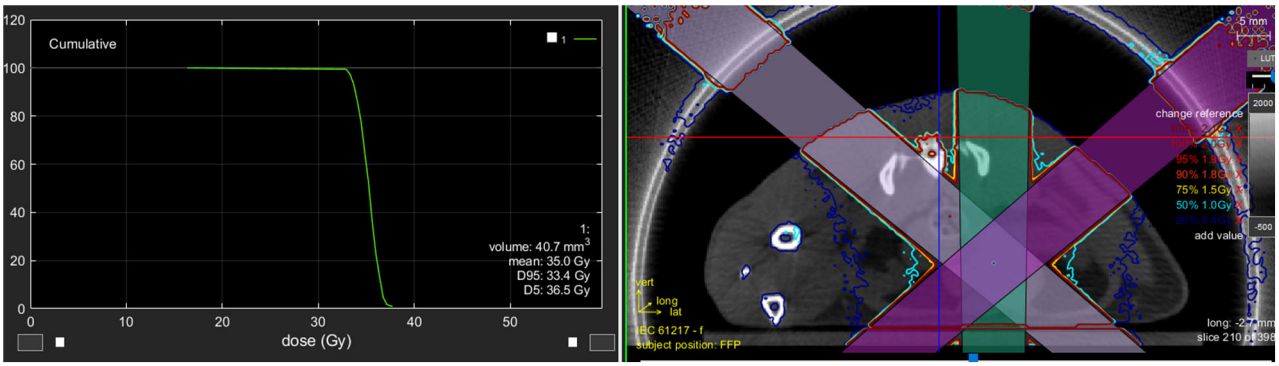

FIGURE 1 | The image shows an example of a planned treatment to the entire rat bladder. The TPS allows the calculation of dose volume histogram (DVH), the visualization of the beams, the dose distributions, etc., similar to a clinical TPS.

TABLE 1 | Search and exclusion strategy used in the bibliographic research on scopus for the current review.

Search and exclusion strategy	Input in the research platform Scopus
Search step 1	
Multiple search in titles, abstracts and keywords of the following subjects:	TITLE-ABS-KEY(
3. Pre-clinical small animal research	"preclinical" OR "rat" OR "mice"
4. External radiotherapy (X-rays therapeutic beam)	"radiotherapy" OR "radiation injuries" OR "radiation dose" OR "radiation-protective agents" OR "ionizing radiation"
5. Urinary tract	"bladder" OR "urethra"
6. Models of radio-induced toxicity	"model" OR "tolerance" OR "toxicity" OR "controlled study" OR "dose response")
Exclusion step 1	
Restriction to the only medical subject area	SUBJAREA (medi)
Exclusion step 2	
Limitation to works published in english	LIMIT-TO (LANGUAGE, "English")
Exclusion step 3	
Reinforcement of the exclusion criteria for subjects outside the scope of the current review:	AND NOT(
7. Bladder cancer	"bladder cancer" OR "bladder carcinoma"
8. Clinical studies	OR "clinical trials" OR "case report"
9. *In vitro* experiments	OR "*in vitro*"
10. Internal radiotherapy	OR "radionuclide" OR "radioactivity" OR "PET" OR "intraoperative"
11. Pharmaceutical studies	OR "radiopharmaceutical" OR "pharmacodynamics"
12. Non-ionizing radiation	OR "electromagnetic")

At the end of the first examination through the evaluation of 78 abstracts, 30 papers were excluded based on the established criteria, resulting in 48 full papers (4 of which are reviews) published in the period 1985–2019.

LITERATURE REVIEW

Methods of Bibliographic Research

In October 2019, the peer-reviewed scientific literature was scrutinized by S.Z. and A.B. for pre-clinical research on *in-vivo* small animal (mouse and rat) models of radiation cystitis. The research platform *Scopus* (Elsevier tool) was used: the search strategy and the multiple keywords combinations used are detailed in **Table 1**. Eligibility was limited to documents in the medical area published in English. Specific exclusion criteria were used to avoid non-pertinent subjects, such as studies relative to bladder cancer, radioactive nuclides or non-ionizing radiation, *in vitro* experiments, pharmaceutical or clinical trials. Of the initial 78 abstracts reviewed, 30 were excluded on the base of the above mentioned criteria, resulting in 48 full papers (4 of which are reviews) published between 1985 and 2019. The articles, despite reporting very different end-points and methods, are grouped into three main topics (i.e., Radiation damage and bladder dysfunction; Pathology and preclinical models; Radioprotective agents) and are summarized in **Tables 2**–**4**, respectively. **Table 5** includes five studies on abscopal/bystander effects retained for completeness, although they are not discussed in the current review.

TABLE 2 | Chronological summary of the pre-clinical cystometric studies about radio-induced toxicity on the normal bladder.

References	Animal model (strain)	Dose set-up	Endpoint (method)	Toxicity timing after RT	Findings
Knowles et al. (37)	Female rat (Wistar)	20-40 Gy in 1 fr. to ureter/trigone delivered by 300 kV X-rays machine through a ventral beam	Hydronephrosis (intravenous urography)	Death: <40 days Hydronephrosis: >42 days	Rate at 23.4 Gy to ureter = 14/16 Rate at 25 Gy to trigone = 9/11 Many rats died with 37.4 Gy to ureter; No death associated with 40 Gy to trigone
Lundbeck et al. (38)	Female Mouse ($C_3D_2F_1$/Bom)	20 Gy in 1 fr. delivered by 250 kV X-rays machine	Reservoir function (transurethral cystometry)	No change in the control group within 200 days. Biphasic change in the irradiated group	Evidence of biphasic change in the bladder reservoir function: acute and late damage
Lundbeck et al. (39)	Female mouse ($C_3D_2F_1$/Bom)	5–30 Gy in 1 fr. delivered by 250 kV X-ray machine through a ventral beam	Reservoir function (transurethral cystometry)	Acute response: 10–14 days (Functions restored after another month) Late response: dependent on the dose	RD_{50} = 17.2 Gy for the acute response. Late toxicity time was dose-dependent: 10–15 Gy, 20 Gy, 25–30 Gy groups were significant different
Stewart et al. (40)	Female mouse (C3H/Hen Af-nu$^+$)	8–16 Gy repeated after 1 day or 3 or 9 months and delivered by 250 kV X-ray machine through a ventral beam	Functional damage (transurethral cystometry)	Early damage: 2 weeks (reirradiation at 9 months after 16Gy) Late damage: undirect relationship with the dose administered in the first treatment and no dependency upon time between treatments	Prolonging the overall treatment time does not result in the prevention of late radiation injury in the bladder
Stewart et al. (41)	Female mouse (C3H/Hen Af-nu$^+$)	10–30 Gy in 1 fr. delivered by 250 kV X-ray machine through a ventral beam	Functional damage (transurethral cystometry)	Acute response: 5–21 days (duration: <1 week) Late response: 16–40 weeks	Acute response rate (20–30 Gy): 20–40% Late response rate (10–15 Gy): <20%
Bentzen et al. (42)	Female mouse ($C_3D_2F_1$/Bom)	1 to 10 fractions for an overall time of 4–4.5 days and a total dose of 5-60 Gy delivered by 250 kV X-ray machine	Reservoir function (transurethral cystometry)	Late response: >30 days Latent period: 35–401 days	α/β = 5.8 Gy Late radiation injury in the mouse urinary bladder was not highly sensitive to change in dose per fraction
Dörr et al. (43)	Female Mouse (C3H/Neu)	Single-dose or fractionated irradiation delivered by Seifert Isovolt 320/20 X-ray machine	Reservoir function (transurethral cystometry)	Early response 7–25 days after ≥10 Gy in 1 fr. Duration of the response: 3–9 days	α/β = = 11.1-12.4 Gy (acute responding tissue)
Vale et al. (44)	Female rat (Wistar)	10, 15, 20, 25 Gy in 1fr. delivered by Pantak 320- kV X-ray generator	Reservoir function (transurethral cystometry)	First reduction: 4 weeks Second reduction: 3–4 months and persistent at 6 months	Biphasic reduction for 15–25 Gy
Dörr et al. (45)	Female Mouse (C3H/Neu)	Four equal-sized dose fractions were applied with intervals of 0–8 h and delivered by Seifert Isovolt 320/20 X-ray machine	Reservoir function (transurethral cystometry)	Acute response: <30 days Half-time of repair = 1.2 h	ED50 = 18.2 Gy for single dose ED50 = 28.1 Gy for 8h protocol $\frac{\alpha}{\beta}$ = 10.4 Gy
Dörr et al. (46)	Female mouse (C3H/Neu)	19 Gy in 1 fr. delivered by Seifert Isovolt 320/20 X-ray machine	Reservoir function (transurethral cystometry)	Complete recovery <30 days, followed by a symptom-free latent time of about 15 weeks	No changes in the diurnal pattern were observed. In the late phase, the absolute capacity and the amplitude of fluctuations decreased
Dörr et al. (47)	Female mouse (C3H/Neu)	Graded single dose delivered by Seifert Isovolt 320/20 X-ray machine	Reservoir function (transurethral cystometry)	Acute response: - 1–15 days (I wave) with mean latent time = 7.1 days - 16–30 days (II wave) with mean latent time = 23.3 days	ED50 = 21.7 Gy (I acute wave) ED50 = 19.3 Gy (II acute wave) ED50 = 18.7 Gy (late response) Response during the second but not the first acute wave correlated with the late response (p = 0.0008)

(Continued)

TABLE 2 | Continued

References	Animal model (strain)	Dose set-up	Endpoint (method)	Toxicity timing after RT	Findings
Dörr et al. (48)	Female Mouse (C3H/Neu)	(i) 1 to 10 fr. applied within 5 days. (ii) 4 equal-sized dose fractions applied with intervals of 0–8 h and delivered by Seifert Isovolt 320/20 X-ray machine	Reservoir function (transurethral cystometry)	Half time of repair: 0.39 h Latent time to chronic functional changes: 12–40 weeks inversely dependent on the BED	(i) repair capacity: $\frac{\alpha}{\beta} = 4.4$ Gy (ii) repair kinetics: $\frac{\alpha}{\beta} = 3.7$ Gy Dose fractionation sparing effect was in the lower range of tissues with a chronic response
Jaal et al. (49, 50)	Female Mouse (C3H/Neu)	20 Gy in 1fr. delivered by Seifert Isovolt 320/20 X-ray machine through a ventral beam	Reservoir function (transurethral cystometry)	Rate = 40% for days 0–15 Rate = 64% for days 16–30 Rate = 71% after 180 days	Irradiation induced significant acute and chronic reduction in bladder capacity by >50%
Rajaganapathy et al. (51)	Female rat (Sprague-Dawley)	20, 30, 40 Gy in 1fr. delivered by SARRP unit through three ventral beams	Micturition frequency (metabolic cage)	Early response: 6 weeks	40 Gy caused reductions in the mean inter-micturition interval by ∼20 min
Zwaans et al. (52)	Female Mouse (C3H/HeN)	20 Gy in 1fr. delivered by SARRP unit through two ventral beams	Micturition frequency (metabolic cage)	Late response: starting at 17 weeks	Micturition frequency in irradiated mice was significantly increased compared to controls. The radiation exposure attenuated the urothelial integrity long-term
Giglio et al. (53)	Female rat (Sprague–Dawley)	20 Gy in 1fr. delivered by 6 MeV linac through two side- field	Functional damage (metabolic cage)	14 days	Irradiation led to urodynamic changes. Water intake and micturition frequency were found not to be correlated

In these studies the endpoint is the functional damage in terms of reservoir function (reduction in the bladder capacity by >50% at a fixed intravesical pressure) and/or micturition frequency.

RT, radiotherapy; RD_{50}, response dose 50%; ED50, radiation dose producing damage in the 50% of cases; dose BED, biologically effective dose; H&E, Hematoxylin & Eosin; SARRP, small animal radiation research platform.

Contribution of Animal Models to the Understanding of the Physio-Pathogenesis of Radiation Cystitis

High energy ionizing radiation affects various bladder cell types, among which urothelial, neuronal, detrusor, and vascular smooth muscle cells; pre-clinical research in the last decades has tried to clarify these processes. At a molecular level, RT-induced injury can be triggered either via direct damage to DNA or other cellular macromolecules (i.e., protein, lipids etc.) causing early cell death and/or functional deficiency, or via an indirect activity, breaking down water atoms into free oxygen radicals and producing oxidative stress (82). The release of free oxygen radicals can cause cell membrane lipid peroxidation or react with DNA, leading in both cases to DNA damage, replication failure and cell death (3). Subsequently, a number of downstream abnormalities of the bladder wall might occur at multiple levels, which can be classified into three consequential phases: (a) an early or acute phase of inflammation, which occurs during or just after the completion of a conventional therapy protocol such as 2 Gy per 5 days/week to a total dose of 60–70 Gy in 6–7 weeks; (b) a symptom-free phase; (c) a late non-reversible, fibrotic phase that develops gradually and can be detected from 6 months to years after RT (48, 83). The former response is transient and often resolves in a few weeks or months. Its symptoms are caused by the activation of the pro-inflammatory cascade. In particular, one of the early stage events is the increase of the inflammatory, proliferative and pro-apoptotic nuclear factor-kappa B (NF-κB), which stimulates endothelial cyclooxygenase (COX2) expression and arachidonic acid conversion into prostaglandins in endothelial cells, determining vasodilatation and increased muscle tone (edema and hyperemia) (60). NF-κB activation might bring to the increase in membrane urothelial intercellular adhesion molecule 1 (ICAM-1) levels in the vascular endothelial cells, prompting and supporting leucocyte infiltration in the lesion (49, 50). These events result in a functional impairment of the organ, and patients therefore experience symptoms such as increased frequency, urgency and dysuria (47). After a symptom-free period, the duration of which is highly variable, a late chronic response might develop. In this phase, at molecular level, uroplakin 3 downregulation on the luminal surface of the bladder urothelium, together with loss of superficial urothelial cells (umbrella cells), produces the disruption of urine-plasma barrier and thus an increased permeability (59, 84, 85) leading to a chemical irritation of the bladder wall caused by urine components. Furthermore, transforming growth factor beta-1 (TGF-β1) expression increase, and the subsequent accumulation of extracellular matrix and collagen deposition eventually supports the development of fibrosis (86, 87).

TABLE 3 | Chronological summary of the pre-clinical immunohistochemical studies about radio-induced toxicity on the normal bladder.

References	Animal model (strain)	Dose set-up	Endpoint (method)	Toxicity timing after RT	Findings
Stewart et al. (41)	Female mouse (C3H/Hen Af-nu^{+})	10-30 Gy in 1 fr. delivered by a 250 kV X-rays machine through a ventral beam	Morphological changes (hematoxylin eosin staining)	2 weeks: no changes 7–12 months: epithelial denudation, hyperplasia, necrosis, fibrosis	The late damage was characterized by epithelial denudation and focal hyperplasia; fibrosis and ulceration were also detectable at higher doses (20–30 Gy)
Vale et al. (44)	Female rat (Wistar)	10, 15, 20, 25 Gy in 1fr. delivered by Pantak 320- kV X-ray generator	Morphological changes (H&E, toluidine blue staining)	6 months	Evidence of increase mast cell density. Fibrosis in 9/18 rats
Crowe et al. (54)	Female rat (Wistar)	15 and 25 Gy in 1 fr. delivered by Pantak HF 320 X-ray generator	Changes in neuropeptides	6 months	Increase in the density of NPY, SP- and TH-immunoreactive nerves in the urinary bladder
Kraft et al. (55)	Mouse (sex n.a.) (C3H/Hen Af-nu+ and C3H/Neu)	25 or 19 Gy (ED80 40 weeks after RT)	Morphological changes (TGF-β expression and collagen content)	Increase in TGF-β: 90–360 days Increase in collagen I and III: >180 days	TGF-beta expression and connective tissue metabolism were important factors determining reduced bladder function after irradiation
Kruse et al. (56)	Female mouse (C3H/Hen Af-nu^{+})	20 Gy to rectum 16 Gy to kidney delivered in 1 fr. by 250-kV X-ray	Telangiectasia (microarray analysis of RNA isolated from pre-irradiated kidney/ rectum)	10–20 weeks	Identification of genes expressed in tissues with manifest vascular damage
Kanai et al. (57)	Rat (Sprague-Dawley) Mouse (nNOS$^{-/-}$, iNOS$^{-/-}$, eNOS$^{-/-}$, C57BL10)	0–50 Gy in 1 or more fr. (1–3 days interval) delivered by 6 MeV linac	Umbrella cells ulceration	n.a.	mtNOS was in the cardiomyocytes and urothelial cells, and can be either protective or detrimental
Jaal et al. (49, 50)	Female mouse (C3H/Neu)	20 Gy in 1fr. delivered by Seifert Isovolt 320/20 X-ray machine	Morphological changes (ICAM-1 expression)	Increasing signal at day 2–4 and 16–28 Permanent signal between 90–360 days	Irradiation induces significant early and late deregulation in ICAM-1 expression levels, preceding bladder functional response
Jaal et al. (58)	Female Mouse (C3H/Neu)	20 Gy in 1fr. delivered by Seifert Isovolt 320/20 X-ray machine	Vasodilatation (COX-2 in blood vessels)	Early: 4–16 days Late: 90–360 days	COX-2 dependent inflammatory response in the bladder wall during the early phase after radiation
Jaal et al. (59)	Female mouse (C3H/Neu)	20 Gy in 1fr. delivered by Seifert Isovolt 320/20 X-ray machine	Decrease in n° of umbrella cells (UP-III)	Early phase: 0–31 days Initial late phase: 90, 120 days	Irradiation resulted in morphological impairment of the urothelial barrier
Jaal et al. (60)	Female Mouse (C3H/Neu)	20 Gy in 1fr. delivered by Seifert Isovolt 320/20 X-ray machine	Amount of collagen (Masson's Trichrome)	In the entire late phase, but most pronounced at day 120 and 180	Suggested neovascularization in the late phase of radiation-induced bladder damage
Soler et al. (61)	Female rat (Lewis)	20 Gy in 1fr. delivered by Cesium isotope-based irradiator collimated by shield on bladder	Amount of collagen (Masson's Trichrome) and vascularization (VonWillebrand factor)	1.5 and 3 months	Anti-Angiogenesis therapy is proposed to prevent and/or treat the pathology of radiation cystitis
Xu et al. (62)	Male mouse (NCRNU)	5 Gy in 5 fr. delivered by 250 kV X-ray machine	Ultrastructural and mitochondrial damage	60 days	Parthenolide enhanced radiosensitivity of prostate tumors but protects healthy tissues (bladder) from radiation

(Continued)

TABLE 3 | Continued

References	Animal model (strain)	Dose set-up	Endpoint (method)	Toxicity timing after RT	Findings
Ozbilgin et al. (63)	Male mouse (Swiss Albino)	10 Gy in 1 fr. delivered by Co^{60} RT	Morphological changes (H&E), POMC immunoreactivity	24 h, 48 h, and 7 days	No morphological alterations. Expression of POMC on the urothelium seems to spare bladder from radiation injuries
Ozbilgin et al. (64)	Male mouse (Swiss Albino)	10 Gy in 1 fr. delivered by Co^{60} RT	Reaction of versican and HB-EGF	7 days	Increase of versican and HB-EGF concentrations may play a role in the side effects of RT
Ozbilgin et al. (65)	Male mouse (Swiss Albino)	10 Gy in 1 fr. delivered by Co^{60} RT	COX-1 and COX-2 immunoreactivity	24 h, 48 h, and 7 days	The expression of COX-1 and COX-2 seems to prevent bladder damage from radiation
Giglio et al. (53)	Female rat (Sprague–Dawley)	20 Gy in 1fr. delivered by 6 MeV linac through two side- field	Extensive immuno-histochemical characterization	16 h−14 days	Irradiation may suppress important immunoregulatory pathways
Rajaganapathy et al. (51)	Female rat (Sprague-Dawley)	20, 30, 40 Gy in 1fr. delivered by SARRP unit through three ventral beams	Morphological changes (H&E)	Early response: 6 weeks	Evidence of degenerative type epithelial changes, urothelial swelling and hyperplasia
Zwaans et al. (52)	Female Mouse (C3H/HeN)	20 Gy in 1fr. delivered by SARRP unit through two ventral beams	Morphological changes (H&E) Fibrosis (Masson Trichrome) Mast cells (toluidine blue staining)	Starting at 17 weeks after treatment	Pathological changes included fibrosis, inflammation, urothelial thinning, and necrosis. The radiation exposure attenuated the long-term urothelial integrity

RT, radiotherapy; ICAM-1, intercellular adhesion molecule 1; mtNOS, mitochondrial nitric oxide synthase; COX, cyclooxygenase; UP-III, uroplakin-III; POMC, Proopiomelanocortin; HB-EGF, heparin-binding EGF-like growth factor; ICAM-1, irradiation on intercellular adhesion molecule 1; H&E, Hematoxylin & Eosin; SARRP, small animal radiation research platform.

Histologically, several phenomena can be detected, such as a combination of urothelial cell denudation and tumor-like epithelial hyperproliferation, vascular damage and hemorrhaging, submucosal telangiectasia, fibrin deposition, formation of ulcers, loss of smooth muscle cells, influx of fibroblasts, collagen accumulation and, eventually, fibrosis (17, 47). All these anomalies lead eventually to hematuria and a permanent reduction of the bladder compliance, which could ultimately result in an impaired ureteric emptying and, thus, renal dysfunction. Moreover, voiding failure can also derive from the progressive underactivity of detrusor muscle, which subsequently becomes acontractile.

Due to the complexity of this condition, current non-invasive treatment options have limited effectiveness and, in certain extreme scenarios, radical cystectomy is required (52).

The establishment of reliable preclinical models mimicking urothelial toxicity (UT) and aimed at understanding all the molecular processes involved in disease progression is fundamental for testing "tailored" therapies. To date, mice and rats have been commonly used for RC modeling, and a positive correlation has been seen between radiation dose (usually in the range of 5–40 Gy) and urothelial changes at early or late post-irradiation time points. However, different experimental methods, endpoints, irradiation doses, dose distribution and sources along with different animal species have been used. Therefore, the full comprehension of RT-induced UT and the availability of comprehensive models that faithfully recapitulate all the pathological paths still represent an unmet need.

Interestingly, dose and fractionation effects were mostly investigated in older studies (**Table 2**) using single fraction or minimally fractionated protocols. No studies on dose and fractionation using modern micro-irradiators have been published to date. Similarly, there are no specific studies dealing with the quantification of bladder volume effects and/or the existence of more sensitive sub-structures.

Each research group developed its own animal model using different strains of rats or mice, as listed in **Tables 2**–**4**. Despite this variability, the general practice was to use a single radiation dose of 20 Gy, roughly corresponding to a fractionated radiotherapy treatment delivering 60 Gy in 30 fractions over 6 weeks (4, 44). Several cystometric studies showed that 20 Gy is a dose sufficient to observe in at least 50% of animals (47, 49, 88), a biphasic response in the acute phase (88) at about 7 and 23 days after RT, respectively (47), and a late phase starting at 4–6 months (44, 49, 83). Interestingly, Dörr et al. highlighted a strong correlation between damage in the second (but not in the first) acute wave and late damage (47).

Some works also studied radiation doses over 20 Gy delivered in 1 fraction (41, 44, 47, 51, 89). This dose escalation was associated with a higher toxicity rate (41) and more severe symptoms in terms of bladder dysfunction (51), degenerative type of epithelial changes (41) and increase of mast cell density (44). Regarding the late response, the latent time was found to be inversely dependent on the dose (48, 89).

The effects of fractionated radiotherapy were investigated in several works (42, 48, 90). Dörr et al. demonstrated that

TABLE 4 | Chronological summary of the pre-clinical studies about radioprotective effects on the normal bladder.

Reference	Animal model (strain)	Set-up	Endpoint (method)	Toxicity timing after RT	Findings
Edrees et al. (66)	Female mouse (C3H)	13–25 Gy in 1 fr. delivered by 250 kV X-ray machine + Cy	Micturition frequency (cystometry), incidence of haematuria	5 months (rad) 1 week (Cy) Early and 9–12 month (rad+Cy)	Cy administered up to 9 months before or after irradiation induced more severe bladder damage than X-rays alone
Malkinson et al. (67)	Male mouse ($B_6D_2F_1$)	2–4.5 Gy/fr. x 10–15 fr. after PGs administration	Murine hair loss	Immediately after the fractionated RT	PGs may provide protection of tissue as bladder mucosa
Horsman et al. (68)	Female mouse (CDFI and C3H)	Nicotinamide injected after local irradiation delivered by 250 kV X-ray irradiator	i) Moist desquamation ii) Reservoir function (transurethral cystometry)	i) 11–30 days ii) 9 months	Best radiosensitization with minimal effect on normal tissues (bladder) at time of nicotinamide peak plasma drug concentrations
Kanai et al. (69)	Female rat (Sprague-Dawley)	35 Gy in 1 fr. delivered by 6 MeV linac + MnSOD transgene injection 24 h before RT	Transepithelial resistance and permeability damage on detrusor function	1, 48, and 96 h 7 and 24 days 6 months	MnSOD transgene allows transepithelial resistance and permeability to recover within 4 weeks and shows baseline pressures and more stable voiding patterns after 6 months
Jaal et al. (70)	Female mouse (C3H/Neu)	Graded radiation doses delivered by Seifert Isovolt 320/20 X-ray machine + rHuKGF	Reservoir function (transurethral cystometry)	Early phase response: 1–30 days Late phase response: 60–360 days	Early: ED50 from 20 to 27 Gy Late: ED50 from 16 to 22 Gy rHuKGF administration before irradiation modified early and late radiation effects
Dinçbaş et al. (71)	Male rat (Wistar)	25 Gy in 5 fr. delivered by Co^{60} teletherapy unit + AF + GEM	Bladder fibrosis (H&E)	4 months	AF may have a beneficial effect in limiting the radio-sensitizing effect of GEM
Rocha et al. (72)	Rat (sex n.a.) (Wistar)	11.64 Gy in 1 fr. delivered by 6 MeV linac + L-glutamine	Amount of collagen (Masson's trichrome, Picro Sirius Red) Immuno-histochemistry	15 days	L-glutamine seems to prevent bladder wall damage
Costa et al. (73)	Male rat (Wistar)	10 Gy in 1 fr. delivered by 10 MeV linac + L-arginine	Morphologic change of blood vessels in the wall (H&E, expression of VEGF and FGF)	16 days	L-arginine was radioprotective
Rajaganapathy et al. (51)	Female rat (Sprague-Dawley)	40 Gy in 1fr. delivered by SARRP unit + liposomal tacrolimus	Micturition frequency(cystometry) Morphological changes (H&E)	2 and 6 weeks	Lipo-tacrolimus treated rats show an increased post- irradiation IMI and minimal edematous changes
Horsman et al. (74)	Male and Female Mice (CDF1)	Graded radiation doses + VDA(CA4P)	Reservoir function (transurethral cystometry)	9 months	ED50 = 14 Gy for bladder VDA has no effect on the early (skin) or late (bladder and lung) tissues responding to radiation
Oscarsson et al. (75)	Female rat (Sprague-Dawley)	20 Gy in 1 fr. delivered by 6 MeV linac + with and without 20 sessions of HBOT	Oxidative stress and pro-fibrotic factors	28 days	HBOT may prevent radiation-induced changes
Sarsarshahi et al. (76)	Female mouse (C3H/Neu)	14-24 Gy in 1 fr. delivered by YXLON Maxishot device + bortezomib	Reservoir function (transurethral cystometry)	Acute response: 6–9 days Late response: 21–24 days	Daily bortezomib injections between days 0–15 resulted in a significant decrease in responders

Several agents were tested in combination with radiation and the effect was measured using various techniques.
RT, radiotherapy; Cy, Cyclophosphamide; PGs, prostaglandins; MnSOD, Manganese superoxide dismutase gene therapy; VEGF, vascular endothelial growth factor; FGF, Wbroblast growth factors; AF, amifostine; GEM, gemcitabine; H&E, hematoxylin & eosin; rHuKGF, palifermin; HBOT, hyperbaric oxygen therapy; CA4P, combretastatin A-4 phosphate; VDA, vascular disrupting agents; SARRP, small animal radiation research platform; IMI, inter- micturition intervals IMI.

when radiation is delivered in equal-sized dose fractions, the radiation dose producing the damage in 50% of animals (ED50) is higher than in single dose irradiation. Furthermore, ED50 was shown to be sensitive to the interval between fractions (90). Other studies highlighted that the sparing effect obtained by dose fractionation results in a lower risk of chronic response (42, 48).

Stewart et al. evaluated the recovery of bladder at late time points and the consequent re-irradiation tolerance in mice and highlighted a possible indirect correlation between

TABLE 5 | Chronological summary of the pre-clinical studies about bystander and abscopal effects: the clonogenic the survival of brain cells after pencil beam and/or microbeam *in-vivo* irradiation (usually using a synchrotron) is compared with that of the corresponding not-targeted bladder cells.

Reference	Animal model (strain)	Set-up	Endpoint (method)	Euthanasia timing after RT	Findings
Singh et al. (77)	Female mouse (C57BL6 and Balb/c)	Whole body irradiation (Co60 source) at single and serial low dose (20mGy-2Gy)	RIBE (clonogenic survival)	24 h	Genotype determined the type of bystander signal/response
Fernandez-Palomo et al. (78)	Rat (sex n.a.) (Wistar)	17.5, 35, 70, 350 Gy delivered by synchrotron on one brain hemisphere	RIBE (clonogenic survival)	4, 8, 12 h	Both MRT and HSR yielded a demonstrable abscopal effect after high doses of irradiation
Mothersill et al. (79)	Male rat (Wistar)	Whole body MRT and HSR on one brain hemisphere (35 and 350 Gy skin-entry doses)	RIBE (proteomics, clonogenic survival)	48 h (hours in cage with uneradicated rats)	Evidence of strong RIBE signal in the contra-lateral brain hemisphere and weaker effects in the distant bladder of the irradiated rats. Proximity to an irradiated animal induced signaling changes in an un-irradiated partner
Fernandez-Palomo et al. (80)	Male rat (Fisher)	MRT (20 or 200 Gy skin-entry doses) on one brain hemisphere with inoculated F98 cells	RIBE/abscopal effects (calcium flux, role of 5HT, clonogenic survival and proteomic profil)	48 h (hours in cage with unirradiated rats)	Membrane related functions were critical for true RIBE expression. Bystander effects (in partner animals) were not the same as abscopal effects (in the irradiated animal)
Fernandez-Palomo et al. (81)	Male/female mouse (NU-Foxn1^{nu})	PB (200 or 1,000 Gy skin-entry doses) and MRT (22 Gy or 110 Gy) on one brain hemisphere with and without glioma injected 7d earlier	RIBE/abscopal effects (calcium flux, clonogenic survival)	2, 12, 48 h	Calcium data did not support a calcium channel mediated mechanism. The presence of a tumor reduced or reversed the effect. The immune response played a role.

Thus, in this field of research the normal bladder does not deal with any direct radiation effect.
RT, radiotherapy; RIBE, radiation-induced bystander effects; PB, Pencil Beam; MRT, microbeam irradiation; HSR, homogenous synchrotron radiation.

long-term injury and radiation dose administered in the first treatment; furthermore the prolongation of the interval time between treatment did not prevent late radiation damage in the bladder (40).

In vivo Functional Evaluation

As in clinical setting, also small animals functional assessment of radiation cystitis can be undertaken. Cystometric evaluation, in both mice and rats (**Table 2**) represents the state of the art for quantifying *in vivo* functional bladder impairment.

Historically, one of the first attempts at assessing urinary frequency was reported in 1978 by Stewart et al. by placing an irradiated mice in a metabolic cage and counting the number and size of urine patches on a paper moving under it (91). Subsequently more precise technologies have been developed (38). Various cystometric models exist, but catheterizing the animals and placing them in metabolic cages is generally necessary. The bladder catheter is connected to a pressure transducer and a microinjection pump. Micturition volumes are recorded with a fluid collector under the metabolic cage. A room-temperature saline solution can be instilled into the bladder constantly at different rates depending on the aims of the investigator. Thus, bladder basal pressure, threshold pressure, flow pressure, maximum micturition pressure, micturition volume and micturition interval can be directly recorded. When male mice or rats (which display slight differences among species) are used, due to the anatomic structure of the urethra in the rodents, surgical implantation of the catheter is generally necessary if bladder catheterization is required; the catheter is positioned at the dome of the bladder and then tunneled subcutaneously to an interscapular region incision (or, less frequently, to the abdomen).

Many examples of the application of this technology in radiation cystitis setting may be found in the literature (**Table 2**). Lundbeck et al. reported one of the first attempts in female mice (doses delivered from 5 to 40 Gy), showing a reduction of reservoir function starting from 20 Gy in both acute (peak at 14 days) and late phase (300 days follow up) (89). Stewart et al. ascertained an increased urinary frequency and a reduced bladder capacity in a mouse model (female mice of strain C3H) after irradiation from 10 to 30 Gy in both early and late time settings (6 to 53 weeks after treatment, each animal was examined every 4/6 weeks) (41). Vale et al. after irradiating four equal groups of nine female Wistar rats at 10, 15, 20 and

25 Gy, performed a weekly cystometric evaluation until 2 months after irradiation and subsequently once every 3 weeks up to 6 months. A biphasic reduction of at least 30% in the bladder compliance index (calculated as volume injected to induce an increase in intravesical pressure of 5 cmH20) was obtained at 4/6 weeks and at 6 months after irradiation in all groups of animals receiving at least 15 Gy (44). Dörr et al. evaluated bladder reservoir function in female mice through cystometry in the dose fractionation setting: four equal-sized doses per fraction with increasing intervals of 0–8 h were applied to female mouse (strain CH3) bladders, and bladder capacity was measured 3 times 2 weeks before irradiation and at 3–4 day intervals during the initial 30 days after irradiation, obtaining a clear dose-response relationship (44, 48, 90).

In conclusion, all the authors seemed to agree that acute damage is confined to only a few days after irradiation, irrespective of the dose delivered, while late toxicity could emerge at different time lapses and with intensity depending on radiation dose and fractionation; in addition, cystometry has to be considered as a feasible, easy to interpret and reliable way to assess RC functional impairment.

Histopathological Model of RC

Several animal models, employing both mouse and rat, have been developed with the aim of investigating the pathological modifications that occur in the bladder after irradiation but a "standard" universally recognized RC model is still lacking. To standardize the evaluation of histologic patterns, which are meant to be surrogates of the functional status of the bladder, morphological scores have been used.

To date, hematoxylin and eosin (H&E), indisputably remains the most informative staining employed, allowing the recognition of macroscopic signs of both early acute and late histological changes. Rajaganapathy et al. described the alterations of the rats' bladder wall 6 weeks after radiation (early inflammatory phase) through an analysis of the organ sections stained with H&E. In their study it was possible to discriminate several pathological features at three different radiation doses (20, 30, and 40 Gy). No sign of inflammation could be detected at the lowest dose (20 Gy), while edematous changes, immune cell infiltration, ectasic blood vessels in the lamina propria and hyperplasic urothelium were evident following 30 Gy irradiation. In addition, the staining highlighted degenerative-type epithelial changes, urothelial cell swelling and small nests of urothelial cells in the lamina propria surrounding blood vessels after 40 Gy radiation (51). Zwaans et al. in their mouse model of chronic radiation-induced cystitis used a scoring method to show the presence of urothelial thinning, ischemic necrosis and inflammation on H&E-stained slide, while Masson trichrome staining, which allows for a better visualization of both collagen deposition and smooth muscle fibers, was employed to score fibrosis (52). Both an intensity-based score (52) or a percentage of bladder wall area score (92), have been used to assess fibrosis.

In order to support such histopathological evidences, immunohistochemical staining can be employed to better visualize features such as urothelium loss and loss of smooth muscle (e.g., with markers COX-1/2 and UP-III) (52, 65). Morphological scores have been implemented, for example, by Zwaans et al. using a simple "positive *vs.* negative" staining assessment (52), and by Jiang et al. using integrated optical density (92).

Many of the single histological features present in the animal models of RC, such as inflammatory infiltrate, submucosal fibrosis, surface ulceration and nests of urothelial cells within the lamina propria referred to as "pseudocarcinomatous urothelial hyperplasia," have also been described in humans by several research groups (93, 94). Moreover, histopathological changes in the human irradiated bladder have also been divided into "early" (predominant $<$12 months after irradiation) and "late" (predominant $>$12 months after irradiation) changes, consistent with the proposed model of RC progression in the animal model (52, 93). However, there are some subtle differences: for example, fibrosis has seldom been reported in humans as an early change that persists into the chronic phase, while in small animal models it occurs in the late phase only (95). This implies that even given the extensive experimentation on animal models, there are some limitations in the application of this knowledge to humans to be considered when planning clinical trials and experimental treatments.

Radioprotective Agents

Great effort has been spent in finding new radioprotective agents (RA) to improve the range of clinical options for the management of radiotherapy-induced toxicity. An RA is natural compound or an artificially synthetized substance able to prevent radiation induced acute and late effects. In other words, RA should protect patients' healthy tissues during treatment and prevent the development of detrimental effects (96). According to the timing of their administration, it is possible to distinguish three classes of RAs. The first class includes agents intended for the prophylaxis of RT injuries, and is therefore administered before exposure to the radiation dose (97). This category comprises compounds with sulfhydryl groups, antioxidant properties or free radical scavengers (98). The second class of RA is represented by mitigators, administered during or shortly after RT, before symptoms appear, and are aimed at minimizing toxicity by preventing or reducing radiation damage on cells or tissues (99). These mitigators are, in fact, directed at hindering a series of cellular insults that stimulate proliferation and immune-inflammatory responses, including DNA repair, apoptosis and regulation of signal transduction cascades (100). The third heterogeneous group comprises symptomatic treatments given after RT.

Currently, the clinical management of RC includes both systemic and local treatments mostly focused on pain and symptomatic relief, which, however, neither prevent the development of RC nor reverse it in case of assumption after RT administration. The approved therapies may vary depending on the degree and the phase of radiation induced bladder damage. Anticholinergic agents and β_3-adrenergic receptor agonists, for instance, are used to attenuate acute phase symptoms such as frequency and urgency. On the other hand, a wide range of drugs are systemically administered to cope with RT induced chronic response. Examples of

this class of pharmaceuticals are represented by WF10, also known as Tetrachlorodecaoxygen (TCDO), a formulation given intravenously able to stimulate natural immunity in order to reduce inflammation; sodium pentosan polysulphate (SPP), a synthetic sulphated polysaccharide that decrease urothelial permeability by replacing defective glycosaminoglycans; tranexamic acid, used to inhibit fibrinolysis and prevent clot urinary retention in patients with hemorragic cystitis (95).

Nevertheless, although systemic treatments are non-invasive and avoid inpatient hospital admission, these therapies had low efficacy often accompanied by dose-dependent toxicity. For this reason, local treatments and bladder irrigation are considered the first line of intervention in all grades of the disease (101), aiming at protect the urothelium, arrest focal bleeding points and remove blood clots. Several agents are employed as intravesical therapies and directed at improving bladder compliance (102) including formalin, aluminum salts, hyaluronic acid, prostaglandins, botulinum toxin, polydeoxyribonucleotides and early placental extract (83, 95).

In recent years, hyperbaric oxygen and laser ablation have also emerged as non-invasive management options able to produce symptom relief and stop the progression of the pathologic process. They are, however, cumbersome for patients, requiring lengthy treatments and, in case of ablation a performance status that typically patients with radiation-induced cystitis do not have (83, 95, 103).

To date, many compounds have promised improvements in preclinical radioprotection research, most belonging to the third treatment category of RAs. For instance, Bortezomib, a potent proteasome inhibitor currently used in clinics for multiple myeloma treatment, is implicated also in the blockade of NF-κB (104–108) and therefore it was recently investigated in a radiation induced urinary bladder dysfunction mouse model (76). The study employs a daily subcutaneous dose of 0.02 mg/ml of Bortezomib given between days 0–15 or 15–30, at the two acute radiation-induced bladder inflammatory waves, after a single graded radiation dose. The aim was to identify the window of time in which the drug was more effective. At cystometry evaluation the most favorable outcome was obtained in case of drug administration at the first acute inflammatory wave (days 0–15), with no significant variation when given in the second, meaning that distinct mechanisms are involved in the acute phases. In 2018, Ikeda et al. investigated the effect of the hormone relaxin in reversing radiation induced bladder fibrosis in adult female C57Bl/6 mice (109). Relaxin is a 6 kDa hormone involved in the relaxation of uterine smooth muscle and in the softening of the pubic symphysis during pregnancy. Although a relaxing effect of the hormone on the bladder has not been demonstrated yet, its receptors were found to be expressed on detrusor cells as well as in the lamina propria and, to a lesser extent, the urothelium. In this study, relaxin 2 was administered to 7-week post-irradiated animals (10 Gy radiation dose) at a concentration of 400 μg/kg/day for 2 weeks. As a result, the treatment increased bladder compliance and bladder wall force generation. The hypothesized mechanism of action involved the activation of specific pathways associated to the activation of relaxin receptors; the stimulation of neoangiogenesis through the phosphorylation of AKT, the expression of platelet derived growth factor (PDGF) and vascular endothelial growth factor (VEGF), the enhancement of contractile function mediated by increased Cav1.2 (i.e., L-type Ca^{2+} channel) and the arrest of profibrotic TGF-β signaling (110) induced by ERK1/2 phosphorylation and upregulation of neuronal Nitric Oxide Syntase (nNOS) and cyclic guanosine monophosphate (cGMP) levels. Tacrolimus, a calcineurin inhibitor that prevents the growth and differentiation of T cells by indirectly blocking IL-2 expression was tested in a RC rat model in which animals received a high radiation dose (40 Gy). In this study, due to its hydrophobic nature, in order to improve drug solubility and delivery and reduce systemic toxicity, Tacrolimus was encapsulated into liposome (51). A significant improvement on the inter-micturition interval was achieved (111). L-arginine, due to its anti-oxidant and anti-inflammatory properties (6, 112, 113), as well as due to its proposed protective effect on endothelium by the stimulation of endothelium-derived relaxing factors (114), was tested in several preclinical studies on pelvic radiation-induced bladder toxicity. In these studies, the amino acid administration triggered nitric oxide formation in animals with impaired endothelial function at basal levels (115), reduced radiation-induced diarrhea in around 40% of rats (116), and prevented bladder modification, restoring the morphology of blood vessels by recovering VEGF and FGF expression in the bladder wall (73).

CONCLUSION AND FUTURE PERSPECTIVES

A brief summary of the revised literature is reported in **Table 6**, along with summarized conclusions. The current review has underlined renewed interest in pre-clinical research on radiation induced urinary toxicity and the bladder response to radiotherapy. In particular, a considerable interest in the development and testing of RA has been increased in recent years, especially for high risk conditions such the use of high doses, as for prostate cancer, and the existence of baseline risk factors, i.e., genetic predisposition or clinical factors (e.g., impaired baseline urinary function, adjuvant or salvage irradiation after prostatectomy). Importantly, a greater effort should be spent in the translation of pre-clinical results into clinical trials. Nonetheless, further pre-clinical studies are needed to clarify the applicability and therapeutic advantages of radioprotective agents in the treatment of radiation cystitis. Future goals will be the identification of novel molecules and strategies to pursue in order to guarantee a broader efficacy at a cellular, tissue, organ and whole organism level.

Despite the availability of micro-irradiators, animal studies on bladder radiation focusing on dose, fractionation and volume effects, are largely lacking. Such investigations deserves greater attention for several reasons, e.g., given the growing interest in hypo-fractionation and ablative therapies, investigations mimicking these situations might help in better understanding the mechanisms of bladder radiation response in these extreme condition; or given some evidences (20) of high sensitivity to moderate hypofractionation (2.3–3.0 Gy/fr), experiments on animal models on this subject might shed light on the issue.

TABLE 6 | Brief summary of the revised literature with some conclusions; unmet needs; future perspectives.

Findings from literature	Conclusions	Future perspectives
Bladder mechanism		
Radiation effect at the molecular level (direct and indirect damage to DNA) is followed by downstream **abnormalities of bladder** wall in three phases: 1) *Early/acute phase: reversible* →Increase of NF-κB →COX2 and prostaglandin expression →Vasodilatation, increased muscle tone →hyperemia, edema →increase of ICAM-1 →leucocyte infiltration →inflammatory symptoms (frequency, urgency, dysuria) 2) *Symptom-free phase* *Late phase: persistent, fibrotic* →UP-III downregulation and loss of umbrella cells →increase of permeability →chemical irritation from urine components →Increase of TGF-β1 expression →accumulation of extracellular matrix and collagen deposition →development of fibrosis →hematuria, permanent reduction of bladder compliance, voiding failure	The **full comprehension of RT-induced urothelial toxicity** and the availability of models that faithfully recapitulate all the pathological paths, both early and late phases, still represent an unmet need. The establishment of reliable preclinical **models mimicking urothelial toxicity** is fundamental for testing more "tailored" novel therapies.	Given the current interest in **hypo-fractionation and ablative therapies**, investigations mimicking extreme hypo-fractionation (e.g., radical doses delivered in 1–5 fractions) should help in better understanding the partially unknown mechanisms of bladder radiation response in these extreme situations. Experiments set to identify the mechanisms underlying **"spatial effects"** would be of paramount importance in possibly guiding plan optimization to selectively reduce the dose to these sub-structures.
Animal models and dose set up: • Each research group developed their own animal model using **different strains of rats or mice**. • Radiation dose was tested in the range **5–40 Gy**. • The general practice was to use a **single radiation dose of 20–25 Gy**, approximately equal to ED50 and estimated to mimic the delivered clinical doses to pelvic tumors. • **Doses over 20 Gy** proved to be associated with a higher toxicity rate and more severe symptoms. • ED50 increases with the **number of fractions** and the **interval between fractions**. • Late radiation injury seemed to be inversely related to the **dose given in the first treatment** and independent of the **interval between treatments**.	Very different experimental settings have been used: a "**standard**" universally recognized RC model is still missing. Even though a single dose of 40 Gy is well above the dose delivered in a clinical setting, the use of **high dose** can be useful for a better understanding of the underlying biological mechanisms.	Despite the availability of micro-irradiators with theoretically significant potentials for high-precision experiments, animal studies focused on gaining a better understanding of **dose, fractionation and volume effects** are largely lacking. **Reliable and reproducible methods** to quantify the **severity of RC** in animal models should be realized.
***In vivo* functional evaluation** • **Acute damage** is confined to only a few weeks after irradiation, irrespective of the dose delivered, with a biphasic response at about 7 and 23 days after RT, respectively. • **late toxicity** could emerge at different time lapses (within 6 month to 1 year) with intensity depending on radiation dose and fractionation. No changes in the **diurnal urinary pattern** were observed during cystometry. If **male mice/rats** are used, a surgical implantation of the catheter is deemed necessary.	Cystometry is the "state-of-the- art" objective tool in evaluating the ***in vivo*** response to radiation damage, in terms of **reservoir function** and/or **micturition frequency.**	**High-quality pre-clinical imaging platforms** are expected to extend the potential of **non-invasive** assessment of RC severity.
Histopathological model of RC • **H&E** (the most informative): recognition of both early acute and late histological changes. • **Masson trichrome**: to assess the level of bladder wall fibrosis as an intensity-based score or as a percentage of bladder wall area score. • **urothelial and inflammation markers** to better visualize the urothelium (e.g., COX-1/2 and UP-III). • Simple **"positive vs. negative" staining** using integrated optical density: to better visualize urothelium loss and loss of smooth muscle.	IHC is the gold standard for the **tracking** of disease progression in preclinical models. There are **limitations in the application of this knowledge to humans** that must be considered when planning clinical trials and experimental therapies.	The interaction between radiation induced reactions, damage repair and the immune system in the case of **combined immune-radiotherapy** is an extremely promising field of investigation, possibly involving several pelvic tumors.

(Continued)

TABLE 6 | Continued

Findings from literature	Conclusions	Future perspectives
Radioprotective agents *Clinical management of RC*: • **Systemic treatments** (e.g., anticholinergic agents and β3-adrenergic receptor agonists, TCDO, SPP, tranexamic acid): non-invasive and circumvent inpatient hospital admission; these therapies suffer from a very low efficacy, often accompanied by dose-dependent toxicity. • **Local treatments** and **bladder irrigation**: considered the first line of intervention in all grades of the disease, aiming at sterilization, arrest of focal bleeding points and removal of blood clots (e.g., intravesical therapies). • **hyperbaric oxygen** and **laser ablation**: emerged as non-invasive management; they are, however, cumbersome for patients requiring lengthy treatments, and a level of fitness that many patients with radiation cystitis do not possess. *Classes of RAs*: • agents for the **prophylaxis** of RT injuries, administered before exposure. • **mitigators** given during or shortly after RT, aimed at minimizing or preventing the effects of radiation on cells/tissues. • **treatments or therapeutic preparations** applied after RT, to ameliorate radio-induced symptoms. *Compounds in radioprotection preclinical research*: • **Bortezomib**: implicated in the NF-κB blockade. • **Hormone relaxin**: reversing fibrosis. • **Tacrolimus** and **L-arginine**: to hinder the production and release of pro-inflammatory cytokines.	RAs **improve the range of clinical options** for the management of the RT-induced toxicity in **combined therapies**.	We must expect the **translation of pre-clinical results into clinical trials** testing the protective effects of RAs, especially in situations where high doses need to be delivered (e.g., prostate cancer) and for patients at higher risk of toxicity due to genetic predisposition or clinical factors (e.g., the impaired baseline urinary function of patients irradiated after prostatectomy). Future goals will be the identification of **novel molecules and strategies** to pursue either alone or in combination in order to guarantee a broader efficacy at a cellular, tissue, organ and whole organism level.

NF-κB, nuclear factor-kappa B; COX2, cyclooxygenase; ICAM-1, intercellular adhesion molecule 1; UP-III, uroplakin 3; TGF-β1, transforming growth factor beta-1; ED50, radiation dose producing the damage in 50% of animals; RC, radiation cystitis; reservoir function, reduction in the bladder capacity by >50% at a fixed intravesical pressure; H&E, hematoxylin and eosin; IHC, immunohistochemistry; RA, radioprotective agent; TCDO, Tetrachlorodecaoxygen; SPP, sodium pentosan polysulphate.

Another significant issue concerns evidence of "spatial" effects suggesting that specific sub-structures (i.e., the trigone) may be more sensitive to radiation (18–20): experiments set to identify the mechanisms underlying these effects would be of paramount importance in guiding plan optimization to selectively reduce the dose to these sub-structures.

A related development that could be useful for further advances in the field is the increasing use of combined therapies, including chemotherapeutic agents and immunotherapy. Testing dose and volume effects in these scenarios is an issue of paramount importance to understand the interaction between drugs and radiation induced reactions, damage repair and immune system.

Another largely unexplored field of investigation is pre-clinical imaging: high quality small animal images before and after radiation delivery may potentially become a powerful, non-invasive, quantitative surrogate for the measurement of radiobiological effects. For the bladder echography as well as targeted optical imaging seem especially promising.

Finally, an attempt should be made to set up reliable and reproducible methods to quantify the severity of RC in animal models. This implies the fulfillment of an easy-to-realize, ideally quick and economical, but at the same time sufficiently robust, quantitative analysis of RC severity both *in vivo*, e.g., by means of ultrasounds and/or MRI, and after the animal's sacrifice, e.g., through the development of a histological quantitative scoring of the radiation-induced lymphocyte infiltrate, collagen matrix deposition and neoangiogenesis.

AUTHOR CONTRIBUTIONS

SZ and ABre performed the literature review and wrote a large part of the manuscript and tables. AES contributed to the preclinical radiotherapy part and coordinated the work. GF, ABri, AS, and FM contributed to the anatomical description of the urinary tract. FS and RL contributed to the section on histopathology. ND, CF, and CC focused on the radiotherapy discussion. CF and CC also supervised the entire work. FB and RV contributed to the section focused on radioprotective agents. All authors contributed to the article and approved the submitted version.

FUNDING

The research leading to these results has received funding from AIRC under IG 2018 - ID. 21441 project – CC.

ACKNOWLEDGMENTS

The authors thank Dr. Frank Bagg for the linguistic revision of the manuscript.

REFERENCES

1. Spampinato S, Fokdal L, Marinovskij E, Axelsen S, Pedersen EM, Pötter R, et al. Assessment of dose to functional sub-structures in the lower urinary tract in locally advanced cervical cancer radiotherapy. *Phys Med.* (2019) 59:127–32. doi: 10.1016/j.ejmp.2019.01.017
2. Budäus L, Bolla M, Bossi A, Cozzarini C, Crook J, Widmark A, et al. Functional outcomes and complications following radiation therapy for prostate cancer: a critical analysis of the literature. *Eur Urol.* (2012) 61:112–27. doi: 10.1016/j.eururo.2011.09.027
3. Baskar R, Dai J, Wenlong N, Yeo R, Yeoh KW. Biological response of cancer cells to radiation treatment. *Front Mol Biosci.* (2014) 1:24. doi: 10.3389/fmolb.2014.00024
4. Ambrus JL, Halpern J, Bardos T, Chmielwicz ZF, Klein E. Radiation sensitizing and radiation protective agents in experimental radiation therapy. *J Med.* (1988) 19:369–81.
5. Grape HH, Dedering A, Jonasson AF. Retest reliability of surface electromyography on the pelvic floor muscles. *Neurourol Urodyn.* (2013) 32:215–23. doi: 10.1002/nau.20648
6. Coman D, Yaplito-Lee J, Boneh A. New indications and controversies in arginine therapy. *Clin Nutr.* (2008) 27:489–96. doi: 10.1016/j.clnu.2008.05.007
7. de Langhe S, de Meerleer G, de Ruyck K, Ost P, Fonteyne V, de Neve W, et al. Integrated models for the prediction of late genitourinary complaints after high-dose intensity modulated radiotherapy for prostate cancer: making informed decisions. *Radiother Oncol.* (2014) 112:95–9. doi: 10.1016/j.radonc.2014.04.005
8. Andersson KE, Arner A. Urinary bladder contraction and relaxation: physiology and pathophysiology. *Physiol Rev.* (2004) 84:935–86. doi: 10.1152/physrev.00038.2003
9. Wein A, Kavoussi L, Alan P, Peters C. *Campbell-Walsh Urology*, 11th edn. Philadelphia, PA: Elsevier (2013).
10. Farsund T, Dahl E. Cell Kinetics of mouse urinary bladder epithelium - III. A histologic and ultrastructural study of bladder epithelium during regeneration after a single dose of cyclophosphamide, with special reference to the mechanism by which polyploid cells are formed. *Virchows Arch B Cell Pathol.* (1978)26:215–23.
11. Roccabianca S, Bush TR. Understanding the mechanics of the bladder through experiments and theoretical models: where we started and where we are heading. *Technology.* (2016) 04:30–41. doi: 10.1142/S2339547816400082
12. Korkmaz I, Rogg B. A simple fluid-mechanical model for the prediction of the stress-strain relation of the male urinary bladder. *J Biomech.* (2007) 40:663–8. doi: 10.1016/j.jbiomech.2006.02.014
13. Parekh A, Cigan AD, Wognum S, Heise RL, Chancellor MB, Sacks MS. Ex vivo deformations of the urinary bladder wall during whole bladder filling: contributions of extracellular matrix and smooth muscle. *J Biomech.* (2010) J43:1708–16. doi: 10.1016/j.jbiomech.2010.02.034
14. Ding HL, Ryder JW, Stull JT, Kamm KE. Signaling processes for initiating smooth muscle contraction upon neural stimulation. *J Biol Chem.* (2009) 284:15541–8. doi: 10.1074/jbc.M900888200
15. Veerasarn V, Boonnuch W, Kakanaporn C. A phase II study to evaluate WF10 in patients with late hemorrhagic radiation cystitis and proctitis. *Gynecol Oncol.* (2006) 100:179–84. doi: 10.1016/j.ygyno.2005.08.014
16. Shadad AK, Sullivan FJ, Martin JD, Egan LJ. Gastrointestinal radiation injury: symptoms, risk factors and mechanisms. *World J Gastroenterol.* (2013) 19:185–98. doi: 10.3748/wjg.v19.i2.185
17. Clement CH, Stewart FA, Akleyev AV, Hauer-Jensen M, Hendry JH, Kleiman NJ, et al. ICRP publication 118: ICRP statement on tissue reactions and early and late effects of radiation in normal tissues and organs - threshold doses for tissue reactions in a radiation protection context. *Ann ICRP.* (2012) 41:1–322. doi: 10.1016/j.icrp.2012.02.001
18. Landoni V, Fiorino C, Cozzarini C, Sanguineti G, Valdagni R, Rancati T. Predicting toxicity in radiotherapy for prostate cancer. *Phys Med.* (2016) 32:521–32. doi: 10.1016/j.ejmp.2016.03.003
19. Rancati T, Palorini F, Cozzarini C, Fiorino C, Valdagni R. Understanding urinary toxicity after radiotherapy for prostate cancer: first steps forward. *Tumori.* (2017) 103:395–404. doi: 10.5301/tj.5000681
20. Rancati T, Fiorino C. *Modelling Radiotherapy Side Effects: Practical Application for Planning Optimisation.* Boca Raton, FL: CRC Press (2019). p. 113–36. doi: 10.1201/b21956-5
21. Cozzarini C, Fiorino C, Deantoni C, Briganti A, Fodor A, La Macchia M, et al. Higher-than-expected severe (Grade 3-4) late urinary toxicity after postprostatectomy hypofractionated radiotherapy: a single-institution analysis of 1176 patients. *Eur Urol.* (2014) 66:1024–30. doi: 10.1016/j.eururo.2014.06.012
22. Viswanathan AN, Yorke ED, Marks LB, Eifel PJ, Shipley WU. Radiation dose-volume effects of the urinary bladder. *Int J Radiat Oncol Biol Phys.* (2010) 76(Suppl. 3):S116–22. doi: 10.1016/j.ijrobp.2009.02.090
23. Cozzarini C, Rancati T, Carillo V, Civardi F, Garibaldi E, Franco P, et al. Multi-variable models predicting specific patient-reported acute urinary symptoms after radiotherapy for prostate cancer: results of a cohort study. *Radiother Oncol.* (2015) 116:185–91. doi: 10.1016/j.radonc.2015.07.048
24. Verhaegen F, Granton P, Tryggestad E. Small animal radiotherapy research platforms. *Phys Med Biol.* (2011) 56:R55–83. doi: 10.1088/0031-9155/56/12/R01
25. van Hoof SJ, Granton PV, Verhaegen F. Development and validation of a treatment planning system for small animal radiotherapy: SmART-Plan. *Radiother Oncol.* (2013) 109:361–6. doi: 10.1016/j.radonc.2013.10.003
26. Graves EE, Zhou H, Chatterjee R, Keall PJ, Gambhir SS, Contag CH, et al. Design and evaluation of a variable aperture collimator for conformal radiotherapy of small animals using a microCT scanner. *Med Phys.* (2007) 34:4359–67. doi: 10.1118/1.2789498
27. Pidikiti R, Stojadinovic S, Speiser M, Song KH, Hager F, Saha D, et al. Dosimetric characterization of an image-guided stereotactic small animal irradiator. *Phys Med Biol.* (2011) 56:2585–99. doi: 10.1088/0031-9155/56/8/016
28. Tillner F, Thute P, Löck S, Dietrich A, Fursov A, Haase R, et al. Precise image-guided irradiation of small animals: a flexible non-profit platform. *Phys Med Biol.* (2016) 61:3084–108. doi: 10.1088/0031-9155/61/8/3084
29. Sharma S, Narayanasamy G, Przybyla B, Webber J, Boerma M, Clarkson R, et al. Advanced small animal conformal radiation therapy device. *Technol Cancer Res Treat.* (2017) 16:45–56. doi: 10.1177/1533034615626011
30. Verhaegen F, Dubois L, Gianolini S, Hill MA, Karger CP, Lauber K, et al. ESTRO ACROP: Technology for precision small animal radiotherapy research: optimal use and challenges. *Radiother Oncol.* (2018) 126:471–8. doi: 10.1016/j.radonc.2017.11.016
31. Pinter C, Lasso A, Wang A, Jaffray D, Fichtinger G. SlicerRT: radiation therapy research toolkit for 3D Slicer. *Med Phys.* (2012) 39:6332–8. doi: 10.1118/1.4754659
32. Bolcaen J, Descamps B, Deblaere K, Boterberg T, Hallaert G, Van den Broecke C, et al. MRI-guided 3D conformal arc micro-irradiation of a F98 glioblastoma rat model using the small animal radiation research platform (SARRP). *J Neurooncol.* (2014) 120:257–66. doi: 10.1007/s11060-014-1552-9
33. Kuntner C, Stout D. Quantitative preclinical PET imaging: opportunities and challenges. *Front Phys.* (2014) 2:12. doi: 10.3389/fphy.2014.00012
34. Franc BL, Acton PD, Mari C, Hasegaway BH. Small-animal SPECT and SPECT/CT: important tools for preclinical investigation. *J Nucl Med.* (2008) 49:1651–63. doi: 10.2967/jnumed.108.055442
35. Kuo C, Coquoz O, Troy TL, Xu H, Rice BW. Three-dimensional reconstruction of *in vivo* bioluminescent sources based on multispectral imaging. *J Biomed Opt.* (2007) 12:024007. doi: 10.1117/1.2717898

36. Ghita M, Brown KH, Kelada OJ, Graves EE, Butterworth KT. Integrating small animal irradiators with functional imaging for advanced preclinical radiotherapy research. *Cancers.* (2019) 11:170. doi: 10.3390/cancers11020170
37. Knowles JF. Radiation-induced hydronephrosis in the rat: a new experimental model. *Int J Radiat Biol.* (1985) 48:737–44.
38. Lundbeck F, Djurhuus JV aeth M. Bladder filling mice: an experimental in vivo model to evaluate the reservoir function of the urinary bladder in a long term study. *J Urol.* (1989) 141:1245–9. doi: 10.1016/S0022-5347(17)41231-6
39. Lundbeck F, Ulsø N, Overgaard J. Cystometric evaluation of early and late irradiation damage to the mouse urinary bladder. *Radiother Oncol.* (1989) 15:383–92. doi: 10.1016/0167-8140(89)90085-6
40. Stewart FA, Oussoren Y, Luts A. Long-term recovery and reirradiation tolerance of mouse bladder. *Int J Radiat Oncol Biol Phys.* (1990) 18:1399–406.
41. Stewart FA, Lundbeck F, Oussoren Y, Luts A. Acute and late radiation damage in mouse bladder: a comparison of urination frequency and cystometry. *Int J Radiat Oncol Biol Phys.* (1991) 21:1211–9.
42. Bentzen SM, Lundbeck F, Christensen LL, Overgaard J. Fractionation sensitivity and latency of late radiation injury to the mouse urinary bladder. *Radiother Oncol.* (1992) 25:301–7.
43. Dorr W, Schultz-Hector S. Early changes in mouse urinary bladder function following fractionated X irradiation. *Radiat Res.* (1992) 131:35–42.
44. Vale JA, Bowsher WG, Liu K, Tomlinson A, Whitfield HN, Trott KR. Post-irradiation bladder dysfunction: development of a rat model. *Urol Res.* (1993) 21:383–8.
45. Dörr W, Dorr W. Impact of time between x-ray fractions on acute changes in the function of the urinary bladder in the mouse. *Radiat Res.* (1995) 141:219. doi: 10.2307/3579051
46. Dörr W, Kraft M. Effects of ageing and x-lrradiation on the diurnal rhythm of mouse urinary bladder capacity. *Urol Int.* (1997) 58:153–9.
47. Dörr W, Beck-Bornholdt H-P. Radiation-induced impairment of urinary bladder function in mice: fine structure of the acute response and consequences on late effects. *Radiat Res.* (1999) 151:461–7.
48. Dörr W, Bentzen SM. Late functional response of mouse urinary bladder to fractionated X-irradiation. *Int J Radiat Biol.* (1999) 75:1307–15.
49. Jaal J, Dörr W. Early and long-term effects of radiation on intercellular adhesion molecule 1 (ICAM-1) expression in mouse urinary bladder endothelium. *Int J Radiat Biol.* (2005) 81:387–95. doi: 10.1080/09553000500147600
50. Jaal J, Brüchner K, Hoinkis C, Dörr W. Radiation-induced variations in urothelial expression of intercellular adhesion molecule 1 (IGAM-1): association with changes in urinary bladder function. *Int J Radiat Biol.* (2004) 80:65–72. doi: 10.1080/09553000310001632921
51. Rajaganapathy BR, Janicki JJ, Levanovich P, Tyagi P, Hafron J, Chancellor MB, et al. Intravesical liposomal tacrolimus protects against radiation cystitis induced by 3-beam targeted bladder radiation. *J Urol.* (2015) 194:578–84. doi: 10.1016/j.juro.2015.03.108
52. Zwaans BMM, Krueger S, Bartolone SN, Chancellor MB, Marples B, Lamb LE. Modeling of chronic radiation-induced cystitis in mice. *Adv Radiat Oncol.* (2016) 1:333–43. doi: 10.1016/j.adro.2016.07.004
53. Giglio D, Wasén C, Mölne J, Suchy D, Swanpalmer J, Jabonero Valbuena J, et al. Downregulation of toll-like receptor 4 and IL-6 following irradiation of the rat urinary bladder. *Clin Exp Pharmacol Physiol.* (2016) 43:698–705. doi: 10.1111/1440-1681.12583
54. Crowe R, Vale J, Trott KR, Soediono P, Robson T, Burnstock G. Radiation-induced changes in neuropeptides in the rat urinary bladder. *J Urol.* (1996) 156:2062–6.
55. Kraft M, Oussoren Y, Stewart FA, Dörr W, Schultz-Hector S. Radiation-induced changes in transforming growth factor β and collagen expression in the murine bladder wall and its correlation with bladder function. *Radiat Res.* (1996) 146:619–27.
56. Kruse JJCM, Te Poele JAM, Russell NS, Boersma LJ, Stewart FA. Microarray analysis to identify molecular mechanisms of radiation-induced microvascular damage in normal tissues. *Int J Radiat Oncol Biol Phys.* (2004) 58:420–6. doi: 10.1016/j.ijrobp.2003.09.031
57. Kanai AJ, Epperly M, Pearce L, Birder L, Zeidel M, Meyers S, et al. Differing roles of mitochondrial nitric oxide synthase in cardiomyocytes and urothelial cells. *Am J Physiol - Hear Circ Physiol.* (2004) 286:13–21. doi: 10.1152/ajpheart.00737.2003
58. Jaal J, Dörr W. Radiation induced inflammatory changes in the mouse bladder: the role of cyclooxygenase-2. *J Urol.* (2006) 175:1529–33. doi: 10.1016/S0022-5347(05)00658-0
59. Jaal J, Dörr W. Radiation-induced damage to mouse urothelial barrier. *Radiother Oncol.* (2006) 80:250–6. doi: 10.1016/j.radonc.2006.07.015
60. Jaal J, Dörr W. Radiation induced late damage to the barrier function of small blood vessels in mouse bladder. *J Urol.* (2006) 176:2696–700. doi: 10.1016/j.juro.2006.07.138
61. Soler R, Vianello A, Füllhase C, Wang Z, Atala A, Soker S, et al. Vascular therapy for radiation cystitis. *Neurourol Urodyn.* (2011) 30:428–34. doi: 10.1002/nau.21002
62. Xu Y, Fang F, Miriyala S, Crooks PA, Oberley TD, Chaiswing L, et al. KEAP1 is a redox sensitive target that arbitrates the opposing radiosensitive effects of parthenolide in normal and cancer cells. *Cancer Res.* (2013) 73:4406–17. doi: 10.1158/0008-5472.CAN-12-4297
63. Ozbilgin MK, Aktas C, Temel M, Önal T, Uluer ET, Vatansever HS, et al. POMC expression of the urothelium of the urinary bladder of mice submitted to pelvic radiation. *Eur J Inflamm.* (2016) 14:34–9. doi: 10.1177/1721727X15624698
64. Ozbilgin MK, Aktas C, Uluer ET, Buyukuysal MC, Gareveran MS, Kurtman C. Influence of radiation exposure during radiotherapy: evidence for the increase of versican and heparin-binding EGF-like growth factor concentrations. *Anal Quant Cytol Histol.* (2016) 38:126–32.
65. Ozbilgin MK, Onal T, Ozcan C, Temel M, Aktas C, Gareveran MS, et al. Effects of cyclooxygenase on the urothelium of the urinary bladder of mice exposed to pelvic radiation. *Anal Quant Cytol Histol.* (2016) 38:103–10.
66. Edrees G, Luts A, Stewart F. Bladder damage in mice after combined treatment with cyclophosphamide and X-rays. The influence of timing and sequence. *Radiother Oncol.* (1988) 11:349–60.
67. Malkinson FD, Geng L, Hanson WR. Prostaglandins protect against murine hair injury produced by ionizing radiation or doxorubicin. *J Invest Dermatol.* (1993) 101(Suppl. 1):S135–7.
68. Horsman MR, Siemann DW, Chaplin DJ, Overgaard J. Nicotinamide as a radiosensitizer in tumours and normal tissues: the importance of drug dose and timing. *Radiother Oncol.* (1997) 45:167–74.
69. Kanai AJ, Zeidel ML, Lavelle JP, Greenberger JS, Birder LA, de Groat WC, et al. Manganese superoxide dismutase gene therapy protects against irradiation-induced cystitis. *Am J Physiol Ren Physiol.* (2002) 283:F1304–12. doi: 10.1152/ajprenal.00228.2002
70. Jaal J, Dörr W. Effect of recombinant human keratinocyte growth factor (rHuKGF, Palifermin) on radiation-induced mouse urinary bladder dysfunction. *Int J Radiat Oncol Biol Phys.* (2007) 69:528–33. doi: 10.1016/j.ijrobp.2007.05.074
71. Dinçbaş FÖ, Öksüz DÇ, Atalar B, Altug T, Ilvan S, Gedik N, et al. The role of amifostine on late normal tissue damage induced by pelvic radiotherapy with concomitant gemcitabine: an *in vivo* study. *Med Oncol.* (2009) 26:402–8. doi: 10.1007/s12032-008-9136-1
72. Rocha BR, Gombar FM, Barcellos LM, Costa WS, Barcellos Sampaio FJ, Ramos CF. Glutamine supplementation prevents collagen expression damage in healthy urinary bladder caused by radiotherapy. *Nutrition.* (2011) 27:809–15. doi: 10.1016/j.nut.2010.07.020
73. Costa WS, Ribeiro MN, Cardoso LEM, Dornas MC, Ramos CF, Gallo CBM, et al. Nutritional supplementation with l-arginine prevents pelvic radiation-induced changes in morphology, density, and regulating factors of blood vessels in the wall of rat bladder. *World J Urol.* (2013) 31:653–8. doi: 10.1007/s00345-012-0938-6
74. Horsman MR. Enhancing the radiation response of tumors but not early or late responding normal tissues using a vascular disrupting agent. *Acta Oncol.* (2017) 56:1634–8. doi: 10.1080/0284186X.2017.1348629
75. Oscarsson N, Ny L, Mölne J, Lind F, Ricksten S-E, Seeman-Lodding H, et al. Hyperbaric oxygen treatment reverses radiation induced pro-fibrotic and oxidative stress responses in a rat model. *Free Radic Biol Med.* (2017) 103:248–55. doi: 10.1016/j.freeradbiomed.2016.12.036
76. Sarsarshahi S, Madjd Z, Bozsaky E, Kowaliuk J, Kuess P, Ghahremani MH, et al. An evaluation of the effect of bortezomib on radiation-induced urinary bladder dysfunction [Untersuchung der wirkung von bortezomib auf die strahleninduzierte harnblasenfunktionsstörung]. *Strahlentherapie Onkol.* (2019) 195:934–9. doi: 10.1007/s00066-019-01497-8

77. Singh H, Saroya R, Smith R, Mantha R, Guindon L, Mitchel REJ, et al. Radiation induced bystander effects in mice given low doses of radiation *in vivo*. *Dose Res.* (2011) 9:225–42. doi: 10.2203/dose-response.09-062.Singh
78. Fernandez-Palomo C, Schültke E, Smith R, Bräuer-Krisch E, Laissue J, Schroll C, et al. Bystander effects in tumor-free and tumor-bearing rat brains following irradiation by synchrotron X-rays. *Int J Radiat Biol.* (2013) 89:445–53. doi: 10.3109/09553002.2013.766770
79. Mothersill C, Fernandez-Palomo C, Fazzari J, Smith R, Schültke E, Bräuer-Krisch E, et al. Transmission of signals from rats receiving high doses of microbeam radiation to cage mates: an inter-mammal bystander effect. *Dose Res.* (2014) 12:72–92. doi: 10.2203/dose-response.13-011.Mothersill
80. Fernandez-Palomo C, Bräuer-Krisch E, Laissue J, Vukmirovic D, Blattmann H, Seymour C, et al. Use of synchrotron medical microbeam irradiation to investigate radiation-induced bystander and abscopal effects *in vivo*. *Phys Med.* (2015) 31:584–95. doi: 10.1016/j.ejmp.2015.03.004
81. Fernandez-Palomo C, Schültke E, Bräuer-Krisch E, Laissue JA, Blattmann H, Seymour C, et al. Investigation of abscopal and bystander effects in immunocompromised mice after exposure to pencilbeam and microbeam synchrotron radiation. *Health Phys.* (2016) 111:149–59. doi: 10.1097/HP.0000000000000525
82. Di Maggio FM, Minafra L, Forte GI, Cammarata FP, Lio D, Messa C, et al. Portrait of inflammatory response to ionizing radiation treatment. *J Inflamm.* (2015) 12:14. doi: 10.1186/s12950-015-0058-3
83. Zwaans BMM, Chancellor MB, Lamb LE. Modeling and treatment of radiation cystitis. *Urology.* (2016) 88:14–21. doi: 10.1016/j.urology.2015.11.00
84. Dörr W, Eckhardt M, Ehme A, Koi S. Pathogenesis of acute radiation effects in the urinary bladder. Experimental results. *Strahlentherapie Onkol.* (1998) 174(Suppl. 3):93–5.
85. Hicks RM. The mammalian urinary bladder: an accommodating organ. *Biol Rev.* (1975) 50:215–46. doi: 10.1111/j.1469-185X.1975.tb01057.x
86. Bentzen SM. Preventing or reducing late side effects of radiation therapy: radiobiology meets molecular pathology. *Nat Rev Cancer.* (2006) 6:702–13. doi: 10.1038/nrc1950
87. Mauviel A. Transforming growth factor-beta: a key mediator of fibrosis. *Methods Mol Med.* (2005) 117:69–80. doi: 10.1385/1-59259-940-0:069
88. Lundbeck F, Djurhuus JC, Vaeth M. Bladder filling in mice: an experimental in vivo model to evaluate the reservoir function of the urinary bladder in a long term study. *J Urol.* (1989) 141:1245–9.
89. Lundbeck F, Ulsø N, Overgaard J. Cystometric evaluation of early and late irradiation damage to the mouse urinary bladder. *Radiother Oncol.* (1989) 15:383–92.
90. Dorr W. Impact of time between X-ray fractions on acute changes in the function of the urinary bladder in the mouse. *Radiat Res.* (1995) 141:219–22.
91. Stewart FA, Michael BD, Denekamp J. Late radiation damage in the mouse bladder as measured by increased urination frequency. *Radiat Res.* (1978) 75:649–59.
92. Jiang X, Chen Y, Zhu H, Wang B, Qu P, Chen R, et al. Sodium tanshinone IIA sulfonate ameliorates bladder fibrosis in a rat model of partial bladder outlet obstruction by inhibiting the TGF-β/Smad pathway activation. *PLoS ONE.* (2015) 10:e0129655. doi: 10.1371/journal.pone.0129655
93. Suresh UR, Smith VJ, Lupton EW, Haboubi NY. Radiation disease of the urinary tract: histological features of 18 cases. *J Clin Pathol.* (1993) 46:228–31. doi: 10.1136/jcp.46.3.228
94. Kryvenko ON, Epstein JI. Pseudocarcinomatous urothelial hyperplasia of the bladder: clinical findings and followup of 70 patients. *J Urol.* (2013) 189:2083–6. doi: 10.1016/j.juro.2012.12.005
95. Pascoe C, Duncan C, Lamb BW, Davis NF, Lynch TH, Murphy DG, et al. Current management of radiation cystitis: a review and practical guide to clinical management. *BJU Int.* (2019) 123:585–94. doi: 10.1111/bju.14516
96. Saaya FM, Xie KT, Tanaka K, Fujita K, Wang B. Research and development of radioprotective agents: a mini-review. *Int J Radiol.* (2017) 4:128–38. doi: 10.17554/j.issn.2313-3406.2017.04.41
97. Stone HB, Moulder JE, Coleman CN, Ang KK, Anscher MS, Barcellos-Hoff MH, et al. Models for evaluating agents intended for the prophylaxis, mitigation and treatment of radiation injuries. *Radiat Res.* (2004)162:711–28. doi: 10.1667/RR3276
98. Patt HM, Tyree EB, Straube RL, Smith DE. Cysteine protection against X irradiation. *Science.* (1949) 110:213–4. doi: 10.1126/science.110.2852.213
99. Chen CC. *Selected Topics in DNA Repair*. InTech (2012). doi: 10.5772/1749
100. Moulder JE, Cohen EP. Future strategies for mitigation and treatment of chronic radiation-induced normal tissue injury. *Semin Radiat Oncol.* (2007) 17:141–8. doi: 10.1016/j.semradonc.2006.11.010
101. Mallick S, Madan R, Julka PK, Rath GK. Radiation induced cystitis and proctitis - prediction, assessment and management. *Asian Pac J Cancer Prev.* 16:5589–94. doi: 10.7314/APJCP.2015.16.14.5589
102. Smit SG, Heyns CF. Management of radiation cystitis. *Nat Rev Urol.* (2010) 7:206–14. doi: 10.1038/nrurol.2010.23
103. Horan N, Cooper JS. *Hyperbaric, Radiation Cystitis [Internet]*. StatPearls. (2018) Available online at: http://www.ncbi.nlm.nih.gov/pubmed/29261976 (accessed Dec 30, 2019).
104. Amiri KI, Horton LW, LaFleur BJ, Sosman JA, Richmond A. Augmenting chemosensitivity of malignant melanoma tumors via proteasome inhibition: implication for bortezomib (VELCADE, PS-341) as a therapeutic agent for malignant melanoma. *Cancer Res.* (2004) 64:4912–8. doi: 10.1158/0008-5472.CAN-04-0673
105. Dai Y, Rahmani M, Grant S. Proteasome inhibitors potentiate leukemic cell apoptosis induced by the cyclin-dependent kinase inhibitor flavopiridol through a SAPK/JNK- and NF-κB-dependent process. *Oncogene.* (2003) 22:7108–22. doi: 10.1038/sj.onc.1206863
106. Fujioka S, Schmidt C, Sclabas GM, Li Z, Pelicano H, Peng B, et al. Stabilization of p53 is a novel mechanism for proapoptotic function of NF-κB. *J Biol Chem.* (2004) 27927549–59. doi: 10.1074/jbc.M313435200
107. Li Q, Verma IM. NF-κB regulation in the immune system. *Nat Rev Immunol.* (2002) 2:725–34. doi: 10.1038/nri910
108. Yamamoto Y, Gaynor RB. IκB kinases: key regulators of the NF-κB pathway. *Trends Biochem Sci.* (2004)29:72–9. doi: 10.1016/j.tibs.2003.12.003
109. Ikeda Y, Zabbarova IV, Birder LA, Wipf P, Getchell SE, Tyagi P, et al. Relaxin-2 therapy reverses radiation-induced fibrosis and restores bladder function in mice. *Neurourol Urodyn.* (2018) 37:2441–51. doi: 10.1002/nau.23721
110. Samuel CS. Relaxin: antifibrotic properties and effects in models of disease. *Clin Med Res.* (2005) 17:241–9. doi: 10.3121/cmr.3.4.241
111. Rico MJ, Lawrence I. Tacrolimus ointment for the treatment of atopic dermatitis: clinical and pharmacologic effects. *Allergy asthma Proc.* (2019) 23:191–7.
112. Zheng P, Yu B, He J, Tian G, Luo Y, Mao X, et al. Protective effects of dietary arginine supplementation against oxidative stress in weaned piglets. *Br J Nutr.* (2013) 109:2253–60. doi: 10.1017/S0007114512004321
113. Cukier RI. A molecular dynamics study of water chain formation in the proton-conducting K channel of cytochrome c oxidase. *Biochim Biophys Acta - Bioenerg.* (2005) 1706:134–46. doi: 10.1016/j.bbabio.2004.10.004
114. de Morais Puga GI, Novais P, Zanesco A. *Efeitos Terapêuticos Da Suplementação De L-Arginina Nas Doenças Cardiovasculares E Endócrino-Metabólicas Therapeutic Effects Of L-Arginine Supplementation on The Cardiovascular and Endocrine-Metabolic Diseases.* 107–14. Available online at: http://www.scielo.mec.pt/pdf/am/v25n3/v25n3a04.pdf (accessed September 15, 2020).
115. Böger RH. The pharmacodynamics of L-arginine. *J Nutr.* (2007) 137(Suppl. 2):1650S−5. doi: 10.1093/jn/137.6.1650S
116. Pinto FCM, Campos-Silva P, de Souza DB, Costa WS, Sampaio FJB. Nutritional supplementation with arginine protects radiation-induced effects. An experimental study. *Acta Cir Bras.* (2016) 31:650–4. doi: 10.1590/S0102-865020160100000002

Conflict of Interest: The authors declare that the research was conducted in the absence of any commercial or financial relationships that could be construed as a potential conflict of interest.

frontiers in Oncology

ORIGINAL RESEARCH
published: 30 October 2020
doi: 10.3389/fonc.2020.575909

External Validation of a Predictive Model for Acute Skin Radiation Toxicity in the REQUITE Breast Cohort

Tim Rattay[1], Petra Seibold[2], Miguel E. Aguado-Barrera[3,4], Manuel Altabas[5], David Azria[6], Gillian C. Barnett[7], Renée Bultijnck[8,9], Jenny Chang-Claude[2,10], Ananya Choudhury[11], Charlotte E. Coles[7], Alison M. Dunning[12], Rebecca M. Elliott[11], Marie-Pierre Farcy Jacquet[13], Sara Gutiérrez-Enríquez[14], Kerstie Johnson[1], Anusha Müller[2], Giselle Post[8], Tiziana Rancati[15], Victoria Reyes[5], Barry S. Rosenstein[16], Dirk De Ruysscher[17,18], Maria C. de Santis[19], Elena Sperk[20], Hilary Stobart[21], R. Paul Symonds[1], Begoña Taboada-Valladares[4,22], Ana Vega[3,4], Liv Veldeman[8,9], Adam J. Webb[23], Catharine M. West[11], Riccardo Valdagni[14,19,24], Christopher J. Talbot[23] and REQUITE consortium*

[1] Cancer Research Centre, University of Leicester, Leicester, United Kingdom, [2] Division of Cancer Epidemiology, German Cancer Research Center (DKFZ), Heidelberg, Germany, [3] Fundación Pública Galega Medicina Xenómica, Santiago de Compostela, Spain, [4] Instituto de Investigación Sanitaria de Santiago de Compostela, Santiago de Compostela, Spain, [5] Radiation Oncology Department, Vall d'Hebron Hospital Universitari, Vall d'Hebron Barcelona Hospital Campus, Barcelona, Spain, [6] Fédération Universitaire d'Oncologie Radiothérapie d'Occitanie Méditérranée, Département d'Oncologie Radiothérapie, ICM Montpellier, INSERM U1194 IRCM, University of Montpellier, Montpellier, France, [7] Department of Oncology, University of Cambridge, Cambridge, United Kingdom, [8] Department of Human Structure and Repair, Ghent University, Ghent, Belgium, [9] Department of Radiation Oncology, Ghent University Hospital, Ghent, Belgium, [10] University Cancer Center Hamburg, University Medical Center Hamburg-Eppendorf, Hamburg, Germany, [11] Translational Radiobiology Group, Division of Cancer Sciences, University of Manchester, Manchester Academic Health Science Centre, The Christie NHS Foundation Trust, Manchester, United Kingdom, [12] Centre for Cancer Genetic Epidemiology, Department of Oncology, Strangeways Research Laboratory, University of Cambridge, Cambridge, United Kingdom, [13] Fédération Universitaire d'Oncologie Radiothérapie d'Occitanie Méditérranée, Département d'Oncologie Radiothérapie, CHU Carémeau, Nîmes, France, [14] Hereditary Cancer Genetics Group, Vall d'Hebron Institute of Oncology (VHIO), Vall d'Hebron Hospital Campus, Barcelona, Spain, [15] Prostate Cancer Program, Fondazione IRCCS Istituto Nazionale dei Tumori, Milan, Italy, [16] Department of Radiation Oncology, Department of Genetics and Genomic Sciences, Icahn School of Medicine at Mount Sinai, New York, NY, United States, [17] MAASTRO Clinic, GROW School for Oncology and Developmental Biology, Maastricht University Medical Center, Maastricht, Netherlands, [18] Department of Radiation Oncology, University Hospitals Leuven/KU Leuven, Leuven, Belgium, [19] Department of Radiation Oncology 1, Fondazione IRCCS Istituto Nazionale dei Tumori, Milan, Italy, [20] Department of Radiation Oncology, Universitätsklinikum Mannheim, Medical Faculty Mannheim, Heidelberg University, Mannheim, Germany, [21] Independent Cancer Patients' Voice, London, United Kingdom, [22] Department of Radiation Oncology, Complexo Hospitalario Universitario de Santiago, Servizo Galego de Saúde (SERGAS), Santiago de Compostela, Spain, [23] Department of Genetics and Genome Biology, University of Leicester, Leicester, United Kingdom, [24] Department of Hematology and Hemato-Oncology, Università degli Studi di Milano, Milan, Italy

OPEN ACCESS

Edited by:
Sharad Goyal, George Washington University, United States

Reviewed by:
Laure Marignol, Trinity College Dublin, Ireland
Jean L. Wright, Johns Hopkins University, United States
Chirag Shah, Cleveland Clinic, United States

***Correspondence:**
Tim Rattay
tr104@le.ac.uk

Specialty section:
This article was submitted to Radiation Oncology, a section of the journal Frontiers in Oncology

Received: *24 June 2020*
Accepted: *15 September 2020*
Published: *30 October 2020*

Citation:
Rattay T, Seibold P, Aguado-Barrera ME, Altabas M, Azria D, Barnett GC, Bultijnck R, Chang-Claude J, Choudhury A, Coles CE, Dunning AM, Elliott RM, Farcy Jacquet M-P, Gutiérrez-Enríquez S, Johnson K, Müller A, Post G, Rancati T, Reyes V, Rosenstein BS, De Ruysscher D, de Santis MC, Sperk E, Stobart H, Symonds RP, Taboada-Valladares B, Vega A, Veldeman L, Webb AJ, West CM, Valdagni R, Talbot CJ and REQUITE consortium (2020) External Validation of a Predictive Model for Acute Skin Radiation Toxicity in the REQUITE Breast Cohort. Front. Oncol. 10:575909. doi: 10.3389/fonc.2020.575909

Background: Acute skin toxicity is a common and usually transient side-effect of breast radiotherapy although, if sufficiently severe, it can affect breast cosmesis, aftercare costs and the patient's quality-of-life. The aim of this study was to develop predictive models for acute skin toxicity using published risk factors and externally validate the models in patients recruited into the prospective multi-center REQUITE (validating pREdictive models and biomarkers of radiotherapy toxicity to reduce side-effects and improve QUalITy of lifE in cancer survivors) study.

Methods: Patient and treatment-related risk factors significantly associated with acute breast radiation toxicity on multivariate analysis were identified in the literature. These

predictors were used to develop risk models for acute erythema and acute desquamation (skin loss) in three Radiogenomics Consortium cohorts of patients treated by breast-conserving surgery and whole breast external beam radiotherapy (n = 2,031). The models were externally validated in the REQUITE breast cancer cohort (n = 2,057).

Results: The final risk model for acute erythema included BMI, breast size, hypo-fractionation, boost, tamoxifen use and smoking status. This model was validated in REQUITE with moderate discrimination (AUC 0.65), calibration and agreement between predicted and observed toxicity (Brier score 0.17). The risk model for acute desquamation, excluding the predictor tamoxifen use, failed to validate in the REQUITE cohort.

Conclusions: While most published prediction research in the field has focused on model development, this study reports successful external validation of a predictive model using clinical risk factors for acute erythema following radiotherapy after breast-conserving surgery. This model retained discriminatory power but will benefit from further re-calibration. A similar model to predict acute desquamation failed to validate in the REQUITE cohort. Future improvements and more accurate predictions are expected through the addition of genetic markers and application of other modeling and machine learning techniques.

Keywords: validation, prediction model, early toxicity, radiotherapy, breast cancer

INTRODUCTION

Survivorship issues and quality-of-life (QoL) are becoming an increasingly important research focus in cancer care (1). Breast cancer survival has improved markedly, with current predicted 10-year survival rates in excess of 80% (2). Over 70% of breast cancer patients undergo radiotherapy, usually in the adjuvant setting following surgery. Radiotherapy reduces the risk of local recurrence and contributes to a reduction in overall mortality (3). Nevertheless, breast radiotherapy can be associated with several side-effects (toxicity). Acute (or early) toxicity includes breast erythema (reddening) and desquamation (skin loss) and occurs within 90 days of treatment (4). While late side-effects of radiotherapy are concerning due to their potential irreversibility, acute toxicity may cause considerable patient morbidity and can have adverse effects on the cosmetic outcome from oncoplastic breast surgery and reconstruction (5, 6). There is some evidence that if sufficiently severe, early toxicity can be associated with clinically significant late toxicity (7). Invariably, surgeons' treatment recommendations are influenced by their perception of potential adjuvant treatment complications such as from radiotherapy (8, 9). Nevertheless, there is considerable variation between individual patients' normal tissue reaction to radiotherapy. Being able to stratify individual patients according to their risk of radiation toxicity would enable breast surgeons to take this information into account when advising patients about the risks and benefits of different surgical treatment options, or even suggest a change to the sequence of surgery and adjuvant treatment including radiotherapy (10).

In the field of medical physics, many radiobiological predictive models have been proposed with the aim of preserving normal tissue, mostly focused on late toxicity. Normal tissue complication probability (NTCP) models, such as the Lyman-Kutcher-Burman (LKB) model, incorporate the linear quadratic (LQ) model of cell killing (11, 12). Many of these dosimetric models have already been integrated into radiotherapy treatment planning systems. They generally take the form of simplified empirical models consisting of dose distribution parameters, and the risk of toxicity is assumed to depend on the mean dose to the respective target organ or the amount of damaged tissue (13).

In prostate radiotherapy, it has been shown that dosimetric models for late rectal toxicity can be improved by including clinical and other treatment risk factors, such as prior abdominal surgery, colorectal disease and diabetes (14, 15). In breast radiotherapy, several studies have investigated the association of clinical and treatment risk factors with acute skin toxicity, although none have reported a clinical prediction model as such (16–25). Integrated clinical prediction models capable of identifying patients at risk of clinically significant side-effects have now been developed in different disease sites, the majority predicting late toxicity with moderate performance (AUC ranging from 0.60 to 0.75) (26–28). There are also an increasing number of published models predicting acute toxicity, although none for breast radiotherapy (29–31).

For surgeons and other clinicians, models that include common clinical and treatment predictors are of particular interest because this obviates the need for detailed patient dosimetry and dose-volume histograms from radiotherapy planning scans. It would allow clinicians to estimate toxicity risk at the time of breast cancer diagnosis and before any treatment is planned. In breast reconstruction surgery, a small number of clinical risk models for various 30-day complications have been

published (32, 33), of which some have been validated for select endpoints (34, 35). However, these models are chiefly designed to predict surgical side-effects, such as implant loss, surgical site infection and seroma, and include radiotherapy as a binary predictor variable only.

In the absence of an available prediction model in the literature, the aim of this study was to develop and externally validate predictive models for acute breast radiation toxicity in the REQUITE study breast cohort using published clinical and treatment predictors of acute skin toxicity in the REQUITE study breast cohort.

METHODS

This study was designed using data from patients who underwent breast-conserving surgery (BCS) and adjuvant external beam radiotherapy (EBRT) enrolled in three Radiogenomics Consortium (RGC) studies and the REQUITE cohort study. Candidate variables associated with acute breast radiation toxicity were identified from the existing literature. In the absence of predictive models in the literature, predictive models for acute radiation toxicity endpoints were first developed in combined RGC patient cohorts, then validated in the REQUITE patient cohort. This was a TRIPOD type 3 study, representing model development and validation using a separate dataset (36).

Model Development Cohorts

The German ISE cohort (16) included 478 breast cancer patients treated with conventional 3D conformal whole breast EBRT plus either photon or electron tumor bed boost (except for 19 patients) recruited into a prospective patient cohort at four centers in Southwest Germany between 1998 and 2001, with documented acute radiotherapy toxicity at baseline, at cumulative doses of 36–42 Gy and 44–50 Gy, at the end of radiotherapy, and 6 weeks following radiotherapy. None of the patients in ISE received chemotherapy. All patients from the ISE cohort were included in this study. The ISE study was approved by the Ethical Committee at the University of Heidelberg, Germany (reference No. 37/98).

The LeND cohort (37) consists of 633 breast cancer patients treated with conventional 3D conformal whole breast EBRT using tangential fields and documented normal tissue toxicity recruited at varying time points (up to several years) after breast radiotherapy ± boost in Leicester, Nottingham and Derby (UK) between 2008 and 2010. Acute toxicity was collected from medical records. After excluding the first 154 patients without data on acute toxicity, and 119 patients who had chest wall radiotherapy following mastectomy, 390 patients treated with EBRT following BCS from the LeND cohort were included in this study. The LeND study was approved by the Research Ethics Committee (reference no. 08/H0405/57).

The Cambridge cohort (19) comprised 1,144 women who received adjuvant whole breast EBRT following BCS as part of the Cambridge IMRT trial (UK) following the standard hypofractionated regimen (40 Gy in 15 fractions), 411 of whom were randomized to manual forward-planned intensity-modulated radiotherapy (IMRT) to improve dose homogeneity (reduce the volumes receiving >107 and <95% of the prescribed dose) in the irradiated breast. The remainder of patients were treated with 3D-conformal radiotherapy using wedged tangential fields. Toxicity was documented weekly during treatment according to the RTOG scale. All patients from the Cambridge cohort were included. The study was approved by the Cambridge Research Ethics Committee and written consent was obtained from all patients to use their data for research purposes.

Validation Cohort

The multicenter REQUITE breast cancer patient cohort was recruited prospectively in seven European countries and the USA between 2014 and 2016. The REQUITE study was conceived as an international multicenter validation cohort for predictive models of radiation toxicity with standardized prospective data collection (38). Patient baseline characteristics and methodology have been described in detail elsewhere (39). All 2,057 enrolled patients were treated with BCS followed by EBRT according to local protocol, approximately half of whom were treated with IMRT, with a lower proportion in France and no IMRT at Italian or US centers. The majority patients received a tumor-bed boost (64%), ranging from <20% at the French, Italian and Spanish centers to over 80% at the Belgian center, given either simultaneously ($n = 257$) or sequentially ($n = 1{,}138$). Patients with invasive breast cancer in Belgium and the UK were treated using the START-B hypofractionated regimen. Although late toxicity was the main endpoint in REQUITE, data collected at the end of radiation treatment was used to document acute toxicity. All patients gave written informed consent. The study was approved by local ethics committees in participating countries (UK NRES Approval 14/NW/0035) and registered at http://www.controlled-trials.com (ISRCTN98496463). Characteristics of all cohorts included in this study are summarized in **Table 1**.

Endpoint Definition

Radiation toxicity in REQUITE was scored using CTCAE (Common Terminology Criteria for Adverse Events; **Table 2**) v4.0 (40). CTCAE v4.0 has separate scales for radiation dermatitis (erythema) and skin ulceration (desquamation), both of which are relevant to the acute response to radiotherapy in the breast. For both LeND and Cambridge cohorts, acute skin toxicity was scored according to the RTOG (Radiation Therapy Oncology Group; **Table 2**) scale, which is mostly based on target organ or body region (e.g., larynx, upper GI, skin) (41). The German ISE study used a modified version of the Common Toxicity Criteria (CTCAE v2.0) scale for erythema, where grade 2 was subdivided into three sub-grades, with 2c being defined as ≥1 moist desquamation or interruption of treatment due to side-effects and grade 2a and 2b comprising moderate and brisk erythema, respectively.

This raised the issue of how to deal with the use of different toxicity scales and assessment time points in the previously assembled cohorts and the REQUITE validation cohort. Where multiple measurements were available, maximum recorded toxicity was used. To ensure comparability with previous studies, the following endpoints were considered where they occurred within 90 days of the start of treatment (acute toxicity) according to the different grading systems:

TABLE 1 | Summary study characteristics of eligible patients from the three RGC derivation cohorts and the REQUITE validation cohort (RT, radiotherapy).

	LeND	ISE	Cambridge	REQUITE
Total patients in cohort (*n*)	663	478	1144	4438
Eligible patients (BCS+EBRT)	409	478	1,144	2,057
Location	Leicester, Nottingham, Derby (UK)	SW Germany	Cambridge (UK)	Western Europe, United States
Study design	Retrospective	Prospective	Prospective	Prospective
Recruitment year (range)	2008–2010	1998–2001	2003–2007	2014–2016
Treatment year (range)	1998–2008	1998–2001	2003–2007	2014–2016
Toxicity assessment scale	RTOG	Modified CTCAE v2	RTOG	CTCAE v4
Toxicity assessment time points	(From records) end-of-RT	Start-of-RT cumulative 36–42 Gy cumulative 44–50 Gy end-of-RT 6 weeks after RT	Weekly during RT end-of RT	Start-of-RT end-of-RT
Age (median, range)	59 (33–87)	61 (27–87)	59 (26–84)	58 (23–90)
Whole breast dose (Gy, median, range)	50 (40–50)	50 (44–56)	40	50 (28.5–56)
Whole breast fractions (median, range)	25 (11–25)	25 (22–29)	15	25 (5–31)
Boost (proportion of patients)	10%	90%	65%	64%
Toxicity scale used	RTOG	CTCAE v2.0	RTOG	CTCAE v4.0
BMI ≥25 (proportion)	66%	48%	63%	54%
Smoker (current or previous)	13%	30%	15%	43%
Chemotherapy	28%	None	20%	30%
Diabetes	8%	6%	5%	6%
Hypertension	35%	32%	Not available	28%
Cardiovascular disease	6%	16%	10%	7%
Tamoxifen use	75%	80%	66%	76%

TABLE 2 | RTOG and CTCAE v4.0 toxicity scales for acute skin reaction and ulceration.

Toxicity	Grade 1	2a	2b	3	4
RTOG Skin	Follicular, faint or dull erythema/epilation/dry desquamation/decreased sweating	Tender or bright erythema ± dry desquamation	Patchy moist desquamation; moderate oedema	Confluent, moist desquamation other than skin folds, pitting edema	Ulceration, hemorrhage, necrosis
CTCAE v4.0 Radiation dermatitis	Faint erythema or dry desquamation	Moderate to brisk erythema or patchy moist desquamation (2c*), mostly confined to skin folds and creases; moderate edema (tenderness is graded separately in the Pain category)		Confluent moist desquamation ≥1.5 cm diameter and not confined to skin folds; pitting edema	Skin necrosis or ulceration of full thickness dermis; may include bleeding not induced by minor trauma or abrasion
CTCAE v4.0 Skin ulceration	Combined area of ulcers <1 cm; non-blanchable erythema of intact skin with associated warmth or oedema	Combined area of ulcers 1–2 cm; partial thickness skin loss involving skin or subcutaneous fat		Combined area of ulcers >2 cm; full-thickness skin loss involving damage to or necrosis of subcutaneous tissue that may extend down to fascia	Any size ulcer with extensive destruction, tissue necrosis, or damage to muscle, bone, or supporting structures with or without full thickness skin loss

**Sub-scales of CTCAE v2.0 used in the ISE study.*

a) Acute erythema: RTOG or CTCAE grade≥2 (at least moderate to brisk erythema);
b) Acute desquamation: RTOG grade≥2b (patchy moist desquamation) or CTCAE grade ≥2c erythema (moist desquamation) or CTCAE grade≥1 skin ulceration, implying that skin integrity has been broken, either over the breast or in the infra-mammary fold.

Selection and Definition of Candidate Predictors

The literature was searched through Medline using the MeSH keywords "radiation injury," "breast neoplasm," "radiotherapy," "radiation tolerance," and "risk factors," and through PubMed using keywords "radiation injury," "normal radiation toxicity," "acute," "radiotherapy," "breast cancer," "radiosensitivity" and

"risk factor" or "predictor" or "radiogenomics." Reference lists from identified papers or review articles were also searched. Candidate predictor variables in the literature were considered for validation where their association with acute breast radiation toxicity endpoints on multivariate analysis was reported in at least one publication.

To ensure comparability of measures of breast size, such as breast diameter or bra size, these were converted to a single continuous variable for the purpose of this study by adding bra cup and band sizes, to represent "sister" sizes equal to the same breast volume (according to http://www.sizechart.com/brasize/sistersize/index.html). For instance, a UK size 34B bra holds an approximate breast volume equal to 32C, ∼390 cc. In the Cambridge trial cohort, breast size was graded as a categorical variable and converted accordingly.

For each patient in the REQUITE and the other three RGC cohorts, information comprising candidate predictor variables and relevant study endpoints were extracted from the data. Hypertension was not recorded in the Cambridge trial cohort, and post-operative infection was not available in the LeND and ISE cohorts. Observations on body mass index (BMI) and breast size were missing from 22 and 17% of patients, respectively, in the three combined RGC cohorts, while information on the remaining candidate predictor variables was missing in between 0.5 and 3% of patients across all cohorts.

Statistical Methods

Both endpoints were considered as dichotomized (binary) outcome measures. Where a patient had multiple measures of acute toxicity within the specified time period, the maximum grade of toxicity recorded was used. Cases with high baseline toxicity defined as grade≥2 were excluded from the analysis. Statistical analyses were carried out in Stata™ version 15.1. Continuous variables are presented as medians (with ranges), and categorical/binary variables as counts and percentages.

In order to minimize bias from analyzing only complete cases, multiple imputation (MI) was used to replace missing values by means of a chained equation approach based on all candidate predictors excluding hypertension (42). Ten imputed datasets were created for missing variables and then combined across all datasets using Rubin's rule to obtain final estimates (43). The number of imputations ($m = 10$) was determined by the percentage of incomplete observations per variable to reduce the error associated with estimating the regression coefficients, standard errors and the resulting p-values (44). On the basis of an estimated 900 cases of acute erythema and 175 cases of acute desquamation in the three combined RGC cohorts, the consideration of nine candidate predictor variables in this analysis satisfied the methodological constraint of at least 10 events per variable (EPV) required to reduce issues with over-fitting in predictive modeling (45).

To develop clinical prediction models, a generalized linear mixed model (GLMM, *xtlogit*) was fitted in the original dataset combining three RGC derivation cohorts to model the probability of each toxicity endpoint. GLMMs are an extension of mixed models and generalized linear models (GLMs) to allow for inclusion of both fixed and random effects across different study cohorts or cohorts enrolling at multiple centers. Like GLMs, a link function is applied, such as the *logit* link. Initially, a full model comprising all included predictor variables was fitted, followed by stepwise backwards elimination to select the candidate variables to include in the final prediction model (with $p < 0.1$ taken conservatively to warrant inclusion). After elimination, each excluded predictor was re-inserted into the final model to further check whether they became statistically significant at this stage.

The equation for the log odds for each acute breast endpoint was formed using the estimated β coefficients multiplied by the predictors included in the model together with the intercept across cohorts. The predicted risk of toxicity can thus be calculated:

$$predicted\ risk = \frac{e^{\log\ odds}}{1 + e^{log\ odds}}$$

Discrimination of the fitted models was assessed by calculating the c-statistic (AUC from the logistic model, plotting sensitivity over 1-specificity) and examining the calibration plot across tenths of predicted risk. A c-statistic of 1 indicates perfect discrimination, whereas 0.5 indicates no discrimination. A calibration slope of 1 indicates perfect calibration and would be expected across the original datasets as the model is being developed in the same data (apparent performance).

To control for optimism (over-fitting), the model development process was repeated in 100 bootstrap samples. Each model was applied to the same bootstrap sample to quantify apparent performance, and then to the original dataset to evaluate test performance (c-statistic and calibration slope) and optimism (difference in test performance and apparent performance). To estimate overall optimism, the average calibration slope across all bootstrap samples was calculated and multiplied as a shrinkage coefficient by each variable's β coefficient and the intercept of the model derived in the original dataset to produce a final model for each toxicity endpoint.

The final models were applied to patients in the REQUITE validation cohort to predict the log odds of acute erythema or acute desquamation based on the presence or absence of one or more of the predictor variables. In this external validation step, the intercept of each final model was re-calibrated by subtracting the estimated intercept of the model in the REQUITE validation cohort. Performance of the model in the validation cohort was again assessed by calculating the c-statistic (AUC) and examining the calibration plot across tenths of predicted risk. Overall accuracy was measured by calculating a Brier score, which is the sum of mean square errors between predicted risk and observed outcome for each patient, with a zero score indicating total accuracy.

RESULTS

The literature search identified 10 studies of between 200 and 1,124 patients examining the association of acute breast radiation toxicity with predictor variables. Most studies reported acute skin toxicity scored according to RTOG, while only two studies used

the CTCAE erythema scale (16, 25). Depending on the published study, the variables associated significantly with toxicity on multivariate analysis were: age (50 and over, dichotomized), body mass index (BMI), breast size or volume, fractionation schedule (hypo- vs. conventional fractionation, dichotomized), use of boost, smoking (ever smoked), and tamoxifen use (see **Table 3**). Chemotherapy showed significant effects but in opposite directions in two studies (19, 46) and was excluded. Interestingly, breast dose was not assessed as a continuous variable in any publication. Hypertension and diabetes were not significant on multivariate analysis in any study. One study used ordinal regression and did not report odds ratios, as endpoints were not dichotomized (20).

Predictive Clinical Model Development and External Validation

The distribution of patients across the three RGC development cohorts and the REQUITE validation cohort according to endpoint is shown in **Table 4**. Across the RGC cohorts (n = 2.031), there were 914 events of acute erythema (grade ≥2, 45.0%) and 175 events of acute desquamation (8.7%). It was noted that the incidence of desquamation was lower in the Cambridge IMRT cohort. In the REQUITE validation cohort, there were 1,969 and 2,057 patient datasets available for the endpoints acute erythema and acute desquamation, respectively. There were 450 patients with acute erythema (grade ≥2 erythema, 22.9%), and 192 patients with acute desquamation (grade 1≥ ulceration or grade ≥3 erythema, 9.3%).

Further detail regarding the distribution of clinical predictors in each cohort is available in **Table 1**. Median patient age in the REQUITE breast cohort was 58 years (range 23–80 years), similar to the RGC cohorts. REQUITE patients were treated with a median dose to the breast of 50 Gy (28.5–56 Gy) in 25 fractions (5–31), which is similar to the LeND and ISE cohorts. Patients in the Cambridge IMRT trial were exclusively treated with 40 Gy in 15 fractions. There was variation in use of boost between the different development cohorts and within the REQUITE multi-center cohort (see Methods). Although most other co-morbidities and co-medications were similarly distributed, the proportion of smokers was higher in the non-UK cohorts, whereas the proportion of overweight patients (BMI ≥25) was higher in the UK cohorts.

Final logistic regression models for both toxicity endpoints following backwards elimination are shown in **Table 5**. At this stage, variables that satisfied the $p < 0.1$ stepwise inclusion threshold in the development cohorts for both endpoints were BMI, breast size, hypo-fractionation, use of boost, and smoking status. Tamoxifen use was associated with acute erythema only (OR 1.25, CI 1.05–1.26; **Table 5**). Age 50 and over was eliminated from both models, acute erythema (OR 1.17, 0.89–1.53, p = 0.253) and acute desquamation (OR 1.45, 0.83–2.53, $p = 0.194$).

Table 6 shows apparent, optimism-corrected (after bootstrapping) and validation performance of both risk prediction models. After correcting for optimism, the final model for acute erythema discriminated patients with and without grade ≥2 erythema undergoing EBRT following BCS with an AUC of 0.645 (CI 0.619–0.667). Agreement between observed and predicted proportions was seen with a calibration slope of 1.0319. The final log odds of acute erythema could be calculated as −2.265 + 0.049*BMI + 0.1*breast_size – 1.565*hypo-fractionation + 0.302*boost + 0.308*smoking + 0.234*tamoxifen. After re-calibrating the intercept, applying the final model to the REQUITE cohort gave a c-statistic (AUC) of 0.651 (CI 0.622–0.680), indicating the model performed equally well on validation, albeit with moderate calibration (slope = 0.665, 0.509–0.821) and a Brier score of 0.172 (**Table 6**). The calibration plot demonstrates that the model slightly over-predicts the probability of acute erythema in the REQUITE validation cohort (**Figure 1**), with a mean predicted probability of 25.7% against an observed incidence of 22.8%.

The final model for acute desquamation developed in the joint RGC cohorts was able to discriminate patients with an optimism-corrected AUC of 0.847 (CI 0.817–0.873) and a calibration slope of 1.043. The log odds of acute desquamation could be calculated as −7.226 + 0.111*BMI + 0.240*breast_size – 2.592*hypo-fractionation + 0.606*boost + 0.435*smoking. Applying the final model to the REQUITE validation cohort with re-calibrated intercept, gave a c-statistic (AUC) of 0.697 (CI 0.658–0.737). This drop in AUC indicates relatively poorer discrimination performance, with equally poorer calibration (slope = 0.376, 0.260–0.492) (**Table 6**). The model significantly under-predicts the probability of acute desquamation in the REQUITE cohort, with a mean predicted probability of 3.0% against and observed incidence of 9.3% (**Figure 2**). The Brier score was 0.085.

DISCUSSION

The aim of this study was to develop and validate predictive models for acute skin erythema and acute desquamation following whole-breast external beam radiotherapy and breast-conserving surgery for breast cancer, which could be used without the need for detailed radiation dosimetry, in order to allow clinicians to estimate toxicity risk at the time of breast cancer diagnosis and before any treatment is planned. Previous work in prostate cancer showed that dosimetric models for radiation toxicity can be improved by adding clinical and co-treatment risk factors (14, 15).

The initial literature search of published predictors significantly associated with acute breast radiation toxicity in multivariate analysis confirmed a number of variables including BMI, breast size or volume, hypo-fractionation (protective), boost and tamoxifen use, and smoking status. Variables relating to BMI and breast size or volume have been most frequently reported in previous smaller cohorts (**Table 3**) as well as published randomized clinical trials (19, 47). Moreover, both aforementioned trials highlighted breast volume as a stand-alone predictor of acute radiation toxicity independent of dose inhomogeneity. Interestingly, none of the previous publications assessed breast dose as predictor in itself, only fractionation schedule. However, findings from the UK breast hypo-fractionation trials and radiobiology have shown that acute toxicity is related to total breast dose (48), not dose per

TABLE 3 | Odds ratios (confidence intervals) of clinical predictor variables for acute breast toxicity reported from multivariate regression in previously published studies with significant associations in bold (BMI, body mass index; fractionation, fractionation treatment schedule).

References	Twardella et al. (16)	Back (17)	Deantonio et al. (18)	Barnett et al. (19)	Terrazzino et al. (21)	Sharp et al. (22)	Tortorelli et al. (23)	Ciammella et al. (24)	De Langhe et al. (25)
N	**478**	**234**	**155**	**1124**	**286**	**390**	**200**	**212**	**377**
Proportion acute breast toxicity*	**17.6%**	**31.4%**	**34.8%**	**36.5%**	**31.1%**	**21.3%**	**31.9%**	**15.0%**	**58.0%**
Age (per year) Age ≥50	0.98 (0.96–1.01)	Not significant**				**2.20 (1.00–4.80)**	0.97 (0.94–1.01)	Not significant	
BMI (per kg/m^2) BMI ≥25 BMI ≥30	**1.09 (1.05–1.13)**	**2.10 (1.00–4.60)**			1.00 (0.92–1.09)	1.10 (0.60–2.10) **4.20 (2.10–8.30)**			**1.09 (not given)**
Breast volume (per liter) Breast volume > median Breast size > median Breast diameter Breast cup size ≥D		**3.60 (1.60–8.10)**		**2.09 (1.60–2.72)**	**1.14 (1.00–1.29)**		1.00 (1.00–1.01)	**2.47 (1.98–6.22)**	**2.83 (not given)**
Fractionation Hypo- vs. conventional			**0.45 (0.23–0.93)**						**0.08 (not given)**
Conventional vs. hypo-						**1.90 (1.00–3.50)**	**2.05 (1.00–4.20)**		
Boost use		Not significant			**4.90 (1.46–16.48)**			0.99 (0.98–1.00)	
Hypertension								Not significant	
Diabetes					Not significant			Not significant	
Smoking	0.86 (0.44–1.70)				Not significant	**2.50 (1.10–5.70)**			**2.71 (not given)**
Postop infection		Not significant		**1.49 (1.08–2.06)**				**3.46 (1.49–8.02)**	
Chemotherapy		Not significant	Not significant	**0.58 (0.41–0.82)**	Not significant	**1.80 (1.01–3.33)**	1.14 (0.53–2.43)	Not significant	0.95 (not given)
Tamoxifen use	1.54 (0.73–3.09)			**1.23 (1.07–1.41)**	Not significant	1.20 (0.70–2.10)	1.23 (0.55–2.77)		

**The proportion of patients with acute breast toxicity is shown according to each study's endpoint definition. **These studies only published p-values but no odds ratios for non-significant associations.*

TABLE 4 | Number of patients by acute skin toxicity in the three RGC derivation cohorts and the REQUITE validation cohort; number and proportion of cases at the end of radiotherapy.

	LeND	ISE	Cambridge	REQUITE
Eligible patients	**409**	**478**	**1144**	**2057**
Acute erythema with RTOG or CTCAE grade ≥2	111 (27.1%)	358 (74.9%)	445 (38.9%)	450 (22.9%)
Acute desquamation with RTOG grade ≥2b or CTCAE grade ≥2c radiation dermatitis or grade ≥1 ulceration	62 (15.2%)	86 (18.0%)	27 (2.4%)	192 (9.3%)

TABLE 5 | Final logistic regression models (GLMM) following backwards elimination ($p < 0.1$) for acute breast toxicity endpoints in the RGC development cohorts.

	Acute erythema				Acute desquamation			
Predictor	**OR**	**CI lower**	**CI upper**	***p*-value**	**OR**	**CI lower**	**CI upper**	***p*-value**
BMI (per kg/m^2)	1.05	1.02	1.08	<0.001	1.11	1.05	1.18	<0.001
Breast size (per sister size)	1.10	1.04	1.17	0.001	1.26	1.12	1.41	<0.001
Hypo-fractionation	0.22	0.05	0.89	0.033	0.08	0.05	0.13	<0.001
Boost use	1.34	1.06	1.69	0.013	1.79	1.24	2.57	0.002
Smoking (ever)	1.35	1.06	1.72	0.016	1.52	1.04	2.22	0.032
Tamoxifen use	1.25	1.01	1.56	0.044				

TABLE 6 | Performance statistics for both predictive models in the RGC development cohorts and external validation performance in REQUITE.

	Acute erythema				Acute desquamation			
Performance	**Apparent**	**Average optimism**	**Optimism-corrected**	**External validation (REQUITE)**	**Apparent**	**Average optimism**	**Optimism-corrected**	**External validation (REQUITE)**
c-statistic (AUC)	0.644	−0.001	0.645	0.651	0.845	−0.002	0.849	0.697
Calibration slope	1.082	−0.050	1.032	0.665	1.067	−0.024	1.043	0.376
Brier score				0.172				0.085

fraction as for late toxicity (7). The protective association with hypo-fractionation reported in the literature is therefore likely due to the reduction in total dose for safe hypo-fractionation. Results of the literature search did not confirm an association with acute breast radiation toxicity for the predictors diabetes, cardiovascular disease and hypertension, whereas in the past radiation sensitivity has at least in part been attributed to the presence of cardiovascular disease or diabetes mellitus, which affects the microvasculature (49). However, it is likely that many patients enrolled in the reported cohorts were also on some form of anti-diabetic agent or a statin. Radioprotective effects of both metformin and gliclazide on human cells have been reported at least *in vitro* (50, 51), and there is evidence that statins may accelerate DNA repair (52) and reduce the expression of pro-inflammatory cytokines (53).

Although several studies have investigated the association of acute breast toxicity with clinical and treatment factors, to date, none have produced a clinical prediction model. Population-based measures of toxicity risk may not accurately reflect risk for an individual patient, but accurate prediction models can inform patients and clinicians about the future course of their condition or illness, thereby helping guide decisions about treatment. For a prediction model to be valuable, it should not only have predictive ability in the development cohort but must also perform well in a validation cohort. In the present study, the model to predict the risk of acute erythema following breast radiotherapy across RGC cohorts performed moderately well in the RGC cohorts and equally in the external REQUITE validation cohort with an AUC of 0.65, while calibration showed moderate agreement between predicted and observed toxicity outcomes in the validation cohort. On the other hand, performance of the model to predict the risk of acute desquamation following breast radiotherapy decreased relatively more in the external validation cohort (AUC = 0.70) than expected from internal validation (optimism-corrected AUC = 0.85), with relatively poor calibration.

Reasons why a predictive model may perform substantially differently between development and validation cohorts include over-fitting, missing important predictor variables, measurement errors of predictors, or differences in the patient cohort case mix. Measurement errors can arise from inter-observer variability across different cohorts and centers as well as use of different scales and time points to assess acute toxicity endpoints. Acute toxicity in both the Cambridge IMRT trial

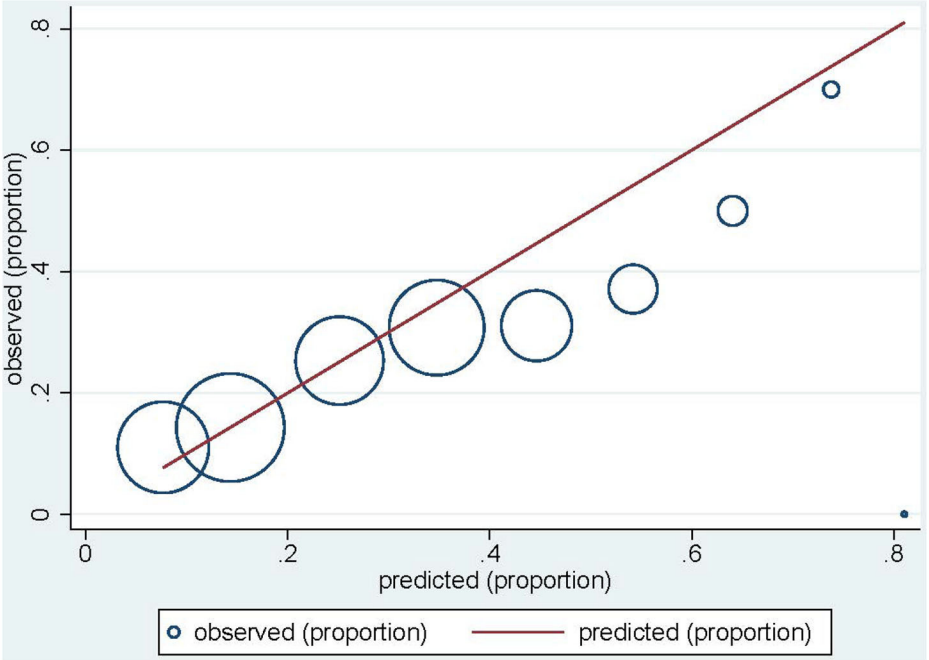

FIGURE 1 | Calibration plot for acute erythema in the REQUITE validation cohort. Circles indicate the observed proportion of acute erythema per tenth of predicted probability. The red line indicates ideal calibration with a slope of 1.

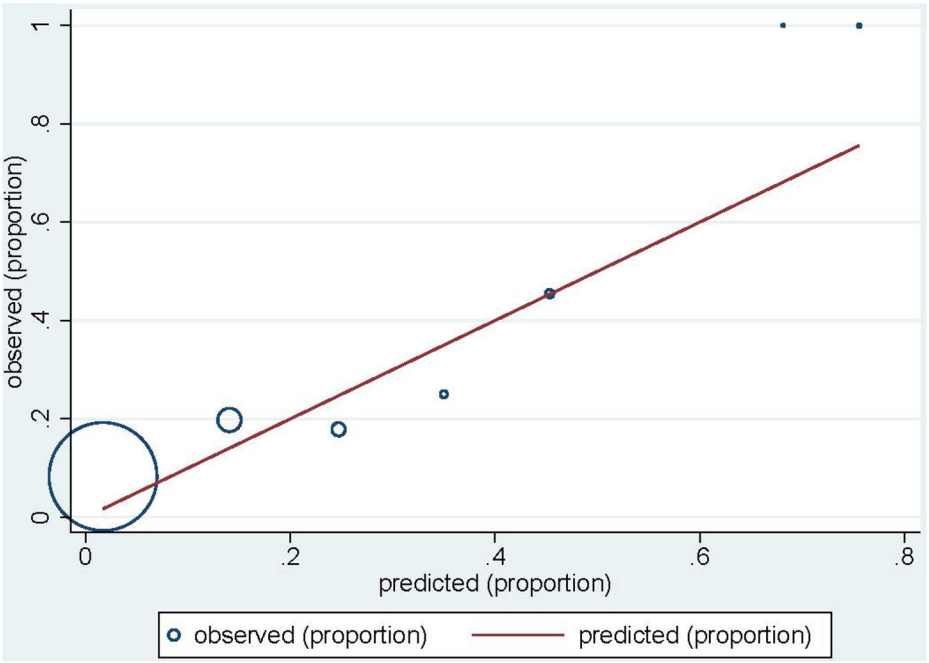

FIGURE 2 | Calibration plot for acute desquamation in the REQUITE validation cohort. Circles indicate the observed proportion of acute desquamation per tenth of predicted probability. The red line indicates ideal calibration with a slope of 1.

and the REQUITE study was assessed in the final week of radiotherapy. The acute reaction may not peak until 1–2 weeks after the end of treatment and hence could have been missed in some patients, although this would not have been the case in the ISE cohort study in which patients were assessed at the end and 6 weeks after the end of treatment. In the

LeND study, acute toxicity was coded retrospectively from the medical notes, which may have led to bias if the original documentation was unclear. In both LeND and the Cambridge IMRT cohorts, toxicity was assessed using the RTOG scale, which does not separate out patients with oedema and might in part explain the lower proportion of cases with grade $\geq$2 erythema in these cohorts compared to the ISE cohort, although the proportion of cases in the REQUITE validation cohort is more similar to that of the LeND and Cambridge cohorts. The ability to detect and grade skin changes is also dependent on skin tone, which is not readily captured in the RTOG and CTCAE scales.

The model developed across the three RGC cohorts in this study included clinically relevant predictors which satisfied the relatively loose criteria for inclusion in the model ($p < 0.1$). The purpose of multivariate prediction modeling is estimation rather than testing for association with risk factors, and it may therefore be reasonable to include clinical predictors despite non-significant association or collinearity, to ensure that important predictors are not missed (54). In order to address over-fitting and to correct for optimism, bootstrapping was used as internal validation technique, but other studies with reasonably large datasets have used split-sample training-validation or cross-validation (55). It is possible but not very likely that a different internal validation method may have produced different results to the bootstrapping method used in the present study.

The value of the c-statistic (AUC) depends not only on the model of interest but also the even distribution of predictor and endpoint variables within a given patient population. Many radiotherapy patients present with a similar constellation of demographics and co-morbidities. They are also treated with similar plans, making discrimination a difficult task. In this study, acute desquamation was a relatively rare event in both the development and validation cohorts (8.7 and 9.3%), while the distribution of acute erythema within each dataset was somewhat more balanced toward cases (45.0 and 22.9%).

The distribution of clinical predictors between cohorts was broadly similar between the three development and validation cohorts, apart from smoking status and BMI, and none of the patients in the ISE cohort received chemotherapy. Overall, the distribution of clinical predictors was also similar to other previously published cohorts (21, 24, 25). Nevertheless, there was considerable heterogeneity between the centers within REQUITE with regards to treatment variables, such as dose fractionation, use of boost, and inclusion of patients who received prior adjuvant chemotherapy, as well as observed toxicity frequencies (39). Differences in radiotherapy techniques over time may have also affected generalizability of the prediction models to the validation cohort, as the patients in the three RGC development cohorts were on average treated more than 10 years before those enrolled in REQUITE. Certainly, there has been widespread update of intensity-modulated radiotherapy (IMRT) over that time, with almost 50% of patients enrolled in REQUITE treated in this way, whereas only some patients in the Cambridge trial cohort were randomized to IMRT and none of the patients in LeND and ISE received IMRT. Because of this and lack of data from previous literature, radiotherapy technique, such as IMRT, was not included in the model development phase.

A mixed modeling (GLMM) approach was chosen in this study to try and address issues of cohort heterogeneity and to relax the assumptions of independence of predictor variables. Using an alternative statistical method such as Lasso techniques, or data mining such as machine learning algorithms, may have identified other predictor variables or potential interactions in patients with several marginal risk factors (56). Machine learning algorithms are used with increasing frequency, in particular in the context of multi-dimensional "big data" such as electronic health records and radiotherapy imaging (57). However, the data available for this study, in particular from the slightly older RGC cohorts, were somewhat more limited and did not reach the multi-dimensionality usually associated with machine learning projects.

Despite these limitations, it is important to note that validation of the predictive model for acute erythema was achieved in the absence of detailed radiation dosimetry and notwithstanding the differences in radiotherapy techniques between treatment centers and countries particularly in the REQUITE cohort. The performance of this model across different cohorts in this study suggests that these findings are reproducible and generalizable beyond that of the original development dataset, whilst acknowledging the tendency for the model to over-predict in the external REQUITE cohort. The calibration plot demonstrates that the model can successfully identify high-risk patients and observed vs. expected rates were still correlated. This suggests that the model for acute erythema will simply benefit from further re-calibration of certain variable coefficients without redesigning the model from scratch. In the case of acute desquamation, further improvements using shrinkage and re-calibration would not affect the model's reduced discriminatory power in the validation cohort. To improve discrimination, the model would need to be revised, for example, by additional adjustment to regression coefficients of predictors with different strength or direction of effect in the RGC development compared to the REQUITE cohorts, stepwise selection of additional predictors, such as those relating to radiotherapy technique (e.g., IMRT), or re-estimation of all regression coefficients in the validation population. These approaches to update the model need to be balanced against the fact that the information in the original model would be neglected and would require further validation elsewhere.

To increase clinical relevance, novel performance measures such as net re-classification improvement (NRI) and net benefit (NB) could also be considered (58). Risk models without recommending clinical decisions are less likely to change treatment decision-making behavior than those that translate risk into a treatment decision recommendation (59). Nevertheless, the clinical risk model presented here without detailed radiation dosimetry can be used in practice relatively simply to predict a patient's probability of acute skin radiation toxicity at the time of breast cancer diagnosis, which can then be taken into account when discussion various treatment options with patients.

CONCLUSIONS

While most published prediction research in the field of local breast cancer treatment toxicity continues to focus solely on model development, this study reports development and external validation of a predictive model for acute erythema following radiotherapy after breast-conserving surgery, which retained its moderate discriminatory power but will benefit from further re-calibration. A similar model to predict acute desquamation using clinical risk factors failed to validate in the REQUITE cohort. While other statistical or machine learning techniques may improve the performance of clinical risk models in the future, more accurate predictions are expected through the addition of genetic markers. This information could be considered when discussing breast cancer treatment options at the outset in particular with patients predicted at high risk of radiation toxicity.

DATA AVAILABILITY STATEMENT

The raw data supporting the conclusions of this article will be made available by the authors, without undue reservation.

ETHICS STATEMENT

The studies involving human participants were reviewed and approved by Manchester North West UK NRES Approval 14/NW/0035. The patients/participants provided their written informed consent to participate in this study.

AUTHOR CONTRIBUTIONS

TRat conceived the study design and wrote the first draft of the paper. TRat and PS analyzed the data. TRat, PS, JC-C, TRan, RS, CW, and CT contributed to the interpretation of the data. CW is lead chief investigator and CT is deputy lead of the REQUITE study. JC-C is chief investigator of the ISE study, CEC is chief investigator of the Cambridge IMRT trial. RS is chief investigator of the LeND study. TRat, MA-B, MA, DA, GB, RB, JC-C, CEC, M-PF, KJ, GP, TRan, VR, BR, DD, MdS, ES, RS, BT-V, RV, and LV contributed patients to the participating studies. HS is the breast cancer patient advocate on the REQUITE study. AM and AW curated the database for the REQUITE study. All authors commented on and approved the final manuscript.

FUNDING

TRat is currently an NIHR Clinical Lecturer. He was previously funded by a National Institute of Health Research (NIHR) Doctoral Research Fellowship (DRF 2014-07-079). This publication presents independent research funded by the NIHR. The views expressed are those of the authors and not necessarily those of the NHS, the NIHR, or the Department of Health. The REQUITE study received funding from European Union's 7th Framework Programme for research, technological development and demonstration under grant agreement no. 601826. The ISE study was supported by the German Office for Radiation Protection, project number St. Sch. 4116 and 4233. The LeND study received funding from Breast Cancer Now (formerly Breast Cancer Campaign) under grant ref. 2007NovPR45.

ACKNOWLEDGMENTS

We sincerely thank all patients who participated in the REQUITE study and all REQUITE staff involved at the following hospitals:

Belgium: Prof. Wilfried de Neve, Dr. Christel Monten, Dr. Pieter Deseyne at Ghent University Hospital; Gilles Defraene, Rita Aerts, Soumia Arredouani, Maarten Lambrecht at KU Leuven.
France: ICM Montpellier, CHU Nîmes (Department of Radiation Oncology, CHU Nîmes, Nîmes, France).
Germany: Praxis für Strahlentherapie an der Stadtklinik Baden-Baden (Dr. Thomas Blaschke); Klinikum Darmstadt GmbH (PD Dr. Christian Weiß); Zentrum für Strahlentherapie Freiburg (Dr. Petra Stegmaier); ViDia Christliche Kliniken Karlsruhe (Prof. Dr. Johannes Claßen); Klinikum der Stadt Ludwigshafen gGmbH (PD Dr. Thomas Schnabel); Universitätsklinikum Mannheim; Strahlentherapie Speyer (Dr. Jörg Schnabel). The researchers at DKFZ also thank Irmgard Helmbold and Dr. Sabine Behrens. ES was previously supported by the Ministry of Science and Arts of the State of Baden-Württemberg (2017–19) through the Brigitte-Schlieben-Lange-Programme.
Italy: Fondazione IRCCS Istituto Nazionale dei Tumori, Milano.
Spain: Santiago: Complexo Hospitalario Universitario de Santiago. AV was supported by Spanish Instituto de Salud Carlos III (ISCIII) funding, an initiative of the Spanish Ministry of Economy and Innovation partially supported by European Regional Development FEDER Funds (INT15/00070, INT16/00154, INT17/00133; PI16/00046; PI13/02030; PI10/00164), and through the Autonomous Government of Galicia (Consolidation and structuring program: IN607B); Barcelona: The authors acknowledge the Cellex Foundation for providing research facilities and equipment and thank the CERCA Programme/Generalitat de Catalunya for institutional support. SG-E was supported by the ISCIII Miguel Servet II Program (CP16/00034).
UK: Cambridge: AD was supported by Cancer Research-UK C8197/A16565. Leicester: University Hospitals Leicester: Support from the HOPE Clinical Trials Unit and Leicester Experimental Cancer Medicine Center (ECMC), Theresa Beaver, Sara Barrows; Manchester: CW was supported by Cancer Research UK (C1094/A18504, C147/A25254). AC and CW are supported by the NIHR Manchester Biomedical Research Center.
USA: Mount Sinai Hospital, New York. LeND cohort: We would like to thank all patients who participated in this study. Cambridge IMRT trial: We would like to acknowledge the work of Miss Jenny Wilkinson, research radiographer who was supported by funding from Breast Cancer Now (formerly Breast Cancer Campaign). We would also like to thank all

the patients who participated in the trial. GB receives funding from the Cancer Research UK Radiation Research Unit at the University of Cambridge (CRUK RadNet: Cambridge, C17918/A28870). CEC was supported by the Cambridge NIHR Biomedical Research Center. German ISE cohort: The researchers at DKFZ thank Ursula Eilber and Irmgard Helmbold, all patients and staff at the participating clinics involved in the project.

REQUITE CONSORTIUM COLLABORATORS

Yolande Lievens[9], Marc van Eijkeren[9], Piet Ost[9], Valérie Fonteyne[9], Christel Monten[9], Wilfried De Neve[9], Stephanie Peeters[18], Karin Haustermans[18], Caroline Weltens[18], Gilles Defraene[18], Maarten Lambrecht[18], Erik van Limberghen[18], Erik Briers[25], Celine Bourgier[6], Muriel Brengues[6], Roxana Draghici[6], Francoise Bons[13], Thomas Blaschke[26], Christian Weiß[27], Irmgard Helmbold[2], Christian Weißenberger[28], Petra Stegmaier[28], Johannes Claßen[29], Ulrich Giesche[29], Marie-Luise Sautter-Bihl[30], Burkhard Neu[30], Thomas Schnabel[31], Michael Ehmann[20], Benjamin Gauter-Fleckenstein[20], Carsten Herskind[20], Marlon Veldwijk[20], Jörg Schäfer[32], Tommaso Giandini[33], Marzia Franceschini[34], Claudia Sangalli[19], Barbara Avuzzi[19], Sara Morlino[19], Laura Lozza[19], Gabriele Pietro[35], Elena Delmastro[35], Elisabetta Garibaldi[35], Alessandro Cicchetti[15], Ben Vanneste[17], Bibiana Piqué-Leiva[5], Meritxel Molla[5], Alexandra Giraldo[5], Monica Ramos[5], Ramon Lobato-Busto[36], Paloma Sosa-Fajardo[4,22], Laura Torrado Moya[4,22], Isabel Dominguez-Rios[22], Irene Fajardo-Paneque[22], Patricia Calvo-Crespo[4,22], Ana Carballo[4,22], Paula Peleteiro[4,22], Olivia-Fuentes-Rios[3,4], Antonio Gomez-Caamano[4,22], Victoria Harrop[37], Debbie Payne[38], Manjusha Keni[39], Samuel Lavers[23], Simon Wright[40], Sridhar Thiagarajan[40], Luis Aznar-Garcia[40], Kiran Kancherla[40], Christopher Kent[40], Subramaniam Vasanthan[40], Donna Appleton[41], Monika Kaushik[41], Frances Kenny[41], Hazem Khout[41], Jaroslaw Krupa[41], Kelly V. Lambert[41], Simon Pilgrim[41], Sheila Shokuhi[41], Kalliope Valassiadou[41], Ion Bioangiu[40], Kufre Sampson[40], Ahmed Osman[40], Corinne Faivre-Finn[42], Karen Foweraker[43], Abigail Pascoe[43], Claire P. Esler[43], Tim Ward[44], Daniel S. Higginson[45], Richard G. Stock[46], Sheryl Green[46]

[25]Patient advocate, Hasselt, Belgium

[26]Praxis für Strahlentherapie, Baden-Baden, Germany

[27]Klinikum Darmstadt, Institut für Radionkologie und Strahlentherapie, Darmstadt, Germany

[28]Zentrum für Strahlentherapie, Karlsruhe, Germany

[29]Klinik für Strahlentherapie, St. Vincentius-Kliniken gAG, Karlsruhe, Germany

[30]Klinik für Radioonkologie und Strahlentherapie, Städtisches Klinikum, Karlsruhe, Germany

[31]Klinik für Strahlentherapie und Radiologische Onkologie, Klinikum der Stadt Ludwigshafen gGmbH, Ludwigshafen, Germany

[32]Strahlentherapie Speyer, Germany

[33]Department of Medical Physics, Fondazione IRCCS Istituto Nazionale dei Tumori, Milan, Italy

[34]Department of Radiotherapy 2, Fondazione IRCCS Istituto Nazionale dei Tumori, Milan, Italy

[35]Department of Radiation Oncology, Fondazione del Piemonte per l'Oncologia Candiolo Cancer Institute, Candiolo (TO), Italy

[36]Department of Medical Physics, Complexo Hospitalario Universitario de Santiago, SERGAS, Santiago de Compostela, Spain

[37]Queen Elizabeth Hospital, University Hospitals Birmingham NHS Trust, Birmingham, United Kingdom

[38]Centre for Integrated Genomic Medical Research (CIGMR), Manchester, United Kingdom

[39]Department of Oncology, Derby Teaching Hospitals NHS Foundation Trust, Derby, United Kingdom

[40]Department of Oncology, Leicester Royal Infirmary, University Hospitals of Leicester NHS Trust, Leicester, United Kingdom

[41]Department of Breast Surgery, Glenfield Hospital, University Hospitals of Leicester NHS Trust, Leicester, United Kingdom

[42]Division of Cancer Sciences, University of Manchester, Manchester, United Kingdom

[43]City Hospital, Nottingham University Hospitals NHS Trust, Nottingham, United Kingdom

[44]Patient advocate, Pelvic Radiation Disease Association, United Kingdom

[45]Department of Radiation Oncology, Memorial Sloan Kettering Cancer Center, New York, NY, United States

[46]Department of Radiation Oncology, The Icahn School of Medicine at Mount Sinai, New York, NY, United States

REFERENCES

1. Rowland JH, Hewitt M, Ganz PA. Cancer survivorship: a new challenge in delivering quality cancer care. *J Clin Oncol.* (2006) 24:5101–4. doi: 10.1200/JCO.2006.09.2700
2. ONS. *Cancer Survival in England: Patients Diagnosed Between 2010 and 2014 and Followed Up to 2015*. London: Office for National Statistics (2016).
3. Darby S, Mcgale P, Correa C, Taylor C, Arriagada R, Clarke M, et al. Effect of radiotherapy after breast-conserving surgery on 10-year recurrence and 15-year breast cancer death: meta-analysis of individual patient data for 10 801 women in 17 randomised trials. *Lancet.* (2011) 378:1707–16. doi: 10.1016/S0140-6736(11)61629-2
4. Knobf MT, Sun Y. A longitudinal study of symptoms and self-care activities in women treated with primary radiotherapy for breast cancer. *Cancer Nurs.* (2005) 28:210–8. doi: 10.1097/00002820-200505000-00010
5. Barry M, Kell MR. Radiotherapy and breast reconstruction: a meta-analysis. *Breast Cancer Res Treat.* (2011) 127:15–22. doi: 10.1007/s10549-011-1401-x
6. Rochlin DH, Jeong AR, Goldberg L, Harris T, Mohan K, Seal S, et al. Postmastectomy radiation therapy and immediate autologous breast reconstruction: integrating perspectives from surgical oncology, radiation oncology, and plastic and reconstructive surgery. *J Surg Oncol.* (2015) 111:251–7. doi: 10.1002/jso.23804
7. Lilla C, Ambrosone CB, Kropp S, Helmbold I, Schmezer P, Von Fournier D, et al. Predictive factors for late normal tissue complications following

radiotherapy for breast cancer. *Breast Cancer Res Treat.* (2007) 106:143–50. doi: 10.1007/s10549-006-9480-9
8. Thomson HJ, Potter S, Greenwood RJ, Bahl A, Barker J, Cawthorn SJ, et al. A prospective longitudinal study of cosmetic outcome in immediate latissimus dorsi breast reconstruction and the influence of radiotherapy. *Ann Surg Oncol.* (2008) 15:1081–91. doi: 10.1245/s10434-007-9772-2
9. Duxbury PJ, Gandhi A, Kirwan CC, Jain Y, Harvey JR. Current attitudes to breast reconstruction surgery for women at risk of post-mastectomy radiotherapy: a survey of UK breast surgeons. *Breast.* (2015) 24:502–12. doi: 10.1016/j.breast.2015.05.002
10. Giacalone PL, Rathat G, Daures JP, Benos P, Azria D, Rouleau C. New concept for immediate breast reconstruction for invasive cancers: feasibility, oncological safety and esthetic outcome of post-neoadjuvant therapy immediate breast reconstruction versus delayed breast reconstruction: a prospective pilot study. *Breast Cancer Res Treat.* (2010) 122:439–51. doi: 10.1007/s10549-010-0951-7
11. Fowler JF. The linear-quadratic formula and progress in fractionated radiotherapy. *Br J Radiol.* (1989) 62:679–94. doi: 10.1259/0007-1285-62-740-679
12. Emami B, Lyman J, Brown A, Coia L, Goitein M, Munzenrider JE, et al. Tolerance of normal tissue to therapeutic irradiation. *Int J Radiat Oncol Biol Phys.* (1991) 21:109–22. doi: 10.1016/0360-3016(91)90171-Y
13. Pastore F, Conson M, D'avino V, Palma G, Liuzzi R, Solla R, et al. Dose-surface analysis for prediction of severe acute radio-induced skin toxicity in breast cancer patients. *Acta Oncol.* (2016) 55:466–73. doi: 10.3109/0284186X.2015.1110253
14. Rancati T, Fiorino C, Fellin G, Vavassori V, Cagna E, Casanova Borca V, et al. Inclusion of clinical risk factors into NTCP modelling of late rectal toxicity after high dose radiotherapy for prostate cancer. *Radiother Oncol.* (2011) 100:124–30. doi: 10.1016/j.radonc.2011.06.032
15. Defraene G, Van Den Bergh L, Al-Mamgani A, Haustermans K, Heemsbergen W, Van Den Heuvel F, et al. The benefits of including clinical factors in rectal normal tissue complication probability modeling after radiotherapy for prostate cancer. *Int J Radiat Oncol Biol Phys.* (2012) 82:1233–42. doi: 10.1016/j.ijrobp.2011.03.056
16. Twardella D, Popanda O, Helmbold I, Ebbeler R, Benner A, Von Fournier D, et al. Personal characteristics, therapy modalities and individual DNA repair capacity as predictive factors of acute skin toxicity in an unselected cohort of breast cancer patients receiving radiotherapy. *Radiother Oncol.* (2003) 69:145–53. doi: 10.1016/S0167-8140(03)00166-X
17. Back M. Impact of radiation therapy on acute toxicity in breast conservation therapy for early breast cancer. *Clin. Oncol.* (2004) 16:12–6. doi: 10.1016/j.clon.2003.08.005
18. Deantonio L, Gambaro G, Beldi D, Masini L, Tunesi S, Magnani C, et al. Hypofractionated radiotherapy after conservative surgery for breast cancer: analysis of acute and late toxicity. *Radiat Oncol.* (2010) 5:112. doi: 10.1186/1748-717X-5-112
19. Barnett GC, Wilkinson JS, Moody AM, Wilson CB, Twyman N, Wishart GC, et al. The Cambridge breast intensity-modulated radiotherapy trial: patient- and treatment-related factors that influence late toxicity. *Clin Oncol.* (2011) 23:662–73. doi: 10.1016/j.clon.2011.04.011
20. Kraus-Tiefenbacher U, Sfintizky A, Welzel G, Simeonova A, Sperk E, Siebenlist K, et al. Factors of influence on acute skin toxicity of breast cancer patients treated with standard three-dimensional conformal radiotherapy (3D-CRT) after breast conserving surgery (BCS). *Radiat Oncol.* (2012) 7:217. doi: 10.1186/1748-717X-7-217
21. Terrazzino S, Mattina PL, Masini L, Caltavuturo T, Gambaro G, Canonico PL, et al. Common variants of eNOS and XRCC1 genes may predict acute skin toxicity in breast cancer patients receiving radiotherapy after breast conserving surgery. *Radiother Oncol.* (2012) 103:199–205. doi: 10.1016/j.radonc.2011.12.002
22. Sharp L, Johansson H, Hatschek T, Bergenmar M. Smoking as an independent risk factor for severe skin reactions due to adjuvant radiotherapy for breast cancer. *Breast.* (2013) 22:634–8. doi: 10.1016/j.breast.2013.07.047
23. Tortorelli G, Di Murro L, Barbarino R, Cicchetti S, Di Cristino D, Falco MD, et al. Standard or hypofractionated radiotherapy in the postoperative treatment of breast cancer: a retrospective analysis of acute skin toxicity and dose inhomogeneities. *BMC Cancer.* (2013) 13:230. doi: 10.1186/1471-2407-13-230
24. Ciammella P, Podgornii A, Galeandro M, Micera R, Ramundo D, Palmieri T, et al. Toxicity and cosmetic outcome of hypofractionated whole-breast radiotherapy: predictive clinical and dosimetric factors. *Radiat Oncol.* (2014) 9:97. doi: 10.1186/1748-717X-9-97
25. De Langhe S, Mulliez T, Veldeman L, Remouchamps V, Van Greveling A, Gilsoul M, et al. Factors modifying the risk for developing acute skin toxicity after whole-breast intensity modulated radiotherapy. *BMC Cancer.* (2014) 14:711. doi: 10.1186/1471-2407-14-711
26. Tomatis S, Rancati T, Fiorino C, Vavassori V, Fellin G, Cagna E, et al. Late rectal bleeding after 3D-CRT for prostate cancer: development of a neural-network-based predictive model. *Phys Med Biol.* (2012) 57:1399–412. doi: 10.1088/0031-9155/57/5/1399
27. De Langhe S, De Meerleer G, De Ruyck K, Ost P, Fonteyne V, De Neve W, et al. Integrated models for the prediction of late genitourinary complaints after high-dose intensity modulated radiotherapy for prostate cancer: making informed decisions. *Radiother Oncol.* (2014) 112:95–9. doi: 10.1016/j.radonc.2014.04.005
28. D'avino V, Palma G, Liuzzi R, Conson M, Doria F, Salvatore M, et al. Prediction of gastrointestinal toxicity after external beam radiotherapy for localized prostate cancer. *Radiat Oncol.* (2015) 10:80. doi: 10.1186/s13014-015-0389-5
29. Dehing-Oberije C, De Ruysscher D, Petit S, Van Meerbeeck J, Vandecasteele K, De Neve W, et al. Development, external validation and clinical usefulness of a practical prediction model for radiation-induced dysphagia in lung cancer patients. *Radiother Oncol.* (2010) 97:455–61. doi: 10.1016/j.radonc.2010.09.028
30. Sheu T, Fuller CD, Mendoza TR, Garden AS, Morrison WH, Beadle BM, et al. Nomogram for predicting symptom severity during radiation therapy for head and neck cancer. *Otolaryngol Head Neck Surg.* (2014) 151:619–26. doi: 10.1177/0194599814545746
31. Wijsman R, Dankers F, Troost EG, Hoffmann AL, Van Der Heijden EH, De Geus-Oei LF, et al. Multivariable normal-tissue complication modeling of acute esophageal toxicity in advanced stage non-small cell lung cancer patients treated with intensity-modulated (chemo-)radiotherapy. *Radiother Oncol.* (2015) 117:49–54. doi: 10.1016/j.radonc.2015.08.010
32. Kim JY, Mlodinow AS, Khavanin N, Hume KM, Simmons CJ, Weiss MJ, et al. Individualized risk of surgical complications: an application of the breast reconstruction risk assessment score. *Plast Reconstr Surg Glob Open.* (2015) 3:e405. doi: 10.1097/GOX.0000000000000351
33. Nelson JA, Chung CU, Fischer JP, Kanchwala SK, Serletti JM, Wu LC. Wound healing complications after autologous breast reconstruction: a model to predict risk. *J Plast Reconstr Aesthet Surg.* (2015) 68:531–9. doi: 10.1016/j.bjps.2014.11.017
34. Khavanin N, Qiu CS, Mlodinow AS, Vu MM, Dorfman RG, Fine NA, et al. External validation of the breast reconstruction risk assessment calculator. *J Plast Reconstr Aesthet Surg.* (2017) 70:876–83. doi: 10.1016/j.bjps.2017.04.010
35. Roy M, Sebastiampillai S, Haykal S, Zhong T, Hofer SOP, O'neill AC. Development and validation of a risk stratification model for immediate microvascular breast reconstruction. *J Surg Oncol.* (2019) 120:1177–83. doi: 10.1002/jso.25714
36. Collins GS, Reitsma JB, Altman DG, Moons KG. Transparent reporting of a multivariable prediction model for individual prognosis or diagnosis (TRIPOD): the TRIPOD statement. *Br J Surg.* (2015) 102:148–58. doi: 10.1002/bjs.9736
37. Tanteles GA, Whitworth J, Mills J, Peat I, Osman A, Mccann GP, et al. Can cutaneous telangiectasiae as late normal-tissue injury predict cardiovascular disease in women receiving radiotherapy for breast cancer? *Br J Cancer.* (2009) 101:403–9. doi: 10.1038/sj.bjc.6605182
38. West C, Azria D, Chang-Claude J, Davidson S, Lambin P, Rosenstein B, et al. The REQUITE project: validating predictive models and biomarkers of radiotherapy toxicity to reduce side-effects and improve quality of life in cancer survivors. *Clin Oncol.* (2014) 26:739–42. doi: 10.1016/j.clon.2014.09.008
39. Seibold P, Webb A, Aguado-Barrera ME, Azria D, Bourgier C, Brengues M, et al. REQUITE: a prospective multicentre cohort study of patients

undergoing radiotherapy for breast, lung or prostate cancer. *Radiother Oncol.* (2019) 138:59–67. doi: 10.1016/j.radonc.2019.04.034
40. NCI. *Common Terminology Criteria for Adverse Events v4.0*. Bethesda, MD: National Cancer Institute; NIH (2009).
41. Cox JD, Stetz J, Pajak TF. Toxicity criteria of the Radiation Therapy Oncology Group (RTOG) and the European Organization for Research and Treatment of Cancer (EORTC). *Int J Radiat Oncol Biol Phys.* (1995) 31:1341–6. doi: 10.1016/0360-3016(95)00060-C
42. Van Buuren S, Oudshoorn K. *Flexible Multivariate Imputation by MICE.* TNO Report. Leiden: TNO Institute (1999).
43. Rubin DB. Multiple imputation after 18+ years. *J Am Stat Assoc.* (1996) 91:473–89. doi: 10.1080/01621459.1996.10476908
44. White IR, Royston P, Wood AM. Multiple imputation using chained equations: issues and guidance for practice. *Stat Med.* (2011) 30:377–99. doi: 10.1002/sim.4067
45. Vergouwe Y, Steyerberg EW, Eijkemans MJ, Habbema JD. Substantial effective sample sizes were required for external validation studies of predictive logistic regression models. *J Clin Epidemiol.* (2005) 58:475–83. doi: 10.1016/j.jclinepi.2004.06.017
46. Sharp L, Johansson H, Landin Y, Moegelin IM, Bergenmar M. Frequency and severity of skin reactions in patients with breast cancer undergoing adjuvant radiotherapy, the usefulness of two assessment instruments - a pilot study. *Eur J Cancer.* (2011) 47:2665–72. doi: 10.1016/j.ejca.2011.06.039
47. Pignol JP, Olivotto I, Rakovitch E, Gardner S, Sixel K, Beckham W, et al. A multicenter randomized trial of breast intensity-modulated radiation therapy to reduce acute radiation dermatitis. *J Clin Oncol.* (2008) 26:2085–92. doi: 10.1200/JCO.2007.15.2488
48. Brunt AM, Wheatley D, Yarnold J, Somaiah N, Kelly S, Harnett A, et al. Acute skin toxicity associated with a 1-week schedule of whole breast radiotherapy compared with a standard 3-week regimen delivered in the UK FAST-Forward Trial. *Radiother Oncol.* (2016) 120:114–8. doi: 10.1016/j.radonc.2016.02.027
49. Chon BH, Loeffler JS. The effect of nonmalignant systemic disease on tolerance to radiation therapy. *Oncologist.* (2002) 7:136–43. doi: 10.1634/theoncologist.7-2-136
50. Cheki M, Shirazi A, Mahmoudzadeh A, Bazzaz JT, Hosseinimehr SJ. The radioprotective effect of metformin against cytotoxicity and genotoxicity induced by ionizing radiation in cultured human blood lymphocytes. *Mutat Res.* (2016) 809:24–32. doi: 10.1016/j.mrgentox.2016.09.001
51. Pouri M, Shaghaghi Z, Ghasemi A, Hosseinimehr SJ. Radioprotective effect of gliclazide as an anti-hyperglycemic agent against genotoxicity induced by ionizing radiation on human lymphocytes. *Cardiovasc Hematol Agents Med Chem.* (2019) 17:40–6. doi: 10.2174/1871525717666190524092918
52. Mahmoudi M, Gorenne I, Mercer J, Figg N, Littlewood T, Bennett M. Statins use a novel Nijmegen breakage syndrome-1-dependent pathway to accelerate DNA repair in vascular smooth muscle cells. *Circ Res.* (2008) 103:717–25. doi: 10.1161/CIRCRESAHA.108.182899
53. Fritz G, Henninger C, Huelsenbeck J. Potential use of HMG-CoA reductase inhibitors (statins) as radioprotective agents. *Br Med Bull.* (2011) 97:17–26. doi: 10.1093/bmb/ldq044
54. Altman DG, Vergouwe Y, Royston P, Moons KG. Prognosis and prognostic research: validating a prognostic model. *BMJ.* (2009) 338:b605. doi: 10.1136/bmj.b605
55. Steyerberg EW, Harrell FE Jr, Borsboom GJ, Eijkemans MJ, Vergouwe Y, Habbema JD. Internal validation of predictive models: efficiency of some procedures for logistic regression analysis. *J Clin Epidemiol.* (2001) 54:774–81. doi: 10.1016/S0895-4356(01)00341-9
56. Mbah C, Thierens H, Thas O, De Neve J, Chang-Claude J, Seibold P, et al. Pitfalls in prediction modeling for normal tissue toxicity in radiation therapy: an illustration with the individual radiation sensitivity and mammary carcinoma risk factor investigation cohorts. *Int J Radiat Oncol Biol Phys.* (2016) 95:1466–76. doi: 10.1016/j.ijrobp.2016.03.034
57. Kang J, Rancati T, Lee S, Oh JH, Kerns SL, Scott JG, et al. Machine learning and radiogenomics: lessons learned and future directions. *Front Oncol.* (2018) 8:228. doi: 10.3389/fonc.2018.00228
58. Cook NR. Use and misuse of the receiver operating characteristic curve in risk prediction. *Circulation.* (2007) 115:928–35. doi: 10.1161/CIRCULATIONAHA.106.672402
59. Moons KG, Altman DG, Vergouwe Y, Royston P. Prognosis and prognostic research: application and impact of prognostic models in clinical practice. *BMJ.* (2009) 338:b606. doi: 10.1136/bmj.b606

Conflict of Interest: DA has been involved in the creation of the start-up NovaGray in 2015. DD is on the advisory board of Astra Zeneca, Bristol-Myers-Squibb, Roche/Genentech, Merck/Pfizer, Celgene, Noxxon, Mologen and has received investigator initiated grants from Bristol-Myers-Squibb, Boehringer Ingelheim, and Astra-Zeneca. ES received General speakers bureau Zeiss Meditec, travel support Zeiss Meditec.

The remaining authors declare that the research was conducted in the absence of any commercial or financial relationships that could be construed as a potential conflict of interest.

frontiers in Oncology

ORIGINAL RESEARCH
published: 05 November 2020
doi: 10.3389/fonc.2020.531660

Targeted Alpha Therapy in mCRPC (Metastatic Castration-Resistant Prostate Cancer) Patients: Predictive Dosimetry and Toxicity Modeling of ^{225}Ac-PSMA (Prostate-Specific Membrane Antigen)

Maria Luisa Belli[1†], Anna Sarnelli[1†], Emilio Mezzenga[1], Francesco Cesarini[1], Paola Caroli[2], Valentina Di Iorio[3], Lidia Strigari[4], Marta Cremonesi[5], Antonino Romeo[6], Silvia Nicolini[2], Federica Matteucci[2], Stefano Severi[2] and Giovanni Paganelli[2]*

[1] Medical Physics Unit, Istituto Scientifico Romagnolo per lo Studio e la Cura dei Tumori (IRST) IRCCS, Meldola, Italy, [2] Nuclear Medicine Unit, Istituto Scientifico Romagnolo per lo Studio e la Cura dei Tumori (IRST) IRCCS, Meldola, Italy, [3] Oncology Pharmacy, Istituto Scientifico Romagnolo per lo Studio e la Cura dei Tumori (IRST) IRCCS, Meldola, Italy, [4] Medical Physics Unit, Policlinico S. Orsola-Malpighi, Bologna, Italy, [5] Radiation Research Unit, European Institute of Oncology (IEO) IRCCS, Milano, Italy, [6] Radiotherapy Unit, Istituto Scientifico Romagnolo per lo Studio e la Cura dei Tumori (IRST) IRCCS, Meldola, Italy

OPEN ACCESS

Edited by:
Ester Orlandi,
Istituto Nazionale dei Tumori (IRCCS), Italy

Reviewed by:
William F. Hartsell,
Northwestern University, United States
Iain Murray,
Royal Marsden NHS Foundation Trust, United Kingdom

***Correspondence:**
Maria Luisa Belli
maria.belli@irst.emr.it

†These authors have contributed equally to this work and share first authorship

Specialty section:
This article was submitted to Radiation Oncology, a section of the journal Frontiers in Oncology

Received: 31 January 2020
Accepted: 20 August 2020
Published: 05 November 2020

Citation:
Belli ML, Sarnelli A, Mezzenga E, Cesarini F, Caroli P, Di Iorio V, Strigari L, Cremonesi M, Romeo A, Nicolini S, Matteucci F, Severi S and Paganelli G (2020) Targeted Alpha Therapy in mCRPC (Metastatic Castration-Resistant Prostate Cancer) Patients: Predictive Dosimetry and Toxicity Modeling of ^{225}Ac-PSMA (Prostate-Specific Membrane Antigen). Front. Oncol. 10:531660. doi: 10.3389/fonc.2020.531660

Radioligand therapy is a type of internal radiotherapy combining a short-range radioisotope labeled to a carrier with a high affinity for a specific receptor expressed on tumor cells. Targeted alpha therapy (TAT) combines a high-linear energy transfer (LET) emitter (^{225}Ac) with a prostate-specific membrane antigen (PSMA) carrier, specifically binding tumor cells in patients with metastatic castration-resistant prostate cancer. Although the antitumor activity of ^{225}Ac-PSMA is well-documented, this treatment is nowadays only used as salvage therapy because the high incidence of xerostomia limits the therapeutic window. Thus, methods to reduce salivary toxicity and models able to describe xerostomia incidence are needed. We recently studied the efficacy of salivary gland protectors administered in combination with ^{177}Lu-PSMA therapy. Starting from these data, we performed a predictive dosimetric evaluation of ^{225}Ac-PSMA to assess the impact of salivary gland protectors in TAT. ^{225}Ac-PSMA predictive dosimetry was performed in 13 patients treated with ^{177}Lu-PSMA. Sequential whole-body planar images were acquired 0.5–1, 16–24, 36–48, and 120 h post-injection. ^{177}Lu time-activity curves were corrected for ^{225}Ac physical decay and assumed in equilibrium for all daughters. The OLINDA/EXM spherical model was used for dose estimation of the parotid and submandibular glands. The dose for each daughter was calculated and summed for the total dose estimation. The biologically effective dose formalism was extended to high-LET emitters. For the total biologically effective dose formalism extended to high-LET emitters, including the contribution of all daughter isotopes, the brachytherapy formalism for a mixture of radionuclides was implemented. Equivalent doses in 2 Gy/fraction (EQD2) were then calculated and compared with the normal tissue complication probability model derived from external beam radiotherapy for grade $\geq$2 xerostomia induction. Median predictive doses were 0.86 Bd_{RBE5}/MBq for parotid glands and 1.05 Bd_{RBE5}/MBq for submandibular glands, with a 53% reduction compared with

previously published data. The results show that the radiobiological model implemented is conservative, as it overestimates the complication rate with respect to the clinical data. Our data shows the possibility of reducing salivary gland uptake in TAT with the coadministration of organ protectors, but these results should be confirmed for TAT with ^{225}Ac-PSMA by carrying out prospective trials with defined toxicity endpoints and dosimetry procedures.

Keywords: target alpha therapy (TAT), prostate-specific membrane antigen (PSMA), xerostomia, theragnostic, protectors, dosimetry

INTRODUCTION

The combination of a short-range radioisotope labeled to a carrier/ligand highly specific for receptors expressed on tumor cells enables "internal" radioligand therapy (RLT) to be delivered to tumors. The increased tumor cells turnover and receptor overexpression induces a high isotope concentration within the tumor (1). Internal radiotherapy is also known as radiometabolic treatment (RMT) when iodine-131 is used in thyroid cancer or peptide receptor radionuclide therapy when radiolabeled peptides such as somatostatin analog are used in neuroendocrine tumors (2). Similarly, prostate-specific membrane antigen (PSMA) is an attractive target for diagnosis and therapy of metastasized prostate cancer (3). The PSMA expression is directly correlated with androgen independence, metastasis, and progression. PSMA, also known as glutamate carboxypeptidase II, is a membrane protease anchored in the cell membrane of prostate cancer cells but not in normal prostate cells. A radiolabeled version of a PSMA ligand (Dota-PSMA-617) has been synthesized and has shown promising properties when labeled with ^{177}Lutetium, a short-range beta-gamma emitter (4, 5).

PSMA-based RLT is thus becoming an attractive therapeutic option for the clinical management of metastatic castration-resistant prostate cancer patients (3, 4, 6, 7). However, as many as 40% of treated patients do not respond to this β-particle therapy (8). The use of high-linear energy transfer (LET) α-emitters to increase local damage to tumor cells and thus enhance treatment efficacy has aroused widespread interest in this setting. In particular, targeted alpha therapy (TAT) combining ^{225}Ac α-emitter with PSMA carrier has proven a promising therapeutic option in terms of disease control for tumors refractory to beta-radiation therapy. Although the antitumor activity of ^{225}Ac-PSMA is well-documented (9), this therapy is now only used as salvage therapy because the high rate of irreversible xerostomia limits the therapeutic window. Kratochwil et al. (8, 9) reported their experience in 40 patients treated with ^{225}Ac-PSMA administrated with an activity ranging from 50 to 200 kBq/kg. Xerostomia was regularly reported with 100 kBq/kg or more per cycle and was considered intolerable with more than 150 kBq/kg (8). The first symptoms of xerostomia appeared 2–5 days post-TAT, lasting for about 2 months. Partial recovery was observed if no additional cycles were added, but some patients had a chronic loss of secretion function (8).

In a prospective study carried out at Istituto Scientifico Romagnolo per lo Studio e la Cura dei Tumori (IRST) (10), ^{177}Lu-PSMA was administered in combination with polyglutamate tablets and ice packs application used as protectors for salivary glands. The gamma emission of ^{177}Lu (208 keV, 11% relative abundance) enabled us to perform dosimetry, acquiring serial post-injection whole-body scans. Polyglutamate tablets were orally administered as a substrate for PSMA receptors, and external ice packs were applied to the neck region (3). The dosimetry evaluation performed on 13 patients showed a lower absorbed dose in both parotid and submandibular glands compared with previously published data (11, 12). The efficacy results of the protectors proposed in our study, especially for salivary glands, were encouraging in the context of TAT, as they could potentially improve treatment management, enabling wider use of this therapeutic approach. As the metabolic uptake of a radioisotope is mainly guided by the carrier (*i.e.,* Dota-PSMA-617), it is reasonable to assume that the organ protectors used for ^{177}Lu-PSMA could also result in a similar reduction in a predicted dose for ^{225}Ac-PSMA treatment. Given that dosimetric imaging is not feasible with ^{225}Ac, where lower gamma emission largely impairs post-injection image acquisition, predictive dosimetry was performed assuming an uptake and retention similar to ^{177}Lu-PSMA dosimetry. In this way, absorbed dose results for ^{177}Lu were converted to ^{225}Ac, including the contribution of the decay chain. A radiobiological evaluation was then performed by comparing biologically effective dose (BED) of TAT [relative biological effectiveness (RBE)-weighted] with external beam radiotherapy (EBRT) schedules. The BED formalism was extended to α-emitters (BED_H) for therapies with a continuous and exponentially decreasing dose rate. To include in the total BED_H the contribution of all daughter isotopes in the ^{225}Ac chain, the formalism adopted in brachytherapy to estimate the BED for a mixture of radionuclides was implemented. The normal tissue complication probability (NTCP) model derived from EBRT data was then applied to TAT data to estimate the impact of salivary gland protectors on the incidence of acute xerostomia as a function of injected activity.

MATERIALS AND METHODS

Main Treatment and Patient's Population Characteristics

From April 2017 to February 2019, we enrolled 43 patients in the first European phase II RLT prospective trial [EudraCt/RSO

number: 2016-002732-32, NCT03454750 (10)] ongoing at our institute (IRST). Patients were stratified on the basis of risk factors. Patients <75 years old unfit to undergo treatment with docetaxel received 5.5 GBq of ^{177}Lu-PSMA-617, whereas those who had already been treated with docetaxel, were older than 75 years, or those who had other risk factors received lower activities ranging from 3.7 to 4.4 GBq of ^{177}Lu-PSMA-617. Patients received four treatment cycles, with a time interval of 8–12 weeks between 2 consecutive cycles. An additional two cycles were performed for patients with no registered adverse effects, no evidence of progressive disease, and who, in the opinion of the investigator, could obtain a clinical benefit. All patients underwent a pretreatment ^{68}Ga-PSMA-HBED-11 whole-body positron emission tomography PET/CT scan. ^{177}Lu-Dota-PSMA-617 radiopharmaceutical infusion was performed slowly intravenously in 15–30 min in a dedicated room using a dedicated pump system (patent US 7,842,023 B2). Additional information are provided in **Appendix**.

Organ-specific drug protectors were administered to reduce organ-at-risk uptake (10–12). For the salivary glands, 30 min before, during, and 4 h after ^{177}Lu-PSMA infusion, ice packs were applied to the neck region (3, 13), and patients were given polyglutamate folate tablets of plant origin (Morgan Pharma Monteviale, Italy). To preserve kidney functionality, a 10% mannitol solution in 500 ml was infused before and after ^{177}Lu-PSMA injection, 250 ml 30 min before therapy and 250 ml 1 h after therapy (14). Additional organ protectors consisted of eye drops (Naaxia Eye Drop Solution 19.6 mg/0.4 ml, Laboratoires Thea, Clermont-Ferrand, France) to limit lacrimal gland uptake, given 30 min before injection, and laxatives (Movicol, Norgine, Norgine Italia., Milano, Italy) to reduce delayed intestinal uptake, given 24 h post-injection.

Dosimetry

^{177}Lu-PSMA (Prostate-Specific Membrane Antigen) Dosimetry

Serial scintigraphic planar images were acquired 0.5–1, 16–24, 36–48, and 120 h post-infusion. Anterior and posterior images were acquired with a single positron emission computed tomography (SPECT) scanner (Discovery NM/CT 670, General Electric Medical System, Haifa, Israel) equipped with a 3/8″-thick NaI (Tl) crystal with a scan speed of 7 cm/min. The emission energy window was centered on 208 keV (20% width), and additional low and scatter energy windows were centered on 175 and 238 keV (10% width), respectively, and used for scatter correction image. Given that Kratochwil et al. (8) did not perform any attenuation correction to their patents' data, no attenuation correction was applied in this study. Details on the dosimetry protocol were published in previous works (11, 12). Structures of interest for dosimetry evaluation were kidneys, liver, parotid glands (PGs), submandibular glands (SGs), red marrow (RM), and whole body (WB). All structures were delineated on subsequent post-injection planar images, whereas RM dosimetry was based on blood samples. The conjugate projection method (15) was used to evaluate the relative uptake of each considered structure at different time points. For each organ, the time–activity curve was derived for residency time evaluation, and the dose calculation was performed according to the medical internal radiation dose (MIRD) formalism (15, 16) using OLINDA/EXM software (v1.1, Nashville, TN, USA) (17). The OLINDA/EXM adult male phantom was used for WB, kidney, liver, and RM dose estimation. For PGs and SGs, the sphere model of unite density was used. The mass of every single structure was derived on the basis of the pretreatment WB CT scan (^{68}Ga-PSMA PET/CT). For paired organs, a mean value between the left and right structures was calculated. The salivary gland dose value was calculated as the mean between PG and SG dose values for each patient. More details are reported in Sarnelli et al. (11). Although the focus of the present study is salivary glands, for the sake of completeness, we reported the predicted dose also for the other considered organs.

^{225}Ac-PSMA (Prostate-Specific Membrane Antigen) Predictive Dosimetry

The dosimetric data obtained for ^{177}Lu-PSMA evaluation were converted into ^{225}Ac-PSMA predictive dosimetry, assuming a similar uptake governed by the PSMA carrier. We used the same method previously published by Kratochwil et al. (8, 18). The ^{177}Lu-PSMA time–activity curves were corrected for ^{177}Lu physical half-life, and the biological time–activity curves were then used for predictive dosimetry of ^{225}Ac. Assuming equilibrium in the decay chain and no translocation during the decay between succeeding disintegrations, the same residence time estimated for ^{225}Ac was used for all the daughters in the ^{225}Ac chain. S-values specific for each daughter were considered to account for different dose contribution. According to the literature data, an RBE factor equal to 5 was used to weight the α-particle dose contribution concerning the γ and β emission (19). The contributions of α, β, and γ radiations were then summed up for each radioisotope, taking into account the branching ratio of 2% for ^{209}Tl and 98% for ^{213}Po. As suggested by the MIRD committee, when a deterministic endpoint is considered (19, 20), we expressed data in Barendsen units (Bd) or Bd/MBq. A suffix indicating the RBE value assumed for α-particle weight was added (e.g., Bd_{RBE5} indicates the use of RBE = 5).

The median values of our data were then compared with previously published findings (8, 9). Unfortunately, there is no consensus regarding the choice of unit expression of the RBE-weighted dose. Consequently, it may thus happen that data reported by different studies are derived with the same approach but are expressed with different units (8, 20). For the sake of simplicity, when comparing our data with those from other studies, we used the unit of Sv_{RBE5}/MBq according to (8).

Radiobiological Model

BED (Biological Effective Dose) Calculation

When comparing the effect of delivered dose with high- or low-LET radiation, the different ability to create biological damage per unit of delivered dose should be taken into account. The radiosensitivity parameters used in the linear-quadratic (LQ) model for high-LET radiation are therefore different from those used for low-LET. The concept of maximum RBE (RBE_M) is used to incorporate this effect for the linear component of the LQ

model in the BED calculation, maximizing the RBE value on cell survival curves (21). We derived RBE_M from the Equation (8) in (22) as follows:

$$RBE_M = RBE_{exp} + \frac{d}{\alpha/\beta}\left(\frac{RBE_{exp}^2 - 1}{RBE_{exp}}\right) \quad (1)$$

where RBE_{exp} is the experimental value of high-LET radiation assumed from literature (19), d is the fractional dose of the reference low-LET radiation, α/β is the ratio of the dose-rate-independent and the dose-rate-dependent term in the LQ model estimated for low-LET radiation (23).

Aiming to compare the effect of TAT delivered dose with the low-LET EBRT schedules, the BED (24, 25) for high-LET (BED_H), continuous and exponentially decreasing dose rate, was calculated using the equation proposed by Dale and Jones (21). The formalism derived for brachytherapy implants with a mixture of radionuclide was used (26–29) to account for all daughter isotopes in the ^{225}Ac decay chain:

$$BED_H = \frac{1}{\lambda}\sum_n (R_0)_n \left\{ RBE_M + \frac{\sum_n \sum_p (R_0)_n (R_0)_p}{(\lambda+\mu)(\alpha/\beta)\left[\sum_n (R_0)_n\right]} \right\} \quad (2)$$

were n and p denote the different daughter in the decay chain, λ the effective half-life (a combination of ^{225}Ac physical and biological half-lives, assumed equal for all the daughter isotopes), and μ the repair time. $(R_0)_n$ is the initial dose rate expressed as follows:

$$(R_0)_n\left[\frac{mGy}{h}\right] = D_n\left[\frac{mGy}{MBq}\right] A_i\left[MBq\right]\ \lambda\left[\frac{1}{h}\right] \quad (3)$$

where D_n is the non-RBE-weighted predicted absorbed dose and A_i the injected activity.

For bi-exponential curve fitting, the λ value corresponding to the slow washout phase (lower value) was used for BED_H calculation. By introducing RBE_M, the calculated BED_H remains compatible with the LQ model and is expressed in the same biological units as for low-LET calculation (Gy), allowing a direct comparison with EBRT schedules (22). For the BED_H calculation, we considered only the α emissions, whereas the β and γ emissions were neglected.

We compared our data with those derived from EBRT schedules for both late [at 1-year post-EBRT, QUANTEC data (30, 31)] and early [at 3-month post-EBRT, Strigari et al. (32)] xerostomia post-treatment. For this purpose, we calculated the BED for low-LET radiation (BED_L) of EBRT as (33):

$$BED_L = D_L\left(1 + \frac{D_L/N}{\alpha/\beta}\right) \quad (4)$$

where D_L is the total dose for low-LET EBRT schedules, and N is the number of fractions.

As QUANTEC (30, 31) reports as dose constraint for xerostomia induction a value calculated on PGs alone, we did not include in this comparison the SG dose values. Whereas, when comparing our data to the model of Strigari et al. (32) that includes both PGs and SGs, the mean value between them was considered for salivary glands dose.

NTCP (Normal-Tissue Complication Probability) Modeling

To compare the data with the NTCP model, the equivalent dose in 2 Gy/fr (EQD2) is calculated as (34):

$$EQD2 = \frac{BED_H}{\left(1 + \frac{2\ Gy}{\alpha/\beta}\right)} \quad (5)$$

The Lyman–Kutcher–Burman formalism (35, 36) was used for the NTCP model as:

$$NTCP = \frac{1}{\sqrt{2\pi}}\int_0^t e^{-x^2/2}dx \quad (6)$$

$$t = \frac{EQD2 - TD50}{m^*TD50} \quad (7)$$

where TD50 is the tolerance dose for a homogenous dose distribution to the organ in which 50% of the patients are likely to experience severe xerostomia, and m is the slope of the dose–response curve.

Data Analysis

In accordance with the clinical protocol active in our institute, all enrolled patients received salivary gland protectors in combination with ^{177}Lu-PSMA. For this reason, no data without drug protectors were available in our patient cohort. To compare the results of predictive dosimetry for ^{225}Ac-PSMA obtained in our patient cohort with those obtained without salivary gland protectors (8), the predictive dose calculated for our patients was rescaled according to the ratio between the mean predicted dose value for salivary glands reported in the study by Kratochwil et al. (8) and the same value estimated in our patient cohort. The BED'_H was then calculated for rescaled predictive doses as previously described. The EBRT-derived NTCP model was then used to estimate the probability of xerostomia for ^{225}Ac-PSMA with and without the administration of the salivary gland protector. Moreover, based on BED_H dependence on injection activity, the impact of different activity concentration levels was evaluated, scaling from 50 to 200 kBq/kg.

RESULTS

Predictive dosimetry evaluation was performed on 13 patients enrolled in the ^{177}Lu-PSMA protocol (nine at the first cycle and four at the second cycle).

Predictive Dose for ^{225}Ac-PSMA

Median (range) mass values of considered structures were 371 g (223–628) for kidneys, 1,830 g (1,132–2,366) for liver, 53 g (33–89) for PGs, 17 g (13–34) for SGs, and 80 kg (72–105) for WB. For paired organs, the sum of the left and right organ is reported. Median (range) effective half-lives were 17.6 h^{-1} (0.07–46.2) for

TABLE 1 | Results of ^{225}Ac-PSMA predictive dosimetric study in terms of Bd_{RBE5}/MBq (11).

	Kidneys (Bd_{RBE5}/MBq)	Liver (Bd_{RBE5}/MBq)	Parotid glands (Bd_{RBE5}/MBq)	Submandibular glands (Bd_{RBE5}/MBq)	Red marrow (Bd_{RBE5}/MBq)	Whole body (Bd_{RBE5}/MBq)
Patient 1	0.67	0.23	1.28	1.52	–	0.11
Patient 2	0.54	0.17	2.43	1.98	0.08	0.05
Patient 3	1.81	0.08	0.64	0.79	0.08	0.04
Patient 4	0.15	0.02	0.70	1.05	0.03	0.02
Patient 5	0.86	0.23	1.16	0.87	0.08	0.04
Patient 6	0.42	0.06	0.86	1.09	0.14	0.09
Patient 7	0.57	0.12	0.57	1.15	0.07	0.02
Patient 8	0.70	0.14	0.52	0.96	0.03	0.03
Patient 9	0.45	0.09	0.49	1.30	0.05	0.04
Patient 10	0.54	0.08	1.11	0.83	0.05	0.04
Patient 11	0.67	0.09	1.39	0.68	–	0.03
Patient 12	1.06	0.24	1.83	1.89	–	0.09
Patient 13	0.73	0.11	0.50	0.42	–	0.02
Median (range)	0.67 (0.15–1.81)	0.11 (0.02–0.24)	0.86 (0.49–2.43)	1.05 (0.42–1.98)	0.07 (0.03–0.14)	0.04 (0.02–0.11)
Mean (SD)	0.71 (0.40)	0.13 (0.07)	1.04 (0.59)	1.12 (0.46)	0.07 (0.03)	0.05 (0.03)

Data were extrapolated from ^{177}Lu-PSMA dosimetry evaluations. OLINDA/EXM adult male phantom was used for the whole-body, kidney, liver, and red marrow dose estimation, whereas spherical model was used for parotid and submandibular glands. Blood sample data were not available for patients 1, 11, 12, and 13. SD, standard deviation.

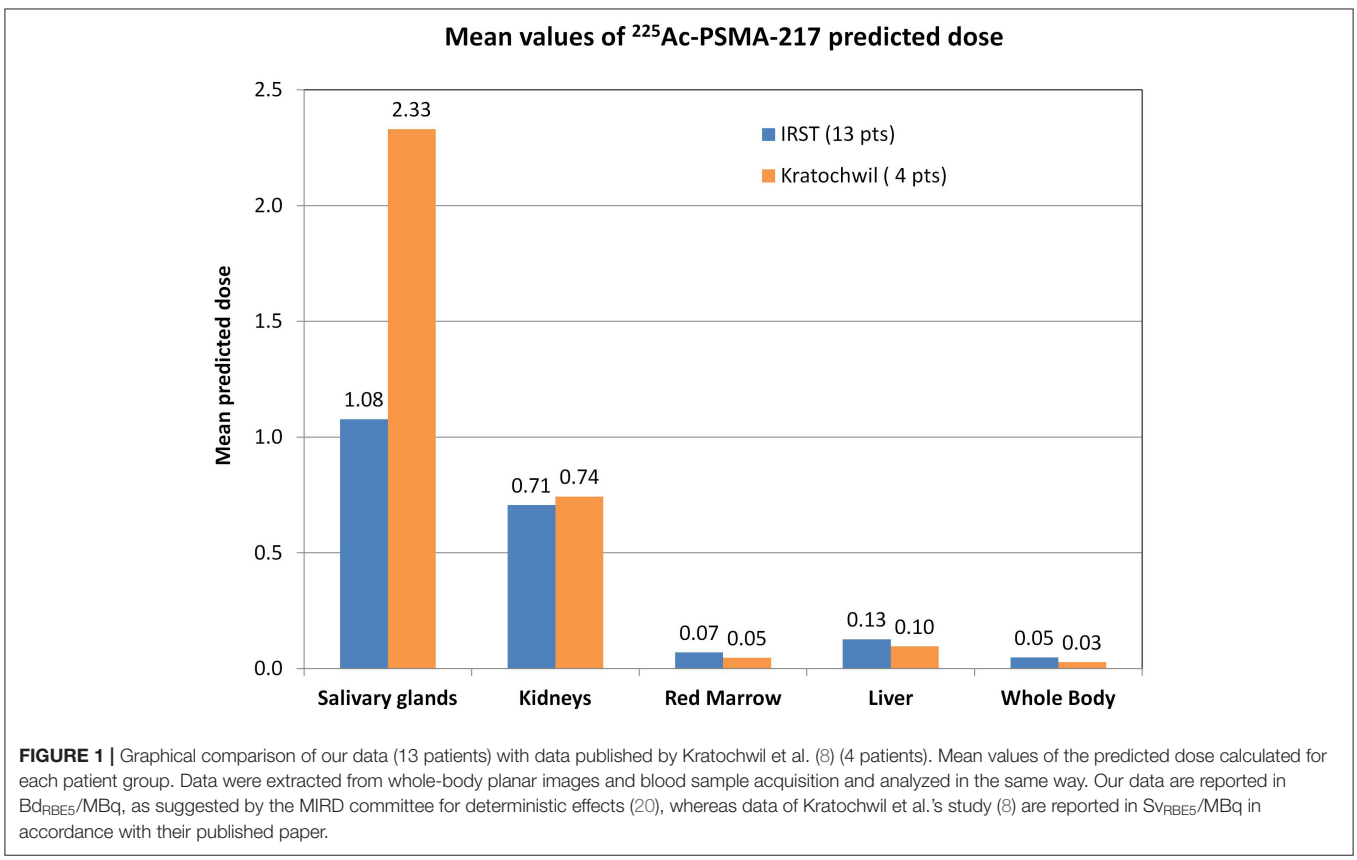

FIGURE 1 | Graphical comparison of our data (13 patients) with data published by Kratochwil et al. (8) (4 patients). Mean values of the predicted dose calculated for each patient group. Data were extracted from whole-body planar images and blood sample acquisition and analyzed in the same way. Our data are reported in Bd_{RBE5}/MBq, as suggested by the MIRD committee for deterministic effects (20), whereas data of Kratochwil et al.'s study (8) are reported in Sv_{RBE5}/MBq in accordance with their published paper.

kidneys, 12.1 h^{-1} (4.2–33.8) for liver, 25.5 h^{-1} (1.7–46.2) for PGs, 10.0 h^{-1} (2.8–32.7) for SGs, 2.1 h^{-1} (0.5–15.2) for RM, and 5.7 h^{-1} (1.4–17.0) for WB. The mean contribution (range) values to the total predictive dose of each single particle emission were 99.47% (98.20–99.79), 0.49% (0.22–1.76), and 0.05% (0.02–0.15) for α, β, and γ, respectively. Median (range) predictive doses were 0.67 Bd_{RBE5}/MBq (0.15–1.81) for kidneys, 0.11 Bd_{RBE5}/MBq (0.02–0.24) for liver, 0.86 Bd_{RBE5}/MBq (0.49–2.43) for PGs, 1.05 Bd_{RBE5}/MBq (0.42–1.98) for SGs, 0.07 Bd_{RBE5}/MBq (0.03–0.14) for RM, and 0.04 Bd_{RBE5}/MBq (0.02–0.11) for WB (**Table 1**).

Figure 1 compares our data with those of Kratochwil et al.'s study (8). The reduced absorbed dose observed with ^{177}Lu-PSMA dosimetry (11, 12) was also confirmed for ^{225}Ac-PSMA predictive dosimetry, with a 53% decreased of predicted dose in salivary glands in our patient group [1.08 vs. 2.33 Sv_{RBE5}/MBq (8), mean values].

Comparison With EBRT Biological Model

Table 2 reports the values of parameters used for BED calculation. Considering xerostomia as a toxicity endpoint, a value of α/β equal to 3 Gy was used (37, 38), whereas a value of 0.46 h^{-1} was used for the μ (39, 40). For high-LET radiation, assuming $RBE_{exp} = 5$ (19), the RBE_M was 8.2. Fractional dose d of the reference low-LET radiation was assumed to be 2 Gy. As predictive dosimetry, an injection activity of 100 kBq/kg was assumed on the basis of single patient weight (8).

Considering this RBE_M value and an injection activity of 100 kBq/kg, the BED_H was calculated for the predictive dose values reported in *Predictive Dose for ^{225}Ac-PSMA With a Prostate-Specific Membrane Antigen*. Median (range) BED_H values were 36.5 Gy (12.4–237.0) for PGs, 55.0 Gy (12.1–203.9) for SGs, and 51.9 Gy (15.9–220.4) for both salivary glands (**Table 3**). A QUANTEC dose constraint of $D_L = 26$ Gy on PGs delivered in N = 30 fractions was considered for EBRT (30, 31) for late xerostomia induction at 1-year post-EBRT. This dose constraint corresponds to a BED_L of 33.5 Gy. For 100 kBq/kg injection activity, 7 of our 13 patients, the PG BED_H was >33.5 Gy. Rescaling data to Kratochwil et al.'s (8) mean predicted dose value (*i.e.,* corresponding to a patient population without salivary gland protectors), the BED'_H for all 13 patients was >33.5 Gy (data not shown).

We used Strigari et al.'s data for NTCP modeling (32). In this model, the dose to the salivary glands is the mean dose of both PGs and SGs and converted into EQD2. Considering a salivary flow reduction of <45% of the initial value at 3-month post-EBRT (grade ≥ 2, G2+) as an endpoint, the fitting parameters were TD50 = 14 Gy_{EQD2} and m = 0.88 [personal communication (32)]. **Figure 2** shows the comparison between the considered NTCP model and the data rescaled to Kratochwil et al.'s (8) mean predicted dose value (**Figure 2A**) and our data (**Figure 2B**). The different activity concentration levels are also indicated. Without the administration of salivary gland protectors, the predicted probability values of acute G2+ xerostomia based on the NTCP model were 97% (95% CI: 79–100%) for A_i equal to 50 kBq/kg and 100% (95% CI: 99–100%) for A_i equal to 100 g, 150, and 200 kBq/kg (**Figure 2A**). The predicted incidence values of xerostomia for TAT combined with salivary gland protectors were 40% (95% CI: 10–48%) for A_i equal to 50 kBq/kg, 94% (95% CI: 72–100%) for A_i equal to 100 kBq/kg, 100% (95% CI: 99–100%) for A_i equal to 150 kBq/kg, and 100% (95% CI: 100–100%) for A_i equal to 200 kBq/kg (**Figure 2B**).

TABLE 2 | Value of parameters used for BED evaluation.

Parameter	Value	Note (reference)
α/β	3 Gy	Xerostomia (37, 38)
μ	0.46 h^{-1}	Repair time (39, 40)
^{225}Ac-PSMA injected activity	100 kBq/kg	(8)
RBE_{exp} high-LET radiation	5	(19)

DISCUSSION

The predictive dosimetry of ^{225}Ac-PSMA confirms the reduction of absorbed dose previously reported in our protocol with ^{177}Lu-PSMA in combination with folic glutamate tablets and ice pack application as salivary gland protectors (11, 12). The conversion from a β/γ emission to an α/β/γ emission could not be calculated with a global scaling factor between ^{177}Lu and ^{225}Ac emissions. In fact, the conversion of ^{177}Lu emission into the decay chain of ^{225}Ac includes daughters emitting α, β, and γ radiations with different branching ratios and different RBE values. Therefore, the scaling factor takes into account the emission of each daughter and is a linear combination of the

TABLE 3 | BED_H calculated for parotid and submandibular glands.

	Parotid glands (Gy)	Submandibular glands (Gy)	Salivary glands (Gy)
Patient 1	56.6	57.8	57.2
Patient 2	237.0	203.9	220.4
Patient 3	15.4	22.0	18.7
Patient 4	42.1	140.5	91.3
Patient 5	36.5	15.7	26.1
Patient 6	22.9	33.8	28.3
Patient 7	27.6	104.7	66.2
Patient 8	22.2	55.0	38.6
Patient 9	12.4	91.3	51.9
Patient 10	49.0	23.4	36.2
Patient 11	125.9	34.0	80.0
Patient 12	142.2	138.2	140.2
Patient 13	19.7	12.1	15.9
Median (range)	36.5 (12.4–237.0)	55.0 (12.1–203.9)	51.9 (15.9–220.4)
Mean (SD)	62.3 (66.5)	71.7 (59.8)	67.0 (57.6)

*Salivary gland BED_H is calculated as mean of parotid and submandibular gland BED_H values. Used parameters are reported in **Table 2**. SD, standard deviation.*

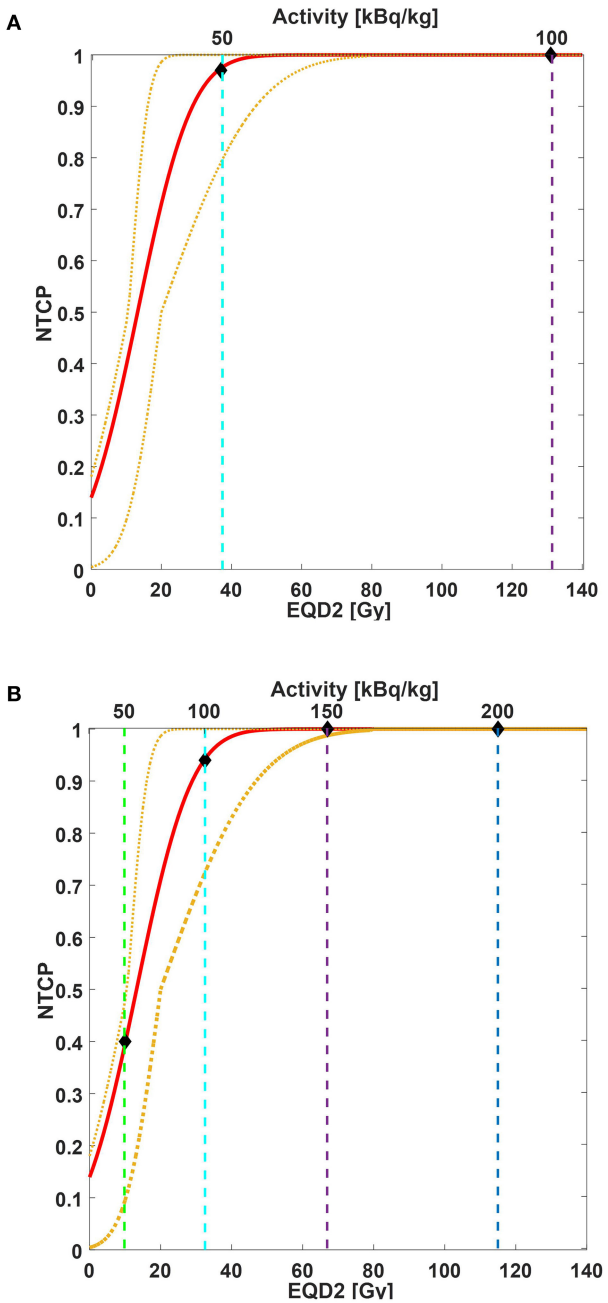

FIGURE 2 | NTCP curve (red line) of acute xerostomia incidence as a function of mean EQD2 values (bottom x-axis) and injected activity (top x-axis). Yellow dotted lines are 95% CI. NTCP model parameters: TD%50 = 14 Gy_{EQD2}, m = 0.88. Considered endpoint: grade ≥ 2 xerostomia 3-month post-EBRT. Considered structures: salivary glands (parotid and submandibular glands together). Both EBRT and TAT doses were converted into EQD2. For EQD2 calculation: **(A)** predictive dose value estimated for our patient cohort and rescaled to Kratochwil et al.'s (8) mean predicted dose value is used; **(B)** predictive dose estimated for our patient cohort is used. Vertical dashed lines correspond to 50 kBq/kg (green line), 100 kBq/kg (cyan line), 150 kBq/kg (purple line), and 200 kBq/kg (blue line). Diamonds indicate the estimated incidence of acute xerostomia based on EBRT NTCP modeling for the injected activities of interest.

different branching ratios of the radiations emitted weighted by the corresponding RBE factor [see Supplementary Table 4 of Supplementary Material in reference (18)]. We obtained a reduction of 53% in predicted dose compared with previously published data, i.e., 1.08 vs. 2.33 Sv_{RBE5}/MBq (8). Kratochwil et al. (8, 9) did not report any use of salivary gland protectors in their study. Therefore, our results differ from those of Kratochwil et al.'s study (8) for the potential sparing effect of both ice pack application and polyglutamate folate administration. The data from both studies are derived with the same dosimetry protocol and procedure and are therefore comparable. Acute xerostomia was identified by Kratochwil et al. (8, 9) as major toxicity impairing treatment, and the authors experimentally identified 100 kBq/kg as an activity concentration threshold capable of avoiding acute toxicity. Kratochwil et al. (8) reported the xerostomia incidence stratified with injection activity only in a subgroup of 16 patients. In particular, four patients were injected with 50 kBq/kg, and none experienced severe xerostomia; four patients were injected with 100 kBq/kg, and none experienced severe xerostomia; two patients were injected with 150 kBq/kg, and one experienced severe xerostomia; and four patients were injected with 200 kBq/kg, and three experienced severe xerostomia.

Comparing our data with the acute tolerance threshold of 17 Sv_{RBE5} reported in Kratochwil et al. (8, 18), we did not expect to find a high-grade xerostomia incidence in our treatment for 100 kBq/kg ^{225}Ac-PSMA injected activity. At the same time, when the EBRT model of acute xerostomia was applied to our data rescaled to Kratochwil's (8) mean predicted dose value, the expected incidence rate was higher than that observed by Kratochwil's group (8). The large discrepancy observed between the clinical data of Kratochwil's study (8) and our model derived from the combination of EBRT and brachytherapy formalisms may arise from different factors.

First of all, we should consider the limited cohort of patients administered ^{225}Ac-PSMA for whom toxicity data were evaluated and stratified with injected activity (16 patients), resulting in a fairly large error in the observed toxicity incidence (8). In addition, we scaled our data with a factor equal to the ratio between the mean value of our population and the one reported in Kratochwil et al.'s (8) study, calculated on dosimetric data for four patients. However, the reduced number of patients included in the dosimetry study of Kratochwil's group (8) (4 patients) may strongly impact the calculated scaling factor between the two patients' populations. Therefore, NTCP values calculated on the rescaled patient population should be considered with caution. In addition, the attenuation correction, which was not considered in the dosimetric analysis, may play a relevant role to account for the discrepancy between the predicted and observed toxicity.

Despite the above issues, other radiobiological considerations may affect the biological evaluation of toxicity induction based on predictive dosimetry estimations for TAT therapy from ^{177}Lu-PSMA data. We assumed that there would be a similar

local uptake and temporal distribution between ^{177}Lu-PSMA and all daughters of the decay chain of ^{225}Ac-PSMA, mainly governed by the PSMA carrier. Although this assumption may be considered sufficiently robust if ^{177}Lu-PSMA and ^{225}Ac-PSMA are considered alone, it is no longer valid for all daughters in the decay chain. In fact, if the link between ^{225}Ac daughters and the PSMA carrier is no longer stable, a significant redistribution of daughter nuclides may occur throughout the body, and, consequently, their uptake may substantially differ from ^{177}Lu-PSMA distribution (41).

Moreover, although a uniform dose distribution was assumed inside each salivary gland, the pre-therapy ^{68}Ga-PSMA-HBED-11 PET/CT (**Supplementary Figure S1**) clearly showed that this was not the case. The standard uptake value distribution of ^{68}Ga-PSMA radiotracer could be considered a surrogate of ^{225}AC-PSMA uptake. Taking into account that the dose delivered in TAT could be considered extremely localized, the non-uniform ^{68}Ga-PSMA standard uptake value distribution could, therefore, also be considered a surrogate of TAT dose distribution. **Supplementary Figure S3** depicts the dose distribution and **Supplementary Figure S4** the dose–volume histogram (DVH) of PGs and SGs in a head-and-neck cancer patient who underwent EBRT. Thanks to the new technology of intensity-modulated radiotherapy (IMRT), EBRT allows sparing a portion of salivary glands and results in a non-uniform dose distribution inside PGs. Beyond the non-uniform distribution, one noticeable aspect is that the portions of salivary glands receiving the high doses in the case of ^{68}Ga-PSMA (**Supplementary Figures S1**, **S2**) are different from the high-dose region in EBRT (**Supplementary Figures S3**, **S4**). For this reason, the considerations achieved on toxicity impact based on tissue damage assumed from EBRT dose distribution should be carefully managed when applied to RLT. A three-dimensional (3D) approach would be favorable to take into account these differences. However, the dosimetry approach based on 2D planar images does not permit differences in regional uptake to be seen, and the dose evaluation is therefore limited to the mean predicted dose evaluation. It is also well-known from EBRT experiences that both the mean dose to PGs and the DVH constraints should be taken into account to reduce the impact of xerostomia caused by the volume effect for parallel organs (42–44). None of these parameters can be evaluated without 3D information on activity uptake. A 3D SPECT imaging with ^{177}Lu-PSMA centered on the neck region is needed to be able to calculate dose distribution and generate a DVH. The uptake information for each voxel derived from 3D SPECT ^{177}Lu imaging can then be converted into ^{225}Ac emission with the same formalism mentioned earlier. However, the limited field-of-view of traditional SPECT scanners does not allow for 3D imaging acquisition of the WB, and SPECT acquisition is generally only centered in the abdominal region to evaluate the dose to the kidneys, other important dose-limiting organs in RLT (45). Fortunately, new SPECT scanners are beginning to emerge that are capable of providing full 3D SPECT imaging along the WB by combining a 3D acquisition with a dynamic longitudinal motion of the patient couch. Another solution could be to perform a hybrid dosimetry evaluation where time–activity curves are evaluated on serial planar images, and the 3D dose distribution is evaluated in a single 3D SPECT acquired at a single time-point post-injection (45). Despite this, even with the conversion of ^{177}Lu 3D dose distribution into ^{225}Ac, another factor to take into consideration is that the local damage performed by low-LET β-particle and γ-emitters is different from the one of α-particle, characterized by clusters of spots with high-energy deposition (8, 46). The presence of hot spots may dramatically change the pattern of tissue damage when changing from a low-LET β/γ-emitter to a high-LET α-emitter, and this difference should also be taken into account.

With regard to the salivary gland composition, it is known that they are mainly composed of adipose tissue, ductal, and acinar cells, able to produce saliva. Histopathological studies of patients treated with EBRT to the neck region have shown that irradiation of salivary glands results in a loss of the acinar cell component (47), which correlates with both volume reduction of the glands and decreased saliva flow. Moreover, van Luijk et al. (48) found that the recovery of radiation-induced xerostomia can be repaired by a pool of stem cells, mainly located in the central region of PGs. The authors showed that the protection of this central zone during EBRT in head-and-neck patients enables organ function to be preserved. All of these factors may play an important role in the functional damage induced by tissue irradiation and warrant further investigation. We considered salivary glands uniform in their composition and radiosensitivity. To better understand the underlying radiobiological process of damage, the interaction between short-range high-LET α-particle and different salivary gland tissue components should be investigated with microdosimetry and autoradiography (19).

Assumptions were also made about the parameters used in BED and NTCP calculation. In a first approximation, we considered a mono-exponential curve fitting capable of describing the long-term organ washout. However, time–activity curves are generally best fitted with bi-exponential curves. An improved model would consider both λ parameters of bi-exponential curve fitting. Furthermore, in the BED_H formalism for the mixture of radionuclide, we assumed the ^{225}Ac λ-value valid for all the daughters in the decay chain. In fact, in our case, the mixture is produced as a consequence of the ^{225}Ac decay, which has life-time significantly longer than one of all the daughter isotopes. Therefore, we assume that the decay rates of all daughter isotopes are dominated by the one of ^{225}Ac.

Moreover, it is important to point out that in our model, the RBE_{exp} was assumed equal to 5, in accordance with previously published studies and MIRD recommendations (19). However, this value, which was extracted from *in vitro* experiments, has never been clinically validated in human subjects (49). For this reason, some authors (49, 50) prefer not to apply an RBE factor to the calculated dose. In our radiobiological model, we adopted the formalism proposed by Dale for BED for high-LET particle, including the RBE_M (22). Carabe-Fernandez et al. (51) published a model that was also the minimum value of RBE (RBE_{min}) and is included in the BED formalism. They

found that the dependence of BED from RBE_{min} has a larger impact on acute toxicity incidence than for the late one. In fact, the RBE_{min} could assume values less than unity, reducing the contribution of the quadratic term in the BED formula. The dependence of BED for a high-LET particle on both RBE_M and RBE_{min} may explain the observed discrepancy between model and clinical data in our study. Further improvements of the present model should consider both terms, RBE_M and RBE_{min}.

Furthermore, the RBE experimental values provided in the literature for α-particles are measured with a single emitter. To our knowledge, no RBE experimental data are reported in the literature for a mixture of different radionuclides with different half-life and the emission of α-particles of different energies.

Lastly, it is possible that the high-dose rate involved with ^{225}Ac TAT could potentially shift the radiobiology effect in a region of RBE plot of overkilling (52). Prospective clinical studies are therefore required to be able to provide clinical data of toxicity impact in combination with dosimetric data.

Palm et al. (19, 53) found that the polonium can diffuse away from the decay site, reducing, therefore, the local damage. Inside the ^{225}Ac decay chain, the ^{213}Po contributes to 30% of the absorbed dose in the sphere model. By removing the ^{213}Po contribution from the radiobiological calculation of the rescaled patient population to the Kratochwil et al. (8) data, the EQD2 of salivary glands for 100-kBq/kg injected activity is reduced of 66%. The corresponding NTCP values then shifted to 71% (95% CI: 50–99%) for A_i equal to 50 kBq/kg, 100% (95% CI: 99–100%) for A_i equal to 100 kBq/kg, and 100% (95% CI: 100–100%) for A_i equal to 150 and 200 kBq/kg (data not shown). Even with the correction proposed by Palm et al. (53), the model remains conservative, as it overestimates the clinical data of Kratochwil et al.'s study (8). A model able to describe the source–target interaction at the microscopic level is therefore required to improve the agreement between the clinical data and the theoretical model (19, 54). As suggested by Kvinnsland et al. (54), a microdosimetry evaluation that takes into account both the energy spectrum and intracellular differences can describe the underplaying biological process in detail, whereas a mean value may not be sufficiently representative.

Finally, the NTCP model based on EBRT also has different issues that should be carefully taken into account. First, there is no consensus regarding TD50 and m fitting parameters in different studies, with values spanning over a wide range (TD50 = 28.4 to 52 Gy, m = 0.10–0.40 for late xerostomia induction) (55). This is due to substantial variability in study design such as differences in treatment modality and dose distribution, dose reporting of the single spared PG or a mean value over both, inclusion or not of SGs and/or oral cavity, salivary measurement methods, considered endpoint, segmentation, inter-gland sensitivity, and/or patient geographical location (55). Given that both PGs and SGs are irradiated in TAT, we compared our data with those obtained using the model developed by Strigari et al. (32), which has the advantage of including both PG and SG mean dose and considering acute grade ≥ 2 xerostomia at 3-month post-EBRT as an endpoint (personal communication).

Methods for salivary glands protection have previously been implemented for both PSMA-based therapy [^{177}Lu-PSMA RLT (3, 56)] and imaging [^{68}Ga-PSMA PET/CT (57)]. However, the efficacy of these methodologies in TAT has never been investigated before, and no toxicity modeling was tested with these settings.

The results we obtained on the mean predictive dose reduction when using protectors specific for salivary glands in combination with ^{177}Lu-PSMA therapy would also appear promising for TAT. However, our results should be confirmed with ^{225}Ac-PSMA therapy data and post-injection evaluation of toxicity and treatment outcome. BED calculation and NTCP modeling overestimate the incidence of high-grade xerostomia reported in some studies, suggesting that further elements should be included in the biological model of tissue damage induced by TAT. Further investigation and appropriate modeling are warranted to describe better the underlying radiobiological process of damage from high-LET therapy. This can be done by carrying out prospective trials with defined toxicity endpoints and dosimetry procedures. At the same time, appropriate NTCP biological models specific for TAT should be developed based on clinical data.

DATA AVAILABILITY STATEMENT

The datasets generated for this study are available on request to the corresponding author.

ETHICS STATEMENT

The studies involving human participants were reviewed and approved by Ethics Committee of Area Vasta Romagna and by the competent Italian regulatory authorities (Ethical approval no. 1704 of 15.02.2017, Protocol IRST 185.03). The patients/participants provided their written informed consent to participate in this study.

AUTHOR CONTRIBUTIONS

MLB: dosimetry, data analysis, and writing. AS: study conception and critical revision of the manuscript for intellectual content. FC: data analysis. EM: dosimetry. GP, FM, and PC: image analysis and diagnosis. VDI: radiopharmaceutical preparation. LS: EBRT modeling. GP, SS, SN, MC, and AR: patient management. All authors: contributed to the article and approved the submitted version.

FUNDING

This work was partially supported by the Fondazione AIRC per la Ricerca sul Cancro, Associazione Italiana per la Ricerca sul Cancro (project code IG20476) and the Italian Ministry of Health (Ricerca Finalizzata, code RF-2016-02364230).

ACKNOWLEDGMENTS

We thank Prof. Kratochwil and Prof. Schmidt for the help in providing a ^{225}Ac dose estimation methodology. The authors thank Gràinne Tierney for editorial assistance.

SUPPLEMENTARY MATERIAL

The Supplementary Material for this article can be found online at: https://www.frontiersin.org/articles/10.3389/fonc.2020.531660/full#supplementary-material

Supplementary Figure 1 | Pre-treatment ^{68}Ga-PSMA-HBED-11 PET/CT image. The non-uniform uptake distribution inside parotid glands is clearly visible.

Supplementary Figure 2 | Cumulative histogram of standard uptake value (SUV) of parotid and submandibular glands.

Supplementary Figure 3 | Dose distribution of a head-and-neck cancer patient treated with helical TomoTherapy (66, 60, and 45 Gy in 30 fractions). Red contour for 60 Gy target, dark-red and cyan contours for right and left PGs respectively. Mean absorbed dose: 25.3, 25.9, 50.6, and 50.1 Gy for right and left PGs, right and left SGs respectively.

Supplementary Figure 4 | Dose-volume histogram (DVH) of parotid and submandibular glands.

REFERENCES

1. Bodei L, Paganelli G, Mariani G. Receptor radionuclide therapy of tumors: a road from basic research to clinical applications. *J Nucl Med.* (2006) 47:375–7. Available online at: http://jnm.snmjournals.org/content/47/3/375.long
2. Kong G, Hicks RJ. Peptide receptor radiotherapy: current approaches and future directions. *Curr Treat Options Oncol.* (2019) 20:77. doi: 10.1007/s11864-019-0677-7
3. Fendler WP, Rahbar K, Herrmann K, Kratochwil C, Eiber M. 177Lu-PSMA radioligand therapy for prostate cancer. *J Nucl Med.* (2017) 58:1196–201. doi: 10.2967/jnumed.117.191023
4. Baum RP, Kulkarni HR, Schuchardt C, Singh A, Wirtz M, Wiessalla S, et al. 177Lu-labeled prostate-specific membrane antigen radioligand therapy of metastatic castration-resistant prostate cancer: safety and efficacy. *J Nucl Med.* (2016) 57:1006–13. doi: 10.2967/jnumed.115.168443
5. Hofman MS, Violet J, Hicks RJ, Ferdinandus J, Ping Thang S, Akhurst T, et al. [177 Lu]-PSMA-617 radionuclide treatment in patients with metastatic castration-resistant prostate cancer (LuPSMA trial): a single-centre, single-arm, phase 2 study. *Lancet Oncol.* (2018) 19:825–33. doi: 10.1016/S1470-2045(18)30198-0
6. Kratochwil C, Giesel FL, Stefanova M, Beneova M, Bronzel M, Afshar-Oromieh A, et al. PSMA-targeted radionuclide therapy of metastatic castration-resistant prostate cancer with 177Lu-labeled PSMA-617. *J Nucl Med.* (2016) 57:1170–6. doi: 10.2967/jnumed.115.171397
7. Paganelli G, De Giorgi U. [177Lu]-PSMA-617 for targeted prostate cancer treatment: a magic bullet? *Lancet Oncol.* (2018) 19:725–6. doi: 10.1016/S1470-2045(18)30268-7
8. Kratochwil C, Bruchertseifer F, Rathke H, Bronzel M, Apostolidis C, Weichert W, et al. Targeted alpha therapy of mCRPC with 225Actinium-PSMA-617: dosimetry estimate and empirical dose finding. *J Nucl Med.* (2017) 58:1624–31. doi: 10.2967/jnumed.117.191395
9. Kratochwil C, Bruchertseifer F, Rathke H, Hohenfellner M, Giesel FL, Haberkorn U, et al. Targeted alpha therapy of mCRPC with 225Actinium-PSMA-617: swimmer-plot analysis suggests efficacy regarding duration of tumor-control. *J Nucl Med.* (2018) 59:795–802. doi: 10.2967/jnumed.117.203539
10. Paganelli G, De Giorgi U. *Radiometabolic Therapy (RMT) With 177Lu PSMA 617 in Advanced Castration Resistant Prostate Cancer (CRPC): Efficacy and Toxicity Evaluation* (EudraCt/RSO number: 2016-002732-32, NCT03454750). Meldola, FC. (2017).
11. Sarnelli A, Belli ML, Di Iorio V, Mezzenga E, Celli M, Severi S, et al. Dosimetry of 177 Lu-PSMA-617 after mannitol infusion and glutamate tablet administration: preliminary results of EUDRACT/RSO 2016-002732-32 IRST protocol. *Molecules.* (2019) 24:621. doi: 10.3390/molecules24030621
12. Paganelli G, Sarnelli A, Severi S, Sansovini M, Belli ML, Monti M, et al. Dosimetry and safety of ^{177}Lu PSMA-617 along with polyglutamate parotid gland protector: preliminary results in metastatic castration-resistant prostate cancer patients. *Eur J Nucl Med Mol Imaging.* (2020). doi: 10.1007/s00259-020-04856-1. [Epub ahead of print].
13. van Kalmthout LWM, Lam MGEH, de Keizer B, Krijger GC, Ververs TFT, de Roos R, et al. Impact of external cooling with icepacks on 68Ga-PSMA uptake in salivary glands. *EJNMMI Res.* (2018) 8:56. doi: 10.1186/s13550-018-0408-2
14. Matteucci F, Mezzenga E, Caroli P, Di Iorio V, Sarnelli A, Celli M, et al. Reduction of 68Ga-PSMA renal uptake with mannitol infusion: preliminary results. *Eur J Nucl Med Mol Imaging.* (2017) 44:2189–94. doi: 10.1007/s00259-017-3791-4
15. Siegel J a, Thomas SR, Stubbs JB, Stabin MG, Hays MT, Koral KF, et al. MIRD pamphlet no. 16: techniques for quantitative radiopharmaceutical biodistribution data acquisition and analysis for use in human radiation dose estimates. *J Nucl Med.* (1999) 40:37S−61S.
16. Bolch WE, Bouchet LG, Robertson JS, Wessels BW, Siegel JA, Howell RW, et al. MIRD Pamphlet No. 17: the dosimetry of nonuniform activity distributions- radionuclide S values at the voxel level. *J Nucl Med.* (1998) 40:11s−36s.
17. Stabin MG, Sparks RB, Crowe E. OLINDA/EXM: the second-generation personal computer software for internal dose assessment in nuclear medicine. *J Nucl Med.* (2005) 46:1023–27. Available online at: http://jnm.snmjournals.org/content/46/6/1023.long
18. Kratochwil C, Schmidt K, Afshar-Oromieh A, Bruchertseifer F, Rathke H, Morgenstern A, et al. Targeted alpha therapy of mCRPC: dosimetry estimate of 213Bismuth-PSMA-617. *Eur J Nucl Med Mol Imaging.* (2018) 45:31–37. doi: 10.1007/s00259-017-3817-y
19. Sgouros G, Roeske JC, McDevitt MR, Palm S, Allen BJ, Fisher DR, et al. MIRD pamphlet no. 22 (Abridged): radiobiology and dosimetry of-particle emitters for targeted radionuclide therapy. *J Nucl Med.* (2010) 51:311–28. doi: 10.2967/jnumed.108.058651
20. Sgouros G, Howell RW, Bolch WE, Fisher DR. MIRD commentary: proposed name for a dosimetry unit applicable to deterministic biological effects–the barendsen (Bd). *J Nucl Med.* (2009) 50:485–7. doi: 10.2967/jnumed.108.057398
21. Dale R, Carabe-Fernandez A. The radiobiology of conventional radiotherapy and its application to radionuclide therapy. *Cancer Biother Radiopharm.* (2005) 20:47–51. doi: 10.1089/cbr.2005.20.47
22. Dale RG, Jones B. The assessment of RBE effects using the concept of biologically effective dose. *Int J Radiat Oncol Biol Phys.* (1999) 43:639–45. doi: 10.1016/S0360-3016(98)00364-2
23. Brenner DJ. The linear-quadratic model is an appropriate methodology for determining isoeffective doses at large doses per fraction. *Semin Radiat Oncol.* (2008) 18:234–9. doi: 10.1016/j.semradonc.2008.04.004
24. Barendsen GW. Dose fractionation, dose rate and iso-effect relationships for normal tissue responses. *Int J Radiat Oncol Biol Phys.* (1982) 8:1981–97. doi: 10.1016/0360-3016(82)90459-X
25. Antipas V, Dale RG, Coles P. A theoretical investigation into the role of tumour radiosensitivity, clonogen repopulation, tumour shrinkage and radionuclide RBE in permanent brachytherapy implants of 125I and 103Pd. *Phys Med.* (2001) 46:2557–69. doi: 10.1088/0031-9155/46/10/304
26. Nath R, Bice WS, Butler WM, Chen Z, Meigooni AS, Narayana V, et al. AAPM recommendations on dose prescription and reporting methods for permanent interstitial brachytherapy for prostate cancer: report of task group 137. *Med Phys.* (2009) 36:5310–22. doi: 10.1118/1.3246613
27. Chen Z, Nath R. Biologically effective dose (BED) for interstitial seed implants containing a mixture of radionuclides with different half-lives. *Int J Radiat Oncol Biol Phys.* (2003) 55:825–34. doi: 10.1016/S0360-3016(02)04282-7

28. Dahle J, Bruland ØS, Larsen RH. Relative biologic effects of low-dose-rate α-emitting 227Th-Rituximab and β-emitting 90Y-tiuexetan-ibritumomab versus external beam X-radiation. *Int J Radiat Oncol Biol Phys.* (2008) 72:186–92. doi: 10.1016/j.ijrobp.2008.05.029
29. Hamacher KA, Sgouros G. A schema for estimating absorbed dose to organs following the administration of radionuclides with multiple unstable daughters: a matrix approach. *Med Phys.* (1999) 26:2526–8. doi: 10.1118/1.598788
30. Drug C, Scherman E, Lee N. RTOG 0912. *A Randomized Phase II Study of Concurrent Intensity Modulated Radiation Therapy (IMRT), Paclitaxel and Pazopanib (NSC 737754)/Placebo, for the Treatment of Anaplastic Thyroid Cancer*. Philadelphia, PA (2010).
31. Wu VWC, Leung KY. A review on the assessment of radiation induced salivary gland damage after radiotherapy. *Front Oncol.* (2019) 9:1090. doi: 10.3389/fonc.2019.01090
32. Strigari L, Benassi M, Arcangeli G, Bruzzaniti V, Giovinazzo G, Marucci L. A novel dose constraint to reduce xerostomia in head-and-neck cancer patients treated with intensity-modulated radiotherapy. *Int J Radiat Oncol Biol Phys.* (2010) 77:269–76. doi: 10.1016/j.ijrobp.2009.07.1734
33. McMahon SJ. The linear quadratic model: usage, interpretation and challenges. *Phys Med Biol.* (2019) 64:01TR01. doi: 10.1088/1361-6560/aaf26a
34. Hobbs RF, Howell RW, Song H, Baechler S, Sgouros G. Redefining relative biological effectiveness in the context of the EQDX formalism: implications for alpha-particle emitter therapy. *Radiat Res.* (2014) 181:90–8. doi: 10.1667/RR13483.1
35. Lyman JT. Complication probability as assessed from dose-volume histograms. *Radiat Res.* (1985) 104:S13–19. doi: 10.2307/3576626
36. Niemierko A, Goitein M. Calculation of normal tissue complication probability and dose-volume histogram reduction schemes for tissues with a critical element architecture. *Radiother Oncol.* (1991) 20:166–76. doi: 10.1016/0167-8140(91)90093-V
37. Joiner M, van der Kogel A. *Basic Clinical Radiobiology*. CRC Press (2009).
38. Herrmann T, Baumann M, Dörr W. *Klinische Strahlenbiologie : Kurz und Bündig*. Elsevier; Urban & Fischer (2006).
39. Dale RG. Dose-rate effects in targeted radiotherapy. *Phys Med Biol.* (1996) 41:1871–84. doi: 10.1088/0031-9155/41/10/001
40. Dale RG. The application of the linear-quadratic dose-effect equation to fractionated and protracted radiotherapy. *Br J Radiol.* (1985) 58:515–28. doi: 10.1259/0007-1285-58-690-515
41. Kruijff RM, Raavé R, Kip A, Molkenboer-Kuenen J, Morgenstern A, Bruchertseifer F, et al. The *in vivo* fate of 225Ac daughter nuclides using polymersomes as a model carrier. *Sci Rep.* (2019) 9:11671. doi: 10.1038/s41598-019-48298-8
42. Viswanathan AN, Oncologist G, Miller BE, Biology T, Weidhaas J, Physics M, et al. Radiation Therapy Oncology Group RTOG 0921. A phase II study of postoperative Intensity Modulated Radiation Therapy (IMRT) with concurrent Cistiplatin and Bevacizumab followed by Carboplatin and Paclitaxel for patients with endometrial cancer. *Cancer*. (2015) 121:2156–63. doi: 10.1002/cncr.29337
43. Broggi S, Salco E, Fiorino C, Belli ML, Richetti F, Dell'Oca I, et al. The shape of parotid DVH predicts the entity of gland deformation during IMRT for head and neck cancers. *Technol Cancer Res Treat.* (2014) 14:683–91. doi: 10.7785/tcrt.2012.500440
44. van Luijk P, Faber H, Schippers JM, Brandenburg S, Langendijk JA, Meertens H, et al. Bath and shower effects in the rat parotid gland explain increased relative risk of parotid gland dysfunction after intensity-modulated radiotherapy. *Int J Radiat Oncol Biol Phys.* (2009) 74:1002–5. doi: 10.1016/j.ijrobp.2009.03.039
45. Belli ML, Mezzenga E, Di Iorio V, Celli M, Caroli P, Canali E, et al. A whole body dosimetry protocol for peptide-receptor radionuclide therapy (PRRT): 2D planar image and hybrid 2D+3D SPECT/CT image methods. *J Vis Exp*. (2020) 158. doi: 10.3791/60477
46. Jaggi JS, Seshan SV, McDevitt MR, LaPerle K, Sgouros G, Scheinberg DA. Renal tubulointerstitial changes after internal irradiation with α-particle-emitting actinium daughters. *J Am Soc Nephrol.* (2005) 16:2677–89. doi: 10.1681/ASN.2004110945
47. Teshima K, Murakami R, Yoshida R, Nakayama H, Hiraki A, Hirai T, et al. Histopathological changes in parotid and submandibular glands of patients treated with preoperative chemoradiation therapy for oral cancer. *J Radiat Res.* (2012) 53:492–6. doi: 10.1269/jrr.11115
48. van Luijk P, Pringle S, Deasy JO, Moiseenko VV, Faber H, Hovan A, et al. Sparing the region of the salivary gland containing stem cells preserves saliva production after radiotherapy for head and neck cancer. *Sci Transl Med.* (2015) 7:305ra147. doi: 10.1126/scitranslmed.aac4441
49. Feinendegen LE, McClure JJ. *Alpha-Emitters for Medical Therapy Workshop*. (1996) Available online at: http://www.osti.gov/energycitations/servlets/purl/458593-T9RCrP/webviewable/.
50. Murray I, Chittenden SJ, Denis-bacelar AM, Hindorf C, Parker CC, Chua S, et al. The potential of 223 Ra and 18 F-fluoride imaging to predict bone lesion response to treatment with 223 Ra-dichloride in castration resistant prostate cancer. *Eur J Nucl Med Mol Imaging.* (2018) 44:1832–44. doi: 10.1007/s00259-017-3744-y
51. Carabe-Fernandez A, Dale RG, Jones B. The incorporation of the concept of minimum RBE (RBEmin) into the linear-quadratic model and the potential for improved radiobiological analysis of high-LET treatments. *Int J Radiat Biol.* (2007) 83:27–39. doi: 10.1080/09553000601087176
52. Mehnati P, Morimito S, Yatagai F, Furusawa Y, Kobayashi Y, Wada S, et al. Exploration of 'over kill effect' of high-LET Ar- and Fe-ions by evaluating the fraction of non-hit cell and interphase death. *J Radiat Res.* (2005) 46:343–50. doi: 10.1269/jrr.46.343
53. Palm S, Humm JL, Rundqvist R, Jacobsson L. Microdosimetry of astatine-211 single-cell irradiation: role of daughter polonium-211 diffusion. *Med Phys.* (2004) 31:218–25. doi: 10.1118/1.1640951
54. Kvinnsland Y, Stokke T, Aurlien E. Radioimmunotherapy with alpha-particle emitters: microdosimetry of cells with a heterogeneous antigen expression and with various diameters of cells and nuclei. *Radiat Res.* (2001) 155:288–96. doi: 10.1667/0033-7587(2001)155[0288:RWAPEM]2.0.CO;2
55. Deasy JO, Moiseenko V, Marks L, Chao KSC, Nam J, Eisbruch A. Radiotherapy dose-volume effects on salivary gland function. *Int J Radiat Oncol Biol Phys.* (2010) 76:58–63. doi: 10.1016/j.ijrobp.2009.06.090
56. Nedelcovych MT, Dash RP, Wu Y, Choi EY, Lapidus RS. JHU-2545 selectively shields salivary glands and kidneys during PSMA- targeted radiotherapy. *bioRxiv*. (2018) 1–36. doi: 10.1101/457085
57. Baum RP, Langbein T, Singh A, Shahinfar M, Schuchardt C, Vol GF, et al. Injection of botulinum toxin for preventing salivary gland toxicity after PSMA radioligand therapy: an empirical proof of a promising concept. *Nucl Med Mol Imaging.* (2018) 52:80–81. doi: 10.1007/s13139-017-0508-3
58. Scher HI, Morris MJ, Stadler WM, Higano C, Basch E, Fizazi K, et al. Trial design and objectives for castration-resistant prostate cancer: updated recommendations from the prostate cancer clinical trials working group 3. *J Clin Oncol.* (2016) 34:1402–18. doi: 10.1200/JCO.2015.64.2702
59. Oken M, Creech R, Tormey D, Horton J, Davis T, McFadden E, et al. Toxicity and response criteria of the eastern cooperative oncology group. *Am J Clin Oncol.* (1982) 5:649–55. doi: 10.1097/00000421-198212000-00014
60. Salvo D, Bui F, Dottorini ME. Norme di Buona Preparazione dei Radiofarmaci in Medicina Nucleare. *Notiziario di Med Nucl Imaging Mol.* (2006) 3.

Conflict of Interest: The authors declare that the research was conducted in the absence of any commercial or financial relationships that could be construed as a potential conflict of interest.

APPENDIX

The study, conducted in accordance with the Declaration of Helsinki and good clinical practice (guidelines, was approved by the Ethics Committee of Area Vasta Romagna and by the competent Italian regulatory authorities (Ethical approval no. 1704 of 15.02.2017, Protocol IRST 185.03). All patients gave written informed consent. Admission criteria were radiological progression (in soft tissue or bone) or biochemical progression (sequence of three prostate-specific antigen rising values from a screening prostate-specific antigen value $\geq$ 2 ng/ml) according to Prostate Cancer Working Group 3 in the pre-study period, refractory or unfit to conventional standard treatments (hormonal or chemotherapeutic treatment such as abiraterone, enzalutamide, and docetaxel). Other eligible criteria were age $\geq$18 years; histological or cytological confirmation of advanced castration-resistant prostate cancer [Prostate Cancer Working Group 3 criteria (58)]; measurable disease (RECIST 1.1 criteria); Eastern Cooperative Oncology Group performance status <2 (59); adequate hematological, liver, and renal functions: hemoglobin $\geq$9 g/dl, absolute neutrophil count $\geq 1.5 \times 10^9$/L, platelets $\geq 100 \times 10^9$/L, bilirubin $\leq$1.5 $\times$ upper normal limit (UNL), alanine aminotransferase and aspartate aminotransferase <2.5 $\times$ UNL (<5 $\times$ UNL in the presence of liver metastases, creatinine <2 mg/dl). Patients treated with chemotherapy and ^{223}Ra radiotherapy within 4 weeks, treated within 2 weeks with palliative radiotherapy, or with the persistence of acute toxicities from any prior therapy (grade >1, Common Terminology Criteria for Adverse Events version 4.03) were excluded.

National good preparation standards [NBP MN (60)] for pharmaceutical products were followed for ^{177}Lu-PSMA-617 production, as required by current Italian legislation. Dota-PSMA-617 was kindly provided by Endocyte Inc. (West Lafayette, IN 47906, USA), and ^{177}Lu was purchased from AAA Severijns (LuMark®, Baarle-Nassau, The Netherlands) or ITG (Endolucinbeta®, Isotope Technologies Garching GmbH, Garching, Germany). The labeling procedure and quality control of the ^{177}Lu-DOTA-PSMA-617 compound were performed in the Radiopharmacy Laboratory of our Institute (11) (IRST Istituto di Ricovero e Cura a Carattere Scientifico, Meldola, Italy).

frontiers in Oncology

ORIGINAL RESEARCH
published: 24 November 2020
doi: 10.3389/fonc.2020.531344

Brainstem NTCP and Dose Constraints for Carbon Ion RT—Application and Translation From Japanese to European RBE-Weighted Dose

Jon Espen Dale[1,2], Silvia Molinelli[3], Barbara Vischioni[3], Viviana Vitolo[3], Maria Bonora[3], Giuseppe Magro[3], Andrea Mairani[3,4], Azusa Hasegawa[3,5], Tatsuya Ohno[6], Olav Dahl[1], Francesca Valvo[3] and Piero Fossati[3,7]*

[1] Department of Clinical Science, Faculty of Medicine, University of Bergen, Bergen, Norway, [2] Department of Oncology and Medical Physics, Haukeland University Hospital, Bergen, Norway, [3] National Center of Oncological Hadrontherapy, Pavia, Italy, [4] Heidelberg Ion-Beam Therapy Center, Heidelberg, Germany, [5] Osaka Heavy Ion Therapy Center, Osaka, Japan, [6] Department of Radiation Oncology, Gunma University Graduate School of Medicine, Gunma, Japan, [7] MedAustron Ion Therapy Center, Wiener Neustadt, Austria

OPEN ACCESS

Edited by:
Ester Orlandi, Instituto Nazionale dei Tumori (IRCSS), Italy

Reviewed by:
Naruhiro Matsufuji, National Institutes for Quantum and Radiological Science and Technology, Japan
Xuanfeng Ding, William Beaumont Hospital, United States

***Correspondence:**
Barbara Vischioni
barbara.vischioni@cnao.it

Specialty section:
This article was submitted to Radiation Oncology, a section of the journal Frontiers in Oncology

Received: *31 January 2020*
Accepted: *04 September 2020*
Published: *24 November 2020*

Citation:
Dale JE, Molinelli S, Vischioni B, Vitolo V, Bonora M, Magro G, Mairani A, Hasegawa A, Ohno T, Dahl O, Valvo F and Fossati P (2020) Brainstem NTCP and Dose Constraints for Carbon Ion RT—Application and Translation From Japanese to European RBE-Weighted Dose. Front. Oncol. 10:531344. doi: 10.3389/fonc.2020.531344

Background and Purpose: The Italian *National Center of Oncological Hadrontherapy* (CNAO) has applied dose constraints for carbon ion RT (CIRT) as defined by Japan's *National Institute of Radiological Sciences* (NIRS). However, these institutions use different models to predict the *relative biological effectiveness* (RBE). CNAO applies the *Local Effect Model I* (LEM I), which in most clinical situations predicts higher RBE than NIRS's *Microdosimetric Kinetic Model* (MKM). Equal constraints therefore become more restrictive at CNAO. Tolerance doses for the brainstem have not been validated for LEM I-weighted dose ($D_{LEM\ I}$). However, brainstem constraints and a *Normal Tissue Complication Probability* (NTCP) model were recently reported for MKM-weighted dose (D_{MKM}), showing that a constraint relaxation to $D_{MKM|0.7\ cm^3}$ <30 Gy (RBE) and $D_{MKM|0.1\ cm^3}$ <40 Gy (RBE) was feasible. The aim of this work was to evaluate the brainstem NTCP associated with CNAO's current clinical practice and to propose new brainstem constraints for LEM I-optimized CIRT at CNAO.

Material and Methods: We reproduced the absorbed dose of 30 representative patient treatment plans from CNAO. Subsequently, we calculated both $D_{LEM\ I}$ and D_{MKM}, and the relationship between D_{MKM} and $D_{LEM\ I}$ for various brainstem dose metrics was analyzed. Furthermore, the NTCP model developed for D_{MKM} was applied to estimate the NTCPs of the delivered plans.

Results: The translation of CNAO treatment plans to D_{MKM} confirmed that the former CNAO constraints were conservative compared with D_{MKM} constraints. Estimated NTCPs

were 0% for all but one case, in which the NTCP was 2%. The relationship $D_{MKM}/D_{LEM\ I}$ could be described by a quadratic regression model which revealed that the validated D_{MKM} constraints corresponded to $D_{LEM\ I|0.7\ cm^3}$ <41 Gy (RBE) (95% CI, 38–44 Gy (RBE)) and $D_{LEM\ I|0.1\ cm^3}$ <49 Gy (RBE) (95% CI, 46–52 Gy (RBE)).

Conclusion: Our study demonstrates that RBE-weighted dose translation is of crucial importance in order to exchange experience and thus harmonize CIRT treatments globally. To mitigate uncertainties involved, we propose to use the lower bound of the 95% CI of the translation estimates, *i.e.*, $D_{LEM\ I|0.7\ cm^3}$ <38 Gy (RBE) and $D_{LEM\ I|0.1\ cm^3}$ <46 Gy (RBE) as brainstem dose constraints for 16 fraction CIRT treatments optimized with LEM I.

Keywords: carbon ion radiotherapy, normal tissue complication probability, dose constraints, local effect model, microdosimetric kinetic model, relative biological effectiveness (RBE), brainstem tolerance

INTRODUCTION

There is an increasing interest in using carbon ion radiotherapy (CIRT) for the treatment of advanced, radioresistant tumors. The physical properties of CIRT allow for delivering a high dose to the tumor, while the finite distal depth dose and sharp lateral penumbra can be utilized to spare nearby organs at risk (OARs) from excessive dose. Furthermore, carbon ions exhibit high linear energy transfer (LET) properties, which lead to more efficient cell killing (higher relative biological effectiveness (RBE)), compared with photon and proton RT. However, there are substantial uncertainties regarding the clinical RBE of carbon ions. Therefore, prescription doses, tolerance doses to OARs, and normal tissue complication probability (NTCP) models based on experience with photon or proton RT may not be applicable to CIRT and should preferably be derived from CIRT data.

Two major approaches have been used for the clinical implementation of CIRT. Spearheaded by the National Institute of Radiological Sciences (NIRS), Chiba, Japan, the Japanese centers are using hypofractionated treatment schedules (16 fractions of 3.6–4.6 Gy (RBE)) in which prescription doses and OAR tolerance doses initially were defined through carefully conducted dose-escalation trials. Originally, the *mixed beam model* (1) was developed to predict the RBE of the passively scattered carbon ion beams with *tumor response* as the relevant endpoint. Later, with the implementation of scanned beam delivery, the *modified microdosimetric kinetic model* (MKM) (2–5) was introduced. Since these two models have been validated for consistency, they are hereby collectively abbreviated as MKM.

In contrast, CIRT at the Gesellschaft für Schwerionenforschung (GSI), Darmstadt, Germany, was initiated with moderately hypofractionated schedules (20–22 fractions of 3.0–3.5 Gy (RBE)) in which the *Local Effect Model Version I* (LEM I) (6, 7) was used to predict the RBE of CIRT for *late responding normal tissues* (*i.e.*, central nervous system tissue). Trusting the LEM I to be sufficiently accurate, dose constraints derived from photon RT could be applied for CIRT treatments. An additional assumption for this approach was that the linear quadratic (LQ) formalism was applicable also for CIRT.

When the *National Center of Oncological Hadrontherapy* (CNAO, Italy) (8) started treating patients with LEM I-optimized CIRT in 2012, the successful treatment approach developed at NIRS was adopted. However, comparative studies show that the LEM I predicts a 5–15% higher RBE in the spread out Bragg peak (SOBP) of a carbon ion beam, relative to the MKM (9, 10). In the entrance region, the RBE predicted by LEM I can be 60% higher (11). Consequently, dependent on the clinical indication, prescription doses at CNAO (reported in LEM I-weighted dose, $D_{LEM\ I}$) were increased 5–15% relative to the prescription doses at NIRS (reported in MKM-weighted dose (D_{MKM})) (9, 10). In contrast, dose constraints to OARs were not adjusted. This was a cautious approach mitigating various uncertainties related to the adaptation of NIRS prescription doses (*i.e.*, differences in RBE model, beam delivery method, dose optimization process, *etc.*).

For the brainstem, the dose constraint at CNAO was therefore set to be <30 Gy (RBE) to no more than 1% of the organ's volume ($D_{LEM\ I|1\%}$), following the tradition of NIRS (12). Since this constraint becomes more restrictive in LEM I-optimized CIRT, CNAO has so far treated more than 1,000 patients with advanced tumors in the head and neck region (for example, skull base, nasopharynx, and sinonasal sites) without experiencing any grade of radiation-induced brainstem injury. Thus, the constraint needs to be updated to provide optimal treatments in cases where the target volume is located close to the brainstem. However, it is challenging to propose new and reasonable constraints since no toxic events have been reported from any institution applying LEM I-weighted doses for CIRT.

Recently, a dose-response analysis of brainstem toxicity following D_{MKM}-optimized CIRT at *Gunma University Heavy Ion Medical Center* (GHMC) (13) was published by Shirai et al. (14). None of the 85 patients included in this analysis experienced symptomatic brainstem toxicity. However, four cases of focal brainstem contrast enhancement were detected on routine magnetic resonance imaging (MRI) during follow-up. This was defined as central nervous system (CNS) necrosis grade 1 events according to the *Common Terminology Criteria for Adverse Events version 4.0* (CTCAE). Even these asymptomatic

events did not occur before the maximum dose ($D_{MKM|max}$) exceeded 48 Gy (RBE), showing that current constraint may be conservative even when applied for D_{MKM}. The brainstem volume receiving more than 30 Gy (RBE) ($V_{30\ Gy\ (RBE)}$) and 40 Gy (RBE) ($V_{40\ Gy\ (RBE)}$) were independent risk factors for this endpoint. Brainstem toxicity of any grade did not occur before $V_{30\ Gy\ (RBE)}$ exceeded 0.7 cm^3 and $V_{40\ Gy\ (RBE)}$ exceeded 0.1 cm^3. Since these values relate to radiologically detectable, but asymptomatic alterations in the brainstem, they may serve as constraints to avoid symptomatic injury. Shirai et al. also fitted their data to the Lyman-Kutcher-Burman (LKB) NTCP model (15–17), resulting in the following model parameters: volume-effect parameter (n) = 0.08, biodiversity parameter (m) = 0.08, and the *equivalent uniform dose* (EUD) corresponding to 50% probability of toxicity (TD50) = 32.4 Gy (RBE).

The goal of this work is therefore to:

1. evaluate the brainstem NTCP associated with CNAOs current clinical practice by applying the NTCP model published by Shirai et al.
2. convert the D_{MKM} validated constraints into $D_{LEM\ I}$, providing guidance for the proposal of new dose constraints to be used at CNAO and other centers applying LEM I.

MATERIAL AND METHODS

Treatment Plan Selection and CIRT at CNAO

The dose distributions of 30 CIRT treatments with target volumes close to the brainstem were included in this study. Details on disease site, histology, and prescription dose are presented in **Table 1**. The treatments were given at CNAO in the period 2013–2014 as part of prospective protocols (CNAO S9/2012/C, CNAO S12/2012/C, and CNAO S15/2012/C) approved by the Regional Ethics Committee. Signed consent was required for participation. The plans were optimized for a prescribed $D_{LEM\ I}$ of 68.8–76.8 Gy (RBE) in 16 fractions (4 fractions/week) using the *syngo*® RT Planning (Siemens Healthcare, Erlangen, Germany) treatment planning system (TPS). Dose constraint for the brainstem was $D_{LEM\ I|1\%} \leq 30$ Gy (RBE). Additionally, a constraint of $D_{LEM\ I|1\%} \leq 35$ Gy (RBE) was applied to a 3-mm planning OAR volume (PRV) for plan optimization purposes.

In general, the strategy to obtain a robust treatment plan is similar at CNAO and GHMC: Multiple beam angles (3 to 4), dominantly originating from the horizontally fixed beam line, are achieved by couch rotation and/or by multiple immobilization positions where the patient's head is positioned either straight or

TABLE 1 | Disease and treatment characteristics.

Case nr.	Histology	Site	Total $D_{LEM\ I}$ (Gy (RBE))	Fraction $D_{LEM\ I}$ (Gy (RBE))
1	Chordoma	Skull base	70.4	4.4
2	Mesenchymal tumor	Frontal sinus	76.8	4.8
3	Chordoma	Skull base	70.4	4.4
4	Chordoma	Skull base	70.4	4.4
5	MPNST	Clivus	76.8	4.8
6	Chordoma	Skull base	70.4	4.4
7	ACC	Meckel's cave	68.8	4.3
8	Chondrosarcoma	Nasal cavity	70.4	4.4
9	Chordoma	Clivus	70.4	4.4
10	Chordoma	Clivus	70.4	4.4
11	Chordoma	Clivus	70.4	4.4
12	ACC	Maxillary sinus	68.8	4.3
13	Chordoma	Clivus	70.4	4.4
14	Chordoma	Clivus	70.4	4.4
15	Chondrosarcoma	Clivus	70.4	4.4
16	Chordoma	Skull base	70.4	4.4
17	ACC	Maxillary sinus	68.8	4.3
18	ACC	Nasopharynx	68,8	4,3
19	Chordoma	Clivus	70.4	4.4
20	Chondrosarcoma	Skull base	70.4	4.4
21	Cordoma	Clivus	70.4	4.4
22	ACC	Maxillary sinus	68.8	4.3
23	ACC	Skull base	68.8	4.3
24	Chordoma	Clivus	70.4	4.4
25	Pleomorphic sarcoma	Clivus	76.8	4.8
26	ACC	Paranasal sinuses	68.8	4.3
27	Chordoma	Clivus	70.4	4.4
28	Acinar cell carcinoma	Ethmoid/nasal cavity	68.8	4.3
29	ACC	Maxillary sinus	68.8	4.3
30	Chordoma	Clivus	70.4	4.4

MPNST, Malignant peripheral nerve sheath tumor; ACC, Adenoid cystic carcinoma.

rotated. Due to particle range uncertainty, beam angles are chosen so that most of the dose to the brainstem originates from the beam's sharp lateral penumbra, rather than the distal dose fall-off. Beams traversing through the brainstem are never used.

Recalculation of RBE-Weighted Dose Distributions

The patients' computed tomography (CT) image files, structure set files, dose files, and plan files were exported from the *syngo*® TPS and imported to the *matRad* open source multimodality radiation TPS (https://e0404.github.io/matRad/) (18) in which the absorbed dose (D_{Abs}) and $D_{LEM\ I}$ were reproduced. The input parameters used clinically for LEM I were applied, *i.e.*, α_γ = 0.1 Gy^{-1}, β_γ = 0.05 Gy^{-2}, D_t = 30 Gy, s_{max} = 3.1 Gy^{-1}, R_n = 5 µm (7). The DVHs of targets and OARs were compared with the corresponding DVHs of the dose distribution from the *syngo*® TPS to ensure correct reproduction of both D_{Abs} and $D_{LEM\ I}$ (results not reported). Secondly, MKM was implemented in the matRad TPS code using the input parameters used clinically (R_d = 0.32 µm, R_n = 3.9 µm, α_0 = 0.172 Gy^{-1}, β = 0.0615 Gy^{-2}, α_r = 0.764 Gy^{-1}, F_{Clin} = 2.39) (2, 11) and D_{MKM} was derived from the exact same absorbed dose and LET spectra. This enabled a direct comparison of each patient's $D_{LEM\ I}$ and D_{MKM} based exclusively on the differences in the RBE modeling.

Estimation of Brainstem NTCP

Using the D_{MKM} distributions, the brainstem NTCP for each treatment plan was calculated by the LKB method, using the model parameters suggested by Shirai et al. (14): n = 0.08, m = 0.08, and TD50 = 32.4 Gy (RBE).

RBE-Weighted Dose Translation

For each brainstem, the $D_{MKM|0.7\ cm^3}$ and $D_{MKM|0.1\ cm^3}$ were plotted as a function of $D_{LEM\ I|0.7\ cm^3}$ and $D_{LEM\ I|0.1\ cm^3}$, respectively. A curve fitting procedure was performed with the software IBM SPSS Statistics for Windows, version 24.0 (IBM Corp., Armonk, NY, U.S.A.) in order to produce a dose translation model.

Verification of Dose Translation Model

As a last step, we wanted to verify that the dose translation model correctly predicted the $D_{LEM\ I}/D_{MKM}$ relationship also for higher brainstem doses than our original data. Therefore, five treatment plans, in which the original $D_{LEM\ I}$ constraint caused suboptimal dose coverage to the clinical target volume (CTV $D_{95\%}$ <95% of prescription dose), were reoptimized applying a new set of $D_{LEM\ I}$ constraints as proposed by this work (see "**RESULTS**"). Subsequently, these new plans were recalculated to D_{MKM}. These procedures, which were conducted exclusively to confirm the relationship of the RBE models, were performed with the RayStation® 6.99 TPS (RaySearch Laboratories AB, Stockholm, Sweden), where both the LEM I and MKM were implemented with the respective model input parameters as mentioned earlier.

RESULTS

Brainstem DVHs in relative and absolute volumes are presented in both $D_{LEM\ I}$ and D_{MKM} in **Figure 1**, showing the substantial decrease in RBE-weighted doses when the MKM is applied as RBE model.

The median brainstem $D_{LEM\ I|1\%}$ was 23.7 Gy (range, 11.2–31.3 (RBE)), which corresponded to only 12.4 Gy (range, 5.5–21.8 (RBE)) in D_{MKM}, highlighting the restraining effect of the original CNAO constraint in achieving optimal CIRT treatments.

Only four of the brainstems received D_{MKM} >30 Gy (RBE), each of them to a volume smaller than 0.05 cm^3. As seen in **Figures 1B, D**, the highest $D_{LEM\ I}$ to the brainstem volumes 0.7 and 0.1 cm^3 were 29 Gy (RBE) and 35 Gy (RBE), respectively, corresponding to 17 Gy (RBE) and 25 Gy (RBE) in D_{MKM}. These modest doses resulted in a very low probability of asymptomatic (grade 1) brainstem injury according to the NTCP model published by Shirai et al. (14): One patient had an NTCP of 2%, while the NTCPs of the remaining 29 patients were close to 0%, see **Figure 2**.

For each patient, the brainstem dose metrics $D_{LEM\ I|0.7\ cm^3}$ and $D_{LEM\ I|0.1\ cm^3}$ were plotted against the corresponding dose metric in D_{MKM} (**Figure 3**). With the assumption that the intercept should be at origin (D_{LEM} = 0 Gy (RBE) when D_{MKM} = 0 Gy (RBE)), we found that the quadratic regression model

$$D_{MKM} = (b1 \times D_{LEM\ \ I}) + (b2 \times [D_{LEM\ \ I}]^2)$$

adequately fit both sets of data (coefficients of determination, $R^2 \geq 0.918$). Extrapolation of the models to the relevant dose levels revealed that a $D_{MKM|0.7\ cm^3}$ of 30 Gy (RBE) and a $D_{MKM|0.1\ cm^3}$ of 40 Gy (RBE) translates into a $D_{LEM\ I|0.7\ cm^3}$ of 41 Gy (RBE) (95% CI, 38–44 Gy (RBE)) and a $D_{LEM\ I|0.1\ cm^3}$ of 49 Gy (RBE) (95% CI, 46–52 Gy (RBE)), respectively.

Subsequently, we reoptimized five of the treatment plans in which the old brainstem constraint ($D_{LEM\ I|1\%}$ <30 Gy (RBE)) caused suboptimal CTV dose coverage. For the reoptimization, new brainstem constraints within the lower half of the 95% CI of the dose translation estimates were applied, *i.e.*, $D_{LEM\ I|0.7\ cm^3}$ <38–41 Gy (RBE) and $D_{LEM\ I|\ cm^3}$ <46–49 Gy (RBE). The relationship of $D_{LEM\ I}$ to D_{MKM} for the dose metrics $D_{0.7\ cm^3}$ and $D_{0.1\ cm^3}$ from the reoptimized plans are plotted as open circles in the scatterplots of **Figure 3**. As can be seen, the values of these data pairs agree with the prediction of the dose translation model. To demonstrate the potential clinical impact of relaxing the constraints, a comparison of the original and reoptimized plans, displayed in both $D_{LEM\ I}$ and $D_{MKM,}$ is presented in **Figure 4**. For this patient, the proportion of the CTV receiving >95% of the prescription dose increased from 74 to 95%.

DISCUSSION

For the implementation of CIRT at CNAO, the goal has been to replicate the successful results achieved at Japanese CIRT centers, by translating NIRS prescription doses into

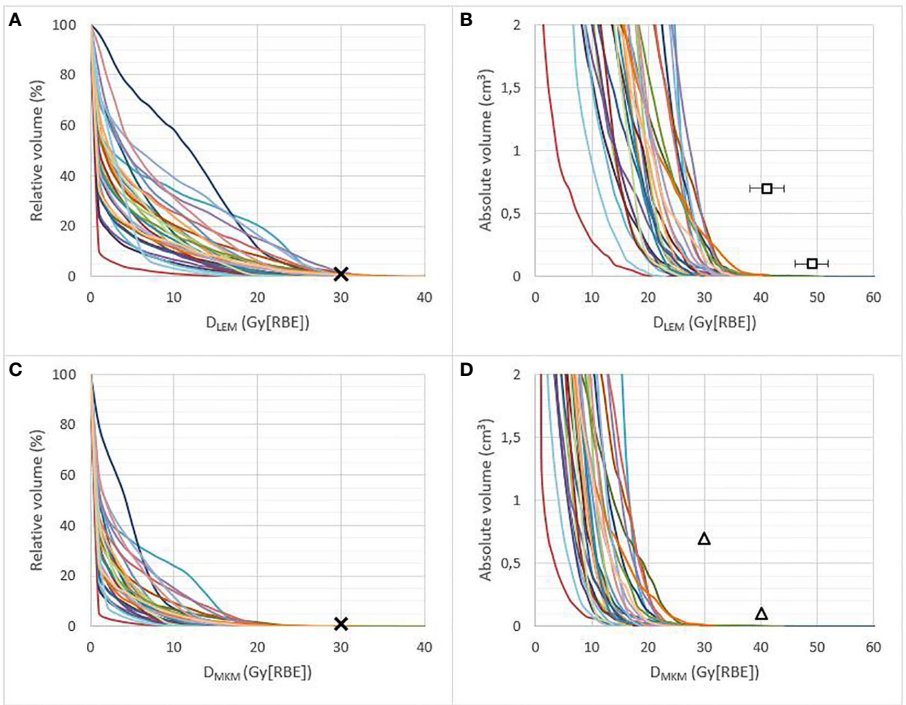

FIGURE 1 | Brainstem DVHs in relative **(A, C)** and absolute volume (≤2 cm^3) **(B, D)** of 30 patients treated at CNAO, presented in $D_{LEM\ I}$ **(A, B)** and D_{MKM} **(C, D)**. Crosses represent the former CNAO and NIRS dose constraint of $D_{1\%}$ ≤30 Gy (RBE). Triangles represent the new D_{MKM} constraints $V_{40\ Gy\ (RBE)}$ <0.1 cm^3 and $V_{30\ Gy\ (RBE)}$ <0.7 cm^3 as defined by Shirai et al. (14). Squares in **(B)** represent the possible new $D_{LEM\ I}$ constraints (error bars, 95% CI) resulting from the dose translation model presented in this work, see **Figure 3**.

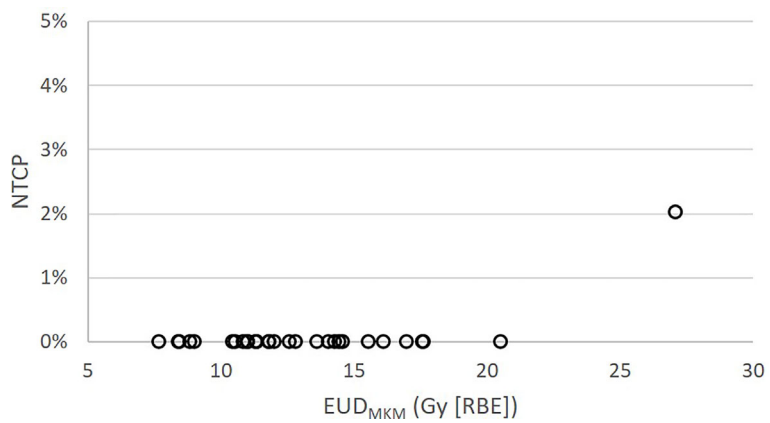

FIGURE 2 | Brainstem NTCP for the 30 patients treated at CNAO as function of EUD_{MKM} according to the NTCP model published by Shirai et al. (14).

equiefficient doses within the LEM I dose prescription system (9, 10). However, initially the OAR dose constraints were not adjusted correspondingly. This study clearly shows that the original brainstem dose constraint applied at CNAO is too conservative compared with the clinical practice in Japanese centers. In a recent publication on skull base chordomas treated at CNAO, Iannalfi et al. found that 92% of the local recurrences were attributable to suboptimal target dose in regions close to the brainstem or optic pathways (19). The estimated 5-year local control (LC) rate was 71%. This is inferior to the results reported by Japanese centers, where 5-year LC rates within the range 76–92% have been reported (20, 21).

Consequently, updated constraints for LEM I-optimized CIRT are urgently needed. In our opinion, due to the lack of publications

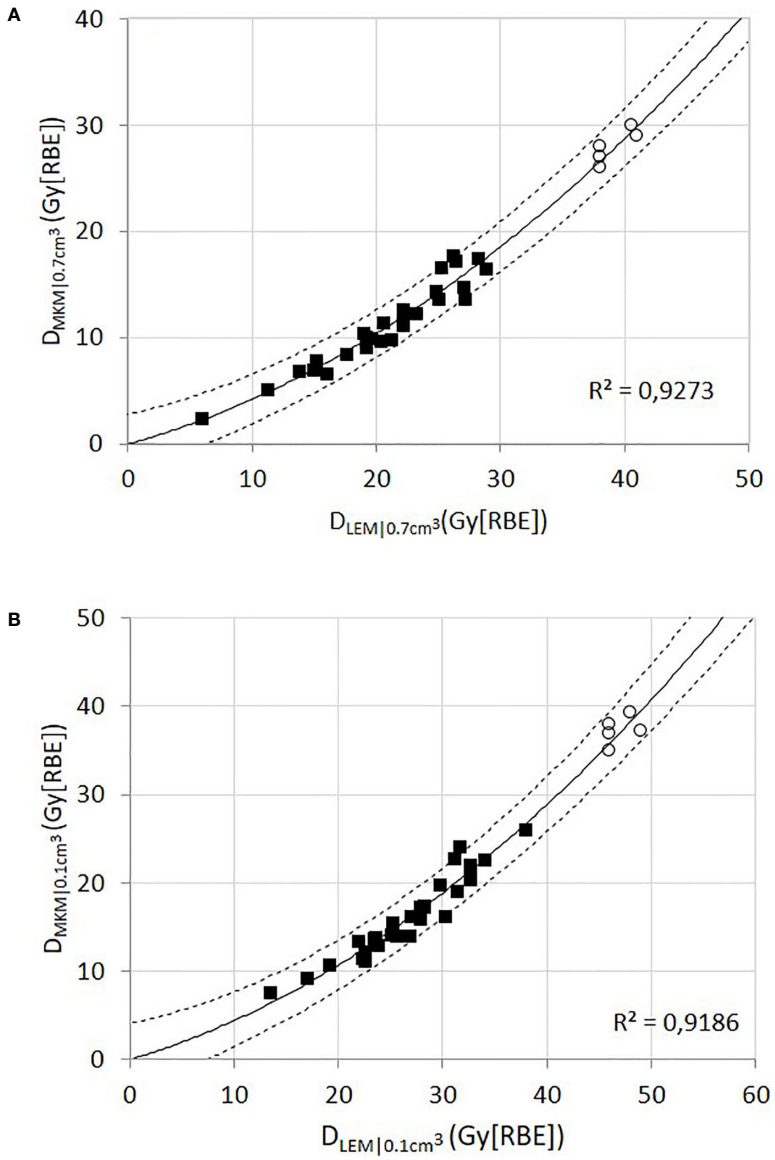

FIGURE 3 | Black squares represent the relationship of $D_{\text{LEM I}}$ to D_{MKM} for the dose metrics $D_{0.7\ cm^3}$ **(A)** and $D_{0.1\ cm^3}$ **(B)** for each individual brainstem. The solid line represents the quadratic function providing the best fit to the data points (black squares), assuming that the intercept should be in the origin. The dashed lines represent the 95% CI. The open circles represent the data collected from the reoptimized plans; these data points were not used for the curve fitting procedure.

addressing brainstem NTCP for LEM I-optimized CIRT, this aim was only achievable by making use of D_{MKM}-validated dose constraints. Relating the CNAO DVHs to the new D_{MKM} constraints defined by Shirai et al. (**Figure 1D**) suggests that doses to the brainstem volumes 0.7 and 0.1 cm^3 potentially could be increased by 13 Gy (RBE) and 15 Gy (RBE) in D_{MKM}, respectively, compared with the former practice at CNAO. According to our dose constraint translation, the corresponding increase in $D_{\text{LEM I}}$ would be approximately 12 Gy (RBE) (95% CI, 9–15 Gy (RBE)) and 14 Gy (RBE) (95% CI, 11–17 Gy (RBE)). This unveils an opportunity for improved target dose coverage, and thus improved treatment outcome, as demonstrated in **Figure 4**.

Recently, the European Particle Therapy Network (EPTN) released a consensus paper for dose constraints to various OARs (22), suggesting a general constraint of $D_{0.03\ cm^3} \leq 54$ Gy (RBE) to the brainstem, with an option to allow for $D_{0.03\ cm^3} \leq 60$ Gy (RBE) to the brainstem surface. Both constraints were expressed in *equivalent dose in 2 Gy fractions* (EQD2), with an assumed α/β ratio of 2 Gy. These guidelines are based on photon and proton RT toxicity data and are not necessarily applicable for CIRT due

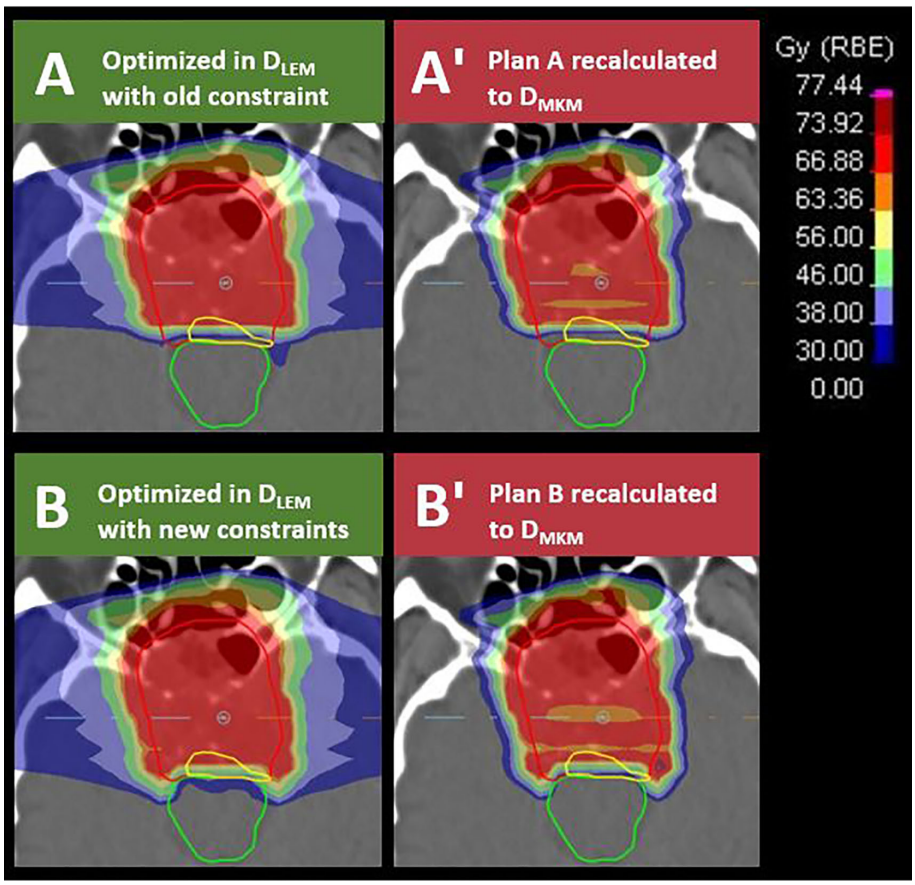

FIGURE 4 | Transversal sections of $D_{LEM\ I}$-optimized treatment plans applying brainstem (green contour) constraints of $D_{LEM\ I|1\%}$ <30 Gy (RBE) in plan **(A)** or $D_{LEM\ I|0.7\ cm^3}$ <38 Gy (RBE) and $D_{LEM|0.1\ cm^3}$ <46 Gy (RBE) in plan **B)**. The dose constraint levels are illustrated by dark blue, light blue, and light green isodose, respectively. Plans were subsequently recalculated to D_{MKM} **(A′, B′)**. Red isodose in plan **(A, B)** represents 95% of the target dose (70.4 Gy (RBE) in $D_{LEM\ I}$). Note the improved dose coverage to the CTV (red contour) and to the part of the CTV in which the tumor recurred (yellow contour) in plan B compared with plan A. Dose to the brainstem remains compliant with the constraints defined by Shirai et al. when evaluated in D_{MKM} **(B′)**.

to the larger uncertainties involved in the prediction of the RBE. However, similar constraints are used for CIRT at the *Heidelberg Ion Beam Therapy Center* (HIT) in Germany (23), building on previous clinical experience of the GSI. Various publications from this institution explicitly report an absence of brainstem toxicity (24, 25). Consequently, these constraints are considered safe for CIRT under HIT's current treatment paradigm, which consists of 20–22 fractions of 3.0–3.5 Gy (RBE) and 5–7 fractions per week. Although HIT also applies LEM I, these constraints may not be safely transferred to the 16 fraction/4 fractions per week treatment schedule of CNAO, as EQD2 conversion may not be sufficiently precise when fraction doses increase, due to uncertainties in the prediction of RBE.

That being said, it is interesting to observe that our translated constraints, when converted into EQD2, relate closely to the EQD2 constraints used in clinical practice at HIT (23), see **Figure 5**.

In 2010, as part of the *Quantitative Analysis of Normal Tissue Effects in the Clinic* (QUANTEC) effort, brainstem constraints and tolerance doses following photon and proton RT were summarized in Figure 1 in the organ-specific paper by Mayo et al. (26). Making use of the LQ model, tolerance doses from either normofractionated treatments or single fractionation stereotactic treatments were extrapolated to provide an approximation for the tolerance dose for hypofractionated treatments. The figure is reused in **Figure 6** of this paper, in which the $D_{LEM\ I|0.1\ cm^3}$ constraint we derived from this work has been superimposed as a red circle. Clearly, our constraint complies with the projections of the LQ model, supporting the capacity of the LEM I to predict the RBE of CIRT for this endpoint with sufficient accuracy.

An advantage of our dose translation approach is that the fractionation regimen at GHMC is similar to that of CNAO, and therefore the uncertainty related to EQD2 conversion can be avoided. Furthermore, both GHMC and CNAO have adopted the traditions of NIRS, in regard to the choice of beam number, angles, and strategies to achieve a robust treatment plan. Lastly, both centers are restricted to the use of fixed beam lines,

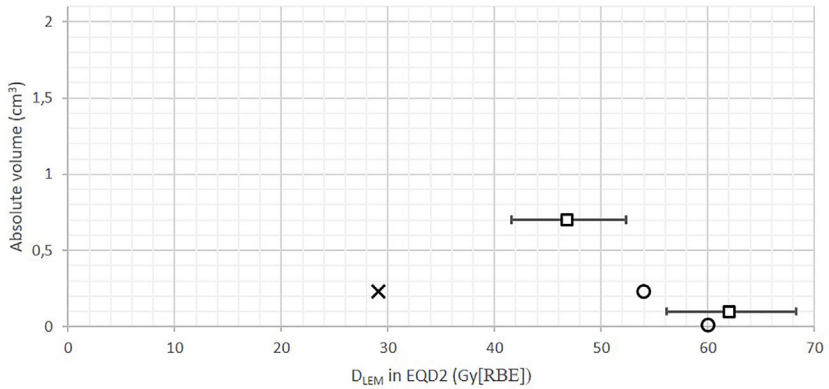

FIGURE 5 | Absolute volume DVH showing old CNAO $D_{LEM\ I|1\%}$ <30 Gy (RBE) constraint (cross) and the translated Shirai constraints $D_{LEM\ I|0.7\ cm^3}$ <41 Gy (RBE) and $D_{LEM\ I|0.1\ cm^3}$ <49 Gy (RBE) (squares, error bars = 95% CI), converted into EQD2 (assuming α/β ratio = 2 Gy) in comparison with the EQD2 constraints applied at HIT as reported by Nikoghosyan et al. (21): $D_{LEM\ I|1\%}$ <54 Gy (RBE) and $D_{LEM\ I|max}$ <60 Gy (RBE) (circles). As an approximation to the absolute volume relating to the $D_{1\%}$ constraints, the median brainstem volume in our data set (26 cm^3) was used. The translated constraints are more closely related to the constraints used at HIT than the old CNAO constraint.

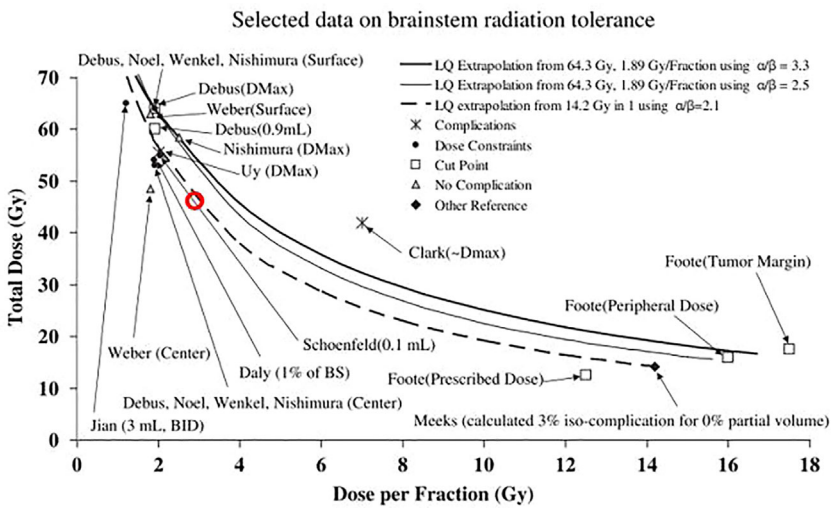

FIGURE 6 | Figure 1 from Mayo et al. (23) reprinted with permission, comparing selected data on brainstem tolerance and dose constraints from stereotactic RT or normofractionated photon or proton RT, compared with the linear quadratic (LQ) model extrapolations. Data points are marked with the corresponding author and dose parameter considered in parenthesis. The $D_{LEM\ I|0.1\ cm^3}$ <46 Gy (RBE) constraint for a 16-fraction LEM I-optimized CIRT, estimated by dose translation of the corresponding D_{MKM} constraint is superimposed as a red circle on the original figure.

whichinevitably restricts the freedom of beam angles and consequently favors harmonization of the treatments at the two centers additionally.

However, our method is affected by unavoidable uncertainties. Firstly, transferring dose constraints from a center with passive scattering beam delivery (PS) to a center with pencil beam scanning (PBS) may be controversial. The beam delivery techniques will inevitably cause differences in the radiation quality (mixture of primary and secondary particles and their corresponding LET values) of the beams, and the distribution and weighting of Bragg peaks may be very dissimilar. However, two studies have confirmed that the biological effect of the carbon ion beams of NIRS, HIT, and CNAO are identical (27, 28).

Secondly, the D_{Abs} underlying the RBE-weighted dose is calculated by different beam models at the two institutions. It has been shown that the D_{Abs} of a given RBE-weighted dose could on average vary about 2.5% in the *target region* of head and neck treatments, depending on the beam model (9). Differences related to beam modeling in the *out-of-target* areas have not been investigated, but one would expect to find more profound deviations in D_{Abs} especially within the lateral penumbra dose fall-off. This region is certainly sensitive to how the lateral spread

of the beam is modeled. This is of importance, since the sharp lateral penumbra of the carbon ion beam typically is utilized to avoid high doses to the brainstem when it is located close to the tumor.

To conclude, these latter issues infer that the D_{MKM} that we reproduce in this work, based on the D_{Abs} of CNAO $D_{LEM\ I}$-optimized treatment plans, are not an exact replica of GHMC treatment plans. Nevertheless, our dose translation approach definitely provides guidance as to how much the $D_{LEM\ I}$ constraints at CNAO may be relaxed in order to match the Japanese constraints. As a measure of caution, we propose the lower bound of the 95% CI of the dose translation estimates, *i.e.*, $D_{LEM\ I|0.7\ cm^3}$ <38 Gy (RBE) and $D_{LEM\ I|0.1\ cm^3}$ <46 Gy (RBE), as possible brainstem constraints for LEM I-optimized CIRT in a 16-fraction schedule. These proposed constraint values imply $D_{LEM\ I}$/D_{MKM} conversion factors of 1.27 and 1.15 for D_{MKM} fraction doses of 1.88 Gy (RBE) and 2.5 Gy (RBE) respectively, which is quite modest compared with the target dose conversion factors found by Steinsträter et al. (29), where conversion factors for the respective fraction doses were found to be >1.44 and >1.21.

Finally, as our conclusions rely on the results of Shirai et al., the limitations described in their study also apply to our work (small number of events, single institution study, *etc.*). Another essential assumption for the application of these constraints is that asymptomatic MRI contrast enhancement does not necessarily evolve into necrosis and therefore constraints that safeguard against this event most certainly will prevent the more meaningful clinical endpoint. Mere contrast enhancement is regarded as evidence of increased permeability of the blood-brain barrier (BBB), which results from radiation-induced alterations in endothelial and glial cell function (30). However, increased permeability does not necessarily lead to parenchymal damage as demonstrated for the spinal cord in a rat model (31). This phenomenon has also been documented for radiation-induced injury of the brain following CIRT, and it is hypothesized that since smaller volumes of CNS tissue is irradiated by particle therapy in comparison with photon RT, the probability of recovery will be higher (32). The observation that the lesions reported by Shirai et al. were reversible or stable in the absence of therapeutic intervention further supports the argument that no real necrosis had occurred.

In this setting, applying the CTCAE term *CNS necrosis grade 1* when only contrast enhancement is evident, as done by Shirai et al., may be confusing and potentially discourage physicians from referring patients to CIRT. However, the CTCAE lacks a proper predefined term to discriminate increased permeability in the BBB from a necrotic process. Moreover, neither the *SOMA-LENT scale* (subterm *MRI* in the *Analytic* scale) (33) nor the *RTOG/EORTC Late Morbidity Scoring Schema* (subterm *Brain*) (34) exhibit sufficient granularity to encompass this distinction. We therefore suggest to apply the CTCAE term *Nervous system disorders—Other*, and specifying it as *Brainstem reaction* as an analogy to the *Temporal lobe reaction* term coined by Gilman et al. (35), in which contrast enhancement would be a grade 1 "reaction," thus avoiding the use of the misleading and more distressing term "necrosis."

CONCLUSIONS

Based on this work, these new constraints, $D_{LEM\ I|0.7\ cm^3}$ <38 Gy (RBE) and $D_{LEM\ I|0.1\ cm^3}$ <46 Gy (RBE), have been implemented in the prospective treatment protocols of CNAO since October 2018. They can serve as constraints also for other centers applying LEM I within CIRT schedules of 16 fractions. Indeed, these constraints have also been selected as the most optimal constraints available and have therefore recently been implemented in clinical practice at the MedAustron Ion Therapy Center (Wiener-Neustadt, Austria) for 16 fractions of CIRT treatment of skull base tumors optimized with LEM I.

This paper highlights a challenge that is unique for CIRT compared with other external beam RT modalities: the exchange of experience between Japanese and European CIRT facilities is severely hampered by the use of disparate RBE models. Fortunately, we anticipate that the recalculation of treatment plans to the alternative RBE model will become substantially less time consuming due to the introduction of such functionality in commercial TPSs. We therefore hope to see future CIRT publications reporting OAR toxicity, NTCP, and related dose metrics in both D_{MKM} and $D_{LEM\ I}$, as our group recently has done for the optic nerve (36). This would accelerate the much needed validation of OAR constraints for both RBE models.

DATA AVAILABILITY STATEMENT

The datasets generated for this study are available on request to the corresponding author.

ETHICS STATEMENT

The patients analyzed in the study cannot be identified as all the research has been conducted with anonymized data. All patients enrolled in the clinical trials at CNAO gave their free informed consent to the treatment and the use of their anonymized data for research purposes. The anonymized patient data used for this study originated from the clinical trials "CNAO S9/2012/C", "CNAO S12/2012/C" and "CNAO S15/2012/C" approved by the CNAO Ethics Committee.

AUTHORS CONTRIBUTIONS

The manuscript was mainly authored by JD with support from PF, SM, OD, TO, and BV. JD performed data analysis. Clinical treatment plans were optimized by medical physicists SM, GM, and AM with FV, MB, VV, BV, and PF as the responsible radiation oncologists. Clinical data were collected by VV, MB, BV, AH, and PF. JD, SM, and GM performed the recalculation of all treatment plans. FV, VV, and BV are

responsible for the treatment protocols and analyzed patient follow-up together with MB and PF. JD, SM, OD, AM, TO, AH, and PF contributed to the development of the study methodology. All authors critically reviewed the manuscript. All authors contributed to the article and approved the submitted version.

FUNDING

This work was supported by grants (grant no: BFS2015PAR02) from the Trond Mohn Foundation, Ytrebygdsvegen 215, Kokstad, Postboks 7150, 5020 BERGEN, Norway, tlf: +47 479 00 111, org.nr: 988 029 327.

REFERENCES

1. Kanai T, Endo M, Minohara S, Miyahara N, Koyama-ito H, Tomura H, et al. Biophysical characteristics of HIMAC clinical irradiation system for heavy-ion radiation therapy. *Int J Radiat Oncol Biol Phys* (1999) 44(1):201–10. doi: 10.1016/S0360-3016(98)00544-6
2. Inaniwa T, Kanematsu N, Matsufuji N, Kanai T, Shirai T, Noda K, et al. Reformulation of a clinical-dose system for carbon-ion radiotherapy treatment planning at the National Institute of Radiological Sciences, Japan. *Phys Med Biol* (2015) 60(8):3271–86. doi: 10.1088/0031-9155/60/8/3271
3. Hawkins RB. A Microdosimetric-Kinetic Model for the Effect of Non-Poisson Distribution of Lethal Lesions on the Variation of RBE with LET. *J Radiat Res* (2003) 160(1):61–69, 9. doi: 10.1667/RR3010
4. Hawkins RB. A microdosimetric-kinetic model of cell death from exposure to ionizing radiation of any LET, with experimental and clinical applications. *Int J Radiat Biol* (1996) 69(6):739–55. doi: 10.1080/095530096145481
5. Hawkins RB. A statistical theory of cell killing by radiation of varying linear energy transfer. *Radiat Res* (1994) 140(3):366–74. doi: 10.2307/3579114
6. Scholz M, Kellerer MA, Kraft-Weyrather W, Kraft G. Computation of cell survival in heavy ion beams for therapy. *Radiat Environ Biophys* (1997) 36 (1):59–66. doi: 10.1007/s004110050055
7. Kramer M, Scholz M. Treatment planning for heavy-ion radiotherapy: calculation and optimization of biologically effective dose. *Phys Med Biol* (2000) 45(11):3319–30. doi: 10.1088/0031-9155/45/11/314
8. Rossi S. The National Centre for Oncological Hadrontherapy (CNAO): Status and perspectives. *Phys Med* (2015) 31(4):333–51. doi: 10.1016/j.ejmp.2015.03.001
9. Molinelli S, Magro G, Mairani A, Matsufuji N, Kanematsu N, Inaniwa T, et al. Dose prescription in carbon ion radiotherapy: How to compare two different RBE-weighted dose calculation systems. *Radiother Oncol* (2016) 120(2):307–12. doi: 10.1016/j.radonc.2016.05.031
10. Fossati P, Molinelli S, Matsufuji N, Ciocca M, Mirandola A, Mairani A, et al. Dose prescription in carbon ion radiotherapy: a planning study to compare NIRS and LEM approaches with a clinically-oriented strategy. *Phys Med Biol* (2012) 57(22):7543–54. doi: 10.1088/0031-9155/57/22/7543
11. Magro G, Dahle T, Molinelli S, Ciocca M, Fossati P, Ferrari A, et al. The FLUKA Monte Carlo code coupled with the NIRS approach for clinical dose calculations in carbon ion therapy. *Phys Med Biol* (2017) 62(9):3814–27. doi: 10.1088/1361-6560/aa642b
12. Koto M, Hasegawa A, Takagi R, Sasahara G, Ikawa H, Mizoe JE, et al. Feasibility of carbon ion radiotherapy for locally advanced sinonasal adenocarcinoma. *Radiother Oncol* (2014) 113(1):60–5. doi: 10.1016/j.radonc.2014.09.009
13. Ohno T, Kanai T, Yamada S, Yusa K, Tashiro M, Shimada H, et al. Carbon Ion Radiotherapy at the Gunma University Heavy Ion Medical Center: New Facility Set-up. *Cancers* (2011) 3(4):4046–60. doi: 10.3390/cancers3044046
14. Shirai K, Fukata K, Adachi A, Saitoh JI, Musha A, Abe T, et al. Dose-volume histogram analysis of brainstem necrosis in head and neck tumors treated using carbon-ion radiotherapy. *Radiother Oncol* (2017) 125(1):36–40. doi: 10.1016/j.radonc.2017.08.014
15. Lyman JT. Complication probability as assessed from dose-volume histograms. *Radiat Res Suppl* (1985) 8:S13–9. doi: 10.2307/3583506
16. Burman C, Kutcher GJ, Emami B, Goitein M. Fitting of normal tissue tolerance data to an analytic function. *Int J Radiat Oncol Biol Phys* (1991) 21(1):123–35. doi: 10.1016/0360-3016(91)90172-Z
17. Niemierko A. Reporting and analyzing dose distributions: a concept of equivalent uniform dose. *Med Phys* (1997) 24(1):103–10. doi: 10.1118/1.598063
18. Wieser H-P, Cisternas E, Wahl N, Ulrich S, Stadler A, Mescher H, et al. Development of the open-source dose calculation and optimization toolkit matRad. *Med Phys* (2017) 44(6):2556–68. doi: 10.1002/mp.12251
19. Iannalfi A, D'Ippolito E, Riva G, Molinelli S, Gandini S, Viselner G, et al. Proton and carbon ions radiotherapy in skull base chordomas: a prospective study based on a dual particle and a patient-customized treatment strategy. *Neuro Oncol* (2020) 22(9):1348–58. doi: 10.1093/neuonc/noaa067
20. Takagi M, Demizu Y, Nagano F, Terashima K, Fujii O, Jin D, et al. Treatment outcomes of proton or carbon ion therapy for skull base chordoma: a retrospective study. *Radiat Oncol* (2018) 13(1):232. doi: 10.1186/s13014-018-1173-0
21. Koto M, Ikawa H, Kaneko T, Hagiwara Y, Hayashi K, Tsuji H, et al. Long-term outcomes of skull base chordoma treated with high-dose carbon-ion radiotherapy. *Head Neck* (2020) 42(9):2607–13. doi: 10.1002/hed.26307
22. Lambrecht M, Eekers DBP, Alapetite C, Burnet NG, Calugaru V, Coremans IEM, et al. Radiation dose constraints for organs at risk in neuro-oncology; the European Particle Therapy Network consensus. *Radiother Oncol* (2018) 128 (1):26–36. doi: 10.1016/j.radonc.2018.05.001
23. Nikoghosyan AV, Karapanagiotou-Schenkel I, Munter MW, Jensen AD, Combs SE, Debus J, et al. Randomised trial of proton vs. carbon ion radiation therapy in patients with chordoma of the skull base, clinical phase III study HIT-1-Study. *BMC Cancer* (2010) 10:607. doi: 10.1186/1471-2407-10-606
24. Schulz-Ertner D, Karger CP, Feuerhake A, Nikoghosyan A, Combs SE, Jakel O, et al. Effectiveness of carbon ion radiotherapy in the treatment of skull-base chordomas. *Int J Radiat Oncol Biol Phys* (2007) 68(2):449–57. doi: 10.1016/j.ijrobp.2006.12.059
25. Uhl M, Mattke M, Welzel T, Oelmann J, Habl G, Jensen AD, et al. High control rate in patients with chondrosarcoma of the skull base after carbon ion therapy: first report of long-term results. *Cancer* (2014) 120(10):1579–85. doi: 10.1002/cncr.28606
26. Mayo C, Yorke E, Merchant TE. Radiation associated brainstem injury. *Int J Radiat Oncol Biol Phys* (2010) 76(3 Suppl):S36–41. doi: 10.1016/j.ijrobp.2009.08.078
27. Uzawa A, Ando K, Koike S, Furusawa Y, Matsumoto Y, Takai N, et al. Comparison of biological effectiveness of carbon-ion beams in Japan and Germany. *Int J Radiat Oncol Biol Phys* (2009) 73(5):1545–51. doi: 10.1016/j.ijrobp.2008.12.021
28. Facoetti A, Vischioni B, Ciocca M, Ferrarini M, Furusawa Y, Mairani A, et al. In vivo radiobiological assessment of the new clinical carbon ion beams at CNAO. *Radiat Prot Dosimetry* (2015) 166(1-4):379–82. doi: 10.1093/rpd/ncv145
29. Steinstrater O, Grun R, Scholz U, Friedrich T, Durante M, Scholz M, et al. Mapping of RBE-weighted doses between HIMAC- and LEM-Based treatment planning systems for carbon ion therapy. *Int J Radiat Oncol Biol Phys* (2012) 84(3):854–60. doi: 10.1016/j.ijrobp.2012.01.038
30. Yuan H, Gaber MW, Boyd K, Wilson CM, Kiani MF, Merchant TE, et al. Effects of fractionated radiation on the brain vasculature in a murine model: blood-brain barrier permeability, astrocyte proliferation, and ultrastructural changes. *Int J Radiat Oncol Biol Phys* (2006) 66(3):860–6. doi: 10.1016/j.ijrobp.2006.06.043
31. Siegal T, Pfeffer MR. Radiation-induced changes in the profile of spinal cord serotonin, prostaglandin synthesis, and vascular permeability. *Int J Radiat Oncol Biol Phys* (1995) 31(1):57–64. doi: 10.1016/0360-3016(94)E0305-4
32. Kishimoto R, Mizoe JE, Komatsu S, Kandatsu S, Obata T, Tsujii H, et al. MR imaging of brain injury induced by carbon ion radiotherapy for head and neck tumors. *Magn Reson Med Sci* (2005) 4(4):159–64. doi: 10.2463/mrms.4.159
33. LENT SOMA tables. *Radiother Oncol* (1995) 35(1):17–60. doi: 10.1016/0167-8140(95)90055-1
34. Cox JD, Stetz J, Pajak TF. Toxicity criteria of the Radiation Therapy Oncology Group (RTOG) and the European Organization for Research

and Treatment of Cancer (EORTC). *Int J Radiat Oncol Biol Phys* 1995 31 (5):1341–6.

35. Gillmann C, Lomax AJ, Weber DC, Jakel O, Karger CP. Dose-response curves for MRI-detected radiation-induced temporal lobe reactions in patients after proton and carbon ion therapy: Does the same RBE-weighted dose lead to the same biological effect? *Radiother Oncol* (2018) 128(1):109–14. doi: 10.1016/j.radonc.2018.01.018
36. Dale JE, Molinelli S, Vitolo V, Vischioni B, Bonora M, Magro G, et al. Optic nerve constraints for carbon ion RT at CNAO - Reporting and relating outcome to European and Japanese RBE. *Radiother Oncol* (2019) 140:175–81. doi: 10.1016/j.radonc.2019.06.028

Conflict of Interest: The authors declare that the research was conducted in the absence of any commercial or financial relationships that could be construed as a potential conflict of interest.

frontiers in Oncology

ORIGINAL RESEARCH
published: 16 December 2020
doi: 10.3389/fonc.2020.589168

NFATC2 Modulates Radiation Sensitivity in Dermal Fibroblasts From Patients With Severe Side Effects of Radiotherapy

*Joshua Dulong[1], Clara Kouakou[1], Yasmina Mesloub[2], Julie Rorteau[1], Sandra Moratille[2], Fabien P. Chevalier[1], Tatiana Vinasco-Sandoval[2], Michèle T. Martin[2] and Jérôme Lamartine[1]**

[1] Laboratory of Tissue Biology and Therapeutic Engineering, CNRS UMR5305, University of Lyon, Claude Bernard University Lyon I, IBCP, Lyon, France, [2] CEA, Genomics and Radiobiology of Keratinopoiesis, DRF/IBFJ/iRCM, Université Paris-Saclay, Evry, France

OPEN ACCESS

Edited by:
Ester Orlandi,
Istituto Nazionale dei Tumori (IRCCS), Italy

Reviewed by:
Michael Wayne Epperly,
University of Pittsburgh, United States
Stuart Samuels,
University of Miami Hospital, United States

***Correspondence:**
Jérôme Lamartine
Jerome.lamartine@univ-lyon1.fr

Specialty section:
This article was submitted to Radiation Oncology, a section of the journal Frontiers in Oncology

Received: 30 July 2020
Accepted: 10 November 2020
Published: 16 December 2020

Citation:
Dulong J, Kouakou C, Mesloub Y, Rorteau J, Moratille S, Chevalier FP, Vinasco-Sandoval T, Martin MT and Lamartine J (2020) NFATC2 Modulates Radiation Sensitivity in Dermal Fibroblasts From Patients With Severe Side Effects of Radiotherapy. Front. Oncol. 10:589168. doi: 10.3389/fonc.2020.589168

Although it is well established that 5 to 15% of radiotherapy patients exhibit severe side-effects in non-cancerous tissues, the molecular mechanisms involved are still poorly known, and the links between cellular and tissue radiosensitivity are still debated. We here studied fibroblasts from non-irradiated skin of patients with severe sequelae of radiotherapy, to determine whether specific basal cell activities might be involved in susceptibility to side-effects in normal tissues. Compared to control cells, patient fibroblasts exhibited higher radiosensitivity together with defects in DNA repair. Transcriptome profiling of dermal fibroblasts from 16 radiotherapy patients with severe side-effects and 8 healthy individuals identified 540 genes specifically deregulated in the patients. Nuclear factor of activated T cells 2 (*NFATC2*) was the most differentially expressed gene, poorly expressed at both transcript and protein level, whereas the *NFATC2* gene region was hypermethylated. Furthermore, *NFATC2* expression correlated with cell survival after irradiation. Finally, silencing *NFATC2* in normal cells by RNA interference led to increased cellular radiosensitivity and defects in DNA repair. This study demonstrates that patients with clinical hypersensitivity also exhibit intrinsic cellular radiosensitivity in their normal skin cells. It further reveals a new role for NFATC2 as a potential regulator of cellular sensitivity to ionizing radiation.

Keywords: radiotherapy, radiosensitivity, human skin fibroblasts, transcriptome, NFATC2, normal tissue side effects

INTRODUCTION

Radiosensitivity is the relative sensitivity of cells, tissues, organs, and organisms to the injurious effects of ionizing radiations. This notion includes very different outcomes according to the scale at which it is analyzed. At cellular level, sensitivity to ionizing radiation is notably evaluated by the rate of immediate or delayed death in irradiated cell cultures and by cell capacity to repair DNA damage. At organism level, radiosensitive individuals are those that develop severe effects in irradiated tissue

whereas the majority of the population exposed to the same dose show no or only mild effects. This is particularly obvious in the context of radiotherapy (RT), the main source of human exposure to high-dose ionizing radiation, where 5–15% of patients exhibit severe side-effects in irradiated normal tissues (1, 2), including fibrosis (3), necrosis, and sometimes radio-induced secondary cancers (4, 5). A central question regarding the multi-scale nature of radiosensitivity is whether intrinsic cellular radiosensitivity is a mirror of organism sensitivity. If that is the case, cellular testing would be a means of identifying radiosensitive patients and predicting deleterious outcome of radiation exposure. Moreover, using cultured cells as models of radiation sensitivity would shed light on the intrinsic mechanisms, which are far from clear. However, to date, data on the correlation between cellular and organism radiosensitivity are contradictory, especially regarding skin fibroblasts, a cell type which has been directly involved in the development of radiotherapy side-effects (6). Previous studies reported higher radiation toxicity in dermal fibroblasts from radiosensitive patients (7–11) and a correlation between clinical grades and cellular radiosensitivity (12, 13). However, other authors reported no difference in dermal fibroblast radiosensitivity between radiosensitive and radio-tolerant individuals (14, 15).

To further investigate this question, we used cutaneous fibroblasts from a collection of RT patients exhibiting severe side-effects of radiotherapy, that were classified according to side-effect severity (16). The first goal of this study was to investigate the link between cellular and individual radiosensitivity. The second goal was to shed light on the complex molecular mechanisms of the cellular response to ionizing radiation.

Here, we investigated the radiation toxicity and the DNA repair ability of skin fibroblasts from patients with RT severe side effect and we observed that patient fibroblasts exhibited higher cell death and profound DNA repair defects compared to normal control cell samples. By a transcriptomic analysis, we identified the transcription factor NFATC2 as being strongly repressed in patient fibroblasts, with hypermethylation on the coding sequence. Finally, we demonstrate that the repression of NFATC2 is able to increase the radiation sensitivity of normal fibroblasts, suggesting that this protein is involved in the establishment of the radiosensitive phenotype.

MATERIALS AND METHODS

Cell Culture

Fibroblasts from patients were obtained from the INSERM UMR1052 COPERNIC cell collection (16). This collection was approved by the regional Ethical Committee (CPP Sud-Est, Lyon, France) and cell lines were declared under the numbers DC2008-585 and DC2011-1437 to the Ministry of Research. The database derived from the COPERNIC collection is protected under the reference IDDN.FR.001.510017.000.D.P.2014.000.10300.

All the anonymous patients were informed and signed consent according to the ethics recommendations. This collection is composed of cancer patients presenting with overreactions in normal tissues after radiotherapy. Severity of side-effects was graded for each patient according to the Common Terminology Criteria for Adverse Events scale, version 4.03 (17). Sampling was performed in non-irradiated, non-photo-exposed anatomical region after local anesthesia. Standardized dermatological punch and untransformed fibroblast cell strains were prepared from skin biopsies. In the present study, 16 breast cancer patient cells were studied, comprising eight cell strains from grade 2 patients, here referenced as P1 to P8, and eight cell strains from grade 3 patients (P9 to P16). Cells were studied between passage 7 to 10 in culture (mean population doublings: 35 to 50), before any senescence occurrence.

As control, primary dermal fibroblasts were obtained from eight non-irradiated female healthy donors (C1 to C8). Surgical samples were obtained from the Hospitals Board of Lyon, France (Hospices Civils de Lyon), with the subjects' informed consent. Cells were subcultured up to seven passages and studied between passage 7 to 10, to have similar age in culture as patient cells (mean population doublings: 35 to 50). As fibroblasts are quiescent cells in the dermis, most studies were performed on confluent cells, in the G0/G1 cell cycle phase, both for patient and control cells.

Cultures were maintained in Dulbecco's Modified Eagle Medium–Glutamax medium (ThermoFisher Scientific, Illkirch, France) supplemented with 10% fetal bovine serum (ThermoFisher) and 1% penicillin/streptomycin (Sigma-Aldrich, Saint-Quentin-Fallavier, France).

Cell Irradiation

Primary dermal fibroblasts were irradiated after reaching confluency with 2 Gy using an XRAD320 X-ray generator (Precision X-Ray, North Brandford, CT, USA) at a dose rate of 0.8 $Gy.min^{-1}$ and then further cultured for indicated times depending on the assay.

Colony Survival Assay

Dermal fibroblasts were irradiated with 2 Gy X-rays after reaching confluency and seeded at low density (5 to 40 cells/cm^2) 24 h after irradiation. Two weeks later, cell cultures were fixed with EtOH 100% for 15 min and stained with hematoxylin/eosin. Only colonies formed by more than 50 fibroblasts were considered for calculating survival fraction at 2 Gy (SF2), expressed as the ratio between colonies formed with and without irradiation.

γH2AX and 53BP1 Foci Assays

Irradiated fibroblasts were further cultured for the indicated times (0, 15 min, 2, 6, and 24 h) and fixed with 4% paraformaldehyde for 15 min. Then, cells were permeabilized (0.1% Triton X-100 and 0.1 M Glycine) and incubated in blocking buffer (5% goat serum, 2% BSA, 0.1% Triton X-100, and 0.05% Tween-20) for 15 min prior to immunostaining with anti-γH2AX antibody (05-636, Millipore) or anti-53BP1 antibody (PA1-46147, ThermoFisher). For immunodetection, goat anti-rabbit IgG or goat anti-mouse IgG Alexa Fluor-488

or -546 conjugated secondary antibody (ThermoFisher) was incubated for 1 h and nuclei were counterstained with 4′-6-diamidino-2-phenylindole dihydrochloride (DAPI). The resulting foci were counted in at least 50 nuclei per condition using an Eclipse Ti-E inverted microscope (Nikon).

DNA Repair Chip Assay

Fibroblast DNA repair was measured on ExSy-SPOT assay (LXRepair). Protein extracts from lysed cells were applied directly on the biochip containing plasmids with well-characterized DNA lesions (8-Oxoguanine, Ethenobase, Abasic site, Glycols, Photoproducts and Cisplatin adducts) and incubated with fluorescent nucleotides to allow DNA repair. Effective DNA repair was quantified for each type of lesion by CT measurement of the resulting fluorescence signal. Thus, fluorescence level was proportional to cell ability to repair the specific DNA damage within the prescribed time.

Transcriptome Analysis

Total RNA was isolated from fibroblasts at confluency with the NucleoSpin RNA plus kit (Macherey–Nagel, Hoerdt, France) or RNeasy Plus Minikit (Qiagen, Courtaboeuf, France) according to the manufacturer's instructions.

For next-generation RNA sequencing at CNRGH (CEA, Evry, France), RNA sequences were captured using a TruSeq RNA Library Prep Kit v2 (Illumina, Evry, France) with input of 1 µg. Paired-end RNA sequencing was performed on HiSeq4000 with 100 bp paired-end reads. Sequencing data quality control was performed using FastQC 0.11.7 before and after adapter trimming by Cutadapt 1.13 (parameters: -q 15 -a 5'-AGA TCG GAA GAG CAC ACG TCT GAA CTC CAG TCA C-3' – 5-AAG ATC GGA AGA GCG TCG TGT AGG GAA AGA GTG TAG ATC TCG GTG GTC GCC GTA TCA TT-3'). The reads were mapped to the human genome (GRCh37/hg19) using HISAT2 2.0.5. For a single gene, sequences were aligned *versus* all known exons of all gene isoforms. The resulting BAM files were sorted by read pairs (using SAMtools 1.3.1) and counted using the HtSeq-count tool of HtSeq 0.6.1.

For transcriptome analysis, filtering was applied to genes with low expression (mean number of reads in the training set <10). Principal component analysis and hierarchical clustering were performed using the R DEseq2 and stats packages. VennDiagram and plots were made using the VennDiagram and ggplot2 packages. Functional annotation of the gene list was performed using the WEB-based GEne SeT AnaLysis Toolkit (WebGestalt) and the KEGG database 2019. Gene Ontology (GO) was performed using the clusterProfiler package in R software (18). GO and KEGG enrichment analyses were based on a false discovery rate (FDR) threshold of <0.05. The Enrichedplot package was used for graphical visualization of the result from enriched analysis. Transcriptome data have been deposited into the GEO database and are available under the accession number GSE154559.

Real-Time Quantitative PCR

An equal amount of total RNA (500 ng) was used as template for reverse transcription with PrimeScriptTM RT reagent kit (Takara, Shiga, Japan) and analyzed by Real-Time QPCR using SYBR® Premix ExTaqII (Takara) on an AriaMx Realtime PCR system (Agilent Genomics, Santa Clara, CA, USA). All primers listed below were provided by Eurogentec. *NFATC2* expression level was normalized to *TBP* and *RPS17* housekeeping gene expression level.

NFATC2f: 5'-TTGGAAGAAAGAACACGCGG-3',
NFATC2r: 5'-GAGCACTCGATGGGGTTAGA-3',
TBPf: 5'-TCAAACCCAGAATTGTTCTCCTTAT-3',
TBPr: 5'-CCTGAATCCCTTTAGAATAGGGTAGA-3',
RPS17f: 5'-CTCTTTTACCAAGGACCCGCC-3',
RPS17r: 5'-AGGTTGGACAGACTGCCGAAG-3'

Protein Extraction and Immunoblotting

Total proteins were extracted using RIPA buffer (50 mM Tris-HCl pH = 8, 150 mM NaCl, 1.5 mM KCl, 1% NP-40, 0.1% SDS, 0.5% sodium deoxycholate, 0.1% Triton X-100, 1 mM EDTA) containing protease inhibitor cocktail (cOmplete mini, Roche Diagnostics) and phosphatase inhibitor cocktail (5 mM NaF, 50 mM β-glycerophosphate, 5 mM orthovanadate). Proteins were quantified using the Pierce BCA Protein Assay Kit (ThermoFisher), loaded on an 8% SDS-polyacrylamide gel and transferred to a nitrocellulose membrane (Bio-rad). The membrane was blocked for 1 h at room temperature in TBS-Tween20 0.1–5% BSA and immunoblotted overnight at 4°C for primary antibodies specific to NFATC2 (#4389, Cell Signaling Technology) or VINCULIN (V9131, Sigma-Aldrich). After washing, goat anti-mouse IgG or goat anti-rabbit IgG HRP-conjugated secondary antibodies (Bio-rad) were incubated for 1 h at room temperature. Proteins were revealed using SuperSignal West Pico PLUS Chemiluminescent Substrate (ThermoFisher) and the signal was detected by the Fusion Fx system (Vilber Smart Imaging). Immunoblot quantifications were performed using GelAnalyzer software.

DNA Extraction and Bisulfite Conversion and HRM PCR

DNA was extracted from fibroblasts using the QIAamp DNA Mini Kit (Qiagen) according to the manufacturer's instructions. To assess methylation of a specific DNA region, DNA was converted with bisulfite treatment, using the EpiTect Bisulfite Kit (Qiagen) according to the manufacturer's instructions. Then, HRM PCR was performed using the EpiTect HRM PCR kit (Qiagen) to amplify the specific DNA region and to measure the melting temperature of the amplicon on an AriaMx Realtime PCR system (Agilent Genomics). One hundred percent methylated DNA, 100% unmethylated DNA, and bisulfite unconverted DNA from the EpiTect Control DNA Set kit (Qiagen) were used as controls. Figures with methylation peaks were produced with Agilent Aria 1.5 Software (Agilent Genomics). Primers were designed with Methyl Primer Express Software v1.0 (ThermoFisher Scientific) and were provided by Eurogentec. The following primers were used for methylation study:

NFATC2mF: 5'-TTTAGATGAATAGTGTTTTGGG-3',
NFATC2mR: 5'-ATTATCATTTCCTTCCTCTACTTC-3'.

RNA Interference

Control fibroblasts were transduced with lentiviral vectors from NFATC2 Human shRNA Plasmid Kit (OriGene). Lentiviral vector particles were produced by the vector facility at SFR BioSciences Gerland-Lyon Sud (Lyon, France) as previously described (19). Control cells were infected at 40% confluency with lentiviral particles (MOI at 10) containing a vector with a shRNA targeting *NFATC2* (sh-*NFATC2*) or a plasmid with a non-effective shRNA sequence (sh-*SCR*) for 12 h. At confluency, cells were trypsinized and seeded in another plate. Then, transduced cells were maintained under puromycin selection for 1 week and then selected cells were amplified for 1 week before analysis.

Statistics

Statistical significance was calculated by Student's t-test, one-way analysis of variance (ANOVA), two-way analysis of variance (ANOVA2), or Pearson correlation using Prism software (version 8.0, GraphPad Software). Mean differences were considered statistically significant when $P < 0.05$. * $P < 0.05$, ** $P < 0.01$, *** $P < 0.001$, **** $P < 0.0001$.

RESULTS

Fibroblasts From Patients With Severe Radiotherapy Side Effects Exhibit Decreased Tolerance to Radiation Toxicity

We analyzed ionizing radiation toxicity in cultured dermal fibroblasts from sixteen breast cancers patients with severe radiotherapy (RT) side-effects (eight grade 2, eight grade 3) and eight control individuals. To estimate radiation-induced toxicity, we used the reference method of colony survival fraction measurement after a standard dose of 2 Gy X-irradiation (SF2). The colony survival assay showed that dermal fibroblasts from the eight control biopsies presented a mean 48% survival fraction, whereas cells from patients with RT over-reaction exhibited significantly lower SF2, with 28 and 27% survival fraction for cells of grade 2 and grade 3 patients respectively (**Figure 1**). Since no significant difference in cellular radiosensitivity was observed between cells from grade 2 and grade 3 patients, the 16 cell strains were pooled for the following experiments.

Fibroblasts From Patients With Severe Radiotherapy Side Effects Exhibit DNA Repair Defects

To study patient cell DNA repair ability, we first performed immunofluorescence against γH2AX and 53BP1, two early markers of DNA double-strand breaks (DSB), in four control and four radiosensitive cell strains after 2 Gy irradiation. The number of γH2AX and 53BP1 foci 15 min after 2 Gy irradiation

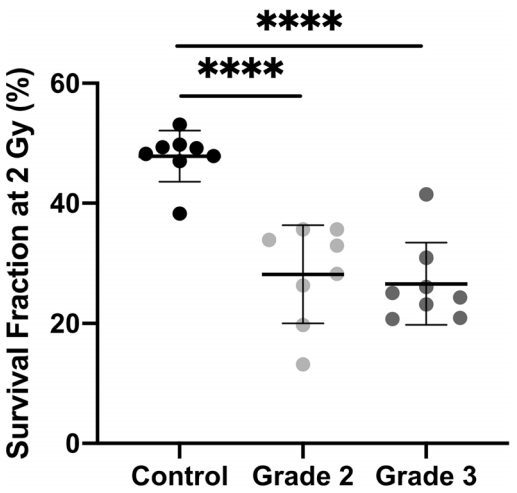

FIGURE 1 | Dermal fibroblasts from patients with severe side-effects of radiotherapy exhibit higher radiosensitivity. Colony survival assays showed that survival fraction at 2 Gy was higher in control cells (n = 8) than in cells from overreacting patients, with no difference according to clinical grade (n = 8 grade 2 and n = 8 grade 3). Results are mean +/– SD. The p-value was calculated by one-way ANOVA. Significant at ****$P < 0.0001$.

was identical in control and patient fibroblasts, with a mean 40 foci per nucleus in both (**Figures 2A, B**). However, more γH2AX foci were detected in patient than control cells 2, 6, and 24 h after irradiation: 2.7, 4.13, and 2.03 additional foci per cell respectively (**Figure 2A**). More 53BP1 foci were also detected 6 and 24 h after 2 Gy irradiation in patient than control fibroblasts: respectively +2.65 and +5.55 foci per cell (**Figure 2B**).

We also assessed patient cell ability to repair various DNA lesions, using the ExSy-SPOT chip, a microsystem developed to measure excision-synthesis activity in immobilized plasmid DNA (20). Repair activity was reflected by the incorporation of fluorescent nucleotides at the lesion site. Fluorescence in plasmids containing 8-oxoGuanine and abasic sites was higher in control than patient samples (**Figure 2C**), and in plasmids containing glycol-damaged bases, although the difference did not quite reach significance ($P = 0.062$) (**Figure 2C**). Thus, ability to repair 8-oxoGuanine, abasic site and glycol-damaged bases, three types of DNA damage induced by oxidative stress and known to be repaired by the BER pathway, seemed to be impaired in dermal fibroblasts from patients with severe radiotherapy side-effects.

Identification of a Specific Transcriptome Profile in Patients' Fibroblasts

To investigate the mechanisms underlying individual radiosensitivity at cellular level, we used next-generation RNA sequencing to profile the whole genome transcriptome of the 16 patient and 8 control fibroblast cultures. Principal component analysis (PCA) of whole gene expression data clearly separated controls from over-reacting patients (**Figure 3A**). However, one patient's cell strain was classified as being in the control group by hierarchical cluster analysis (**Figure 3B**). Within the patient

group, there was no clear separation between grades 2 and 3, whether on PCA or hierarchical cluster analysis (**Figures 3A, B**).

We identified 1,338 genes differentially expressed (adjusted p-value <0.05) between fibroblasts from grade 2 patients and controls (**Figure 3C**), and 804 genes differentially expressed between fibroblasts from grade 3 patients and controls (**Figure 3C**). Five hundred forty of these differentially expressed genes were in common between grade 2 patients *vs* controls and grade 3 patients *vs* controls (**Figure 3C** and **Supplementary Table S1**). Interestingly, no genes were differentially expressed between

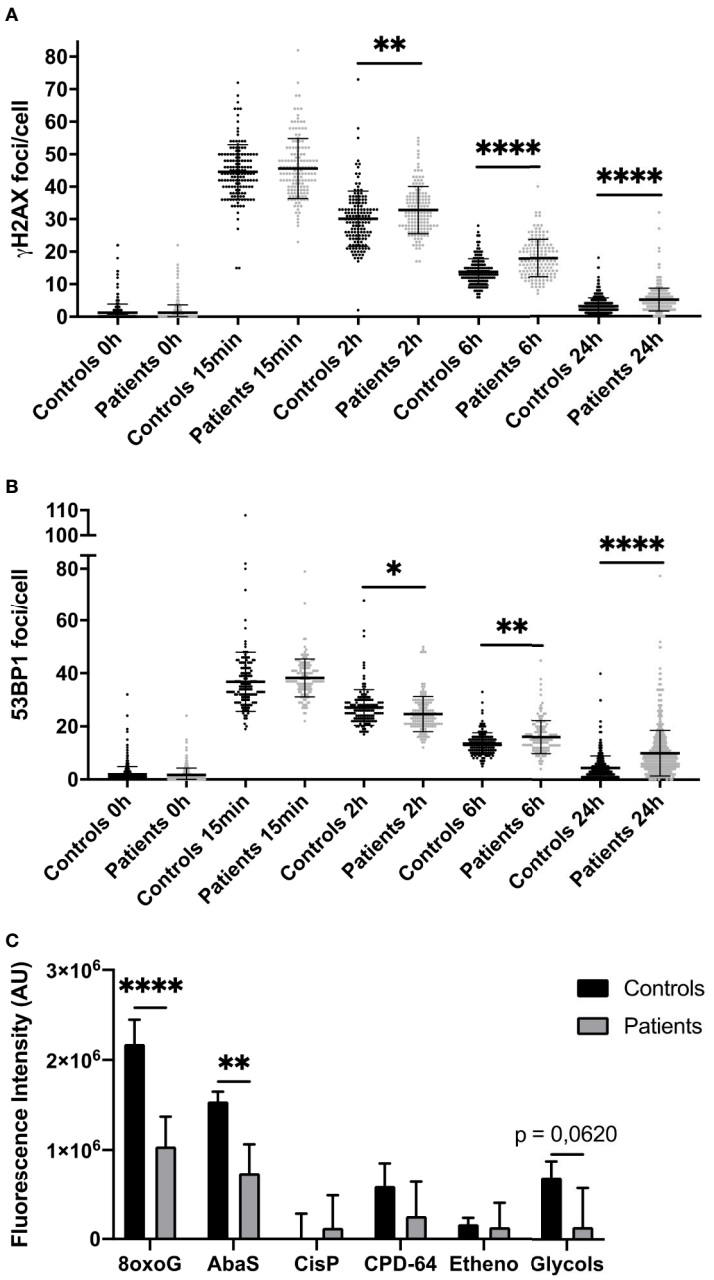

FIGURE 2 | Impaired DNA repair in dermal fibroblasts from overreacting patients. Immunofluorescence detection of γH2AX **(A)** and 53BP1 **(B)** foci, investigated 0 h, 15 min, 2, 6, and 24 h after 2 Gy irradiation in cells from patients with severe radiotherapy side-effects. The number of foci was assessed in at least 100 cells in four normal (C1, C2, C4, and C8) and four patient cell strains (P1, P6, P10, and P15). Results are mean +/– SD. The p-value was calculated by one-way ANOVA. Significant at $^{*}P < 0.05$, $^{**}P < 0.01$, and $^{****}P < 0.0001$. **(C)** DNA damage repair ability was measured using the ExSy-SPOT chip. Fluorescence was proportional to cell ability to repair indicated DNA lesions. 8oxoG, 8-oxoGuanine; AbaS, Abasic site; CisP, Cisplatin adducts; CPD-64, Cyclobutane pyrimidine dimer - pyrimidine-(6,4)-pyrimidone photoproducts; Etheno, Etheno adducts. Results are mean +/– SD from four control fibroblast strains (C1, C2, C4, and C6) and four radiosensitive fibroblast strains (P2, P7, P8, and P10). The p-value was calculated by Student's t-test. Significant at $^{**}P < 0.01$ and $^{****}P < 0.0001$.

grade 2 and grade 3 patients, in agreement with the PCA and hierarchical cluster classification of the transcriptome data.

Four hundred forty-five of the 540 differentially expressed genes were protein-coding and were used for functional enrichment analysis. Gene ontology analysis highlighted 93 significantly enriched GO biological processes with FDR <0.05 (**Figure S1 Supplementary data**). Functions with the smallest FDRs comprised regulation of GTPase activity regulation, of organ development and of cell adhesion and junction (**Figure S1 Supplementary data**). All these functions might be involved in cellular radiation toxicity, but correspond to multiple intracellular pathways. We then searched for enriched pathways involving the 445 differentially expressed protein-coding genes using the WebGestalt and the KEGG database 2019. We found only one significantly enriched pathway (**Supplementary Table S2**): Arrhythmogenic right ventricular cardiomyopathy (adjusted p-value 0.0065733—10 genes out 72 modulated), a pathology of cardiac muscles with progressive loss of myocytes replaced by adipocytes. Systematic analysis of our gene list revealed that none of these genes was directly involved in any known genetic syndrome leading to increased radiosensitivity.

NFATC2 Is Downregulated in Patient Cells and Correlated With Radiosensitivity

Among the most differentially expressed genes between control and patient fibroblasts identified by our RNA sequencing approach, we focused on *NFATC2*, which encodes a transcription factor initially described in T-cell activation and involved in numerous cellular functions such as apoptosis and the cell cycle (21). We therefore carefully analyzed NFATC2 gene and protein expression in patient cells extracted from non-irradiated skin. Dermal fibroblasts from patients with severe radiotherapy side-effects exhibited much lower *NFATC2* gene expression than control cells (**Figure 4A**). Similarly, NFATC2 protein expression was lower in patient's cells (**Figures 4B, C**). NFATC2 gene and protein expressions were assessed after irradiation to determine whether *NFATC2* could be a radiation-responding gene, potentially involved in cellular radiation response. *NFATC2* gene overexpression was detected in response to 2 Gy irradiation, with a 4-fold peak at 3 h in control fibroblasts and a 15-fold peak in patient fibroblasts, with return to baseline after 24 h (**Figure 4D**). NFATC2 protein was detected in greater quantities (×1.8) after 2 Gy irradiation with a peak between 3 and 6 h in normal fibroblasts, but the difference was not statistically significant due to interindividual variability (P = 0.1192 and P = 0.1553, respectively) (**Figures 4E, F**). Furthermore, NFATC2 protein was barely detected in cells from radiosensitive patients (**Figures 4E, F**). Interestingly, there was a significant correlation between NFATC2 transcriptional expression and irradiated cell survival (Pearson correlation coefficient, R^2 = 0.4949, P = 0.0001254) (**Figure 4G**), suggesting a possible role for NFATC2 in cellular radiosensitivity. Taken together, these results suggest that *NAFTC2* is a radiation-responding gene potentially involved in cellular response to ionizing radiation.

NFATC2 Is Hypermethylated in Patient Fibroblasts

To elucidate the regulatory mechanisms underlying *NFATC2* differential expression in non-irradiated fibroblasts from controls and patients, we compared gene methylation level between patients and controls. The methylation pattern of the *NFATC2* gene region was extracted from genome-wide methylation profiling using methylation bead chips performed on patient and control fibroblasts (data not shown), identifying 34 differentially methylated sites (CpGs) (33 hyper- and 1 hypo-methylated) (**Figure 5**). This hypermethylation of the *NFATC2* gene in patients' fibroblasts was consistent with its lower gene expression. Interestingly, the upstream region of the transcription starting site (TSS) exhibited the same methylation profile in patient and control cells (**Figure 5**). However, among the hypermethylated CpGs, cg00418183, cg00401091, cg11086066, cg10226546, cg11074047, cg18302534, cg16419175, cg21610125, cg15497991, cg26408896, cg22243637, cg09740920, cg00498368, cg08637147, cg09465142, cg03986956, and cg00689890 belong to gene regions identified as promoter-associated regions according to the ENCODE consortium. This hypermethylation of these regulatory regions could, at least in part, explain the weak expression of *NFATC2* in patient fibroblasts.

To confirm these results by an independent method, we performed HRM PCR to evaluate the methylation state of the CpG00498368 in four patient and two control cell strains. HRM PCR is a PCR measuring the melting temperature of a specific amplicon. After bisulfite conversion, an amplicon comprising a methylated CpG would exhibit a higher melting temperature than an amplicon with an unmethylated CpG. We detected a higher melting temperature peak, corresponding to a methylated state of this CpG in patient fibroblasts and to an unmethylated state in control fibroblasts (**Figure S2B Supplementary data**), in agreement with the global methylome data (**Figure S2A Supplementary data**).

These results suggest that NFATC2 down-regulation could, at least in part, be due to hypermethylation of the gene in fibroblasts from patients with severe radiotherapy side-effects.

NFATC2 Silencing in Normal Dermal Fibroblasts Leads to Increased Cellular Radiosensitivity and DNA DSB Defects

To evaluate the functional impact of NFATC2 in cellular radiosensitivity, *NFATC2* expression was silenced in cells from healthy individuals by stable RNA interference mediated by a lentiviral vector. We tested four lentiviral vectors, each containing a different short hairpin RNA (shRNA) targeting *NFATC2*, and chose the most efficient in terms of silencing for the further experiments (**Figure S3 Supplementary data**). NFATC2 expression was reduced by 48% on average at gene level (**Figure 6A**) and by 70% on average at protein level in transduced fibroblasts expressing the shRNA targeting the *NFATC2* transcript (**Figures 6B, C**). Colony survival assays revealed that cells with lower *NFATC2* expression (HNF sh-*NFATC2*) exhibited a significantly lower SF2 compared to their

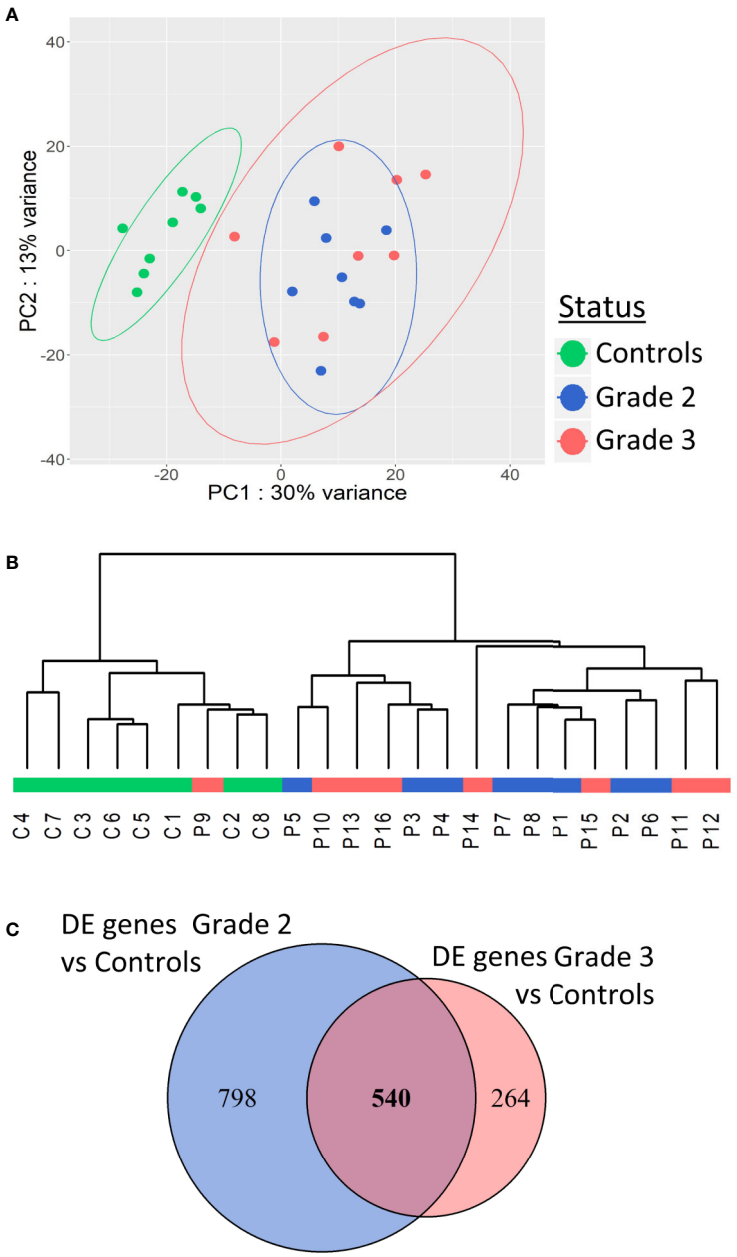

FIGURE 3 | Patients with severe radiotherapy side-effects show a specific transcriptome profile. Principal component analysis **(A)** and hierarchical clustering **(B)** of patients and controls based on RNA sequencing data. **(C)** Venn diagram showing the 540 differentially expressed genes in common between grade 2 vs control and grade 3 vs control RNAseq data.

control (HNF sh-*SCR*) (20% decrease in cell survival in response to irradiation) (**Figure 6D**). To better understand the molecular mechanisms of this cell death elevation in sh-NFTAC2 expressing cells, we investigated their DNA DSB repair ability, and detected more residual γH2AX and 53BP1 foci 24 h after 2 Gy irradiation in HNF sh-*NFATC2* cells than in control cells (HNF sh-*SCR*) (respectively, +1.49 γH2AX and +1.46 53BP1 foci per nucleus on average) (**Figures 6E, F**), corresponding to an excess of residual unrepaired DNA double-strand breaks. These results suggest that the *NFACT2* down-regulation observed in patient cells is involved in their cellular radiation sensitivity.

DISCUSSION

The mechanisms responsible for individual sensitivity to ionizing radiations are not yet fully elucidated. The present study investigated the radiation sensitivity of dermal fibroblasts from

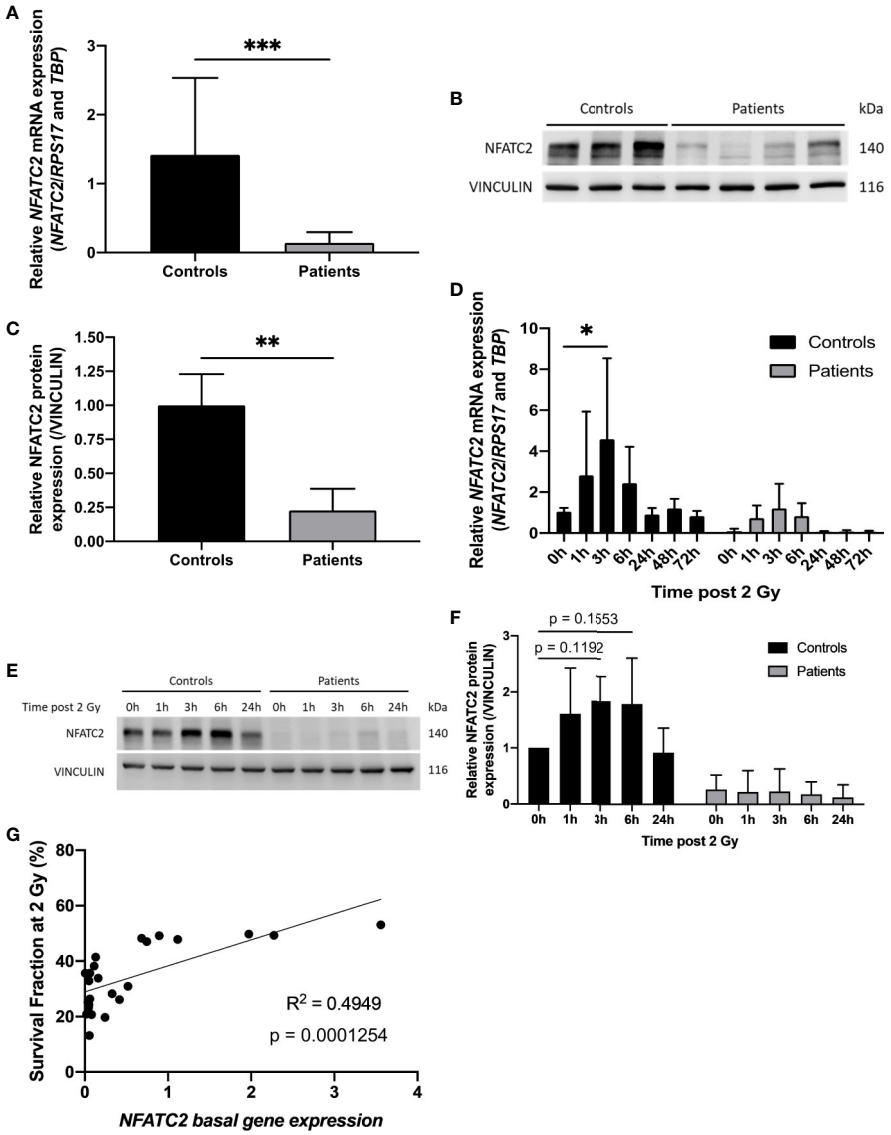

FIGURE 4 | NFATC2 downregulation in fibroblasts from overreacting patients. **(A)** *NFATC2* mRNA levels were measured by RTqPCR in control cells (n = 8) and in fibroblasts from patients with severe radiotherapy side-effects (n = 16). Results are mean +/– SD. The p-value was calculated by Student's t-test. Significant at $^{***}P < 0.001$. **(B)** NFATC2 protein expression was evaluated by immunoblotting in control (n = 3) and patient fibroblasts (n = 4) and quantified **(C)**, with VINCULIN as loading control. Results are mean +/– SD. The p-value was calculated by Student's t-test. Significant at $^{**}P < 0.01$. **(D)** *NFATC2* gene expression was assessed at various time points after 2 Gy irradiation in three control cell strains (C1, C5, and C8) and three cell strains from overreacting patients (P7, P8, and P10). Results are mean +/– SD. The p-value was calculated by two-way ANOVA. Significant at $^{*}P < 0.05$. **(E)** Representative image of immunoblotting analysis of NFATC2 protein expression at various time points after 2 Gy irradiation on one control cell strain (C4) and one patient cell strain (P8) and quantification **(F)**. Results are mean +/– SD from three independent immunoblotting analyses of three control (C4, C5, and C8) and three patient fibroblast strains (P6, P8, and P10). The p-value was calculated by two-way ANOVA. **(G)** Pearson correlation between *NFATC2* gene expression and SF2.

patients showing severe side-effects of radiotherapy (RT). A key result was that patient dermal fibroblasts were intrinsically more radiosensitive than cells from healthy individuals. We also detected more γH2AX and 53BP1 foci from 6 to 24 h after irradiation in patient dermal fibroblasts, suggesting slower DNA DSB repair ability.

DNA DSB repair abilities in cells from radiosensitive patients have been widely studied. Some authors identified a link between residual unrepaired DNA DSB and risk of severe RT side-effects (16, 22, 23), whereas others found no DNA DSB repair defect in cells from radiosensitive patients (24–26). Once again, these differences could be due to differences in the methods used to assess DSB repair ability, highlighting the necessity of more standardized protocols, especially regarding cell culture conditions, type of irradiation and DSB detection kinetics (27).

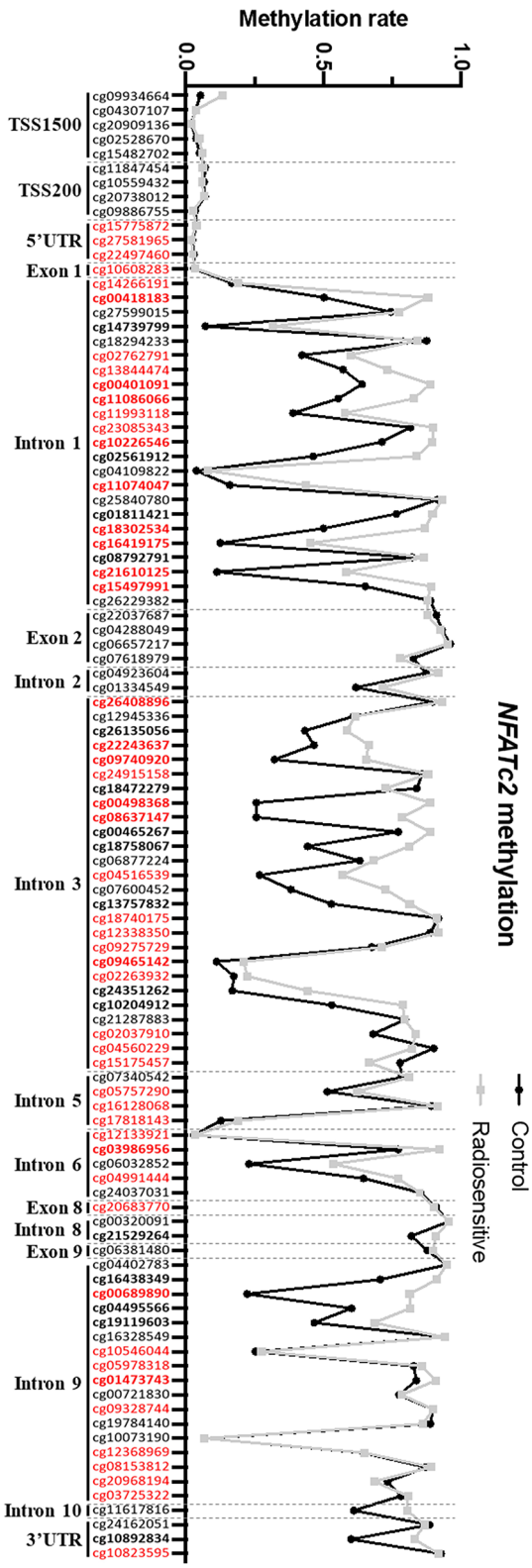

FIGURE 5 | *NFATC2* is hypermethylated in patient fibroblasts. *NFATC2* methylation in cells from patients with severe radiotherapy side-effects (n = 16) and controls (n = 8) were investigated on genome-wide methylation analysis. CpG sites in bold are differentially methylated between control and patient cells. CpG sites in red are part of promoter-associated regions defined by the ENCODE consortium.

Moreover, using the ExSy-SPOT assay, we showed that cells from patients with severe RT side-effects also exhibited repair defects for 8-oxoGuanine, abasic sites, and glycol-damaged bases. All these types of DNA damage, induced by ionizing radiation and the resulting oxidative stress, are usually repaired by base excision repair mechanisms (28). Batar et al. showed that a decrease in *XRCC1* expression, an actor in base excision repair, was associated with acute side-effects in breast cancer patients (29). However, no *XRCC1* differential expression was detected between control and patient fibroblasts and further investigations will be needed to elucidate at which level dermal fibroblasts from radiosensitive patients fail in their base excision repair mechanism.

Patient cells exhibited a specific transcriptome profile compared to controls, with no segregation at transcriptional level between clinical grades 2 and 3. Side-effect severity is probably highly multifactorial and modulated by complex interaction between intrinsic and extrinsic factors during radiotherapy treatment. This could explain why we were not able to distinguish clinical grades on transcriptome analysis of patients' cells obtained several months after end of treatment. Nevertheless, we were able to identify 540 genes differentially

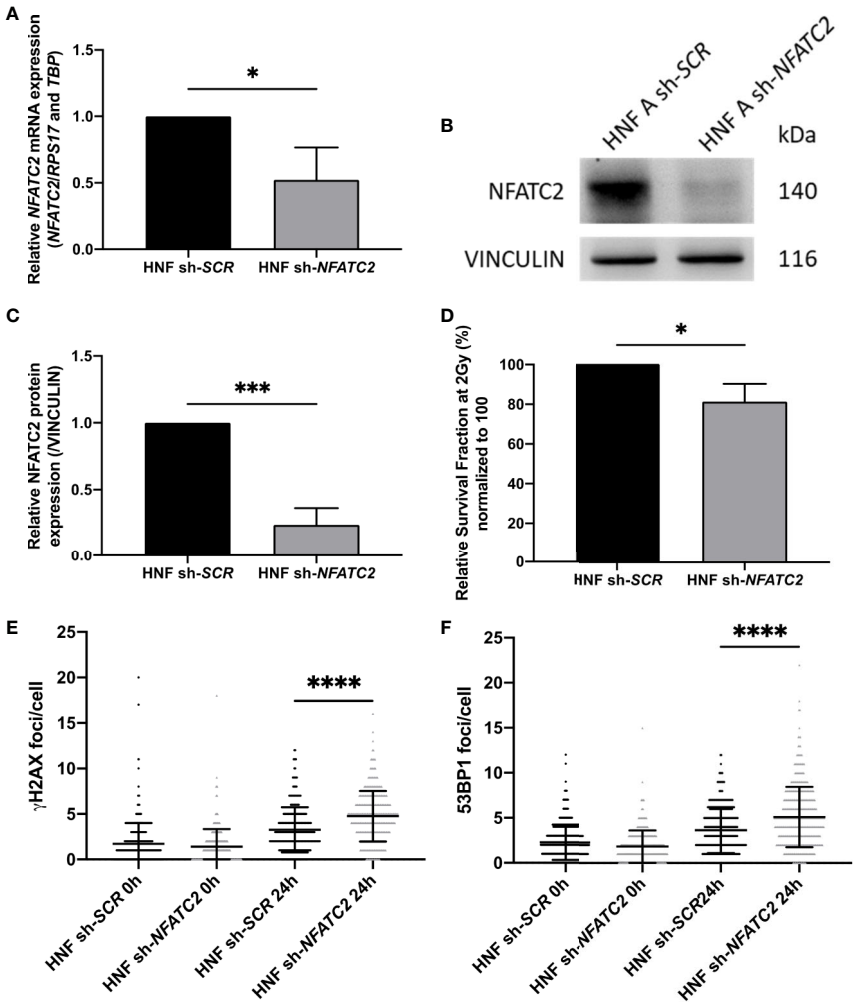

FIGURE 6 | NFATC2 downregulation leads to cellular radiosensitivity. **(A)** *NFATC2* mRNA levels were measured by RT-qPCR in three control fibroblast strains (HNF) infected with a lentiviral vector carrying either a shRNA scramble (sh-*SCR*) sequence or a shRNA targeting *NFATC2* (sh-*NFATC2*). Results are mean +/– SD. The p-value was calculated using a Student's t-test. Significant at $^{*}P < 0.05$. **(B)** Representative image of immunoblotting analysis of NFATC2 protein expression in one control cell strain (HNF A) infected with lentiviral vectors sh-*SCR* or sh-*NFATC2*, and quantification **(C)**. Results are mean +/– SD from immunoblotting analysis of three different cell strains infected with lentiviral vectors sh-*SCR* or sh-*NFATC2*. The p-value was calculated using a Student's t-test. Significant at $^{***}P < 0.001$. **(D)** Lower SF2 was measured by colony survival assays in cells infected with lentiviral vector sh-*NFATC2* compared to cells infected with lentiviral vector sh-*SCR*. Results are mean +/– SD from three cell strains. The p-value was calculated using a Student's t-test. Significant at $^{*}P < 0.05$. More numerous γH2AX **(E)** and 53BP1 **(F)** residual foci, investigated by immunofluorescence, 24 h after 2 Gy irradiation in fibroblasts infected with lentiviral vector sh-*NFATC2*. Assessed in at least 100 cells in three cell strains infected with lentiviral vectors sh-*SCR* or sh-*NFATC2*. Results are mean +/– SD. The p-value was calculated using a two-way ANOVA. Significant at $^{****}P < 0.0001$.

expressed between dermal fibroblasts from grade 2 and 3 patients *versus* controls. This list of genes is a potentially valuable resource for identifying new modulators of radiation toxicity in tissues and cells. Surprisingly, only one biological process, arrhythmogenic right ventricular cardiomyopathy (ARVC), was significantly over-represented in this gene list. ARVC is a non-genetic disease without any evidence of associated radiosensitivity. The link between ARVC and individual radiation response seems to be incidental, but it has been shown that inhibition of the Wnt pathway is a causal mechanism in ARVC (30), and it is clearly established that the Wnt pathway plays an important role in cell survival after irradiation, as previously shown in several cell types (31–33).

The main limitation of this transcriptome study is the relatively small number of patients analyzed, with 16 patients who suffered severe RT side-effects and 8 control samples. Nevertheless, this study allowed us to identify 540 genes differentially expressed between controls and patients, including NFATC2. We recently analyzed the expression of *NFATC2* in dermal fibroblasts from 22 additional patients and 8 controls and confirmed the strong repression of this gene in the patient's cells (fold change 4.07, p-value 3.21 E-1).

Transcriptome analysis identified *NFATC2* as one of the genes most differentially expressed between cells from over-reacting patients and controls. We confirmed that NFATC2 expression at gene and protein levels at basal state was lower in fibroblasts from patients with severe RT side-effects, and that *NFATC2* gene expression was modulated in response to irradiation. Furthermore, we highlighted the global hypermethylated state of *NFATC2* in patient fibroblasts, suggesting a role of methylation in the regulation of NFATC2 expression. Particularly, 17 CpG sites located in the promoter-associated regions defined by the ENCODE consortium (34) were identified as hypermethylated in patient fibroblasts. These promoter-associated regions were identified by ChIP-seq analysis against transcription factors in 91 different cell lines. Several transcription factors were identified by the ENCODE consortium as able to recognize the DNA region where the 17 CpG sites are located, including CTCF, E2F6, ZBTB7A, ZNF143, JUND, MEF2A, EGR1, RUNX3, and EBF1. ChIP analysis against these transcription factors in irradiated fibroblasts and at basal state would be of interest to elucidate the regulatory mechanisms of *NFATC2* expression modulated by epigenetic mechanisms.

Moreover, the present study showed that *NFATC2* silencing using RNA interference leads to increased cellular radiosensitivity and to a defect in DNA DSB repair. To our knowledge, this was the first study linking NFATC2 and cellular sensitivity to ionizing radiation. NFAT family members have been shown to be able to induce *GJA1* and *GADD45A* gene expressions in response to ionizing radiation (35, 36) and NFATC2 has been shown to induce *IL-5* expression in response to ionizing radiation (37). However, NFAT response to UV irradiation has been more thoroughly studied. It has been shown that NFAT positively regulates apoptosis in response to UV-radiation in keratinocytes (38) but, in contrast, inhibiting NFAT signaling promoted apoptosis in response to UV irradiation in a human embryonic fibroblast cell line (39). Moreover, inhibiting NFAT signaling has been shown to reduce keratinocyte ability to repair UV-induced DNA damages (40, 41). However, these studies used chemical inhibitors of NFAT signaling, while the specific roles of each NFAT family member in response to radiation remain unknown.

NFATC2 has been shown to regulate apoptosis and cell cycle progression, two major mechanisms involved in cellular radiosensitivity. NFATC2 controls the expression of *FASLG*, a pro-apoptotic regulator (42, 43), and of *CFLAR*, *BCL2A1*, and *MDM2*, known for their anti-apoptotic abilities (44–46). Moreover, NFATC2 can also regulate *TNFA* and *NR4A1* expression, both known for their dual pro- and anti-apoptotic roles (47, 48). Furthermore, NFATC2 has been shown to regulate cell cycle progression positively by inducing expression of *CDK6* (49) or inhibiting expression of *CDK4* (50), or negatively by inducing expression of *CDKN1A* (51) or repressing expression of *CCNA2* (52) and $p15^{INK4b}$ (53). NFATC2 has also been reported in positive or negative regulation of *MYC* expression, promoting or blocking cell cycle progression (54). These dual roles of NFATC2 in apoptosis and cell cycle control highlight the importance of its different isoforms and partners. One limit of our functional study of NFATC2 is the use of a shRNA targeting a region common to all the known isoforms of this protein. Further experiments using isoform-specific shRNAs will be necessary to decipher the relative role of the different variants of NFATC2 in fibroblast sensitivity to ionizing radiations.

In a 2016 study, Gabriel et al. investigated NFATC2 isoform C partners in a Jurkat human T-cell line (55). In addition to transcription factors, the authors pointed out new potential NFATC2 partners, including several actors of DNA damage response: notably those involved in DNA DSB repair, such as XRCC5/Ku80 and PRKDC, and in base or nucleotide excision repair, such as RFC, LIG3, and XRCC1. They also found an interaction between NFATC2 and PARP1, which is involved in recognition of DNA damage, and RPA, which binds to single-strand DNA during DNA repair. Interestingly, the authors detected these associations between actors of DNA damage response and NFATC2, but not with NFATC1, which suggests a specific role for NFATC2 in the DNA damage response (55). We performed preliminary experiments to clarify the interactions between NFATC2 and a few DNA repair proteins such as XRCC1 and XRCC5 in irradiated and non-irradiated fibroblasts, but did not observe any consistent co-immunoprecipitation (data not shown). Further specific investigations will be necessary to clarify these putative interactions, using tagged versions of the NFATC2 protein.

The present study found increased cellular radiosensitivity and a defect in DNA repair in dermal fibroblasts from patients with severe side-effects of RT, and highlighted a specific transcriptome profile in patient fibroblasts. These data pave the way for cellular and molecular strategies to identify radiosensitive patients. The study also showed the involvement of NFATC2 in cellular sensitivity to ionizing radiation and in DNA repair. However, the mechanisms by which NFATC2 contributes to the cellular response to ionizing radiation

remain to be clarified, notably concerning its interactions with actors of the DNA damage response, and its target genes as transcription factor. For the latter, investigating molecular pathways known to be involved in the development of RT complication in normal tissues, such as TGF-β and WNT, would be particularly relevant.

DATA AVAILABILITY STATEMENT

The data presented in the study are deposited in the Gene Expression Omnibus repository, accession number GSE154559.

ETHICS STATEMENT

The studies involving human participants were reviewed and approved by the regional Ethical Committee (CPP Sud-Est, Lyon, France), and cell lines were declared under the numbers DC2008-585 and DC2011-1437 to the Ministry of Research. The patients/participants provided their written informed consent to participate in this study.

AUTHOR CONTRIBUTIONS

JL, JD, and MTM designed the study. JD, CK, YM, JR, SM, TVS, and FPC acquired, analyzed, and interpreted the data. JD, JR, FPC, MTM, and JL critically revised the manuscript for important intellectual content. JL and MTM obtained funding. CK, SM, MTM, and JL provided the administrative, technical, and material support. JL is the guarantor of this work and, as such, has full access to all of the data and the accuracy of the data analysis. All authors contributed to the article and approved the submitted version.

ACKNOWLEDGMENTS

We thank Dr Nicolas Foray (INSERM, Lyon) for helpful support and discussion. We thank CEA CNRGH (Evry, France) for support. Christine Oger (PRABI, University of Lyon), Pascal Soularue (CEA, LGRK, Evry), and Olivier Alibert (CEA, CNRGH, Evry) helped in the analysis of the RNAseq data. We also thank Gisèle Froment, Didier Nègre, and Caroline Costa from the lentivectors production facility/SFR Biosciences Gerland - Lyon Sud (UMS3444/US8). The study was supported by a grant from La Ligue Contre le Cancer, Comité de Saône-et-Loire, and by ANR-RSNR-INDIRA.

SUPPLEMENTARY MATERIAL

The Supplementary Material for this article can be found online at: https://www.frontiersin.org/articles/10.3389/fonc.2020.589168/full#supplementary-material

REFERENCES

1. Bentzen SM. Preventing or reducing late side effects of radiation therapy: radiobiology meets molecular pathology. *Nat Rev Cancer* (2006) 6:702–13. doi: 10.1038/nrc1950
2. Schaake W, Wiegman EM, de Groot M, van der Laan HP, van der Schans CP, van den Bergh ACM, et al. The impact of gastrointestinal and genitourinary toxicity on health related quality of life among irradiated prostate cancer patients. *Radiother Oncol* (2014) 110:284–90. doi: 10.1016/j.radonc.2013.11.011
3. Martin M, Lefaix J, Delanian S. TGF-beta1 and radiation fibrosis: a master switch and a specific therapeutic target? *Int J Radiat Oncol Biol Phys* (2000) 47:277–90. doi: 10.1016/s0360-3016(00)00435-1
4. Jonathan Leventhal MD. Radiation Dermatitis: Recognition, Prevention, and Management(2017). Available at: https://www.cancernetwork.com/article/radiation-dermatitis-recognition-prevention-and-management (Accessed April 1, 2020).
5. Partl R, Regitnig P, Tauber G, Pötscher M, Bjelic-Radisic V, Kapp KS. Radiation-induced morphea—a rare but severe late effect of adjuvant breast irradiation. *Strahlenther Onkol* (2018) 194:1060–5. doi: 10.1007/s00066-018-1336-9
6. Delanian S, Martin M, Bravard A, Luccioni C, Lefaix J-L. Cu/Zn superoxide dismutase modulates phenotypic changes in cultured fibroblasts from human skin with chronic radiotherapy damage. *Radiother Oncol* (2001) 58:325–31. doi: 10.1016/S0167-8140(00)00332-7
7. Smith KC, Hahn GM, Hoppe RT, Earle JD. Radiosensitivity in vitro of human fibroblasts derived from patients with a severe skin reaction to radiation therapy. *Int J Radiat Oncol Biol Phys* (1980) 6:1573–5. doi: 10.1016/0360-3016(80)90017-6
8. Woods WG, Byrne TD, Kim TH. Sensitivity of cultured cells to gamma radiation in a patient exhibiting marked in vivo radiation sensitivity. *Cancer* (1988) 62:2341–5. doi: 10.1002/1097-0142(19881201)62:11<2341::aid-cncr2820621114>3.0.co;2-w
9. Loeffler JS, Harris JR, Dahlberg WK, Little JB. In vitro radiosensitivity of human diploid fibroblasts derived from women with unusually sensitive clinical responses to definitive radiation therapy for breast cancer. *Radiat Res* (1990) 121:227–31. doi: 10.2307/3577508
10. Plowman PN, Bridges BA, Arlett CF, Hinney A, Kingston JE. An instance of clinical radiation morbidity and cellular radiosensitivity, not associated with ataxia-telangiectasia. *Br J Radiol* (1990) 63:624–8. doi: 10.1259/0007-1285-63-752-624
11. Vulin A, Sedkaoui M, Moratille S, Sevenet N, Soularue P, Rigaud O, et al. Severe PATCHED1 Deficiency in Cancer-Prone Gorlin Patient Cells Results in Intrinsic Radiosensitivity. *Int J Radiat Oncol Biol Phys* (2018) 102:417–25. doi: 10.1016/j.ijrobp.2018.05.057
12. Burnet NG, Wurm R, Yarnold JR, Peacock JH, Nyman J, Turesson I. Prediction of normal-tissue tolerance to radiotherapy from in-vitro cellular radiation sensitivity. *Lancet* (1992) 339:1570–1. doi: 10.1016/0140-6736(92)91833-T
13. Geara FB, Peters LJ, Ang KK, Wike JL, Brock WA. Prospective comparison of in vitro normal cell radiosensitivity and normal tissue reactions in radiotherapy patients. *Int J Radiat Oncol Biol Phys* (1993) 27:1173–9. doi: 10.1016/0360-3016(93)90540-c
14. Russell NS, Grummels A, Hart AAM, Smolders IJH, Borger J, Bartelink H, et al. Low predictive value of intrinsic fibroblast radiosensitivity for fibrosis development following radiotherapy for breast cancer. *Int J Radiat Biol* (1998) 73:661–70. doi: 10.1080/095530098141915
15. Peacock J, Ashton A, Bliss J, Bush C, Eady J, Jackson C, et al. Cellular radiosensitivity and complication risk after curative radiotherapy. *Radiother Oncol* (2000) 55:173–8. doi: 10.1016/S0167-8140(00)00173-0
16. COPERNIC project investigators, Granzotto A, Benadjaoud MA, Vogin G, Devic C, Ferlazzo ML, et al. Influence of Nucleoshuttling of the ATM Protein in the Healthy Tissues Response to Radiation Therapy: Toward a Molecular

Classification of Human Radiosensitivity. *Int J Radiat Oncol Biol Phys* (2016) 94:450–60. doi: 10.1016/j.ijrobp.2015.11.013
17. Common Terminology Criteria for Adverse Events (CTCAE).80.
18. Yu G, Wang L-G, Han Y, He Q-Y. clusterProfiler: an R Package for Comparing Biological Themes Among Gene Clusters. *OMICS* (2012) 16:284–7. doi: 10.1089/omi.2011.0118
19. Fusil F, Calattini S, Amirache F, Mancip J, Costa C, Robbins JB, et al. A Lentiviral Vector Allowing Physiologically Regulated Membrane-anchored and Secreted Antibody Expression Depending on B-cell Maturation Status. *Mol Ther* (2015) 23:1734–47. doi: 10.1038/mt.2015.148
20. Millau J-F, Raffin A-L, Caillat S, Claudet C, Arras G, Ugolin N, et al. A microarray to measure repair of damaged plasmids by cell lysates. *Lab Chip* (2008) 8:1713–22. doi: 10.1039/b806634e
21. Mognol GP, Carneiro FRG, Robbs BK, Faget DV, Viola JPB. Cell cycle and apoptosis regulation by NFAT transcription factors: new roles for an old player. *Cell Death Dis* (2016) 7:e2199. doi: 10.1038/cddis.2016.97
22. Bourton EC, Plowman PN, Smith D, Arlett CF, Parris CN. Prolonged expression of the γ-H2AX DNA repair biomarker correlates with excess acute and chronic toxicity from radiotherapy treatment. *Int J Cancer* (2011) 129:2928–34. doi: 10.1002/ijc.25953
23. Li P, Du C, Xu W, Shi Z, Zhang Q, Li Z, et al. Correlation of dynamic changes in γ-H2AX expression in peripheral blood lymphocytes from head and neck cancer patients with radiation-induced oral mucositis. *Radiat Oncol* (2013) 8:155. doi: 10.1186/1748-717X-8-155
24. Olive PL, Banáth JP, Keyes M. Residual γH2AX after irradiation of human lymphocytes and monocytes in vitro and its relation to late effects after prostate brachytherapy. *Radiother Oncol* (2008) 86:336–46. doi: 10.1016/j.radonc.2007.09.002
25. Werbrouck J, De Ruyck K, Beels L, Vral A, Van Eijkeren M, De Neve W, et al. Prediction of late normal tissue complications in RT treated gynaecological cancer patients: Potential of the γ-H2AX foci assay and association with chromosomal radiosensitivity. *Oncol Rep* (2010) 23:571–8. doi: 10.3892/or_00000671
26. Vasireddy RS, Sprung CN, Cempaka NL, Chao M, McKay MJ. H2AX phosphorylation screen of cells from radiosensitive cancer patients reveals a novel DNA double-strand break repair cellular phenotype. *Br J Cancer* (2010) 102:1511–8. doi: 10.1038/sj.bjc.6605666
27. Habash M, Bohorquez LC, Kyriakou E, Kron T, Martin OA, Blyth BJ. Clinical and Functional Assays of Radiosensitivity and Radiation-Induced Second Cancer. *Cancers (Basel)* (2017) 9(11):147. doi: 10.3390/cancers9110147
28. Ravanat J-L. Endogenous natural and radiation-induced DNA lesions: differences and similarities and possible implications for human health and radiological protection. *Radioprotection* (2018) 53:241–8. doi: 10.1051/radiopro/2018039
29. Batar B, Guven G, Eroz S, Bese NS, Guven M. Decreased DNA repair gene XRCC1 expression is associated with radiotherapy-induced acute side effects in breast cancer patients. *Gene* (2016) 582:33–7. doi: 10.1016/j.gene.2016.01.040
30. van Tintelen JP, Hofstra RM, Wiesfeld AC, van den Berg MP, Hauer RN, Jongbloed JD. Molecular genetics of arrhythmogenic right ventricular cardiomyopathy: emerging horizon? *Curr Opin Cardiol* (2007) 22:185–92. doi: 10.1097/HCO.0b013e3280d942c4
31. Chang HW, Roh J-L, Jeong E-J, Lee S, Kim S-W, Choi S-H, et al. Wnt signaling controls radiosensitivity via cyclooxygenase-2-mediated Ku expression in head and neck cancer. *Int J Cancer* (2008) 122:100–7. doi: 10.1002/ijc.23069
32. Gurung A, Uddin F, Hill RP, Ferguson PC, Alman BA. β-Catenin Is a Mediator of the Response of Fibroblasts to Irradiation. *Am J Pathol* (2009) 174:248–55. doi: 10.2353/ajpath.2009.080576
33. Karimaian A, Majidinia M, Bannazadeh Baghi H, Yousefi B. The crosstalk between Wnt/β-catenin signaling pathway with DNA damage response and oxidative stress: Implications in cancer therapy. *DNA Repair (Amst)* (2017) 51:14–9. doi: 10.1016/j.dnarep.2017.01.003
34. ENCODE consortium. An Integrated Encyclopedia of DNA Elements in the Human Genome. *Nature* (2012) 489:57–74. doi: 10.1038/nature11247
35. Glover D, Little JB, Lavin MF, Gueven N. Low dose ionizing radiation-induced activation of connexin 43 expression. *Int J Radiat Biol* (2003) 79:955–64. doi: 10.1080/09553000310001632895
36. Daino K, Ichimura S, Nenoi M. Comprehensive Search for X-ray-responsive Elements and Binding Factors in the Regulatory Region of the GADD45a Gene. *J Radiat Res* (2003) 44:311–8. doi: 10.1269/jrr.44.311
37. Lu-Hesselmann J, Messer G, van Beuningen D, Kind P, Peter RU. Transcriptional regulation of the human IL5 gene by ionizing radiation in Jurkat T cells: evidence for repression by an NF-AT-like element. *Radiat Res* (1997) 148:531–42. doi: 10.2307/3579728
38. Flockhart RJ, Diffey BL, Farr PM, Lloyd J, Reynolds NJ. NFAT regulates induction of COX-2 and apoptosis of keratinocytes in response to ultraviolet radiation exposure. *FASEB J* (2008) 22:4218–27. doi: 10.1096/fj.08-113076
39. Mazière C, Morlière P, Louandre C, Conte M-A, Gomilla C, Santus R, et al. Low UVA doses activate the transcription factor NFAT in human fibroblasts by a calcium-calcineurin pathway. *Free Radic Biol Med* (2005) 39:1629–37. doi: 10.1016/j.freeradbiomed.2005.08.003
40. Yarosh DB, Pena AV, Nay SL, Canning MT, Brown DA. Calcineurin inhibitors decrease DNA repair and apoptosis in human keratinocytes following ultraviolet B irradiation. *J Invest Dermatol* (2005) 125:1020–5. doi: 10.1111/j.0022-202X.2005.23858.x
41. Canning MT, Nay SL, Peña AV, Yarosh DB. Calcineurin inhibitors reduce nuclear localization of transcription factor NFAT in UV-irradiated keratinocytes and reduce DNA repair. *J Mol Histol* (2006) 37:285–91. doi: 10.1007/s10735-006-9034-9
42. Latinis KM, Carr LL, Peterson EJ, Norian LA, Eliason SL, Koretzky GA. Regulation of CD95 (Fas) ligand expression by TCR-mediated signaling events. *J Immunol* (1997) 158:4602–11.
43. Holtz-Heppelmann CJ, Algeciras A, Badley AD, Paya CV. Transcriptional Regulation of the Human FasL Promoter-Enhancer Region. *J Biol Chem* (1998) 273:4416–23. doi: 10.1074/jbc.273.8.4416
44. Ueffing N, Schuster M, Keil E, Schulze-Osthoff K, Schmitz I. Up-regulation of c-FLIPshort by NFAT contributes to apoptosis resistance of short-term activated T cells. *Blood* (2008) 112:690–8. doi: 10.1182/blood-2008-02-141382
45. Ullerås E, Karlberg M, Möller Westerberg C, Alfredsson J, Gerondakis S, Strasser A, et al. NFAT but not NF-κB is critical for transcriptional induction of the prosurvival gene A1 after IgE receptor activation in mast cells. *Blood* (2008) 111:3081–9. doi: 10.1182/blood-2006-10-053371
46. Zhang X, Zhang Z, Cheng J, Li M, Wang W, Xu W, et al. Transcription Factor NFAT1 Activates the mdm2 Oncogene Independent of p53. *J Biol Chem* (2012) 287:30468–76. doi: 10.1074/jbc.M112.373738
47. Youn H-D, Chatila TA, Liu JO. Integration of calcineurin and MEF2 signals by the coactivator p300 during T-cell apoptosis. *EMBO J* (2000) 19:4323–31. doi: 10.1093/emboj/19.16.4323
48. Wu Q, Liu S, Ye X, Huang Z, Su W. Dual roles of Nur77 in selective regulation of apoptosis and cell cycle by TPA and ATRA in gastric cancer cells. *Carcinogenesis* (2002) 23:1583–92. doi: 10.1093/carcin/23.10.1583
49. Baumgart, Chen N, Zhang J-S, Billadeau DD, Gaisina I, Kozikowski AP, et al. GSK-3β governs inflammation-induced NFATc2 signaling hubs to promote pancreatic cancer progression. *Mol Cancer Ther* (2016) 15:491–502. doi: 10.1158/1535-7163.MCT-15-0309
50. Baksh S, Widlund HR, Frazer-Abel AA, Du J, Fosmire S, Fisher DE, et al. NFATc2-Mediated Repression of Cyclin-Dependent Kinase 4 Expression. *Mol Cell* (2002) 10:1071–81. doi: 10.1016/S1097-2765(02)00701-3
51. Santini MP, Talora C, Seki T, Bolgan L, Dotto GP. Cross talk among calcineurin, Sp1/Sp3, and NFAT in control of p21WAF1/CIP1 expression in keratinocyte differentiation. *Proc Natl Acad Sci U S A* (2001) 98:9575–80. doi: 10.1073/pnas.161299698
52. Carvalho LDS, Teixeira LK, Carrossini N, Caldeira ATN, Ansel KM, Rao A, et al. The NFAT1 transcription factor is a repressor of cyclin A2 gene expression. *Cell Cycle* (2007) 6:1789–95. doi: 10.4161/cc.6.14.4473
53. Baumgart GE, Singh G, Chen N-M, Reutlinger K, Zhang J, Billadeau, et al. Restricted Heterochromatin Formation Links NFATc2 Repressor Activity With Growth Promotion in Pancreatic Cancer. *Gastroenterology* (2012) 142:388–98.e17. doi: 10.1053/j.gastro.2011.11.001
54. Mognol, de Araujo-Souza PS, Robbs BK, Teixeira LK, Viola JPB. Transcriptional regulation of the c-Myc promoter by NFAT1 involves negative and positive NFAT-responsive elements. *Cell Cycle* (2012) 11:1014–28. doi: 10.4161/cc.11.5.19518

55. Gabriel CH, Gross F, Karl M, Stephanowitz H, Hennig AF, Weber M, et al. Identification of Novel Nuclear Factor of Activated T Cell (NFAT)-associated Proteins in T Cells. *J Biol Chem* (2016) 291:24172–87. doi: 10.1074/jbc.M116.739326

Conflict of Interest: The authors declare that the research was conducted in the absence of any commercial or financial relationships that could be construed as a potential conflict of interest.

frontiers in Oncology

ORIGINAL RESEARCH
published: 17 December 2020
doi: 10.3389/fonc.2020.596013

A Novel Nomogram Model Based on Cone-Beam CT Radiomics Analysis Technology for Predicting Radiation Pneumonitis in Esophageal Cancer Patients Undergoing Radiotherapy

*Feng Du[1,2], Ning Tang[1], Yuzhong Cui[3], Wei Wang[3], Yingjie Zhang[3], Zhenxiang Li[3] and Jianbin Li[3]**

[1] Department of Radiation Oncology, School of Clinical Medicine, Cheeloo College of Medicine, Shandong University, Jinan, China, [2] Department of Radiation Oncology, Zibo Municipal Hospital, Zibo, China, [3] Department of Radiation Oncology, Shandong Cancer Hospital and Institute, Shandong First Medical University and Shandong Academy of Medical Sciences, Jinan, China

OPEN ACCESS

Edited by:
Tiziana Rancati, Istituto Nazionale dei Tumori (IRCCS), Italy

Reviewed by:
Gilles Defraene, KU Leuven, Belgium
Irina Vergalasova, Rutgers Cancer Institute of New Jersey, United States

***Correspondence:**
Jianbin Li
lijianbin@msn.com

Specialty section:
This article was submitted to Radiation Oncology, a section of the journal Frontiers in Oncology

Received: *18 August 2020*
Accepted: *04 November 2020*
Published: *17 December 2020*

Citation:
Du F, Tang N, Cui Y, Wang W, Zhang Y, Li Z and Li J (2020) A Novel Nomogram Model Based on Cone-Beam CT Radiomics Analysis Technology for Predicting Radiation Pneumonitis in Esophageal Cancer Patients Undergoing Radiotherapy. Front. Oncol. 10:596013. doi: 10.3389/fonc.2020.596013

Purpose: We quantitatively analyzed the characteristics of cone-beam computed tomography (CBCT) radiomics in different periods during radiotherapy (RT) and then built a novel nomogram model integrating clinical features and dosimetric parameters for predicting radiation pneumonitis (RP) in patients with esophageal squamous cell carcinoma (ESCC).

Methods: At our institute, a retrospective study was conducted on 96 ESCC patients for whom we had complete clinical feature and dosimetric parameter data. CBCT images of each patient in three different periods of RT were obtained, the images were segmented using both lungs as the region of interest (ROI), and 851 image features were extracted. The least absolute shrinkage selection operator (LASSO) was applied to identify candidate radiomics features, and logistic regression analyses were applied to construct the rad-score. The optimal period for the rad-score, clinical features, and dosimetric parameters were selected to construct the nomogram model and then the receiver operating characteristic (ROC) curve was used to evaluate the prediction capacity of the model. Calibration curves and decision curves were used to demonstrate the discriminatory and clinical benefit ratios, respectively.

Results: The relative volume of total lung treated with ≥5 Gy (V5), mean lung dose (MLD), and tumor stage were independent predictors of RP and were finally incorporated into the nomogram. When the three time periods were modeled, the first period was better than the others. In the primary cohort, the area under the ROC curve (AUC) was 0.700 (95% confidence interval (CI) 0.568–0.832), and in the independent validation cohort, the AUC was 0.765 (95% CI 0.588–0.941). In the nomogram model that integrates clinical features and dosimetric parameters, the AUC in the primary cohort was 0.836 (95% CI 0.700–0.918), and the AUC in the validation cohort was 0.905 (95% CI 0.799–1.000). The

nomogram model exhibits excellent performance. Calibration curves indicate a favorable consistency between the nomogram prediction and the actual outcomes. The decision curve exhibits satisfactory clinical utility.

Conclusion: The radiomics model based on early lung CBCT is a potentially valuable tool for predicting RP. V5, MLD, and tumor stage have certain predictive effects for RP. The developed nomogram model has a better prediction ability than any of the other predictors and can be used as a quantitative model to predict RP.

Keywords: esophageal cancer, cone beam computed tomography, radiation pneumonitis, prediction model, radiomics

INTRODUCTION

Among malignant tumors, the incidence rate of esophageal cancer (EC) is the seventh highest, and the mortality rate is sixth worldwide (1). Radiotherapy (RT) is still one of the main treatments for locally advanced EC (2, 3). However, radiation pneumonitis (RP) is one of the major toxicities of thoracic radiation therapy. If RP occurs, it seriously affects the patient's quality of life and survival prognosis (4). Therefore, it is imperative for EC patients undergoing RT to identify this toxicity at the earliest possible time. More importantly, the accurate prediction of RP is essential to facilitate individualized radiation dosing that leads to maximized therapeutic gain. At present, the risk assessment of RP is mainly predicted by using lung dosimetric parameters (5, 6), such as the relative volume of total lung irradiated above a specified threshold dose (V_X) or mean lung dose (MLD): Although several metrics have appeared promising, the results vary across institutions, so these metrics do not seem to be perfect at predicting RP (7, 8). In addition to dosimetric parameters, some clinical features (tumor stage, smoking history, preexisting lung diseases, concurrent chemotherapy, and radiation dose) are also considered to be related to RP occurrence. However, the consensus on the comparative importance of these related predictors remains unavailable at present. Consequently, in order to individually and precisely discern RP, an accurate predictive model incorporating multiple types of factors with superior clinical utility is urgently needed.

Computed tomography (CT) images play an essential role in the diagnosis and treatment of RP. As early as the end of the 20th century, RP could be identified by CT. However, RP cannot be predicted by superficial CT manifestations. Therefore, the focus of later research is on the accurate prediction of RP (9). In recent years, with the rapid development of radiomics analysis technology, increasing attention has been paid to the research of RT effect and side effect predictions based on radiomics features (10–13). Among them, one study found that there is a dose-dependent relationship between the changes in some radiomics features and RP ≥2 grade determined by extracting local lung CT images after RT (12). Another study successfully established a differential model of high- and low-risk RP by analyzing the region of interest (ROI) of the whole lung tissue before RT (13). In short, radiomics features can capture the capability of lung texture features, which help describe the potential RP risk (14, 15).

At present, cone-beam computed tomography (CBCT) has become a routine online method of image-guided radiotherapy (IGRT) for EC. If we can perform quantitative analysis on CBCT radiomics features in a certain period of RT and then combine these radiomics features with clinical features and dosimetric parameters to predict RP in EC, it will help guide clinical treatment strategies in a timely manner.

Therefore, the initial aim of this study was to investigate whether the early changes in CBCT radiomics features could be used as potential markers for predicting RP. In the present study, a comprehensive nomogram, which is a conveniently applicable predictive model integrating CBCT radiomics features, clinical features, and dosimetric parameters, was built for the individualized risk assessment and precise prediction of RP.

MATERIALS AND METHODS

Patients

The entire cohort of this retrospective study was obtained from the records of our institutional picture archiving and communication system (PACS) from January 2017 to June 2019, which was used to identify esophageal squamous cell carcinoma (ESCC) patients receiving RT treatment. The inclusion criteria were as follows: (1) Karnofsky performance score (KPS) ≥70, (2) no previous history of thoracic RT, (3) intensity-modulated radiotherapy (IMRT) and received ≥50 Gy RT, and (4) CBCT scan performed at least once a week during RT with the scanning range of the CBCT imaging including at least two thirds of the lungs. The exclusion criteria were as follows: (1) low image quality, (2) general pulmonary infection unrelated to RT, and (3) treatment break of more than 7 days during RT. A total of 96 consecutive patients with thoracic middle segment ESCC were identified and divided into two cohorts at a 7:3 proportion using computer-generated random numbers. Sixty-seven patients were allocated to the primary cohort, and 29 patients were allocated to the verification cohort. Our institutional research ethics board approved this retrospective study (SDTHEC201703014). It waived the need to obtain informed consent from the patients due to the retrospective nature of the investigation (retrospective single-institution cohort study).

Clinical Data and RT Parameters

The clinical data were all acquired from the institute's medical records. Specifically, clinicopathological parameters included age, sex, KPS, smoking status, diabetes history, chronic obstructive lung disease (COPD), pathological diagnosis, tumor location, TNM stage, radiation dose, and concurrent chemoradiotherapy lack thereof. In addition, the lung dosimetric parameters involved in this study included V5–V40 (relative volume of total lung treated with ≥5–40 Gy) and MLD. In short, the parameters mentioned above were used to establish a comprehensive nomogram after univariate analysis or least absolute shrinkage selection operator (LASSO) feature selection.

The Eclipse Treatment Planning System (Varian Medical Systems, Palo Alto, CA, Version 13.5.35) was adopted for RT planning design. IMRT adopts a fixed-field, static intensity modulation technique, and 5–7 fields of coplanar irradiation are uniformly divided according to the specific situation in each case. The required target parameters are then set, and the dose distribution is obtained by inverse calculation of the treatment planning system. The dose distribution is then graded (stratified), and each field is decomposed into a series of subfields. IMRT does not include sIMRT or volumetric intensity-modulated arc therapy (VMAT). The target area includes tumor volume (GTV), including CT imaging of visible esophageal tumors and positive lymph nodes. The clinical target volume (CTV) refers to the upper and lower expansion of the esophageal tumor by 3 cm and 6 mm around the tumor and related lymphatic drainage area. The planned target volume (PTV) is formed by CTV extending 8 mm outward. IMRT was administered by a Varian Linac Accelerator with a 6-MVX ray and 95% PTV, and radiation doses of 50–66 Gy (median dose of 60 Gy) and 1.8–2.0 Gy/fraction 5 times/week were prescribed.

Normal tissue constraints were prioritized in the following order for treatment planning purposes: maximum spinal cord dose of 45 Gy, relative volume of total lung treated with ≥5 Gy (V5) ≤60%, relative volume of total lung treated with ≥20 Gy (V20) ≤28%, MLD ≤20 Gy, relative volume of the heart treated with ≥30 Gy (V30) ≤40%, and relative volume of the heart treated with ≥40 Gy (V40) ≤30%.

Follow-up and Evaluation of RP

Follow-up items included chest CT, physical examination, and clinical symptoms. Patients were evaluated weekly during RT, followed up at 1 month after completion of the initial treatment, and then followed up every 2–3 months until at least 6 months after the end of RT. The grading of RP was confirmed by two senior oncologists and one radiologist. The National Cancer Institute Common Terminology Criteria for Adverse Events 4.03 (CTCAE 4.03) was used to evaluate the degree of RP. In the present study, grade ≥2 was used as the cutoff for diagnosing RP.

CBCT Scanning Method and Image Acquisition

Using the on-board imager (OBI) system mounted on the Varian Trilogy medical linear accelerator, the hardware portion included a diagnostic (kV) level X-ray source (KVS) and an amorphous silicon flat-panel kV detector (KVD). The CBCT image was obtained by rotating the frame at an angle. This is a slow CBCT acquisition setting. The acquisition time is 67 s, and the patient keeps breathing evenly during this process. Standard body scan conditions were voltage (125 kVp), current (80 mA), exposure time (13 ms), exposure (680 mAs), rotation angle (178°–182°), pixel matrix size (384×384), field of view (FOV, 45×18 cm), slice thickness (2.5 mm), and fan-beam type (half-fan). Among fan-beam types, the half-fan mode was used for the image acquisition of lung tissue structures larger than 24 cm. In this study, lung CBCT image acquisition was carried out in three different periods, and then the images were imported into 3D Slicer (version 4.10.2; http://www.slicer.org) in a DICOM format to extract and analyze the radiomics features. It should be noted that these three different periods were artificially divided according to the experimental design and corresponded to the early stages: the third, fourth, and fifth weeks of RT (PTV prescription dose range of EC: 18–22 Gy, 27–32 Gy, and 36–44 Gy).

Image Segmentation and Feature Extraction

Images from both lungs were segmented by a semiautomatic segmentation method (16, 17) based on a threshold-based algorithm. The specific steps are as follows: First, the background was removed to obtain the internal region of the chest. Second, the appropriate threshold was found to segment the lung and the tissues outside the lung contour to the greatest extent. Finally, the manual segmentation method (18) was used to erase the extra parts outside the large trachea and lung parenchyma to obtain both lungs as the ROI. Image segmentation was performed by an experienced radiologist and then verified by a senior radiologist. All features were extracted by using the radiomics plug-in in 3D Slicer. A total of 851 radiomics features were extracted, including 13 morphological features, 18 histogram features, 74 original texture features, and 746 high-order features (wavelet transform features).

Radiomics Feature Selection and Radiomics Signature Construction

First, the extracted radiomics features were preprocessed. Based on the Spearman rank correlation test, the features with correlations greater than 0.9 and multicollinearity were deleted, and independent features were preliminarily screened. Meanwhile, based on the Mann–Whitney *U* test, the characteristics with significant differences between the RP (≥2 grade) and non-RP (<2 grade) groups were screened out. Finally, the LASSO method (19) was used to select the final features, and the RP prediction model of rad-score was constructed based on logistic regression analysis. The LASSO method minimizes the sum of squared residuals by using the case in which the sum of the absolute values of the coefficients is less than the tuning parameter (λ). To prevent overfitting of the model, (20–22) during model building, features are selected by constantly adjusting λ. With the increasing penalty, more regression coefficients are reduced to zero, (23, 24) and then the remaining nonzero coefficient is selected. The nonzero coefficient of the selected features is the rad-score. Each patient's rad-score is calculated as a linear combination of selected features that have their own coefficient weighting.

In this study, 50 iterations of 10-fold nested cross-validation were utilized, similarly to Xu et al. (25). Random sampling was conducted in an attempt to balance the class distributions within the cross-validation partitions. The cross-validation loop provides a profile of model performance. It serves to estimate how well the LASSO applied to a given set of candidate predictors may generalize to other data sets. Model performance was assessed by computing the area under the curve (AUC) for each constructed model on a test partition. The inner cross-validation loop was applied to determine the optimal value for λ such that the resulting model was guarded against overfitting. The value of λ for each cross-validation partition was selected by determining the value that produced the most regularized model such that the AUC was within one standard error of the maximum (26). The use of 50 resampled iterations with 10-fold nested cross-validation constructs 500 models used to generate a distribution of AUC values to estimate how well model construction with LASSO generalizes to other data sets.

Construction and Validation of the Nomogram

First, the prediction efficiency of the three different periods was compared, and then the best period was selected. Second, 96 patients were divided into the RP (39 cases) and non-RP (57 cases) groups, and 16 clinical features and dosimetric parameters were collected. The best clinical features and dosimetric parameters were determined by LASSO feature selection. Finally, a comprehensive nomogram was established. The receiver operating characteristic (ROC) curve was used to evaluate the prediction capacity of the model. The calibration curve was used to determine whether the predicted and observed probabilities for RP were in concordance. The decision curve was performed to evaluate the clinical benefit ratio of the nomogram.

This research process can be divided into four parts: image acquisition, ROI segmentation, feature extraction, and radiomics model construction as shown in **Figure 1**.

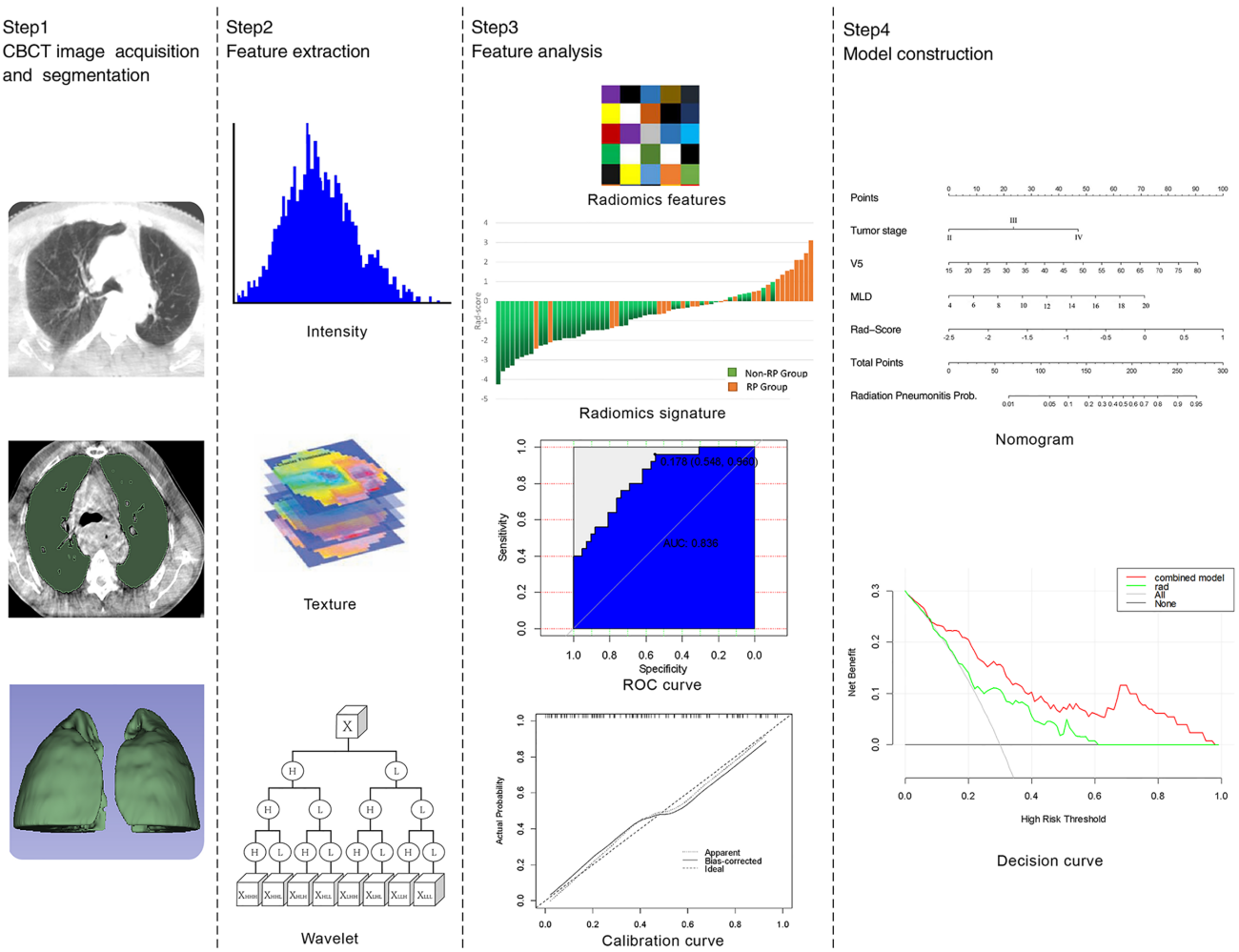

FIGURE 1 | Flow chart of radiomics.

Statistical Analysis

All statistical analyses were based on SPSS 20.0 (IBM, Armonk, NY, USA) or R software (R Foundation for Statistical Computing, Vienna, Austria, https://www.R-project.org/). The χ^2 test or Fisher exact probability test was used to classify data between the two groups. Two independent-sample *t* tests were used for counting data (continuous data). The Mann–Whitney *U* test was used to compare the differences in clinical features between the primary and validation cohorts. The model was evaluated with respect to sensitivity, specificity, ROC curve, and 95% confidence interval (CI). *P* values ≤ 0.05 were considered statistically significant.

RESULTS

Analysis of Clinical Features and Dosimetric Parameters Associated With RP

The 96 patients were divided into RP (39 cases) and non-RP (57 cases) groups, and 9 clinical features and 7 dosimetric parameters that might be related to the occurrence of RP were included. Univariate analysis showed that tumor stage was correlated with ≥2 grade RP (χ^2 = 2.650, *P* = 0.008), and other factors, including age, sex, concurrent chemoradiotherapy or lack thereof, COPD status, smoking status, and RT dose, showed no significant differences between the two groups (all *P*s > 0.05). V5, V10, V15, V20, V30, and MLD of both lungs were associated with the occurrence of grade ≥2 RP (all *P*s < 0.05). The characteristics of the enrolled population are listed in **Tables 1** and **2**.

There were no significant differences in age, sex, tumor stage, V5, and MLD between the primary group and the validation group, which indicates that the groupings were reasonable (all *P*s > 0.05) as shown in **Table 3**. Seven factors (tumor stage, V5, V10, V15, V20, V30, and MLD) remained after univariate analysis. The LASSO feature selection method was used to screen these seven factors, and three potential factors (V5, MLD, and tumor stage) remained as shown in **Figures 2A, B**. The AUC values of prediction efficiency for V5, MLD, and tumor stage were 0.698, 0.685, and 0.662, respectively. To observe the overall predictive performance of V5, MLD, and tumor stage, we established a full clinical–dosimetric feature combined model. The AUC value of the combined model was 0.764 as shown in **Figure 2C**.

Radiomics Feature Extraction/Selection at Different Periods and Radiomics Signature Building

In the first period (PTV dose: 18–22 Gy), a total of 851 radiomics features were extracted from the patients. First, correlations greater than 0.9 features were deleted, resulting in a total of 220 features remaining. Second, linear features were removed, and 96 features remained. Then, 21 features remained after using the rank-sum test. Finally, the remaining two features after LASSO selection were used to build the radiomics model as shown in **Figures 3A, B**. The two features are original first-order skewness and original GLSZM-small area emphasis. The model was built as follows: Rad-score = -0.924 e+00×Skewness - 7.047 e+00×Small Area Emphasis +

TABLE 1 | Univariate analysis of baseline clinical features of patients and RP.

Factor	*N*	RP		χ^2 value	*P* value
		<2 grade	≥2 grade		
Sex	96	57	39	2.767	0.096
Male	81	51	30		
Female	15	6	9		
Age (years)	96			1.619	0.203
<60	21	15	6		
≥60	75	42	33		
Stage				2.650	0.008
II	19	15	4		
III	48	30	18		
IV	29	12	17		
Smoking history	96			0.198	0.656
No	54	31	23		
Yes	42	26	16		
COPD	96			1.436	0.231
No	81	46	35		
Yes	15	11	4		
Diabetes	96			0.318	0.573
No	88	53	35		
Yes	8	4	4		
Hypertension	96			0.606	0.436
No	83	48	35		
Yes	13	9	4		
Concurrent Chemotherapy	96				
No	71	41	30	0.300	0.584
Yes	25	16	9		
Delivered Dose (Gy)	96			1.867	0.172
<60	45	30	15		
≥60	51	27	24		

COPD, chronic obstructive lung disease.

TABLE 2 | Single factor analysis of DVH and RP.

Lung DVH	RP		*P* value	χ^2 value
	<2 grade	≥2 grade		
V5	48.95 ± 10.56	59.39 ± 10.00	0.00	-4.91
V10	33.64 ± 7.70	40.92 ± 7.95	0.00	-4.46
V15	25.34 ± 6.52	30.77 ± 6.96	0.00	-3.85
V20	18.81 ± 5.47	22.47 ± 4.82	0.00	-3.47
V30	9.61 ± 4.40	12.16 ± 5.00	0.01	-2.58
V40	3.80 ± 2.49	4.58 ± 3.24	0.21	-1.25
MLD (cGy)	1016.47 ± 218.82	1260.87 ± 267.38	0.00	-4.72

MLD, mean lung dose; V5, V10, V15, V20, V30, V40 = relative volume of total lung treated with ≥5, 10, 15, 20, 30, and 40 Gy.

TABLE 3 | Comparison of sex, age, tumor stage, V5, and MLD between the primary and the verification cohort.

Factor	Primary cohort	Verification cohort	χ^2 value	*P* value
Age (years)	65.33 ± 9.37	68.62 ± 8.89	-1.64	0.11
Sex (*N*)	67	29	0.11	0.75
Male	56	25		
Female	11	4		
Stage			3.54	0.17
II	13	6		
III	30	18		
IV	24	5		
V5	52.35 ± 11.27	55.14 ± 12.01	-1.07	0.29
MLD (Gy)	11.06 ± 2.61	11.38 ± 2.85	-0.52	0.61

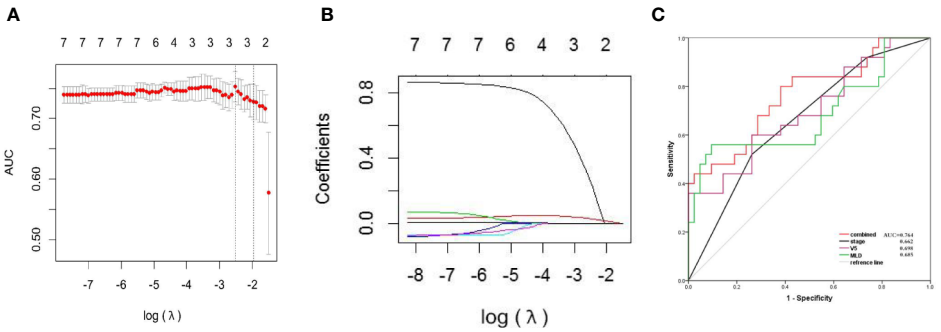

FIGURE 2 | LASSO characteristic selection of clinical features and dosimetric parameters **(A, B)**. ROC curve of V5, MLD, tumor stage, and combined model **(C)**.

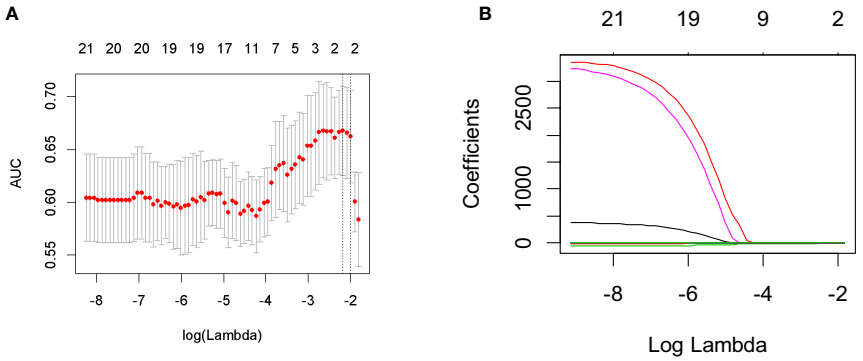

FIGURE 3 | Feature screening of radiomics in the first period. By adjusting the different penalty parameter (λ) to obtain a high-performance model, the radiomics characteristics with the highest predictive performance were obtained. Radiomics feature convergence diagram **(A)**. Each curve represents the trajectory of the coefficient of each independent variable **(B)**.

4.5329. Rad-scores for each patient in the primary cohort and validation cohort are shown in **Figures 4A, B**.

In the second period (PTV dose: 27–32 Gy), a total of 851 radiomics features were extracted from the patients. First, correlations greater than 0.9 features were deleted, resulting in a total of 222 features remaining. Second, linear features were removed, and 96 features remained. Then, 10 features remained after using the rank-sum test. Finally, the remaining five features (voxel volume, smallest axis length, small dependence low gray-level emphasis, large area low gray-level emphasis, and busyness) after LASSO selection were used to build the radiomics model. The model was built as follows: Rad-score = -1.996 e-07×voxel volume - 4.036 e-03×smallest axis length + 5.376 e+01×small dependence low gray-level emphasis + 1.718 e-07×large area low gray-level emphasis - 2.473 e-04×busyness + 1.041 e+00.

In the third period (PTV dose: 36–44 Gy), a total of 851 radiomics features were extracted from the patients. First, correlations greater than 0.9 features were deleted, resulting in a total of 220 features remaining. Second, linear features were removed, and 96 features remained. Then, 43 features remained after using the rank-sum test. Finally, the remaining six features (gray-level nonuniformity, small dependence low gray-level emphasis, cluster shape, uniformity, entropy, and size zone nonuniformity) after LASSO selection were used to build the radiomics model. The model was built as follows: Rad-score = +4.680 e-07×gray-level nonuniformity + 1.087 e+01×small dependence low gray-level emphasis - 7.913 e-04×cluster shape + 1.401 e+00×uniformity + 1.406 e+00×entropy - 2.207 e-05×size zone nonuniformity - 4.776 e+00.

Validation of Radiomics Signature at Different Periods

In the first period, the predictive efficacy of the model was as follows: In the primary cohort, the AUC was 0.700 (95% CI 0.568–0.832), the sensitivity was 61.5%, and the specificity was 75.0%. In the validation cohort, the AUC was 0.765 (95% CI 0.588–0.941), the sensitivity was 84.6%, and the specificity was 64.7% as shown in **Table 4** and **Figures 5A, B**.

In the second period, the predictive efficacy of the model was as follows: In the primary cohort, the AUC was 0.663 (95% CI 0.530–0.797), the sensitivity was 90.6%, and the specificity was

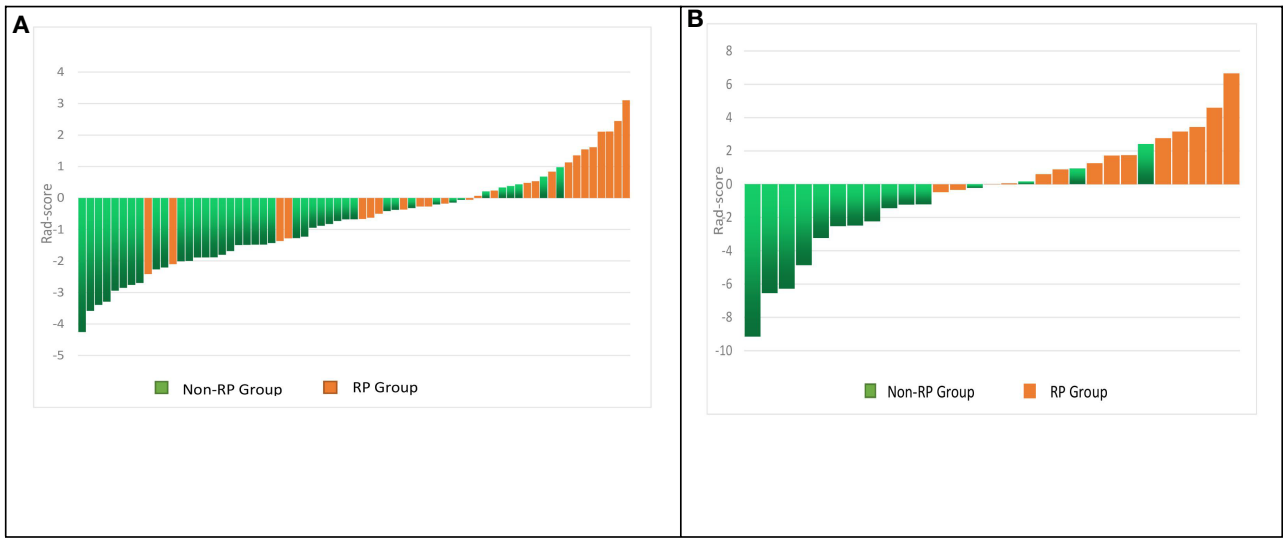

FIGURE 4 | Rad-score for each patient in the primary and validation cohorts. Green bars show scores for patients without RP, and orange bars show scores for those with RP **(A, B)**.

TABLE 4 | ROC curve parameters of the radiomics model and nomogram.

Classification	Primary cohort				Validation cohort			
	AUC	95% CI	Sensitivity	Specificity	AUC	95% CI	Sensitivity	Specificity
First period	0.700	0.568-0.832	61.5%	75.0%	0.765	0.588-0.941	84.6%	64.7%
Second period	0.663	0.530-0.797	90.6%	42.9%	0.604	0.356-0.851	85.7%	50.0%
Third period	0.699	0.573-0.826	66.7%	70.3%	0.756	0.561-0.950	66.7%	80.0%
Nomogram	0.836	0.700-0.918	96.0%	54.8%	0.905	0.799-1.000	92.9%	73.3%

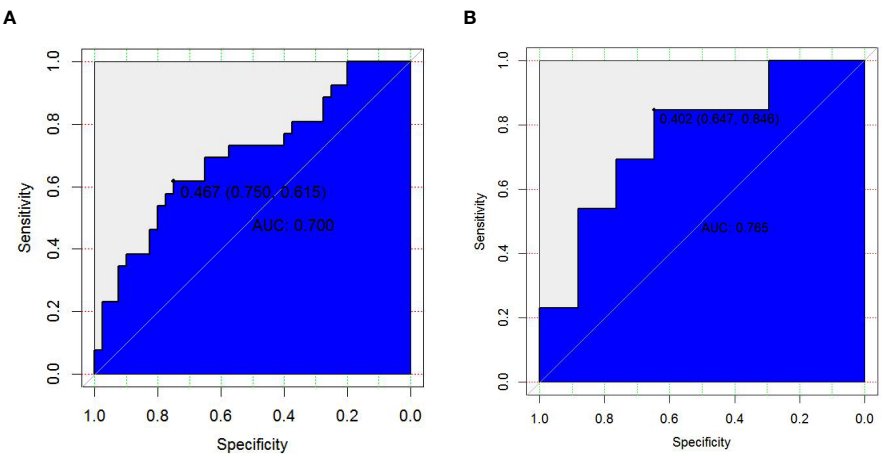

FIGURE 5 | ROC curve of radiomics features in the first period of RT **(A, B)**.

42.9%. In the validation cohort, the AUC was 0.604 (95% CI 0.356–0.851), the sensitivity was 85.7%, and the specificity 50.0%.

In the third period, the predictive efficacy of the model was as follows: In the primary cohort, the AUC was 0.699 (95% CI 0.573–0.826), the sensitivity was 66.7%, and the specificity was 70.3%. In the validation cohort, the AUC was 0.756 (95% CI 0.561–0.950), the sensitivity was 66.7%, and the specificity was 80.0% as shown in **Table 4**.

By comparing the prediction efficiency of the AUC in three periods, it is obvious that the prediction efficiency in the first period is better than those in the second and third periods in both the primary and validation cohorts. To reflect the importance of the early prediction of RP in clinical practice, the first-period rad-score and three essential features (V5, MLD, and tumor stage) were used to establish a comprehensive nomogram model.

The Incremental Value of the Radiomics Signature When Added to the Comprehensive Nomogram

The AUC values of dosimetric parameters (V5, MLD) and clinical features (tumor stage) were 0.698, 0.685, and 0.662, respectively. The AUC values of the full clinical–dosimetric feature combined model was 0.764. In addition, the AUC values of the radiomics signature at three different periods were 0.700, 0.663, and 0.699, respectively (primary cohort). It can be seen that the single clinical features, dosimetric parameters, or full clinical–dosimetric combined model are not ideal in predicting the risk of RP. To this end, we created a comprehensive nomogram that integrates dosimetric parameters and clinical features with the radiomics signature from the first period. The results show that, in the primary cohort, the AUC of our nomogram was 0.836 (95% CI: 0.700–0.918), and in the validation cohort, the AUC was 0.905 (95% CI: 0.799–1.000) as shown in **Table 4** and **Figures 6B, C**. There is no doubt that the comprehensive nomogram, incorporating radiomics features, significantly improves the ability of conventional dosimetric parameters and clinical features to predict the risk of RP. The graphical form of the nomogram is shown in **Figure 6A**. More importantly, the calibration curve is produced as shown in **Figure 6D**. The diagonal dotted line represents an ideal evaluation, and the other two lines next to it represent the performance of the nomogram. A closer fit to the diagonal dotted line indicates a better evaluation. In summary, this calibration curve shows favorable consistency between the predicted RP and the actual observation.

How to Make Clinical Decisions

The clinical decision curve analysis of the nomogram is shown in **Figure 6E**, which shows the patient's benefits when the physician makes the judgment. It shows that, if the probability of the domain value is 10%, the benefit of using the nomogram to predict the efficacy of RP is higher than that of radiomics features or other parameters alone. In short, this decision curve exhibits satisfactory positive net benefits of the nomogram at the threshold probabilities.

DISCUSSION

A single index based on lung dosimetric parameters is not the "gold standard" to judge the occurrence of PR risk; however, radiomics can extract image data to characterize the standard tissue structure, including typical lung structures. They may produce clinically relevant improvements in predicting treatment-related toxicities (13). This makes up for the deficiency of dose-volume parameter prediction to a great extent. Some previous studies, (12, 13) respectively, report the relationship between the changes in some second- or higher-order eigenvalues of lung cancer after and before RT and the occurrence of RP. Unfortunately, due to the limitations of detection techniques or other factors, it is not possible to establish predictive models for clinical practice. In this study, we used an automated computer extraction algorithm and digital quantitative analysis technology to obtain high-quality information to comprehensively evaluate various characteristics of tumor and normal tissue responses (14, 27). More importantly, we constructed a comprehensive nomogram model based on CBCT radiomics features in combination with clinical features and dosimetric parameters to accurately predict RP in EC patients treated with RT. To the best of our knowledge, this is the first study of the early prediction of RP by using IGRT to obtain CBCT imaging information in different periods of RT. Importantly, this comprehensive nomogram model is superior to single clinical features and lung dosimetric parameters in RP prediction.

We selected CBCT images from three different periods and extracted the radiomics features. The primary purpose was to find the first radiomics features that can independently predict RP; however, after selecting the radiomics features in different periods, it is found that each period has its own independent set of feature parameters related to RP. We believe that, in addition to the influence of radiation dose factors, whether these characteristics vary with changes in the RT process is still uncertain. It is gratifying that we found the best prediction of RP to be in the first period of radiomics characteristics. Two important features can be found in the early stage of low-dose RT of lung tissue: Although this may differ from our initial expectation of the experimental results, the results are fascinating. This result is similar to the findings of Cunliffe et al. (12) and Jenkins et al (28). They found that AUC values in low- and medium-dose areas of the lung were different between RP and non-RP patients even though these AUC values appeared in areas with lower visible changes. These first radiomics features may be able to be used to explain or screen out those susceptible to RP due to intrinsic genetic mutations.

In regard to the susceptible population of RP, we must devote attention to the sensitivity of lung tissue to RT. At present, the radiosensitivity of lung tissue has been reported (29, 30), and it is considered to be a potential influencing factor for RP occurrence. This difference in the sensitivity of lung tissue to radiation constitutes our different understanding of the probability of RP. In two groups of patients with different radiosensitivity of lung tissue, we cannot judge the probability of RP by standard clinical features and lung dosimetric parameters. However,

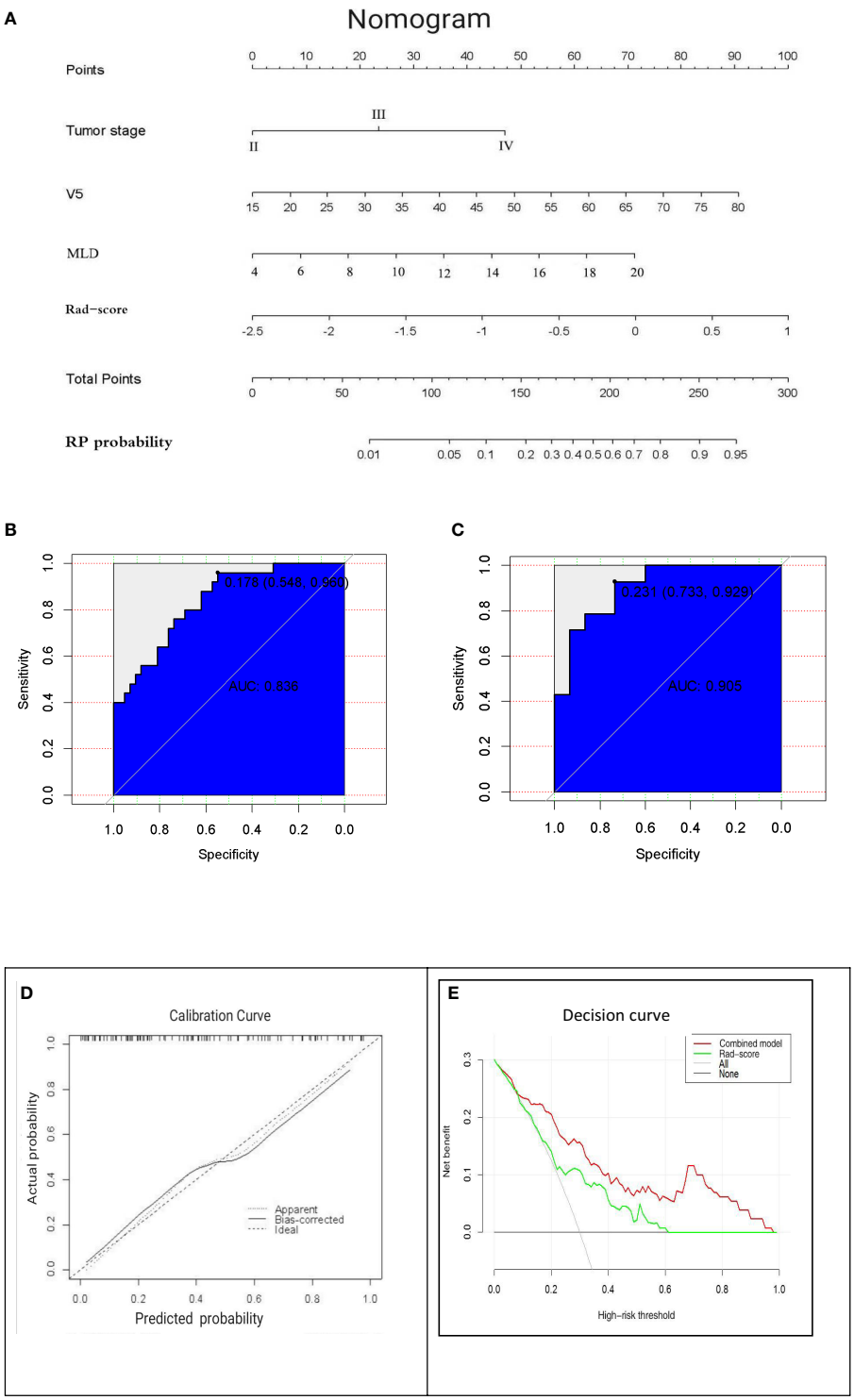

FIGURE 6 | **(A)** The comprehensive nomogram incorporates V5, MLD, tumor stage, and rad-score (the first period) to predict the risk of RP in EC patients. V5: relative volume of total lung treated with ≥5 Gy; MLD: mean lung dose. **(B, C)** ROC curves of the comprehensive nomogram in the primary and validation cohorts. **(D)** Calibration curves of the comprehensive nomogram with the addition of V5, MLD, tumor stage, and radiomics features. The diagonal dotted line represents an ideal evaluation, and the other two lines next to it represent the performance of the nomogram. A closer fit to the diagonal dotted line indicates a better evaluation. **(E)** Decision curves of the radiomics features model and the combination model (comprehensive nomogram) predicting RP. The *y*-axis represents the net benefit. The red curve represents the comprehensive nomogram, and the green line represents the radiomics features model. The horizontal black line indicates that the assumption is valid. The oblique gray line indicates that the assumption is invalid.

radiomics can analyze the data by extracting features from CT images of the lung, thus providing a powerful method for the noninvasive description of lung tissue radiosensitivity. This may be why the radiomics features are superior to the clinical features and dosimetric parameters in current studies. In this study, this advantage in AUC value, sensitivity, and specificity performance is not particularly good, but through our research analysis, radiomics features of RP risk prediction cannot be ignored.

The successful establishment of the prediction model is based on the standardization of data collection and the rationalization of data processing. First, we should consider that the feature extraction data are affected by CT parameters (31) because the CT features may be different under different image-acquisition conditions. In this study, based on the CBCT of the Varian accelerators in our center, these devices have the same tube voltage, tube current, exposure time, exposure amount, and pixel matrix size, which can help control for the differences between the scanners and acquisition parameters. Second, to develop the radiomics signature, a total of 851 candidate features were reduced to a set of only a few potential descriptors by using the LASSO logistic regression model to realize feature selection by constantly adjusting the regularization parameter λ to make the weight coefficient of the feature approach zero. The LASSO (20) logistic regression model is suitable for analyzing large sets of radiomics features with a relatively small sample size, and it is designed to avoid overfitting high-dimensional data (21, 32). At the same time, the LASSO logistic regression model allows the radiomics signature to be constructed by combining the selected features, so it allows the model to more easily identify the most closely related features in patients with RP. Finally, the nested cross-validation method (25) was used for internal validation to improve the accuracy of the model.

It should be noted that the difference in the irradiation mode (3-D conformal radiation therapy and IMRT) affects the potential dose distribution of the lung, which may affect the selection of clinical features and dosimetric parameters as risk characteristics of RP. This can be quickly confirmed by comparing Tucker et al. (33) and Shane et al. (13) where, in the former, 75% received 3-D conformal radiation therapy, and the latter 83% received IMRT. Therefore, it seems complicated to establish a general model with good discriminant performance under different technical conditions.

The clinical factors (age, tumor stage, KPS score, chronic lung disease, diabetes, chemotherapy lack thereof) and lung dosimetric parameters (V5, V10, V20, MLD) related to RP are reported in previous studies. To provide better help for the oncologist, we designed a clinical nomogram to combine the above available RP risk factors with radiomics features. Therefore, we aim to establish a combined model, maximizing clinical utility and accuracy of prediction ability, and so the initial experimental design was not expected to rely solely on the radiomics model as the final prediction model. Of course, judging from the AUC value, sensitivity, and specificity of the radiomics model in each period of RT, these characteristics alone are not perfect in predicting RP. Dose-volume histogram (DVH) metrics have been extensively observed and reported to be correlated with RP despite the current data and research reports not being sufficient to provide specific and safe standard doses (34). Chargari et al. (35) find that V5 is a risk factor for acute or chronic lung toxicity. Cho et al. (6) find that MLD is the most related factor that predicts RP rather than V5, V10, or V20. Some clinical features have emerged as important risk factors contributing to RP progression. Some studies show that smoking is related to the severity of RP (36, 37). Takeda et al. (38) and Kimura et al. (39) report that COPD is a significant risk factor for RP in patients with EC after RT. In this study, we find that smoking status, COPD, and concurrent chemoradiotherapy are not correlated with the incidence of RP, and so these factors are not included in our combined model, but this does not mean that they are not important. After LASSO logistic regression analysis, several significant variables, including V5, MLD, and tumor stage, were integrated into the nomogram to predict PR. The results were as follows: clinical-dose characteristic model (AUC values: V5 = 0.698, MLD = 0.685, tumor stage = 0.662), radiomics model (primary cohort AUC 0.700, validation cohort AUC 0.765), and nomogram (primary cohort AUC 0.836, validation cohort AUC 0.905). The nomogram demonstrates a better ability to predict RP than the other models.

How to use this information in the treatment plan or alternative program to help clinicians is our greatest concern. Fortunately, the goal of radiomics is to develop a decision-making tool that meets the needs of clinicians. This is because such a tool could combine radiomics features with other patient characteristics to improve the capability of the decision support model (15, 40). We show that radiomics features complement clinical features and lung dosimetric parameters, helping to provide better predictive ability for RP. The clinical decision curve of this nomogram shows that the effectiveness of the nomogram in predicting RP is higher than that of using radiomic characteristics or other parameters alone. In short, under the threshold probability, the decision curve exhibits a satisfactory positive net benefit of the nomogram.

Our results demonstrate the potential value of radiomics techniques in the risk prediction of RP patients. If more clinical variables are included in the nomogram, there will be more room for future development of this model, and the resulting prediction effect will be better. A recent study (41) by another of our teams found that subjective global assessment score (SGA), pulmonary fibrosis score (PFS), planning target volume/total lung volume (PTV/LV), MLD, and ratio of change regarding systemic immune inflammation index at 4 weeks (4w SII) were potential valuable markers in predicting severe acute radiation pneumonitis (SARP). Subsequently, the team developed a nomogram and corresponding risk classification system with superior prediction ability for SARP. In the next step, we will consider combining the research results of this team with radiomics to establish a new RP prediction model for better clinical application.

Although our study has many strengths, several limitations should be addressed here. First, the sample size is small, which can lead to the inability to apply nonlinear classifiers, such as neural networks (42, 43). Because a nonlinear classifier uses a more extensive data set, it is beneficial to improve the accuracy of the RP model. Second, our analysis does not account for two-way

or higher-order interactions between features. If interactions between features had been identified, the interaction terms that were most strongly associated with the outcome interactions would have been selected when we constructed the radiomics signature, and this could have improved performance. However, uncovering the interactions of multiple attributes is a challenging problem. Third, we used a validation cohort that was drawn from the same institution as the primary cohort, which prevented us from investigating the generalizability of the results to other institutions and settings. In addition, there is a lack of sufficient external data validation. Fourth, selection bias occurred when strict criteria were used, and this may affect the model training. For instance, all patients are middle thoracic EC patients, which limits the application of this method to patients with cervical, upper, and lower thoracic segment EC radiotherapy. Also, all patients experienced uniform CBCT imaging scanners and parameters, which does not guarantee the reproducibility and stability of radiomics features under other conditions. In the future, we should conduct a prospective, multicenter, large-cohort study to further develop and validate nomograms in terms of predicting RP.

As a future study, we will add different types of patients, including those with different EC locations (cervical, upper thoracic, lower thoracic segments) and different RT techniques (3DCRT, TOMO, VMAT). We will also include more laboratory indicators that may reflect RP, such as inflammatory indexes and immune inflammatory indexes. In terms of basic research, we should also improve the model of radiomics, especially the combination of radiomics and genomics. The former focuses on medical imaging of the normal tissues or tumors and performs diagnosis and prognosis based on quantitative imaging features, and the latter discovers and notes the gene sequences to study the function and structure of genomes of the diseases. Besides this, if we can combine available radiation metabolomics (44) with functional CT (45, 46) radiomics features, it may help us understand the differences in radiation sensitivity and tissue cell metabolism in order to establish a more robust prediction model. Therefore, it can be predicted that the combination of multiple omics will be the best plan for the future diagnosis and treatment of diseases and the prediction of complications.

CONCLUSIONS

CT radiomics has powerful data-processing and analysis abilities. In this context, we explored a method to predict RP based on the lung CBCT radiomics features for EC patients. More importantly, we used this method to successfully build and validate a novel nomogram with good predictive value, which can help clinicians identify high-risk RP patients early and guide personalized treatment and clinical decisions.

DATA AVAILABILITY STATEMENT

The raw data supporting the conclusions of this article will be made available by the authors, without undue reservation.

AUTHOR CONTRIBUTIONS

FD and NT are responsible for analyzing data and writing papers. JL designed experiments to guide the writing and revision of papers. WW directed the writing and revision of papers. YC, YZ, and ZL were responsible for radiomics diagnosis and radiomics data processing of patients. All authors contributed to the article and approved the submitted version.

FUNDING

Funding was obtained from the National Key Research Program of China (No. 2016YFC0904700), the National Natural Science Foundation of China (No. 81773287), and The Key Research Development Program of Shandong Province (No. 2016GSF201093).

REFERENCES

1. Bray F, Ferlay J, Soerjomataram I, Siegel RL, Torre LA, Jemal A. Global cancer statistics 2018: GLOBOCAN estimates of incidence and mortality worldwide for 36 cancers in 185 countries. *CA Cancer J Clin* (2018) 68(6):394–424. doi: 10.3322/caac.21492
2. Ajani JA, D'Amico TA, Bentrem DJ, Chao J, Corvera C, Das P, et al. Esophageal and Esophagogastric Junction Cancers, Version 2.2019,NCCN Clinical Practice Guidelines in Oncology. *J Natl Compr Canc Netw* (2019) 17 (7)855–83. doi: 10.6004/jnccn.2019.0033
3. Deng W, Lin SH. Advances in radiotherapy for esophageal cancer. *Ann Transl Med* (2018) 6(4):79. doi: 10.21037/atm.2017.11.28
4. Tonison JJ, Fischer SG, Viehrig M, Welz S, Boeke S, Zwirner K, et al. Radiation pneumonitis after intensity-modulated radiotherapy for esophageal cancer: institutional data and a systematic review. *Sci Rep* (2019) 9(1):2255. doi: 10.1038/s41598-018-38414-5
5. Zhang Y, Wang H, Huang X, Zhang Q, Ren R, Sun R, et al. Dosimetric comparison of TomoDirect, helical tomotherapy, VMAT,and ff-IMRT for upper thoracic esophageal carcinoma. *Med Dosim* (2019) 44(2):167–72. doi: 10.1016/j.meddos.2018.05.001
6. Cho WK, Oh D, Kim HK, Ahn YC, Noh JM, Shim YM, et al. Dosimetric predictors for postoperative pulmonary complications in esophageal cancer following neoadjuvant chemoradiotherapy and surgery. *Radiother Oncol* (2019) 133:87–92. doi: 10.1016/j.radonc.2019.01.005
7. Rodrigues G, Lock M, D'Souza D, Yu E, Dyk JV. Prediction of radiation pneumonitis by dose-volume histogram parameters in lung cancer-A systematic review. *Radiother Oncol* (2004) 71(2):127–38. doi: 10.1016/j.radonc.2004.02.015
8. Senan S, Cardenal F, Vansteenkiste J, Stigt J, Akyol F, Neve WD. A randomized phase II study comparing induction or consolidation chemotherapy with cisplatindocetaxel,plus radical concurrent chemoradiotherapy with cisplatin-docetaxel,in patients with unresectable locally advanced non-small-cell lung cancer. *Ann Oncol* (2011) 22:553–8. doi: 10.1093/annonc/mdq388
9. Graham M V, Purdy JA, Emami B, Harms W, Bosch W, Lockett MA. Clinical dose-volume histogram analysis for pneumonitis after 3D treament for non-small cell lung cancer(NSCLC). *Int J Radiat Oncol Biol Phys* (1999) 45(2):323–9. doi: 10.1016/s0360-3016(99)00183-2
10. Bashir U, Siddique MM, Mclean E, Goh V, Cook GJ. Imaging heterogeneity in lung cancer:techniques,applications,and challenges. *Am J Roentgenol* (2016) 207(3):534–43. doi: 10.2214/AJR.15.15864

11. Yip SS, Aerts HJ. Applications and limitations of radiomics. *Phys Med Biol* (2016) 61(13):R150–66. doi: 10.1088/0031-9155/61/13/R150
12. Cunliffe A, Armato SG, Castillo R, Pham N, Guerrero T, Al-Hallaq HA. Lung texture in serial thoracic computed tomography scans:correlation of radiomics-based features with radiation therapy dose and radiation pneumonitis development. *Int J Radiat Oncol Biol Phys* (2015) 91(5):1048–56. doi: 10.1016/j.ijrobp.2014.11.030
13. Krafft SP, Rao A, Stingo F, Briere TM, Court LE, Liao Z, et al. The utility of quantitative CT radiomics features for improved prediction of radiation pneumonitis. *Med Phys* (2018) 45(11):5317–24. doi: 10.1002/mp.13150
14. Lambin P, Rios-Velazquez E, Leijenaar R, Carvalho S, van Stiphout RG, Granton P, et al. Radiomics: Extracting more information from medical images using advanced feature analysis. *Eur J Cancer* (2012) 48(4):441–6. doi: 10.1016/j.ejca.2011.11.036
15. Gillies RJ, Kinahan PE, Hricak H. Radiomics:images are more than pictures,they are data. *Radiology* (2016) 278(2):563–77. doi: 10.1148/radiol.2015151169
16. Parmar C, Rios Velazquez E, Leijenaar R, Jermoumi M, Carvalho S, Mak RH, et al. Robust radiomics feature quantification using semiautomatic volumetric segmentation. *PloS One* (2014) 9(7):e102107. doi: 10.1371/journal.pone.0102107
17. Doumou G, Siddiques M, Tsoumpas C, Goh V, Cook GJ. The precision of textural analysis in (18)F-FDG-PET scans of oesophageal cancer. *Eur Radiol* (2015) 25(9):2805–12. doi: 10.1007/s00330-015-3681-8
18. Coroller TP, Grossmann P, Hou Y, Velazquez ER, Leijenaar RTH, Hermann G, et al. CT-based radiomic signature predicts distant metastasis in lung adenocarcinoma. *Radiother Oncol* (2015) 114(3):345–50. doi: 10.1016/j.radonc.2015.02.015
19. Tibshirani R. Regression Shrinkage and Selection via the Lasso:a retrospective. *J Roy Statist Soc Ser B* (1996) 58(1):267–88. doi: 10.1111/j.1467-9868.2011.00771.x
20. Gui J, Li H. Penalized Cox regression analysis in the high-dimensional and low-sample size settings, with applications to microarray gene expression data. *Bioinformatics* (2005) 21(13):3001–8. doi: 10.1093/bioinformatics/bti422
21. Hepp T, Schmid M, Gefeller O, Waldmann E, Mayr A. Approaches to regularized regression–a comparison between gradient boosting and the Lasso. *Methods Inf Med* (2016) 55(5):422–30. doi: 10.3414/ME16-01-0033
22. Ndhlovu ZM, Chibnik LB, Proudfoot J, Vine S, McMullen A, Cesa K, et al. High-dimensionai immunomonitonitoring models of HIV-1-specific CD8 T-cell responses accurately identify subjects achieving spontaneous viral control. *Blood* (2013) 121(5):801–11. doi: 10.1182/blood-2012-06-436295
23. Kumamaru KK, Saboo SS, Aghayev A, Cai P, Quesada CG, George E, et al. CT pulmonary angiography-based scoring system to predict the prognosis of acute pulmonary embolism. *J Cardiovasc Comput Tomogr* (2016) 10(6):473–9. doi: 10.1016/j.jcct.2016.08.007
24. Vasquez MM, Hu C, Roe DJ, Chen Z, Halonen M, Guerra S. Least absolute shrinkage and selection operator type methods for the identification of serum biomarkers of overweight and obesity: simulation and application. *BMC Med Res Methodol* (2016) 16(1):154. doi: 10.1186/s12874-016-0254-8
25. Xu C-J, van der Schaaf A, van't Veld AA, Langendijk JA, Schilstra C. Statistical validation of normal tissue complication probability models. *Int J Radiat Oncol Biol Phys* (2012) 84(1):e123–9. doi: 10.1016/j.ijrobp.2012.02.022
26. Friedman J, Hastie T, Tibshirani R. Regularization Paths for Generalized Linear Models via Coordinate Descent. *J Stat software* (2010) 33(1):1–22. doi: 10.1016/j.jspi.2009.07.020
27. Aerts HJ, Velazquez ER, Leijenaar RT, Parmar C, Grossmann P, Carvalho S, et al. Decoding tumour phenotype by noninvasive imaging using aquantitative radiomics approach. *Nat Commun* (2014) 5:4006. doi: 10.1038/ncomms5006
28. Jenkins P, Welsch A. Computed tomography appearance of early radiation injury to the lung: Correlation with clinical and dosimetric factors. *Int J Radiat Oncol Biol Phys* (2011) 81(1):97–103. doi: 10.1016/j.ijrobp.2010.05.017
29. Xu L, Jiang J, Li Y, Zhang L, Li Z, Xian J, et al. Genetic variants of SP-D confer susceptibility to radiation pneumonitis in lung cancer patients undergoing thoracic radiation therapy. *Cancer Med* (2019) 8(5):2599–611. doi: 10.1002/cam4.2088
30. Yin M, Liao Z, Liu Z, Wang L, O'Reilly M, Gomez D, et al. Genetic variants of the nonhomologous end joining gene LIG4 and severe radiation pneumonitis in nonsmall cell lung cancer patients treated with definitive radiotherapy. *Cancer* (2012) 118:528–35. doi: 10.1002/cncr.26214
31. Mackin D, Fave XB, Zhang L, Fried D, Yang J, Taylor B, et al. Measuring computed tomography scanner variability of radiomics features. *Invest Radiol* (2015) 50:(11):757–65. doi: 10.1097/RLI.0000000000000180
32. Daghir-Wojtkowiak E, Wiczling P, Bocian S, Kubik Ł, Kośliński P, Bocian S, et al. Least absolute shrinkage and selection operator and dimensionality reduction techniques in quantitative structure retention relationship modeling of retention in hydrophilic interaction liquid chromatography. *J Chromatogr A* (2015) 1403:54–62. doi: 10.1016/j.chroma.2015.05.025
33. Tucker S L, Liao Z, Dinh J, Bian SX, Mohan R, Martel MK, et al. Is there an impact of heart exposure on the incidence of radiation pneumonitis? Analysis of data from a large clinical cohort. *Acta Oncol* (2014) 53(5):590–6. doi: 10.3109/0284186X.2013.831185
34. Zhao J, Yorke ED, Li L, Kavanagh BD, Li XA, Das S, et al. Simpe factors associated with radiatio-reduced lung toxicity after stereotactic body radiation therapy of the thorax:a pooled analysis of 88 studies. *Int J Radiat Oncol Biol Phys* (2016) 95(5):1357–66. doi: 10.1016/j.ijrobp.2016.03.024
35. Chargari C, Riet F, Mazevet M, Morel E, Lepechoux C, Deutsch E. Complications of thoracic radiotherapy. *Presse Med* (2013) 42(9 pt 2):e342–51. doi: 10.1016/j.lpm.2013.06.012
36. Tucker S L, Liu HH, Liao Z, Wei X, Wang S, Jin H, et al. Analysis of radiation pneumonitis risk using a generalized lyman model. *Int J Radiat Oncol Biol Phys* (2008) 72(2):568–74. doi: 10.1016/j.ijrobp.2008.04.053
37. Jin H, Tucker SL, Liu HH, Wei X, Yom SS, Wang S, et al. Dose-volume thresholds and smoking status for the risk of treatment-related pneumonitis in inoperable non-small cell lung cancer treated with definitive radiotherapy. *Radiother Oncol* (2009) 919(3):427–32. doi: 10.1016/j.radonc.2008.09.009
38. Takeda A, Kunieda E, Ohashi T, Aoki Y, Oku Y, Enomoto T, et al. Severe COPD is correlated with mild radiation pneumonitis following stereotactic body radiotherapy. *Chest* (2012) 141(4):858–66. doi: 10.1378/chest.11-1193
39. Kimura T, Togami T, Takashima H, Nishiyama Y, Ohkawa M, Nagata Y. Radiation pneumonitis in patients with lung and mediastinal tumours:a retrospective study of risk factors focused on pulmonary emphysema. *Br J Radiol* (2012) 85(1010):135–41. doi: 10.1259/bjr/32629867
40. Permuth JB, Choi J, Balarunathan Y, Kim J, Chen DT, Chen L, et al. Combining radiomic features with a miRNA classifier may improve prediction of malignant pathology for pancreatic intraductal papillary mucinous neoplasms. *Oncotarget* (2016) 7:85785–97. doi: 10.18632/oncotarget.11768
41. Wang L, Liang S, Li C, Sun X, Pang L, Meng X, et al. A novel nomogram and risk classification system predicting radiation pneumonitis in patients with esophageal cancer receiving radiotherapy. *Int J Radiat Oncol Biol Phys* (2019) 105(5):1074–85. doi: 10.1016/j.ijrobp.2019.08.024
42. Dreiseitl S, Ohno-Machado L. Logistic regression and artificial neural network classifications models: A methodology review. *J BioMed Inform* (2002) 35(5-6):352–9. doi: 10.1016/s1532-0464(03)00034-0
43. Ayer T, Chhatwal J, Alagoz O, Jr CEK, Woods RW, Burnside ES. Informatics in radiology:Comparison of logistic regression and artificial neural network models in breast cancer risk estimation. *Radiographics* (2010) 30(1):13–22. doi: 10.1148/rg.301095057
44. Coy S L, Cheema AK, Tyburski JB, Laiakis EC, Collins SP, Fornace A Jr. Radiation metabolomics and its potential in biodosimetry. *Int J Radiat Biol* (2011) 87(8):802–23. doi: 10.3109/09553002.2011.556177
45. Hoover DA, Reid RH, Wong E, Stitt L, Sabondjian E, Rodrigues GB, et al. SPECT-based functional lung imaging for the prediction of radiation pneumonitis: A clinical and dosimetric correlation. *J Med Imaging Radiat Oncol* (2014) 58(2):214–22. doi: 10.1111/1754-9485.12145
46. Castillo R, Pham N, Ansari S, Meshkov D, Castillo S, Li M, et al. Pre-radiotherapy FDG PET predicts radiation pneumonitis in lung cancer. *Radiat Oncol* (2014) 9:74. doi: 10.1186/1748-717X-9-74

Conflict of Interest: The authors declare that the research was conducted in the absence of any commercial or financial relationships that could be construed as a potential conflict of interest.

Advantages of publishing in Frontiers

OPEN ACCESS
Articles are free to read for greatest visibility and readership

FAST PUBLICATION
Around 90 days from submission to decision

HIGH QUALITY PEER-REVIEW
Rigorous, collaborative, and constructive peer-review

TRANSPARENT PEER-REVIEW
Editors and reviewers acknowledged by name on published articles

Frontiers
Avenue du Tribunal-Fédéral 34
1005 Lausanne | Switzerland

Visit us: www.frontiersin.org
Contact us: frontiersin.org/about/contact

REPRODUCIBILITY OF RESEARCH
Support open data and methods to enhance research reproducibility

DIGITAL PUBLISHING
Articles designed for optimal readership across devices

FOLLOW US
@frontiersin

IMPACT METRICS
Advanced article metrics track visibility across digital media

EXTENSIVE PROMOTION
Marketing and promotion of impactful research

LOOP RESEARCH NETWORK
Our network increases your article's readership